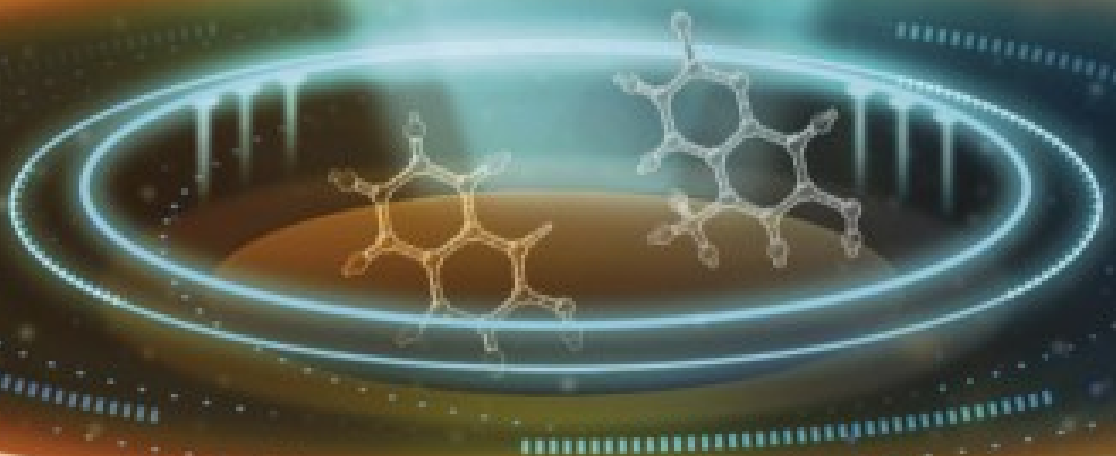
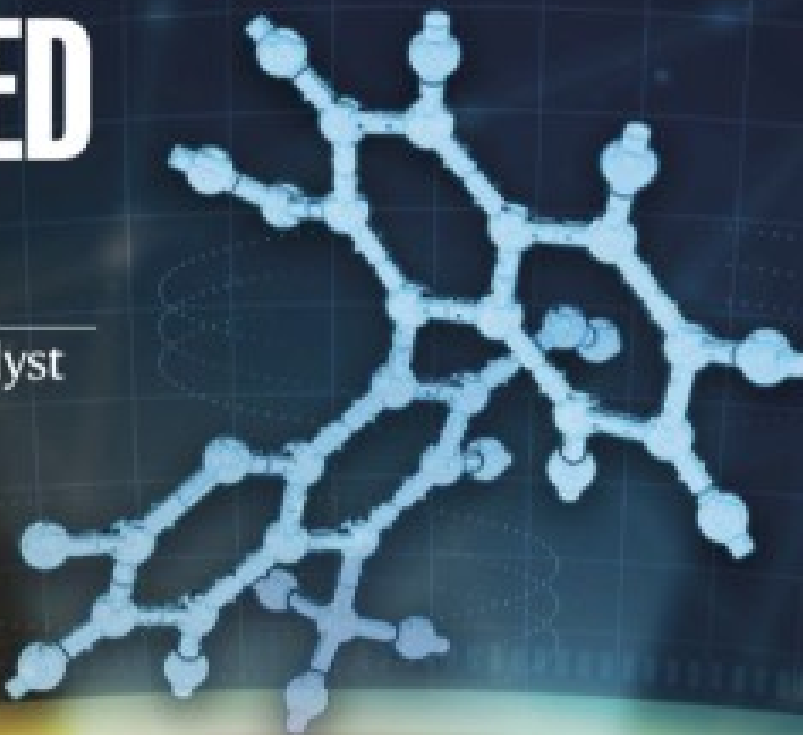


# nature

## ENHANCED ENZYME

Engineered biocatalyst offers efficient way to form biaryl compounds



**Coronavirus**  
Inside the pipeline producing new drugs to treat COVID-19

**G20 stimulus**  
Plans for economic recovery renege on emissions promise

**Chicxulub impact**  
Northern spring marked the demise of the dinosaurs

# Nature.2022.03.05

[ Sat, 05 Mar 2022]

- [This Week](#)
- [News in Focus](#)
- [Opinion](#)
- [Work](#)
- [Research](#)
- [Amendments & Corrections](#)

# This Week

- **[Wanted: better systems for turning evidence into action](#)** [ 28 February 2022]  
Editorial • The pandemic created a colossal demand for scientific evidence to inform decision-making. Now researchers are mapping out what went wrong and what needs to change.
- **[Nature is trialling transparent peer review — the early results are encouraging](#)** [ 01 March 2022]  
Editorial • Last year, nearly half of Nature authors agreed to publish anonymous referee reports. We hope that more will consider doing so this year.
- **[Climate change won't wait for future innovation — we need action now](#)** [ 28 February 2022]  
World View • Governments must focus on solutions that are already working, even when they aren't glamorous or supported by powerful lobbyists.
- **[First quadruple asteroid found hiding in plain sight](#)** [ 22 February 2022]  
Research Highlight • A dive into old data reveals that the space rock Elektra has not two moons, but three.
- **[Engineered microbes put waste to good use — and help the climate](#)** [ 23 February 2022]  
Research Highlight • Ethanol-producing bacteria endowed with extra enzymes convert unwanted gases into useful compounds.
- **[Timekeeping rats estimate how long a task will take](#)** [ 24 February 2022]  
Research Highlight • The rodents learn from their mistakes to become accurate at judging the time needed to execute a lever push.
- **[How colonialism fed the flames of Australia's catastrophic wildfires](#)** [ 24 February 2022]  
Research Highlight • The arrival of British settlers disrupted Indigenous burning practices, setting the stage for large and destructive blazes.
- **[Extreme rains are drenching China's booming cities](#)** [ 23 February 2022]  
Research Highlight • The Yangtze River Delta, the nation's economic powerhouse, is soaked by heavy rainstorms more often today than 50 years ago.

- **The surprisingly huge reptile that prowled the Jurassic skies** [ 23 February 2022]

Research Highlight • Pterosaurs living during the Jurassic period were thought to have been relatively small, but a stunning new skeleton shows otherwise.

- **Venus flytrap snaps shut at synthetic neuron's command**

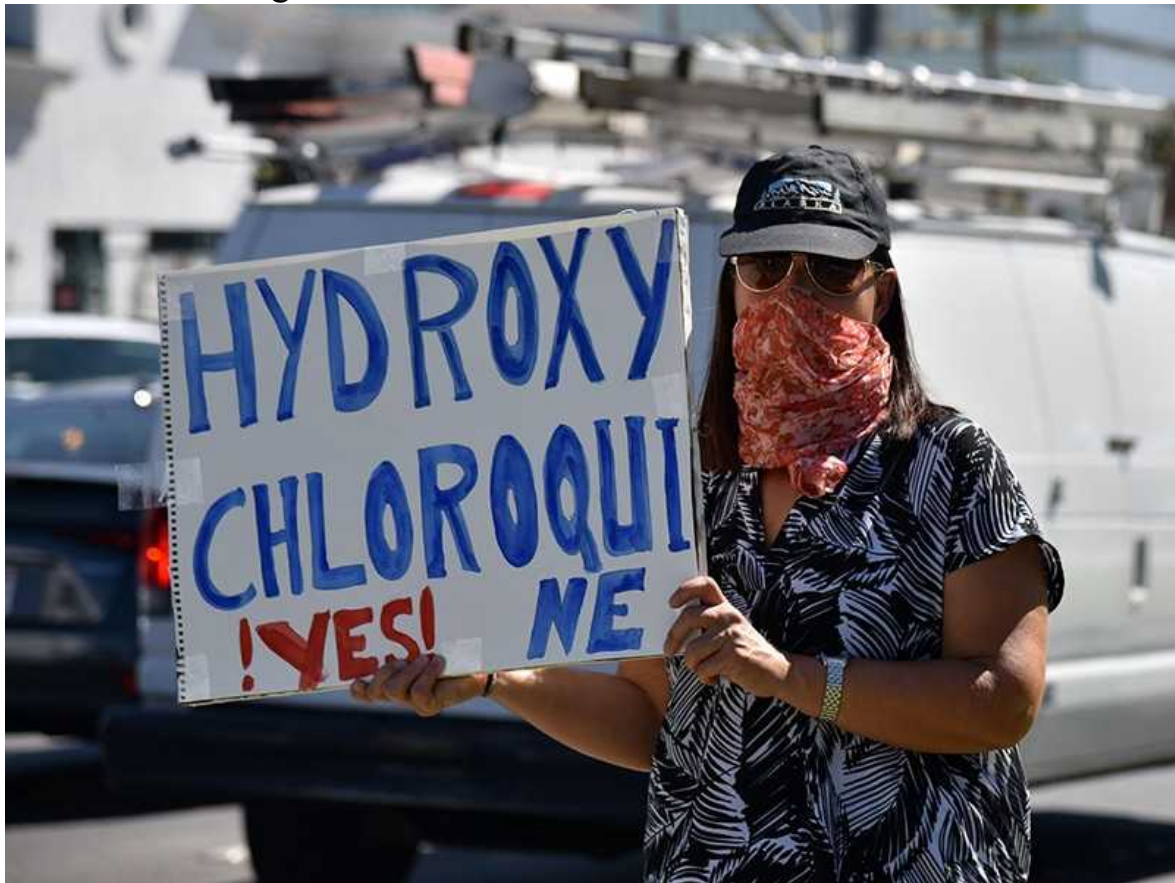
[ 23 February 2022]

Research Highlight • Organic material proves superior to silicon for carrying ‘nerve’ signals to the carnivorous plant’s maw.

- EDITORIAL
- 28 February 2022

# Wanted: better systems for turning evidence into action

The pandemic created a colossal demand for scientific evidence to inform decision-making. Now researchers are mapping out what went wrong and what needs to change.



Misinformation — such as the idea that the antimalarial drug hydroxychloroquine can prevent or treat COVID-19 — has flourished during the pandemic. Credit: Alamy

There's a saying in medicine that decisions were once made by GOBSAT: good old boys sat around a table, pontificating about their own (usually biased) opinions. The GOBSAT method is elitist and exclusionary, and it means that no one knows on what solid evidence, if any, a decision is based. Sadly, this way of making decisions has been on full display in many countries over the past two years.

During the pandemic, governments, businesses and people worldwide have needed rigorous evidence quickly to inform their decisions — on what treatments work for COVID-19, say, or how best to educate children safely. But [that pressure has exposed weaknesses](#) in the world's systems for producing, synthesizing, communicating and using evidence for decision-making. Although research has been essential during the pandemic, too much of it has been of poor quality or hasn't addressed pressing questions. Researchers who produce evidence syntheses — authoritative reports that summarize a body of research — have been unable to keep up with the pace of new studies. Misinformation has flourished, and politicians and others have often been unable to access the evidence they need.

But researchers are on the case. In the past couple of months, three reports have been published that show what can be done to improve evidence-informed decisions, not only during a pandemic, but in many spheres of public policy, including combating climate change, reducing inequality and improving global health. The reports are ambitious — idealistic, even. But together, they visualize an efficient machinery that can supply fast but rigorous evidence, on time, to those who need it. And they outline a road map to get there, putting equity at the centre and highlighting the very different needs of countries around the world.

## The evidence ecosystem

In [one report](#) from the Global Commission on Evidence to Address Societal Challenges, a group of 25 people — ranging from politicians to statisticians to citizen leaders — across 6 continents proposes improvements for almost every aspect of the evidence ecosystem. One priority recommendation is for multilateral organizations to provide commitment and greater support for the use of research evidence in making decisions — such as the way the

Intergovernmental Panel on Climate Change assesses climate science for policymakers.

Under this global umbrella, the commission recommends that every nation have its own processes to support the use of good evidence. Of course, many nations already do, in the form of science advisers and data-analytics teams attached to government departments. But a common missing ingredient, as the commission rightly points out, is a central agency to help to coordinate these efforts and get the right evidence to those who need it at the right time.

Many of these recommendations are echoed in a call to action issued in December by the health-policy groups that make up the World Health Organization Evidence-informed Policy Network (EVIPNet) and in a report, published in February, by Cochrane, a world-leading supplier of evidence syntheses in health. Cochrane is keen, in particular, to develop evidence-synthesis units in low- and middle-income countries. Only 3–4% of Cochrane review authors were from such countries between 2018 and 2021, an imbalance that needs to be corrected.

## A pragmatic approach

Many organizations in low- and middle-income countries are already bridging the chasm between researchers who generate evidence and decision makers who could use it. The Center for Rapid Evidence Synthesis (ACRES) at Makerere University in Uganda is one of them. It receives requests from policymakers and sends back a rapid synthesis of relevant evidence within days or weeks. It has influenced Ugandan policies ranging from food fortification to tuberculosis diagnosis. Health-policy researcher Rhona Mijumbi-Deve, who founded the centre and now advises other nations on setting up similar outfits, told *Nature* that what sets it apart is the way it provides evidence that policymakers need, tailored for Uganda, at the pace they need it. And it is rightly pragmatic, willing to produce a good review on time, rather than the perfect review too late.

Across the Atlantic, a Latin American evidence hub has been taking shape, co-directed by Laura Boeira, who leads the Instituto Veredas, a non-profit organization focused on evidence-informed policymaking in São Paulo,

Brazil. Boeira and her colleagues are seeing a growing appetite for evidence from public officials, despite — or perhaps because of — Brazilian President Jair Bolsonaro’s open disdain for evidence, such as that on COVID-19 vaccines.

Each country needs a mechanism for supplying evidence that is appropriate to its systems of governance and wider needs, but there are some common, essential ingredients too — such as the need for trusted, long-term relationships between researchers and decision makers. Politicians, says Boeira, typically want to call their favourite expert and ask them what to do. By building trust, she wants to make sure that their first call is instead aimed at finding the bestavailable evidence.

The risk for the global evidence commission is that its recommendations are so ambitious that they seem unfeasible or overwhelming. The commissioners are already receiving questions from countries about where to start. A good first step is for a nation or region to take stock of what has worked during the pandemic — the bright spots, such as the centres in Uganda and Brazil — and then figure out what hasn’t worked and what could be done to fill the gaps.

During the pandemic, too many decisions have been made by GOBSATs or by other questionable means. Lessons learnt from COVID-19 provide an opportunity for change, for injecting more-rigorous research and evidence into the way that decisions are reached. We can all start by asking the GOBSATs for the evidence on which their statements are based.

*Nature* **603**, 7–8 (2022)

doi: <https://doi.org/10.1038/d41586-022-00559-9>

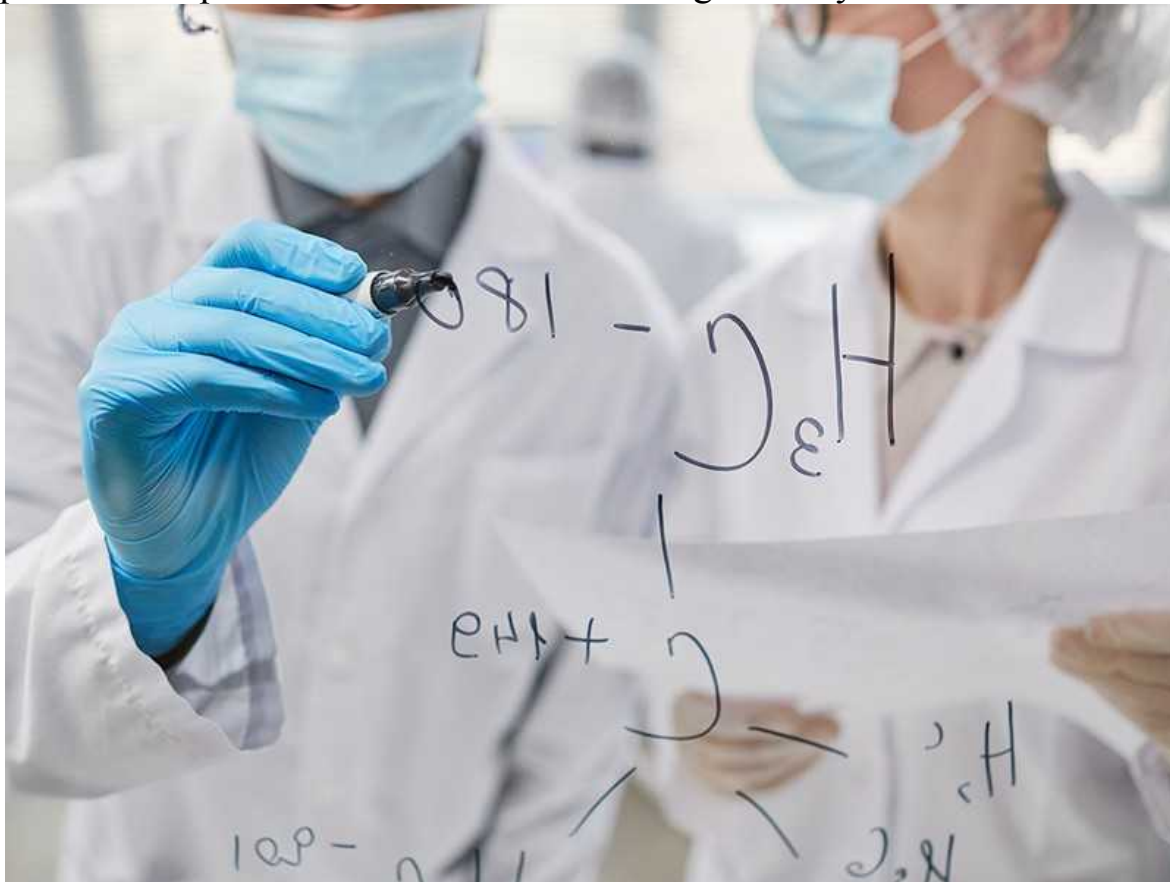
---

This article was downloaded by **calibre** from <https://www.nature.com/articles/d41586-022-00559-9>

- EDITORIAL
- 01 March 2022

# ***Nature* is trialling transparent peer review — the early results are encouraging**

Last year, nearly half of *Nature* authors agreed to publish anonymous referee reports. We hope that more will consider doing so this year.



According to one study, reviewers in total do tens of millions of hours of peer review each year.Credit: Getty

Research papers are the product of lengthy discussions between authors and reviewers — guided by editors. These peer-review conversations can last for months at a time and are essential to progress in research. There is widespread agreement that the robustness and clarity of papers are enhanced in this process.

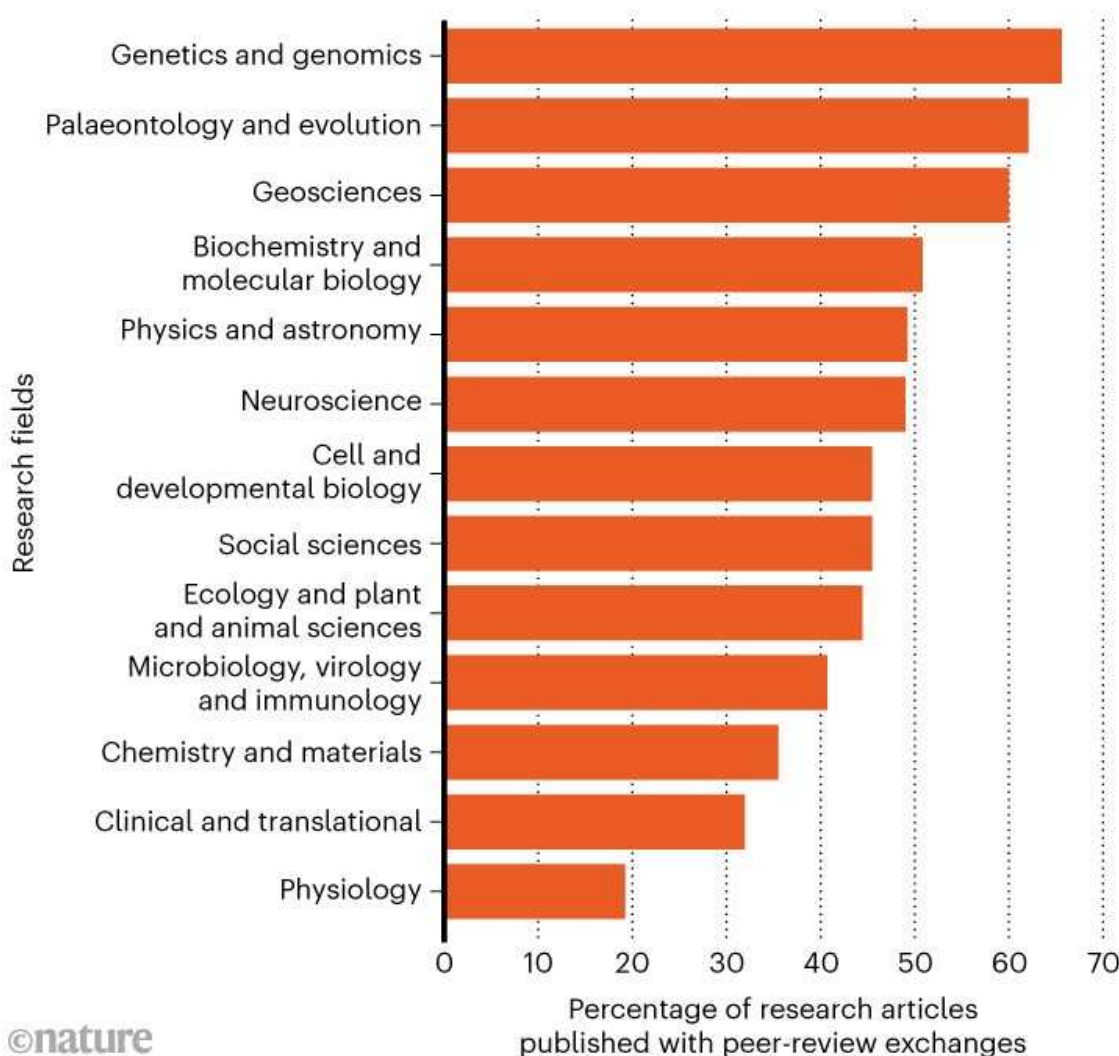
Peer-review exchanges are mostly kept confidential, meaning that the wider research community and the world have few opportunities to learn what is said in them. Such opacity can fuel perceptions of secrecy in publishing — and leaves reviewers and their key role in science publication underappreciated. It also robs early-career researchers of the opportunity to engage with examples of the inner workings of a process that is key to their career development.

In an attempt to change things, *Nature Communications* has since 2016 been encouraging authors to publish peer-review exchanges. In February 2020, and to the widespread approval of Twitter's science community, [Nature announced that it would offer a similar opportunity](#). Authors of new manuscript submissions can now have anonymous referee reports — and their own responses to these reports — published at the same time as their manuscript. Those who agree to act as reviewers know that both anonymous reports and anonymized exchanges with authors might be published. Referees can also choose to be named, should they desire.

A full year's data are now in, and the results are encouraging. During 2021, nearly half (46%) of authors chose to publish their discussions with reviewers, although there is variation between disciplines (see 'Peer review opens up'). Early data suggest more will do so in 2022. This is a promising trend. And we strongly encourage more researchers to take this opportunity to publish their exchanges. Last year, some 69% of *Nature Communication's* published research articles were accompanied by anonymous peer-review reports together with author–reviewer exchanges, including manuscripts in life sciences (73% of published papers), chemistry (59%), physics (64%) and Earth sciences (77%).

## PEER REVIEW OPENS UP

In 2021 and 2022, transparent peer-review comments were published alongside many *Nature* research articles. In total, 447 out of 974 articles in 2021 were published with anonymous referee reports. By 1 February 2022, it was 30 out of 61 articles.



Source: Springer Nature

The benefits to research are huge. Opening up peer review promotes more transparency, and is valuable to researchers who study peer-review systems. It is also valuable to early-career researchers more broadly. Each set of reports is a real-life example, a guide to how to provide authors with constructive feedback in a collegial manner.

Publishing peer-review exchanges, in addition, recognizes the effort that goes into the endeavour. Peer review is integral to being a researcher. Making reviewers' work public illustrates the lengths that researchers will go in the service of scholarship. According to one study, reviewers in total do tens of millions of hours of peer review each year ([B. Aczel et al. Res. Integr. Peer Rev. 6, 14; 2021](#)). Yet this contribution is rarely recognized in research evaluation systems. As we have reported, [there is growing interest in reforming these systems](#) to better represent how science is done. If more researchers agree to open up their peer-review exchanges, we can all play a part in making that happen.

*Nature* **603**, 8 (2022)

*doi:* <https://doi.org/10.1038/d41586-022-00493-w>

---

This article was downloaded by **calibre** from <https://www.nature.com/articles/d41586-022-00493-w>

| [Section menu](#) | [Main menu](#) |

- WORLD VIEW
- 28 February 2022

# Climate change won't wait for future innovation — we need action now



Governments must focus on solutions that are already working, even when they aren't glamorous or supported by powerful lobbyists.

- [Marie Claire Brisbois](#) 0

Reading national climate plans feels like perusing corporate advertising brochures. There is an ever-increasing focus on the promise of innovation: hydrogen fuel, new nuclear technologies and carbon capture and storage, the plans claim, will close the gap between what the world needs and what renewables can provide.

Yes, alternative energy sources and carbon removal will be crucial for decarbonization. But let's not pretend they'll be here fast enough to cap temperature rise at 1.5 °C above pre-industrial levels. Politicians and researchers also need to do more with techniques that are already established — highly effective, publicly supported ways to cut energy use.

One estimate suggests that steps such as increasing use of home insulation, public transport, appliance repair and animal-free protein could reduce emissions by 40–80% in the building, transport, industry and food sectors ([F. Creutzig et al. \*Nature Clim. Change\* 12, 36–46; 2022](#)). Measures to cut energy use can make citizens healthier and happier, and can ease the burden of the rising cost of energy. But they are neglected.

US President Joe Biden's Build Back Better plan heavily finances technologies to produce clean hydrogen and supergrids (which carry large amounts of electricity), with expectations of high economic returns. The UK Ten Point Plan for a Green Industrial Revolution also targets innovations, from carbon capture to electric vehicles. These plans acknowledge the crucial but boring role of reducing energy use, but do little to bring it about. On 28 February, the Intergovernmental Panel on Climate Change released a report on the impacts of climate change and how to mitigate them; I predict that responses will emphasize flashy innovation over familiar established strategies.

This dynamic was evident on Transport Day at the COP26 climate-change conference in Glasgow, UK, last year. The official agenda featured technologies such as electric vehicles and new jet fuels. Cycling, walking and public transport were mentioned only when a bottom-up effort by 350 organizations squeezed one line into the official declaration. By then, it was too late to steer the conversation.

Why do governments neglect proven practices to bet big on technological fixes unlikely to arrive on time? I study the intersection of power, politics and environmental decision-making, and that's the question I've focused on for more than a decade.

Of the hundreds of strategy plans I've analysed over the five years I've been studying energy, almost every single one ensures three things. First,

that global citizens will still buy a lot of energy. Second, that control of energy resources will remain concentrated among a few industry players. Third, that energy-intensive companies and their shareholders will still make huge profits.

It's no secret that energy industries are powerful political actors, or that governments overwhelmingly measure national progress by economic growth. Less well-known is that this encourages politicians to produce climate strategies that prioritize high economic returns over absolute carbon reductions. There are examples from around the world of industry lobbying to weaken carbon targets, to block the phasing out of coal and even to label fossil-fuel-guzzling natural-gas plants as green investments.

Unglamorous solutions have few politically powerful advocates. Their economic benefits come more from reducing costs than from increasing growth, and tend to be spread across sectors and accrue to less-powerful interests. For example, proposed programmes to retrofit homes in the United Kingdom and Spain to be more energy efficient are projected to create half a million jobs each, most of which would be in small or medium-sized enterprises. National savings as air pollution falls are realized in health and environment budgets, not growth projections.

Governments do sometimes prioritize broad benefits. Italy is offering tax deductions of 110% to finance home energy retrofits. Cities including Paris, Milan, Detroit and Montreal are scraping together money to fund cycle lanes and pedestrian spaces. But these small interventions are not enough. Few governments are making serious financial investments.

Here's where the research community can step up. One way to counter the fixation on profitable rather than proven climate solutions is for analysts and researchers assessing policy options to build in metrics of environmental sustainability, social connection, health and other indicators of well-being. There are a wealth of relevant measures, such as the Organisation for Economic Co-operation and Development's Better Life Index. These should be implemented and advanced widely.

An emerging research base suggests that governments can maintain logistical and social services even when economic output is static. We need

more social-science research on how to encourage political support for policies that don't promote growth. Researchers must supply case studies, models and ways to craft policy around energy use that consider people as citizens, not simply consumers.

Unglamorous solutions are effective; critics can't say they are a bad idea. Instead, they argue that green innovation is the only way to mobilize the private capital and ingenuity needed to solve the climate crisis. But the evidence is clear: the planet needs us to do more to implement what's already working.

*Nature* **603**, 9 (2022)

*doi:* <https://doi.org/10.1038/d41586-022-00560-2>

---

This article was downloaded by **calibre** from <https://www.nature.com/articles/d41586-022-00560-2>

| [Section menu](#) | [Main menu](#) |

- RESEARCH HIGHLIGHT
- 22 February 2022

# First quadruple asteroid found hiding in plain sight

A dive into old data reveals that the space rock Elektra has not two moons, but three.

 Between Mars and Jupiter lie some of the relics of the early Solar System: the main asteroid belt.

A newly discovered moon (orbit depicted in blue; artist's illustration) raises the asteroid Elektra's moon count to a chart-topping three. Credit: ESO/Berdeu *et al.*, Yang *et al.*

Astronomers have discovered an unprecedented three moons in orbit around an asteroid<sup>1</sup>.

## Access options

Subscribe to Nature+

Get immediate online access to the entire Nature family of 50+ journals

\$29.99

monthly

[Subscribe](#)

Subscribe to Journal

Get full journal access for 1 year

\$199.00

only \$3.90 per issue

[Subscribe](#)

All prices are NET prices.

VAT will be added later in the checkout.

Tax calculation will be finalised during checkout.

Buy article

Get time limited or full article access on ReadCube.

\$32.00

[Buy](#)

All prices are NET prices.

### **Additional access options:**

- [Log in](#)
- [Learn about institutional subscriptions](#)

*Nature* **603**, 10 (2022)

*doi:* <https://doi.org/10.1038/d41586-022-00487-8>

## **References**

1. Berdeu, A., Langlois, M. & Vachier, F. *Astron. Astrophys.* **658**, L4 (2022).

---

This article was downloaded by **calibre** from <https://www.nature.com/articles/d41586-022-00487-8>

- RESEARCH HIGHLIGHT
- 23 February 2022

# Engineered microbes put waste to good use — and help the climate

Ethanol-producing bacteria endowed with extra enzymes convert unwanted gases into useful compounds.

 LanzaTech Freedom Pines Facility, an industrial site with lots of pipes and containers.

At this pilot reactor, engineered bacteria convert industrial waste gases to industrially useful products. Credit: LanzaTech

Modified bacteria can turn waste gases, including carbon dioxide, into the valuable chemicals acetone and isopropanol — on a large scale<sup>1</sup>.

## Access options

Subscribe to Nature+

Get immediate online access to the entire Nature family of 50+ journals

\$29.99

monthly

[Subscribe](#)

Subscribe to Journal

Get full journal access for 1 year

\$199.00

only \$3.90 per issue

### Subscribe

All prices are NET prices.

VAT will be added later in the checkout.

Tax calculation will be finalised during checkout.

Buy article

Get time limited or full article access on ReadCube.

\$32.00

### Buy

All prices are NET prices.

### **Additional access options:**

- [Log in](#)
- [Learn about institutional subscriptions](#)

*Nature* **603**, 10 (2022)

*doi:* <https://doi.org/10.1038/d41586-022-00488-7>

## References

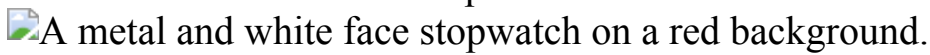
1. Liew, F. E. *et al.* *Nature Biotechnol.* <https://doi.org/10.1038/s41587-021-01195-w> (2022).
2. Marcellin, E. *et al.* *Green Chem.* **18**, 3020–3028 (2016).

| [Section menu](#) | [Main menu](#) |

- RESEARCH HIGHLIGHT
- 24 February 2022

# Timekeeping rats estimate how long a task will take

The rodents learn from their mistakes to become accurate at judging the time needed to execute a lever push.



Off by only a whisker: rats keep track of elapsed time and the errors they make in assessing it. Credit: Martin Poole/Getty

Rats can estimate how long they need to complete a task, helping them to stick to deadlines<sup>1</sup>.

## Access options

Subscribe to Nature+

Get immediate online access to the entire Nature family of 50+ journals

\$29.99

monthly

[Subscribe](#)

Subscribe to Journal

Get full journal access for 1 year

\$199.00

only \$3.90 per issue

## Subscribe

All prices are NET prices.

VAT will be added later in the checkout.

Tax calculation will be finalised during checkout.

## Buy article

Get time limited or full article access on ReadCube.

\$32.00

## Buy

All prices are NET prices.

## Additional access options:

- [Log in](#)
- [Learn about institutional subscriptions](#)

*Nature* **603**, 10 (2022)

*doi:* <https://doi.org/10.1038/d41586-022-00490-z>

## References

1. Kononowicz, T. W., van Wassenhove, V. & Doyère, V. *Proc. Natl Acad. Sci. USA* **119**, e2108850119 (2022).

---

This article was downloaded by **calibre** from <https://www.nature.com/articles/d41586-022-00490-z>

- RESEARCH HIGHLIGHT
- 24 February 2022

# How colonialism fed the flames of Australia's catastrophic wildfires

The arrival of British settlers disrupted Indigenous burning practices, setting the stage for large and destructive blazes.



Flames char bush land in southeastern Australia during the deadly barrage of fires that hit the region in late 2019 and early 2020. Credit: Mark Graham/Bloomberg via Getty

The unprecedented fires that devastated parts of Australia in 2020 can be attributed in part to colonialism<sup>1</sup>.

## Access options

Subscribe to Nature+

Get immediate online access to the entire Nature family of 50+ journals

\$29.99

monthly

[Subscribe](#)

Subscribe to Journal

Get full journal access for 1 year

\$199.00

only \$3.90 per issue

[Subscribe](#)

All prices are NET prices.

VAT will be added later in the checkout.

Tax calculation will be finalised during checkout.

Buy article

Get time limited or full article access on ReadCube.

\$32.00

[Buy](#)

All prices are NET prices.

### **Additional access options:**

- [Log in](#)
- [Learn about institutional subscriptions](#)

*Nature* **603**, 10 (2022)

*doi:* <https://doi.org/10.1038/d41586-022-00509-5>

## **References**

1. Mariani, M. *et al.* *Front. Ecol. Environ.* <https://doi.org/10.1002/fee.2395> (2022).

---

This article was downloaded by **calibre** from <https://www.nature.com/articles/d41586-022-00509-5>

- RESEARCH HIGHLIGHT
- 23 February 2022

# Extreme rains are drenching China's booming cities

The Yangtze River Delta, the nation's economic powerhouse, is soaked by heavy rainstorms more often today than 50 years ago.



A worker inspects waterlogged steps on July 6, 2020 in Shanghai, China during a yellow alert for rainstorms.

A storm deluges Shanghai, the largest city in China's Yangtze River Delta. Urban sprawl in the region might be adding to rainfall intensity. Credit: Yin Liqin/China News Service via Getty

Intense rains are becoming more common in the heavily developed region that is China's economic powerhouse, perhaps in part because of rampant urbanization<sup>1</sup>.

## Access options

Subscribe to Nature+

Get immediate online access to the entire Nature family of 50+ journals

\$29.99

monthly

[Subscribe](#)

Subscribe to Journal

Get full journal access for 1 year

\$199.00

only \$3.90 per issue

[Subscribe](#)

All prices are NET prices.

VAT will be added later in the checkout.

Tax calculation will be finalised during checkout.

Buy article

Get time limited or full article access on ReadCube.

\$32.00

[Buy](#)

All prices are NET prices.

### **Additional access options:**

- [Log in](#)
- [Learn about institutional subscriptions](#)

*Nature* **603**, 11 (2022)

*doi:* <https://doi.org/10.1038/d41586-022-00489-6>

## **References**

1. Yu, X. *et al.* *Geophys. Res. Lett.* <https://doi.org/10.1029/2021GL097046> (2022).

| [Section menu](#) | [Main menu](#) |

- RESEARCH HIGHLIGHT
- 23 February 2022

# The surprisingly huge reptile that prowled the Jurassic skies

Pterosaurs living during the Jurassic period were thought to have been relatively small, but a stunning new skeleton shows otherwise.



The Jurassic pterosaur *Dearc sgiathanach* had a wingspan comparable to that of the largest living birds. Credit: Natalia Jagielska

A newly discovered pterosaur is the world's largest-known reptile to have roamed the skies some 170 million years ago<sup>1</sup>.

## Access options

Subscribe to Nature+

Get immediate online access to the entire Nature family of 50+ journals

\$29.99

monthly

[Subscribe](#)

Subscribe to Journal

Get full journal access for 1 year

\$199.00

only \$3.90 per issue

## Subscribe

All prices are NET prices.

VAT will be added later in the checkout.

Tax calculation will be finalised during checkout.

## Buy article

Get time limited or full article access on ReadCube.

\$32.00

## Buy

All prices are NET prices.

## Additional access options:

- [Log in](#)
- [Learn about institutional subscriptions](#)

*Nature* **603**, 11 (2022)

doi: <https://doi.org/10.1038/d41586-022-00506-8>

## References

1. Jagielska, N. *et al.* *Curr. Biol.* <https://doi.org/10.1016/j.cub.2022.01.073> (2022).

---

This article was downloaded by **calibre** from <https://www.nature.com/articles/d41586-022-00506-8>

- RESEARCH HIGHLIGHT
- 23 February 2022

# Venus flytrap snaps shut at synthetic neuron's command

Organic material proves superior to silicon for carrying ‘nerve’ signals to the carnivorous plant’s maw.

 Modulation of Venus flytrap using the artificial neuron, where the flytrap is open and attached to the wires providing current.

An electrical signal can prompt an artificial neuron to close a Venus flytrap.  
Credit: P. C. Harikesh *et al.*/*Nature Commun.*

Carbon-based artificial nerve cells can trigger the chomp of a Venus flytrap and might improve intelligent soft robots<sup>1</sup>.

## Access options

Subscribe to Nature+

Get immediate online access to the entire Nature family of 50+ journals

\$29.99

monthly

[Subscribe](#)

Subscribe to Journal

Get full journal access for 1 year

\$199.00

only \$3.90 per issue

[Subscribe](#)

All prices are NET prices.

VAT will be added later in the checkout.

Tax calculation will be finalised during checkout.

Buy article

Get time limited or full article access on ReadCube.

\$32.00

[Buy](#)

All prices are NET prices.

### **Additional access options:**

- [Log in](#)
- [Learn about institutional subscriptions](#)

*Nature* **603**, 11 (2022)

*doi:* [\*https://doi.org/10.1038/d41586-022-00491-y\*](https://doi.org/10.1038/d41586-022-00491-y)

## **References**

1. Harikesh, P. C. *et al.* *Nature Commun.* **13**, 901 (2022).

---

This article was downloaded by **calibre** from <https://www.nature.com/articles/d41586-022-00491-y>.

# News in Focus

- **[COVID reinfections, sneezing hamsters and huge methane emissions](#)** [ 02 March 2022]  
News Round-Up • The latest science news, in brief.
- **[Wuhan market was epicentre of pandemic's start, studies suggest](#)** [ 27 February 2022]  
News • Report authors say that the coronavirus SARS-CoV-2 jumped to people from animals sold at the market on two occasions in late 2019 — but some scientists want more definitive evidence.
- **[Fossil fish reveal timing of asteroid that killed the dinosaurs](#)** [ 23 February 2022]  
News • The discovery is likely to reignite controversy over the US site where the fossils were found.
- **[A year on Mars: How NASA's Perseverance hit a geological jackpot](#)** [ 17 February 2022]  
News • The rover collected exciting rock samples on the first leg of its epic journey. Next, it will turn towards an ancient river delta to look for past life.
- **[Asteroids, Hubble rival and Moon base: China sets out space agenda](#)** [ 18 February 2022]  
News • In the next five years, the nation hopes to launch a robotic craft to an asteroid and two lunar missions.
- **[Two scientists will replace disgraced US science adviser Eric Lander](#)** [ 17 February 2022]  
News • Celebrated sociologist Alondra Nelson and genome leader Francis Collins will temporarily split Lander's duties.
- **[Omicron's lasting mysteries: four questions scientists are racing to answer](#)** [ 24 February 2022]  
News Feature • The fast-moving variant poses new puzzles in viral transmission, severity and evolution.
- **[Hundreds of COVID trials could provide a deluge of new drugs](#)** [ 01 March 2022]

News Feature • Two years into the pandemic, the COVID-19 drugs pipeline is primed to pump out novel treatments — and fresh uses for familiar therapies.

---

| [Next section](#) | [Main menu](#) | [Previous section](#) |

- NEWS ROUND-UP
- 02 March 2022

# COVID reinfections, sneezing hamsters and huge methane emissions

The latest science news, in brief.



Cases of coronavirus reinfection are increasing around the world.Credit: Carlo Allegri/Reuters

## COVID reinfections surge during Omicron wave

Since the Omicron variant of SARS-CoV-2 was first detected, the number of people reinfected with the coronavirus has been rising sharply — a trend that was not observed with previous variants. Researchers say that [Omicron is probably driving the surge](#) because it can evade the body's immune defences.

In England, more than 650,000 people have probably been infected twice; most of them were reinfected in the past two months, according to data collected by the UK Health Security Agency. The agency considers an infection a ‘possible reinfection’ if it took place at least three months after a previous one. Before mid-November, reinfections accounted for about 1% of reported cases of COVID-19, but the rate has now increased to around 10%.

“The ability of Omicron to infect people with either vaccine- or infection-derived immunity is a key part of what made the recent surge so large,” says Marm Kilpatrick, an infectious-disease researcher at the University of California, Santa Cruz.

Measuring reinfection rates helps to assess “how infections might surge”, says Catherine Bennett, an epidemiologist at Deakin University in Melbourne, Australia.

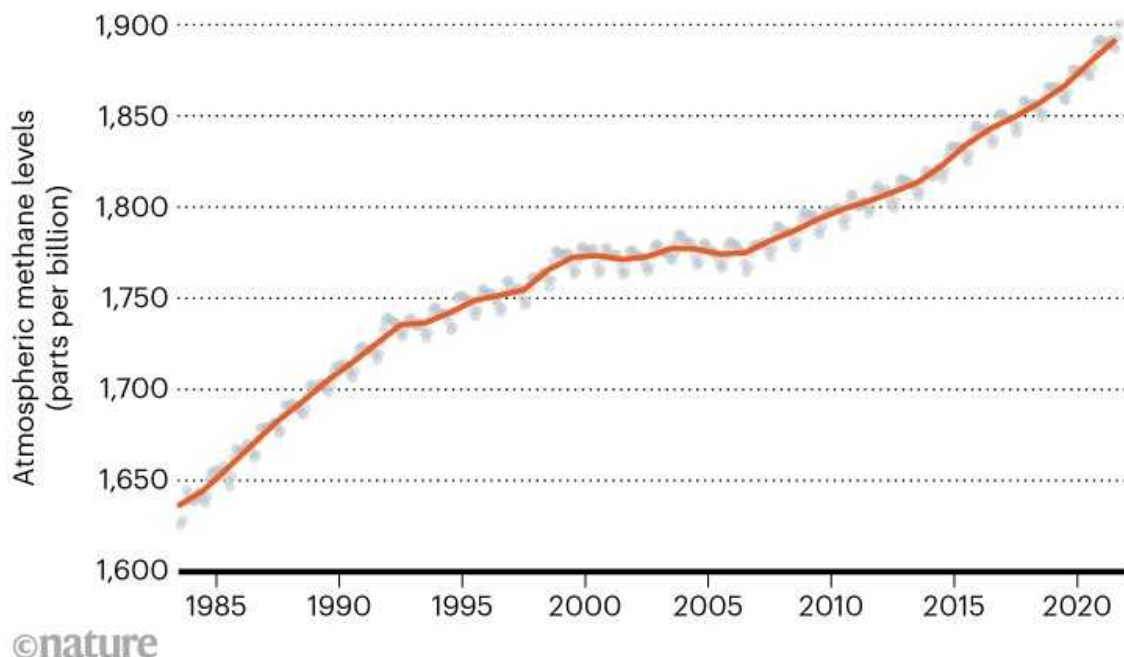
## **‘Dangerously fast’ growth in atmospheric methane**

Methane concentrations in the atmosphere [raced past 1,900 parts per billion last year](#), nearly triple pre-industrial levels, according to data released in January by the US National Oceanic and Atmospheric Administration. Scientists say the grim milestone underscores the importance of a pledge made at last year’s COP26 climate summit to curb emissions of methane, a greenhouse gas at least 28 times as potent as carbon dioxide.

The growth of methane emissions slowed around the turn of the millennium, but began a rapid and mysterious uptick around 2007. The spike has caused many researchers to worry that global warming is creating a feedback mechanism that will cause ever more methane to be released, making it even harder to rein in rising temperatures.

## A WORRYING TREND

Atmospheric methane levels have been rising since the Industrial Revolution. Growth slowed between 1999 and 2006, but methane levels have increased sharply since 2007. Neither trend is well understood.



Source: NOAA

“Methane levels are growing dangerously fast,” says Euan Nisbet, an Earth scientist at Royal Holloway, University of London, in Egham, UK.

Some researchers think that much of the increase in the past 15 years might be due to microbial sources, rather than the extraction of fossil fuels. The emissions are a major threat to the world’s goal of limiting global warming to 1.5–2 °C over pre-industrial temperatures.



A suspected outbreak at a pet shop in January led to a cull of hamsters in Hong Kong. Credit: Chan Long Hei/Bloomberg/Getty

## Sneezing hamsters sparked Hong Kong COVID outbreak

Pet hamsters probably carried the Delta variant of SARS-CoV-2 into Hong Kong and sparked a human COVID-19 outbreak, according to a genomic analysis of viral samples from the rodents. The research confirms earlier fears that a pet shop was the source of the outbreak, which had, by early February, infected about 50 people and led to the culling of some 2,000 hamsters across the city.

Hamsters are highly susceptible to SARS-CoV-2 and so are a popular model for studying the virus. But the Hong Kong study — posted online as a preprint and yet to be peer reviewed — is the first to show that hamsters can become infected outside the laboratory, and that they can pass the virus on, both to other hamsters and to humans (H.-L. Yen et al. Preprint at Social Science Research Network <https://doi.org/10.13140/RG.2.2.30350.48000>; 2022). Hamsters are only

the second animal known to be able to infect people, after mink. In late 2020, small outbreaks of COVID-19 in people in Denmark and the Netherlands were linked to farmed mink, sparking panic and mass culls.

The latest study points to the pet trade as a route for viral spread, says co-author Leo Poon, a virologist at the University of Hong Kong. But “to be fair to the hamsters”, people are still much more likely to be infected by each other than by pets, he says.

*Nature* **603**, 13 (2022)

*doi:* <https://doi.org/10.1038/d41586-022-00561-1>

---

This article was downloaded by **calibre** from <https://www.nature.com/articles/d41586-022-00561-1>

| [Section menu](#) | [Main menu](#) |

- NEWS
- 27 February 2022

# Wuhan market was epicentre of pandemic's start, studies suggest

Report authors say that the coronavirus SARS-CoV-2 jumped to people from animals sold at the market on two occasions in late 2019 — but some scientists want more definitive evidence.

- [Amy Maxmen](#)



Police in Wuhan, China, shut down the Huanan Seafood Wholesale Market on 1 January, 2020. Credit: Noel Celis/AFP via Getty

Scientists have released three studies that reveal intriguing new clues about how the COVID-19 pandemic started. Two of the reports trace the outbreak back to a massive market that sold live animals, among other goods, in Wuhan, China<sup>1,2</sup>, and a third suggests that the coronavirus SARS-CoV-2 spilled over from animals — possibly those sold at the market — to humans at least twice in November or December 2019<sup>3</sup>. Posted on 25 and 26 February, all three are preprints, and so have not been published in a peer-reviewed journal.

These analyses add weight to original suspicions that the pandemic began at the Huanan Seafood Wholesale Market, which many of the people who were infected earliest with SARS-CoV-2 had visited. The preprints contain genetic analyses of coronavirus samples collected from the market and from people infected in December 2019 and January 2020, as well as geolocation analyses connecting many of the samples to a section of the market where live animals were sold. Taken together, these lines of evidence point towards the market as the source of the outbreak — a situation akin to that seen in the epidemic of severe acute respiratory syndrome (SARS) in 2002–04, for which animal markets were found to be ground zero — says Kristian Andersen, a virologist at the Scripps Research Institute in La Jolla, California, and an author on two of the reports. “This is extremely strong evidence,” he says.

However, none of the studies contains definitive evidence about what type of animal might have harboured the virus before it spread to humans. Andersen speculates that the culprits could be raccoon dogs, squat dog-like mammals used for food and their fur in China. One of the studies he co-authored<sup>2</sup> suggests that raccoon dogs were sold in a section of the market where several positive samples were collected. And reports<sup>4</sup> show that the animals can harbour other types of coronavirus.

Nevertheless, some virologists say that the new evidence pointing to the Huanan market doesn’t rule out an alternative hypothesis. They say that the market could just have been the location of a massive amplifying event, in which an infected person spread the virus to many other people, rather than the site of the original spillover.

“Analysis-wise, this is excellent work, but it remains open to interpretation,” says Vincent Munster, a virologist at the Rocky Mountain Laboratories, a division of the National Institutes of Health in Hamilton, Montana. He says that searching for SARS-CoV-2 and antibodies against it in blood samples collected from animals sold at the market, and from people who sold animals at the market, could provide more-definitive evidence of COVID-19’s origins. The number of positive samples from the market does suggest an animal source, Munster says. But he is frustrated that more-thorough investigations haven’t already been conducted: “We are talking about a pandemic that has upended the lives of so many people.”

## Ground zero?

In early January 2020, Chinese authorities identified the Huanan market as a potential source of a viral outbreak because most people infected with COVID-19 at that time had been there in the days before they began to show symptoms, or were in contact with people who had been. Hoping to stem the outbreak, the authorities closed the market. Researchers then collected samples from poultry, snakes, badgers, giant salamanders, Siamese crocodiles and other animals sold there. They also swabbed drains, cages, toilets and vendors’ stalls in search of the pathogen. Following an investigation led by the World Health Organization (WHO), [researchers released a report in March 2021](#) showing that all of the nearly 200 samples collected directly from animals were negative, but that around 1,000 environmental samples from the stalls and other areas of the market were positive.



Researchers speculate that an intermediate animal such as a raccoon dog could have passed the coronavirus SARS-CoV-2 to humans. Raccoon dogs have been sold at the Huanan market. Credit: Edwin Giesbers/Nature Picture Library/Science Photo Library

A team in China including researchers at China's Center for Disease Control and Prevention (CDC) has now sequenced genetic material recovered from those positive samples, and released the results in a preprint posted on 25 February<sup>1</sup>. The scientists confirm that the samples contain SARS-CoV-2 sequences almost identical to those that have been circulating in humans. Furthermore, they show that the two original virus lineages circulating at the start of the pandemic, called A and B, were both present at the market.

“It’s a nice piece of work,” says Ray Yip, an epidemiologist and a former director of the China branch of the US Centers for Disease Control and Prevention. “They’ve confirmed that the Huanan market was indeed a very important spreading location.”

As soon as the report from China had been posted online, Andersen and his colleagues rushed to post manuscripts they had been working on for weeks.

In one<sup>2</sup>, the team zeroed in on the southwestern section of the Huanan market, where live animals were sold as recently as 2019, as being the potential epicentre of the outbreak. The researchers arrived at this conclusion by compiling information on the first known COVID-19 cases in China, as reported by various sources, including the WHO investigation, newspaper articles, and audio and video recordings of doctors and patients in Wuhan. This geospatial analysis found that 156 cases that occurred in December 2019 clustered tightly around the market, with cases gradually becoming more dispersed across Wuhan during January and February 2020.

The authors also examined the locations of the positive samples collected in the market, as reported in the WHO study, and fleshed out information about the potential surroundings of these spots by collecting business registration information, photographs of the market before it closed and scientific reports that have emerged since the WHO's investigation. For example, one paper published last year<sup>5</sup> documented some 47,000 animals — including 31 protected species — sold in Wuhan markets between 2017 and 2019.

One major finding reported by Andersen and colleagues is the mapping of five positive samples from the market to a single stall that sold live animals, and, more specifically, to a metal cage, to carts used to move animals and to a machine used to remove birds' feathers<sup>2</sup>. One of the report's co-authors, virologist Eddie Holmes at the University of Sydney in Australia, had been to this stall in 2014 and snapped photographs — included in this study — of a live raccoon dog in a metal cage, stacked above crates of poultry, with the whole assembly sitting on top of sewer drains. Notably, in the study by researchers at the China CDC, sewage at the market tested positive for SARS-CoV-2.

In a second report<sup>3</sup>, Andersen and his colleagues concluded that, genetically, lineage A and lineage B of SARS-CoV-2 are too different from one another for one to have evolved into the other quickly in humans. Therefore, they suggest that the coronavirus must have evolved in non-human animals and that the two lineages spread to humans separately. For a few reasons, including the fact that lineage B was much more prevalent in January 2020, the authors suggest that it spilled over into humans before lineage A. Other outbreaks of coronaviruses, such as the SARS and Middle East respiratory

syndrome (MERS) epidemics, also resulted from repeated introductions from wildlife, the paper notes.

Taking all of the new data together, and adding a degree of speculation, Andersen suggests that raccoon dogs could have been infected on a farm that then sold the animals at the markets in Wuhan in November or December 2019, and that the virus might have jumped to people handling them or to buyers. On at least two occasions, those infections could have spread from an index case to other people, he says.

## **‘As good as it gets’**

Over the past year, Michael Worobey, a virologist at the University of Arizona in Tucson and a co-author on the papers with Andersen<sup>2,3</sup>, says that his thinking on the origins of COVID-19 has shifted. In May 2021, he led a letter published in *Science*<sup>6</sup> in which he and others pressed the scientific community to keep an open mind about whether the pandemic stemmed from a laboratory, [a controversial hypothesis](#) suggesting that SARS-CoV-2 was either created in a lab or was accidentally or intentionally released by researchers at the Wuhan Institute of Virology. “You want to take this kind of thing seriously,” he explains.

But since then, other evidence has come to light that supports a zoonotic origin story similar to that of HIV, Zika virus, Ebola virus and multiple influenza viruses, he says. “When you look at all of the evidence, it is clear that this started at the market.” Separate lines of analysis point to it, he says, and it’s extremely improbable that two distinct lineages of SARS-CoV-2 could have been derived from a laboratory and then coincidentally ended up at the market.

Nonetheless, Munster says he is not completely convinced of two spillover events because the virus might have evolved from one lineage into the other in a person who was immunocompromised. He adds that more data collected from people and animals is needed to answer this question, and to show that the first spillover occurred at the Huanan market. David Relman, a microbiologist at Stanford University in California, agrees that the preprints

are not definitive, and that they exclude the possibility that people were infected prior to the outbreak at the market, but went undiagnosed.

Holmes fears that additional samples from early human cases and from animals might never materialize. Last July, for example, [Chinese officials said](#) that they planned to analyse patient blood samples from 2019, stored at the Wuhan Blood Center — but if that study has been conducted, it has yet to be made public. “This is as good as it gets,” Holmes says. “What we should focus on now is trying to keep these events from happening again.”

*Nature* **603**, 15-16 (2022)

doi: <https://doi.org/10.1038/d41586-022-00584-8>

## References

1. Gao, G. *et al.* Preprint at Research Square  
<https://doi.org/10.21203/rs.3.rs-1370392/v1> (2022).
2. Worobey, M. *et al.* Preprint at Zenodo  
<https://doi.org/10.5281/zenodo.6299600> (2022).
3. Pekar, J. E. *et al.* Preprint at Zenodo  
<https://doi.org/10.5281/zenodo.6291628> (2022).
4. He, W.-T. *et al.* *Cell* <https://doi.org/10.1016/j.cell.2022.02.014> (2022).
5. Xiao, X., Newman, C., Buesching, C. D., Macdonald, D. W. & Zhou, Z.-M. *Sci. Rep.* **11**, 11898 (2021).
6. Bloom, J. D. *et al.* *Science* **372**, 694 (2021).

---

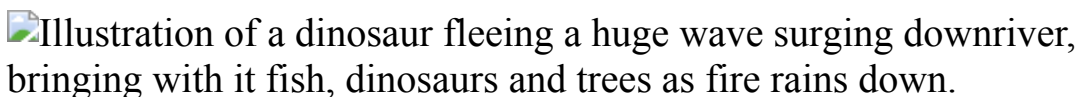
This article was downloaded by **calibre** from <https://www.nature.com/articles/d41586-022-00584-8>

- NEWS
- 23 February 2022

# Fossil fish reveal timing of asteroid that killed the dinosaurs

The discovery is likely to reignite controversy over the US site where the fossils were found.

- [Colin Barras](#)



Evidence suggests an asteroid impact that killed off most dinosaurs might have happened in spring. Credit: Joschua Knüppe

Winter began in spring for many animals during the final year of the age of dinosaurs. Palaeontologists studying fossilized fish suggest that spring was in full bloom in the Northern Hemisphere when an asteroid slammed into Earth, triggering a devastating global winter and mass extinction.

But the conclusions are likely to stir controversy among some researchers, partly because the fossils come from Tanis, an extraordinary yet contentious geological site in North Dakota. Some were puzzled by the results, published in *Nature* on 23 February<sup>1</sup>, which are essentially identical to those of a separate study published in *Scientific Reports* last December<sup>2</sup> by another research group working at Tanis. Neither paper cites the other.

## Big news

News of Tanis' discovery first hit the headlines in [\*The New Yorker\* magazine in 2019](#). The team behind the discovery, led by Robert DePalma,

now a PhD student at the University of Manchester, UK, then published a description of the site in a scientific journal<sup>3</sup>. They said Tanis captured what happened just minutes to hours after the asteroid struck Mexico's Yucatán Peninsula about 66 million years ago.

According to the 2019 paper, the impact generated 10-metre-tall waves in a shallow sea that stretched across what is now the southern and eastern United States. As one of these waves surged up a river valley in what is now North Dakota, it swept up the organisms in its path, along with plenty of mud and sand. The wave then retreated and dumped the material, forming the Tanis site.

The research came under intense scrutiny because no other site on Earth is thought to preserve a detailed record of the day of impact. But many researchers note that the 2019 paper did not include a detailed description of the site's geology, making it difficult to assess whether the geology can really be tied to the impact or another unknown catastrophe that occurred perhaps thousands of years earlier. "For a site of such potential importance, I'd really like to see a long-format paper that dives deep into the sedimentology and stratigraphy of the site, and supports it with lots of imagery and data," says Thomas Tobin, a geologist at the University of Alabama in Tuscaloosa. He says this is particularly important given that a limited number of researchers to date have had an opportunity to visit Tanis.

DePalma says that an upcoming study will expand on the description of the site given in 2019. He also acknowledges there is a "misconception" that he is restricting access to the site, but he insists this is not the case. "In fact, the access has been more open than is typical practice," he says.

One researcher who has had access is Melanie During, who is now pursuing a PhD in palaeontology at Uppsala University in Sweden. In August 2017, while she was at the Vrije Universiteit Amsterdam, she had an opportunity to visit Tanis because her instructor, geologist Jan Smit, had previously worked with DePalma at the site. "It looks like a car wreck frozen in time. It's insane," says During. "There are fishes folded around tree branches — you can tell that this wave displaced everything."

## Fossil record

During wondered whether a geological record formed on the day of impact would preserve evidence that could pinpoint the event to a particular season. She says the growth patterns of certain fossilized fish bones at Tanis can reveal the season in which the fish died. The bones grow rapidly in spring when food is abundant, but slowly in winter when food is scarce — creating a microscopic ‘line of arrested growth’ (LAG) in the bone tissue.

During collected fossilized fish from Tanis and then, working with Smit and other colleagues, produced high-resolution micro-computerized-tomography models of three paddlefish jawbones and three sturgeon pectoral fin spines. The researchers say it was possible to identify LAGs in the six bones and show that all six fish had died shortly after beginning a new period of growth. This suggests their deaths — and, by implication, the asteroid impact — occurred during the Northern Hemisphere’s spring.

During says the findings could offer clues about why the impact-triggered extinction wiped out some animals, including all non-avian dinosaurs, but not others. She speculates that the impact’s timing might have been devastating for species in the Northern Hemisphere that had young to care for. There is also some evidence that Southern Hemisphere ecosystems recovered twice as fast after the extinction, write the researchers.

“I think their argument [about the season of death] is convincing,” says Michael Newbrey, a biologist at Columbus State University in Georgia who is familiar with using LAGs to study fish. He says he would have liked to see a larger sample size, but acknowledges the difficulty in accessing and preparing samples from the fossil record.

But LAGs are contentious, says a postdoctoral researcher who understands bone analysis and the geology of the Tanis region. They have requested anonymity given the controversy of the site. “There is no uniform, agreed-upon definition of what a LAG is or how you identify one,” they say — and neither is there agreement on how often and why LAGs form. As such, the researcher questions the strength of the spring-impact hypothesis.

## Double trouble?

Several researchers have pointed out that the study is nearly identical to the study led by DePalma that was published last year<sup>2</sup>. This earlier study also examined LAGs in fish fossils from Tanis and used them to link the impact event to spring, or possibly summer. “Adding to this bizarre overlap is the conspicuous absence of any mention of the DePalma *et al.* paper by the During *et al.* paper,” the postdoc says.

During points out that her team’s paper was submitted for publication before the DePalma team submitted theirs. “Ours is the prior work and does not in any respect rest on the data or conclusions of DePalma *et al.*,” she says, adding that her team therefore felt no need to cite the DePalma *et al.* study — although the new paper acknowledges DePalma for providing guidance in the field and access to specimens.

“Similarities in the studies might be expected to some extent when considering that the second study was born from the same site and used specimens on loan from our study area,” says DePalma. He adds that the studies “complement” and “independently reinforce each other”.

*Nature* **603**, 17 (2022)

doi: <https://doi.org/10.1038/d41586-022-00511-x>

## References

1. During, M. A. D. *et al.* *Nature* <https://doi.org/10.1038/s41586-022-04446-1> (2022).
2. DePalma, R. A. *et al.* *Sci. Rep.* **11**, 23704 (2021).
3. DePalma, R.A. *et al.* *Proc. Natl Acad. Sci. USA* **116**, 8190–8199 (2019).

| [Section menu](#) | [Main menu](#) |

- NEWS
- 17 February 2022

# A year on Mars: How NASA's Perseverance hit a geological jackpot

The rover collected exciting rock samples on the first leg of its epic journey. Next, it will turn towards an ancient river delta to look for past life.

- [Alexandra Witze](#)



During its first Earth year on Mars, the Perseverance rover has used its sampling arm to collect rock cores and explore the red planet's geochemistry. Credit: NASA/JPL-Caltech

Since [landing on Mars one year ago](#), NASA's Perseverance rover has travelled more than 3 kilometres across rocky terrain, [recorded the first flight on the planet](#) by a helicopter and collected six precious rock samples that — if all goes well — will one day be returned to Earth, along with many more, for study.

Perseverance [touched down in Jezero Crater](#), just north of the Martian equator, on 18 February 2021 [with the goal of searching for signs of past life](#). Researchers intended the US\$2.7-billion rover to look for these signs in an ancient delta, where a river that once flowed into the crater deposited sediments and rocks — an environment that could have supported life. But the rover hasn't reached it yet.

## SAMPLING MARS

NASA's Perseverance rover has drilled and collected three pairs of rock samples in Jezero Crater on Mars, the first Martian rocks ever intended to be brought back to Earth for scientific analysis. The rover will soon head to its ultimate destination, an ancient river delta, to look for signs of past life.



Image source: NASA/JPL-Caltech

Instead, Perseverance has spent the year rolling around the bottom of the crater, making a host of surprising discoveries — one of which is that Jezero's floor is made of igneous rocks. These formed as molten rock cooled and solidified billions of years ago. Some researchers had thought that the crater floor would be made of sedimentary rock, created as wind or water deposited layers of sediment over time. But the rover found a different history for the landscape.

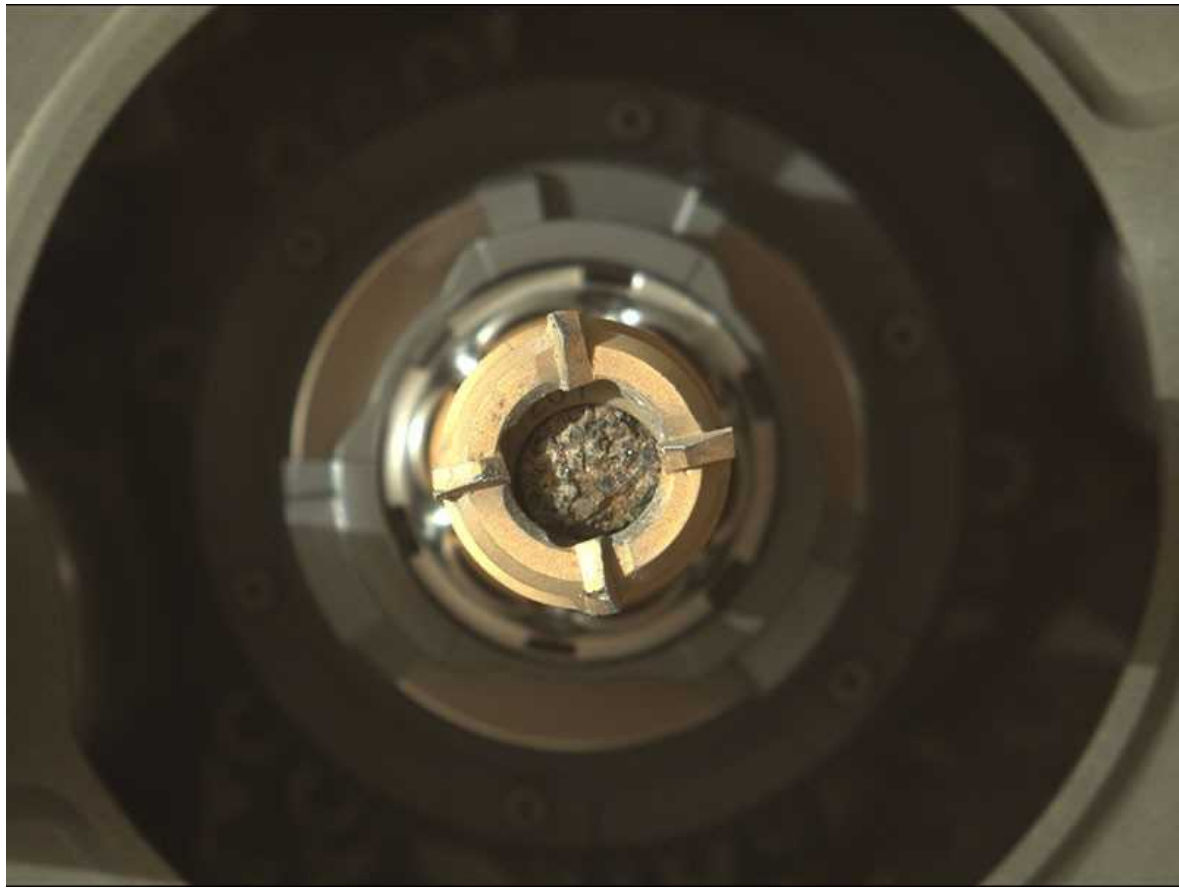
Igneous rocks are important because scientists can analyse the radioactive decay of elements inside them to determine how old the rocks are. If and when Perseverance's samples come back to Earth, researchers will be able to date rocks from specific places on the surface of Mars for the first time.

Before the rover landed, mission scientists didn't know they were going to hit an igneous jackpot. "Jezero delivered," says Katie Stack Morgan, the mission's deputy project scientist at the Jet Propulsion Laboratory in Pasadena, California.

## A fiery past

Scientists discovered that Jezero's floor wasn't what they expected when the rover began preparing to drill its first sample in August. Exploring the area's geology, Perseverance ground into a piece of Martian rock to reveal a fresh surface. It looked like an igneous rock on Earth that had salt-rimmed holes in it — holes that had probably formed as water flowed through the rock. That meant the rover was looking at an ancient volcanic rock that had interacted with water, indicating a life-friendly environment such as had never been seen on Mars. "That was a great moment for the mission," says Stack Morgan. "Those are ideal places to be looking for signs of ancient rock-hosted life."

But when Perseverance tried to drill a core, the material crumbled and slid out of the sampling device. Because the sampling procedure was automated, the rover ended up with an empty but sealed tube, which mission scientists tried to put a positive spin on, labelling it a sample of Mars's atmosphere.



Perseverance collected its sixth rock core (shown here, held in the rover's sampling mechanism) last month. Credit: NASA/JPL-Caltech/ASU

“You can’t really give Mars a wish list,” says Tanja Bosak, a geobiologist at the Massachusetts Institute of Technology in Cambridge. “Mars gives you what it wants to give you.”

A month later, Perseverance successfully [drilled its first pair of cores](#), into a similar igneous rock that had been altered by water (see ‘Sampling Mars’). This rock formation, called Maaz, covers much of Jezero’s floor.

The rover then drove south and west, skirting a dune-ridden area called Seitah, and collected two more pairs of samples. (It collects pairs to increase the potential that one of the samples will be returned to Earth.) Mission scientists had thought that Seitah’s rocks would be sedimentary, because visually they seemed to be composed of different layers. But as soon as Perseverance ground away at some of the Seitah rocks, another surprise emerged. They, too, were igneous.

Using various instruments to analyse the rocks' chemical composition, Perseverance found chunky grains of one mineral, called olivine, encased in another, called pyroxene. These minerals are generally found in igneous rocks or volcanic areas on Earth. That's strong evidence that the Seitah rocks formed as a large body of molten rock cooled, says Stack Morgan. Olivine crystals would have formed first, and sunk towards the bottom of the cooling magma, and then pyroxene would have formed around them — creating layered rocks that appear sedimentary.

The Seitah rocks, like the Maaz rocks, also show signs of having interacted with water in the past. They might even — as reported at a December meeting of the American Geophysical Union by Eva Scheller, a geologist at the California Institute of Technology in Pasadena — contain organic molecules, probably produced through non-biological processes, such as those seen in some Martian meteorites.

## Pressure mounts

All told, Perseverance is supposed to collect at least 30 rock, dirt and atmosphere samples. It will lay them down in one or more places for future missions to retrieve, in what could be the first sample return from Mars. Getting the cores to Earth will be an elaborate process requiring another rover to pick them up, a rocket to launch them into Mars orbit, and a spacecraft to capture them and fly them back to Earth; this would happen no earlier than 2031. NASA and the European Space Agency are collaborating on the plan, and NASA announced this month that it had chosen a contractor to build the rocket that will lift the samples into Mars orbit.

“I’m just super-excited that we’re finally taking the first steps towards collecting and hopefully bringing back samples from Mars,” says Meenakshi Wadhwa, a planetary scientist at Arizona State University in Tempe and NASA’s principal scientist for the Mars sample-return programme. “We already have some really great samples to assess the question of whether there was ancient life.”

Despite the rover’s success so far, pressure is mounting for it to get to the long-awaited delta. Perseverance is making its way there now as quickly as

possible; earlier this month, it set a record for long-distance driving on Mars, travelling more than 240 metres in a day. Even so, it probably won't get to the delta until April.

Time is of the essence because Perseverance has only about one Earth year remaining to meet the timetable for accomplishing its main to-do list: get to the delta, collect samples there, and drive up onto the crater rim to place them somewhere for pick-up. The rover is currently retracing its steps towards its landing site: it will collect another pair of cores from Maaz along the way, and then detour around the dune-filled region to reach the delta. Perseverance is working at a much faster pace than NASA's previous Mars rover, Curiosity, which has been exploring Gale Crater since it landed in 2012. "We have to keep on moving," Bosak says.



Some pebbles jammed Perseverance's drilling mechanism in January. But it shook them loose, as shown in this GIF, recorded with one of the rover's cameras.Credit: NASA/JPL-Caltech/ASU/MSSS

Although operations have mostly been smooth, some small glitches have occurred, besides the initial failed attempt to collect a rock core. In December, some pebbles fell out during a coring attempt and jammed some of the mechanisms in the rover's sampling equipment. Engineers eventually got Perseverance to shake the pebbles loose to fix the problem. And in recent weeks, says José Antonio Rodríguez Manfredi, principal investigator of the rover's weather instrument at the Centre for Astrobiology in Madrid, surprisingly strong winds kicked dust and small pebbles into several of the rover's wind sensors, damaging them.

Perseverance's sidekick, the tiny helicopter named Ingenuity, continues to plug along. Researchers intended the craft to make five flights over 30 days. But it has so far made 19 flights and travelled more than 3.8 kilometres. It is currently staged ahead of the rover and will be used, if it continues to survive, to scout routes that the rover might take once it gets to the Jezero delta to collect more cores.

“The delta samples will be spectacular,” Bosak says. “I can’t wait. I really can’t wait.”

*Nature* **603**, 18-19 (2022)

*doi:* <https://doi.org/10.1038/d41586-022-00469-w>

---

This article was downloaded by **calibre** from <https://www.nature.com/articles/d41586-022-00469-w>

- NEWS
- 18 February 2022

# Asteroids, Hubble rival and Moon base: China sets out space agenda

In the next five years, the nation hopes to launch a robotic craft to an asteroid and two lunar missions.

- [Elizabeth Gibney](#)



China's Tiangong Space Station.Credit: Xinhua/eyevine

China has had a bumper few years in space exploration, and its ambitions are about to get bolder. The China National Space Administration has released an overview of its plans for the next five years, which include launching a robotic craft to an asteroid, building a space telescope to rival

the Hubble and laying the foundations for a space-based gravitational-wave detector.

The missions were highlighted in a white paper, '[China's Space Program: A 2021 Perspective](#)', released last month. The plans continue the country's trend in emphasizing missions with science at their heart, rather than technology development and applications, says Shuang-Nan Zhang, an astronomer at the Institute of High Energy Physics in Beijing. "This is a very good sign," he says. "It's a continuous increase in investment in exploration of the Universe."

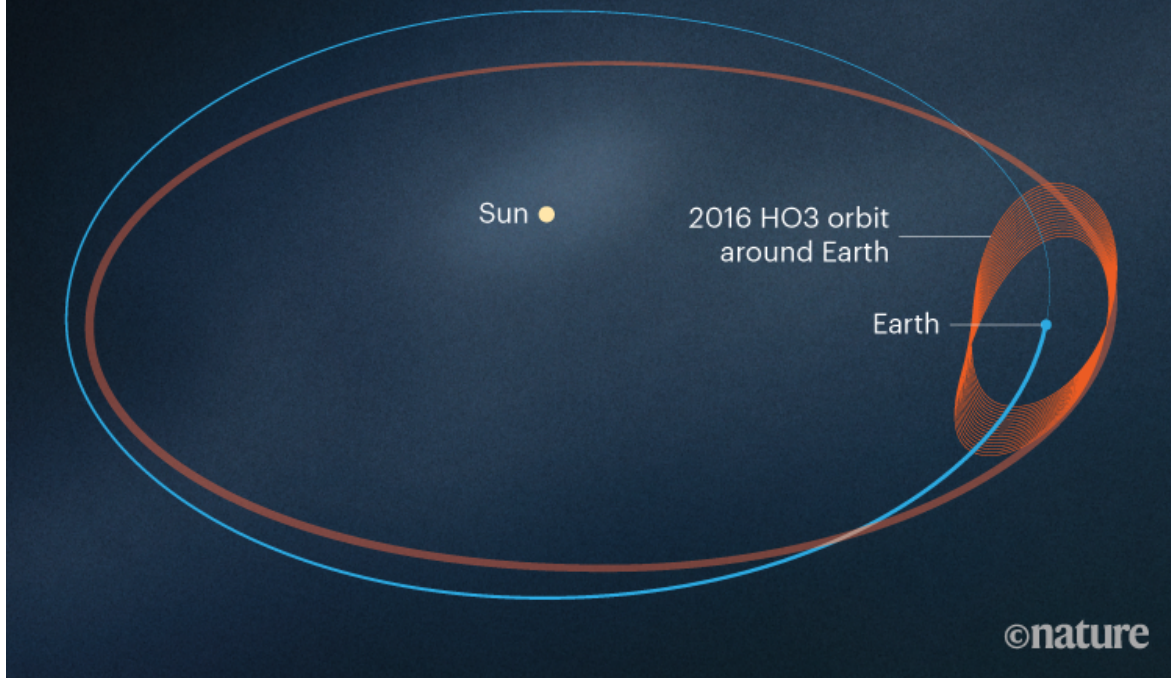
*Nature* looks at five of the most ambitious projects.

## Visit an asteroid

China aims to launch asteroid probes to sample near-Earth asteroids and study icy comets that have asteroid-like orbits. The mission, which will probably be named ZhengHe after a Ming-dynasty Chinese explorer, would be the country's [first to visit an asteroid](#), and could launch as soon as 2024. It will follow in the wake of Japan's successful [Hayabusa asteroid missions](#) and [NASA's OSIRIS-Rex](#), which is due to return space rocks to Earth next year.

## EARTH'S PET ROCK

China plans to launch a mission that would collect material from the asteroid 2016 HO<sub>3</sub> and return it to Earth. The rock is a 'quasi-satellite' of Earth that loops around the planet as it orbits the Sun.



©nature

ZhengHe will fly for ten years, first landing on an ancient asteroid known as HO<sub>3</sub> or Kamo'olewa, which loops around Earth as a quasi-satellite (see 'Earth's pet rock'). Scientists hope that studying it will give them an insight into conditions in the early Solar System. ZhengHe will anchor itself on the asteroid before scooping up its sample, according to a correspondence<sup>1</sup> published in *Nature Astronomy* last year. ZhengHe will return to Earth's orbit in 2026 to drop off its spoils, which will parachute to the ground. The craft will then sling-shot around Earth and Mars and travel to comet 311P/PANSTARRS in deep space.

## Towards a lunar base

Not content with returning the [first lunar samples](#) to Earth since the 1970s, China approved three more lunar missions in December, all focusing on the Moon's south pole, where the country is considering [building a lunar base](#).

Chang'e-7, set to launch in 2024, will carry out a detailed survey of the Moon's south pole, including mapping the distribution of ice in its shadowy craters. Chang'e-6 will follow, aiming to bring back polar soil samples. The ice is a treasure trove for scientists, who can use it to study the Moon's history, and for prospectors, who hope to use it as rocket fuel and to supply lunar bases.

Work will also begin on Chang'e-8, which is not scheduled to fly until 2030; this will test "core technologies" for a crewed international lunar research station — the focus of China's lunar programme beyond 2025. Russia and China will sign an intergovernmental agreement on building a research base together "as soon as possible this year", said Wu Yanhua, vice-administrator of the China National Space Administration (CNSA), at the press conference to launch the white paper. He stressed, however, that the venture was open to all nations.

Wu added that China wants to broaden and deepen international collaboration, including on lunar exploration; on China's space station, Tiangong, which is under construction; and on planetary exploration.

## Mars and beyond

China made its first leap into interplanetary space with the Tianwen-1 orbiter, which dropped a lander containing the [Zhurong rover on Mars](#) in May. According to the white paper, China will complete research for sending a craft to Mars to sample rocks and return them to Earth. This mission could launch in 2028. (NASA's Perseverance rover [collected](#) the first Mars rocks in 2021. The agency hopes to bring them back to Earth as part of a joint mission with the European Space Agency (ESA), [launching in 2026.](#))

The white paper also lays out China's plans to eventually probe further into the solar system. The next five years will see the completion of key research for a mission to explore Jupiter and its ocean-filled moon system. Press reports suggest that this mission could launch as early as 2029 — meaning that it would join [ESA's JUICE](#) and [NASA's Europa Clipper mission](#), scheduled to fly in 2023 and 2024. "Deep space is certainly another area

China sees there are a lot of opportunities for scientific breakthroughs,” says Zhang.

The country has also set its sights on exploring the boundary of the Solar System. China’s funding agencies have yet to confirm this, or the Jupiter mission, but “a mention in the plan is certainly helpful”, says Zhan Hu, an astronomer at the National Astronomical Observatories in Beijing.

## A new Hubble: the Xuntian space telescope

China also plans to launch a space telescope called Xuntian, whose name means ‘survey the heavens’. This will image in the same wavelengths — ultraviolet, visible and infrared — as those used by NASA’s Hubble Space Telescope.

Slightly smaller than Hubble, Xuntian will not quite match its predecessor’s resolution; but, at any one time, Xuntian will capture a patch of sky 300 times larger. That will allow it to probe a much greater volume of the Universe than Hubble, says Zhan, who works on Xuntian.

Most of Xuntian’s first 10 years will be devoted to understanding the history and evolution of the Universe through a wide survey of the sky. The telescope will periodically dock with China’s space station, Tiangong, for refuelling and maintenance. Zhan says that the team plans to deliver the telescope by the end of 2023, ready for launch in 2024. “The schedule is very tight,” he says.

## Detecting gravitational waves in space

China wants to further develop plans to launch a space-based gravitational-wave detector, called Taiji, in the early 2030s. If launched then, it would be the first of its kind. Such a mission would observe lower-frequency waves than those seen by ground-based detectors such as [Advanced LIGO](#), allowing it to detect higher-mass black holes, including those in the early Universe.

But the experiment would be complex: spotting ripples in space-time will mean detecting shifts of just a few trillionths of a metre in the distances between [three spacecraft](#), positioned 3 million kilometres apart from each other in the shape of a triangle.

An [initial pilot satellite](#), called Taiji-1, completed its mission successfully in 2019, and researchers now hope to fly a two-satellite mission in 2024–25 to test the necessary precision technologies. This will “remove all the technical obstacles” for the ultimate Taiji mission, says Yue-Liang Wu, a physicist at the University of the Chinese Academy of Sciences in Beijing.

ESA has long planned its own gravitational-wave observatory, LISA, and has already flown a [successful pathfinder](#). But LISA is not scheduled to launch until 2037. Together, the two networks could be used to measure the Hubble constant, which describes the expansion of the Universe, with much greater accuracy than ground-based detectors can, say researchers behind the mission.

*Nature* **603**, 19–20 (2022)

*doi:* <https://doi.org/10.1038/d41586-022-00439-2>

## References

1. Zhang, T. *et al.* *Nature Astron.* **5**, 730–731 (2021).

---

This article was downloaded by **calibre** from <https://www.nature.com/articles/d41586-022-00439-2>

- NEWS
- 17 February 2022

# Two scientists will replace disgraced US science adviser Eric Lander

Celebrated sociologist Alondra Nelson and genome leader Francis Collins will temporarily split Lander's duties.

- [Lauren Wolf](#),
- [Jeff Tollefson](#) &
- [Amy Maxmen](#)



Francis Collins (left) retired in December from the helm of the US National Institutes of Health, and Alondra Nelson is a deputy director in the White

House Office of Science and Technology Policy.Credit: Michael Kovac/Getty, Matt Slocum/AP/Shutterstock

US President Joe Biden has replaced his disgraced science adviser, Eric Lander, with two scientists who will split Lander's duties "until permanent leadership is nominated and confirmed", [according to the White House](#).

Alondra Nelson, deputy director for science and society at the Office of Science and Technology Policy (OSTP), which Lander led, will become acting director of the agency. And Francis Collins, who led the US National Institutes of Health [before retiring in December](#), will temporarily become Biden's science adviser and co-chair the President's Council of Advisors on Science and Technology (PCAST).

Lander [resigned on 7 February](#), after the [news outlet Politico revealed](#) that, according to a White House investigation, he had violated the Biden administration's Safe and Respectful Workplace Policy by mistreating staff members at the OSTP. In his resignation letter, Lander acknowledged that things he had said to team members "crossed the line at times into being disrespectful and demeaning".

Biden moved swiftly to name interim replacements for Lander, who had been leading some of the president's priority science initiatives — in particular, the creation of the Advanced Research Projects Agency for Health (ARPA-H), a high-risk, high-reward biomedical innovations agency; and [the revamping of his 'Cancer Moonshot' programme](#), which launched five years ago and has the new goal of decreasing cancer deaths by at least 50% in the next 25 years.

The OSTP did not answer *Nature*'s query about why Lander's duties have been split between two people.

Since the agency was established in 1976, its director has also gone by the title of science adviser to the president. The OSTP director oversees a staff of roughly 150 people who are charged with coordinating scientific activities across the federal government and ensuring that the president and the executive branch have access to the best available scientific information as they make decisions and craft federal policies. The role of presidential

science adviser has varied by administration. Both Lander and John Holdren, science adviser under former president Barack Obama, also served as ‘assistant to the president’, a role that granted them more direct access to the Oval Office. Biden had also elevated Lander to his cabinet, a first for an OSTP director.

Kenneth Bernard, an epidemiologist and biodefence researcher who has worked for the US government under several presidential administrations, says that Lander’s swift, interim replacements make sense. Although he doesn’t have inside knowledge, he speculates that Biden might have chosen Collins because of his grounding in biomedical laboratory research and his extended experience heading a government agency. And Collins, Bernard suggests, might not have wanted to manage the OSTP, having just retired from the NIH. He adds that Nelson is well suited to running the OSTP, having been deputy director for the past year.

The White House announcement said: “The selections are responsive to the dual importance of a strong OSTP that can drive science and technology solutions to our greatest challenges — and the very specific attention the President wants to give to the creation of a new ARPA-H research and discovery agency, the building of support for a Cancer Moonshot 2.0, the search for a new head of NIH, and the broad advisory work of PCAST.”

Nelson is a prominent sociologist, whose selection by Biden as an OSTP deputy drew praise from the scientific community. She has studied the societal impact of emerging technology and the effect of racism on science and medicine. As OSTP deputy director for science and society, she co-leads a task force charged with bolstering scientific-integrity policies and protecting scientists from political interference across the federal government.

Collins was director of the NIH under three US presidents, serving for longer than any other presidentially appointed head of the biomedical agency. He built a reputation as a shrewd spokesperson for scientific research and steered the NIH through the early stages of the COVID-19 pandemic. Known for leading the Human Genome Project in the 1990s and early 2000s, he had returned to his laboratory at the National Human Genome Research Institute to continue his research after retiring.

Neal Lane, a physicist at Rice University in Houston, Texas, who served as science adviser to former president Bill Clinton, says that splitting Lander's duties is not a permanent solution. "The director of OSTP has always been, and should continue to be, the president's science adviser," he says. "OSTP is the one agency in the federal government that has the expertise to provide advice on all aspects of US science and technology."

*Nature* **603**, 21 (2022)

*doi:* <https://doi.org/10.1038/d41586-022-00484-x>

---

This article was downloaded by **calibre** from <https://www.nature.com/articles/d41586-022-00484-x>

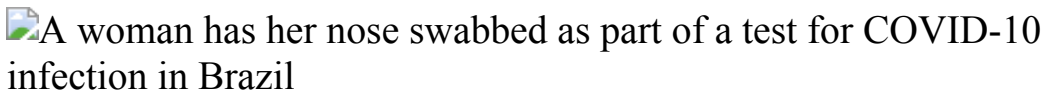
| [Section menu](#) | [Main menu](#) |

- NEWS FEATURE
- 24 February 2022

# Omicron's lasting mysteries: four questions scientists are racing to answer

The fast-moving variant poses new puzzles in viral transmission, severity and evolution.

- [Amber Dance](#) ✉



Omicron infects the cells of the nose, throat and lungs differently from former variants. Credit: Lucas Landau/Reuters/Alamy

Infection rates with the Omicron variant of the coronavirus SARS-CoV-2 are plummeting in many countries around the world. But scientists are still struggling to understand how it spread so rapidly and what it might do next, especially because the subvariant known as BA.2 is rising in some places.

Unlike previous variants of concern, Omicron often infects people who possess antibodies against earlier SARS-CoV-2 versions, acquired through infection or vaccination. In the three months that scientists have been aware of Omicron, they've learnt a lot, but most work so far has focused on the parent Omicron strain or on BA.1. Researchers still have a number of pressing questions.

In people, Omicron seems to be highly contagious — BA.2 even more so than BA.1 — but to cause less severe disease than other variants. How does it manage that? Studies on this and on how the variant interacts with host

cells and immune systems could lead to better medicines or improved vaccines. And laboratory experiments that put artificial pressures on the virus, to see what mutations arise, offer hints about what variants might appear as SARS-CoV-2 continues to evolve.

“The virus has changed,” says Salim Abdool Karim, an epidemiologist at the Centre for the AIDS Programme of Research in South Africa in Durban. “It enters cells differently, it infects lungs differently, it infects the nose differently.”

Here, *Nature* highlights some of the key questions for scientists to tackle about Omicron and what might come next.

## How is it so transmissible?

Much of Omicron’s success must come down to the dozens of mutations that separate it from previous variants and enable it to evade host antibodies, particularly the neutralizing ones that bind to the virus’s outer spike protein and block cell entry. That means that despite widespread immunity to earlier SARS-CoV-2 versions, there are more available hosts for Omicron to hop between, compared with when the Delta variant was dominant.

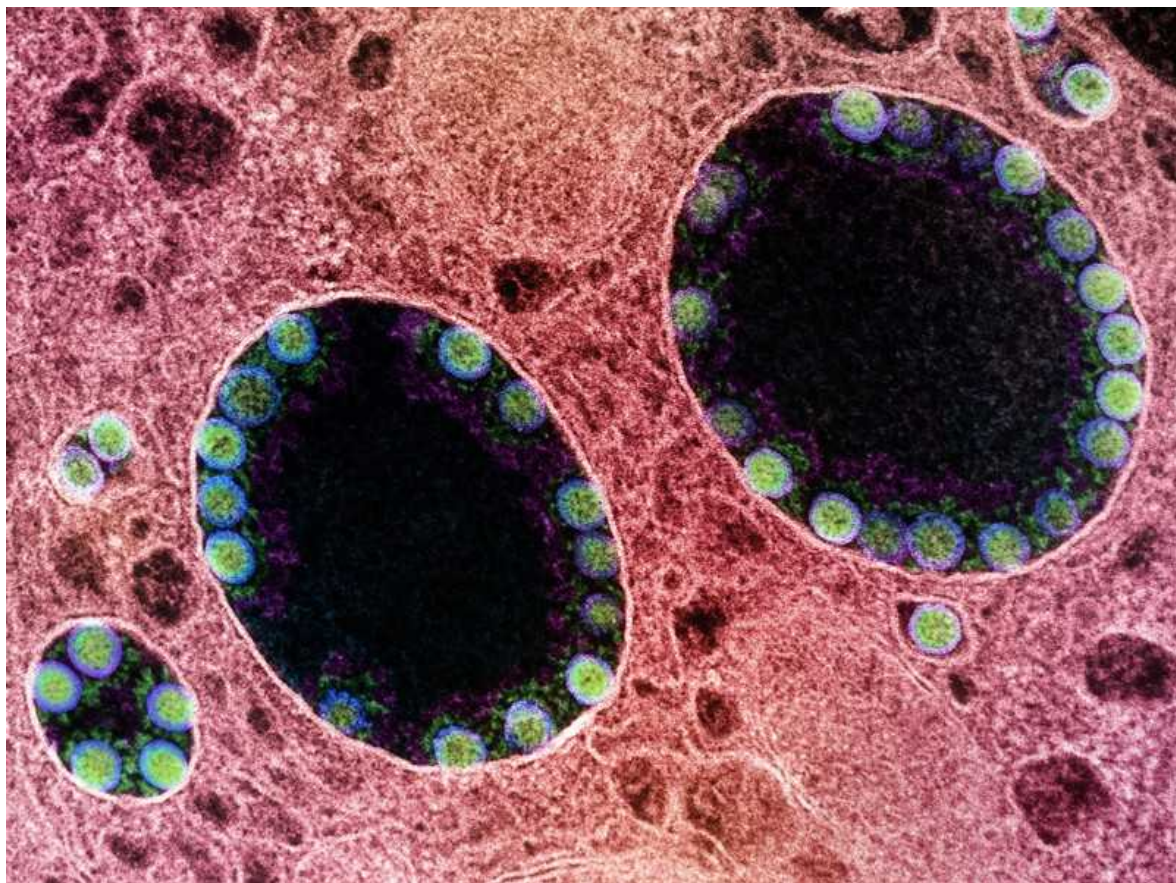
But there might also be something inherent in Omicron’s biology that makes it highly transmissible regardless of human immunity. This could be a change to how a person infected with the coronavirus transmits it, how another receives it, or both.

On the transmission side, one idea is that this variant creates a higher concentration of viral particles in the nose, so that infected individuals release more coronavirus with every exhalation. Data on this point have been mixed.

One result in favour of this hypothesis comes from a study<sup>1</sup> of human lung and bronchial tissues led by Michael Chan, a virologist at the University of Hong Kong. The data suggest that Omicron replicates faster in the upper respiratory system than all previous forms of the virus.

Researchers led by Wendy Barclay, a virologist at Imperial College London, observed that Omicron replicates faster than Delta in cultures of nose cells<sup>2</sup>.

But some studies reported that immunologically naive hamsters had fewer virus particles — none of which were infectious — in their lungs compared with previous variants<sup>3</sup>. Other studies<sup>4,5</sup> in people indicate that Omicron produces the same or lower levels of infectious viral particles as Delta does in the upper respiratory tract.



SARS-CoV-2 particles (green) inside a cellular endosome. Credit: NIAID ([CC BY 2.0](#))

As for the potential receivers of those infectious particles, Barclay suggests that Omicron's transmission strength might be linked to how it enters cells. Earlier versions of SARS-CoV-2 relied on a cellular receptor, ACE2, to bind to the cells, and on a cellular enzyme called TMPRSS2 to cleave its spike protein, granting the virus entry. Omicron has mostly abandoned the

TMPRSS2 route. Instead, cells swallow it whole, and it lands in intracellular bubbles called endosomes<sup>[2,6](#)</sup>.

Many cells in the nose make ACE2 but not TMPRSS2, Barclay says. That could give Omicron an edge as soon as it's inhaled, allowing it to set up shop without reaching the lungs and other organs where TMPRSS2 is more widely expressed. This could, in part, explain why Omicron can pass so easily between people and how it so rapidly establishes infection.

## Is it less severe? If so, why?

Hospitalization and death rates for Omicron, compared with those for previous variants, seem to suggest that it is a weaker strain. But because many people have some level of immunity, through COVID-19 vaccination or previous infection, it's challenging to untangle how much of that reduced severity stems from people's immune systems being preconditioned to take on the virus, and how much from some inherent feature of the virus itself.

"It's much more difficult to have a 'clean' genetic and immunological study," says Jean-Laurent Casanova, a paediatric immunologist at the Rockefeller University in New York City.

Scientists at Case Western Reserve University School of Medicine in Cleveland, Ohio, attempted to control for these factors by looking at first-time COVID-19 cases in children younger than 5 years old, who are not yet eligible for vaccination<sup>[7](#)</sup>. Omicron infections were less severe than Delta cases in terms of rates of emergency-department visits, admissions to hospital or intensive-care units, and need for mechanical ventilation.

In another study<sup>[8](#)</sup>, researchers in South Africa analysed hospitalization and death risk for infected adults during the Omicron wave and during earlier surges. Adjusting their data to account for previous infections, vaccination and other factors, they estimated that 25% of Omicron's reduced risk of severe disease or death was due to something intrinsic to the virus itself.

What blunted Omicron's fangs? Chan's team found that, although the variant is successful in the upper respiratory system, it was less able to replicate in

lung tissue<sup>1</sup>. And studies in rodents found less inflammation and damage to the lungs<sup>3</sup>.

In people, Omicron's relative inability to colonize or damage the lungs seems to result in fewer cases of dangerous pneumonia and respiratory distress, but in higher numbers of annoying head colds.

Another feature that might underlie Omicron's reduced severity, says Barclay, is its inability to fuse individual lung cells together into larger blobs called syncytia. Previous coronavirus variants did this, and because these aggregates were present in the lungs of people who died of severe illness, some scientists propose that this aggregation contributes to symptoms or helps the virus to spread. But the fusion relies on TMPRSS2, and Omicron infections don't seem to result in the same levels of syncytium formation<sup>2</sup>.

## What is the complete immune response to Omicron?

One of the body's key defences against pathogens is a molecule called interferon, which cells produce when they detect an invader. Interferon tells infected cells to ramp up their own defences — for example, by keeping viruses trapped in endosomes. Interferon also delivers a warning signal to uninfected neighbouring cells so that they can do the same.

Previous variants were able to avoid or disable many of interferon's effects. Some research suggests that Omicron has lost some of that advantage<sup>9</sup>, although other experiments find that it's better equipped to withstand interferon's effects<sup>10</sup>.

Researchers are also mapping the parts of the virus that get the attention of T cells. The viral proteins recognized by T cells seem not to have changed much in Omicron<sup>11</sup>, compared with previous SARS-CoV-2 variants.

That's good news, because although T cells are slower than antibodies to respond to a recurring threat, they're effective once they get going. This helps to stop breakthrough infections from becoming severe.

Understanding the parts of SARS-CoV-2 that rarely mutate and serve as strong T-cell activators could help vaccine designers to create [new formulations to induce this long-lasting form of immunity](#) against current and future variants.

## What comes next?

The overall Omicron data so far suggest to Barclay that Omicron could be highly contagious early on in the infection because it starts out strong. But it's possible that the viral load, along with the variant's ability to infect other cells or other people, quickly drops as it attempts to spread beyond the upper airways or as it encounters interferon.

"Omicron is very good at getting into the cells of the nose," she says. "Once it's in there, actually, I don't think that Omicron is a terribly fit virus."

The diminished severity has provided a thin silver lining to the Omicron surge, but most experts think that this won't be the final variant of concern. There are two likely scenarios going forward, says Jesse Bloom, an evolutionary virologist at the Fred Hutchinson Cancer Research Center in Seattle, Washington. One is that Omicron continues to evolve, creating some sort of Omicron-plus variant that is worse than BA. 1 or BA.2. The other possibility is that a new, unrelated variant appears.

The latter is what's happened with each variant of concern so far. "It suggests that there's a huge amount of plasticity in the virus," says Lucy Thorne, a virologist at University College London. "It's got different evolutionary options."

With dozens of mutations, Omicron explored more of the evolutionary space than the other variants. Many of Omicron's mutations ought to make it less fit, but it thrives, probably because other mutations mitigate those disadvantages.

What evolutionary options might it still have left to try? One way to make educated guesses is to let the virus evolve under controlled laboratory conditions. For example, researchers at the University of Alabama at Birmingham found, after growing the virus in several rounds of cell culture,

that the original SARS-CoV-2 strain picked up the ability to bind to heparan sulfate, a molecule on the surface of all cells<sup>[12](#)</sup>. This cultured virus still used ACE2, but the extra binding partner made it better at infecting cells.

As the study authors note, changes in cell-culture dishes don't necessarily mean that the virus would be any better at infecting animals or people; it's possible the mutations might make it inept in other ways. Thus, this type of work does not fall under the strictest definition of 'gain-of-function research of concern'.

Researchers can also put pressure on the virus in the lab, allowing it to evolve in the presence of antibodies or antiviral drugs. For example, scientists passed an early SARS-CoV-2 strain from dish to dish in the presence of the antiviral remdesivir, and the virus readily developed a mutation that made it less sensitive to the drug<sup>[13](#)</sup>.

These kinds of experiment enable researchers to predict how the virus might evolve. Finding such mutations in the lab doesn't mean they will occur in nature, but scientists tracking coronavirus genetics through surveillance can keep an eye out for them.



Animals such as hamsters might be hosts for Omicron. Credit: Louise Delmotte/Getty

SARS-CoV-2 is known to infect several animal species, [including mink, deer and hamsters](#). Some scientists think that Omicron could have passed through an animal host or hosts before it was first detected in South Africa last November. Other researchers are wondering whether it might infiltrate even more species than it is known to and then move back to humans again, potentially bringing new and dangerous adaptations.

“We have to address the elephant in the room, quite literally: where else has the virus gone, and what is it doing in those species?” says Jason Kindrachuk, a virologist at the University of Manitoba in Winnipeg, Canada, who is part of a team tackling this question. The group is checking wildlife samples for Omicron and is also testing how the virus’s spike interacts with ACE2 proteins from different species.

As for severity, there’s no guarantee that it will continue to diminish. Chan is keeping an eye on pathogenicity using the virus’s temperature preference as a clue. Viruses that stick to the upper airways replicate well at a cool 33 °C and tend to cause a milder infection. Those that prefer the 37 °C of the lungs are likely to be more virulent. The original Omicron variant doesn’t seem to grow better at either temperature, says Chan, but he’s checking its descendants now.

Whatever happens next, these and other questions will keep scientists busy with Omicron for months to come. Most current research is still preliminary, awaiting peer review and confirmation in other labs.

After all, researchers were still trying to understand Delta when Omicron emerged, notes Kindrachuk. “We’ve only really known this variant since the end of November,” he says. “We don’t know a lot yet.”

*Nature* **603**, 22-24 (2022)

*doi:* <https://doi.org/10.1038/d41586-022-00428-5>

## References

1. Hui, K. P. Y. *et al.* *Nature* <https://doi.org/10.1038/s41586-022-04479-6> (2022).
2. Peacock, T. P. *et al.* Preprint at bioRxiv  
<https://doi.org/10.1101/2021.12.31.474653> (2022).
3. Abdelnabi, R. *et al.* *Antiviral Res.* **198**, 105253 (2022).
4. Hay, J. A. *et al.* Preprint at medRxiv  
<https://doi.org/10.1101/2022.01.13.22269257> (2022).
5. Puhach, O. *et al.* Preprint at medRxiv  
<https://doi.org/10.1101/2022.01.10.22269010> (2022).
6. Willet, B. J. *et al.* Preprint at medRxiv  
<https://doi.org/10.1101/2022.01.03.21268111> (2022).
7. Wang, L. *et al.* Preprint at medRxiv  
<https://doi.org/10.1101/2022.01.12.22269179> (2022).
8. Davies, M.-A. *et al.* Preprint at medRxiv  
<https://doi.org/10.1101/2022.01.12.22269148> (2022).
9. Bojkova, D. *et al.* *Cell Res.* <https://doi.org/10.1038/s41422-022-00619-9> (2022).
10. Shalamova, L. *et al.* Preprint at bioRxiv  
<https://doi.org/10.1101/2022.01.20.476754> (2022).
11. Choi, S. J. *et al.* *Cell. Mol. Immunol.* <https://doi.org/10.1038/s41423-022-00838-5> (2022).
12. Shiliaev, N. *et al.* *J. Virol.* **95**, e01357-21 (2021).
13. Szemiel, A. M. *et al.* *PLoS Pathog.* **17**, e1009929 (2021).

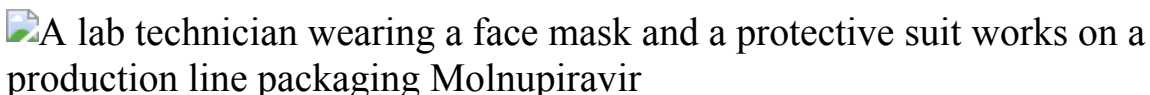
| [Section menu](#) | [Main menu](#) |

- NEWS FEATURE
- 01 March 2022

# Hundreds of COVID trials could provide a deluge of new drugs

Two years into the pandemic, the COVID-19 drugs pipeline is primed to pump out novel treatments — and fresh uses for familiar therapies.

- [Heidi Ledford](#)



A lab technician works on the production of molnupiravir, an oral antiviral drug that some countries have authorized for use against COVID-19. Credit: Amr Abdallah Dalsh/Reuters/Alamy

It takes Lawrence Tabak about 15 minutes to rattle off all the potential COVID-19 treatments being tested in the clinical trial programme he oversees: a lengthy, tongue-twisting list that includes drugs to disarm the virus, to soothe inflammation and to stop blood clots. Over the past two years, the ACTIV programme, run by the US National Institutes of Health (NIH), has included more than 30 studies — 13 of them ongoing — of therapeutic agents chosen from a list of 800 candidates. Several of the studies are due to report results in the first half of the year.

And that's just in his programme; hundreds more are in progress around the world. Whether those results are positive or negative, Tabak says, 2022 is poised to provide some much-needed clarity on how best to treat COVID-19. “The next three to four months are, we hope, going to be very exciting,” says Tabak, acting director of the NIH in Bethesda, Maryland. “Even when a trial does not show efficacy, that’s still incredibly important information. It tells you what not to use.”

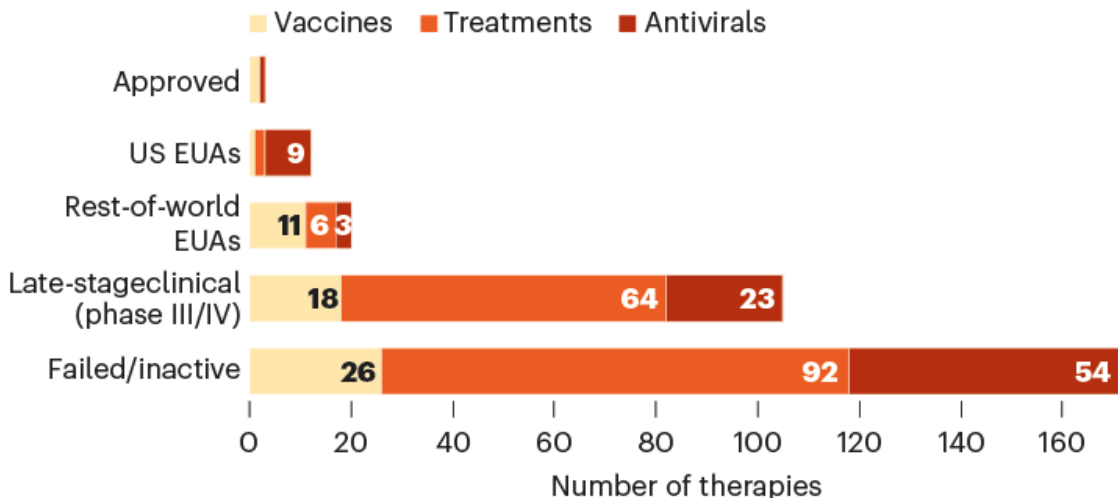
Nearly two years into the pandemic, that information is still badly needed: with more than one million new infections and thousands of deaths around the world each day, COVID-19 continues to strain health-care systems and exact a terrible human toll. Researchers have developed a handful of options — including two oral antiviral drugs, Paxlovid and molnupiravir, authorized in some countries in the past couple of months — that help in certain situations. But gaps remain, and researchers think that this year will bring new drugs and new uses for older drugs, including better treatments for mild COVID-19.

And although vaccines remain the most important way to rein in the pandemic, there is still a desperate need for better therapies [to treat people who cannot](#) — or [choose not to](#) — access the vaccines, whose immune systems cannot respond fully to vaccination, or who experience breakthrough infections. “The main tool in combating the pandemic is prevention, and the main tool in prevention is vaccination,” says Taher Entezari-Maleki, who studies clinical pharmacy at Tabriz University of Medical Sciences in Iran. “But new medications can fill in when vaccines do not work — for example against new variants.”

Over time, researchers have ramped up clinical-trial infrastructure, and repeated surges of the coronavirus SARS-CoV-2 have ensured a ready pool of potential study participants. The result has been an accelerated drug pipeline, says Tabak (see ‘Bursting pipeline’). “It has been two years, which feels like a long time for everybody,” says Paul Verdin, head of consulting and analytics at the London-based pharmaceutical analytics firm Evaluate. “But in the grand scheme of drug development, that’s not very long.”

## BURSTING PIPELINE

Researchers have devised and trialled a litany of compounds against COVID-19 — antivirals to disrupt the virus itself, treatments to improve disease symptoms, and vaccines that provide immunity. More than 100 are in late-stage trials, and a handful have emergency-use authorization (EUA) or are approved.



Data as of 24 February 2022

©nature

Source: BIO COVID-19 Therapeutic Development Tracker

## Trickle becomes flood

Early in the pandemic, much research focused on finding ways to treat people who were seriously ill with COVID-19, to save lives and ease pressures on hospitals. In mid-2020, scientists found that a steroid called dexamethasone tamps down supercharged immune responses that can contribute to late stages of severe disease, and [reduces deaths](#) in people in this group<sup>1</sup>. Such steroids remain the most effective treatments for reducing COVID-19 deaths.

Other drugs target the virus more directly but must be administered by medical professionals, limiting their use. The [antiviral drug remdesivir](#) (Veklury), made by Gilead Sciences in Foster City, California, is given as an infusion, and so was reserved, until recently, only for people hospitalized with COVID-19. (On 21 January, the US Food and Drug Administration

(FDA) authorized remdesivir for outpatient treatment of people at high risk of COVID-19 complications.)

Several firms have developed monoclonal antibodies — mass-produced versions of the neutralizing antibodies that the immune system pumps out to bind to and disable SARS-CoV-2. These therapies offered [another early route to treatment](#), and more than 200 monoclonal antibodies are now under development or authorized. But they are expensive compared with other treatments, are in short supply, and often have to be infused. One recent exception is a long-lasting combination of two monoclonal antibodies, called Evusheld. This drug, made by AstraZeneca in Cambridge, UK, can be injected into muscle, and was authorized by the FDA last December for prevention of COVID-19 in people at high risk of exposure to SARS-CoV-2.

With time, the focus began to shift to drugs that could be used outside a hospital setting to treat mild illness, in the hope of preventing progression to more severe disease. In late 2021, [two antiviral treatments](#) — Lagevrio (molnupiravir), developed by Merck, based in Kenilworth, New Jersey, and Ridgeback Biotherapeutics in Miami, Florida; and Paxlovid (a combination of two drugs, nirmatrelvir and ritonavir), developed by Pfizer, based in New York City — became available as pills that could be taken at home.

Neither drug is a panacea, notes José Carlos Menéndez Ramos, who studies pharmacy at the Complutense University of Madrid. A laboratory study<sup>2</sup> has suggested that molnupiravir might be able to cause mutations in human DNA, leading regulators to advise against its use during pregnancy. Some countries, including France and India, have chosen not to authorize it. And Paxlovid's use could be limited because it might interact with a wide range of commonly used medications.



A nurse administers a monoclonal-antibody treatment at a mobile clinic in Detroit, Michigan last December. Credit: Kimberly P. Mitchell/Detroit Free Press/TNS/ZUMA/eyevine

Luckily, the two could soon have company. Many antivirals in trials target one of two key viral proteins, with the aim of stopping the virus from replicating. Like molnupiravir, some of these target a protein called RNA-dependent RNA polymerase. About 40 candidates are under development, says Chengyuan Liang, who studies pharmacy at Shaanxi University of Science and Technology in Xi'an, China. Another roughly 180 molecules act like Paxlovid and block the SARS-CoV-2 main protease protein, which is responsible for clipping viral proteins into their final, functional forms. Of these protease inhibitors, the one that has progressed furthest is S-217622, made by Shionogi in Osaka, Japan, which is in late-stage clinical trials.

Other antiviral medications with a fresh set of targets are working their way along the pipeline. Some of them have been selected to [block the human proteins that SARS-CoV-2 uses to infiltrate cells](#), rather than viral proteins. For example, a cancer drug called plitidepsin targets a human protein called eEF1A, which is involved in making proteins and is important for the

replication of several viral pathogens. Plitidepsin has been shown to reduce SARS-CoV-2 replication in mice<sup>3</sup>, and is now in phase III clinical trials.

Targeting human proteins such as eEF1A could make it more difficult for the virus to mutate to evade the drug than when viral proteins are the target, says Ramos. “On the flip side, targeting a host protein can lead to toxicity,” he adds. In the case of plitidepsin, Ramos is hopeful that the dose required to restrict SARS-CoV-2 replication is low enough, and treatment duration short enough, for the drug to be a safe antiviral.

Researchers hope to target a smattering of other viral and human proteins important for SARS-CoV-2 replication. For example, the drug camostat, made by Ono Pharmaceutical in Osaka, inhibits a human protease, called TMPRSS2, that SARS-CoV-2 and several other coronaviruses use to enter human cells. Camostat is already used in Japan to treat non-viral conditions such as pancreatitis.

## New combinations

Some familiar COVID-19 antivirals could find fresh uses, either in a formulation that makes them easy to administer, or in different patient groups. Antivirals such as remdesivir seem to work best when given earlier in the course of infection, before severe disease sets in; researchers are working on oral formulations to see whether this definitely is the case.

Conversely, researchers also want to know whether the new oral antivirals could improve outcomes for people with severe COVID-19. Clinical trials of molnupiravir in people who have been hospitalized have suggested<sup>4</sup> that these drugs would not work against moderate or severe illness, when the immune system is contributing to the damage. But epidemiologist and infectious-disease specialist Peter Horby at the University of Oxford, UK, says that the studies of people in hospital might have been too small for researchers to draw a firm conclusion. It’s a common problem during the pandemic, he says: many investigators launched quick, small trials, enrolling too few participants to yield clear answers. Some treatments were abandoned prematurely. “The studies weren’t big enough, and stuff was being ditched way too early in our opinion,” he says.

Horby is one of the lead investigators on the UK RECOVERY trial — a large, multitherapy trial in people hospitalized with COVID-19.

RECOVERY will test molnupiravir and eventually Paxlovid, he says. Treating sicker people could be the best way to make the most of these scarce drugs. Most infected people won't develop severe disease and there is no definitive way to tell who will; giving the drug to people with mild disease might not yield as much benefit as treating those who are severely ill. While supplies of the drugs are low, he says, "you've got to target your use of a limited and expensive resource".

The RECOVERY trial will also begin to unpick whether these antivirals work synergistically when given together. Some participants in the trial will receive one of the drugs; others might receive a combination of the two, or one of the antivirals together with a monoclonal antibody. Researchers hope that combining antivirals can boost their effectiveness and reduce the chances that the virus will develop resistance to the drugs. "We don't have many antiviral options," says Horby. "If we lost any, it would be a disaster."

Researchers are exploring other options for those hospitalized with COVID-19. Treatments at this late stage often focus on the immune system, which, whipped into a frenzy by the viral infection, can begin to harm the body's own tissues. Anti-inflammatory drugs are top of the list. RECOVERY is now looking at higher doses of steroids such as dexamethasone, and several trials are studying whether diabetes drugs called SGLT2 inhibitors — also thought to have anti-inflammatory properties — help people with moderate to severe COVID-19.

## Reuse and repurpose

Globally, some of the most important trials are those that study widely available drugs developed to treat other diseases. For Philippe Guérin, director of the Infectious Diseases Data Observatory at the University of Oxford, it has been frustrating to see that many large clinical trials are focused on therapies that, in a lot of countries, will be too expensive to buy or too difficult to administer. "There is a clear disconnect between the needs of lower- to middle-income countries and the level of research," he says.

“Most of the large funding was focused on the needs of high-income countries.”



A health-care worker tests samples from people with COVID-19 as part of the ANTICOV trial.Credit: Kenny Mbala/DNDi

This was reflected in the early attention given to people with severe COVID-19, who were coming to hospitals and being treated in intensive care units (ICUs). “In low-income countries, you don’t have ICU capacity,” says Guérin. “What you want to do is try to prevent the non-severe patients from becoming severe, and that was not clearly the priority of the funders.”

Much of the early research on treating mild COVID-19 focused on monoclonal antibodies, notes public-health specialist Borna Nyaoke, clinical operations representative for East Africa at the Drugs for Neglected Diseases initiative, a non-profit organization in Nairobi. But these drugs pose a challenge in lower- and middle-income countries, she says, because of their cost, and because they need to be stored at low temperatures and administered by trained medical personnel. And the newer, oral antivirals promise to be less expensive, but are still in short supply.

For more practical solutions, Nyaoke looks to the ANTICOV trial, which is enrolling participants in 19 sites across 13 countries in sub-Saharan Africa. The trial is looking at a range of repurposed treatments, including the anti-parasitic drug ivermectin; an inhaled steroid called budesonide; and the antidepressant fluoxetine. (Other trials, including one run by ACTIV, are testing a similar antidepressant, called fluvoxamine, which has shown promise in some early clinical trials.)

Some of these treatments [have already been tested](#) — and sometimes failed — in smaller clinical trials. Ivermectin, in particular, has become a [popular but controversial COVID-19 treatment](#) in many countries, despite clinical trials indicating that the drug does not work as an antiviral in early stages of infection. Both ACTIV and ANTICOV are testing the treatment anew. ACTIV is running a trial in people with mild to moderate COVID-19, and results are due in the next few months. “No matter what we find, that will be of interest to many people,” says Tabak. The ANTICOV trial will test ivermectin for its potential anti-inflammatory properties in people seriously ill with COVID-19, and will combine it with an antimalarial drug. Preclinical data have been promising, says Nyaoke. “Combining drugs with different mechanisms of action increases a treatment’s chances of success,” she says.

Drug developers still face challenges when it comes to finding COVID-19 therapies. For instance, there is a [shortage of non-human primates](#) to use for research, and the costs of animals have skyrocketed, says Liang.

And although clinical-trial planners are not short of participants, running a trial in a pandemic is complicated: emerging viral variants can change the spectrum of symptoms, the severity of disease and the population that’s most affected. In some cases, variants have rendered COVID-19 therapies — particularly [some of the monoclonal antibodies](#) — obsolete. By contrast, broader-acting drugs such as remdesivir, which was developed in 2015 and tested against severe acute respiratory syndrome (SARS) and Middle East respiratory syndrome (MERS) in animal models, and against Ebola in humans, could be useful tools in future pandemics. In the middle of this chaos, it’s hard to know which of the many therapies in current trials will be successful, says Verdin. “The whole thing is such a big churning bubble; the

goal posts are constantly moving,” he says. “It’s very difficult to pick a winner.”

*Nature* **603**, 25–27 (2022)

*doi:* <https://doi.org/10.1038/d41586-022-00562-0>

## References

1. RECOVERY Collaborative Group *N. Engl. J. Med.* **384**, 693–704 (2021).
2. Zhou, S. *et al.* *J. Infect Dis.* **224**, 415–419 (2021).
3. White, K. M. *et al.* *Science* **371**, 926–931 (2021).
4. Arribas, J. R. *et al.* *N. Engl. J. Med. Evid.* <https://doi.org/10.1056/EVIDoa2100044> (2021).

---

This article was downloaded by **calibre** from <https://www.nature.com/articles/d41586-022-00562-0>

| [Section menu](#) | [Main menu](#) |

# Opinion

- **[G20's US\\$14-trillion economic stimulus reneges on emissions pledges](#)** [ 02 March 2022]  
Comment • Analysis of pandemic economic recovery packages from the 20 largest economies reveals that governments are not spending on emissions cuts despite promises to ‘build back better’.
- **[Disaggregate data on Asian Americans — for science and scientists](#)** [ 01 March 2022]  
Correspondence •
- **[Doctoral students benefit from international publishing](#)** [ 01 March 2022]  
Correspondence •
- **[Chile: new cabinet is rich in scientists and women](#)** [ 01 March 2022]  
Correspondence •
- **[Contrarian Botox pioneer remembered](#)** [ 01 March 2022]  
Correspondence •

- COMMENT
- 02 March 2022

# G20's US\$14-trillion economic stimulus reneges on emissions pledges

Analysis of pandemic economic recovery packages from the 20 largest economies reveals that governments are not spending on emissions cuts despite promises to ‘build back better’.

- [Jonas M. Nahm](#) <sup>0</sup>,
- [Scot M. Miller](#) <sup>1</sup> &
- [Johannes Urpelainen](#) <sup>2</sup>



An excavator at a coal mine in Indonesia. The country holds the 2022 presidency of the G20 group of largest economies. Credit: Afriadi Hikmal/NurPhoto/Getty

Governments are spending unprecedented amounts to escape the recession caused by the COVID-19 pandemic. In 2020 and 2021, the G20 group of the 20 largest economies spent at least US\$14 trillion — close to China’s annual gross domestic product. Much of that total, rightly, went to shoring up health-care systems, wages and welfare. But climate action was widely promised, too — including ‘green new deals’ and ‘building back better’.

Our analysis suggests that, so far, those promises have not been met. We created an inventory of fiscal stimulus spending during the COVID-19 pandemic in G20 economies, and classified measures according to their likely impacts on greenhouse-gas emissions.

Overall, we found that only 6% of total stimulus spending (or about \$860 billion) has been allocated to areas that will also cut emissions, including electrifying vehicles, making buildings more energy efficient and installing renewables. Worse, almost 3% of stimulus funding has targeted activities that are likely to increase global emissions, such as subsidizing the coal industry. And there's been little change in strategies as nations have shifted from economic rescue mode during lockdowns to recovery, as shops and other businesses have reopened.

Today's green investments are [proportionately less than those that followed previous recessions](#). After the global financial crisis in 2007–09, for example, 16% of global stimulus spending was directed at emissions cuts (or about \$520 billion of \$3.25 trillion in total)<sup>1</sup>. If a similar share had been committed today, the total would be \$2.2 trillion — more than double what has been pledged towards reducing emissions.

Global emissions must peak within four years to avoid catastrophic climate change (see [go.nature.com/3h9dqs](https://go.nature.com/3h9dqs)). Current rates of green investment are not enough to reach 'net zero' emissions by 2050 and limit warming to 1.5 °C — that would require around \$7 trillion during 2020–24<sup>2</sup>. As of early this year, governments have spent much more than that in responding to COVID-19, but only one-ninth of what is needed on climate mitigation.

Current stimulus packages are also failing to ready economies for a low-carbon world. Long-term investments in infrastructure, transport electrification, building efficiency and clean-energy technologies will open up new sources of economic growth<sup>3</sup>. For instance, in 2021, the global market for renewable-energy technologies — including wind and solar — reached \$366 billion, making it a lucrative area (see also [go.nature.com/3jczjx](https://go.nature.com/3jczjx)). Jobs are also created, for example, in constructing, retrofitting, installing and maintaining renewables. In 2020, the renewable-energy industry employed almost 900,000 workers in the United States and more than 12 million people globally (see [go.nature.com/3h9fejw](https://go.nature.com/3h9fejw)).

It is not too late to change course. Now that vaccines, antivirals, masks and more could be offering a path out of the pandemic (at least on paper), national economies have a prime opportunity to shift to a low-carbon footing. Governments have demonstrated that they are willing and able to

mobilize substantial resources to combat a global crisis. Some nations, especially in Europe, have spent generously to boost green growth. Major US investments have been passed as part of President Joe Biden's infrastructure package; more might yet be released by Congress.

Here we outline our findings, lessons and research priorities. We call on all governments to combine economic and climate objectives in upcoming recovery bills — even cheap measures can be effective, such as making bailouts conditional on emissions reductions. Researchers need to improve their understanding of why responses to this COVID-19 recession are different to others, to help make economies more resilient to future shocks.

## Stimulus study

Our database covers national fiscal stimulus efforts for G20 economies between 1 January 2020 and 31 December 2021 (see Supplementary information for details). We focus on the G20 economies because these account for more than 80% of global emissions (see [go.nature.com/3bnjnut](https://go.nature.com/3bnjnut)) and 85% of global economic activity. For each bill, we recorded the date of passage, the amount and the target sector or sectors.

We judged whether the impacts would cut emissions, increase them or have no effect. Emissions-reducing policies include measures that promote energy sources generating fewer emissions and that boost energy efficiency (such as building wind turbines or insulating homes), or those that decrease activities that emit greenhouse gases (such as flying or driving). Measures that increase emissions support conventional fossil-fuel industries or encourage greater energy consumption (for example, by reducing petrol taxes). Emissions-neutral policies (such as wage premiums for essential workers in Russia) had no direct impact on emissions or an indeterminate net impact on activities that emit greenhouse gases.

We evaluated whether these policies would be short term or longer-lived. The former are typically one-off and temporary bailouts (of airlines, for example). The latter include permanent policy changes and construction of major infrastructure that will alter the economy (such as high-speed railways or wind turbines).



Argentina invested in railway expansion during the COVID-19 pandemic to create jobs and improve train reliability.Credit: Martin Zabala/Xinhua/eyevine

We included only direct responses to the pandemic. For example, India dedicated almost \$14 billion to propping up its coal industry during the economic downturn, including modernizing mining infrastructure, attracting private-sector investment and reducing coal prices. By contrast, France earmarked \$66 million to subsidize bicycle parking and repairs — to encourage green transportation in citizens who shied away from public transport during the pandemic.

We used government press releases, legislative text and quotes from officials to exclude unrelated measures. We also excluded state and local measures, to focus on the large scale and avoid double-counting.

Our study does not include all climate-related spending during the pandemic. We focus on fiscal spending only and exclude other policy tools — including monetary policy and loans —through which governments can have an effect on emissions. Our research also excludes non-pandemic-

related climate spending, which at times required us to make difficult decisions on which measures to count as stimulus spending. Finally, our estimates are based on government spending announcements, particularly for long-term spending packages. Actual investments might end up differing from the numbers presented here.

## Same old

We found that, of the \$14 trillion G20 governments have pledged to fiscal stimulus since the beginning of the pandemic, less than \$1 trillion was allocated to recovery programmes that have direct or indirect climate objectives (see ‘G20 stimulus spend’). Of this amount, just over one-quarter (27%) targets measures that will cut emissions directly — for example, through grants to install insulation and energy-efficient heating systems in homes, as in the United Kingdom and Germany.

### G20 STIMULUS SPEND

Governments of the 20 largest economies spent US\$14 trillion on fiscal recovery in 2020–21 in response to the COVID-19 pandemic. Less than \$1 trillion (6%) went to policies that will reduce emissions. Most of those impacts will be indirect and depend on consumer behaviour.

#### Effect on emissions



#### Impact of spending on emissions cuts



©nature

Source: Analysis by J. Nahm *et al.*

Most of the rest of the allocation (72%) has indirect impacts. These hinge on consumer behaviour and will require more regulatory and financial incentives. Examples include investments in Germany to construct electric-vehicle charging stations as part of its Coronavirus Recovery Package. Argentina spent on expanding railways to create jobs during the pandemic, while improving the reliability and safety of passenger rail.

The remaining 1% (\$10.6 billion) went to research and development (R&D). Such efforts might yield technological breakthroughs in the future, but are unlikely to affect global emissions before 2030. Examples include \$2.2 billion in South Korea for green innovation research (such as on carbon capture and renewables), and a \$216-million boost to hydrogen-power research in Australia. This \$10.6-billion global sum is similar to the US National Science Foundation's budget request for 2022<sup>4</sup>. It is much less than the combined R&D spending of countries in the Organisation for Economic Co-operation and Development, which totalled \$1.45 trillion in 2019 (see [go.nature.com/2suftd2](https://go.nature.com/2suftd2)).

The vast majority of recovery spending (91%) did not seek to shift greenhouse-gas emissions. Often passed in large omnibus bills, such measures included funding for strained health-care systems, as expected during a pandemic. Most went to propping up the status quo: tax breaks, subsidies, business bailouts and wages paid to workers or companies to avoid lay-offs.

Little has changed since the start of pandemic. In the first six months of 2020, green recovery measures accounted for 5% of overall stimulus spending. That rose to 12% in the second half of the year, largely because the European Union passed its large emissions-reducing spending package. The share fell back to 3% in 2021.

As restrictions have lifted, new rounds of stimulus packages have paid more attention to economic recovery and rebuilding. Still, few contained climate provisions. For instance, almost all G20 economies provided financial support to domestic airlines, but only France made its support conditional on meeting climate goals by asking Air France to cease domestic flights on routes that compete with high-speed rail. No environmental conditions or

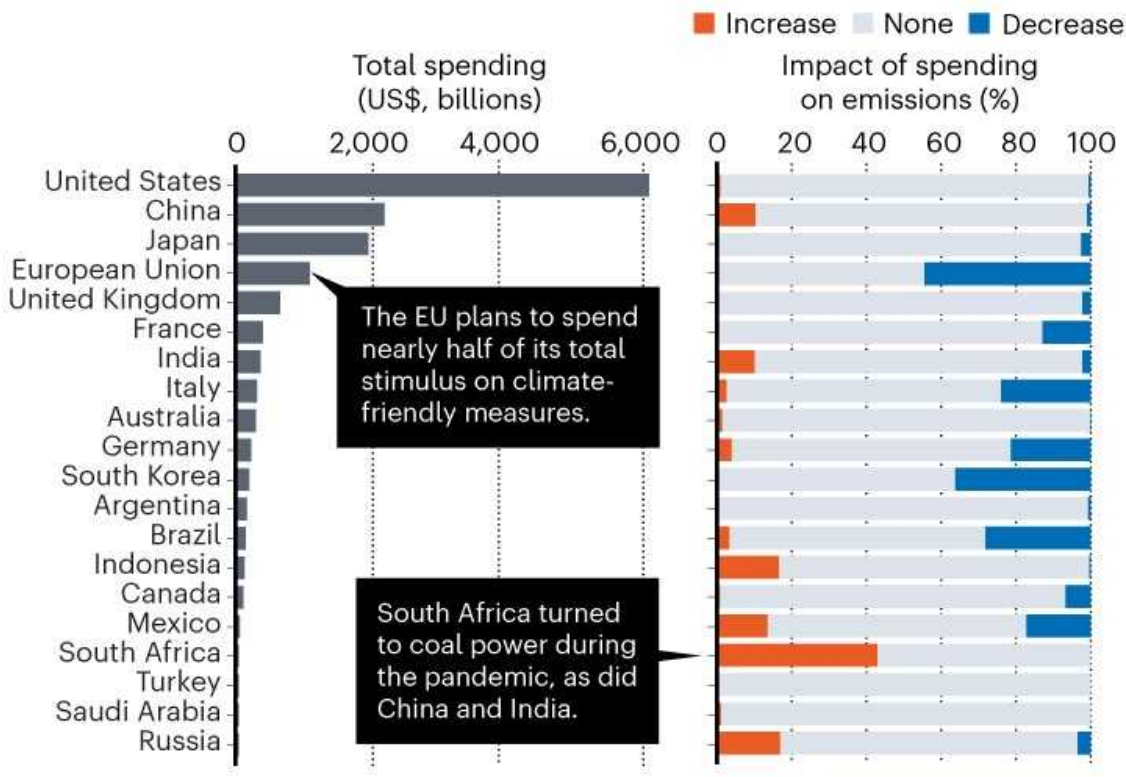
incentives were attached to the US Paycheck Protection Program or to Russia's support for its construction sector, for instance.

## Leaders and laggards

Not all countries known for ambitious climate policies, for instance through strong commitments under the Paris climate agreement, stepped up to the plate. But some governments did more than others. The European Union and South Korea led the pack (see 'Varying investments'). Each dedicated more than 30% of their COVID-19 fiscal stimulus to emissions-reducing measures — even though each had already invested nearly 60% and nearly 70% of their 2009 stimulus, respectively, in such projects<sup>1</sup>. Brazil, Germany and Italy invested more than 20%, Mexico and France over 10%. In absolute terms, the EU has pledged just shy of \$500 billion on emissions-reducing measures, while Italy has committed \$70 billion and France nearly \$50 billion.

## VARYING INVESTMENTS

Countries that rely on fossil fuels often boosted sectors that increase emissions, despite stated commitments to limit global average temperature rise.



©nature

Source: Analysis by J. Nahm *et al.*

Such nations have, smartly, used stimulus packages to address many sectors at once. For example, Germany's budget will promote wind- and solar-energy deployment, energy-efficient buildings, electric and hydrogen-powered vehicles and more-efficient buses and aeroplanes.

At the other extreme, economies that are laggards are those dependent on fossil fuels, such as India, China and South Africa. China cut electricity prices by 5% in 2020 to ease financial stresses. It asked coal mines to increase production to help to stabilize prices. India delayed the deadline for coal power plants to implement air-pollution control measures. South Africa earmarked \$11.4 billion in guarantees to buy electricity from power plants (largely coal) in the face of plummeting demand, while decreasing purchases of wind power.

The middle of the pack holds the most surprises. The United States, Japan, Canada and the United Kingdom each committed less than 10% of recovery funds to emissions-reducing causes. These small investments stand in stark contrast to their official commitments to the Paris climate goals.

This gap is concerning in the United States and China. Together, they account for more than 35% of total emissions (see [go.nature.com/3bnjnut](https://go.nature.com/3bnjnut)) and 59% of global stimulus spending. In this pandemic, China directed much of its stimulus to boosting new emissions-neutral sectors, including 5G mobile-phone networks, artificial intelligence and data centres. Yet in 2009, its priorities were high-speed rail, grid modernization, waste management and the solar industry.

That said, hopeful signs are emerging from the Biden administration and Chinese president Xi Jinping. In 2020, China announced its first official net-zero carbon goal and, in 2021, alone installed more offshore wind power than the rest of the world has done since 2016<sup>5</sup>. The United States rejoined the Paris agreement in 2021 and included investments in public transit, vehicle electrification and grid modernization in its infrastructure bill. Other climate legislation remains stalled in Congress.

But the United States and China have also committed large sums to supporting fossil-fuel-intensive industries and infrastructure projects in their recovery packages. These include unconditional bailouts for US domestic airlines and investments in Chinese roads and industrial parks. Such measures could have been conditional on meeting emissions goals or targeted at green industries.

## Missed opportunity

Why have governments missed this chance to restructure their economies? The answer requires further research. Historically, governments have often prioritized economic growth over environmental and climate policy<sup>6</sup>. Yet the view that emissions reductions and economic recovery are irreconcilable is incorrect. It is also at odds with growing concerns about the vulnerability of global supply chains that have led governments to build up domestic

manufacturing, particularly in clean technology sectors, for which the world depends on China.

The COVID-19 recession was worse than previous ones, and different in cause. Spending decisions have focused on weathering a short-term health crisis and fighting economic fires. Structural problems in the economy lay behind the 2007–09 financial crisis, and received more attention.

Changing political landscapes are another factor. For example, having already invested heavily in clean-energy sectors after 2009, a country such as China might not feel the need to do so again so soon<sup>7</sup>. US presidents have come and gone. Congressional gridlock has stymied progress on President Biden's climate agenda in 2021. In 2009, former US president Barack Obama was able to pass climate-friendly recovery measures with greater congressional majorities.

## Paths forward

There is still time for improvement. Four lessons can be learnt from recovery efforts.

First, governments should apply environmental conditions to stimulus bills. It is cheap and effective. As France has shown for aviation, attaching climate targets to corporate bailouts can shift entire sectors onto more sustainable trajectories at minimal cost to governments.

Second, governments should focus on recovery measures that have direct emissions impacts<sup>8</sup>. They should accelerate public spending on renewable energy to reduce the consumption of fossil fuels and increase the energy efficiency of housing, as in South Korea's Green New Deal. Or they could invest in vehicle electrification, as Germany has done by purchasing electric vehicles for government fleets.

Third, governments should position their economies strategically to compete in a post-carbon world. That means investing in low-carbon industries. It also requires building institutions to make economies more resilient to future shocks, and to help those who rely on fossil-fuel-based industries to

transition to new livelihoods. The EU recovery programme, for instance, offers grants, loans and subsidies to new industrial sectors, for instance by creating a European battery-supply chain. The EU has also pledged to use a portion of proceeds from the European emissions-trading scheme to fund training programmes and compensate those who lose employment as a result of the energy transition.

Fourth, the climate community, economists and social scientists need to examine the reasons behind the current drop in emissions-reducing recovery spending. Why are there large cross-national differences in approaches to stimulus, even between countries that have similar political institutions and levels of economic development? What kinds of investment will yield the best outcomes for both climate and economic recovery?

As the COVID-19 pandemic is showing, governments that turn a blind eye to risks fail to guard their citizens' lives and livelihoods.

*Nature* **603**, 28–31 (2022)

doi: <https://doi.org/10.1038/d41586-022-00540-6>

## References

1. Jaeger, J., Westphal, M. I. & Park, C. *Lessons Learned on Green Stimulus: Case Studies from the Global Financial Crisis* (World Resources Institute, 2020).
2. Andrijevic, M., Schleussner, C.-F., Gidden, M. J., McCollum, D. L. & Rogelj, J. *Science* **370**, 298–300 (2020).
3. Meckling, J. & Allan, B. B. *Nature Clim. Change* **10**, 434–438 (2020).
4. US National Science Foundation. *FY 2022 Budget Request to Congress* (NSF, 2021).
5. Vetter, D. ‘China Built More Offshore Wind In 2021 Than Every Other Country Built In 5 Years.’ *Forbes* (26 January 2022).

6. Mol, A. P. J. *Environ. Polit.* **25**, 48–68 (2016).
7. Nahm, J. *Collaborative Advantage: Forging Green Industries in the New Global Economy* (Oxford Univ. Press, 2021).
8. Hepburn, C., O'Callaghan, B., Stern, N., Stiglitz, J. & Zenghelis, D. *Oxford Rev. Econ. Pol.* **36**, S359–S381 (2020).

---

This article was downloaded by **calibre** from <https://www.nature.com/articles/d41586-022-00540-6>

| [Section menu](#) | [Main menu](#) |

- CORRESPONDENCE
- 01 March 2022

# Disaggregate data on Asian Americans — for science and scientists

- [Kao Lee Yang](#) 

Data on Asian Americans in the United States are aggregated across dozens of ethnicities and languages with roots in Asia. In my experience as a Hmong American researcher, this practice is suboptimal for science and scientists.

## Access options

Subscribe to Nature+

Get immediate online access to the entire Nature family of 50+ journals

\$29.99

monthly

[Subscribe](#)

Subscribe to Journal

Get full journal access for 1 year

\$199.00

only \$3.90 per issue

## Subscribe

All prices are NET prices.

VAT will be added later in the checkout.

Tax calculation will be finalised during checkout.

Buy article

Get time limited or full article access on ReadCube.

\$32.00

## Buy

All prices are NET prices.

## **Additional access options:**

- [Log in](#)
- [Learn about institutional subscriptions](#)

*Nature* **603**, 32 (2022)

*doi:* <https://doi.org/10.1038/d41586-022-00539-z>

---

This article was downloaded by **calibre** from <https://www.nature.com/articles/d41586-022-00539-z>

- CORRESPONDENCE
- 01 March 2022

# Doctoral students benefit from international publishing

- [Serhii Nazarovets](#) ORCID: <http://orcid.org/0000-0002-5067-4498> 0

The current terrifying situation in Ukraine threatens to halt my nation's research activities ([Nature 602, 555–556; 2022](#)).

## Access options

Subscribe to Nature+

Get immediate online access to the entire Nature family of 50+ journals

\$29.99

monthly

[Subscribe](#)

Subscribe to Journal

Get full journal access for 1 year

\$199.00

only \$3.90 per issue

[Subscribe](#)

All prices are NET prices.  
VAT will be added later in the checkout.  
Tax calculation will be finalised during checkout.

Buy article

Get time limited or full article access on ReadCube.

\$32.00

[Buy](#)

All prices are NET prices.

### **Additional access options:**

- [Log in](#)
- [Learn about institutional subscriptions](#)

*Nature* **603**, 32 (2022)

*doi:* <https://doi.org/10.1038/d41586-022-00538-0>

---

This article was downloaded by **calibre** from <https://www.nature.com/articles/d41586-022-00538-0>

| [Section menu](#) | [Main menu](#) |

- CORRESPONDENCE
- 01 March 2022

# Chile: new cabinet is rich in scientists and women

- [Cristián Bonacic](#) 

Chile's incoming government has appointed Maisa Rojas — a leading climate-change researcher — as its new minister of the environment to help speed up progress towards a green economy. Rojas has been involved in the 26th United Nations Climate Change Conference of the Parties (COP26) and in the latest report by the Intergovernmental Panel on Climate Change. She joins a cabinet now dominated by women (for the first time in the country's history) and by graduates who studied abroad under Chile's 30-year-old science scholarship programme.

## Access options

Subscribe to Nature+

Get immediate online access to the entire Nature family of 50+ journals

\$29.99

monthly

[Subscribe](#)

Subscribe to Journal

Get full journal access for 1 year

\$199.00

only \$3.90 per issue

[Subscribe](#)

All prices are NET prices.

VAT will be added later in the checkout.

Tax calculation will be finalised during checkout.

Buy article

Get time limited or full article access on ReadCube.

\$32.00

[Buy](#)

All prices are NET prices.

### **Additional access options:**

- [Log in](#)
- [Learn about institutional subscriptions](#)

*Nature* **603**, 32 (2022)

*doi:* <https://doi.org/10.1038/d41586-022-00536-2>

---

This article was downloaded by **calibre** from <https://www.nature.com/articles/d41586-022-00536-2>

- CORRESPONDENCE
- 01 March 2022

# Contrarian Botox pioneer remembered

- [Eric A. Johnson](#)<sup>0</sup> &
- [Dirk Dressler](#)<sup>1</sup>

Undeterred by the apparent absurdity of using the world's deadliest known poison as a clinical treatment, Alan Brown Scott — who died last December, aged 89 — first developed botulinum toxin as a treatment for involuntary muscle hyperactivity. This treatment can now be used for at least 26 conditions in 6 medical specialties.

## Access options

Subscribe to Nature+

Get immediate online access to the entire Nature family of 50+ journals

\$29.99

monthly

[Subscribe](#)

Subscribe to Journal

Get full journal access for 1 year

\$199.00

only \$3.90 per issue

## Subscribe

All prices are NET prices.

VAT will be added later in the checkout.

Tax calculation will be finalised during checkout.

Buy article

Get time limited or full article access on ReadCube.

\$32.00

## Buy

All prices are NET prices.

## **Additional access options:**

- [Log in](#)
- [Learn about institutional subscriptions](#)

*Nature* **603**, 32 (2022)

*doi:* <https://doi.org/10.1038/d41586-022-00596-4>

---

This article was downloaded by **calibre** from <https://www.nature.com/articles/d41586-022-00596-4>

# Work

- **[Rooting African science and technology education in cultures and languages](#)** [ 15 February 2022]  
Career Feature • The continent's role in the global economy depends on development from within.
- **[The wise counsel that can drive public-health research in Kenya](#)** [ 09 February 2022]  
Career Feature • Finding the right working culture pays dividends when trying to juggle academia and parenthood in Africa.
- **[Advance Kenyan science by seizing opportunities to collaborate](#)** [ 14 February 2022]  
Career Feature • How networks can help to win research grants and equip labs in Africa.
- **[Capacity building to boost science in Ethiopia](#)** [ 10 February 2022]  
Career Feature • Experience gained overseas can be used to develop home-grown solutions to local challenges.
- **[Cut the tyranny of copy-and-paste with these coding tools](#)** [ 28 February 2022]  
Technology Feature • ‘Executable manuscripts’ insert results directly into documents, eliminating common mistakes.
- **[Protector of giant salamander](#)** [ 28 February 2022]  
Where I Work • Wansheng Jiang studies the endangered Chinese giant salamander to better protect its habitat.

- CAREER FEATURE
- 15 February 2022

# Rooting African science and technology education in cultures and languages

The continent's role in the global economy depends on development from within.

- [Kendall Powell](#) 0

[Find a new job](#)



Molecular biologist and entrepreneur Khady Sall helps to guide students towards jobs in biotechnology and artificial intelligence. Credit: Ricci Shryock for *Nature*

## Voices from Africa

In the final article of this eight-part series about the career experiences of African women scientists, Khady Sall explains how seeing the 2018 superhero film Black Panther contributed to her decision to return to her native Senegal and develop her career there. The film depicts an African nation, posing as a developing country while creating advanced technologies.

Sall is an entrepreneur and molecular biologist at the Virtual University of Senegal in Dakar. She founded a non-profit organization called Science Education Exchange for Sustainable Development (SeeSD) to promote science, technology, engineering, arts and maths (STEAM) education, critical thinking and scientific literacy to young people in Senegal. She also founded an innovation lab named Ubbil.

I did my PhD at Oregon State University in Corvallis on the genetics of seed dormancy and drought tolerance. When I finished in 2017, I hesitated a bit about a career in academia. It wouldn't be satisfying for me if it had no direct impact on my community. I wasn't motivated to apply for many postdocs because I felt like that would be doing a PhD 2.0 — I didn't want to commit to another four years. But I knew that I would also struggle to build a research career from nothing if I came back to Senegal.

Seeing the action film Black Panther triggered something in me. The vision it portrays — of how local language, culture and ancestral knowledge can be integrated with science — was something I had spoken about at many conferences. About two months later, I woke up one day and bought a plane ticket home.

People think that development in Africa should look like that in the United States or France. But is everything going well in those places right now? We are always going to be behind if we are aiming for ‘the United States in 2022’. Sustainable development has to be rooted in the culture, preserving

local languages and integrating ancestral practices that are good for the environment. It has to resemble you and where you want your country to go. You can get there by being authentic and you can do that by teaching science in the local language, such as Wolof, a language of Senegal, Gambia and Mauritania.

This is the reason I came back to grow SeeSD. Compared with getting a job in the United States, working in Senegal is not predictable or stable. It's seriously not easy — the day-to-day is a struggle.

But, I chose the struggle. I was pushing myself and pushing my SeeSD colleagues, too. We were young, we lacked experience, we made mistakes, but we learnt by doing. I've grown so much since I came back. You have to negotiate the lack of funding, human resources and training. We started something out of nothing.

You have to navigate the politics, too. Some people associate having ambitions with becoming a politician and they can suspect you of having a different motive. This can make local funders skittish about supporting your organization.

But we clearly need to expand science, technology, engineering and mathematics education. The ramifications of the COVID-19 pandemic are showing us the dangers of not guiding students towards jobs in biotechnology and artificial intelligence that will define the future. If we are not part of the global economy, leveraging knowledge to create technologies, then we are doomed.

Gender bias is an issue for women everywhere, and here I also encounter bias against young people. I try to overcome these biases by speaking through my work. It's not my personality to promote myself on social media as an influencer or at international conferences.

Instead, I push my work ahead. Sometimes people don't know who is behind the work. But eventually, it's your achievements that validate you. If you prove you can do it, you show that you are a capable person. This is why I was asked to set up master's and bachelor's degree programmes in molecular genetics and bioinformatics at the Virtual University. We are

working to set up the laboratory space for both teaching courses and research. These programmes are not yet established, and everything has to be started from scratch.

I don't have kids of my own because I'm so focused on my work. I'm satisfied that I get to be independent. I can have an idea, work on it and see it become a reality. I like that.

I work with a lot of women and, as a supervisor, I have to be flexible because they have so much going on with their families. There needs to be more female-founded businesses out there to accommodate women better, because women give so much back to businesses.

The hardest part about being a female entrepreneur is that you will definitely need to work twice as hard as a man to succeed. People will tend to underestimate you. But at some point, you should be unapologetic about your leadership. Just get the work done. Show your organizational skills.

In 2020, I led a project to manufacture face shields for health-care workers across Senegal for protection against COVID-19. It required coordinating several organizations. Some people doubted that, as a young woman, I could be an assertive leader. At one point, I had to reaffirm that I was in charge and keep us going. Not everyone liked that, but who cares? Once you reach your goal, you have proven yourself.

And you need to find something that really fires you up — work that you find amazing. That will give you the drive and energy you need to get ahead of the older men.

The experience you gain from your PhD can be applied to the African context: 'we are in start-up countries'. The skills I learned doing my master's and PhD — starting something from scratch, trying to get a publication and gaining independence and critical thinking — those expertise are much needed here. They are extremely useful for getting things done.

*doi: <https://doi.org/10.1038/d41586-022-00449-0>*

This interview has been edited for length and clarity.

---

This article was downloaded by **calibre** from <https://www.nature.com/articles/d41586-022-00449-0>

| [Section menu](#) | [Main menu](#) |

- CAREER FEATURE
- 09 February 2022

# The wise counsel that can drive public-health research in Kenya

Finding the right working culture pays dividends when trying to juggle academia and parenthood in Africa.

- [Kendall Powell](#) 0

[Find a new job](#)



Elizabeth Kimani-Murage had to learn to find time to do all the necessary work.Credit: African Population and Health Research Centre

## **Voices from Africa**

In the fifth instalment of an eight-part series about African women in science, Elizabeth Kimani-Murage, head of maternal and child well-being at the African Population and Health Research Center (APHRC) in Nairobi, describes the importance of quiet hours to write as an early-career public-health researcher.

After I got my master's degree in 2004 from Moi University in Eldoret, Kenya, I took a three-year research traineeship at the APHRC while I applied for PhD programmes.

My focus at the APHRC was on food insecurity and malnutrition in the urban poor in Nairobi. For my PhD, I got a scholarship to the University of the Witwatersrand (Wits) in Johannesburg, South Africa, to investigate the double burden of malnutrition — stemming from obesity in adolescents and under-nutrition in young children.

When I was admitted to my PhD programme in 2007, my child was 2 years old. My husband said he would help to take care of the baby, and we decided the child would grow up in Kenya. I knew I had to finish my PhD within three years. I negotiated alternating three months in South Africa with two months working remotely from Kenya. It was really hectic. I worked past midnight many nights.

But it was worth the effort, because Wits provides a high-quality education and I could complete the programme in a short time. In Kenya, it can take up to ten years to get a PhD and many people give up. I also wanted to gain experience outside Kenya.

When I returned to the APHRC in 2010, my colleagues called me a publishing machine. I was a prolific writer and I was able to publish my master's and PhD work. I have also partnered with a lot of co-authors.

I pass along my mum's advice to me: nothing good comes along easily. You have to be diligent and work hard. You cannot sit back and expect results. As a young researcher, I learnt to find time to do the work, managing projects and logistics during the day, and finding quiet time to learn the science of writing.

I got into that culture of working, finding an hour or two in the evenings to write a few paragraphs. If you don't find that time, you'll never write.

Work-life balance is a big challenge for all researchers, but as a woman here, you also have the major responsibility of your family. I promote exclusive breastfeeding for the first six months of a baby's life in my work, and was keen to do this when my second child was born. But it's a real challenge when you are working. I had to wake up early to express breast milk, go home to breastfeed at lunchtime and then express again after work and stay up until midnight to feed the baby. It was exhausting and difficult.

My workplace had some policies that were supportive of pregnant mothers, but we didn't have a breastfeeding room on site at that time. Now we do, and my research in this area helped to influence that. Kenya's policies for working mothers are generally supportive, but there could be improvements, such as extending maternity leave beyond three months. The APHRC has just started an on-site childcare facility for babies.

Women are respected as much as men at my workplace, but for true gender equality to happen, institutions might need policies to ensure that women's careers advance at the same rate as men's. Women take leave to care for children, they do the reproductive work and most of the care in those first years. For example, as part of evaluations for promotions, policies could take into account that extra work that women do.

*Nature* **603**, 188-189 (2022)

*doi:* <https://doi.org/10.1038/d41586-022-00392-0>

This interview has been edited for length and clarity.

---

This article was downloaded by **calibre** from <https://www.nature.com/articles/d41586-022-00392-0>

- CAREER FEATURE
- 14 February 2022

# Advance Kenyan science by seizing opportunities to collaborate

How networks can help to win research grants and equip labs in Africa.

- [Kendall Powell](#) <sup>0</sup>

[Find a new job](#)



Environmental scientist Veronica Okello develops sustainable approaches to clean up heavy metals.Credit: Esther Sweeney for *Nature*

**Voices from Africa**

Some Kenyans have a tendency to equate quietness with being nice, says analytical environmental chemist Veronica Okello at Machakos University in Kenya. She urges young researchers to be less timid, air their views and approach their professors for professional opportunities. In this seventh article of eight describing the career experiences of African women in science, Okello describes how support from family members enabled her to study abroad, and how she cultivates the networks she forged overseas to foster collaborations.

I was a part-time lecturer at Masinde Muliro University of Science and Technology in Kakamega, Kenya, when I was offered a PhD fellowship at Binghamton University in New York in 2008. By then, I was married, with two boys, aged 3 and 5.

My husband and my late mother were so supportive. They said, “You go. We’re going to help you.” Every summer, my husband came to the United States with the children, and every Christmas he sent my ticket to visit home. He sent money for my car and apartment, and called every day: if it was 7 p.m., my fellow graduate students knew who was calling when my phone rang. I returned to Kenya in December 2014 and became a lecturer at Machakos University in February 2015. I teach undergraduate and graduate students analytical and environmental chemistry and the fundamentals of nanotechnology. I founded the Go Green Chemistry Club for students; club members plant trees and do environmental clean-ups and science projects.

My research focuses on developing green, sustainable approaches to clean up heavy metals, such as chromium, arsenic and lead, that pollute the environment. For example, chromium-6 is a carcinogen, but chromium-3 is benign, so we are looking for environmentally friendly compounds that can reduce chromium-6 to chromium-3.

Doing research after returning to Kenya has been challenging. I had many more publications on my CV during my PhD programme than in the time after it. But collaboration has done wonders. I have relied on my US network to help me win six grants to adequately equip our laboratory from scratch. Collaborating with established professors here and at other universities in Kenya has also helped me. A group of lecturers, hired at my

university between 2015 and 2018, write grants together to buy equipment for research and teaching.

I tell young female researchers in Kenya that there are many opportunities — but you have to step out of your comfort zone and look for them. They will not come to you. You have to put in the work.

Often, I see people raised in Kenya who are timid and scared of approaching their professors. They think that being quiet is being nice. But I advise young researchers to have a great personality and to respectfully talk and air their views. Approaching professors for opportunities is a way to be on the right path. And once an opportunity comes, grab it and run with it.

Young women who have already started their families can face big challenges. I advise these women to see whether their spouses can support them in pursuing further studies — not necessarily abroad, but maybe in their own country.

Once early-career researchers have a university position, they should identify someone at their institution to be their mentor. For me, this was Zachary Getenga, an analytical chemist who has consistently guided me on how to write grant proposals. He watches out for me. I'm in my eighth year as a lecturer and should have been promoted already. But in our promotion system, single-author papers count for more than grants or publications with multiple authors. I feel so demotivated by this. But he tells me to keep going, to build my profile.

The policy committees of Kenyan universities are typically dominated by men. If I sat on one of these committees, I would change the promotion policy to award points to people who bring in grants and equipment to the university. I have brought in analytical equipment, including an electrochemical analyser, worth more than US\$28,000 — that is a lot of service to the university!

As a woman in science, the most limiting factor we have is time. Writing grants takes a lot of time and effort that competes with my teaching, administrative meetings and family time. I try to create my own time — this

is why I'm doing this interview on Zoom from my car. You have to create the time when you want to succeed.

*Nature* **603**, 189-190 (2022)

*doi:* <https://doi.org/10.1038/d41586-022-00451-6>

This interview has been edited for length and clarity.

---

This article was downloaded by **calibre** from <https://www.nature.com/articles/d41586-022-00451-6>

| [Section menu](#) | [Main menu](#) |

- CAREER FEATURE
- 10 February 2022

# Capacity building to boost science in Ethiopia

Experience gained overseas can be used to develop home-grown solutions to local challenges.

- [Kendall Powell](#) ✉

[Find a new job](#)



Aster Tsegaye encourages young researchers to apply for opportunities to work in overseas laboratories and with high-tech equipment. Credit: Maheder Haileselassie for *Nature*

## Voices from Africa

In the sixth of eight articles about the career experiences of female scientists in Africa, Aster Tsegaye, an immuno-haematology researcher at Addis Ababa University and a fellow of the Ethiopian Academy of Sciences, describes how her mother's support and encouragement enabled her to study abroad. She also offers advice on how to work during political unrest.

When I graduated from Addis Ababa University with a biology degree in 1987, I was assigned to a haematology laboratory in what was then the Ethiopian National Research Institute of Health (which now forms part of the Ethiopian Public Health Institute). In those days, when you graduated from higher education you were assigned a job. I didn't know anything about haematology. All I knew was that it was an 'ology'.

A lesson for the younger generation is that if you don't get what you like, like what you get. I had to learn on the job from senior lab technicians who were always busy. So, by doing all the 'busy work' jobs, such as clerical work and washing lab equipment, I made sure the technicians had time in the afternoons to teach me and check my work. Even though I had a higher academic degree, I admitted my limitations, acknowledged their expertise and respected them. In the evenings, I taught myself from a textbook. Two years later, I was teaching a haematology course at the institute's School of Medical Laboratory Technology. Next, I started a master's thesis on anaemia caused by hookworm infection.

At that time, in the mid-1990s, HIV was gripping sub-Saharan Africa. I had a chance to work on the Ethiopia–Netherlands AIDS Research Project, a decade-long collaboration to conduct research on HIV/AIDS, which set up an HIV reference laboratory in Ethiopia and trained Ethiopian researchers in epidemiology. Through that programme, I began my PhD at the University of Amsterdam in 2000. It meant starting when my second baby was 11 months old and my older son was almost 3. My mum, who never finished secondary school, said, "Go for it." She offered to look after my kids.

Still, it was hard to leave them. The first time you go away, you can promise them you'll bring chocolates back. But after that, they beg you not to go. My

PhD was a sandwich programme, which meant spending three months in Amsterdam and nine months in Ethiopia for each of the four years.

Now, there are opportunities to do a PhD in Ethiopia, but I think having exposure and experience in international laboratories, and working with other scientists and with high-tech equipment is important. I would advise young researchers to develop their research and then apply for grants or scholarships for international opportunities.

Doing science is even more challenging amid unrest, but we should contribute to peace and stability wherever we can. It's important not to panic and to stay calm. Social media should be used to promote peace and not to disseminate negative or fake news.

Whatever challenge we have, there is always a solution. When I returned to Addis Ababa University in 2007 and joined the school of medical laboratory sciences as a professor, it was one of the least-equipped schools on campus. I proposed that we standardized what we were teaching on our courses across other major universities in Ethiopia for training medical lab professionals to work on HIV/AIDS, and we did that in partnership with the American Society for Clinical Pathology based in Chicago, Illinois.

Although I've had opportunities to work in high-tech labs, I preferred to build the capacity of my department here. I am a firm believer in capacity building. We convinced management at the Centers for Disease Control and Prevention in Ethiopia (the US public-health agency established a presence here in 2001) that our students needed hands-on experience. I coordinated the procurement and distribution of immune-cell-count analysers and clinical chemistry equipment to eight universities that taught medical laboratory science. I didn't build my own lab, but I'm satisfied with what I did at that stage, because now we are harvesting that expertise.

*Nature* **603**, 190 (2022)

*doi:* <https://doi.org/10.1038/d41586-022-00401-2>

This interview has been edited for length and clarity.

---

This article was downloaded by **calibre** from <https://www.nature.com/articles/d41586-022-00401-2>

| [Section menu](#) | [Main menu](#) |

- TECHNOLOGY FEATURE
- 28 February 2022

# Cut the tyranny of copy-and-paste with these coding tools

‘Executable manuscripts’ insert results directly into documents, eliminating common mistakes.

- [Jeffrey M. Perkel](#)

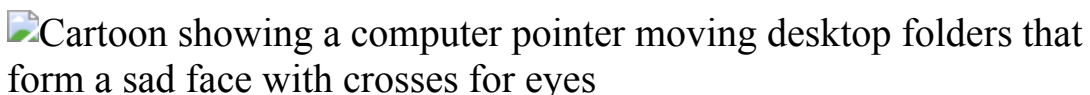


Illustration by The Project Twins

If you’ve written a scientific manuscript, there’s a good chance you’re familiar with the app-switching two-step that happens when you copy your data from one program and paste them into another. That time-tested workflow does the job, but it isn’t always the most efficient process.

Perhaps you receive new samples and need to update your numbers. Or maybe you have to fix an error you made when processing your data. In any event, you must repeat the analysis, then comb through the manuscript line by line to find all the values that are now out of date. Oversights are inevitable.

Many tech-savvy researchers take a different path. These researchers use computational notebook systems such as R Markdown, Jupyter Book and Observable to create ‘executable manuscripts’, which insert data as the document is rendered, rather than copying and pasting them in. As long as the underlying data are up to date and the computations accurate, so, too, will be the final product.

Bjørn Peare Bartholdy, a bioarchaeologist at Leiden University in the Netherlands, used that approach when preparing a preprint he posted on bioRxiv last October ([B. P. Bartholdy and A. G. Henry Preprint at bioRxiv https://doi.org/hf5d; 2021](#)). As he wrote up his findings on what starch granules in dental calculus can tell us about diet, Bartholdy realized that he had made a mistake in extrapolating the final counts. “All of the numbers changed,” he says. But because those values were computed in R Markdown, it took him all of two minutes to correct his work. “I don’t know how much time that would have saved,” he adds.

It’s not the easiest way to write a paper, Bartholdy concedes. It requires computational know-how and a steep learning curve. And flexibility is needed when collaborating with less tech-savvy co-authors. But many argue that the pay-off is worth the investment. “It reduces the amount of stupid manual things that you have to do,” says Sarah Pederzani, a geochemist at the Max Planck Institute for Evolutionary Anthropology in Leipzig, Germany. Bartholdy concurs: “I now work infinitely more efficiently than I did before.”

## Transparency

Researchers in the physical sciences and mathematics have long blended workflow engines such as Make and Snakemake with the LaTeX typesetting system to create beautifully formatted PDFs ready to post on the arXiv preprint server. But LaTeX is an unforgiving language. Today, many researchers write in Markdown, which is easier to learn, and then convert that into LaTeX and other outputs. R Markdown, so named because it includes and can execute R code; Jupyter Book, a tool that was created to build online books from Jupyter Notebooks and text files; and Observable, a commercial JavaScript notebook system, all use Markdown to format text.

Ben Marwick, an archaeologist at the University of Washington in Seattle, has written “around a dozen” papers using R Markdown. He says that the workflow dovetails with his broader interest in open science and scientific transparency. Data science, he says, involves multiple “very small decisions” — data cleaning and filtering steps, for instance, which are crucially important, but difficult to document. And journal page limits

preclude exposition. But by blending code, data and text in a single document, researchers can show just how their results were generated. “It’s an extremely efficient way to communicate as much of the process as we can,” Marwick says. “It makes your analyses and everything much cleaner and easier to reproduce,” says Pederzani, “because you’re basically making a self-contained analysis file and manuscript in one.”

## Version control

Executable documents, like all software code, can be posted to the platform GitHub. They can be version-controlled when the document changes, and rendered into multiple output formats. Using BibTeX, a bibliographic format supported by most citation managers, researchers can build bibliographies. And using ‘styles’, they can format documents to meet journal specifications. I created an example R Markdown manuscript (see [go.nature.com/3jkjkt9](https://go.nature.com/3jkjkt9)), which can be converted to HTML, Word or PDF with a template used by Springer Nature, which publishes *Nature*. (See [go.nature.com/3jgf2es](https://go.nature.com/3jgf2es) for a comparable manuscript in Observable.)

Although text and code can be contained in a single file, many authors separate those elements. R Markdown, for instance, allows authors to import ‘child’ documents into a manuscript, which simplifies version control and collaboration, says Mine Çetinkaya-Rundel, a statistician at Duke University in Durham, North Carolina. (Our example notebook uses this approach.)

Authors can also ‘cache’ blocks of code that are computationally intensive, as well as import pre-built images and data rather than computing them anew with each build. Taylor Reiter, a computational biologist at the University of Colorado Anschutz Medical Campus in Aurora, compiled her PhD thesis in R Markdown by cobbling together figures she had created throughout her studies, shortening her thesis build time from about 12 minutes to 30 seconds. “These eleven-and-a-half extra minutes were key to my mental sanity during the dissertation-writing period,” she jokes.

Tiffany Timbers, a statistician at the University of British Columbia in Vancouver, Canada, says that executable manuscripts provide transparency

by detailing how results were generated and making it straightforward to replicate them. “You really lack this when you use something like Word or a Google Doc for writing a manuscript that involves data analysis,” she says.

And perhaps nowhere is that transparency clearer than when programming code is used to insert the relevant numbers into the text as the document builds — a technique known as inline execution. “In the ‘compute in R and type in Word’ workflow, the human in-between is responsible for making sure the latest results are reflected in the document. That’s a lot of copying and pasting and keeping track of stuff,” says Çetinkaya-Rundel. But with inline execution, “there’s really no way to break that reproducibility, because as you update your code and you render your document, you end up with the latest results”.

R Markdown, Jupyter Book and Observable all support inline code execution. Authors could, for instance, indicate the number of samples in a study by counting the rows in a table, or insert the version number of a computational package in their methods. “The inline code just completely allows you to sleep well at night,” Marwick says.

## Features and formats

RStudio, a development environment for R (free for academic users), includes a bare-bones what-you-see-is-what-you-get visual editor to ease the R Markdown writing process. A toolbar provides basic formatting options such as bold and italic, as well as the ability to insert tables and citations. Libraries such as ‘Bookdown’ (an R package that automatically numbers document sections, figures and tables when creating online books) and ‘Rticles’ (which provides article templates for Springer Nature and several other scientific publishers), enhance the experience. Observable provides a slick browser-based editing environment, whereas Jupyter Book uses a blend of browser and command-line tools.

Whatever the platform, executable manuscripts require technical skill and speciality tools. Bartholdy’s paper, he notes, required several years of work. “I’m not gonna lie, it was a little painful. And it is a steep learning curve.”

Mariana Montes, a linguist at the Catholic University of Leuven in Belgium, advises starting small, for instance by writing up individual experiments or analyses. “Do it for a report for yourself while you get comfortable with R Markdown, and do not start with R Markdown with your thesis — that’s going to be crazy,” she says.

Formatting can be particularly painful. R Markdown uses a tool called Pandoc to transform Markdown into the desired output, often through a LaTeX intermediate, and it’s easy to fall foul of the LaTeX rendering engine. A misplaced backslash, for instance, can lead to “strange error messages that people have a hard time understanding”, Pederzani says.

## Collaboration tricks

The other main difficulty involves collaboration. Computed manuscripts are generally written in plain-text editors rather than in word processors, and collaborative writing and commenting are rarely supported. (Observable is an exception, allowing Google Docs-style collaboration.) Instead, collaborators can make comments in the form of GitHub ‘pull requests’ — suggested code (or text) changes that can be reviewed and incorporated into the document directly. That’s how Reiter worked with one of her thesis advisers, computational biologist C. Titus Brown. But for her other, less tech-savvy adviser, she knit her thesis into a Word document and then manually folded the suggestions back into R Markdown.

As an alternative to pull requests, Timbers suggests that collaborators take advantage of GitHub’s ‘issues’ interface, which is conventionally used to discuss bugs and suggest features. “You don’t need any version-control skills to open an issue, it’s like posting on a forum,” she says.

Developers have created tools that can help to ease the collaborative workflow. The Trackdown package, for instance, can push and pull R Markdown files to Google Docs so that collaborators can work on them. A package called Redoc provides similar functionality for Word documents. RStudio is also developing a next-generation tool called [Quarto](#), which helps users to build computational documents with Python, R and JavaScript through integration with Jupyter, Observable and an R package

called Knitr. According to chief executive J. J. Allaire, planned improvements will ease researchers' ability to collaborate by allowing them to review Quarto manuscripts in an editor "that will kind of look and feel a lot like Google Docs".

The bottom line is that computed manuscripts can be a powerful tool for scientific writing. But they're not for everyone. Reiter found it a relatively easy way to turn text into a dissertation, but she's adept at using computational tools. "For the trade-off of not having to format my thesis, in a heartbeat I would do that again," she says. But would she advise others to use it? "Soft recommend," she laughs.

*Nature* **603**, 191-192 (2022)

*doi:* <https://doi.org/10.1038/d41586-022-00563-z>

---

This article was downloaded by **calibre** from <https://www.nature.com/articles/d41586-022-00563-z>

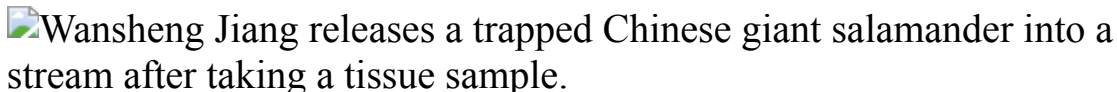
| [Section menu](#) | [Main menu](#) |

- WHERE I WORK
- 28 February 2022

# Protector of giant salamander

Wansheng Jiang studies the endangered Chinese giant salamander to better protect its habitat.

- [Andy Tay](#) <sup>0</sup>



Wansheng Jiang is an associate professor at Jishou University. Credit: Wu Huiyuan/Sixth Tone

I study the Chinese giant salamander (*Andrias davidianus*), which is native to the Yangtze River Basin of central China. This particular species is critically endangered in the wild owing to habitat loss and overcatching — a particular problem is their use in traditional Chinese medicine. My research focuses on the salamander's conservation biology and evolutionary ecology.

In this photo, I am releasing a Chinese giant salamander at the Golden Whip River in Zhangjiajie National Forest Park on an early morning in September 2021. My team and I caught the salamander the night before, to measure its size and collect tissue samples for genetic analyses.

My interest in aquatic animals started as a child. I grew up in a rural village in Hunan province, and I remember spending most of my childhood playing and fishing near my home. Because of this, I knew where each fish species lived in nearby rivers and lakes, and it sparked my interest in river ecology.

I'm employed as an associate professor at Jishou University, where I lead a team dedicated to researching this species of salamander. Wild salamanders

are quiet, nocturnal animals that live in remote areas. This makes studying them challenging. My team tried many creative ways to track down the animals, including walking along riverbanks with torches and photographing salamanders under water — but these techniques didn't work as well as we needed them to. We eventually found that the best way to trap wild salamanders is to use small live fish and chicken livers as bait. The research is challenging, but we've learnt to be patient and celebrate every small success we have.

Studying Chinese giant salamanders has also taught me an important life lesson: adapt to thrive. When food is abundant, the salamanders grow rapidly; when food is scarce, they can go up to 11 months without feeding. In my personal life and work, I have experienced successes and failures, and taking on that lesson has been useful.

*Nature* **603**, 194 (2022)

*doi:* <https://doi.org/10.1038/d41586-022-00564-y>

---

This article was downloaded by **calibre** from <https://www.nature.com/articles/d41586-022-00564-y>.

| [Section menu](#) | [Main menu](#) |

# Research

- **[Mechanism underlying a risk gene in neurodegeneration](#)** [ 23 February 2022]  
News & Views • Messenger RNA from the gene UNC13A is misprocessed in people who have neurodegenerative diseases known as ALS and FTD. The discovery could explain the disease risk associated with variants in this gene.
- **[Plasmas primed for rapid pulse production](#)** [ 02 March 2022]  
News & Views • A plasma-based device is set to challenge particle accelerators that generate high-quality light pulses, with evidence that the cheaper plasma platform can run at competitive repetition rates.
- **[From the archive](#)** [ 01 March 2022]  
News & Views • Nature's pages feature a look at some books for travellers, and success reported in the effort to preserve a Stone Age monument.
- **[Isotopes tracked on a sub-nanometre scale using electron spectroscopy](#)** [ 02 March 2022]  
News & Views • Measurements of atomic vibrations can now identify chemical isotopes on a sub-nanometre scale in an electron microscope. An innovative approach makes use of this resolution to build and track isotopic domains.
- **[Light-dependent development is tailored in visual neurons](#)** [ 18 February 2022]  
News & Views • When mouse pups first open their eyes, what they see shapes neuronal connectivity. A study shows that this visual experience has cell-type-specific effects, acting only on a subset of malleable neurons.
- **[Lung microbes mediate spinal-cord autoimmunity](#)** [ 23 February 2022]  
News & Views • Lung bacteria modulate the activity of immune cells in the central nervous system in a rodent model of autoimmunity. This finding might shed light on the neuroinflammation associated with multiple sclerosis.
- **[Progress and prospects in magnetic topological materials](#)** [ 02 March 2022]  
Review Article • Recent theoretical and experimental progress in identifying and understanding magnetic topological materials is reviewed, highlighting the antiferromagnetic topological insulator MnBi<sub>2</sub>Te<sub>4</sub> and the ferromagnetic Weyl semimetal Co<sub>3</sub>Sn<sub>2</sub>S<sub>2</sub>, and future research directions are discussed.

- **A persistent ultraviolet outflow from an accreting neutron star binary transient** [ 02 March 2022]

Article • A persistent, blue-shifted absorption feature is reported in time-resolved UV spectroscopy of the neutron star binary Swift J1858.6-0814, revealing a warm, moderately ionized component in the accretion disk that is wind driven from this system.

- **Recovery time of a plasma-wakefield accelerator** [ 02 March 2022]

Article • Relaxation of a perturbed plasma back to its initial state over nanosecond timescales establishes that megahertz repetition rates are supported, and high luminosities and brilliances are in principle attainable with plasma-wakefield accelerator facilities.

- **High-density switchable skyrmion-like polar nanodomains integrated on silicon** [ 02 March 2022]

Article • Two types of skyrmion-like polar nanodomain are observed in oxide bilayers transferred onto silicon, and these nanodomains, with distinct resistive behaviour, can be converted to each other under an external electric field.

- **Imaging of isotope diffusion using atomic-scale vibrational spectroscopy** [ 02 March 2022]

Article • Vibrational electron energy-loss spectroscopy is used to distinguish two stable isotopes of carbon and to monitor their diffusion with subnanometre spatial resolution.

- **All-perovskite tandem solar cells with improved grain surface passivation** [ 17 January 2022]

Article • A certified efficiency of 26.4% in all-perovskite tandem solar cells, exceeding that of the best-performing single-junction perovskite solar cells, is achieved by control over surface defects in the Pb–Sn subcell.

- **Biocatalytic oxidative cross-coupling reactions for biaryl bond formation** [ 02 March 2022]

Article • A study presents a biocatalytic method for the formation of sterically hindered biaryl bonds, providing a tunable approach for assembling molecules with catalyst-controlled reactivity, site selectivity and atroposelectivity.

- **A wet heterogeneous mantle creates a habitable world in the Hadean** [ 02 March 2022]

Article • A hydrated, heterogeneous mantle resulting from magma ocean solidification is shown to be key to the rapid formation of Earth's habitable surface environment during the Hadean era.

- **The Mesozoic terminated in boreal spring** [ 23 February 2022]

Article • Examination of fish that died on the day the Mesozoic ended reveal that the impact that caused the Cretaceous–Palaeogene mass extinction occurred during boreal spring.

- **Genetic associations of protein-coding variants in human disease** [ 23 February 2022]
 

Article • A meta-analysis combining whole-exome sequencing data from UK Biobank participants and imputed genotypes from FinnGen participants enables identification of genetic associations with human disease in the rare and low-frequency allelic spectrum
- **Determinants of emissions pathways in the coupled climate–social system** [ 16 February 2022]
 

Article • A stylized model of the climate–social system could help to understand policy and emissions futures.
- **A global timing mechanism regulates cell-type-specific wiring programmes** [ 23 February 2022]
 

Article • Integration of a global temporal transcriptional module with cell-type-specific transcription factors influences neuronal wiring in the fly visual system.
- **A biophysical account of multiplication by a single neuron** [ 23 February 2022]
 

Article • Release from shunting inhibition and coincident excitation implement a multiplication-like synaptic interaction in motion-sensing neurons of *Drosophila melanogaster*.
- **TDP-43 represses cryptic exon inclusion in the FTD–ALS gene UNC13A** [ 23 February 2022]
 

Article • TDP-43 controls an exon splicing event in UNC13A that results in the inclusion of a cryptic exon associated with frontotemporal dementia and amyotrophic lateral sclerosis.
- **TDP-43 loss and ALS-risk SNPs drive mis-splicing and depletion of UNC13A** [ 23 February 2022]
 

Article • Risk variants for ALS and FTD in the synaptic gene UNC13A increase the expression of an UNC13A cryptic exon in neurons with TDP-43 depletion.
- **The lung microbiome regulates brain autoimmunity** [ 23 February 2022]
 

Article • Work in experimental autoimmune models shows that the lung microbiome is linked to immune reactivity in the brain through a mechanism in which the balance of pulmonary microorganisms regulates the activation state of microglia.
- **The cGAS–STING pathway drives type I IFN immunopathology in COVID-19** [ 19 January 2022]
 

Article • The cGAS–STING pathway has a central role in the pathogenesis of severe COVID-19 by driving the increase in type I interferons that occurs in the later stages of SARS-CoV-2 infection.

- **Twin study reveals non-heritable immune perturbations in multiple sclerosis** [ 16 February 2022]  
Article • In monozygotic twins discordant for multiple sclerosis, the influence of genetic predisposition and environmental factors is determined using matched-pair analyses.
- **Low-dose metformin targets the lysosomal AMPK pathway through PEN2** [ 23 February 2022]  
Article • The molecular target of the antidiabetic medicine metformin is identified as PEN2, a subunit of  $\gamma$ -secretases, and the PEN2–ATP6AP1 axis offers potential targets for screening for metformin substitutes.
- **Effective drug combinations in breast, colon and pancreatic cancer cells** [ 23 February 2022]  
Article • A survey of potency and efficacy of 2,025 clinically relevant two-drug combinations against 125 molecularly characterized breast, colorectal and pancreatic cancer cell lines identifies rare synergistic effects of anticancer drugs, informing rational combination treatments for specific cancer subtypes.
- **Structure and receptor recognition by the Lassa virus spike complex** [ 16 February 2022]  
Article • The structure of the complete native spike complex of Lassa virus reveals its membrane topology and the matriglycan-depended recognition of its  $\alpha$ -dystroglycan cellular receptor.
- **Structural architecture of the human NALCN channelosome** [ 20 December 2021]  
Article • The structure of the human NALCN channelosome and a model of the gating mechanism are determined.

- NEWS AND VIEWS
- 23 February 2022

# Mechanism underlying a risk gene in neurodegeneration

Messenger RNA from the gene *UNC13A* is misprocessed in people who have neurodegenerative diseases known as ALS and FTD. The discovery could explain the disease risk associated with variants in this gene.

- [Noa Lipstein](#)    [ORCID: http://orcid.org/0000-0002-0755-5899](#) 

Two devastating neurodegenerative diseases, motor neuron disease (amyotrophic lateral sclerosis; ALS) and frontotemporal dementia (FTD), share common risk factors and involve similar cellular abnormalities.

Despite immense efforts, research has identified only a few genes in which variants are linked to the risk of developing these diseases. One such gene is *UNC13A*, variations in which have been strongly associated with the risk<sup>1,2</sup> of both ALS and FTD, and with faster disease progression<sup>3</sup>. Writing in *Nature*, [Brown et al.](#)<sup>4</sup> and [Ma et al.](#)<sup>5</sup> identify a functional link between *UNC13A* and the activity of TDP-43, a protein involved in neurodegeneration; they also provide evidence to explain the risk brought about by variations in *UNC13A*. Their work brings together disparate information to provide a more coherent picture of how ALS and FTD might progress.

## Access options

Subscribe to Nature+

Get immediate online access to the entire Nature family of 50+ journals

\$29.99

monthly

[Subscribe](#)

Subscribe to Journal

Get full journal access for 1 year

\$199.00

only \$3.90 per issue

[Subscribe](#)

All prices are NET prices.

VAT will be added later in the checkout.

Tax calculation will be finalised during checkout.

Buy article

Get time limited or full article access on ReadCube.

\$32.00

[Buy](#)

All prices are NET prices.

### **Additional access options:**

- [Log in](#)
- [Learn about institutional subscriptions](#)

*Nature* **603**, 33-34 (2022)

*doi:* [\*https://doi.org/10.1038/d41586-022-00383-1\*](https://doi.org/10.1038/d41586-022-00383-1)

# References

1. Diekstra, F. P. *et al.* *Ann. Neurol.* **76**, 120–133 (2014).
2. van Es, M. A. *et al.* *Nature Genet.* **41**, 1083–1087 (2009).
3. Diekstra, F. P. *et al.* *Neurobiol. Aging* **33**, 630.e3–630.e8 (2012).
4. Brown, A.-L. *et al.* *Nature* <https://doi.org/10.1038/s41586-022-04436-3> (2022).
5. Ma, X. R. *et al.* *Nature* <https://doi.org/10.1038/s41586-022-04424-7> (2022).
6. Neumann, M. *et al.* *Science* **314**, 130–133 (2006).
7. Polymenidou, M. *et al.* *Nature Neurosci.* **14**, 459–468 (2011).
8. Augustin, I., Rosenmund, C., Südhof, T. C. & Brose, N. *Nature* **400**, 457–461 (1999).
9. Lipstein, N. *et al.* *Neuron* **109**, 3980–4000 (2021).
10. Varoqueaux, F., Sons, M. S., Plomp, J. J. & Brose, N. *Mol. Cell. Biol.* **25**, 5973–5984 (2005).
11. Sigler, A. *et al.* *Neuron* **94**, 304–311 (2017).
12. Nakashima-Yasuda, H. *et al.* *Acta Neuropathol.* **114**, 221–229 (2007).

---

This article was downloaded by **calibre** from <https://www.nature.com/articles/d41586-022-00383-1>

- NEWS AND VIEWS
- 02 March 2022

# Plasmas primed for rapid pulse production

A plasma-based device is set to challenge particle accelerators that generate high-quality light pulses, with evidence that the cheaper plasma platform can run at competitive repetition rates.

- [Michael Litos](#) 0

Particle accelerators are usually associated with the discovery of fundamental particles, but they also have a long history of powering light sources. One such source is the free-electron laser, in which a high-energy beam of electrons from a linear accelerator generates ultrashort X-ray laser pulses by travelling through a series of magnets. However, conventional accelerators are expensive and unwieldy, needing up to one kilometre of space under Earth's surface, and a smaller, cheaper accelerator based on plasma (ionized gas) might be capable of doing the job. The plasma in such a device needs to settle before each new interaction with the electron beam, but the interactions must be repeated at a high rate to power a free-electron laser that has sufficient average brilliance. [Writing in Nature](#), D'Arcy *et al.*<sup>1</sup> report that the maximum repetition rate of a plasma-based accelerator could be as high as one million times per second — or even higher, putting it comfortably in the realm of nearly all potential applications.

## Access options

Subscribe to Nature+

Get immediate online access to the entire Nature family of 50+ journals

\$29.99

monthly

[Subscribe](#)

Subscribe to Journal

Get full journal access for 1 year

\$199.00

only \$3.90 per issue

[Subscribe](#)

All prices are NET prices.

VAT will be added later in the checkout.

Tax calculation will be finalised during checkout.

Buy article

Get time limited or full article access on ReadCube.

\$32.00

[Buy](#)

All prices are NET prices.

### **Additional access options:**

- [Log in](#)
- [Learn about institutional subscriptions](#)

*Nature* **603**, 34-35 (2022)

*doi:* <https://doi.org/10.1038/d41586-022-00544-2>

# References

1. D'Arcy, R. *et al.* *Nature* **603**, 58–62 (2022).
2. Lindstrøm, C. A. *et al.* *Phys. Rev. Lett.* **126**, 014801 (2021).
3. Gonsalves, A. J. *et al.* *Phys. Rev. Lett.* **122**, 084801 (2019).
4. Litos, M. *et al.* *Nature* **515**, 92–95 (2014).
5. Wang, W. *et al.* *Nature* **595**, 516–520 (2021).
6. Rovige, L. *et al.* *Phys. Rev. Accel. Beams* **23**, 093401 (2020).

---

This article was downloaded by **calibre** from <https://www.nature.com/articles/d41586-022-00544-2>

| [Section menu](#) | [Main menu](#) |

- NEWS AND VIEWS
- 01 March 2022

## From the archive

*Nature's* pages feature a look at some books for travellers, and success reported in the effort to preserve a Stone Age monument.

**100 years ago**

### Access options

Subscribe to Nature+

Get immediate online access to the entire Nature family of 50+ journals

\$29.99

monthly

[Subscribe](#)

Subscribe to Journal

Get full journal access for 1 year

\$199.00

only \$3.90 per issue

[Subscribe](#)

All prices are NET prices.

VAT will be added later in the checkout.

Tax calculation will be finalised during checkout.

Buy article

Get time limited or full article access on ReadCube.

\$32.00

[Buy](#)

All prices are NET prices.

### **Additional access options:**

- [Log in](#)
- [Learn about institutional subscriptions](#)

*Nature* **603**, 35 (2022)

*doi:* <https://doi.org/10.1038/d41586-022-00546-0>

---

This article was downloaded by **calibre** from <https://www.nature.com/articles/d41586-022-00546-0>

| [Section menu](#) | [Main menu](#) |

- NEWS AND VIEWS
- 02 March 2022

# Isotopes tracked on a sub-nanometre scale using electron spectroscopy

Measurements of atomic vibrations can now identify chemical isotopes on a sub-nanometre scale in an electron microscope. An innovative approach makes use of this resolution to build and track isotopic domains.

- [Jordan A. Hachtel](#) <sup>0</sup>

The isotopes of an atom have the same number of protons, but different numbers of neutrons. Changing the neutron count changes the mass of an atom, but it doesn't have a pronounced effect on its chemical properties. As a result, isotopes feature in a host of techniques used in biological and materials sciences, where they function as atomic-scale labels that can track specific compounds in heterogeneous samples and can trace chemical-reaction pathways. To make the most of isotopic labelling, isotopes must be detected with high spatial resolution. [Writing in Nature](#), Senga *et al.*<sup>1</sup> report that, using a specialized electron microscopy technique, they have identified isotopic labels with sub-nanometre spatial resolution, allowing the behaviour of the labelled atoms to be revealed as they move around the crystal.

## Access options

Subscribe to Nature+

Get immediate online access to the entire Nature family of 50+ journals

\$29.99

monthly

[Subscribe](#)

Subscribe to Journal

Get full journal access for 1 year

\$199.00

only \$3.90 per issue

[Subscribe](#)

All prices are NET prices.

VAT will be added later in the checkout.

Tax calculation will be finalised during checkout.

Buy article

Get time limited or full article access on ReadCube.

\$32.00

[Buy](#)

All prices are NET prices.

### **Additional access options:**

- [Log in](#)
- [Learn about institutional subscriptions](#)

*Nature* **603**, 36-37 (2022)

*doi:* <https://doi.org/10.1038/d41586-022-00545-1>

# References

1. Senga, R. *et al.* *Nature* **603**, 68–72 (2022).
2. Poplawsky, J. D. *et al.* *Scr. Mater.* **210**, 114411 (2022).
3. Zhang, R. *et al.* *Nature* **498**, 82–86 (2013).
4. Krivanek, O. L. *et al.* *Nature* **514**, 209–212 (2014).
5. Lagos, M. J., Trügler, A., Hohenester, U. & Batson, P. E. *Nature* **543**, 529–532 (2017).
6. Li, X. *et al.* *Science* **371**, 1364–1367 (2021).
7. Hoglund, E. R. *et al.* *Nature* **601**, 556–561 (2022).
8. Cheng, Z. *et al.* *Nature Commun.* **12**, 6901 (2021).
9. Qi, R. *et al.* *Nature* **599**, 399–403 (2021).
10. Yan, X. *et al.* *Nature* **589**, 65–69 (2021).
11. Hage, F. S., Radtke, G., Kepaptsoglou, D. M., Lazzeri, M. & Ramasse, Q. M. *Science* **367**, 1124–1127 (2020).
12. Hachtel, J. A. *et al.* *Science* **363**, 525–528 (2019).
13. Zan, R., Ramasse, Q. M., Bangert, U. & Novoselov, K. S. *Nano Lett.* **12**, 3936–3940 (2012).
14. Gan Y., Sun, L. & Banhart, F. *Small* **4**, 587–591 (2008).

---

This article was downloaded by **calibre** from <https://www.nature.com/articles/d41586-022-00545-1>

- NEWS AND VIEWS
- 18 February 2022

# Light-dependent development is tailored in visual neurons

When mouse pups first open their eyes, what they see shapes neuronal connectivity. A study shows that this visual experience has cell-type-specific effects, acting only on a subset of malleable neurons.

- [Sergi Roig Puiggros](#) ORCID: <http://orcid.org/0000-0001-5909-218X><sup>0</sup> &
- [Denis Jabaudon](#) ORCID: <http://orcid.org/0000-0003-2438-4769><sup>1</sup>

Environmental stimuli have a crucial role in shaping a developing organism's behaviour. Birds readily accept foster parents — even human ones — provided they see them at birth<sup>1</sup>. Cats raised in an environment consisting only of vertical stripes are later unable to see horizontal lines<sup>2</sup>. Even (brainless) bacteria must react to changes in environmental lactose to keep on thriving and dividing<sup>3</sup>. Distinguishing inborn (nature) from acquired (nurture) facets of development is thus a fundamental quest in biology, and particularly so in the developing brain. But, despite decades of research, we do not understand precisely how the environment shapes the brain at the molecular, cellular and circuit levels. [Writing in Cell](#), Cheng *et al.*<sup>4</sup> take on this challenge by investigating how postnatal visual experience affects distinct neuronal cell types in the maturing mouse brain.

## Access options

Subscribe to Nature+

Get immediate online access to the entire Nature family of 50+ journals

\$29.99

monthly

[Subscribe](#)

Subscribe to Journal

Get full journal access for 1 year

\$199.00

only \$3.90 per issue

[Subscribe](#)

All prices are NET prices.

VAT will be added later in the checkout.

Tax calculation will be finalised during checkout.

Buy article

Get time limited or full article access on ReadCube.

\$32.00

[Buy](#)

All prices are NET prices.

### **Additional access options:**

- [Log in](#)
- [Learn about institutional subscriptions](#)

*Nature* **603**, 37-38 (2022)

*doi:* <https://doi.org/10.1038/d41586-022-00463-2>

# References

1. Lorenz, K. *J. Ornithol.* **83**, 137–213 (1935).
2. Blakemore, C. & Cooper, G. F. *Nature* **228**, 477–478 (1970).
3. Jacob, F. & Monod, J. *J. Mol. Biol.* **3**, 318–356 (1961).
4. Cheng, S. *et al.* *Cell* **185**, 311–327 (2022).
5. Ding, J. *et al.* *Nature Biotechnol.* **38**, 737–746 (2020).
6. Jabaudon, D. *Nature Commun.* **8**, 16042 (2017).
7. Espinosa, J. S. & Stryker, M. P. *Neuron* **75**, 230–249 (2012).
8. Lin, Y. *et al.* *Nature* **455**, 1198–1204 (2008).
9. Reh, R. K. *et al.* *Proc. Natl Acad. Sci. USA* **117**, 23242–23251 (2020).
10. Davis, M. F. *et al.* *Neuron* **86**, 1055–1066 (2015).

---

This article was downloaded by **calibre** from <https://www.nature.com/articles/d41586-022-00463-2>

| [Section menu](#) | [Main menu](#) |

- NEWS AND VIEWS
- 23 February 2022

# Lung microbes mediate spinal-cord autoimmunity

Lung bacteria modulate the activity of immune cells in the central nervous system in a rodent model of autoimmunity. This finding might shed light on the neuroinflammation associated with multiple sclerosis.

- [Aubrey M. Schonhoff](#) <sup>0</sup> &
- [Sarkis K. Mazmanian](#) <sup>1</sup>

Chronic, uncontrolled inflammation of healthy tissues can lead to damage and autoimmune disease. There is growing evidence that both autoimmunity and the development of normal immune responses in humans are linked to the microbiome — the community of trillions of microorganisms that colonize body surfaces. Most research so far has focused on bacteria living in the gut, with microbial communities in the colon being the most diverse and abundant. There is evidence<sup>1–3</sup> that interactions between the microbiome and the brain have a role in some brain disorders and in complex behaviours such as sociability, although most such studies have focused on the gut–brain axis in animal models.

## Access options

Subscribe to Nature+

Get immediate online access to the entire Nature family of 50+ journals

\$29.99

monthly

## Subscribe

Subscribe to Journal

Get full journal access for 1 year

\$199.00

only \$3.90 per issue

## Subscribe

All prices are NET prices.

VAT will be added later in the checkout.

Tax calculation will be finalised during checkout.

Buy article

Get time limited or full article access on ReadCube.

\$32.00

## Buy

All prices are NET prices.

## **Additional access options:**

- [Log in](#)
- [Learn about institutional subscriptions](#)

*Nature* **603**, 38-40 (2022)

*doi:* <https://doi.org/10.1038/d41586-022-00468-x>

## **References**

1. Lee, Y. K., Menezes, J. S., Umesaki, Y. & Mazmanian, S. K. *Proc. Natl Acad. Sci. USA* **108** (Suppl. 1), 4615–4622 (2011).
2. Cekanaviciute, E. *et al.* *Proc. Natl Acad. Sci. USA* **114**, 10713–10718 (2017).
3. Berer, K. *et al.* *Nature* **479**, 538–541 (2011).
4. Hosang, L. *et al.* *Nature* <https://doi.org/10.1038/s41586-022-04427-4> (2022).
5. Gollwitzer, E. S. *et al.* *Nature Med.* **20**, 642–647 (2014).
6. Odoardi, F. *et al.* *Nature* **488**, 675–679 (2012).
7. Sender, R., Fuchs, S. & Milo, R. *Cell* **164**, 337–340 (2016).
8. Englehardt, B. & Ransohoff, R. M. *Trends Immunol.* **33**, 579–589 (2012).
9. Prinz, M. *et al.* *Immunity* **28**, 675–686 (2008).
10. Wendeln, A.-C. *et al.* *Nature* **556**, 332–338 (2018).
11. Vatanen, T. *et al.* *Cell* **165**, 842–853 (2016).
12. Mundt, S. *et al.* *Sci. Immunol.* **4**, eaau8380 (2019).

---

This article was downloaded by **calibre** from <https://www.nature.com/articles/d41586-022-00468-x>

- Review Article
- [Published: 02 March 2022](#)

# Progress and prospects in magnetic topological materials

- [B. Andrei Bernevig](#) [ORCID: orcid.org/0000-0001-6337-4024<sup>1</sup>](#),
- [Claudia Felser](#) [ORCID: orcid.org/0000-0002-8200-2063<sup>2</sup>](#) &
- [Haim Beidenkopf](#) [ORCID: orcid.org/0000-0003-0139-1835<sup>3</sup>](#)

[Nature](#) volume **603**, pages 41–51 (2022)

- 2021 Accesses
- 98 Altmetric
- [Metrics details](#)

## Subjects

- [Topological matter](#)

## Abstract

Magnetic topological materials represent a class of compounds with properties that are strongly influenced by the topology of their electronic wavefunctions coupled with the magnetic spin configuration. Such materials can support chiral electronic channels of perfect conduction, and can be used for an array of applications, from information storage and control to dissipationless spin and charge transport. Here we review the theoretical and experimental progress achieved in the field of magnetic topological materials, beginning with the theoretical prediction of the

quantum anomalous Hall effect without Landau levels, and leading to the recent discoveries of magnetic Weyl semimetals and antiferromagnetic topological insulators. We outline recent theoretical progress that has resulted in the tabulation of, for the first time, all magnetic symmetry group representations and topology. We describe several experiments realizing Chern insulators, Weyl and Dirac magnetic semimetals, and an array of axionic and higher-order topological phases of matter, and we survey future perspectives.

This is a preview of subscription content

## Access options

Subscribe to Nature+

Get immediate online access to the entire Nature family of 50+ journals

\$29.99

monthly

[Subscribe](#)

Subscribe to Journal

Get full journal access for 1 year

\$199.00

only \$3.90 per issue

[Subscribe](#)

All prices are NET prices.

VAT will be added later in the checkout.

Tax calculation will be finalised during checkout.

Buy article

Get time limited or full article access on ReadCube.

\$32.00

[Buy](#)

All prices are NET prices.

### Additional access options:

- [Log in](#)
- [Learn about institutional subscriptions](#)

**Fig. 1: Interplay between magnetic orders and topology.**



**Fig. 2: Magnetic topological insulators—realizations and  $\text{MnBi}_2\text{Te}_4$  case study.**

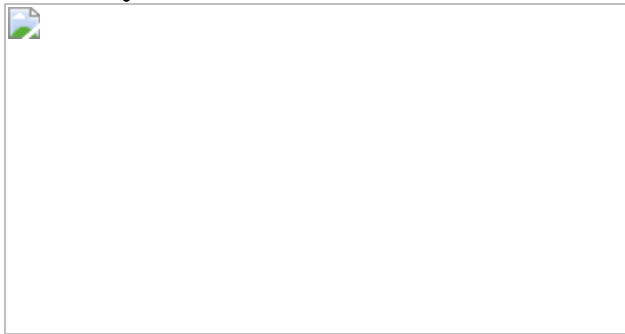
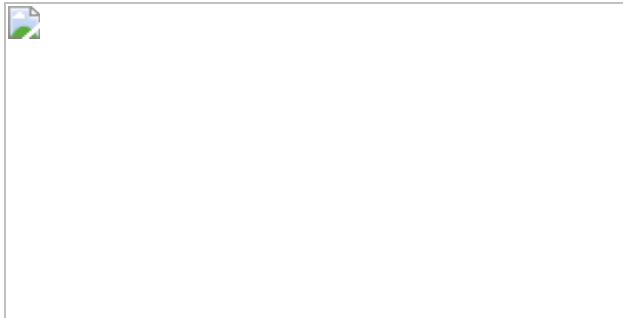


**Fig. 3: Magnetic topological semimetals— $\text{Co}_3\text{Sn}_2\text{S}_2$  case study.**



## References

1. Kane, C. L. & Mele, E. J. Quantum spin Hall effect in graphene. *Phys. Rev. Lett.* **95**, 226801 (2005).
2. Bernevig, B. A., Hughes, T. L. & Zhang, S.-C. Quantum spin Hall effect and topological phase transition in HgTe quantum wells. *Science* **314**, 1757–1761 (2006).
3. Kitaev, A. Y. U. Fault-tolerant quantum computation by anyons. *Ann. Phys.* **303**, 2–30 (2003). **This paper shows how to implement topological quantum computing in magnetic superconducting systems.**
4. Pesin, D. & MacDonald, A. H. Spintronics and pseudospintronics in graphene and topological insulators. *Nat. Mater.* **11**, 409–416 (2012).
5. Rajamathi, C. R. et al. Weyl semimetals as hydrogen evolution catalysts. *Adv. Mater.* **29**, 1606202 (2017). **This paper represents the first application of a Weyl semimetal for catalysis.**
6. Xu, Y. et al. High-throughput calculations of magnetic topological materials. *Nature* **586**, 702–707 (2020). **This paper represents the first high-throughput magnetic topological calculations.**
7. Elcoro, L. et al. Magnetic topological quantum chemistry. *Nat. Commun.* **12**, 5965 (2021). **This paper develops the full theory of topological insulators and metals in magnetic groups.**

8. Watanabe, H., Po, H. C. & Vishwanath, A. Structure and topology of band structures in the 1651 magnetic space groups. *Sci. Adv.* **4**, aat8685 (2018).
9. Morali, N. et al. Fermi-arc diversity on surface terminations of the magnetic Weyl semimetal  $\text{Co}_3\text{Sn}_2\text{S}_2$ . *Science* **365**, 1286–1291 (2019).  
**This paper shows the relevance of the distinct surface potentials imposed by three different terminations on the modification of the Fermi-arc contour and Weyl node connectivity.**
10. Otkrov, M. M. et al. Prediction and observation of an antiferromagnetic topological insulator. *Nature* **576**, 416–422 (2019).  
**This paper predicts and realizes an antiferromagnetic topological insulator in a bulk material for the first time.**
11. Noky, J., Zhang, Y., Gooth, J., Felser, C. & Sun, Y. Giant anomalous Hall and Nernst effect in magnetic cubic Heusler compounds. *npj Comput. Mater.* **6**, 77 (2020). **This paper systematically investigates the Berry curvature of all magnetic Heusler compounds.**
12. Haldane, F. D. M. Model for a quantum Hall Effect without Landau levels: condensed-matter realization of the “parity anomaly”. *Phys. Rev. Lett.* **61**, 2015–2018 (1988). **This paper realizes the first model of a magnetic topological insulators (Chern insulators).**
13. Chang, C.-Z. et al. Experimental observation of the quantum anomalous Hall effect in a magnetic topological insulator. *Science* **340**, 167–170 (2013).
14. Checkelsky, J. G. et al. Trajectory of the anomalous Hall effect towards the quantized state in a ferromagnetic topological insulator. *Nat. Phys.* **10**, 731–736 (2014).
15. Deng, Y. et al. Quantum anomalous Hall effect in intrinsic magnetic topological insulator  $\text{MnBi}_2\text{Te}_4$ . *Science* **367**, 895–900 (2020).
16. Gong, Y. et al. Experimental realization of an intrinsic magnetic topological insulator. *Chin. Phys. Lett.* **36**, 076801 (2019).

17. Chang, C.-Z. & Li, M. Quantum anomalous Hall effect in time-reversal-symmetry breaking topological insulators. *J. Phys. Condens. Matter* **28**, 123002 (2016).
18. Hor, Y. S. et al. Development of ferromagnetism in the doped topological insulator  $\text{Bi}_{2-x}\text{Mn}_x\text{Te}_3$ . *Phys. Rev. B* **81**, 195203 (2010).
19. Yu, R. et al. Quantized anomalous Hall effect in magnetic topological insulators. *Science* **329**, 61–64 (2010).
20. Chang, C.-Z. et al. Thin films of magnetically doped topological insulator with carrier-independent long-range ferromagnetic order. *Adv. Mater.* **25**, 1065–1070 (2013).
21. Mong, R. S. K., Essin, A. M. & Moore, J. E. Antiferromagnetic topological insulators. *Phys. Rev. B* **81**, 245209 (2010). **This paper describes the first model of an antiferromagnetic topological insulator.**
22. Fang, C., Gilbert, M. J. & Bernevig, B. A. Topological insulators with commensurate antiferromagnetism. *Phys. Rev. B* **88**, 085406 (2013).
23. Bradley, C. & Cracknell, A. *The Mathematical Theory of Symmetry in Solids: Representation Theory for Point Groups and Space Groups* (Clarendon, 1972).
24. Otkrov, M. M. et al. Highly-ordered wide bandgap materials for quantized anomalous Hall and magnetoelectric effects. *2D Mater.* **4**, 025082 (2017).
25. Otkrov, M. M. et al. Unique thickness-dependent properties of the van der Waals interlayer antiferromagnet  $\text{MnBi}_2\text{Te}_4$  films. *Phys. Rev. Lett.* **122**, 107202 (2019).
26. Li, J. et al. Intrinsic magnetic topological insulators in van der Waals layered  $\text{MnBi}_2\text{Te}_4$ -family materials. *Sci. Adv.* **5**, aaw5685 (2019).

27. Zhang, D. et al. Topological axion states in the magnetic insulator  $\text{MnBi}_2\text{Te}_4$  with the quantized magnetoelectric effect. *Phys. Rev. Lett.* **122**, 206401 (2019).
28. Ge, J. et al. High-Chern-number and high-temperature quantum Hall effect without Landau levels. *Natl Sci. Rev.* **7**, 1280–1287 (2020).
29. Qi, X.-L., Hughes, T. L. & Zhang, S.-C. Topological field theory of time-reversal invariant insulators. *Phys. Rev. B* **78**, 195424 (2008).
30. Benalcazar, W. A., Bernevig, B. A. & Hughes, T. L. Quantized electric multipole insulators. *Science* **357**, 61–66 (2017).
31. Hughes, T. L., Prodan, E. & Bernevig, B. A. Inversion-symmetric topological insulators. *Phys. Rev. B* **83**, 245132 (2011).
32. Turner, A. M., Zhang, Y., Mong, R. S. K. & Vishwanath, A. Quantized response and topology of magnetic insulators with inversion symmetry. *Phys. Rev. B* **85**, 165120 (2012).
33. Zhang, F., Kane, C. L. & Mele, E. J. Surface state magnetization and chiral edge states on topological insulators. *Phys. Rev. Lett.* **110**, 046404 (2013).
34. Fu, L., Kane, C. L. & Mele, E. J. Topological insulators in three dimensions. *Phys. Rev. Lett.* **98**, 106803 (2007).
35. Fu, L. & Kane, C. L. Topological insulators with inversion symmetry. *Phys. Rev. B* **76**, 045302 (2007).
36. Coh, S. & Vanderbilt, D. Canonical magnetic insulators with isotropic magnetoelectric coupling. *Phys. Rev. B* **88**, 121106 (2013).
37. Essin, A. M., Moore, J. E. & Vanderbilt, D. Magnetoelectric polarizability and axion electrodynamics in crystalline insulators. *Phys. Rev. Lett.* **102**, 146805 (2009).

38. Schindler, F. et al. Higher-order topological insulators. *Sci. Adv.* **4**, aat0346 (2018).
39. Po, H. C., Vishwanath, A. & Watanabe, H. Symmetry-based indicators of band topology in the 230 space groups. *Nat. Commun.* **8**, 50 (2017).
40. Wang, Z., Wieder, B. J., Li, J., Yan, B. & Bernevig, B. A. Higher-order topology, monopole nodal lines, and the origin of large Fermi arcs in transition metal dichalcogenides  $X\text{Te}_2$  ( $X = \text{Mo}, \text{W}$ ). *Phys. Rev. Lett.* **123**, 186401 (2019).
41. Turner, A. M., Zhang, Y. & Vishwanath, A. Entanglement and inversion symmetry in topological insulators. *Phys. Rev. B* **82**, 241102 (2010).
42. Wieder, B. J. & Bernevig, B. A. The axion insulator as a pump of fragile topology. Preprint at <https://arxiv.org/abs/1810.02373> (2018).
43. Mogi, M. et al. A magnetic heterostructure of topological insulators as a candidate for an axion insulator. *Nat. Mater.* **16**, 516–521 (2017).  
**This paper realizes the first step towards the realization of an axion insulator by engineered heterostructures with modulation-doped topological insulator films.**
44. Xiao, D. et al. Realization of the axion insulator state in quantum anomalous Hall sandwich heterostructures. *Phys. Rev. Lett.* **120**, 056801 (2018).
45. Xu, S.-Y. et al. Hedgehog spin texture and Berry's phase tuning in a magnetic topological insulator. *Nat. Phys.* **8**, 616–622 (2012).
46. Wang, Z. & Zhang, S.-C. Chiral anomaly, charge density waves, and axion strings from Weyl semimetals. *Phys. Rev. B* **87**, 161107 (2013).
47. Gooth, J. et al. Axionic charge-density wave in the Weyl semimetal  $(\text{TaSe}_4)^2\text{I}$ . *Nature* **575**, 315–319 (2019). **First realization of an axion quasiparticle in a charge-density wave Weyl semimetal.**

48. Shi, W. et al. A charge-density-wave topological semimetal. *Nat. Phys.* **17**, 381–387 (2021).
49. Ahn, J. & Yang, B.-J. Symmetry representation approach to topological invariants in  $C_{2z}T$ -symmetric systems. *Phys. Rev. B* **99**, 235125 (2019).
50. Varnava, N., Souza, I. & Vanderbilt, D. Axion coupling in the hybrid Wannier representation. *Phys. Rev. B* **101**, 155130 (2020).
51. Shiozaki, K., Sato, M. & Gomi, K. Topological crystalline materials: general formulation, module structure, and wallpaper groups. *Phys. Rev. B* **95**, 235425 (2017).
52. Fang, C. & Fu, L. New classes of three-dimensional topological crystalline insulators: nonsymmorphic and magnetic. *Phys. Rev. B* **91**, 161105 (2015). **This paper realizes the first models of rotational anomaly topological insulators.**
53. Zhang, R.-X., Wu, F. & Das Sarma, S. Möbius insulator and higher-order topology in  $MnBi_{2n}Te_{3n+1}$ . *Phys. Rev. Lett.* **124**, 136407 (2020). **This paper predicts several topological phases in the MnBiTe family.**
54. Aliev, Z. S. et al. Novel ternary layered manganese bismuth tellurides of the MnTe-Bi<sub>2</sub>Te<sub>3</sub> system: synthesis and crystal structure. *J. Alloys Compd.* **789**, 443–450 (2019).
55. Klimovskikh, I. I. et al. Tunable 3D/2D magnetism in the  $(MnBi_2Te_4)(Bi_2Te_3)_m$  topological insulator family. *npj Quantum Mater.* **12**, 20 (2019).
56. Wang, Z., Alexandradinata, A., Cava, R. J. & Bernevig, B. A. Hourglass fermions. *Nature* **532**, 189–194 (2016).
57. Wieder, B. J. et al. Wallpaper fermions and the nonsymmorphic Dirac insulator. *Science* **361**, 246–251 (2018).

58. Ma, J. et al. Experimental evidence of hourglass fermion in the candidate nonsymmorphic topological insulator KHgSb. *Sci. Adv.* **3**, e1602415 (2017).
59. Liang, S. et al. A gap-protected zero-Hall effect state in the quantum limit of the non-symmorphic metal KHgSb. *Nat. Mater.* **18**, 443–447 (2019).
60. Hu, C. et al. Realization of an intrinsic ferromagnetic topological state in MnBi<sub>8</sub>Te<sub>13</sub>. *Sci. Adv.* **6**, aba4275 (2020).
61. Fang, C. & Fu, L. New classes of topological crystalline insulators having surface rotation anomaly. *Sci. Adv.* **5**, aat2374 (2019).
62. Wei, P. et al. Exchange-coupling-induced symmetry breaking in topological insulators. *Phys. Rev. Lett.* **110**, 186807 (2013).
63. Katmis, F. et al. A high-temperature ferromagnetic topological insulating phase by proximity coupling. *Nature* **533**, 513–516 (2016).
64. Lang, M. et al. Proximity induced high-temperature magnetic order in topological insulator – ferrimagnetic insulator heterostructure. *Nano Lett.* **14**, 3459–3465 (2014).
65. Tang, S. et al. Quantum spin Hall state in monolayer 1T'-WTe<sub>2</sub>. *Nat. Phys.* **13**, 683–687 (2017).
66. HiraHara, T. et al. Large-gap magnetic topological heterostructure formed by subsurface incorporation of a ferromagnetic layer. *Nano Lett.* **17**, 3493–3500 (2017).
67. HiraHara, T. et al. Fabrication of a novel magnetic topological heterostructure and temperature evolution of its massive Dirac cone. *Nat. Commun.* **11**, 4821 (2020).
68. Krieger, J. A. et al. Spectroscopic perspective on the interplay between electronic and magnetic properties of magnetically doped topological insulators. *Phys. Rev. B* **96**, 184402 (2017).

69. Alegria, L. D. et al. Large anomalous Hall effect in ferromagnetic insulator-topological insulator heterostructures. *Appl. Phys. Lett.* **105**, 053512 (2014).
70. Wolf, S. et al. Spintronics: a spin-based electronics vision for the future. *Science* **294**, 1488–1495 (2001).
71. Tokura, Y., Yasuda, K. & Tsukazaki, A. Magnetic topological insulators. *Nat. Rev. Phys.* **1**, 126–143 (2019). **This paper reviews the basic concepts of magnetic topological insulators, their experimental realization and the verification of their emergent properties.**
72. Chang, C.-Z. et al. High-precision realization of robust quantum anomalous Hall state in a hard ferromagnetic topological insulator. *Nat. Mater.* **14**, 473–477 (2015).
73. Chen, Y. L. et al. Massive Dirac fermion on the surface of a magnetically doped topological insulator. *Science* **329**, 659–662 (2010).
74. Lachman, E. O. et al. Visualization of superparamagnetic dynamics in magnetic topological insulators. *Sci. Adv.* **1**, e1500740 (2015).
75. Beidenkopf, H. et al. Spatial fluctuations of helical Dirac fermions on the surface of topological insulators. *Nat. Phys.* **7**, 939–943 (2011).
76. Lee, I. et al. Imaging Dirac-mass disorder from magnetic dopant atoms in the ferromagnetic topological insulator  $\text{Cr}_x(\text{Bi}_{0.1}\text{Sb}_{0.9})_{2-x}\text{Te}_3$ . *Proc. Natl Acad. Sci.* **112**, 1316–1321 (2015).
77. Rienks, E. D. L. et al. Large magnetic gap at the Dirac point in  $\text{Bi}_2\text{Te}_3/\text{MnBi}_2\text{Te}_4$  heterostructures. *Nature* **576**, 423–428 (2019).
78. Lee, S. H. et al. Spin scattering and noncollinear spin structure-induced intrinsic anomalous Hall effect in antiferromagnetic topological insulator  $\text{MnBi}_2\text{Te}_4$ . *Phys. Rev. Res.* **1**, 012011 (2019).

79. Li, H. et al. Dirac surface states in intrinsic magnetic topological insulators  $\text{EuSn}_2\text{As}_2$  and  $\text{MnBi}_{2n}\text{Te}_{3n+1}$ . *Phys. Rev. X* **9**, 041039 (2019).
80. Yan, J.-Q. et al. Crystal growth and magnetic structure of  $\text{MnBi}_2\text{Te}_4$ . *Phys. Rev. Mater.* **3**, 064202 (2019).
81. Yuan, Y. et al. Electronic states and magnetic response of  $\text{MnBi}_2\text{Te}_4$  by scanning tunneling microscopy and spectroscopy. *Nano Lett.* **20**, 3271–3277 (2020).
82. Liu, C. et al. Robust axion insulator and Chern insulator phases in a two-dimensional antiferromagnetic topological insulator. *Nat. Mater.* **19**, 522–527 (2020).
83. Lin, X. & Ni, J. Layer-dependent intrinsic anomalous Hall effect in  $\text{Fe}_3\text{GeTe}_2$ . *Phys. Rev. B* **100**, 085403 (2019).
84. Xu, J., Phelan, W. A. & Chien, C.-L. Large anomalous Nernst effect in a van der Waals ferromagnet  $\text{Fe}_3\text{GeTe}_2$ . *Nano Lett.* **19**, 8250–8254 (2019).
85. Deng, Y. et al. Gate-tunable room-temperature ferromagnetism in two-dimensional  $\text{Fe}_3\text{GeTe}_2$ . *Nature* **563**, 94–99 (2018).
86. Kim, K. et al. Large anomalous Hall current induced by topological nodal lines in a ferromagnetic van der Waals semimetal. *Nat. Mater.* **17**, 794–799 (2018).
87. Wang, L.-L. et al. Single pair of Weyl fermions in the half-metallic semimetal  $\text{EuCd}_2\text{As}_2$ . *Phys. Rev. B* **99**, 245147 (2019).
88. Hua, G. et al. Dirac semimetal in type-IV magnetic space groups. *Phys. Rev. B* **98**, 201116 (2018).
89. Ma, J. et al. Emergence of nontrivial low-energy Dirac fermions in antiferromagnetic  $\text{EuCd}_2\text{As}_2$ . *Adv. Mater.* **32**, 1907565 (2020).

90. Xu, Y., Song, Z., Wang, Z., Weng, H. & Dai, X. Higher-order topology of the axion insulator EuIn<sub>2</sub>As<sub>2</sub>. *Phys. Rev. Lett.* **122**, 256402 (2019).
91. Gui, X. et al. A new magnetic topological quantum material candidate by design. *ACS Cent. Sci.* **5**, 900–910 (2019).
92. Sato, T. et al. Signature of band inversion in the antiferromagnetic phase of axion insulator candidate EuIn<sub>2</sub>As<sub>2</sub>. *Phys. Rev. Res.* **2**, 033342 (2020).
93. Nagaosa, N., Sinova, J., Onoda, S., MacDonald, A. H. & Ong, N. P. Anomalous Hall effect. *Rev. Mod. Phys.* **82**, 1539–1592 (2010).
94. Berry, M. V. Quantal phase factors accompanying adiabatic changes. *Proc. R. Soc. Lond. A* **392**, 45–57 (1984).
95. Murakami, S. Phase transition between the quantum spin Hall and insulator phases in 3D: emergence of a topological gapless phase. *New J. Phys.* **9**, 356 (2007).
96. Wan, X., Turner, A. M., Vishwanath, A. & Savrasov, S. Y. Topological semimetal and Fermi-arc surface states in the electronic structure of pyrochlore iridates. *Phys. Rev. B* **83**, 205101 (2011).
97. Burkov, A. A. & Balents, L. Weyl semimetal in a topological insulator multilayer. *Phys. Rev. Lett.* **107**, 127205 (2011).
98. Yang, K.-Y., Lu, Y.-M. & Ran, Y. Quantum Hall effects in a Weyl semimetal: possible application in pyrochlore iridates. *Phys. Rev. B* **84**, 075129 (2011).
99. Li, X. et al. Anomalous Nernst and Righi–Leduc effects in Mn<sub>3</sub>Sn: Berry curvature and entropy flow. *Phys. Rev. Lett.* **119**, 056601 (2017).
100. Sharma, G., Goswami, P. & Tewari, S. Nernst and magnetothermal conductivity in a lattice model of Weyl fermions. *Phys. Rev. B* **93**, 035116 (2016).

101. Sakai, A. et al. Giant anomalous Nernst effect and quantum-critical scaling in a ferromagnetic semimetal. *Nat. Phys.* **14**, 1119–1124 (2018).
102. Noky, J., Gayles, J., Felser, C. & Sun, Y. Strong anomalous Nernst effect in collinear magnetic Weyl semimetals without net magnetic moments. *Phys. Rev. B* **97**, 220405 (2018).
103. Fang, C., Gilbert, M. J., Dai, X. & Bernevig, B. A. Multi-Weyl topological semimetals stabilized by point group symmetry. *Phys. Rev. Lett.* **108**, 266802 (2012).
104. Solin, N. I. & Chebotaev, N. M. Magnetoresistance and Hall effect of the magnetic semiconductor  $\text{HgCr}_2\text{Se}_4$  in strong magnetic fields. *Phys. Solid State* **39**, 754–758 (1997).
105. Kübler, J. & Felser, C. Non-collinear antiferromagnets and the anomalous Hall effect. *Europhys. Lett.* **108**, 67001 (2014).
106. Chen, H., Niu, Q. & MacDonald, A. H. Anomalous Hall effect arising from noncollinear antiferromagnetism. *Phys. Rev. Lett.* **112**, 017205 (2014).
107. Zhang, Y. et al. Strong anisotropic anomalous Hall effect and spin Hall effect in the chiral antiferromagnetic compounds  $\text{Mn}_3X$  ( $X = \text{Ge}, \text{Sn}, \text{Ga}, \text{Ir}, \text{Rh}$ , and  $\text{Pt}$ ). *Phys. Rev. B* **95**, 075128 (2017).
108. Yang, H. et al. Topological Weyl semimetals in the chiral antiferromagnetic materials  $\text{Mn}_3\text{Ge}$  and  $\text{Mn}_3\text{Sn}$ . *New J. Phys.* **19**, 015008 (2017).
109. Tang, P., Zhou, Q., Xu, G. & Zhang, S.-C. Dirac fermions in an antiferromagnetic semimetal. *Nat. Phys.* **12**, 1100–1104 (2016).
110. Belopolski, I. et al. Discovery of topological Weyl fermion lines and drumhead surface states in a room temperature magnet. *Science* **365**, 1278–1281 (2019).

111. Nie, S., Weng, H. & Prinz, F. B. Topological nodal-line semimetals in ferromagnetic rare-earth-metal monohalides. *Phys. Rev. B* **99**, 035125 (2019).
112. Bradlyn, B. et al. Beyond Dirac and Weyl fermions: unconventional quasiparticles in conventional crystals. *Science* **353**, aaf5037 (2016).
113. Cano, J., Bradlyn, B. & Vergniory, M. G. Multifold nodal points in magnetic materials. *APL Mater.* **7**, 101125 (2019).
114. Wieder, B. J., Kim, Y., Rappe, A. M. & Kane, C. L. Double Dirac semimetals in three dimensions. *Phys. Rev. Lett.* **116**, 186402 (2016).
115. Wieder, B. J. et al. Strong and fragile topological Dirac semimetals with higher-order Fermi arcs. *Nat. Commun.* **11**, 627 (2020).
116. Lin, M. & Hughes, T. L. Topological quadrupolar semimetals. *Phys. Rev. B* **98**, 241103 (2018).
117. Liu, E. et al. Giant anomalous Hall effect in a ferromagnetic kagome-lattice semimetal. *Nat. Phys.* **14**, 1125–1131 (2018).
118. Liu, D. F. et al. Magnetic Weyl semimetal phase in a Kagomé crystal. *Science* **365**, 1282–1285 (2019).
119. Guin, S. N. et al. Zero-field Nernst effect in a ferromagnetic kagome-lattice Weyl-semimetal  $\text{Co}_3\text{Sn}_2\text{S}_2$ . *Adv. Mater.* **31**, 1806622 (2019).
120. Howard, S. et al. Evidence for one-dimensional chiral edge states in a magnetic Weyl semimetal  $\text{Co}_3\text{Sn}_2\text{S}_2$ . *Nat. Commun.* **12**, 4269 (2021).
121. Muechler, L. et al. Emerging chiral edge states from the confinement of a magnetic Weyl semimetal in  $\text{Co}_3\text{Sn}_2\text{S}_2$ . *Phys. Rev. B* **101**, 115106 (2020).
122. Ma, D.-S. et al. Spin-orbit-induced topological flat bands in line and split graphs of bipartite lattices. *Phys. Rev. Lett.* **125**, 266403 (2020).

123. Xu, Y. et al. Electronic correlations and flattened band in magnetic Weyl semimetal  $\text{Co}_3\text{Sn}_2\text{S}_2$ . *Nat. Commun.* **11**, 3985 (2019).
124. Yin, J. X. et al. Negative flat band magnetism in a spin–orbit-coupled correlated kagome magnet. *Nat. Phys.* **15**, 443–448 (2019).
125. Li, G. et al. Surface states in bulk single crystal of topological semimetal  $\text{Co}_3\text{Sn}_2\text{S}_2$  toward water oxidation. *Sci. Adv.* **5**, eaaw9867 (2019).
126. Wang, Q. et al. Large intrinsic anomalous Hall effect in half-metallic ferromagnet  $\text{Co}_3\text{Sn}_2\text{S}_2$  with magnetic Weyl fermions. *Nat. Commun.* **9**, 3681 (2018).
127. Nie, S., Xu, G., Prinz, F. B. & Zhang, S.-C. Topological semimetal in honeycomb lattice  $\text{LnSi}$ . *Proc. Natl Acad. Sci.* **114**, 10596–10600 (2017).
128. Kang, M. et al. Dirac fermions and flat bands in the ideal kagome metal  $\text{FeSn}$ . *Nat. Mater.* **19**, 163–169 (2020).
129. Ye, L. et al. Massive Dirac fermions in a ferromagnetic kagome metal. *Nature* **555**, 638–642 (2018). **The paper discusses surface and bulk Dirac fermions as well as flat bands in the antiferromagnetic kagome metal  $\text{FeSn}$ .**
130. Nakatsuji, S., Kiyohara, N. & Higo, T. Large anomalous Hall effect in a non-collinear antiferromagnet at room temperature. *Nature* **527**, 212–215 (2015). **First report of a large anomalous Hall effect in an antiferromagnet  $\text{Mn}_3\text{Sn}$  with vanishingly small magnetization.**
131. Nayak, A. K. et al. Large anomalous Hall effect driven by a nonvanishing Berry curvature in the noncollinear antiferromagnet  $\text{Mn}_3\text{Ge}$ . *Sci. Adv.* **2**, e1501870 (2016).
132. Liu, Z. et al. Orbital-selective Dirac fermions and extremely flat bands in frustrated kagome-lattice metal  $\text{CoSn}$ . *Nat. Commun.* **11**, 4002

(2020).

133. Yin, J.-X. et al. Quantum-limit Chern topological magnetism in  $\text{TbMn}_6\text{Sn}_6$ . *Nature* **583**, 533–536 (2020). **A topological kagome magnet with strong out-of-plane magnetization realized in  $\text{TbMn}_6\text{Sn}_6$  and identified by scanning tunnelling microscopy.**
134. Asaba, T. et al. Anomalous Hall effect in the kagome ferrimagnet  $\text{GdMn}_6\text{Sn}_6$ . *Phys. Rev. B* **101**, 174415 (2020).
135. Ma, W. et al. Rare earth engineering in  $R\text{Mn}_6\text{Sn}_6$  ( $R = \text{Gd-Tm, Lu}$ ) topological kagome magnets. *Phys. Rev. Lett.* **126**, 246602 (2021).
136. Yin, J.-X. et al. Giant and anisotropic spin–orbit tunability in a strongly correlated kagome magnet. *Nature* **562**, 91–95 (2018).
137. Wang, Z. et al. Time-reversal-breaking Weyl fermions in magnetic Heusler alloys. *Phys. Rev. Lett.* **117**, 236401 (2016). **This paper reports the first prediction of ferromagnetic Weyl semimetal.**
138. Kübler, J. & Felser, C. Weyl points in the ferromagnetic Heusler compound  $\text{Co}_2\text{MnAl}$ . *Europhys. Lett.* **114**, 47005 (2016).
139. Graf, T., Felser, C. & Parkin, S. S. P. Simple rules for the understanding of Heusler compounds. *Prog. Solid State Chem.* **39**, 1–50 (2011). **This article summarizes the wide range of properties in the family of Heusler compounds.**
140. Li, P. et al. Giant room temperature anomalous Hall effect and tunable topology in a ferromagnetic topological semimetal  $\text{Co}_2\text{MnAl}$ . *Nat. Commun.* **11**, 3476 (2020).
141. Manna, K., Sun, Y., Muechler, L., Kübler, J. & Felser, C. Heusler, Weyl and Berry. *Nat. Rev. Mater.* **3**, 244–256 (2018).
142. Guin, S. N. et al. Anomalous Nernst effect beyond the magnetization scaling relation in the ferromagnetic Heusler compound  $\text{Co}_2\text{MnGa}$ .

143. Manna, K. et al. From colossal to zero: controlling the anomalous Hall effect in magnetic Heusler compounds via Berry curvature design. *Phys. Rev. X* **8**, 041045 (2018).
144. Sakai, A. et al. Iron-based binary ferromagnets for transverse thermoelectric conversion. *Nature* **581**, 53–57 (2020).
145. Hirschberger, M. et al. The chiral anomaly and thermopower of Weyl fermions in the half-Heusler GdPtBi. *Nat. Mater.* **15**, 1161–1165 (2016).
146. Liang, S. et al. Experimental tests of the chiral anomaly magnetoresistance in the Dirac–Weyl semimetals Na<sub>3</sub>Bi and GdPtBi. *Phys. Rev. X* **8**, 031002 (2018).
147. Shekhar, C. et al. Anomalous Hall effect in Weyl semimetal half-Heusler compounds RPtBi ( $R = \text{Gd}$  and  $\text{Nd}$ ). *Proc. Natl Acad. Sci. USA* **115**, 9140–9144 (2018).
148. Kumar, N., Guin, S. N., Felser, C. & Shekhar, C. Planar Hall effect in the Weyl semimetal GdPtBi. *Phys. Rev. B* **98**, 041103 (2018).
149. Schindler, C. et al. Anisotropic electrical and thermal magnetotransport in the magnetic semimetal GdPtBi. *Phys. Rev. B* **101**, 125119 (2020).
150. Yu, J., Yan, B. & Liu, C.-X. Model Hamiltonian and time reversal breaking topological phases of antiferromagnetic half-Heusler materials. *Phys. Rev. B* **95**, 235158 (2017).
151. Kuroda, K. et al. Evidence for magnetic Weyl fermions in a correlated metal. *Nat. Mater.* **16**, 1090–1095 (2017).
152. Ikhlas, M. et al. Large anomalous Nernst effect at room temperature in a chiral antiferromagnet. *Nat. Phys.* **13**, 1085–1090 (2017).

153. Higo, T. et al. Large magneto-optical Kerr effect and imaging of magnetic octupole domains in an antiferromagnetic metal. *Nat. Photonics* **12**, 73–78 (2018).
154. Šmejkal, L., Mokrousov, Y., Yan, B. & MacDonald, A. H. Topological antiferromagnetic spintronics. *Nat. Phys.* **14**, 242–251 (2018).
155. Suzuki, T. et al. Singular angular magnetoresistance in a magnetic nodal semimetal. *Science* **365**, 377–381 (2019).
156. Puphal, P. et al. Topological magnetic phase in the candidate Weyl semimetal CeAlGe. *Phys. Rev. Lett.* **124**, 017202 (2020).
157. Sanchez, D. S. et al. Observation of Weyl fermions in a magnetic non-centrosymmetric crystal. *Nat. Commun.* **11**, 3356 (2020).
158. Xu, S.-Y. et al. Discovery of Lorentz-violating type II Weyl fermions in LaAlGe. *Sci. Adv.* **3**, e1603266 (2017).
159. Guo, H., Ritter, C. & Komarek, A. C. Direct determination of the spin structure of  $\text{Nd}_2\text{Ir}_2\text{O}_7$  by means of neutron diffraction. *Phys. Rev. B* **94**, 161102 (2016).
160. Goswami, P., Roy, B. & Das Sarma, S. Competing orders and topology in the global phase diagram of pyrochlore iridates. *Phys. Rev. B* **95**, 085120 (2017).
161. Ueda, K. et al. Magnetic-field induced multiple topological phases in pyrochlore iridates with Mott criticality. *Nat. Commun.* **8**, 15515 (2017).
162. Savary, L., Moon, E. G. & Balents, L. New type of quantum criticality in the pyrochlore iridates. *Phys. Rev. X* **4**, 041027 (2014).
163. Matsuhira, K. et al. Metal–insulator transition in pyrochlore iridates  $\text{Ln}_2\text{Ir}_2\text{O}_7$  ( $\text{Ln} = \text{Nd}, \text{Sm}, \text{and Eu}$ ). *J. Phys. Soc. Jpn.* **76**, 043706 (2007).

164. Nakayama, M. et al. Slater to Mott crossover in the metal to insulator transition of  $\text{Nd}_2\text{Ir}_2\text{O}_7$ . *Phys. Rev. Lett.* **117**, 056403 (2016).
165. Tian, Z. et al. Field-induced quantum metal–insulator transition in the pyrochlore iridate  $\text{Nd}_2\text{Ir}_2\text{O}_7$ . *Nat. Phys.* **12**, 134–138 (2016).
166. Ma, E. Y. et al. Mobile metallic domain walls in an all-in-all-out magnetic insulator. *Science* **350**, 538–541 (2015).
167. Yamaji, Y. & Imada, M. Metallic interface emerging at magnetic domain wall of antiferromagnetic insulator: fate of extinct Weyl electrons. *Phys. Rev. X* **4**, 021035 (2014).
168. Li, J. et al. Intrinsic magnetic topological insulators in van der Waals layered  $\text{MnBi}_2\text{Te}_4$ -family materials. *Sci. Adv.* **5**, aaw5685 (2019).
169. Song, Z., Zhang, T., Fang, Z. & Fang, C. Quantitative mappings between symmetry and topology in solids. *Nat. Commun.* **9**, 3530 (2018).
170. Song, Z.-D., Elcoro, L., Xu, Y.-F., Regnault, N. & Bernevig, B. A. Fragile phases as affine monoids: classification and material examples. *Phys. Rev. X* **10**, 031001 (2020).
171. Song, Z.-D., Elcoro, L. & Bernevig, B. A. Twisted bulk-boundary correspondence of fragile topology. *Science* **367**, 794–797 (2020).
172. Suzuki, T. et al. Large anomalous Hall effect in a half-Heusler antiferromagnet. *Nat. Phys.* **12**, 1119–1123 (2016).
173. Vilanova Vidal, E., Stryganyuk, G., Schneider, H., Felser, C. & Jakob, G. Exploring  $\text{Co}_2\text{MnAl}$  Heusler compound for anomalous Hall effect sensors. *Appl. Phys. Lett.* **99**, 132509 (2011).
174. Wuttke, C. et al. Berry curvature unravelled by the anomalous Nernst effect in  $\text{Mn}_3\text{Ge}$ . *Phys. Rev. B* **100**, 085111 (2019).

175. Bradlyn, B. et al. Topological quantum chemistry. *Nature* **547**, 298–305 (2017).
176. Vergniory, M. G. et al. Graph theory data for topological quantum chemistry. *Phys. Rev. E* **96**, 023310 (2017).
177. Bradlyn, B., Wang, Z., Cano, J. & Bernevig, B. A. Disconnected elementary band representations, fragile topology, and Wilson loops as topological indices: an example on the triangular lattice. *Phys. Rev. B* **99**, 045140 (2019).
178. Kruthoff, J., de Boer, J., van Wezel, J., Kane, C. L. & Slager, R.-J. Topological classification of crystalline insulators through band structure combinatorics. *Phys. Rev. X* **7**, 041069 (2017).
179. Khalaf, E., Po, H. C., Vishwanath, A. & Watanabe, H. Symmetry indicators and anomalous surface states of topological crystalline insulators. *Phys. Rev. X* **8**, 031070 (2018).
180. Kenzelmann, M. et al. Magnetic inversion symmetry breaking and ferroelectricity in  $\text{TbMnO}_3$ . *Phys. Rev. Lett.* **95**, 087206 (2005).
181. Gallego, S. V. et al. MAGNDATA: towards a database of magnetic structures. I. The commensurate case. *J. Appl. Crystallogr.* **49**, 1750–1776 (2016).
182. Belopolski, I. et al. Discovery of topological Weyl fermion lines and drumhead surface states in a room temperature magnet. *Science* **365**, 1278–1281 (2019). **This is the first proof of a ferromagnetic nodal line half metal with surface states that take the form of drumheads via ARPES in  $\text{Co}_2\text{MnGa}$ .**

## Acknowledgements

Work from B.A.B. on magnetic topology is mainly supported by DOE grant no. DE-SC0016239. Further support comes from the Schmidt Fund for Innovative Research, Simons Investigator grant no. 404513, the Packard

Foundation, the Gordon and Betty Moore Foundation through grant no. GBMF8685 towards the Princeton theory programme, the NSF-EAGER no. DMR 1643312, NSF-MRSEC nos DMR-1420541 and DMR2011750, ONR no. N00014-20-1-2303, BSF Israel US Foundation no. 2018226, and the Princeton Global Network Funds. C.F. was supported by the ERC Advanced grant no. 742068 ‘TOPMAT’ and by the Deutsche Forschungsgemeinschaft (DFG, German Research Foundation) under Germany’s Excellence Strategy through the Würzburg–Dresden Cluster of Excellence on Complexity and Topology in Quantum Matter—ct.qmat (EXC 2147, project-id 390858490). H.B. acknowledges support from the European Research Council (ERC) under the European Union’s Horizon 2020 research and innovation programme (grant agreement no. 678702), and the German–Israeli Foundation (GIF, I-1364-303.7/2016).

## Author information

### Affiliations

1. Department of Physics, Princeton University, Princeton, NJ, USA  
B. Andrei Bernevig
2. Max Plank Institute for Chemical Physics of Solids, Dresden,  
Germany  
Claudia Felser
3. Department of Condensed Matter Physics, Weizmann Institute of  
Science, Rehovot, Israel  
Haim Beidenkopf

### Contributions

B.A.B., C.F. and H.B. wrote the review.

### Corresponding author

Correspondence to [B. Andrei Bernevig](#).

## Ethics declarations

### Competing interests

The authors declare no competing interests.

### Peer review

### Peer review information

*Nature* thanks Shuang Jia and the other, anonymous, reviewer(s) for their contribution to the peer review of this work.

### Additional information

**Publisher's note** Springer Nature remains neutral with regard to jurisdictional claims in published maps and institutional affiliations.

### Supplementary information

#### [Supplementary Information](#)

This Supplementary Information file contains Appendix A: Magnetic Group Theory and Magnetic Topology; Appendix B: Magnetic Topological Insulators: Correlated Chern Insulators in Moiré Systems; Appendix C: Semimetal Predictions; and additional references.

### Rights and permissions

#### [Reprints and Permissions](#)

### About this article

## Cite this article

Bernevig, B.A., Felser, C. & Beidenkopf, H. Progress and prospects in magnetic topological materials. *Nature* **603**, 41–51 (2022).  
<https://doi.org/10.1038/s41586-021-04105-x>

- Received: 08 December 2020
- Accepted: 06 October 2021
- Published: 02 March 2022
- Issue Date: 03 March 2022
- DOI: <https://doi.org/10.1038/s41586-021-04105-x>

## Share this article

Anyone you share the following link with will be able to read this content:

[Get shareable link](#)

Sorry, a shareable link is not currently available for this article.

[Copy to clipboard](#)

Provided by the Springer Nature SharedIt content-sharing initiative

---

This article was downloaded by **calibre** from <https://www.nature.com/articles/s41586-021-04105-x>

- Article
- [Published: 02 March 2022](#)

# A persistent ultraviolet outflow from an accreting neutron star binary transient

- [N. Castro Segura](#) ORCID: [orcid.org/0000-0002-5870-0443<sup>1</sup>](https://orcid.org/0000-0002-5870-0443),
- [C. Knigge<sup>1</sup>](#),
- [K. S. Long](#) ORCID: [orcid.org/0000-0002-4134-864X<sup>2,3</sup>](https://orcid.org/0000-0002-4134-864X),
- [D. Altamirano](#) ORCID: [orcid.org/0000-0002-3422-0074<sup>1</sup>](https://orcid.org/0000-0002-3422-0074),
- [M. Armas Padilla<sup>4,5</sup>](#),
- [C. Bailyn<sup>6</sup>](#),
- [D. A. H. Buckley](#) ORCID: [orcid.org/0000-0002-7004-9956<sup>7</sup>](https://orcid.org/0000-0002-7004-9956),
- [D. J. K. Buisson<sup>1</sup>](#),
- [J. Casares](#) ORCID: [orcid.org/0000-0001-5031-0128<sup>4,5</sup>](https://orcid.org/0000-0001-5031-0128),
- [P. Charles<sup>1</sup>](#),
- [J. A. Combi<sup>8</sup>](#),
- [V. A. Cúneo](#) ORCID: [orcid.org/0000-0002-1813-9137<sup>4,5</sup>](https://orcid.org/0000-0002-1813-9137),
- [N. D. Degenaar](#) ORCID: [orcid.org/0000-0002-0092-3548<sup>9</sup>](https://orcid.org/0000-0002-0092-3548),
- [S. del Palacio<sup>8</sup>](#),
- [M. Díaz Trigo<sup>10</sup>](#),
- [R. Fender<sup>11</sup>](#),
- [P. Gandhi<sup>1</sup>](#),
- [M. Georganti<sup>1</sup>](#),
- [C. Gutiérrez<sup>1,12,13</sup>](#),
- [J. V. Hernandez Santisteban](#) ORCID: [orcid.org/0000-0002-6733-5556<sup>14</sup>](https://orcid.org/0000-0002-6733-5556),
- [F. Jiménez-Ibarra<sup>15,16</sup>](#),
- [J. Matthews<sup>17</sup>](#),

- [M. Méndez](#) ORCID: orcid.org/0000-0003-2187-2708<sup>18</sup>,
- [M. Middleton](#)<sup>1</sup>,
- [T. Muñoz-Darias](#)<sup>4,5</sup>,
- [M. Özbey Arabaci](#)<sup>1</sup>,
- [M. Pahari](#)<sup>1,19</sup>,
- [L. Rhodes](#)<sup>11</sup>,
- [T. D. Russell](#) ORCID: orcid.org/0000-0002-7930-2276<sup>9,20</sup>,
- [S. Scaringi](#)<sup>21</sup>,
- [J. van den Eijnden](#)<sup>9,11</sup>,
- [G. Vasilopoulos](#) ORCID: orcid.org/0000-0003-3902-3915<sup>6,22</sup>,
- [F. M. Vincentelli](#)<sup>1</sup> &
- [P. Wiseman](#)<sup>1</sup>

*Nature* volume **603**, pages 52–57 (2022)

- 458 Accesses
- 303 Altmetric
- [Metrics details](#)

## Subjects

- [Astrophysical disks](#)
- [Compact astrophysical objects](#)
- [High-energy astrophysics](#)

## Abstract

All disc-accreting astrophysical objects produce powerful disc winds. In compact binaries containing neutron stars or black holes, accretion often takes place during violent outbursts. The main disc wind signatures during these eruptions are blue-shifted X-ray absorption lines, which are preferentially seen in disc-dominated ‘soft states’<sup>1,2</sup>. By contrast, optical wind-formed lines have recently been detected in ‘hard states’, when a hot corona dominates the luminosity<sup>3</sup>. The relationship between these

signatures is unknown, and no erupting system has as yet revealed wind-formed lines between the X-ray and optical bands, despite the many strong resonance transitions in this ultraviolet (UV) region<sup>4</sup>. Here we report that the transient neutron star binary Swift J1858.6-0814 exhibits wind-formed, blue-shifted absorption lines associated with C iv, N v and He ii in time-resolved UV spectroscopy during a luminous hard state, which we interpret as a warm, moderately ionized outflow component in this state.

Simultaneously observed optical lines also display transient blue-shifted absorption. Decomposing the UV data into constant and variable components, the blue-shifted absorption is associated with the former. This implies that the outflow is not associated with the luminous flares in the data. The joint presence of UV and optical wind features reveals a multi-phase and/or spatially stratified evaporative outflow from the outer disc<sup>5</sup>. This type of persistent mass loss across all accretion states has been predicted by radiation–hydrodynamic simulations<sup>6</sup> and helps to explain the shorter-than-expected duration of outbursts<sup>7</sup>.

This is a preview of subscription content

## Access options

Subscribe to Nature+

Get immediate online access to the entire Nature family of 50+ journals

\$29.99

monthly

[Subscribe](#)

Subscribe to Journal

Get full journal access for 1 year

\$199.00

only \$3.90 per issue

[Subscribe](#)

All prices are NET prices.

VAT will be added later in the checkout.

Tax calculation will be finalised during checkout.

Buy article

Get time limited or full article access on ReadCube.

\$32.00

[Buy](#)

All prices are NET prices.

**Additional access options:**

- [Log in](#)
- [Learn about institutional subscriptions](#)

**Fig. 1: Overview light curves of the X-ray transient Swift J1858.6–0814.**

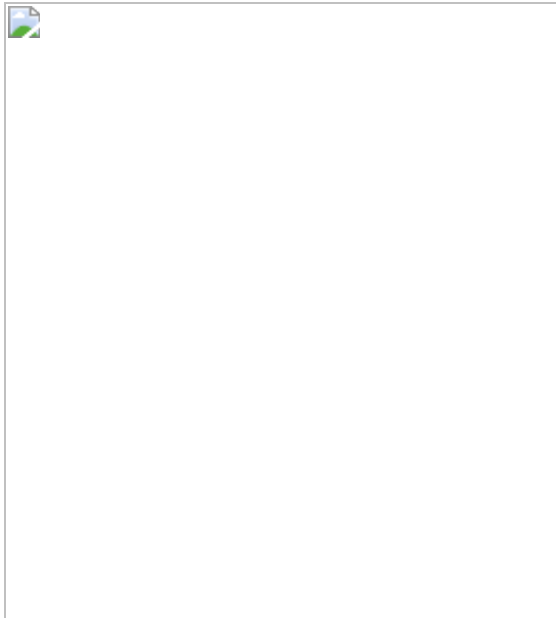


**Fig. 2:** Apparently transient optical wind signatures.



**Fig. 3:** Average far-UV spectrum of Swift J1858.6–0814 during the luminous hard state.

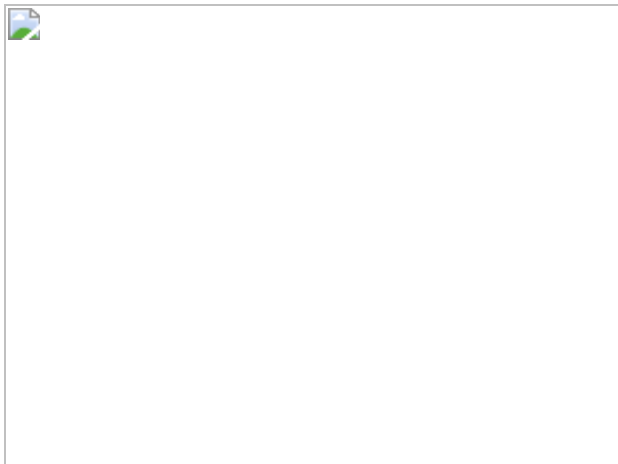
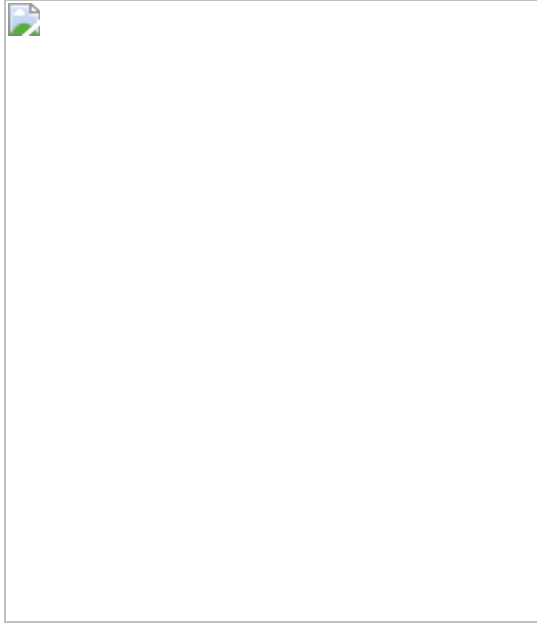


**Fig. 4: Spectral decomposition into a constant (blue) and flaring component (red).**



## Data availability

The data underlying this article are publicly available at [https://archive.stsci.edu/hst/search.php\\_program](https://archive.stsci.edu/hst/search.php_program) ID 15984 for HST/FUV data, <http://archive.eso.org/cms.html> program 190ID 2103.D-5052(A) for VLT/X-Shooter and <https://gtc.sdc.cab.inta-csic.es/gtc/> program ID GTC23-19A for GTC/OSIRIS. X-ray data from NICER used all the OBSIDs starting with 120040, 220040, 320040 and 359201 accessible from HIESARC ([https://heasarc.gsfc.nasa.gov/docs/nicer/nicer\\_archive.html](https://heasarc.gsfc.nasa.gov/docs/nicer/nicer_archive.html)). [Source data](#) are provided with this paper.

## Code availability

Codes used for the analysis are available from the corresponding author upon reasonable request.

## References

1. Ponti, G. et al. Ubiquitous equatorial accretion disc winds in black hole soft states. *MNRAS* **422**, L11–L15 (2012).
2. Homan, J. et al. Evidence for simultaneous jets and disk winds in luminous low-mass x-ray binaries. *Astrophys. J.* **830**, L5 (2016).
3. Muñoz-Darias, T. et al. The changing-look optical wind of the flaring x-ray transient Swift J1858.6-0814. *Astrophys. J.* **893**, L19 (2020).
4. Long, K. S. & Knigge, C. Modeling the spectral signatures of accretion disk winds: a new Monte Carlo approach. *Astrophys. J.* **579**, 725–740 (2002).
5. Waters, T., Proga, D. & Dannen, R. Multiphase AGN winds from x-ray-irradiated disk atmospheres. *Astrophys. J.* **914**, 62 (2021).
6. Higginbottom, N. et al. Thermal and radiation driving can produce observable disc winds in hard-state X-ray binaries. *MNRAS* **492**, 5271–5279 (2020).
7. Tetarenko, B. E., Lasota, J. P., Heinke, C. O., Dubus, G. & Sivakoff, G. R. Strong disk winds traced throughout outbursts in black-hole X-ray binaries. *Nature* **554**, 69–72 (2018).
8. Gehrels, N. et al. The Swift gamma-ray burst mission. *Astrophys. J.* **611**, 1005–1020 (2004).
9. Krimm, H. A. et al. Swift reports the detection of a new galactic transient source Swift J1858.6-0814. *The Astronomer's Telegram* **12151**, 1 (2018).
10. Bright, J. et al. AMI-LA radio observations of the galactic X-ray transient Swift J1858.6-0814. *The Astronomer's Telegram* **12184**, 1 (2018).
11. Vasilopoulos, G., Bailyn, C. & Milburn, J. Swift J1858.6-0814: Localization and variability of the optical counterpart. *The Astronomer's Telegram* **12164**, 1 (2018).

12. Kennea, J. A. & Krimm, H. A. Swift J1858.6-0814: Swift XRT and UVOT localization. *The Astronomer's Telegram* **12160**, 1 (2018).
13. Buisson, D. J. K. et al. Discovery of thermonuclear (Type I) X-ray bursts in the X-ray binary Swift J1858.6-0814 observed with NICER and NuSTAR. *MNRAS* **499**, 793–803 (2020).
14. Buisson, D. J. K. et al. Dips and eclipses in the X-ray binary Swift J1858.6-0814 observed with NICER. *MNRAS* **503**, 5600–5610 (2021).
15. Ludlam, R. M. et al. Initial NICER observation of the new X-ray transient Swift J1858.6-0814. *The Astronomer's Telegram* **12158**, 1 (2018).
16. Motta, S. E. et al. Swift observations of V404 Cyg during the 2015 outburst: X-ray outflows from super-Eddington accretion. *MNRAS* **471**, 1797–1818 (2017).
17. Hare, J. et al. NuSTAR observations of the transient galactic black hole binary candidate Swift J1858.6–0814: a new sibling of V404 Cyg and V4641 Sgr? *Astrophys. J.* **890**, 57 (2020).
18. van den Eijnden, J. et al. The variable radio counterpart of Swift J1858.6-0814. *MNRAS* **496**, 4127–4140 (2020).
19. Begelman, M. C., McKee, C. F. & Shields, G. A. Compton heated winds and coronae above accretion disks. I. Dynamics. *Astrophys. J.* **271**, 70–88 (1983).
20. Done, C., Gierliński, M. & Kubota, A. Modelling the behaviour of accretion flows in X-ray binaries. Everything you always wanted to know about accretion but were afraid to ask. *Astron. Astrophys. Rev.* **15**, 1–66 (2007).
21. Higginbottom, N. & Proga, D. Coronae and winds from irradiated disks in x-ray binaries. *Astrophys. J.* **807**, 107 (2015).

22. Buisson, D. J. K. et al. Soft X-ray emission lines in the X-ray binary Swift J1858.6-0814 observed with XMM-Newton Reflection Grating Spectrometer: disc atmosphere or wind? *MNRAS* **498**, 68–76 (2020).
23. Muñoz-Darias, T. et al. Regulation of black-hole accretion by a disk wind during a violent outburst of V404 Cygni. *Nature* **534**, 75–78 (2016).
24. Shields, G. A., McKee, C. F., Lin, D. N. C. & Begelman, M. C. Compton-heated winds and coronae above accretion disks. III. Instability and oscillations. *Astrophys. J.* **306**, 90–106 (1986).
25. Ganguly, S. & Proga, D. On the wind-driven relaxation cycle in accretion disks. *Astrophys. J.* **890**, 54 (2020).
26. Ioannou, Z. et al. Understanding the LMXB X2127+119 in M 15. II. The UV data. *Astron. Astrophys.* **399**, 211–218 (2003).
27. Neilsen, J. et al. A NICER view of a highly absorbed flare in GRS 1915+105. *Astrophys. J.* **902**, 152 (2020).
28. Dubus, G., Done, C., Tetarenko, B. E. & Hameury, J.-M. The impact of thermal winds on the outburst lightcurves of black hole X-ray binaries. *Astron. Astrophys.* **632**, A40 (2019).
29. Luketic, S., Proga, D., Kallman, T. R., Raymond, J. C. & Miller, J. M. On the properties of thermal disk winds in x-ray transient sources: a case study of GRO J1655-40. *Astrophys. J.* **719**, 515–522 (2010).
30. Done, C., Tomaru, R. & Takahashi, T. Thermal winds in stellar mass black hole and neutron star binary systems. *MNRAS* **473**, 838–848 (2018).
31. Charles, P. et al. Hot, dense He II outflows during the 2017 outburst of the X-ray transient Swift J1357.2-0933. *MNRAS* **489**, L47–L52 (2019).
32. Green, J. C. et al. The Cosmic Origins Spectrograph. *Astrophys. J.* **744**, 60 (2012).

33. Eracleous, M. & Horne, K. The speedy magnetic propeller in the cataclysmic variable AE Aquarii. *Astrophys. J.* **471**, 427–446 (1996).
34. Vernet, J. et al. X-shooter, the new wide band intermediate resolution spectrograph at the ESO Very Large Telescope. *Astron. Astrophys.* **536**, A105 (2011).
35. Cepa, J. et al. In *Optical and IR Telescope Instrumentation and Detectors* Vol. 4008 of *Society of Photo-Optical Instrumentation Engineers (SPIE) Conference Series* (eds Iye, M. & Moorwood, A. F.) 623–631 (SPIE, 2000); <https://doi.org/10.1117/12.395520>
36. Freudling, W. et al. Automated data reduction workflows for astronomy. The ESO Reflex environment. *Astron. Astrophys.* **559**, A96 (2013).
37. Drew, J. E. Inclination and orbital-phase-dependent resonance line-profile calculations applied to cataclysmic variable winds. *MNRAS* **224**, 595–632 (1987).
38. Done, C. In *Accretion Processes in Astrophysics* (eds González Martínez-País, I., Shahbaz, T. & Casares Velázquez, J.) 184–227 (Cambridge Univ. Press, 2014).
39. Woods, D. T., Klein, R. I., Castor, J. I., McKee, C. F. & Bell, J. B. X-ray–heated coronae and winds from accretion disks: time-dependent two-dimensional hydrodynamics with adaptive mesh refinement. *Astrophys. J.* **461**, 767–804 (1996).
40. Proga, D. & Kallman, T. R. On the role of the ultraviolet and x-ray radiation in driving a disk wind in x-ray binaries. *Astrophys. J.* **565**, 455–470 (2002).
41. Frank, J., King, A. & Raine, D. J. *Accretion Power in Astrophysics* 3rd edn (Cambridge Univ. Press, 2002).
42. Ashman, K. M., Bird, C. M. & Zepf, S. E. Detecting bimodality in astrometrical datasets. *Astron. J.* **108**, 2348–2361 (1994).

## Acknowledgements

N.C.S. and C.K. acknowledge support from the Science and Technology Facilities Council (STFC), and from STFC grant ST/M001326/1. Partial support for K.S.L.’s effort on the project was provided by NASA through grant numbers HST-GO-15984 and HST-GO-16066 from the Space Telescope Science Institute, which is operated by AURA, Inc., under NASA contract NAS 5-26555. N.C.S. thanks T. Royle for helping to coordinate the time-critical observations in this article. N.D.D. acknowledges support from a Vidi grant for the Netherlands Organization for Scientific Research (NWO). J.V.H.S. acknowledges support from STFC grant ST/R000824/1. M.A.P., J.C., F.J.-I. and T.M.D. acknowledge support from grants AYA2017-83216-P and PID2020-120323GB-I00. T.M.-D. also acknowledges RYC-2015-18148 and EUR2021-122010. T.M.-D. and M.A.P. acknowledge support from grants with references ProID2020010104 and ProID2021010132. J.M. acknowledges a Herchel Smith Fellowship at Cambridge. T.D.R. acknowledges a financial contribution from the agreement ASI-INAF n.2017-14-H.0. J.v.d.E. is supported by a Lee Hysan Junior Research Fellowship from St Hilda’s College, Oxford. G.V. acknowledges support by NASA grants 80NSSC20K1107, 80NSSC20K0803 and 80NSSC21K0213. M.Ö.A. acknowledges support from the Royal Society through the Newton International Fellowship program. J.A.C. acknowledges support from grants PICT-2017-2865 (ANPCyT), PID2019-105510GB-C32/AEI/10.13039/501100011033 and FQM-322, as well as FEDER funds.

## Author information

### Affiliations

1. Department of Physics & Astronomy, University of Southampton, Southampton, UK

N. Castro Segura, C. Knigge, D. Altamirano, D. J. K. Buisson, P. Charles, P. Gandhi, M. Georganti, C. Gutiérrez, M. Middleton, M. Özbeý Arabacı, M. Pahari, F. M. Vincentelli & P. Wiseman

2. Space Telescope Science Institute, Baltimore, MD, USA

K. S. Long

3. Eureka Scientific, Inc., Oakland, CA, USA

K. S. Long

4. Instituto de Astrofísica de Canarias, La Laguna, Tenerife, Spain

M. Armas Padilla, J. Casares, V. A. Cúneo & T. Muñoz-Darias

5. Departamento de Astrofísica, Universidad de La Laguna, La Laguna, Tenerife, Spain

M. Armas Padilla, J. Casares, V. A. Cúneo & T. Muñoz-Darias

6. Department of Astronomy, Yale University, New Haven, CT, USA

C. Bailyn & G. Vasilopoulos

7. South African Astronomical Observatory, Cape Town, South Africa

D. A. H. Buckley

8. Instituto Argentino de Radioastronomía (CONICET; CICPBA; UNLP), Villa Elisa, Argentina

J. A. Combi & S. del Palacio

9. Anton Pannekoek Institute for Astronomy, University of Amsterdam, Amsterdam, The Netherlands

N. D. Degenaar, T. D. Russell & J. van den Eijnden

10. ESO, Garching bei München, Germany

M. Díaz Trigo

11. Astrophysics, Department of Physics, University of Oxford, Oxford, UK

R. Fender, L. Rhodes & J. van den Eijnden

12. Finnish Centre for Astronomy with ESO (FINCA), University of Turku, Turku, Finland

C. Gutiérrez

13. Tuorla Observatory, Department of Physics and Astronomy, University of Turku, Turku, Finland

C. Gutiérrez

14. SUPA School of Physics & Astronomy, University of St Andrews, St Andrews, UK

J. V. Hernandez Santisteban

15. Department of Physics and Astronomy, Macquarie University, Sydney, New South Wales, Australia

F. Jiménez-Ibarra

16. Research Centre in Astronomy, Astrophysics and Astrophotonics, Macquarie University, Sydney, New South Wales, Australia

F. Jiménez-Ibarra

17. Institute of Astronomy, University of Cambridge, Cambridge, UK

J. Matthews

18. Kapteyn Astronomical Institute, University of Groningen, Groningen, The Netherlands

M. Méndez

19. Department of Physics, IIT Hyderabad, Hyderabad, India

M. Pahari

20. INAF, Istituto di Astrofisica Spaziale e Fisica Cosmica, Palermo, Italy

T. D. Russell

21. Centre for Extragalactic Astronomy, Department of Physics, Durham University, Durham, UK

S. Scaringi

22. Université de Strasbourg, CNRS, Observatoire Astronomique de Strasbourg, UMR 7550, Strasbourg, France

G. Vasilopoulos

## Contributions

N.C.S. and C.K. wrote the original proposal, performed the data analysis and wrote the paper with significant feedback from K.S.L., D.A., F.M.V., S.d.P., J.M. and M. Middleton M.A.P., J.C., F.J.-I. and T.M.-D. provided the GTC data. J.V.H.S. reduced the X-Shooter data and assisted in designing the observations. D.J.K.B. and D.A. provided the X-ray data. D.A.H.B., J.A.C., V.A.C., N.D.D., S.d.P., M.D.T., R.F., C.G., J.V.H.S., M.P., M.Ö.A., L.R., T.D.R., J.v.d.E., F.M.V., M. Méndez, C.B., P.C., P.G., M.G., S.S., G.V. and P.W. assisted in proposing and planning the multiwavelength observations. All authors contributed to the original proposal, discussed the results and commented on the manuscript.

## Corresponding author

Correspondence to [N. Castro Segura](#).

## Ethics declarations

## Competing interests

The authors declare no competing interests.

## Peer review

### Peer review information

*Nature* thanks Daniel Proga and the other, anonymous, reviewer(s) for their contribution to the peer review of this work. Peer reviewer reports are available.

## Additional information

**Publisher's note** Springer Nature remains neutral with regard to jurisdictional claims in published maps and institutional affiliations.

## Extended data figures and tables

### [Extended Data Fig. 1 The logarithmic far-UV flux distribution of J1858 during our observations.](#)

The distribution is clearly bimodal, consistent with the visual impression from the light curve (Fig. 1b) of the variability being due to a flaring component that is superposed on a roughly constant component. The grey line is the optimal decomposition of the distribution into two Gaussians, as suggested by the KMM algorithm<sup>42</sup>. The blue and red lines correspond to the individual Gaussians. KMM rejects the null hypothesis of a single component with extremely high significance ( $p < 10^{-43}$ ).

### [Source data](#)

### [Extended Data Fig. 2 The far-UV continuum and driving light curves.](#)

The black histogram shows the light curve of Swift J1858.6–0814 constructed from three broad wavelength regions that exclude the three strongest emission lines ( $\text{N v } \lambda 1240$ ,  $\text{Si iv } \lambda 1400$  and  $\text{He ii } \lambda 1640$ ). The specific regions used were  $\lambda\lambda 1290 \text{ \AA} - 1390 \text{ \AA}$ ,  $1410 \text{ \AA} - 1630 \text{ \AA}$ ,  $1660 \text{ \AA} - 1850 \text{ \AA}$ . The light curve is shown normalized to an estimate of the underlying constant level ( $80 \text{ c s}^{-1}$ ). The driving light curve used in the decomposition,  $D(t)$ , was constructed from this and is shown as the red curve. It was obtained by subtracting the estimate of the constant level, setting any slightly negative values to zero, and using a 5-point, 2nd order Savitzky-Golay filter to produce a slightly smoother, higher S/N version of the light curve.

## [Source data](#)

# **Supplementary information**

## [Peer Review Information](#)

## **Source data**

### [Source Data Fig. 1](#)

### [Source Data Fig. 2](#)

### [Source Data Fig. 3](#)

### [Source Data Fig. 4](#)

### [Source Data Extended Data Fig. 1](#)

### [Source Data Extended Data Fig. 2](#)

## **Rights and permissions**

### [Reprints and Permissions](#)

## About this article

### Cite this article

Castro Segura, N., Knigge, C., Long, K.S. *et al.* A persistent ultraviolet outflow from an accreting neutron star binary transient. *Nature* **603**, 52–57 (2022). <https://doi.org/10.1038/s41586-021-04324-2>

- Received: 09 July 2021
- Accepted: 09 December 2021
- Published: 02 March 2022
- Issue Date: 03 March 2022
- DOI: <https://doi.org/10.1038/s41586-021-04324-2>

### Share this article

Anyone you share the following link with will be able to read this content:

[Get shareable link](#)

Sorry, a shareable link is not currently available for this article.

[Copy to clipboard](#)

Provided by the Springer Nature SharedIt content-sharing initiative

---

This article was downloaded by **calibre** from <https://www.nature.com/articles/s41586-021-04324-2>

- Article
- Open Access
- [Published: 02 March 2022](#)

# Recovery time of a plasma-wakefield accelerator

- [R. D'Arcy](#) [ORCID: orcid.org/0000-0002-7224-8334<sup>1</sup>](#),
- [J. Chappell<sup>2</sup>](#),
- [J. Beinortaitė<sup>1,2</sup>](#),
- [S. Diederichs](#) [ORCID: orcid.org/0000-0001-9079-0461<sup>1,3</sup>](#),
- [G. Boyle<sup>1</sup>](#),
- [B. Foster<sup>4</sup>](#),
- [M. J. Garland<sup>1</sup>](#),
- [P. Gonzalez Caminal<sup>1,3</sup>](#),
- [C. A. Lindstrøm](#) [ORCID: orcid.org/0000-0002-0769-0425<sup>1</sup>](#),
- [G. Loisch](#) [ORCID: orcid.org/0000-0002-6178-2339<sup>1</sup>](#),
- [S. Schreiber](#) [ORCID: orcid.org/0000-0001-7705-649X<sup>1</sup>](#),
- [S. Schröder](#) [ORCID: orcid.org/0000-0002-0649-9995<sup>1</sup>](#),
- [R. J. Shalloo](#) [ORCID: orcid.org/0000-0002-9568-3814<sup>1</sup>](#),
- [M. Thévenet](#) [ORCID: orcid.org/0000-0001-7216-2277<sup>1</sup>](#),
- [S. Wesch<sup>1</sup>](#),
- [M. Wing<sup>1,2</sup>](#) &
- [J. Osterhoff](#) [ORCID: orcid.org/0000-0002-7684-0140<sup>1</sup>](#)

[Nature](#) volume 603, pages 58–62 (2022)

- 69 Altmetric
- [Metrics details](#)

## Subjects

- [Experimental particle physics](#)
- [Plasma-based accelerators](#)

## Abstract

The interaction of intense particle bunches with plasma can give rise to plasma wakes<sup>1,2</sup> capable of sustaining gigavolt-per-metre electric fields<sup>3,4</sup>, which are orders of magnitude higher than provided by state-of-the-art radio-frequency technology<sup>5</sup>. Plasma wakefields can, therefore, strongly accelerate charged particles and offer the opportunity to reach higher particle energies with smaller and hence more widely available accelerator facilities. However, the luminosity and brilliance demands of high-energy physics and photon science require particle bunches to be accelerated at repetition rates of thousands or even millions per second, which are orders of magnitude higher than demonstrated with plasma-wakefield technology<sup>6,7</sup>. Here we investigate the upper limit on repetition rates of beam-driven plasma accelerators by measuring the time it takes for the plasma to recover to its initial state after perturbation by a wakefield. The many-nanosecond-level recovery time measured establishes the in-principle attainability of megahertz rates of acceleration in plasmas. The experimental signatures of the perturbation are well described by simulations of a temporally evolving parabolic ion channel, transferring energy from the collapsing wake to the surrounding media. This result establishes that plasma-wakefield modules could be developed as feasible high-repetition-rate energy boosters at current and future particle-physics and photon-science facilities.

[Download PDF](#)

## Main

Radio-frequency (RF) accelerator technology has driven material-science and particle-physics research for the past century. Maximizing accelerated charge per second maximizes the brilliance of free-electron lasers<sup>8,9</sup> and the luminosity of future linear colliders<sup>10</sup>. The high quality factor of metallic super-conducting RF cavities, maintaining up to  $10^{11}$  electromagnetic oscillations before substantial dissipation<sup>11</sup>, enables the efficient extraction of energy over long bunch trains at high repetition rates. However, because of electrical breakdowns, such cavities are incapable of sustaining electric fields greater than about 40 megavolts-per-metre ( $\text{MV m}^{-1}$ )<sup>5</sup>, thus necessitating large facilities to reach high particle energies.

Plasma wakes<sup>1,2</sup> driven by intense particle bunches<sup>3,4</sup> represent a disruptive development owing to their ability to sustain gigavolt-per-metre ( $\text{GV m}^{-1}$ ) electric fields. To exceed the luminosity and brilliance demands of current facilities, however, plasma-acceleration techniques must also be capable of accelerating particle bunches at high repetition rates. The electromagnetic fields in plasma, unlike those in RF cavities, are significantly damped after only a few oscillations, at which point the

plasma wake collapses and its stored energy dissipates into the surrounding media. Therefore, it is essential to use the first oscillation of the wakefield for acceleration and then wait for the perturbed background plasma to recover to approximately its initial state before the next acceleration. This recovery time places an upper limit on the maximum achievable repetition rate of plasma accelerators.

During excitation of a particle-beam-driven plasma wake, electrons and ions are separated by the space-charge field of the intense, relativistic particle beam. On the timescale of this motion, defined by the plasma-electron frequency, the plasma ions are typically treated as being stationary. On longer timescales, however, the plasma ions move towards the beam axis<sup>12,13,14,15</sup>, impelled there by the strong radial electric fields of the beam and the decaying plasma wave. The timescale of this movement is defined by the mass and charge of the ions and the strength of the radial fields. After the on-axis ion density reaches a maximum, the ion wave continues to propagate outwards, assisted by the pressure gradient between regions of differing plasma density and temperature, until uniform conditions are re-established. Laser-based optical-probing techniques have been used to observe the onset of ion motion<sup>16</sup> and subsequent ion acoustic waves<sup>17</sup> in the form of on-axis electron-density peaks. To measure the collective ion motion, a diagnostic technique based on the interaction of multiple electron bunches with plasma has been developed.

The collective motion of ions was measured at the plasma-wakefield research facility FLASHForward<sup>18</sup>. The initial plasma, with electron density  $1.75 \times 10^{16} \text{ cm}^{-3}$ , was generated by sending a high-voltage discharge through a capillary filled with argon gas ([Methods](#)). A large-amplitude, non-linear wakefield ( $1.6 \text{ GV m}^{-1}$ ) was then driven by an intense leading electron bunch (1.5 kA peak current), produced by a photocathode laser temporally locked to the plasma generation, and accelerated by the FLASH linac to 1,061 MeV (ref. <sup>19</sup>). A probe bunch, with different parameters to the leading bunch, was produced by a second photocathode laser and placed in a later RF bucket ([Methods](#)). The probe bunch (accelerated to 1,054 MeV) was bisected into a pair of bunches in the FLASHForward experimental beamline—the first ‘driving probe’ bunch driving a subsequent non-linear wakefield and the second ‘trailing probe’ bunch travelling behind in its wake. The two probe bunches propagated through the perturbed plasma at varying times after the leading bunch (Fig. 1), thereby driving a second plasma wake the properties of which depend on the state of the perturbed plasma. By analysing the two probe bunches, the perturbed plasma can be sampled with temporal resolution defined by the 1.3 GHz frequency of the RF accelerating cavities in the FLASH linac. The recovery time of the plasma is defined as the point at which the properties of the probe bunches are consistent with those measured after interaction with an unperturbed plasma, that is, in the absence of the leading bunch.

**Fig. 1: Conceptual representation of the plasma probe process.**

 figure 1



For the perturbed measurements, a leading bunch drives a wakefield, which in turn stimulates motion of the plasma ions. The two probe bunches sample the perturbed plasma in increments of 0.77 ns after the temporally locked leading bunch. For the unperturbed measurements, the procedure is the same but without the presence of the leading bunch. The rendering was performed using VisualPIC<sup>33</sup>.

The results of a scan varying the separation of the leading and probe bunches can be seen in Fig. 2, which was generated by dispersing all three bunches in a dipole magnet, focusing them on a scintillating screen after the interaction and subtracting the overlapping energy spectra, averaged over many bunches, of the leading bunch from that of the driving probe bunch ([Methods](#)). In the case of the unperturbed plasma, both the energy spectra and transverse distributions (Fig. 2a) remain approximately constant over the duration of the 160 ns scan (see Extended Data Fig. 1 for separations 70–160 ns), with gradual changes due to the slow dynamic evolution of the background plasma as it undergoes recombination and is gradually expelled from the open capillary ends<sup>20</sup>. However, in the case of the perturbed plasma, the energy spectra and transverse distributions (Fig. 2b) vary significantly over the same timescale until approximately 63 ns, at which point all residuals are compatible with zero (Fig. 2c),

indicating that the probe-bunch properties are consistent with those of the unperturbed case. That this is the case over longer timescales, up to 160 ns, can be seen in Fig. 2c and Extended Data Fig. 1. The recovery time for this operational state translates to an interbunch repetition-rate upper limit of  $O(10 \text{ MHz})$ .

**Fig. 2: Recovery time of a beam-driven plasma wake.**

---

 **figure 2**

**a**, The energy spectra and transverse distributions of the probe bunches after interaction with an unperturbed plasma. **b**, The same as in **a** but after interaction with a plasma perturbed by the leading bunch. Imperfections in the procedure used to subtract the overlapping spectra of the leading bunch from the driving probe bunch

([Methods](#)) lead to small systematic differences between the energy spectra of **a** and **b** at late timescales, for example, in the large betatron-mismatch band at approximately 1,030 MeV. Larger trailing-probe-bunch charge is also seen in **b** at shorter timescales due to higher coupling between the plasma and downstream capturing optics. **c**, The residuals ([Methods](#)) between the energy spectra and transverse bunch size of both the unperturbed and perturbed datasets. Extended data up to 160 ns is shown on a compressed horizontal timescale in the right-hand panel. The error bar represents the standard error of the mean. The recovery time, indicated by the black dashed vertical line, is reached when all three residuals are consistent with zero. The three experimental signatures of ion motion are enumerated in **b**, with orange dashed bands for the first signature added to **a** and **b** to guide the eye.

---

The dominant physics mechanisms and timescales defining the ion motion can be understood from the features of Fig. 2. The timescale over which an on-axis ion-density peak is generated depends on the longitudinally integrated radial fields of the electron bunch and plasma wave. Considering only the fields generated by the leading electron bunch, it is estimated that the on-axis ion density for a singly ionized argon plasma will reach its maximum at  $0.5 \pm 0.2$  ns ([Methods](#))—an upper-bound estimate yet still outside the 0.77 ns temporal resolution of the diagnostic. The ensuing expansion of the on-axis spike manifests itself as an outwardly propagating ion acoustic wave<sup>21</sup>. As this wave propagates outwards, the on-axis ion density is expected to fall and be subsequently replenished by inwardly streaming cold plasma, essentially unperturbed by the initial wakefield. The speed of each counter-propagating wave is proportional to  $\sqrt{T_e/m_i}$ , where  $T_e$  is the plasma-electron temperature and  $m_i$  is the plasma-ion mass<sup>21,22</sup>. On the basis of the results of previous investigations<sup>12,13,14,15,16,17</sup>, we describe the temporally evolving non-uniformity of the radial density profile to lowest order (that is, parabolic) with the form  $n(r) = n_0(1 + \alpha r^2)$ , where the on-axis ion density  $n_0$  and curvature of the channel  $\alpha$  are time dependent and  $r$  represents the radial distance from the axis.

Ideally, self-consistent particle-in-cell (PIC) simulations of a wakefield driven by the leading bunch, followed by the evolution of the plasma over tens of nanoseconds, would be carried out to understand the details of Fig. 2. However, such simulations are out of reach using current numerical methods owing to prohibitively high computational demands and the accumulation of debilitating numerical noise<sup>23</sup>. In light of this, our approach is to show that the results can be plausibly attributed to ion motion by investigating the experimental signatures of Fig. 2, using them to quantify  $n_0$  and  $\alpha$  through the application of non-linear<sup>24,25</sup> and linear<sup>4</sup> plasma-wakefield theory, respectively, and testing the efficacy of the derived profiles by using them as initial conditions in PIC simulations of the probe process over short timescales. The three experimental signatures investigated are labelled in Fig. 2: (1) betatron-mismatch

bands of the driving-probe-bunch energy spectra; (2) transverse size of the trailing probe bunch; (3) mean-energy evolution of the two probe bunches.

The first signature is a manifestation of the head-to-tail growth of the focusing force acting on the head of the driver during the build-up of the wakefield, which results in differing betatron-oscillation frequencies for each longitudinal beam slice in that region. The energies at which these bands of raised intensity appear are constant, not only over the slowly decaying density range of Fig. 2 but also over many orders of magnitude beyond (Extended Data Fig. 2), illustrating that they are independent of the on-axis density. This is due to the low-density head of the driving probe bunch producing a linear wakefield response in that region: for the slice experiencing a given deceleration, the betatron wavelength at the position of this slice does not depend on the density ([Methods](#)). In the perturbed case, the energy of these bands shifts as a function of separation, and this shift occurs most significantly at shorter bunch separations. This is a result of the non-linear focusing force generated by the parabolic ion density either increasing or decreasing off axis. The deviation in energy of these bands from the unperturbed values may be used to determine the  $\alpha$  parameter of the parabola at each separation ([Methods](#)).

The second signature relates to the transverse size of the trailing probe bunch. As implied by the trailing-probe-bunch energy spectra (Fig. 2a), the unperturbed on-axis plasma density gradually decreases over time. The longitudinal-wakefield amplitude experienced by the trailing probe bunch correspondingly decreases and its betatron-oscillation frequency is modified. It therefore accrues a betatron phase over the plasma length that varies with  $n_0$ , resulting in a differing divergence and transverse size at the plasma exit. In the perturbed case of Fig. 2b, the change in transverse beam size is much more pronounced than the unperturbed case, indicating a significant change of  $n_0$  during this time. As such, the transverse beam size provides an experimental signature for  $n_0$  that is independent of  $\alpha$ , because the transverse size of the trailing bunch is small compared with that of the parabolic channel ([Methods](#)).

Figure 3 shows experimental results obtained by operating with beam conditions designed to amplify the first two experimental signatures:  $\alpha$  is determined by increasing the beam size of the driving-probe-bunch head at the plasma entrance, such that it samples a larger transverse range of the parabolic ion profile while still remaining small relative to the parabolic channel width;  $n_0$  is measured by reducing the length of the trailing probe bunch, such that it samples a smaller longitudinal-wakefield phase range and, therefore, the oscillations remain mostly coherent. Figure 3 shows that the magnitude of both the betatron-mismatch-band shift and trailing-probe-bunch transverse oscillations have increased compared with Fig. 2, while the third experimental signature—the large relative change in the mean energies of the driving and trailing probe bunches—has been maintained. This third signature arises from a

combination of the variable  $n_0$  and  $\alpha$ , which modifies both the extent and electric field of the plasma cavity. In the case of the largest energy change at approximately 10 ns separation,  $n_0$  and  $\alpha$  combine to lengthen the wakefield cavity and reduce the electric-field strengths observed by both probe bunches compared with the unperturbed case. This drop in the accelerating field reduces the mean energy of the trailing bunch from approximately 1.10 GeV to approximately 1.07 GeV.

**Fig. 3: Derivation of the parabolic ion channel properties.**

---

 **figure 3**

---

**a**, Energy spectra and transverse distributions of the driving and trailing probe bunches after interaction with the same perturbed plasma sampled in Fig. [2b](#). Differences between the spectra and transverse distributions of Fig. [2b](#) arise from modification to the probe bunches made to enhance the strength of the experimental signatures. **b**, Curvature and on-axis ion-density values derived from the first two experimental

signatures ([Methods](#)) highlighted in **a**. The line fits were calculated with a cubic spline. The error bars reflect the experimental uncertainties, which are dominated by the fits to measurements of the relative trailing beam size and the position of the focal lines. Values derived from separations with significant charge loss (>50%), which therefore carry an additional systematic uncertainty beyond the fitting errors shown, are highlighted in grey. This primarily occurs (1) at short timescales for both probe bunches due to their interaction with the decreasing off-axis focusing forces of the on-axis density spike and (2) at approximately 20 ns for the highly divergent trailing probe bunch owing to clipping in the capturing quadrupoles downstream of the plasma capillary.

The values of  $n_0$  and  $\alpha$  with associated uncertainties—corresponding to the first two experimental signatures of Fig. [3a](#)—are derived for each separation by using a fit-function based on non-linear and linear plasma-wakefield theory, respectively (Fig. [3b](#)) ([Methods](#)). At the shortest separations,  $n_0$  is higher than the unperturbed value and  $\alpha$  is negative, both of which indicate that the probe beam is sampling the end of the on-axis peak at short times. Beyond this time the ion channel begins to form, with the on-axis density decreasing to a minimum and the curvature increasing to a maximum by approximately 10 ns. Once the channel reaches this deepest point, the inwardly propagating cold plasma refills the depleted channel, with the on-axis ion density and curvature slowly tending back towards their unperturbed values.

The derived values of Fig. [3b](#) were used to construct an evolving two-dimensional density map (Fig. [4a](#)), used as input for PIC simulations over short timescales to test their validity. For accurate modelling, six-dimensional (6D) distributions of both the driving and trailing bunches were reconstructed from transverse- and longitudinal-phase-space measurements ([Methods](#)). The simulation results are shown in Fig. [4b](#), with the corresponding experimental signatures overlaid. The third experimental signature, which was not used in the derivation of the parabolic ion channel, is compared with the corresponding simulated values in Fig. [4c](#). The disagreement at the very earliest times is caused by initial charge loss, as described in Fig. [3b](#). The excellent agreement for later times provides independent validation of the derivation procedure and the physics model.

**Fig. 4: Numerical reconstruction of the experimental results.**

---

 **figure 4**

**a**, The radial-ion-density map interpolated from the experimental results of Fig. 3**b**. **b**, The simulated energy spectra and transverse distributions of the probe bunches after interaction with the radial-ion-density map of **a**. The mean values and uncertainties of the experimental betatron-mismatch band (white error bars) as well as the r.m.s. values

of the experimental transverse beam size (red solid lines) are overlaid, demonstrating good agreement with experiment except at approximately 20 ns in the transverse distribution, at which time some of the charge of the highly divergent trailing probe bunch is lost owing to clipping in the capturing quadrupoles downstream of the plasma capillary. **c**, A comparison of the third experimental (exp.) signature of Fig. 3a—not used in the fitting procedures for  $n_0$  and  $\alpha$ —with the equivalent simulated (sim.) values of **b**. Error bars represent the standard error of the mean. As in Fig. 3b, the grey data points highlight separations at which some of the charge was lost.

The success of the evolving-ion-channel model establishes that ion motion is the key mechanism in understanding the experimental data. Thus, the timescales involved should depend on the ion mass and plasma temperature<sup>21,22</sup>. Argon was selected for this study to match the temporal range of the diagnostic. However, by operating with, for example, hydrogen, the recovery time should be reduced by a factor of  $\sqrt{m_{Ar}/m_H} \approx 6$ , that is, to approximately 10 ns. The timescales of the on-axis peak and refilling of the channel are also expected to depend on the wakefield strength and initial plasma-electron density. A detailed parametric assessment of these dependencies will be a topic of future study.

The results reported here place an upper limit on the interbunch repetition rate for plasma-wakefield accelerators arising from fundamental plasma-physics processes. To operate a future plasma-based facility at high repetition rates, however, other factors must also be taken into account. One such example is cumulative heating of the plasma from the acceleration of long bunch trains. PIC simulations explored elsewhere<sup>26,27,28</sup> suggest that thermal effects of  $O(100$  eV) are not expected to modify significantly the acceleration process of the accelerating bunch but temperature effects beyond this range remain unexplored. Another important consideration is the macroscopic effect of this heat deposition, which could lead to damage of the plasma source if left untreated. Any possible effects of plasma heating, both on the plasma-wakefield properties and the structural integrity of the plasma cell, may be mitigated by running with bunch trains, as indeed is proposed for both the ILC<sup>29</sup> and CLIC<sup>30</sup> accelerators. Each bunch train would contain many bunches separated by the recovery time (at minimum), with each bunch train separated by a time sufficient to enable any heating effects to be reduced to an acceptable level. Furthermore, plasma sources designed specifically with high repetition rate in mind<sup>31,32</sup> may be utilized, for which the cooling dynamics would be entirely different to the source type used here but the motion of the ions, as characterized in this work, would be unchanged. The importance of the results reported here is to establish that fundamental plasma-physics processes central to the operation of plasma accelerators do not preclude their application to current and future high-repetition-rate facilities.

In summary, we have measured the recovery time of a  $\text{GV m}^{-1}$  gradient beam-driven plasma accelerator to be 63 ns in an argon plasma of density  $1.75 \times 10^{16} \text{ cm}^{-3}$ . Simulations confirm that the data can be explained by the long-term evolution of a parabolic ion profile produced by the transfer of energy in the system after the plasma wake breaks down. The return of the perturbed plasma to the unperturbed state in such a timescale establishes that megahertz interbunch repetition rates are supported and hence luminosities and brilliances beyond the state of the art are in principle attainable in plasma-wakefield-accelerator facilities of the future.

## Methods

### Plasma generation and characterization

A high-voltage discharge was used to create the plasma, ignited by a thyratron switch operating at a breakdown voltage of 25 kV, supplying approximately 500 A for a duration of 400 ns. The plasma was contained within a 1.5-mm-diameter, 50-mm-long capillary milled from two slabs of sapphire, mounted in a PEEK plastic holder, all mounted on a hexapod platform for high-precision alignment. A continuous flow of argon was supplied through two internal gas inlets from a buffer volume at a 10 mbar backing pressure. The gas escaped the open-ended capillary through holed copper electrodes (cathode upstream, anode downstream) into a large 500-mm-diameter vacuum chamber pumped to an ambient pressure of  $4.3 \times 10^{-3}$  mbar. Broadening of spectral lines<sup>34</sup> enabled the density at the longitudinal centre of the plasma cell to be resolved<sup>35</sup>. The profile and evolution of the plasma density were recorded from the start of the discharge (0  $\mu\text{s}$ ) and to just after the arrival time of the electron beam (2.6  $\mu\text{s}$  after discharge). The argon was doped with 3% hydrogen (defined by atomic density) to spectrally broaden the H-alpha line. The density measurements were fitted to obtain the plasma density,  $(1.75 \pm 0.27) \times 10^{16} \text{ cm}^{-3}$ , at the arrival time of the electron beam<sup>20</sup>.

### Electron-bunch generation and transport

The leading and probe electron bunches were generated by two distinct photocathode lasers. The maximum repetition rate of the two individual photocathode lasers<sup>36</sup> is 1 and 3 MHz, which is defined by the fastest rate at which the Pockels-cell drivers can pick pulses from the laser oscillator. However, the base low-level frequency of the FLASH facility is 1.3 GHz. The 3 MHz limit of a single photocathode laser can, therefore, be overcome by placing separate photocathode-laser pulses in consecutive 1.3 GHz RF buckets. This defines the 0.77 ns (1/1.3 GHz) resolution of the perturbation diagnostic. The timing between the leading bunch and the probe bunch can be increased by incrementally shifting to later RF buckets in 0.77 ns steps. The

two lasers produce pulses of differing root mean square (r.m.s.) length, 4 and 6 ps, which translates directly into electron bunches of differing length. To compensate for variable space-charge effects in the early stages of the FLASH superconducting linac arising from electron bunches of different length but equal charge, the electron bunch charges were scaled accordingly to be 700 pC (leading) and 900 pC (probe). These two bunches were then accelerated to a mean particle energy of 1,061 MeV and 1,054 MeV, respectively. The bunches were compressed in two magnetic chicanes. A kicker magnet was used to extract the bunches into the dispersive section of the FLASHForward beamline, where a set of three collimators were used to manipulate the bunch-current profile—one wedge to bisect the probe bunch and two outer blocks to remove high- and low-energy electrons<sup>37</sup>. The exact positioning of the three wedges was varied slightly between the two working points of Fig. 2 (WP1) and Fig. 3 (WP2) to accentuate certain experimental signals. For both working points, the remaining charge in the leading bunch was constant at 590 pC. For WP1, the probe bunch charges after scraping were 320 pC (driving) and 90 pC (trailing). For WP2, they were 242 pC (driving) and 48 pC (trailing). In addition, the final-focussing quadrupoles were modified to enlarge the head of the driving beam at the plasma entrance. This also reduced the density of the head of the leading bunch such that the strength of the wakefield it generated was correspondingly reduced by 3% (as measured by the maximumenergy loss of the leading bunch in the electron spectrometer). As the probe bunch had a linear correlation in longitudinal phase space, its length could be reduced to reach that desired for WP2 by cutting away energy slices from the rear of the bunch. Toroids were used to measure the bunch charge before and after the energy collimation. A set of quadrupoles was used to tightly focus the beam at the location of the plasma cell. These matching quadrupoles were set to focus the beam to a waist close to the plasma entrance. The waist location and beta function were then measured and fine-tuned with a precision of  $O(10\text{ mm})$  using a new jitter-based measurement technique<sup>38</sup>. The same two cavity-based beam-position monitors (50 cm upstream and 50 cm downstream of the plasma) were used for beam alignment. Five differential pumping stations enabled a windowless vacuum-to-plasma transition, ensuring high beam quality while also meeting the ultrahigh vacuum requirements of the superconducting FLASH accelerator.

## Electron imaging spectrometer

A dipole magnet was used to perform energy dispersion of the beam vertically onto a LANEX (fine) screen mounted just outside the 1-mm-thick stainless-steel vacuum chamber wall, approximately 3 m downstream of the plasma cell. Five quadrupoles (acting as a triplet) located just upstream of the dipole were used to point-to-point image the beam from the plasma-cell exit (the object plane) to the screen (the image plane) with a magnification of  $R_{11} = -5$  (horizontally) and  $R_{33} = -0.97$  (vertically), where  $R$  is the object-to-image-plane transfer matrix. The spatial resolution of the

optical system was approximately 50  $\mu\text{m}$  (that is, approximately 2 pixels), corresponding to an energy resolution of 0.05% for particles close to the imaged energy. Away from this imaged energy, the energy resolution degrades depending on the vertical divergence of the bunch. The recorded two-dimensional images in the ( $x$ ,  $E$ ) plane may be collapsed onto a single axis to produce a spectral density map in either  $x$  or  $E$ . The stacking of these maps—in this case a function of bunch separation—is displayed as a waterfall plot in Figs. [2a,b](#), [3a](#) and [4b](#).

## Spectrometer image subtraction

In these measurements, multiple bunches interact with the electron-spectrometer scintillating screen in its scintillation lifetime (measured to be approximately 380  $\mu\text{s}$ ), leading to overlapping signals in both space and time. A subtraction technique was developed<sup>39</sup> to enable reconstruction of the spectra of the probe bunch. This technique uses  $O(100)$  measurements of only the leading bunch to predict its scintillation signal (based on its charge) and remove this from the spectrometer images in the case of the perturbed plasma. This subtraction process contributes to the systematic uncertainty included in calculations of the energy and transverse distributions of the probe bunch and is of the order of 10%; the magnitude of the systematic uncertainty is calculated by pixel-by-pixel comparisons of the measured scintillation signal of the leading bunch only and its corresponding predicted signal for each of the  $O(100)$  events. Imperfections in this subtraction procedure lead to small differences in the driving-probe-bunch energy spectra (Fig. [2a](#) versus Fig. [2b](#)). The three-bunch setup used here (a single leading bunch followed by two probe bunches) means the scintillation signal from the trailing probe bunch is unaffected by the subtraction procedure (as there is no overlap of the trailing probe bunch with any other bunch on the scintillation screen) and hence its properties provide the cleanest signal, motivating its use to define the relaxation of the perturbation. All properties of the trailing bunches are compared with optics set to image an energy of 1,100 MeV to improve the resolution of the trailing probe bunch. However, comparisons between the mean energies of the driving probe bunch in the perturbed and unperturbed cases (orange data points in Fig. [2c](#)) are performed with a spectrometer imaging energy of 1,050 MeV. In this case, the subtraction technique is more accurate (with a few per cent systematic uncertainty) as the change in imaging energy minimizes imaging errors in the driving-probe-bunch spectra.

## Definition of residuals

Three separate residuals are used to define the convergence of the perturbed plasma to the unperturbed state. The first two correspond to measurements of the change in mean energy of the driving and trailing probe bunches. This is referred to as the ‘relative energy change’ in Fig. [2c](#) and is calculated from

$$\$ \$ \frac{\{\mu\}_E - \{\mu\}_{E,\{rm{p}\}}}{\Delta \{\mu\}_E}, \$ \$$$

where  $\{\mu\}_E / \{\mu\}_{E,\{rm{p}\}}$  represents the mean energy of the unperturbed (u) or perturbed (p) bunch and  $\Delta \{\mu\}_E$  represents the average energy gain and loss of the trailing and driving probe bunch, respectively, in the unperturbed scheme relative to the energy of that bunch without plasma interaction. The third residual is the ‘relative transverse bunch size’, calculated from

$$\$ \$ \frac{\{\sigma\}_x - \{\sigma\}_{x,\{rm{p}\}}}{\{\sigma\}_{x,\{rm{u}\}}}, \$ \$$$

where  $\{\sigma\}_x / \{\sigma\}_{x,\{rm{p}\}}$  represents the transverse size of the trailing probe bunch in the unperturbed (u) or perturbed (p) scheme measured in the plane of the electron spectrometer. The bunch separation beyond which all three residuals return to, and remain at, zero within experimental uncertainties is defined as the recovery time of the plasma.

## Timescale for the formation of an on-axis density spike

In a plasma-wakefield accelerator, ions inside the plasma wake focus the electrons in the passing beam. In the process, the beam electrons will also exert an equal but opposite force on the ions, which varies both in time,  $t$ , and in space,  $r$ . Assuming, for simplicity, a cylindrical bunch of area  $2\{\pi\} \{\sigma\}_r^2$  and a current profile  $I(t)$ , the radial force on the ions in the radius of the beam is

$$\$ \$ F_r(t,r) = \frac{e Z_i \{rm{i}\} I(t)}{4\{\pi\} c \{\sigma\}_r^2 \varepsilon_0}, \$ \$$$

where  $Z_i$  is the ionization state of the ions, and  $e$ ,  $c$  and  $\varepsilon_0$  are the electron charge, speed of light in a vacuum and permittivity, respectively. Rosenzweig et al.<sup>14</sup> used a similar starting point to model the motion of ions within the initial plasma cavity. However, in the present study the motion of the ions is negligible on the timescale of the plasma-electron frequency. Instead, the total radial impulse,

$$\$ \$ \varDelta p_r(t,r) = \int F_r(t,r) dt = \frac{e Z_i Q r}{4\{\pi\} c \{\sigma\}_r^2 \varepsilon_0}, \$ \$$$

induces a (non-relativistic) radial ion velocity  $\varDelta v_r = \varDelta p_r / m_i$ , where  $m_i$  is the ion mass and  $Q = \int dt \{rm{d}\}$  is the total bunch charge. Assuming that plasma electrons do not significantly alter the collective ion motion, the ions are all ‘focused’ onto the axis in a time

$$\$ \$ \varDelta t = \frac{r}{v_r} = \frac{4\pi c \varepsilon_0 m_i \sigma_r^2 e Z_i Q}{\$ \$}$$

which represents an approximate upper bound to the timescale of the on-axis ion-peak generation. For this experiment (Fig. 2), operating in singly ionized argon ( $Z_i = 1$ ), ( $m_i = 6.64 \times 10^{-26} \text{ kg}$ ) with an average leading-bunch charge of 590 pC and r.m.s. transverse beam size of  $5 \pm 1 \mu\text{m}$ , the resulting formation time for the density spike is estimated to be approximately  $0.5 \pm 0.2 \text{ ns}$ .

## Origin of the density-independent betatron-mismatch bands

The driving probe bunch occupies a large range of wakefield phase, and hence longitudinal-field amplitude, for the range of plasma-electron densities used in the experiments. As a result, the betatron phase advance, and, therefore, the divergence of individual energy slices, varies significantly across the bunch at the plasma exit. When fixing the focal energy of the capturing optics, this variation manifests itself as bands of raised intensity at the spectrometer screen, separated by an  $n\pi$  phase advance. In the unperturbed case, the energy at which these bands appear is constant over an orders-of-magnitude plasma-density range (Extended Data Fig. 2). This is due to the linear wakefield response generated by the head of the driving probe bunch, which is relatively low in density because of the coherent synchrotron radiation induced during the transport of the bunch to the plasma.

In this regime, the focusing and decelerating fields at a given longitudinal slice are linked with the focusing-field strength<sup>40,41</sup>, which is approximated as

$$\$ \$ \frac{F(r)}{r} = - \left( \frac{8\varepsilon_0 L \varDelta \lambda^3}{n_b w^2} \right)^{1/2}, \$ \$$$

where  $L$  is the length of the beam,  $\varDelta \lambda$  is the magnitude of deceleration of that slice,  $n_{b0}$  is the peak bunch density and  $w$  is the width of the beam. In this region of the driving probe bunch, the current profile can be approximated as being longitudinally triangular ( $L = 60 \mu\text{m}$ ) and transversely Gaussian (r.m.s.  $w = 40 \mu\text{m}$ ), with a charge of 125 pC (giving  $n_{b0} \approx 1.2 \times 10^{16} \text{ cm}^{-3}$ ). To obtain this expression, one can get the analytic expression for the pseudo-potential in the beam using Green functions<sup>40</sup> and extract the corresponding transverse and focusing forces. The expression can then be readily derived. With these values, the model predicts three shifts of  $\pi$  in the final phase of betatron oscillation over the head of the bunch, all separated by approximately 10 MeV, that is, in good agreement with the experimental results of Fig. 3a.

## Quantification of the betatron-mismatch bands

The energy of the main betatron-mismatch band in the perturbed-plasma case (Fig. 3a) is calculated for each separation by fitting a peak to the spectrometer image projected onto the energy-dispersed axis. The mean energy of these bands is given by the peak of the fit, with error bars representing the average full-width at half-maximum of the peak. Both the mean energy and errors are overlaid on the simulated spectra of Fig. 4b. These values are the signature used to derive the curvature of the evolving radial ion profile (see the following subsection). At bunch separations around 10 ns, multiple focal lines appear in a small energy range in the spectra, leading to a systematic increase in the average full-width at half-maximum. At the shortest timescales, a large fraction of the driving-probe-bunch charge is lost and hence the identification of the peaks in the spectra carries an associated higher uncertainty.

## Derivation of ion-channel-profile parameters

The first two experimental signatures—(1) the modification of the energy slice that is maximally focused by the post-plasma imaging optics due to the betatron mismatch, and (2) the oscillations of the r.m.s. transverse size of the trailing probe bunch—are a result of the motion of electrons in the probe bunches as they propagate in the plasma:

In the first experimental signature, an electron that propagates in the linear portion of the wakefield, that is, at the head of the driving probe bunch, undergoes transverse oscillations due to the focusing force provided by the wakefield. In the presence of a parabolic transverse-plasma-density profile,  $n(r) = n_0(1 + ar^2)$ , the focusing force at a given longitudinal slice for a uniform density profile is modified by the factor  $(1 + ar^2)$ . As such, the energies of the longitudinal slices that exit the plasma having acquired the appropriate betatron phase to correspond to bands of raised intensity observed on the spectrometer depend on  $\alpha$  through the relation

$$\$ \$ \{\varDelta\}_{\alpha,i} = \{\varDelta\}_{0,i} \{(1+\alpha r^2)\}^{2/3}, \$ \$$$

where  $\{\varDelta\}_{\alpha,i}$  and  $\{\varDelta\}_{0,i}$  are the deceleration of slice  $i$  in a plasma with a non-zero and zero curvature, respectively. This enables reconstruction of the curvature as a function of the separation between the leading and probe bunches by fitting to the difference in energy between the band of raised intensity for the perturbed case and that in the equivalent unperturbed case.

In the second experimental signature, the trailing bunch has a low  $O(\text{mm mrad})$  emittance and is focused to a centimetre-scale  $\beta$ -function at the entrance of the plasma; hence, it has a transverse size of approximately  $8 \mu\text{m}$ , which is much smaller than even the steepest ion channel found in the experiment, where an increase of approximately 5% is predicted in the size of the trailing bunch and a doubling in density from the value on axis occurs at a radial position of approximately  $40 \mu\text{m}$ . The trailing probe

bunch therefore experiences limited changes to its off-axis focusing force due to the presence of the parabolic channel (confirmed in PIC simulations) and its divergence as a function of the on-axis plasma density follows the relation

$$\text{propto } <\!\!\text{RetainOpenmmlfenced separators="" open="|" close="|"?}\kappa_{\beta} \sin\!\!>\!\!|<\!\!\text{RetainOpenmmlfenced separators="" open="(" close=")"?}>(\kappa_{\beta} L)\!\!<\!\!\text{rm{p}}\!\!>\!\!$$

for a fixed plasma length  $L_p$ , where  $\kappa_{\beta} = \omega_{\beta}/c$ . The plasma length is assumed to be constant over the  $O(100 \text{ ns})$  timescale considered here. The divergence of the bunch at the plasma exit directly relates to the r.m.s. transverse size measured in the plane of the electron spectrometer. Bunches with minimal and maximal divergence at the exit of the plasma can be focused to both small and large sizes and high and low intensities, respectively, at the scintillating screen. Therefore, the measured oscillations in the transverse size of the trailing probe bunch (Fig. 3a) can be correlated to extrema of the divergence of the trailing probe bunch at the plasma exit. This enables reconstruction of the on-axis plasma density as a function of the separation between the leading and probe bunches.

As the two experimental signatures are decoupled, the relevant equations can, therefore, be solved independently through numerical fitting of each equation to the pertinent experimental observable, that is, the energy of the betatron-mismatch bands for  $\alpha$  and the r.m.s. transverse beam size for  $n_0$  (Fig. 3a). The fitted values of the parabolic channel (and the associated fitting errors) are shown in Fig. 3b.

## 6D beam reconstruction

For accurate modelling of the plasma acceleration process, robust measurements of both the transverse and longitudinal phase spaces are required. A series of 11 quadrupoles downstream of the plasma cell was used to transport the electron bunches to an X-band transverse deflection structure (X-TDS)<sup>42</sup>, where the beam was streaked onto a cerium-doped gadolinium aluminium gallium garnet screen for measurements of the longitudinal phase space. The energy-dispersed axis of the longitudinal phase space was provided by a dipole located between the X-TDS and the screen. The total length of the bunch was approximately 195  $\mu\text{m}$  with a peak current of 1.5 kA for the leading bunch and 420  $\mu\text{m}$  with a peak current of 1 kA for the unscraped probe bunch. The X-TDS has the feature of being able to streak in all transverse directions. As such, it was possible to derive slice information of the horizontal and vertical planes of the beam by streaking in the vertical and horizontal directions, respectively. Slice emittance measurements were performed in both planes for the leading and probe bunches, providing beam size and emittance information for every 8  $\mu\text{m}$  slice. The X-

TDS was only operated with non-plasma-interacted bunches and relaxed beam focusing due to the complexity of transporting high-divergence bunches the full distance (33 m) from the plasma to the X-TDS measurement screen.

## Particle-in-cell simulations

The 3D quasi-static PIC code HiPACE++ (ref. 43) was used to simulate the full evolution of the beam–plasma interaction. The input beam was generated based on the 6D phase-space information of the experimentally characterized beams. It was modelled with  $2 \times 10^6$  constant-weight macro-particles. A 32-mm-long flat-top plasma-density profile of height  $1.75 \times 10^{16} \text{ cm}^{-3}$  was estimated based on density measurements (see above). The plasma was sampled with 16 particles per cell. A simulation box of size  $600 \times 600 \times 480 \mu\text{m}^3$  (in  $x \times y \times \xi$ , where  $\xi = z - ct$  represents the co-moving frame) was resolved by a grid of  $512 \times 512 \times 512$  cells, evolved with a constant time step of  $4.5\omega_p^{-1}$ , where  $\omega_p$  is the plasma frequency.

## Data availability

The data presented in this paper and the other findings of this study are available from the corresponding author upon reasonable request.

## Code availability

All codes written for use in this study are available from the corresponding author upon reasonable request.

## References

1. Tajima, T. & Dawson, J. M. Laser electron accelerator. *Phys. Rev. Lett.* **43**, 267–270 (1979).
2. Esarey, E., Schroeder, C. B. & Leemans, W. P. Physics of laser-driven plasma-based electron accelerators. *Rev. Mod. Phys.* **81**, 1229 (2009).
3. Chen, P., Dawson, J. M., Huff, R. W. & Katsouleas, T. Acceleration of electrons by the interaction of a bunched electron beam with a plasma. *Phys. Rev. Lett.* **54**, 693–696 (1985).
4. Ruth, R. D., Chao, A. W., Morton, P. L. & Wilson, P. B. A plasma wake field accelerator. *Part. Accel.* **17**, 171–189 (1985).

5. Padamsee, H., Knobloch, J. & Hays, T. *RF Superconductivity for Accelerators* (John Wiley and Sons, 1998).
6. Lindstrøm, C. A. et al. Energy-spread preservation and high efficiency in a plasma-wakefield accelerator. *Phys. Rev. Lett.* **126**, 014801 (2021).
7. Litos, M. et al. High-efficiency acceleration of an electron beam in a plasma wakefield accelerator. *Nature* **515**, 92–95 (2014).
8. Ackermann, S. et al. Operation of a free-electron laser from the extreme ultraviolet to the water window. *Nat. Photon.* **1**, 336–342 (2007).
9. Decking, W. et al. A MHz-repetition-rate hard X-ray free-electron laser driven by a superconducting linear accelerator. *Nat. Photon.* **14**, 650 (2020).
10. Brau, J. et al. International Linear Collider reference design report volume 1: executive summary. Preprint at <https://arxiv.org/abs/0712.1950> (2007).
11. Romanenko, A., Grassellino, A., Crawford, A. C., Sergatskov, D. A. & Melnychuk, O. Ultra-high quality factors in superconducting niobium cavities in ambient magnetic fields up to 190 mG. *Appl. Phys. Lett.* **105**, 234103 (2014).
12. Gorbunov, L. M., Mora, P. & Solodov, A. A. Plasma ion dynamics in the wake of a short laser pulse. *Phys. Rev. Lett.* **88**, 15 (2001).
13. Gorbunov, L. M., Mora, P. & Solodov, A. A. Dynamics of a plasma channel created by the wakefield of a short laser pulse. *Phys. Plasmas* **10**, 1124 (2003).
14. Rosenzweig, J. B. et al. Effects of ion motion in intense beam-driven plasma wakefield accelerators. *Phys. Rev. Lett.* **95**, 195002 (2005).
15. Vieira, J., Fonseca, R. A., Mori, W. B. & Silva, L. O. Ion motion in self modulated plasma wakefield accelerators. *Phys. Rev. Lett.* **109**, 145005 (2012).
16. Zgadzaj, R. et al. Dissipation of electron-beam-driven plasma wakes. *Nat. Commun.* **11**, 4753 (2020).
17. Gilljohann, M. F. et al. Direct observation of plasma waves and dynamics induced by laser-accelerated electron beams. *Phys. Rev. X* **9**, 011046 (2019).
18. D'Arcy, R. et al. FLASHForward: plasma wakefield accelerator science for high-average-power applications. *Phil. Trans. R. Soc. A* **377**, 20180392 (2019).

19. Faatz, B. et al. Simultaneous operation of two soft x-ray free-electron lasers driven by one linear accelerator. *New J. Phys.* **18**, 062002 (2016).
20. Garland, J. M. et al. Combining laser interferometry and plasma spectroscopy for spatially resolved high-sensitivity plasma density measurements in discharge capillaries. *Rev. Sci. Instrum.* **92**, 013505 (2021).
21. Phelps, A. V. The diffusion of charged particles in collisional plasmas: free and ambipolar diffusion at low and moderate pressures. *J. Res. Natl Inst. Stand. Technol.* **95**, 407–431 (1999).
22. Braginskii, S. I. *Reviews of Plasma Physics* (Consultants Bureau, 1965).
23. Cormier-Michel, E. et al. Unphysical kinetic effects in particle-in-cell modeling of laser wakefield accelerators. *Phys. Rev. E* **78**, 016404 (2008).
24. Rosenzweig, J. B. Nonlinear plasma dynamics in the plasma wakefield accelerator. *Phys. Rev. Lett.* **58**, 555 (1987).
25. Lu, W., Huang, C., Zhou, M., Mori, W. B. & Katsouleas, T. Nonlinear theory for relativistic plasma wakefields in the blowout regime. *Phys. Rev. Lett.* **96**, 165002 (2006).
26. Lotov, K. V. Fine wakefield structure in the blowout regime of plasma wakefield accelerators. *Phys. Rev. ST Accel. Beams* **6**, 061301 (2003).
27. Jain, N. et al. Plasma wakefield acceleration studies using the quasi-static code WAKE. *Phys. Plasmas* **22**, 023103 (2015).
28. Esarey, E. et al. Thermal effects in plasma-based accelerators. *Phys. Plasmas* **14**, 056707 (2007).
29. Phinney, N. *ILC Reference design report: accelerator executive summary. ICFA Beam Dyn. Newslett.* **42**, 7–29 (2007).
30. Aicheler, M. et al. *A Multi-TeV Linear Collider Based on CLIC Technology: CLIC Conceptual Design Report* (SLAC, 2014); <https://doi.org/10.2172/1120127>
31. Shalloo, R. J. et al. Hydrodynamic optical-field-ionized plasma channels. *Phys. Rev. E* **97**, 053203 (2018).
32. Picksley, A. et al. Meter-scale conditioned hydrodynamic optical-field-ionized plasma channels. *Phys. Rev. E* **102**, 053201 (2020).

33. Ferran Pouso, A. et al. VisualPIC: a new data visualizer and post-processor for particle-in-cell codes. In *IPAC'17, Copenhagen, Denmark, May 2017* (eds Arduini, G. et al.) 1696–1698 (JACoW, 2017).
34. Stark, J. & Wendt, G. Observations of the effect of the electric field on spectral lines II. Transverse effect. *Ann. Phys.* **348**, 7 (1914).
35. Griem, H. *Spectral Line Broadening By Plasmas* (Elsevier Science, 1974).
36. Will, I., Templin, H. I., Schreiber, S. & Sandner, W. Photoinjector drive laser of the FLASH FEL. *Opt. Express* **19**, 23770–23781 (2011).
37. Schröder, S. et al. Tunable and precise two-bunch generation at FLASHForward. *J. Phys. Conf. Ser.* **1596**, 012002 (2020).
38. Lindström, C. A. et al. Matching small  $\beta$  functions using centroid jitter and two beam position monitors. *Phys. Rev. Accel. Beams* **23**, 052802 (2020).
39. Chappell, J. *Experimental Study of Long Timescale Plasma Wakefield Evolution*. PhD Thesis, Univ. College London (2021).
40. Gorbunov, L. M. & Kirsanov, V. I. Excitation of plasma waves by an electromagnetic wave packet. *Sov. Phys. JETP* **66.2**, 290–294 (1987).
41. Sprangle, P. et al. Laser wakefield acceleration and relativistic optical guiding. In *AIP Conference Proceedings* Vol. 175 (eds Roberson, C. W. & Driscoll, C. F.) 231–245 (American Institute of Physics, 1988).
42. Marchetti, B. et al. Experimental demonstration of novel beam characterization using a polarizable X-band transverse deflection structure. *Sci. Rep.* **11**, 3560 (2021).
43. Diederichs, S. et al. HiPACE++: a portable, 3D quasi-static particle-in-cell code. Preprint at <https://arxiv.org/abs/2109.10277> (2021).

## Acknowledgements

We thank M. Dinter, S. Karstensen, S. Kottler, K. Ludwig, F. Marutzky, A. Rahali, V. Rybnikov, A. Schleiermacher, the FLASH management, and the DESY FH and M divisions for their scientific, engineering and technical support. We also thank C. Benedetti and C. B. Schroeder for their input on long-term-plasma-evolution theory. We thank W. Leemans for his help finalizing the manuscript. We also thank R. Jonas and K. Klose for developing the 1.3 GHz phase shifters to enable the diagnostic. This

work was supported by Helmholtz ARD and the Helmholtz IuVF ZT-0009 programme, as well as the Maxwell computational resources at DESY. This work was supported in parts by a Leverhulme Trust Research Project grant no. RPG-2017-143. We acknowledge the use of the UCL Kathleen High Performance Computing Facilities (Kathleen@UCL), and associated support services, in the completion of this work.

## Funding

Open access funding provided by Deutsches Elektronen-Synchrotron (DESY).

## Author information

### Affiliations

1. Deutsches Elektronen-Synchrotron DESY, Hamburg, Germany

R. D'Arcy, J. Beinortaite, S. Diederichs, G. Boyle, M. J. Garland, P. Gonzalez Caminal, C. A. Lindstrøm, G. Loisch, S. Schreiber, S. Schröder, R. J. Shalloo, M. Thévenet, S. Wesch, M. Wing & J. Osterhoff

2. University College London, London, UK

J. Chappell, J. Beinortaite & M. Wing

3. Universität Hamburg, Hamburg, Germany

S. Diederichs & P. Gonzalez Caminal

4. John Adams Institute, Department of Physics, University of Oxford, Oxford, UK

B. Foster

### Contributions

J.C., R.D. and J.O. conceived the experiment. J.C. wrote all data-taking scripts. J.B., R.D. and G.L. performed the experiment with help from J.C., M.J.G., P.G.C., C.A.L., S. Schröder, and S.W. J.C. performed all data analysis. Simulations were performed by J.C. with the help of S.D. and J.B. The manuscript was written by J.C. and R.D. with assistance from B.F., C.A.L., J.O., R.J.S. and M.W. The 6D beam reconstruction was performed by P.G.C. S.W. oversaw the technical development of the experimental infrastructure. M.J.G. and G.L. performed the plasma-density characterization. S.D. implemented parabolic-channel functionality to HiPACE++. R.J.S. conceived the

illustration in Fig. 1 with help with its creation from S.D. G.B. provided crucial theoretical insights into long-term plasma evolution. C.A.L. quantified the timescale of the on-axis ion-density peak and wrote the equivalent methods section. S. Schreiber developed the 1.3 GHz bucket-jumping routine essential for the diagnostic. M.T. and J.C. demonstrated the density independence of the betatron-mismatch bands. R.D. and J.O. supervised the project and personnel. J.C. was supervised by M.W. All authors discussed the results in the paper.

## Corresponding author

Correspondence to [R. D'Arcy](#).

## Ethics declarations

## Competing interests

The authors declare no competing interests.

## Peer review information

*Nature* thanks Anthony Gonsalves and the other, anonymous, reviewer(s) for their contribution to the peer review of this work. Peer reviewer reports are available.

## Additional information

**Publisher's note** Springer Nature remains neutral with regard to jurisdictional claims in published maps and institutional affiliations.

## Extended data figures and tables

### [Extended Data Fig. 1 Continued recovery time scan \(as in Fig. 2\).](#)

**a**, The energy spectra and transverse distributions of the probe bunches after interaction with an unperturbed plasma. The results are those from a dataset taken shortly after that of Fig. 2, extending the data range from 87.7 ns to 152.3 ns in 9.23 ns steps. **b**, The same as in **a** but after interaction with a plasma perturbed by the leading bunch. Imperfections in the procedure used to subtract the overlapping spectra of the leading bunch from the driving bunch (see [Methods](#)) lead to small systematic differences between the energy spectra of **a** and **b** at low driver energies. Some trailing-bunch charge is lost at higher energies for the shortest bunch separation due to

clipping in the quadrupoles. The similarity of the spectra and distributions plus the permanence of approximately zero residuals (see Fig. 2c) confirm that i) the ion motion has fully decayed and ii) no other perturbative plasma effects arising from the leading wakefield, which would cause deviation of the perturbed from the unperturbed case, occur within the measured timescale. Furthermore, according to PIC simulations such experimental uncertainties translate to a 1% difference in the longitudinally-integrated plasma density experienced by the probe bunch.

## **Extended Data Fig. 2 Constant betatron-mismatch bands for variable plasma density.**

Energy spectra of the unscraped probe bunch of a working point similar to that of Fig. 2 as a function of delay after the start of the plasma-generating high-voltage discharge. The timing is scanned over a  $\sim 3$   $\mu\text{s}$  range, corresponding to a density decay of  $\sim 10^{17}$  to  $\sim 10^{15} \text{ cm}^{-3}$ . The far-left spectra of high intensity at  $t < 0$  represent discharge times after the beam has already traversed the capillary—effectively a *plasma off* state. The betatron-mismatch bands of increased intensity at constant energy—highlighted by orange dashed lines—indicate that the betatron oscillations of the driving-beam head are independent of plasma density and may therefore be used as a signal for the curvature of the channel.

## **Supplementary information**

### **Peer Review File**

## **Rights and permissions**

**Open Access** This article is licensed under a Creative Commons Attribution 4.0 International License, which permits use, sharing, adaptation, distribution and reproduction in any medium or format, as long as you give appropriate credit to the original author(s) and the source, provide a link to the Creative Commons license, and indicate if changes were made. The images or other third party material in this article are included in the article's Creative Commons license, unless indicated otherwise in a credit line to the material. If material is not included in the article's Creative Commons license and your intended use is not permitted by statutory regulation or exceeds the permitted use, you will need to obtain permission directly from the copyright holder. To view a copy of this license, visit <http://creativecommons.org/licenses/by/4.0/>.

### **Reprints and Permissions**

## About this article

### Cite this article

D'Arcy, R., Chappell, J., Beinortaite, J. *et al.* Recovery time of a plasma-wakefield accelerator. *Nature* **603**, 58–62 (2022). <https://doi.org/10.1038/s41586-021-04348-8>

- Received: 30 June 2021
- Accepted: 13 December 2021
- Published: 02 March 2022
- Issue Date: 03 March 2022
- DOI: <https://doi.org/10.1038/s41586-021-04348-8>

### Share this article

Anyone you share the following link with will be able to read this content:

[Get shareable link](#)

Sorry, a shareable link is not currently available for this article.

[Copy to clipboard](#)

Provided by the Springer Nature SharedIt content-sharing initiative

### [\*\*Plasmas primed for rapid pulse production\*\*](#)

- Michael Litos

News & Views 02 Mar 2022

---

This article was downloaded by **calibre** from <https://www.nature.com/articles/s41586-021-04348-8>

- Article
- [Published: 02 March 2022](#)

# High-density switchable skyrmion-like polar nanodomains integrated on silicon

- [Lu Han<sup>1,2</sup>](#),
- [Christopher Addiego](#) ORCID: [orcid.org/0000-0001-7966-0121<sup>3</sup>](https://orcid.org/0000-0001-7966-0121),
- [Sergei Prokhorenko](#) ORCID: [orcid.org/0000-0003-3911-0795<sup>4</sup>](https://orcid.org/0000-0003-3911-0795),
- [Meiyu Wang<sup>1,2</sup>](#),
- [Hanyu Fu<sup>1,2</sup>](#),
- [Yousra Nahas](#) ORCID: [orcid.org/0000-0001-8878-9760<sup>4</sup>](https://orcid.org/0000-0001-8878-9760),
- [Xingxu Yan](#) ORCID: [orcid.org/0000-0001-7991-4849<sup>5,6</sup>](https://orcid.org/0000-0001-7991-4849),
- [Songhua Cai](#) ORCID: [orcid.org/0000-0003-3839-2030<sup>7</sup>](https://orcid.org/0000-0003-3839-2030),
- [Tianqi Wei<sup>1,2</sup>](#),
- [Yanhan Fang<sup>1,2</sup>](#),
- [Huazhan Liu<sup>1,2</sup>](#),
- [Dianxiang Ji](#) ORCID: [orcid.org/0000-0002-8334-2043<sup>7</sup>](https://orcid.org/0000-0002-8334-2043),
- [Wei Guo<sup>1,2</sup>](#),
- [Zhengbin Gu<sup>1,2</sup>](#),
- [Yurong Yang<sup>1,2</sup>](#),
- [Peng Wang](#) ORCID: [orcid.org/0000-0003-0788-6687<sup>1,2,8</sup>](https://orcid.org/0000-0003-0788-6687),
- [Laurent Bellaiche](#) ORCID: [orcid.org/0000-0002-6181-2024<sup>4</sup>](https://orcid.org/0000-0002-6181-2024),
- [Yanfeng Chen](#) ORCID: [orcid.org/0000-0001-7365-0221<sup>1,2</sup>](https://orcid.org/0000-0001-7365-0221),
- [Di Wu](#) ORCID: [orcid.org/0000-0003-3619-1411<sup>1,2</sup>](https://orcid.org/0000-0003-3619-1411),
- [Yuefeng Nie](#) ORCID: [orcid.org/0000-0002-9948-9904<sup>1,2</sup>](https://orcid.org/0000-0002-9948-9904) &
- [Xiaoqing Pan](#) ORCID: [orcid.org/0000-0002-0965-8568<sup>3,5,6</sup>](https://orcid.org/0000-0002-0965-8568)

- 2438 Accesses
- 24 Altmetric
- [Metrics details](#)

## Subjects

- [Condensed-matter physics](#)
- [Materials for devices](#)

## Abstract

Topological domains in ferroelectrics<sup>1,2,3,4,5</sup> have received much attention recently owing to their novel functionalities and potential applications<sup>6,7</sup> in electronic devices. So far, however, such topological polar structures have been observed only in superlattices grown on oxide substrates, which limits their applications in silicon-based electronics. Here we report the realization of room-temperature skyrmion-like polar nanodomains in lead titanate/strontium titanate bilayers transferred onto silicon. Moreover, an external electric field can reversibly switch these nanodomains into the other type of polar texture, which substantially modifies their resistive behaviours. The polar-configuration-modulated resistance is ascribed to the distinct band bending and charge carrier distribution in the core of the two types of polar texture. The integration of high-density (more than 200 gigabits per square inch) switchable skyrmion-like polar nanodomains on silicon may enable non-volatile memory applications using topological polar structures in oxides.

This is a preview of subscription content

## Access options

Subscribe to Nature+

Get immediate online access to the entire Nature family of 50+ journals

\$29.99

monthly

[Subscribe](#)

Subscribe to Journal

Get full journal access for 1 year

\$199.00

only \$3.90 per issue

[Subscribe](#)

All prices are NET prices.

VAT will be added later in the checkout.

Tax calculation will be finalised during checkout.

Buy article

Get time limited or full article access on ReadCube.

\$32.00

[Buy](#)

All prices are NET prices.

### **Additional access options:**

- [Log in](#)
- [Learn about institutional subscriptions](#)

**Fig. 1: High-density polar nanodomains in a PTO<sub>20</sub>/STO<sub>10</sub> bilayer from PFM measurements.**

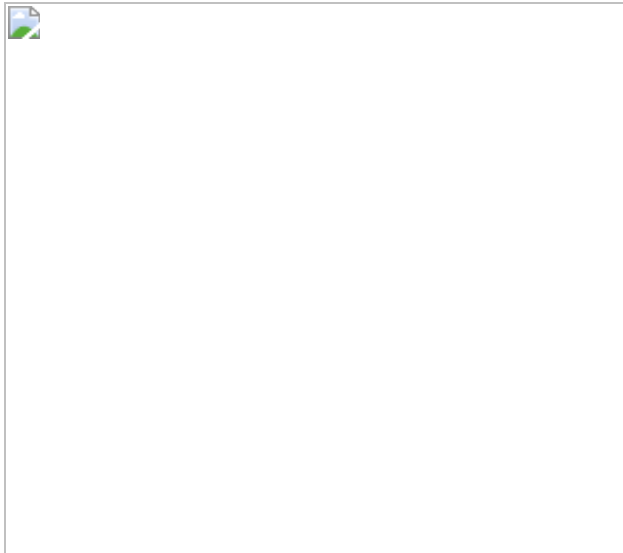


**Fig. 2: Polarization mapping of polar nanodomains in a  $\text{PTO}_{20}/\text{STO}_{10}$  bilayer by vector PFM and 4D STEM.**

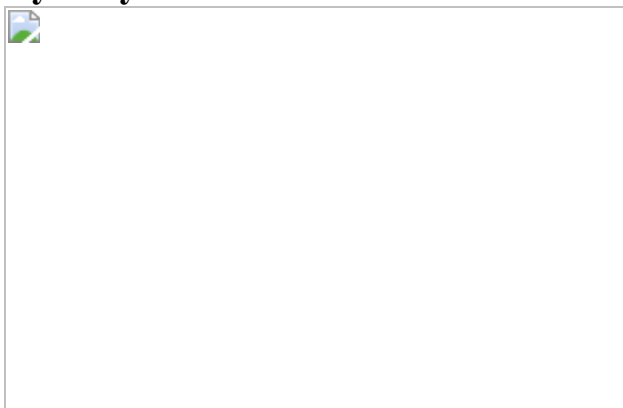


**Fig. 3: Effective Hamiltonian model simulations of skyrmion-like nanodomains in PTO/STO bilayers.**

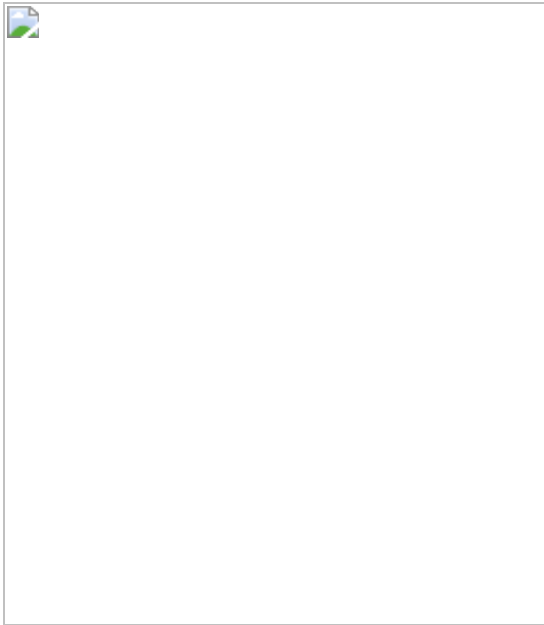


**Fig. 4: Resistive behaviours of the polar nanodomains integrated on silicon.**



## Data availability

The data that support the plots within this paper and other findings of this study are available from the corresponding authors upon reasonable request.

## Code availability

All the code or mathematical algorithm files within this paper are available from the corresponding authors upon reasonable request.

## References

1. Tang, Y. L. et al. Observation of a periodic array of flux-closure quadrants in strained ferroelectric PbTiO<sub>3</sub> films. *Science* **348**, 547–551 (2015).

2. Yadav, A. K. et al. Observation of polar vortices in oxide superlattices. *Nature* **530**, 198–201 (2016).
3. Nahas, Y., Prokhorenko, S., Fischer, J., Xu, B. & Bellaiche, L. Inverse transition of labyrinthine domain patterns in ferroelectric thin films. *Nature* **577**, 47–51 (2020).
4. Das, S. et al. Observation of room-temperature polar skyrmions. *Nature* **568**, 368–372 (2019).
5. Wang, Y. J. et al. Polar meron lattice in strained oxide ferroelectrics. *Nat. Mater.* **19**, 881–886 (2020).
6. Seidel, J. et al. Conduction at domain walls in oxide multiferroics. *Nat. Mater.* **8**, 229–234 (2009).
7. Zubko, P. et al. Negative capacitance in multidomain ferroelectric superlattices. *Nature* **534**, 524–528 (2016).
8. Eliseev, E. A. et al. Labyrinthine domains in ferroelectric nanoparticles: manifestation of a gradient-induced morphological transition. *Phys. Rev. B* **98**, 054101 (2018).
9. Wei, X. K. et al. Neel-like domain walls in ferroelectric  $\text{Pb}(\text{Zr},\text{Ti})\text{O}_3$  single crystals. *Nat. Commun.* **7**, 12385 (2016).
10. Prokhorenko, S., Nahas, Y. & Bellaiche, L. Fluctuations and topological defects in proper ferroelectric crystals. *Phys. Rev. Lett.* **118**, 147601 (2017).
11. Zhang, Q. et al. Nanoscale bubble domains and topological transitions in ultrathin ferroelectric films. *Adv. Mater.* **29**, 1702375 (2017).
12. Peters, J. J. P., Apachitei, G., Beanland, R., Alexe, M. & Sanchez, A. M. Polarization curling and flux closures in multiferroic tunnel junctions. *Nat. Commun.* **7**, 13484 (2016).

13. Xu, R., Karthik, J., Damodaran, A. R. & Martin, L. W. Stationary domain wall contribution to enhanced ferroelectric susceptibility. *Nat. Commun.* **5**, 3120 (2014).
14. Wada, S., Yako, K., Yokoo, K., Kakemoto, H. & Tsurumi, T. Domain wall engineering in barium titanate single crystals for enhanced piezoelectric properties. *Ferroelectrics* **334**, 17–27 (2006).
15. Naumov, I. I., Bellaiche, L. & Fu, H. Unusual phase transitions in ferroelectric nanodisks and nanorods. *Nature* **432**, 737–740 (2004).
16. Stachiotti, M. G. & Sepliarsky, M. Toroidal ferroelectricity in PbTiO<sub>3</sub> nanoparticles. *Phys. Rev. Lett.* **106**, 137601 (2011).
17. Lu, D. et al. Synthesis of freestanding single-crystal perovskite films and heterostructures by etching of sacrificial water-soluble layers. *Nat. Mater.* **15**, 1255–1260 (2016).
18. Kim, K. E. et al. Configurable topological textures in strain graded ferroelectric nanoplates. *Nat. Commun.* **9**, 403 (2018).
19. Kim, J., You, M., Kim, K.-E., Chu, K. & Yang, C.-H. Artificial creation and separation of a single vortex–antivortex pair in a ferroelectric flatland. *npjQuantum Mater.* **4**, 29 (2019).
20. Tsuda, K., Yasuhara, A. & Tanaka, M. Two-dimensional mapping of polarizations of rhombohedral nanostructures in the tetragonal phase of BaTiO<sub>3</sub> by the combined use of the scanning transmission electron microscopy and convergent-beam electron diffraction methods. *Appl. Phys. Lett.* **103**, 082908 (2013).
21. Yadav, A. K. et al. Spatially resolved steady-state negative capacitance. *Nature* **565**, 468–471 (2019).
22. Kalinin, S. V. et al. Spatial resolution, information limit, and contrast transfer in piezoresponse force microscopy. *Nanotechnology* **17**, 3400–3411 (2006).

23. Tian, L. et al. Nanoscale polarization profile across a 180° ferroelectric domain wall extracted by quantitative piezoelectric force microscopy. *J. Appl. Phys.* **104**, 074110 (2008).
24. Lee, D. et al. Emergence of room-temperature ferroelectricity at reduced dimensions. *Science* **349**, 1314–1317 (2015).
25. Kim, S. D., Hwang, G. T., Song, K., Chang, K. J. & Choi, S. Y. Inverse size-dependence of piezoelectricity in single BaTiO<sub>3</sub> nanoparticles. *Nano Energy* **58**, 78–84 (2019).
26. Zhong, W., Vanderbilt, D. & Rabe, K. M. Phase transitions in BaTiO<sub>3</sub> from first principles. *Phys. Rev. Lett.* **73**, 1861–1864 (1994).
27. Bellaiche, L., Garcia, A. & Vanderbilt, D. Finite-temperature properties of Pb(Zr<sub>1-x</sub>Ti<sub>x</sub>)O<sub>3</sub> alloys from first principles. *Phys. Rev. Lett.* **84**, 5427–5430 (2000).
28. Mermin, N. D. The topological theory of defects in ordered media. *Rev. Mod. Phys.* **51**, 591–648 (1979).
29. Prosandeev, S. & Bellaiche, L. Asymmetric screening of the depolarizing field in a ferroelectric thin film. *Phys. Rev. B* **75**, 172109 (2007).
30. Nahas, Y. et al. Topology and control of self-assembled domain patterns in low-dimensional ferroelectrics. *Nat. Commun.* **11**, 5779 (2020).
31. Kornev, I., Fu, H. & Bellaiche, L. Ultrathin films of ferroelectric solid solutions under a residual depolarizing field. *Phys. Rev. Lett.* **93**, 196104 (2004).
32. Hsing, G. H.-C. *Strain and Defect Engineering for Tailored Electrical Properties in Perovskite Oxide Thin Films and Superlattices*. PhD Thesis, State Univ. New York at Stony Brook (2017).

33. Edwards, D. et al. Giant resistive switching in mixed phase BiFeO<sub>3</sub> via phase population control. *Nanoscale* **10**, 17629 (2018).
34. Crassous, A., Sluka, T., Tagantsev, A. K. & Setter, N. Polarization charge as a reconfigurable quasi-dopant in ferroelectric thin films. *Nat. Nanotechnol.* **10**, 614–618 (2015).
35. Ma, J. et al. Controllable conductive readout in self-assembled, topologically confined ferroelectric domain walls. *Nat. Nanotechnol.* **13**, 947–952 (2018).
36. Zhang, Q. et al. Deterministic switching of ferroelectric bubble nanodomains. *Adv. Funct. Mater.* **29**, 1808573 (2019).
37. Li, Z. et al. High-density array of ferroelectric nanodots with robust and reversibly switchable topological domain states. *Sci. Adv.* **3**, e1700919 (2017).
38. Ding, L. L. et al. Characterization and control of vortex and antivortex domain defects in quadrilateral ferroelectric nanodots. *Phys. Rev. Mater.* **3**, 104417 (2019).
39. Rodriguez, B. J., Callahan, C., Kalinin, S. V. & Proksch, R. Dual-frequency resonance-tracking atomic force microscopy. *Nanotechnology* **18**, 475504 (2007).
40. Waghmare, U. V. & Rabe, K. M. Ab initio statistical mechanics of the ferroelectric phase transition in PbTiO<sub>3</sub>. *Phys. Rev. B* **55**, 6161 (1997).
41. Zhong, W., Vanderbilt, D. & Rabe, K. M. First-principles theory of ferroelectric phase transitions for perovskites: the case of BaTiO<sub>3</sub>. *Phys. Rev. B* **52**, 6301 (1995).
42. Nishimatsu, T., Grünebohm, A., Waghmare, U. V. & Kubo, M. Molecular dynamics simulations of chemically disordered ferroelectric (Ba,Sr)TiO<sub>3</sub> with a semi-empirical effective Hamiltonian. *J. Phys. Soc. Jpn* **85**, 114714 (2016).

43. Ponomareva, I., Naumov, I. I., Kornev, I., Fu, H. & Bellaiche, L. Atomistic treatment of depolarizing energy and field in ferroelectric nanostructures. *Phys. Rev. B* **72**, 140102(R) (2005).
44. Xu, B. et al. Intrinsic polarization switching mechanisms in BiFeO<sub>3</sub>. *Phys. Rev. B* **95**, 104104 (2017).
45. Prokhorenko, S., Kalke, K., Nahas, Y. & Bellaiche, L. Large scale hybrid Monte Carlo simulations for structure and property prediction. *npj Comput. Mater.* **4**, 80 (2018).
46. Manton, N. & Schwarz, N. in *Topological Solitons* Ch. 3 (eds Manton, N. & Sutcliffe, P.) 506 (Cambridge Univ. Press, 2004).
47. Nahas, Y. et al. Discovery of stable skyrmionic state in ferroelectric nanocomposites. *Nat. Commun.* **6**, 8542 (2015).
48. Berg, B. & Lüscher, M. Definition and statistical distributions of a topological number in the lattice O(3)  $\sigma$ -model. *Nucl. Phys. B* **190**, 412–424 (1981).
49. Kiselev, N. S. Experimental observation of chiral magnetic bobbers in B20-type FeGe. *Nat. Nanotechnol.* **13**, 451–455 (2018).

## Acknowledgements

We thank L. Chen for discussions, and H. Huyan at UCI for assisting with the TEM experiments. This work was supported by the National Natural Science Foundation of China (grant numbers 11774153, 11861161004, 51772143, 51725203, 51721001, 11874207 and U1932115), the National Key R&D Program of China (grant numbers 2021YFA1400400 and 2020YFA0711504) and the Fundamental Research Funds for the Central Universities (0213-14380198). Y. Nie is supported by High Level Entrepreneurial and Innovative Talents Introduction, Jiangsu Province; C.A., X.Y. and X.P. acknowledge funding from the Department of Energy (DOE) under grant DE-SC0014430, and the NSF under grant number DMR-2034738. The 4D STEM experiments was conducted using facilities

and instrumentation at the UC Irvine Materials Research Institute (IMRI) supported in part by the National Science Foundation through the Materials Research Science and Engineering Center programme (DMR-2011967); Researchers at the University of Arkansas acknowledge DARPA grant number HR0011727183-D18AP00010 (TEE Program), the Vannevar Bush Faculty Fellowship (VBFF) grant number N00014-20-1-2834 from the Department of Defense, and ARO grant number W911NF-21-2-0162 (ETHOS). Computations were made possible thanks to the use of the Arkansas High Performance Computing Center, HPCC resources of Nanjing University and the Arkansas Economic Development Commission. S.C. acknowledges the support of startup grants from the Department of Applied Physics at the Hong Kong Polytechnic University, the General Research Fund (grant number 15306021) from the Hong Kong Research Grant Council, the National Natural Science Foundation of China (grant number 12104381) and the open subject of the National Laboratory of Solid State Microstructures, Nanjing University (M34001).

## Author information

### Affiliations

1. National Laboratory of Solid State Microstructures, Jiangsu Key Laboratory of Artificial Functional Materials, College of Engineering and Applied Sciences, Nanjing University, Nanjing, People's Republic of China

Lu Han, Meiyu Wang, Hanyu Fu, Tianqi Wei, Yanhan Fang, Huazhan Liu, Wei Guo, Zhengbin Gu, Yurong Yang, Peng Wang, Yanfeng Chen, Di Wu & Yuefeng Nie

2. Collaborative Innovation Center of Advanced Microstructures, Nanjing University, Nanjing, People's Republic of China

Lu Han, Meiyu Wang, Hanyu Fu, Tianqi Wei, Yanhan Fang, Huazhan Liu, Wei Guo, Zhengbin Gu, Yurong Yang, Peng Wang, Yanfeng Chen, Di Wu & Yuefeng Nie

3. Department of Physics and Astronomy, University of California,  
Irvine, CA, USA

Christopher Addiego & Xiaoqing Pan

4. Physics Department and Institute for Nanoscience and Engineering,  
University of Arkansas, Fayetteville, AR, USA

Sergei Prokhorenko, Yousra Nahas & Laurent Bellaiche

5. Department of Materials Science and Engineering, University of  
California, Irvine, CA, USA

Xingxu Yan & Xiaoqing Pan

6. Irvine Materials Research Institute, University of California, Irvine,  
CA, USA

Xingxu Yan & Xiaoqing Pan

7. Department of Applied Physics, The Hong Kong Polytechnic  
University, Hong Kong SAR, People's Republic of China

Songhua Cai & Dianxiang Ji

8. Department of Physics, University of Warwick, Coventry CV4 7AL,  
UK

Peng Wang

## Contributions

Y. Nie conceived the idea and directed the project with X.P., Y.C. and D.W. L.H. synthesized the samples and characterized the crystalline structure with the help of Y.F., H.L., D.J. and W.G. under the supervision of Y. Nie, X.P. and Z.G. L.H. performed the PFM and CAFM measurements and data analysis with the help of H.F. under the supervision of D.W. and Y. Nie. C.A. performed 4D STEM measurements and data analysis with the help of

X.Y. under the supervision of X.P. M.W. performed the selected area electron diffraction and S/TEM measurements with the help of S.C. under the supervision of P.W. and X.P. S.P., Y. Nahas and Y.Y. performed and discussed the effective Hamiltonian model simulations under the supervision of L.B. T.W. helped with the lithography processing. Y. Nie and L.H. wrote the manuscript. All authors discussed the data and contributed to the manuscript.

## Corresponding authors

Correspondence to [Di Wu](#), [Yuefeng Nie](#) or [Xiaoqing Pan](#).

## Ethics declarations

### Competing interests

The authors declare no competing interests.

### Peer review

### Peer review information

*Nature* thanks Matthew Dawber, Si-Young Choi and Anna Morozovska for their contribution to the peer review of this work.

## Additional information

**Publisher's note** Springer Nature remains neutral with regard to jurisdictional claims in published maps and institutional affiliations.

## Extended data figures and tables

[Extended Data Fig. 1 Growth and transfer of freestanding PTO/STO bilayers.](#)

**a**, Schematic illustration of the process of heterostructure growth and membrane lift-off. The PTO/STO heterostructure is first grown on  $\text{TiO}_2$ -terminated (001) STO substrates with a SAO water-soluble sacrificial layer (left) and then the bilayer is attached to a supporting polymer and released from the substrate by dissolving away the SAO layer by water (middle). Finally, the bilayer is transferred onto the desired substrate (right). **b**, The Reflection High Energy Electron Diffraction (RHEED) patterns for as-grown PTO(16 u.c.)/STO(10 u.c.)/SAO(6 u.c.) film on (001) STO substrate. **c**, Atomic force microscopy characterization of (001) STO substrate (left) and as-grown films (right) showing an atomically smooth surface with unit cell step terraces. Scale bar, 1  $\mu\text{m}$ . **d**, Low-magnification planar-view HADDF image of the freestanding  $(\text{PbTiO}_3)_{20}/(\text{SrTiO}_3)_{10}$  bilayer transferred to a holey carbon TEM grid and selected area electron diffraction (SAED) taken along [001] zone axis (inset), showing the single-crystal structure of the bilayer. Scale bar, 1  $\mu\text{m}$ .

### Extended Data Fig. 2 Simulation of vector fields for two distinct divergent domains.

**a**, Simulation of vector fields for a quad divergent domain. **b**, Simulation of vector fields for a skyrmion-like bubble domain. **c**, Calculation of the divergence from vector PFM image.

### Extended Data Fig. 3 Direct visualization of topological polar textures by vector piezoelectric force microscope (PFM).

**a**, Schematic of angle-resolved lateral PFM. In-plane (IP) PFM real part signal was collected experimentally as a function of tip orientation angle  $\varphi$  and then the amplitude and the phase delay were determined by trigonometric curve fitting, i.e.  $A$  and  $\theta$  in  $A\cos(\varphi-\theta+\pi/2)$ . Piezoresponse vector field can be constructed by finding IP vector components ( $A\cos\theta$ ,  $A\sin\theta$ ) as a function of position. **b**, IP piezoresponse vector map for a centre-divergent domain showing the centre-divergent nanodomain. **c**, The trigonometric curve fitting for four representative points that are denoted as red spots in **b**.

## Extended Data Fig. 4 Characterization of a centre-convergent type nanodomain.

**a**, Polarization mapping by 4D-STEM. **b**, The projected electric field calculated from the (000) diffraction peak. **c**, The projected charge density calculated from the electric field based on Gauss's law. Scale bar, 5 nm. **d**, Atomically resolved plane-view HADDF-STEM image of the PTO<sub>20</sub>/STO<sub>10</sub> bilayer. Scale bar, 2 nm. **e**, The PACBED pattern extracted from the region of the centre-convergent domain shown in **a–c**.

## Extended Data Fig. 5 Spatial resolution in PFM.

**a**, i) SEM image of an unused spherelike PFM tip. Scale bar, 500 nm. ii) The radius  $r$  of the contact circle for a weak indentation ( $h \sim 1\text{--}2$  nm) is used to characterize the radius  $r$  of the tip. Scale bar, 50 nm. **b**, Electric field distribution at the tip simulated by finite element modelling (FEM). Labels near the curves designate potential values. Scale bar, 10 nm. **c**, Schematic image of the PFM tip scanning across a nanodomain. The measured size is proportional to the tip radius.

## Extended Data Fig. 6 Topological characterization of the centre-divergent domains and interfacial skyrmion-like nanodomain (polar Bobber) obtained computationally (via the effective Hamiltonian).

**a**, (001)-plane resolved polar structure of the centre divergent domains in the vicinity of the STO/PTO interface. The first, second and third PTO layers counting from the interface are indicated with labels  $z = 1, 2$ , and 3, respectively. **b**, The in-plane projected polar structure superimposed with the distribution of the Pontryagin topological charge density. The arrows correspond to the in-plane-projected dipoles coloured according to their out-of-plane component; red and purple colours correspond to [001] and [00–1] oriented dipoles, respectively. **c**, Dependence of the interpolated polar angle  $\theta$  between the local dipole and [001] axis on the distance  $R$  from the central axis of the domain. **d**, The dependence of the interpolated Pontryagin charge density  $\langle \{\rho\}_{\langle\{S_k\}\rangle} \rangle$  on the distance  $R$  from the

central axis of the domain. **e**, The plane-resolved Skyrmion number of a single centre-divergent domain as a function of the distance from the domain centre. **f**, Schematic illustration of the topology of centre-divergent domains (left). Each  $z \geq 2$  cross section of the domain reveals a 2D Néel skyrmion-like structure characterized by an integer Skyrmion number. The domain tip at the PTO/STO interface pins an anti-hedgehog-like Bloch point.

### Extended Data Fig. 7 Simulated dipolar structure of the centre-convergent domains.

**a**, The [100]–[001] cross-section of the simulated centre-divergent domain (Néel skyrmion). **b**, Artificially prepared partially switched dipolar configuration. **c**, Cross-section of the relaxed dipolar structure of the centre-convergent domain (submerged Néel bubble). **d**, Above and below the bubble (grey circle), the local dipoles are inclined (yellow arrows) towards and away from the central revolution axis (grey line), respectively. Red (purple) arrows indicate the polarization within (above) the bubble at its axis. **e**, The in-plane distribution of the thickness-averaged polarization. **f**, In-plane projection of the thickness averaged polarization.

### Extended Data Fig. 8 Thickness dependence of the polar texture in $\text{PTO}_n/\text{STO}_{10}$ ( $n = 12, 16, 20$ ) bilayers transferred on silicon and crystal structures of pure freestanding PTO and PTO/STO bilayer.

The surface morphology, in-plane PFM amplitude and phase images of **(a)**  $n = 20$ , **(b)**  $n = 16$ , **(c)**  $n = 12$  bilayer films. Only the 20 u.c. PTO/10 u.c. STO shows circular shape polar textures. Scale bar, 30 nm. X-ray diffraction  $2\theta\text{-}\omega$  scans around (002) (left) and (101) (right) diffraction peaks for **(d)** freestanding 20 u.c. PTO film and **(e)** freestanding  $(\text{PbTiO}_3)_{20}/(\text{SrTiO}_3)_{10}$  bilayer. Schematic images showing the crystal structures of **(f)** freestanding 20 u.c. PTO film and **(g)** freestanding  $(\text{PbTiO}_3)_{20}/(\text{SrTiO}_3)_{10}$  bilayer.

## Extended Data Fig. 9 Reversible switching of topological nanodomains.

**a**, Schematic images illustrating the reversible switching of the topological domains by external electric field: The coexistence of two types of nanodomains in pristine bilayer (i) were first switched into all centre-divergent nanodomains by a scan with +5 V bias voltage (ii) and then further switched to all centre-convergent nanodomains by a scan with -5 V bias voltage (iii). **b-d**, Vertical PFM amplitude (VPFM-amp.), vertical phase (VPFM-pha.), lateral PFM amplitude (LPFM-amp.) and lateral phase (LPFM-pha.) images for three corresponding cases shown in (a). The centre-divergent (centre-convergent) domains are marked by red (blue) circles. Scale bar, 100 nm. **e**, VPFM-amp. (upper left), VPFM-pha. (bottom left), LPFM-amp. (upper right) and LPFM-pha. (bottom right) images taken under an a.c. amplitude of 500 mV for one single skyrmion-like polar nanodomain after applying the 0 V, -1 V, -4 V, -2 V, +1 V and +4 V DC voltage. Scale bar, 20 nm. **f**, Hysteresis loop of the skyrmion-like polar nanodomain.

## Extended Data Fig. 10 Domain structures and switching behaviour in a PTO/STO bilayer transferred on a P-doped silicon wafer after a standard electron beam lithography process.

**a**, Schematic images showing standard lithography process on the ferroelectric bilayer transferred on a P-doped silicon wafer. **b**, Quadrat patterns on a P-doped silicon wafer, inset shows the topography of a single piece. Scale bar, 10  $\mu$ m. **c**, Vertical PFM amplitude (VPFM-amp.) and phase (VPFM-pha.), lateral PFM amplitude (LPFM-amp.) and phase (LPFM-pha.) images for the freestanding  $\text{PTO}_{20}/\text{STO}_{10}$  bilayers transferred on P-doped silicon substrate. Scale bar, 100 nm.

## Rights and permissions

### Reprints and Permissions

## About this article

### Cite this article

Han, L., Addiego, C., Prokhorenko, S. *et al.* High-density switchable skyrmion-like polar nanodomains integrated on silicon. *Nature* **603**, 63–67 (2022). <https://doi.org/10.1038/s41586-021-04338-w>

- Received: 24 January 2021
- Accepted: 10 December 2021
- Published: 02 March 2022
- Issue Date: 03 March 2022
- DOI: <https://doi.org/10.1038/s41586-021-04338-w>

### Share this article

Anyone you share the following link with will be able to read this content:

[Get shareable link](#)

Sorry, a shareable link is not currently available for this article.

[Copy to clipboard](#)

Provided by the Springer Nature SharedIt content-sharing initiative

---

This article was downloaded by **calibre** from <https://www.nature.com/articles/s41586-021-04338-w>

- Article
- [Published: 02 March 2022](#)

# Imaging of isotope diffusion using atomic-scale vibrational spectroscopy

- [Ryosuke Senga](#) [ORCID: orcid.org/0000-0001-9225-4144](#)<sup>1</sup>,
- [Yung-Chang Lin](#) [ORCID: orcid.org/0000-0002-3968-7239](#)<sup>1</sup>,
- [Shigeyuki Morishita](#) [ORCID: orcid.org/0000-0001-9705-4942](#)<sup>2</sup>,
- [Ryuichi Kato](#)<sup>1</sup>,
- [Takatoshi Yamada](#) [ORCID: orcid.org/0000-0003-2828-6744](#)<sup>1</sup>,
- [Masataka Hasegawa](#)<sup>1</sup> &
- [Kazu Suenaga](#) [ORCID: orcid.org/0000-0002-6107-1123](#)<sup>3</sup>

[Nature](#) volume **603**, pages 68–72 (2022)

- 1415 Accesses
- 28 Altmetric
- [Metrics details](#)

## Subjects

- [Characterization and analytical techniques](#)
- [Imaging techniques](#)
- [Nanofabrication and nanopatterning](#)
- [Synthesis of graphene](#)

## Abstract

The spatial resolutions of even the most sensitive isotope analysis techniques based on light or ion probes are limited to a few hundred nanometres. Although vibrational spectroscopy using electron probes has achieved higher spatial resolution<sup>1,2,3</sup>, the detection of isotopes at the atomic level<sup>4</sup> has been challenging so far. Here we show the unambiguous isotopic imaging of <sup>12</sup>C carbon atoms embedded in <sup>13</sup>C graphene and the monitoring of their self-diffusion via atomic-level vibrational spectroscopy. We first grow a domain of <sup>12</sup>C carbon atoms in a pre-existing crack of <sup>13</sup>C graphene, which is then annealed at 600 degrees Celsius for several hours. Using scanning transmission electron microscopy–electron energy loss spectroscopy, we obtain an isotope map that confirms the segregation of <sup>12</sup>C atoms that diffused rapidly. The map also indicates that the graphene layer becomes isotopically homogeneous over 100-nanometre regions after 2 hours. Our results demonstrate the high mobility of carbon atoms during growth and annealing via self-diffusion. This imaging technique can provide a fundamental methodology for nanoisotope engineering and monitoring, which will aid in the creation of isotope labels and tracing at the nanoscale.

This is a preview of subscription content

## Access options

Subscribe to Nature+

Get immediate online access to the entire Nature family of 50+ journals

\$29.99

monthly

[Subscribe](#)

Subscribe to Journal

Get full journal access for 1 year

\$199.00

only \$3.90 per issue

[Subscribe](#)

All prices are NET prices.

VAT will be added later in the checkout.

Tax calculation will be finalised during checkout.

Buy article

Get time limited or full article access on ReadCube.

\$32.00

[Buy](#)

All prices are NET prices.

### **Additional access options:**

- [Log in](#)
- [Learn about institutional subscriptions](#)

**Fig. 1: Comparison of  $^{12}\text{C}$  and  $^{13}\text{C}$  graphene by dark-field EELS.**

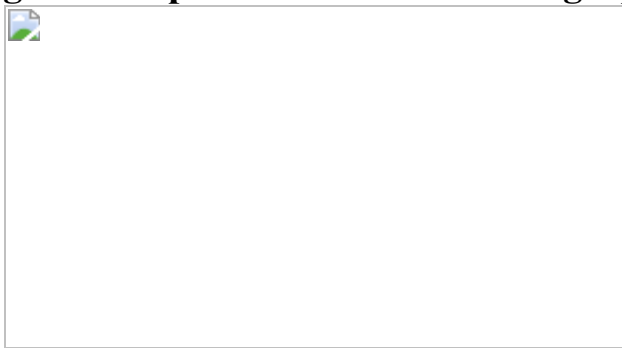


**Fig. 2: In situ growth of isotope nanodomains.**

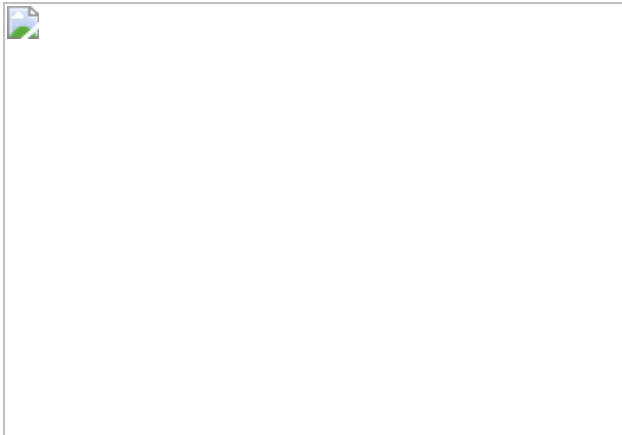


**Fig. 3: Isotopic mapping of single-layer graphene.**

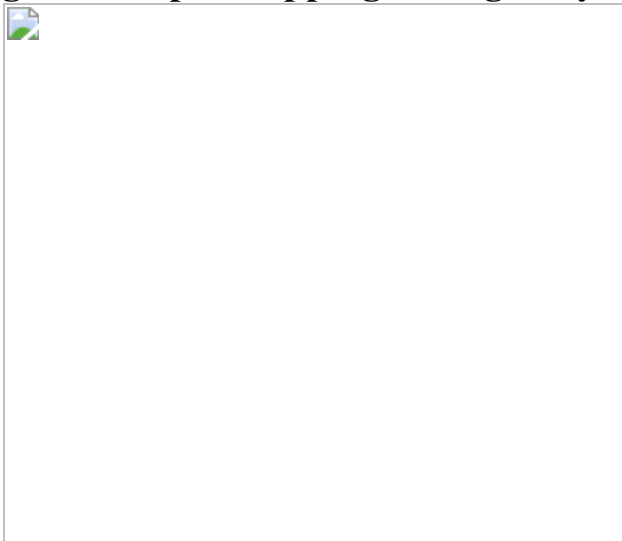


**Fig. 4: Self-diffusion of carbon atoms in graphene.**

## Data availability

The datasets generated and/or analysed during this study are provided with the paper as source data. [Source data](#) are provided with this paper.

## Code availability

Quantum ESPRESSO is an open-source suite of computational tools available at [www.quantum-espresso.org](http://www.quantum-espresso.org).

## References

1. Hage, F. S., Radtke, G., Kepaptsoglou, D. M., Lazzeri, M. & Ramasse, Q. M. Single-atom vibrational spectroscopy in the scanning transmission electron microscope. *Science* **367**, 1124–1127 (2020).
2. Yan, X. et al. Single-defect phonons imaged by electron microscopy. *Nature* **589**, 65–69 (2021).
3. Venkatraman, K., Levin, B. D. A., March, K., Rez, P. & Crozier, P. A. Vibrational spectroscopy at atomic resolution with electron impact scattering. *Nat. Phys.* **15**, 1237–1241 (2019).
4. Hachtel, J. A. et al. Identification of site-specific isotopic labels by vibrational spectroscopy in the electron microscope. *Science* **363**, 525–528 (2019).
5. Ong, S.-E. et al. Stable isotope labeling by amino acids in cell culture, SILAC, as a simple and accurate approach to expression proteomics. *Mol. Cell. Proteomics* **1**, 376–386 (2002).
6. Li, X., Cai, W., Colombo, L. & Ruoff, R. S. Evolution of graphene growth on Ni and Cu by carbon isotope labeling. *Nano Lett.* **9**, 4268–4272 (2009).
7. Li, Q. et al. Growth of adlayer graphene on Cu studied by carbon isotope labeling. *Nano Lett.* **13**, 486–490 (2013).
8. Wiederhold, J. G. Metal stable isotope signatures as tracers in environmental geochemistry. *Environ. Sci. Technol.* **49**, 2606–2624 (2015).

9. Krogh, T. E. A low-contamination method for hydrothermal decomposition of zircon and extraction of U and Pb for isotopic age determinations. *Geochim. Cosmochim. Acta* **87**, 485–494 (1973).
10. Susi, T. et al. Isotope analysis in the transmission electron microscope. *Nat. Commun.* **7**, 13040 (2016).
11. Krivanek, O. L. et al. Vibrational spectroscopy in the electron microscope. *Nature* **514**, 209–212 (2014).
12. Senga, R. et al. Position and momentum mapping of vibrations in graphene nanostructures. *Nature* **573**, 247–250 (2019).
13. Zhang, H., Lee, G., Fonseca, A. F., Borders, T. L. & Cho, K. Isotope effect on the thermal conductivity of graphene. *J. Nanomater.* **2010**, 537657 (2010).
14. Liu, Z. et al. In situ observation of step-edge in-plane growth of graphene in a STEM. *Nat. Commun.* **5**, 4055 (2014).
15. Garvie, L. A. J., Craven, A. J. & Brydson, R. Use of electron-energy loss near-edge fine structure in the study of minerals. *Am. Mineral.* **79**, 411–425 (1994).
16. Kimoto, K., Sekiguchi, T. & Aoyama, T. Chemical shift mapping of Si L and K edges using spatially resolved EELS and energy-filtering TEM. *J. Electron Microsc.* **46**, 369–374 (1997).
17. Lichtert, S. & Verbeeck, J. Statistical consequences of applying a PCA noise filter on EELS spectrum images. *Ultramicroscopy* **125**, 35–42 (2013).
18. Gan, Y., Sun, L. & Banhart, F. One- and two-dimensional diffusion of metal atoms in graphene. *Small* **4**, 587–591 (2008).
19. Dienes, G. J. Mechanism for self-diffusion in graphite. *J. Appl. Phys.* **23**, 1194–1200 (1952).

20. Banhart, F., Kotakoski, J. & Krasheninnikov, A. V. Structural defects in graphene. *ACS Nano* **5**, 26–41 (2011).
21. Konečná, A., Iyikanat, F. & de Abajo, F. J. G. Atomic-scale vibrational mapping and isotope identification with electron beams. *ACS Nano* **15**, 9890–9899 (2021).
22. Zan, R., Ramasse, Q. M., Bangert, U. & Novoselov, K. S. Graphene reknits its holes. *Nano Lett.* **12**, 3936–3940 (2012).
23. Giannozzi, P. et al. Quantum ESPRESSO: a modular and open-source software project for quantum simulations of materials. *J. Phys. Condens. Matter* **21**, 395502 (2009).

## Acknowledgements

This work was supported by JST-PRESTO (JPMJPR2009), JST-CREST (JPMJCR20B1, JPMJCR1993), JSPS KAKENHI (16H06333, 21H05235), ER-C “MORE-TEM” and NEDO (JPNP16010) projects.

## Author information

### Affiliations

1. Nanomaterials Research Institute, National Institute of Advanced Industrial Science and Technology (AIST), Ibaraki, Japan  
Ryosuke Senga, Yung-Chang Lin, Ryuichi Kato, Takatoshi Yamada & Masataka Hasegawa
2. JEOL Ltd, Tokyo, Japan  
Shigeyuki Morishita
3. The Institute of Scientific and Industrial Research (ISIR), Osaka University, Ibaraki, Japan

Kazu Suenaga

## Contributions

R.S. and K.S. designed the experiments. R.S. performed the in situ graphene growth in TEM. R.S. and S.M. performed EEL spectroscopy. R.S. analysed the data. R.S., Y.-C.L. and R.K. prepared the samples on the TEM grid. R.K., T.Y. and M.H. prepared the samples by CVD. R.S. and K.S. co-wrote the paper. All authors commented on the manuscript.

## Corresponding authors

Correspondence to [Ryosuke Senga](#) or [Kazu Suenaga](#).

## Ethics declarations

## Competing interests

The authors declare no competing interests.

## Peer review

## Peer review information

*Nature* thanks F. Javier Garcia de Abajo, Jordan Hachtel and Quentin Ramasse for their contribution to the peer review of this work.

## Additional information

**Publisher's note** Springer Nature remains neutral with regard to jurisdictional claims in published maps and institutional affiliations.

## Extended data figures and tables

## Extended Data Fig. 1 EEL spectra including zero-loss peaks at bright field and dark field.

**a**, EEL spectrum at bright field without samples. **b, c**, Linear- and log-scaled EEL spectra at dark field on  $^{13}\text{C}$  graphene. The natural width of the zero-loss peak in the ideal on-axis condition has been shown. As an instrumental function, the zero-loss half-width is 18 meV, whereas it is 45 meV in the off-axis condition (with sample). The zero-loss peak in the off-axis is an ambiguous concept and cannot be detected without a sample.

[Source data](#)

## Extended Data Fig. 2 EEL vibrational spectra for 1 layer (1L) and 2 layers (2L) graphene made of $^{12}\text{C}$ , $^{13}\text{C}$ and both stacked 2L ( $^{12}\text{C}/^{13}\text{C}$ ).

**a**, Comparison of the optical modes (H-peak) in the vibrational spectra of all the samples including 1L graphene shown in Fig. 1. The energy shift of approximately 7–8 meV between isotopes was found in 2L as in the case of 1L. The H-peak in 2L consists of two components due to possible contributions from the TO mode due to LO–TO splitting or the high-energy component of the LA mode. **b**, Line shape analysis of the vibration spectra obtained from 2L samples, where a rough component analysis by Voigt function is possible as in the case of 1L shown in Fig. 1. In this case, four components were used for the fittings: the L-peak, which is mainly the contribution of acoustic phonons, the two H-peaks mentioned above, and the peak that appears between them, which is considered to be the contribution of out-of-plane ZO mode.

[Source data](#)

## Extended Data Fig. 3 Orientation dependence of vibrational spectra obtained by dark-field EELS.

The signal is almost identical regardless of the position of the EELS collection aperture (green, red and black); therefore, the in-plane orientation

of graphene hardly affects the fitting parameters. The lattice defects in graphene also do not affect these parameters, except for the acoustic vibration mode in the lower peak, which is considered negligible.

[Source data](#)

**Extended Data Fig. 4 Simulated phonon dispersion and PDOS.**

The phonon dispersion (left) and PDOS (right) of  $^{12}\text{C}$  and  $^{13}\text{C}$  graphene obtained by DFPT calculations in Quantum Espresso. The energy difference between  $^{12}\text{C}$  and  $^{13}\text{C}$  graphene is 7.7 meV at the highest energy peak in PDOS corresponding to the LO mode and 6.7 meV at the second highest energy peak which is mainly contributed from the LO/TO mode. The interatomic force constants calculated from DFPT is, for instance, 52.4 eV  $\text{\AA}^{-2}$  for the in-plane direction at  $\Gamma$ . This calculation was performed to estimate the energy shift of the PDOS of  $^{12}\text{C}$  and  $^{13}\text{C}$  with the simple model. To reproduce the experimental spectra, full calculation considering the charge modulation in the higher-order Brillouin Zone is necessary, although such calculation is beyond the scope of this study and is not addressed here.

[Source data](#)

**Extended Data Fig. 5 Probe size and possible isotope configurations at the probed region.**

**a**, Comparison of probe and pixel size with graphene lattice. When the electron beam is fixed on an atom with our probe condition in which the probe size is increased to gain the current, the resulting spectrum contains the signal of the nearest three atoms in addition to that of the atom at the centre of the probe. Thus, a single spectrum roughly consists of the average signal of four atoms. The momentum space was also integrated up to  $3.5 \text{\AA}^{-1}$ . Therefore, the spatial resolution was influenced by the integration effect in both real and momentum space. Based on a study by Hage et al. using silicon single atoms on graphene, when the probe size is sufficiently small, a localized signal at the single atom level can be obtained in the dark-field

EELS condition<sup>1</sup>. **b**, Isotope combinations of the four atoms. The colour distribution at the top in **b** corresponds to that used in Figs. 3, 4. The corresponding vibrational energies of the LO/TO mode at  $\Gamma$  are calculated by DFPT and shown on the bottom line in **b**. When all four atoms are  $^{12}\text{C}$  or  $^{13}\text{C}$ , the energy difference of the H-peak between them is the largest and detectable with more than 90% of confidence level. If any one or two of the four atoms belong to different isotopes, the peak positions are between them. In this case, there are six possible configurations, as shown in **b**.

[Source data](#)

**Extended Data Fig. 6 Isotope colour maps before and after filtering.**

**a, b**, The isotope colour map in Fig. 3 before and after median filtering, respectively.

[Source data](#)

**Extended Data Fig. 7 Composition of residual gas in the TEM chamber measured by quadrupole mass spectroscopy.**

The residual gases include hydrocarbons such as  $\text{CH}_x$  and  $\text{C}_2\text{H}_x$ .

[Source data](#)

**Extended Data Fig. 8 Two-dimensional vibrational spectroscopy across a grain boundary.**

**a**, TEM image of  $^{13}\text{C}$  graphene involving a grain boundary. The grain boundary extends from the top right to the bottom left of the image. The crystal orientation is rotated by approximately 16° across the grain boundary comprised of 5–7 membered rings, as indicated by the yellow lines. **b**, Annular dark-field image obtained by performing a STEM-EELS two-dimensional scan at the same position as in **a**. **c**, Colour map of the high-energy peak positions corresponding to **b**. **d**, The EEL spectra taken

from positions 1–3 in **b** are shown. The H-peaks in all three spectra are almost identical.

[Source data](#)

**Extended Data Fig. 9 H-peak position mapping on a crack of  $^{12}\text{C}$  graphene embedded by in-situ graphene growth in TEM.**

**a, b,** TEM image of initial  $^{12}\text{C}$  graphene including a crack and the same position after the nanodomain growth, respectively. The newly grown domain contains prolific defects involving 5–7 membered rings, as shown in **c**. **d**, Annular dark-field image obtained by performing a STEM-EELS two-dimensional scan at the same position as in **b**. **e**, Colour map showing the position of the high-energy peak without noise filtering. The peak positions are almost uniform over the whole area, including the newly grown region.

[Source data](#)

**Extended Data Fig. 10 Noise level quantifications of the measurements.**

**a, b,** The variation of the measured vibrational peak positions for line scans with an exposure time of 1 s per pixel on  $^{12}\text{C}$  and  $^{13}\text{C}$  graphene, respectively. The standard deviations  $\sigma$  for 500 data points are 2.1 meV for  $^{12}\text{C}$  and 2.0 meV for  $^{13}\text{C}$  graphene, which is three times smaller than the energy shift  $S$  between  $^{12}\text{C}$  and  $^{13}\text{C}$  graphene  $\sim$ 8 meV. Because the standard deviations of the measured points are based on fitting and contain errors, then the confidence intervals cannot be directly measured around those data points. This statistical analysis, however, simply proves the high detection level of  $^{12}\text{C}$  atoms in case of 4 atoms and will give a standard for future experiments. Note that the purities of these samples are both over 99%, and thus, the peaking data points may be attributed to 1% of the isotopes in the samples. **c**, The variation of the measured vibrational peak positions on  $^{13}\text{C}$  graphene (corresponding to Fig. 4a) shows a  $\sigma$  of 3.0 meV at an exposure time of 0.5 s. Note that the data points at the crack are excluded.

## Source data

**Extended Data Table 1 Fitted results of the vibrational spectra obtained from  $^{12}\text{C}$  and  $^{13}\text{C}$  graphene**

## **Source data**

[Source Data Fig. 1](#)

[Source Data Fig. 2](#)

[Source Data Fig. 3](#)

[Source Data Fig. 4](#)

[Source Data Extended Data Fig. 1](#)

[Source Data Extended Data Fig. 2](#)

[Source Data Extended Data Fig. 3](#)

[Source Data Extended Data Fig. 4](#)

[Source Data Extended Data Fig. 5](#)

[Source Data Extended Data Fig. 6](#)

[Source Data Extended Data Fig. 7](#)

[Source Data Extended Data Fig. 8](#)

[Source Data Extended Data Fig. 9](#)

[Source Data Extended Data Fig. 10](#)

# Rights and permissions

[Reprints and Permissions](#)

## About this article

### Cite this article

Senga, R., Lin, YC., Morishita, S. *et al.* Imaging of isotope diffusion using atomic-scale vibrational spectroscopy. *Nature* **603**, 68–72 (2022).  
<https://doi.org/10.1038/s41586-022-04405-w>

- Received: 22 July 2021
- Accepted: 05 January 2022
- Published: 02 March 2022
- Issue Date: 03 March 2022
- DOI: <https://doi.org/10.1038/s41586-022-04405-w>

### Share this article

Anyone you share the following link with will be able to read this content:

[Get shareable link](#)

Sorry, a shareable link is not currently available for this article.

[Copy to clipboard](#)

Provided by the Springer Nature SharedIt content-sharing initiative

[\*\*Isotopes tracked on a sub-nanometre scale using electron spectroscopy\*\*](#)

- Jordan A. Hachtel

## News & Views 02 Mar 2022

---

This article was downloaded by **calibre** from <https://www.nature.com/articles/s41586-022-04405-w>

| [Section menu](#) | [Main menu](#) |

- Article
- [Published: 17 January 2022](#)

# All-perovskite tandem solar cells with improved grain surface passivation

- [Renxing Lin<sup>1</sup>](#) na1,
- [Jian Xu<sup>2</sup>](#) na1,
- [Mingyang Wei](#) [ORCID: orcid.org/0000-0003-4820-2210](#)<sup>2</sup> na1,
- [Yurui Wang<sup>1</sup>](#) na1,
- [Zhengyuan Qin<sup>3</sup>](#) na1,
- [Zhou Liu<sup>1</sup>](#),
- [Jinlong Wu<sup>1</sup>](#),
- [Ke Xiao<sup>1,4</sup>](#),
- [Bin Chen](#) [ORCID: orcid.org/0000-0002-2106-7664](#)<sup>2</sup>,
- [So Min Park<sup>2</sup>](#),
- [Gang Chen](#) [ORCID: orcid.org/0000-0001-8112-3579](#)<sup>5</sup>,
- [Harindi R. Atapattu<sup>6</sup>](#),
- [Kenneth R. Graham<sup>6</sup>](#),
- [Jun Xu<sup>4</sup>](#),
- [Jia Zhu](#) [ORCID: orcid.org/0000-0002-2871-4369](#)<sup>1</sup>,
- [Ludong Li<sup>1</sup>](#),
- [Chunfeng Zhang](#) [ORCID: orcid.org/0000-0001-9030-5606](#)<sup>3</sup>,
- [Edward H. Sargent](#) [ORCID: orcid.org/0000-0003-0396-6495](#)<sup>2</sup> &
- [Hairen Tan](#) [ORCID: orcid.org/0000-0003-0821-476X](#)<sup>1,7</sup>

*Nature* volume 603, pages 73–78 (2022)

- 12k Accesses

- 1 Citations
- 53 Altmetric
- [Metrics details](#)

## Subjects

- [Photovoltaics](#)
- [Solar cells](#)

## Abstract

All-perovskite tandem solar cells hold the promise of surpassing the efficiency limits of single-junction solar cells<sup>1,2,3</sup>; however, until now, the best-performing all-perovskite tandem solar cells have exhibited lower certified efficiency than have single-junction perovskite solar cells<sup>4,5</sup>. A thick mixed Pb–Sn narrow-bandgap subcell is needed to achieve high photocurrent density in tandem solar cells<sup>6</sup>, yet this is challenging owing to the short carrier diffusion length within Pb–Sn perovskites. Here we develop ammonium-cation-passivated Pb–Sn perovskites with long diffusion lengths, enabling subcells that have an absorber thickness of approximately 1.2 μm. Molecular dynamics simulations indicate that widely used phenethylammonium cations are only partially adsorbed on the surface defective sites at perovskite crystallization temperatures. The passivator adsorption is predicted to be enhanced using 4-trifluoromethyl-phenylammonium (CF<sub>3</sub>-PA), which exhibits a stronger perovskite surface-passivator interaction than does phenethylammonium. By adding a small amount of CF<sub>3</sub>-PA into the precursor solution, we increase the carrier diffusion length within Pb–Sn perovskites twofold, to over 5 μm, and increase the efficiency of Pb–Sn perovskite solar cells to over 22%. We report a certified efficiency of 26.4% in all-perovskite tandem solar cells, which exceeds that of the best-performing single-junction perovskite solar cells. Encapsulated tandem devices retain more than 90% of their initial performance after 600 h of operation at the maximum power point under 1 Sun illumination in ambient conditions.

This is a preview of subscription content

## Access options

Subscribe to Nature+

Get immediate online access to the entire Nature family of 50+ journals

\$29.99

monthly

[Subscribe](#)

Subscribe to Journal

Get full journal access for 1 year

\$199.00

only \$3.90 per issue

[Subscribe](#)

All prices are NET prices.

VAT will be added later in the checkout.

Tax calculation will be finalised during checkout.

Buy article

Get time limited or full article access on ReadCube.

\$32.00

[Buy](#)

All prices are NET prices.

## **Additional access options:**

- [Log in](#)
- [Learn about institutional subscriptions](#)

**Fig. 1: Interaction between passivator and Pb–Sn perovskite surface.**



**Fig. 2: PV performance of Pb–Sn perovskite solar cells.**

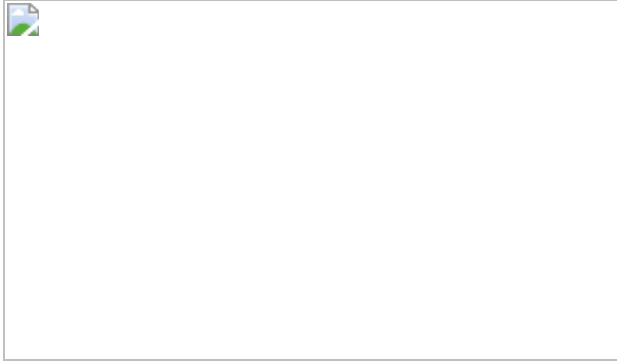


**Fig. 3: Characterization of mixed Pb–Sn perovskite films with passivating agents.**

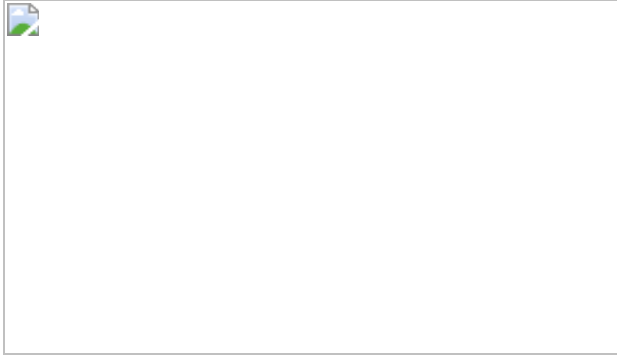


**Fig. 4: PV performance and stability of all-perovskite tandem solar cells with CF3-PA additive.**



## Data availability

The data that support the findings of this study are available from the corresponding authors on reasonable request.

## References

1. Albrecht, S. & Rech, B. Perovskite solar cells: on top of commercial photovoltaics. *Nat. Energy* **2**, 16196 (2017).
2. Wang, R. et al. Prospects for metal halide perovskite-based tandem solar cells. *Nat. Photonics* **15**, 411–425 (2021).
3. Jošt, M., Kegelmann, L., Korte, L. & Albrecht, S. Monolithic perovskite tandem solar cells: a review of the present status and advanced characterization methods toward 30% efficiency. *Adv. Energy Mater.* **10**, 1904102 (2020).
4. Lin, R. et al. Monolithic all-perovskite tandem solar cells with 24.8% efficiency exploiting comproportionation to suppress Sn(II) oxidation in precursor ink. *Nat. Energy* **4**, 864–873 (2019).
5. Min, H. et al. Perovskite solar cells with atomically coherent interlayers on  $\text{SnO}_2$  electrodes. *Nature* **598**, 444–450 (2021).

6. Yang, Z. et al. Enhancing electron diffusion length in narrow-bandgap perovskites for efficient monolithic perovskite tandem solar cells. *Nat. Commun.* **10**, 4498 (2019).
7. Eperon, G. E. et al. Perovskite-perovskite tandem photovoltaics with optimized band gaps. *Science* **354**, 861–865 (2016).
8. Li, Z. et al. Cost analysis of perovskite tandem photovoltaics. *Joule* **2**, 1559–1572 (2018).
9. Green, M. A. et al. Solar cell efficiency tables (version 58). *Prog. Photovoltaics Res. Appl.* **29**, 657–667 (2021).
10. Xiao, K. et al. All-perovskite tandem solar cells with 24.2% certified efficiency and area over 1 cm<sup>2</sup> using surface-anchoring zwitterionic antioxidant. *Nat. Energy* **5**, 870–880 (2020).
11. Tong, J. et al. Carrier lifetimes of >1 μs in Sn-Pb perovskites enable efficient all-perovskite tandem solar cells. *Science* **364**, 475–479 (2019).
12. Yu, Z. et al. Simplified interconnection structure based on C<sub>60</sub>/SnO<sub>2-x</sub> for all-perovskite tandem solar cells. *Nat. Energy* **5**, 657–665 (2020).
13. Li, C. et al. Low-bandgap mixed tin–lead iodide perovskites with reduced methylammonium for simultaneous enhancement of solar cell efficiency and stability. *Nat. Energy* **5**, 768–776 (2020).
14. Liu, H. et al. Modulated crystallization and reduced voc deficit of mixed lead–tin perovskite solar cells with antioxidant caffeic acid. *ACS Energy Lett.* **6**, 2907–2916 (2021).
15. Kapil, G. et al. Tin-lead perovskite fabricated via ethylenediamine interlayer guides to the solar cell efficiency of 21.74%. *Adv. Energy Mater.* **11**, 2101069 (2021).
16. Kirchartz, T. & Rau, U. What makes a good solar cell? *Adv. Energy Mater.* **8**, 1703385 (2018).

17. Kirchartz, T., Bisquert, J., Mora-Sero, I. & Garcia-Belmonte, G. Classification of solar cells according to mechanisms of charge separation and charge collection. *Phys. Chem. Chem. Phys.* **17**, 4007–4014 (2015).
18. Aydin, E., Bastiani, M. & Wolf, S. Defect and contact passivation for perovskite solar cells. *Adv. Mater.* **31**, 1900428 (2019).
19. Ni, Z., Xu, S. & Huang, J. Resolving spatial and energetic distributions of trap states in metal halide perovskite solar cells. *Science* **371**, 1352–1358 (2021).
20. Yang, Y. et al. Top and bottom surfaces limit carrier lifetime in lead iodide perovskite films. *Nat. Energy* **2**, 16207 (2017).
21. Ricciarelli, D., Meggiolaro, D., Ambrosio, F. & De Angelis, F. Instability of tin iodide perovskites: bulk p-doping versus surface tin oxidation. *ACS Energy Lett.* **5**, 2787–2795 (2020).
22. Savill, K. J., Ulatowski, A. M. & Herz, L. M. Optoelectronic properties of tin–lead halide perovskites. *ACS Energy Lett.* **6**, 2413–2426 (2021).
23. Zong, Y., Zhou, Z., Chen, M., Padture, N. P. & Zhou, Y. Lewis-adduct mediated grain-boundary functionalization for efficient ideal-bandgap perovskite solar cells with superior stability. *Adv. Energy Mater.* **8**, 1800997 (2018).
24. Luo, D., Su, R., Zhang, W., Gong, Q. & Zhu, R. Minimizing non-radiative recombination losses in perovskite solar cells. *Nat. Rev. Mater.* **5**, 44–60 (2020).
25. Gao, F., Zhao, Y., Zhang, X. & You, J. Recent progresses on defect passivation toward efficient perovskite solar cells. *Adv. Energy Mater.* **10**, 1902650 (2019).
26. Chen, J. & Park, N.-G. Materials and methods for interface engineering toward stable and efficient perovskite solar cells. *ACS*

*Energy Lett.* **5**, 2742–2786 (2020).

27. Li, C. et al. Vertically aligned 2D/3D Pb–Sn perovskites with enhanced charge extraction and suppressed phase segregation for efficient printable solar cells. *ACS Energy Lett.* **5**, 1386–1395 (2020).
28. Park, S. M., Abtahi, A., Boehm, A. M. & Graham, K. R. Surface ligands for methylammonium lead iodide films: surface coverage, energetics, and photovoltaic performance. *ACS Energy Lett.* **5**, 799–806 (2020).
29. Wang, R. et al. Constructive molecular configurations for surface-defect passivation of perovskite photovoltaics. *Science* **366**, 1509–1513 (2019).
30. Wei, M. et al. Combining efficiency and stability in mixed tin–lead perovskite solar cells by capping grains with an ultrathin 2D layer. *Adv. Mater.* **32**, 1907058 (2020).
31. Chen, B., Rudd, P. N., Yang, S., Yuan, Y. & Huang, J. Imperfections and their passivation in halide perovskite solar cells. *Chem. Soc. Rev.* **48**, 3842–3867 (2019).
32. Jiang, Q. et al. Surface passivation of perovskite film for efficient solar cells. *Nat. Photonics* **13**, 460–466 (2019).
33. Abate, A. et al. Supramolecular halogen bond passivation of organic-inorganic halide perovskite solar cells. *Nano Lett.* **14**, 3247–3254 (2014).
34. Walsh, A., Scanlon, D. O., Chen, S., Gong, X. G. & Wei, S. Self-regulation mechanism for charged point defects in hybrid halide perovskites. *Angew. Chemie* **127**, 1811–1814 (2015).
35. Wehrenfennig, C., Eperon, G. E., Johnston, M. B., Snaith, H. J. & Herz, L. M. High charge carrier mobilities and lifetimes in organolead trihalide perovskites. *Adv. Mater.* **26**, 1584–1589 (2014).

36. Hempel, H., Hages, C. J., Eichberger, R., Repins, I. & Unold, T. Minority and majority charge carrier mobility in Cu<sub>2</sub>ZnSnSe<sub>4</sub> revealed by terahertz spectroscopy. *Sci. Rep.* **8**, 14476 (2018).
37. Al-Ashouri, A. et al. Monolithic perovskite/silicon tandem solar cell with >29% efficiency by enhanced hole extraction. *Science* **370**, 1300–1309 (2020).
38. Palmstrom, A. F. et al. Enabling flexible all-perovskite tandem solar cells. *Joule* **3**, 2193–2204 (2019).
39. Gao, H. et al. Thermally stable all-perovskite tandem solar cells fully using metal oxide charge transport layers and tunnel junction. *Sol. RRL* **5**, 2100814 (2021).
40. Kühne, T. D. et al. CP2K: an electronic structure and molecular dynamics software package -Quickstep: Efficient and accurate electronic structure calculations. *J. Chem. Phys.* **152**, 194103 (2020).
41. Nosé, S. A unified formulation of the constant temperature molecular dynamics methods. *J. Chem. Phys.* **81**, 511–519 (1984).
42. VandeVondele, J. & Hutter, J. Gaussian basis sets for accurate calculations on molecular systems in gas and condensed phases. *J. Chem. Phys.* **127**, 114105 (2007).
43. Goedecker, S. & Teter, M. Separable dual-space Gaussian pseudopotentials. *Phys. Rev. B* **54**, 1703–1710 (1996).
44. Kresse, G. & Furthmüller, J. Efficient iterative schemes for ab initio total-energy calculations using a plane-wave basis set. *Phys. Rev. B* **54**, 11169–11186 (1996).
45. Perdew, J. P., Burke, K. & Ernzerhof, M. Generalized gradient approximation made simple. *Phys. Rev. Lett.* **77**, 3865–3868 (1996).
46. Lee, K., Murray, É. D., Kong, L., Lundqvist, B. I. & Langreth, D. C. Higher-accuracy van der Waals density functional. *Phys. Rev. B* **82**, 3–

6 (2010).

47. Lu, T. & Chen, F. Multiwfn: a multifunctional wavefunction analyzer. *J. Comput. Chem.* **33**, 580–592 (2012).
48. Han, Q. et al. Low-temperature processed inorganic hole transport layer for efficient and stable mixed Pb-Sn low-bandgap perovskite solar cells. *Sci. Bull.* **64**, 1399–1401 (2019).
49. Santbergen, R. et al. GenPro4 optical model for solar cell simulation and its application to multijunction solar cells. *IEEE J. Photovolt.* **7**, 919–926 (2017).

## Acknowledgements

This work was financially supported by the National Key R&D Program of China (grant no. 2018YFB1500102), the National Natural Science Foundation of China (grant nos. 61974063 and 61921005), the Natural Science Foundation of Jiangsu Province (grant nos. BK20202008 and BK20190315), the Technology Innovation Fund of Nanjing University, Fundamental Research Funds for the Central Universities (grant nos. 0213/14380206 and 0205/14380252), the Frontiers Science Center for Critical Earth Material Cycling Fund (grant no. DLTD2109), the Program A for Outstanding PhD Candidate of Nanjing University, and the Program for Innovative Talents and Entrepreneur in Jiangsu. The work at the University of Toronto was supported by the US Department of the Navy, Office of Naval Research (grant no. N00014-20-1-2572). SciNet is funded by the Canada Foundation for Innovation under the auspices of Compute Canada. K.R.G., S.M.P. and H.R.A. acknowledge the US Department of Energy, Office of Basic Energy Sciences under grant no. DE-SC0018208 for supporting the photoelectron spectroscopy measurements.

## Author information

### Author notes

1. These authors contributed equally: Renxing Lin, Jian Xu, Mingyang Wei, Yurui Wang, Zhengyuan Qin

## Affiliations

1. National Laboratory of Solid State Microstructures, Collaborative Innovation Center of Advanced Microstructures, Jiangsu Key Laboratory of Artificial Functional Materials, College of Engineering and Applied Sciences, Nanjing University, Nanjing, China

Renxing Lin, Yurui Wang, Zhou Liu, Jinlong Wu, Ke Xiao, Jia Zhu, Ludong Li & Hairen Tan

2. Department of Electrical and Computer Engineering, University of Toronto, Toronto, Ontario, Canada

Jian Xu, Mingyang Wei, Bin Chen, So Min Park & Edward H. Sargent

3. School of Physics, Nanjing University, Nanjing, China

Zhengyuan Qin & Chunfeng Zhang

4. School of Electronic Science and Engineering, Nanjing University, Nanjing, China

Ke Xiao & Jun Xu

5. School of Physical Science and Technology, Shanghai Tech University, Shanghai, China

Gang Chen

6. Department of Chemistry, University of Kentucky, Lexington, Kentucky, USA

Harindi R. Atapattu & Kenneth R. Graham

7. Frontiers Science Center for Critical Earth Material Cycling, Nanjing University, Nanjing, China

Hairen Tan

## Contributions

H.T. conceived and directed the overall project. R.L. and Y.W. fabricated all the devices and conducted the characterization. Jian X. carried out the DFT simulation. M.W. performed Tof-SIMS, PL and PL-decay characterization. Z.Q. and C.Z. performed the terahertz measurements and analysis. Z.L. and G.C. carried out the grazing-incidence wide-angle X-ray scattering measurements. J.W., Z.L., K.X., B.C., Jun X., J.Z. and L.L. carried out device fabrication and materials characterization. S.M.P., H.R.A. and K.R.G. performed angle-dependent XPS characterization and analysis. E.H.S. and H.T. supervised the project and assisted in data analysis. R.L., M.W., Jian X., E.H.S. and H.T. wrote the manuscript. All authors discussed the results and commented on the paper.

## Corresponding authors

Correspondence to [Edward H. Sargent](#) or [Hairen Tan](#).

## Ethics declarations

## Competing interests

The authors declare no competing interests.

## Peer review

## Peer review information

*Nature* thanks the anonymous reviewers for their contribution to the peer review of this work.

## Additional information

**Publisher's note** Springer Nature remains neutral with regard to jurisdictional claims in published maps and institutional affiliations.

## Extended data figures and tables

### Extended Data Fig. 1 Optical simulation of all-perovskite tandem solar cells.

The implied photocurrent density ( $J_{sc}$ ) of tandems was calculated as function of wide-bandgap and narrow-bandgap perovskite layer thicknesses.

### Extended Data Fig. 2 PCEs of mixed Pb-Sn perovskite solar cells with various concentrations of passivating agents.

**a**, PEA; **b**, PA; **c**, CF3-PA. The absorber layer thickness is ~1,200 nm.

### Extended Data Fig. 3 Performance of control and CF3-PA mixed Pb-Sn perovskite solar cells with various absorber thicknesses.

For regular thinner Pb-Sn perovskite solar cells (thicknesses of 750 and 900 nm), the diffusion lengths are sufficiently long to ensure charge transport within devices. This agrees with the finding that no obvious improvement was observed in regular thinner devices after we added the CF3-PA passivating agent. The abrupt drop in performance at the thickness of 1.45  $\mu\text{m}$  comes because the precursor solution fails to form high-quality films, a result of finite solubility of metal halides in DMF/DMSO solvent.

### Extended Data Fig. 4 Performance of champion mixed Pb-Sn perovskite solar cells.

**a**, EQE spectra of champion control and CF3-PA mixed Pb-Sn solar cells. The EQE values of CF3-PA device are substantially higher than those of previous works at wavelengths above 800 nm, mainly due to the use of

thicker absorber while maintaining sufficient carrier transport. It is noted that such a high  $J_{sc}$  value is obtained herein together with high  $V_{oc}$  and FF even when using a 1,200 nm absorber. **b**, Reverse and forward  $J-V$  curves of the champion CF3-PA mixed Pb-Sn solar cell. **c**, The steady-state PCE of the champion CF3-PA device.

### Extended Data Fig. 5 Characterization of control and CF3-PA mixed Pb-Sn perovskite films.

**a–b**, Cross-sectional SEM images of 1200-nm-thick (a) control and (b) CF3-PA mixed Pb-Sn perovskite solar cells. **c**, The F 1s XPS spectra of the control and CF3-PA perovskite films. **d**, TOF-SIMS spectra of mixed Pb-Sn perovskite film with CF3-PA additive. The additive is accumulated on the top perovskite surface and at the perovskite/HTL interface.

### Extended Data Fig. 6 Schematic of angle-dependent XPS measurements.

**a**, Schematic of angle-dependent XPS measurements with dashed yellow lines indicating the relative photoelectron probing depth. Angles were defined as normal of the sample to detector. **b–c**, Angle-dependent XPS spectra of the Sn 3d at detector take-off angle  $\theta = 0, 45$ , and  $75^\circ$  for (b) control and (c) CF3-PA perovskite films. Red peaks are fitted to  $\text{Sn}^{2+}$  and the blue peaks are fitted to  $\text{Sn}^{4+}$ .

### Extended Data Fig. 7 Photovoltaic performance of wide-bandgap perovskite solar cells.

**a**, Statistics of PV parameters among 34 devices. **b, c**,  $J-V$  and EQE curves of the best-performing device.

### Extended Data Fig. 8 Photovoltaic performance of all-perovskite tandem solar cells.

**a**, The PCE histogram of all-perovskite tandem solar cells (96 devices) with 1,200-nm-thick NBG subcell. The devices were measured with a mask

having aperture area of 0.049 cm<sup>2</sup>. **b**, Steady-state output of the champion all-perovskite tandem solar over 600 s. The device exhibited a stabilized PCE of 26.6%.

## **Extended Data Fig. 9 Photovoltaic performance of large-area all-perovskite tandem solar cells.**

**a**, EQE spectra of large-area tandem solar cell. **b**, PCE distribution of 21 large-area tandem devices.

## **Extended Data Table 1 Photovoltaic parameters of champion WBG subcell, NBG subcell and all-perovskite tandem solar cell**

## **Supplementary information**

### **Supplementary Information**

Supplementary Notes 1–5, Figs. 1–21, Tables 1–5 and References.

## **Rights and permissions**

### **Reprints and Permissions**

## **About this article**

### **Cite this article**

Lin, R., Xu, J., Wei, M. *et al.* All-perovskite tandem solar cells with improved grain surface passivation. *Nature* **603**, 73–78 (2022). <https://doi.org/10.1038/s41586-021-04372-8>

- Received: 01 August 2021
- Accepted: 20 December 2021

- Published: 17 January 2022
- Issue Date: 03 March 2022
- DOI: <https://doi.org/10.1038/s41586-021-04372-8>

## Share this article

Anyone you share the following link with will be able to read this content:

[Get shareable link](#)

Sorry, a shareable link is not currently available for this article.

[Copy to clipboard](#)

Provided by the Springer Nature SharedIt content-sharing initiative

---

This article was downloaded by **calibre** from <https://www.nature.com/articles/s41586-021-04372-8>

| [Section menu](#) | [Main menu](#) |

- Article
- [Published: 02 March 2022](#)

# Biocatalytic oxidative cross-coupling reactions for biaryl bond formation

- [Lara E. Zetzsche](#) ORCID: [orcid.org/0000-0002-1644-7769<sup>1,2 na1</sup>](https://orcid.org/0000-0002-1644-7769),
- [Jessica A. Yazarians](#) ORCID: [orcid.org/0000-0001-8129-8483<sup>1,3 na1</sup>](https://orcid.org/0000-0001-8129-8483),
- [Suman Chakrabarty](#) ORCID: [orcid.org/0000-0002-6611-3839<sup>1</sup>](https://orcid.org/0000-0002-6611-3839),
- [Meagan E. Hinze](#) ORCID: [orcid.org/0000-0003-4448-058X<sup>1</sup>](https://orcid.org/0000-0003-4448-058X),
- [Lauren A. M. Murray](#) ORCID: [orcid.org/0000-0003-3249-0828<sup>1</sup>](https://orcid.org/0000-0003-3249-0828),
- [April L. Lukowski](#)<sup>1,2</sup>,
- [Leo A. Joyce](#) ORCID: [orcid.org/0000-0002-8649-4894<sup>4</sup>](https://orcid.org/0000-0002-8649-4894) &
- [Alison R. H. Narayan](#) ORCID: [orcid.org/0000-0001-8290-0077<sup>1,2,3</sup>](https://orcid.org/0000-0001-8290-0077)

[Nature](#) volume 603, pages 79–85 (2022)

- 6247 Accesses
- 109 Altmetric
- [Metrics details](#)

## Subjects

- [Biocatalysis](#)

## Abstract

Biaryl compounds, with two connected aromatic rings, are found across medicine, materials science and asymmetric catalysis<sup>1,2</sup>. The necessity of joining arene building blocks to access these valuable compounds has inspired several approaches for biaryl bond formation and challenged chemists to develop increasingly concise and robust methods for this task<sup>3</sup>. Oxidative coupling of two C–H bonds offers an efficient strategy for the formation of a biaryl C–C bond; however, fundamental challenges remain in controlling the reactivity and selectivity for uniting a given pair of substrates<sup>4,5</sup>. Biocatalytic oxidative cross-coupling reactions have the potential to overcome limitations inherent to numerous small-molecule-mediated methods by providing a paradigm with catalyst-controlled selectivity<sup>6</sup>. Here we disclose a strategy for biocatalytic cross-coupling through oxidative C–C bond formation using cytochrome P450 enzymes. We demonstrate the ability to catalyse cross-coupling reactions on a panel of phenolic substrates using natural P450 catalysts. Moreover, we engineer a P450 to possess the desired reactivity, site selectivity and atroposelectivity by transforming a low-yielding, unselective reaction into a highly efficient and selective process. This streamlined method for constructing sterically hindered biaryl bonds provides a programmable platform for assembling molecules with catalyst-controlled reactivity and selectivity.

This is a preview of subscription content

## Access options

Subscribe to Nature+

Get immediate online access to the entire Nature family of 50+ journals

\$29.99

monthly

[Subscribe](#)

Subscribe to Journal

Get full journal access for 1 year

\$199.00

only \$3.90 per issue

[Subscribe](#)

All prices are NET prices.

VAT will be added later in the checkout.

Tax calculation will be finalised during checkout.

Buy article

Get time limited or full article access on ReadCube.

\$32.00

[Buy](#)

All prices are NET prices.

### **Additional access options:**

- [Log in](#)
- [Learn about institutional subscriptions](#)

**Fig. 1: Biaryl bond formation through direct oxidative cross-coupling.**

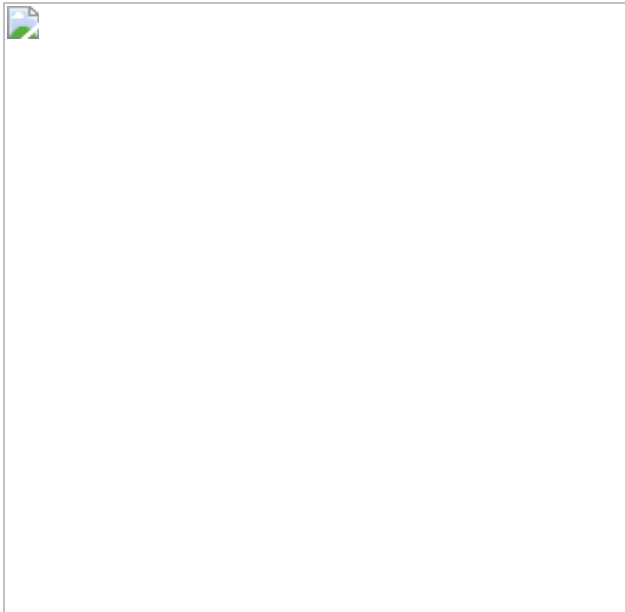


**Fig. 2: Scope of oxidative cross-coupling reactions catalysed by wild-type P450 KtnC.**

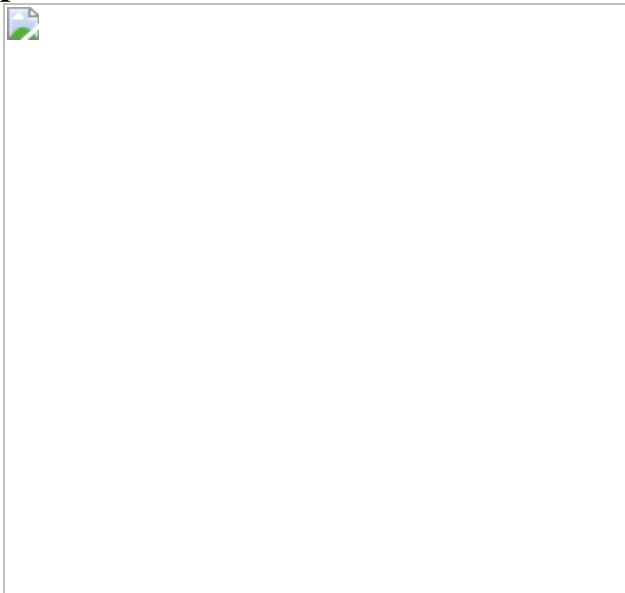


**Fig. 3: Engineering P450 biocatalysts for improved activity and selectivity.**

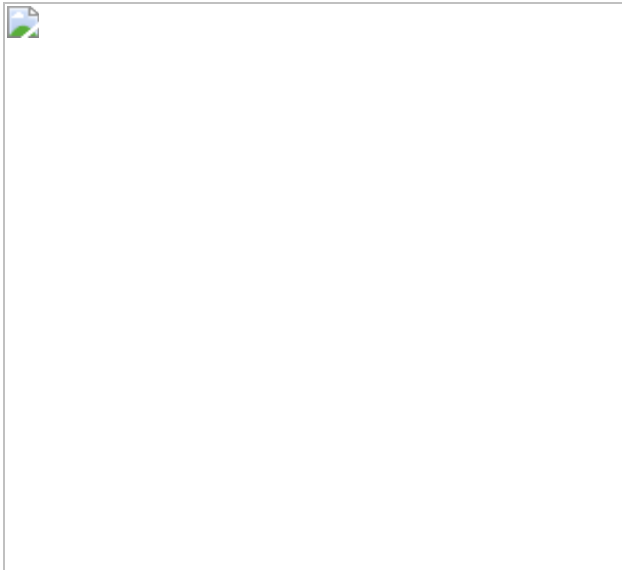
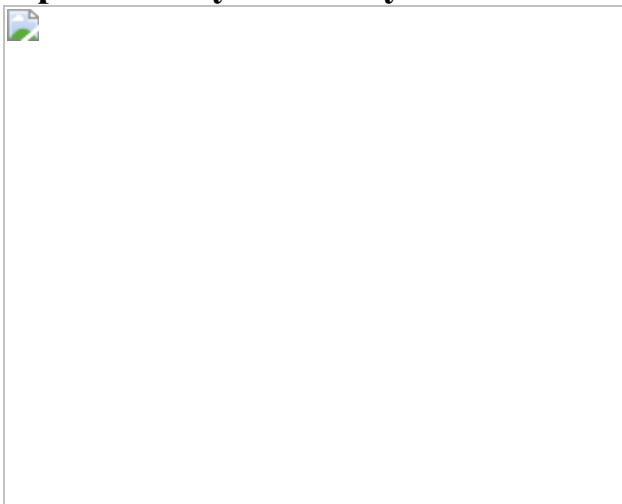


**Fig. 4: Exploring alternative sequence space for catalysts with complementary reactivity.**



## Data availability

Raw data associated with biocatalytic reactions and protein engineering efforts supporting the conclusions of this work are available from the corresponding author upon reasonable request.

## References

1. Yet, L. *Privileged Structures in Drug Discovery: Medicinal Chemistry and Synthesis* 1st edn, 83–154 (Wiley, 2018).

2. Yoon, T. P. & Jacobsen, E. N. Privileged chiral catalysts. *Science* **299**, 1691–1693 (2003).
3. Ashenhurst, J. A. Intermolecular oxidative cross-coupling of arenes. *Chem. Soc. Rev.* **39**, 540–548 (2010).
4. Kozlowski, M. C. Oxidative coupling in complexity building transforms. *Acc. Chem. Res.* **50**, 638–643 (2017).
5. Yang, Y., Lan, J. & You, J. Oxidative C–H/C–H coupling reactions between two (hetero)arenes. *Chem. Rev.* **117**, 8787–8863 (2017).
6. Hüttel, W. & Müller, M. Regio- and stereoselective intermolecular phenol coupling enzymes in secondary metabolite biosynthesis. *Nat. Prod. Rep.* **38**, 1011–1043 (2021).
7. Lunxiang, Y. & Liebscher, J. Carbon–carbon coupling reactions catalyzed by heterogeneous palladium catalysts. *Chem. Rev.* **107**, 133–173 (2007).
8. Boström, J., Brown, D. G., Young, R. J. & Keserü, G. M. Expanding the medicinal chemistry synthetic toolbox. *Nat. Rev. Drug Discov.* **17**, 709–727 (2018).
9. Yin, J., Rainka, M. P., Zhang, X.-X. & Buchwald, S. L. A highly active Suzuki catalyst for the synthesis of sterically hindered biaryls: novel ligand coordination. *J. Am. Chem. Soc.* **124**, 1162–1163 (2002).
10. Cammidge, A. N. & Crépy, K. V. L. Synthesis of chiral binaphthalenes using the asymmetric Suzuki reaction. *Tetrahedron* **60**, 4377–4386 (2004).
11. Martin, R. & Buchwald, S. L. Palladium-catalyzed Suzuki–Miyaura cross-coupling reactions employing dialkylbiaryl phosphine ligands. *Acc. Chem. Res.* **41**, 1461–1473 (2008).
12. Valente, C. et al. The development of bulky palladium NHC complexes for the most-challenging cross-coupling reactions. *Angew.*

*Chem. Int. Ed.* **51**, 3314–3332 (2012).

13. Patel, N. D. et al. Computationally assisted mechanistic investigation and development of Pd-catalyzed asymmetric Suzuki–Miyaura and Negishi cross-coupling reactions for tetra-*ortho*-substituted biaryl synthesis. *ACS Catal.* **8**, 10190–10209 (2018).
14. Ackermann, L., Potukuchi, H. K., Althammer, A., Born, R. & Mayer, P. Tetra-*ortho*-substituted biaryls through palladium-catalyzed Suzuki–Miyaura couplings with a diaminochlorophosphine ligand. *Org. Lett.* **12**, 1004–1007 (2010).
15. Brown, D. G. & Boström, J. Analysis of past and present synthetic methodologies on medicinal chemistry: where have all the new reactions gone? *J. Med. Chem.* **59**, 4443–4458 (2016).
16. Lee, Y. E., Cao, T., Torruellas, C. & Kozlowski, M. C. Selective oxidative homo- and cross-coupling of phenols with aerobic catalysts. *J. Am. Chem. Soc.* **136**, 6782–6785 (2014).
17. Nieves-Quinones, Y. et al. Chromium-salen catalyzed cross-coupling of phenols: mechanism and origin of the selectivity. *J. Am. Chem. Soc.* **141**, 10016–10032 (2019).
18. Shalit, H., Dyadyuk, A. & Pappo, D. Selective oxidative phenol coupling by iron catalysis. *J. Org. Chem.* **84**, 1677–1686 (2019).
19. Reiss, H. et al. Cobalt(II)[salen]-catalyzed selective aerobic oxidative cross-coupling between electron-rich phenols and 2-naphthols. *J. Org. Chem.* **84**, 7950–7960 (2019).
20. Röckl, J. L., Schollmeyer, D., Franke, R. & Waldvogel, S. R. Dehydrogenative anodic C–C coupling of phenols bearing electron-withdrawing groups. *Angew. Chem. Int. Ed.* **59**, 315–319 (2020).
21. Kang, H. et al. Enantioselective vanadium-catalyzed oxidative coupling: development and mechanistic insights. *J. Org. Chem.* **83**, 14362–14384 (2018).

22. Libman, A. et al. Synthetic and predictive approach to unsymmetrical biphenols by iron-catalyzed chelated radical–anion oxidative coupling. *J. Am. Chem. Soc.* **137**, 11453–11460 (2015).
23. Morimoto, K., Sakamoto, K., Ohshika, T., Dohi, T. & Kita, Y. Organooiodine(III)-catalyzed oxidative phenol–arene and phenol–phenol cross-coupling reaction. *Angew. Chem. Int. Ed.* **55**, 3652–3656 (2016).
24. More, N. Y. & Jeganmohan, M. Oxidative cross-coupling of two different phenols: an efficient route to unsymmetrical biphenols. *Org. Lett.* **17**, 3042–3045 (2015).
25. Egami, H. & Katsuki, T. Iron-catalyzed asymmetric aerobic oxidation: oxidative coupling of 2-naphthols. *J. Am. Chem. Soc.* **131**, 6082–6083 (2009).
26. Hovorka, M., Günterova, J. & Zavada, J. Highly selective oxidative cross-coupling of substituted 2-naphthols: a convenient approach to unsymmetrical 1, 1'-binaphthalene-2, 2'-diols. *Tetrahedron Lett.* **31**, 413–416 (1990).
27. Li, X., Hewgley, J. B., Mulrooney, C. A., Yang, J. & Kozlowski, M. C. Enantioselective oxidative biaryl coupling reactions catalyzed by 1,5-diazadecalin metal complexes: efficient formation of chiral functionalized BINOL derivatives. *J. Org. Chem.* **68**, 5500–5511 (2003).
28. Tian, J.-M. et al. Copper-complex-catalyzed asymmetric aerobic oxidative cross-coupling of 2-naphthols: enantioselective synthesis of 3,3'-substituted C1-symmetric BINOLs. *Angew. Chem. Int. Ed.* **58**, 11023–11027 (2019).
29. Bringmann, G. et al. Atroposelective synthesis of axially chiral biaryl compounds. *Angew. Chem. Int. Ed.* **44**, 5384–5427 (2005).
30. Kočovský, P., Vyskočil, Š. & Smrčina, M. Non-symmetrically substituted 1,1'-binaphthyls in enantioselective catalysis. *Chem. Rev.* **103**, 3213–3246 (2003).

31. Kozlowski, M. C., Morgan, B. J. & Linton, E. C. Total synthesis of chiral biaryl natural products by asymmetric biaryl coupling. *Chem. Soc. Rev.* **38**, 3193–3207 (2009).
32. Bringmann, G., Gulder, T., Gulder, T. A. M. & Breuning, M. Atroposelective total synthesis of axially chiral biaryl natural products. *Chem. Rev.* **111**, 563–639 (2011).
33. Aldemir, H., Richarz, R. & Gulder, T. A. The biocatalytic repertoire of natural biaryl formation. *Angew. Chem. Int. Ed.* **53**, 8286–8293 (2014).
34. Mate, D. M. & Alcalde, M. Laccase: a multi-purpose biocatalyst at the forefront of biotechnology. *Microp. Biotechnol.* **10**, 1457–1467 (2017).
35. Sagui, F. et al. Laccase-catalyzed coupling of catharanthine and vindoline: an efficient approach to the bisindole alkaloid anhydrovinblastine. *Tetrahedron* **65**, 312–317 (2009).
36. Obermaier, S., Thiele, W., Fürtges, L. & Müller, M. Enantioselective phenol coupling by laccases in the biosynthesis of fungal dimeric naphthopyrones. *Angew. Chem. Int. Ed.* **58**, 9125–9128 (2019).
37. Fasan, R. Tuning P450 enzymes as oxidation catalysts. *ACS Catal.* **2**, 647–666 (2012).
38. Gil Girol, C. et al. Regio- and stereoselective oxidative phenol coupling in *Aspergillus niger*. *Angew. Chem. Int. Ed.* **51**, 9788–9791 (2012).
39. Mazzaferro, L. S., Huttel, W., Fries, A. & Müller, M. Cytochrome P450-catalyzed regio- and stereoselective phenol coupling of fungal natural products. *J. Am. Chem. Soc.* **137**, 12289–12295 (2015).
40. Chakrabarty, S., Wang, Y., Perkins, J. C. & Narayan, A. R. H. Scalable biocatalytic C–H oxyfunctionalization reactions. *Chem. Soc. Rev.* **49**, 8137–8155 (2020).

41. Noji, M., Nakajima, M. & Koga, K. A new catalytic system for aerobic oxidative coupling of 2-naphthol derivatives by the use of CuCl-amine complex: a practical synthesis of binaphthol derivatives. *Tetrahedron Lett.* **35**, 7983–7984 (1994).
42. Nakajima, M. Synthesis and application of novel biaryl compounds with axial chirality as catalysts in enantioselective reactions. *Yakugaku Zasshi* **120**, 68–75 (2000).
43. Langeslay, R. R. et al. Catalytic applications of vanadium: a mechanistic perspective. *Chem. Rev.* **119**, 2128–2191 (2018).
44. Shannon, P. et al. Cytoscape: a software environment for integrated models of biomolecular interaction networks. *Genome Res.* **13**, 2498–2504 (2003).
45. Gerlt, J. A. et al. Enzyme Function Initiative-Enzyme Similarity Tool (EFI-EST): a web tool for generating protein sequence similarity networks. *Biochim. Biophys. Acta* **1854**, 1019–1037 (2015).
46. Zallot, R., Oberg, N. O. & Gerlt, J. A. ‘Democratized’ genomic enzymology web tools for functional assignment. *Curr. Opin. Chem. Biol.* **47**, 77–85 (2018).
47. Zallot, R., Oberg, N. & Gerlt, J. A. The EFI web resource for genomic enzymology tools: leveraging protein, genome, and metagenome databases to discover novel enzymes and metabolic pathways. *Biochemistry* **58**, 4169–4182 (2019).
48. Funa, N., Funabashi, M., Ohnishi, Y. & Horinouchi, S. Biosynthesis of hexahydroxyperylenequinone melanin via oxidative aryl coupling by cytochrome P-450 in *Streptomyces griseus*. *J. Bacteriol.* **187**, 8149–8155 (2005).
49. Zhao, B. et al. Binding of two flaviolin substrate molecules, oxidative coupling, and crystal structure of *Streptomyces coelicolor* A3(2) cytochrome P450 158A2. *J. Biol. Chem.* **280**, 11599–11607 (2005).

50. Li, S., Podust, L. M. & Sherman, D. H. Engineering and analysis of a self-sufficient biosynthetic cytochrome P450 PikC fused to the RhFRED reductase domain. *J. Am. Chem. Soc.* **129**, 12940–12941 (2007).

## Acknowledgements

This research was supported by funds from the University of Michigan's Life Sciences Institute and the Chemistry Department, Alfred P. Sloan Foundation, and Research Corporation Cottrell Scholars programme. Initial studies on the selectivity of dimerization reactions were supported by the National Institutes of Health (NIH; R35 GM124880), and protein engineering (rounds 4–7) and bioinformatic-based library generation were supported by generous funds from the Novartis Global Scholars Program. L.E.Z. is grateful to the NIH National Center for Complementary and Integrative Health (F31AT010973), J.A.Y. thanks the National Science Foundation Graduate Research Fellowship Program, A.L.L. acknowledges the Rackham Graduate School (University of Michigan) and the NIH (F31 NS111906) for funding. We thank M. Müller for supplying the expression vector containing KtnC and D. Sherman for supplying the expression vector containing RhFRed. We thank E. A. Meucci, E. C. Bornowski and J. B. Pyser for assistance with the synthesis of substrates and C.-H. Chiang for help with acquisition of circular dichroism spectra.

## Author information

### Author notes

1. These authors contributed equally: Lara E. Zetzsche, Jessica A. Yazarians

## Affiliations

1. Life Sciences Institute, University of Michigan, Ann Arbor, MI, USA

Lara E. Zetzsche, Jessica A. Yazarians, Suman Chakrabarty, Meagan E. Hinze, Lauren A. M. Murray, April L. Lukowski & Alison R. H. Narayan

2. Program in Chemical Biology, University of Michigan, Ann Arbor, MI, USA

Lara E. Zetzsche, April L. Lukowski & Alison R. H. Narayan

3. Department of Chemistry, University of Michigan, Ann Arbor, MI, USA

Jessica A. Yazarians & Alison R. H. Narayan

4. Arrowhead Pharmaceuticals, Inc., Madison, WI, USA

Leo A. Joyce

## Contributions

L.E.Z., J.A.Y., S.C., M.E.H. and A.R.H.N. designed experiments and wrote the manuscript with feedback from all authors. L.E.Z. and A.L.L. generated yeast strains used in this work. L.E.Z. performed protein engineering and generated SSNs presented in this work. L.E.Z., J.A.Y., M.E.H. and L.A.M.M. conducted biocatalytic reactions. J.A.Y., S.C. and M.E.H. synthesized substrates and racemic product standards. S.C. carried out product isolation from preparative-scale biocatalytic reactions. L.A.J. calculated circular dichroism spectra and assigned the absolute configuration of products.

## Corresponding author

Correspondence to [Alison R. H. Narayan](#).

## Ethics declarations

## Competing interests

The authors declare no competing interests.

## Peer review

### Peer review information

*Nature* thanks Nicholas Turner and the other, anonymous, reviewer(s) for their contribution to the peer review of this work.

## Additional information

**Publisher's note** Springer Nature remains neutral with regard to jurisdictional claims in published maps and institutional affiliations.

## Supplementary information

### Supplementary Information

This file contains the following sections: I. Chemical synthesis; II. Protein sequences, expression, and purification; III. Biocatalytic reactions with fungal P450 KtnC; IV. Directed evolution of KtnC; V. Biocatalytic reactions with P450–RhFRed enzymes; VI. Preparative-scale biocatalytic reactions; VII. Assignment of absolute configurations; VIII.  $^1\text{H}$  NMR and  $^{13}\text{C}$  NMR spectra of compounds; and IX. References.

## Rights and permissions

### Reprints and Permissions

## About this article

### Cite this article

Zetzsche, L.E., Yazarians, J.A., Chakrabarty, S. *et al.* Biocatalytic oxidative cross-coupling reactions for biaryl bond formation. *Nature* **603**, 79–85 (2022). <https://doi.org/10.1038/s41586-021-04365-7>

- Received: 24 June 2020
- Accepted: 08 December 2021
- Published: 02 March 2022
- Issue Date: 03 March 2022
- DOI: <https://doi.org/10.1038/s41586-021-04365-7>

## Share this article

Anyone you share the following link with will be able to read this content:

[Get shareable link](#)

Sorry, a shareable link is not currently available for this article.

[Copy to clipboard](#)

Provided by the Springer Nature SharedIt content-sharing initiative

---

This article was downloaded by **calibre** from <https://www.nature.com/articles/s41586-021-04365-7>

- Article
- [Published: 02 March 2022](#)

# A wet heterogeneous mantle creates a habitable world in the Hadean

- [Yoshinori Miyazaki](#) ORCID: [orcid.org/0000-0001-8325-8549](https://orcid.org/0000-0001-8325-8549)<sup>1,2</sup> &
- [Jun Korenaga](#) ORCID: [orcid.org/0000-0002-4785-2273](https://orcid.org/0000-0002-4785-2273)<sup>1</sup>

[Nature](#) volume **603**, pages 86–90 (2022)

- 983 Accesses
- 1 Citations
- 243 Altmetric
- [Metrics details](#)

## Subjects

- [Carbon cycle](#)
- [Geodynamics](#)

## Abstract

The Hadean eon, following the global-scale melting of the mantle<sup>1,2,3</sup>, is expected to be a dynamic period, during which Earth experienced vastly different conditions. Geologic records, however, suggest that the surface environment of Earth was already similar to the present by the middle of the Hadean<sup>4,5</sup>. Under what conditions a harsh surface environment could turn into a habitable one remains uncertain<sup>6</sup>. Here we show that a hydrated

mantle with small-scale chemical heterogeneity, created as a result of magma ocean solidification, is the key to ocean formation, the onset of plate tectonics and the rapid removal of greenhouse gases, which are all essential to create a habitable environment on terrestrial planets. When the mantle is wet and dominated by high-magnesium pyroxenites, the removal of carbon dioxide from the atmosphere is expected to be more than ten times faster than the case of a pyrolytic homogeneous mantle and could be completed within 160 million years. Such a chemically heterogeneous mantle would also produce oceanic crust rich in olivine, which is reactive with ocean water and promotes serpentinization. Therefore, conditions similar to the Lost City hydrothermal field<sup>7,8,9</sup> may have existed globally in the Hadean seafloor.

This is a preview of subscription content

## Access options

Subscribe to Nature+

Get immediate online access to the entire Nature family of 50+ journals

\$29.99

monthly

[Subscribe](#)

Subscribe to Journal

Get full journal access for 1 year

\$199.00

only \$3.90 per issue

[Subscribe](#)

All prices are NET prices.  
VAT will be added later in the checkout.  
Tax calculation will be finalised during checkout.

Buy article

Get time limited or full article access on ReadCube.

\$32.00

[Buy](#)

All prices are NET prices.

### **Additional access options:**

- [Log in](#)
- [Learn about institutional subscriptions](#)

**Fig. 1: Schematic illustration of how a magma ocean solidifies with the evolution of atmosphere.**

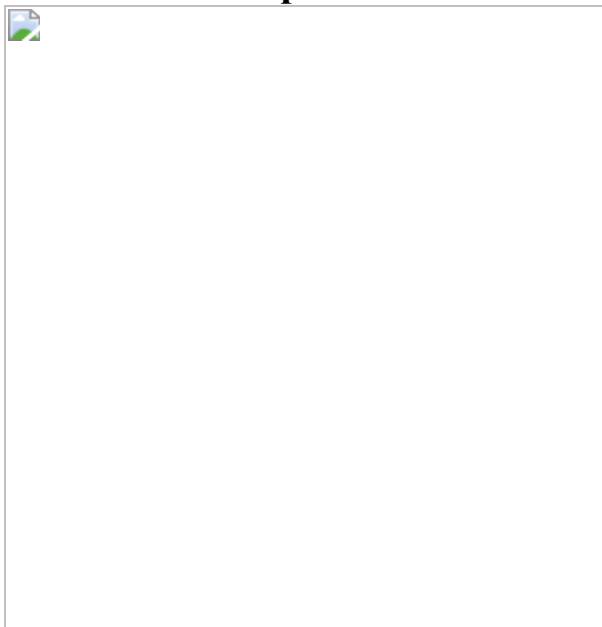


**Fig. 2: Mantle degassing considering the effect of the rheological transition.**

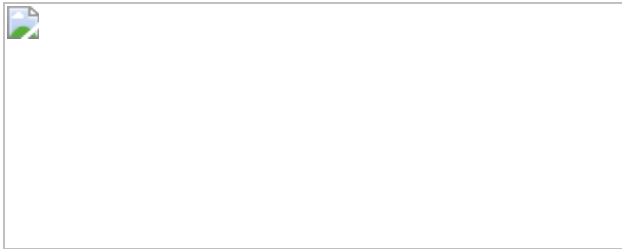


**Fig. 3: Crustal thickness and plate velocity of chemically heterogeneous and pyrolytic (homogeneous) mantles.**

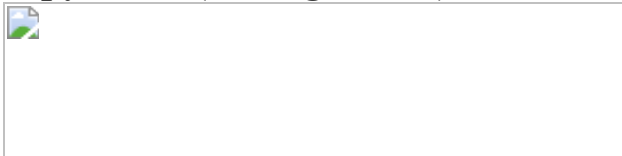
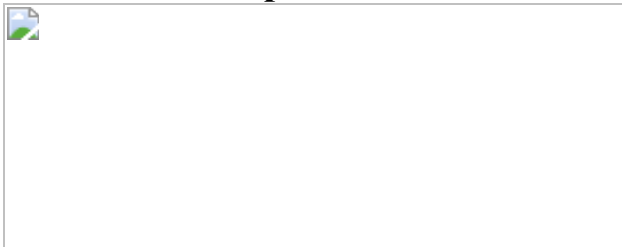


**Fig. 4: Evolutions of atmospheric composition and surface temperature after the onset of plate tectonics.**



## Data availability

All relevant data are provided in the paper. Codes to reproduce the results are available at <https://github.com/yoshi-miyazaki/Hadean-evolution/>. The Gibbs energy minimization code is available at <https://github.com/yoshi-miyazaki/GibbsE-minimization/>. [Source data](#) are provided with this paper.

## References

1. Matsui, T. & Abe, Y. Evolution of an impact-induced atmosphere and magma ocean on the accreting Earth. *Nature* **319**, 303–305 (1986).
2. Tonks, W. B. & Melosh, H. J. Magma ocean formation due to giant impacts. *J. Geophys. Res.* **98**, 5319–5333 (1993).
3. Canup, R. M. & Asphaug, E. Origin of the Moon in a giant impact near the end of the Earth’s formation. *Nature* **412**, 708–712 (2001).

4. Wilde, S. A., Valley, J. W., Peck, W. H. & Graham, C. M. Evidence from detrital zircons for the existence of continental crust and oceans on the Earth 4.4 Gyr ago. *Nature* **409**, 175–178 (2001).
5. Harrison, T. M. The Hadean crust: Evidence from >4 Ga zircons. *Annu. Rev. Earth Planet. Sci.* **37**, 479–505 (2009).
6. Sleep, N. H. & Zahnle, K. Carbon dioxide cycling and implications for climate on ancient Earth. *J. Geophys. Res.* **106**, 1373–1399 (2001).
7. Kelley, D. S. et al. A serpentinite-hosted ecosystem: the Lost City Hydrothermal Field. *Science* **307**, 1428–1434 (2005).
8. Proskurowski, G. et al. Abiogenic hydrocarbon production at Lost City hydrothermal field. *Science* **319**, 604–607 (2008).
9. Klein, F., Grozeva, N. G. & Seewald, J. S. Abiotic methane synthesis and serpentinization in olivine-hosted fluid inclusions. *Proc. Natl Acad. Sci.* **116**, 17666–17672 (2019).
10. Raymond, S. N., Schlichting, H. E., Hersant, F. & Selsis, F. Dynamical and collisional constraints on a stochastic late veneer on the terrestrial planets. *Icarus* **226**, 671–681 (2013).
11. Krissansen-Totton, J., Arney, G. N. & Catling, D. C. Constraining the climate and ocean pH of the early Earth with a geological carbon cycle model. *Proc. Natl Acad. Sci.* **115**, 4105–4110 (2018).
12. Elkins-Tanton, L. T. Linked magma ocean solidification and atmospheric growth for Earth and Mars. *Earth Planet. Sci. Lett.* **271**, 181–191 (2008).
13. Lebrun, T. et al. Thermal evolution of an early magma ocean in interaction with the atmosphere. *J. Geophys. Res. Planet.* **118**, 1155–1176 (2013).
14. Hamano, K., Abe, Y. & Genda, H. Emergence of two types of terrestrial planet on solidification of magma ocean. *Nature* **497**, 607–

610 (2013).

15. Salvador, A. et al. The relative influence of H<sub>2</sub>O and CO<sub>2</sub> on the primitive surface conditions and evolution of rocky planets. *J. Geophys. Res. Planet.* **122**, 1458–1486 (2017).
16. Bower, D. J. et al. Linking the evolution of terrestrial interiors and an early outgassed atmosphere to astrophysical observations. *Astron. Astrophys.* **631**, A103 (2019).
17. Hirschmann, M. M. Magma ocean influence on early atmosphere mass and composition. *Earth Planet. Sci. Lett.* **341–344**, 48–57 (2012).
18. Deng, J., Du, Z., Karki, B. B., Ghosh, D. B. & Lee, K. K. A magma ocean origin to divergent redox evolutions of rocky planetary bodies and early atmospheres. *Nat. Commun.* **11**, 2007 (2020).
19. Abe, Y. Physical state of the very early Earth. *Lithos* **30**, 223–235 (1993).
20. Catling, D. C. & Zahnle, K. J. The Archean atmosphere. *Sci. Adv.* **6**, eaax1420 (2020).
21. Solomatov, V. S. In *Treatise on Geophysics*. Volume 9: Evolution of the Earth 1st edn (ed. Schubert G.) 91–119 (Elsevier, 2007).
22. Hier-Majumder, S. & Hirschmann, M. M. The origin of volatiles in the Earth's mantle. *Geochem. Geophys. Geosyst.* **18**, 3078–3092 (2017).
23. Kawamoto, T. & Holloway, J. R. Melting temperature and partial melt chemistry to H<sub>2</sub>O-saturated mantle peridotite to 11 gigapascals. *Science* **276**, 240–243 (1997).
24. Katz, R. F., Spiegelman, M. & Langmuir, C. H. A new parameterization of hydrous mantle melting. *Geochem. Geophys. Geosyst.* **4**, 1073 (2003).

25. Hirschmann, M. M. & Dasgupta, R. The H/C ratios of Earth's near-surface and deep reservoirs, and consequences for deep Earth volatile cycles. *Chem. Geol.* **262**, 4–16 (2009).
26. Korenaga, J., Planavsky, N. J. & Evans, D. A. D. Global water cycle and the coevolution of the Earth's interior and surface environment. *Philos. Trans. R. Soc. A* **375**, 20150393 (2017).
27. Maurice, M. et al. Onset of solid-state mantle convection and mixing during magma ocean solidification. *J. Geophys. Res. Planet.* **122**, 577–598 (2017).
28. Miyazaki, Y. & Korenaga, J. On the timescale of magma ocean solidification and its chemical consequences: 2. Compositional differentiation under crystal accumulation and matrix compaction. *J. Geophys. Res. Solid Earth* **124**, 3399–3419 (2019).
29. Blank, J. G. & Brooker, R. A. In *Reviews in Mineralogy and Geochemistry. Volume 30: Volatiles in Magmas* (eds Carroll, M. R. & Holloway, J. R.) 157–186 (Mineralogical Society of America, 1994).
30. Abe, Y. In *Evolution of the Earth and Planets* (eds Takahashi, E. et al.) 41–54 (AGU, 1993).
31. Hirth, G. & Kohlstedt, D. L. Water in the oceanic upper mantle: implications for rheology, melt extraction and the evolution of the lithosphere. *Earth Planet. Sci. Lett.* **144**, 93–108 (1996).
32. Jain, C., Korenaga, J. & Karato, S.-i Global analysis of experimental data on the rheology of olivine aggregates. *J. Geophys. Res. Solid Earth* **124**, 310–334 (2019).
33. Korenaga, J. Thermal evolution with a hydrating mantle and the initiation of plate tectonics in the early Earth. *J. Geophys. Res.* **116**, B12403 (2011).
34. Korenaga, J. Plate tectonics and surface environment: role of the oceanic upper mantle. *Earth Sci. Rev.* **205**, 103185 (2020).

35. Zahnle, K. et al. Emergence of a habitable planet. *Space Sci. Rev.* **129**, 35–78 (2007).
36. Korenaga, J. Energetics of mantle convection and the fate of fossil heat. *Geophys. Res. Lett.* **30**, 1437 (2003).
37. Bradley, D. C. Passive margins through earth history. *Earth Sci. Rev.* **91**, 1–26 (2008).
38. Herzberg, C., Condie, K. & Korenaga, J. Thermal history of the Earth and its petrological expression. *Earth Planet. Sci. Lett.* **292**, 79–88 (2010).
39. Pehrsson, S. J., Eglington, B. M., Evans, D. A., Huston, D. & Reddy, S. M. Metallogeny and its link to orogenic style during the Nuna supercontinent cycle. *Geol. Soc. Spec. Publ.* **424**, 83–94 (2016).
40. Plesa, A.-C., Tosi, N. & Breuer, D. Can a fractionally crystallized magma ocean explain the thermo-chemical evolution of Mars? *Earth Planet. Sci. Lett.* **403**, 225–235 (2014).
41. Ghiorso, M. S., Hirschmann, M. M., Reiners, P. W. & Kress, V. C. III The pMELTS: A revision of MELTS for improved calculation of phase relations and major element partitioning related to partial melting of the mantle to 3 GPa. *Geochem. Geophys. Geosyst.* **3**, 1–35 (2002).
42. Gualda, G. A., Ghiorso, M. S., Lemons, R. V. & Carley, T. L. Rhyolite-MELTS: a modified calibration of MELTS optimized for silica-rich, fluid-bearing magmatic systems. *J. Petrol.* **53**, 875–890 (2012).
43. Korenaga, J. In Archean Geodynamics and Environments (eds Benn, K. et al.) 7–32 (AGU, 2006).
44. Davies, G. F. On the emergence of plate tectonics. *Geology* **20**, 963–966 (1992).
45. Korenaga, J. Scaling of plate tectonic convection with pseudoplastic rheology. *J. Geophys. Res.* **115**, B11405 (2010).

46. Diamond, L. W. & Akinfiev, N. N. Solubility of CO<sub>2</sub> in water from −1.5 to 100 °C and from 0.1 to 100 MPa: evaluation of literature data and thermodynamic modelling. *Fluid Phase Equilib.* **208**, 265–290 (2003).
47. Alt, J. C. & Teagle, D. A. The uptake of carbon during alteration of ocean crust. *Geochim. Cosmochim. Acta* **63**, 1527–1535 (1999).
48. Sleep, N. H., Meibom, A., Fridriksson, T., Coleman, R. G. & Bird, D. K. H<sub>2</sub>-rich fluids from serpentinization: geochemical and biotic implications. *Proc. Natl Acad. Sci.* **101**, 12818–12823 (2004).
49. Schulte, M., Blake, D., Hoehler, T. & McCollom, T. Serpentinization and its implications for life on the early Earth and Mars. *Astrobiology* **6**, 364–376 (2006).
50. Lambert, J. B., Gurusamy-Thangavelu, S. A. & Ma, K. The silicate-mediated formose reaction: bottom-up synthesis of sugar silicates. *Science* **327**, 984–986 (2010).
51. Davies, G. F. Gravitational depletion of the early Earth’s upper mantle and the viability of early plate tectonics. *Earth Planet. Sci. Lett.* **243**, 376–382 (2006).
52. Zahnle, K. J., Kasting, J. F. & Pollack, J. B. Evolution of a steam atmosphere during Earth’s accretion. *Icarus* **74**, 62–97 (1988).
53. Dullien, F. A. L. Porous Media: Fluid Transport and Pore Structure 2nd edn (Academic, 1992).
54. Zahnle, K. J., Lupu, R., Dobrovolskis, A. & Sleep, N. H. The tethered Moon. *Earth Planet. Sci. Lett.* **427**, 74–82 (2015).
55. Trønnes, R. G. & Frost, D. J. Peridotite melting and mineral-melt partitioning of major and minor elements at 22–24.5 GPa. *Earth Planet. Sci. Lett.* **197**, 117–131 (2002).

56. Corgne, A., Liebske, C., Wood, B. J., Rubie, D. C. & Frost, D. J. Silicate perovskite-melt partitioning of trace elements and geochemical signature of a deep perovskitic reservoir. *Geochim. Cosmochim. Acta* **69**, 485–496 (2005).
57. Parsons, B. Causes and consequences of the relation between area and age of the ocean floor. *J. Geophys. Res.* **87**, 289–302 (1982).
58. Zhang, G., Mei, S. & Song, M. Effect of water on the dislocation creep of enstatite aggregates at 300 MPa. *Geophys. Res. Lett.* **47**, e2019GL085895 (2020).
59. Aubaud, C., Hauri, E. H. & Hirschmann, M. M. Hydrogen partition coefficients between nominally anhydrous minerals and basaltic melts. *Geophys. Res. Lett.* **31**, L20611 (2004).
60. de Capitani, C. & Petrakakis, K. The computation of equilibrium assemblage diagrams with Theriak/Domino software. *Am. Mineral.* **95**, 1006–1016 (2010).
61. McKenzie, D. The generation and compaction of partially molten rock. *J. Petrol.* **25**, 713–765 (1984).
62. Christensen, U. R. Thermal evolution models for the Earth. *J. Geophys. Res.* **90**, 2995–3007 (1985).
63. Korenaga, J. Thermal cracking and the deep hydration of oceanic lithosphere: A key to the generation of plate tectonics? *J. Geophys. Res.* **112**, B05408 (2007).
64. Tackley, P. J. In Treatise on Geophysics: Volume 7: Mantle Dynamics 2nd edn (ed. Schubert G.) 521–585 (Elsevier, 2015).
65. Nakajima, S., Hayashi, Y.-Y. & Abe, Y. A study on the “runaway greenhouse effect” with a one-dimensional radiative–convective equilibrium model. *J. Atmos. Sci.* **49**, 2256–2266 (1992).

66. Johnson, S. S., Mischna, M. A., Grove, T. L. & Zuber, M. T. Sulfur-induced greenhouse warming on early Mars. *J. Geophys. Res. Planet.* **113**, E08005 (2008).
67. Abe, Y. & Matsui, T. The formation of an impact-generated H<sub>2</sub>O atmosphere and its implications for the early thermal history of the Earth. *J. Geophys. Res. Suppl.* **90**, C545–C559 (1985).
68. Dasgupta, R. & Hirschmann, M. M. The deep carbon cycle and melting in Earth's interior. *Earth Planet. Sci. Lett.* **298**, 1–13 (2010).
69. Kelemen, P. B. & Manning, C. E. Reevaluating carbon fluxes in subduction zones, what goes down, mostly comes up. *Proc. Natl Acad. Sci.* **112**, E3997–E4006 (2015).
70. Sleep, N. H., Zahnle, K. & Neuhoff, P. S. Initiation of clement surface conditions on the earliest Earth. *Proc. Natl Acad. Sci.* **98**, 3666–3672 (2001).
71. Peterson, M. N. A. Calcite: rates of dissolution in a vertical profile in the central Pacific. *Science* **154**, 1542–1544 (1966).
72. Andersson, A. J. In *Treatise on Geochemistry. Volume 8: The Oceans and Marine Geochemistry* 2nd edn (eds Holland, H. D. & Turekian, K.) 519–542 (Elsevier, 2014).
73. Kelemen, P. B. et al. Rates and mechanisms of mineral carbonation in peridotite: natural processes and recipes for enhanced, in situ CO<sub>2</sub> capture and storage. *Annu. Rev. Earth Planet. Sci.* **39**, 545–576 (2011).
74. Syracuse, E. M., van Keken, P. E. & Abers, G. A. The global range of subduction zone thermal models. *Phys. Earth Planet. Inter.* **183**, 73–90 (2010).
75. Dasgupta, R., Hirschmann, M. M. & Withers, A. C. Deep global cycling of carbon constrained by the solidus of anhydrous, carbonated eclogite under upper mantle conditions. *Earth Planet. Sci. Lett.* **227**, 73–85 (2004).

76. Korenaga, J. On the extent of mantle hydration caused by plate bending. *Earth Planet. Sci. Lett.* **457**, 1–9 (2017).
77. Miller, N. C., Lizarralde, D., Collins, J. A., Holbrook, W. S. & Van Avendonk, H. J. Limited mantle hydration by bending faults at the middle America trench. *J. Geophys. Res. Solid Earth* **126**, e2020JB020982 (2021).
78. Miyazaki, Y. & Korenaga, J. Effects of chemistry on vertical dust motion in early protoplanetary disks. *Astrophys. J.* **849**, 41 (2017).
79. Wirth, E. A. & Korenaga, J. Small-scale convection in the subduction zone mantle wedge. *Earth Planet. Sci. Lett.* **357–358**, 111–118 (2012).
80. Lyubetskaya, T. & Korenaga, J. Chemical composition of Earth's primitive mantle and its variance: 1. Method and results. *J. Geophys. Res.* **112**, B03211 (2007).
81. Gale, A., Dalton, C. A., Langmuir, C. H., Su, Y. & Schilling, J.-G. The mean composition of ocean ridge basalts. *Geochem. Geophys. Geosyst.* **14**, 489–518 (2013).

## Acknowledgements

This work was sponsored by the US National Aeronautics and Space Administration under Cooperative Agreement No. 80NSSC19M0069 issued through the Science Mission Directorate and the National Science Foundation under grant EAR-1753916. This work was also supported in part by the facilities and staff of the Yale University Faculty of Arts and Sciences High Performance Computing Center. Y.M. was supported by the Stanback Postdoctoral Fellowship from Caltech Center for Comparative Planetary Evolution. The authors thank N. Sleep and M. Hirschmann for providing constructive comments, which were helpful to substantially improve the accuracy of the manuscript.

## Author information

## Affiliations

1. Department of Earth and Planetary Sciences, Yale University, New Haven, CT, USA

Yoshinori Miyazaki & Jun Korenaga

2. Division of Geological and Planetary Sciences, California Institute of Technology, Pasadena, CA, USA

Yoshinori Miyazaki

## Contributions

Y.M. and J.K. designed the study, discussed the results, and wrote the manuscript. Y.M. performed calculations.

## Corresponding author

Correspondence to [Yoshinori Miyazaki](#).

## Ethics declarations

## Competing interests

The authors declare no competing financial interests.

## Peer review

## Peer review information

*Nature* thanks Marc Hirschmann and Norman Sleep for their contribution to the peer review of this work. Peer reviewer reports are available.

## Additional information

**Publisher's note** Springer Nature remains neutral with regard to jurisdictional claims in published maps and institutional affiliations.

## Extended data figures and tables

### Extended Data Fig. 1 The thermal structure of the chemically heterogeneous mantle plotted together with contours of melt fraction.

**a–c**, Melt fraction is shown for two components of the mantle: high-Mg# pyroxenite matrix (**a**) and Fe-rich blobs (**c**), and water content remaining in the solid phase of the high-Mg# matrix (**b**). The melt fractions of high-Mg# matrix and Fe-rich blobs are estimated using the Rhyolite-MELTS model<sup>42</sup>. The dry (grey solid) and wet (0.1 wt%; grey dashed) adiabats are calculated with a potential temperature of 1,600 °C, using equation (17). For the wet adiabat of the high-Mg# matrix, two modes of melting are considered, batch (dotted) and fractional (dashed), and for the latter, we assume that 90% of melt would escape from the mantle for every 0.1 GPa of ascent when the degree of melting is greater than 1%. The fraction of melt escaping the system is insensitive to the thickness of complete dehydration, and values between 10% and 99.9% would yield a thickness within 0.1 GPa of what is predicted in this figure. **d**, Schematic illustration of the compositional structure of the mantle during and after the solidification of a magma ocean under fractional crystallization. The mantle experiences global-scale chemical stratification, leaving an Fe-rich layer near the surface. Such stratification is subject to the Rayleigh–Taylor (RT) instability, resulting in the dripping-like descent of Fe-rich materials. This period corresponds to Fig. 1a. These droplets would solidify as they sink through the mantle (left) and be mixed with high-Mg# cumulates. When the surface becomes rheologically solid (Fig. 1b), the mantle would have a structure with small-scale chemical heterogeneity, embedded in high-Mg# matrix (right).

### Extended Data Fig. 2 Thermal structure of a pyrolytic (chemically homogeneous) mantle when a melt-dominated layer disappears.

The figure describes when the entire mantle starts to behave rheologically as solid, which corresponds to a potential temperature of  $\sim 1,600$  °C. **a–c**, The profiles of temperature (**a**), melt fraction (**b**) and water content (**c**) are shown for both dry (grey solid) and wet (0.1 wt%; grey dotted and dashed) mantles, together with the solidus (blue) and liquidus of pyrolite (red). The solidus of a wet mantle (blue dashed) is estimated using equation (18) and a melt/mineral partitioning coefficient of  $D = 0.005$ . Two modes of melting are considered for the wet mantle, batch (dotted) and fractional (dashed). Temperature profiles would be adiabatic as a result of the Rayleigh–Taylor instability, and melt fraction is estimated using a model of ref. <sup>24</sup> with the mass fraction of clinopyroxene of 19 wt%. For fractional melting, we assume that 90% of melt would escape from the mantle for every 0.1 GPa of ascent when the degree of melting is greater than 1%.

### Extended Data Fig. 3 The subduction geotherm during the Hadean with the stability field of carbonates.

$P$ – $T$  paths are calculated assuming a dip angle of 45° using the model of ref. <sup>79</sup> (see [Methods](#) for details). We consider (1) a mantle potential temperature of 1,350 °C with a plate age of 10 Myr, a velocity of 5 cm yr<sup>-1</sup>, and a surface temperature of 0 °C (blue), (2) a potential temperature of 1,600 °C with a plate age of 10 Myr, a velocity of 50 cm yr<sup>-1</sup>, and a surface temperature of 230 °C (red solid), and (3) a potential temperature of 1,600 °C with a plate age of 100 Myr, a velocity of 5 cm yr<sup>-1</sup>, and a surface temperature of 230 °C (red dashed), representing the present-day young slab, the Hadean slab of the chemically heterogeneous mantle, and that of a homogeneous pyrolytic mantle, respectively.  $P$ – $T$  paths of the heterogeneous and homogenous mantles are similar because rapid plate motion mitigates the heating of the slab from the surrounding mantle. The solidus of carbonate melt is adopted from ref. <sup>75</sup> (black dotted), and the decomposition of magnesite under the presence of quartz is calculated using Theriak-Domino<sup>60</sup> (grey dotted).

### Extended Data Fig. 4 The profiles of Al<sub>2</sub>O<sub>3</sub>(red) and CaO (blue) contents after magma ocean solidification.

Profiles before the onset of small-scale Rayleigh–Taylor instabilities are shown. The top 500 km of the mantle becomes the source for iron-rich blobs, whereas the lower mantle composition corresponds to the high-Mg# matrix in the main text. We assume that newly formed crystals in the magma ocean would stack at the base of the melt-dominated layer (Fig. 1a). Initial concentrations of  $\text{Al}_2\text{O}_3$  3.5 wt% and  $\text{CaO}$  2.8 wt%<sup>80</sup> are assumed (dashed lines), and partitioning coefficients between melt and bridgemanite are calculated from the experimental results of Trønnes and Frost<sup>55</sup> and Corgne et al<sup>56</sup>. Shaded areas represent uncertainties, which are calculated using partitioning coefficients 30% larger and smaller values than the mean estimated values ( $D_{\text{Al/Si}} = 0.78$  and  $D_{\text{Ca/Si}} = 0.16$ ).

### **Extended Data Fig. 5 Effective viscosity contrast across the lithosphere and the criteria for plate tectonics.**

Effective viscosity contrast is shown (equation (14)) as a function of the internal Rayleigh number, together with the corresponding mantle potential temperature. The thickness of depleted lithospheric mantle  $h_m$  in equation (14) is different between chemically homogeneous (grey) and heterogeneous mantles (red), and the values of  $h_m$  are shown in Fig. 3b. The criteria for plate tectonics ( $\Delta\eta_{L,\text{crit}}$  in equation (20)) is also plotted with a dotted line.

**Extended Data Table 1 The evolution of  $\text{CO}_2$  and  $\text{H}_2\text{O}$  budgets**

**Extended Data Table 2 Compositions of high-Mg# pyroxenite, iron-rich blobs and their differentiated components**

## **Supplementary information**

**Peer Review File**

## **Source data**

**Source Data Fig. 2**

## Source Data Fig. 3

## Source Data Fig. 4

## Rights and permissions

### Reprints and Permissions

## About this article

### Cite this article

Miyazaki, Y., Korenaga, J. A wet heterogeneous mantle creates a habitable world in the Hadean. *Nature* **603**, 86–90 (2022).  
<https://doi.org/10.1038/s41586-021-04371-9>

- Received: 03 August 2020
- Accepted: 20 December 2021
- Published: 02 March 2022
- Issue Date: 03 March 2022
- DOI: <https://doi.org/10.1038/s41586-021-04371-9>

## Share this article

Anyone you share the following link with will be able to read this content:

[Get shareable link](#)

Sorry, a shareable link is not currently available for this article.

[Copy to clipboard](#)

Provided by the Springer Nature SharedIt content-sharing initiative

---

This article was downloaded by **calibre** from <https://www.nature.com/articles/s41586-021-04371-9>

| [Section menu](#) | [Main menu](#) |

- Article
- Open Access
- [Published: 23 February 2022](#)

# The Mesozoic terminated in boreal spring

- [Melanie A. D. During](#) [ORCID: orcid.org/0000-0002-1438-6018<sup>1,2</sup>](#),
- [Jan Smit](#) [ORCID: orcid.org/0000-0002-6070-4865<sup>1</sup>](#),
- [Dennis F. A. E. Voeten](#) [ORCID: orcid.org/0000-0002-2090-2824<sup>2,3</sup>](#),
- [Camille Berruyer<sup>3</sup>](#),
- [Paul Tafforeau](#) [ORCID: orcid.org/0000-0002-5962-1683<sup>3</sup>](#),
- [Sophie Sanchez](#) [ORCID: orcid.org/0000-0002-3611-6836<sup>2,3</sup>](#),
- [Koen H. W. Stein<sup>4,5</sup>](#),
- [Suzan J. A. Verdegaal-Warmerdam<sup>1</sup>](#) &
- [Jeroen H. J. L. van der Lubbe](#) [ORCID: orcid.org/0000-0001-7545-6502<sup>1,6</sup>](#)

*Nature* volume 603, pages 91–94 (2022)

- 35k Accesses
- 1898 Altmetric
- [Metrics details](#)

## Subjects

- [Biogeochemistry](#)
- [Evolution](#)

## Abstract

The Cretaceous–Palaeogene mass extinction around 66 million years ago was triggered by the Chicxulub asteroid impact on the present-day Yucatán Peninsula<sup>1,2</sup>. This event caused the highly selective extinction that eliminated about 76% of species<sup>3,4</sup>, including all non-avian dinosaurs, pterosaurs, ammonites, rudists and most marine reptiles. The timing of the impact and its aftermath have been studied mainly

on millennial timescales, leaving the season of the impact unconstrained. Here, by studying fishes that died on the day the Mesozoic era ended, we demonstrate that the impact that caused the Cretaceous–Palaeogene mass extinction took place during boreal spring. Osteohistology together with stable isotope records of exceptionally preserved perichondral and dermal bones in acipenseriform fishes from the Tanis impact-induced seiche deposits<sup>5</sup> reveal annual cyclicity across the final years of the Cretaceous period. Annual life cycles, including seasonal timing and duration of reproduction, feeding, hibernation and aestivation, vary strongly across latest Cretaceous biotic clades. We postulate that the timing of the Chicxulub impact in boreal spring and austral autumn was a major influence on selective biotic survival across the Cretaceous–Palaeogene boundary.

[Download PDF](#)

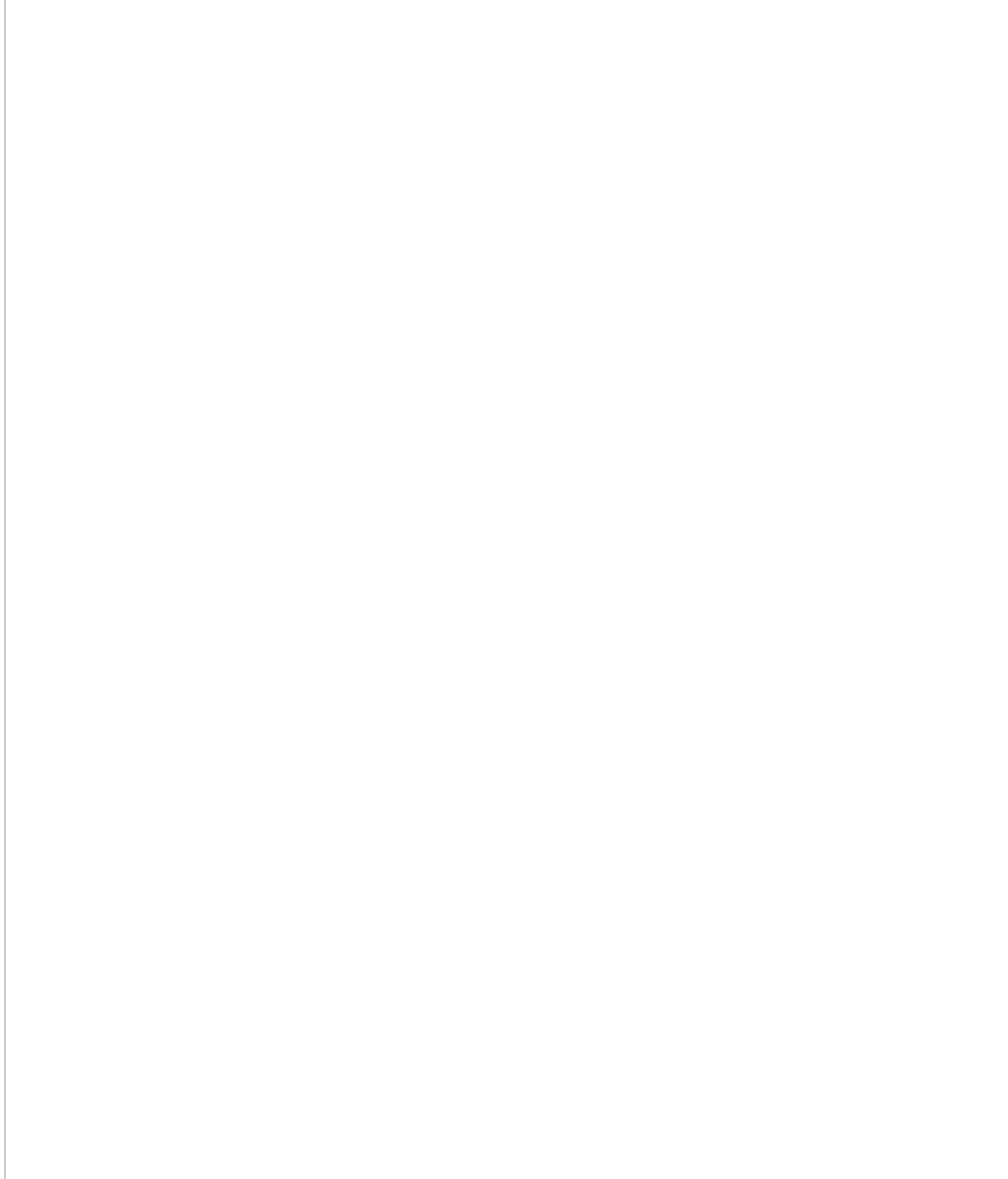
## Main

The Cretaceous-Palaeogene (K–Pg) mass extinction event affected biodiversity with high but poorly understood taxonomic selectivity. Among archosaurs, for example, all pterosaurs and non-avian dinosaurs succumbed in the K–Pg mass extinction, while crocodilians and birds survived into the Palaeogene period<sup>3,4</sup>. Direct consequences of the impact, including impact glass fallout, large-scale forest fires and tsunamis, are geologically documented more than 3,500 km from the Chicxulub impact crater<sup>5,6,7,8</sup>. Although direct effects of the impact devastated a vast geographical area, the global mass extinction probably unfolded during its aftermath, which involved rapid climatic deterioration estimated to have lasted up to several thousands of years<sup>9,10,11</sup>. Whether seasonal timing of the onset of these marked changes affected the selectivity of the K–Pg extinction could not yet be established owing to the lack of suitable records.

The Tanis event deposit in North Dakota (USA) is an exceptional seiche deposit preserving a rich thanatocoenosis (that is, a mass death assemblage) of latest Cretaceous biota at the top of the Hell Creek Formation. The majority of macrofossils encountered at the Tanis locality represent direct casualties of the K–Pg bolide impact that were buried within the impact-induced seiche deposit<sup>5</sup>. Tens of minutes after the impact, the seiche agitated large volumes of water and soil in the estuary of the Tanis river<sup>5</sup>. As the seiche proceeded upstream, it advected bones, teeth, bivalves, ammonites, benthic foraminifera (Extended Data Fig. [1a–c](#)) and plant matter in the suspended load while impact spherules rained down from the sky<sup>5</sup>. Within the thanatocoenotic accumulation, abundant acipenseriforms—sturgeons and paddlefishes—became oriented along the seiche flow directions and buried alive with numerous impact spherules in their gills<sup>5</sup> (Fig. [1](#), Extended Data Fig. [2a, b](#)).

**Fig. 1: Reconstruction of a paddlefish with impact spherules in the gill rakers.**

 figure 1



- a**, Three-dimensional rendering of paddlefish FAU.DGS.ND.161.4559.T in left lateral view with the location of a higher-resolution scan (depicted in **b**) indicated (white outline). **b**, Three-dimensional rendering of the subopercular and gills in **a** with

trapped impact spherules (yellow). Scale bars, 2 cm. Two-dimensional tomographic data and fully annotated three-dimensional renderings are provided in Extended Data Fig. 2. A three-dimensional animated rendering of FAU.DGS.ND.161.4559.T is provided as Supplementary Video 1.

During the Maastrichtian (that is, the last age of the Cretaceous), the climate of present-day North Dakota involved four seasons that were documented in tree-ring records recovered from other Upper Cretaceous sites in the Hell Creek Formation<sup>12,13</sup>. Tanis was located at approximately 50° N during the latest Cretaceous and experienced distinct seasonality in rainfall and temperature<sup>14</sup>. Regional air temperatures were reconstructed to range from 4–6 °C in winter up to an average of about 19 °C in summer<sup>13,14</sup>. To uncover the season of the K–Pg bolide impact, we analysed osteohistological records of acipenseriform bone apposition in three paddlefish dentaries and three sturgeon pectoral fin spines that were excavated at the Tanis site in 2017 (Extended Data Fig. 1d–j). These skeletal elements preserve unaltered growth records from embryonic development up to death, making them highly suitable for life history reconstructions<sup>15,16</sup>.

## Growth records of end-Cretaceous fishes

To trace appositional growth and pinpoint the season in which bone apposition terminated, we first assessed the preservation of bone growth patterns across the studied specimens. We prepared dermal bone slices of six acipenseriform specimens as microscopic slides and subjected these to osteohistological assessment, during which lines of arrested growth (LAGs) were easily recognized (Fig. 2). To corroborate the annual nature of the LAGs using virtual high-resolution osteohistology<sup>17,18</sup>, three-dimensional (3D) volumes were produced with propagation phase-contrast synchrotron radiation micro-computed tomography<sup>19</sup> on beamline BM05 of the European Synchrotron Radiation Facility, France. The 3D nature of the synchrotron data enables optimal projection of the bone deposition pattern across multiple cross-sectional planes and resolved the exact relationship between seasonality and cyclical bone apposition in superb detail<sup>20</sup>. In addition, virtual osteohistology allowed us to visualize the seasonal fluctuations of osteocyte lacunar density and volume, which are poorly expressed in the physical 2D thin sections<sup>18</sup> (Fig. 3c, d). The osteohistological data (Figs. 2, 3, Extended Data Figs. 3–6) were complemented with an incremental carbon isotope record extracted from one of the paddlefish dentaries (VUA.GG.2017.X-2724).

**Fig. 2: Osteohistological thin sections of five acipenseriform fishes.**

---

 **figure 2**

**a–e**, Thin sections in transmitted light of VUA.GG.2017.MDX-3 (**a**), VUA.GG.2017.X-2743M (**b**), VUA.GG.2017.X-2744M (**c**), VUA.GG.2017.X-2733A (**d**) and VUA.GG.2017.X-2733B (**e**), showing congruent pacing of bone apposition during the final years of life, terminating in spring. Red arrows indicate LAGs. Scale bars, 0.5 mm.

**Fig. 3: Carbon isotope record alongside the incremental growth profiles across the dentary of paddlefish VUA.GG.2017.X-2724.**

---

 **figure 3**

**a**,  $\delta^{13}\text{C}$  record expressed as ‰ on the Vienna Pee Dee Belemnite (VPDB) reference scale. The colour gradient highlights the theoretical range between maximum values during seasonal (summer) trophic increase of  $^{13}\text{C}$  (yellow) and minimum values during trophic decrease of  $^{13}\text{C}$  (winter) (blue). **b**, Virtual thick section (average-value projection with 0.1-mm depth) showing growth zones during the favourable growth seasons and annuli and LAGs outside the favourable growth seasons. **c**, Cell density map<sup>51</sup> of a virtual thick section (minimum-value projection with 0.2-mm depth) showing fluctuating osteocyte lacunar densities and sizes, with higher densities and largest sizes recorded during the favourable growth seasons (orange) and lower densities and smaller sizes outside the favourable growth seasons (purple). A comparative image of a larger section of bone with scale is provided in Extended Data Fig. 6. **d**, Microscopic thin section in transmitted light showing LAGs (red arrows) and a single growth mark indicated (bracket) spanning the distance between two subsequent LAGs and including a zone and an annulus (Extended Data Fig. 10b). Scanning data visualized in **b** and **c** were obtained approximately 10-mm distal from the physically sectioned thin slice of **d**, which itself was located directly proximal to the thick section sampled for **a**. Scale bars, 1 mm. Corresponding osteohistological data of the other five sampled acipenseriform fishes are presented in Extended Data Figs. 3–5.

The tomographic data show that impact spherules associated with the paddlefish skeleton are present exclusively in its gill rakers<sup>5</sup> and are absent elsewhere in the preserved specimen (Fig. 1). The absence of impact spherules outside the gill rakers demonstrates that spherules were filtered out of the surrounding waters but had not yet proceeded into the oral cavity or further down the digestive tract, and had not impacted the fish carcasses during perimortem exposure. Impact spherule accumulation in the gill rakers and the arrival of the seiche waves must therefore have occurred simultaneously<sup>5</sup>, which implies that the acipenseriforms were alive and foraging during the bolide impact and the last minutes of the Cretaceous.

## Well-conserved bone growth archives

The degree of preservation of the sampled acipenseriform bones was assessed using micro-X-ray fluorescence (Methods, Extended Data Figs. 7–9), which would reveal potential taphonomic elemental exchange that may have affected the primary stable isotope composition. The micro-X-ray fluorescence maps show that Fe and Mn oxides are present in the bone vascular canals and surrounding sediments (Extended Data Fig. 8), but have not invaded the bone apatite ( $\text{Ca}_5(\text{PO}_4,\text{CO}_3)_3(\text{OH},\text{F},\text{Cl})$ ). Detrital components, characterized by high concentrations of K and Si, remain restricted to the sediment matrix (Extended Data Fig. 8f–j). The bone apatite conserves a highly homogeneous distribution of P and Ca (Extended Data Fig. 9), which corroborates the

unaltered preservation of these apatitic tissues. Skeletal remains of the paddlefishes and sturgeons thus experienced negligible diagenetic alteration, probably as a consequence of rapid burial and possibly aided by early Mn and Fe oxide seam formation<sup>21,22</sup>. The exquisite 3D preservation of delicate structures, including non-ossified tissues that originally enveloped the brain (Extended Data Fig. 2c–f), further demonstrates the excellent preservation of the fossils and absence of taphonomic reorganization<sup>23</sup>.

## Consistent records of a spring death

Paddlefish dentaries form through perichondral ossification around the Meckel's cartilage<sup>24</sup>. Sturgeon pectoral fin spines consist of dermal bone—an intramembranous skeletal tissue that forms in the mesenchyme (mesodermal embryonic tissue)<sup>25</sup>. Unlike endochondral bone, perichondral and dermal bone do not originate through mineralization of cartilaginous precursors<sup>26,27,28</sup> but grow exclusively through incremental bone matrix apposition by secretion of a row of osteoblasts<sup>24,26,27,28</sup>. The thickness of one annual growth mark cumulatively spans a thick (favourable) growth zone, a thinner (slowly deposited) annulus and, ultimately, a LAG<sup>20</sup>. Our microscopic and virtual osteohistological data consistently show that the six fishes perished (that is, stopped growing) while forming a growth zone shortly after a LAG was deposited (Figs. 2, 3, Extended Data Figs. 3–6), which coincides with an early stage of the favourable growth season<sup>20</sup>. The outermost cortices of all six acipenseriform individuals studied here also exhibit increasing osteocyte lacunar densities and sizes towards their periosteal surfaces (Fig. 3c, Extended Data Figs. 5, 6). In all specimens, this density remained lower than the highest densities and average sizes recorded in previous years (Fig. 3c, Extended Data Figs. 3–6, 10b). As osteocyte lacunar density and size patterns were consistently cyclical across the preceding years during which they peaked at the climaxes of the growth seasons, the last recorded growth season had thus not yet climaxed at the time of death (Figs. 2, 3, Extended Data Figs. 3–6, 10b).

The inferred annual growth cycles are independently corroborated by a stable carbon isotope ( $\delta^{13}\text{C}_{\text{sc}}$ ) archive that recorded several years of seasonal dietary fluctuations in growing bone. Paddlefish VUA.GG.2017.X-2724 also yielded, in addition to this  $\delta^{13}\text{C}_{\text{sc}}$  archive, an oxygen isotope ( $\delta^{18}\text{O}_{\text{sc}}$ ) record across the final six years of its life (Supplementary Data Table 1, Extended Data Fig. 10a, Methods). The low and constant  $\delta^{18}\text{O}_{\text{sc}}$  values in VUA.GG.2017.X-2724 reflect exclusive inhabitation of freshwater environments by the paddlefishes. This implies that their osteohistological records must have captured seasonal variability rather than, for example, migration between saline and freshwater habitats. Although modern sturgeons are known to have anadromous lifestyles<sup>29,30</sup>, this remains to be confirmed for the fossil sturgeons at

Tanis, as isotopic data from sturgeon pectoral fin spines could not be secured (Methods, ‘Micromill’). Notably, the osteohistological records of all our sturgeons and paddlefishes converge on the same annual growth phase, despite their potential different lifestyles.

Like their modern-day relatives, the latest Maastrichtian paddlefishes of Tanis were filter feeders that presumably consumed copepods and other zooplankton<sup>29,30,31</sup>. These fishes probably experienced an annual feeding pattern, determined by fluctuating food availability, that peaked between spring and autumn<sup>31</sup>. During maximum productivity, ingested zooplankton enriches the growing skeleton of filter-feeding fishes with <sup>13</sup>C relative to <sup>12</sup>C<sup>32,33</sup>. Thus, the cyclically elevated <sup>13</sup>C/<sup>12</sup>C ratios in paddlefish VUA.GG.2017.X-2724 (Fig. 3a) reflect distinct episodes of high food availability and consumption. Carbon isotope records across the growth record of Paddlefish VUA.GG.2017.X-2724 indicate that peak annual growth rate was not yet attained and the feeding season had thus not yet climaxed—corroborating a boreal spring death.

## Implications for selective K–Pg survival

The Chicxulub bolide impact caused a global heat pulse that ignited widespread wildfires<sup>9,34</sup>. After this heat wave, the last boreal spring of the Mesozoic transitioned to a global impact winter<sup>10</sup>. Although a June timing for the K–Pg impact has been suggested on the basis of palaeobotanical indications for anomalous freezing in this region (Wyoming, USA)<sup>35</sup>, the palaeobotanical identities, taphonomic inferences and stratigraphic assumptions underlying that conclusion have since all been refuted<sup>36,37,38,39</sup>. Moreover, post-impact cooling happened in the first months to decades following the K–Pg impact<sup>10</sup>, which renders proxies registering post-impact freezing conditions asynchronous with the impact event itself.

A suite of impact-induced phenomena contributed to the K–Pg extinction on differing timescales<sup>40,41</sup>. In the days to months following the impact, its instantaneous effects, such as intense infrared radiation caused by ejecta reentry<sup>34</sup>, resulting wildfires<sup>9,34</sup> and the spread of sulfurous aerosols leading to acid precipitation<sup>42</sup> must have predominantly afflicted the exposed continental environments. Although negotiating these hostile conditions would not have guaranteed survival, an early clade-wide eradication would always have meant immediate extinction<sup>41</sup>.

The seasonal timing of the catastrophic end-Cretaceous bolide impact places the event at a particularly sensitive stage for biological life cycles in the Northern Hemisphere. In many taxa, annual reproduction and growth take place during spring. Species with longer incubation times, such as non-avian reptiles, including pterosaurs and most dinosaurs, were arguably more vulnerable to sudden environmental perturbations than

other groups<sup>43</sup> (for example, birds). Southern Hemisphere ecosystems, which were struck during austral autumn, appear to have recovered up to twice as fast as Northern Hemisphere communities<sup>44</sup>, consistent with a seasonal effect on biotic recovery.

Subterranean sheltering conceivably contributed to the cynodont survival of the Permo-Triassic (PT) crisis<sup>45</sup>. Similarly, large-scale wildfires raging across the Southern Hemisphere<sup>9,34,41</sup> may have been evaded by hibernating mammals that were already sheltered in burrows<sup>34,41</sup> in anticipation of austral winter. Additional modes of seasonal dormancy, torpor and/or aestivation, which are nowadays practised by various mammals<sup>46,47</sup> as well as certain amphibians, birds and crocodilians<sup>48</sup>, could have facilitated further underground survival. In the aftermath of the K–Pg event, ecological networks collapsed from the bottom up. Floral necrosis<sup>9</sup> and extinction immediately affected species dependent on primary producers, while some animals capable of exploiting alternative resources—for example, certain birds and mammals<sup>49,50</sup>—persisted.

## Conclusions

Seasonal timing of the Chicxulub impact in boreal spring and austral autumn will aid in further calibrating evolutionary models exploring the selectivity of the K–Pg extinction and the asymmetry in extinction and recovery patterns between the two hemispheres. Decoupling short- and long-term effects of the bolide impact on the K–Pg mass extinction will also aid in identifying extinction risks and modes of ecological deterioration caused by the forthcoming global climate change. The uniquely constrained Tanis site<sup>5</sup> offers valuable proxies for reconstructing the environmental, climatological and biological conditions that prevailed locally when the Mesozoic ended.

## Methods

### Fieldwork

Excavation at the Tanis locality in south-western North Dakota took place between 10 August and 20 August 2017. Sections of dentaries of paddlefishes and pectoral fin spines of sturgeons were collected in the field for histological study.

### Thin sectioning

Four out of the six samples were excavated from the sediment matrix. These included all sturgeon pectoral fin spines (VUA.GG.2017.X-2743M, VUA.GG.2017.X-2744M,

and VUA.GG.2017.MDX-3) and one of the paddlefish dentaries (VUA.GG.2017.X-2724). Paddlefish dentaries VUA.GG.2017.X-2733A and VUA.GG.2017.X-2733B, belong to two individuals, were uncovered aligned to each other and fractured upon discovery. To avoid further damage, the samples were embedded in epoxy resin prior to thin sectioning. All specimens were cut with a diamond saw and polished to obtain microscopic thin sections (about 50- $\mu$ m thick) and thick sections for micromilling (about 200- $\mu$ m thick). See Extended Data Fig. 1e-j for images of the specimens and the sampling locations.

## Osteohistological analysis

In the acipenseriform dermal bones examined in this study, annual growth cyclicity can be traced through growth marks (GMs).

A GM spans a single growth cycle that typically lasts one year and can be divided into a zone, an annulus, and a LAG<sup>20,52</sup>. The zone is deposited during a period of relative rapid growth in the active or favourable growth season<sup>20</sup>. The annulus is subsequently formed when growth slows down towards the end of the growth season<sup>20</sup>. Finally, a LAG forms when growth periodically ceases until the next growth season starts and a new zone is deposited<sup>20</sup>.

During the formation of a growth zone, the density and volumes of osteocyte lacunae (OL; subcircular dark features in Extended Data Fig. 10a) initially increase when growth accelerates. Subsequently, towards and into the annulus, OL density and volume decrease as growth slows down<sup>18</sup>. Because a LAG coincides with a temporary arrest of local osteogenesis, it is only expressed when deposition of a new growth zone has commenced. All six studied specimens show a LAG relatively close to the outermost partial growth zone.

In fossil bone, LAGs often appear as sharply defined dark lines<sup>53</sup> that typically constitute a poorly coherent interface between adjacent bone layers, thus facilitating (local) delamination between adjacent cortical layers<sup>53</sup>. During fossilization, percolation products can accumulate in these gaps and thereby (locally) accentuate the LAGs<sup>51,53</sup> (figure 31.3G of ref. 52). Based on this well-understood expression of LAGs (that we recognize from our own experience as well; S.S. personal observation), we have consistently identified the LAGs as locally stained dark lines that may be associated with circumferentially propagated cracked surfaces which are oriented parallel to the periosteal deposits.

Besides cyclical seasonal factors that synchronize GM accretion, stress may induce additional diapause stages that result in supplementary marks within a single year<sup>54</sup>. Cessation of growth for the duration of several weeks can provoke the formation of a

LAG<sup>54</sup>. However, such non-cyclical marks “tend to be haphazard rather than regular (that is, they do not reflect a particular spacing or rhythm)” and do not encircle the cortex of the skeletal element but “tend to be locally confined to an arc”<sup>55</sup>.

As the studied bones yield only regularly spaced GMs along their complete circumference, we confidently identify the preserved GMs as annual cycles. Moreover, the fluctuating quantified density and volumes of osteocyte lacunae (Extended Data Fig. 6d–f) and the carbon isotopic record (Fig. 3a, Extended Data Fig. 10a) across the final seven years of growth of VUA.GG.2017.X-2724 are exclusively consistent with the identification of annual LAGs in corresponding physical thin sections. In all studied specimens, bone growth terminated during the process of zonal bone growth.

## Micro-X-ray fluorescence

Fragments of the paddlefish and sturgeon samples that remained after thin sectioning were analysed with microX-ray fluorescence. High-resolution elemental mapping was conducted using a Bruker M4 Tornado 2D spectrometer at 50 kV and 600 µA, without a filter, and at an acquisition rate of 20 µm per 5 ms at the Vrije Universiteit Brussel.

## Micromill

The growth increments were sampled in the thick sections (about 200-µm thick) at the highest possible accuracy using a Micromill (Merkantek). Drill transects were assigned in the accompanying software and after each individual sample was collected, the drill bit was cleaned with ethanol. Not all thick sections were suitable for micromilling. The lobed anatomy of the sturgeon fin spines (VUA.GG.2017.X-2743M and VUA.GG.2017.X-2744M) proved too complex to reliably sample single growth increments with the micromill. Paddlefish dentaries VUA.GG.2017.X-2733A and VUA.GG.2017.X-2733B only exposed a few growth lines that were too narrow to sample with the micromill. Sturgeon pectoral fin spine VUA.GG.2017.MDX-3 and paddlefish dentary VUA.GG.2017.X-2724 were sampled up to the outermost growth increment.

## Stable isotope analysis

Micromilled hydroxyapatite samples of specimen VUA.GG.2017.X-2724 weighing about 50 µg were placed in Exetainer vials (Labco) and flushed with purified helium gas. For reference, the analysed amounts of structural carbonate are equivalent to about 5 µg of CaCO<sub>3</sub>. Orthophosphoric acid was subsequently added and allowed to react for 24 h at 45 °C. VUA.GG.2017.MDX-3 was routinely analysed with a Thermo Finnigan Delta<sup>plus</sup> mass spectrometer connected to a Thermo Finnigan GasBench II at the Earth Sciences Stable Isotope Laboratory (Vrije Universiteit, Amsterdam).

However, the amount of CO<sub>2</sub> generated was found to be too small to permit reliable isotopic determinations. To alleviate this, the GasBench was provisionally interfaced with a cold trap in which the CO<sub>2</sub> was frozen with liquid nitrogen during a 2 min period. After trapping for 2 min, an accurate single-pulse measurement was performed for each of the apatitic samples and standards. Each isotopic sample determination was preceded by six pulses of monitoring CO<sub>2</sub> with a calibrated isotopic composition to assure stable conditions of the mass spectrometer. The isotopic measurements of the weighted micromilled samples were bracketed by the analyses of the inter-laboratorial apatite standard (Ag-Lox) to account for the linearity effect<sup>56</sup>. After corrections, the uncertainties for δ<sup>13</sup>C and δ<sup>18</sup>O of the Ag-Lox (*n* = 4) were 0.16 ‰ and 0.39 ‰ (1 s.d.) respectively. Although the amount of extracted and analysed structural carbonate remains insufficient for optimal isotopic determination, the relatively large recovered δ<sup>13</sup>C variability still yields a meaningful record across the appositional bone archive. The δ<sup>18</sup>O values of structural carbonate, unlike those of phosphate (PO<sub>4</sub>)<sup>57</sup>, do not offer a sensitive palaeo-environmental proxy for accurate seasonal temperature reconstructions<sup>58</sup>. However, the relatively constant δ<sup>18</sup>O values of structural carbonate precludes large δ<sup>18</sup>O changes in ambient water, such as shifts between freshwater and saline environments.

## Propagation phase-contrast synchrotron radiation micro-computed tomography

Paddlefish specimen FAU.DGS.ND.161.4559.T lacks the paddle-shaped rostrum and all aspects caudal to the pectoral girdle. FAU.DGS.ND.161.4559.T was provided by the Palm Beach Museum of Natural History. Data acquisition took place in May 2018 on Beamline BM05 of the European Synchrotron Radiation Facility, Grenoble, France<sup>59</sup>. The complete specimen was scanned at an average energy of 132 keV using the white beam of BM05 filtered with 0.4 mm of Mo and 9 mm of Cu. The detector was composed of a 2-mm-thick LuAG:Ce scintillator optically coupled to a PCO edge 4.2 CLHS sCMOS camera. The resulting voxel size was 43.5 μm. To obtain sufficient propagation phasecontrast, the distance between the sample and the detector was set at 5 m. A total of 205 scans, each consisting of 5,000 projections taken at 7-ms intervals, were performed with a vertical displacement of 1.4 mm at a vertical field of view of 2.8 mm to ensure a double scan of the complete samples. Scans were performed in half-acquisition mode to enlarge the lateral field of view. The volume was reconstructed using a single-distance phase retrieval algorithm coupled with filtered back projection as implemented in the ESRF software PyHST2. Vertical concatenation, 16-bit conversion, and ring artefact corrections were performed using MATLAB scripts developed in-house. The gill region and impact spherules were subsequently scanned at a voxel size of 13.67 μm (filters: 0.4 mm of Mo and 6 mm of

Cu, scintillator: LuAG:Ce, 500- $\mu$ m thick, detected energy: 166 keV, propagation distance: 2.5 m). The samples were scanned in half-acquisition mode in two columns of 77 scans, each consisting of 4,998 projections with exposure times of 0.05 s, that were laterally concatenated after reconstruction. Finally, sample (VUA.GG.2017.X-2724) from the paddlefish dentaries and (VUA.GG.2017.MDX-3, VUA.GG.2017.X-2743M and VUA.GG.2017.X-2744M) of the sturgeon pectoral fin spines were scanned at 4.35  $\mu$ m voxel size for osteohistological analysis<sup>60</sup> (filters: 3.5 mm of Al plus 11 bars Al with a diameter of 5 mm, scintillator: LuAG:Ce scintillator, 500- $\mu$ m thick, detected energy: 92 keV, propagation distance: 1.5 m). The samples were scanned in half-acquisition mode in one single column of 22 scans, each consisting of 4,998 projections with exposure times of 60 ms.

Digital 3D extraction of the bones and impact spherules was performed in VGStudio MAX 3.2 (Volume Graphics). VGStudio MAX 3.2 furthermore enabled the creation of virtual thick sections of the osteohistological samples through the ‘thick slab-mode’, which captures the maximum, average, or minimum, grey-level values along the desired field depth. Virtual thick sections were obtained from the average grey-level values at a thickness of 100  $\mu$ m following optimal 3D alignment of the annuli and LAGs. Additional virtual thick sections were created from the minimum grey-level values at a thickness of 200  $\mu$ m to best resolve the sizes and distributions of osteocyte lacunae. A coloured map of the density of the osteocyte lacunar distribution was created with a Gaussian filter<sup>51</sup>. Finally, we visualized the annual cyclicity of osteocyte lacunar volumes<sup>18</sup> in paddlefish dentary VUA.GG.2017.X-2724. As the resolution of our data (voxel size of 4.35  $\mu$ m; appropriate for assessing GMs and osteocyte lacunar distributions) is sixfold lower than that used for earlier osteocyte lacunar volumetric quantification in fish bones<sup>18</sup> (voxel size of 0.7  $\mu$ m), our result should be considered with appropriate care. Closely spaced (large) osteocyte lacunae may occasionally be conjoined and additional phenomena in the broad size range of osteocyte lacunae may be incidentally included in the visualized distribution. Moreover, in tomographic data, osteocyte lacunae are delimited by slight colour gradients (rather than discrete lines) that scale with voxel size. Because the outermost feature fringe contributes disproportionately to recovered volumes, these values are somewhat skewed relative to the original osteocyte lacunar volumes, which likely produces exaggerated volume values. Therefore, although all rendered features were extracted with a single thresholding operation and relative patterns are conservatively retained, absolute volume values are best considered in a comparative context.

## Reporting summary

Further information on research design is available in the [Nature Research Reporting Summary](#) linked to this paper.

## Data availability

All isotopic, geochemical, and osteohistological data are included in the paper and Extended Data. Tomographic data of FAU.DGS.ND.161.4559.T, VUA.GG.2017.X-2724, VUA.GG.2017.MDX-3, VUA.GG.2017.X-2743M, and VUA.GG.2017.X-2744M are available at <https://doi.org/10.5281/zenodo.5776294> and the <http://paleo.esrf.eu> database.

## References

1. Alvarez, L. W., Alvarez, W., Asaro, F. & Michel, H. V. Extraterrestrial cause for the Cretaceous–Tertiary extinction. *Science* **208**, 1095–1108 (1980).
2. Smit, J. & Hertogen, J. An extraterrestrial event at the Cretaceous–Tertiary boundary. *Nature* **285**, 198–200 (1980).
3. Raup, D. M. Biological extinction in earth history. *Science* **231**, 1528–1533 (1986).
4. Schulte, P. et al. The Chicxulub asteroid impact and mass extinction at the Cretaceous–Paleogene boundary. *Science* **327**, 1214–1218 (2010).
5. DePalma, R. A. et al. A seismically induced onshore surge deposit at the KPg boundary, North Dakota. *Proc. Natl Acad. Sci. USA* **116**, 8190–8199 (2019).
6. Smit, J. et al. Tektite-bearing, deep-water clastic unit at the Cretaceous–Tertiary boundary in northeastern Mexico. *Geology* **20**, 99–103 (1992).
7. Alvarez, W. in *The Cretaceous-Tertiary Event and Other Catastrophes in Earth History* (eds Ryder, G. et al.) 141–150 (Geological Society of America, 1996).
8. Smit, J. The global stratigraphy of the Cretaceous–Tertiary boundary impact ejecta. *Annu. Rev. Earth Planet. Sci.* **27**, 75–113 (1999).
9. Morgan, J., Artemieva, N. & Goldin, T. Revisiting wildfires at the K–Pg boundary. *J. Geophys. Res.* **118**, 1508–1520 (2013).
10. Vellekoop, J. et al. Rapid short-term cooling following the Chicxulub impact at the Cretaceous–Paleogene boundary. *Proc. Natl Acad. Sci. USA* **111**, 7537–7541 (2014).
11. Vellekoop, J. et al. Evidence for Cretaceous-Paleogene boundary bolide ‘impact winter’ conditions from New Jersey, USA. *Geology* **44**, 619–622 (2016).

12. Golovneva, L. B. The Maastrichtian (Late Cretaceous) climate in the northern hemisphere. *J. Geol. Soc. Lond.* **181**, 43–54 (2000).
13. Wolfe, J. A. & Upchurch Jr, G. R. North American nonmarine climates and vegetation during the Late Cretaceous. *Palaeogeogr. Palaeocl.* **61**, 33–77 (1987).
14. Hallam, A. A review of Mesozoic climates. *J. Geol. Soc. London* **142**, 433–445 (1985).
15. Adams, L. A. Age determination and rate of growth in *Polyodon spathula*, by means of the growth rings of the otoliths and dentary bone. *Am. Midl. Nat.* **28**, 617–630 (1942).
16. Bakhshalizadeh, S., Bani, A., Abdolmalaki, S. & Moltschaniwskyj, N. Identifying major events in two sturgeons' life using pectoral fin spine ring structure: exploring the use of a non-destructive method. *Environ. Sci. Pollut. R* **24**, 18554–18562 (2017).
17. Sanchez, S., Ahlberg, P. E., Trinajstic, K. M., Mirone, A. & Tafforeau, P. Three-dimensional synchrotron virtual paleohistology: a new insight into the world of fossil bone microstructures. *Microsc. Microanal.* **18**, 1095–1105 (2012).
18. Davesne, D., Schmitt, A. D., Fernandez, V., Benson, R. B. & Sanchez, S. Three-dimensional characterization of osteocyte volumes at multiple scales, and its relationship with bone biology and genome evolution in ray-finned fishes. *J. Evol. Biol.* **33**, 808–830 (2020).
19. Tafforeau, P., Bentaleb, I., Jaeger, J.-J. & Martin, C. Nature of enamel laminations and mineralization in rhinoceros enamel using histology and X-ray synchrotron microtomography: potential implications for palaeoenvironmental isotopic studies. *Palaeogeogr. Palaeocl.* **246**, 206–227 (2007).
20. Castanet, J. *Bone—Volume 7: Bone Growth* (ed. Hall, B. K.) 245–283 (CRC Press, 1993).
21. Hedges, R. E. Bone diagenesis: an overview of processes. *Archaeometry* **44**, 319–328 (2002).
22. Dumont, M. et al. Synchrotron XRF analyses of element distribution in fossilized sauropod dinosaur bones. *Powder Diffr.* **24**, 130–134 (2009).
23. Pradel, A. et al. Skull and brain of a 300-million-year-old chimaeroid fish revealed by synchrotron holotomography. *Proc. Natl Acad. Sci. USA* **106**, 5224–5228 (2009).

24. Weigle, J. & Franz-Odendaal, T. A. Functional bone histology of zebrafish reveals two types of endochondral ossification, different types of osteoblast clusters and a new bone type. *J. Anat.* **229**, 92–103 (2016).
25. Enlow, D. H. *The Human Face. An Account of the Postnatal Growth and Development of the Craniofacial Skeleton* (Harper and Row, 1968).
26. Grande, L. & Bemis, W. E. Osteology and phylogenetic relationships of fossil and recent paddlefishes (Polyodontidae) with comments on the interrelationships of Acipenseriformes. *J. Vert. Paleo.* **11**, 1–121 (1991).
27. De Ricqlès, A. J., Meunier, F. J., Castanet, J. & Francillon-Vieillot, H. *Bone 3, Bone Matrix and Bone Specific Products* (CRC Press, 1991).
28. Hall, B. K. *Bones and Cartilage: Developmental and Evolutionary Skeletal Biology* (Elsevier, 2005).
29. Bemis, W. E. & Kynard, B. Sturgeon rivers: an introduction to acipenseriform biogeography and life history. *Environ. Biol. Fish.* **48**, 167–183 (1997).
30. LeBreton, G. T., Beamish, F. W. H. & McKinley, S. R. (eds) *Sturgeons and paddlefish of North America*, Vol. 27 (Springer, 2004)
31. Blackwell, B. G., Murphy, B. R. & Pitman, V. M. Suitability of food resources and physicochemical parameters in the lower Trinity River, Texas for paddlefish. *J. Freshw. Ecol.* **10**, 163–175 (1995).
32. Fry, B. & Sherr, E. B.  $\delta^{13}\text{C}$  measurements as indicators of carbon flow in marine and freshwater ecosystems. *Ecol. Stud.* [https://doi.org/10.1007/978-1-4612-3498-2\\_12](https://doi.org/10.1007/978-1-4612-3498-2_12) (1989).
33. Finlay, J. C. Stable-carbon-isotope ratios of river biota: implications for energy flow in lotic food webs. *Ecology* **82**, 1052–1064 (2001).
34. Robertson, D. S., Lewis, W. M., Sheehan, P. M. & Toon, O. B. K-Pg extinction: reevaluation of the heat-fire hypothesis. *J. Geophys. Res.* **118**, 329–336 (2013).
35. Wolfe, J. A. Palaeobotanical evidence for a June 'impact winter' at the Cretaceous/Tertiary boundary. *Nature* **352**, 420–423 (1991).
36. Nichols, D. J. Plants at the K/T boundary. *Nature* **356**, 295–295 (1992).
37. Hickey, L. J. & McWeney, L. J. Plants at the K/T boundary. *Nature* **356**, 295–296 (1992).

38. McIver, E. E. Paleobotanical evidence for ecosystem disruption at the Cretaceous–Tertiary boundary from Wood Mountain, Saskatchewan, Canada. *Can. J. Earth Sci.* **36**, 775–789 (1999).
39. Upchurch, G. R., Lomax, B. H. & Beerling, D. J. Paleobotanical evidence for climatic change across the Cretaceous–Tertiary boundary, North America: twenty years after Wolfe and Upchurch. *Cour. Forsch. Senck* **258**, 57 (2007).
40. Kring, D. A. The Chicxulub impact event and its environmental consequences at the Cretaceous–Tertiary boundary. *Palaeogeogr. Palaeocl.* **255**, 4–21 (2007).
41. Robertson, D. S., McKenna, M. C., Toon, O. B., Hope, S. & Lillegraven, J. A. Survival in the first hours of the Cenozoic. *Geol. Soc. Am. Bull.* **116**, 760–768 (2004).
42. D'Hondt, S., Pilson, M. E., Sigurdsson, H., Hanson Jr, A. K. & Carey, S. Surface-water acidification and extinction at the Cretaceous–Tertiary boundary. *Geology* **22**, 983–986 (1994).
43. Erickson, G. M., Zelenitsky, D. K., Kay, D. I. & Norell, M. A. Dinosaur incubation periods directly determined from growth-line counts in embryonic teeth show reptilian-grade development. *Proc. Natl Acad. Sci. USA* **114**, 540–545 (2017).
44. Donovan, M. P., Iglesias, A., Wilf, P., Labandeira, C. C. & Cúneo, N. R. Rapid recovery of Patagonian plant–insect associations after the end-Cretaceous extinction. *Nat. Ecol. Evol.* **1**, 0012 (2016).
45. Fernandez, V. et al. Synchrotron reveals Early Triassic odd couple: injured amphibian and aestivating therapsid share burrow. *PLoS ONE* **8**, e64978 (2013).
46. Nowack, J., Cooper, C. E. & Geiser, F. Cool echidnas survive the fire. *Proc. R. Soc. B* **283**, 20160382 (2016).
47. Lovegrove, B. G., Lobban, K. D. & Levesque, D. L. Mammal survival at the Cretaceous–Palaeogene boundary: metabolic homeostasis in prolonged tropical hibernation in tenrecs. *Proc. R. Soc. B* **281**, 20141304 (2014).
48. Withers, P. C. & Cooper, C. in *Encyclopedia of Ecology* (eds Jorgensen, S. E. & Fath, B.) 952–957 (Elsevier, 2008).
49. Field, D. J. et al. Early evolution of modern birds structured by global forest collapse at the end-Cretaceous mass extinction. *Curr. Biol.* **28**, 1825–1831 (2018).

50. Schleuning, M. et al. Ecological networks are more sensitive to plant than to animal extinction under climate change. *Nat. Commun.* **7**, 13965 (2016).
51. Sanchez, S. et al. 3D microstructural architecture of muscle attachments in extant and fossil vertebrates revealed by synchrotron microtomography. *PLoS ONE* **8**, e56992 (2013).
52. de Buffrénil, V., Quilhac, A. & Castanet, J. in *Vertebrate Skeletal Histology and Paleohistology* (eds de Buffrénil, V. et al.) 626–645 (Routledge, 2021).
53. Lee, A. H. & O'Connor, P. M. Bone histology confirms determinate growth and small body size in the noasaurid theropod *Masiakasaurus knopfleri*. *J. Vertebr. Paleontol.* **33**, 865–876 (2013).
54. Klevezal, G. A. & Stewart, B. S. Patterns and calibration of layering in tooth cementum of female northern elephant seals, *Mirounga angustirostris*. *J. Mammal.* **75**, 483–487 (1994).
55. Woodward, H. N., Padian, K. and Lee, A. H. In *Bone Histology of Fossil Tetrapods—Advancing Methods, Analysis and Interpretation* (eds Padian, K. & E. T. Lamm) 195–215 (Univ. California Press, 2013).
56. Vonhof, H. B. et al. High-precision stable isotope analysis of < 5 µg CaCO<sub>3</sub> samples by continuous-flow mass spectrometry. *Rapid Commun. Mass Spectr.* **34**, e8878 (2020).
57. Pucéat, E. et al. Revised phosphate–water fractionation equation reassessing paleotemperatures derived from biogenic apatite. *Earth Planet. Sci. Lett.* **298**, 135–142 (2010).
58. Vennemann, T. W., Hegner, E., Cliff, G. & Benz, G. W. Isotopic composition of recent shark teeth as a proxy for environmental conditions. *Geochim. Cosmochim. Acta* **65**, 1583–1599 (2001).
59. Tafforeau, P. et al. Applications of X-ray synchrotron microtomography for non-destructive 3D studies of paleontological specimens. *Appl. Phys. A* **83**, 195–202 (2006).
60. Tafforeau, P. & Smith, T. M. Nondestructive imaging of hominoid dental microstructure using phase contrast X-ray synchrotron microtomography. *J. Hum. Evol.* **54**, 272–278 (2008).

## Acknowledgements

M.A.D.D. was partially funded by an EAVP Research Grant (ERG) awarded by the European Association of Vertebrate Palaeontologists. D.F.A.E.V. gratefully acknowledges support from the Wenner-Gren Foundation through fellowships UPD2018-250 and UPD2019-0076. VGStudio Max (Volume Graphics, Germany) and the Porosity/Inclusion Analysis module were funded by the Vetenskapsrådet through grants 2015-04335; 2019-04595 to S.S. We thank R. DePalma for providing guidance in the field and access to the specimens. We acknowledge the ESRF for provisioning beamtime at BM05. We thank V. Fernandez and K. Chapelle for their assistance with the segmentation in VGStudio; B. Lacet for help with the preparation of the thin and thick sections; M. Hagen for the use of her sedimentology laboratory and the microbalance for weeks in a row; F. Peeters for assistance in photographing the thin sections while sharing his thoughts on the project; and P. Ahlberg for his advice, labelling of the paddlefish bones, fruitful discussions and invaluable consultation.

## Funding

Open access funding provided by Uppsala University.

## Author information

### Affiliations

1. Department of Earth Sciences, Faculty of Science, Vrije Universiteit Amsterdam, Amsterdam, the Netherlands

Melanie A. D. During, Jan Smit, Suzan J. A. Verdegaal-Warmerdam & Jeroen H. J. L. van der Lubbe

2. Subdepartment of Evolution and Development, Department of Organismal Biology, Evolutionary Biology Centre, Uppsala University, Uppsala, Sweden

Melanie A. D. During, Dennis F. A. E. Voeten & Sophie Sanchez

3. European Synchrotron Radiation Facility, Grenoble, France

Dennis F. A. E. Voeten, Camille Berruyer, Paul Tafforeau & Sophie Sanchez

4. Royal Belgian Institute of Natural Sciences, Directorate ‘Earth and History of Life’, Brussels, Belgium

Koen H. W. Stein

5. Earth System Science—AMGC, Vrije Universiteit Brussel, Brussels, Belgium

Koen H. W. Stein

6. School of Earth and Environmental Sciences, Cardiff University, Cardiff, UK

Jeroen H. J. L. van der Lubbe

## Contributions

M.A.D.D., J.S. and H.J.L.v.d.L. conceived and designed the project. Materials were excavated by M.A.D.D. in 2017. M.A.D.D., D.F.A.E.V., C.B. and P.T. performed the synchrotron experiments. K.H.W.S. and M.A.D.D. performed the micro X-ray fluorescence analysis. M.A.D.D. sampled the specimens with the micromill. M.A.D.D., S.J.A.V.-W. and H.J.L.v.d.L performed the isotope analyses. P.T. processed and reconstructed the raw propagation phase contrast synchrotron radiation micro computed tomography scanning data. M.A.D.D. and D.F.A.E.V. segmented the scanning data. M.A.D.D., J.S., D.F.A.E.V., S.S. and H.J.L.v.d.L. analysed the data. S.S. created Fig. [3c](#) and Extended Data Fig. [8a–c](#). D.F.A.E.V. created Extended Data Fig. [8d–f](#). M.A.D.D. created all other figures. All authors discussed the interpretations. M.A.D.D., D.F.A.E.V. and H.J.L.v.d.L. wrote the manuscript. All authors provided a critical review and approved the final draft of the manuscript.

## Corresponding author

Correspondence to [Melanie A. D. During](#).

## Ethics declarations

## Competing interests

The authors declare no competing interests.

## Peer review

## Peer review information

*Nature* thanks Donald Davesne, Lauren Sallan and the other, anonymous, reviewers for their contribution to the peer review of this work. Peer reviewer reports are available.

## Additional information

**Publisher's note** Springer Nature remains neutral with regard to jurisdictional claims in published maps and institutional affiliations.

## Extended data figures and tables

### [Extended Data Fig. 1 Benthic foraminifera and acipenseriforms in the field at the Tanis locality and their respective sampling locations.](#)

**a,b,c**, and **d**, undetermined benthic foraminifera recovered from the Tanis deposit. Scale bars 1 mm. **e**, Sturgeon pectoral fin spines VUA.GG.2017.X-2743M and VUA.GG.2017.X-2744M, preserved in anatomical position, relative to their respective sturgeon carcasses in the Tanis deposit. **f**, Perichondral sturgeon bone sample VUA.GG.2017.MDX-3. **g**, perichondral sturgeon bone sample VUA.GG.2017.X-2743M. **h**, Perichondral sturgeon bone sample VUA.GG.2017.X-2744M. **i**, Dermal paddlefish bone sample VUA.GG.2017.X-2724. **j**, VUA.GG.2017.X-2733A in left lateral (left) and right lateral (right) view (sampling locations indicated between lines). The sediment matrix of sample VUA.GG.2017.X-2733A (bottom) also contains specimen VUA.GG.2017.X-2733B (covered). The fragile bone-bearing matrix was stabilised in epoxy resin prior to cutting, which obscured VUA.GG.2017.X-2733B from view. Scale bars 1 cm.

### [Extended Data Fig. 2 PPC- SR \$\mu\$ CT data of FAU.DGS.ND.161.4559.T, a partial paddlefish from the Tanis locality.](#)

**a**, Orthogonal virtual thin sections (100  $\mu$ m thick, average-value projections) obtained in front, top, and right view. **b**, Impact spherules in virtual thin sections of **a**, indicated with yellow circles. Scale bars **a** 1 mm. **c**, Three-dimensional rendering (in left lateral view) with virtual cross sections of **d** (blue), **e** (green), and **f** (red) indicated. **d**, Coronal virtual slice. **e**, Sagittal virtual slice. **f**, Axial virtual slice, brain-enveloping tissues indicated with red arrows. **g**, Three-dimensional rendering in right lateral view with anatomical labels. **h**, Three-dimensional rendering in left lateral view with anatomical labels.

### [Extended Data Fig. 3 Osteohistology of acipenseriforms from the Tanis locality.](#)

**a**, Thin section of paddlefish dentary VUA.GG.2017.X-2724 under transmitted light. **b**, Detail of VUA.GG.2017.X-2724 thin section (white box in **a**), scale bar 100  $\mu$ m. **c**,

Detail of VUA.GG.2017.X-2724 thin section (white box in **b**), scale bar 100 µm. **d**, Thin section of sturgeon pectoral fin spine VUA.GG.2017.MDX-3 under transmitted light. **e**, Detail of VUA.GG.2017.MDX-3 thin section (white box in **d**), scale bar 100 µm. **f**, Detail of VUA.GG.2017.MDX-3 thin section (white box in **e**), scale bar 100 µm. **g**, Thin section of paddlefish dentary VUA.GG.2017.X-2733A under transmitted light. **h**, Detail of VUA.GG.2017.X-2733A thin section (white box in **g**) with red arrows indicating Lines of Arrested Growth (LAGs), scale bar 100 µm. **i**, Detail of VUA.GG.2017.X-2724 thin section (white box in **h**), scale bar 100 µm.

#### [Extended Data Fig. 4 Osteohistology of acipenseriforms from the Tanis locality.](#)

**a**, Thin section of paddlefish dentary VUA.GG.2017.X-2733B under transmitted light. **b**, Detail of VUA.GG.2017.X-2733B thin section (white box in **a**) with red arrows indicating Lines of Arrested Growth (LAGs), scale bar 100 µm. **c**, Detail of VUA.GG.2017.X-2733B thin section (white box in **b**), scale bar 100 µm. **d**, Thin section of sturgeon pectoral fin spine VUA.GG.2017.X-2743M under transmitted light. **e**, Detail of VUA.GG.2017.X-2743M thin section (white box in **d**), scale bar 100 µm. **f**, Detail of VUA.GG.2017.X-2743M thin section (white box in **e**), scale bar 100 under transmitted light. **g**, Thin section of sturgeon pectoral fin spine VUA.GG.2017.X-2744M under transmitted light. **h**, Detail of VUA.GG.2017.X-2744M thin section (white box in **g**), scale bar 100 µm. **i**, Detail of VUA.GG.2017.X-2744M thin section (white box in **h**), scale bar 100 µm.

#### [Extended Data Fig. 5 PPC-SRµCT virtual osteohistology of acipenseriforms from the Tanis locality at 4.53 µm voxel size.](#)

**a**, Virtual thin section (100 µm thick, average-value projection; avp 100) of paddlefish dentary VUA.GG.2017.X-2724. **b**, Virtual thin section (avp 100) of sturgeon pectoral fin spine VUA.GG.2017.MDX-3. **c**, Virtual thin section (avp 100) of sturgeon pectoral fin spine VUA.GG.2017.X-2743M. **d**, Virtual thin section (avp 100) of sturgeon pectoral fin spine VUA.GG.2017.X-2744M. **e**, Thin section, virtual thin section, and virtual thick section of sturgeon pectoral fin spine VUA.GG.2017.MDX-3. **e,I**, Microscopic thin section under transmitted light showing LAGs. **e,II**, Virtual thin section (avp 100) showing LAGs. **e,III**, Virtual thick section (minimum-value projection with 200 µm depth (mvp 200)) showing oscillating osteocyte lacunar densities and sizes, with highest densities and largest sizes recorded during the favourable growth seasons and lowest densities and smallest sizes outside the favourable growth seasons. **f**, Thin section, virtual thin section, and virtual thick section of sturgeon pectoral fin spine VUA.GG.2017.X-2743M. **f,I**, Microscopic thin section under transmitted light showing LAGs. **f,II**, Virtual thin section (avp 100) showing LAGs. **f,III**, Virtual thick section (mvp 200) showing oscillating osteocyte

lacunar densities and sizes, with highest densities and largest sizes recorded during the favourable growth seasons and lowest densities and smallest sizes outside the favourable growth seasons. **g**, Thin section, virtual thin section, and virtual thick section of sturgeon pectoral fin spine VUA.GG.2017.X-2744M.**g,I**. Microscopic thin section under transmitted light showing LAGs. **g,II**. Virtual thin section (avp 100) showing LAGs. **g,III**. Virtual thick section (mvp 200) showing oscillating osteocyte lacunar densities and sizes, with highest densities and largest sizes recorded during the favourable growth seasons and lowest densities and smallest sizes outside the favourable growth seasons. Scanning data visualised in **e,II,III**, **f,II,III**, and **g,II,III**, were obtained approximately 10 mm distal to the physical thin sections in **e,I**, **f,I**, and **g,I**, respectively. Red arrows indicate LAGs, green arrows indicate concentrations of larger osteocyte lacunae. Scale bars in **e**, **f**, and **g**, 1 mm.

#### **Extended Data Fig. 6 Osteocyte lacunar density and volume distribution in paddlefish dentary VUA.GG.2017.X-2724 revealed by PPC-SR $\mu$ CT.**

**a**, Virtual thin section (100  $\mu$ m thick, average-value projection) with osteohistological features indicated. **b**, Segmented osteocyte lacunar distribution (black dots). **c**, Osteocyte lacunar density ma 54= Sanchez et al., 2013 p<sup>54</sup> with gradient scale. **d**, Virtual thick section (100  $\mu$ m thick, minimum-value projection). **e**, Three-dimensional osteocyte lacunar distribution at **d** (depth circa 1230  $\mu$ m), colour-coded by volume. **f**, Oscillating osteocyte lacunar volumes towards periosteal margin (10-point moving average) in dashed box in **e**. Successive annual growth climaxes (green arrows) and growth cessations (LAGs; red arrows) indicated. Typical annual maximum osteocyte lacunar volumes and highest osteocyte lacunar densities were not yet achieved in the year of death, indicating that growth ceased prior to the annual growth climax projected to occur during summer. Because the data resolution (voxel size of 4.35  $\mu$ m: appropriate for assessing growth marks and osteocyte lacunar distributions) is sixfold lower than that demonstrated in detailed osteocyte lacunar volume reconstructions<sup>18</sup> (voxel size of 0.7  $\mu$ m), these results should be considered qualitatively.

#### **Extended Data Fig. 7 Micro-X-ray fluorescence spectra of acipenseriform elements from the Tanis locality.**

**a**, Elemental spectrum of paddlefish dentary VUA.GG.2017.X-2724. **b**, Elemental spectrum of sturgeon pectoral fin spine VUA.GG.2017.MDX-3. **c**, Elemental spectrum of paddlefish dentary VUA.GG.2017.X-2733A, VUA.GG.2017.X-2733B, and surrounding matrix. **d**, Elemental spectrum of sturgeon pectoral fin spine VUA.GG.2017.X-2743M. **e**, Elemental spectrum of sturgeon pectoral fin spine VUA.GG.2017.X-2744M.

**Extended Data Fig. 8 Elemental distribution maps of acipenseriform elements from the Tanis locality obtained with micro-X-ray fluorescence.**

**a**, Ca, P, and Mn distribution in paddlefish dentary VUA.GG.2017.X-2724. **b**, Ca, P, and Mn distribution in sturgeon pectoral fin spine VUA.GG.2017.MDX-3. **c**, Ca, P, and Mn distribution in paddlefish dentaries VUA.GG.2017.X-2733A, VUA.GG.2017.X-2733B, and the surrounding sediment matrix. **d**, Ca, P, and Mn distribution in sturgeon pectoral fin spine VUA.GG.2017.X-2743M. **e**, Ca, P, and Mn distribution in sturgeon pectoral fin spine VUA.GG.2017.X-2744M. **f**, K, Si, and Fe distribution in paddlefish dentary VUA.GG.2017.X-2724. **g**, K, Si, and Fe distribution in sturgeon pectoral fin spine VUA.GG.2017.MDX-3. **h**, K, Si, and Fe distribution in paddlefish dentaries VUA.GG.2017.X-2733A, VUA.GG.2017.X-2733B and the surrounding sediment matrix. **i**, K, Si, and Fe distribution in sturgeon pectoral fin spine VUA.GG.2017.X-2743M. **j**, K, Si, and Fe distribution in sturgeon pectoral fin spine VUA.GG.2017.X-2744M.

**Extended Data Fig. 9 Elemental heat maps of acipenseriform elements from the Tanis locality, obtained with micro-X-ray fluorescence, showing homogenous distributions of Ca and P.**

**a**, Ca heat map of paddlefish dentary X-2723. **b**, Ca heat map of sturgeon pectoral fin spine VUA.GG.2017.MDX-3. **c**, Ca heat map of paddlefish dentaries VUA.GG.2017.X-2733A, VUA.GG.2017.X-2733B, and the surrounding sediment matrix. **d**, Ca heat map of sturgeon pectoral fin spine VUA.GG.2017.X-2743M. **e**, Ca heat map of sturgeon pectoral fin spine VUA.GG.2017.X-2744M. **f**, P heat map of paddlefish dentary VUA.GG.2017.X-2724. **g**, P heat map of sturgeon pectoral fin spine VUA.GG.2017.MDX-3. **h**, P heat map of paddlefish dentaries VUA.GG.2017.X-2733A, VUA.GG.2017.X-2733B, and the surrounding sediment matrix. **i**, P heat map of sturgeon pectoral fin spine VUA.GG.2017.X-2743M. **j**, P heat map of sturgeon pectoral fin spine VUA.GG.2017.X-2744M. Red and blue indicate higher, respectively lower abundance of Ca (**a**, **b**, **c**, **d**, and **e**) and P (**f**, **g**, **h**, **i**, and **j**).

**Extended Data Fig. 10  $\delta^{13}\text{C}_{\text{sc}}$  and  $\delta^{18}\text{O}_{\text{sc}}$  data of structurally-bound carbonate across the growth record in paddlefish dentary VUA.GG.2017.X-2724 and osteohistological diagram of paddlefish dentary VUA.GG.2017.X-2724.**

**a**, Incremental records of the carbon ( $\delta^{13}\text{C}_{\text{sc}}$ ; left) and oxygen ( $\delta^{18}\text{O}_{\text{sc}}$ ; right) isotopic composition of structurally-bound carbonate in the apatitic matrix of

VUA.GG.2017.X-2724 with uncertainty limits (1 s.d.). The seasonal cyclicity of  $\delta^{13}\text{C}_{\text{sc}}$  that reflects alternations in seasonal food availability is, to a lesser extent, also expressed in the  $\delta^{18}\text{O}_{\text{sc}}$  record. **b**, Schematic diagram of paddlefish dentary VUA.GG.2017.X-2724 with osteohistological features indicated. In the acipenseriform dermal bones examined in this study, annual growth cyclicity can be traced through Growth Marks (GMs). A GM spans a single growth cycle that typically lasts one year and can be divided into a zone, an annulus, and a LAG<sup>20,52</sup>. The zone is deposited during a period of relative rapid growth in the active or favourable growth season<sup>20</sup>. The annulus is subsequently formed when growth slows down towards the end of the growth season<sup>20</sup>. Finally, a LAG forms when growth periodically ceases until the next growth season starts and a new zone is deposited<sup>20</sup>.

## Supplementary information

[Reporting Summary](#)

[Supplementary Data Table](#)

[Peer Review File](#)

[Supplementary Video 1](#)

V1. 3D reconstruction of paddlefish FAU.DGS.ND.161.4559.T showing impact spherules trapped in its gill rakers

## Rights and permissions

**Open Access** This article is licensed under a Creative Commons Attribution 4.0 International License, which permits use, sharing, adaptation, distribution and reproduction in any medium or format, as long as you give appropriate credit to the original author(s) and the source, provide a link to the Creative Commons license, and indicate if changes were made. The images or other third party material in this article are included in the article's Creative Commons license, unless indicated otherwise in a credit line to the material. If material is not included in the article's Creative Commons license and your intended use is not permitted by statutory regulation or exceeds the permitted use, you will need to obtain permission directly from the copyright holder. To view a copy of this license, visit <http://creativecommons.org/licenses/by/4.0/>.

[Reprints and Permissions](#)

## About this article

### Cite this article

During, M.A.D., Smit, J., Voeten, D.F.A.E. *et al.* The Mesozoic terminated in boreal spring. *Nature* **603**, 91–94 (2022). <https://doi.org/10.1038/s41586-022-04446-1>

- Received: 22 June 2021
- Accepted: 19 January 2022
- Published: 23 February 2022
- Issue Date: 03 March 2022
- DOI: <https://doi.org/10.1038/s41586-022-04446-1>

### Share this article

Anyone you share the following link with will be able to read this content:

[Get shareable link](#)

Sorry, a shareable link is not currently available for this article.

[Copy to clipboard](#)

Provided by the Springer Nature SharedIt content-sharing initiative

### [Dinosaur-destroying asteroid struck in spring](#)

- Nick Petrić Howe
- Benjamin Thompson

Nature Podcast 23 Feb 2022

---

This article was downloaded by **calibre** from <https://www.nature.com/articles/s41586-022-04446-1>

- Article
- Open Access
- [Published: 23 February 2022](#)

# Genetic associations of protein-coding variants in human disease

- [Benjamin B. Sun](#) ORCID: [orcid.org/0000-0001-6347-2281<sup>1,2</sup>](https://orcid.org/0000-0001-6347-2281),
- [Mitja I. Kurki<sup>3,4,5,6</sup>](#),
- [Christopher N. Foley<sup>7,8</sup>](#),
- [Asma Mechakra<sup>9</sup>](#),
- [Chia-Yen Chen<sup>1</sup>](#),
- [Eric Marshall<sup>1</sup>](#),
- [Jemma B. Wilk<sup>1</sup>](#),
- [Biogen Biobank Team](#),
- [Mohamed Chahine](#) ORCID: [orcid.org/0000-0002-9500-2839<sup>10</sup>](https://orcid.org/0000-0002-9500-2839),
- [Philippe Chevalier<sup>9</sup>](#),
- [Georges Christé](#) ORCID: [orcid.org/0000-0003-2235-235X<sup>9</sup>](https://orcid.org/0000-0003-2235-235X),
- [FinnGen](#),
- [Aarno Palotie](#) ORCID: [orcid.org/0000-0002-2527-5874<sup>3,4,5,6</sup>](https://orcid.org/0000-0002-2527-5874),
- [Mark J. Daly<sup>3,4,5,6</sup>](#) &
- [Heiko Runz](#) ORCID: [orcid.org/0000-0002-2133-7345<sup>1</sup>](https://orcid.org/0000-0002-2133-7345)

[Nature](#) volume 603, pages 95–102 (2022)

- 19k Accesses
- 122 Altmetric
- [Metrics details](#)

## Subjects

- [Diseases](#)
- [Genetic association study](#)
- [Genetic predisposition to disease](#)
- [Genetic variation](#)

## Abstract

Genome-wide association studies (GWAS) have identified thousands of genetic variants linked to the risk of human disease. However, GWAS have so far remained largely underpowered in relation to identifying associations in the rare and low-frequency allelic spectrum and have lacked the resolution to trace causal mechanisms to underlying genes<sup>1</sup>. Here we combined whole-exome sequencing in 392,814 UK Biobank participants with imputed genotypes from 260,405 FinnGen participants (653,219 total individuals) to conduct association meta-analyses for 744 disease endpoints across the protein-coding allelic frequency spectrum, bridging the gap between common and rare variant studies. We identified 975 associations, with more than one-third being previously unreported. We demonstrate population-level relevance for mutations previously ascribed to causing single-gene disorders, map GWAS associations to likely causal genes, explain disease mechanisms, and systematically relate disease associations to levels of 117 biomarkers and clinical-stage drug targets. Combining sequencing and genotyping in two population biobanks enabled us to benefit from increased power to detect and explain disease associations, validate findings through replication and propose medical actionability for rare genetic variants. Our study provides a compendium of protein-coding variant associations for future insights into disease biology and drug discovery.

[Download PDF](#)

## Main

Inherited variations in protein-coding and non-coding DNA have a role in the risk, onset and progression of human disease. Traditionally, geneticists have dichotomized diseases as either caused by coding mutations in single genes that tend to be rare, highly penetrant and frequently compromise survival and reproduction (often termed ‘Mendelian’ diseases), or as common diseases that show a complex pattern of inheritance influenced by the joint contributions of hundreds of low-impact, typically non-coding genetic variants (often termed ‘complex’ diseases). For both rare and common conditions, large human cohorts systematically characterized for a respective trait of interest have enabled the identification of thousands of disease-relevant variants through either sequencing-based approaches or GWAS. Nevertheless, the exact causal alleles and mechanisms that underlie associations of genetic variants to disease have so far remained largely elusive<sup>1</sup>.

In recent years, population biobanks have been added to the toolkit for disease gene discovery. Biobanks provide the opportunity to simultaneously investigate multiple traits and diseases at once and uncover relationships between previously unconnected

phenotypes. For instance, the UK Biobank (UKB) is a resource that captures detailed phenotype information matched to genetic data for more than 500,000 individuals and, since its inception, has facilitated biomedical discoveries at an unprecedented scale<sup>2</sup>. We and others have recently reported on the ongoing efforts to sequence the exomes of all UKB participants and link genetic findings to a broad range of phenotypes<sup>3,4,5,6</sup>. We also established FinnGen (FG) (<https://www.finngen.fi>), an academic–industry collaboration to identify genotype–phenotype correlations in the Finnish founder population with the aim of better understanding how the genome affects health. Finland is a well-established genetic isolate and a unique gene pool distinguishes Finns from other Europeans<sup>7</sup>. The distinct Finnish haplotype structure is characterized by large blocks of co-inherited DNA in linkage disequilibrium and an enrichment for alleles that are rare in other populations, but can still be confidently imputed from genotyping data even in the rare and ultra-rare allele frequency spectrum<sup>8,9,10</sup>. Through combining imputed genotypes with detailed phenotypes ascertained through national registries, FG holds the promise to provide particular insights into the so far little examined allele frequency spectrum between 0.1 and 2%, where both sequencing studies and GWAS have so far remained largely underpowered in relation to identifying associations with disease. This spectrum includes many coding variants with moderate to large effect sizes that can help identify causal genes in GWAS loci, provide mechanistic insights into disease pathologies, and potentially bridge rare and common diseases.

Here, we have leveraged the combined power of UKB and FG to investigate how rare and low-frequency variants in protein-coding regions of the genome contribute to the risk for human traits and diseases. Using data from a total of 653,219 individuals, we tested how approximately 48,000 coding variants identified in both biobanks through either whole-exome sequencing or genotype imputation associate with 744 distinct disease endpoints. Disease associations were compared against information from rare disease, biomarker and drug target resources and complemented by deep dives into distinct disease mechanisms of individual genes and coding variants. Our results showcase the benefits of combining large population cohorts to discover and replicate novel associations, explain disease mechanisms across a range of common and rare diseases, and shed light on a substantial gap in the allelic spectrum that neither genotyping nor sequencing studies have previously been able to address.

## Coding associations with human disease

An overview of the study design and basic demographics are provided in Extended Data Fig. 1, Supplementary Table 1. In brief, we systematically harmonised disease phenotypes across UKB and FG using Phecode and ICD10 mappings and retained 744 specific disease endpoints grouped into 580 disease clusters (Methods, Supplementary Table 2). Disease case counts relative to cohort size showed good correlations both

overall between UKB and FG (Spearman's  $\rho=0.65$ ,  $P<5.3\times10^{-90}$ ) and across distinct disease groups (Extended Data Fig. 2).

We performed coding-wide association studies (CWAS) across 744 disease endpoints over a mean of 48,189 (range: 25,309–89,993) ([Methods](#), Supplementary Table 2) post-quality control coding variants across the allele frequency spectrum derived from whole-exome sequencing of 392,814 European ancestry individuals in UKB and meta-analysed these data with summary results from up to 260,405 individuals in FG ([Methods](#), Supplementary Table 2).

We identified 975 associations (534 variants in 301 distinct regions across 148 disease clusters; 620 distinct region-disease cluster associations) meeting genome-wide significance ( $P<5\times10^{-8}$ ), and 717 associations (378 variants in 231 distinct regions across 121 disease clusters; 445 distinct region-disease cluster associations) at a conservative (Bonferroni) multiple testing threshold of  $P<2\times10^{-9}$  (correcting for the number of approximate independent tests) ([Methods](#), Fig. 1a, Supplementary File 1 (interactive), Supplementary Table 3). The distributions of coding variant annotation categories were largely similar for variants with at least one significant association ( $P<5\times10^{-8}$ ) relative to all variants tested, with missense variants showing a higher fraction of significant variants than in-frame insertion–deletions or predicted loss-of-function (pLOF) variants (Extended Data Fig. 3). Inflation was well controlled with a mean genomic inflation factor of 1.04 (5th–95th percentiles: 1.00–1.09; Extended Data Fig. 4a). Effect sizes were generally well aligned between UKB and FG (Spearman's  $\rho=0.90$ ,  $P<10^{-300}$ ) (Extended Data Fig. 4b). Minor allele frequencies (MAFs) of lead variants correlated well overall between UKB and FG (Spearman's  $\rho=0.97$ ,  $P<10^{-300}$ ) (Fig. 1b), especially for variants with  $MAF>1\%$ , yet as expected<sup>9</sup> from genetic differences between Finns and non-Finnish Europeans (NFEs) this correlation was reduced for variants with  $MAF<1\%$  (Spearman's  $\rho=0.32$ ,  $P=0.023$ ).

**Fig. 1: Coding genetic associations with disease.**

---

 **figure 1**

**a**, Summary of sentinel variant associations. Size of the point is proportional to effect size.  $-\log_{10}(P)$  capped at  $-\log_{10}(10^{-50})$ . Labels highlight pleiotropic associations ( $\geq 5$  trait clusters). Colours indicate disease groups. Shapes indicate novel and known (grey circles) associations. Dotted horizontal lines indicate  $-\log_{10}(2 \times 10^{-9})$  (brown) and  $-\log_{10}(5 \times 10^{-8})$  (grey). **b**, Comparison of sentinel variant MAF between UKB and FG data. **c**, Effect size against MAF of sentinel variants. Dashed lines indicate MAF of 0.1% (left) and 1% (right). Genes for coding variant associations with absolute effect size greater than 2 or MAF less than 0.1% are labelled. **d**, Surface plot of effects of cohort specific allele enrichment on inverse variant weighted (IVW) meta-analysis  $z$ -scores (IVW uplift) across MAFs (up to MAF 1%). Uplift is defined as the ratio of meta-analysed IVW  $z$ -score to the  $z$ -score of an individual study (details in [Supplementary Information](#)). **e**, Density plot of MAF for sentinel variants for known versus novel associations. Interactive Manhattan plot for novel associations and allelic enrichment surface plots are provided as Supplementary Files [1](#), [2](#).

Across all diseases, we found generally larger effect sizes for low frequency and rare variants (Fig. [1c](#)). Of the 975 identified associations, 387 (39.7% at  $P < 5 \times 10^{-8}$ , 270 out of 717 (37.7%) at  $P < 2 \times 10^{-9}$ ) would not have been detected if analysed in UKB (61.5% at  $P > 5 \times 10^{-8}$ ; 60.1% at  $P > 2 \times 10^{-9}$ ) or FG (59.6% at  $P > 5 \times 10^{-8}$ ; 58.6% at  $P > 2 \times 10^{-9}$ ) alone. We found 13 associations (across 11 genes) with log odds ratios greater than 2 (Fig. [1c](#)). Of these, 12 associated variants had MAF < 1%, and only the

haemochromatosis variant rs1800562 showed frequency ranges traditionally interrogated in GWAS (MAF of 7.9% (UKB) and 3.7% (FG)). Several variants with large effect sizes reside in well studied disease genes such as *BRCA1* (breast cancer), *IDH2* (myeloid leukaemia), *VWF* (von Willebrand disease) or *HFE* (disorders of iron metabolism), proposing that carriers could benefit from clinical monitoring for associated conditions. Association testing within UKB and FG individually would have yielded 318 and 479 associations, respectively, at  $P < 5 \times 10^{-8}$  (Supplementary Tables 4, 5). Thus, our combined approach using both biobanks increased the number of significant findings by approximately threefold for UKB and twofold for FG. Of the 318 and 479 significant sentinel variants in UKB and FG, 252 (72.6%) and 258 (53.9%) replicated at  $P < 0.05$  in FG and UKB, respectively (Supplementary Tables 4, 5), further highlighting the strength of our approach to yield results that are more robust through replication than findings derived from a single biobank.

Our study benefits from population enrichment of rare alleles in Finns versus NFEs (and vice versa) that increases the power for association discovery. Using a combination of theoretical analyses and empirical simulations, we show that by leveraging population-enriched variants we could increase inverse-variance weighted meta-analysis Z-scores and hence our ability to detect underlying associations ([Supplementary Information](#)). The gain in power from enriched alleles was present across a range of rare MAFs (0.01–1%), with the strongest power gain in the rare and ultra-rare MAF range of 0.01% to 0.25% (Fig. 1d, Extended Data Fig. 5, [Supplementary Information](#), Supplementary Files 2a–c (interactive)). Notably, we demonstrate both theoretically and in practice that gains in power due to allele enrichment remain even after adjusting for power gains due to increased sample size (Supplementary Fig. 2 (MAF enrichment on Z-scores), Extended Data Fig. 5d). Of the sentinel variants, we found 73 (33 in UKB and 40 in FG) to be enriched by more than twofold and 23 (8 in UKB and 15 in FG) by more than fourfold relative to the other biobank (Fig. 1b, [Supplementary Table 6](#)). Most highly population-enriched variants are rare (MAF<1%) or low frequency (MAF 1–5%), whereby 20 out of 23 variants with more than fourfold population enrichment (13 in FG and 7 in UKB) had MAF <1% (Table 1, [Supplementary Table 6](#)). In comparison, 52 out of the total of 534 (9.7%) sentinel variants had MAF<1% in either UKB or FG, of which 15 and 23 were enriched by more than twofold in UKB and FG, respectively ([Supplementary Table 6](#)).

**Table 1 Genes with sentinel variants enriched more than fourfold in either UKB or FG datasets**

We systematically cross-referenced our results with previously described GWAS associations (via GWAS Catalog<sup>11</sup> and PhenoScanner<sup>12</sup>) and disease relevance as reported in ClinVar<sup>13</sup> ([Methods](#)). In total, we found that 216 out of 620 (34.8%) distinct region–disease cluster associations (at  $P < 5 \times 10^{-8}$ ) had not previously been

reported (130 out of 445 (29.2%) at  $P < 2 \times 10^{-9}$ ). Out of the 216 distinct loci, 177 (104 out of 130 at  $P < 2 \times 10^{-9}$ ) were in genes not previously mapped to the respective diseases (Fig. 1a, Supplementary Table 3, Supplementary File 1 (interactive)). Of the novel associations at GWAS significance ( $P < 5 \times 10^{-8}$ ), roughly one-third had MAF  $< 5\%$  in either UKB or FG and 15% had MAF  $< 1\%$  (Supplementary Table 3). Notably, in UKB, 17% of known (19% in FG) and 31% of novel (28% in FG) associations had a MAF  $< 5\%$ . Correspondingly, in UKB, 5% of known (6% in FG) and 15% of novel (10% in FG) associations had a MAF  $< 1\%$ , highlighting the power gained through our approach especially in the low and rare allele frequency spectrum (Fig. 1e, Supplementary Table 3).

Mapping associations to genes, we found a total of 482 unique genes associated with the 148 disease clusters. Approximately 92% of the associated regions for each disease cluster (excluding the major histocompatibility complex (*MHC*) cluster) harbour a single gene with coding associations (Extended Data Fig. 6a). The majority of gene loci (81.2% at  $P < 5 \times 10^{-8}$ ; *MHC* region counted as one locus) were associated with a single disease cluster (Extended Data Fig. 6b). Thirteen loci were associated with at least five trait clusters (at  $P < 5 \times 10^{-8}$ ), including well established pleiotropic regions such as the *MHC*, *APOE*, *PTPN22*, *GCKR*, *SH2B3* and *FUT2* (Fig. 1a). For instance, in addition to a known association with breast cancer, we found variants in *CHEK2* to be associated with the risk of colorectal and thyroid cancers, uterine leiomyoma, benign meningeal tumours and ovarian cysts. Also, in addition to a known association with prostate hyperplasia, we found an *ODF3* missense variant (rs72878024, MAF = 7.5% (UKB) and 7.7% (FG)) to be associated with risk of uterine leiomyoma, benign meningeal tumour, lipoma and polyps in the female genital tract (Supplementary Table 3).

Harnessing the added power of UKB and FG, we were able to detect GWAS associations for rare variants previously only annotated as causal for single-gene diseases, establishing a disease relevance for these variants at the population level. Of the 534 distinct variants with significant disease associations in our study ( $P < 5 \times 10^{-8}$ ), 152 (28.5%) had previously been linked to diseases in ClinVar. For 46 (30.3%) of these variants, the associated disease cluster matched with a previously reported phenotype in ClinVar. Notably, only 7 of these 46 variants (in *GJB2*, *ABCC6*, *BRCA1*, *SERPINA1*, *FLG*, *IDH2* and *MYOC*) had a previous annotation as either pathogenic or probably pathogenic (Supplementary Table 7), with 15 others annotated as benign. For the remaining 106 ClinVar-listed variants, 29 (27.4%) showed associations to conditions putatively related to those listed in ClinVar (Supplementary Table 7, Methods). For 17 variants, the medical relevance had been reported in ClinVar for the associated conditions, with 3 being classified as pathogenic or probably pathogenic and 14 classified either as benign or having ‘conflicting interpretation of pathogenicity’ for the associated trait (Supplementary Tables 3, 7).

For instance, we found a rare missense variant annotated as showing conflicting pathogenicity in ClinVar in *VWF* (rs1800386:C; Tyr1584Cys; MAF = 0.44% (UKB) and 0.47% (FG)) to be associated with the risk of von Willebrand disease<sup>13</sup> ( $\log(\text{odds ratio (OR)}) = 2.09$ ,  $P = 8.7 \times 10^{-9}$ ). We also assessed the medical actionability of associated genes as defined in the latest American College of Medical Genetics and Genomics (ACMG) guidelines<sup>14</sup> and found 15 coding variants with significant associations in 11 ACMG genes (Supplementary Table 2). Thirteen of these associations (one pathogenic (*BRCA1*), four conflicting evidence of pathogenicity and eight benign or probably benign) had prior ClinVar reports to a matching or putatively related condition, and for several our results proposed extended phenotypes. For example, we found that carriers of the rare missense variant rs370890951 (Ile1131Thr; MAF = 0.097% (UKB) and 0.29% (FG)) in *MYBPC3*, in which mutations cause hypertrophic cardiomyopathy, showed an approximately threefold increased risk ( $P = 9.8 \times 10^{-13}$ ) for coagulation defects (Supplementary Tables 3, 7). Together, these findings highlight that population-scale analyses like ours can help refine pathogenicity assignments through contributing quantitative, rather than qualitative, information on relative disease risks for variant carriers, or establish an ‘allelic series’ for medically actionable genes.

Seventeen of the twenty-three genes with highly population-enriched sentinel variants (Table 1) were listed as disease genes at Online Mendelian Inheritance in Man (OMIM). Of these, ten (*CHEK2*, *DBH*, *SCL24A5*, *CFI*, *FLG*, *XPA*, *F10*, *BRCA1*, *SCN5A* and *CACNA1D*) showed associations with conditions identical or related to the respective Mendelian disease, revealing a relevance of the associated variants on the population level. For instance, we found the missense variant rs77273740 in *DBH* (enriched by more than 50-fold in FG)—a gene associated with orthostatic hypotension—to be associated with reduced risk of hypertension ( $\log(\text{OR}) = -0.19$ ,  $P = 1.3 \times 10^{-23}$ ), and an in-frame deletion (rs1250342280) in *CACNA1D* (enriched by 4.3× in UKB)—a gene associated with primary aldosteronism—was associated with increased risk of hypertension ( $\log(\text{OR}) = 0.19$ ,  $P = 2.0 \times 10^{-8}$ ) (Table 1).

## Biomedical insights through CWAS

We leveraged the coding variant associations identified in our study to generate biological insights for a range of distinct genes, pathways and diseases and in the following exemplify the broad utility of our resource with a set of selected use cases.

### Coagulation proteins in pulmonary embolism

We found known and novel associations with pulmonary embolism risk, including two rare variant associations (average MAF < 1%) in genes encoding components of the

coagulation cascade at the convergent common pathway (Extended Data Fig. 7). For instance, we discovered a rare missense mutation in *F10*, enriched by approximately fivefold in FG (rs61753266:A; Glu142Lys; MAF = 0.33% (UKB) and 1.85% (FG)), and a venous thromboembolism risk-reducing variant in *F5* (rs4525:C, His865Arg; MAF = 27.2% (UKB) and 22.3% (FG)), to be protective against pulmonary embolism ( $\log(\text{OR})_{F10} = -0.44$ ,  $P_{F10} = 2.9 \times 10^{-9}$ ;  $\log(\text{OR})_{F5} = -0.14$ ,  $P_{F5} = 1.2 \times 10^{-15}$ ). The effects of these associations on the levels of their respective circulating factors and thromboembolic diseases, Mendelian randomization analyses that support developing drugs inhibiting factors V and X for pulmonary embolism and findings on additional clotting factors are discussed in ([Supplementary Information](#) ‘New roles for coagulation proteins in PE’).

## Rare variants yield mechanistic insights

We interrogated the sentinel variants identified in this study for associations with 117 quantitative biomarkers spanning eight categories in UKB (Supplementary Table 8). At a multiple testing adjusted threshold of  $P < 1 \times 10^{-6}$ , we found 112 of the biomarkers to be associated with at least one of 433 sentinel variants across 247 regions (Fig. 2a, Supplementary Table 9, [Supplementary Information](#)). Ninety-five of the regions were associated with five or more biomarker categories (Extended Data Fig. 6c, Supplementary Table 9), including pleiotropic disease loci such as *MHC*, *APOE*, *GCKR*, *SH2B3* and *FUT2*.

**Fig. 2: Biomarker associations with sentinel variants.**

 figure 2

**a**, Heat map of sentinel associations with biomarkers. Only significant associations ( $P < 10^{-6}$ ) are shown. Colours on the left axis indicate chromosomes, with cyan indicating the MHC region. Colours on the right axis indicate sentinel association with disease by group. Colours along the top indicate the category of biomarkers. **b**, Forest plot of associations (unadjusted regression effect estimates with 95% confidence intervals (CI)) between *SLC34A1* deletion (rs1460573878) with haematological and biochemistry biomarkers. associations with  $P < 0.05$  are shown. **c**, Forest plot of associations (unadjusted regression effect estimate with 95% confidence interval (CI)) between *CHEK2* deletion (rs555607708) with haematological biomarkers. Unadjusted  $P$  values are shown. Disease associations  $n = 653,219$  biologically independent samples. Specific sample sizes for biomarker associations are listed in Supplementary Table 8. IGF-1, insulin-like growth factor 1; LDL, low-density lipoprotein; SHBG, sex hormone binding globulin.

### SLC34A1 deletion and fluid biomarkers

Cross-referencing disease with biomarker associations provided mechanistic insights into novel findings. For instance, a low-frequency in-frame deletion in *SLC34A1* (rs1460573878; MAF = 2.6% (UKB) and 2.7% (FG); p.Val91\_AlA97del) coding for

the sodium phosphate cotransporter NPT2a expressed in proximal tubular cells was associated with increased risk of renal ( $\log(\text{OR}) = 0.24, P = 4.0 \times 10^{-9}$ ) and urinary tract stones ( $\log(\text{OR}) = 0.21, P = 6.8 \times 10^{-9}$ ). The deletion has previously been implicated in hypercalciuric renal stones<sup>15,16</sup> and autosomal recessive idiopathic infantile hypercalcaemia<sup>17</sup> in family studies. The variant is also associated with increased serum calcium ( $\beta = 0.047, P = 5.4 \times 10^{-11}$ ) and reduced phosphate ( $\beta = -0.075, P = 3.3 \times 10^{-26}$ ), consistent with a disrupted function or cell surface expression of the transporter<sup>17</sup> (Fig. 2b). We further find associations with increased levels of serum urate ( $\beta = 0.048, P = 4.5 \times 10^{-17}$ ), also suggesting an increased risk of uric acid stones. Additionally, we found associations with increased erythrocyte count ( $\beta = 0.035, P = 4.7 \times 10^{-10}$ ), haemoglobin concentration ( $\beta = 0.033, P = 7.7 \times 10^{-10}$ ) and haematocrit percentage ( $\beta = 0.036, P = 9.9 \times 10^{-11}$ ), suggesting increased renal-driven erythropoiesis (Fig. 2b). Serum creatinine was not increased in carriers of the deletion ( $\beta = -0.07, P = 3.6 \times 10^{-33}$ ), suggesting that renal function is not adversely affected in deletion carriers. Among 11,114 renal or ureteric, and 13,319 urinary tract stone cases, we identified 735 (renal or ureteric) and 863 (urinary tract) carriers of the deletion who may benefit from clinical interventions targeting NPT2A-related pathways and monitoring for disturbed biochemical and haematological biomarkers.

## CHEK2 deletion and haematological signs

A frameshift deletion in *CHEK2* (rs555607708; MAF = 0.64% (FG), 0.24% (UKB)) that increases breast cancer risk has also been previously implicated in myeloproliferative neoplasms through GWAS<sup>18</sup> and lymphoid leukaemia in a candidate variant study<sup>19</sup>. Consistently, we found nominally significant associations with risks of both, myeloid ( $\log(\text{OR}) = 1.52, P = 9.5 \times 10^{-8}$ ) and lymphoid ( $\log(\text{OR}) = 1.38, P = 3.1 \times 10^{-7}$ ) leukaemia, but also multiple myeloma ( $\log(\text{OR}) = 1.07, P = 5.1 \times 10^{-5}$ ) and non-Hodgkin lymphoma ( $\log(\text{OR}) = 0.81, P = 4.7 \times 10^{-4}$ ). Association of rs555607708 with clinical haematology traits showed statistically significant associations with increased blood cell counts for both myeloid (leukocytes, neutrophils and platelets at  $P < 1 \times 10^{-6}$ ; monocyte and erythrocytes at  $P < 1 \times 10^{-3}$ ) and lymphoid (lymphocytes,  $P = 5.7 \times 10^{-17}$ ) lineages (Fig. 2c). Furthermore, we found associations with increased mean platelet volume ( $P = 1.3 \times 10^{-16}$ ) and platelet distribution width ( $P = 5.2 \times 10^{-13}$ ), consistent with increased platelet activation and previous associations of mean platelet volume and platelet distribution width with chronic myeloid leukaemia<sup>20</sup>. We also found associations with decreased mean corpuscular haemoglobin ( $P = 7.8 \times 10^{-12}$ ) and mean corpuscular volume ( $P = 5.3 \times 10^{-10}$ ), suggesting that predisposition to haematological cancers by loss of *CHEK2* function is accompanied by a microcytic red blood cell phenotype (Fig. 2c).

## Coding associations aid drug development

We cross-referenced genes with significant coding variant associations with drug targets<sup>21</sup>. We found 66 genes with trait cluster associations that are the targets of either approved drugs (26 genes) or drugs currently being tested in clinical trials (40 genes), 14 of which are in phase III trials (Supplementary Table 10). We found a statistically significant enrichment of significant genes in our study that were also approved drug targets (26 out of 482, compared with a background of 569 approved targets out of 19,955 genes, OR = 1.9,  $P = 0.0024$ ), which is in line with previous estimates of a higher success rate for drug targets supported by genetics<sup>22,23</sup>. Sensitivity analyses using more stringent association  $P$ -value thresholds further increased these probability estimates ( $P = 5 \times 10^{-9}$  (OR = 2.3,  $P = 0.00070$ );  $P = 5 \times 10^{-10}$  (OR = 2.5,  $P = 0.00037$ )), supporting previous observations of higher likelihood of therapeutic success with stronger genetic associations (Supplementary Table 11). Specific examples are highlighted in the [Supplementary Information](#).

Atrial fibrillation (AF). GWAS have yielded a sizeable number of loci<sup>24,25</sup>. We chose AF to exemplify how results from our study can further elucidate the genetics and biological basis of one distinct human trait. Notably, we report several coding variant associations (Supplementary Table 3) in which prior GWAS<sup>24,25</sup> had fallen short for resolving GWAS loci to coding genes and explaining disease mechanisms.

### METTL11B methylase missense variant in AF

The AF GWAS sentinel variant rs72700114 is an intergenic variant located between *METTL11B* and *LINC01142* with no obvious candidate gene<sup>24,25,26</sup>. Our study revealed that a low-frequency missense variant in the methylase *METTL11B* (rs41272485:G; Ile127Met; MAF = 3.9% (UKB) and 3.8% (FG)) was associated with increased AF risk ( $\log(\text{OR}) = 0.14$ ,  $P = 4.0 \times 10^{-11}$ ). This variant locates to the enzyme's S-adenosylmethionine–S-adenosyl-l-homocysteine ligand-binding site<sup>27</sup> and is expected to perturb methylation of other AF risk genes with N-terminal (Ala/Pro/Ser)-Pro-Lys methylation motifs that are enriched in cardiomyocytes ([Methods](#), Supplementary Table 12, [Supplementary Results](#)), which probably explains the association.

### Rare variants and ion channel AF loci

Within the *SCN5A*–*SCN10A* locus, we replicated a common missense variant in *SCN10A* (rs6795970:A; Ala1073Val; MAF = 40.0% (UKB) and 44.6% (FG)) that was previously described as prolonging cardiac conduction<sup>28</sup>. Additionally, we found associations with reduced AF risk ( $\log(\text{OR}) = -0.06$ ,  $P = 2.1 \times 10^{-12}$ ), reduced pulse

rate ( $\beta = -0.02$ ,  $P = 4.8 \times 10^{-18}$ ), and a suggestive signal for increased risk of atrioventricular block ( $\log(\text{OR}) = 0.10$ ,  $P = 1.9 \times 10^{-7}$ ). It is thus tempting to speculate that loss of function of Nav1.8—the sodium channel encoded by *SCN10A*—blunts the effects of vagus nerve activity on the atria. In addition, we found a rare, enriched missense variant in FG (rs45620037:A; Thr220Ile; MAF = 0.11% (UKB) and 0.47% (FG); SIFT = 0.03, PolyPhen = 0.96) in *SCN5A*—which encodes the cardiac sodium channel Nav1.5—to be associated with decreased risk of AF ( $\log(\text{OR}) = -0.65$ ,  $P = 1.3 \times 10^{-12}$ ). This missense variant resides within the voltage sensing segment of *SCN5A*, causes a partial loss of function of the Nav1.5 channel in atrial cells and has been associated with dilated cardiomyopathy<sup>29</sup> and conduction defects including sick sinus syndrome and atrial standstill<sup>30</sup> in family studies with bradycardic changes. Consistently, we found a nominal association with reduced pulse rate ( $\beta = -0.078$ ,  $P = 0.023$ ), suggesting that protective effects of the variant will be most beneficial for the common tachycardic form of AF through reducing pulse rate. The *SCN10A* and *SCN5A* variants found here are probably both moderators of AF risk that act by different mechanisms. Potential mechanisms underlying further AF loci are described in [Supplementary Discussion](#).

### Genetic effects underlying AF and pulse

To further evaluate the hypothesis that distinct genetic mechanisms underlying AF risk inversely modulate pulse rate, we adjusted the clustered Mendelian randomization<sup>31</sup> (MR-Clust) algorithm to better accommodate rare-variants. We then related expectation maximization clustering of AF associated variants with homogenous directional effects on pulse rate ([Methods](#)). We found clusters of CWAS AF sentinel variants in *SCN10A* (rs6795970) and *HCN4* (rs151004999) as two genetic components of AF that can increase and decrease pulse rate, respectively (Fig. 3, Supplementary Table 13). Identifying components of AF with diverging directionality on pulse rate matches clinical observations that AF can be caused by both tachycardia and bradycardia<sup>32</sup>. Using sentinel variants from a recent AF GWAS<sup>24</sup> for sensitivity analyses yielded concordant patterns. By integrating CWAS and GWAS sentinel variants for AF we found additional clusters with differing effects on pulse rate. Expectedly, within the AF GWAS loci<sup>24</sup>, the two rare missense alleles in *HCN4* (rs151004999:T,  $\log(\text{OR}) = 0.72$ ) and *SCN5A* (rs45620037:A,  $\log(\text{OR}) = -0.65$ ) identified in our study had much larger effect sizes on AF risk than the respective non-coding sentinel GWAS variants (rs74022964:T (*HCN4* locus),  $\log(\text{OR}) = 0.12$ ; rs6790396:C (*SCN5A* and *SCN10A* locus),  $\log(\text{OR}) = -0.058$ ) (Fig. 3).

**Fig. 3: Genetic and functional insights into atrial fibrillation.**

---

 **figure 3**

Clustered Mendelian randomization plot of association of atrial fibrillation loci with pulse rate. Only variants with cluster inclusion probability greater than 0.7 are included. Top left, CWAS loci (sentinels). Top right, overlapping CWAS and atrial fibrillation GWAS loci. Bottom left, all atrial fibrillation GWAS loci from Nielsen et al.<sup>49</sup> (with zoomed inset). Bottom right, all atrial fibrillation GWAS loci with permuted pulse (null, with zoomed inset).

### Functional effects of PITX2c(Pro41Ser)

Finally, we found a rare missense variant in *PITX2* as associated with increased risk of AF ( $\log(\text{OR}) = 0.38$ ,  $P = 1.1 \times 10^{-9}$ ). This variant is enriched nearly 50-fold in FG (rs143452464:A; Pro41Ser; MAF = 0.023% (UKB) and 1.1% (FG)) and was independently identified in a French family with AF ([Supplementary Information](#)), whereas GWAS had linked intergenic variants between *PITX2* and *FAM241A* to AF risk. *PITX2* is a bicoid type homeobox transcription factor previously assumed to play a role in cardiac rhythm control<sup>33</sup>. The Pro41Ser variant lies in the N-terminal domain

that is only present in the PITX2c isoform expressed in cardiac muscle. In reporter assays comparing the ability of PITX2c wild-type and Pro41Ser protein constructs to transactivate a luciferase reporter plasmid containing a putative PITX2c-binding element, PITX2c(Pro41Ser) showed an approximately 2.4-fold higher activation of the reporter than the wild type ( $P = 0.006$ , Extended Data Fig. 8). This effect was abrogated upon deletion of the putative PITX2c-binding site. In cultured cardiac muscle HL-1 cells, the Pro41Ser mutation increased the transcription of several presumed PITX2c target genes (Supplementary Table 14, [Supplementary Information](#)). Together, these results are consistent with a putative gain-of-function mechanism of Pro41Ser on PITX2c transactivation potential and AF risk.

## Discussion

Here we have conducted the largest association study of protein-coding genetic variants so far against hundreds of disease endpoints ascertained from two massive population biobanks, UK Biobank and FinnGen. We report novel disease associations, most notably in the rare and low-allelic frequency spectrum, replicate and assign putative causalities to many previously reported GWAS associations, and leverage the insights gained to elucidate disease mechanisms, demonstrating that the step from association to biological insight may be considerably shorter for coding variant association studies than it has traditionally been for GWAS. In addition to a substantial gain in power over previous studies, our analyses benefit from replication between two population cohorts, increasing the robustness of our findings and setting the stage for future similar studies in ethnically more diverse populations.

Notably, our study identifies both pathogenic variants residing in monogenic disease genes to impact the risk for related complex conditions as well as new, probably causal sentinel variants within GWAS loci in genes with known and novel biological roles in the respective GWAS trait. With this, our study is one of the first to help bridge the gap between common and rare disease genetics across a broad range of conditions and provides support for the hypothesis that the genetic architecture of many diseases is continuous<sup>1</sup>. Of the 975 associations identified in our study, 145 are driven by unique variants in the so far little-interrogated rare and low-allelic frequency spectrum between 0.1 and 2% that neither GWAS nor sequencing studies have been able to thoroughly interrogate across a range of diseases and that is hypothesized to contribute to the ‘missing heritability’ of many human diseases<sup>34</sup>.

Our approach benefits considerably from the Finnish genetic background, where certain alleles are stochastically enriched to unusually high allele frequencies<sup>6,7,8</sup>, at times exceeding population frequencies in the UK Biobank by more than 50-fold. Our theoretical and empirical results suggest the increasing utility of enriched variants for identifying associations quantitatively towards lower allelic frequencies. Notably, we

identify the most prominent relative power gain in the rarest variant frequency spectrum, highlighting a role for sequencing studies and integrating additional population cohorts with enriched variants for identifying novel disease associations at scale. We identify several alleles with comparatively high effect sizes and a prevalence in the population that warrants follow-up, both experimentally as well as potentially directly in clinical settings to help improve disease outcomes. For instance, our data propose that 6.5% of UKB and FG participants with kidney or urinary tract stones, conditions debilitating more than 15% of men and 5% of women by 70 years of age<sup>35</sup>, carry a deletion in *SLC34A1*. Monitoring patients for the clinical biomarkers identified here as associated with this deletion might help to differentiate aetiologies and guide individualized treatments. Similarly, coding variant associations identified in our study may serve as an attractive source to generate hypotheses for drug discovery programs. Our results support previous studies<sup>22,23</sup> that drug targets supported by human genetics have an increased likelihood of success, which can be considered particularly high when the genetic effect on a drug target closely mimics that of a pharmacological intervention<sup>36</sup>.

Our results foreshadow the discovery of many additional coding and non-coding associations from cross-biobank analyses at even larger sample sizes. With the continued growth of population biobanks with comprehensive health data in non-European populations, the emergence of more and more cost-effective technologies for sequencing and genotyping, and computational advances to analyse genetic and non-genetic data at scale, future studies will be able to assess the genetic contribution to health and disease at even finer resolution.

## Methods

### Samples and participants

UKB is a UK population study of approximately 500,000 participants aged 40–69 years at recruitment<sup>2</sup>. Participant data (with informed consent) include genomic, electronic health record linkage, blood, urine and infection biomarkers, physical and anthropometric measurements, imaging data and various other intermediate phenotypes that are constantly being updated. Further details are available at <https://biobank.ndph.ox.ac.uk/showcase/>. Analyses in this study were conducted under UK Biobank Approved Project number 26041. Ethic protocols are provided by the UK Biobank Ethics Advisory Committee (<https://www.ukbiobank.ac.uk/learn-more-about-uk-biobank/about-us/ethics>).

FG is a public-private partnership project combining electronic health record and registry data from six regional and three Finnish biobanks. Participant data (with informed consent) include genomics and health records linked to disease endpoints.

Further details are available at <https://www.finngen.fi/>. More details on FG and ethics protocols are provided in [Supplementary Information](#). We used data from FG participants with completed genetic measurements (R5 data release) and imputation (R6 data release). FinnGen participants provided informed consent for biobank research. Recruitment protocols followed the biobank protocols approved by Fimea, the National Supervisory Authority for Welfare and Health. The Coordinating Ethics Committee of the Hospital District of Helsinki and Uusimaa (HUS) approved the FinnGen study protocol Nr HUS/990/2017. The FinnGen study is approved by Finnish Institute for Health and Welfare.

## Disease phenotypes

FG phenotypes were automatically mapped to those used in the Pan UKBB (<https://pan.ukbb.broadinstitute.org/>) project. Pan UKBB phenotypes are a combination of Phecodes<sup>37</sup> and ICD10 codes. Phecodes were translated to ICD10 ([https://phewascatalog.org/phecodes\\_icd10](https://phewascatalog.org/phecodes_icd10), v.2.1) and mapping was based on ICD-10 definitions for FG endpoints obtained from cause of death, hospital discharge and cancer registries. For disease definition consistency, we reproduced the same Phecode maps using the same ICD-10 definitions in UKB. In particular, we expertly curated 15 neurological phenotypes using ICD10 codes. We retained phenotypes where the similarity score (Jaccard index:  $ICD10_{FG} \cap ICD10_{UKB} / ICD10_{FG} \cup ICD10_{UKB}$ ) was  $>0.7$  and additionally excluded spontaneous deliveries and abortions.

Phecodes and ICD10 coded phenotypes were first mapped to unified disease names and disease groups using mappings from Phecode, PheWAS and icd R packages followed by manual curation of unmapped traits and diseases groups, mismatched and duplicate entries. Disease endpoints were mapped to Experimental Factor Ontology (EFO) terms using mappings from EMBL-EBI and Open Targets based on exact disease entry matches followed by manual curation of unmapped traits.

Disease trait clusters were determined through first calculating the phenotypic similarity via the cosine similarity, then determining clusters via hierarchical clustering on the distance matrix (1-similarity) using the Ward algorithm and cutting the hierarchical tree, after inspection, at height 0.8 to provide the most semantically meaningful clusters.

## Genetic data processing

### UKB genetic QC

UKB genotyping and imputation were performed as described previously<sup>2</sup>. Whole-exome sequencing data for UKB participants were generated at the Regeneron

Genetics Center (RGC) as part of a collaboration between AbbVie, Alnylam Pharmaceuticals, AstraZeneca, Biogen, Bristol-Myers Squibb, Pfizer, Regeneron and Takeda with the UK Biobank. Whole-exome sequencing data were processed using the RGC SBP pipeline as described<sup>3,38</sup>. RGC generated a QC-passing ‘Goldilocks’ set of genetic variants from a total of 454,803 sequenced UK Biobank participants for analysis. Additional quality control (QC) steps were performed prior to association analyses as detailed below.

## FG genetic QC

Samples were genotyped with Illumina and Affymetrix arrays (Thermo Fisher Scientific). Genotype calls were made with GenCall and zCall algorithms for Illumina and AxiomGT1 algorithm for Affymetrix data. Sample, genotyping as well as imputation procedures and QC are detailed in [Supplementary Information](#).

## Coding variant selection

GnomAD v.2.0 variant annotations were used for FinnGen variants<sup>39</sup>. The following gnomAD annotation categories are included: pLOF, low-confidence loss-of-function (LC), in-frame insertion–deletion, missense, start lost, stop lost, stop gained. Variants have been filtered to imputation INFO score > 0.6. Additional variant annotations were performed using variant effect predictor (VEP)<sup>40</sup> with SIFT and PolyPhen scores averaged across the canonical annotations.

## Disease endpoint association analyses

For optimized meta-analyses with FG, analyses in UKB were performed in the subset of exome-sequence UKB participants with white European ancestry for consistency with FG ( $n = 392,814$ ). We used REGENIE v1.0.6.7 for association analyses via a two-step procedure as detailed in ref. <sup>41</sup>. In brief, the first step fits a whole genome regression model for individual trait predictions based on genetic data using the leave one chromosome out (LOCO) scheme. We used a set of high-quality genotyped variants: MAF > 5%, MAC > 100, genotyping rate >99%, Hardy–Weinberg equilibrium (HWE) test  $p > 10^{-15}$ , <5% missingness and linkage-disequilibrium pruning (1,000 variant windows, 100 sliding windows and  $r^2 < 0.8$ ). Traits where the step 1 regression failed to converge due to case imbalances were subsequently excluded from subsequent analyses. The LOCO phenotypic predictions were used as offsets in step 2 which performs variant association analyses using the approximate Firth regression detailed in ref. <sup>41</sup> when the  $P$  value from the standard logistic regression score test is below 0.01. Standard errors were computed from the effect size estimate and the likelihood ratio test  $P$ -value. To avoid issues related to severe case

imbalance and extremely rare variants, we limited association test to phenotypes with  $>100$  cases and for variants with MAC  $\geq 5$  in total samples and MAC  $\geq 3$  in cases and controls. The number of variants used for analyses varies for different diseases as a result of the MAC cut-off for different disease prevalence. The association models in both steps also included the following covariates: age, age $^2$ , sex, age\*sex, age $^2$ \*sex, first 10 genetic principal components (PCs).

Association analyses in FG were performed using mixed model logistic regression method SAIGE v0.39<sup>42</sup>. Age, sex, 10 PCs and genotyping batches were used as covariates. For null model computation for each endpoint each genotyping batch was included as a covariate for an endpoint if there were at least 10 cases and 10 controls in that batch to avoid convergence issues. One genotyping batch need be excluded from covariates to not have them saturated. We excluded Thermo Fisher batch 16 as it was not enriched for any particular endpoints. For calculating the genetic relationship matrix, only variants imputed with an INFO score  $>0.95$  in all batches were used. Variants with  $>3\%$  missing genotypes were excluded as well as variants with MAF  $< 1\%$ . The remaining variants were linkage-disequilibrium pruned with a 1-Mb window and  $r^2$  threshold of 0.1. This resulted in a set of 59,037 well-imputed not rare variants for GRM calculation. SAIGE options for null computation were: “LOCO=false, numMarkers=30, traceCVcutoff=0.0025, ratioCVcutoff=0.001”. Association tests were performed phenotypes with case counts  $>100$  and for variants with minimum allele count of 3 and imputation INFO  $>0.6$  were used.

We additionally performed sex-specific associations for a subset of gender-specific diseases (60 female diseases and in 50 disease clusters, 14 male diseases and in 13 disease clusters) in both FG and UKB using the same approach without inclusion of sex-related covariates (Supplementary Table 2)

We performed fixed-effect inverse-variance meta-analysis combining summary effect sizes and standard errors for overlapping variants with matched alleles across FG and UKB using METAL<sup>43</sup>.

## Definition and refinement of significant regions

To define significance, we used a combination of (1) multiple testing corrected threshold of  $P < 2 \times 10^{-9}$  (that is,  $0.05 / (\text{approximately } 26.8 \times 10^6)$ , the sum of the mean number of variants tested per disease cluster)), to account for the fact that some traits are highly correlated disease subtypes, (2) concordant direction of effect between UKB and FG associations, and (3)  $P < 0.05$  in both UKB and FG.

We defined independent trait associations through linkage-disequilibrium-based ( $r^2 = 0.1$ ) clumping  $\pm 500$  kb around the lead variants using PLINK<sup>44</sup>, excluding the HLA

region (chr6:25.5-34.0Mb) which is treated as one region due to complex and extensive linkage-disequilibrium patterns. We then merged overlapping independent regions ( $\pm 500$  kb) and further restricted each independent variant ( $r^2 = 0.1$ ) to the most significant sentinel variant for each unique gene. For overlapping genetic regions that are associated with multiple disease endpoints (pleiotropy), to be conservative in reporting the number of associations we merged the overlapping (independent) regions to form a single distinct region (indexed by the region ID column in Supplementary Table 3).

## Cross-reference with known associations

We cross-referenced the sentinel variants and their proxies ( $r^2 > 0.2$ ) for significant associations ( $P < 5 \times 10^{-8}$ ) of mapped EFO terms and their descendants in GWAS Catalog<sup>11</sup> and PhenoScanner<sup>12</sup>. To be more conservative with reporting of novel associations, we also considered whether the most-severe associated gene in our analyses were reported in GWAS Catalog and PhenoScanner. In addition, we also queried our sentinel variants in ClinVar<sup>13</sup> to define known associations with rarer genetic diseases and further manually curated novel associations (where the association is a novel variant association and a novel gene association) for previous genome-wide significant ( $P < 5 \times 10^{-8}$ ) associations.

To assess medical actionability of associated genes, we cross-referenced the associated genes with the latest ACMG v3. (75 unique genes linked to 82 conditions, linked to cancer ( $n = 28$ ), cardiovascular ( $n = 34$ ), metabolic ( $n = 3$ ), or miscellaneous conditions ( $n = 8$ )). This list was supplemented by 20 ‘ACMG watchlist genes’<sup>14</sup> for which evidence for inclusion to ACMG 3.0 list was considered too preliminary based on either technical, penetrance or clinical management concerns

## Biomarker associations of lead variants

For the lead sentinel variants, we performed association analyses using the two-step REGENIE approach described above with 117 biomarkers including anthropometric traits, physical measurements, clinical haematology measurements, blood and urine biomarkers available in UKB (detailed in Supplementary Table 8). Additional biochemistry subgroupings were based on UKB biochemistry subcategories:  
[https://www.ukbiobank.ac.uk/media/oiudpjqa/bcm023\\_ukb\\_biomarker\\_panel\\_website\\_v1-0-aug-2015-edit-2018.pdf](https://www.ukbiobank.ac.uk/media/oiudpjqa/bcm023_ukb_biomarker_panel_website_v1-0-aug-2015-edit-2018.pdf)

## Drug target mapping and enrichment

We mapped the annotated gene for each sentinel variant to drugs using the therapeutic target database (TTD)<sup>21</sup>. We retained only drugs which have been approved or are in clinical trial stages. For enrichment analysis of approved drugs with genetic associations, we used Fisher's exact test on the proportion of significant genes targeted by approved drug against a background of all approved drugs in TTD<sup>21</sup> ( $n = 595$ ) and 20,437 protein coding genes from Ensembl annotations<sup>45</sup>.

## Mendelian randomization analyses

### *F5* and *F10* effects on pulmonary embolism

The missense variants rs4525 and rs61753266 in *F5* and *F10* genes were taken as genetic instruments for Mendelian randomization analyses. To assess potential that each factor level is causally associated with pulmonary embolism we used two-sample Mendelian randomization using summary statistics, with effect of the variants on their respective factor levels obtained from previous large scale (protein quantitative trait loci) pQTL studies<sup>46,47</sup>. Let  $\beta_{XY}$  denote the estimated causal effect of a factor level on pulmonary embolism risk and  $\beta_X$ ,  $\beta_Y$  be the genetic association with a factor level (FV, FX or FXa) and pulmonary embolism risk respectively. Then, the Mendelian randomization ratio-estimate of  $\beta_{XY}$  is given by:

$$\frac{\beta_Y}{\beta_X} = \frac{\beta_{XY}}{\beta_X}$$

where the corresponding standard error  $\text{se}(\beta_{XY})$ , computed to leading order, is:

$$\text{se}(\beta_{XY}) = \sqrt{\frac{\text{se}(\beta_Y)}{\text{se}(\beta_X)}}$$

### Clustered Mendelian randomization

To assess evidence of several distinct causal mechanisms by which AF may influence pulse rate (PR) we used MR-Clust<sup>31</sup>. In brief, MR-Clust is a purpose-built clustering algorithm for use in univariate Mendelian randomization analyses. It extends the typical Mendelian randomization assumption that a risk factor can influence an outcome via a single causal mechanism<sup>48</sup> to a framework that allows one or more mechanisms to be detected. When a risk-factor affects an outcome via several mechanisms, the set of two-stage ratio-estimates can be divided into clusters, such that variants within each cluster have similar ratio-estimates. As shown in<sup>31</sup>, two or more variants are members of the same cluster if and only if they affect the outcome via the

same distinct causal pathway. Moreover, the estimated causal effect from a cluster is proportional to the total causal effect of the mechanism on the outcome. We included variants within clusters where the probability of inclusion >0.7. We used MR-Clust algorithm allowing for singletons/outlier variants to be identified as their own ‘clusters’ to reflect the large but biologically plausible effect sizes seen with rare and low-frequency variants.

## Bioinformatic analyses for *METTL11B*

We searched [Ala/Pro/Ser]-Pro-Lys motif containing proteins using the ‘peptide search’ function on UniProt<sup>49</sup>, filtering for reviewed Swiss-Prot proteins and proteins listed in Human Protein Atlas<sup>50</sup> (HPA) ( $n = 7,656$ ). We obtained genes with elevated expression in cardiomyocytes ( $n = 880$ ) from HPA based on the criteria: ‘cell\_type\_category\_rna: cardiomyocytes; cell type enriched, group enriched, cell type enhanced’ as defined by HPA at <https://www.proteinatlas.org/humanproteome/celltype/Muscle+cells#cardiomyocytes> (accessed 20th March 2021) with filtering for those with valid UniProt IDs (Swiss-Prot,  $n = 863$ ). Enrichment test was performed using Fisher’s exact test. Additionally, we performed enrichment analyses using any [Ala/Pro/Ser]-Pro-Lys motif positioned within the N-terminal half of the protein ( $n = 4,786$ ).

**Additional methods** Additional methods on further FinnGen QC; theoretical description and simulation of the effect of MAF enrichment on inverse-variance weighted (IVW) meta-analysis Z-scores; and functional characterization of PITX2c(Pro41Ser) are provided in the [Supplementary Information](#).

## Reporting summary

Further information on research design is available in the [Nature Research Reporting Summary](#) linked to this paper.

## Data availability

Full summary association results of this study are accessible at <https://doi.org/10.5281/zenodo.5571000>. Summary and individual-level whole-exome sequencing data from UKB participants have been deposited with UKB and will be freely available to approved researchers via The UK Biobank Research Analysis Platform (<https://www.ukbiobank.ac.uk/enable-your-research/research-analysis-platform>). FG summary association results are being released bi-annually via [https://www.finngen.fi/en/access\\_results](https://www.finngen.fi/en/access_results) and can be explored in a public results browser (<https://r5.finngen.fi>). All analyses in this manuscript which rely on variants

that were directly interrogated through chip-based genotyping with the FG array rely on FG data freeze 5 (from 11 May 2021). Analyses in this manuscript that are based on imputed variants rely on FG data freeze 6, which is anticipated to become public in November 2021. Individual-level genotypes and register data from FG participants can be accessed by approved researchers via the Fingenious portal (<https://site.fingenious.fi/en/>) hosted by the Finnish Biobank Cooperative FinBB (<https://finbb.fi/en/>). Data release to FinBB is timed to the bi-annual public release of FG summary results which occurs twelve months after FG consortium members can start working with the data. Further datasets underlying this study have been derived from: Therapeutic Target Database (<http://db.idrblab.net/ttd/>); Phecode-ICD10 data ([https://phewascatalog.org/phecodes\\_icd10](https://phewascatalog.org/phecodes_icd10)); GWAS Catalog (<https://www.ebi.ac.uk/gwas/>); PhenoScanner (<http://www.phenoscanner.medschl.cam.ac.uk/>); ClinVar (<https://www.ncbi.nlm.nih.gov/clinvar/>); gnomAD (<https://gnomad.broadinstitute.org/>); Human Protein Atlas (<https://www.proteinatlas.org/>); and Ensembl (<https://www.ensembl.org/index.html>).

## Code availability

Custom analysis scripts used are available at <https://github.com/cnfoley/Sun-et-al-2021-protein-coding-variants-in-human-disease>.

## References

1. Claussnitzer, M. et al. A brief history of human disease genetics. *Nature* **577**, 179–189 (2020).
2. Bycroft, C. et al. The UK Biobank resource with deep phenotyping and genomic data. *Nature* **562**, 203–209 (2018).
3. Van Hout, C. V. et al. Exome sequencing and characterization of 49,960 individuals in the UK Biobank. *Nature* **586**, 749–756 (2020).
4. Szustakowski, J. D. et al. Advancing human genetics research and drug discovery through exome sequencing of the UK Biobank. *Nat. Genet.* **53**, 942–948 (2021).
5. Wang, Q. et al. Rare variant contribution to human disease in 281,104 UK Biobank exomes. *Nature* **597**, 527–532 (2021).
6. Karczewski, K. J. et al. Systematic single-variant and gene-based association testing of 3,700 phenotypes in 281,850 UK Biobank exomes. Preprint at <https://doi.org/10.1101/2021.06.19.21259117> (2021).

7. Peltonen, L., Jalanko, A. & Varilo, T. Molecular genetics of the Finnish disease heritage. *Hum. Mol. Genet.* **8**, 1913–1923 (1999).
8. Lim, E. T. et al. Distribution and medical impact of loss-of-function variants in the Finnish founder population. *PLoS Genet.* **10**, e1004494 (2014).
9. Locke, A. E. et al. Exome sequencing of Finnish isolates enhances rare-variant association power. *Nature* **572**, 323–328 (2019).
10. Hassan, S. et al. High-resolution population-specific recombination rates and their effect on phasing and genotype imputation. *Eur. J. Hum. Genet.* **29**, 615–624 (2020).
11. Buniello, A. et al. The NHGRI-EBI GWAS Catalog of published genome-wide association studies, targeted arrays and summary statistics 2019. *Nucleic Acids Res.* **47**, D1005–D1012 (2019).
12. Staley, J. R. et al. PhenoScanner: a database of human genotype-phenotype associations. *Bioinformatics* **32**, 3207–3209 (2016).
13. Landrum, M. J. et al. ClinVar: improving access to variant interpretations and supporting evidence. *Nucleic Acids Res.* **46**, D1062–D1067 (2018).
14. Miller, D. T. et al. ACMG SF v3.0 list for reporting of secondary findings in clinical exome and genome sequencing: a policy statement of the American College of Medical Genetics and Genomics (ACMG). *Genet. Med.* **23**, 1381–1390 (2021).
15. Lapointe, J. Y. et al. NPT2a gene variation in calcium nephrolithiasis with renal phosphate leak. *Kidney Int.* **69**, 2261–2267 (2006).
16. Halbritter, J. et al. Fourteen monogenic genes account for 15% of nephrolithiasis/nephrocalcinosis. *J. Am. Soc. Nephrol.* **26**, 543–551 (2015).
17. Schlingmann, K. P. et al. Autosomal-recessive mutations in *SLC34A1* encoding sodium-phosphate cotransporter 2A cause idiopathic infantile hypercalcemia. *J. Am. Soc. Nephrol.* **27**, 604–614 (2016).
18. Hinds, D. A. et al. Germ line variants predispose to both JAK2 V617F clonal hematopoiesis and myeloproliferative neoplasms. *Blood* **128**, 1121–1128 (2016).
19. Sellick, G. S., Sullivan, K., Catovsky, D. & Houlston, R. S. CHEK2\*1100delC and risk of chronic lymphocytic leukemia. *Leuk. Lymphoma* **47**, 2659–2660 (2006).

20. Yan, K. et al. Normal platelet counts mask abnormal thrombopoiesis in patients with chronic myeloid leukemia. *Oncol. Lett.* **10**, 2390–2394 (2015).
21. Wang, Y. et al. Therapeutic target database 2020: enriched resource for facilitating research and early development of targeted therapeutics. *Nucleic Acids Res.* **48**, D1031–D1041 (2020).
22. Nelson, M. R. et al. The support of human genetic evidence for approved drug indications. *Nat. Genet.* **47**, 856–860 (2015).
23. King, E. A., Davis, J. W. & Degner, J. F. Are drug targets with genetic support twice as likely to be approved? Revised estimates of the impact of genetic support for drug mechanisms on the probability of drug approval. *PLoS Genet.* **15**, e1008489 (2019).
24. Nielsen, J. B. et al. Biobank-driven genomic discovery yields new insight into atrial fibrillation biology. *Nat. Genet.* **50**, 1234–1239 (2018).
25. Roselli, C. et al. Multi-ethnic genome-wide association study for atrial fibrillation. *Nat. Genet.* **50**, 1225–1233 (2018).
26. Thorolfsdottir, R. B. et al. A missense variant in PLEC increases risk of atrial fibrillation. *J. Am. Coll. Cardiol.* **70**, 2157–2168 (2017).
27. Dong, C. et al. An asparagine/glycine switch governs product specificity of human N-terminal methyltransferase NTMT2. *Commun. Biol.* **1**, 183 (2018).
28. Chambers, J. C. et al. Genetic variation in SCN10A influences cardiac conduction. *Nat. Genet.* **42**, 149–152 (2010).
29. Olson, T. M. et al. Sodium channel mutations and susceptibility to heart failure and atrial fibrillation. *JAMA* **293**, 447–454 (2005).
30. Zaklyazminskaya, E. & Dzemeshkevich, S. The role of mutations in the *SCN5A* gene in cardiomyopathies. *Biochim. Biophys. Acta* **1863**, 1799–1805 (2016).
31. Foley, C. N., Mason, A. M., Kirk, P. D. W. & Burgess, S. MR-Clust: clustering of genetic variants in Mendelian randomization with similar causal estimates. *Bioinformatics* **37**, 531–541 (2020).
32. Sidhu, S. & Marine, J. E. Evaluating and managing bradycardia. *Trends Cardiovasc. Med.* **30**, 265–272 (2020).

33. Syeda, F., Kirchhof, P. & Fabritz, L. PITX2-dependent gene regulation in atrial fibrillation and rhythm control. *J. Physiol.* **595**, 4019–4026 (2017).
34. Eichler, E. E. et al. Missing heritability and strategies for finding the underlying causes of complex disease. *Nat. Rev. Genet.* **11**, 446–450 (2010).
35. Howles, S. A. & Thakker, R. V. Genetics of kidney stone disease. *Nat. Rev. Urol.* **17**, 407–421 (2020).
36. Plenge, R. M., Scolnick, E. M. & Altshuler, D. Validating therapeutic targets through human genetics. *Nat. Rev. Drug Discov.* **12**, 581–594 (2013).
37. Denny, J. C. et al. Systematic comparison of genome-wide association study of electronic medical record data and genome-wide association study data. *Nat. Biotechnol.* **31**, 1102–1110 (2013).
38. Kosmicki, J. A. et al. A catalog of associations between rare coding variants and COVID-19 outcomes. Preprint at <https://doi.org/10.1101/2020.10.28.20221804> (2021).
39. Karczewski, K. J. et al. The mutational constraint spectrum quantified from variation in 141,456 humans. *Nature* **581**, 434–443 (2020).
40. McLaren, W. et al. The Ensembl variant effect predictor. *Genome Biol.* **17**, 122 (2016).
41. Mbatchou, J. et al. Computationally efficient whole-genome regression for quantitative and binary traits. *Nat. Genet.* **53**, 1097–1103 (2021).
42. Zhou, W. et al. Efficiently controlling for case-control imbalance and sample relatedness in large-scale genetic association studies. *Nat. Genet.* **50**, 1335–1341 (2018).
43. Willer, C. J., Li, Y. & Abecasis, G. R. METAL: fast and efficient meta-analysis of genomewide association scans. *Bioinformatics* **26**, 2190–2191 (2010).
44. Chang, C. C. et al. Second-generation PLINK: rising to the challenge of larger and richer datasets. *Gigascience* **4**, 7 (2015).
45. Yates, A. D. et al. Ensembl 2020. *Nucleic Acids Res.* **48**, D682–D688 (2020).
46. Sun, B. B. et al. Genomic atlas of the human plasma proteome. *Nature* **558**, 73–79 (2018).

47. Suhre, K. et al. Connecting genetic risk to disease end points through the human blood plasma proteome. *Nat. Commun.* **8**, 14357–14357 (2017).
48. Burgess, S., Foley, C. N. & Zuber, V. Inferring causal relationships between risk factors and outcomes from genome-wide association study data. *Annu. Rev. Genomics Hum. Genet.* **19**, 303–327 (2018).
49. UniProt, C. UniProt: the universal protein knowledgebase in 2021. *Nucleic Acids Res.* **49**, D480–D489 (2021).
50. Uhlen, M. et al. Tissue-based map of the human proteome. *Science* **347**, 1260419 (2015).

## Acknowledgements

We thank all the participants, contributors and researchers of UK Biobank and FinnGen (and its participating biobanks) for making data available for this study. We thank the UK Biobank Exome Sequencing Consortium (AbbVie, Alnylam Pharmaceuticals, AstraZeneca, Biogen, Bristol-Myers Squibb, Pfizer, Regeneron and Takeda) for generation of the whole-exome sequencing data and Regeneron Genetics Centre for initial quality control of the exome sequencing data. The FinnGen project is funded by two grants from Business Finland (HUS 4685/31/2016 and UH 4386/31/2016) and the following industry partners: AbbVie, AstraZeneca UK, Biogen MA, Celgene, Celgene International II, Genentech, Merck Sharp & Dohme, Pfizer, GlaxoSmithKline Intellectual Property Development, Sanofi US Services, Maze Therapeutics, Janssen Biotech and Novartis. We thank S. Lemmelä for her contribution to FinnGen data curation; and Y.-Q. Yang, T. Footz, M. Walter, A. Aránega, F. Hernández-Torres, E. Morel and G. Millat for their contributions to the functional characterization of PITX2c. PITX2 functional work was supported in part by grants from the National Natural Science Fund of China (81070153), the Personnel Development Foundation of Shanghai, China (2010019) and the Key Program of Basic Research of Shanghai, China (10JC1414002), and by the Canadian Institutes of Health Research (grants MOP-111072 and MOP-130373 to M.C.). Asma Mechakra was supported by a bursary of the French Ministry of Research and Technology (MRT).

## Author information

### Affiliations

1. Translational Biology, Research and Development, Biogen Inc., Cambridge, MA, USA

Benjamin B. Sun, Chia-Yen Chen, Eric Marshall, Jemma B. Wilk, Benjamin B. Sun, Chia-Yen Ghen, Eric Marshall, Jemma B. Wilk, Heiko Runz & Heiko Runz

2. BHF Cardiovascular Epidemiology Unit, Department of Public Health and Primary Care, University of Cambridge, Cambridge, UK

Benjamin B. Sun & Benjamin B. Sun

3. Psychiatric and Neurodevelopmental Genetics Unit, Massachusetts General Hospital, Boston, MA, USA

Mitja I. Kurki, Mitja I. Kurki, Aarno Palotie, Mark J. Daly, Aarno Palotie & Mark J. Daly

4. The Stanley Center for Psychiatric Research, The Broad Institute of MIT and Harvard, Cambridge, MA, USA

Mitja I. Kurki, Mitja I. Kurki, Aarno Palotie, Mark J. Daly, Aarno Palotie & Mark J. Daly

5. Institute for Molecular Medicine Finland (FIMM), University of Helsinki, Helsinki, Finland

Mitja I. Kurki, Mitja I. Kurki, Aarno Palotie, Mark J. Daly, Aarno Palotie & Mark J. Daly

6. Analytic and Translational Genetics Unit, Department of Medicine, Massachusetts General Hospital, Boston, MA, USA

Mitja I. Kurki, Mitja I. Kurki, Aarno Palotie, Mark J. Daly, Aarno Palotie & Mark J. Daly

7. MRC Biostatistics Unit, School of Clinical Medicine, University of Cambridge, Cambridge, UK

Christopher N. Foley

8. Optima Partners, Edinburgh, UK

Christopher N. Foley

9. Université de Lyon 1, Université Lyon 1, INSERM, CNRS, INMG, Lyon, France

Asma Mechakra, Philippe Chevalier & Georges Christé

10. CERVO Brain Research Center and Department of Medicine, Faculty of Medicine, Université Laval, Quebec City, Quebec, Canada

Mohamed Chahine

## Consortia

### Biogen Biobank Team

- Benjamin B. Sun
- , Chia-Yen Ghen
- , Eric Marshall
- , Jemma B. Wilk
- & Heiko Runz

### FinnGen

- Mitja I. Kurki
- , Aarno Palotie
- & Mark J. Daly

## Contributions

Conceptualization and experimental design: B.B.S. and H.R. Methodology: B.B.S., H.R., C.N.F., C.-Y.C. and M.J.D. Analysis: B.B.S., M.I.K., C.N.F., A.M., C.-Y.C., E.M., J.B.W. and Biogen Biobank Team. Experimental work: A.M., G.C., M.C. and P.C. FinnGen protocols and analysis: M.I.K., A.P., M.J.D. and FinnGen. Writing: B.B.S. and H.R. All authors critically reviewed the manuscript.

## Corresponding authors

Correspondence to [Benjamin B. Sun](#) or [Heiko Runz](#).

## Ethics declarations

## Competing interests

B.B.S., H.R., C.-Y.C., E.M., J.W. and members of the Biogen Biobank Team are employees of Biogen. M.J.D. is a founder of Maze Therapeutics. The other authors declare no competing interests.

# Peer review

## Peer review information

*Nature* thanks Loic Yengo and the other, anonymous, reviewers for their contribution to the peer review of this work. Peer review reports are available.

## Additional information

**Publisher's note** Springer Nature remains neutral with regard to jurisdictional claims in published maps and institutional affiliations.

## Extended data figures and tables

### [Extended Data Fig. 1](#)

UKB and FG study overview.

### [Extended Data Fig. 2 Case count comparison between UKB and FG across disease groups.](#)

Diseases within each group are listed in Supplementary Table 2. Only cases >100 in UKB/FG are included. *R*: Spearman's correlation for FG R5 (red) and R6 (blue).

### [Extended Data Fig. 3 Distribution of variant annotation categories.](#)

**Left**: all variants tested. **Right**: variants with at least 1 significant association ( $p < 5 \times 10^{-8}$ ). pLOF: predicted loss of function. LC: low confidence loss of function.

### [Extended Data Fig. 4 Inflation factors and FG-UKB effect size comparisons.](#)

(a) Distribution of inflation factors of CWAS meta-analysis. (b) Effect size comparison between UKB and FG. Inset: zoomed in on small effect sizes. *R*: Spearman's rank correlation (two-sided test),  $p = 4.4 \times 10^{-351}$ .

### [Extended Data Fig. 5 Surface plot of effects of cohort specific allele enrichment on inverse variant weighted meta-analysis z-scores \(IVW uplift\) across MAFs \(up to MAF 1%\).](#)

Uplift is defined as the ratio of meta-analysed IVW Z-score to the Z-score of an individual study. **(a)** Theoretically predicted IVW uplift. **(b)** Observed IVW uplift. **(c)** Median absolute relative error (MARE, %) between simulated and theoretical IVW uplift values. For each combination of MAF and allelic enrichment, we simulated 1000 datasets for two binary variables reflecting disease status for two studies. Study sample size and disease prevalence were fixed (matching values estimates from UKB and FG), genomic effects were randomly sampled from the set of positive effect sizes in UKB and FG (Supplementary Table 3), MAF was varied from 0.01% to 1% and allele enrichment (in the smaller study) ranged from 1 to 50. **(d)** Comparison of Z-scores for randomly subsetted UKB data meta-analysed with FinnGen (UKBxFG) against subsetted UKB meta-analysed with sample size matched UKB cohort (UKBxUKB') across allele fold enrichments for sentinel associations (Supplementary Table 3) with MAF<0.1. Y-axis ( $\log_{10}$ (FG/UKB meta Z ratio)):

$\log_{10}(Z_{\text{UKBxFG}}/Z_{\text{UKBxUKB}'})$ . X-axis (MAF enrichment ratio): allelic fold enrichment (FE) where pink side denotes greater enrichment in UKB, blue side denotes greater enrichment in FG. Each box plot presents the median, first and third quartiles, with upper and lower whiskers representing 1.5x inter-quartile range above and below the third and first quartiles respectively. N for each boxplot from left to right: 88, 99, 212, 453, 213, 71, 126, 158.

### Extended Data Fig. 6 Histogram of genes with associations, disease and biomarker associations per region.

**(a)** Number of genes with coding associations per region. Each disease cluster counted separately. MHC region excluded. **(b)** Number of associated trait clusters ( $p < 5 \times 10^{-8}$ ) per region. Inset shows zoomed in x-scale between 0-12 trait cluster associations per region. **(c)** Number of associated biomarker groups per locus ( $p < 1 \times 10^{-6}$ ). *MHC*: Major Histocompatibility Complex.

### Extended Data Fig. 7

**(a) Simplified diagram of the coagulation cascade.** Factors (in roman numerals, “a” represents activated) with genetic association with PE highlighted in orange. Blue line (round end) indicates inhibitory effect of APC on VIIIa and Va. **(b)** Schematic of potential pathway from missense variants in *F5* and *F10* to PE risk. Factor V Leiden variant had null associations with F5 levels ( $\beta_{\text{F5 levels}} = 0.21, p = 0.091$ ). Dashed blue lines suggest effect of the variants on PE risk which we assume under MR framework acts through factor levels (solid blue lines). Grey box and arrows represent known pathway for Factor V Leiden mutation. *GOF*: Gain of function, *APC*: Activated protein C, *MR*: Mendelian randomisation, *PE*: Pulmonary embolism.

## [Extended Data Fig. 8 In vitro functional effects of the PITX2c Pro41Ser variant \(rs143452464\).](#)

(a) Schematic of the location of the Pro41Ser variant in PITX2c as compared with the PITX2a splicing isoform. Numbers below each row indicate AA number from N-terminal (left) to C-terminal (right). AD1: common sequence, HD: homeodomain, ID1: transcriptional inhibitory domain 1, AD2: second common sequence, ID2: transcriptional inhibitory domain 2. Pro41Ser lies within the terminal domain (grey), near the 5-amino acid LAMAS (single amino acid code) sequence (33 to 37 red), which is important for transcriptional activity of the N-terminal of PITX2c. (b) Reporter gene assays: TM-1 cells (Transformed human trabecular meshwork cells) were co-transfected with a firefly luciferase reporter plasmid containing a PITX2c binding element, a  $\beta$ -galactosidase control vector and expression vector for PTIX2c (wild-type, Pro41Ser (P41S) or empty control vector (EV)). The activity of firefly luciferase upon activation by PITX2c ( $n = 3$  transfections per condition) was normalized to  $\beta$ -galactosidase. Experiments with a truncated reporter construct ("−163/+165Δ"), containing a deletion of 8bp within the predicted PITX2 binding site, are shown as additional control. Data are presented as mean values  $\pm$  SEM, unadjusted *p*-value derived from two-sided t-test (EVΔ vs EV: 0.122; WTΔ vs WT: 0.074; P41SΔ vs P41S: 0.018; WT vs EV: 0.015; P41S vs WT: 0.0056; WTΔ vs EVΔ: 0.002; P41SΔ vs WTΔ: 0.0005).

## Supplementary information

### Supplementary Information

This file contains Supplementary Methods, results and discussions, Supplementary Figs. 1–6, full legends for Supplementary Tables 1–14, Biobank contributions to FinnGen, FinnGen ethics statement details, a list of FinnGen consortium contributors, PITX2 Function Study Group contributors, a list of Biogen Biobank Team contributors and Supplementary References.

### Reporting Summary

### Supplementary File 1

Interactive Manhattan plot summary of novel sentinel associations. Size of the point is proportional to effect size.  $-\log_{10}(p)$  capped at  $-\log_{10}(10^{-50})$ . Colours indicate disease groups (click [select/deselect trace]/double click [isolate one trace] on the legend to toggle selection). “+” indicate novel variant and gene, “×” indicate novel variant ( $r^2 < 0.2$ ) not reported in GWAS Catalog/PhenoScanner for the disease. Dotted

horizontal lines indicate  $-\log_{10}(2 \times 10^{-9})$  [brown] and  $-\log_{10}(5 \times 10^{-8})$  [grey]. Hover over the points for detailed information and double click/click on colors/shape in the legends to filter on select groups. Tooltip is available at top right for additional interactive options including: zooming and panning, selection, toggling multiple highlighting of nearby regions on hover and saving as static images.

## Supplementary Tables

Supplementary Tables 1–14 – see Supplementary Information document for full table descriptions.

## Peer Review File

### Supplementary File 2

This zipped file contains Supplementary Files 2a–c which show interactive surface plot of effects of cohort specific allele enrichment on inverse variant weighted meta-analysis z-scores (IVW uplift) across MAFs (up to MAF 1%). Uplift is defined as the ratio of meta-analysed IVW Z-score to the Z-score of an individual study. (a) theoretically predicted IVW uplift. (b) observed IVW uplift. (c) Median absolute relative error (MARE, %) between simulated and theoretical IVW uplift values. For each combination of MAF and allelic enrichment, we simulated 1,000 datasets for two binary variables reflecting disease status. Study sample size and disease prevalence were fixed (matching values estimates from UKB and FG), genomic effects were randomly sampled from the set of positive effect sizes in UKB and FG (Supplementary Table 3), MAF was varied from 0.01% to 1% and allele enrichment (in the smaller study) ranged from 1 to 50. Tooltip is available at top right for additional interactive options including zooming, panning and saving as static images.

## Rights and permissions

**Open Access** This article is licensed under a Creative Commons Attribution 4.0 International License, which permits use, sharing, adaptation, distribution and reproduction in any medium or format, as long as you give appropriate credit to the original author(s) and the source, provide a link to the Creative Commons license, and indicate if changes were made. The images or other third party material in this article are included in the article's Creative Commons license, unless indicated otherwise in a credit line to the material. If material is not included in the article's Creative Commons license and your intended use is not permitted by statutory regulation or exceeds the permitted use, you will need to obtain permission directly from the copyright holder. To view a copy of this license, visit <http://creativecommons.org/licenses/by/4.0/>.

## [Reprints and Permissions](#)

## About this article

### Cite this article

Sun, B.B., Kurki, M.I., Foley, C.N. *et al.* Genetic associations of protein-coding variants in human disease. *Nature* **603**, 95–102 (2022).  
<https://doi.org/10.1038/s41586-022-04394-w>

- Received: 25 May 2021
- Accepted: 20 December 2021
- Published: 23 February 2022
- Issue Date: 03 March 2022
- DOI: <https://doi.org/10.1038/s41586-022-04394-w>

### Share this article

Anyone you share the following link with will be able to read this content:

[Get shareable link](#)

Sorry, a shareable link is not currently available for this article.

[Copy to clipboard](#)

Provided by the Springer Nature SharedIt content-sharing initiative

---

This article was downloaded by **calibre** from <https://www.nature.com/articles/s41586-022-04394-w>

- Article
- [Published: 16 February 2022](#)

# Determinants of emissions pathways in the coupled climate–social system

- [Frances C. Moore](#) [ORCID: orcid.org/0000-0003-3866-9642<sup>1</sup>](#),
- [Katherine Lacasse](#) [ORCID: orcid.org/0000-0002-3413-9815<sup>2</sup>](#),
- [Katharine J. Mach<sup>3,4</sup>](#),
- [Yoon Ah Shin](#) [ORCID: orcid.org/0000-0002-2173-6207<sup>5</sup>](#),
- [Louis J. Gross<sup>6,7</sup>](#) &
- [Brian Beckage](#) [ORCID: orcid.org/0000-0002-5908-6924<sup>8,9,10</sup>](#)

[Nature](#) volume 603, pages 103–111 (2022)

- 15k Accesses
- 512 Altmetric
- [Metrics details](#)

## Subjects

- [Climate change](#)
- [Environmental social sciences](#)
- [Socioeconomic scenarios](#)

## Abstract

The ambition and effectiveness of climate policies will be essential in determining greenhouse gas emissions and, as a consequence, the scale of climate change impacts<sup>1,2</sup>. However, the socio-politico-technical processes that will determine climate policy and emissions trajectories are treated as exogenous in almost all climate change modelling<sup>3,4</sup>. Here we identify relevant feedback processes documented across a range of disciplines and connect them in a stylized model of the climate–social system. An analysis of model behaviour reveals the potential for nonlinearities and tipping points that are particularly associated with connections across the individual, community,

national and global scales represented. These connections can be decisive for determining policy and emissions outcomes. After partly constraining the model parameter space using observations, we simulate 100,000 possible future policy and emissions trajectories. These fall into 5 clusters with warming in 2100 ranging between 1.8 °C and 3.6 °C above the 1880–1910 average. Public perceptions of climate change, the future cost and effectiveness of mitigation technologies, and the responsiveness of political institutions emerge as important in explaining variation in emissions pathways and therefore the constraints on warming over the twenty-first century.

[Download PDF](#)

## Main

The global trajectory of anthropogenic greenhouse gas emissions is the most important determinant of projected global temperature increases in this century and beyond, swamping the magnitude of internal climate variability or model differences<sup>1</sup>. However, this key driver of Earth's future climate is treated as exogenous in almost all climate science<sup>3</sup>. Moreover, although emissions pathways arise from complex interactions among social, political, economic and technical systems, these elements are often analysed separately within disciplinary silos, neglecting interactions and feedback that can give rise to or stymie rapid change<sup>5</sup>. Understanding the potential for nonlinear dynamics in the socio-technical systems producing both greenhouse gases and climate policy is essential for identifying high-impact intervention points and better informing policy<sup>4,6,7</sup>. However, the coupling and interaction among social, political, economic, technical and climate systems—and their implications for emissions and temperature trajectories over the twenty-first century—have not been widely examined (although refs. <sup>2,8,9</sup> provide some exceptions).

Evidence regarding the likely emissions path over the twenty-first century is mixed. On the one hand, although emissions growth may have decelerated in recent years, with some evidence of declining emissions in a few advanced economies, global emissions continue to grow<sup>10</sup>. National commitments under the Paris Agreement remain inadequate to meet either the 1.5-°C or 2-°C temperature target<sup>11</sup> and it is unclear whether government policies are yet sufficient to deliver on these emissions pledges<sup>12</sup>. Carbon dioxide emissions from energy infrastructure currently in place or under development will exceed the 1.5-°C carbon budget, and standard energy-system models struggle to simulate pathways that meet either temperature target without the widespread deployment of negative emissions technologies that are highly speculative<sup>13,14,15</sup>. The pace of decarbonization that is required to meet the Paris

temperature targets vastly exceeds anything in the historical record at the global scale<sup>16</sup>.

On the other hand, specific cases of very rapid change in energy systems do exist, with accelerating deployment as market or policy conditions shift and technology costs fall. Path dependencies, increasing returns to scale and learning-by-doing cost reductions can produce sudden, tipping-point-like transitions that cannot be extrapolated from past system behaviour<sup>17,18</sup>. Recent examples include the rapid fall in coal generation in the UK electricity mix and the dominance of electric vehicles sales in Norway<sup>19,20</sup>. Standard energy models, which mostly rely on linear extrapolations of past behaviour, repeatedly underpredict the rate of renewable energy growth<sup>21</sup>. Historically, technological innovation and government policies often motivated by energy security concerns<sup>22</sup> have also, in notable cases, spurred rapid shifts in energy systems, one of the fastest examples of which being the transition to kerosene lighting in the nineteenth century<sup>23</sup>.

Social norms that shape individual behaviour and preferences can exhibit similar tipping-point style dynamics<sup>24</sup>. These changes, via collective action operating through political institutions, could in turn affect the regulatory and market conditions in which energy technologies compete. The presence of both positive and negative feedback processes within the political system has also been documented, as policy changes can both create new interest groups and activate incumbents against further change<sup>25,26,27</sup>.

These coupled feedback processes could give rise to complex behaviour and a wide range of plausible emissions pathways but, although the space of possibility is wide, that does not mean it is unknowable. Our goal is to model the drivers of potential emissions scenarios over the twenty-first century and, in doing so, shed light on how both climate policy and emissions arise from more fundamental socio-politico-technical forces and the key parameters governing these dynamics.

The main contributions are threefold. First, we present a stylized model of the coupled climate–social system, focusing on coupling across individual to global scales and on feedback processes documented across a wide range of relevant disciplinary literatures. This model is distinct from previous work that represents feedback processes within energy systems<sup>28</sup> or between the climate, the economy and emissions pathways<sup>29</sup> in that climate policy is still specified exogenously in these applications. By contrast, in this model, climate policy and greenhouse gas emissions arise endogenously from the coupled interaction of the climate, social, political and energy systems.

Second, we used this model to systematically examine potential dynamics of the system, highlighting feedback, connections and thresholds across different

components. Finally, after partially constraining the set of parameter values using historical data, we examined the space of possible emissions and policy trajectories over the twenty-first century arising from the model. These fall into five clusters associated with particular parameter combinations, enabling these future trajectories to be classified on the basis of their underlying social, political and technical characteristics. Overall, we find that the socio-politico-technical feedback processes can be decisive determinants of climate policy and emissions futures. Our parameterized model implies a high likelihood of accelerating emissions reductions over the twenty-first century, moving the world decisively away from a no-policy, business-as-usual baseline.

## Feedback and model structure

The positive and negative feedback processes operating within the coupled climate–social system are critical to understanding system behaviour and dynamics. The feedback processes that are represented in the model were identified in a two-step process. First, potentially relevant system feedback processes were described during a four-day interdisciplinary workshop. Second, targeted searches were conducted across relevant literatures in psychology, economics, sociology, law, political science and engineering to evaluate the evidentiary literature for or against candidate feedback processes, resulting in eight key feedback processes being included in the final model. This section briefly describes each feedback process, and Table 1 and Fig. 1 describe how these feedback processes are coupled together in the model and the model structure.

**Table 1 Description of the climate–social model components and key parameters**  
**Fig. 1: The climate–social model components and feedback processes.**

 figure 1

Components are shown in black and the model feedback processes in green. Feedback processes are identified as positive (+) (that is, reinforcing) or negative (−) (that is, dampening). The black arrow shows a connection between components (policy-adoption effect) that is not directly part of a particular feedback process. Descriptions of the components and key parameters governing both feedback strength and component behaviour are given in Table 1.

## Social-conformity feedback

The social networks in which individuals are embedded at home, work, school or leisure have a strong influence on opinions and behaviour<sup>30,31</sup>. Social norms (that is, representations of the dominant or acceptable practices or opinions within a social group) are costly for individuals to violate and, over the long term, can shape individual identities, habits and world-views<sup>32,33</sup>. Studies in the USA have shown that perceived social consensus, that is, the degree to which individuals believe a particular opinion or action is dominant within their social group, can partially explain belief in climate change and support for climate policies<sup>34</sup>. A large body of literature has also shown that social norms are one important determinant of the probability that an individual engages in pro-environmental behaviour, such as conserving energy or adopting solar panels<sup>35,36,37</sup>. A tendency towards social conformity can lead to tipping-point-type dynamics in which a system transitions suddenly from a previously stable state given a sufficient critical mass of proponents of the alternate norm<sup>24,38</sup>. The model includes the social conformity effect in two ways: formation of public opinion regarding climate policy and individual decisions on adopting pro-climate behaviour (Fig. 1).

## Climate change perception feedback

The anthropogenic influence on the Earth's climate system is increasingly apparent<sup>39,40,41</sup>. Assessments of the contribution of anthropogenic warming to the probability of particular extreme events are increasingly routine<sup>42</sup>. It has been hypothesized that this emerging signal of climate change in people's everyday experience of weather might lead to widespread acknowledgement of the existence of global warming and possibly, by extension, support for mitigation policy<sup>43</sup>. A large number of studies have connected stated belief in global warming with local temperature anomalies: people appear to be able to identify local warming<sup>44,45</sup> and are more likely to report believing in climate change if the weather is (or is perceived to be) unusually warm<sup>46,47,48,49</sup>. In effect, people appear to be using their personal experience of weather as evidence informing their belief in climate change<sup>49</sup>.

However, this so-called ‘local warming effect’ is complicated<sup>50</sup>. Several papers have found evidence that interpretations of weather events are filtered through pre-existing partisan identities or ideologies<sup>45,51,52</sup>. This suggests the presence of motivated reasoning (that is, the rejection of new information that contradicts pre-existing beliefs) in the processing of climate-change-related information<sup>53,54</sup>. Moreover, the perception of weather anomalies might well be complicated by a ‘shifting-baselines’ effect in which people’s perception of normal conditions is quickly updated on the basis of recent experience of weather<sup>55</sup>.

## Political interest feedback

The large-scale emissions reductions that are required to stabilize the climate system cannot be accomplished by individuals acting alone, meaning the question of how individual support or opposition to climate policy translates into collective action through the political system is critical. This process is not straightforward—it is subject to political–economic constraints operating through complex political and government institutions and cannot be modelled as a simple linear function of public opinion<sup>56,57,58</sup>. The political economy literature has documented a positive feedback effect in which initial policy change establishes powerful interests able to lobby against policy reversal and for further change, the establishment of the wind energy industry in Texas being one example<sup>26,27</sup>. Although most examples in the literature are ones of reinforcing feedback processes, Stokes<sup>27</sup> also documents instances of balancing feedback processes—where small policy changes activate powerful incumbents to lobby against further changes that threaten their interests.

## Credibility-enhancing display feedback

Although the ability of individuals to alter the trajectory of greenhouse gas emissions is limited, individual adoption of pro-environmental behaviours can have spillover effects to the larger social network. Changing behaviour to better align one’s consumption or practices with how one believes society ought to function can strengthen this moral identity and send a normative signal to other community members about desirable collective outcomes<sup>59,60</sup>. Engaging in costly personal actions aligned with collective goals can act as ‘credibility enhancing displays’, increasing the persuasiveness of the actor. Kraft-Todd et al.<sup>61</sup> use this framework to explain why community ambassadors promoting solar panel installation were more effective if they had installed solar themselves. For climate change more generally, Attari, Krantz and Weber<sup>62,63</sup> found that the personal carbon footprints of researchers advocating climate policy affects their credibility and the impact of their message.

## Expressive force of law feedback

To the extent legal or judicial institutions are perceived as legitimate, changes in laws coming out of them can provide information about desirable or common attitudes within the population, feeding back to reinforce the attitudes or behaviour of the society that produced them. Tankard and Paluck<sup>64</sup> identify signals from governing institutions as one of three sources of information about community norms. Legal scholars have developed the theory of the ‘expressive function’ of law—the idea that law and regulation work on society not only by punishing undesirable behaviour but also by signalling what kind of behaviour is praiseworthy and what is reprehensible<sup>65,66,67</sup>. This signal is particularly important if individuals have imperfect information about the distribution of attitudes or behaviour within a reference population<sup>67,68</sup>. Several papers have found evidence for feedback from changes in laws and regulations to the perception of social norms, attitudes or behaviour, including the legalization of gay marriage<sup>69,70</sup>, smoking bans<sup>71</sup> and the COVID-19 lockdowns<sup>72</sup>.

## **Endogenous cost-reduction feedback**

New energy technologies are often expensive, but also tend to exhibit price declines with installed capacity. This ‘learning-by-doing’ effect has been widely documented in the energy systems literature and is incorporated into some energy system models<sup>73</sup>. Falling costs are attributed to the combination of economies of scale, lower input costs and efficiencies in the production process and design<sup>74</sup>. This is a reinforcing feedback process, where small initial deployments, possibly driven by subsidies or regulatory requirements, lower costs and enable further deployment. Rubin et al.<sup>75</sup> reviewed estimated learning rates (that is, the fractional reduction in cost for a doubling of installed capacity) for 11 generation technologies and found ranges between –11% and 47% with many estimates falling in the 2% to 20% range.

## **Temperature–emissions feedback**

The effects of climate change are expected to be widely felt across geographical regions and economic sectors. These impacts themselves might well affect the capacity of the economy to produce emissions. Most notably, some work has suggested large effects of warming on economic growth<sup>76,77</sup>, which could substantially reduce the level of economic production over time with a corresponding reduction in greenhouse gas emissions. However, other effects through the impact of warming on energy demand<sup>78</sup> or on the carbon intensity of energy production<sup>79,80</sup> might either partially offset or exacerbate this effect. Woodard et al.<sup>8</sup> provide a central estimate of these combined effects of a 3.1% decline in emissions per degree of warming, with upper and lower bounds ranging from –10.2% to 0.1%.

The model developed here is designed to investigate the complex, emergent behaviour of the coupled climate–social system, including the feedback processes described above. Figure 1 shows the six major model components that operate across four interconnected scales: individual (cognition component), social (opinion and adoption components), national (policy component) and global (emissions and climate components). Descriptions of processes and key parameters in each component are given in Table 1, and equations and parameters are fully documented in the [Methods](#) and the ‘Model documentation’ section of the [Supplementary Information](#).

## Tipping points, interactions and thresholds

The coupled feedback processes across model components described above can produce complex, highly nonlinear behaviour that depends sensitively on interactions across social, political and technical systems. We begin by demonstrating this behaviour through three systematic explorations of the model parameter space, designed to highlight interactions across scales and model components. These values were chosen deliberately to highlight tipping-point and threshold behaviour in the model and are not necessarily the most likely or representative values. Constraints on the distribution of parameter values are discussed in the next section. Each panel in Fig. 2 shows model output, systematically varying 2–3 parameters while keeping all of the other model parameters fixed at the values given in Extended Data Table 1.

**Fig. 2: Tipping points and thresholds in model behaviour.**

 figure 2

- a**, Illustration of a tipping point associated with individual adoption of behavioural change by climate policy supporters through the credibility-enhancing display feedback. **b**, The interactions between endogenous cost reductions in the energy sector

and the opinion (fraction of climate policy supporters) and policy (status quo bias) components. **c**, The effect of the climate perception feedback and specific cognitive biases on public opinion. Model parameters that are not mentioned in each figure panel are kept constant for all of the model runs at the values shown in Extended Data Table 1.

## Individual behavioural change

Figure 2a demonstrates the potential for tipping points associated with individuals' adoption of behavioural change. The primary effect of behaviour change on emissions is small, reflecting the limited control that individuals have over how societies produce and use energy. The COVID-19 lockdowns, a global and unprecedented change in mobility and consumption patterns, temporarily reduced global CO<sub>2</sub> emissions by somewhere between 9% and 17% (refs. 81,82), providing a possible upper bound on the effect of behavioural change on reducing carbon footprints. As emissions under our RCP7 baseline almost double by 2100, this is clearly insufficient to provide the deep decarbonization needed to stabilize global temperatures, even under universal adoption.

However, Fig. 2a demonstrates that, under some conditions, the willingness of climate policy supporters to undertake costly personal pro-climate behavioural change can be decisive in triggering positive feedback processes that tip the system into a sustainable state. This interaction operates through the credibility-enhancing display feedback from adoption to opinion; if this feedback is small or absent, then no amount of individual action can drive major emissions reduction. However, if this feedback is strong, then behavioural change by climate policy supporters persuades more people to support climate policy, an effect that triggers a cascade of positive feedback processes in the opinion (social-conformity feedback) and mitigation (learning by doing) components that drive emissions to zero by 2100.

## Learning by doing

Figure 2b illustrates interaction effects between technological change in the energy system, public opinion dynamics and the responsiveness of political institutions. On average, larger endogenous cost reductions lead to larger emissions reduction. However, as this technological feedback must be initiated by climate policy, there is a threshold effect—a large nonlinear change in model behaviour at a particular parameter value—associated with the fraction of the population supporting climate policy. Below a threshold level of support, there is no policy driving the initial deployment required to kickstart the cost-reduction feedback. Moreover, even beyond this threshold, higher levels of support lead to faster deployment and a larger effect of

endogenous cost reductions (indicated by the steepening of the contour lines at the top of the figure). The two panels in Fig. 2b highlight how the characteristics of political institutions affect this relationship: those that are less responsive to public opinion (that is, high status quo bias) (Fig. 2b bottom) have a higher threshold for policy support and ramp up climate policy more slowly, leading to higher cumulative emissions over the twenty-first century, even in the presence of a strong cost-reduction feedback in the energy sector.

### Perception of climate change

Figure 2c illustrates how information from the climate system might influence public opinion dynamics if observation of the weather affects support for climate policy (that is, the climate perception feedback). The existence of this feedback can have a decisive influence on opinion dynamics, as illustrated by the threshold behaviour at zero. Model behaviour is substantively different even for very small effects of perceived weather on climate policy opinion compared with model behaviour with no perception effect. However, this is moderated substantially in the presence of cognitive biases that can fully offset the cognition feedback. In model runs using a fixed baseline for the perception of temperature anomalies (Fig. 2c left), the population unanimously favours climate policy, regardless of biased assimilation, because the perceived weather changes are so large.

The presence of shifting baselines (Fig. 2c right) complicates this effect. In particular, when biased assimilation is large, a stronger perception feedback leads to more climate policy opposers in 2050 compared with if that feedback were weaker or absent. This is because, if baselines shift and people compare current weather only to the past 8 years, they will periodically perceive unusually cold anomalies due to natural weather variability, even though temperatures are warm relative to a fixed, preindustrial baseline<sup>55</sup>. In the presence of biased assimilation, these perceived cold anomalies reinforce the belief of climate policy opposers in their position, leading to persistence of this opinion group.

### Constraining the parameter space

The illustrations in the previous section highlight how coupled socio-politico-technical feedback processes across components and scales in the climate–social system can produce nonlinear behaviour leading to a wide range of twenty-first century emission trajectories. This complexity characterizes the space of possible climate outcomes when climate policy is modelled as an endogenous product of more fundamental social and political forces. However, identifying outcomes that are more or less likely within this range requires placing some bounds on the model parameters.

The model is a highly aggregated and abstracted representation of the coupled climate–social system, meaning that parameterization is not straightforward. We performed two exercises based on hindcasting performance to partially and probabilistically constrain the parameter space. The first exercise used the population-weighted time series of public opinion on climate change in nine OECD countries (the USA, Canada, France, Germany, Italy, Spain, the UK, Australia and Japan) between 2013 and 2020 from Pew Research Center<sup>83</sup> and the emissions-weighted average carbon price for the same countries over the same period<sup>84</sup> to jointly constrain nine parameters in the cognition, opinion and policy components.

The second exercise used recent estimates of the effect of Swedish carbon prices on emissions to constrain two parameters in the emissions component<sup>85</sup>. Although only a tiny fraction of global emissions, the Swedish case is important because Sweden has had the world’s highest carbon price for several decades<sup>84</sup>, enabling estimates of the effect of high and sustained carbon prices on emissions. As the model includes a single abatement cost function, this exercise implicitly assumes that the Swedish abatement costs are more widely generalizable, a potential weakness of this calibration point.

For each hindcasting exercise, relevant model components are run in a Monte Carlo mode, sampling independently from the set of possible parameter values. Model output for each run is then compared to the observed time-series and parameter combinations are weighted on the basis of the distance between model output and observed data ([Methods](#)). Differences between the unweighted and weighted parameter distributions provide an indication of the extent to which observations provide constraints on the parameter value.

Extended Data Figures [1](#) and [2](#) give the results of these exercises. Extended Data Figure [1a](#) shows how the dynamics of public opinion provide some constraint on both the social conformity and cognition feedback. Public opinion on climate policy over the last decade suggests a population socially sorted within opinion groups (that is, slightly higher network homophily parameter) with relatively slow movement between groups (that is, low persuasive force) and a relatively small role for the individual perception of climate change in opinion formation (low evidence parameter). The exercise is less informative regarding parameters in the policy component, although there is some evidence of status quo bias in the political system.

The exercise also constrains the covariance between parameters (Extended Data Fig. [1b](#)). For example, there is covariance between the network homophily, persuasive force and shifting baseline parameters—consistency with observed changes in OECD climate opinion over time requires that opinion groups are socially separated, movement between opinion groups is slow or cognitive biases like shifting baselines limit the role of observed climate change in driving public opinion. Extended Data

Figure 2 shows the results of the second hindcasting exercise on the emissions parameters, which suggests a low value for the contemporaneous effect of policy on emissions (maximum mitigation rate), but is uninformative about the persistence of those emissions reductions (maximum mitigation time).

## Future emissions pathways

We used the partially constrained parameter space to probabilistically examine emissions trajectories over the twenty-first century. We performed 100,000 runs of the model, drawing from the joint distribution of the set of hindcast parameters and sampling uniformly over an additional 11 parameters, mostly within the adoption component (with the exception of a triangular distribution for the temperature–emissions feedback based on Woodard et al.<sup>8</sup>). The model is initialized using 2020 public opinion<sup>83</sup> and emissions data and run until 2100, with parameter values fixed for each model run. We used  $k$ -means clustering to group together model runs with similar trajectories of climate policy and emissions over the twenty-first century, identifying five distinct pathway types ([Methods](#)). A focus on clusters of similar policy and emissions pathways strikes a balance between exploring and explaining the diverse range of model behaviours while avoiding an undue focus on either the central tendency or the extremes of model outcomes.

Figure 3 shows the mean policy and emissions trajectories for the five clusters. The model parameter values characteristic to each cluster indicate the socio-politico-technical states determining each policy–emissions trajectory. These parameter values are shown visually in Extended Data Fig. 3. Table 2 describes the different pathways and gives end-of-century warming under the mean emissions scenario in each cluster.

**Fig. 3: Future emissions pathways in the coupled climate–social system.**



Policy (left) and global CO<sub>2</sub> emissions (right) trajectories from 100,000 Monte Carlo runs of the coupled climate–social model, clustered into 5 clusters using *k*-means clustering. The line thickness corresponds to the size of the cluster.

[Source data](#)

**Table 2 Descriptions of distinguishing characteristics, frequency and temperature outcomes**

The modal policy–emissions trajectory emerging from the model, 48% of model runs, has global emissions peaking in the 2030s and dropping steeply over the 2040–2060 period, resulting in 2100 warming of 2.3 °C above 1880–1910 levels. The 2030–2050 emissions pathway displays a perhaps remarkable similarity to recent estimates of the effect of current climate policies or stated nationally determined contributions.

Sognnaes et al.<sup>11</sup> estimate these result in fossil-fuel CO<sub>2</sub> emissions between 30–36 Gt CO<sub>2</sub> in 2030 and between 23–40 Gt CO<sub>2</sub> in 2050. Assuming that fossil fuels constitute 90% of total CO<sub>2</sub> emissions, equivalent values for the modal path trajectory are 38 Gt CO<sub>2</sub> in 2030 and 30 Gt CO<sub>2</sub> in 2050. This congruency arises despite the fact that current and stated climate policies are not input into the model and do not constrain model behaviour.

The second and third most frequent clusters highlight the role of feedback processes discussed above. The ‘aggressive action’ trajectory is characterized by a strong social-conformity feedback in the opinion component through a high persuasive force parameter, leading to rapid diffusion of support for climate policy that—combined with effective and globally deployed mitigation technologies—drives emissions down faster than in the modal path, limiting warming to below the 2 °C temperature target. By contrast, the ‘technical challenges’ trajectory is characterized by a weak or absent learning-by-doing cost reduction feedback within the energy sector, as well as expensive and ineffective mitigation technologies. This pathway has the same climate policy trajectory as the modal path, but the absence of the technical-change feedback driving costs down over time leads to much greater emissions and warming of 3 °C by 2100.

Two other trajectories (‘delayed recognition’ and ‘little and late’) exhibit multi-decade delays in climate policy, producing higher emissions over the century. These trajectories (which together constitute just over 5% of model runs), tend to be characterized by weak social conformity feedback in public opinion (through high network homophily and low persuasive force), cognitive biases limiting any effect of perceived climate change in increasing support for climate policy and an unresponsive political system (high status quo bias) that slows climate policy even as public support increases.

Examining the set of parameters that distinguish the clusters of policy and emissions trajectories from each other (Table 1 and Extended Data Fig. 3) reveals an important role for parameters associated with the opinion, mitigation, cognition and policy components, particularly the strength of social conformity (for example, network homophily and persuasive force), the strength of mitigation technology feedback and effectiveness (for example, learning by doing, mitigation rate and lag time), the responsiveness of political institutions (for example, status quo bias) and the role of cognitive biases (for example, shifting baselines and biased assimilation). Parameters from the adoption component notably do not tend to be distinguishing characteristics of policy and emissions pathways. Thus, although the model can exhibit tipping-point behaviour in which individual adoption of behavioural change can be decisive in driving the system towards zero emissions (Fig. 2a), the particular conditions that are necessary for this model behaviour do not appear to be common after constraining the model parameters using the hindcasting exercise.

Drivers of variance in model behaviour were further explored by fitting random-forest models to two outputs of the 100,000 Monte Carlo runs of the calibrated model: policy in 2030 and cumulative emissions over 2020–2100. Normalized values of the 22 model parameters are used as explanatory variables. Extended Data Figure 4 gives the minimum depth distributions for the most important 10 variables for each model. As with the clustering analysis, variables related to opinion dynamics (persuasive force and network homophily), responsiveness of the political system (status quo bias and political-interest feedback), individual perception of climate change (shifting baselines and evidence effect) and mitigation technologies emerge as important in explaining variation in policy and emissions trajectories over the twenty-first century.

## Discussion and conclusions

The trajectory of global greenhouse gas emissions over the twenty-first century will result from the complex interaction of technologies, governments, markets, individuals and communities. Although a range of disciplines have documented relevant feedback processes, the dynamics of the full system will depend on connections across components and scales. These coupled feedback processes can give rise to complex behaviour with, in some cases, sensitive dependence on parameter values and initial conditions. Even further uncertainties and more complex behaviour could emerge if parameter values were allowed to drift or change over time, for example, due to the evolution or reform of political institutions, a dynamic not explored in this analysis.

However, despite the wide range of plausible behaviour, systematic exploration of the model parameter space combined with observational constraints on parameter values where possible can bound the space of probable outcomes. Despite uncertainties in many parameters, none of the policy–emissions clusters that we identified represent a

pure business-as-usual world without climate policy. Even the highest-emission cluster produces warming in 2100 that is lower than the RCP7 business-as-usual baseline of 3.9 °C. The vast majority of runs (98%) produce warming of more than half a degree lower, although these warming estimates are sensitive to uncertainties in the climate system, including the climate sensitivity and the representation of carbon-cycle feedback, as well as the treatment of non-CO<sub>2</sub> greenhouse gases ([Methods](#)). Identified emissions trajectories, even the aggressive action scenario, fail to meet the more ambitious Paris Agreement target of limiting warming to 1.5 °C above pre-industrial levels. This result is not surprising, as all 1.5-°C-consistent emissions scenarios from energy system models include the widespread deployment of negative emissions technology, which is not represented in our model<sup>[86](#)</sup>. However, we do estimate a substantial probability of meeting the 2 °C Paris Agreement target—28% of our Monte Carlo runs result in 2091–2100 warming below 2 °C above 1880–1910 levels.

We therefore find that socio-politico-technical feedback processes can be decisive for climate policy and emissions outcomes. Yet, they require a distinct and deliberate modelling approach. Exploring emissions pathways as an endogenous outcome of the coupled climate–social system differs from the typical use of emissions scenarios as exogenous inputs into either energy–economic or general circulation models. This paper seeks to explain alternative emissions and policy trajectories as the product of more fundamental social, political, technical and economic processes. Doing so requires an integrated multidisciplinary perspective—almost all of our identified clusters have distinguishing parameters from more than one model component, implying that the interaction between these subsystems is key in driving variance in potential twenty-first century emissions pathways. Further work to enhance this modelling framework could improve the climate model to better represent non-CO<sub>2</sub> forcing and carbon-cycle feedback and would expand the carbon pricing data used for calibration of the policy and mitigation components.

## Methods

Model components and the feedback processes between and within components were identified from a review of literature across relevant fields including social and cognitive psychology, economics, sociology, law, political science and energy systems engineering<sup>[8,24,26,27,31,32,33,34,35,36,37,38,39,40,41,42,43,44,45,46,47,48,49,50,51,52,53,54,55,56,57,58,59,60,61,62,63,64,65,66,67,68,69,70,71,72,73,74,75,76,78](#)</sup>. The climate–social model was developed using relationships and feedback processes identified from this review (illustrated in Fig. 1, described in Table 1 and documented in the ‘Model documentation’ section of the [Supplementary Information](#)). Specific parameterizations or functional forms were derived from the literature where available. These are (1) parameterization of the temperature-emissions feedback using Woodard et al.<sup>[8](#)</sup>; (2) parameterization of the

shifting-baseline effect using Moore et al.<sup>55</sup>; (3) parameterization of the learning-by-doing effect using Rubin et al.<sup>75</sup>; and (4) use of a logistic uptake curve to represent uptake of individual behaviour change as commonly used in the technology adoption literature<sup>95</sup>. However, in many cases, only qualitative descriptions or relationships were described in the literature. In these cases (normative force of law feedback, political interest feedback, social norm effect, social homophily, status quo bias, credibility-enhancing display feedback and biased assimilation), we attempted to translate the relationships into appropriate functional forms, described in more detail in the ‘Extended model documentation’ section of the [Supplementary Information](#).

The behaviour of the model, particularly the potential for cross-component feedback processes and tipping points was investigated using systematic sweeps of the parameters shown in Fig. 2, keeping all of the other model parameters fixed. Other model parameters for this part of the analysis were deliberately chosen to demonstrate the existence of tipping or threshold behaviour following an informal, qualitative exploration of the parameter space and are given in Extended Data Table 1. The parameters that were varied in this analysis were chosen to exemplify thresholds and tipping-point behaviour as well as the interactions that moderate those effects.

Two hindcasting exercises were conducted to partially constrain some key model parameters (given in Extended Data Figs. 1 and 2) using historical data. The first used time series of public opinion on climate change and carbon prices from 2013 to 2020 for nine OECD countries (the USA, Canada, Japan, Australia, the UK, Germany, France, Italy and Spain) to jointly constrain nine parameters in the opinion, policy and cognition components. Opinion data came from the Pew Research Center<sup>83</sup>, which asked respondents whether they thought global climate change was a major threat, a minor threat or not a threat. These three categories were mapped onto those supporting, neutral or opposed to climate policy and data from nine countries were aggregated into a single population-weighted time series<sup>96</sup>. Carbon price data come from the World Bank Carbon Pricing Dashboard and we calculate a single, emissions-weighted carbon price for the nine OECD countries between 2013 and 2020 (ref. <sup>84</sup>). This constrains the calibration to only explicit carbon prices based on taxes or emissions trading schemes, ignoring implicit carbon prices arising through other forms of climate and energy regulation, for which data are not readily available.

The model was initialized using carbon prices and opinion distribution from 2013 and then run 20,000 times, sampling from the distributions over nine model parameters (given in Extended Data Fig. 1). We use uniform prior distributions over the parameters, except in a couple of cases for which parameters are structurally related to each other (specifically the ‘weak persuasive force’ is constrained to be smaller than the ‘strong persuasive force’ and the ‘political interest feedback’ is constrained to be smaller than the ‘status quo bias’) or where some prior evidence suggests non-uniform

distributions. Specifically, we used informative prior distributions for the network homophily parameter, placing higher weight on larger values (that is, more social separation between opinion groups<sup>97,98</sup>) and for the shifting baselines parameter, placing more weight on the existence of shifting baselines<sup>55</sup>. For each model run, we defined a probability weight associated with the parameters based on its error in predicting 2014–2020 opinion and policy (that is, carbon prices) relative to the set of all 20,000 runs (details are provided in the ‘Weighting scheme for hindcast parameter constraints’ section of the [Supplementary Information](#)). Initial distributions and weighted distributions based on hindcasting performance are given in Extended Data Fig. 1a.

A second tuning exercise was performed for two parameters in the emissions component (maximum mitigation rate and maximum mitigation time) using evidence from Andersson<sup>85</sup> on the effect of the Swedish carbon price over the period 1991–2005. Andersson estimates that carbon pricing reduced emissions by 12.5% in 2005. The emissions component was forced with observed Swedish carbon prices over this time period and run 10,000 times, sampling from independent uniform distributions over the two mitigation parameters. A weighting scheme based on the difference in the modelled mitigation rate in 2005 and the estimated effect of the policy in Andersson<sup>85</sup> was applied to the initial uniform distributions, shown in Extended Data Fig. 2. As with the first calibration exercise, this again relies on only explicit carbon tax levels, ignoring the effects of fuel taxes or the shadow costs of other climate or energy regulation.

To evaluate the effectiveness of the parameter-tuning process for parameters in the opinion, policy and cognition components, we also performed a leave-one-out cross-validation of the model. Component parameters were tuned after dropping data from each year between 2014 and 2020 in sequence. The trained model was then run 20,000 times in Monte Carlo mode to predict the missing year value. We find that the average out-of-sample root mean squared error is US \$2.5 for the carbon price and 5.4 percentage points for the combined neutral and opposed opinion groups.

Finally, a full Monte Carlo analysis of the model was performed. Parameters partly constrained in the hindcasting exercises were drawn from the weighted distributions shown in Extended Data Figs. 1 and 2. An additional 11 parameters (primarily in the adoption component, and listed in the ‘Monte Carlo parameter sampling details’ section of the [Supplementary Information](#)) were drawn from independent uniform distributions (with the exception of a triangular distribution for the temperature–emissions feedback based on Woodard et al.<sup>8</sup>). The model was run 100,000 times, initialized using opinion distribution in 2020 and running until 2100.

Clusters of similar policy and emissions trajectories were identified by concatenating the two time series for each model run, scaling each column and applying  $k$ -means clustering to the resulting data frame. We decided on 5 clusters based on reductions in the within-cluster variance for 2–9 clusters (Extended Data Fig. 5). Characteristic parameter values for each cluster (Extended Data Fig. 3) were identified by first scaling the parameter values across all runs and then plotting average values for each cluster. Values close to zero mean that the model runs within the cluster have parameter values close to the ensemble average, whereas high or low values suggest sorting of those ensemble runs into the cluster and that these values are therefore important in producing the policy–emissions trajectory associated with that cluster.

The temperature outcomes for emissions pathways reported in Table 2 depend on how forcing from non-CO<sub>2</sub> greenhouse gases are assumed to change with CO<sub>2</sub> emissions. Following the 2016 DICE model<sup>99</sup>, non-CO<sub>2</sub> forcings appear in the model as an ‘exogenous forcing’ term applied on top of radiative forcing from CO<sub>2</sub>. We allow this forcing to vary with CO<sub>2</sub> emissions based on a fitted relationship between reductions in CO<sub>2</sub> and reductions in CH<sub>4</sub> and N<sub>2</sub>O observed in the SSP-RCP emissions database<sup>100</sup>, which suggests that these gases are reduced at approximately half the rate of CO<sub>2</sub> (Extended Data Fig. 6). The sensitivity of 2091–2100 temperature estimates to this modelling choice is shown in Extended Data Table 2.

Moreover, the DICE climate model used in the coupled climate–social model and to estimate warming in Table 2 has a slow temperature response and lacks representation of carbon-cycle feedback<sup>101</sup>. Thus, in Extended Data Table 2, we also show 2091–2100 warming under the five emissions trajectories using the MAGICC v.7 climate model, which includes saturation of the land and ocean carbon sinks, a more complete treatment of non-CO<sub>2</sub> forcing and is calibrated to reproduce behaviour of much larger general circulation models<sup>94,102</sup>. End-of-century warming on the basis of the DICE model is well within the uncertainty range based on 100 Monte Carlo runs of MAGICC. The largest difference with median MAGICC warming is 0.2 °C for the aggressive action pathway. All of the other scenarios are within 0.1 °C of the median.

The coupled climate–social model is coded in R (v.3.6.3). Model output and behaviour were also analysed using the tidyverse, randomForest and randomForestExplainer packages. Figure 3 and Extended Data Figs. 3, 4 and 6 were made using the ggplot2 package.

## Reporting summary

Further information on research design is available in the [Nature Research Reporting Summary](#) linked to this paper.

## Data availability

All data used in the Article are publicly available online (<https://doi.org/10.24433/CO.5602083.v1>). [Source data](#) are provided with this paper.

## Code availability

Model code and code to reproduce the analysis in this Article are provided in an online repository (<https://doi.org/10.24433/CO.5602083.v1>).

## References

1. Collins, M. et al. in *Climate Change 2013: The Physical Science Basis. Contribution of Working Group 1 to the Fifth Assessment Report of the Intergovernmental Panel on Climate Change* (eds Stocker, T. F. et al.) 1029–1136 (Cambridge Univ. Press, 2013).
2. Beckage, B. et al. Linking models of human behaviour and climate alters projected climate change. *Nat. Clim. Change* **8**, 79–84 (2018).
3. Beckage, B. et al. The Earth has humans, so why don't our climate models? *Clim. Change* **163**, 181–188 (2020).
4. Peng, W. et al. Climate policy models need to get real about people—here's how. *Nature* **594**, 174–176 (2021).
5. Geels, F. W., Sovacool, B., Schwanen, T. & Sorrell, S. Sociotechnical transitions for deep decarbonization. *Science* **357**, 1242–1244 (2017).
6. Farmer, J. D. et al. Sensitive intervention points in the post-carbon transition. *Science* **364**, 132–134 (2019).
7. Otto, I. M. et al. Social tipping dynamics for stabilizing Earth's climate by 2050. *Proc. Natl Acad. Sci. USA* **117**, 2354–2365 (2020).
8. Woodard, D. L., Davis, S. J. & Randerson, J. T. Economic carbon cycle feedbacks may offset additional warming from natural feedbacks. *Proc. Natl Acad. Sci. USA* **116**, 759–764 (2019).
9. Howard, P. & Livermore, M. A. Sociopolitical feedbacks and climate change. *Harvard Environ. Law Rev.* **43**, 119–174 (2019).

10. Friedlingstein, P. et al. Global carbon budget 2020. *Earth Syst. Sci. Data* **12**, 3269–3340 (2020).
11. Sognnaes, I. et al. A multi-model analysis of long-term emissions and warming. *Nat. Clim. Change* **8**, 493 (2021).
12. Victor, D. G. et al. Prove Paris was more than paper promises. *Nature* **548**, 25–27 (2017).
13. Field, C. B. & Mach, K. J. Climate: rightsizing carbon dioxide removal. *Science* **356**, 706–707 (2017).
14. Tong, D. et al. Committed emissions from existing energy infrastructure jeopardize 1.5 °C climate target. *Nature* **572**, 373–377 (2019).
15. Smith, S. M. A case for transparent net-zero carbon targets. *Commun. Earth Environ.* **2**, 24 (2021).
16. IPCC. in *Special Report on Global Warming of 1.5 °C* (eds Masson-Delmotte, V. et al.) p15 (WMO, 2018).
17. Strauch, Y. Beyond the low-carbon niche: global tipping points in the rise of wind, solar, and electric vehicles to regime scale systems. *Energy Res. Soc. Sci.* **62**, 101364 (2020).
18. Fiddaman, T. S. Exploring policy options with a behavioral climate-economy model. *Syst. Dyn. Rev.* **18**, 243–267 (2002).
19. Brauers, H., Oei, P.-Y. & Walk, P. Comparing coal phase-out pathways: the United Kingdom's and Germany's diverging transitions. *Environ. Innov. Soc. Transitions* **37**, 238–253 (2020).
20. Sperling, D. Electric vehicles: approaching the tipping point. *Bull. At. Sci.* **74**, 11–18 (2018).
21. Hoekstra, A., Steinbuch, M. & Verbong, G. Creating agent-based energy transition management models that can uncover profitable pathways to climate change mitigation. *Complexity* **2017**, 1967645 (2017).
22. Vinichenko, V., Cherp, A. & Jewell, J. Historical precedents and feasibility of rapid coal and gas decline required for the 1.5 °C target. *One Earth* **4**, 1477–1490 (2021).

23. Fouquet, R. Historical energy transitions: speed, prices and system transformation. *Energy Res. Soc. Sci.* **22**, 7–12 (2016).
24. Centola, D., Becker, J., Brackbill, D. & Baronchelli, A. Experimental evidence for tipping points in social convention. *Science* **360**, 1116–1119 (2018).
25. Hacker, J. S. & Pierson, P. Policy feedback in an age of polarization. *Ann. Am. Acad. Pol. Soc. Sci.* **685**, 8–28 (2019).
26. Pierson, P. When effect becomes cause: policy feedback and political change. *World Polit.* **45**, 595–628 (1993).
27. Stokes, L. C. *Short Circuiting Policy: Interest Groups and the Battle Over Clean Energy and Climate Policy in the American States* (Oxford Univ. Press, 2020).
28. Berglund, C. & Söderholm, P. Modeling technical change in energy system analysis: analyzing the introduction of learning-by-doing in bottom-up energy models. *Energy Policy* **34**, 1344–1356 (2006).
29. EN-ROADS, <https://en-roads.climateinteractive.org/scenario.html> (Climate Interactive, accessed 16 November 2021).
30. Latané, B. The psychology of social impact. *Am. Psychol.* **36**, 343–356 (1981).
31. Mason, W. A., Conrey, F. R. & Smith, E. R. Situating social influence processes: dynamic, multidirectional flows of influence within social networks. *Personal. Soc. Psychol. Rev.* **11**, 279–300 (2007).
32. Bénabou, R. & Tirole, J. Incentives and prosocial behavior. *Am. Econ. Rev.* **96**, 1652–1678 (2006).
33. McDonald, R. I. & Crandall, C. S. Social norms and social influence. *Curr. Opin. Behav. Sci.* **3**, 147–151 (2015).
34. Goldberg, M. H., van der Linden, S., Leiserowitz, A. & Maibach, E. Perceived social consensus can reduce ideological biases on climate change. *Environ. Behav.* **52**, 495–517 (2020).
35. Bamberg, S. & Moser, G. Twenty years after Hines, Hungerford and Tomera: a new meta-analysis of psycho-social determinants of pro-environmental behavior. *J. Environ. Psychol.* **27**, 14–25 (2007).
36. Schultz, P. W., Nolan, J. M. & Cialdini, R. B. The constructive, destructive, and reconstructive power of social norms. *Psychol. Sci.* **10**, 429–434 (2007).

37. Bollinger, B. & Gillingham, K. Peer-effects in the diffusion of solar photovoltaics. *Mark. Sci.* **31**, 900–912 (2012).
38. Andreoni, J., Nikiforakis, N. & Siegenthaler, S. Predicting social tipping and norm change in controlled experiments. *Proc. Natl Acad. Sci. USA* **118**, e2014893118 (2021).
39. Santer, B. D. et al. Identifying human influences on atmospheric temperature. *Proc. Natl Acad. Sci. USA* **110**, 26–33 (2013).
40. Marvel, K. & Bonfils, C. Identifying external influences on global precipitation. *Proc. Natl Acad. Sci. USA* **110**, 19301–19306 (2013).
41. Parmesan, C. & Yohe, G. A globally coherent fingerprint of climate change impacts across natural systems. *Nature* **421**, 37–42 (2003).
42. Diffenbaugh, N. S. et al. Quantifying the influence of global warming on unprecedented extreme climate events. *Proc. Natl Acad. Sci. USA* **114**, 4881–4886 (2017).
43. Ricke K. L. & Caldeira K. Natural climate variability and future climate policy. *Nat. Clim. Chang.* **4**, 333–338 (2014).
44. Howe, P. D., Markowitz, E. M., Lee, T. M., Ko, C.-Y. & Leiserowitz, A. Global perceptions of local temperature change. *Nat. Clim. Change* **3**, 352–356 (2012).
45. Howe, P. D. & Leiserowitz, A. Who remembers a hot summer or a cold winter? The asymmetric effect of beliefs about global warming on perceptions of local climate conditions in the U.S. *Glob. Environ. Change* **23**, 1488–1500 (2013).
46. Deryugina, T. How do people update? The effects of local weather fluctuations on beliefs about global warming. *Clim. Change* **118**, 397–416 (2013).
47. Kaufmann, R. K. et al. Spatial heterogeneity of climate change as an experiential basis for skepticism. *Proc. Natl Acad. Sci. USA* **114**, 67–71 (2017).
48. Hamilton, L. C. & Stampone, M. D. Blowin' in the wind: short-term weather and belief in anthropogenic climate change. *Weather Clim. Soc.* **5**, 112–119 (2013).
49. Zaval, L., Keenan, E. A., Johnson, E. J. & Weber, E. U. How warm days increase belief in global warming. *Nat. Clim. Change* **4**, 143–147 (2014).
50. Howe, P. D., Marlon, J. R., Mildenberger, M. & Shield, B. S. How will climate change shape climate opinion? *Environ. Res. Lett.* **14**, 113001 (2019).

51. McCright, A. M., Dunlap, R. E. & Xiao, C. The impacts of temperature anomalies and political orientation on perceived winter warming. *Nat. Clim. Change* **4**, 1077–1081 (2014).
52. Hazlett, C. & Mildenberger, M. Wildfire exposure increases pro-environment voting within Democratic but not Republican areas. *Am. Polit. Sci. Rev.* **114**, 1359–1365 (2020).
53. Druckman, J. N. & McGrath, M. C. The evidence for motivated reasoning in climate change preference formation. *Nat. Clim. Change* **9**, 111–119 (2019).
54. Kahan, D. M., Jenkins-Smith, H. & Braman, D. Cultural cognition of scientific consensus. *J. Risk Res.* **14**, 147–174 (2011).
55. Moore, F. C., Obradovich, N., Lehner, F. & Baylis, P. Rapidly declining remarkableability of temperature anomalies may obscure public perception of climate change. *Proc. Natl Acad. Sci. USA* **116**, 4905–4910 (2019).
56. Mildenberger, M. *Carbon Captured: How Business and Labor Control Climate Politics* (MIT Press, 2020).
57. Hertel-Fernandez, A., Mildenberger, M. & Stokes, L. C. Legislative staff and representation in Congress. *Am. Polit. Sci. Rev.* **113**, 1–18 (2018).
58. Jenkins, J. D. Political economy constraints on carbon pricing policies: what are the implications for economic efficiency, environmental efficacy, and climate policy design? *Energy Policy* **69**, 467–477 (2014).
59. Truelove, H. B., Carrico, A. R., Weber, E. U., Raimi, K. T. & Vandenbergh, M. P. Positive and negative spillover of pro-environmental behavior: an integrative review and theoretical framework. *Glob. Environ. Change* **29**, 127–138 (2014).
60. Sparkman, G. & Walton, G. M. Dynamic norms promote sustainable behavior, even if it is counternormative. *Psychol. Sci.* **28**, 1663–1674 (2017).
61. Kraft-Todd, G. T., Bollinger, B., Gillingham, K., Lamp, S. & Rand, D. G. Credibility-enhancing displays promote the provision of non-normative public goods. *Nature* **563**, 245–248 (2018).
62. Attari, S. Z., Krantz, D. H. & Weber, E. U. Statements about climate researchers' carbon footprints affect their credibility and the impact of their advice. *Clim. Change* **138**, 325–338 (2016).

63. Attari, S. Z., Krantz, D. H. & Weber, E. U. Climate change communicators' carbon footprints affect their audience's policy support. *Clim. Change* **154**, 529–545 (2019).
64. Tankard, M. E. & Paluck, E. L. Norm perception as a vehicle for social change. *Soc. Issues Policy Rev.* **10**, 181–211 (2016).
65. Kahan, D. M. What do alternative sanctions mean? *Univ. Chicago Law Rev.* **63**, 591–653 (1996).
66. Sunstein, C. R. On the expressive function of law. *Univ. PA Law Rev.* **281**, 2021–2054 (1996).
67. McAdams, R. H. An attitudinal theory of expressive law. *Oregon Law Rev.* **79**, 339–390 (2000).
68. Posner, E. A. Symbols, signals, and social norms in politics and the law. *J. Legal Stud.* **27**, 765–797 (1998).
69. Ofosu, E. K., Chambers, M. K., Chen, J. M. & Hehman, E. Same-sex marriage legalization associated with reduced implicit and explicit antigay bias. *Proc. Natl Acad. Sci. USA* **116**, 8846–8851 (2019).
70. Tankard, M. E. & Paluck, E. L. The effect of a supreme court decision regarding gay marriage on social norms and personal attitudes. *Psychol. Sci.* **28**, 1334–1344 (2017).
71. Orbell, S. et al. Social–cognitive beliefs, alcohol, and tobacco use: a prospective community study of change following a ban on smoking in public places. *Health Psychol.* **28**, 753–761 (2009).
72. Galbiati, R., Henry, E., Jacquemet, N. & Lobeck, M. How laws affect the perception of norms: empirical evidence from the lockdown. *PLoS ONE* **16**, e0256624 (2021).
73. Trancik, J. E. Scale and innovation in the energy sector: a focus on photovoltaics and nuclear fission. *Environ. Res. Lett.* **1**, 014009 (2006).
74. Yeh, S. & Rubin, E. S. A review of uncertainties in technology experience curves. *Energy Econ.* **34**, 762–771 (2012).
75. Rubin, E. S., Azevedo, I. M. L., Jaramillo, P. & Yeh, S. A review of learning rates for electricity supply technologies. *Energy Policy* **86**, 198–218 (2015).

76. Dell, M., Jones, B. F. & Olken, B. A. Temperature shocks and economic growth: evidence from the last half century. *Am. Econ. J. Macroecon.* **4**, 66–95 (2012).
77. Burke, M., Hsiang, S. M. & Miguel, E. Global non-linear effect of temperature on economic production. *Nature* **527**, 235–239 (2015).
78. Rode, A. et al. Estimating a social cost of carbon for global energy consumption. *Nature* **598**, 308–314 (2021).
79. Hardin, E. et al. California drought increases CO<sub>2</sub> footprint of energy. *Sustain. Cities Soc.* **28**, 450–452 (2017).
80. Mideksa, T. K. & Kallbekken, S. The impact of climate change on the electricity market: a review. *Energy Policy* **38**, 3579–3585 (2010).
81. Le Quéré, C. et al. Temporary reduction in daily global CO<sub>2</sub> emissions during the COVID-19 forced confinement. *Nat. Clim. Change* **10**, 647–653 (2020).
82. Liu, Z. et al. Near-real-time monitoring of global CO<sub>2</sub> emissions reveals the effects of the COVID-19 pandemic. *Nat. Commun.* **11**, 5172 (2020).
83. Fagan, M. & Huang, C. *Many Globally are as Concerned About Climate Change as About the Spread of Infectious Diseases*, <https://www.pewresearch.org/fact-tank/2020/10/16/many-globally-are-as-concerned-about-climate-change-as-about-the-spread-of-infectious-diseases/> (Pew Research Center, 2020).
84. World Bank. *Carbon Pricing Dashboard* <https://carbonpricingdashboard.worldbank.org/> (World Bank, 2021).
85. Andersson, J. J. Carbon taxes and CO<sub>2</sub> emissions: Sweden as a case study. *Am. Econ. J. Econ. Policy* **11**, 1–30 (2019).
86. Hilaire, J. et al. Negative emissions and international climate goals—learning from and about mitigation scenarios. *Clim. Change* **157**, 189–219 (2019).
87. Leiserowitz, A. A. et al. *Politics & Global Warming, March 2018* (Yale Univ. & George Mason Univ., 2018).
88. Jurkowitz, M., Mitchell, A., Shearer, E. & Walker, M. *U.S. Media Polarization and the 2020 Election: A Nation Divided* (Pew Research Center, 2020).
89. Lang, C. & Pearson-Merkowitz, S. Partisan sorting in the United States, 1972–2012: new evidence from a dynamic analysis. *Polit. Geogr.* **48**, 119–129 (2015).

90. Fernandez, B. R. & Rodrik, D. Resistance to reform: status quo bias in the presence of individual-specific uncertainty. *Am. Econ. Rev.* **81**, 1146–1155 (1991).
91. Hausfather, Z. & Peters, G. P. Emissions—the ‘business as usual’ story is misleading. *Nature* **577**, 618–620 (2020).
92. Nordhaus, W. D. *A Question of Balance: Weighing the Options on Global Warming Policy* (Yale Univ. Press, 2008).
93. Cai, Y. & Lontzek, T. S. The social cost of carbon with economic and climate risks. *J. Polit. Econ.* **127**, 2684–2734 (2019).
94. Meinshausen, M. et al. The shared socio-economic pathway (SSP) greenhouse gas concentrations and their extensions to 2500. *Geosci. Model Dev.* **13**, 3571–3605 (2020).
95. Rogers, E. M. *Diffusion of Innovations* (Free Press, 2003).
96. UN Population Division. *World Population Prospects 2019*, <https://population.un.org/wpp/Download/Standard/Population/> (UN, 2019).
97. Halberstam, Y. & Knight, B. Homophily, group size, and the diffusion of political information in social networks: evidence from Twitter. *J. Public Econ.* **143**, 73–88 (2016).
98. Huber, G. A. & Malhotra, N. Political homophily in social relationships: evidence from online dating behavior. *J. Polit.* **79**, 269–283 (2017).
99. Nordhaus, W. D. Revisiting the social cost of carbon. *Proc. Natl Acad. Sci. USA* **114**, 1518–1523 (2017).
100. SSP Public Database—Version 2.0, <https://tntcat.iiasa.ac.at/SspDb>, accessed 24 November 2021 (IIASA, 2018).
101. Dietz, S., van der Ploeg, F., Rezai, A. & Venmans, F. Are economists getting climate dynamics right and does it matter? *J. Assoc. Environ. Resour. Econ.* **8**, 895–921 (2021).
102. Meinshausen, M., Raper, S. C. B. & Wigley, T. M. L. Emulating coupled atmosphere-ocean and carbon cycle models with a simpler model, MAGICC6—part 1: model description and calibration. *Atmos. Chem. Phys.* **11**, 1417–1456 (2011).

103. Meinshausen, M. et al. The RCP greenhouse gas concentrations and their extensions from 1765 to 2300. *Clim. Change* **109**, 213–241 (2011).
104. MAGICC, <https://live.magicc.org> (Climate Resource, accessed 10 December 2021).

## Acknowledgements

We thank S. Metcalf, D. Rothman, T. Franck and A. Kinzig for discussions and comments on this work. This work resulted from a working group supported by the National Socio-Environmental Synthesis Center (SESYNC) under funding received from the National Science Foundation (NSF) DBI-1052875. F.C.M. acknowledges the support of NSF (award no. 1924378). K.L. acknowledges the support of the NSF under EPSCoR Cooperative Agreement OIA-1655221. L.J.G. acknowledges the support of NSF (award no. 1300426 to the National Institute for Mathematical and Biological Synthesis). B.B. acknowledges the support of the National Science Foundation through VT EPSCoR (award no. 1556770).

## Author information

### Affiliations

1. Department of Environmental Science and Policy, University of California, Davis, CA, USA  
Frances C. Moore
2. Department of Psychology, Rhode Island College, Providence, RI, USA  
Katherine Lacasse
3. Department of Environmental Science and Policy, Rosenstiel School of Marine and Atmospheric Science, University of Miami, Miami, FL, USA  
Katharine J. Mach
4. Leonard and Jayne Abess Center for Ecosystem Science and Policy, University of Miami, Miami, FL, USA  
Katharine J. Mach
5. Global Futures Laboratory, Arizona State University, Tempe, AZ, USA

Yoon Ah Shin

6. Department of Ecology and Evolutionary Biology, University of Tennessee,  
Knoxville, TN, USA

Louis J. Gross

7. Department of Mathematics, University of Tennessee, Knoxville, TN, USA

Louis J. Gross

8. Department of Plant Biology, University of Vermont, Burlington, VT, USA

Brian Beckage

9. Department of Computer Science, University of Vermont, Burlington, VT, USA

Brian Beckage

10. Gund Institute for Environment, University of Vermont, Burlington, VT, USA

Brian Beckage

## Contributions

All of the authors contributed to the conceptual design of the model. F.C.M., K.L., K.J.M. and Y.A.S. performed the literature review of evidence for feedback processes. F.C.M. coded the model, analysed results and generated the figures. All of the authors contributed to writing the manuscript.

## Corresponding author

Correspondence to [Frances C. Moore](#).

## Ethics declarations

## Competing interests

The authors declare no competing interests.

## Peer review

## Peer review information

*Nature* thanks Gernot Wagner and the other, anonymous, reviewer(s) for their contribution to the peer review of this work. Peer reviewer reports are available.

## Additional information

**Publisher's note** Springer Nature remains neutral with regard to jurisdictional claims in published maps and institutional affiliations.

## Extended data figures and tables

### [Extended Data Fig. 1 Results of the first hindcasting exercise to constrain parameters in the opinion, policy, and cognition components.](#)

**a)** Parameter distributions before (prior) and after (posterior) weighting based on fit with observed public opinion and policy trajectories over 2013–2020 for nine OECD nations (US, Canada, Japan, Australia, UK, Germany, France, Spain and Italy). **b)** Covariance of parameters after weighting based on model performance. Covariance of the unweighted parameters is zero as they are drawn independently, meaning covariance of the weighted distribution is induced by model performance of particular parameter combinations.

### [Extended Data Fig. 2 Results of the second hindcasting exercise to constrain parameters in the mitigation component.](#)

Parameter distributions before (prior) and after (posterior) weighting based on distance from observed response of Swedish emissions to carbon pricing based on Andersson<sup>85</sup>.

### [Extended Data Fig. 3 Characteristic parameter combinations for the policy-emissions trajectory clusters.](#)

Average parameter values by policy-emissions trajectory cluster for the 100,000 Monte Carlo model runs, after normalizing by subtracting the mean and dividing by the standard deviation of parameter values across all samples. High or low values imply that those parameters values are important in producing the trajectories in that particular cluster.

## [Extended Data Fig. 4 Minimum depth distributions for random forest models.](#)

Minimum depth distributions (level at which a variable first appears in the regression tree) for two random forest models of the 100,000 Monte Carlo runs, for the 2030 carbon price (left) and cumulative emissions 2020–2100 (right). Both random forest models include standardized values of all 22 model parameters varied in the Monte Carlo analysis. Figures show the 10 variables with lowest average minimum depth.

## [Extended Data Fig. 5 Total within-cluster sum of squares for 2–9 clusters.](#)

Five clusters were chosen based on the reduction in slope for larger number of clusters.

## [Extended Data Fig. 6 Relationship between fractional reductions in CO<sub>2</sub> from RCP7 and fractional reductions in CH<sub>4</sub> and N<sub>2</sub>O based on emissions from the SSP Database.](#)

The fitted relationship is used to scale the exogenous forcing term in the climate model that parameterizes forcing from non-CO<sub>2</sub> greenhouse gases.

**Extended Data Table 1** Parameter values used to highlight tipping points and thresholds used for model runs shown in Fig. 2 in main text

**Extended Data Table 2** Sensitivity of 2091–2100 Temperatures (°C relative to 1880–1910 baseline) to alternate modelling choices

## **Supplementary information**

### [Supplementary Information](#)

The weighting scheme for hindcast parameter constraints; Monte Carlo parameter sampling details; extended model documentation; and Supplementary Notes and Supplementary Equations.

### [Reporting Summary](#)

### [Peer Review File](#)

# Source data

## [Source Data Fig. 3](#)

# Rights and permissions

## [Reprints and Permissions](#)

# About this article

## Cite this article

Moore, F.C., Lacasse, K., Mach, K.J. *et al.* Determinants of emissions pathways in the coupled climate–social system. *Nature* **603**, 103–111 (2022).  
<https://doi.org/10.1038/s41586-022-04423-8>

- Received: 28 July 2021
- Accepted: 12 January 2022
- Published: 16 February 2022
- Issue Date: 03 March 2022
- DOI: <https://doi.org/10.1038/s41586-022-04423-8>

## Share this article

Anyone you share the following link with will be able to read this content:

[Get shareable link](#)

Sorry, a shareable link is not currently available for this article.

[Copy to clipboard](#)

Provided by the Springer Nature SharedIt content-sharing initiative

[\*\*Social, political and technical feedback processes will drive future climate policies and emissions\*\*](#)

Research Briefing 16 Feb 2022

## **Tongan volcano eruption leaves scientists with unanswered questions**

- Benjamin Thompson
- Nick Petrić Howe

Nature Podcast 16 Feb 2022

---

This article was downloaded by **calibre** from <https://www.nature.com/articles/s41586-022-04423-8>

| [Section menu](#) | [Main menu](#) |

- Article
- [Published: 23 February 2022](#)

# A global timing mechanism regulates cell-type-specific wiring programmes

- [Saumya Jain](#)<sup>1,2</sup> natl,
- [Ying Lin](#)<sup>1,3</sup> natl,
- [Yerbol Z. Kurmangaliyev](#)<sup>2</sup>,
- [Javier Valdes-Aleman](#) ORCID: orcid.org/0000-0002-1577-1057<sup>1,2</sup>,
- [Samuel A. LoCascio](#)<sup>1</sup>,
- [Parmis Mirshahidi](#)<sup>1</sup>,
- [Brianna Parrington](#)<sup>1</sup> &
- [S. Lawrence Zipursky](#) ORCID: orcid.org/0000-0001-5630-7181<sup>1,2</sup>

[Nature](#) volume 603, pages 112–118 (2022)

- 3459 Accesses
- 51 Altmetric
- [Metrics details](#)

## Subjects

- [Development of the nervous system](#)
- [Molecular neuroscience](#)

## Abstract

The assembly of neural circuits is dependent on precise spatiotemporal expression of cell recognition molecules<sup>1,2,3,4,5</sup>. Factors controlling cell type specificity have been identified<sup>6,7,8</sup>, but how timing is determined remains unknown. Here we describe induction of a cascade of transcription factors by a steroid hormone (ecdysone) in all fly visual system neurons spanning target recognition and synaptogenesis. We demonstrate through single-cell sequencing that the ecdysone pathway regulates the expression of a common set of targets required for synaptic maturation and cell-type-specific targets enriched for cell-surface proteins regulating wiring specificity. Transcription factors in the cascade regulate the expression of the same wiring genes in complex ways, including activation in one cell type and repression in another. We show that disruption of the ecdysone pathway generates specific defects in dendritic and axonal processes and synaptic connectivity, with the order of transcription factor expression correlating with sequential steps in wiring. We also identify shared targets of a cell-type-specific transcription factor and the ecdysone pathway that regulate specificity. We propose that neurons integrate a global temporal transcriptional module with cell-type-specific transcription factors to generate different cell-type-specific patterns of cell recognition molecules regulating wiring.

This is a preview of subscription content

## Access options

Subscribe to Nature+

Get immediate online access to the entire Nature family of 50+ journals

\$29.99

monthly

[Subscribe](#)

Subscribe to Journal

Get full journal access for 1 year

\$199.00

only \$3.90 per issue

[Subscribe](#)

All prices are NET prices.

VAT will be added later in the checkout.

Tax calculation will be finalised during checkout.

Buy article

Get time limited or full article access on ReadCube.

\$32.00

[Buy](#)

All prices are NET prices.

### **Additional access options:**

- [Log in](#)
- [Learn about institutional subscriptions](#)

**Fig. 1: Dynamic expression of wiring genes and ecdysone pathway TFs.**

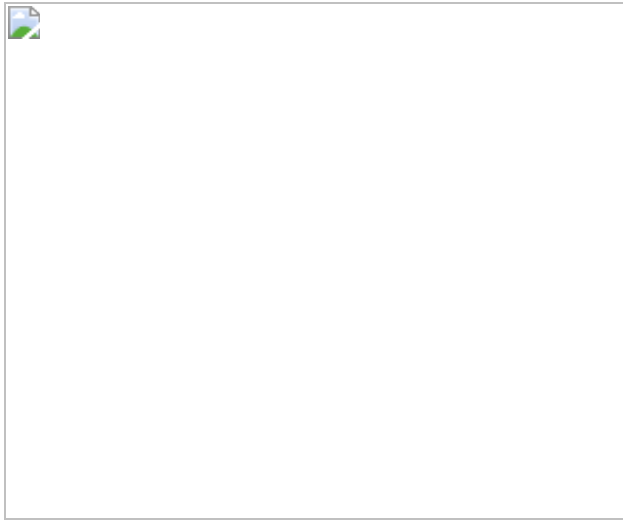


**Fig. 2: Ecdysone pathway TFs control multiple aspects of wiring.**



**Fig. 3: Common and cell-type-specific targets of the ecdysone pathway.**

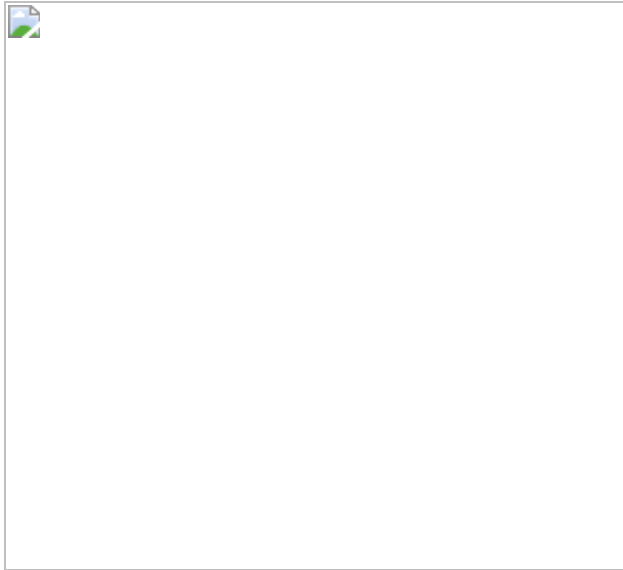
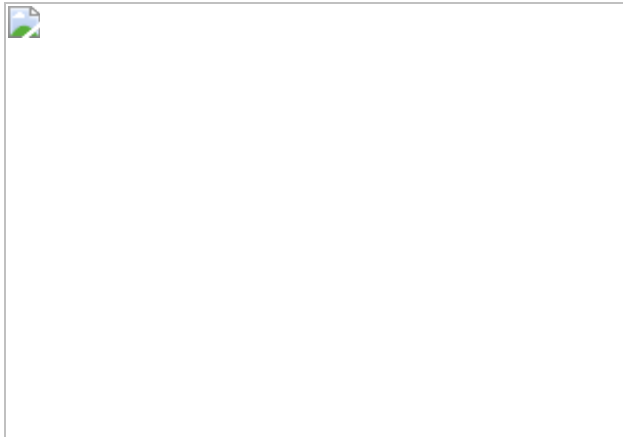


**Fig. 4: Screening of genes co-regulated by EcR and Erm for wiring regulators.**



## Data availability

All raw sequencing data are available under Gene Expression Omnibus (GEO) accession [GSE190714](#). Gene expression tables for all sequencing experiments are provided in Supplementary Tables [6–9](#). Raw data for all other experiments are available on request. [Source data](#) are provided with this paper.

## Code availability

Code used in this work is available on request.

## References

1. Südhof, T. C. Towards an understanding of synapse formation. *Neuron* **100**, 276–293 (2018).
2. Zipursky, S. L. & Sanes, J. R. Chemoaffinity revisited: dscams, protocadherins, and neural circuit assembly. *Cell* **143**, 343–353 (2010).
3. Hassan, B. A. & Hiesinger, P. R. Beyond molecular codes: simple rules to wire complex brains. *Cell* **163**, 285–291 (2015).
4. Li, H. et al. Classifying *Drosophila* olfactory projection neuron subtypes by single-cell RNA sequencing. *Cell* **171**, 1206–1220 (2017).

5. Özel, M. N. et al. Neuronal diversity and convergence in a visual system developmental atlas. *Nature* **589**, 88–95 (2020).
6. Hobert, O. Terminal selectors of neuronal identity. *Curr. Top. Devel. Biol.* **116**, 455–475 (2016).
7. Hong, W. & Luo, L. Genetic control of wiring specificity in the fly olfactory system. *Genetics* **196**, 17–29 (2014).
8. Dasen, J. S. & Jessell, T. M. Hox networks and the origins of motor neuron diversity. *Curr. Top. Devel. Biol.* **88**, 169–200 (2009).
9. Larkin, A. et al. FlyBase: updates to the *Drosophila melanogaster* knowledge base. *Nucleic Acids Res.* **49**, D899–D907 (2020).
10. Scheffer, L. K. et al. A connectome and analysis of the adult *Drosophila* central brain. *eLife* **9**, e57443 (2020).
11. Kurmangaliyev, Y. Z., Yoo, J., Valdes-Aleman, J., Sanfilippo, P. & Zipursky, S. L. Transcriptional programs of circuit assembly in the *Drosophila* visual system. *Neuron* **108**, 1045–1057 (2020).
12. Reilly, M. B., Cros, C., Varol, E., Yemini, E. & Hobert, O. Unique homeobox codes delineate all the neuron classes of *C. elegans*. *Nature* **584**, 595–601 (2020).
13. Truman, J. W., Talbot, W. S., Fahrbach, S. E. & Hogness, D. S. Ecdysone receptor expression in the CNS correlates with stage-specific responses to ecdysteroids during *Drosophila* and *Manduca* development. *Development* **120**, 219–234 (1994).
14. Riddiford, L. M., Cherbas, P. & Truman, J. W. Ecdysone receptors and their biological actions. *Vitam. Horm.* **60**, 1–73 (2000).
15. Agawa, Y. et al. *Drosophila* Blimp-1 is a transient transcriptional repressor that controls timing of the ecdysone-induced developmental pathway. *Mol. Cell. Biol.* **27**, 8739–8747 (2007).

16. Pak, M. D. & Gilbert, L. I. A developmental analysis of ecdysteroids during the metamorphosis of extit *Drosophila melanogaster*. *J. Liq. Chromatogr.* **10**, 2591–2611 (1987).
17. Rabinovich, D., Yaniv, S. P., Alyagor, I. & Schuldiner, O. Nitric oxide as a switching mechanism between axon degeneration and regrowth during developmental remodeling. *Cell* **164**, 170–182 (2016).
18. Shlyueva, D. et al. Hormone-responsive enhancer-activity maps reveal predictive motifs, indirect repression, and targeting of closed chromatin. *Mol. Cell* **54**, 180–192 (2014).
19. Cherbas, L., Hu, X., Zhimulev, I., Belyaeva, E. & Cherbas, P. EcR isoforms in *Drosophila*: testing tissue-specific requirements by targeted blockade and rescue. *Development* **130**, 271–284 (2003).
20. Xu, C. et al. Control of synaptic specificity by establishing a relative preference for synaptic partners. *Neuron* **103**, 865–877 (2019).
21. Nern, A., Zhu, Y. & Zipursky, S. L. Local N-cadherin interactions mediate distinct steps in the targeting of lamina neurons. *Neuron* **58**, 34–41 (2008).
22. Fisher, Y. E. et al. FlpStop, a tool for conditional gene control in *Drosophila*. *eLife* **6**, e22279 (2017).
23. Bender, M., Imam, F. B., Talbot, W. S., Ganetzky, B. & Hogness, D. S. *Drosophila* ecdysone receptor mutations reveal functional differences among receptor isoforms. *Cell* **91**, 777–788 (1997).
24. Yao, T. P. et al. Functional ecdysone receptor is the product of *EcR* and *Ultraspiracle* genes. *Nature* **366**, 476–479 (1993).
25. Schwabe, T., Borycz, J. A., Meinertzhagen, I. A. & Clandinin, T. R. Differential adhesion determines the organization of synaptic fascicles in the *Drosophila* visual system. *Curr. Biol.* **24**, 1304–1313 (2014).

26. White, K. P., Hurban, P., Watanabe, T. & Hogness, D. S. Coordination of *Drosophila* metamorphosis by two ecdysone-induced nuclear receptors. *Science* **276**, 114–117 (1997).
27. Takemura, S. et al. Synaptic circuits and their variations within different columns in the visual system of *Drosophila*. *Proc. Natl Acad. Sci. USA* **112**, 13711–13716 (2015).
28. Tan, L. et al. Ig superfamily ligand and receptor pairs expressed in synaptic partners in *Drosophila*. *Cell* **163**, 1756–1769 (2015).
29. Lee, C. W. & Peng, H. B. The function of mitochondria in presynaptic development at the neuromuscular junction. *Mol. Biol. Cell* **19**, 150–158 (2008).
30. Rangaraju, V., Lauterbach, M. & Schuman, E. M. Spatially stable mitochondrial compartments fuel local translation during plasticity. *Cell* **176**, 73–84 (2019).
31. Gowrisankaran, S. & Milosevic, I. Regulation of synaptic vesicle acidification at the neuronal synapse. *IUBMB Life* **72**, 568–576 (2020).
32. Özel, M. N., Langen, M., Hassan, B. A. & Hiesinger, P. R. Filopodial dynamics and growth cone stabilization in *Drosophila* visual circuit development. *eLife* **4**, e10721 (2015).
33. Peng, J. et al. *Drosophila* Fezf coordinates laminar-specific connectivity through cell-intrinsic and cell-extrinsic mechanisms. *eLife* **7**, e33962 (2018).
34. Akin, O. & Zipursky, S. L. Frazzled promotes growth cone attachment at the source of a Netrin gradient in the *Drosophila* visual system. *eLife* **5**, e20762 (2016).
35. Moffatt, N. S. C., Bruinsma, E., Uhl, C., Obermann, W. M. J. & Toft, D. Role of the cochaperone Tpr2 in Hsp90 chaperoning. *Biochemistry* **47**, 8203–8213 (2008).

36. Suzuki, M., Suzuki, H., Sugimoto, Y. & Sugiyama, Y. ABCG2 transports sulfated conjugates of steroids and xenobiotics. *J. Biol. Chem.* **278**, 22644–22649 (2003).
37. Alyagor, I. et al. Combining developmental and perturbation-Seq uncovers transcriptional modules orchestrating neuronal remodeling. *Dev. Cell* **47**, 38–52 (2018).
38. Uyehara, C. M. & McKay, D. J. Direct and widespread role for the nuclear receptor EcR in mediating the response to ecdysone in *Drosophila*. *Proc. Natl Acad. Sci. USA* **116**, 9893–9902 (2019).
39. Syed, M. H., Mark, B. & Doe, C. Q. Steroid hormone induction of temporal gene expression in *Drosophila* brain neuroblasts generates neuronal and glial diversity. *eLife* **6**, e26287 (2017).
40. Altmann, C. R. & Brivanlou, A. H. Neural patterning in the vertebrate embryo. *Int. Rev. Cytol.* **203**, 447–482 (2001).
41. Briscoe, J. & Small, S. Morphogen rules: design principles of gradient-mediated embryo patterning. *Development* **142**, 3996–4009 (2015).
42. Gaunt, S. J. *Hox* cluster genes and collinearities throughout the tree of animal life. *Int. J. Dev. Biol.* **62**, 673–683 (2018).
43. Miranda, A. & Sousa, N. Maternal hormonal milieu influence on fetal brain development. *Brain Behav.* **8**, e00920 (2018).
44. Akin, O. & Zipursky, S. L. Activity regulates brain development in the fly. *Curr. Opin. Genet. Dev.* **65**, 8–13 (2020).
45. Ting, C.-Y. et al. Photoreceptor-derived activin promotes dendritic termination and restricts the receptive fields of first-order interneurons in *Drosophila*. *Neuron* **81**, 830–846 (2014).
46. Mizumoto, K. & Shen, K. Two Wnts instruct topographic synaptic innervation in *C. elegans*. *Cell Rep.* **5**, 389–396 (2013).

47. Umemori, H., Linhoff, M. W., Ornitz, D. M. & Sanes, J. R. FGF22 and its close relatives are presynaptic organizing molecules in the mammalian brain. *Cell* **118**, 257–270 (2004).
48. Picelli, S. et al. Full-length RNA-seq from single cells using Smart-seq2. *Nat. Protoc.* **9**, 171–181 (2014).
49. Buenrostro, J. D., Giresi, P. G., Zaba, L. C., Chang, H. Y. & Greenleaf, W. J. Transposition of native chromatin for fast and sensitive epigenomic profiling of open chromatin, DNA-binding proteins and nucleosome position. *Nat. Methods* **10**, 1213–1218 (2013).
50. Ambrosini, G., Groux, R. & Bucher, P. PWMScan: a fast tool for scanning entire genomes with a position-specific weight matrix. *Bioinformatics* **34**, 2483–2484 (2018).
51. Butler, A., Hoffman, P., Smibert, P., Papalexi, E. & Satija, R. Integrating single-cell transcriptomic data across different conditions, technologies, and species. *Nat. Biotechnol.* **36**, 411–420 (2018).
52. Xu, S. et al. Interactions between the Ig-superfamily proteins DIP- $\alpha$  and Dpr6/10 regulate assembly of neural circuits. *Neuron* **100**, 1369–1384 (2018).
53. Santiago, I. J. et al. *Drosophila* Fezf functions as a transcriptional repressor to direct layer-specific synaptic connectivity in the fly visual system. *Proc. Natl Acad. Sci USA* **118**, e2025530118 (2021).

## Acknowledgements

We thank M. Y. Pecot (Harvard), N. Yamanaka (UC Riverside), D. L. Black (UCLA), E. M. De Robertis (UCLA), L. M. Riddiford (University of Washington) and J. W. Truman (Janelia Research Campus) for helpful discussions. We thank O. Schuldiner (Weizmann Institute of Science) and members of the Zipursky laboratory for feedback on the manuscript and M. Diaz de la Loza for help with figure illustrations. Figure 2 and Extended Data Fig. 3 were designed using resources from Flaticon.com. We would

like to specifically acknowledge J. Yoo (Zipursky laboratory) and R. Hodge (Jones laboratory, UCLA) for help with ATAC-seq library preparation and immunostaining. We also thank the BSCRC Sequencing Core (UCLA) and the TCGB core (UCLA) for help with library preparation and sequencing; the BSCRC FACS core (UCLA) and the Witte laboratory (UCLA) for assistance with FACS purification of lamina neurons; and IDRE Statistics Consulting (UCLA) and B. Balliu (UCLA) for assistance with the statistical analysis of data. Reagents provided by O. Akin (UCLA), F. A. Laski (UCLA), H. Wang (Duke-NUS), M. Y. Pecot (Harvard), C. S. Thummel (University of Utah) and G. J. Bashaw (University of Pennsylvania) and fly lines from the Bloomington *Drosophila* Stock Center were critical for this work. This work was supported by NIH T32-NS048004 Neurobehavioral Genetics Training Grant (S.J.), the Helen Hay Whitney Foundation (S.J.) and a Whitcome Fellowship (Y.L.). S.L.Z. is an investigator of the Howard Hughes Medical Institute.

## Author information

### Author notes

1. These authors contributed equally: Saumya Jain, Ying Lin

### Affiliations

1. Department of Biological Chemistry, University of California, Los Angeles, CA, USA

Saumya Jain, Ying Lin, Javier Valdes-Aleman, Samuel A. LoCascio, Parmis Mirshahidi, Brianna Parrington & S. Lawrence Zipursky

2. Howard Hughes Medical Institute, David Geffen School of Medicine, University of California, Los Angeles, CA, USA

Saumya Jain, Yerbol Z. Kurmangaliyev, Javier Valdes-Aleman & S. Lawrence Zipursky

3. Molecular Biology Institute, University of California, Los Angeles,  
CA, USA

Ying Lin

## Contributions

S.J., Y.L., Y.Z.K., J.V.-A. and S.L.Z. designed experiments. S.J., Y.L., P.M., S.A.L., J.V.-A. and B.P. acquired data. S.J., Y.L., J.V.-A. and Y.K. analysed the data. S.J., Y.L. and S.L.Z. wrote the manuscript with input from all co-authors.

## Corresponding author

Correspondence to [S. Lawrence Zipursky](#).

## Ethics declarations

## Competing interests

The authors declare no competing interests.

## Peer review

## Peer review information

*Nature* thanks the anonymous reviewers for their contribution to the peer review of this work.

## Additional information

**Publisher's note** Springer Nature remains neutral with regard to jurisdictional claims in published maps and institutional affiliations.

## Extended data figures and tables

## Extended Data Fig. 1 Developmental expression of EcR-pathway TFs and bulk ATAC-Seq data.

**a**, Images showing immunostaining for EcR-B1, EcR-A, Hr3 and Ftz-f1 at the indicated time points. Scale bar, 50 $\mu$ m. Note: EcR-A positive cells at 36hAPF are glia. **b**, Comparison of replicates of bulk RNA-Seq of L1 neurons at 40hAPF, 60hAPF and 72hAPF. Values given are Spearman correlation values (see [Methods](#)). **c**, Coverage tracks from L1 bulk RNA-Seq in the *EcR* locus at 40hAPF, 60hAPF and 72hAPF. *EcR-A*, *EcR-B1* and *EcR-B2* transcripts are shown, and *EcR-B1* specific exon is highlighted. **d**, Comparison of replicates of bulk ATAC-Seq data of L1 neurons at 40hAPF, 60hAPF and 72hAPF. Values shown are Spearman correlation values (see [Methods](#)). **e**, Comparison of change of ATAC-seq peak coverage (for regions with dynamic coverage over time) and change in expression of nearest gene.  $\log_2$ (fold change RPKM of nearest gene) vs  $\log_2$ (fold change ATAC-seq peak coverage) between 40hAPF and 60hAPF, and 60hAPF and 72hAPF. **f**, Pearson's correlation coefficient. **g**, p-values (two-sided Hypergeometric test) for enrichment of binding motifs of EcR-usp complex, Hr3 and Nr5a1 (mammalian homolog for Ftz-f1) amongst the following sets of ATAC-Seq peaks: peaks going down from 40hAPF to 60hAPF, peaks going up from 40hAPF to 60hAPF, peaks going down from 60hAPF to 72hAPF, peaks going up from 60hAPF to 72hAPF, and peaks invariant over time. Red: occurrence of motif is higher than expected by chance, blue: occurrence of motif is lower than expected by chance (see [Methods](#)).

## Extended Data Fig. 2 Analysis of morphology and DIP- $\beta$ expression with or without EcR<sup>DN</sup> expression.

**a**, Morphology of lamina neurons (L1-L5) in wildtype (WT) brains and upon pan-lamina expression (using 9B08 Gal4) of EcR<sup>DN</sup>, EcR<sup>DN</sup> + *EcR-B1* cDNA or *EcR* RNAi. Arrowhead in inset points to M3 medulla layer. Note: loss of arborization in M3 with EcR<sup>DN</sup> is likely due to loss of driver expression in L3 neurons (see Extended Data Fig. [2b](#)). **b**, Morphology of L3 neurons with or without EcR<sup>DN</sup> expression using an L3-specific driver

(*9D03 Gal4*). Note, in adults *9D03 Gal4* also labels some L2 neurons. This is not the case during development (see Extended Data Fig. 11f,g) **a, b**, Arrowhead points to M3 layer in the medulla. Scale bar, 50µm. **c**, Effect of EcR<sup>DN</sup> expression on morphology of T4/T5 neurons. Four layers in the lobula plate, a, b, c and d, are marked with red, yellow, blue and pink arrowheads, respectively. Cartoons of one T4 (purple neuron, top) and one T5 neuron (purple neuron, bottom) are shown to highlight wildtype morphology. Scale bar, 20 µm. **d**, *DIP-β* mRNA expression in L1-L5 neurons across development with or without pan-lamina expression of EcR<sup>DN</sup> (from scRNA-Seq based transcriptomic analyses, see Fig. 3, Extended Data Fig. 4, 5). \* significant difference between control and EcR<sup>DN</sup> (change in expression > 2-fold, p-value < 0.05, two-sided Wilcoxon rank sum test). **e**, Staining using anti-DIP-β antibody at the indicated time points in development with or without pan lamina expression of EcR<sup>DN</sup>. Inset shows the lamina neuropil. Arrowhead points to proximal lamina neuropil, positive for DIP-β staining at 72hAPF. Note that staining is largely absent from the lamina neuropil (yellow arrowheads). The level of *DIP-β* RNA is reduced in EcR<sup>DN</sup> at 48 but rises to near normal levels again at 72 h. We assume that the decrease in RNA leads to a lag in the accumulation of DIP-β protein. Scale bar, 50 µm. **f**, EcR-usp complex binding motif within the first intron of *DIP-β* (FDR < 10<sup>-7</sup>, see [Methods](#)). For number of replicates and exact p-values, see Supplementary Table 10.

### [Extended Data Fig. 3 Analysis of wiring defects in L5 with or without disruption of Ecdysone-pathway TFs.](#)

**a**, Different L5 arborization defects and their distributions under the given genotypes (see Fig. 2g). All transgenes are expressed using an L5-specific driver (pan-lamina driver is used for data in Fig. 2g). n = number of neurons. \*\*, p-value < 0.001. **b**, schematic showing the *EcR*<sup>FlpStop</sup> allele. FlpStop cassette is inserted in the first common intron of *EcR* (grey bar shows insertion site, *Mi{MIC}EcRMI05320*). Cells expressing Gal4, within which a stochastic, heat-shock FLP recombinase-mediated flipping of the cassette occurs, express tdTom. **c**, Ca<sup>2+</sup> response from Tm3 (measured using GCaMP6s) upon optogenetic stimulation of L5 with (blue line) or without (red line) EcR<sup>DN</sup> expression in L5. GCaMP6s responses were

measured in 3 regions of interest (ROI). ROI 1, ROI 2 and ROI 3 span medulla layers M1, M5 and M10 respectively. (WT, 19 animals; EcR<sup>DN</sup>, 17 animals.) **d**, Ca<sup>2+</sup> response from Dm13 and Dm18 (common LexA driver used yields expression in both Dm13 and Dm18, see Supplementary Table 1) upon optogenetic stimulation of L5 with (blue line) or without (red line) EcR<sup>DN</sup> expression in L5. ROI 1 spans M1 and measures response from Dm18. ROI 2 spans M5 and measures response from Dm13. (WT, 19 animals; EcR<sup>DN</sup>, 17 animals.) Note: weak response from Dm18 upon stimulation of L5 irrespective of condition. **c, d**, Amplitude of relative peak response for each condition is quantified. There is no significant difference between WT and EcR<sup>DN</sup> for any comparison shown here. For Dm13 response, see Fig. 2j. For all box-plots, solid line depicts median, while the upper and lower bounds of the box depict the third and first quantile of the data spread respectively. p-value from two-sided Student's t-test. For number of replicates and exact p-values, see Supplementary Table 10.

### **Extended Data Fig. 4 Approach for identification of EcR and Hr3 targets using scRNA-Seq.**

**a**, Scheme for scRNA-Seq based transcriptomic analysis of WT and mutant lamina neurons (see Kurmangaliyev *et al*<sup>11</sup>. and methods). GFP vs forward scatter 2-D plot showing criteria used to enrich for lamina neurons by FACS is shown on the right. ‘Cells’ highlighted in purple were excluded despite being GFP+ due to their small size. **b**, tSNE plots showing WT L1-L5 clusters at 24, 36, 48, 60, 72, 84 and 96 hAPF (Adult). **c**, Log(expression) of previously identified lamina neuron type-specific genes in L1-L5 clusters identified at each time point over development (see Tan *et al*<sup>32</sup>.). **d**, Comparison of lamina neuron transcriptomes generated by scRNA-Seq in this study and by scRNA-Seq in Kurmangaliyev *et al*. Values given are Spearman correlation values. For all box-plots, solid line depicts median, while the upper and lower bounds of the box depict the third and first quantile of the data spread respectively.

### **Extended Data Fig. 5 scRNA-Seq-based analysis of WT and EcR<sup>DN</sup> expressing lamina neurons.**

**a**, tSNE plots showing WT and EcR<sup>DN</sup>-expressing L1-L5 clusters at 24, 48, 72 and 96 hAPF (Adult). **b**, Number of genes up or downregulated in EcR<sup>DN</sup> in L1-L5 neurons. **c**, Expression of *EcR* in EcR<sup>DN</sup>-expressing lamina neurons at 48hAPF normalized to mean expression of *EcR* in wildtype cells at 48hAPF (done separately for each lamina neuron-type). Red dots, mean of data spread. Increase in *EcR* expression in EcR<sup>DN</sup>-expressing cells over wildtype is expected to be due to the expression of the *EcR<sup>DN</sup>* transgene. Note the poor induction of *EcR<sup>DN</sup>* in L2 neurons. p-value from two-sided Student's t-test (with Bonferroni correction for multiple comparisons) are stated in the figure for comparison between L2 and other lamina neuron-types. The difference between *EcR<sup>DN</sup>* expression in L2 and L3 neurons is not significant likely due to the low cell numbers of EcR<sup>DN</sup>-expressing L3 neurons. **d**, Volcano plots showing significant gene expression changes in L1-L5 neurons throughout development. Red dots: fold change > 2 and p-value < 0.05. **e**, Log(expression) of lamina neuron-type specific TFs with (blue) or without (red) EcR<sup>DN</sup>. Note no change in expression of TFs ± EcR<sup>DN</sup>. **f**, Log(expression) of TFs in the Ecdysone-pathway in WT (red lines) and EcR<sup>DN</sup>-expressing (blue lines) L1-L5 neurons. \*, p-value < 0.05, fold change > 2. For all statistical tests, see Supplementary Table 7 for number of cells for each cell-type, time-point and condition. For all box-plots, solid line depicts median, while the upper and lower bounds of the box depict the third and first quantile of the data spread respectively. **d, f**, p-value from two-sided Wilcoxon rank sum test.

### Extended Data Fig. 6 scRNA-Seq-based analysis of *w* RNAi and *EcR* RNAi expressing lamina neurons.

**a**, tSNE plots showing *w* RNAi and *EcR* RNAi-expressing L1-L5 clusters at 24, 48, 72 and 96 hAPF (Adult). **b**, Number of genes up or downregulated in *EcR* RNAi in L1-L5 neurons. **c**, Image showing optic lobe (top) stained using an antibody targeting all EcR isoforms (grey) at 24hAPF. Box with green dotted outline marks the region containing lamina neuron cell-bodies. This region is magnified in bottom two panels. Lamina neurons are labeled in magenta. Scale bar, 50 µm. **d**, Volcano plots showing significant gene expression changes in L1-L5 neurons throughout development. Red dots: fold change > 2 and p-value < 0.05. **e**, Log(expression) of lamina neuron-

type specific TFs with (blue) or without (red) *EcR* RNAi. Note no change in expression of TFs  $\pm$  *EcR* RNAi. **f**, Log(expression) of TFs in the Ecdysone-pathway in WT (red lines) and *EcR* RNAi-expressing (blue lines) L1-L5 neurons. \*, p-value  $< 0.05$ , fold change  $> 2$ . For all statistical tests, see Supplementary Table 8 for number of cells for each cell-type, time-point and condition. For all box-plots, solid line depicts median, while the upper and lower bounds of the box depict the third and first quantile of the data spread respectively. **d, f**, p-value from two-sided Wilcoxon rank sum test. For number of replicates and exact p-values, see Supplementary Table 10.

### Extended Data Fig. 7 scRNA-Seq-based analysis of *w* RNAi and *Hr3* RNAi expressing lamina neurons.

**a**, tSNE plots showing *w* RNAi and *Hr3* RNAi-expressing L1-L5 clusters at 24, 48, 72 and 96 hAPF (Adult). **b**, Number of genes up or downregulated in *Hr3* RNAi in L1-L5 neurons. **c**, Image showing optic lobe (top) stained using an antibody targeting *Hr3* (grey) at 24hAPF. Box with green dotted outline marks the region containing lamina neuron cell-bodies. This region is magnified in bottom two panels. Lamina neurons are labeled in magenta. Scale bar, 50  $\mu$ m. **d**, Volcano plots showing significant gene expression changes in L1-L5 neurons throughout development. Red dots: fold change  $> 2$  and p-value  $< 0.05$ . **e**, Log(expression) of lamina neuron-type specific TFs with (blue) or without (red) *Hr3* RNAi. Note no change in expression of TFs  $\pm$  *Hr3* RNAi. **f**, Log(expression) of TFs in the Ecdysone-pathway in WT (red lines) and *Hr3* RNAi-expressing (blue lines) L1-L5 neurons. \*, p-value  $< 0.05$ , fold change  $> 2$ . For all statistical tests, see Supplementary Table 9 for number of cells for each cell-type, time-point and condition. For all box-plots, solid line depicts median, while the upper and lower bounds of the box depict the third and first quantile of the data spread respectively. **d, f**, p-value from two-sided Wilcoxon rank sum test. For number of replicates and exact p-values, see Supplementary Table 10.

### Extended Data Fig. 8 Comparison of genes affected by EcR<sup>DN</sup>, EcR RNAi and Hr3 RNAi.

**a**, Top, Venn diagram showing overlap between genes downregulated by EcR<sup>DN</sup> and *EcR* RNAi across all time points and lamina neuron-types. Below,  $\log_2(\text{normalized expression in } w \text{ RNAi}/\text{EcR RNAi})$  vs  $\log_2(\text{normalized expression in WT/EcR}^{\text{DN}})$  for L1-L5 neurons throughout development. Correlation coefficient, R, is given for comparisons where p < 0.05. **b**, Top, Venn diagram showing overlap between genes downregulated by EcR<sup>DN</sup> and *Hr3* RNAi across all time points and lamina neuron-types. Below,  $\log_2(\text{normalized expression in } w \text{ RNAi}/\text{Hr3 RNAi})$  vs  $\log_2(\text{normalized expression in WT/EcR}^{\text{DN}})$  for L1-L5 neurons throughout development. Correlation coefficient, R, is given for comparisons where p < 0.05. **c**, Cell-type variability vs Temporal dynamicity plot for *EcR* RNAi-affected genes (fold change > 2, p-value < 0.05). Cell-type Specific (blue) and Common (red) targets are shown. Darker colors: genes reduced in *EcR* RNAi, lighter colors: genes increased in *EcR* RNAi. **d**, Cell-type variability vs Temporal dynamicity plot for *Hr3* RNAi-affected genes (fold change > 2, p-value < 0.05). Cell-type Specific (blue) and Common (red) targets are shown. Darker colors: genes reduced in *Hr3* RNAi, lighter colors: genes increased in *Hr3* RNAi. **e**, Maximum change in expression of Ecdysone-pathway TFs in L1-L5 neurons with EcR<sup>DN</sup>, *EcR* RNAi and *Hr3* RNAi. Note that *EcR* RNAi often has weaker effect on TF expression as compared to EcR<sup>DN</sup>. p-value from two-sided Wilcoxon rank sum test.

### Extended Data Fig. 9 Clusters of genes most affected by EcR<sup>DN</sup>, EcR RNAi and Hr3 RNAi.

All genes expressed in L1-L5 neurons (done separately for each cell-type) were clustered into groups (using k-means clustering) based on their expression dynamics (see [Methods](#)). Clusters that show maximum upregulation or downregulation with EcR<sup>DN</sup> are shown in **a – c** (clusters are indicated in numbers above each graph). Also shown are clusters unchanged by EcR<sup>DN</sup>. For each panel: left, light grey lines, relative expression of all genes in the cluster; black line, mean of relative expression of all genes in the cluster. Right, red line, mean relative expression in control; blue line, mean relative expression with perturbation. Shades are SEM. d, examples of dynamic wiring genes that are not affected by EcR<sup>DN</sup>.

**d**, Plots showing maximum change in expression [ $\log_2(\text{WT}/\text{EcR}^{\text{DN}})$ ] caused by EcR<sup>DN</sup> vs the temporal dynamicity of the gene (calculated separately for each cell-type). Shown in red are wiring genes. Colored region on the plot represents genes not affected by EcR<sup>DN</sup>. Note many genes including wiring genes (especially in L1, L3 and L4) with high temporal dynamicity scores that are not affected by EcR<sup>DN</sup>.

### Extended Data Fig. 10 Families of genes affected by Ecdysone-pathway and verification using *ex vivo* culture of pupal brain.

**a**, Relative WT expression (left), change in expression with EcR<sup>DN</sup> (center), and change in expression with *Hr3* RNAi (right) shown as heat maps for all genes expressed in L3-L5 neurons belonging to the specified gene categories at 48hAPF. Examples of genes belonging to the Dpr family, Side-Beat family and cell-type specific transcription factors are shown separately. **b**, Expression of some genes involved in ATP synthesis and vacuolar ATPase biology are shown with and without EcR<sup>DN</sup> in L1-L5 neurons across development. \*, fold change between WT and EcR<sup>DN</sup> > 2, p-value < 0.05. Note: expression in adults is not significantly affected by EcR<sup>DN</sup>. p-value from two-sided Wilcoxon rank sum test. **c**, Left, schematic of experimental setup (see [Methods](#)). Briefly, brains are dissected at 22hAPF then incubated for 26h in media  $\pm$  20E (20 HydroxyEcdysone, active form of Ecdysone). Right, optic lobes stained for EcR-B1, Hr3 and Ftz-f1 cultured *ex vivo*  $\pm$  20E. Scale bar, 50 $\mu$ m. **d**, Left, Staining for CARPB and *dpr6* reporters (reporter lines, see [Methods](#)) in lamina neuron cell-bodies  $\pm$  20E. Scale bar, 10 $\mu$ m. Right, CARPB and *dpr6* expression with (blue) or without (red) EcR<sup>DN</sup>. \*, fold change between WT and EcR<sup>DN</sup> > 2, p-value < 0.05, two-sided Wilcoxon rank sum test. Note: *dpr6* expression is unchanged in L2 with pan-lamina expression of EcR<sup>DN</sup>, however staining in brains cultured *ex vivo* without 20E in the medium shows reduced protein expression in L2 (Bab2 positive cell-bodies). This is consistent with weak activity of the pan-lamina driver (*9B08 Gal4*) in L2 at 48hAPF leading to ineffective inhibition of the Ecdysone-pathway (see Extended Data Fig. [5c](#)). For number of replicates and exact p-values, see Supplementary Table [10](#).

## Extended Data Fig. 11 Genes expressed in L3 required for R8 wiring and model figure.

**a**, R8 presynaptic sites (Brp, green)  $\pm$  EcR<sup>DN</sup> expression in L3. Right, quantification of Brp puncta number under the conditions shown. Scale bar, 5  $\mu$ m. (WT, 58 neurons; EcR<sup>DN</sup>, 47 neurons). **b**, Total number of presynaptic sites (Brp puncta) in R8 neurons with WT, NetB overexpressing, or EcR<sup>DN</sup> and NetB-expressing L3 neurons. NetB overexpression is unable to rescue the reduction in R8 presynaptic sites seen with expression of EcR<sup>DN</sup> in L3 neurons. **a, b**, p-value (two-sided Student's t-test) is given. **c, d**, Distributions of R8 axon terminal depth in *w* RNAi (red) or with expression of other RNAi (as shown, blue) in L3 neurons. p-values (two-sided Kolmogorov-Smirnov test) are given and number of neurons/ conditions are given. ns = Not significant. **c**, RNAi against TFs in the Ecdysone-pathway. **d**, Results from RNAi screen showing genes that did not significantly increase R8 axon depth. Note that *nrm* RNAi yields a subtle reduction in R8 axon depth. Numbers of neurons/ condition are given. For all box-plots, solid line depicts median, while the upper and lower bounds of the box depict the third and first quantile of the data spread respectively. **e**, Expression of *NetA* and *NetB* in L3 with (blue) or without (red) EcR<sup>DN</sup> expression. \*, fold change between WT and EcR<sup>DN</sup>  $>$  2, p-value  $<$  0.05, two-sided Wilcoxon rank sum test. **f**, Staining using anti-NetB antibody (magenta) at the indicated times in development. Marker for M6 medulla layer (24B10, grey) and L3 neurons labeled with GFP (green) are shown. **g**, Staining using anti-NetB antibody (magenta)  $\pm$  EcR<sup>DN</sup> expression only in L3. L3 neurons labeled with GFP (green) are shown. **f, g**, Scale bar, 50  $\mu$ m. Yellow arrowhead, M3 medulla layer. For number of replicates and exact p-values, see Supplementary Table 10. **h**, Model for temporal regulation of wiring genes. Temporally-regulated TFs (grey triangle) controlled by various external cues such as neural activity, cell-cell interactions and endocrine signals (e.g. Ecdysone) work together with cell-type specific TFs (red and blue proteins). Their combined activity controls the timing and cell-type specificity of wiring gene (such as the ones coding for cell recognition molecules) expression.

## Supplementary information

## **Supplementary Information**

This file contains Supplementary Fig. 1.

## **Reporting Summary**

### **Supplementary Table 1**

Fly strains used in this study.

### **Supplementary Table 2**

Temporal dynamicity and cell type variability scores.

### **Supplementary Table 3**

Wiring genes.

### **Supplementary Table 4**

Gene Ontology and Reactome analyses.

### **Supplementary Table 5**

L1 bulk ATAC-seq data.

### **Supplementary Table 6**

scRNA-seq data for wild-type lamina neurons.

### **Supplementary Table 7**

scRNA-seq data for wild-type versus EcR<sup>DN</sup>-expressing lamina neurons.

### **Supplementary Table 8**

scRNA-seq data for wild-type versus *EcR* RNAi-expressing lamina neurons.

## **Supplementary Table 9**

scRNA-seq data for wild-type versus *Hr3* RNAi-expressing lamina neurons.

## **Supplementary Table 10**

Number of neurons and animals per condition and exact *P* values for all comparisons described in this study.

## **Source data**

### **Source Data Fig. 2**

### **Source Data Fig. 4**

## **Rights and permissions**

### **Reprints and Permissions**

## **About this article**

### **Cite this article**

Jain, S., Lin, Y., Kurmangaliyev, Y.Z. *et al.* A global timing mechanism regulates cell-type-specific wiring programmes. *Nature* **603**, 112–118 (2022). <https://doi.org/10.1038/s41586-022-04418-5>

- Received: 18 September 2020
- Accepted: 10 January 2022

- Published: 23 February 2022
- Issue Date: 03 March 2022
- DOI: <https://doi.org/10.1038/s41586-022-04418-5>

## Share this article

Anyone you share the following link with will be able to read this content:

[Get shareable link](#)

Sorry, a shareable link is not currently available for this article.

[Copy to clipboard](#)

Provided by the Springer Nature SharedIt content-sharing initiative

---

This article was downloaded by **calibre** from <https://www.nature.com/articles/s41586-022-04418-5>

| [Section menu](#) | [Main menu](#) |

- Article
- Open Access
- [Published: 23 February 2022](#)

# A biophysical account of multiplication by a single neuron

- [Lukas N. Groschner](#) ORCID: [orcid.org/0000-0002-4325-0232<sup>1</sup>](https://orcid.org/0000-0002-4325-0232)
- [Jonatan G. Malis](#) ORCID: [orcid.org/0000-0002-1636-6248<sup>1</sup>](https://orcid.org/0000-0002-1636-6248)
- [Birte Zuidinga](#) ORCID: [orcid.org/0000-0002-8214-3747<sup>1</sup>](https://orcid.org/0000-0002-8214-3747) &
- [Alexander Borst](#) ORCID: [orcid.org/0000-0001-5537-8973<sup>1</sup>](https://orcid.org/0000-0001-5537-8973)

*Nature* volume 603, pages 119–123 (2022)

- 10k Accesses
- 169 Altmetric
- [Metrics details](#)

## Subjects

- [Biophysical models](#)
- [Motion detection](#)
- [Neural circuits](#)

## Abstract

Nonlinear, multiplication-like operations carried out by individual nerve cells greatly enhance the computational power of a neural system<sup>1,2,3</sup>, but our understanding of their biophysical implementation is scant. Here we pursue this problem in the *Drosophila melanogaster* ON motion vision circuit<sup>4,5</sup>, in which we record the membrane potentials of direction-selective T4 neurons and of their columnar input elements<sup>6,7</sup> in response to visual and pharmacological stimuli *in vivo*. Our electrophysiological measurements and conductance-based simulations provide evidence for a passive supralinear interaction between two distinct types of synapse on T4 dendrites. We show that this multiplication-like nonlinearity arises from the

coincidence of cholinergic excitation and release from glutamatergic inhibition. The latter depends on the expression of the glutamate-gated chloride channel GluCl $\alpha$ <sup>8,9</sup> in T4 neurons, which sharpens the directional tuning of the cells and shapes the optomotor behaviour of the animals. Interacting pairs of shunting inhibitory and excitatory synapses have long been postulated as an analogue approximation of a multiplication, which is integral to theories of motion detection<sup>10,11</sup>, sound localization<sup>12</sup> and sensorimotor control<sup>13</sup>.

[Download PDF](#)

## Main

Motion vision in insects represents a textbook example<sup>14</sup> of nonlinear signal processing by a single neuron. Each photoreceptor of the compound eye captures changes in light intensity, but it is blind to the direction of motion. To compute visual motion, the signals of at least two neighbouring photoreceptors must be processed nonlinearly by a downstream local motion detector (Fig. 1a). In the Hassenstein–Reichardt model<sup>10</sup>, multiplication ensures detector output only if the two signals coincide. The coincidence results from asymmetric temporal filtering of the input signals and the sequence of photoreceptor activation, one after the other, as it unfolds during visual motion in the detector’s preferred direction (PD). The Barlow–Levick model of motion vision, which was first proposed for the rabbit retina<sup>15</sup>, uses a divisive nonlinearity to cancel responses to motion in the detector’s null direction (ND).

**Fig. 1: Receptive fields of direction-selective T4 neurons and their presynaptic partners.**

---

 **figure 1**

**a**, The circuit architecture for visual ON motion detection involving a multiplicative interaction ( $\times$ ) between synapses of glutamatergic Mi9 and synapses of cholinergic Mi1/Tm3 neurons and a divisive interaction ( $\div$ ) between synapses of Mi1/Tm3 and synapses of GABAergic C3/Mi4 neurons. Non-columnar inputs from T4, TmY15 and CT1 neurons are shaded. The dashed lines show the column borders. **b**, A T4 dendrite

with subcellular segregation of glutamatergic (green), cholinergic (red) and GABAergic synapses (blue). Data from ref. [7](#). **c**, Targeted patch-clamp recording *in vivo* during visual stimulation. **d**, Average spatial receptive fields of input neuron classes obtained by reverse correlation (corr.) of membrane potentials and white-noise stimuli. AU, arbitrary units. **e**, The average spatial receptive fields of T4 neurons (left) representing cross-sections of the spatiotemporal receptive field (right) at two time points (dashed lines). **f**, Exemplary membrane potential recordings of T4 neurons in response to visual stimulation with square-wave gratings moving in the directions indicated on top. **g**, Directional (left) and frequency tuning (right) of T4 neurons based on the change in membrane potential ( $\Delta V_m$ ) in response to visual stimulation with square-wave gratings. Data are mean  $\pm$  s.e.m.  $n$  values indicate the number of cells.

### Source data

The visual system of *Drosophila* is compatible with both models (Fig. [1a](#)). T4 neurons, which are functionally equivalent to the nonlinear stages of both models, respond selectively to luminance increments moving in one out of four cardinal directions<sup>5</sup>. Their direction selectivity arises in the second optic neuropil<sup>5,16,17</sup>, where spatial information is preserved in a retinotopic columnar organization<sup>18</sup>. Each T4 dendrite innervates approximately seven columns—at least three in a row along the neuron’s PD<sup>6</sup> (Fig. [1b](#))—and, therefore, samples from multiple adjacent points in visual space. Recent studies<sup>6,7</sup> identified most—if not all—columnar medulla intrinsic (Mi), transmedullary (Tm) and centrifugal (C) neurons that form synapses at distinct locations along a T4 neuron’s dendrite: glutamatergic Mi9 neurons at the distal branches (where stimuli moving in the T4 cell’s PD first affect its membrane potential), cholinergic Tm3 and Mi1 neurons at the centre, and GABAergic Mi4 and C3 neurons at the proximal segment (Fig. [1b](#)). The emerging three-legged circuit motif involves a divisive interaction between cholinergic and GABAergic synapses and a multiplicative interaction between glutamatergic and cholinergic synapses<sup>17,19,20,21,22</sup> (Fig. [1a,b](#)). However, crucial assumptions concerning the multiplicative term of this model<sup>21</sup> remain untested: (1) the multiplication-like synaptic interaction involves disinhibition; (2) the supralinearity arises from the T4 cells’ passive membrane properties; and (3) it sharpens the directional tuning of the neurons and the optomotor acuity of the animal.

The first assumption, that multiplication requires release from inhibition, hinges on the conditions that the signals carried by glutamatergic Mi9 neurons are of opposite polarity to those of the other input elements and that glutamate controls the input resistance of T4 neurons through shunting inhibition<sup>23</sup>. Direct measurements of input resistance and membrane voltage are possible only through patch-clamp experiments, which we conducted *in vivo* in tethered flies, guided by cell-type-specific expression of green fluorescent protein (GFP; Extended Data Fig. [1a](#)). We recorded the membrane

potentials of T4 cells and of their presynaptic partners while projecting a 60 Hz spatiotemporal binary white-noise stimulus with a pixel size of  $2.8^\circ$  onto the fly's eye. To characterize the receptive fields of the neurons, we cross-correlated the luminance of each pixel with the recorded voltage (Fig. 1c–e and Extended Data Fig. 1b). We found that the membrane potentials of Tm3, Mi1, Mi4 and C3 neurons were positively correlated with luminance, whereas those of Mi9 neurons were anticorrelated (Fig. 1d). The negative correlation was due to a rapid hyperpolarization following increments in luminance, as opposed to a possible depolarization in response to luminance decrements (Extended Data Fig. 2). Thus, the Mi9 neuron maintains a degree of continuous activity in darkness that ceases abruptly when the centre of its receptive field is stimulated by light. Yet, while the delayed inhibition mediated by GABAergic inputs<sup>24</sup> was clearly discernible in the spatiotemporal receptive fields of direction-selective T4 neurons (Fig. 1e–g), the contribution of Mi9 neurons was not immediately apparent.

To test the effect of glutamate—and, indirectly, that of Mi9—on T4 neurons, we applied the neurotransmitter directly to T4 dendrites (Fig. 2a). Pneumatic ejection of glutamate transiently hyperpolarized T4 cells by  $3.72 \pm 0.61$  mV (mean  $\pm$  s.e.m.; Fig. 2b,c). The mild hyperpolarization was paralleled by a 25.27% decrease in input resistance, which was fully reversible. Repeated applications of glutamate enabled us to toggle T4 cells between states of high and low resistance (Fig. 2d,e). Targeted RNA interference (RNAi) with transcripts of *GluCl $\alpha$* <sup>8</sup>, the most highly expressed glutamate receptor gene in T4 neurons<sup>25,26,27,28</sup>, blocked glutamate-gated whole-cell currents (Fig. 2f) and abolished the effects of glutamate on membrane potential and input resistance (Fig. 2b,c,e), while leaving the morphology of T4 cells intact (Extended Data Fig. 3). Importantly, post-transcriptional silencing of *GluCl $\alpha$*  caused an average 11.94 mV depolarization of the resting membrane potential (Fig. 2g) and an increase in input resistance from  $5.28 \pm 0.12$  to  $6.70 \pm 0.16$  G $\Omega$  (mean  $\pm$  s.e.m.; Fig. 2h), measured under dark conditions. This speaks for a persistent release of glutamate in the dark that keeps GluCl $\alpha$  channels open and clamps the membrane potential of T4 neurons close to the equilibrium potential of chloride—a GluCl $\alpha$ -mediated short circuit that curtails any excitation, unless glutamatergic Mi9 neurons are switched off first.

**Fig. 2: Glutamate controls T4 neuron excitability through GluCl $\alpha$ .**

---

 **figure 2**

**a**, Glutamate application during whole-cell recording. **b**, Membrane potential traces of exemplary T4 neurons in response to 100 ms glutamate pulses (Glu) in flies expressing *GFP* (black; T4 > *GFP*, full genotypes are provided in the [Methods](#)) or *GFP* + *GluCla*<sup>RNAi</sup> (teal; T4 > *GluCla*<sup>RNAi</sup>) under T4-cell-specific GAL4 control. Ten technical replicates per genotype are shown. **c**, The average membrane potentials of T4 neurons expressing *GFP* (black) or *GFP* + *GluCla*<sup>RNAi</sup> (teal) before and after glutamate application (green). A significant effect of glutamate, determined using a two-tailed paired Student's *t*-test, is indicated;  $*P = 2.1 \times 10^{-6}$ . The light lines represent individual cells. The dark lines represent the mean  $\pm$  s.e.m. **d**, Voltage responses of one exemplary T4 neuron to current steps (top) without (left) and with (right) prior glutamate application. **e**, Input resistances of T4 neurons expressing *GFP* (black) or *GFP* + *GluCla*<sup>RNAi</sup> (teal) during (+) and in between (-) repeated glutamate

applications. The light lines represent individual cells. The dark lines represent the mean  $\pm$  s.e.m. Two-way repeated-measures analysis of variance (ANOVA) detected a significant effect of glutamate ( $P = 3.5 \times 10^{-12}$ ) and a significant glutamate  $\times$  genotype interaction ( $P = 1.6 \times 10^{-11}$ ). **f**, Average whole-cell currents in response to 100 ms glutamate pulses at different voltages (left and middle) and current–voltage relationships (right) of T4 neurons expressing *GFP* (black) or *GFP + GluCl $\alpha$ <sup>RNAi</sup>* (teal). Data are mean  $\pm$  s.e.m. **g, h**, Resting membrane potentials (**g**) and input resistances (**h**) of T4 neurons expressing *GFP* (black) or *GFP + GluCl $\alpha$ <sup>RNAi</sup>* (teal) measured under dark conditions. Significant differences between genotypes, determined using two-tailed Mann–Whitney *U*-tests, are indicated; \* $P = 3.4 \times 10^{-23}$  (**g**), \* $P = 4.8 \times 10^{-11}$  (**h**). *n* values indicate the number of cells.

### Source data

To break down the precise temporal sequences of synaptic signals evoked by visual stimulation, we obtained membrane potential recordings while moving contrast edges through the T4 neuron’s receptive field in its PD and ND (Fig. 3). Bright ON and dark OFF edges travelling at a velocity of  $30^\circ \text{ s}^{-1}$  revealed distinct, fingerprint-like signatures of electrical activity. To explain these signatures in terms of their underlying synaptic conductances, we subjected the five columnar input elements of T4 cells to an identical set of stimuli (Fig. 3a). Our reconstructions of the receptive fields of the cells (Extended Data Fig. 1b) enabled a post hoc alignment of their responses, which we used to recreate the direction-dependent input sequences that are expected to shape the voltage responses of a T4 cell (Fig. 3b,c). With all input signals and the respective reversal potentials at hand (Extended Data Fig. 4a–d), we simulated the electrical equivalent circuit of a passive single-compartment T4 neuron (Fig. 3b,c and Extended Data Fig. 5a). Measured membrane voltages of presynaptic neurons were transformed into postsynaptic conductance values using two free parameters per neuron: a gain (that is, synaptic weight) and a threshold below which no transmission occurred. The T4 neurons’ electrically compact morphology (Extended Data Fig. 4e,f) led us to neglect the membrane capacitance. After estimating the model parameters on the basis of a least-squares fit to the average voltage responses of T4 neurons, we quantified parameter uncertainty using an artificial neural network<sup>29</sup>. Examination of the full range of parameter combinations compatible with our measurements confirmed the estimated values, which fell within regions of high conditional probability (Extended Data Fig. 6). In agreement with our second assumption, the voltage responses of T4 neurons to all four stimuli were captured by our passive conductance-based model (Fig. 3b,c), which naturally joins an excitatory and an inhibitory signal in a supralinear manner. While, in a passive membrane, two excitatory inputs are bound to combine sublinearly (Extended Data Fig. 5b), the coincidence of an excitatory input with the release from an inhibitory one will almost invariably yield a supralinear response<sup>1,21</sup> (Extended Data Fig. 5c). Exceptions are rare and can occur only under

conditions in which the reversal potential of the excitatory current is closer to the leak reversal potential than that of the inhibitory current (Extended Data Fig. 5d,e and [Supplementary Equations](#)). For ON edge motion in the PD, a brief interval of minimal inhibitory conductance—a window of opportunity<sup>30</sup>—opened up (Fig. 3b). The transient lack of inhibition led to the amplification of excitatory inputs from Mi1 and Tm3 neurons during the upstroke of the T4 cell’s voltage trajectory (Fig. 3b and Extended Data Fig. 7). Intuitively, this can be explained by the coincident drop in overall conductance or, in other words, the increase in input resistance.

**Fig. 3: Conductance-based T4 neuron model.**

 figure 3



**a**, Aligned membrane voltage ( $V_m$ ) responses of columnar T4 input neurons to ON and OFF edges moving at  $30^\circ \text{ s}^{-1}$ . Time course of normalized light intensity at the receptive field centre is shown at the top. The light lines represent individual cells. The dark lines represent the mean. **b, c**, Conductance-based biophysical simulations of the membrane voltage ( $V_m$ ) of a T4 neuron in response to ON (b) and OFF (c) edge motion. Input signals were time-shifted, as evident from light intensities at receptive field centres (top), to simulate visual motion in the T4 neuron’s PD and ND, respectively. The voltage signals of presynaptic neurons were converted into

normalized postsynaptic conductances ( $g/g_{\text{leak}}$ , centre) using a threshold and gain obtained by fitting the model (dashed pink) to measured T4 voltage responses (solid black, bottom). Conductance values are mean and area under curve. Voltage values are mean  $\pm$  s.e.m. The arrowhead in **b** marks the window of opportunity when a minimum of shunting inhibition (green/blue) coincides with excitation (red).  $n$  values indicate the number of cells.

#### Source data.

Direct evidence for the predicted increase in resistance (Extended Data Fig. 8) was obtained using current-clamp experiments. We took advantage of each T4 neuron's stereotyped responses to moving edges and presented the fly with repeated episodes of identical visual stimulation. Varying the holding current in between episodes enabled us to obtain time-locked measurements of membrane potential and resistance (Fig. 4 and Extended Data Fig. 9). For ON edges moving in the neuron's PD, the input resistance revealed a distinct peak that preceded the depolarizing voltage excursion and amounted to approximately 147% of the initial resistance (Fig. 4). Under all other conditions, the T4 cell experienced, if anything, a dip in excitability (Fig. 4). RNAi-mediated silencing of *GluCl $\alpha$*  pre-empted the increase in that the resistance of *GluCl $\alpha$* -deficient T4 neurons at the baseline was already equivalent to the peak values reached by wild-type neurons (Fig. 4). Owing to the shift in resting potential towards the reversal potential of acetylcholine-induced currents, depletion of *GluCl $\alpha$*  also reduced the membrane potential response amplitude from  $18.10 \pm 0.77$  mV in wild-type T4 neurons to  $13.63 \pm 1.05$  mV in *GluCl $\alpha$* <sup>RNAi</sup>-expressing T4 neurons (mean  $\pm$  s.e.m.;  $n = 53$  and  $n = 30$  cells, respectively;  $P = 0.0008$ , two-tailed Mann–Whitney *U*-test).

**Fig. 4: A *GluCl $\alpha$* -dependent input resistance peak.**

 figure 4



**a**, Simultaneously measured membrane potentials ( $V_m$ , solid lines) and input resistances ( $R_{in}$ , dashed lines) of T4 neurons expressing *GFP* (black) or *GFP + GluCl $\alpha$ <sup>RNAi</sup>* (teal) in response to ON (top) and OFF (bottom) edges moving at  $30^\circ \text{ s}^{-1}$  in the neurons' PD and ND. Data are mean  $\pm$  s.e.m.  $n$  values indicate the number of cells. **b**, The average membrane potential ( $V_m$ ) as a function of input resistance ( $R_{in}$ ) of T4 neurons shown in **a** in response to ON (top) and OFF (bottom) edges moving in the PD (left) and ND (right). The arrowheads mark the input resistance peak.

#### Source data

The ability to restrict the arithmetic repertoire of T4 neurons by interfering with the abundance of *GluCl $\alpha$*  enabled us to test the prediction that multiplication sharpens directional tuning. We moved bright edges at a speed of  $30^\circ \text{ s}^{-1}$  in 36 evenly spaced directions while recording the membrane potentials of GFP-labelled wild-type and *GluCl $\alpha$ <sup>RNAi</sup>*-expressing T4 neurons (Fig. 5a–c). RNAi targeting transcripts of *Nmdar1*, which encodes a glutamate-gated cation channel with negligible expression in T4 cells<sup>25,26,27,28</sup>, was used as an additional control. Silencing *GluCl $\alpha$*  in T4 cells *in vivo* replicated the effect of silencing Mi9 neurons *in silico*—it broadened the directional tuning curve (Fig. 5a). Response amplitudes of wild-type and *Nmdar1<sup>RNAi</sup>*-expressing neurons declined steeply with increasing angular distance from PD, to 72.97% and 72.74% at a deviation of  $60^\circ$ , respectively. The decline was much shallower in *GluCl $\alpha$ <sup>RNAi</sup>*-expressing T4 neurons of which the response amplitudes at  $\text{PD} \pm 60^\circ$  still averaged 89.62% of the corresponding PD responses (Fig. 5a). Rather than enhancing voltage responses to visual motion in the PD, the presence of *GluCl $\alpha$*  attenuated responses to motion in all other directions, an effect that was especially obvious at those directions not affected by inhibition from Mi4 and C3 neurons (Fig. 5a–c). This was reflected in a significant reduction of the T4 neurons' directional tuning indices ( $L_{dir}$ ) in the absence of *GluCl $\alpha$*  compared with the wild-type controls ( $P = 0.0002$ , Kruskal–Wallis test followed by Dunn's multiple-comparisons test; Fig. 5c).

**Fig. 5: GluCl $\alpha$  sharpens directional tuning of T4 neurons and optomotor behaviour.**

---

 figure 5

**a**, T4 input organization in the presence (top left) and absence of Mi9 neurons (top right). Bottom, directional tuning of T4 neurons expressing *GFP* (black) or *GFP* + *GluCla*<sup>RNAi</sup> (teal) on the basis of membrane potential responses to ON edges moving at 30° s<sup>-1</sup>. Data are mean ± s.e.m. *n* values indicate the number of cells. The pink

dashed lines show model predictions. **b**, Exemplary membrane voltage ( $V_m$ ) recordings from T4 neurons in **c** in response to ON edges moving in the indicated directions (arrowheads). **c**, Peak membrane voltages of T4 neurons expressing *GFP* (black), *GFP + GluCl $\alpha$ <sup>RNAi</sup>* (T4 > *GluCl $\alpha$ <sup>RNAi</sup>*, teal) or *GFP + Nmdar1<sup>RNAi</sup>* (T4 > *Nmdar1<sup>RNAi</sup>*; grey) as a function of the direction of ON edge motion (left). Data are mean ± s.e.m. Right, directional tuning ( $L_{dir}$ ) for all genotypes. Kruskal–Wallis test followed by Dunn’s multiple-comparisons test detected a significant difference of T4 > *GluCl $\alpha$ <sup>RNAi</sup>* from T4 > *GFP*; \* $P$  = 0.0002. The circles show individual cells. The bars show the mean ± s.e.m.  $n$  values indicate the number of cells. **d**, Open-loop optomotor behaviour. **e**, Average virtual walking trajectories of flies expressing *GluCl $\alpha$ <sup>RNAi</sup>* in T4/T5 cells (teal,  $n$  = 20) and of their parental controls (back and grey,  $n$  = 19 and  $n$  = 18, respectively) in response to ON edge motion at a 22.5° angle. **f**, The angular velocities of flies expressing *GluCl $\alpha$ <sup>RNAi</sup>* (teal) or *Nmdar1<sup>RNAi</sup>* (grey) in T4/T5 neurons, and of their parental controls (black/grey), as a function of stimulus direction and polarity (top). Data are mean ± s.e.m. Bottom, absolute angular velocities scaled by horizontal stimulus components. For moving ON edges, one-way ANOVA followed by Holm–Šídák’s multiple comparisons test detected a significant difference of flies expressing *GluCl $\alpha$ <sup>RNAi</sup>* in T4/T5 cells from both parental controls; \* $P$  = 0.0105. The circles represent individual flies. The bars show the mean ± s.e.m.  $n$  values indicate the number of flies. **g**, Closed-loop bar fixation behaviour. **h**, Exemplary bar trajectories (832 trials and 16 flies per genotype, top) and the overall bar position probabilities (bottom) for flies expressing *GluCl $\alpha$ <sup>RNAi</sup>* in T4/T5 cells (teal) and their parental controls (back/grey). Probabilities are mean ± s.e.m. of flies in **i**. **i**, The percentage of the time that the bar occupied a 60° central window (fixation in front, dashed lines in **h**). Welch’s ANOVA followed by Dunnett’s T3 multiple comparisons test detected a significant difference of flies expressing *GluCl $\alpha$ <sup>RNAi</sup>* in T4/T5 cells from both parental controls; \* $P$  = 0.0042. The dashed line indicates the chance level. The circles represent individual flies. The bars show mean ± s.e.m.  $n$  values indicate the number of flies.

### Source data

The impact of this intervention on the flies’ optomotor responses offered an opportunity to link a molecular mechanism to behavioural performance. Walking on a spherical treadmill (Fig. [5d](#)), flies expressing *GluCl $\alpha$ <sup>RNAi</sup>* in T4 neurons and their OFF-responsive T5 twins under control of *R39H12-GAL4* (Extended Data Fig. [10a](#)) overestimated the velocity of bright, but not of dark, edges moving in different directions. In their attempt to compensate for the perceived egomotion, animals that carried both the *GAL4* and the *UAS-GluCl $\alpha$ <sup>RNAi</sup>* transgene rotated the treadmill excessively about the vertical axis and strayed off the virtual paths of their parental controls (Fig. [5e,f](#)). The angular velocities of animals of all other genotypes, including

those expressing *Nmdar1*<sup>RNAi</sup> in T4/T5 neurons, were indistinguishable (Fig. 5f). In contrast to ON-responsive T4 neurons, which are speckled with GluCl $\alpha$  receptors at both dendritic and axonal compartments, T5 neurons feature the receptor exclusively at their axon terminals<sup>31</sup>. It follows that the impairment of optomotor acuity specific to moving ON edges can, in all likelihood, be attributed to a process that is localized to the dendrites of T4 neurons.

To test the ability of animals with a T4/T5-cell-restricted GluCl $\alpha$  deficiency to hold a steady course under closed-loop conditions, we took advantage of the flies' tendency to approach a dark vertical bar, a behaviour that depends on T4/T5 neurons<sup>32,33</sup>. When given the opportunity to control the bar position through their walking behaviour (Fig. 5g), control animals had a clear preference for holding the bar in front of them at  $0 \pm 30^\circ$ . By contrast, flies expressing *GluCl $\alpha$* <sup>RNAi</sup> in T4/T5 neurons failed to maintain a stable bearing relative to the bar (Fig. 5h) despite moving at a comparable pace (Extended Data Fig. 10b). We corroborated this discovery using another, more specific split GAL4 line (Extended Data Fig. 10c–e). Independent of the driver line used, animals with a T4/T5-cell-restricted GluCl $\alpha$ -deficiency performed at chance level (Fig. 5i and Extended Data Fig. 10f). In accordance with our third assumption, locking T4 neurons in a state of high gain (Figs. 2h and 4) resulted in exaggerated optomotor responses (Fig. 5d–f) and impaired performance as the animals navigated a virtual environment (Fig. 5g–i). These observations reveal the behavioural significance of a multiplication-like operation in a specific type of neuron.

## Discussion

Nervous systems rely on nonlinearities to process information<sup>1</sup>. A multiplication-like operation—possibly the simplest form of nonlinearity—is implicated in the transformation of eye-centric into head-centric coordinates<sup>13</sup>, the localization of sound<sup>12</sup>, the combination of multisensory signals<sup>34,35</sup> and the detection of visual motion<sup>10</sup>. The biophysical underpinnings of such an operation in a single neuron are by and large unclear. One exception is the looming detector of locusts, in which—just like on a slide rule—the sum of two logarithmically scaled signals is exponentially transformed into spike rates<sup>36</sup>. Other multiplicative synaptic interactions involve NMDA receptors<sup>37,38</sup>. Both mechanisms are contingent on threshold-like nonlinearities in the current–voltage relationships of ion channels: the gating of tetrodotoxin-sensitive sodium channels in the former and the magnesium block of NMDA receptors in the latter case. Here, we describe a multiplication-like nonlinearity that is independent of thresholds.

Using the visual circuit of the fruit fly as an example<sup>5</sup>, we took advantage of the neurons' compact sizes, their known connectivity<sup>6</sup> and our ability to manipulate them

genetically to study the biophysical basis of the multiplication step in a Hassenstein–Reichardt detector<sup>10</sup>. We recorded the membrane potentials of ON motion-sensitive T4 neurons and of their columnar input elements in response to a defined set of visual stimuli. Our measurements of both pre- and postsynaptic voltages obviated the need for assumptions regarding the temporal dynamics of input signals when modelling the detector’s output. The voltage responses of T4 neurons were reproduced rather faithfully by our passive conductance-based model (Figs. 3b, c and 5a). Discrepancies between simulation and reality could be due to selective synaptic delays or the 15% of dendritic inputs from wide-field TmY15 and CT1 neurons<sup>6,7,39</sup>, which were not taken into account. In the model, as in our data, the supralinearity arises from the coincidence of excitation and release from shunting inhibition<sup>23</sup>. Such ‘multiplicative disinhibition’ constitutes the inverse operation of divisive inhibition. It is free from the voltage dependence that often limits threshold-based systems<sup>40</sup> and less sensitive to changing signal amplitudes<sup>21</sup> (Extended Data Fig. 5c). More broadly, theory invokes multiplication as a strategy to gate information flow<sup>41,42</sup>. The passive biophysical mechanism that we propose could lend itself to other systems, such as the logical conjunction of chemosensory signals<sup>43</sup> or the gating of cortical afferents<sup>44</sup>. Motion vision in flies may provide one of many cases of multiplicative disinhibition.

## Methods

### Fly husbandry and genotypes

Flies were cultivated on a cornmeal, molasses and yeast medium under a 12 h–12 h light–dark cycle at 25 °C and 60% humidity. All of the experiments were carried out on female flies bearing at least one wild-type allele of the *white* gene. The experimenters were not blinded.

*Drosophila melanogaster* of the following genotypes were used to target transgene expression to the respective types of neuron:  $P\{R48A07-p65.AD\}attP40$ ,  $P\{10XUAS-IVS-mCD8::GFP\}su(Hw)attP5$ ;  $P\{VT046779-GAL4.DBD\}attP2$  was used to label Mi9 neurons,  $P\{R13E12-p65.AD\}attP40/+$ ;  $P\{R59C10-GAL4.DBD\}attP2/P\{40XUAS-IVS-mCD8::GFP\}attP2$  was used to label Tm3 neurons,  $P\{R19F01-p65.AD\}attP40/+$ ;  $P\{R71D01-GAL4.DBD\}attP2/P\{40XUAS-IVS-mCD8::GFP\}attP2$  was used to label Mi1 neurons,  $P\{R48A07-p65.AD\}attP40$ ,  $P\{10XUAS-IVS-mCD8::GFP\}su(Hw)attP5$ ;  $P\{R13F11-GAL4.DBD\}attP2$  was used to label Mi4 neurons,  $P\{R26H02-p65.AD\}attP40/+$ ;  $P\{R29G11-GAL4.DBD\}attP2/P\{40XUAS-IVS-mCD8::GFP\}attP2$  was used to label C3 neurons and  $P\{R42F06-p65.AD\}attP40$ ,  $P\{10XUAS-IVS-mCD8::GFP\}su(Hw)attP5$ ;  $P\{VT037588-GAL4.DBD\}attP2$  (abbreviated T4 > GFP) was used to label T4 neurons, with a preference for subtypes T4c and T4d<sup>17,27,45,46</sup>. In electrophysiological experiments,  $P\{TRiP.HMC03585\}attP40/P\{R42F06-$

*p65.AD}attP40, P{10XUAS-IVS-mCD8::GFP}su(Hw)attP5; P{VT037588-GAL4.DBD}attP2/+* (abbreviated T4 > *GluCl $\alpha$ <sup>RNAi</sup>*) and *P{TRiP.HMS02199}attP2/P{R42F06-p65.AD}attP40, P{10XUAS-IVS-mCD8::GFP}su(Hw)attP5; P{VT037588-GAL4.DBD}attP2/+* (abbreviated T4 > *Nmdar1<sup>RNAi</sup>*) were used to silence the expression of *GluCl $\alpha$*  and *Nmdar1*, respectively<sup>47</sup>.

In behavioural experiments, *P{UAS-Dcr-2.D}2; P{R39H12-GAL4}attP2* (abbreviated T4/T5 >), which yields strong and comprehensive expression in T4 and T5 neurons, was used to drive either *P{TRiP.HMC03585}attP40* (abbreviated *GluCl $\alpha$ <sup>RNAi</sup>*) or *P{TRiP.HMS02199}attP2* (abbreviated *Nmdar1<sup>RNAi</sup>*). For the experiments in Extended Data Fig. 10c–f, *P{R59E08-p65.AD}attP40; P{R42F06-GAL4.DBD}attP2* was used as the driver line. All flies, including the parental controls, were heterozygous for the respective transgenes. *P{UAS-Dcr-2.D}2/P{10XUAS-IVS-mCD8::GFP}su(Hw)attP5; P{R39H12-GAL4}attP2/+* and *P{R59E08-p65.AD}attP40/P{10XUAS-IVS-mCD8::GFP}su(Hw)attP5; P{R42F06-GAL4.DBD}attP2/+* were used to visualize the expression pattern of the respective driver lines immunohistochemically.

With the exception of the strain used to label C3 (a gift from A. Nern and M. Reiser), all of the flies were obtained from the Bloomington *Drosophila* Stock Center.

## Histology

Brains of female flies (aged 1–3 days) were dissected in phosphate-buffered saline (PBS; 137 mM NaCl, 3 mM KCl, 8 mM Na<sub>2</sub>HPO<sub>4</sub>, 1.5 mM KH<sub>2</sub>PO<sub>4</sub>, pH 7.3) and fixed in 4% (w/v) paraformaldehyde in PBS overnight at 4 °C, followed by four 30 min washes in PBS containing 0.2% (v/v) Triton X-100 (PBT). To label biocytin-filled neurons, the samples were incubated with DyLight 633-conjugated streptavidin (21844, Invitrogen, 1:200) for 48 h at 4 °C, followed by four 30 min washes in PBT. To visualize GFP expression patterns driven by *R39H12-GAL4* and *R59E08-AD; R42F06-DBD*, brains were fixed for 25 min at room temperature and blocked in PBT containing 10% normal goat serum (NGS) overnight at 4 °C. Synaptic structures and GFP were labelled, first with mouse anti-bruchpilot antibodies (nc82, AB2314866, Developmental Studies Hybridoma Bank, 1:20) and chicken anti-GFP antibodies (600-901-215S, Rockland, 1:400), respectively, for 48 h and then with Atto 647N-conjugated goat anti-mouse IgG antibodies (610-156-040, Rockland, 1:300) and Alexa 488-conjugated goat anti-chicken IgY antibodies (A-11039, Invitrogen, 1:500), respectively, for 72 h, both diluted in PBT containing 5% NGS, at 4 °C. Immunodecorated samples were mounted in Vectashield antifade mounting medium (Vector Laboratories) and imaged on a Leica TCS SP8 confocal microscope equipped with an HCX PL APO ×63/1.30 NA glycerol-immersion objective (506353, Leica).

Micrographs were acquired using the Leica Application Suite X (Leica) and processed using the Fiji distribution of ImageJ (v.2.0)<sup>48</sup>.

## Patch-clamp recordings

For whole-cell recordings *in vivo*<sup>49,50</sup>, female flies aged 2–24 h post-eclosion were cold-anaesthetized and fixed to a custom, laser-cut polyoxymethylene mount with soft thermoplastic wax (Agar Scientific). The preparation was submerged in extracellular solution (pH 7.3) containing 5 mM TES, 103 mM NaCl, 3 mM KCl, 26 mM NaHCO<sub>3</sub>, 1 mM NaH<sub>2</sub>PO<sub>4</sub>, 1.5 mM CaCl<sub>2</sub>, 4 mM MgCl<sub>2</sub>, 10 mM trehalose, 10 mM glucose and 7 mM sucrose (280 mOsM, equilibrated with 5% CO<sub>2</sub> and 95% O<sub>2</sub>). Cuticle, adipose tissue and trachea were surgically removed in a window large enough to expose the left dorsal optic lobe. Patch pipettes (15–20 MΩ) were fabricated from borosilicate glass capillaries with outer and inner diameters of 1.5 mm and 1.17 mm or 0.86 mm, respectively, using a P-97 (Sutter Instruments) or a PC-10 (Narishige) micropipette puller. Pipettes were polished using a microforge (MF-830, Narishige) and filled with solution (pH 7.3) containing 10 mM HEPES, 140 mM potassium aspartate, 1 mM KCl, 4 mM MgATP, 0.5 mM Na<sub>3</sub>GTP, 1 mM EGTA and 10 mM biocytin (265 mOsM).

Green fluorescent somata were targeted visually using a combination of bright-field and epifluorescence microscopy on an InVivo SliceScope (Scientifica) or an Axio Scope.A1 microscope (Zeiss), each equipped with a ×60/1.0 NA water-immersion objective (LUMPLFLN60XW, Olympus) and an LQ-HXP 120 light source (Leistungselektronik Jena). Transillumination was achieved by butt-coupling a white LED (MCWHD5, Thorlabs) to a liquid light guide, the far end of which was positioned caudally at a distance of 1 cm to the fly allowing for an unobstructed field of view. To gain access to cell membranes, a micropipette was used to make a small incision in the perineural sheath. Signals were recorded at room temperature (21–23 °C) with a MultiClamp 700B amplifier, low-pass-filtered and sampled at 10 kHz using a Digidata 1550B digitizer controlled through pCLAMP 11 software (all from Molecular Devices). Data were corrected for the liquid junction potential and analysed using custom-written software in Python v.3.7 (Python Software Foundation) using NumPy v.1.15, Pandas v.0.25, SciPy v.1.3, Matplotlib v.3.0 and pyABF v.2.1 (<https://pypi.org/project/pyabf/>). After temporal alignment, current-clamp data were analysed at a sampling rate of 1 kHz. The most negative membrane potential recorded within 2 min after break-in, in darkness and in the absence of a holding current was taken to represent the resting potential. Only cells with a measured resting potential that was more negative than −25 mV were characterized further. Input resistances, as plotted in Fig. 2, were calculated on the basis of linear fits to the steady-state voltage changes elicited by 1 s steps of hyperpolarizing currents (2 pA increments, starting at −10 pA). In voltage-clamp recordings, voltage steps were applied 2 s in advance of pharmacological applications and linear leak currents were subtracted.

## Visual stimulation in electrophysiological experiments

Visual stimuli were projected with two mirrors onto a cylindrical screen using two DLP Lightcrafter 3000 pico projectors (Texas Instruments) as previously described<sup>20</sup>. The screen covered 180° in azimuth and 105° in elevation of the fly's left frontal visual field and doubled as a Faraday shield. Restricting the projectors to the green channel (500–600 nm) allowed for a refresh rate of 180 Hz at 8-bit colour depth and a maximal luminance of 1,274 cd m<sup>-2</sup>. The average luminance of stimuli, which were presented in full contrast, was set to an 8-bit greyscale value of 128 corresponding to an average luminance of ~637 cd m<sup>-2</sup>. Stimuli were created and predistorted to account for the curvature of the screen using the Panda3D game engine in Python v.2.7.

Receptive fields were located and characterized using a binary white-noise stimulus with a pixel size of 2.8° × 2.8°. Samples were drawn at a rate of 60 Hz and projected onto the screen for durations ranging from 3 min to 20 min. Stimuli and simultaneously recorded membrane potentials were time-locked using a continuously recorded trigger signal on the screen. Stimulus files were exported after lossless compression and cross-correlated to each neuron's recorded membrane voltage using standard techniques for reverse correlation in Python (v.3.7)<sup>20</sup>. Slow voltage drifts were corrected post hoc by subtracting a low-pass-filtered version of the signal obtained using a Gaussian blur with a standard deviation of 60 s. The reverse correlation was calculated as

$$\$\$K(x,\tau) = \int_0^T S(x,t-\tau) V_m(t) dt, \$\$$$

where  $V_m$  denotes the neuron's baseline-subtracted membrane voltage at time point  $t$  and  $S$  denotes the stimulus at position  $x$  and time point  $t - \tau$  for values of  $\tau$  ranging from -0.5 to +3.0 s. The resulting spatiotemporal receptive fields were converted into standard scores. Only neurons with clear standard score peaks (typically >4 s.d. from the mean) and with receptive field centres >8 px (22.48°) from the bezel of the screen were included in the analysis to guarantee full coverage of the surround. Receptive fields were normalized and aligned in space using the extremum (that is, the maximum or minimum with the highest absolute value) of the standard score as a point of reference, which was placed at 0°. After cropping the individual spatial receptive fields to the largest common region holding data from all neurons, scores were averaged across neurons of one class. For Fig. 1, averages were upsampled by a factor of 10 by linear interpolation and smoothed with a Gaussian filter (1.8 px s.d.). For direction-selective T4 neurons, individual receptive fields were rotated in space to align along the neurons' PDs; therefore, in Fig. 1e, azimuth and elevation do not necessarily correspond to horizontal and vertical coordinates on the screen, but to coordinates parallel and orthogonal to the T4 cell's PD.

To determine a neuron's PD, square-wave gratings with a spatial wavelength of  $30^\circ$  spanning the full extent of the screen were moved at a temporal frequency of 1 Hz in eight different directions separated by  $45^\circ$ . The neuron's peak membrane voltage during motion, after subtracting a 1 s prestimulus baseline, was taken to represent the magnitude of a Euclidean vector  $\mathbf{v}(\phi)$  pointing in the direction given by the angle of rotation  $\phi$  of the associated stimulus. PD was defined as the direction of the resultant of all individual vectors. Temporal frequency tuning curves were measured using gratings of the above properties that were moved alternatingly in PD and ND (that is,  $\text{PD} + 180^\circ$ ) at temporal frequencies ranging from 0.5 Hz to 16.0 Hz.  $\Delta V_m$  was defined as the absolute difference between the maximal and minimal membrane potential.

The fine-grained directional tuning curves in Fig. 5 were assessed using ON edges moving at  $30^\circ \text{ s}^{-1}$  in 36 evenly spaced directions. Membrane potentials were recorded in the presence of a constant holding current of  $-1 \text{ pA}$ , which enabled stable recordings over extended periods of time. In Fig. 5c,  $|\mathbf{v}(\phi)|$  was defined as the maximum of a Voigt profile fit to the membrane potential in a 700 ms time window surrounding the peak response during motion in the respective direction using the VoigtModel function of the lmfit.models module in Python v.3.7. Thus the readout incorporated more data points than just the maxima of the raw traces. To make directional tuning curves comparable between experiments and genotypes, each neuron's PD was aligned post hoc to  $0^\circ$  and its tuning curve was minimum–maximum normalized. Directional tuning was quantified as the magnitude of the resultant vector divided by the sum of the individual vectors' magnitudes:

$$\$ \$ \{L\}_{\{\{\rm{dir}\}\}} = \frac{\sum_{\phi} |\mathbf{v}(\phi)|}{\sum_{\phi} |\mathbf{v}(\phi)|} \$ \$$$

For the experiments in Fig. 3, bright (ON) and dark (OFF) edges were moved across the screen at a velocity of  $30^\circ \text{ s}^{-1}$ . The responses of individual neurons of one type were temporally aligned based on the cross-correlation maximum between the time derivative of the low-pass-filtered membrane potential of each neuron and that of one hand-picked template neuron in response to ON edges (moving in PD for T4 cells). The responses of different input neuron classes were aligned based on the relative distances of the template neurons' receptive field centres on the screen. Correct alignment was verified by recording light intensities from a  $5^\circ$ -wide area of the screen located at the respective template neuron's receptive field centre using a custom-built photodiode under identical stimulus conditions.

Time-locked measurements of a T4 neuron's membrane potential and input resistance (Fig. 4 and Extended Data Fig. 9) were achieved through repeated presentations of identical stimuli with varying holding current amplitudes ranging from  $-5$  to  $0 \text{ pA}$ . The slope of a linear regression of voltages onto holding currents provided a measure

of the neuron's input resistance at each time point. For experiments with only two different holding current amplitudes, the slope of the regression is equivalent to the input resistance calculated as  $\Delta V_m/\Delta I$ , where  $\Delta V_m$  denotes the change in membrane potential and  $\Delta I$  denotes the change in holding current in between repetitions. Resistances shown in Fig. 4 were smoothed with a Gaussian filter (13 ms s.d.). Input resistances did not change significantly throughout recording sessions. The difference in input resistance between the start and the end of recording sessions averaged at  $0.28 \pm 0.56 \text{ G}\Omega$  (mean  $\pm$  s.e.m.,  $n = 30$  cells;  $P = 0.6143$ , two-tailed paired Student's  $t$ -test).

## Pharmacology

For applications of glutamate, acetylcholine and GABA, a micropipette with a bore diameter of 5  $\mu\text{m}$  was filled with 1 mM of neurotransmitter (dissolved in extracellular solution) and aimed at the GFP-labelled T4 dendrites in layer 10 of the medulla. To elicit transient neurotransmitter responses in patch-clamped T4 neurons, pressure (50 kPa) was applied in 100 ms pulses using a PDES-02DX pneumatic drug ejection system (NPI Electronic). For long-lasting responses during input resistance measurements, pulse times were increased to 500 ms. Two wild-type neurons were lost after the third glutamate application during patch-clamp recordings for Fig. 2e and were excluded from the repeated-measures analysis.

## Multi-compartment model

We built a passive compartmental model of a T4 neuron (Extended Data Fig. 4c, d) in Python v.3.7 to account for possible space-clamp problems due to neuronal morphology in voltage-clamp experiments and to assess signal propagation between dendrite and soma (Extended Data Fig. 4e, f). The model was based on an electron microscopic reconstruction<sup>7</sup> ([http://neuromorpho.org/neuron\\_info.jsp?neuron\\_name=T4a-25\\_85](http://neuromorpho.org/neuron_info.jsp?neuron_name=T4a-25_85)) and comprised 2,012 compartments. A connectivity matrix, which held values of 1 where two compartments were connected and values of 0 otherwise, was used as a template to calculate a conductance matrix  $M$ . The latter was based on the three-dimensional coordinates and the length as well as the diameter of each compartment assuming, unless stated otherwise, an axial resistivity ( $R_a$ ) of 150  $\Omega$  cm, a membrane resistance ( $R_m$ ) of 28 k $\Omega$  cm<sup>2</sup>, and a specific membrane capacitance ( $C_m$ ) of 1  $\mu\text{F cm}^{-2}$ . All parameters were on the same scale as those commonly used to model *Drosophila* neurons<sup>51</sup> and were considered to be uniform across the entire cell. Varying  $R_a$  and  $R_m$  over a biophysically plausible range had negligible effects on model output (Extended Data Fig. 4f, g).

The voltage vector  $\mathbf{V}_m(t)$  indicating the membrane potential of each compartment and at each time point  $t$  was determined by using the `sparse.linalg.spsolve` function of the SciPy v.1.3 module to iteratively solve the matrix equation  $M \times \mathbf{V}_m(t) = \mathbf{V}_m(t - 1) \times \mathbf{c}_m / \Delta t + E_{\text{leak}} \times \mathbf{g}_{\text{leak}} + \mathbf{I}(t)$ , where  $\mathbf{V}_m(t - 1)$  denotes the voltage vector at the previous time point,  $\mathbf{c}_m$  is the vector holding the specific capacitances of all compartments,  $\Delta t$  denotes the time step,  $E_{\text{leak}}$  denotes the leak reversal potential,  $\mathbf{g}_{\text{leak}}$  denotes the vector holding the specific transmembrane leak conductances of all compartments and  $\mathbf{I}(t)$  is the vector indicating the current injected at time point  $t$  into each compartment.

Simulations were performed with a fixed  $\Delta t$  of 0.1 ms. If only steady-state was considered, the diagonal of the conductance matrix  $M$  held no capacitive conductances and the right side of the equation simplified to  $E_{\text{leak}} \times \mathbf{g}_{\text{leak}} + \mathbf{I}(t)$ . At the time of transmitter application, synaptic conductances were added both to the diagonal of the conductance matrix and, multiplied by the reversal potential of the current, to the right side of the equation.

To simulate voltage clamp, the current injected at the soma was calculated on the basis of the difference between the chosen command voltage  $V_{\text{cmd}}$  and the actual potential at the soma  $V_{m,\text{soma}}$  using a proportional-integral control loop that served to emulate a voltage-clamp amplifier in Python v.3.7. The current to be injected at time point  $t$  was calculated as  $I(t) = K_p \times (V_{\text{cmd}}(t) - V_{m,\text{soma}}(t)) + K_i \times I(t - 1)$ ; where  $K_p$  denotes the proportional gain and  $K_i$  the integral gain. With values of  $2 \times 10^9$  and 1 for  $K_p$  and  $K_i$ , respectively,  $V_{m,\text{soma}}$  could be clamped reliably at the desired  $V_{\text{cmd}}$  under all conditions and synaptic inputs.

## Single-compartment model

Recorded membrane voltages of input neurons were averaged, minimum–maximum normalized (retaining the signal ratios across stimuli) and converted into relative conductances using a rectilinear transfer function with two free parameters per neuron: a threshold below which all conductances were set to 0 and a gain (that is, a scaling factor). Taking into account an average inter-ommatidial angle  $\theta$  of  $4.8^\circ$  (refs. [52,53](#)) and the edge velocity  $v$  of  $30^\circ \text{ s}^{-1}$ , conductances of Mi9 neurons and those of Mi4 and C3 neurons were advanced or delayed in time, respectively, by  $\Delta t$  relative to those of Mi1 and Tm3 neurons, depending on the angle  $\varphi$  of the virtual edge:  $\Delta t = \theta \cos \varphi / v$ .

For each stimulus condition, the membrane potential of the T4 neuron was calculated as

$$\$\{V\}_{m}=\frac{\{E\}_{\{\rm{Glu}\}}}{\{g\}_{\{\rm{Mi9}\}}}+\{E\}_{\{\rm{ACh}\}}, \\ (\{g\}_{\{\rm{Tm3}\}}+\{g\}_{\{\rm{Mi1}\}})+\{E\}_{\{\rm{GABA}\}}\},$$

$$(\{g\}_{\rm Mi4} + \{g\}_{\rm C3}) + E_{\rm leak} \{g\}_{\rm Mi9} + \{g\}_{\rm Tm3} + \{g\}_{\rm Mi1} + \{g\}_{\rm Mi4} + \{g\}_{\rm C3} + \{g\}_{\rm leak}), \$$$

where  $g$  denotes the relative conductance associated with each input neuron and  $E$  denotes the reversal potential of the respective synaptic current with  $E_{\text{Glu}} = -71$  mV,  $E_{\text{ACh}} = -21$  mV and  $E_{\text{GABA}} = -68$  mV as measured/modelled in voltage-clamp experiments (Extended Data Fig. 4a–d). Owing to the compact size of a T4 neuron, the small amplitudes of capacitive currents (in relation to the steady-state amplitudes) and their short time constants (in relation to those of synaptic currents) eliminated the need for a differential equation to calculate  $V_m$ . Free parameters (thresholds, gains,  $E_{\text{leak}}$  and  $g_{\text{leak}}$ ) were estimated from a least-squares fit to measured membrane voltage traces of T4 neurons, computed with the help of the optimize.minimize function of the SciPy v.1.3 module and hand-tuned using a FaderPort 16-channel mix production controller (Presonus). Upper and lower bounds for parameter values were set to 0 and 1 for thresholds, 0 and 2 for gains,  $-80$  mV and  $-45$  mV for  $E_{\text{leak}}$ , and 0 and 3 for  $g_{\text{leak}}$ , respectively. The parameters used for the simulations shown in Figs. 3b, c and 5a and Extended Data Figs. 7b, c and 8 were as follows:  $\text{Mi9}_{\text{gain}} = 0.92$ ,  $\text{Tm3}_{\text{gain}} = 0.35$ ,  $\text{Mi1}_{\text{gain}} = 0.65$ ,  $\text{Mi4}_{\text{gain}} = 1.10$ ,  $\text{C3}_{\text{gain}} = 1.49$ ,  $\text{Mi9}_{\text{thld}} = 0.20$ ,  $\text{Tm3}_{\text{thld}} = 0.35$ ,  $\text{Mi1}_{\text{thld}} = 0.88$ ,  $\text{Mi4}_{\text{thld}} = 0.44$ ,  $\text{C3}_{\text{thld}} = 0.70$ ,  $E_{\text{leak}} = -65.0$  mV and  $g_{\text{leak}} = 0.50$ , where ‘thld’ refers to the respective threshold values.

To validate our choice of parameters and to quantify the sensitivity, robustness and uniqueness of parameter sets, we resorted to simulation-based inference<sup>29</sup>, which enabled us to examine the full range of possible parameter combinations. We used 20,000 model simulations, drawing parameters from uniform distributions within the above bounds, to train the artificial neural network implemented in the sequential neural posterior estimation (SNPE) algorithm of the software package sbi (v.0.8)<sup>54</sup>. On the basis of Bayesian inference, SNPE provided a conditional probability distribution  $P(\alpha|V_{\text{data}})$ , which is high for parameter sets  $\alpha$  that are consistent with the experimentally measured voltage traces  $V_{\text{data}}$ , but close to zero otherwise. To visualize  $P(\alpha|V_{\text{data}})$  we drew 10,000 sample parameter sets that are compatible with  $V_{\text{data}}$  and compared them to our chosen parameters (Extended Data Fig. 6). All of the simulations were written in Python v.3.7.

## Behaviour

Female flies (aged 1–5 days) were cold-immobilized and attached to a pin with light-curing composite glue (Sinfony Opaque Dentin, 3M) using dental curing light (440 nm, New Woodpecker). Five independent locomotion recorders<sup>32</sup> were operated in

parallel. In each recorder, a tethered fly was positioned on top of an air-suspended polyurethane sphere with a diameter of 6 mm and a weight of around 40 mg. The sphere floated freely on an air stream supplied by a rotary vane pump (G6/01-K-EB9L, Gardner Denver Thomas) through an inlet at the bottom of a concave holder, allowing the walking fly to rotate the sphere about any axis through its centre. The rotation of the spherical treadmill, lit by an infrared LED (JET-800-10, Roithner Electronics), was tracked at 4 kHz and digitized at 200 Hz using a custom-designed system based on two optical computer mouse sensors focused on two 1 mm<sup>2</sup> equatorial squares at ±30° from the centre of the sphere<sup>55</sup>. A camera (GRAS-20S4M-C, Point Grey Research) was used to facilitate proper positioning of the fly on the ball. To encourage prolonged walking, the air temperature surrounding the fly was maintained at 34 ± 0.1 °C using a custom-built air conditioning system with a Peltier heater (QC-127-1.4-6.0MS, Quick-Cool) and a thermometer positioned below the sphere.

Visual stimuli were presented with a refresh rate of 120 Hz on three liquid crystal displays (2233RZ, Samsung) arranged vertically to form a U-shaped visual arena surrounding the fly, which spanned approximately 270° in azimuth and 120° in elevation of the fly's visual field at a resolution of <0.1°. The maximal luminance of the displays was 131 cd m<sup>-2</sup>; the average intensity of stimuli, which were presented at a Michelson contrast of 50%, was set to an 8-bit greyscale value of 100. Stimuli were created, and predistorted to mimic a cylindrical panorama, using the Panda3D game engine in Python v.2.7.

In open-loop experiments, ON and OFF edges were moved at a velocity of 60° s<sup>-1</sup> in 16 evenly spaced directions. Owing to the geometry of the visual arena, full translation of edges at different angles required variable amounts of time. Thus, to limit stimulus durations to 5 s, an edge of which the direction of motion deviated from the cardinal directions was initialized with a small segment of the edge already present in one of the outer corners (never covering any part of the central display). Edges started moving 0.5 s after stimulus initialization and crossed the arena within 5 s. In a single experiment (~80 min), flies experienced 50 trials of either ON or OFF edges moving in all 16 directions in a pseudorandom order. The first 15 trials were used to equilibrate the temperature and to accustom the fly to the treadmill and were excluded from analyses. As inclusion criteria, we used a forward walking speed of ≥0.15 cm s<sup>-1</sup> on a trial-by-trial basis and a minimum of ten trials per fly. To correct for a possible constant turning bias, the time-averaged rotational velocity of each full trial (comprising all 16 directions) was subtracted from all measurements of the corresponding trial. The optomotor response was quantified as the average rotational velocity during 5 s of edge motion in the corresponding direction. The slope of a linear regression of optomotor responses onto the absolute horizontal stimulus components

$|\cos\varphi|$  served as a single measure of an animal's angular velocity across different edge angles  $\varphi$ .

In closed-loop experiments, bar-fixation was assessed using a 10°-wide dark vertical bar, the position of which along the azimuth was controlled in real time by the rotation of the spherical treadmill ( $\Delta$ bar position = –rotation about  $z$  axis, updated every ~9 ms). The bar appeared at a random position between –180° and 180° at the start of each 20 s trial, during which the fly could control the bar's position through its walking behaviour. One experiment (~60 min) consisted of 180 trials, the first 40 of which were not analysed, as they served to equilibrate the temperature and to accustom the fly to the virtual environment. For the results presented in Extended Data Fig. 10d–f, each experiment consisted of 80 longer multi-stimulus trials, the first 10 of which were excluded. Only trials with a forward walking velocity of  $\geq 0.40 \text{ cm s}^{-1}$  and flies with at least 50 (20 for Extended Data Fig. 10d–f) of such trials were included in the analysis. To avoid possible turning bias (for example, due to skewed mounting), flies whose average turning deviated from zero by  $> 10^\circ \text{ s}^{-1}$  were excluded. Probability density functions of bar positions were calculated for each 20 s trial using a bin width of 5° before averaging over trials. The measure ‘fixation in front’ was obtained by summing the probabilities of finding the bar in a 60° window in front of the fly and averaging these probabilities over trials.

## Statistics and reproducibility

Statistical tests were performed in Prism v.9.2 (GraphPad). Details, including test statistics, degrees of freedom and exact  $P$  values for statistical analyses of data shown in Figs. 2 and 5 and Extended Data Fig. 10 are reported in Supplementary Tables 1 and 2.

Data were assessed for normality and equality of variances using Shapiro–Wilk and Brown–Forsythe tests, respectively. Two groups of normally distributed data were compared using two-tailed Student's  $t$ -tests (paired if applicable). Two groups of nonparametric data were compared using two-tailed Mann–Whitney  $U$ -tests for independent datasets and using Wilcoxon matched-pairs signed-ranks test for paired datasets. Differences between the means of multiple independent groups of data that met the assumptions of normality and equality of variances were compared using one-way ANOVA followed by Holm–Šídák's multiple-comparisons test. Where the assumptions of normality or of equality of variances were violated, group means were compared using Kruskal–Wallis tests followed by Dunn's multiple-comparisons test or by Welch's ANOVA followed by Dunnett's T3 multiple-comparisons test, respectively. Reported  $P$  values were corrected for multiple comparisons. Data shown in Fig. 2e were analysed using two-way repeated measures ANOVA with Geisser–

Greenhouse correction. For multiple comparisons with parental controls, the highest of two  $P$  values was reported in the figure legend.

No sample size calculations were performed before experimentation. Sample sizes were chosen to match or exceed standard sample sizes in the field. Sample sizes in electrophysiological experiments correspond to the number of cells, each of which was recorded in a different animal. Sample sizes in behavioural experiments correspond to the number of flies. The investigators were not blinded. Randomization was not applicable, because flies were grouped on the basis of genotype. In open-loop behavioural experiments (Fig. 5d–f) and all experiments involving two directions of visual stimuli, stimulus directions were alternated randomly; all of the remaining visual stimuli were presented in a strict sequence to enable quick, intuitive interpretation (Figs. 1f and 5b). Two wild-type neurons were lost after the third glutamate application during patch-clamp recordings for Fig. 2e and were excluded from the repeated-measures analysis. Six cells were lost during voltage-clamp experiments shown in Fig. 2f and Extended Data Fig. 4b due to pneumatic ejection. The current–voltage relationships of those cells do not include all, but at least six, data points per cell.

## Reporting summary

Further information on research design is available in the [Nature Research Reporting Summary](#) linked to this paper.

## Data availability

Data are available at the Edmond Open Research Data Repository of the Max Planck Society (<https://doi.org/10.17617/3.8g>). [Source data](#) are provided with this paper.

## Code availability

Custom-written code is available at the Edmond Open Research Data Repository of the Max Planck Society (<https://doi.org/10.17617/3.8g>).

## References

1. Koch, C. & Poggio, T. Multiplying with Synapses and Neurons. In *Single Neuron Computation* (eds Mckenna T. et al.) 315–345 (Academic Press, 1992).
2. Koch, C. & Segev, I. The role of single neurons in information processing. *Nat. Neurosci.* **3**, 1171–1177 (2000).

3. London, M. & Häusser, M. Dendritic computation. *Annu. Rev. Neurosci.* **28**, 503–532 (2005).
4. Joesch, M., Schnell, B., Raghu, S. V., Reiff, D. F. & Borst, A. ON and OFF pathways in *Drosophila* motion vision. *Nature* **468**, 300–304 (2010).
5. Maisak, M. S. et al. A directional tuning map of *Drosophila* elementary motion detectors. *Nature* **500**, 212–216 (2013).
6. Takemura, S.-Y. et al. The comprehensive connectome of a neural substrate for ‘ON’ motion detection in *Drosophila*. *eLife* **6**, e24394 (2017).
7. Shinomiya, K. et al. Comparisons between the ON- and OFF-edge motion pathways in the *Drosophila* brain. *eLife* **8**, e40025 (2019).
8. Cully, D. F., Paress, P. S., Liu, K. K., Schaeffer, J. M. & Arena, J. P. Identification of a *Drosophila melanogaster* glutamate-gated chloride channel sensitive to the antiparasitic agent avermectin. *J. Biol. Chem.* **271**, 20187–20191 (1996).
9. Liu, W. W. & Wilson, R. I. Glutamate is an inhibitory neurotransmitter in the *Drosophila* olfactory system. *Proc. Natl Acad. Sci. USA* **110**, 10294–10299 (2013).
10. Hassenstein, B. & Reichardt, W. Systemtheoretische Analyse der Zeit-, Reihenfolgen- und Vorzeichenauswertung bei der Bewegungsperzeption des Rüsselkäfers *Chlorophanus*. *Z. Naturforsch. B* **11**, 513–524 (1956).
11. Borst, A., Haag, J. & Reiff, D. F. Fly motion vision. *Annu. Rev. Neurosci.* **33**, 49–70 (2010).
12. Peña, J. L. & Konishi, M. Auditory spatial receptive fields created by multiplication. *Science* **292**, 249–252 (2001).
13. Andersen, R. A., Essick, G. K. & Siegel, R. M. Encoding of spatial location by posterior parietal neurons. *Science* **230**, 456–458 (1985).
14. Luo, L. *Principles of Neurobiology* (Garland Science, 2020).
15. Barlow, H. B. & Levick, W. R. The mechanism of directionally selective units in rabbit’s retina. *J. Physiol.* **178**, 477–504 (1965).
16. Fisher, Y. E., Silies, M. & Clandinin, T. R. Orientation selectivity sharpens motion detection in *Drosophila*. *Neuron* **88**, 390–402 (2015).

17. Strother, J. A. et al. The emergence of directional selectivity in the visual motion pathway of *Drosophila*. *Neuron* **94**, 168–182 (2017).
18. Fischbach, K.-F. & Dittrich, A. P. M. The optic lobe of *Drosophila melanogaster*. I. A Golgi analysis of wild-type structure. *Cell Tissue Res.* **258**, 441–475 (1989).
19. Haag, J., Arenz, A., Serbe, E., Gabbiani, F. & Borst, A. Complementary mechanisms create direction selectivity in the fly. *eLife* **5**, e17421 (2016).
20. Arenz, A., Drews, M. S., Richter, F. G., Ammer, G. & Borst, A. The temporal tuning of the *Drosophila* motion detectors is determined by the dynamics of their input elements. *Curr. Biol.* **27**, 929–944 (2017).
21. Borst, A. A biophysical mechanism for preferred direction enhancement in fly motion vision. *PLoS Comput. Biol.* **14**, e1006240 (2018).
22. Zavatone-Veth, J. A., Badwan, B. A. & Clark, D. A. A minimal synaptic model for direction selective neurons in *Drosophila*. *J. Vis.* **20**, 1–22 (2020).
23. Torre, V. & Poggio, T. A synaptic mechanism possibly underlying directional selectivity to motion. *Proc. R. Soc. Lond. B* **202**, 409–416 (1978).
24. Gruntman, E., Romani, S. & Reiser, M. B. Simple integration of fast excitation and offset, delayed inhibition computes directional selectivity in *Drosophila*. *Nat. Neurosci.* **21**, 250–257 (2018).
25. Pankova, K. & Borst, A. RNA-seq transcriptome analysis of direction-selective T4/T5 neurons in *Drosophila*. *PLoS ONE* **11**, e0163986 (2016).
26. Davis, F. P. et al. A genetic, genomic, and computational resource for exploring neural circuit function. *eLife* **9**, e50901 (2020).
27. Hörmann, N. et al. A combinatorial code of transcription factors specifies subtypes of visual motion-sensing neurons in *Drosophila*. *Development* **147**, dev186296 (2020).
28. Özal, M. N. et al. Neuronal diversity and convergence in a visual system developmental atlas. *Nature* **589**, 88–95 (2021).
29. Gonçalves, P. J. et al. Training deep neural density estimators to identify mechanistic models of neural dynamics. *eLife* **9**, e56261 (2020).
30. Denève, S. & Machens, C. K. Efficient codes and balanced networks. *Nat. Neurosci.* **19**, 375–382 (2016).

31. Fendl, S., Vieira, R. M. & Borst, A. Conditional protein tagging methods reveal highly specific subcellular distribution of ion channels in motion-sensing neurons. *eLife* **9**, e62953 (2020).
32. Bahl, A., Ammer, G., Schilling, T. & Borst, A. Object tracking in motion-blind flies. *Nat. Neurosci.* **16**, 730–738 (2013).
33. Fenk, L. M., Poehlmann, A. & Straw, A. D. Asymmetric processing of visual motion for simultaneous object and background responses. *Curr. Biol.* **24**, 2913–2919 (2014).
34. Huston, S. J. & Krapp, H. G. Nonlinear integration of visual and haltere inputs in fly neck motor neurons. *J. Neurosci.* **29**, 13097–13105 (2009).
35. Haag, J., Wertz, A. & Borst, A. Central gating of fly optomotor response. *Proc. Natl Acad. Sci. USA* **107**, 20104–20109 (2010).
36. Gabbiani, F., Krapp, H. G., Koch, C. & Laurent, G. Multiplicative computation in a visual neuron sensitive to looming. *Nature* **420**, 320–324 (2002).
37. Lavzin, M., Rapoport, S., Polsky, A., Garion, L. & Schiller, J. Nonlinear dendritic processing determines angular tuning of barrel cortex neurons *in vivo*. *Nature* **490**, 397–401 (2012).
38. Poleg-Polsky, A. & Diamond, J. S. NMDA receptors multiplicatively scale visual signals and enhance directional motion discrimination in retinal ganglion cells. *Neuron* **89**, 1277–1290 (2016).
39. Meier, M. & Borst, A. Extreme compartmentalization in a *Drosophila* amacrine cell. *Curr. Biol.* **29**, 1545–1550 (2019).
40. Srinivasan, M. V. & Bernard, G. D. A proposed mechanism for multiplication of neural signals. *Biol. Cybern.* **21**, 227–236 (1976).
41. Abbott, L. F. Where Are the Switches on This Thing? In *23 Problems in Systems Neuroscience* (eds van Hemmen, J. L. & Sejnowski, T. J.) 423–431 (Oxford University Press, 2006).
42. Schnupp, J. W. & King, A. J. Neural processing: the logic of multiplication in single neurons. *Curr. Biol.* **11**, R640–R642 (2001).
43. Dobosiewicz, M., Liu, Q. & Bargmann, C. I. Reliability of an interneuron response depends on an integrated sensory state. *eLife* **8**, e50566 (2019).

44. Pi, H.-J. et al. Cortical interneurons that specialize in disinhibitory control. *Nature* **503**, 521–524 (2013).
45. Tuthill, J. C., Nern, A., Holtz, S. L., Rubin, G. M. & Reiser, M. B. Contributions of the 12 neuron classes in the fly lamina to motion vision. *Neuron* **79**, 128–140 (2013).
46. Schilling, T., Ali, A. H., Leonhardt, A., Borst, A. & Pujol-Martí, J. Transcriptional control of morphological properties of direction-selective T4/T5 neurons in *Drosophila*. *Development* **146**, dev.169763 (2019).
47. Ni, J.-Q. et al. A genome-scale shRNA resource for transgenic RNAi in *Drosophila*. *Nat. Methods* **8**, 405–407 (2011).
48. Schindelin, J. et al. Fiji: an open-source platform for biological-image analysis. *Nat. Methods* **9**, 676–682 (2012).
49. Wilson, R. I., Turner, G. C. & Laurent, G. Transformation of olfactory representations in the *Drosophila* antennal lobe. *Science* **303**, 366–370 (2004).
50. Groschner, L. N., Chan Wah Hak, L., Bogacz, R., DasGupta, S. & Miesenböck, G. Dendritic integration of sensory evidence in perceptual decision-making. *Cell* **173**, 894–905 (2018).
51. Gouwens, N. W. & Wilson, R. I. Signal propagation in *Drosophila* central neurons. *J. Neurosci.* **29**, 6239–6249 (2009).
52. Götz, K. G. Optomotorische Untersuchung des visuellen Systems einiger Augenmutanten der Fruchtfliege *Drosophila*. *Kybernetik* **2**, 77–92 (1964).
53. Land, M. F. Visual acuity in insects. *Annu. Rev. Entomol.* **42**, 147–177 (1997).
54. Tejero-Cantero, A. et al. sbi: A toolkit for simulation-based inference. *J. Open Source Softw.* **5**, 2505 (2020).
55. Seelig, J. D. et al. Two-photon calcium imaging from head-fixed *Drosophila* during optomotor walking behavior. *Nat. Methods* **7**, 535–540 (2010).

## Acknowledgements

We thank A. Nern, M. Reiser, G. Rubin, L. Luo and T. Schilling for flies; M. Drews and A. Leonhardt for software; S. Prech for technical assistance; and G. Ammer, N. Hörmann and J. Pujol-Martí for discussions. This work was supported by the Max

Planck Society, an EMBO Long-Term Fellowship ALTF 365-2019 to L.N.G. and by the European Union's Horizon 2020 programme under the Marie Skłodowska-Curie Action MOVIS grant agreement no. 896143 to L.N.G. Flies obtained from the Bloomington *Drosophila* Stock Center (NIH P40OD018537) were used in this study.

## Funding

Open access funding provided by the Max Planck Society.

## Author information

### Author notes

1. These authors contributed equally: Lukas N. Groschner, Jonatan G. Malis

### Affiliations

1. Max Planck Institute of Neurobiology, Martinsried, Germany

Lukas N. Groschner, Jonatan G. Malis, Birte Zuidinga & Alexander Borst

### Contributions

L.N.G., J.G.M. and A.B. conceived the study, designed experiments and ran model simulations. L.N.G. and J.G.M. performed and analysed electrophysiological recordings. L.N.G., J.G.M. and B.Z. performed histological analyses and B.Z. conducted and analysed behavioural experiments. The manuscript was written by L.N.G. and edited by all of the authors, chiefly by B.Z.

### Corresponding authors

Correspondence to [Lukas N. Groschner](#) or [Alexander Borst](#).

## Ethics declarations

### Competing interests

The authors declare no competing interests.

## Peer review

## Peer review information

*Nature* thanks Holger Krapp and Botond Roska for their contribution to the peer review of this work.

## Additional information

**Publisher's note** Springer Nature remains neutral with regard to jurisdictional claims in published maps and institutional affiliations.

## Extended data figures and tables

### [Extended Data Fig. 1 Neuronal morphologies and receptive fields of the ON motion detection circuit.](#)

**a**, Maximum intensity projections of confocal stacks with GFP expression in the respective neuronal population (green) and single biocytin-filled neurons (white) recovered after patch-clamp recordings. Scale bars, 20  $\mu\text{m}$ . Micrographs are representative of independent experiments in different flies (Mi9:  $n = 5$ , Tm3:  $n = 3$ , Mi1:  $n = 3$ , Mi4:  $n = 4$ , C3:  $n = 3$ , T4:  $n = 7$ ). **b**, Individual spatial receptive fields of T4 and their columnar input neurons obtained by reverse correlation (corr.) of membrane potentials and white noise stimuli. AU, arbitrary units. Filtered averages are shown in Fig. [1d, e](#).

[Source data](#)

### [Extended Data Fig. 2 Mi9 neurons hyperpolarize in response to luminance increments.](#)

Membrane potential responses of the same Mi9 neurons to increments (left) and decrements in luminance (right) presented in a 5° circle at the centre of the neurons' receptive fields on a dark or bright background, respectively. Traces on top are normalized light intensities at the respective receptive field centre. The light lines represent technical replicates; the dark lines represent the mean;  $n = 14$  technical replicates/2 cells/2 flies. Note the difference in membrane potential depending on the baseline luminance.

[Source data](#)

### Extended Data Fig. 3 Morphology of wild-type and GluCl $\alpha$ -deficient T4 neurons.

Maximum intensity projections of representative confocal stacks of T4 neurons expressing GFP (left) or GFP and GluCl $\alpha$ <sup>RNAi</sup> (right), each containing an individual biocytin-filled neuron (white) recovered after patch-clamp recording. The soma of the GluCl $\alpha$ <sup>RNAi</sup>-expressing neuron was lost during pipette removal. Scale bars, 20  $\mu$ m. Micrographs are representative of independent experiments in different flies (T4 > GFP;  $n = 7$  and T4 > GFP + GluCl $\alpha$ <sup>RNAi</sup>;  $n = 3$ ). At the light microscopic level, no obvious genotype-specific morphological differences were detectable.

### Extended Data Fig. 4 Measured and modelled T4 whole-cell currents in response to three types of neurotransmitter.

**a**, Placement of pipettes for neurotransmitter application during whole-cell recording. **b**, Average whole-cell currents of T4 neurons in response to 100 ms applications of neurotransmitter to the dendrite at different holding potentials (left) and full current-voltage relationships (right). Coloured dashed lines are linear fits to measurements taken at membrane potentials in the physiologically observed range between -100 and -40 mV. Filled triangles denote reversal potentials obtained by linear fits to currents measured at the soma ( $E_{rev\ Soma}$ ). Data are mean  $\pm$  s.e.m.  $n$  values indicate the number of cells. The inward rectification of GABA-induced currents could be due to coupling of GABA<sub>B</sub> receptors to inwardly-rectifying potassium channels. **c**, Electron microscopic reconstruction of a T4 neuron<sup>7</sup> used for compartmental modelling. Pipettes indicate approximate locations of conductances and the recording site for simulations in **d**. **d**, Somatic currents at different holding potentials simulated during 100 ms openings of conductances at the electron microscopically-determined synaptic sites corresponding to the respective transmitter (left) and current-voltage relationships (right). Conductances were adjusted in order to approximate measured reversal potentials at the soma. Filled triangles denote modelled reversal potentials at the soma ( $E_{rev\ Soma}$ ); open triangles denote corresponding reversal potentials at the dendritic root ( $E_{rev\ Dend.}$ ). Note the predicted deviation of  $E_{rev\ Soma}$  from  $E_{rev\ Dend.}$  for currents induced by acetylcholine, but not for currents induced by glutamate or GABA. **e**, Pipettes indicate locations of recording sites on the compartmental model (**c**) for simulations in **f**. **f**, Ratio of somatic to dendritic membrane potential in response to dendritic injection of 10 pA of depolarizing current as a function of membrane resistance ( $R_m$ ) and axial resistivity ( $R_a$ ) in the model. Note that soma and dendrite were quasi-isopotential (ratio > 0.9) across a wide range of parameters. Asterisk indicates parameter set used for simulations in **d**. **g**, Modelled somatic input resistance as a function of  $R_m$  and  $R_a$ . Solid and dashed lines correspond to the measured mean

input resistance  $\pm$  s.d. for wild-type T4 neurons (as shown in Fig. 2h). Asterisk indicates parameter set used for simulations in d.

[Source data](#)

[\*\*Extended Data Fig. 5 Nonlinear response properties of model circuits.\*\*](#)

**a**, Resistor-capacitor equivalent circuit of a passive T4 neuron used for simulations in Fig. 3b, c, and 5a and Extended Data Figs. 6, 7, and 8.  $E_{\text{Glu}}$ ,  $E_{\text{ACh}}$ , and  $E_{\text{GABA}}$  denote the equilibrium potentials and  $g_{\text{Glu}}$ ,  $g_{\text{ACh}}$ , and  $g_{\text{GABA}}$  denote the conductances associated with glutamate, acetylcholine and GABA, respectively. The signals of Mi9 neurons control  $g_{\text{Glu}}$ , the signals of Tm3 and Mi1 neurons control  $g_{\text{ACh}}$ , and those of C3 and Mi4 neurons act on  $g_{\text{GABA}}$ .  $V_m$ , membrane potential;  $C_m$ , membrane capacitance;  $g_{\text{leak}}$ , leak conductance. **b, c**, Top: Equivalent circuits of two passive isopotential neurons. One neuron (**b**) receives two input signals  $x$  and  $y$ , which control the excitatory conductances  $g_{\text{exc}1}$  and  $g_{\text{exc}2}$ , respectively. The other neuron (**c**) receives one input signal  $x$  controlling the excitatory conductance  $g_{\text{exc}}$  and another input signal  $y$  of opposite polarity that controls the inhibitory conductance  $g_{\text{inh}}$ .  $E_{\text{exc}}$ ,  $E_{\text{inh}}$ , and  $E_{\text{leak}}$  are the equilibrium potentials of excitatory, inhibitory, and leak currents, respectively. Bottom: Nonlinearity as a function of signal amplitude for two excitatory conductances (**b**) and for one excitatory and the release from an inhibitory conductance (**c**). Nonlinearity was defined as the difference between the voltage response to both coincident inputs and the sum of the responses to each individual input. Equilibrium potentials were set to  $E_{\text{exc}} - E_{\text{leak}} = 50$  mV and  $E_{\text{inh}} - E_{\text{leak}} = -10$  mV. **d, e**, Nonlinearity of the circuit in **c** as a function of  $E_{\text{exc}}$  and  $E_{\text{inh}}$ . Conductances were set to  $g_{\text{exc}} = g_{\text{inh}} = g_{\text{leak}}$  (**d**) or  $g_{\text{exc}} = g_{\text{inh}} = 0.5 \times g_{\text{leak}}$  (**e**). Disinhibition supports supralinear responses over a wide range of equilibrium potentials and input signal amplitudes.

[Source data](#)

[\*\*Extended Data Fig. 6 Free parameters of the conductance-based T4 neuron model.\*\*](#)

Samples ( $n = 10,000$ ) drawn from conditional probability distributions of input neuron gains and thresholds, leak reversal potential ( $E_{\text{leak}}$ ), and leak conductance ( $g_{\text{leak}}$ ) consistent with measured voltage traces of T4 neurons inferred by deep neural density estimation<sup>29</sup>. Histograms of individual parameter distributions are shown at the bottom; the remaining panels each contain the relationship between two respective

parameters. Pink arrowheads and crosses indicate model parameters used for simulations shown in Figs. 3b, c, and 5a and Extended Data Figs. 7b, c, and 8.

[Source data](#)

**Extended Data Fig. 7 A direction-selective ‘window of opportunity’.**

**a**, Schematic columnar organization of T4 neuron inputs. Synapses from Mi9 neurons (green), Tm3/Mi1 neurons (red), and Mi4 /C3 neurons (blue) are each separated by one column (hexagons) resulting in direction-dependent time differences during visual motion. Arrows indicate the directions of edge motion in corresponding panels in **b** and **c**. **b, c**, Top: Normalized T4 cell conductances ( $g/g_{\text{leak}}$ ) of respective input synapses during ON (**b**) and OFF edge motion (**c**) at a velocity of  $30^\circ \text{ s}^{-1}$  in the directions indicated in **a** using the same model parameters as in Figs. 3b, c, and 5a and Extended Data Fig. 8. Data are mean and area under curve. Arrowheads in **b** mark the coincidence of increased excitability and cholinergic excitatory input (red). Bottom: T4 cell membrane voltage ( $V_m$ ) responses predicted by the model.

[Source data](#)

**Extended Data Fig. 8 Predicted relationship between membrane potential and input resistance during edge motion.**

Simulated T4 cell membrane potential ( $V_m$ ) as a function of input resistance ( $R_{\text{in}}$ ) in response to ON (top) and OFF edges (bottom) moving at  $30^\circ \text{ s}^{-1}$  in the preferred (PD, left) and the null direction (ND, right) of the model. The arrowhead marks the peak in input resistance.

[Source data](#)

**Extended Data Fig. 9 Input resistance measurements during visual stimulation.**

Holding currents (solid lines, top), membrane potentials (solid lines, centre), and input resistances (dashed lines, bottom) of exemplary T4 neurons expressing either *GFP* (**a**) or *GFP + GluCl $\alpha$ RNAi* (**b**). To obtain input resistance measurements at high temporal resolution, neurons were subjected to at least two repetitions of identical visual stimulation while recording their membrane potentials. In this case, the stimulus was an ON edge moving at  $30^\circ \text{ s}^{-1}$  in the neuron’s preferred direction. The holding current  $I$  was altered in between the first (#1) and the second repetition (#2) by  $\Delta I = -1 \text{ pA}$ . The input resistance  $R_{\text{in}}$  at each time point was calculated as  $\Delta V_m/\Delta I$ , where  $\Delta V_m$

denotes the difference in membrane potential between repetitions (shaded areas/dashed arrows in **a**).

### [Source data](#)

## [Extended Data Fig. 10 GAL4 expression patterns, walking speeds, and bar fixation.](#)

**a**, Confocal cross section through the optic lobe of a fly expressing *GFP* (green) under control of *R39H12-GAL4* (T4/T5 >) as used in behavioural experiments in Fig. [5d–i](#). Synaptic structures were counterstained with an antibody against bruchpilot (grey). Scale bar, 40 µm. The micrograph is representative of 8 biological replicates. **b**, Average forward walking speeds of flies expressing *GluCl $\alpha$ <sup>RNAi</sup>* (teal) or *Nmdar1<sup>RNAi</sup>* (grey) in T4/T5 neurons and their parental controls (black/grey) during closed-loop bar fixation experiments in Fig. [5h, i](#). **c**, Confocal cross section through the optic lobe of a fly expressing *GFP* (green) under control of the split GAL4 line *R59E08-AD; R42F06-DBD*. Synaptic structures were counterstained with an antibody against bruchpilot (grey). Scale bar, 40 µm. The micrograph is representative of 5 biological replicates. **d**, Average forward walking speeds of flies expressing *GluCl $\alpha$ <sup>RNAi</sup>* (teal) under control of *R59E08-AD; R42F06-DBD* and their parental controls (black/grey) during closed-loop bar fixation in **e**, **f**. **e**, Exemplary bar trajectories (242 trials and 11 flies per genotype, top) and the overall bar position probabilities (bottom) for flies expressing *GluCl $\alpha$ <sup>RNAi</sup>* (teal) under control of *R59E08-AD; R42F06-DBD* and their parental controls (back/grey). Data are mean ± s.e.m. of flies in **f**. **f**, The percentage of time that the bar occupied a central 60° window (fixation in front, dashed lines in **e**). The dashed line indicates the chance level. Circles, individual flies; bars, mean ± s.e.m. Asterisk denotes a significant difference from both parental controls ( $P = 0.0012$ , one-way ANOVA followed by Holm–Šídák’s multiple comparisons test).  $n$  values indicate the number of flies.

### [Source data](#)

## Supplementary information

### [Supplementary Information](#)

This file contains Supplementary Equations and Supplementary Tables 1 and 2.

### [Reporting Summary](#)

## Source data

[Source Data Fig. 1](#)

[Source Data Fig. 2](#)

[Source Data Fig. 3](#)

[Source Data Fig. 4](#)

[Source Data Fig. 5](#)

[Source Data Extended Data Fig. 1](#)

[Source Data Extended Data Fig. 2](#)

[Source Data Extended Data Fig. 4](#)

[Source Data Extended Data Fig. 5](#)

[Source Data Extended Data Fig. 6](#)

[Source Data Extended Data Fig. 7](#)

[Source Data Extended Data Fig. 8](#)

[Source Data Extended Data Fig. 9](#)

[Source Data Extended Data Fig. 10](#)

## Rights and permissions

**Open Access** This article is licensed under a Creative Commons Attribution 4.0 International License, which permits use, sharing, adaptation, distribution and reproduction in any medium or format, as long as you give appropriate credit to the original author(s) and the source, provide a link to the Creative Commons license, and indicate if changes were made. The images or other third party material in this article are included in the article's Creative Commons license, unless indicated otherwise in a credit line to the material. If material is not included in the article's Creative Commons license and your intended use is not permitted by statutory regulation or exceeds the permitted use, you will need to obtain permission directly from the copyright holder. To view a copy of this license, visit <http://creativecommons.org/licenses/by/4.0/>.

## [Reprints and Permissions](#)

## About this article

### Cite this article

Groschner, L.N., Malis, J.G., Zuidinga, B. *et al.* A biophysical account of multiplication by a single neuron. *Nature* **603**, 119–123 (2022).  
<https://doi.org/10.1038/s41586-022-04428-3>

- Received: 21 June 2021
- Accepted: 14 January 2022
- Published: 23 February 2022
- Issue Date: 03 March 2022
- DOI: <https://doi.org/10.1038/s41586-022-04428-3>

### Share this article

Anyone you share the following link with will be able to read this content:

[Get shareable link](#)

Sorry, a shareable link is not currently available for this article.

[Copy to clipboard](#)

Provided by the Springer Nature SharedIt content-sharing initiative

---

This article was downloaded by **calibre** from <https://www.nature.com/articles/s41586-022-04428-3>

- Article
- Open Access
- [Published: 23 February 2022](#)

# TDP-43 represses cryptic exon inclusion in the FTD–ALS gene *UNC13A*

- [X. Rosa Ma](#) ORCID: [orcid.org/0000-0001-8297-4279<sup>1</sup>](https://orcid.org/0000-0001-8297-4279)<sup>nal</sup>,
- [Mercedes Prudencio](#) ORCID: [orcid.org/0000-0002-4894-4858<sup>2,3</sup>](https://orcid.org/0000-0002-4894-4858)<sup>nal</sup>,
- [Yuka Koike](#) ORCID: [orcid.org/0000-0002-5067-8579<sup>2,3</sup>](https://orcid.org/0000-0002-5067-8579)<sup>nal</sup>,
- [Sarat C. Vatsavayai](#)<sup>4,5</sup>,
- [Garam Kim](#) ORCID: [orcid.org/0000-0001-5907-1127<sup>1,6</sup>](https://orcid.org/0000-0001-5907-1127),
- [Fred Harbinski](#)<sup>7</sup>,
- [Adam Briner](#) ORCID: [orcid.org/0000-0002-4760-5037<sup>1,8</sup>](https://orcid.org/0000-0002-4760-5037),
- [Caitlin M. Rodriguez](#)<sup>1</sup>,
- [Caiwei Guo](#)<sup>1</sup>,
- [Tetsuya Akiyama](#) ORCID: [orcid.org/0000-0002-8076-1242<sup>1</sup>](https://orcid.org/0000-0002-8076-1242),
- [H. Broder Schmidt](#)<sup>9</sup>,
- [Beryl B. Cummings](#)<sup>7</sup>,
- [David W. Wyatt](#)<sup>7</sup>,
- [Katherine Kurylo](#)<sup>7</sup>,
- [Georgiana Miller](#)<sup>7</sup>,
- [Shila Mekhoubad](#)<sup>7</sup>,
- [Nathan Sallee](#)<sup>7</sup>,
- [Gemechu Mekonnen](#)<sup>10,11</sup>,
- [Laura Ganser](#)<sup>12</sup>,
- [Jack D. Rubien](#) ORCID: [orcid.org/0000-0003-1203-0445<sup>13</sup>](https://orcid.org/0000-0003-1203-0445),
- [Karen Jansen-West](#)<sup>2</sup>,
- [Casey N. Cook](#)<sup>2,3</sup>,
- [Sarah Pickles](#)<sup>2,3</sup>,
- [Björn Oskarsson](#) ORCID: [orcid.org/0000-0002-1725-9866<sup>14</sup>](https://orcid.org/0000-0002-1725-9866),
- [Neill R. Graff-Radford](#)<sup>14</sup>,
- [Bradley F. Boeve](#) ORCID: [orcid.org/0000-0002-4153-8187<sup>15</sup>](https://orcid.org/0000-0002-4153-8187),
- [David S. Knopman](#) ORCID: [orcid.org/0000-0002-6544-066X<sup>15</sup>](https://orcid.org/0000-0002-6544-066X),
- [Ronald C. Petersen](#)<sup>15</sup>,

- [Dennis W. Dickson](#) [ORCID: orcid.org/0000-0001-7189-7917<sup>2,3</sup>](#),
- [James Shorter<sup>13</sup>](#),
- [Sua Myong<sup>10,11,12</sup>](#),
- [Eric M. Green](#) [ORCID: orcid.org/0000-0001-7874-9482<sup>7</sup>](#),
- [William W. Seeley<sup>4,5</sup>](#),
- [Leonard Petrucelli](#) [<sup>2,3</sup>](#) &
- [Aaron D. Gitler](#) [ORCID: orcid.org/0000-0001-8603-1526<sup>1</sup>](#)

*Nature* volume 603, pages 124–130 (2022)

- 27k Accesses
- 3 Citations
- 169 Altmetric
- [Metrics details](#)

## Subjects

- [Amyotrophic lateral sclerosis](#)
- [Neurodegeneration](#)
- [RNA splicing](#)
- [Transcriptomics](#)

## Abstract

A hallmark pathological feature of the neurodegenerative diseases amyotrophic lateral sclerosis (ALS) and frontotemporal dementia (FTD) is the depletion of RNA-binding protein TDP-43 from the nucleus of neurons in the brain and spinal cord<sup>1</sup>. A major function of TDP-43 is as a repressor of cryptic exon inclusion during RNA splicing<sup>2,3,4</sup>. Single nucleotide polymorphisms in *UNC13A* are among the strongest hits associated with FTD and ALS in human genome-wide association studies<sup>5,6</sup>, but how those variants increase risk for disease is unknown. Here we show that TDP-43 represses a cryptic exon-splicing event in *UNC13A*. Loss of TDP-43 from the nucleus in human brain, neuronal cell lines and motor neurons derived from induced pluripotent stem cells resulted in the inclusion of a cryptic exon in *UNC13A* mRNA and reduced *UNC13A* protein expression. The top variants associated with FTD or ALS risk in humans are located in the intron harbouring the cryptic exon, and we show that they increase *UNC13A* cryptic exon splicing in the face of TDP-43 dysfunction. Together, our data provide a direct functional link between one of the strongest genetic

risk factors for FTD and ALS (*UNC13A* genetic variants), and loss of TDP-43 function.

[Download PDF](#)

## Main

TDP-43, encoded by the *TARDBP* gene, is an abundant, ubiquitously expressed RNA-binding protein that normally localizes to the nucleus. It has a role in fundamental RNA-processing activities, including RNA transcription, alternative splicing and RNA transport<sup>7</sup>. A major splicing regulatory function of TDP-43 is to repress the inclusion of cryptic exons during splicing<sup>2,8,9,10</sup>. Unlike normal conserved exons, these cryptic exons occur in introns and are normally excluded from mature mRNAs. When TDP-43 is depleted from cells, these cryptic exons get spliced into messenger RNAs, often introducing frame shifts and premature termination, or even reduced RNA stability. However, the key cryptic splicing events that are integral to disease pathogenesis remain unknown.

*STMN2*—which encodes stathmin 2, a regulator of microtubule stability—is the gene whose expression is most significantly reduced when TDP-43 is depleted from neurons<sup>3,4</sup>. *STMN2* harbours a cryptic exon (exon 2a) that is normally excluded from the mature *STMN2* mRNA. The first intron of *STMN2* contains a TDP-43 binding site. When TDP-43 is lost or its function is impaired, exon2a gets incorporated into the mature mRNA. Exon 2a harbours a stop codon and a polyadenylation signal—this results in truncated *STMN2* mRNA and eightfold reduction<sup>3</sup> of stathmin 2. Aberrant splicing and reduced stathmin 2 levels seem to be a major feature of sporadic and familial cases of ALS (except those with *SOD1* mutations)<sup>3,4</sup> and in frontotemporal lobar degeneration (FTLD) due to TDP-43 proteinopathy<sup>11</sup> (FTLD-TDP). The discovery of *STMN2* cryptic exon splicing in ALS and FTLD-TDP highlights a key mRNA target—we aimed to identify other possible mRNA targets.

To discover cryptic splicing targets regulated by TDP-43 that may also have a role in disease pathogenesis, we used a recently generated RNA sequencing (RNA-seq) dataset<sup>12</sup>. To generate this dataset, fluorescence-activated cell sorting (FACS) was used to enrich neuronal nuclei with and without TDP-43 from postmortem brain tissue from patients with FTD and ALS (FTD–ALS); RNA-seq was performed to compare the transcriptomic profiles of TDP-43-positive and TDP-43-negative neuronal nuclei. This identified several differentially expressed genes<sup>12</sup>. We re-analysed the data to identify novel alternative splicing events affected by the loss of nuclear TDP-43. We performed splicing analyses using two pipelines, MAJIQ<sup>13</sup> and LeafCutter<sup>14</sup>, designed to detect novel splicing events (Fig. 1a). We identified 266 alternative splicing events

( $P(\Delta\Psi > 0.1) > 0.95$ ; where  $\Delta\Psi$  signifies changes of local splicing variations between two conditions) with MAJIQ and 152 with LeafCutter ( $P < 0.05$ ). There were 66 alternatively spliced genes in common between the two analyses (Fig. 1b), probably because each tool uses different definitions for transcript variations and different criteria to control for false positives (Supplementary Note 1). These genes have at least one region that both tools identified to be alternatively spliced (Supplementary Table 1). Among the alternatively spliced genes identified by both tools were *STMN2* and *POLDIP3*, both of which have been extensively validated as bona fide targets of splicing by TDP-43<sup>3,4,11,15</sup>.

**Fig. 1:** Nuclear depletion of TDP-43 causes CE inclusion in *UNC13A* RNA and reduced expression of *UNC13A* protein.

 figure 1

- a**, Splicing analyses were performed on RNA-sequencing results from TDP-43-positive and TDP-43-negative neuronal nuclei isolated from frontal cortices of seven patients with FTD or FTD–ALS. Some illustrations were created with BioRender.com.
- b**, Sixty-six alternatively spliced genes identified by both MAJIQ ( $P(\Delta\Psi > 0.1) > 0.95$ ) and LeafCutter ( $P < 0.05$ ). Genes in blue are previously validated TDP-43 splicing targets<sup>3,4,11,15</sup>. **c, f**, RT–qPCR confirmed inclusion of CE in *UNC13A* mRNA upon TDP-43 depletion in SH-SY5Y cells ( $n = 5$  cell culture experiments for each

condition; two sided-Welch two-sample *t*-test; mean ± s.e.m.) (**c**) and in 3 independent lines of iPSC-MNs ( $n = 2$  independent cell culture experiments, each with 2 technical replicates for each iPSC-MN) (**f**). *RPLP0* was used to normalize RT-qPCR. Three-way ANOVA; mean ± s.e.m. *TDP-43* is also known as *TARDBP*. **d, e, g, h**, Immunoblotting for *UNC13A* and *TDP-43* protein levels in SH-SY5Y cells (**d**; quantified in **e**) and iPSC-MNs (**g**; quantified in **h**) treated with scramble (shScramble) or *TDP-43* shRNA ( $n = 3$  independent cell culture experiments for each condition). *GAPDH* served as a loading control. Two-sided Welch two-sample *t*-test, mean ± s.e.m. Gel source data are shown in Supplementary Fig. [1a, b](#).

### Source data

*UNC13A* was one of the genes with the most significant levels of alternative splicing (MAJIQ  $\Delta\Psi = 0.779$ ; LeafCutter  $\Delta\Psi = 0.8360$ ;  $P < 0.0001$ ) in neurons with nuclear *TDP-43* depletion (Fig. [1b](#)). Depletion of *TDP-43* resulted in the inclusion of a 128-bp or a 178-bp cryptic exon between the canonical exons 20 and 21 (hg38; chr19: 17642414–17642541 (128bp); chr19: 17642591–17642414 (178 bp)) (Extended Data Fig. [1a–e](#), Supplementary Note [2](#)). The two cryptic exons share the same 3' end but the 178-bp cryptic exon is 50 bp longer than the 128-bp cryptic exon at the 5' end. The cryptic exons were almost completely absent in wild-type neuronal nuclei (Fig. [1f](#)) and are not present in any of the known human isoforms of *UNC13A*<sup>[16](#)</sup>. Furthermore, analysis of ultraviolet cross-linking and immunoprecipitation (iCLIP) data for *TDP-43*<sup>[17](#)</sup> provides evidence that *TDP-43* binds directly to the intron harbouring these cryptic exons (shown by mapped reads) (Extended Data Fig. [1g](#)). Because of the much higher abundance of the 128-bp cryptic exon in the RNA-seq data that we analysed, we focused our analyses on this cryptic exon, which we refer to as CE. Intron 20–21 of *UNC13A* and the CE sequence are conserved among most primates (Extended Data Fig. [2a, b](#)) but not in mouse (Extended Data Fig. [2c, d](#)), similar to *STMN2* and other cryptic splicing targets of *TDP-43*<sup>[2,3,4](#)</sup>. Together, these results suggest that *TDP-43* functions to repress the inclusion of a cryptic exon in the *UNC13A* mRNA.

To determine whether *TDP-43* directly regulates this *UNC13A* cryptic splicing event, we used short hairpin RNA (shRNA) to reduce *TDP-43* levels in SH-SY5Y cells and quantitative PCR with reverse transcription (RT-qPCR) to detect CE inclusion in *UNC13A* transcript. CE was present in cells with *TDP-43* depletion but not in cells treated with control shRNA (Fig. [1e](#)). Along with the increase in CE, there was a corresponding decrease in the amount of the canonical *UNC13A* transcript upon *TDP-43* depletion (Fig. [1c](#)). By immunoblotting, we also observed a marked reduction in *UNC13A* protein in *TDP-43*-depleted cells (Fig. [1d, e](#)). Reducing levels of *TDP-43* in motor neurons derived from induced pluripotent stem cells (iPSC-MNs) (Fig. [1f–h](#), Extended Data Fig. [3a, b](#), Supplementary Table [3](#)) and excitatory neurons (i<sup>3</sup>Ns) derived from human induced pluripotent stem (iPS) cells (Extended Data Fig. [3c](#)) also

resulted in CE inclusion and a reduction in *UNC13A* mRNA and protein. We confirmed insertion of the cryptic exon sequences into the mature transcript by amplicon sequencing of the product of reverse transcription with PCR (RT–PCR) (Extended Data Fig. 3d; see Supplementary Note 2) and demonstrated that the insertions introduce premature stop codons (Extended Data Fig. 3f–i), consistent with the observed decrease in *UNC13A* protein. *UNC13A* gene expression is probably regulated at multiple levels beyond simply inclusion of the cryptic exons. Other aspects of the cryptic exon-inclusion event (for example, aberrant peptides produced from it) could cause defects, although we do not yet have evidence that such peptides are produced. Thus, lowering levels of TDP-43 in human cells and neurons causes inclusion of CE in the *UNC13A* transcript, resulting in decreased *UNC13A* protein.

*UNC13A* belongs to a family of genes originally discovered in *Caenorhabditis elegans* and was named on the basis of the uncoordinated (*unc*) movements exhibited by animals with mutations in these genes<sup>18</sup>, owing to deficits in neurotransmitter release. *UNC13A* encodes a large multidomain protein that is expressed in the nervous system, where it localizes to most synapses in the central nervous system and neuromuscular junctions, and has an essential role in the vesicle priming step, prior to synaptic vesicle fusion<sup>19,20,21,22</sup>. *UNC13A* is an essential neuronal protein because mice lacking Unc13a (also called Munc13-1) exhibit functional deficits at glutamatergic synapses, demonstrated by a lack of fusion-competent synaptic vesicles, and die within a few hours of birth<sup>21</sup>. Our data suggest that depletion of TDP-43 leads to loss of this critical synaptic protein. As well as *UNC13A*, several other genes encoding synaptic proteins are mis-spliced upon TDP-43 depletion (Fig. 1b). We validated the splicing events in three of these genes (*KALRN*, *RAPGEF6* and *SYT7*) in induced pluripotent stem (iPS) cell-derived neurons (iNs) using RT–qPCR (Extended Data Fig. 4), providing evidence that disruption of synaptic function could be a major mechanism in the pathogenesis of ALS and FTD.

To extend our analysis of *UNC13A* cryptic exon inclusion to a larger collection of patient samples, we first analysed a series of 117 frontal cortex brain samples from the Mayo Clinic Brain Bank using RT–qPCR and a pair of primers that detects the shared 3' end of the cryptic exons. We found a significant increase in *UNC13A* cryptic exon in the frontal cortices of patients with FTLD-TDP compared with healthy controls (Fig. 2a, Extended Data Fig. 5a). Next, we analysed brain samples from the New York Genome Center (NYGC). We interrogated RNA-seq data from 1,151 tissue samples from 413 individuals (with multiple tissues per individual; see Supplementary Note 3), 330 of whom are patients with ALS or FTD. We detected *UNC13A* splice variants in nearly 50% of the frontal and temporal cortical tissues donated by patients with neuropathologically confirmed FTLD-TDP (Fig. 2b) and in some of the patients with ALS whose pathology has not been confirmed (Extended Data Fig. 5b). Notably, we did not observe *UNC13A* splice variants in any of the samples from patients with

FTLD associated with FUS (FTLD-FUS) ( $n = 9$ ) or TAU (FTLD-TAU) ( $n = 18$ ) or ALS associated with SOD1 (ALS-SOD1) ( $n = 22$ ), nor in any of the control samples ( $n = 197$ ) (Fig. 2b). Using the same criteria, we detected the known *STMN2* cryptic exon<sup>3,4</sup> in tissues from these patients, and the majority of the *UNC13A* splice variant containing tissues also contained the *STMN2* splice variant (Supplementary Table 2). Hyperphosphorylated TDP-43 (pTDP-43) is a key feature of the pathology of these diseases<sup>1</sup>. We found a strong association between higher levels of pTDP-43 and higher levels of *UNC13A* CE inclusion in patients with FTLD-TDP (Spearman's  $\rho = 0.610$ ,  $P < 0.0001$ ) (Extended Data Fig. 2c). Thus, *UNC13A* CE inclusion is a robust and specific facet of pathobiology in TDP-43 proteinopathies.

**Fig. 2: *UNC13A* CE inclusion in human TDP-43 proteinopathies.**

---

 **figure 2**

**a**, *UNC13A* CE expression level is increased in the frontal cortices of patients with FTLD-TDP. *GAPDH* and *RPLP0* were used to normalize the RT–qPCR (two-tailed Mann–Whitney test, mean  $\pm$  95% confidence interval). The schematic to the right shows the localization of the primer pair (arrows) used for the RT–qPCR assay.

---

Healthy:  $n = 27$ ; sporadic FTLD-TDP:  $n = 34$ ; *C9ORF72*+ FTLD-TDP:  $n = 47$ ; *GRN*+ FTLD-TDP:  $n = 9$ . **b**, *UNC13A* CE is detected in nearly 50% of frontal cortical tissues and temporal cortical tissues from neuropathologically confirmed FTLD-TDP patients in bulk RNA-sequencing from the NYGC ALS Consortium cohort. CE is absent in tissues from healthy controls and patients with FTLD-FUS, FTLD-TAU or ALS-SOD1.

### Source data

To visualize the *UNC13A* CE within single cells in the human brain, we designed custom BaseScope *in situ* hybridization probes that specifically bind to the exon 20–CE junction (Fig. 3a) or the exon 20–exon 21 junction (Extended Data Fig. 6c). We used these probes for *in situ* hybridization, combined with immunofluorescence for NeuN (to detect neuronal nuclei) and TDP-43. We stained sections from the medial frontal pole of four patients with FTLD-TDP and three controls (Supplementary Table 4). In neurons showing loss of nuclear TDP-43 and accompanying cytoplasmic TDP-43 inclusions, we observed *UNC13A* CE-containing mRNA splice variants in the nucleus (Fig. 3b, Extended Data Fig. 6a). We observed between one and four CE-containing mRNA puncta per nucleus. We did not observe puncta in the cytoplasm, perhaps because CE introduces a premature stop codon, which could lead to nonsense-mediated decay. Controls, however, had universally normal nuclear TDP-43 staining and showed no evidence of *UNC13A* cryptic splicing (Fig. 3b, Extended Data Fig. 6b). Next, we sought to determine whether TDP-43 nuclear depletion is associated with reduced expression of canonical *UNC13A* mRNA. In control brain tissue, *UNC13A* mRNA was widely expressed in neurons across cortical layers (Extended Data Fig. 6d, e). In patients, we saw a trend for reduced *UNC13A* mRNA in neurons showing TDP-43 pathology compared with neighbouring neurons with normal nuclear TDP-43 (Extended Data Fig. 6d, e), consistent with the RT–qPCR data (Fig. 1c, f). These findings suggest that cryptic splicing of *UNC13A* is absent from controls and, in patients, is seen exclusively in neurons showing depleted nuclear TDP-43.

**Fig. 3: *UNC13A* cryptic splicing is associated with loss of nuclear TDP-43 in patients with FTD and motor neuron disease.**

---

 **figure 3**

---

**a**, The design of the *UNC13A* e20/CE BaseScope probe targeting the alternatively spliced *UNC13A* transcript. Each Z binds to the transcript independently, and both must be in close proximity for successful signal amplification, ensuring binding specificity. **b**, BaseScope *in situ* hybridization using the *UNC13A* e20/CE probe, combined with immunofluorescence for TDP-43 and NeuN, was performed on sections from the medial frontal pole of patients with FTD and motor neuron disease

(FTD–MND) and healthy controls. Representative images illustrate the presence of *UNC13A* CE (arrowheads) in neurons showing depletion of nuclear TDP-43. Neurons with normal nuclear TDP-43 in patients and controls show no CE signal (arrows). Images are maximum intensity projections of a confocal image z-stack. Scale bar, 10 µm. Images representative of six non-overlapping images from each individual. We optimized *UNC13A* probes on two cases and two controls in three separate experiments, with similar findings.

*UNC13A* is one of the top hits for ALS and FTD–ALS in multiple genome-wide association studies<sup>5,6,23,24,25,26</sup> (GWAS). Single nucleotide polymorphisms (SNPs) in *UNC13A* are associated with increased risk of sporadic ALS<sup>5</sup> and sporadic FTLD-TDP pathology, especially type B, the subtype associated with FTD–ALS<sup>6</sup>. In addition to increasing susceptibility to ALS, SNPs in *UNC13A* are associated with shorter survival in patients with ALS<sup>27,28,29,30</sup>. But the mechanism by which genetic variation in *UNC13A* increases risk for ALS and FTD is unknown. Notably, the two most significantly associated SNPs, rs12608932 (A>C) and rs12973192 (C>G), are both located in the same intron that we found harbours CE, with rs12973192 located in CE itself (Fig. 4a,c). This immediately suggested that these SNPs (or other nearby genetic variations tagged by these SNPs) might make *UNC13A* more vulnerable to CE inclusion upon TDP-43 depletion. To test this, we analysed the percentage of RNA-seq reads that mapped to intron 20–21 that support the inclusion of CE (Extended Data Fig. 7a,b). Among the seven patients included in the initial splicing analysis (Fig. 1a), two out of three who were homozygous (G/G) and the one patient who was heterozygous (C/G) for the risk allele at rs12973192, showed inclusion of CE in almost every *UNC13A* mRNA that was mapped to intron 20–21. By contrast, the three other patients who were homozygous for the reference allele (C/C) showed much less inclusion of CE (Extended Data Fig. 7a,b). Another way to directly assess the effect of the *UNC13A* risk alleles on CE inclusion is to measure allele imbalance in RNAs from individuals who are heterozygous for the risk allele. Two of the iPSC-MN lines that we used to detect CE inclusion upon TDP-43 knockdown (iPSC-MN1 and iPSC-MN3; Fig. 1h) are heterozygous (C/G) at rs12973192. We performed amplicon sequencing of the RT–PCR product that spans CE and analysed the allele distribution from these two samples (Extended Data Fig. 3d,e) as well as the one patient sample from the original RNA-seq dataset (Fig. 1a) that is heterozygous (C/G) at rs12973192 (Extended Data Fig. 7b). We found a significant difference between the percentage of risk and reference alleles in the spliced variant, with higher inclusion of the risk allele (Fig. 4b, Extended Data Fig. 7c).

**Fig. 4: *UNC13A* risk haplotype associated with ALS or FTD susceptibility potentiates CE inclusion when TDP-43 is dysfunctional.**

---

 **figure 4**

**a**, LocusZoom plot showing SNPs associated with ALS or FTD in *UNC13A*. SNPs are coloured on the basis of levels of linkage equilibrium; SNPs rs12608932 and rs12973192 are in strong linkage disequilibrium (LD). **b**, There is a higher percentage inclusion of the risk allele (G) at rs12973192 in the *UNC13A* splice variant ( $n = 3$  biologically independent samples; two-sided paired *t*-test; mean  $\pm$  s.e.m.). Quantification in Extended Data Fig. 7c. **c**, Location of rs56041637 relative to the two known FTD–ALS GWAS hits and *UNC13A* CE. **d**, Design of *UNC13A* CE minigene reporter constructs and location of the primer pair used for RT–PCR. Black (reference alleles) and blue (risk alleles) triangles represent the genetic variants as shown in c. **e**, Splicing of minigene reporters was assessed in wild-type (WT) and TDP-43<sup>−/−</sup> HEK 293T cells. In addition to the inclusion of CE (2), some splice variants showed inclusion of one of the other two cryptic splicing products (3 and 4) (Extended Data Figs. 1a–e, 3a, Supplementary Note 2). The risk haplotype-carrying minigene showed an almost complete loss of canonical splicing product (1) and an increase in alternatively spliced products (2, 3 and 4).  $n = 2$  independent cell culture experiments for each condition. **f**, Top, survival curves of FTLD-TDP patients stratified on the basis of the number of risk haplotypes. Heterozygous (1) and homozygous (2) patients had shorter survival time after disease onset ( $n = 205$ , Mayo Clinic Brain Bank; score (log-rank) test,  $P = 0.004$ ). Dashed lines mark median survival for each genotype. Risk haplotype effect is modelled additively using Cox multivariable analysis adjusted for

genetic mutations, sex and age at onset. Bottom, risk table. Summary results of the analysis are shown in Extended Data Fig. 10b.

### Source data

Given this evidence for an effect of the risk allele on CE inclusion, we extended our analysis by genotyping patients with FTLD-TDP harbouring CE ( $n = 86$ ) in the Mayo Clinic Brain Bank dataset for the *UNC13A* risk alleles at rs12973192 and rs12608932. Because these two SNPs are in high linkage disequilibrium in the European population<sup>31</sup>, we consider them to be on the same haplotype. Thus, we refer to the haplotype that contains reference alleles at both SNPs as the reference haplotype, and the haplotype that contains risk alleles as the risk haplotype. We excluded the one patient who is homozygous for the reference allele (C/C) at rs12973192 but heterozygous (A/C) at rs12608932. The remaining patients ( $n = 85$ ) have exactly the same number of risk alleles at both loci, indicating that it's very likely that they are carriers of the reference haplotype or the risk haplotype. Using a multiple linear regression model, we found a strong positive correlation ( $\beta = 0.175$ ,  $P = 0.0290$ ) between the number of risk haplotypes and the abundance of *UNC13A* CE inclusion measured by RT–qPCR (Extended Data Fig. 7e). Together, these data suggest that genetic variation in *UNC13A* that increases risk for ALS and FTD in humans promotes CE inclusion upon nuclear depletion of TDP-43.

GWAS SNPs typically do not cause the trait but rather ‘tag’ other neighbouring genetic variation<sup>32</sup>. Thus, a major challenge in human genetics is to go from a GWAS hit to identifying the causative genetic variation that increases risk for disease<sup>33</sup>. A LocusZoom<sup>34</sup> plot (Fig. 4a) generated using results from an ALS GWAS<sup>35</sup> suggests that the strongest association signal on *UNC13A* is indeed in the region surrounding the two lead SNPs (rs12973192 and rs12608932). To identify other genetic variants in intron 20–21 that might also cause risk for disease by influencing CE inclusion but were not included in the original GWAS, we analysed genetic variants identified in whole genome sequencing data of 297 ALS patients of European descent (Answer ALS; <https://www.answersals.org>). We searched for novel genetic variants that could be tagged by the two SNPs by looking for other loci in intron 20–21 that are in linkage disequilibrium with both rs12608932 and rs12973192. We found one that fit these criteria: rs56041637 (Extended Data Fig. 7d). rs56041637 is a CATC-repeat insertion in intron 20–21. Most frequently there are six CATC repeats in this region. In the patient dataset, we observed that patients who are homozygous for the risk alleles at both rs12608932 and rs12973192 tend to have 3 to 5 additional CATC repeats; patients who are homozygous for reference alleles at both rs12608932 and rs12973192 tend to have only 0 to 2 additional repeats (Fig. 4c; CATC is shown as GATG because *UNC13A* is on the reverse strand). Thus, in addition to the two lead GWAS SNPs (rs12608932 and rs12973192), we now nominate rs56041637 as potentially

contributing to risk for disease by making *UNC13A* more vulnerable to CE inclusion when TDP-43 is depleted from the nucleus.

To directly test whether these three variants in *UNC13A*—which are part of the risk haplotype—increase CE inclusion upon TDP-43 depletion, we synthesized minigene reporter constructs (Fig. 4d). The reporter uses a bidirectional promoter to co-express eGFP containing a canonical intron and mCherry that is interrupted by *UNC13A* intron 20–21 from either the reference haplotype or the risk haplotype. Because *UNC13A* is on the reverse strand, the reference alleles and the risk alleles are the reverse complement of the genotypes reported on dbSNP—for example, in intron 20–21 of *UNC13A*, the reference allele at rs12973192 is G and the corresponding risk allele is C. We transfected wild-type and TDP-43-knock-out ( $\text{TDP43}^{-/-}$ ) HEK 293T cells<sup>36</sup> with each minigene reporter construct. Using RT–PCR, we found that both versions of intron 20–21 were efficiently spliced out in wild-type cells (Fig. 4e, lanes 1–4). However, in  $\text{TDP43}^{-/-}$  cells there was a decrease in completely intron-free splicing products and a concomitant increase in cryptic splicing products (Fig. 4e, lanes 5–6). Of note, in  $\text{TDP43}^{-/-}$  cells transfected with the minigene construct harbouring the risk haplotype in the intron, there was an even greater decrease in complete intron 20–21 splicing, and a proportional increase in cryptic splicing products (Fig. 4e, lanes 7–8; see Supplementary Note 2). The transcript levels of the eGFP control remained constant across all conditions, verifying equal reporter expression levels and the integrity of the splicing machinery independent of TDP-43.

To define the effect of each individual risk variant on splicing, we generated six additional minigene reporters, each carrying a different combination of the reference and risk alleles (individually, two at a time, or all three). Using RT–qPCR, we found that the risk variant in CE (rs12973192) had the strongest effect on CE inclusion in cells lacking TDP-43. The other variants also contributed to mis-splicing, but in a non-additive way, and the largest effect was with the construct harbouring all three risk variants (Extended Data Fig. 8). Expression of full-length TDP-43 rescued the splicing defects, whereas an RNA binding-deficient mutant did not (Extended Data Fig. 9). Together, these results provide direct functional evidence that TDP-43 regulates splicing of *UNC13A* intron 20–21 and that genetic variants associated with ALS and FTD susceptibility in humans potentiate cryptic exon inclusion when TDP-43 is dysfunctional.

To directly test whether the risk variants affected TDP-43 binding, we performed quantitative electrophoretic mobility shift assays (EMSA). We incubated radioactively labelled RNA probes containing reference or risk versions of sequences within the *UNC13A* CE or intronic region with recombinant full-length TDP-43. This resulted in a mobility shift, indicating that TDP-43 can bind to these sequences (Extended Data Fig. 10a). TDP-43 binds the reference and risk versions of the CE probe with similar

affinity but the intronic risk allele results in a minor reduction in affinity (Extended Data Fig. 10a). TDP-43 had lower affinity for the probe containing the risk allele at rs56041637 compared with the probe containing the reference allele (Fig. 4g). Overall, TDP-43 has a much higher affinity for the intron sequence compared with the exon or repeat sequence. The diminished binding affinity of TDP-43 to risk alleles of the intron and repeat sequence may contribute to the increased cryptic splicing found in ALS and FTD. We note that these in vitro binding results are somewhat different from those reported in the accompanying Article by Brown and colleagues<sup>37</sup>. Our use of full-length TDP-43, which can be prone to aggregation (although our maltose-binding protein (MBP)-tagged TDP-43 is soluble) but contains additional domains that are important for TDP-43 function, differs from the one used by Brown and colleagues, which contains only the TDP-43 RNA-recognition motifs (RRMs). Future studies will be required to explore how TDP-43 regulates the cryptic splicing of *UNC13A* and other splicing targets and the effect of different genetic variations on TDP-43 binding in vivo.

To examine whether these SNPs affect survival in patients with FTLD-TDP, we evaluated the association of the risk haplotype with survival time after disease onset using data from the Mayo Clinic Brain Bank ( $n = 205$ ). Using Cox multivariable analysis adjusting for other factors known to influence survival (genetic mutations, sex and age at onset), the risk haplotype was associated with survival time under an additive model (Fig. 4f). The number of risk haplotypes an individual carries was a strong prognostic factor (Extended Data Fig. 10b). The association remained significant under a dominant model (Extended Data Fig. 10c,d) and a recessive model (Extended Data Fig. 10e,f), indicating that carrying the risk haplotype reduces patient survival time after disease onset, consistent with previous analyses<sup>27,28,29,30</sup>. Thus, as suggested by previous studies<sup>28,30,38</sup>, genetic variants in *UNC13A* that increase cryptic exon inclusion are associated with decreased survival in patients.

Here we have found that TDP-43 regulates a cryptic splicing event in the FTD–ALS risk gene *UNC13A*. The most significant genetic variants associated with disease risk are located within the intron harbouring the cryptic exon itself. Brain samples from patients with FTLD-TDP carrying these SNPs exhibited more *UNC13A* CE inclusion than those from patients with FTLD-TDP lacking the risk alleles. These risk alleles seem insufficient to cause CE inclusion because CE is not detected extensively in RNA-seq data from healthy control samples<sup>16</sup> (GTEx) and our functional studies indicate that TDP-43 dysfunction is required for substantial CE inclusion. Instead, the *UNC13A* risk alleles exert a TDP-43 loss-of-function-dependent disease-modifying effect. We propose that *UNC13A* risk alleles might act as a kind of Achilles' heel, not causing problems until TDP-43 becomes dysfunctional. The discovery of a novel TDP-43-dependent cryptic splicing event in a bona fide FTD–ALS risk gene opens up a multitude of new directions for validating *UNC13A* as a biomarker and therapeutic

target in ALS and FTD. This cryptic exon inclusion event—similar to that of *STMN2*<sup>3,4</sup>—is not conserved in mouse, so will require studies in human neuron models to test whether blocking *UNC13A* cryptic splicing is sufficient to rescue phenotypes associated with loss of TDP-43 function. It is possible that a full rescue of TDP-43 function will require restoration of more than one cryptic splicing target (for example, *STMN2*, *UNC13A* and perhaps some of the others (Fig. 1b)). But the human genetics data (Fig. 4f) showing a dose-dependent decrease in survival in individuals carrying *UNC13A* risk alleles indicate that *UNC13A* is a key target of TDP-43. We note that *UNC13A* is more highly expressed in the frontal cortex (transcripts per million (TPM) = 530.2) than in the spinal cord<sup>16</sup> (TPM = 35.54). One picture that might emerge is that the cryptic target *STMN2* could have a key role in lower motor neurons in the spinal cord, whereas *UNC13A* could have a key role in the brain. Perhaps some combination of effects could contribute to ALS or FTD. It remains unknown why TDP-43 pathology is associated with ALS, FTLD-TDP, or even other aging-related neuropathological changes<sup>39</sup>. TDP-43-dysfunction-related cryptic splicing plays out across the diverse regional and neuronal landscape of the human brain. It is tempting to speculate that in addition to *STMN2* and *UNC13A*, there could be specific portfolios of other important cryptic exon splicing events (and genetic variations that increase or decrease susceptibility to some of these events) that contribute to heterogeneity in clinical manifestation of TDP-43 dysfunction.

## Methods

All materials used in this study are available upon request.

### RNA-seq alignment and splicing analysis

The detailed pipeline v2.0.1 for RNA-seq alignment and splicing analysis is available on [https://github.com/emc2cube/Bioinformatics/sh\\_RNAseq.sh](https://github.com/emc2cube/Bioinformatics/sh_RNAseq.sh). FASTQ files were downloaded from the Gene Expression Omnibus (GEO) database (GSE126543). Adaptors in FASTQ files were removed using trimmomatic (0.39) (ILLUMINACLIP:TruSeq3-PE.fa:2:30:10 LEADING:3 TRAILING:3 SLIDINGWINDOW:4:15 MINLEN:36). The quality of the resulting files was evaluated using FastQC (v0.11.9). RNA-seq reads were mapped to the human (hg38) using STAR v2.7.3a following ENCODE standard options, read counts were generated using RSEM v1.3.1, and differential expression analysis was performed in R v4.0.2 using the DESeq2 package v1.28.1<sup>40</sup>.

### Splicing analysis

MAJIQ

Alternative splicing events were analysed using MAJIQ (2.2) and VOILA<sup>13</sup>. In brief, uniquely mapped, junction-spanning reads were used by MAJIQ with the following parameters: ‘majiq build -c config–min-intronic-cov 1–simplify’, to construct splice graphs for transcripts by using the UCSC transcriptome annotation (release 82) supplemented with de novo detected junctions. Here, de novo refers to junctions that were not in the UCSC transcriptome annotation but had sufficient evidence in the RNA-seq data (–min-intronic-cov 1). Distinct local splice variations (LSVs) were identified in gene splice graphs, and the MAJIQ quantifier ‘majiq psi’ estimated the fraction of each junction in each LSV, denoted as percent spliced in (PSI or  $\Psi$ ), in each RNA-seq sample. The changes in each junction’s PSI ( $\Delta$ PSI or  $\Delta\Psi$ ) between the two conditions (TDP-43-positive neuronal nuclei versus TDP-43-negative neuronal nuclei) were calculated by using the command ‘majiq deltapsi’. The gene splice graphs and the posterior distributions of PSI and  $\Delta$ PSI were visualized using VOILA.

## LeafCutter

LeafCutter is available as commit 249fc26 on <https://github.com/davidaknowles/leafcutter>. Using RNA-seq reads aligned as previously described, reads that span exon–exon junctions and map with a minimum of 6 nt into each exon were extracted from the alignment (bam) files using filter\_cs.py with the default settings. Intron clustering was performed using the default settings in leafcutter\_cluster.py. Differential excision of the introns between the two conditions (TDP-43-positive neuronal nuclei versus TDP-43-negative neuronal nuclei) were calculated using leafcutter\_ds.R.

## Sashimi plot

RNA-seq densities along the exons were plotted using the sashimi\_plot function included in the MISO package (misopy 0.5.4). In the sashimi plot, introns are scaled down by a factor of 15 and exons are scaled down by a factor of 5. RNA-seq read densities across exons are scaled by the number of mapped reads in the sample and are measured in RPKM units. Slight modifications were made to plot\_gene.py and plot\_settings.py within the sashimi\_plot directory of the MISO package to highlight the RNA-seq density plot. The modified sashimi\_plot directory is available at (<https://github.com/roxaxma/TDP-43-UNC13A-2021>).

## Cell culture

SH-SY5Y (ATCC) cells were grown in DMEM/F12 media supplemented with Glutamax (Thermo Scientific), 10% fetal bovine serum and 10% penicillin–streptomycin at 37 °C, 5% CO<sub>2</sub>. For shRNA treatments, cells were plated on day 0,

transduced with shRNA on day 2 followed by media refresh on day 3, and collected for readout (RT-qPCR and immunoblotting) on day 6. HEK 293T TDP-43 knockout cells and parent HEK 293T cells were generated as described<sup>36</sup>. The cells were cultured in DMEM medium (Gibco 10564011) supplemented with 10% fetal bovine serum, 1% penicillin–streptomycin, 2 mM l-glutamine (Gemini Biosciences) and 1× MEM non-essential amino acids solution (Gibco) at 37 °C, 5% CO<sub>2</sub>.

## iPS cell maintenance and differentiation into iPSC-MNs

iPS cell lines were obtained from public biobanks (GM25256-Corriell Institute; NDS00262, NDS00209-NINDS) and maintained in mTeSR1 media (StemCell Technologies) on Matrigel (Corning). iPS cells were fed daily and split every 4–7 days using ReLeSR (StemCell Technologies) according to the manufacturer's instructions. Differentiation of iPS cells into motor neurons was carried out as previously described<sup>41</sup>. In brief, iPS cells were dissociated and placed in ultra-low adhesion flasks (Corning) to form 3D spheroids in media containing DMEMF12/Neurobasal (Thermo Fisher), N2 Supplement (Thermo Fisher), and B-27 Supplement-Xeno free (Thermo Fisher). Small molecules were added to induce neuronal progenitor patterning of the spheroids, (LDN193189, SB-431542, Chir99021), followed by motor neuron induction (with retinoic acid, Smo agonist and DAPT). After 14 days, neuronal spheroids were dissociated with Papain and DNase (Worthington Biochemical) and plated on poly-d-lysine/laminin coated plates in Neurobasal Medium (Thermo Fisher) containing neurotrophic factors (BDNF, GDNF and CNTF; R&D Systems). For viral transductions, neuronal cultures were incubated for 18 h with media containing lentivirus particles for shScramble, or shTDP-43. Infection efficiency of over 90% was assessed by RFP expression. Neuronal cultures were analysed for RNA and protein 7 days post transduction.

## shRNA cloning, lentiviral packaging, and cellular transduction for detecting the *UNC13A* splice variant

shRNA sequences were originated from the Broad GPP Portal (TDP-43: AGATCTTAAGACTGGTCATT, scramble: GATATCGCTCTACTAGTAAG). To clone, complementary oligonucleotides were synthesized to generate 4-nt overhangs, annealed and ligated into pRSITCH (Tet inducible U6) or pRSI16 (constitutive U6) (Collecta). Ligations were transformed into Stbl3 chemically competent cells (Thermo Scientific) and grown at 30 °C. Large scale plasmid generation was performed using Maxiprep columns (Promega), with purified plasmid used as input for lentiviral packaging with second generation packaging plasmids psPAX2 and pMD2.G (Collecta), transduced with Lipofectamine 2000 (Invitrogen) in Lenti-X 293T cells (Takara). Viral supernatant was collected at 48 and 72 h post transfection and

concentrated using Lenti-X Concentrator (Takara). Viral titer was established by serial dilution in relevant cell lines and readout of percentage of BFP+ cells by flow cytometry, with a dilution achieving a minimum of 80% BFP+ cells selected for experiments.

## Immunoblotting

SH-SY5Y cells and iPSCs-MNs were transfected and treated as above before lysis. Cells were lysed in ice-cold RIPA buffer (Sigma-Aldrich R0278) supplemented with a protease inhibitor cocktail (Thermo Fisher 78429) and phosphatase inhibitor (Thermo Fisher 78426). After pelleting lysates at maximum speed on a table-top centrifuge for 15 min at 4 °C, bicinchoninic acid (Invitrogen 23225) assays were conducted to determine protein concentrations. 60 µg (SH-SY5Y) and 30 µg (iPSCs-MNs) protein of each sample was denatured for 10 min at 70 °C in LDS sample buffer (Invitrogen NP0008) containing 2.5% 2-mercaptoethanol (Sigma-Aldrich). These samples were loaded onto 4–12% Bis–Tris gels (Thermo Fisher NP0335BOX) for gel electrophoresis, then transferred onto 0.45-µm nitrocellulose membranes (Bio-Rad 162-0115) at 100 V for 2 h using the wet transfer method (Bio-Rad Mini Trans-Blot Electrophoretic Cell 170-3930). Membranes were blocked in Odyssey Blocking Buffer (LiCOR 927-40010) for 1 h then incubated overnight at room temperature in blocking buffer containing antibodies against UNC13A (1:500, Proteintech 55053-1-AP), TDP-43 (1:1,000, Abnova H00023435-M01), or GAPDH (1:1,000, Cell Signaling Technologies 5174S). Membranes were subsequently incubated in blocking buffer containing horseradish peroxidase (HRP)-conjugated anti-mouse IgG (H+L) (1:2,000, Fisher 62-6520) or HRP-conjugated anti-rabbit IgG (H+L) (1:2,000, Life Technologies 31462) for 1 h. ECL Prime kit (Invitrogen) was used for development of blots, which were imaged using ChemiDox XRS+ System (Bio-Rad). The intensity of bands was quantified using Fiji, and then normalized to the corresponding controls.

## RNA extraction, cDNA synthesis and RT–qPCR or RT–PCR for detecting the *UNC13A* splice variant in iPSC-MNs

Total RNA was extracted using RNeasy Micro kit (Qiagen) per manufacturer's instructions, with lysate passed through a QIAshredder column (Qiagen) to maximize yield. RNA was quantified by Nanodrop (Thermo Scientific), with 75 ng used for cDNA synthesis with SuperScript IV VILO Master Mix (Thermo Scientific).

Quantitative PCR was run with 6 ng cDNA input in a 20 µl reaction using PowerTrack SYBR Green Master Mix (Thermo Scientific) with readout on a QuantStudio 6 Flex using standard cycling parameters (95 °C for 2 min, 40 cycles of 95 °C for 15 s and 60 °C for 60 s), followed by standard dissociation (95 °C for 15 s at 1.6 °C s<sup>-1</sup>, 60 °C for 60 s at 1.6 °C s<sup>-1</sup>, 95 °C for 15 s at 0.075 °C s<sup>-1</sup>).  $\Delta\Delta C_t$  was calculated with the

housekeeper gene *RPLP0* as control and relevant shScramble as reference; measured  $C_t$  values greater than 40 were set to 40 for visualizations. See Supplementary Table 6 for primers.

PCR was conducted with 15 ng cDNA input in a 100  $\mu$ l reaction using NEBNext Ultra II Q5 Master Mix (New England Biolabs), with the following cycling parameters: initial denaturation: 98 °C for 30 s; 40 cycles: 98 °C for 10 s, 64 °C for 30 s, 72 °C for 20 s; final extension: 72 °C for 2 min. The resulting products were visualized on a 1.5% TAE gel. See Supplementary Table 6 for primers.

### **Human iPS cell-derived neurons for detecting *UNC13A* splice variants**

cDNA was available from CRISPRi-i<sup>3</sup>Neuron iPS cells (i<sup>3</sup>N) generated from our previous publication<sup>11</sup>, in which TDP-43 is downregulated to about 50%. RT-qPCR was performed using SYBR GreenER qPCR SuperMix (Invitrogen). Samples were run in triplicate, and RT-qPCR reactions were run on a QuantStudio 7 Flex Real-Time PCR System (Applied Biosystems). Relative quantification was determined using the  $\Delta\Delta C_t$  method and normalized to the endogenous controls *RPLP0* and *GAPDH*. We normalized relative transcript levels for wild-type *UNC13A* to that of the neurons treated with control sgRNA (mean set to 1). See Supplementary Table 6 for primers.

### **Cell culture for validating additional splicing events in iPS cell-derived neurons**

We used an induced neuron (iN) system previously established for rapidly differentiating human iPS cells into functional cortical neurons<sup>42</sup>. In brief, iPS cells (without disease mutation) were cultured using feeder-free conditions on Matrigel (Fisher Scientific CB-40230) using mTeSR1 media (Stemcell Technologies 85850). Cells were transduced with a Tet-On induction system that allows expression of the transcription factor NGN2. Cells were dissociated on day 3 of differentiation and replated on Matrigel-coated tissue culture plates in Neurobasal Medium (Thermo Fisher) containing neurotrophic factors, BDNF and GDNF (R&D Systems) with viral transductions for shScramble or shTDP-43. RNA and protein were extracted 7 days after transduction.

### **shRNA cloning, lentiviral packaging, and cellular transduction for validating additional splicing events**

The lentiviral plasmid targeting *TARDBP* (Millipore-Sigma TRCN0000016038) and Scramble (CAACAAGATGAAGAGCACCAA) were packaged using third generation packaging plasmids (pMDLg/pRRE, pRSV-Rev, pMD2.G) and transduced with

Lipofectamine 3000 (Invitrogen) into HEK 293T cells cultured under standard conditions (DMEM, 10% FBS, penicillin–streptomycin). Viral supernatant was collected at 48 and 72 h post-transfection and concentrated 1:100 using Lenti-X Concentrator (Takara).

## **RNA extraction, cDNA synthesis and RT–qPCR for validating additional splicing events**

Total RNA was extracted using RNeasy Micro kit (Qiagen) and reverse transcribed into cDNA using High-Capacity cDNA Reverse Transcription Kits (Invitrogen). Quantitative PCR was run with 2 ng cDNA input in a 10 µl reaction using PowerTrack SYBR Green Master Mix (Thermo Scientific) with readout on a QuantStudio 6 Flex using standard cycling parameters.  $\Delta\Delta C_t$  was calculated with *RPLP0* or *GAPDH* as housekeeper gene controls and relevant shScramble transduced condition as reference; measured  $C_t$  values greater than 40 were set to 40 for visualizations. See Supplementary Table [6](#) for primers used for detecting mis-spliced transcripts and normal splicing transcripts, and primers used for internal controls.

## **Amplicon sequencing of the splice variants**

Splice variants in iPSC-MNs were established by PCR amplification from UNC13A exon 19 to exon 21 (UNC13A\_19\_21 FWD 5'-3'= CAACCTGGACAAGCGAACTG, UNC13A\_19\_21 RVS 5'-3'= GGGCTGTCTCATCGTAGTAAAC). Resulting products were purified using Wizard SV Gel and PCR Clean-Up columns (Promega) and submitted for NGS (Amplicon EZ, Genewiz). Adaptors in FASTQ files were removed using trimomatic (0.39) (ILLUMINACLIP:TruSeq3-PE.fa:2:30:10 LEADING:3 TRAILING:3 SLIDINGWINDOW:4:15 MINLEN:36). The quality of the resulting files was then evaluated using FastQC (v0.11.9). The sequencing reads were then mapped to the human (hg38) using STAR v2.7.3a following ENCODE standard options. Uniquely mapped reads were then filtered for using the command ‘samtools view -b -q 255’. The Sashimi Plot were then generated using the sashimi plot function in IGV (2.8.0) with the minimum junction coverage set to 20.

## **Post-mortem brain tissues for detecting *UNC13A* splice variant**

Post-mortem brain tissues from patients with FTLD-TDP and cognitively normal control individuals were obtained from the Mayo Clinic Florida Brain Bank. Diagnosis was independently ascertained by trained neurologists and neuropathologists upon neurological and pathological examinations, respectively. Written informed consent was given by all participants or authorized family members and all protocols were approved by the Mayo Clinic Institution Review Board and Ethics Committee.

Complementary DNA (cDNA) obtained from 500 ng of RNA (RIN  $\geq$  7.0) from medial frontal cortex was available from a previous study, as well as matching pTDP-43 data from the same samples<sup>43</sup>. Following standard protocols, RT-qPCR was conducted using SYBR GreenER qPCR SuperMix (Invitrogen) for all samples in triplicates. RT-qPCR reactions were run in a QuantStudio 7 Flex Real-Time PCR System (Applied Biosystems). Relative quantification was determined using the  $\Delta\Delta C_t$  method and normalized to the endogenous controls *RPLP0* and *GAPDH*. We normalized relative transcript levels to that of the healthy controls (mean set to 1). See Supplementary Table 6 for primers.

## Quantification of *UNC13A* splice variants in bulk RNA sequencing

RNA-seq data generated by NYGC ALS Consortium cohort were downloaded from the NCBI Gene Expression Omnibus (GEO) database (GSE137810, GSE124439, GSE116622 and GSE153960). We used the 1658 available and quality-controlled samples classified as described<sup>11</sup>. After pre-processing and aligning the reads to human (hg38) as described previously, we estimated the expression of the full-length *UNC13A* using RSEM (v1.3.2). PCR duplicates were removed using MarkDuplicates from Picard Tools (2.23.0) using the command ‘MarkDuplicates REMOVE\_DUPLICATES=true CREATE\_INDEX=true’. We then filtered for uniquely mapped reads using the command ‘samtools view -b -q 255’. Reads that span either exon 19–exon 20 junction, exon 20–CE junction, CE–exon 21 junction or exon 20–exon 21 junction were quantified using bedtools (2.27.1) using the command ‘bedtools intersect -split’. Because of the relatively low level of expression of *UNC13A* in post-mortem tissues and the heterogeneity of the tissues, it is possible that not all tissues have enough detectable *UNC13A* for us to detect the splice variants. Since *UNC13A* contains more than 40 exons and RNA-seq coverages of mRNA transcripts are often not uniformly distributed<sup>44</sup>, we looked at reads spanning the exon 19–exon 20 junction, which is included in both the canonical isoform variant and the splice variant, and there is a strong correlation (Pearson’s  $r = 0.99$ ) between the numbers of reads mapped to the exon 19–exon 20 junction and the exon 20–exon 21 junction. We observed that samples that have at least 2 reads spanning either exon 20–CE junction or CE–exon 21 junction have at least either *UNC13A* TPM = 1.55 or 20 reads spanning exon 19–exon 20 junction. Therefore, we selected the 1,151 samples that had a TPM  $\geq 1.55$ , or at least 20 reads mapped to the exon 19–exon 20 junction as samples suitable for *UNC13A* splice variant analysis.

## In situ hybridization *UNC13A* CE analysis in postmortem brain samples

### Patients and diagnostic neuropathological assessment

Postmortem brain tissue samples used for this study were obtained from the University of California San Francisco (UCSF) Neurodegenerative Disease Brain Bank (Supplementary Table 4). Supplementary Table 4 provides demographic, clinical, and neuropathological information. Consent for brain donation was obtained from subjects or their surrogate decision makers in accordance to the Declaration of Helsinki, and following a procedure approved by the UCSF Committee on Human Research. Brains were cut fresh into 1 cm thick coronal slabs, and alternate slices were fixed in 10% neutral buffered formalin for 72 h. Blocks from the medial frontal pole were dissected from the fixed coronal slabs, cryoprotected in graded sucrose solutions, frozen, and cut into 50 µm thick sections as described previously<sup>45</sup>. Clinical and neuropathological diagnosis were performed as described previously<sup>45</sup>. Subjects were selected on the basis of clinical and neuropathological assessment. Patients selected had a primary clinical diagnosis of behavioural variant frontotemporal dementia (bvFTD) with or without amyotrophic lateral sclerosis or motor neuron disease and a neuropathological diagnosis of FTLD-TDP, type B. We excluded subjects if they had a known disease-causing mutation, post-mortem interval  $\geq 24$  h, Alzheimer's disease neuropathologic change > low, Thal amyloid phase > 2, Braak neurofibrillary tangle stage > 4, CERAD neuritic plaque density > sparse, and Lewy body disease > brainstem predominant<sup>45</sup>.

### In situ hybridization and immunofluorescence

To detect single RNA molecules, a BaseScope Red Assay kit (ACDBIO, USA) was used. One 50 µm thick fixed frozen tissue section from each subject was used for staining. Experiments were performed under RNase-free conditions as appropriate. Probes that target the transcript of interest, *UNC13A*, specific to either the mRNA (exon 20–exon 21 junction) or the cryptic exon containing spliced target (exon 20–cryptic exon junction) were used. Positive (*Homo Sapiens PPIB*) and negative (*Escherichia coli DapB*) control probes were also included. In situ hybridization was performed based on vendor specifications for the BaseScope Red Assay kit. In brief, frozen tissue sections were washed in PBS and placed under an LED grow light (HTG Supply, LED-6B240) chamber for 48 h at 4 °C to quench tissue autofluorescence. Sections were quickly rinsed in PBS and blocked for endogenous peroxidase activity. Sections were transferred on to slides and dried overnight. Slides were subjected to target retrieval and protease treatment and advanced to ISH. Probes were detected with TSA Plus-Cy3 (Akoya Biosciences), and subjected to immunofluorescence staining with antibodies to TDP-43 (rabbit polyclonal, Proteintech, RRID: AB\_615042, dilution 1:4,000, catalogue (cat.) no. 10782-2-AP) and NeuN (Guinea pig polyclonal, Synaptic Systems, dilution 1:500; cat. no. 266004), and counterstained with DAPI (Life Technologies) for nuclei.

### Image acquisition and analysis

Z-stack images were captured using a Leica SP8 confocal microscope with an  $63\times$  oil immersion objective (1.4 NA). For RNA probes, image capture settings were established during initial acquisition based on PPIB and DAPB signal and remained constant across *UNC13A* probes and subjects. TDP-43 and NeuN image capture settings were modified based on staining intensity differences between cases. For each case, 6 non-overlapping Z-stack images were captured across cortical layers 2–3. RNA puncta for the *UNC13A* cryptic exon were quantified using the ‘analyze particle’ plugin in ImageJ. In brief, all images were adjusted for brightness using similar parameters and converted to maximum intensity Z-projections, images were adjusted for auto-threshold (intermodes), and puncta were counted (size: 6-infinity, circularity: 0–1).

## Linkage disequilibrium analysis

Recalibrated VCF files of 297 ALS patients of European descent generated by GATK HaplotypeCallers were downloaded from Answer ALS in July 2020 (<https://www.answerals.org>). VCFtools (0.1.16) were used to filter for sites that are in intron 20–21. The filtered VCF files were merged using BCFtools (1.8). Since there are sites that contain more than 2 alleles, we tested for genotype independence using the chi-squared statistics by using the command ‘vcftools–geno-chisq–min-alleles 2–max-alleles 8’. We found two additional SNPs, rs56041637 ( $P < 0.0001$  with rs12608932,  $P < 0.0001$  with rs12973192), and rs62121687 ( $P < 0.0001$  with rs12608932,  $P < 0.0001$  with rs12973192) that are in linkage disequilibrium with both. However, since rs62121687 was included in a GWAS and has a  $P$ -value<sup>35</sup> of 0.0186585, we excluded it from further analysis.

## Determination of rs12608932 and rs12973192 SNP genotype in human postmortem brain

Genomic DNA (gDNA) was extracted from human frontal cortex using Wizard Genomic DNA Purification Kit (Promega), according to the manufacturer’s instructions. TaqMan SNP genotyping assays were performed on 20 ng of gDNA per assay, using a commercial pre-mixture consisting of a primer pair and VIC or FAM-labelled probes specific for each SNP (cat. no. 4351379, assay ID 43881386\_10 for rs12608932 and 11514504\_10 for rs12973192, Thermo Fisher Scientific), and run on a QuantStudio 7 Flex Real-Time PCR system (Applied Biosystems), according to the manufacturer’s instructions. The PCR programs were 60 °C for 30 s, 95 °C for 10 min, 40 cycles of 95 °C for 15 s and, 60 °C (rs12973192) or 62.5 °C for 1 min (rs12608932), and 60 °C for 30 s.

## Splicing reporter assay

Minigene constructs were designed in silico, synthesized by GenScript and sub-cloned into a vector with the GFP splicing control. HEK 293T TDP-43 knockout cells and the parent HEK 293T cells were seeded into standard P12 tissue culture plates (at  $1.6 \times 10^5$  cells per well), allowed to adhere overnight, and transfected with the indicated splicing reporter constructs (400 ng per well) using Lipofectamine 3000 transfection reagent (Invitrogen). Each reporter comprised one of the splicing modules (shown in Fig. 4d), which is expressed from a bidirectional promoter. Twenty-four hours after transfection, RNA was extracted from these cells using PureLink RNA Mini Kit (Life Technologies) according to the manufacturer's protocol, with on-column PureLink DNase (Invitrogen) treatment. The RNA was reverse transcribed into cDNA using the High Capacity cDNA Reverse Transcription Kit (Invitrogen) according to the manufacturers' instructions. PCRs were performed using OneTaq 2X Master Mix with Standard Buffer (NEB) with the following cycling parameters: denaturation: 94 °C for 30 s; 30 cycles: 94 °C for 20 s, 54 °C for 30 s, 68 °C for 30 s; final extension: 68 °C for 5 min on a Mastercycler Pro (Eppendorf) thermocycler PCR machine. PCR products were separated by electrophoresis on a 1.5% TAE gel and imaged ChemiDox XRS+ System (Bio-Rad). See Supplementary Table 6 for primers.

### Assay to assess the effect of variants at rs12973192, rs12608932 and rs56041637 on splicing

Additional minigene constructs shown in Extended Data Fig. 8 were either generated using site-directed mutagenesis (New England Biolabs, E0554S) or synthesized by GenScript, and sub-cloned into the vector with the GFP splicing control. HEK 293T TDP-43 knockout cells and the parent HEK 293T cells were seeded into standard P12 tissue culture plates (at  $5 \times 10^5$  cells per well), allowed to adhere overnight and transfected with the indicated splicing reporter constructs (400 ng per well) using Lipofectamine 3000 transfection reagent (Invitrogen). Twenty-four hours after transfection, RNA was extracted from these cells using PureLink RNA Mini Kit (Life Technologies) according to the manufacturer's protocol, with on-column PureLink DNase treatment. The RNA was reverse transcribed into cDNA using the High Capacity cDNA Reverse Transcription Kit (Invitrogen) according to the manufacturers' instructions. The *UNC13A* cryptic exon signal was measured using a pair of primers that detect the junction of the CE and the immediately downstream mCherry exon. The splicing of eGFP was measured using a pair of primers that detect the junction of the first and second exons of eGFP. A pair of primers that mapped within the second exon of eGFP was used to measure the transfection efficiency of the splicing reporter construct and was used as a normalizer.  $\Delta\Delta C_t$  was calculated using the cryptic exon signal level or the splicing of eGFP in the HEK 293T TDP-43 knockout cells expressing the reference haplotype-carrying reporter as reference. See Supplementary Table 6 for primers.

## Rescue of *UNC13A* splicing using TDP-43 overexpression constructs

HEK 293T TDP-43 knockout cells and the parent (wild-type) HEK 293T cells were seeded into standard P12 tissue culture plates (at  $5 \times 10^5$  cells per well), allowed to adhere overnight and transfected with the splicing reporter construct carrying the reference haplotype (400 ng per well; Fig. 4e) and the indicated TDP-43 overexpression constructs (600 ng per well) using Lipofectamine 3000 transfection reagent (Invitrogen). Twenty-four hours after transfection, RNA was extracted from these cells using PureLink RNA Mini Kit (Life Technologies) according to the manufacturer's protocol, with on-column PureLink DNase treatment. The RNA was reverse transcribed into cDNA using the High Capacity cDNA Reverse Transcription Kit (Invitrogen) according to the manufacturers' instructions. Quantitative PCR was run with 8 ng cDNA input in a 10  $\mu$ l reaction using PowerTrack SYBR Green Master Mix (Thermo Scientific) with readout on a QuantStudio 6 Flex using standard cycling parameters.

The *UNC13A* cryptic exon signal was measured using a pair of primers that detect the junction of the CE and the mCherry exon immediately downstream of it. A pair of primers that are mapped within the second exon of eGFP was used to measure the transfection efficiency of the splicing reporter construct, and was used as a normalizer.  $\Delta\Delta C_t$  was calculated using the cryptic exon signal level in the wild-type HEK 293T cells without TDP-43 overexpression constructs as reference. See Supplementary Table 6 for primers.

The expression levels of the overexpression constructs were measured using a pair of primers that detect the second exon of TDP-43. The primers do detect the endogenous TDP-43 but since the HEK 293T TDP-43 knockout cells do not have TDP-43 expression as shown previously<sup>36</sup>, using the primers do not interfere with the measurement of the expression levels of TDP-43 constructs in the knockout cells.  $\Delta\Delta C_t$  was calculated using the TDP-43 expression level in the HEK 293T TDP-43 knockout cells with full length TDP-43 overexpression constructs as reference. *RPLP0* and *GAPDH* were used as internal controls. See Supplementary Table 6 for primers.

## Generation of pTB *UNC13A* minigene construct

The pTB *UNC13A* minigene construct containing the human *UNC13A* cryptic exon sequence and the nucleotide flanking sequences upstream (50 bp at the end of intron 19, the entirety of exon 20, and the entirety of intron 20 sequence upstream of the cryptic exon) and downstream (approximately 300-bp intron 20) of the cryptic exon were amplified from human genomic DNA using the following primers: FWD 5'-3', AGGTCAATGCAC TGCTATA GTGGAAAGTTC and RVS 5'-3', CTTACATATGTAATA ACTCAACCAC ACTTCCATC; and subcloned into the NdeI

site of the pTB vector. We have previously used a similar approach to study TDP-43 splicing regulation of other TDP-43 targets<sup>46</sup>.

## Rescue of *UNC13A* splicing using the pTB minigene and TDP-43 overexpression constructs

HeLa cells were grown in Opti-MEM I Reduced Serum Medium, GlutaMAX Supplement (Gibco) plus 10% fetal bovine serum (Sigma), and 1% penicillin/streptomycin (Gibco). For double-transfection and knockdown experiments, cells were first transfected with 1.0 µg of pTB *UNC13A* minigene construct and 1.0 µg of one of the following plasmids: GFP, GFP-TDP-43 or GFP-TDP-43 5FL constructs to express GFP-tagged TDP-43 proteins have been previously described<sup>46,47</sup>, in serum-free media and using Lipofectamine 2000 following the manufacturer's instructions (Invitrogen). Four hours following transfection, media was replaced with complete media containing siLentfect (Bio-Rad) and siRNA complexes (AllStars Neg. Control siRNA or siRNA against *TARDBP* 3' untranslated region, a region not included in the TDP-43 overexpression constructs) (Qiagen) following the manufacturer's protocol. Cycloheximide (Sigma) was added at a final concentration of 100 µg ml<sup>-1</sup> at 6 h prior to collecting the cells. Then RNA was extracted from the cells using TRIzol Reagent (Zymo Research), following the manufacturer's instructions. Approximately 1 µg of RNA was converted into cDNA using the High Capacity cDNA Reverse Transcription Kit with RNA inhibitor (Applied Biosystems). The RT-qPCR assay was performed on cDNA (diluted 1:40) with SYBR GreenER qPCR SuperMix (Invitrogen) using QuantStudio7 Flex Real-Time PCR System (Applied Biosystems). All samples were analysed in triplicates. The RT-qPCR program was as follows: 50 °C for 2 min, 95 °C for 10 min, and 40 cycles of 95 °C for 15 s and 60 °C for 1 min. For dissociation curves, a dissociation stage of 95 °C for 15 s, 60 °C for 1 min and 95 °C for 15 s was added at the end of the program. Relative quantification was determined using the  $\Delta\Delta C_t$  method and normalized to the endogenous controls *RPLP0* and *GAPDH*. We normalized relative transcript levels for wild-type *UNC13A* and GFP to that of the control siRNA condition (mean set to 1). See Supplementary Table 6 for primers.

## In vitro TDP-43 binding studies

### Cloning

The plasmid encoding TDP43 as a C-terminal MBP-tagged protein (TDP43-MBP-His<sub>6</sub>) was purchased from Addgene (#104480).

### Bacterial growth and protein expression

The wild-type TDP-43 expression plasmid was transformed into *E. coli* One Shot BL21 Star (DE3) cells (ThermoFisher). Transformed *E. coli* were grown at 37 °C in 1 l of LB media supplemented with 0.2% dextrose and 50 µg ml<sup>-1</sup> kanamycin until absorbance at 600 nm reached 0.5–0.6. The culture was then incubated at 4 °C for 30–45 min. TDP-43 expression was induced with 1 mM IPTG for 16 h at 4 °C. Cells were collected by centrifugation.

### Recombinant TDP-43 purification

Wild-type TDP-43–MBP was purified as described<sup>48</sup>. In brief, cell pellets were resuspended in lysis buffer 1 M NaCl, 20 mM Tris (pH 8.0), 10 mM imidazole, 10% glycerol and 2.5 mM 2-mercaptoethanol and supplemented with cOmplete, EDTA-free protease inhibitor cocktail tablets (Roche) then lysed via sonication. Cell lysates were centrifuged at 31,400g at 4 °C for 1 h, filtered, then purified with FPLC using a XK 50/20 column (Cytiva) packed with Ni-NTA agarose beads (Qiagen) which were equilibrated in lysis buffer. TDP-43 was recovered via a 0–80% gradient elution using 1 M NaCl, 20 mM TrisHCl (pH 8.0), 10 mM imidazole, 10% glycerol and 2.5 mM 2-mercaptoethanol as the base buffer and 1 M NaCl, 20 mM TrisHCl (pH 8.0), 500 mM imidazole, 10% glycerol, and 2.5 mM 2-mercaptoethanol as the elution buffer. Eluted protein was concentrated using Amicon Ultra-15 centrifugal filters, MWCO 50 kDa (Millipore), filtered and further purified with size-exclusion chromatography using a 26/600 Superdex 200 pg column (Cytiva) equilibrated with 300 mM NaCl, 20 mM TrisHCl (pH 8.0) and 1 mM DTT. The second out of three peaks, as evaluated by absorbance at 280 nm, was collected, spin concentrated as before, aliquoted, flash frozen in liquid N<sub>2</sub>, and stored at –80 °C until further use. Protein concentrations were determined using absorbance at 280 nm (Nanodrop) and purity was determined by running samples on a 4–20% SDS–PAGE gel and visualized with Coomassie stain.

### Electrophoresis mobility shift assay

EMSA was used to compare TDP-43 binding to the reference and risk RNA sequences for reference and risk alleles of CE (rs12973192), intron (rs12608932), and repeat sequences (rs56041637) (see Supplementary Table 5). Increasing TDP-43 concentrations ranging from 0–4 mM were incubated with a constant 1 nM concentration of RNA in buffer (50 mM Tris-HCl, pH 7.5, 100 mM KCl, 2 mM MgCl<sub>2</sub>, 100 mM β-mercaptoethanol, 0.1 mg ml<sup>-1</sup> BSA) for 30 min at room temperature. RNA is dual-labelled (Cy3 and Cy5) and contains an 18-nucleotide partial duplex on the 3' end. Reactions were mixed with loading dye and run on a 6% non-denaturing polyacrylamide gel and imaged using fluorescence mode (Cy5) on a Typhoon scanner. Bound fractions were determined using the Analyze Gel plugin in

ImageJ and normalized to the total intensity per lane. Apparent binding affinities were calculated using the ‘Specific binding with Hill slope’ function in Graphpad.

## Statistical methods

Survival curves were compared using the coxph function in the survival (3.1.12) R package, which fits a multivariable Cox proportional hazards model that contains sex, reported genetic mutations and age at onset, and performs a score (log-rank) test. Effect sizes are reported as the hazard ratios. Proportional Hazards assumptions were tested using cox.zph function. The survival curves were plotted using ggsurvplot in survminer (v.0.4.8) R package. Linear mixed effects models were analysed using lmerTest R package (3.1.3). Statistical analyses were performed using R (version 4.0.0), or Prism 8 (GraphPad), which were also used to generate graphs.

## Reporting summary

Further information on research design is available in the [Nature Research Reporting Summary](#) linked to this paper.

## Data availability

The amplicon sequencing data has been deposited in the Gene Expression Omnibus (GEO) at [GSE182976](#). RNA-seq data for splicing analysis is available at [GSE126543](#). RNA-seq data generated by NYGC ALS Consortium cohort is available at [GSE137810](#), [GSE124439](#), [GSE116622](#) and [GSE153960](#). [Source data](#) are provided with this paper.

## Code availability

All codes used in this study are available at (<https://github.com/roaxma/TDP-43-UNC13A-2021>) and (<https://doi.org/10.5281/zenodo.5770954>).

## References

1. Neumann, M. et al. Ubiquitinated TDP-43 in frontotemporal lobar degeneration and amyotrophic lateral sclerosis. *Science* **314**, 130–133 (2006).
2. Ling, J. P., Pletnikova, O., Troncoso, J. C. & Wong, P. C. TDP-43 repression of nonconserved cryptic exons is compromised in ALS–FTD. *Science* **349**, 650–655 (2015).

3. Melamed, Z. et al. Premature polyadenylation-mediated loss of stathmin-2 is a hallmark of TDP-43-dependent neurodegeneration. *Nat. Neurosci.* **22**, 180–190 (2019).
4. Klim, J. R. et al. ALS-implicated protein TDP-43 sustains levels of STMN2, a mediator of motor neuron growth and repair. *Nat. Neurosci.* **22**, 167–179 (2019).
5. Van Es, M. A. et al. Genome-wide association study identifies 19p13.3 (*UNC13A*) and 9p21.2 as susceptibility loci for sporadic amyotrophic lateral sclerosis. *Nat. Genet.* **41**, 1083–1087 (2009).
6. Diekstra, F. P. et al. C9orf72 and *UNC13A* are shared risk loci for amyotrophic lateral sclerosis and frontotemporal dementia: A genome-wide meta-analysis. *Ann. Neurol.* **76**, 120–133 (2014).
7. Lagier-Tourenne, C., Polymenidou, M. & Cleveland, D. W. TDP-43 and FUS/TLS: emerging roles in RNA processing and neurodegeneration. *Hum. Mol. Genet.* **19**, 46–64 (2010).
8. Donde, A. et al. Splicing repression is a major function of TDP-43 in motor neurons. *Acta Neuropathol.* **138**, 813–826 (2019).
9. Sun, M. et al. Cryptic exon incorporation occurs in Alzheimer’s brain lacking TDP-43 inclusion but exhibiting nuclear clearance of TDP-43. *Acta Neuropathol.* **133**, 923–931 (2017).
10. Jeong, Y. H. et al. Tdp-43 cryptic exons are highly variable between cell types. *Mol. Neurodegener.* **12**, 13 (2017).
11. Prudencio, M. et al. Truncated stathmin-2 is a marker of TDP-43 pathology in frontotemporal dementia. *J. Clin. Invest.* **130**, 6080–6092 (2020).
12. Liu, E. Y. et al. Loss of nuclear TDP-43 is associated with decondensation of LINE retrotransposons. *Cell Rep.* **27**, 1409–1421 (2019).
13. Vaquero-Garcia, J. et al. A new view of transcriptome complexity and regulation through the lens of local splicing variations. *eLife* **5**, e11752 (2016).
14. Li, Y. I. et al. Annotation-free quantification of RNA splicing using LeafCutter. *Nat. Genet.* **50**, 151–158 (2018).
15. Shiga, A. et al. Alteration of POLDIP3 splicing associated with loss of function of TDP-43 in tissues affected with ALS. *PLoS ONE* **7**, e43120 (2012).

16. Carithers, L. J. et al. A novel approach to high-quality postmortem tissue procurement: the GTEx project. *Biopreserv. Biobank* **13**, 311–319 (2015).
17. Tollervey, J. R. et al. Characterizing the RNA targets and position-dependent splicing regulation by TDP-43. *Nat. Neurosci.* **14**, 452–458 (2011).
18. Brenner, S. The genetics of *Caenorhabditis elegans*. *Genetics* **77**, 95–104 (1974).
19. Lipstein, N. et al. Synaptic UNC13A protein variant causes increased neurotransmission and dyskinetic movement disorder. *J. Clin. Invest.* **127**, 1005–1018 (2017).
20. Deng, L., Kaeser, P. S., Xu, W. & Südhof, T. C. RIM proteins activate vesicle priming by reversing autoinhibitory homodimerization of munc13. *Neuron* **69**, 317–331 (2011).
21. Augustin, I., Rosenmund, C., Südhof, T. C. & Brose, N. Munc13-1 is essential for fusion competence of glutamatergic synaptic vesicles. *Nature* **400**, 457–461 (1999).
22. Böhme, M. A. et al. Active zone scaffolds differentially accumulate Unc13 isoforms to tune Ca<sup>2+</sup> channel-vesicle coupling. *Nat. Neurosci.* **19**, 1311–1320 (2016).
23. Nicolas, A. et al. Genome-wide analyses identify *KIF5A* as a novel ALS gene. *Neuron* **97**, 1268–1283 (2018).
24. Placek, K. et al. *UNC13A* polymorphism contributes to frontotemporal disease in sporadic amyotrophic lateral sclerosis. *Neurobiol. Aging* **73**, 190–199 (2019).
25. Pottier, C. et al. Genome-wide analyses as part of the international FTLD–TDP whole-genome sequencing consortium reveals novel disease risk factors and increases support for immune dysfunction in FTLD. *Acta Neuropathol.* **137**, 879–899 (2019).
26. van Blitterswijk, M. et al. Genetic modifiers in carriers of repeat expansions in the C9ORF72 gene. *Mol. Neurodegener.* **9**, 38 (2014).
27. Vidal-Taboada, J. M. et al. *UNC13A* confers risk for sporadic ALS and influences survival in a Spanish cohort. *J. Neurol.* **262**, 2285–2292 (2015).
28. Yang, B. et al. *UNC13A* variant rs12608932 is associated with increased risk of amyotrophic lateral sclerosis and reduced patient survival: a meta-analysis. *Neurol. Sci.* **40**, 2293–2302 (2019).

29. Tan, H. et al. The distinct traits of the *UNC13A* polymorphism in amyotrophic lateral sclerosis. *Ann. Neurol.* **88**, 796–806 (2020).
30. Diekstra, F. P. et al. UNC13A is a modifier of survival in amyotrophic lateral sclerosis. *Neurobiol. Aging* **33**, 630.e3–630.e8 (2012).
31. Auton, A. et al. A global reference for human genetic variation. *Nature* **526**, 68–74 (2015).
32. Schaid, D. J., Chen, W. & Larson, N. B. From genome-wide associations to candidate causal variants by statistical fine-mapping. *Nat. Rev. Genet.* **19**, 491–504 (2018).
33. Gallagher, M. D. & Chen-Plotkin, A. S. The post-GWAS era: from association to function. *Am. J. Hum. Genet.* **102**, 717–730 (2018).
34. Pruim, R. J. et al. LocusZoom: regional visualization of genome-wide association scan results. *Bioinformatics* **26**, 2336–2337 (2011).
35. Van Rheenen, W. et al. Genome-wide association analyses identify new risk variants and the genetic architecture of amyotrophic lateral sclerosis. *Nat. Genet.* **48**, 1043–1048 (2016).
36. Schmidt, H. B., Barreau, A. & Rohatgi, R. Phase separation-deficient TDP43 remains functional in splicing. *Nat. Commun.* **10**, 4890 (2019).
37. Brown, A.-L. et al. TDP-43 loss and ALS-risk SNPs drive mis-splicing and depletion of UNC13A. *Nature* <https://doi.org/10.1038/s41586-022-04436-3> (2022).
38. Chiò, A. et al. UNC13A influences survival in Italian amyotrophic lateral sclerosis patients: a population-based study. *Neurobiol. Aging* **34**, 357.e1–5 (2013).
39. Nelson, P. T. et al. Limbic-predominant age-related TDP-43 encephalopathy (LATE): Consensus working group report. *Brain* **142**, 1503–1527 (2019).
40. Love, M. I., Huber, W. & Anders, S. Moderated estimation of fold change and dispersion for RNA-seq data with DESeq2. *Genome Biol.* **15**, 550 (2014).
41. Maury, Y. et al. Combinatorial analysis of developmental cues efficiently converts human pluripotent stem cells into multiple neuronal subtypes. *Nat. Biotechnol.* **33**, 89–96 (2015).

42. Bieri, G. et al. LRRK2 modifies  $\alpha$ -syn pathology and spread in mouse models and human neurons. *Acta Neuropathol.* **137**, 961–980 (2019).
43. Prudencio, M. et al. Repetitive element transcripts are elevated in the brain of C9orf72 ALS/FTLD patients. *Hum. Mol. Genet.* **26**, 3421–3431 (2017).
44. Hansen, K. D., Brenner, S. E. & Dudoit, S. Biases in Illumina transcriptome sequencing caused by random hexamer priming. *Nucleic Acids Res.* **38**, e131 (2010).
45. Nana, A. L. et al. Neurons selectively targeted in frontotemporal dementia reveal early stage TDP-43 pathobiology. *Acta Neuropathol.* **137**, 27–46 (2019).
46. Prudencio, M. et al. Misregulation of human sortilin splicing leads to the generation of a nonfunctional progranulin receptor. *Proc. Natl Acad. Sci. USA* **109**, 21510–21515 (2012).
47. Zhang, Y. J. et al. Aberrant cleavage of TDP-43 enhances aggregation and cellular toxicity. *Proc. Natl Acad. Sci. USA* **106**, 7607–7612 (2009).
48. Hallegger, M. et al. TDP-43 condensation properties specify its RNA-binding and regulatory repertoire. *Cell* **184**, 4680–4696 (2021).
49. Kent, W. J. et al. The Human Genome Browser at UCSC. *Genome Res.* **12**, 996–1006 (2002).
50. Seyfried, N. T. et al. Multiplex SILAC analysis of a cellular TDP-43 proteinopathy model reveals protein inclusions associated with SUMOylation and diverse polyubiquitin chains. *Mol. Cell. Proteomics* **9**, 705–718 (2010).
51. Ayala, Y. M. et al. TDP-43 regulates its mRNA levels through a negative feedback loop. *EMBO J.* **30**, 277–288 (2011).

## Acknowledgements

This work was supported by NIH grants R35NS097263(10) (A.D.G.), R35NS097273(17) (L.P.), U54NS123743 (A.D.G., L.P., M.P. and W.W.S.), P01NS084974 (L.P.), R01NS104437 (W.W.S.), RF1NS120992 (M.P.), F32 NS116208-02 (C.M.R.), T32 GM007231 (G. Mekonnen), 2T32AG047126-06A1 (T.A.), F32GM139268 (L.G.), RF1AG071326 (S. Myong.), RF1NS113636 (S. Myong.), the Robert Packard Center for ALS Research at Johns Hopkins (L.P., J.S. and A.D.G.), P30AG06267 (R.C.P.), U01AG006786 (R.C.P.), 2T32HG000044-21 NIHGRI training grant (X.R.M.), the Brain Rejuvenation Project of the Wu Tsai Neurosciences Institute

(A.D.G.), Target ALS (J.S.), Amyotrophic Lateral Sclerosis Association (J.S.), and the Office of the Assistant Secretary of Defense for Health Affairs through the Amyotrophic Lateral Sclerosis Research Program (W81XWH-20-1-0242 to J.S.). G.K. is supported by a fellowship from the Stanford Knight-Hennessy Scholars Program. A.B. is supported by a Fulbright Future Scholarship. Y.K. is supported by Milton Safenowitz Postdoctoral Fellowship Program from the Amyotrophic Lateral Sclerosis Association (21-PDF-582). S.P. is supported by a BrightFocus ADR Grant (A2020279F). T.A. is supported by a fellowship from the Takeda Science Foundation. The UCSF Neurodegenerative Disease Brain Bank receives funding support from NIH grants P30AG062422, P01AG019724, U01AG057195 and U19AG063911, as well as the Rainwater Charitable Foundation and the Bluefield Project to Cure FTD. Some of the computing for this project was performed on the Sherlock cluster. We would like to thank Stanford University and the Stanford Research Computing Center for providing computational resources and support that contributed to these research results.

## Author information

### Author notes

1. These authors contributed equally: X. Rosa Ma, Mercedes Prudencio, Yuka Koike

### Affiliations

1. Department of Genetics, Stanford University School of Medicine, Stanford, CA, USA

X. Rosa Ma, Garam Kim, Adam Briner, Caitlin M. Rodriguez, Caiwei Guo, Tetsuya Akiyama & Aaron D. Gitler

2. Department of Neuroscience, Mayo Clinic, Jacksonville, FL, USA

Mercedes Prudencio, Yuka Koike, Karen Jansen-West, Casey N. Cook, Sarah Pickles, Dennis W. Dickson & Leonard Petrucelli

3. Neuroscience Graduate Program, Mayo Clinic Graduate School of Biomedical Sciences, Jacksonville, FL, USA

Mercedes Prudencio, Yuka Koike, Casey N. Cook, Sarah Pickles, Dennis W. Dickson & Leonard Petrucelli

4. Department of Neurology, University of California San Francisco, San Francisco, CA, USA

Sarat C. Vatsavayai & William W. Seeley

5. Department of Pathology, University of California San Francisco, San Francisco, CA, USA

Sarat C. Vatsavayai & William W. Seeley

6. Neurosciences Interdepartmental Program, Stanford University School of Medicine, Stanford, CA, USA

Garam Kim

7. Maze Therapeutics, South San Francisco, CA, USA

Fred Harbinski, Beryl B. Cummings, David W. Wyatt, Katherine Kurylo, Georgiana Miller, Shila Mekhoubad, Nathan Sallee & Eric M. Green

8. Clem Jones Centre for Ageing Dementia Research (CJCADR), Queensland Brain Institute (QBI), The University of Queensland, Brisbane, Queensland, Australia

Adam Briner

9. Department of Biochemistry, Stanford University School of Medicine, Stanford, CA, USA

H. Broder Schmidt

10. Program in Cell, Molecular, Developmental Biology, and Biophysics, Johns Hopkins University, Baltimore, MD, USA

Gemechu Mekonnen & Sua Myong

11. Department of Biology, Johns Hopkins University, Baltimore, MD, USA

Gemechu Mekonnen & Sua Myong

12. Department of Biophysics, Johns Hopkins University, Baltimore, MD, USA

Laura Ganser & Sua Myong

13. Department of Biochemistry and Biophysics, Perelman School of Medicine, University of Pennsylvania, Philadelphia, PA, USA

Jack D. Rubien & James Shorter

14. Department of Neurology, Mayo Clinic, Jacksonville, FL, USA

Björn Oskarsson & Neill R. Graff-Radford

15. Department of Neurology, Mayo Clinic, Rochester, MN, USA

Bradley F. Boeve, David S. Knopman & Ronald C. Petersen

## Contributions

X.R.M., M.P., L.P. and A.D.G. designed the experiments. X.R.M. and A.D.G. wrote the paper. X.R.M., M.P., Y.K. performed experiments and analysed data. S.C.V. and W.W.S. performed and analysed the *UNC13A* BaseScope experiments on patient samples. G.K. performed the *UNC13A* immunoblotting experiments. C.M.R. helped perform RT-PCR analyses. F.H., D.W.W., K.K., G.M., S.M., N.S. and E.M.G. performed TDP-43 knockdown experiments and analysed data. A.B. and H.B.S. performed some of the minigene reporter assays. C.G. analysed additional TDP-43 target genes. T.A. generated and analysed induced neurons for TDP-43 knockdown experiments. B.B.C. helped with *UNC13A* human genetics analyses. G.M., L.G., J.D.R., J.S. and S.M. performed TDP-43 RNA-binding studies and analysed data. K.J.-W., C.N.C. and S.P. generated TDP-43 splicing reporter constructs. B.O., N.R.G-R., B.F.B., D.S.K., R.C.P. and D.W.D. contributed patient samples.

## Corresponding authors

Correspondence to [Leonard Petrucelli](#) or [Aaron D. Gitler](#).

## Ethics declarations

### Competing interests

A.D.G. is a scientific founder of Maze Therapeutics. X.R.M. served as a consultant for Maze Therapeutics. M.P. and L.P. serve as consultants for Target ALS. F.H., B.B.C., D.W.W., K.K., G. Miller, S. Mekhoubad, N.S. and E.G. are employees of Maze Therapeutics, which has filed a patent (63/171,522) on methods to modulate splicing of *UNC13A*.

## Peer review

### Peer review information

*Nature* thanks Noa Lipstein, Magdalini Polymenidou and the other, anonymous, reviewers for their contribution to the peer review of this work. Peer reviewer reports are available.

## Additional information

**Publisher's note** Springer Nature remains neutral with regard to jurisdictional claims in published maps and institutional affiliations.

## Extended data figures and tables

[Extended Data Fig. 1 Splicing analysis using MAJIQ demonstrates inclusion of cryptic exon between exon 20 and exon 21 of UNC13A.](#)

**(a, b)** Depletion of TDP-43 introduces two alternative 3' splicing acceptors in the intron 20–21: one is near chr19:17642591( $\Delta\Psi = 0.05246$ ) and the other one is near chr19:17642541( $\Delta\Psi = 0.49267$ ). **(c, d)** An alternative 5' splicing donor is also introduced near chr19:17642414 ( $\Delta\Psi = 0.7763$ ). See Supplementary Note 2. **(a, c)** Splice graphs showing the inclusion of the cryptic exon (CE) between exon 20 and exon 21 of *UNC13A*. **(b, d)** Violin plots corresponding to (a and c) respectively. Each violin in (b and d) represents the posterior probability distribution of the expected relative inclusion (PSI or  $\Psi$ ) for the color matching junction in the splice graph. The tails of each violin represent the 10th and 90th percentile. The box represents the interquartile range with the line in the middle indicating the median. The white circles mark the expected PSI ( $E[\Psi]$ ). The change in the relative inclusion level of each junction between two conditions is referred to as  $\Delta\Psi$  or  $\Delta\text{PSI}$ <sup>13</sup>. **(e)** The three versions of cryptic exons resulting from the loss of TDP-43. **(f)** Visualization of RNA-sequencing alignment between exon 20 and exon 21 in *UNC13A* (hg38). Libraries were generated as described in Fig. 1a. CE, cryptic exon. **(g)** iCLIP for TDP-43 (from Tollervy et al.<sup>17</sup>) indicates that TDP-43 binds to intron 20–21. The sequence shown is an example of a region in intron 20-21 that is frequently bound by TDP-43 (shown by mapped reads from ERR039843, ERR039845 and ERR039855).

### Extended Data Fig. 2 Intron 20-21 of *UNC13A* is conserved among most primates.

The Primates Multiz Alignment & Conservation track on UCSC<sup>49</sup> genome browser (<http://genome.ucsc.edu>) includes 30 mammals, 27 of which are primates. **(a)** Exon 20 and exon 21 of *UNC13A* is well conserved among mammals. The location of the 128 bp cryptic exon is highlighted in red. However, intron 20-21 **(a)**, the cryptic exon **(b)**, and the splicing acceptor site (highlighted in blue) upstream of the cryptic exon **(c)** and splicing donor site (highlighted in blue) downstream of the cryptic exon **(d)** are only conserved in primates.

### Extended Data Fig. 3 Depletion of TDP-43 from iPSC derived motor neurons (iPSC-MNs) and iPSC derived neurons (i<sup>3</sup>Ns).

## leads to cryptic exon inclusion in *UNC13A*.

**(a)** RT-PCR confirmed the expression of the cryptic exon-containing *UNC13A* splice variant upon TDP-43 depletion in three independent iPSC-MNs (n = 4 independent cell culture experiments for each condition). Gel picture shows results from all 4 experiments performed. In addition to the splice variant containing the 128 bp and 178 bp cryptic exons, we also detected inclusion of the complete intron upstream of the cryptic exon (Fig. 4e, Supplementary Note 2). The 128 bp and 178 bp cryptic exons cannot be distinguished here but they are detected through amplicon sequencing the corresponding band (**d**). The PCR products represented by each band are marked to the left of each gel. The location of the PCR primer pair used is shown on top of each gel image. **(b)** The PCR primer pairs spanning the cryptic exon and exon 21 junction confirms cryptic exon inclusion only occurs upon TDP-43 knockdown. For gel source data, see Supplementary Fig. 1c,d. **(c)** RT-qPCR analyses confirmed the inclusion of *UNC13A* cryptic exon upon TDP-43 depletion in iPSC derived neurons (i3Ns). TDP-43 was depleted by expressing two different sgRNAs: sgTDP-43-guide1 and sgTDP-43-guide2 in i<sup>3</sup>Ns stably expressing CRISPR inactivation machinery (CRISPRi). *RPLP0* and *GAPDH* were used to normalize RT-qPCR. (n = 3 independent cell culture experiments for each condition; Ordinary one-way ANOVA with Dunnett's multiple comparisons test, mean ± s.e.m.). **(d)** Sashimi plot visualization of the alignment (hg38) of the amplicon (2 × 250 bp) sequencing reads of the sequences amplified using primers (blue) shown in (e). Both the 128 bp and the 178 bp cryptic exons were supported by the sequencing reads. **(e)** Schematic of the exons amplified by the primers (blue). **(f, h)** DNA sequence of the 128 bp and 178 bp cryptic exons and their flanking exons. The sequences are color coded according to (e). **(g, i)** The amino acid sequences correspond to the DNA sequences in (f, h). The asterisks indicate stop codons are encountered.

Source data

## Extended Data Fig. 4 Validation of additional splicing targets.

**(a–f)** Depletion of TDP-43 introduces cryptic exons into *KALRN* mRNA and *SYT7* mRNA; In *RAPGEF6*, TDP-43 depletion leads to a decrease in

the usage of the exon AE (for alternative exon) between exon 21 and exon 22 of the isoform ENST0000509018.6. Exon AE does exist in some other isoforms of *RAPGEF6*, indicating the depletion of TDP-43 could lead to changes in isoform composition. **(b, d, f)** Violin plots corresponding to **(a, c, e)**, respectively. Each violin in **(b, d, f)** represents the posterior probability distribution of the expected relative inclusion (PSI or  $\Psi$ ) for the color matching junction in the splice graph. The tails of each violin represent the 10th and 90th percentile. The box represents the interquartile range with the line in the middle indicating the median. The white circles mark the expected PSI ( $E[\Psi]$ ). The change in the relative inclusion level of each junction between two conditions is referred to as  $\Delta\Psi$  or  $\Delta\text{PSI}$ <sup>13</sup>. **(g-i)** RT-qPCR analyses confirmed changes in exon usage upon TDP-43 depletion in iPSC-derived neurons. *RPLP0* and *GAPDH* were used to normalize RT-PCR. (n = 3 independent cell culture experiments for each condition, two sided-Welch Two Sample t-test, mean ± s.e.m.).

[Source data](#)

**Extended Data Fig. 5 *UNC13A* cryptic exon inclusion is detected in disease relevant tissues of FTLD-TDP, ALS/FTLD, ALS-TDP and ALS/AD patients, and is correlated with phosphorylated TDP-43 levels in frontal cortices of FTLD-TDP patients.**

**(a)** *UNC13A* cryptic exon expression level is significantly increased in the frontal cortices of patients with FTD and ALS/FTD clinical diagnoses (Mayo Clinic Brain Bank). *GAPDH* and *RPLP0* were used to normalize RT-qPCR (the sample size of each group is listed under the corresponding group; two-tailed Mann-Whitney test, mean ± 95% confidence interval). The schematic on top shows the localization of the primer pair (arrows) used for the RT-qPCR assay. **(b)** *UNC13A* splice variants are observed in ALS patients with unconfirmed pathology. ALS-FTLD refers to patients who have concurrent FTD and ALS. ALS patients were categorized based on whether they carry *SOD1* mutations (ALS-SOD1 (Fig. 2b) vs. ALS-TDP). ALS-AD refers to ALS patients with suspected Alzheimer's disease. The diagnoses of these patients (NYGC) are not neuropathologically

confirmed. Therefore, it is unclear whether TDP-43 mislocalization is present. **(c)** *UNC13A* cryptic exon signal is positively correlated with phosphorylated TDP-43 levels in frontal cortices of FTLD-TDP patients in Mayo Clinic Brain Bank (Spearman's rho = 0.610, n = 90, p-values were calculated by one-sided t-test). Data points are colored according to patients' reported genetic mutations. The correlation within each genetic mutation group and the corresponding p-value and sample size is also shown.

[Source data](#)

[Extended Data Fig. 6 \*UNC13A\* cryptic splicing is associated with loss of nuclear TDP-43 in patients with FTD and motor neuron disease \(MND\).](#)

**(a)** Additional patients and control subjects used in the study (but not shown in Fig. 3), demonstrating *UNC13A* cryptic splicing. Scale bar equals 10  $\mu$ m. **(b)** Quantification of *UNC13A* cryptic exon BaseScope<sup>TM</sup> in situ hybridization. Six non-overlapping Z-stack images from layer 2–3 of medial frontal pole were captured, per subject, using a 63X oil objective and flattened into a maximum intensity projection image. Puncta counts per image were derived using the “analyze particle” plugin in ImageJ. Each data point represents the number of *UNC13A* cryptic exon puncta in a single image. Cryptic exon quantity varies between patients but always exceeds the technical background of the assay, as observed in controls. (n = 6 non-overlapping Z-stack images; Linear mixed model, mean  $\pm$  s.d.). **(c)** The design of the *UNC13A* e20/e21 BaseScope<sup>TM</sup> probe targeting canonical *UNC13A* transcript. Each “Z” binds to the transcript independently. Both “Z”s must be in close proximity for successful signal amplification, ensuring binding specificity. **(d)** Representative images showing expression of *UNC13A* mRNA in layer 2–3 neurons from the medial frontal pole using the probe shown in **(b)**. *UNC13A* mRNA expression is restricted to neurons (arrows) and is decreased in cells exhibiting TDP-43 nuclear depletion. Arrowheads represent neurons with loss of nuclear TDP-43 and accompanying cytoplasmic inclusions, and arrows indicate neurons with normal nuclear TDP-43. Images are maximum intensity projections of a confocal image Z-stack. Scale bar equals 10  $\mu$ m. **(e)** Quantification of

*UNC13A* mRNA BaseScope™ in situ hybridization. *UNC13A* mRNA puncta were quantified as described in **(b)**. Each data point represents the number of *UNC13A* mRNA puncta in a single image. This suggests some variability in *UNC13A* mRNA levels potentially attributable to technical or biological factors. More importantly, the control *UNC13A* mRNA levels suggest that failure to detect *UNC13A* cryptic exons in controls is not due to nonspecific RNA degradation. There is variability of *UNC13A* mRNA detected per sample but we observe a trend of reduced *UNC13A* mRNA in patient samples compared to controls. (Linear mixed model, mean  $\pm$  s.d.). The final BaseScope™ experimental run was performed once involving all the cases and controls. Six non-overlapping images were captured from each individual, and representative images are shown. *UNC13A* probes were first optimized by testing them on 2 cases and 2 controls in 3 separate pilot experiments, showing similar findings.

#### Source data

#### Extended Data Fig. 7 Levels of *UNC13A* cryptic exon inclusion are influenced by the number of risk haplotypes.

**(a)** Visualization of RNA-Seq alignment between exon 20 and exon 21 of *UNC13A*. RNA-Seq libraries were generated from TDP-43-negative neuronal nuclei as described in Fig. [1a](#). **(b)** Samples that are heterozygous (C/G) or homozygous (G/G) at rs12973192 have higher relative inclusion ( $\Psi$ ) of the cryptic exon except for SRR8571945. Information about the patients were obtained from Liu et al. [12](#). **(c)** Percentages of C and G alleles in the *UNC13A* spliced variants in TDP-43 depleted iPSC-MNs and SRR8571950 neuronal nuclei. Exact binomial test was done for each replicate to test whether the observed difference in percentages differ from what was expected if both alleles are equally included in the cryptic exon. **(d)** rs56041637 and rs62121687 are in strong linkage disequilibrium with both GWAS hits in intron 20-21 of *UNC13A* (Method). Along the axes of the heatplot are all loci that show variation among the 297 patients from Answer ALS in July 2020. Each tile represents the p-value from the corresponding Chi-Square test. P-value  $< 0.05$  are shown in yellow and others are shown in blue or gray. Red and blue blocks highlight the associations of rs12608932 and rs12973192 with other genetic variants in

intron 20-21 respectively. Significant associations common to both are circled in black. **(e)** The summary results of multiple linear regression modeling the effects of the number of *UNC13A* risk alleles on the abundance of *UNC13A* cryptic exon inclusion measured by RT-qPCR. A multivariable model was derived adjusting for phosphorylated TDP-43 levels (pTDP-43), sex, known genetic mutations, disease types, and the age of onset. As shown in Extended Data Fig. 5c, pTDP-43 levels have a strong effect on the abundance of *UNC13A* cryptic exon inclusion. Normality of residuals is tested by Shapiro-Wilk normality test (p-value = 0.2014).

[Source data](#)

[\*\*Extended Data Fig. 8 The impact of variants at rs12973192, rs12608932 and rs56041637 on splicing.\*\*](#)

**(a)** Diagrams showing the design of the *UNC13A* minigene reporter constructs used to assess the impact of the variants at each locus. The complete design of the reporter construct is shown in Fig. 4d. For clarity, the mCherry and GFP exons that are closest to the promoter (blue in Fig. 4d) are labeled as exon 1, and the downstream exon are labeled as exon 2. REF is the reporter that carries the reference haplotype. M-1 to M-3 carry a single risk variant. M-4 to M-6 carry two risk variants. M-7 carries all three variants, the risk haplotype. **(b, c)** The locations of the RT-qPCR primer pairs used to detect the inclusion of the cryptic exon **(b)** and the splicing of EGFP **(c, shown in black)**. **(d, e)** The expression level of the cryptic exon **(d)** or the splicing of EGFP **(e)** in each condition is calculated with reference to the expression level of cryptic exon or the splicing of EGFP from the WT construct in TDP-43-/ HEK-293T cells. The expression of the reporter construct measured using a pair of primers aligned to the second exon of EGFP **(c, shown in green)** was used to normalize RT-qPCR. The cryptic exon expression levels of each pair of reporters expressed within the same cell line were compared. The splicing of EGFP remained constant across all conditions, verifying equal reporter expression levels and the integrity of the splicing machinery independent of TDP-43.

[Source data](#)

## Extended Data Fig. 9 TDP-43-dependent minigene splicing reporter assay in HEK293T cells and HeLa cells.

**(a)** Schematic of various TDP-43 overexpression constructs used in HEK293T cells. RRM1&RRM2: RNA recognition motifs 1 & 2; IDR: intrinsically disordered region; adapted from<sup>50</sup>. The RT-qPCR primers (red arrows) for measuring the expression levels of the TDP-43 overexpression constructs are mapped to the second exon of *TARDBP*. The primer pair can detect all the TDP-43 overexpression constructs, including the endogenous TDP-43. Since the HEK293T TDP-43 knock-out cells do not have TDP-43<sup>36</sup>, using the primers does not interfere with measurement of TDP-43 construct expression levels in TDP-43<sup>-/-</sup> HEK293T. **(b)** Expression of full-length TDP-43 rescued the splicing defects in HEK293T. TDP-43 lacking both RREMs (TDP-43 ΔRRMs) exacerbates the splicing defects and TDP-43 lacking the IDR (TDP-43 ΔIDR) has a much weaker rescue effect compared to full length TDP-43. **(c)** The expression levels of the second exon of TDP-43 across different conditions in HEK293T measured by RT-qPCR. The expression levels differ significantly, possibly due to the autoregulation of TDP-43<sup>51</sup>. Despite the variability, the full length TDP-43 is significantly better at reducing the cryptic exon in *UNC13A* compared to TDP-43 ΔRRMs and TDP-43 ΔIDR. (n = 4 independent cell culture experiments for each condition in **(b, c)**). **(d)** Schematic of the pTB *UNC13A* minigene construct in HeLa cells. The pTB *UNC13A* minigene construct containing *UNC13A* cryptic exon sequence and the flanking sequences upstream (from 50 bp at the end of intron 19 to the cryptic exon) and downstream (~300 bp intron 20) were expressed using the pTB vector, which we have previously used to study TDP-43 splicing regulation of other TDP-43 targets<sup>47</sup>. **(e)** Depletion of TDP-43 by siRNA in HeLa cells resulted in inclusion of the cryptic exon, which was rescued by expressing an siRNA-resistant form of TDP-43 (GFP-TDP-43) but not by an RNA-binding deficient mutant TDP-43 (GFP-TDP-43-5FL). **(f)** RT-qPCR of GFP demonstrating expressions of the constructs are similar across different conditions. (n = 3 independent cell culture experiments in **(e, f)**). *GAPDH* and *RPLP0* were used to normalize RT-qPCR in **(c)** and **(f)**. For all RT-PCR analysis, two-way ANOVA with Dunnett's multiple comparisons test was used for all RT-qPCR analysis, mean ± s.e.m.).

## [Source data](#)

### **Extended Data Fig. 10 UNC13A risk haplotype is associated with diminished binding affinity of TDP-43 and reduced survival time of FTLD-TDP patients.**

**(a)** Reference vs. risk allele RNA binding assay using electrophoretic mobility shift assay (EMSA). Exponentially increasing concentrations (0–8  $\mu$ M) of purified TDP-43 were incubated with 1 nM Cy5 labeled RNA substrate for the reference and risk alleles of CE (rs12973192), intron (rs12608932), and repeat sequences (rs56041637) (see [Methods](#)). 8 mM values were excluded in plots due to significant aggregation at this concentration. The total bound population was quantified at each TDP-43 condition and used to plot the binding curve and calculate the apparent binding affinity,  $K_{D\ app}$ . Experiments were performed three times for introns and two times for exons and repeats, which produced similar results. For gel source data, see Supplementary Fig. [1g](#). **(b)** *UNC13A* risk haplotype is associated with reduced survival time of FTLD-TDP patients. Summary results of Cox multivariable analysis (adjusted for genetic mutations, sex and age at onset) of an additive model. **(c, e)** Survival curves of FTLD-TDP patients ( $n = 205$ , Mayo Clinic Brain Bank), according to a dominant model **(c)** and a recessive model **(e)** and their corresponding risk tables. Summary results of Cox multivariable analysis (adjusted for genetic mutations, sex and age at onset) of a dominant model **(d)** and a recessive model **(f)**. Both the dominant model **(c, d)** and the recessive model **(e, f)** show that the presence of the risk haplotype can reduce the survival of FTLD-TDP patients. Dashed lines mark the median survival for each genotype. Log rank p-values were calculated using Score (logrank) test. **(b, d, f)** The significance of each factor was calculated by Wald test.

## [Source data](#)

## **Supplementary information**

### [Supplementary Information](#)

This file contains Supplementary Tables 3–5 and Supplementary Notes 1–3.

## **Reporting Summary**

### **Supplementary Fig. 1**

Uncropped images of immunoblots, PCR gels, and images of EMSA presented in this study.

### **Peer Review File**

### **Supplementary Table 1**

List of genes alternatively spliced in the absence of TDP-43 identified by both MAJIQ and LeafCutter

### **Supplementary Table 2**

Detection of *STMN2* and *UNC13A* splice variants in bulk RNA-sequencing of patient tissues from the NYGC ALS Consortium cohort

### **Supplementary Table 6**

List of all the primers used in the study

## **Source data**

### **Source Data Fig. 1**

### **Source Data Fig. 2**

### **Source Data Fig. 4**

### **Source Data Extended Data Fig. 3**

[\*\*Source Data Extended Data Fig. 4\*\*](#)

[\*\*Source Data Extended Data Fig. 5\*\*](#)

[\*\*Source Data Extended Data Fig. 6\*\*](#)

[\*\*Source Data Extended Data Fig. 7\*\*](#)

[\*\*Source Data Extended Data Fig. 8\*\*](#)

[\*\*Source Data Extended Data Fig. 9\*\*](#)

[\*\*Source Data Extended Data Fig. 10\*\*](#)

## Rights and permissions

**Open Access** This article is licensed under a Creative Commons Attribution 4.0 International License, which permits use, sharing, adaptation, distribution and reproduction in any medium or format, as long as you give appropriate credit to the original author(s) and the source, provide a link to the Creative Commons license, and indicate if changes were made. The images or other third party material in this article are included in the article's Creative Commons license, unless indicated otherwise in a credit line to the material. If material is not included in the article's Creative Commons license and your intended use is not permitted by statutory regulation or exceeds the permitted use, you will need to obtain permission directly from the copyright holder. To view a copy of this license, visit <http://creativecommons.org/licenses/by/4.0/>.

[Reprints and Permissions](#)

## About this article

[\*\*Cite this article\*\*](#)

Ma, X.R., Prudencio, M., Koike, Y. *et al.* TDP-43 represses cryptic exon inclusion in the FTD–ALS gene *UNC13A*. *Nature* **603**, 124–130 (2022). <https://doi.org/10.1038/s41586-022-04424-7>

- Received: 02 April 2021
- Accepted: 13 January 2022
- Published: 23 February 2022
- Issue Date: 03 March 2022
- DOI: <https://doi.org/10.1038/s41586-022-04424-7>

## Share this article

Anyone you share the following link with will be able to read this content:

[Get shareable link](#)

Sorry, a shareable link is not currently available for this article.

[Copy to clipboard](#)

Provided by the Springer Nature SharedIt content-sharing initiative

## Further reading

- [RNA targets of TDP-43: Which one is more important in neurodegeneration?](#)

- Dilara Halim
- Fen-Biao Gao

*Translational Neurodegeneration* (2022)

- [Mechanism underlying a risk gene in neurodegeneration](#)

- Noa Lipstein

*Nature* (2022)

- **TDP-43 loss and ALS-risk SNPs drive mis-splicing and depletion of UNC13A**

- Anna-Leigh Brown
- Oscar G. Wilkins
- Pietro Fratta

*Nature* (2022)

## **TDP-43 loss and ALS-risk SNPs drive mis-splicing and depletion of UNC13A**

- Anna-Leigh Brown
- Oscar G. Wilkins
- Pietro Fratta

Article Open Access 23 Feb 2022

## **Mechanism underlying a risk gene in neurodegeneration**

- Noa Lipstein

News & Views 23 Feb 2022

---

This article was downloaded by **calibre** from <https://www.nature.com/articles/s41586-022-04424-7>

- Article
- Open Access
- [Published: 23 February 2022](#)

# TDP-43 loss and ALS-risk SNPs drive mis-splicing and depletion of UNC13A

- [Anna-Leigh Brown<sup>1</sup>](#)<sup>nal</sup>,
- [Oscar G. Wilkins<sup>1,2</sup>](#)<sup>nal</sup>,
- [Matthew J. Keuss<sup>1</sup>](#)<sup>nal</sup>,
- [Sarah E. Hill](#) [ORCID: orcid.org/0000-0002-8499-7455<sup>3</sup>](#)<sup>nal</sup>,
- [Matteo Zanovello<sup>1</sup>](#),
- [Weaverly Colleen Lee<sup>1</sup>](#),
- [Alexander Bampton<sup>4,5</sup>](#),
- [Flora C. Y. Lee<sup>1,2</sup>](#),
- [Laura Masino<sup>2</sup>](#),
- [Yue A. Qi<sup>6</sup>](#),
- [Sam Bryce-Smith<sup>1</sup>](#),
- [Ariana Gatt<sup>4,5</sup>](#),
- [Martina Hallegger<sup>1,2</sup>](#),
- [Delphine Fagegaltier<sup>7</sup>](#),
- [Hemali Phatnani<sup>7</sup>](#),
- [NYGC ALS Consortium](#),
- [Jia Newcombe](#) [ORCID: orcid.org/0000-0001-9609-7975<sup>8</sup>](#),
- [Emil K. Gustavsson<sup>4,9</sup>](#),
- [Sahba Seddighi<sup>3,10</sup>](#),
- [Joel F. Reyes<sup>3</sup>](#),
- [Steven L. Coon<sup>11</sup>](#),
- [Daniel Ramos<sup>3,6</sup>](#),
- [Giampietro Schiavo](#) [ORCID: orcid.org/0000-0002-4319-8745<sup>1,12</sup>](#),
- [Elizabeth M. C. Fisher<sup>1</sup>](#),
- [Towfique Raj](#) [ORCID: orcid.org/0000-0002-9355-5704<sup>13,14,15,16</sup>](#),
- [Maria Secrier](#) [ORCID: orcid.org/0000-0003-2758-1741<sup>17</sup>](#),
- [Tammaryn Lashley<sup>4,5</sup>](#),
- [Jernej Ule](#) [ORCID: orcid.org/0000-0002-2452-4277<sup>1,2,18</sup>](#),

- [Emanuele Buratti](#) [ORCID: orcid.org/0000-0002-1356-9074<sup>19</sup>](#),
- [Jack Humphrey<sup>13,14,15,16</sup>](#),
- [Michael E. Ward<sup>3</sup>](#) &
- [Pietro Fratta](#) [ORCID: orcid.org/0000-0002-8762-8188<sup>1</sup>](#)

*Nature* volume **603**, pages 131–137 (2022)

- 32k Accesses
- 3 Citations
- 333 Altmetric
- [Metrics details](#)

## Subjects

- [Amyotrophic lateral sclerosis](#)
- [Neurodegeneration](#)

## Abstract

Variants of *UNC13A*, a critical gene for synapse function, increase the risk of amyotrophic lateral sclerosis and frontotemporal dementia<sup>1,2,3</sup>, two related neurodegenerative diseases defined by mislocalization of the RNA-binding protein TDP-43<sup>4,5</sup>. Here we show that TDP-43 depletion induces robust inclusion of a cryptic exon in *UNC13A*, resulting in nonsense-mediated decay and loss of *UNC13A* protein. Two common intronic *UNC13A* polymorphisms strongly associated with amyotrophic lateral sclerosis and frontotemporal dementia risk overlap with TDP-43 binding sites. These polymorphisms potentiate cryptic exon inclusion, both in cultured cells and in brains and spinal cords from patients with these conditions. Our findings, which demonstrate a genetic link between loss of nuclear TDP-43 function and disease, reveal the mechanism by which *UNC13A* variants exacerbate the effects of decreased TDP-43 function. They further provide a promising therapeutic target for TDP-43 proteinopathies.

[Download PDF](#)

## Main

Amyotrophic lateral sclerosis (ALS) and frontotemporal dementia (FTD) are devastating adult-onset neurodegenerative disorders with shared genetic causes and common pathological aggregates<sup>6</sup>. Genome-wide association studies (GWAS) have repeatedly demonstrated a shared risk locus for ALS and FTD in the crucial synaptic gene *UNC13A*, although the mechanism underlying this association has remained unknown<sup>1,2,3</sup>.

ALS and FTD are pathologically defined by cytoplasmic aggregation and nuclear depletion of TAR DNA-binding protein 43 (TDP-43) in more than 97% of ALS cases and 45% of FTD cases<sup>4,5</sup> (frontotemporal lobar degeneration (FTLD) due to TDP-43 proteinopathy (FTLD-TDP)). TDP-43 is an RNA-binding protein (RBP) that resides primarily in the nucleus and has key regulatory roles in RNA metabolism, including as a splicing repressor. Upon loss of nuclear TDP-43—an early pathological feature in TDP-43-associated ALS (ALS-TDP) and FTLD-TDP—non-conserved intronic sequences are de-repressed and erroneously included in mature RNAs. These events are referred to as cryptic exons (CEs) and often lead to premature stop codons and transcript degradation, or premature polyadenylation<sup>7</sup>. One such CE occurs in the stathmin 2 (*STMN2*) transcript<sup>8,9</sup>. This *STMN2* CE is selectively expressed in affected tissue, and its level correlates with TDP-43 phosphorylation, enabling it to serve as a functional readout for TDP-43 proteinopathy<sup>8,9,10</sup>. However, a link between CEs and disease risk has not yet been established.

Here we report the presence of a CE in *UNC13A*, which is present at high levels in neurons from patients with ALS and FTLD-TDP. This CE promotes nonsense-mediated decay (NMD) and *UNC13A* transcript and protein loss. Notably, intronic risk-associated single nucleotide polymorphisms (SNPs) for ALS and FTD in *UNC13A* promote increased inclusion of this CE. Collectively, our findings reveal the molecular mechanism behind one of the top GWAS hits for ALS and FTD and provide a promising new therapeutic target for TDP-43 proteinopathies.

## ***UNC13A* cryptic exon production on TDP-43 knockdown**

To identify novel CEs promoted by TDP-43 depletion, we performed RNA sequencing (RNA-seq) on human induced pluripotent stem (iPS) cell-derived cortical-like i<sup>3</sup>Neurons, in which we reduced TDP-43 expression using CRISPR inhibition<sup>11,12,13</sup> (CRISPRi). Differential splicing and expression analyses identified 179 CEs, including several that have been reported previously, in genes including *AGRN*, *RAP1GAP*, *PFKP* and *STMN2*<sup>7,8,14</sup> (Fig. 1a, Supplementary Data 1,2). We examined splicing, expression, ALS GWAS<sup>15</sup> risk genes and diagnostic panel genes for ALS and FTD<sup>16</sup>. Of the 179 CE-harbouring genes, only the synaptic gene *UNC13A* was also an ALS–FTD risk gene (Fig. 1b,c, Supplementary Table 1). *UNC13A* polymorphisms

modify both disease risk and progression in ALS and FTLD-TDP<sup>1,2,3,15,17,18,19</sup>, suggesting a potential functional relationship between TDP-43, *UNC13A* and disease risk. Inspection of *UNC13A* splicing revealed the presence of a CE, occurring in two forms distinguishable by their size, between exons 20 and 21 after TDP-43 knockdown (Fig. 1b), and increased intron retention between exons 31 and 32 (Extended Data Fig. 1a). One ALS-TDP and FTLD-TDP risk SNP—*rs12973192*<sup>15</sup>—lies 16 bp inside the CE (hereafter referred to as the CE SNP). Another SNP—*rs12608932*<sup>1</sup>—is located 534 bp downstream of the donor splice site of the CE within the same intron (hereafter referred to as the intronic SNP) (Fig. 1c). There are five polymorphisms associated with ALS risk in *UNC13A*<sup>15</sup>. All are in high linkage disequilibrium with both the CE and intronic SNPs in European populations, with an allele frequency of 0.3423 and 0.3651, respectively<sup>20</sup> (Fig. 1d). The proximity of the disease-associated SNPs to the *UNC13A* CE suggests that the SNPs may influence *UNC13A* splicing. Of note, we also observed robust mis-splicing in *UNC13B*, which encodes another member of the UNC13 synaptic protein family (Fig. 1e,f). TDP-43 knockdown led to the inclusion of an annotated frame-shift-inducing exon between exons 10 and 11 in *UNC13B*, hereafter referred to as the *UNC13B* frameshift exon (FSE), and increased intron retention between exon 21 and 22 (Fig. 1e,f, Extended Data Fig. 1b).

**Fig. 1: TDP-43 depletion in neurons leads to altered splicing in synaptic genes *UNC13A* and *UNC13B*.**

---

 **figure 1**

**a**, Differential splicing analysis by MAJIQ<sup>33</sup> in control ( $n = 4$ ) and CRISPRi TDP-43 depleted (KD) ( $n = 3$ ) iPS cell-derived cortical-like i<sup>3</sup>Neurons. Each point denotes a splice junction. **b**, Representative sashimi plots showing cryptic exon (CE) inclusion between exons 20 and 21 of *UNC13A* upon TDP-43 knockdown. **c, f**, Schematics showing intron retention (IR) (orange; bottom), TDP-43 binding region<sup>22</sup> (green), and two ALS- and FTLD-associated SNPs (red) in *UNC13A* (**c**) and *UNC13B* (**f**). **d**, LocusZoom plot of the *UNC13A* locus in the most recent ALS GWAS<sup>15</sup>; the dashed line indicates the risk threshold used in that study. Lead SNP *rs12973192* is plotted as a purple diamond, other SNPs are coloured by linkage disequilibrium (LD) with *rs12973192* in European individuals from 1000 Genomes. Ref. var., reference variant. **e**, Representative sashimi plot of *UNC13B* showing inclusion of the FSE upon TDP-43 knockdown. **g**, BaseScope detection of *UNC13A* CE (white puncta) in control (top) and TDP-43-knockdown (bottom) i<sup>3</sup>Neurons co-stained for TDP-43 (green), neuronal processes (stained for TUBB3, pink) and nuclei (blue). Scale bar, 5 μm. **h**, Quantification of RT–PCR products using iPS cell-derived neurons made from an independent iPS cell line, NCRM5, with a non-targeting control short guide RNA (sgRNA) (sgTARDBP–), an intermediate TDP-43 knockdown (sgTARDBP+) or stronger TDP-43 knockdown (sgTARDBP++). Data are mean ± s.e.m. sgControl,  $n =$

6; sgTARDBP+,  $n = 5$ ; sgTARDBP++,  $n = 6$ ; one-way ANOVA with multiple comparisons. \* $P < 0.05$ , \*\* $P < 0.01$ , \*\*\* $P < 0.001$ , \*\*\*\* $P < 0.0001$ . **i**, Schematic of nanopore long reads quantified in **j**, Extended Data Figs. [2d,e](#), [5e,f](#). **j**, Percentage of targeted *UNC13A* long reads with TDP-43-regulated splice events that contain CE, intron retention or both in TDP-43-knockdown SH-SY5Y cells.

### [Source data](#)

We validated the *UNC13A* CE in i<sup>3</sup>Neurons by in situ hybridization, which showed a primarily nuclear localization and occurred predominantly in TDP-43-knockdown neurons (Fig. [1g](#), Extended Data Fig. [1c](#)). To confirm the CE was not restricted to neurons derived from a single iPS cell line, we performed TDP-43 knockdown in independent i<sup>3</sup>Neurons using two different guides leading to different levels of TDP-43 knockdown (Extended Data Fig. [1d,e](#)). CE expression was restricted to cells with TDP-43 knockdown in both lines, and correlated with the level of TDP-43 knockdown (Fig. [1h](#), Extended Data Fig. [1f,g](#)). We also detected these splicing changes in RNA-seq data we generated from TDP-43 depleted SH-SY5Y and SK-N-DZ neuronal lines, and publicly available RNA-seq from iPS cell-derived motor neurons<sup>9</sup> and SK-N-DZ datasets<sup>21</sup> (Extended Data Fig. [1h-k](#), Supplementary Table [2](#)). We note that the expression of these events was lowest in the SH-SY5Y experiment, which also showed the weakest TDP-43 knockdown (Extended Data Fig. [1l](#)). Using stronger TDP-43 knockdown, we validated the *UNC13A* CE by PCR with reverse transcription (RT-PCR) and Sanger sequencing in SH-SY5Y and SK-N-DZ cell lines (Extended Data Fig. [2a](#)).

In support of a direct role for TDP-43 regulation of *UNC13A* and *UNC13B*, we found multiple TDP-43-binding peaks<sup>22</sup> both downstream and within the body of the *UNC13A* CE (Fig. [1c](#)) and intron retention (Extended Data Fig. [1a](#)). Additionally, TDP-43-binding peaks<sup>22</sup> were present near both splice events in *UNC13B* (Fig. [1f](#), Extended Data Fig. [1b](#)). Additional iCLIP of endogenous TDP-43 in SH-SY5Y cells confirmed enhanced binding near the *UNC13A* CE and intron retention and *UNC13B* FSE and intron retention (Extended Data Fig. [2b,c](#)). We next tested whether the *UNC13A* intron retention and CE events co-occurred in transcripts. Using targeted long-read sequencing, we determined that although co-regulated, *UNC13A* CE and intron retention occurred largely independently from each other (Fig. [1l,j](#); Extended Data Fig. [2d,e](#)).

## ***UNC13A* is downregulated on TDP-43 knockdown**

Next, we examined whether incorrect splicing of *UNC13A* and *UNC13B* affected transcript levels in neurons and neuron-like cells. TDP-43 knockdown significantly reduced *UNC13A* RNA abundance in the three experiments with the highest levels of

cryptic splicing (false discovery rate (FDR)  $< 0.0001$ ; Extended Data Figs. [1h](#), [3a](#)). Similarly, *UNC13B* RNA was significantly downregulated in four datasets (FDR  $< 0.0001$ ) (Extended Data Fig. [3b](#)). We confirmed these results by quantitative PCR (qPCR) in i<sup>3</sup>Neurons, and SH-SY5Y and SK-N-DZ cell lines (Extended Data Figs. [1d](#), [e](#), [3c](#), [d](#)). The number of ribosome footprints aligning to *UNC13A* and *UNC13B* was also reduced after TDP-43 knockdown (Fig. [2a](#), Extended Data Fig. [3e](#), [Supplementary Data 3](#); FDR  $< 0.05$ ). Notably, TDP-43 knockdown decreased expression of *UNC13A* and *UNC13B* at the protein level in a dose-dependent manner, as assessed by quantitative proteomics (Fig. [2b](#)).

**Fig. 2: *UNC13A* and *UNC13B* are downregulated after TDP-43 knockdown owing to the production of NMD-sensitive transcripts.**

 [figure 2](#)

**a**, Ribosome profiling of TDP-43-knockdown i<sup>3</sup>Neurons shows a reduction in ribosome occupancy of *STMN2*, *UNC13A* and *UNC13B* transcripts. **b**, Mass spectrometry-based proteomic analysis shows dose-dependent reduction in protein abundance of *UNC13A* and TDP-43 upon TDP-43 knockdown in i<sup>3</sup>Neurons.  $n = 6$  biological replicates. Two-sample *t*-test. **c**, Protein and RNA quantification of TDP-43, *UNC13A* and *UNC13B* in SH-SY5Y with varying levels of doxycycline-inducible

TDP-43 knockdown.  $n = 3$  biological replicates. **d**, Transcript expression upon treatment with CHX suggests that *UNC13A* and *UNC13B*, but not *STMN2*, are sensitive to NMD. *HNRNPL* is used as a positive control.  $n = 7$  biological replicates (*UNC13A*, *HNRNPL* and *STMN2*) and 8 biological replicates (*UNC13B*). One-sample *t*-test. Data are mean  $\pm$  s.e.m. (**b–d**).

### Source data

To assess the relation between TDP-43 reduction and UNC13 splicing, RNA and protein levels, we assayed SH-SY5Y cells with increasing amounts of TDP-43 knockdown. We found that changes in *UNC13A* paralleled those of TDP-43, whereas *UNC13B* levels were less affected (Fig. 2c, Extended Data Fig. 3f, Supplementary Fig. 1). *UNC13A* CE inclusion and intron retention increased on TDP-43 knockdown, with the CE being detected only after more than 50% TDP-43 loss, whereas *UNC13B* FSE and intron retention were not robustly detected until more than 90% of TDP-43 expression was lost (Fig. 2c, Extended Data Fig. 3g).

To assess whether the amount of *UNC13A* CE expression was underestimated owing to efficient transcript degradation, we investigated whether it promoted NMD, as predicted by the presence of a premature termination codon. Knockdown of the key NMD factor *UPF1* or cycloheximide (CHX) treatment—which stalls translation and impairs NMD—increased the amount of *UNC13A* CE and *UNC13B* FSE, which also leads to a PTC at the beginning of exon 11, confirming that both *UNC13A* and *UNC13B* were targeted by NMD (Fig. 2d, Extended Data Fig. 3h, i). Conversely, CHX treatment and *UPF1* knockdown did not alter levels of the aberrant *STMN2* transcript, which was not predicted to undergo NMD (Fig. 2d, Extended Data Fig. 3h). Of note, CHX treatment of SH-SY5Y cells with the least TDP-43 knockdown (Fig. 2c) enabled detection of the *UNC13A* CE, supporting the notion that its occurrence may be underestimated owing to efficient degradation (Extended Data Fig. 3j, k).

Together, these data suggest that TDP-43 has an essential role in ensuring the correct pre-mRNA splicing of *UNC13A* and *UNC13B*, thereby maintaining normal expression of these key presynaptic proteins.

## ***UNC13A* cryptic exon in patient neurons**

To test whether the *UNC13A* CE could be detected in tissues from patients affected by TDP-43 pathology, we first analysed RNA-seq data from neuronal nuclei sorted from frontal cortices of patients with ALS–FTLD<sup>23</sup>. We compared the levels of *UNC13A* CE to the levels of a CE in *STMN2* known to be regulated by TDP-43. Both *STMN2* and *UNC13A* CEs were found exclusively in TDP-43-depleted nuclei. Although the lack of NMD activity in the nucleus means that the nuclear splicing ratio may not

reflect that of the whole cell, in some cases, the *UNC13A* CE percent spliced in (PSI ( $\Psi$ )) reached 100% (Fig. 3a). This suggests that there is a substantial loss of *UNC13A* expression in the subpopulation of neurons with TDP-43 pathology in human patients with ALS–FTLD.

**Fig. 3: *UNC13A* CE is highly expressed in tissues from patients with ALS or FTLD and correlates with known markers of TDP-43 loss of function.**

 figure 3



**a**, *UNC13A* and *STMN2* CE expression from a published dataset of frontal cortex neuronal nuclei from patients with ALS or FTLD sorted according to TDP-43 expression<sup>23</sup>. **b**, *UNC13A* CE expression in bulk RNA-seq from the NYGC ALS Consortium data normalized by library size across disease and tissue samples. ALS cases are stratified by mutation status, FTLD cases are stratified by pathological subtype. **c**, CE expression throughout ALS-TDP and FTLD-TDP cases across tissue, number of tissue samples in brackets. **d**, BaseScope detection of *UNC13A* CE (red foci) in FTLD-TDP (9 individuals) but not control (5 individuals) or non-TDP FTLD (FTLD-TAU) (4 individuals) frontal cortex samples and quantification of background-

corrected foci frequency between groups. Scale bar, 10 µm. Data are mean ± s.e.m. (**b–d**); Wilcoxon test.

### Source data

Next, we quantified *UNC13A* CE inclusion in bulk RNA-seq data from the New York Genome Center (NYGC) ALS Consortium, which contains 1,349 brain and spinal cord tissues from a total of 377 individuals, including those with ALS or FTLD and controls. The *UNC13A* CE was detected exclusively in tissues from individuals with FTLD-TDP and ALS-TDP (89% and 38% of individuals, respectively), and not in individuals with non-TDP ALS (caused by *SOD1* and *FUS* mutations), FTLD associated with TAU (FTLD-TAU), FTLD associated with FUS (FTLD-FUS) or controls. There were no systematic differences across tissues between controls and non-TDP ALS or FTLD and ALS-TDP or FTLD-TDP in confounding factors such as library depth, RNA integrity number or cellular composition, which could explain the *UNC13A* CE specificity (Extended Data Fig. [4a–d](#)). The lower detection rate in ALS compared with FTLD is possibly owing to the lower expression of *UNC13A* in the spinal cord (Extended Data Fig. [4a](#)), although differences in NMD efficiency between cortical and spinal regions could also affect detection rate<sup>24</sup>. *UNC13A* CE was more likely to be detected in bulk samples that had been sequenced with 125-bp rather than 100-bp paired-end reads, but other technical factors did not systematically affect detection (Extended Data Fig. [5a–d](#)).

*UNC13A* CE expression mirrored the known tissue distribution of TDP-43 aggregation and nuclear clearance<sup>25</sup>: it was specific to ALS-TDP spinal cord and motor cortex, as well as FTLD-TDP frontal and temporal cortices, but was absent from the cerebellum in both disease and control states (Fig. [3b](#)). Furthermore, although the *UNC13A* CE induces NMD (unlike the *STMN2* CE) it was detected at similar levels to the *STMN2* CE in cortical regions, whereas *STMN2* CE was more abundant in the spinal cord (Fig. [3c](#)). Targeted long-read sequencing of *UNC13A* in FTLD frontal cortex revealed that the CE and intron retention events can co-occur but, as in SH-SY5Y cells, they are mostly detected independently (Extended Data Fig. [5e,f](#)). Thus, pathological *UNC13A* CEs occur *in vivo* and are specific to neurodegenerative disease subtypes in which mislocalization and nuclear depletion of TDP-43 occurs.

We next assessed expression of the *UNC13B* FSE across the NYGC dataset. We detected no increase in the *UNC13B* FSE in pathological ALS-TDP or FTLD-TDP tissues. However, the presence throughout control and ALS or FTD brains of a shorter isoform of the CE that included the FSE, which was absent in our *in vitro* experiments, may mask underlying changes (Extended Data Fig. [6a–c](#)).

We also evaluated both *UNC13A* and *UNC13B* intron retention events from bulk RNA-seq. Unlike the CE, both intron retention events were also detected in control

brains, making it difficult to determine whether TDP-43 pathology increased intron retention (Extended Data Fig. 7a, b).

We next investigated whether *UNC13A* CEs could be visualized by *in situ* hybridization in brains from patients with FTLD, using the same probe used for iPS cell-derived neurons. We detected red foci in cortical neurons at a significantly higher frequency in FTLD-TDP relative to both neurologically normal controls (Kruskal–Wallis test,  $P = 0.021$ ) and non-TDP FTLD (FTLD-TAU) ( $P = 0.010$ ) (Fig. 3d).

To assess whether *UNC13A* CE levels in bulk tissue were related to the level of TDP-43 proteinopathy, we used the *STMN2* CE PSI as a proxy. The PSI of *STMN2* CE correlates with the cryptic PSI of other well-known TDP-43 induced CEs, such as those in *RAP1GAP* and *PFKP*<sup>7,9,14</sup> (Extended Data Fig. 7c,d) and correlates with the amount of phosphorylated TDP-43 in patient samples<sup>10</sup>. As expected, across the NYGC ALS Consortium samples we observed a significant positive correlation between the level of *STMN2* CE PSI and *UNC13A* CE PSI across the NYGC ALS Consortium samples ( $\rho = 0.56$ ,  $P = 2.9 \times 10^{-7}$ ,  $n = 72$  cortical samples) (Extended Data Fig. 7e).

Collectively, our analysis reveals a strong relationship between TDP-43 pathology and the level of *UNC13A* CE, supporting a model with direct regulation of *UNC13A* mRNA splicing by TDP-43.

## ***UNC13A* risk SNPs exacerbate cryptic splicing**

To test whether the ALS–FTD risk SNPs in *UNC13A* promote cryptic splicing, thereby explaining their link to disease, we assessed *UNC13A* CE levels across different genotypes. We found significantly increased *UNC13A* CE in cases homozygous for CE rs12973192 (G) and intronic rs12608932 (C) SNPs ( $P = 0.028$ , Wilcoxon test) (Extended Data Fig. 8a, Supplementary Table 4). To ensure that this was not owing to more severe TDP-43 loss of function in these samples, we normalized *UNC13A* CE by the level of *STMN2* cryptic splicing, a well-established product of TDP-43 loss of function. Again, we found significantly increased *UNC13A* CE in cases with homozygous risk variants ( $P < 0.001$ , Wilcoxon test) (Fig. 4a, Extended Data Fig. 8b). Next, we performed targeted RNA-seq on *UNC13A* CE from temporal cortices of ten FTLD-TDP patients who were heterozygous in the risk allele and four controls (Supplementary Table 5). There was no detection of the CE in the control samples, and in the patient samples we detected significant biases towards reads containing the risk allele ( $P < 0.05$ , single-tailed binomial test) in six samples, with a seventh sample approaching significance (Fig. 4b), suggesting that the two ALS- and FTLD-linked variants promote cryptic splicing *in vivo*.

**Fig. 4: *UNC13A* ALS and FTD risk variants enhance *UNC13A* CE splicing in patients and in vitro by altering TDP-43 pre-mRNA binding.**

 figure 4

**a**, Ratio of *UNC13A* and *STMN2* CE  $\Psi$  in ALS-TDP and FTLD-TDP cortex, split by genotype for *UNC13A* risk alleles. In box plots, the centre line shows the median, box edges delineate 25th and 75th percentiles and Tukey whiskers are plotted. **b**, Unique cDNAs from targeted RNA-seq in ten patients with FTLD-TDP who are heterozygous for the risk SNP within the *UNC13A* cryptic exon. Single-tailed binomial tests.

Patients 1, 5 and 7 carry the C9orf72 hexanucleotide repeat. **c**, Schematic of *UNC13A* minigenes containing exon 20, intron 20 and exon 21 and combinations of *UNC13A* alleles. **d, e**, Representative image (**d**) and quantification (**e**) of RT–PCR products from *UNC13A* minigenes in SH-SY5Y cells with or without TDP-43 knockdown. Data are mean  $\pm$  s.e.m. Each variant was compared with the healthy minigene with which it was co-transfected and results were compared with an unpaired *t*-test ( $n = 3$  biological replicates). **f**, TDP-43 iCLIP of SH-SY5Y cells containing 2R and 2H minigenes. Top, average crosslink density. Middle, average density change 2R for – 2H (20-nt rolling window, units are crosslinks per 1,000). Bottom, predicted TDP-43 binding footprints (UGNNUG motif). **g**, Average change in E-value (measure of binding enrichment) across proteins for heptamers containing risk or healthy CE SNP alleles. TDP-43 is indicated in red. **h**, Binding affinities between TDP-43 and 14-nt RNA containing the CE ( $n = 4$ ) or intronic ( $n = 3$ ) healthy or risk sequences measured by isothermal titration calorimetry. Data are mean  $\pm$  s.d.; two-sample *t*-test. **i, j**, Representative image (**i**) and quantification (**j**) of RT–PCR products from *UNC13A* minigenes with mutated UGNNUG TDP-43 binding motifs as shown in **f**. Data are mean  $\pm$  s.e.m.;  $n = 3$  biological replicates; statistical analysis as in (**d, e**).

### Source data

To directly assess whether the risk SNPs increase CE inclusion, we performed minigene experiments. Using two minigenes containing *UNC13A* exon 20, intron 20 and exon 21, with and without the two ALS- and FTLD-linked variants, we determined that the risk variants enhanced CE upon TDP-43 loss (Extended Data Fig. [8c](#)). To examine whether the CE SNP, intronic SNP or short tandem repeat expansion rs56041637—which is in linkage disequilibrium with the two SNPs<sup>[26](#)</sup>—are responsible for promoting the CE inclusion, we generated minigenes featuring different combinations of these genomic variants (Fig. [4c](#)). Using quantitative analysis of RT–PCR products, we found that both the CE SNP and, to a lesser extent, the intronic SNP independently promoted CE inclusion, with the highest overall levels detected for the 2R minigene (Fig. [4d, e](#), Extended Data Fig. [8d](#)).

TDP-43 can both inhibit and promote splicing by binding to pre-mRNA. We performed TDP-43 iCLIP in HEK 293T cells expressing either the 2R or the 2H minigene to fine map TDP-43 binding to *UNC13A* intron 20 and investigate whether the risk SNPs have an effect on this interaction. In agreement with our iCLIP data of endogenous *UNC13A* in SH-SY5Y cells (Extended Data Fig. [2b](#)), we observed an enrichment of crosslinks within the approximately 800-nucleotide UG-rich region containing both SNPs in intron 20 (Fig. [4f](#)). When comparing 2R with 2H, the largest fractional changes were near each SNP (Extended Data Fig. [8e](#)). We detected a 21% decrease in total TDP-43 crosslinks centred around the CE SNP and a 73% increase upstream of the intronic SNP (Fig. [4f](#), Extended Data Fig. [8f](#); 50-nucleotide windows).

These data suggest these two disease-risk SNPs distort the pattern of TDP-43–RNA interactions, decreasing TDP-43 binding near the CE donor splice site.

To explore whether these two SNPs directly influence TDP-43 binding, we analysed a dataset of in vitro RNA heptamer–RBP binding enrichments. We examined the effect of the SNPs on relative RBP enrichment<sup>27</sup> by comparing healthy versus risk SNP-containing heptamers. When investigating which RBPs were most affected in their RNA binding enrichment by the CE risk SNP, TDP-43 had the third largest decrease of any RBP, with only two non-mammalian RBPs showing a larger decrease (Fig. 4g, Extended Data Fig. 8g). The intronic SNP did not strongly affect TDP-43 binding, although data was only available for 2 out of 7 possible heptamers (Extended Data Fig. 8h, i). To verify that the CE SNP directly inhibited TDP-43 binding, we performed isothermal titration calorimetry using recombinant TDP-43 and short RNAs. We observed nanomolar binding affinity in all cases, with an increased dissociation constant ( $K_d$ ) (lower binding affinity) for the CE SNP region ( $P = 0.023$ , two-sample  $t$ -test) and a trend of decreasing  $K_d$  for the intronic SNP region ( $P = 0.052$ ) when the risk variants were present (Fig. 4h, Extended Data Fig. 9a–d, [Supplementary Data 4](#)). Last, to test whether TDP-43 binding to the CE SNP region is critical for CE repression, we mutated the UGNNUG TDP-43-binding motif in this region, leading to significantly increased CE inclusion (Fig. 4i, j, Extended Data Fig. 9e). Together these data suggest that the risk SNPs modulate TDP-43 binding, in part via direct changes in binding affinity, exacerbating *UNC13A* CE inclusion.

## Discussion

Our results support a model in which *UNC13A* SNPs and TDP-43 loss synergistically drive cryptic exon inclusion in *UNC13A* transcripts, thereby reducing expression of a synaptic gene that is critical for normal neuronal function.

In this model, when nuclear TDP-43 levels are normal in healthy individuals, TDP-43 binds efficiently to *UNC13A* pre-mRNA, even in the presence of risk SNPs, thus preventing CE splicing. Conversely, severe nuclear depletion of TDP-43 in end-stage disease induces CE inclusion in all cases. However, in the setting of partial TDP-43 loss that occurs early in degenerating neurons, risk-associated intronic and CE risk SNPs alter TDP-43 binding to *UNC13A* pre-mRNA, exacerbating CE inclusion in these transcripts. The ensuing loss of *UNC13A* protein—which is critical for normal synaptic activity—at earlier disease stages may explain the associated risk effect of these SNPs. Notably, we found that both risk alleles for these SNPs independently and additively promoted cryptic splicing in vitro. Further, when the two variants are not co-inherited, as seen in individuals from east Asia with ALS, an attenuated effect is observed<sup>19</sup>. A similar phenomenon, in which SNP pairs both contribute to risk, has

been widely studied at the APOE locus in Alzheimer's disease<sup>28</sup>. Clarification of single versus additive effects of co-inherited SNPs regarding effects on CE inclusion, as well as contributions of other RBPs, will require future investigation.

UNC13 family proteins are highly conserved across metazoans and are essential for calcium-triggered synaptic vesicle release<sup>29</sup>. In mice, single knockout of *Unc13a* blocks action potential-induced neurotransmitter release from the majority of glutamatergic hippocampal synapses<sup>30</sup>. Double knockout of *Unc13a* and *Unc13b* inhibits both excitatory and inhibitory synaptic transmission in hippocampal neurons and greatly impairs transmission at neuromuscular junctions<sup>31,32</sup>. In TDP-43-depleted neuronal nuclei derived from patients with ALS or FTLD, which reflect transcript expression before NMD, the *UNC13A* CE is present in up to 100% of transcripts, suggesting that expression of functional *UNC13A* is markedly reduced, which could affect normal synaptic transmission.

TDP-43 loss induces hundreds of splicing changes, several of which have also been detected in brains of patients with ALS or FTLD. However, it has remained unclear whether these events—even those that occur in essential neuronal genes—contribute to disease pathogenesis. The fact that genetic variation modulating *UNC13A* CE levels influences the rate of ALS progression strongly supports the role of *UNC13A* downregulation as an important effector of neurotoxicity mediated by TDP-43 loss. The *UNC13A* CE is thus a promising target for therapies that modulate splicing, potentially applicable to 97% of ALS cases and approximately half of FTD cases. These findings are also of interest to other neurodegenerative diseases—such as Alzheimer's disease, Parkinson's disease and chronic traumatic encephalopathy—in which TDP-43 depletion occurs in a substantial fraction of cases.

## Methods

### Human iPS cell culture

All policies of the NIH Intramural research program were followed for the procurement and use of iPS cells. For most studies, the iPS cells used were from the WTC11 line, derived from a healthy 30-year-old male, and obtained from the Coriell cell repository. Informed consent was obtained from the donor. We confirmed the WTC11 line contained no ALS–FTD mutations in the ALS and FTD risk genes in Supplementary Table 1. For key experiments, an independent line was used, NCRM5. NCRM5 was derived from umbilical cord blood from NIH Center for Regenerative Medicine (CRM), Bethesda, MD, USA. Informed consent was obtained from the donor. All culture procedures were conducted as previously<sup>11</sup>. In brief, iPS cells were grown on tissue culture dishes coated with human embryonic stem cell-qualified

Matrigel (Corning, catalogue no. 354277). They were maintained in Essential 8 Medium (E8; Thermo Fisher Scientific, catalogue (cat.) no. A1517001) supplemented with 10 µM ROCK inhibitor (RI; Y-27632; Selleckchem, cat. no. S1049) in a 37 °C, 5% CO<sub>2</sub> incubator. Medium was replaced every 1–2 days as needed. Cells were passaged with accutase (Life Technologies, cat. no. A1110501), 5–10 min treatment at 37 °C. Accutase was removed and cells were washed with PBS before re-plating. Following dissociation, cells were plated in E8 media supplemented with 10 µM RI to promote survival. RI was removed once cells grew into colonies of 5–10 cells.

The following cell line and DNA samples were obtained from the NIGMS Human Genetic Cell Repository at the Coriell Institute for Medical Research: GM25256.

## Data

Publicly available data were obtained from the Gene Expression Omnibus (GEO): iPS cell MNs<sup>9</sup>, GSE121569; SK-N-DZ<sup>b</sup>, GSE97262; FACS-sorted frontal cortex neuronal nuclei, GSE126543; Riboseq, E-MTAB-10235; targeted RNA-seq, E-MTAB-10237; minigene TDP-43 iCLIP, E-MTAB-10297; SH-SY5Y TDP-43 iCLIP, E-MTAB-11243; and *UNC13A*-targeted nanopore, E-MTAB-11244.

## CRISPRi knockdown in human iPS cells

The human iPS cells used in this study were previously engineered<sup>11,13</sup> to express mouse or human neurogenin-2 (NGN2) under a doxycycline-inducible promoter, as well as an enzymatically dead Cas9 (+/– CAG-dCas9-BFP-KRAB)<sup>12</sup>. For WTC11 these were integrated at the AAVS1 safe harbour and the CLYBL promoter safe harbour respectively, while for NCRM5, these were both integrated at the CLYBL promoter safe harbour.

To achieve knockdown, sgRNAs targeting either *TARDBP*/TDP-43, *UPF1* or a non-targeting control guide were delivered to iPS cells by lentiviral transduction. To make the virus, Lenti-X human embryonic kidney (HEK) cells were transfected with the sgRNA plasmids using Lipofectamine 3000 (Life Technologies, cat. no. L3000150), then cultured for 2–3 days in the following media: DMEM, high glucose GlutaMAX Supplement media (Life Technologies, cat. no. 10566024) with 10% FBS (Sigma, cat. no. TMS-013-B), supplemented with viral boost reagent (ALSTEM, cat. no. VB100). Virus was then concentrated from the media 1:10 in PBS using Lenti-X concentrator (Takara Bio, cat. no. 631231), aliquoted and stored at –80 °C for future use.

The sgRNAs were cloned into either pU6-sgRNA EF1Alpha-puro-T2A-BFP vector<sup>12,37</sup> (gift from J. Weissman; Addgene 60955) or a modified version containing a human U6 promoter, a blasticidin (Bsd) resistance gene, and eGFP. sgRNA sequences

were as follows: non-targeting control: GTCCACCCTTATCTAGGCTA, *UPF1*: GGCCAGACGCAGACGCC, and *TARDBP*: GGGAAAGTCAGCCGTGAGACC (strong guide), and GCUGCCTAGCGGGTGAGTCG (weaker guide). The stronger *TARDBP* guide was used in all cases unless otherwise stated.

Virus was delivered to iPS cells in suspension following an accutase split. Cells were plated and cultured overnight. The following morning, cells were washed with PBS and media was changed to E8 or E8+RI depending on cell density. Two days after lentiviral delivery, cells were selected overnight with either puromycin ( $10\text{ }\mu\text{g ml}^{-1}$ ) or blasticidin ( $50\text{--}100\text{ }\mu\text{g ml}^{-1}$ ). iPS cells were then expanded 1–2 days before initiating neuronal differentiation. Knockdown efficiency was tested at iPS cell and neuronal stages using immunofluorescence, qPCR and observed in RNA-seq data.

## iPS cell-derived i<sup>3</sup>Neuron differentiation and culture

To initiate neuronal differentiation, 20–25 million iPS cells per 15 cm plate were individualized using accutase on day 0 and re-plated onto Matrigel-coated tissue culture dishes in N2 differentiation media containing: knockout DMEM/F12 media (Life Technologies Corporation, cat. no. 12660012) with N2 supplement (Life Technologies Corporation, cat. no. 17502048), 1× GlutaMAX (Thermofisher Scientific, cat. no. 35050061), 1× MEM nonessential amino acids (NEAA) (Thermofisher Scientific, cat. no. 11140050), 10  $\mu\text{M}$  ROCK inhibitor (Y-27632; Selleckchem, cat. no. S1049) and 2  $\mu\text{g ml}^{-1}$  doxycycline (Clontech, cat. no. 631311). Media was changed daily during this stage.

On day 3 pre-neuron cells were replated onto dishes coated with freshly made poly-L-ornithine (PLO; 0.1 mg ml<sup>-1</sup>; Sigma, cat. no. P3655-10MG), either 96-well plates (50,000 per well), 6-well dishes (2 million per well), or 15 cm dishes (45 million per plate), in i<sup>3</sup>Neuron Culture Media: BrainPhys media (Stemcell Technologies, cat. no. 05790) supplemented with 1× B27 Plus Supplement (ThermoFisher Scientific, cat. no. A3582801), 10 ng ml<sup>-1</sup> BDNF (PeproTech, cat. no. 450-02), 10 ng ml<sup>-1</sup> NT-3 (PeproTech, cat. no. 450-03), 1  $\mu\text{g ml}^{-1}$  mouse laminin (Sigma, cat. no. L2020-1MG), and 2  $\mu\text{g ml}^{-1}$  doxycycline (Clontech, cat. no. 631311). i<sup>3</sup>Neurons were then fed three times a week by half media changes. i<sup>3</sup>Neuron were then collected on day 7 or 17 after the addition of doxycycline or 4 or 14 days after re-plating.

## Generation of stable TDP-43-knockdown cell line

SH-SY5Y and SK-N-DZ cells were transduced with SmartVector lentivirus (V3IHSHEG\_6494503) containing a doxycycline-inducible shRNA cassette for TDP-43. Transduced cells were selected with puromycin ( $1\text{ }\mu\text{g ml}^{-1}$ ) for one week. For

doxycycline dose–response experiments, the pool of TDP-43-knockdown SH-SY5Y cells were plated as single cells and expanded to obtain a clonal population.

## Depletion of TDP-43 from immortalized human cell lines

SH-SY5Y cells for RT–qPCR validations and western blots were grown in DMEM/F12 containing Glutamax (Thermo) supplemented with 10% FBS (Thermo). For induction of shRNA against TDP-43 cells were treated with 5 µg ml<sup>-1</sup> doxycycline hydralate (Sigma D9891). After 3 days medium was replaced with Neurobasal (Thermo) supplemented with B27 (Thermo) to induce differentiation. After a further 7 days, cells were collected for protein or RNA. For doxycycline dose response experiments, doxycycline was used at concentrations of 12.5 ng ml<sup>-1</sup>, 18.75 ng ml<sup>-1</sup>, 21 ng ml<sup>-1</sup>, 25 ng ml<sup>-1</sup>, and 75 ng ml<sup>-1</sup>. SH-SY5Y and SK-N-DZ cells for RNA-seq experiments were treated with siRNA, as previously described<sup>21</sup>.

## RNA sequencing, differential gene expression and splicing analysis

For RNA-seq experiments of i<sup>3</sup>Neurons, the i<sup>3</sup>Neurons were grown on 96-well dishes. For collection on day 17, media was completely removed, and wells were treated with tri-reagent (100 µl per well) (Zymo research corporation, cat. no. R2050-1-200). Then 5 wells were pooled together for each biological replicate: control ( $n = 4$ ); TDP-43 knockdown ( $n = 3$ ). To isolate RNA, we used a Direct-zol RNA miniprep kit (Zymo Research Corporation, cat. no. R2052), following manufacturer’s instructions including the optional DNase step. Note: one knockdown replicate did not pass RNA quality controls and so was not submitted for sequencing, resulting in a total of  $n = 3$  samples for this condition. Sequencing libraries were prepared with polyA enrichment using a TruSeq Stranded mRNA Prep Kit (Illumina) and sequenced ( $2 \times 75$  bp) on an Illumina HiSeq 2500 machine.

Samples were quality trimmed using Fastp with the parameter “qualified\_quality\_phred: 10”, and aligned to the GRCh38 genome build using STAR (v2.7.0f)<sup>38</sup> with gene models from GENCODE v31<sup>39</sup>. Gene expression was quantified using FeatureCounts<sup>40</sup> using gene models from GENCODE v31. Any gene which did not have an expression of at least 0.5 counts per million (CPM) in more than 2 samples was removed. For differential gene expression analysis, all samples were run in the same manner using the standard DESeq2<sup>41</sup> workflow without additional covariates, except for the Klim MNs dataset<sup>9</sup>, where we included the day of differentiation. The DESeq2 median of ratios, which controls for both sequencing depth and RNA composition, was used to normalize gene counts. Differential expression was defined at a Benjamini–Hochberg false discovery rate < 0.1. Salmon (v1.5.1)<sup>42</sup> using an index built from GENCODE v34<sup>39</sup> was used to assess the isoform

expression of *UNC13B*. Our alignment pipeline is implemented in Snakemake version 5.5.4<sup>43</sup> and available at: [https://github.com/frattalab/rna\\_seq\\_snakemake](https://github.com/frattalab/rna_seq_snakemake).

STAR aligned BAMs were used as input to MAJIQ (v2.1)<sup>33</sup> for differential splicing analysis using the GRCh38 reference genome. A threshold of 10%  $\Delta\Psi$  was used for calling the probability of significant change between groups. The results of the deltaPSI module were then parsed using custom R scripts to obtain  $\Psi$  and probability of change for each junction. Cryptic splicing was defined as junctions with  $\Psi < 5\%$  in control samples,  $\Delta\Psi > 10\%$ , and the junction was unannotated in GENCODE v31. Our splicing pipeline is implemented in Snakemake version 5.5.4 and available at: <https://github.com/frattalab/splicing>.

Counts for specific junctions were tallied by parsing the STAR splice junction output tables using bedtools<sup>44</sup>. Splice junction parsing pipeline is implemented in Snakemake version 5.5.4 and available at:

[https://github.com/frattalab/bedops\\_parse\\_star\\_junctions](https://github.com/frattalab/bedops_parse_star_junctions).  $\Psi$  was evaluated using coordinates in Supplementary Table 6:

```
$$\psi = \frac{\text{rm}\{I\} \text{rm}\{n\} \text{rm}\{c\} \text{rm}\{l\} \text{rm}\{u\} \text{rm}\{s\} \text{rm}\{i\} \text{rm}\{o\} \text{rm}\{n\} \text{rm}\{r\} \text{rm}\{e\} \text{rm}\{a\} \text{rm}\{d\} \text{rm}\{s\} \text{rm}\{I\} \text{rm}\{n\} \text{rm}\{c\} \text{rm}\{l\} \text{rm}\{u\} \text{rm}\{s\} \text{rm}\{i\} \text{rm}\{o\} \text{rm}\{n\} \text{rm}\{r\} \text{rm}\{e\} \text{rm}\{a\} \text{rm}\{d\} \text{rm}\{s\} + \text{rm}\{e\} \text{rm}\{x\} \text{rm}\{c\} \text{rm}\{l\} \text{rm}\{u\} \text{rm}\{s\} \text{rm}\{i\} \text{rm}\{o\} \text{rm}\{n\} \text{rm}\{r\} \text{rm}\{e\} \text{rm}\{a\} \text{rm}\{d\}}{\text{rm}\{s\} \text{rm}\{i\} \text{rm}\{o\} \text{rm}\{n\} \text{rm}\{r\} \text{rm}\{e\} \text{rm}\{a\} \text{rm}\{d\}} \text{rm}\{s\} \text{rm}\{i\} \text{rm}\{o\} \text{rm}\{n\} \text{rm}\{r\} \text{rm}\{e\} \text{rm}\{a\} \text{rm}\{d\} \text{rm}\{s\} } $$
```

Intron retention was assessed using IRFinder<sup>36</sup> with gene models from GENCODE v31.

## Analysis of published iCLIP data

Cross-linked read files from TDP-43 iCLIP experiments in SH-SY5Y and human neuronal stem cells<sup>22</sup> were processed using iCount v2.0.1.dev implemented in Snakemake version 5.5.4, available at [https://github.com/frattalab/pipeline\\_iclip](https://github.com/frattalab/pipeline_iclip). Sites of cross-linked reads from all replicates were merged into a single file using iCount group command. Significant positions of cross-link read density with respect to the same gene (GENCODE v34 annotations) were then identified using the iCount peaks command with default parameters.

## Western blot

SH-SY5Y cells were lysed directly in the sample loading buffer (Thermo NP0008). Lysates were heated at 95 °C for 5 min with 100 mM DTT. If required lysates were

passed through a QIAshredder (Qiagen) to shear DNA. Lysates were resolved on 4–12% Bis-Tris Gels (Thermo) or homemade 6% Bis-Tris gels and transferred to 0.45 µm PVDF (Millipore) membranes. After blocking with 5% milk, blots were probed with antibodies (Rb anti-UNC13A (Synaptic Systems 126 103) 1:2,000; Rb anti-UNC13B (abcam ab97924) 1:1,000; Rat anti-Tubulin (abcam ab6161 clone YOL1/34) 1:5,000, Mouse anti-TDP-43 (abcam ab104223 clone 3H8) 1:5,000) for 2 h at room temperature. After washing, blots were probed with HRP conjugated secondary antibodies (Goat anti-Rabbit HRP (Bio-Rad 1706515) 1:10,000; Goat anti-Mouse HRP (Bio-Rad 1706516) 1:10,000; Rabbit anti-Rat HRP (Dako P0450) 1:10,000) and developed with Chemiluminescent substrate (Merck Millipore WBKLS0500) on a ChemiDoc Imaging System (Bio-Rad). Band intensity was measured with ImageJ (NIH version 2.0.0-rc-69).

## RT-qPCR

RNA was extracted from SH-SY5Y and SK-N-DZ cells with a RNeasy kit (Qiagen) or from i<sup>3</sup>Neurons on day 7 after the initiation of differentiation using a Direct-zol RNA miniprep kit (Zymo Research R2052) following the manufacturer's protocol including the on-column DNA digestion step. RNA concentrations were measured by Nanodrop and 500–1,000 ng of RNA was used for reverse transcription. First strand cDNA synthesis was performed with SSIV (Thermo 18090050), RevertAid (Thermo K1622) or High-Capacity cDNA Reverse Transcription Kit (Thermo 4368814) using random hexamer primers and following the manufacturer's protocol including all optional steps. Gene expression analysis was performed by qPCR using Taqman Multiplex Universal Master Mix (Thermo 4461882) or Taqman Universal PCR Master Mix (Thermo 4304437) and TaqMan assays (UNC13A-Fam Hs00392638\_m1, UNC13B-Fam Hs01066405\_m1, TDP-43-Vic Hs00606522\_m1, GAPDH-Jun assay 4485713, TDP-43-FAM Hs00606522\_m1, UPF1-FAM Hs00161289\_m1, HPRT1-FAM Hs02800695\_m1) on a QuantStudio 5 or a QuantStudio 6 Flex Real-Time PCR system (Applied Biosystems) and quantified using the  $\Delta\Delta C_t$  method<sup>45</sup>.

## RT-PCR

RNA extraction and cDNA synthesis was performed as described under 'RT-qPCR'. *UNC13A* CE was amplified with a forward primer in exon 20 (5'-CAAGCGAACTGACAAATCTGCCGTGTCG-3') and reverse primer in exon 21 (5'-GGCATCGTCACCCTGGCATCTGG-3'). *UNC13A* intron retention was amplified with a forward primer in exon 30 (5'-ATGCCCTATTCTCCTGCTCC-3') and a reverse primer that spans the exon 32–33 junction (5'-CATCCAGCTCCTTCCTCCC-3'). *UNC13B* FSE was amplified with forward primer (5'-TCCGAGCAGTTACCAAGGTT-3') and reverse primer (5'-GCTGTCAATGCCATAGAGCC-3'). *UNC13B* intron retention was amplified with a

forward primer that spans the exon 19–20 junction (5'-CAGGCCATGACGCCTTG-3') and a reverse primer in exon 22 (5'-GATTTAAGTCCTGAAGCCGTT-3'). For Sanger sequencing, *UNC13A* CE was amplified with exon 19 forward primer (5'-GACATCAAATCCCCGTGAA-3') and exon 22 reverse primer (5'-CATTGATGTTGGCGAGCAGG-3'). Amplicons were resolved by agarose gel and the bands corresponding to the short and long form of the cryptic exon were excised and purified (NEB T1030L). The *UNC13A* exon 22 reverse primer (5'-ATACTGGAGGAGAGGCAGG-3') was used for sequencing reactions. PCR products were resolved on a TapeStation 4200 (Agilent) and bands were quantified with TapeStation Systems Software v3.2 (Agilent).

### Nonsense-mediated decay inhibition

For the SH-SY5Y experiment, 10 days after the induction of shRNA against TDP-43 with 1 µg ml<sup>-1</sup> doxycyline hydralate (Sigma D9891-1G), cells were treated either with 100 µM CHX or DMSO<sup>46</sup> for 6 h before collecting the RNA with a RNeasy Minikit (Qiagen). Reverse transcription was performed using RevertAid cDNA synthesis kit (Thermo), and transcript levels were quantified by qPCR (QuantStudio 5 Real-Time PCR system, Applied Biosystems) using the ΔΔC<sub>t</sub> method<sup>45</sup>. Using Reffinder (<https://www.heartcure.com.au/reffinder/>), we identified *GAPDH* as the most stable endogenous control across our conditions of interest; the forward *GAPDH* primer used was 5'-CACCAAGGGCTGCTTTAACT-3', and the reverse primer was 5'-GACAAGCTTCCCCTCTCAG-3'. Since it has been shown to undergo NMD<sup>47</sup>, *HNRNPL* NMD transcript was used as a positive control. The *UNC13B* experiment was subsequently performed, following the same method.

For the TDP-43-UPF1 double siRNA knockdown, SH-SY5Y cells were transfected with 40 pM TDP-43 siRNA and either 40 pM control or 40 pM UPF1 siRNAs, and collected after 96 h. Similarly to our experiment with CHX, we used a qPCR approach with *GAPDH* as endogenous control and *HNRNPL* as positive control. To assess TDP-43 and UPF1 levels, we used the following primers: TDP-43 forward, 5'-GATGGTGTGACTGCAAACCTTC-3'; TDP-43 reverse, 5'-CAGCTCATCCTCAGTCATGTC-3'; *UPF1* forward, 5'-TCGAGGAAGATGAAGAACACAC-3', and *UPF1* reverse, 5'-TCCGTTGCAGAACCACTTC-3'.

For both experiments in SH-SY5Y cells, *UNC13A* CE was amplified with a forward primer in exon 20 (5'-CAAGCGAACTGACAAATCTGCCGTGTCG-3') and reverse primer within the CE (5'-CCTGGAAAGAACTCTTATCCCCAGGAACTAGTTGTTG-3'); *UNC13B* FSE was amplified with a forward primer in exon 10 (5'-TCCGAGCAGTTACCAAGGTT-3') and reverse primer within the FSE (5'-GAAAAGCGAGGAGCCCTTCAG-3');

*STMN2* CE was amplified with a forward primer in exon 1 (5'-GCTCTCTCCGCTGCTGTAG-3') and reverse primer within the cryptic exon (5'-CTGTCTCTCTCTCGCACA-3'); *HNRNPL* NMD transcript was amplified with a forward primer in the NMD-inducing exon (5'-GGTCGCAGTGTATGTTGATG-3') and reverse primer in exon 7 (5'-GGCGTTGTTGGGGTTGCT-3').

For i<sup>3</sup>Neuron experiments, iPS cells were infected sequentially, first with either control or a TDP-43 targeting sgRNA in the human pU6-sgRNA EF1A-Bsd-T2A-eGFP backbone, and then second with either a control or UPF1-targeting sgRNA in the bovine pU6-sgRNA EF1A-puro-T2A-BFP backbone for a total of 4 groups: control/control, control/UPF1, TDP43/control, TDP43/UPF1. Two days following each infection, iPS cells were selected with either blasticidin (first infection) or puromycin and blasticidin (second infection) (see 'CRISPRi knockdown in human iPS cells' for further details). iPS cells were then differentiated and neurons were collected in tri-reagent on day 7 after differentiation. Then RNA was isolated and cDNA was made (see 'RT-qPCR'). Then samples were analysed for differential gene expression and splicing by qPCR or PCR followed by Agilent bioanalyzer measurements to assess differences in band sizes resulting from cryptic exon splicing. PCR products were diluted 1:10 in nuclease-free water and resolved on a Bioanalyzer 2100 (Agilent). Bands were quantified with Agilent 2100 Software (Version B.02.08.SI648) using High sensitivity DNA Assay (Version 1.03). UNC13A primers are listed under RT-PCR.

## Quantification of TDP-43, UNC13A and UNC13B using quantitative proteomics

i<sup>3</sup>Neurons were collected from 6-well plates on day 17 after the initiation of differentiation. One or two wells were pooled for each biological replicate,  $n=6$  for each control and TDP-43-knockdown neurons. To collect cells, wells were washed with PBS, and then SP3 protein extraction was performed to extract intracellular proteins. In brief, we collected and lysed using a very stringent buffer (50 mM HEPES, 50 mM NaCl, 5 mM EDTA 1% SDS, 1% Triton X-100, 1% NP-40, 1% Tween 20, 1% deoxycholate and 1% glycerol) supplemental with cOmplete protease inhibitor cocktail at 1 tablet/10 ml ratio. The cell lysate was reduced by 10 mM dithiothreitol (30 min, 60 °C) and alkylated using 20 mM iodoacetamide (30 min, dark, room temperature). The denatured proteins were captured by hydrophilic magnetic beads, and tryptic on-beads digestion was conducted for 16 h at 37 °C. We injected 1 µg resulting peptides to a nano liquid chromatography for separation, and subsequently those tryptic peptides were analyzed on an Orbitrap Eclipse mass spectrometer coupled with a FAIMS interface using data-dependent acquisition (DDA) and data-independent acquisition (DIA) controlled by Xcalibur v4.3. The peptides were separated on a 120 min LC gradient with 2-35% solvent B (0.1% FA, 5% DMSO

in acetonitrile), and FAIMS's compensation voltages were set to -50, -65 and -80. For DDA, we used MS1 resolution at 12,000 and cycle time was selected for 3 s, MS2 fragments were acquired by linear ion trap. For DIA, we used 8 *m/z* isolation windows (400–1,000 *m/z* range), cycle time was set to 3 s, and MS2 resolution was set to 30,000. The DDA and DIA MS raw files were searched against Uniprot-Human-Proteome\_UP000005640 database with 1% FDR using Proteome Discoverer (v2.4) and Spectronaut (v14.1), respectively. The raw intensity of quantified peptides was normalized by total peptides intensity identified in the same sample. The DDA quantified TDP-43- and UNC13A-derived unique and sharing peptides were parsed out and used for protein quantification. Specifically, we visualized and quantified the unique peptides of UNC13A using their MS/MS fragment ion intensity acquired by DIA.

## Nanopore sequencing and analysis

RNA from four FTLD-TDP patient samples and four SHSY-5Y samples (two with doxycycline-induced TDP-43 knockdown and two untreated controls) was reverse transcribed using Superscript IV (Thermo Fisher Scientific) using a specific reverse transcription primer following the manufacturer recommendations, but with the volumes halved. Following heat inactivation of the reverse transcriptase, the samples were treated with RNase H (NEB) for 20 min at 37 °C, then diluted fourfold with Phusion HF mastermix (Thermo Fisher Scientific). Two rounds of nested PCR were performed to generate pure amplicons spanning the exon upstream of the CE and the exon downstream of the TDP-43 regulated intron retention, with thermolabile exoI treatment in between (NEB). To ensure complete amplification of amplicons, a 10 min extension time was used (approximately 10× longer than recommended by the manufacturer's protocol). Nanopore-compatible overhangs were then added by PCR and the products were validated by agarose electrophoresis, followed by barcode addition using primers 5–12 from the Nanopore PCR barcoding kit (SQK-PBK004). Following ligase-free rapid adaptor addition (SQK-PBK004) the products were loaded onto and sequenced with a MinION. Demultiplexing and basecalling was performed in real time using the GUPPY basecaller.

Raw fastqs were aligned to a section of chromosome 19 containing the entire UNC13A gene (17690344-17599328; GRCh38.p13) using Minimap2<sup>48</sup> with settings “-ax splice”. Downstream analysis was performed using a custom R script ([https://github.com/frattalab/unc13a\\_cryptic\\_splicing](https://github.com/frattalab/unc13a_cryptic_splicing)) that quantified alignment to the regions of interest (the CE, the intron retention and their flanking exons), filtering for reads that were long enough to contain both the CE and intron retention so as not to bias the analysis against reads containing both events. Correct assignment was verified manually by visualizing differently classified reads.

Reverse transcription primer, CACATTGCCTGTGCCCTAAC; nested PCR 1 forward, GACGTGTGGTACAACCTGGA; nested PCR 1 reverse,

CACTCTTCAATGTGCGGCTG; nested PCR 2 forward,  
CTGACAAATCTGCCGTGTCG; nested PCR 2 reverse,  
GAAGCTGGTAGCAAACACCC; add overhang forward,  
TTTCTGTTGGTGCTGATATTGC CTGACAAATCTGCCGTGTCG; add  
overhang reverse, ACTTGCCTGTCGCTATCTTC  
GAAGCTGGTAGCAAACACCC.

## Ribosome profiling

For ribosome-profiling experiments, i<sup>3</sup>Neurons were grown on 15 cm plates, one plate per biological replicate for control ( $n = 4$ ) and TDP-43-knockdown ( $n = 4$ ) neurons. On day 17, i<sup>3</sup>Neuron culture medium was replaced 90 min before collecting the neurons to boost translation. Then the medium was removed, cells were washed with cold PBS, PBS was removed and 900  $\mu$ l of cold lysis buffer (20 mM Tris pH 7.4, 150 mM NaCl, 5 mM MgCl<sub>2</sub>, 1 mM DTT (freshly made), 100  $\mu$ g ml<sup>-1</sup> CHX, 1% TX100; 25 U ml<sup>-1</sup> Turbo DNase I) was added to each 15 cm plate. Lysed cells were scraped and pipetted into microcentrifuge tubes on ice. Cells were then passed through a 26-gauge needle 10 times, and then centrifuged twice at 19,000g at 4 °C, for 10 min, each time moving the supernatant to a fresh tube. Tubes containing supernatant were flash frozen in liquid nitrogen and stored at -80 °C until processing.

Ribosome footprints from three biological replicates of both TDP-43-knockdown control samples were generated and purified as described, using a sucrose cushion<sup>49</sup> and a customized library preparation method based on revised iCLIP<sup>50</sup>. No ribosomal RNA depletion step was performed, and libraries were sequenced on an Illumina Hi-Seq 4000 machine (SR100). Reads were demultiplexed and adaptor/quality trimmed using Ultraplex<sup>51</sup>, then aligned with Bowtie2<sup>52</sup> against a reference file containing abundant ncRNAs that are common contaminants of ribosome profiling, including rRNAs. Reads that did not pre-map were then aligned against the human genome with STAR<sup>38</sup> and the resulting BAM files were deduplicated with UMI-tools<sup>53</sup>. Multi-mapping reads were discarded and reads 28–30 nt in length were selected for analysis. FeatureCounts<sup>44</sup> was used to count footprints aligning to annotated coding sequences, and DESeq2<sup>41</sup> was used

for differential expression analysis, using default parameters in both cases. Periodicity analysis was performed using a custom R script, using transcriptome-aligned bam files. Raw data have been uploaded to E-MTAB-10235.

## ALS and FTD panel genes

To find ALS and FTD ‘green’ panel genes—those with diagnostic level of evidence that have been approached for testing by NHS in England—‘Amyotrophic lateral sclerosis/motor neuron disease (Version 1.33)’ and ‘Early onset dementia (encompassing fronto-temporal dementia and prion disease) (Version 1.48)’ were downloaded from PanelApp<sup>16</sup>.

## Genome-wide association study data

Harmonized summary statistics for the latest ALS GWAS<sup>15</sup> were downloaded from the NHGRI-EBI GWAS catalogue<sup>54</sup> (accession GCST005647). Locus plots were created using LocusZoom<sup>55</sup>, using linkage disequilibrium values from the 1000 Genomes European superpopulation<sup>56</sup>.

## NYGC ALS Consortium RNA-seq cohort

Our analysis contains 377 patients with 1,349 neurological tissue samples from the NYGC ALS dataset, including non-neurological disease controls, FTLD, ALS, FTD with ALS (ALS-FTLD), or ALS with suspected Alzheimer’s disease (ALS-AD). Patients with FTD were classified according to a pathologist’s diagnosis of FTD with TDP-43 inclusions (FTLD-TDP), or those with FUS or Tau aggregates. ALS samples were divided into the following subcategories using the available Consortium metadata: ALS with or without reported SOD1 or FUS mutations. All non-SOD1 or FUS ALS samples were grouped as ALS-TDP in this work for simplicity, although reporting of postmortem TDP-43 inclusions was not systematic and therefore not integrated into the metadata. Confirmed TDP-43 pathology postmortem was reported for all FTLD-TDP samples.

Sample processing, library preparation, and RNA-seq quality control have been extensively described in previous papers<sup>[10,57](#)</sup>. In brief, RNA was extracted from flash-frozen postmortem tissue using TRIzol (Thermo Fisher Scientific) chloroform, and RNA-Seq libraries were prepared from 500 ng total RNA using the KAPA Stranded RNA-Seq Kit with RiboErase (KAPA Biosystems) for ribosomal RNA depletion. Pooled libraries (average insert size: 375 bp) passing the quality criteria were sequenced either on an Illumina HiSeq 2500 (125 bp paired end) or an Illumina NovaSeq (100 bp paired end). The samples had a median sequencing depth of 42 million read pairs, with a range between 16 and 167 million read pairs.

Samples were uniformly processed, including adapter trimming with Trimmomatic and alignment to the hg38 genome build using STAR (2.7.2a)<sup>[38](#)</sup> with indexes from GENCODE v30. Extensive quality control was performed using SAMtools<sup>[58](#)</sup> and Picard Tools<sup>[59](#)</sup> to confirm sex and tissue of origin.

Uniquely mapped reads within the *UNC13A* locus were extracted from each sample using SAMtools. Any read marked as a PCR duplicate by Picard Tools was discarded. Splice junction reads were then extracted with RegTools<sup>[60](#)</sup> using a minimum of 8 bp as an anchor on each side of the junction and a maximum intron size of 500 kb. Junctions from each sample were then clustered together using LeafCutter<sup>[61](#)</sup> with relaxed junction filtering (minimum total reads per junction = 30, minimum fraction of total cluster reads = 0.0001). This produced a matrix of junction counts across all samples.

The CE was considered detected in a sample if there was at least one uniquely mapped spliced read supporting either the short CE acceptor or the CE donor. As the long CE acceptor was detected consistently in control cerebellum samples, as part of an unannotated cerebellum-enriched 35 bp exon containing a stop codon between exons 20 and 21(Extended Data Fig. [10 a, b](#)), we excluded the long CE acceptor for quantification of *UNC13A* CE  $\Psi$  in patient tissue. Only samples with at least 30 spliced reads at the exon locus were included for correlations. In Fig. [4a](#), only cortical samples that were concordant for genotypes at *rs12973192* and *rs12608932*, had both *STMN2* and *UNC13A* CE detected, and had at least 30 spliced reads at

the exon locus were included in the analysis. Cell-type deconvolution was performed using the top 100 most specific marker genes from neurons, astrocytes, oligodendrocytes, endothelial cells and microglia derived by single-cell RNA sequencing<sup>62</sup> with the dtangle<sup>63</sup>. The NYGC ALS Consortium samples presented in this work were acquired through various IRB protocols from member sites and the Target ALS postmortem tissue core and transferred to the NYGC in accordance with all applicable foreign, domestic, federal, state, and local laws and regulations for processing, sequencing, and analyses. The Biomedical Research Alliance of New York (BRANY) IRB serves as the central ethics oversight body for NYGC ALS Consortium. Ethical approval was given and is effective until 22 August 2022. Informed consent has been obtained from all participants.

## Ethics

Brains were donated to the Queen Square Brain Bank (QSBB) for Neurological Disorders (QSBB) and the NeuroResource tissue bank (UCL Queen Square Institute of Neurology). All tissue samples were donated with the full informed consent. Accompanying clinical and demographic data of all cases used in this study were stored electronically in compliance with the 2018 Data Protection Act and are summarized in Supplementary Table 5. Ethical approval for the study was obtained from the NHS research ethics committee (RNEC) and in accordance with the Human Tissue Authority's codes of practice and standards under license number 12198. We have conformed with all relevant ethical regulations related to informed consent and anonymization of patient data analysed in the manuscript.

## Gene transcript model harmonization

To ensure consistency between RNA-seq, re-analysis of published iCLIP data, and the NYGC ALS Consortium RNA-seq cohort, we confirmed that both the ENSEMBL gene minor version and transcripts for *UNC13A* and *UNC13B* are identical between the three GENCODE annotations used across our team.

## BaseScope assay

To validate a BaseScope assay for *UNC13A* cryptic exons, we first performed the assay in i<sup>3</sup>Neurons with CRISPRi depletion of control or a non-targeting guide. Neurons were plated on 8-well IBIDI slides, 0.2 million per well and then fixed with 4% paraformaldehyde for 10 min on day 7 after the initiation of differentiation. Neurons were then dehydrated and stored for ~1 week at -20C. Neurons were then rehydrated and pretreated following the recommendations of the RNAscope® Assay for Adherent Cells, using 30% hydrogen peroxide for 8 min and a 1:15 dilution of the RNAscope Protease III. Then the BaseScope v2-RED assay was performed using our *UNC13A* CE target probe (BA-Hs-*UNC13A*-O1-1zz-st) according to manufacturer guidelines (Advanced Cell Diagnostics). Following fast red solution, wells were washed 2× with PBS, and incubated overnight at 4 °C in 0.5% Triton-X and 3% BSA containing primary antibodies: rabbit TDP43 (proteintech 12892-1-AP, 1:1,000 dilution) and mouse TUBB3 (Biolegend 801201, 1:5,000 dilution). The next morning, wells were washed three times with PBS and treated with secondary antibodies Alexa Fluor 488 anti-rabbit (Jackson Immuno 711-545-152) and Alexa Fluor 647 anti-mouse (Jackson Immuno 715-605-151), and Hoechst 33342 (Thermo Scientific) at 1:10,000 dilution for 1 h at room temperature. Wells were then washed 3× with PBS and imaged on an inverted spinning disk confocal microscope (Nikon Eclipse T1), using a 60× 1.40 NA oil-immersion objective. Confocal images were then processed in FIJI.

Frozen tissue from the frontal cortex of FTLD-TDP ( $n = 9$ ), FTLD-TAU ( $n = 4$ ) and control ( $n = 5$ ) cases were sectioned at 10 µm thickness onto Plus+Frost microslides (Solmedia). Immediately prior to use, sections were dried at room temperature and fixed for 15 min in pre-chilled 4% paraformaldehyde. Sections were then dehydrated in increasing grades of ethanol and pre-treated with RNAscope hydrogen peroxide (10 min, room temperature) and protease IV (30 min, room temperature). The BaseScope v2-RED assay was performed using our *UNC13A* CE target probe (BA-Hs-*UNC13A*-O1-1zz-st) according to manufacturer guidelines with no modifications (Advanced Cell Diagnostics,). Sections were nuclei counterstained in Mayer's haematoxylin (BDH) and mounted (VectaMount). Slides were also incubated with a positive control probe (Hs-PPIB-1 ZZ) targeting a common housekeeping gene and a negative control probe (DapB-1 ZZ) which targets a bacterial gene to assess background

signal (<1–2 foci per approximately 100 nuclei). Representative images were taken at  $\times 60$  magnification.

Hybridized sections were imaged and analysed blinded to disease status. Slides were scanned using an Olympus VS120 slide scanner at  $\times 20$  magnification and equal sized ( $34.5\text{ mm}^2$ ) regions of interest were extracted from the centre of each section. The total number of red foci, which should identify single transcripts harbouring the *UNC13A* CE event, were manually counted in ImageJ (v1.52p). Foci frequency was background-corrected by subtracting the signal obtained with the negative control probe in the same experiment.

## **UNC13A genotypes in the NYGC ALS Consortium**

Whole-genome sequencing was carried out for all donors, from DNA extracted from blood or brain tissue. Full details of sample preparation and quality control will be published in a future manuscript. In brief, paired-end 150-bp reads were aligned to the GRCh38 human reference using the Burrows-Wheeler Aligner (BWA-MEM v0.7.15)<sup>64</sup> and processed using the GATK best-practices workflow. This includes marking of duplicate reads by the use of Picard tools<sup>59</sup> (v2.4.1), followed by local realignment around indels, and base quality score recalibration using the Genome Analysis Toolkit<sup>65,66</sup> (v3.5). Genotypes for *rs12608932* and *rs12973192* were then extracted for the samples.

## **Targeted RNA-seq**

RNA was isolated from temporal cortex tissue of 10 FTLD-TDP and 4 control brains (6 male, 4 female, average age at death  $70.6 \pm 5.8$  yr, average disease duration  $10.98 \pm 5.9$  yr) full metadata provide in [Supplementary Table 5](#). Fifty milligrams of flash-frozen tissue was homogenized in  $700\text{ }\mu\text{l}$  of Qiazol (Qiagen) using a TissueRuptor II (Qiagen). Chloroform was added and RNA subsequently extracted following the spin-column protocol from the miRNeasy kit with DNase digestion (Qiagen). RNA was eluted off the column in  $50\text{ }\mu\text{l}$  of RNase-free water. RNA quantity and quality were evaluated using a spectrophotometer.

Purified RNA was reverse transcribed with Superscript IV (Thermo Fisher Scientific) using either sequence-specific primers containing sample-specific barcodes or random hexamers, following the manufacturer recommendations. Unique molecular identifiers (UMIs) and part of the P5 Illumina sequence were added either during first- or second-strand-synthesis (with Phusion HF 2× Master Mix) respectively. Barcoded primers were removed with exonuclease I treatment (NEB; 30 min) and subsequently bead-size selection of RT-PCR products (TotalPureNGS, Omega Biotek). Three rounds of nested PCR using Phusion HF 2× Master Mix (New England Biolabs) were used to obtain highly specific amplicons for the *UNC13A* cryptic, followed by gel extraction and a final round of PCR in which the full length P3/P5 Illumina sequences were added. Samples were sequenced with an Illumina HiSeq 4000 machine (SR100).

Raw reads were demultiplexed, adaptor/quality trimmed and UMIs were extracted with Ultraplex<sup>51</sup>, then aligned to the hg38 genome with STAR<sup>38</sup>. To control for mapping biases, a VCF containing rs12973192 was used and alignments that failed to pass WASP filtering were ignored. Reads were deduplicated via analysis of UMIs with a custom R script; to avoid erroneous detection of UMIs due to sequencing errors, UMI sequences with significant similarity to greatly more abundant UMIs were discarded—this methodology was tested using simulated data, and final results were manually verified. Raw reads for targeted RNA-seq are available at E-MTAB-10237.

Primers used are listed in [Supplementary Table 7](#).

## Splicing reporters

One variant of the *UNC13A* exon 20, intron 20 and exon 21 sequence was synthesized and cloned into a pIRES-EGFP vector (Clontech) by BioCat. The repeat expansion, containing four extra copies of the CATC repeats (ten instead of the six found in the reference genome), was added via Gibson assembly of a PCR-linearized plasmid and a dsDNA insert generated by annealing two synthesized ssDNA oligos (oligos used: unc13mg\_bb\_FWD: AATGGGTGGGTGGATGAATGGAAGGATG, unc13mg\_bb\_REV: TCTACCCATCTGACTATCAACAAATTCCACC,

Unc13\_Repeat\_add\_AntiSense:

CCCACCCCATTCCATCCATTGTCCATCTGCCTATAACATCCATCCATCC  
ATCCATCCATCCATCCATCCATCCATCTACCTATCTACCCATC,

Unc13\_Repeat\_add\_Sense:

GATGGGTAGATAGGTAGATGGATGGATGGATGGATGGATGGATGG

ATGGATGGATGTATAAGCAGATGGACAAATGGATGAATGGGTGGG

). Plasmids with all four possible combinations of the SNPs were then

generated by PCR-based site directed mutagenesis (primers used:

healthy\_exon\_SNP\_REV: CTTTTATCTACTCATCACTCATTTC,

healthy\_exon\_SNP\_FWD: GATGGATGGAGAGATGGG,

healthy\_intron\_SNP\_REV: CCATCCATTTCGTCTGTC,

healthy\_intron\_SNP\_FWD: TTGGATAAATTGATGGGTGGATG.

risk\_exon\_SNP\_FWD: CATGGATGGAGAGATGGG,

risk\_exon\_SNP\_REV: CTTTTATCTACTCATCACTCATTTC). Plasmids

were propagated in Stbl3 bacteria (Thermo Fisher Scientific) grown at 30

°C due to the observed instability of the plasmids in DH5alpha cells grown

at 37 °C. Similarly, the two UG/UC mutants were generated by PCR-based site directed mutagenesis of the ‘healthy’ plasmid (primers used:

UG\_UC\_1\_F: CGATGGAGAGATGGGTGAG, UG\_UC\_1\_R:

ATCCTTTATCTACTCATCAC, UG\_UC\_2\_F:

CGAGAGATGGGTGAGTAC, UG\_UC\_2\_R:

ATCCATCCTTTATCTACTC). All plasmids were verified by Sanger sequencing.

To reduce the impact of sample-to-sample variation on our analysis, we generated (via PCR site-directed mutagenesis) a modified healthy minigene with an alternative primer binding site downstream of the *UNC13A* sequence, before the polyA site, which had no detectable impact on CE splicing. This enabled co-transfection of 1. a minigene featuring a specific combination of variants and 2. the modified control (healthy) minigene into the same population of cells; the cryptic splicing level of each could then be determined by specific RT–PCR amplification of each minigene from the same cDNA, thus ensuring that the observed differences between variants did not simply reflect differences between cells grown in different dishes.

TDP-43 inducible knockdown SH-SY5Y cells were electroporated with 1.5 µg each of the variant and healthy minigene DNA with the Ingenio

electroporation kit (Mirus) using the A-023 setting on an Amaxa II nucleofector (Lonza). The cells were then left untreated or treated for 6 days with 1 µg ml<sup>-1</sup> doxycycline before RNA extraction. Reverse transcription was performed with RevertAid (Thermo Scientific) and cDNA was amplified by nested PCR with minigene-specific primers (5'-TCCTCACTCTGACGAGG-3' and 5'-CATGGCGGTCGACCTAG-3' or 5'-TGGTCGCCATACTGTCATG-3' (for the healthy cotransfection control)) followed by *UNC13A*-specific primers 5'-CAAGCGAACTGACAAATCTGCCGTGTCG-3' and 5'-CGACACGGCAGATTGTCAGTCGCTTG-3'. PCR products were resolved on a TapeStation 4200 (Agilent) and bands were quantified with TapeStation Systems Software v3.2 (Agilent).

## Heptamer analysis

Binding enrichment *E*-scores were downloaded from Ray et al. (2013)<sup>27</sup>. Seven-nucleotide sequences that overlapped with either the exonic or intronic SNPs were extracted using a sliding-window approach. Using a custom R script ([https://github.com/frattalab/unc13a\\_cryptic\\_splicing/](https://github.com/frattalab/unc13a_cryptic_splicing/)), the average *E*-scores for each RBP were calculated for each set of 7-mers, and the RBPs were ranked by effect size of the SNPs on average *E*-score.

## TDP-43 protein purification

His-tagged human TDP-43 (amino acids 102 to 269) was expressed in BL21-DE3 Gold *Escherichia coli* (Agilent) as previously described<sup>67</sup>. Bacteria were lysed by 2 h of gentle shaking in lysis buffer (50 mM sodium phosphate pH 8, 300 mM NaCl, 30 mM imidazole, 1 M urea, 1% v/v Triton X-100, 5 mM β-mercaptoethanol, with Roche EDTA-free cOmplete protease inhibitor) at room temperature. Samples were centrifuged at 16,000 rpm in a Beckman 25.50 rotor at 4 °C for 10 min, and the supernatant was clarified by vacuum filtration (0.22 µm).

The clarified lysate was loaded onto a 5 ml His-Trap HP column (Cytiva) equilibrated with buffer A (50 mM sodium phosphate pH 8, 300 mM NaCl, 20 mM imidazole) using an AKTA Pure system, and eluted with a linear gradient of 0-100% buffer B (50 mM sodium phosphate pH 8, 300 mM

NaCl, 500 mM imidazole) over 90 column volumes. The relevant fractions were then analysed by SDS-PAGE and then either extensively dialysed (3.5 kDa cutoff) against isothermal titration calorimetry (ITC) buffer (50 mM sodium phosphate pH 7.4, 100 mM NaCl, 1 mM TCEP) at 4 °C, or flash frozen in liquid nitrogen.

## Isothermal titration calorimetry

RNAs with sequences 5'-AAGGAUGGAUGGAG-3' (CE SNP healthy), 5'-AAGCAUGGAUGGAG-3' (CE SNP risk), 5'-AAAAAAUGGAUGGUUGGAU-3' (intron SNP healthy) and 5'-AAAAAAUGGAUGGGUGGAU-3' (intron SNP risk) were synthesized by Merck, resuspended in Ultrapure water, then dialysed against the same stock of ITC buffer used for TDP-43 dialysis (above) overnight at 4 °C using 1 kDa Pur-a-lyzer tubes (Merck). Protein and RNA concentrations after dialysis were calculated by A280 and A260 absorbance respectively. ITC measurements were performed on a MicroCal PEAQ-ITC calorimeter (Malvern Panalytical). Titrations were performed at 25 °C with TDP-43 (9.6–12 µM) in the cell and RNA (96–120 µM) in the syringe. Data were analysed using the MicroCal PEAQ-ITC analysis software using nonlinear regression with the One set of sites model. For each experiment, the heat associated with ligand dilution was measured and subtracted from the raw data.

## iCLIP of SH-SH5Y and minigene-transfected HEK 293T cells

SH-SY5Y cells were grown to 80% confluence in two 10 cm dishes. HEK 293T cells were grown to 80% confluence and transfected with either the 2× healthy or 2× risk minigenes using Lipofectamine 3000 (Thermofisher Scientific). Each replicate consisted of 2× 3.5 cm dishes, with two replicates per sample, for eight dishes total. Plasmid (1.25 µg) was used for each dish, measured via Nanodrop (Thermo Fisher Scientific), combined with 2.5 µl of Lipofectamine 3000 and P3000 reagent diluted in 250 µl (2 × 125 µl) of Opti-MEM I following the manufacturer protocol (Thermo Fisher Scientific). Cells were UV crosslinked on ice and subjected to iCLIP analysis following the iiCLIP protocol<sup>50</sup>. In brief, medium RNase I was added to cell lysate for RNA fragmentation. Immunoprecipitations were

performed with 4 µg of TDP-43 antibody ((Proteintech, Rabbit anti-TDP-43 cat. no. 10782-2-AP) coupled with 100 µl of protein A or G dynabeads (for SH-SY5Y or HEK 293T, respectively) per sample. The complexes were then size-separated with SDS-PAGE and visualized by Odyssey scanning. cDNA was synthesized with Superscript IV Reverse Transcriptase (Life Technologies). cDNA was then circularized. After PCR amplification, libraries were removed from primers with Ampure beads and QCed for sequencing. Libraries were sequenced on an Illumina HiSeq4000 machine (SR100).

For SH-SH5Y iCLIP, downstream analysis was performed with the iMAPS server. For data from HEK 293T cells, after demultiplexing the reads with Ultraplex, we initially aligned to the human genome using STAR<sup>38</sup>, which showed that >5% of uniquely aligned reads mapped solely to the genomic region that is contained in the minigene. Given the high prior probability of reads mapping to the minigene, we therefore instead used Bowtie2 to align to the respective minigene sequences alone, thus minimizing mis-mapping biases that could be caused by the SNPs<sup>52</sup> with settings “--norc --no-unal --rdg 50,50 --rfg 50,50 --score-min L,-2,-0.2 --end-to-end -N 1”, then filtered for reads with no alignment gaps, and length >25 nt. Due to the exceptional read depth and high library complexity, we did not perform PCR deduplication to avoid UMI saturation at signal peaks. All downstream analysis was performed using custom R scripts; to avoid biases due to differing transfection efficiencies, crosslink densities were normalized by the total number of minigene crosslinks for each sample. Raw data are available at E-MTAB-10297.

## Reporting summary

Further information on research design is available in the [Nature Research Reporting Summary](#) linked to this paper.

## Data availability

A minimum dataset to reproduce analyses is freely available at[https://github.com/frattalab/unc13a\\_cryptic\\_splicing/tree/main/data](https://github.com/frattalab/unc13a_cryptic_splicing/tree/main/data).

RNA-seq data for i3Neurons, SH-SY5Y and SK-N-DZ<sup>a</sup> are available through the European Nucleotide Archive (ENA) under accession [PRJEB42763](#). NYGC ALS Consortium RNA-seq: RNA-seq data generated through the NYGC ALS Consortium in this study can be accessed via the NCBI GEO database ([GSE137810](#), [GSE124439](#), [GSE116622](#) and [GSE153960](#)). To request immediate access to new data generated by the NYGC ALS Consortium and for samples provided through the Target ALS Postmortem Core, complete a genetic data request form at CGND\_help@nygenome.org. NYGC ALS Consortium genotypes for the common SNPs in this study *rs129731921* and *rs12608932* are available at [https://github.com/frattalab/unc13a\\_cryptic\\_splicing/blob/main/data/nygc\\_junction\\_information.csv](https://github.com/frattalab/unc13a_cryptic_splicing/blob/main/data/nygc_junction_information.csv). [Source data](#) are provided with this paper.

## Code availability

Analysis code and data to reproduce figures are freely available at [https://github.com/frattalab/unc13a\\_cryptic\\_splicing/](https://github.com/frattalab/unc13a_cryptic_splicing/). The tool for demultiplexing iCLIP reads is freely available at <https://github.com/ulelab/ultraplex>. Snakemake pipelines to perform RNA-seq alignment, splicing and parsing splice junction files are freely available at [https://github.com/frattalab/rna\\_seq\\_snakemake/](https://github.com/frattalab/rna_seq_snakemake/), <https://github.com/frattalab/splicing/> and [https://github.com/frattalab/bedops\\_parse\\_star\\_junctions/](https://github.com/frattalab/bedops_parse_star_junctions/). The Snakemake pipeline for analysing publicly available iCLIP is available at [https://github.com/frattalab/pipeline\\_iclip](https://github.com/frattalab/pipeline_iclip).

## References

1. van Es, M. A. et al. Genome-wide association study identifies 19p13.3 (*UNC13A*) and 9p21.2 as susceptibility loci for sporadic amyotrophic lateral sclerosis. *Nat. Genet.* **41**, 1083–1087 (2009).
2. Pottier, C. et al. Genome-wide analyses as part of the international FTLD-TDP whole-genome sequencing consortium reveals novel disease risk factors and increases support for immune dysfunction in FTLD. *Acta Neuropathol.* **137**, 879–899 (2019).

3. Diekstra, F. P. et al. C9orf72 and *UNC13A* are shared risk loci for ALS and FTD: a genome-wide meta-analysis. *Ann. Neurol.* **76**, 120–133 (2014).
4. Tan, R. H., Ke, Y. D., Ittner, L. M. & Halliday, G. M. ALS/FTLD: experimental models and reality. *Acta Neuropathol.* **133**, 177–196 (2017).
5. Neumann, M. et al. Ubiquitinated TDP-43 in frontotemporal lobar degeneration and amyotrophic lateral sclerosis. *Science* **314**, 130–133 (2006).
6. Ji, A.-L., Zhang, X., Chen, W.-W. & Huang, W.-J. Genetics insight into the amyotrophic lateral sclerosis/frontotemporal dementia spectrum. *J. Med. Genet.* **54**, 145–154 (2017).
7. Ling, J. P., Pletnikova, O., Troncoso, J. C. & Wong, P. C. TDP-43 repression of nonconserved cryptic exons is compromised in ALS-FTD. *Science* **349**, 650–655 (2015).
8. Melamed, Z. et al. Premature polyadenylation-mediated loss of stathmin-2 is a hallmark of TDP-43-dependent neurodegeneration. *Nat. Neurosci.* **22**, 180–190 (2019).
9. Klim, J. R. et al. ALS-implicated protein TDP-43 sustains levels of STMN2, a mediator of motor neuron growth and repair. *Nat. Neurosci.* **22**, 167–179 (2019).
10. Prudencio, M. et al. Truncated stathmin-2 is a marker of TDP-43 pathology in frontotemporal dementia. *J. Clin. Invest.* **130**, 6080–6092 (2020).
11. Fernandopulle, M. S. et al. Transcription factor-mediated differentiation of human iPSCs into neurons. *Curr. Protoc. Cell Biol.* **79**, e51 (2018).
12. Tian, R. et al. CRISPR interference-based platform for multimodal genetic screens in human iPSC-derived Neurons. *Neuron* **104**, 239–

255.e12 (2019).

13. Wang, C. et al. Scalable production of iPSC-derived human neurons to identify Tau-lowering compounds by high-content screening. *Stem Cell Rep.* **9**, 1221–1233 (2017).
14. Humphrey, J., Emmett, W., Fratta, P., Isaacs, A. M. & Plagnol, V. Quantitative analysis of cryptic splicing associated with TDP-43 depletion. *BMC Med. Genomics* **10**, 38 (2017).
15. Nicolas, A. et al. Genome-wide analyses identify *KIF5A* as a novel ALS gene. *Neuron* **97**, 1268–1283.e6 (2018).
16. Martin, A. R. et al. PanelApp crowdsources expert knowledge to establish consensus diagnostic gene panels. *Nat. Genet.* **51**, 1560–1565 (2019).
17. Diekstra, F. P. et al. UNC13A is a modifier of survival in amyotrophic lateral sclerosis. *Neurobiol. Aging* **33**, 630.e3-8 (2012).
18. Placek, K. et al. *UNC13A* polymorphism contributes to frontotemporal disease in sporadic amyotrophic lateral sclerosis. *Neurobiol. Aging* **73**, 190–199 (2019).
19. Yang, B. et al. *UNC13A* variant rs12608932 is associated with increased risk of amyotrophic lateral sclerosis and reduced patient survival: a meta-analysis. *Neurol. Sci.* **40**, 2293–2302 (2019).
20. Karczewski, K. J. et al. The mutational constraint spectrum quantified from variation in 141,456 humans. *Nature* **581**, 434–443 (2020).
21. Appucher, C. et al. Major hnRNP proteins act as general TDP-43 functional modifiers both in *Drosophila* and human neuronal cells. *Nucleic Acids Res.* **45**, 8026–8045 (2017).
22. Tollervey, J. R. et al. Characterising the RNA targets and position-dependent splicing regulation by TDP-43; implications for neurodegenerative diseases. *Nat. Neurosci.* **14**, 452–458 (2011).

23. Liu, E. Y. et al. Loss of nuclear TDP-43 is associated with decondensation of LINE retrotransposons. *Cell Rep.* **27**, 1409–1421.e6 (2019).
24. Zetoune, A. B. et al. Comparison of nonsense-mediated mRNA decay efficiency in various murine tissues. *BMC Genet.* **9**, 83 (2008).
25. Couratier, P., Corcia, P., Lautrette, G., Nicol, M. & Marin, B. ALS and frontotemporal dementia belong to a common disease spectrum. *Rev. Neurol.* **173**, 273–279 (2017).
26. Ma, X. R. et al. TDP-43 represses cryptic exon inclusion in the FTD–ALS gene *UNC13A*. *Nature* <https://doi.org/10.1038/s41586-022-04424-7> (2022).
27. Ray, D. et al. A compendium of RNA-binding motifs for decoding gene regulation. *Nature* **499**, 172–177 (2013).
28. Corder, E. H. et al. Gene dose of apolipoprotein E type 4 allele and the risk of Alzheimer’s disease in late onset families. *Science* **261**, 921–923 (1993).
29. Dittman, J. S. Unc13: a multifunctional synaptic marvel. *Curr. Opin. Neurobiol.* **57**, 17–25 (2019).
30. Augustin, I., Rosenmund, C., Südhof, T. C. & Brose, N. Munc13-1 is essential for fusion competence of glutamatergic synaptic vesicles. *Nature* **400**, 457–461 (1999).
31. Varoqueaux, F. et al. Total arrest of spontaneous and evoked synaptic transmission but normal synaptogenesis in the absence of Munc13-mediated vesicle priming. *Proc. Natl Acad. Sci. USA* **99**, 9037–9042 (2002).
32. Varoqueaux, F., Sons, M. S., Plomp, J. J. & Brose, N. Aberrant morphology and residual transmitter release at the Munc13-deficient mouse neuromuscular synapse. *Mol. Cell. Biol.* **25**, 5973–5984 (2005).

33. Vaquero-Garcia, J. et al. A new view of transcriptome complexity and regulation through the lens of local splicing variations. *eLife* **5**, e11752 (2016).
34. Thorvaldsdóttir, H., Robinson, J. T. & Mesirov, J. P. Integrative Genomics Viewer (IGV): high-performance genomics data visualization and exploration. *Brief. Bioinform.* **14**, 178–192 (2013).
35. Rodriguez, J. M. et al. APPRIS 2017: principal isoforms for multiple gene sets. *Nucleic Acids Res.* **46**, D213–D217 (2018).
36. Middleton, R. et al. IRFinder: assessing the impact of intron retention on mammalian gene expression. *Genome Biol.* **18**, 51 (2017).
37. Gilbert, L. A. et al. Genome-scale CRISPR-mediated control of gene repression and activation. *Cell* **159**, 647–661 (2014).
38. Dobin, A. et al. STAR: ultrafast universal RNA-seq aligner. *Bioinformatics* **29**, 15–21 (2013).
39. Frankish, A. et al. GENCODE reference annotation for the human and mouse genomes. *Nucleic Acids Res.* **47**, D766–D773 (2019).
40. Liao, Y., Smyth, G. K. & Shi, W. featureCounts: an efficient general purpose program for assigning sequence reads to genomic features. *Bioinformatics* **30**, 923–930 (2014).
41. Love, M. I., Huber, W. & Anders, S. Moderated estimation of fold change and dispersion for RNA-seq data with DESeq2. *Genome Biol.* **15**, 550 (2014).
42. Patro, R., Duggal, G., Love, M. I., Irizarry, R. A. & Kingsford, C. Salmon provides fast and bias-aware quantification of transcript expression. *Nat. Methods* **14**, 417–419 (2017).
43. Mölder, F. et al. Sustainable data analysis with Snakemake. *F1000Research* **10**, 33 (2021).

44. Quinlan, A. R. & Hall, I. M. BEDTools: a flexible suite of utilities for comparing genomic features. *Bioinformatics* **26**, 841–842 (2010).
45. Livak, K. J. & Schmittgen, T. D. Analysis of relative gene expression data using real-time quantitative PCR and the  $2^{-\Delta\Delta CT}$  method. *Methods* **25**, 402–408 (2001).
46. Pereverzev, A. P. et al. Method for quantitative analysis of nonsense-mediated mRNA decay at the single cell level. *Sci. Rep.* **5**, 7729 (2015).
47. Humphrey, J. et al. FUS ALS-causative mutations impair FUS autoregulation and splicing factor networks through intron retention. *Nucleic Acids Res.* **48**, 6889–6905 (2020).
48. Li, H. Minimap2: pairwise alignment for nucleotide sequences. *Bioinformatics* **34**, 3094–3100 (2018).
49. McGlincy, N. J. & Ingolia, N. T. Transcriptome-wide measurement of translation by ribosome profiling. *Methods* **126**, 112–129 (2017).
50. Lee, F. C. Y. et al. An improved iCLIP protocol. Preprint at <https://doi.org/10.1101/2021.08.27.457890> (2021).
51. Wilkins, O. G., Capitanchik, C., Luscombe, N. M. & Ule, J. Ultraplex: A rapid, flexible, all-in-one fastq demultiplexer. *Wellcome Open Res.* **6**, 141 (2021).
52. Langmead, B. & Salzberg, S. L. Fast gapped-read alignment with Bowtie 2. *Nat. Methods* **9**, 357–359 (2012).
53. Smith, T., Heger, A. & Sudbery, I. UMI-tools: modeling sequencing errors in Unique Molecular Identifiers to improve quantification accuracy. *Genome Res.* **27**, 491–499 2017).
54. Buniello, A. et al. The NHGRI-EBI GWAS catalog of published genome-wide association studies, targeted arrays and summary statistics 2019. *Nucleic Acids Res.* **47**, D1005–D1012 (2019).

55. Pruij, R. J. et al. LocusZoom: regional visualization of genome-wide association scan results. *Bioinformatics* **26**, 2336–2337 (2010).
56. 1000 Genomes Project Consortium. A global reference for human genetic variation. *Nature* **526**, 68–74 (2015).
57. Tam, O. H. et al. Postmortem cortex samples identify distinct molecular subtypes of ALS: retrotransposon activation, oxidative stress, and activated glia. *Cell Rep.* **29**, 1164–1177.e5 (2019).
58. Li, H. et al. The Sequence Alignment/Map format and SAMtools. *Bioinformatics* **25**, 2078–2079 (2009).
59. Picard toolkit. Broad Institute, GitHub Repository  
<https://broadinstitute.github.io/picard/> (Broad Institute, 2019).
60. Cotto, K. C. et al. RegTools: Integrated analysis of genomic and transcriptomic data for the discovery of splicing variants in cancer. Preprint at <https://doi.org/10.1101/436634> (2021)
61. Li, Y. I. et al. Annotation-free quantification of RNA splicing using LeafCutter. *Nat. Genet.* **50**, 151–158 (2018).
62. Darmanis, S. et al. A survey of human brain transcriptome diversity at the single cell level. *Proc. Natl Acad. Sci. USA* **112**, 7285–7290 (2015).
63. Hunt, G. J., Freytag, S., Bahlo, M. & Gagnon-Bartsch, J. A. dtangle: accurate and robust cell type deconvolution. *Bioinformatics* **35**, 2093–2099 (2019).
64. Li, H. Aligning sequence reads, clone sequences and assembly contigs with BWA-MEM. Preprint at <https://arxiv.org/abs/1303.3997> (2013).
65. DePristo, M. A. et al. A framework for variation discovery and genotyping using next-generation DNA sequencing data. *Nat. Genet.* **43**, 491–498 (2011).

66. McKenna, A. et al. The Genome Analysis Toolkit: a MapReduce framework for analyzing next-generation DNA sequencing data. *Genome Res.* **20**, 1297–1303 (2010).
67. Lukavsky, P. J. et al. Molecular basis of UG-rich RNA recognition by the human splicing factor TDP-43. *Nat. Struct. Mol. Biol.* **20**, 1443–1449 (2013).

## Acknowledgements

We thank F. Allain for the His-tagged TDP-43 plasmid; C. Stuani, F. Weissmann, M. Watson and K. Stott for guidance on TDP-43 purification and ITC; A. Isaacs and P. Whiting for support with shRNA experiments; N. Seyfried for input on proteomic experiments; and J. Vargas for his scientific insights and engaging conversations. This work was supported by grants from UK Medical Research Council MR/R005184/1 (E.M.C.F. and P.F.), FC001002 (J.U.); NIH U54NS123743 (P.F.); UK Motor Neurone Disease Association (P.F.); Rosetrees Trust (P.F. and A.G.); Chan Zuckerberg Initiative (M.E.W.); The Robert Packard Center for ALS Research (M.E.W., P.F. and E.M.C.F.); AriSLA (E.B.); Alzheimers Society (A.G.); NIH T32 GM136577 (S.S.); NIH National Institute of Aging R56-AG055824 and U01-AG068880 (J.H. and T.R.) European Union’s Horizon 2020 research and innovation programme 835300 (J.U.); Cancer Research UK FC001002 (J.U.); Wellcome Trust FC001002 (J.U.); Collaborative Center for X-linked Dystonia-Parkinsonism (W.C.L. and E.M.C.F.). P.F. is supported by a UK Medical Research Council Senior Clinical Fellowship and Lady Edith Wolfson Fellowship (MR/M008606/1 and MR/S006508/1), the UCLH NIHR Biomedical Research Centre; M.E.W. and S.E.H. are supported by the NIH Intramural Research Program of the National Institutes of Neurological Disorders and Stroke; O.G.W. is supported by a Wellcome Trust Studentship; M.Z. is supported by the Neurological Research Trust; S.C. is supported by NIH Intramural Research Program of the Eunice Kennedy Shriver National Institute of Child Health and Human Development; A.B. is supported by Eisai and the Wolfson Foundation; S.E.H. is supported by a Brightfocus Foundation postdoctoral research fellowship; T.L. is supported by an Alzheimer’s Research UK senior fellowship; G.S. is supported by a Wellcome Trust Investigator Award

(107116/Z/15/Z) and UK Dementia Research Institute Foundation award (UKDRI-1005); M.S. is supported by a UKRI Future Leaders Fellowship (MR/T042184/1); S.B.-S. is supported by a UK Motor Neurone Disease Association and Masonic Charitable Foundation PhD Studentship (893-792); M.H. is supported by a Lady Edith Wolfson Senior Non-Clinical Fellowship (959-799); S.S. is supported by the NIH Oxford–Cambridge Scholars Program.

## Author information

### Author notes

1. These authors contributed equally: Anna-Leigh Brown, Oscar G. Wilkins, Matthew J. Keuss, Sarah E. Hill

### Affiliations

1. UCL Queen Square Motor Neuron Disease Centre, Department of Neuromuscular Diseases, UCL Queen Square Institute of Neurology, UCL, London, UK

Anna-Leigh Brown, Oscar G. Wilkins, Matthew J. Keuss, Matteo Zanovello, Weaverly Colleen Lee, Flora C. Y. Lee, Sam Bryce-Smith, Martina Hallegger, Pietro Fratta, Giampietro Schiavo, Elizabeth M. C. Fisher, Jernej Ule & Pietro Fratta

2. The Francis Crick Institute, London, UK

Oscar G. Wilkins, Flora C. Y. Lee, Laura Masino, Martina Hallegger & Jernej Ule

3. National Institute of Neurological Disorders and Stroke, NIH, Bethesda, MD, USA

Sarah E. Hill, Sahba Seddighi, Joel F. Reyes, Daniel Ramos & Michael E. Ward

4. Queen Square Brain Bank, UCL Queen Square Institute of Neurology,  
University College London, London, UK

Alexander Bampton, Ariana Gatt, Emil K. Gustavsson & Tammaryn  
Lashley

5. Department of Neurodegenerative Disease, UCL Queen Square  
Institute of Neurology, University College London, London, UK

Alexander Bampton, Ariana Gatt & Tammaryn Lashley

6. Center for Alzheimer's and Related Dementias, National Institutes of  
Health, Bethesda, MD, USA

Yue A. Qi & Daniel Ramos

7. Center for Genomics of Neurodegenerative Disease, New York  
Genome Center (NYGC), New York, NY, USA

Delphine Fagegaltier, Hemali Phatnani & Hemali Phatnani

8. NeuroResource, Department of Neuroinflammation, UCL Queen  
Square Institute of Neurology, London, UK

Jia Newcombe

9. Great Ormond Street Institute of Child Health, Genetics and Genomic  
Medicine, University College London, London, UK

Emil K. Gustavsson

10. Medical Scientist Training Program, Johns Hopkins University School  
of Medicine, Baltimore, MD, USA

Sahba Seddighi

11. Molecular Genomics Core, Eunice Kennedy Shriver National Institute  
of Child Health and Human Development, NIH, Bethesda, MD, USA

Steven L. Coon

12. UK Dementia Research Institute, University College London, London, UK

Giampietro Schiavo

13. Nash Family Department of Neuroscience and Friedman Brain Institute, Icahn School of Medicine at Mount Sinai, New York, NY, USA

John Crary, Towfique Raj, Towfique Raj & Jack Humphrey

14. Ronald M. Loeb Center for Alzheimer's Disease, Icahn School of Medicine at Mount Sinai, New York, NY, USA

John Crary, Towfique Raj, Towfique Raj & Jack Humphrey

15. Department of Genetics and Genomic Sciences and Icahn Institute for Data Science and Genomic Technology, Icahn School of Medicine at Mount Sinai, New York, NY, USA

Towfique Raj, Towfique Raj & Jack Humphrey

16. Estelle and Daniel Maggin Department of Neurology, Icahn School of Medicine at Mount Sinai, New York, NY, USA

Towfique Raj, Towfique Raj & Jack Humphrey

17. Department of Genetics, Evolution and Environment, UCL Genetics Institute, University College London, London, UK

Maria Secrier

18. Department of Molecular Biology and Nanobiotechnology, National Institute of Chemistry, Ljubljana, Slovenia

Jernej Ule

19. Molecular Pathology Lab, International Centre for Genetic Engineering and Biotechnology (ICGEB), Trieste, Italy

Emanuele Buratti

20. Department of Neurology, Lewis Katz School of Medicine, Temple University, Philadelphia, PA, USA

Justin Kwan

21. Cedars-Sinai Department of Biomedical Sciences, Board of Governors Regenerative Medicine Institute and Brain Program, Cedars-Sinai Medical Center, University of California, Los Angeles, CA, USA

Dhruv Sareen

22. Department of Medicine, University of California, Los Angeles, CA, USA

Dhruv Sareen

23. Department of Biochemistry and Molecular Biology, Penn State Institute for Personalized Medicine, The Pennsylvania State University, Hershey, PA, USA

James R. Broach

24. Department of Neurology, The Pennsylvania State University, Hershey, PA, USA

Zachary Simmons

25. Department of Neurology, Henry Ford Health System, Detroit, MI, USA

Ximena Arcila-Londono

26. Department of Pathology and Laboratory Medicine, Perelman School of Medicine, University of Pennsylvania, Philadelphia, PA, USA

Edward B. Lee & Vivianna M. Van Deerlin

27. Department of Neurology, Center for Motor Neuron Biology and Disease, Institute for Genomic Medicine, Columbia University, New York, NY, USA

Neil A. Shneider

28. Department of Biological Engineering, Massachusetts Institute of Technology, Cambridge, MA, USA

Ernest Fraenkel

29. Department of Neurology, Johns Hopkins School of Medicine, Baltimore, MD, USA

Lyle W. Ostrow

30. Department of Neurogenetics, Academic Medical Centre, Amsterdam, The Netherlands

Frank Baas

31. Leiden University Medical Center, Leiden, The Netherlands

Frank Baas

32. Department of Medicine, Lung Biology Center, University of California, San Francisco, CA, USA

Noah Zaitlen

33. ALS Multidisciplinary Clinic, Neuromuscular Division, Department of Neurology, Harvard Medical School, Boston, MA, USA

James D. Berry

34. Neurological Clinical Research Institute, Massachusetts General Hospital, Boston, MA, USA

James D. Berry & Suma Babu

35. Centre for Neuroscience and Trauma, Blizard Institute, Barts, Queen Mary University of London, London, UK

Andrea Malaspina

36. The London School of Medicine and Dentistry, Queen Mary University of London, London, UK

Andrea Malaspina

37. Department of Neurology, Basildon University Hospital, Basildon, UK

Andrea Malaspina

38. The Jackson Laboratory, Bar Harbor, ME, USA

Gregory A. Cox

39. Department of Psychiatry and Human Behavior, Department of Biological Chemistry, School of Medicine, University of California, Irvine, CA, USA

Leslie M. Thompson

40. Department of Neurobiology and Behavior, School of Biological Sciences, University of California, Irvine, CA, USA

Leslie M. Thompson

41. Taube/Koret Center for Neurodegenerative Disease Research, Roddenberry Center for Stem Cell Biology and Medicine, Gladstone Institute, San Francisco, CA, USA

Steve Finkbeiner

42. Department of Neurology and Sensory Organs, University of Thessaly, Thessaly, Greece

Efthimios Dardiotis

43. Department of Neurology, Washington University in St Louis, St Louis, MO, USA

Timothy M. Miller

44. Centre for Clinical Brain Sciences, Anne Rowling Regenerative Neurology Clinic, Euan MacDonald Centre for Motor Neurone Disease Research, University of Edinburgh, Edinburgh, UK

Siddharthan Chandran & Suvankar Pal

45. Department of Molecular Genetics, Weizmann Institute of Science, Rehovot, Israel

Eran Hornstein

46. Department of Neurology, Icahn School of Medicine at Mount Sinai, New York, NY, USA

Daniel J. MacGowan

47. Center for Neurodegenerative Disorders, Department of Neurology, the Lewis Katz School of Medicine, Temple University, Philadelphia, PA, USA

Terry Heiman-Patterson

48. Cold Spring Harbor Laboratory, Cold Spring Harbor, NY, USA

Molly G. Hammell

49. Ann Romney Center for Neurologic Diseases, Brigham and Women's Hospital, Harvard Medical School, Boston, MA, USA

Nikolaos. A. Patsopoulos & Oleg Butovsky

50. Department of Anesthesiology, Stony Brook University, Stony Brook, NY, USA

Joshua Dubnau

51. Section of Infections of the Nervous System, National Institute of Neurological Disorders and Stroke, NIH, Bethesda, MD, USA

Avindra Nath

52. Department of Neurology, Barrow Neurological Institute, St Joseph's Hospital, Phoenix, AZ, USA

Robert Bowser

53. Medical Center, Department of Neurobiology, Barrow Neurological Institute, St Joseph's Hospital and Medical Center, Phoenix, AZ, USA

Robert Bowser

54. Department of Neurology, Division of Neuromuscular Medicine, Columbia University, New York, NY, USA

Matthew Harms

55. Department of Neuropathology, Academic Medical Center, University of Amsterdam, Amsterdam, The Netherlands

Eleonora Aronica

56. Department of Biology and Veterinary and Biomedical Sciences, The Pennsylvania State University, University Park, PA, USA

Mary Poss

57. New York Stem Cell Foundation, Department of Bioengineering, School of Engineering and Applied Sciences, University of Pennsylvania, Philadelphia, PA, USA

Jennifer Phillips-Cremins

58. Department of Pathology, Fishberg Department of Neuroscience, Icahn School of Medicine at Mount Sinai, New York, NY, USA

John Crary

59. Department of Neurology, Harvard Medical School, Neurological Clinical Research Institute, Massachusetts General Hospital, Boston, MA, USA

Nazem Atassi

60. Department of Neurology, Hospital for Special Surgery, New York, NY, USA

Dale J. Lange

61. Weill Cornell Medical Center, New York, NY, USA

Dale J. Lange

62. Medical Genetics, Atlantic Health System, Morristown Medical Center, Morristown, NJ, USA

Darius J. Adams

63. Overlook Medical Center, Summit, NJ, USA

Darius J. Adams

64. Center of Clinical Research, Experimental Surgery and Translational Research, Biomedical Research Foundation of the Academy of Athens (BRFAA), Athens, Greece

Leonidas Stefanis

65. 1st Department of Neurology, Eginition Hospital, Medical School, National and Kapodistrian University of Athens, Athens, Greece

Leonidas Stefanis

66. Neuromuscular/EMG service and ALS/Motor Neuron Disease Clinic,  
Hebrew University-Hadassah Medical Center, Jerusalem, Israel

Marc Gotkine

67. Board of Governors Regenerative Medicine Institute, Los Angeles,  
CA, USA

Robert H. Baloh

68. Department of Neurology, Cedars-Sinai Medical Center, Los Angeles,  
CA, USA

Robert H. Baloh

69. Harvard Medical School, Department of Physical Medicine and  
Rehabilitation, Spaulding Rehabilitation Hospital, Boston, MA, USA

Sabrina Paganoni

70. Center for Cellular and Molecular Therapeutics, Children's Hospital of  
Philadelphia, Philadelphia, PA, USA

Ophir Shalem

71. Department of Genetics, Perelman School of Medicine, University of  
Pennsylvania, Philadelphia, PA, USA

Ophir Shalem

72. Centre for Clinical Brain Sciences, University of Edinburgh,  
Edinburgh, UK

Colin Smith

73. Euan MacDonald Centre for Motor Neurone Disease Research,  
University of Edinburgh, Edinburgh, UK

Colin Smith

74. Department of Genetics and Genomic Sciences, Icahn Institute of Data Science and Genomic Technology, Icahn School of Medicine at Mount Sinai, New York, NY, USA

Bin Zhang

75. Department of Neuropathology, Georgetown Brain Bank, Georgetown Lombardi Comprehensive Cancer Center, Georgetown University Medical Center, Washington, DC, USA

Brent Harris

76. Neuroradiology Section, Department of Radiology and Biomedical Imaging, University of California, San Francisco, San Francisco, CA, USA

Iris Broce

77. Neuromuscular Diseases Unit, Department of Neurology, Tel Aviv Sourasky Medical Center, Sackler Faculty of Medicine, Tel-Aviv University, Tel-Aviv, Israel

Vivian Drory

78. Department of Neuroscience, University of California San Diego, La Jolla, CA, USA

John Ravits

79. Department of Neurology, University of Pennsylvania Perelman School of Medicine, Philadelphia, PA, USA

Corey McMillan

80. Department of Neurology, Columbia University Medical Center, New York, NY, USA

Vilas Menon

81. Department of Pharmaceutical Chemistry, University of California San Francisco, San Francisco, CA, USA

Lani Wu & Steven Altschuler

82. Hadassah Hebrew University, Jerusalem, Israel

Yossef Lerner

83. Department of Translational Neuroscience, Barrow Neurological Institute, Phoenix, AZ, USA

Rita Sattler

84. The Translational Genomics Research Institute (TGen), Phoenix, AZ, USA

Kendall Van Keuren-Jensen

85. Broad Institute, Cambridge, MA, USA

Orit Rozenblatt-Rosen & Kerstin Lindblad-Toh

86. Massachusetts General Hospital, Boston, MA, USA

Katharine Nicholson

87. Institute of Molecular Medicine, Feinstein Institutes for Medical Research, Northwell Health, Manhasset, NY, USA

Peter Gregersen

88. Korea Advanced Institute of Science and Technology (KAIST), Daejeon, South Korea

Jeong-Ho Lee

89. Perron Institute for Neurological and Translational Science, Nedlands,  
Western Australia, Australia

Sulev Kokos

90. Integrative Immunobiology Section, National Institute of Allergy and  
Infectious Disease, NIH, Bethesda, MD, USA

Stephen Muljo

## **Consortia**

### **NYGC ALS Consortium**

- Hemali Phatnani
- , Justin Kwan
- , Dhruv Sareen
- , James R. Broach
- , Zachary Simmons
- , Ximena Arcila-Londono
- , Edward B. Lee
- , Vivianna M. Van Deerlin
- , Neil A. Shneider
- , Ernest Fraenkel
- , Lyle W. Ostrow
- , Frank Baas
- , Noah Zaitlen
- , James D. Berry
- , Andrea Malaspina
- , Pietro Fratta
- , Gregory A. Cox
- , Leslie M. Thompson
- , Steve Finkbeiner
- , Efthimios Dardiotis
- , Timothy M. Miller
- , Siddharthan Chandran
- , Suvankar Pal

- , Eran Hornstein
- , Daniel J. MacGowan
- , Terry Heiman-Patterson
- , Molly G. Hammell
- , Nikolaos. A. Patsopoulos
- , Oleg Butovsky
- , Joshua Dubnau
- , Avindra Nath
- , Robert Bowser
- , Matthew Harms
- , Eleonora Aronica
- , Mary Poss
- , Jennifer Phillips-Cremins
- , John Crary
- , Nazem Atassi
- , Dale J. Lange
- , Darius J. Adams
- , Leonidas Stefanis
- , Marc Gotkine
- , Robert H. Baloh
- , Suma Babu
- , Towfique Raj
- , Sabrina Paganoni
- , Ophir Shalem
- , Colin Smith
- , Bin Zhang
- , Brent Harris
- , Iris Broce
- , Vivian Drory
- , John Ravits
- , Corey McMillan
- , Vilas Menon
- , Lani Wu
- , Steven Altschuler
- , Yossef Lerner
- , Rita Sattler
- , Kendall Van Keuren-Jensen

- , Orit Rozenblatt-Rosen
- , Kerstin Lindblad-Toh
- , Katharine Nicholson
- , Peter Gregersen
- , Jeong-Ho Lee
- , Sulev Kokos
- & Stephen Muljo

## **Contributions**

Conceptualization: A.-L.B., O.G.W., M.J.K., S.E.H., J.H., M.E.W. and P.F.  
Data curation: A.-L.B., O.G.W., M.Z., W.C.L. and S.B.-S. Formal analysis:  
A.-L.B., O.G.W., M.J.K., M.Z., W.C.L., S.B.-S., A.B., M.H., E.K.G., S.S.,  
J.F.R., S.L.C. and D.R. Funding acquisition: P.F., M.E.W. and E.B.  
Investigation: A.-L.B., O.G.W., M.J.K., S.E.H., M.Z., W.C.L., F.C.Y.L.,  
L.M., Y.A.Q., S.B.-S., A.B., A.G., M.H., E.K.G., S.S., J.F.R., S.L.C., D.R.,  
E.K.G. and S.L.C. Methodology: A.-L.B., O.G.W., M.J.K., S.E.H., J.H.,  
M.E.W. and P.F. Project administration: P.F. and M.E.W. Resources: H.P.,  
T.L., E.B., D.F. and J.N. Software: A.-L.B., O.G.W., M.Z., S.B.-S., J.H. and  
M.J.K. Supervision: P.F., M.E.W., J.H., J.U., M.S., T.R., T.L., E.M.C.F.,  
G.S. and T.F. Visualization: A.-L.B., O.G.W., M.J.K., W.C.L. and S.E.H.  
Writing, original draft: A.-L.B., O.G.W., M.J.K., M.E.W. and P.F. Writing,  
review and editing: S.E.H., W.C.L., E.B., J.U., J.H., M.E.W., P.F. A.-L.B.,  
O.G.W. M.J.K. and S.E.H. contributed equally; therefore each may place  
their name first in author order when referencing this manuscript in  
personal communications.

## **Corresponding authors**

Correspondence to [Michael E. Ward](#) or [Pietro Fratta](#).

## **Ethics declarations**

### **Competing interests**

A patent application related to this work has been filed. The technology described in this work has been protected in the patent PCT/EP2021/084908 and UK patent 2117758.9 (patent applicant, UCL Business Ltd and NIH; status pending), in which A.-L.B., O.G.W., M.J.K., S.E.H., M.E.W. and P.F. are named as inventors. The other authors declare no competing interests.

## **Peer review**

## Peer review information

*Nature* thanks Noa Lipstein, Magdalini Polymenidou and the other, anonymous, reviewers for their contribution to the peer review of this work. Peer review reports are available.

## Additional information

**Publisher's note** Springer Nature remains neutral with regard to jurisdictional claims in published maps and institutional affiliations.

## Extended data figures and tables

### [Extended Data Fig. 1 UNC13A and UNC13B are misspliced after TDP-43 knockdown across neuronal lines.](#)

**(a, b)** RNA-seq traces from IGV<sup>34</sup> of representative samples from control (top) and *TARDBP* KD (bottom) in i<sup>3</sup>Neurons showing intron retention in *UNC13A* (A) (mean  $4.50 \pm 1.50$  increased IR in KD) and *UNC13B* (mean  $1.86 \pm 0.63$  increased IR in KD)(B), overlaid with published TDP-43 iCLIP peaks<sup>22</sup> **(c)** Histogram showing number of basescope cryptic foci per nuclei in control (blue) and TDP-43 KD (grey) in WTC11-derived i<sup>3</sup>Neurons,  $p < 0.0001$  unpaired t-test. **(d, e)** RT-qPCR levels of *TARDBP* and *UNC13A* with a non-targeting control sgRNA (sgTARDBP –), an intermediate TDP-43 KD (sgTARDBP +) or a higher TDP-43 KD (sgTARDBP++) in WTC11-derived **(d)** and NCRM-5-derived i<sup>3</sup>Neurons **(e)**.  $n = 4$  biological replicates sgTARDBP – **(d)**,  $n = 6$  biological replicates sgTARDBP – **(e)**, sgTARDBP + **(d, e)** and ++ **(d, e)**. plotted as means  $\pm$  SEM. **(f)** Representative images of *UNC13A* CE RT-PCR products **(g)** Quantification of the lower gel in **(f)** plotted as means  $\pm$  SEM,  $n = 6$  biological replicates non-targeting control sgRNA (sgTARDBP –), sgTARDBP +, sgTARDBP++. Upper gel is quantified in Fig. [1h](#). One-way ANOVA with multiple comparisons. **(h–k)** Expression of TDP-43 regulated splicing in *UNC13A***(h, i)** and *UNC13B***(j, k)** across neuronal datasets<sup>9,21</sup> in control (blue) and TDP-43 KD (yellow). Intron retention (IR)**(i, k)** and CE and fsE

PSI (**h, j**) significantly increase after TDP-43 depletion in most experiments, Wilcoxon test (**I**) Relative gene expression levels for *TARDBP* across neuronal datasets<sup>9,21</sup>. Normalized RNA counts are shown as relative to control mean. Numbers show log<sub>2</sub> fold change calculated by DESeq2. Significance shown as adjusted p-values from DESeq2. For (h-l) biological replicates are: iPSC MN Ctrl KD n = 12, TDP-43 KD n = 6; i<sup>3</sup>N Ctrl KD n = 4, TDP-43 KD n = 3; SH-SY5Y, SK-N-DZ<sup>a</sup>, and SK-N-DZ<sup>b</sup> Ctrl KD n = 3, TDP-43 KD n = 3, Significance levels reported as \* (p < 0.05) \*\* (p < 0.01) \*\*\* (p < 0.001) \*\*\*\* (p < 0.0001).

### **Extended Data Fig. 2 Validation of *UNC13A* and *UNC13B* mislicing after TDP-43 KD across multiple neuronal cell lines.**

Targeted nanopore sequencing reveals *UNC13A* CE and IR events occur largely independently in-vitro. (**a**) Sanger sequencing of cryptic bands in both SH-SY5Y and SK-N-DZ cells confirm the CE splice junctions. (**b, c**) Crosslink density across *UNC13A* (chr19) (**b**) and *UNC13B* (chr9) (**c**) genomic loci from novel iCLIP on endogenous TDP-43 in SH-SY5Y cells. Crosslink densities for both genes show peaks at the CE/fsE (red) and retained introns (blue). Coordinates shown in hg38. (**d**) Percentage of all targeted *UNC13A* long reads in SH-SY5Y cells containing either neither CE nor IR, both, or either CE or IR. Most reads in both control and TDP-43 KD contain neither event, and while IR event is present in controls, CE is only detected in TDP-43 KD. (**e**) Representative trace in TDP-43 KD of *UNC13A* targeted long reads showing transcript containing either the CE or IR, and transcripts with neither.

### **Extended Data Fig. 3 Reduction of *UNC13A* and *UNC13B* after TDP-43 knockdown correlates with TDP-43 levels and is caused by nonsense-mediated decay.**

Relative gene expression levels for *UNC13A* (**a**) and *UNC13B* (**b**) after TDP-43 knockdown across neuronal cell lines<sup>9,21</sup>. Normalized RNA counts are shown as relative to control mean. Numbers show log fold change calculated by DESeq2. Significance shown as adjusted p-values from DESeq2. Number of replicates as in Extended data Fig. 1 H-L (**c, d**) RT-

qPCR analysis shows *TDP-43*, *UNC13A* and *UNC13B* gene expression is reduced by *TARDBP* shRNA knockdown in both SH-SY5Y and SK-N-DZ human cell lines. Graphs represent the means ± SEM, n = 6 biological replicates, one sample t-test. (e) The 5' ends of 29 nt reads relative to the annotated start codon from a representative ribosome profiling dataset (TDP-43 KD replicate B). As expected, we detected strong three-nucleotide periodicity, and a strong enrichment of reads across the annotated coding sequence relative to the upstream untranslated region. (f) *UNC13A*, *UNC13B*, and *TDP-43* protein levels, measured by Western Blot, with varying levels of DOX-inducible *TDP-43* knockdown in SH-SY5Y cells. Tubulin is used as endogenous control, n = 3. For gel source data, see Supplementary Figure 1. (g) Quantification of RT-PCR products from the transcripts containing *UNC13A* CE, *UNC13A* intron retention, *UNC13B* fsE, and *UNC13B* intron retention, with varying levels of DOX-inducible *TDP-43* knockdown in SH-SY5Y cells. Graphs represent the means ± SEM n = 3 biological replicates. (h) UPF1 siRNA knock-down led to the rescue of *hnRNPL* (positive control), *UNC13A*, and *UNC13B* transcripts, but not *STMN2*. Graphs represent the means ± SEM, n = 4 biological replicates, one-sample t-test. (i) *UNC13A* CE containing-transcript PSI is increased after UPF1 knockdown in i<sup>3</sup>Neurons. Graphs represent the means ± SEM, n = 6 biological replicates. (j) RT-PCR products from *UNC13A* in the setting of mild *TDP-43* knockdown ("+", as for Figure 2C and S4G) with the addition of either DMSO (control) or CHX (NMD inhibition). (k) Quantification of (j) Graphs represent the means ± SEM, n = 4 biological replicates. Significance levels reported as \* (p < 0.05) \*\* (p < 0.01) \*\*\* (p < 0.001) \*\*\*\* (p < 0.0001).

### Extended Data Fig. 4 Sample technical factors in NYGC tissue samples do not vary in a systematic way.

(a) *UNC13A* expression across tissues and disease subtypes in the NYGC ALS Consortium RNA-seq dataset. Expression normalised as transcripts per million (TPM). Cortical regions have noticeably higher *UNC13A* expression than the spinal cord. (b) total RNA-seq library size (log<sub>10</sub> scaled) (c) RNA integrity score (RIN) (d) Cell type decomposition across NYGC ALS Consortium RNA-seq dataset. While there are differences between tissues and disease-subtypes on these technical factors, specificity

of *UNC13A* CE detection to tissues presumed to contain TDP-43 proteinopathy cannot be explained by these technical factors. Box plots (**a–d**): boundaries 25–75th percentiles; midline, median; whiskers, Tukey style. Wilcoxon test, significance levels reported as \* ( $p < 0.05$ ) \*\* ( $p < 0.01$ ) \*\*\* ( $p < 0.001$ ) \*\*\*\* ( $p < 0.0001$ ).

**Extended Data Fig. 5 Differences in sample technical factors where *UNC13A* CE was detected and undetected vary between cortical and spinal tissues.**

Targeted long reads in FTLD frontal cortex show that *UNC13A* CE and IR occur independently in-vivo. (a) Detection rate of *UNC13A* CE across tissues by RNA sequencing platform and read length. *UNC13A* CE was more likely to be detected in cervical spinal cord and motor cortex when sequenced on machines with 125 bp compared to 100 bp. (b) No significant differences in total RNA-seq library size (log10 scaled). (c) RNA integrity score (RIN) was significantly lower in motor and temporal cortices in samples where *UNC13A* was detected. (d) Cell type decomposition revealed that samples with *UNC13A* CE detected had a higher proportion of neurons in cervical and lumbar spinal cord, whereas in frontal, temporal, and motor cortex samples with *UNC13A* CE detected had a lower proportion of neurons, and in motor and temporal cortex samples with *UNC13A* CE detected had a higher proportion of astrocytes. Astrocy. - Astrocytes, Endothi. - Endothelial, Microgl. - Microglia. Neur. - Neurons, Oligodendr. - Oligodendrycytes. P-values shown are from Fisher's exact test (a) or Wilcoxon test (b–d). N tissue samples show below in brackets. Box plots (a–d): boundaries 25–75th percentiles; midline, median; whiskers, Tukey style. (e) Percentage of targeted *UNC13A* long reads with TDP-43 regulated splice events that contain either both, CE, or IR in four in FTLD frontal cortices. (f) Percentage of all targeted *UNC13A* long reads in (a) containing neither CE nor IR, both, or either CE or IR.

**Extended Data Fig. 6 Expression of shorter *UNC13B* isoform in human neuronal tissue masks detection of *UNC13B* fsE across NYGC tissue samples.**

**(a)** Expression of splice junction reads supporting the *UNC13B* fsE across tissues and disease subtypes. Junction counts are normalised by library size in millions (junctions per million). Expression of *UNC13B* fsE is present across controls and ALS/FTLD-non-TDP tissues. Wilcoxon test, significance levels reported as \* ( $p < 0.05$ ) \*\* ( $p < 0.01$ ) \*\*\* ( $p < 0.001$ ) \*\*\*\* ( $p < 0.0001$ ). **(b)** Diagram showing three of the *UNC13B* transcripts, including the APPRIS<sup>35</sup> principal isoform *UNC13B-207* (blue), the NMD sensitive isoform *UNC13B-208* (green), and the shorter isoform *UNC13B-210* which shares the fsE (light green highlight) and one of the splicing junctions supporting the fsE as *UNC13B-208*. **(c)** Expression of three *UNC13B* isoforms across NYGC cohort and in the five in vitro TDP-43 knockdowns experiments<sup>9,21</sup>. *UNC13B-210* is expressed across in vivo human tissues, whereas there is almost no expression of *UNC13B-210* in any of the in vitro experiments. Box plots **(a, c)**: boundaries 25–75th percentiles; midline, median; whiskers, Tukey style.

### **Extended Data Fig. 7 TDP-43 regulated *UNC13A* and *UNC13B* introns are expressed across human neuronal tissues in NYGC tissue samples.**

*STMN2* CE PSI correlates with TDP-43 regulated cryptics across NYGC RNA-seq dataset. IRratio<sup>36</sup> in *UNC13A* exon 31–32 **(a)** and *UNC13B* exon 21–22 **(b)** across NYGC tissue samples. *UNC13A* IR was lower in ALS-TDP cases than in controls in cervical spinal, frontal and motor cortices, and higher in FTLD-TDP cases than controls in frontal and temporal cortices. Possibly this reflects differences in the effects of cell type composition in disease state. Box plots **(a, b)**: boundaries 25–75th percentiles; midline, median; whiskers, Tukey style.. Wilcoxon test, significance levels reported as \* ( $p < 0.05$ ) \*\* ( $p < 0.01$ ) \*\*\* ( $p < 0.001$ ) \*\*\*\* ( $p < 0.0001$ ). **(c–e)** Correlation in ALS/FTLD-TDP cortex between *RAP1GAP* CE **(c)**, *PFKP* CE **(d)**, and *UNC13A* CE **(e)** with *STMN2* CE PSI in patients with at least 30 spliced reads across the CE locus. Spearman’s correlation.

### **Extended Data Fig. 8 *UNC13A* risk alleles increase *UNC13A* CE expression after TDP-43 depletion by altering TDP-43**

## binding affinity across the UNC13A CE-containing intron.

(a) *UNC13A* CE PSI by genotype (Wilcoxon test) Box plots: boundaries 25-75th percentiles; midline, median; whiskers, Tukey style. (b) Effect of CE or intronic SNP on the correlation between STMN2 and *UNC13A* CE PSI in ALS/FTD cortex in samples with at least 30 junction reads across the CE locus. Spearman's correlation. (c) Raw tapestation gel images of *UNC13A* CE products in 2H and 2R minigines and quantification of the PCR products. Graphs represent the means  $\pm$  SEM(n = 3 biological replicates); Two-way ANOVA (d) Raw tapestation gel images corresponding to Fig. 4e. Two sets of primers were used to amplify either control (top row) or mutant minigene (bottom row). Left panel: single transfections were performed to ensure primer specificity. Right panel: three biological replicates of the double transfections. (e) Fractional changes at iCLIP peaks for 2R versus 2H minigene (mean and 75% confidence interval shown). Peaks that are within 50nt of each SNP are highlighted. (f) Mean crosslink density around the exonic (top) and intronic (bottom) SNPs in the 2H (red) and 2R (blue) minigenes, relative to the 5' end of minigene (error bars = standard deviation; dashed lines show SNP positions). (g, h) Individual TDP-43 E-scores for the CE (g) and intronic (h) heptamers for which there was data<sup>27</sup> (i) Average change in E-value (measure of binding enrichment) across proteins for heptamers containing risk/healthy intronic SNP allele; TDP-43 is indicated in red. Significance levels reported as \* (p < 0.05) \*\* (p < 0.01) \*\*\* (p < 0.001) \*\*\*\* (p < 0.0001).

## Extended Data Fig. 9 Binding of TDP-43 to SNP-containing intronic RNA.

(a-d) ITC measurement of the interaction of TDP-43 with 14-nt RNA containing the CE SNP (a, b) and intronic SNP (c, d) healthy sequence. A representative data set is reported, with raw data (a, c) and integrated heat plot (b, d). Circles indicate the integrated heat; the curve represents the best fit. (e) Raw Tapestation gel images corresponding to Fig. 4j. For each experiment, two RT-PCRs were performed with a different primer set which either amplified a control minigene (top row; minigene 2H) or a mutant minigene (bottom row). Left: single transfections to ensure specificity of primers for either the control or the mutant minigene. Right: Three

replicates of double transfections with control minigene 2H and either mutant minigene.

## **Extended Data Fig. 10 One of the splice junctions for UNC13A CE overlaps with an unannotated exon expressed in control cerebellum.**

(a) Expression of splice junction reads supporting the *UNC13A* CE across tissues and disease subtypes. Junction counts are normalised by library size in millions (junctions per million). The long novel acceptor junction is expressed across all disease subtypes in the cerebellum. Box plots: boundaries 25–75th percentiles; midline, median; whiskers, Tukey style. (b) Example RNA-seq traces from IGV showing *UNC13A* cerebellar exon which shares the long novel acceptor junction as the *UNC13A* CE.

## **Supplementary information**

### **Supplementary Figure 1**

Uncropped immunoblots from Extended Data Fig. 3f. Red dashed boxes indicate regions shown in the figure. UNC13B, Tubulin and TDP-43 are from the same membrane. UNC13A is blotted on a separate membrane.

### **Reporting Summary**

### **Peer Review File**

### **Supplementary Table 1**

Gene expression and cryptic splicing status of ALS and FTLD associated genes in i<sup>3</sup>Neurons.

### **Supplementary Table 2**

Cell lines used in this study.

## **Supplementary Table 3**

Effect of read length on *UNC13A* CE detection in ALS/FTLD-TDP.

## **Supplementary Table 4**

Relationship between *UNC13A* CE PSI in patients and *UNC13A* risk SNPs and known covariates.

## **Supplementary Table 5**

Metadata targeted RNA-seq.

## **Supplementary Table 6**

Hg38 coordinates for splice junctions used to calculate PSI.

## **Supplementary Table 7**

Primers used for targeted RNA-seq in temporal cortex of 10 FTLD-TDP brains.

## **Supplementary Data 1**

List of differentially spliced junctions between control and TDP-43-knockdown i3Neurons (Fig. 1a).

## **Supplementary Data 2**

List of differentially expressed genes between control and TDP-43-knockdown i3Neurons (Fig. 1b).

## **Supplementary Data 3**

List of differentially ribosomal profiling genes between control and TDP-43-knockdown i3Neurons (Fig 2c).

## **Supplementary Data 4**

Average thermodynamic parameters obtained from ITC experiments.

## **Source data**

**Source Data Fig. 1**

**Source Data Fig. 2**

**Source Data Fig. 3**

**Source Data Fig. 4**

## **Rights and permissions**

**Open Access** This article is licensed under a Creative Commons Attribution 4.0 International License, which permits use, sharing, adaptation, distribution and reproduction in any medium or format, as long as you give appropriate credit to the original author(s) and the source, provide a link to the Creative Commons license, and indicate if changes were made. The images or other third party material in this article are included in the article's Creative Commons license, unless indicated otherwise in a credit line to the material. If material is not included in the article's Creative Commons license and your intended use is not permitted by statutory regulation or exceeds the permitted use, you will need to obtain permission directly from the copyright holder. To view a copy of this license, visit <http://creativecommons.org/licenses/by/4.0/>.

**Reprints and Permissions**

## **About this article**

**Cite this article**

Brown, AL., Wilkins, O.G., Keuss, M.J. *et al.* TDP-43 loss and ALS-risk SNPs drive mis-splicing and depletion of UNC13A. *Nature* **603**, 131–137 (2022). <https://doi.org/10.1038/s41586-022-04436-3>

- Received: 02 April 2021
- Accepted: 18 January 2022
- Published: 23 February 2022
- Issue Date: 03 March 2022
- DOI: <https://doi.org/10.1038/s41586-022-04436-3>

## Share this article

Anyone you share the following link with will be able to read this content:

[Get shareable link](#)

Sorry, a shareable link is not currently available for this article.

[Copy to clipboard](#)

Provided by the Springer Nature SharedIt content-sharing initiative

## Further reading

- [RNA targets of TDP-43: Which one is more important in neurodegeneration?](#)

- Dilara Halim
  - Fen-Biao Gao

*Translational Neurodegeneration* (2022)

- [Mechanism underlying a risk gene in neurodegeneration](#)

- Noa Lipstein

*Nature* (2022)

- **TDP-43 represses cryptic exon inclusion in the FTD–ALS gene UNC13A**

- X. Rosa Ma
- Mercedes Prudencio
- Aaron D. Gitler

*Nature* (2022)

## **TDP-43 represses cryptic exon inclusion in the FTD–ALS gene UNC13A**

- X. Rosa Ma
- Mercedes Prudencio
- Aaron D. Gitler

Article Open Access 23 Feb 2022

## **Mechanism underlying a risk gene in neurodegeneration**

- Noa Lipstein

News & Views 23 Feb 2022

---

This article was downloaded by **calibre** from <https://www.nature.com/articles/s41586-022-04436-3>

- Article
- [Published: 23 February 2022](#)

# The lung microbiome regulates brain autoimmunity

- [Leon Hosang<sup>1</sup>](#),
- [Roger Cugota Canals<sup>1</sup>](#),
- [Felicia Joy van der Flier<sup>1</sup>](#),
- [Jacqueline Hollensteiner<sup>2</sup>](#),
- [Rolf Daniel<sup>2</sup>](#),
- [Alexander Flügel](#) ORCID: orcid.org/0000-0001-5387-1860<sup>1 na1</sup> &
- [Francesca Odoardi](#) <sup>1,3 na1</sup>

[Nature](#) volume **603**, pages 138–144 (2022)

- 9793 Accesses
- 1 Citations
- 379 Altmetric
- [Metrics details](#)

## Subjects

- [Autoimmunity](#)
- [Neuroimmunology](#)

## Abstract

Lung infections and smoking are risk factors for multiple sclerosis, a T-cell-mediated autoimmune disease of the central nervous system<sup>1</sup>. In addition, the lung serves as a niche for the disease-inducing T cells for long-term survival and for maturation into migration-competent effector T cells<sup>2</sup>. Why the lung tissue in particular has such an important role in an autoimmune disease of the brain is not yet known. Here we detected a tight interconnection between the lung microbiota and the immune reactivity of the brain. A dysregulation in the lung microbiome significantly influenced the susceptibility of rats to developing autoimmune disease of the central nervous system. Shifting the microbiota towards lipopolysaccharide-enriched phyla by local treatment with neomycin induced a type-I-interferon-primed state in brain-resident microglial cells. Their responsiveness towards autoimmune-dominated stimulation by type II interferons was impaired, which led to decreased proinflammatory response, immune cell recruitment and clinical signs. Suppressing lipopolysaccharide-producing lung phyla with polymyxin B led to disease aggravation, whereas addition of lipopolysaccharide-enriched phyla or lipopolysaccharide recapitulated the neomycin effect. Our data demonstrate the existence of a lung–brain axis in which the pulmonary microbiome regulates the immune reactivity of the central nervous tissue and thereby influences its susceptibility to autoimmune disease development.

This is a preview of subscription content

## Access options

Subscribe to Nature+

Get immediate online access to the entire Nature family of 50+ journals

\$29.99

monthly

[Subscribe](#)

Subscribe to Journal

Get full journal access for 1 year

\$199.00

only \$3.90 per issue

[Subscribe](#)

All prices are NET prices.

VAT will be added later in the checkout.

Tax calculation will be finalised during checkout.

Buy article

Get time limited or full article access on ReadCube.

\$32.00

[Buy](#)

All prices are NET prices.

### **Additional access options:**

- [Log in](#)
- [Learn about institutional subscriptions](#)

**Fig. 1: Manipulations of the lung microbiota affect CNS autoimmunity.**

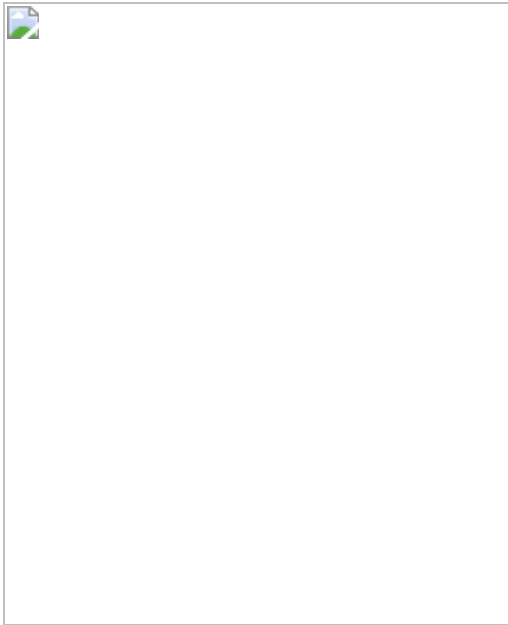


**Fig. 2: Lung dysbiosis does not influence T cell activation and migration.**

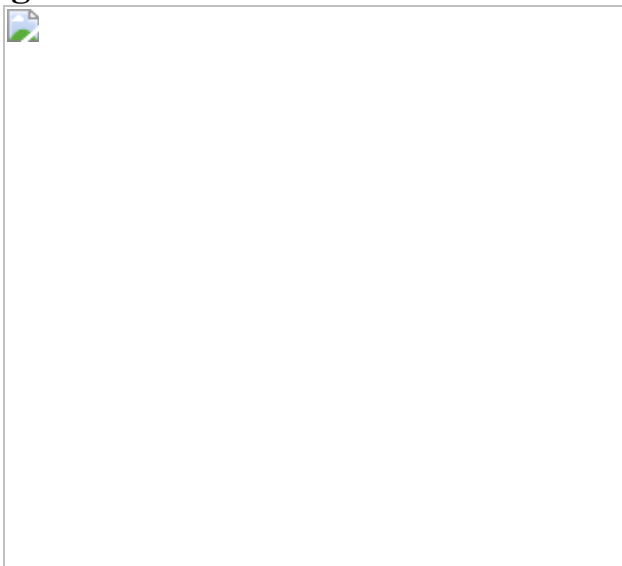


**Fig. 3: Lung dysbiosis affects microglia immune reactivity.**

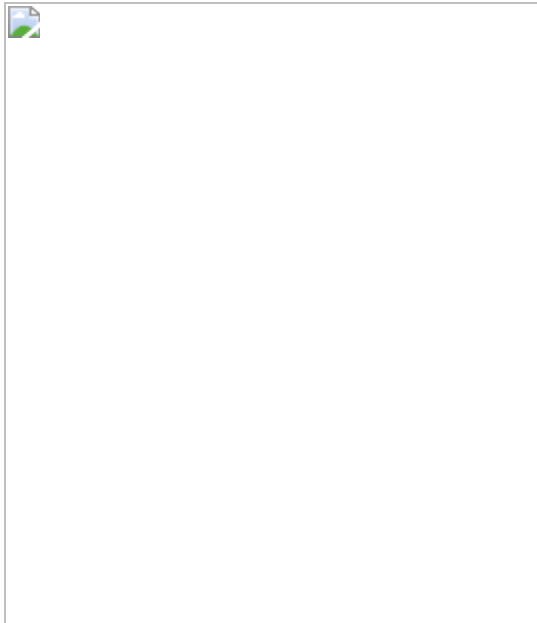


**Fig. 4: Lung dysbiosis shifts microglia to a type I IFN signature.**

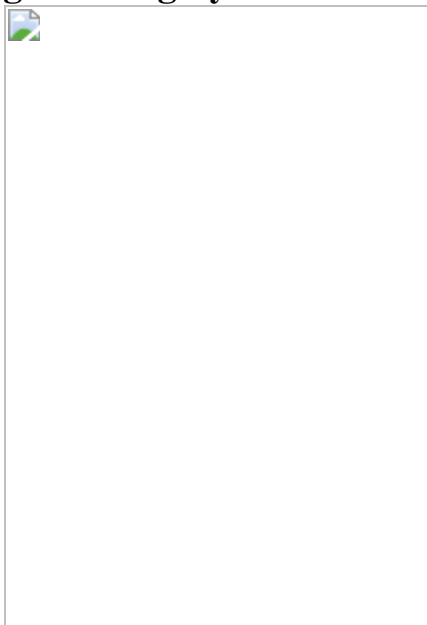
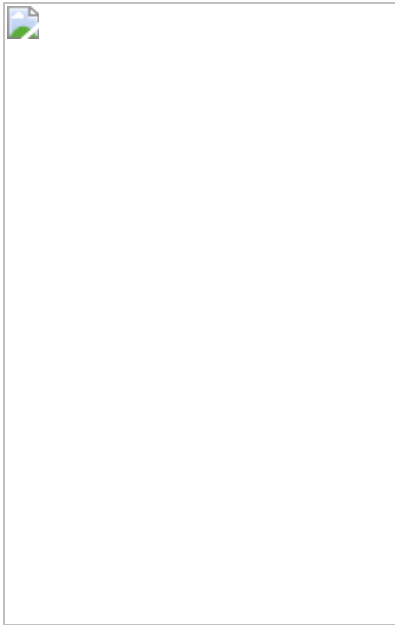


**Fig. 5: Pulmonary LPS controls CNS autoimmunity.**



## Data availability

RNA-seq datasets have been deposited online in the Gene Expression Omnibus (GEO) and BioProject with accession codes [GSE191287](#), [GSE192411](#) and [PRJNA789820](#). [Source data](#) are provided with this paper.

## References

1. Olsson, T., Barcellos, L. F. & Alfredsson, L. Interactions between genetic, lifestyle and environmental risk factors for multiple sclerosis. *Nat. Rev. Neurol.* **13**, 25–36 (2017).
2. Odoardi, F. et al. T cells become licensed in the lung to enter the central nervous system. *Nature* **488**, 675–679 (2012).
3. O'Dwyer, D. N., Dickson, R. P. & Moore, B. B. The lung microbiome, immunity, and the pathogenesis of chronic lung disease. *J. Immunol.* **196**, 4839–4847 (2016).
4. Jin, C. et al. Commensal microbiota promote lung cancer development via  $\gamma\delta$  T cells. *Cell* **176**, 998–1013 (2019).

5. Yokote, H. et al. NKT cell-dependent amelioration of a mouse model of multiple sclerosis by altering gut flora. *Am. J. Pathol.* **173**, 1714–1723 (2008).
6. Ochoa-Repáraz, J. et al. Role of gut commensal microflora in the development of experimental autoimmune encephalomyelitis. *J. Immunol.* **183**, 6041–6050 (2009).
7. Berer, K. et al. Commensal microbiota and myelin autoantigen cooperate to trigger autoimmune demyelination. *Nature* **479**, 538–541 (2011).
8. Rothhammer, V. et al. Type I interferons and microbial metabolites of tryptophan modulate astrocyte activity and central nervous system inflammation via the aryl hydrocarbon receptor. *Nat. Med.* **22**, 586–597 (2016).
9. Miyauchi, E. et al. Gut microorganisms act together to exacerbate inflammation in spinal cords. *Nature* **585**, 102–106 (2020).
10. Flügel, A., Willem, M., Berkowicz, T. & Wekerle, H. Gene transfer into CD4+ T lymphocytes: green fluorescent protein-engineered, encephalitogenic T cells illuminate brain autoimmune responses. *Nat. Med.* **5**, 843–847 (1999).
11. Lodygin, D. et al. β-Synuclein-reactive T cells induce autoimmune CNS grey matter degeneration. *Nature* **566**, 503–508 (2019).
12. Bartholomäus, I. et al. Effector T cell interactions with meningeal vascular structures in nascent autoimmune CNS lesions. *Nature* **462**, 94–98 (2009).
13. Kivisäkk, P. et al. Localizing central nervous system immune surveillance: meningeal antigen-presenting cells activate T cells during experimental autoimmune encephalomyelitis. *Ann. Neurol.* **65**, 457–469 (2009).

14. Lodygin, D. et al. A combination of fluorescent NFAT and H2B sensors uncovers dynamics of T cell activation in real time during CNS autoimmunity. *Nat. Med.* **19**, 784–790 (2013).
15. Starosom, S. C. et al. Galectin-1 deactivates classically activated microglia and protects from inflammation-induced neurodegeneration. *Immunity* **37**, 249–263 (2012).
16. Kawakami, N. et al. The activation status of neuroantigen-specific T cells in the target organ determines the clinical outcome of autoimmune encephalomyelitis. *J. Exp. Med.* **199**, 185–197 (2004).
17. Odoardi, F. et al. Instant effect of soluble antigen on effector T cells in peripheral immune organs during immunotherapy of autoimmune encephalomyelitis. *Proc. Natl Acad. Sci. USA* **104**, 920–925 (2007).
18. Heppner, F. L. et al. Experimental autoimmune encephalomyelitis repressed by microglial paralysis. *Nat. Med.* **11**, 146–152 (2005).
19. Hanisch, U. K. & Kettenmann, H. Microglia: active sensor and versatile effector cells in the normal and pathologic brain. *Nat. Neurosci.* **10**, 1387–1394 (2007).
20. Rock, R. B. et al. Transcriptional response of human microglial cells to interferon- $\gamma$ . *Genes Immun.* **6**, 712–719 (2005).
21. Popovic, N. et al. Inhibition of autoimmune encephalomyelitis by a tetracycline. *Ann. Neurol.* **51**, 215–223 (2002).
22. Elmore, M. R. et al. Colony-stimulating factor 1 receptor signaling is necessary for microglia viability, unmasking a microglia progenitor cell in the adult brain. *Neuron* **82**, 380–397 (2014).
23. Prinz, M. et al. Distinct and nonredundant in vivo functions of IFNAR on myeloid cells limit autoimmunity in the central nervous system. *Immunity* **28**, 675–686 (2008).

24. Khoroshii, R. et al. Induction of endogenous type I interferon within the central nervous system plays a protective role in experimental autoimmune encephalomyelitis. *Acta Neuropathol.* **130**, 107–118 (2015).
25. McNab, F., Mayer-Barber, K., Sher, A., Wack, A. & O'Garra, A. Type I interferons in infectious disease. *Nat. Rev. Immunol.* **15**, 87–103 (2015).
26. Bradley, K. C. et al. Microbiota-driven tonic interferon signals in lung stromal cells protect from influenza virus infection. *Cell Rep.* **28**, 245–256 (2019).
27. d'Hennezel, E., Abubucker, S., Murphy, L. O. & Cullen, T. W. Total lipopolysaccharide from the human gut microbiome silences toll-like receptor signaling. *mSystems* **2**, e00046-17 (2017).
28. Yang, D. et al. Dysregulated lung commensal bacteria drive interleukin-17B production to promote pulmonary fibrosis through their outer membrane vesicles. *Immunity* **50**, 692–706 (2019).
29. Bhor, V. M., Thomas, C. J., Surolia, N. & Surolia, A. Polymyxin B: an ode to an old antidote for endotoxic shock. *Mol. Biosyst.* **1**, 213–222 (2005).
30. Vargas-Caraveo, A. et al. Lipopolysaccharide enters the rat brain by a lipoprotein-mediated transport mechanism in physiological conditions. *Sci. Rep.* **7**, 13113 (2017).
31. Sandiego, C. M. et al. Imaging robust microglial activation after lipopolysaccharide administration in humans with PET. *Proc. Natl Acad. Sci. USA* **112**, 12468–12473 (2015).
32. Dickson, R. P., Erb-Downward, J. R., Martinez, F. J. & Huffnagle, G. B. The microbiome and the respiratory tract. *Annu. Rev. Physiol* **78**, 481–504 (2016).

33. Belkaid, Y. & Hand, T. W. Role of the microbiota in immunity and inflammation. *Cell* **157**, 121–141 (2014).
34. Erny, D. et al. Host microbiota constantly control maturation and function of microglia in the CNS. *Nat. Neurosci.* **18**, 965–977 (2015).
35. Braniste, V. et al. The gut microbiota influences blood–brain barrier permeability in mice. *Sci. Transl. Med.* **6**, 263ra158 (2014).
36. Wang, Y. et al. An intestinal commensal symbiosis factor controls neuroinflammation via TLR2-mediated CD39 signalling. *Nat. Commun.* **5**, 4432 (2014).
37. Luu, M. et al. The short-chain fatty acid pentanoate suppresses autoimmunity by modulating the metabolic-epigenetic crosstalk in lymphocytes. *Nat. Commun.* **10**, 760 (2019).
38. Sonner, J. K. et al. Dietary tryptophan links encephalogenicity of autoreactive T cells with gut microbial ecology. *Nat. Commun.* **10**, 4877 (2019).
39. Jakimovski, D., Kolb, C., Ramanathan, M., Zivadinov, R. & Weinstock-Guttman, B. Interferon  $\beta$  for multiple sclerosis. *Cold Spring Harb. Perspect. Med.* **8**, a032003 (2018).
40. Guo, B., Chang, E. Y. & Cheng, G. The type I IFN induction pathway constrains Th17-mediated autoimmune inflammation in mice. *J. Clin. Invest.* **118**, 1680–1690 (2008).
41. Bauer, H., Horowitz, R. E., Levenson, S. M. & Popper, H. The response of the lymphatic tissue to the microbial flora. Studies on germfree mice. *Am. J. Pathol.* **42**, 471–483 (1963).
42. Smith, K., McCoy, K. D. & Macpherson, A. J. Use of axenic animals in studying the adaptation of mammals to their commensal intestinal microbiota. *Semin. Immunol.* **19**, 59–69 (2007).

43. Kennedy, E. A., King, K. Y. & Baldridge, M. T. Mouse microbiota models: comparing germ-free mice and antibiotics treatment as tools for modifying gut bacteria. *Front. Physiol.* **9**, 1534 (2018).
44. Wypych, T. P., Wickramasinghe, L. C. & Marsland, B. J. The influence of the microbiome on respiratory health. *Nat. Immunol.* **20**, 1279–1290 (2019).
45. Balmer, M. L. et al. The liver may act as a firewall mediating mutualism between the host and its gut commensal microbiota. *Sci. Transl. Med.* **6**, 237ra266 (2014).
46. Määttä, J. A., Coffey, E. T., Hermonen, J. A., Salmi, A. A. & Hinkkanen, A. E. Detection of myelin basic protein isoforms by organic concentration. *Biochem. Biophys. Res. Commun.* **238**, 498–502 (1997).
47. Murray, C. et al. Interdependent and independent roles of type I interferons and IL-6 in innate immune, neuroinflammatory and sickness behaviour responses to systemic poly I:C. *Brain Behav. Immun.* **48**, 274–286 (2015).
48. Rittirsch, D. et al. Acute lung injury induced by lipopolysaccharide is independent of complement activation. *J. Immunol.* **180**, 7664–7672 (2008).
49. Klindworth, A. et al. Evaluation of general 16S ribosomal RNA gene PCR primers for classical and next-generation sequencing-based diversity studies. *Nucleic Acids Res.* **41**, e1 (2013).
50. von Hoyningen-Huene, A. J. E. et al. Bacterial succession along a sediment porewater gradient at Lake Neusiedl in Austria. *Sci. Data* **6**, 163 (2019).
51. Rognes, T., Flouri, T., Nichols, B., Quince, C. & Mahé, F. VSEARCH: a versatile open source tool for metagenomics. *PeerJ* **4**, e2584 (2016).

52. Yilmaz, P. et al. The SILVA and “All-species Living Tree Project (LTP)” taxonomic frameworks. *Nucleic Acids Res.* **42**, D643–D648 (2014).
53. Quast, C. et al. The SILVA ribosomal RNA gene database project: improved data processing and web-based tools. *Nucleic Acids Res.* **41**, D590–D596 (2013).
54. Chen, L. et al. GMPR: a robust normalization method for zero-inflated count data with application to microbiome sequencing data. *PeerJ* **6**, e4600 (2018).
55. Andersen, K. S., Kirkegaard, R. H., Karst, S. M. & Albertsen, M. ampvis2: an R package to analyse and visualise 16S rRNA amplicon data. Preprint at <https://doi.org/10.1101/299537> (2018).
56. Wickham, H. *ggplot2: Elegant Graphics for Data Analysis* (Springer, 2016).
57. Schläger, C. et al. Effector T-cell trafficking between the leptomeninges and the cerebrospinal fluid. *Nature* **530**, 349–353 (2016).
58. Cabeza, R. et al. An RNA sequencing transcriptome analysis reveals novel insights into molecular aspects of the nitrate impact on the nodule activity of *Medicago truncatula*. *Plant Physiol.* **164**, 400–411 (2014).
59. Love, M. I., Huber, W. & Anders, S. Moderated estimation of fold change and dispersion for RNA-seq data with DESeq2. *Genome Biol.* **15**, 550 (2014).
60. Huang, D. W., Sherman, B. T. & Lempicki, R. A. Systematic and integrative analysis of large gene lists using DAVID bioinformatics resources. *Nat. Protoc.* **4**, 44–57 (2009).
61. Doorn, K. J. et al. Brain region-specific gene expression profiles in freshly isolated rat microglia. *Front. Cell. Neurosci.* **9**, 84 (2015).

62. Klinkert, W. E. et al. TNF- $\alpha$  receptor fusion protein prevents experimental auto-immune encephalomyelitis and demyelination in Lewis rats: an overview. *J. Neuroimmunol.* **72**, 163–168 (1997).

## Acknowledgements

We thank S. Schwarz for helping in the quantification of the *tuf* gene expression; M. Ulisse for contributing to characterizing the lung immune milieu; G. Salinas for performing the transcriptome analyses; O. Shomroni for the analysis of the transcriptome data; S. Hamann, M. Weig and M. Heinemann for technical assistance; A. Poeblein for performing the 16S rRNA sequencing; D. Schneider for providing the bioinformatic amplicon processing pipeline; D. Miljković for helping with animal experiments and reading the manuscript; and C. Ludwig for text editing. This work was supported by the Deutsche Forschungsgemeinschaft (DFG, German Research Foundation) RK-Grant FL 377/3-1; FL 377/2-2; SFB 1328/1 project A01, project no. 335447717; OD 87/1-1, OD 87/3-1; SFB TRR 274/1 2020 projects A03 and A04, project no. 408885537; and by the European Commission under the European Union’s Horizon 2020 research and innovation programme, grant agreement no. 101021345 (T-Neuron). L.H. is supported by the Klaus Faber Stiftung.

## Author information

### Author notes

1. These authors contributed equally: Alexander Flügel, Francesca Odoardi

## Affiliations

1. Institute for Neuroimmunology and Multiple Sclerosis Research, University Medical Center Göttingen, Göttingen, Germany

Leon Hosang, Roger Cugota Canals, Felicia Joy van der Flier, Alexander Flügel & Francesca Odoardi

2. Department of Genomic and Applied Microbiology, University of Göttingen, Göttingen, Germany

Jacqueline Hollensteiner & Rolf Daniel

3. Center for Biostructural Imaging of Neurodegeneration, University Medical Center Göttingen, Göttingen, Germany

Francesca Odoardi

## Contributions

L.H. performed most experimental work and together with A.F. and F.O. wrote the paper. R.C.C. contributed to immune cell characterizations by quantitative PCR analyses and flow cytometry and by performing EAE experiments. F.J.v.d.F. performed the intravital TPLSM and supported L.H. with inducing and analysing autoimmune models. J.H. contributed with the microbiome analyses, and R.D. contributed with his expertise in microbiome biology and interpretation of the microbiota sequencing data. A.F. together with F.O. designed the study, coordinated the experimental work and wrote the manuscript with inputs from co-authors.

## Corresponding authors

Correspondence to [Alexander Flügel](#) or [Francesca Odoardi](#).

## Ethics declarations

## Competing interests

The authors declare no competing interests.

## Peer review

## Peer review information

*Nature* thanks Sarkis Mazmanian, Vijay Kuchroo and the other, anonymous, reviewer(s) for their contribution to the peer review of this work.

## Additional information

**Publisher's note** Springer Nature remains neutral with regard to jurisdictional claims in published maps and institutional affiliations.

## Extended data figures and tables

### Extended Data Fig. 1 Establishment of a lung EAE model and targeted manipulation of the lung microbiome.

**a**, Lung EAE. Rats were intravenously (i.v.) transferred with resting T<sub>MBP</sub> cells and 6 h later were intratracheally (i.tr.) immunized with CFA ± MBP. Clinical parameters: Body weight change (lines) and clinical scores (bars) over the EAE course, incidence (%), onset (days after immunization), peak score, cumulative score. Mean ± s.e.m. Representative data of 3 independent experiments.  $n = 4$  (−MBP);  $n = 5$  (+MBP). ND, not determinable. **b–e**, I.tr. neomycin (Neo) treatment does not change the lung immune cell composition. Lung samples were isolated from rats i.tr. treated for 7 days with PBS or neomycin. **b**, Number of endogenous αβTCR<sup>+</sup> CD4<sup>+</sup> and CD8<sup>+</sup> T cells, CD45RA<sup>+</sup> B cells, CD11b<sup>+</sup> ED9<sup>−</sup> interstitial macrophages, CD11b<sup>+</sup> ED9<sup>+</sup> MΦ (alveolar macrophages and infiltrating monocytes) and RP3<sup>+</sup> neutrophils. Flow cytometry. Mean ± s.e.m. **c**, Percentage expression of FoxP3, IFNγ and IL17 in endogenous αβTCR<sup>+</sup> CD4<sup>+</sup> and CD8<sup>+</sup> T cells. Flow cytometry. IFNγ and IL17 were analysed in steady state condition and upon stimulation with PMA and Ionomycin (PMA/I). Mean ± s.e.m. **d, e**, Corresponding surface expression of the activation markers CD134 (OX40) and CD25 (IL2R) by flow cytometry (d) and expression of the indicated cytokines measured by quantitative PCR (e) Mean ± s.e.m. **b–e**, Cumulative data of 2 independent experiments.  $n = 5$  (all groups). **f**, I.tr. treatment for 7 days with PBS or neomycin does not change MHC expression in lung immune cells. Expression of the indicated genes in total lung, pulmonary stromal cells (CD45<sup>−</sup>), as well as lymphoid (CD45<sup>+</sup>)

CD11b<sup>-</sup>) or myeloid (CD45<sup>+</sup> CD11b<sup>+</sup>) hematopoietic pulmonary cell populations. Quantitative PCR. Housekeeping gene: β-actin. Mean ± s.e.m. Cumulative data of 3 independent experiments.  $n = 9\text{--}14$  (PBS);  $n = 8\text{--}12$  (Neo) per condition. **a–f**, Statistical significance determined by unpaired two-tailed *t*-test (Gaussian distribution) and Mann–Whitney test (non-Gaussian distribution). \* $P < 0.05$ , \*\* $P < 0.01$ , \*\*\* $P < 0.001$ .

## [Source data](#)

### **Extended Data Fig. 2 Neomycin treatment outside the lung does not affect CNS autoimmunity.**

**a, b**, Oral treatment with neomycin does not ameliorate EAE. **a**, Left, PCA of the microbiota composition of faecal samples from rats that were orally treated with neomycin (1 or 10 mg) or PBS for 7 days. Middle, corresponding Shannon and phylogenetic diversity indices. Right, quantification of bacterial abundance based on *tuf* gene expression via 16S rRNA-based quantitative PCR. Mean ± s.e.m. Cumulative data of 2 independent experiments.  $n = 6$  (all groups). **b**, Clinical parameters observed in lung EAE of rats pre-treated orally with PBS or neomycin (1 or 10 mg) for 7 days. Mean ± s.e.m. Cumulative data of 2 independent experiments.  $n = 8$  (PBS, 1 mg Neo);  $n = 7$  (10 mg Neo). **c, d**, I.tr. neomycin treatment does not affect T<sub>MBP</sub> cell proliferation and effector function. **c**, Quantification of T<sub>MBP</sub> cells cultured in presence of neomycin at the indicated concentrations. Flow cytometry on D2, D3 and D4 after antigen challenge. Representative data of 2 independent experiments.  $n = 3$  (all groups). **d**, Clinical outcome of EAE induced by transfer of T<sub>MBP</sub> cells previously stimulated in vitro in presence of neomycin at the indicated concentrations. Clinical parameters. Mean ± s.e.m. Representative data of 3 independent experiments.  $n = 3$  (both groups). **e, f**, Subcutaneous (s.c.) treatment with neomycin does not affect EAE. **e**, Lung EAE was induced in rats s.c. pre-treated for 7 days with PBS or neomycin. Clinical parameters. Mean ± s.e.m. Representative data of 3 independent experiments.  $n = 5$  (both groups). **f**, Rats s.c. pre-treated for 7 days with PBS or neomycin were i.v. transferred with resting T<sub>MBP</sub> cells. 6 h later, they were s.c. immunized with MBP. Clinical parameters. Mean ± s.e.m. Representative

data of 3 independent experiments.  $n = 3$  (both groups). **a–d**, Statistical significance determined by one-way ANOVA with Tukey's multiple comparisons test (Gaussian distribution) and Kruskal–Wallis test with Dunn's multiple comparisons test (non-Gaussian distribution). **e, f**, Statistical significance determined by unpaired two-tailed *t*-test (Gaussian distribution) and Mann–Whitney test (non-Gaussian distribution). \* $P < 0.05$ , \*\* $P < 0.01$ , \*\*\* $P < 0.001$ .

[Source data](#)

**Extended Data Fig. 3 Lung dysbiosis does not modify T cell activation and expression profile in the lung.**

**a–e**, Lung EAE was induced in rats that were pre-treated i.tr. with neomycin or PBS for 7 days. **a**, Lung immunization induces reprogramming in the gene expression profile of  $T_{MBP}$  cells. Volcano plots depicting the differential gene expression profiles of lung-derived  $T_{MBP}$  cells from PBS- (left) or neomycin- (right) pre-treated rats between D1 and D0 after immunization. Red and blue dots represent significantly up- or downregulated genes ( $P < 0.05$ ), respectively. Indicated are representative genes involved in cell division and cell cycle. **b, c**, Genes differentially expressed after immunization are mainly involved in cell cycle. **b**, Significantly regulated KEGG pathways for genes upregulated between D1 versus D0 after immunization in  $T_{MBP}$  cells isolated from lung of PBS- (left) or neomycin-treated (right) rats. Bold, pathways significantly enriched in both treatments. **c**, Heat map of the 50 most upregulated genes in D1 versus D0 after immunization in PBS- and neomycin-treated rats. **d**, Lung immunization does not change effector T cell differentiation. Total reads of transcription factors, cytokines and chemokine receptors in  $T_{MBP}$  cells isolated from lung of PBS- or neomycin-treated rats on D0 and D1 after immunization Mean  $\pm$  s.e.m.  $n = 3$  (all groups). **e**, I.tr. neomycin treatment does not impair  $T_{MBP}$  cell activation and migratory program. Relative expression of chemokine receptors and genes involved in cell cycle and cell egress in  $T_{MBP}$  cells isolated from the lung of PBS- or neomycin-pre-treated rats on D1 after immunization. Quantitative PCR. Mean  $\pm$  s.e.m. Representative data of two independent experiments.  $n = 3$  (PBS);  $n = 4$

(Neo) per condition. **d, e**, Statistical significance determined by unpaired two-tailed *t*-test. \**P*<0.05.

[Source data](#)

**Extended Data Fig. 4 Lung dysbiosis does not impair the lung immune response after immunization but impairs grey matter autoimmunity.**

**a–f**, Lung EAE was induced in rats pre-treated i.tr. with PBS or neomycin. Characterization of the lung immune milieu was performed 24 h after i.tr. immunization. **a**, Lung EAE was induced in rats that were pre-treated i.tr. with neomycin or PBS for 7 days. **b–d**, Lung microbiome dysbiosis does not impair local T cell responses. **b**, Absolute numbers of T<sub>MBP</sub> cells and endogenous αβTCR<sup>+</sup> CD4<sup>+</sup> and CD8<sup>+</sup> T cells. Flow cytometry. **c**, Corresponding percentage expression of FoxP3 and proinflammatory cytokines in stimulated (PMA/I) or non-stimulated T cell subsets. Flow cytometry. Representative data from 2 independent experiments. *n*=5 (all groups). **d**, Relative expression of the indicated T cell lineage-signature cytokines in each T cell subset. Quantitative PCR. Housekeeping gene: β-actin. Mean ± s.e.m. **e–g**, Representative data from 2 independent experiments. *n*=5 (all groups). **e, f**, Lung microbiome dysbiosis does not impair local myeloid cell responses. **e**, Absolute number of CD11b<sup>+</sup> ED9<sup>−</sup> interstitial macrophages, CD11b<sup>+</sup> ED9<sup>+</sup> MΦ and RP3<sup>+</sup> neutrophils. Flow cytometry. **f**, Corresponding expression of chemokines, iNOS (*Nos2*), MHC-II (*Rt1ba*) and M2 macrophage markers. Quantitative PCR. Housekeeping gene: β-actin. **e–f**, Mean ± s.e.m. Representative data of 2 independent experiments. *n*=5 (all groups). **g, h**, Lung dysbiosis prevents T<sub>MBP</sub> cell entry into the CNS and ameliorates peripheral EAE induced by s.c. immunization. Rats were i.tr. treated with neomycin or PBS for 7 days. Subsequently, they were i.v. transferred with resting T<sub>MBP</sub> cells and s.c. immunized with MBP. **g**, Clinical parameters. Mean ± s.e.m. Representative data of 3 independent experiments. *n*=4 (both groups). **h**, Number of T<sub>MBP</sub> cells detected in the indicated organs by flow cytometry on D11 after immunization. Mean ± s.e.m. Representative data of 3 independent experiments. *n*=3 (both groups). **i, j**, I.tr. neomycin treatment reduces

$T_{bSYN}$  cell entry in the brain and ameliorates autoimmune grey matter disease. Grey matter autoimmunity was induced in rats pre-treated with neomycin or PBS by transfer of  $T_{bSYN}$  cells. **i**, Clinical parameters. Mean  $\pm$  s.e.m. Cumulative data of 2 independent experiments.  $n = 6$  (both groups). **j**, Quantification of the indicated immune cell subsets in blood or brain on D5 after transfer. Flow cytometry. Mean  $\pm$  s.e.m. Representative data of 2 independent experiments.  $n = 4$  (both groups). **b–j**, Statistical significance determined by unpaired two-tailed *t*-test (Gaussian distribution) and Mann–Whitney test (non-Gaussian distribution). \* $P < 0.05$ , \*\* $P < 0.01$ , \*\*\* $P < 0.001$ .

[Source data](#)

**Extended Data Fig. 5 Lung dysbiosis affects neither T cell and endothelial cell interactions at the CNS borders nor the barrier integrity.**

**a, b**, I.tr. neomycin treatment does not influence the expression of either chemokine receptors or adhesion molecules in  $T_{MBP}$  cells. Lung EAE or transfer EAE were induced in PBS- or neomycin-pre-treated rats. **a**, Chemokine receptor and integrin expression in  $T_{MBP}$  cells isolated from blood on D5 after immunization (lung EAE,  $n = 5$  per condition) or D4 after transfer (transfer EAE,  $n = 4$  per condition). Quantitative PCR.

Housekeeping gene:  $\beta$ -actin. Mean  $\pm$  s.e.m. Representative data of 2 independent experiments. **b**, Corresponding protein expression of LFA-1 and VLA-4. Flow cytometry. Representative data of 2 independent experiments. **c, d**, I.tr. neomycin treatment does not affect T cell motility at the CNS borders.  $T_{MBP}$  (c) or  $T_{OVA}$  (d) cells were i.v. transferred into rats pre-treated with PBS or neomycin. **c**, Intravascular  $T_{MBP}$  cell motility was recorded in the leptomeninges by TPLSM on D2.5 post transfer. Depicted are representative time-projection images over a period of 30 min, percentage of crawling versus rolling cells ( $n = 8$  videos per group) and quantification of the indicated motility parameters. Number of analysed T cells is indicated. Mean  $\pm$  s.e.m. Representative data of 2 independent experiments.  $n = 2\text{--}4$  (both groups). Turquoise,  $T_{MBP}$  cells; Red, 70 kDa Texas Red Dextran labelled vessels; Blue, Collagen. **d**,

Intravascular (upper panel) and extravascular (lower panel)  $T_{OVA}$  cell motility was recorded in the leptomeninges by TPLSM on D3 and D4 post transfer, respectively. Time projection images over a period of 30 min, percentage of crawling versus rolling cells ( $n = 9$  videos per group) and intravascular and extravascular motility parameters derived from the indicated number of T cells. Mean  $\pm$  s.e.m. Turquoise,  $T_{OVA}$  cells; Red, 70 kDa Texas Red Dextran labelled vessels; Blue, Collagen. **e**, I.tr. neomycin treatment does not affect  $T_{OVA}$  cell diapedesis. Intravital TPLSM overviews and corresponding magnified pictures depicting the distribution of  $T_{OVA}$  cells (turquoise) in the leptomeningeal milieu at the indicated time points post transfer in PBS- or neomycin- pre-treated rats. Red, 70 kDa dextran Texas-Red labelled vessels; Blue, Collagen. Arrows, Representative  $T_{OVA}$  cells. Graph, Corresponding quantification of  $T_{OVA}$  cells in the extravascular environment. Each dot represents a single 30 min video. Mean  $\pm$  SEM. Representative data of two independent experiments.  $n = 8$  (both groups). **f**, I.tr. neomycin treatment does not change the expression of tight junction molecules and integrin ligands. Expression of the indicated genes in endothelial cells isolated from spinal cord leptomeninges and parenchyma of rats pre-treated for 7 days with PBS or neomycin. Quantitative PCR. Housekeeping gene:  $\beta$ -actin. Mean  $\pm$  s.e.m. Cumulative data of 4 independent experiments.  $n = 17-18$  (all groups). **g**, I.tr. neomycin treatment does not alter the permeability of leptomeningeal vessels. Intravital TPLSM overviews and corresponding magnified pictures of the thoracic spinal cord recorded 7 days after i.tr. PBS or neomycin treatment. Images were acquired 0, 30, 60 and 90 min after i.v. injection of 3 kDa Texas Red Dextran. No leakage of the dye was observed at any time point. Representative images from two independent experiments. **a, e, f**, Statistical significance determined by unpaired two-tailed *t*-test (Gaussian distribution) and Mann–Whitney test (non-Gaussian distribution). **c, d**, Statistical significance of percentage crawling versus rolling was determined with a two-way ANOVA; for the other motility parameters unpaired two-tailed *t*-test (Gaussian distribution) and Mann–Whitney test (non-Gaussian distribution) were used.

[Source data](#)

## Extended Data Fig. 6 Lung dysbiosis induces quantitative but not qualitative changes in the immune infiltrates in the CNS.

**a**, I.tr. neomycin treatment reduces T<sub>MBP</sub> cell-mediated CNS inflammation. Expression of iNOS (*Nos2*), MHC-II (*Rt1ba*), chemokines, proinflammatory cytokines and regulatory genes in total spinal cord at the initiation stage of the EAE (i.e. 24 h after the onset of the clinical symptoms). Quantitative PCR. Housekeeping gene: β-actin. Mean ± s.e.m.  $n = 11$  (PBS);  $n = 9$  (Neo). **b, c**, T cell responses in the CNS are not affected by lung dysbiosis in transfer EAE. EAE was induced in rats pre-treated i.tr. with neomycin or PBS by transfer of T<sub>MBP</sub> cells. Immune cell characterization was performed at the initiation stage of the disease. **b**, Percentage of T<sub>MBP</sub> cells, endogenous αβTCR<sup>+</sup> CD4<sup>+</sup> and CD8<sup>+</sup> T cells expressing FoxP3 and proinflammatory cytokines (steady state and PMA/I-stimulated conditions) in the CNS and in the indicated peripheral compartments. Flow cytometry. Mean ± s.e.m. Representative data of 2 independent experiments.  $n = 5$  (all groups). **c**, Corresponding expression of the specified T cell lineage signature cytokines in the indicated T cell subsets isolated from the spinal cord. Quantitative PCR. Housekeeping gene: β-actin. Mean ± s.e.m.  $n = 2–4$  (all groups). **d**, Myeloid cells recruited to the CNS are not impaired by lung dysbiosis. Expression of iNOS (*Nos2*), MHC-II (*Rt1ba*), chemokines, M2 macrophage marker and IFNβ in spleen-derived CD45<sup>high</sup> CD11b<sup>+</sup> MΦ and in CNS-derived CD45<sup>high</sup> CD11b<sup>+</sup> MΦ at the initiation stage of EAE. Quantitative PCR. Housekeeping gene: β-actin. Mean ± s.e.m. Representative data of 2 independent experiments.  $n = 3–4$  (PBS);  $n = 4$  (Neo) per condition. **e**, T cell response in the CNS is not affected by lung dysbiosis also in lung active EAE. Lung EAE was induced in rats pre-treated i.tr. with neomycin or PBS. Immune cell analysis was performed at the initiation stage of the disease. **e**, Percentage of T<sub>MBP</sub> cells, endogenous αβTCR<sup>+</sup> CD4<sup>+</sup> and CD8<sup>+</sup> T cells expressing FoxP3 and proinflammatory cytokines (steady state and PMA/I-stimulated conditions) in the CNS and in the indicated peripheral compartments. Flow cytometry. Mean ± s.e.m. Representative data of 2 independent experiments.  $n = 5$  (all groups). **f**, Corresponding expression of the specified T cell lineage-signature cytokines measured as in c. Quantitative PCR. Mean ± s.e.m.  $n = 2–5$  (all groups). **g**, Myeloid cells recruited to the CNS are not functionally

impaired. Expression of the indicated genes measured as in d in spleen-derived CD45<sup>high</sup> CD11b<sup>+</sup> MΦ and in CNS-derived CD45<sup>high</sup> CD11b<sup>+</sup> MΦ. Quantitative PCR. Mean ± s.e.m. Representative data of 2 independent experiments.  $n = 2–5$  (all groups). **a–g**, Statistical significance was determined by unpaired two-tailed *t*-test (Gaussian distribution) and Mann–Whitney test (non-Gaussian distribution). \**P* < 0.05, \*\*\**P* < 0.001; ND, not detected.

[Source data](#)

**Extended Data Fig. 7 Lung dysbiosis induces changes in microglial morphology and expression profile.**

**a**, I.tr. neomycin treatment dampens microglial response in EAE. EAE was induced in rats pre-treated i.tr. with neomycin or PBS by transfer of T<sub>MBP</sub> cells. Confocal images acquired in spinal cord white matter and grey matter depicting the morphology of Iba1<sup>+</sup> microglia (red) at the peak of EAE. **b, c**, PLX3397 ameliorates EAE but does not add to the disease-ameliorating effects of i.tr. neomycin treatment. **b**, Quantification of CD45<sup>low</sup> CD11b<sup>+</sup> microglia in the brain after 7 days of oral treatment with PLX3397 or vehicle. Flow cytometry. Mean ± s.e.m. Cumulative data of 3 independent experiments.  $n = 9$  (both groups). **c**, Rats were treated orally with PLX3397 or vehicle and i.tr. with neomycin or PBS. After 7 days EAE was induced by transfer of T<sub>MBP</sub> cells. The treatments were continued throughout the entire disease course. Clinical parameters. Mean ± s.e.m. Cumulative data of 2 independent experiments.  $n = 10$  (vehicle and PBS, vehicle and Neo);  $n = 9$  (PLX and PBS);  $n = 11$  (PLX and Neo). **d**, I.tr. neomycin treatment does not induce quantitative microglia changes. Rats were treated i.tr. with PBS or neomycin for 7 days. Histological quantification of Iba1<sup>+</sup> microglia in the grey matter of the spinal cord ( $n = 5$  (PBS);  $n = 6$  (Neo)), and cytofluorometric quantification of CD45<sup>low</sup> CD11b<sup>+</sup> microglia in the spinal cord ( $n = 10$  (PBS);  $n = 9$  (Neo)). Mean ± s.e.m. **e, f**, I.tr. neomycin treatment changes microglia morphology in spinal cord and brain cortex without EAE induction. Rats were treated i.tr. with PBS or neomycin for 7 days. **e**, Quantification of the indicated morphological parameters extracted from confocal images of microglia in

the spinal cord of PBS- or neomycin-pre-treated rats. Mean  $\pm$  s.e.m. 16 cells from 3 different rats per group were analysed. **f**, Iba1<sup>+</sup> microglia in cortical grey matter after 7 days of i.tr. treatment with PBS or neomycin. Representative confocal 3D-reconstructions and corresponding morphological parameters derived from 13 cells from 3 different rats per group. Mean  $\pm$  s.e.m. **g**, I.tr. neomycin treatment induces a type I IFN signature in spinal cord microglia. Significantly enriched ( $P < 0.05$ ) GO terms belonging to biological processes (BP) in genes upregulated in microglia of rats treated with neomycin compared to PBS. **h**, I.tr. neomycin treatment induces type I IFN-stimulated gene expression in brain-derived microglia. Differential expression of the indicated genes in microglial cells sorted from the brain of rats pre-treated with PBS or neomycin. Representative data of 2 independent experiments. Quantitative PCR. Housekeeping gene:  $\beta$ -actin. Mean  $\pm$  s.e.m.  $n = 5$  (both groups). **i**, I.tr. neomycin treatment induces upregulation of type I IFN-stimulated genes in the total spinal cord. Comparison of differential gene expression between neomycin- and PBS-treated rats. Light red dots, genes significantly upregulated ( $P < 0.05$ ) but below the 0.5-fold change cut-off. Type I IFN-regulated genes are indicated. Bold, genes upregulated in both spinal cord and sorted microglia (Fig. [4b](#)). **j**, Lung dysbiosis does not induce a shift to a type I IFN profile in astrocytes. Expression of type I IFN-regulated genes,  $\beta$ 2MG (*B2m*), MHC-II (*Rt1ba*), and TNF. Note that no signal was detectable in most of the samples. Cumulative data of 2 independent experiments.  $n = 6$  (PBS);  $n = 7$  (Neo) per condition. **b**, **d**, **e**, **h**, **j**, Statistical significance determined by unpaired two-tailed *t*-test (Gaussian distribution) and Mann–Whitney test (non-Gaussian distribution). **c**, Statistical significance determined by one-way ANOVA with Tukey’s multiple comparisons test. \* $P < 0.05$ , \*\* $P < 0.01$ , \*\*\* $P < 0.001$ ; ND, not detected.

#### Source data

#### Extended Data Fig. 8 Effects of lung dysbiosis on microglia and the lung milieu.

**a**, I.tr. neomycin treatment reduces microglial reactivity towards inflammatory cytokines in the CNS. Rats were i.tr. treated daily with

neomycin or PBS. After 7 days, PBS or TNF & IFN $\gamma$  were administered intrathecally (i.th.). Percentage of MHC-II $^+$  CD45 $^{\text{low}}$  CD11b $^+$  microglia and number of CD45 $^{\text{high}}$  CD11b $^+$  M $\Phi$  in spinal cord and brain 4 h and 18 h after i.th. injection. Flow cytometry. Mean  $\pm$  s.e.m. Representative data from 3 independent experiments. For each CNS compartment,  $n = 4$  (PBS and PBS);  $n = 5$  (PBS and TNF & IFN $\gamma$ );  $n = 3$  (Neo and PBS);  $n = 5$  (Neo and TNF & IFN $\gamma$ ). **b**, Lung dysbiosis impairs the capacity of microglia to respond to proinflammatory stimuli in vitro. Microglial cells, isolated from rats treated for 7 days with PBS or neomycin, were stimulated in vitro with increasing doses of IFN $\gamma$ . Expression of chemokines, cytokines  $\beta$ 2MG (*B2m*), MHC-II (*Rt1ba*) and iNOS (*Nos2*) 4h after stimulation. Quantitative PCR. Representative data of 2 independent experiments. Each value represents the pooled microglia of at least 6 rats per group. **c**, Oral administration of inactivated *P. melaninogenica* does not affect EAE. EAE was induced by transfer of T<sub>MBP</sub> cells. Clinical parameters after daily oral treatment started 7 days before T<sub>MBP</sub> cell transfer and continued throughout the entire disease course. Mean  $\pm$  s.e.m. Cumulative data of 2 independent experiments.  $n = 5$  (PBS);  $n = 4$  (*P. melaninogenica*). **d**, Neomycin treatment increases pulmonary LPS. Concentration of LPS in BALF of rats treated for 7 days with PBS, neomycin or vancomycin (Vanco). ELISA. Mean  $\pm$  s.e.m. Cumulative data of 2 independent experiments.  $n = 9$  (PBS);  $n = 6$  (Vanco);  $n = 8$  (Neo). **e**, Neomycin treatment induces a shift to a type I IFN phenotype in pulmonary immune cells. Expression of type I IFN-stimulated genes in pulmonary stromal cells (CD45 $^-$ ) and immune cell subsets in PBS- or neomycin-pre-treated rats. Quantitative PCR. Housekeeping gene:  $\beta$ -actin. Mean  $\pm$  s.e.m. Cumulative data of 3 independent experiments.  $n = 4\text{--}13$  (PBS);  $n = 4\text{--}11$  (Neo) per condition. **a, c, e**, Statistical significance determined by unpaired two-tailed *t*-test (Gaussian distribution) and Mann–Whitney test (non-Gaussian distribution). **d**, Statistical significance determined by one-way ANOVA with Tukey’s multiple comparisons test. \* $P < 0.05$ , \*\* $P < 0.01$ , \*\*\* $P < 0.001$ .

[Source data](#)

## Extended Data Fig. 9 Vancomycin does not induce a shift towards LPS and does not affect CNS autoimmunity.

**a, b**, Vancomycin does not increase LPS producing phyla in the lung microbiota. **a**, Average relative abundance of bacterial phyla of lung microbiota in rats treated with PBS or vancomycin for 7 days. **b**, Corresponding heat map depicting the most regulated inhabitants of lung microbiota at family level. **c, d**, I.tr. vancomycin treatment does not affect the microglial gene expression profile. **c**, Volcano plots depicting the differential expression profile between vancomycin- and PBS-pre-treated rats in spinal cord derived CD45<sup>low</sup> CD11b<sup>+</sup> microglia or in total spinal cord. **d**, Expression of type I IFN-regulated genes in CD45<sup>low</sup> CD11b<sup>+</sup> microglial cells isolated from the spinal cord of rats pre-treated i.tr. for 7 days with PBS or vancomycin. Quantitative PCR. Please note that the experiment was performed in parallel with the one depicted in Fig. 4c and therefore the values in the PBS group are the same. Housekeeping gene:  $\beta$ -actin. Mean  $\pm$  s.e.m. Cumulative data of 3 independent experiments.  $n = 5$ –12 (PBS);  $n = 5$ –11 (Vanco) per condition. **e, f**, I.tr. vancomycin treatment does not affect transfer EAE or EAE induced via the lung. **e**, Transfer EAE was induced in rats pre-treated i.tr. with PBS or vancomycin for 7 days. Clinical parameters. Mean  $\pm$  s.e.m. Representative data of 3 independent experiments.  $n = 6$  (both groups). **f**, Lung EAE was induced in rats pre-treated i.tr. with PBS or vancomycin for 7 days. Clinical parameters. Mean  $\pm$  s.e.m. Representative data of 3 independent experiments.  $n = 3$  (both groups). **g**, Oral treatment with vancomycin does not affect EAE. Transfer EAE was induced in rats pre-treated orally with PBS or vancomycin for 7 days. Clinical parameters. Mean  $\pm$  s.e.m. Cumulative data of 2 independent experiments.  $n = 8$  (PBS);  $n = 8$  (1 mg Vanco);  $n = 7$  (10 mg Vanco). **d–f**, Statistical significance determined by unpaired two-tailed *t*-test (Gaussian distribution) and Mann–Whitney test (non-Gaussian distribution). **g**, Statistical significance determined by one-way ANOVA with Tukey’s multiple comparisons test. \* $P < 0.05$ , \*\* $P < 0.01$ , \*\*\* $P < 0.001$ .

[Source data](#)

## Extended Data Fig. 10 LPS regulates EAE severity.

**a**, I.tr. treatment with polymyxin B aggravates EAE. Transfer EAE was induced in rats pre-treated i.tr. for 7 days with polymyxin B or PBS. Clinical parameters. Mean  $\pm$  s.e.m. Cumulative data of 3 independent experiments.  $n = 11$  (PBS);  $n = 14$  (polymyxin B). **b**, I.tr. treatment with *E. coli* LPS ameliorates EAE. Transfer EAE was induced in rats pre-treated daily i.tr. for 7 days with LPS or PBS. The treatment was continued throughout the entire disease course. Clinical parameters. Mean  $\pm$  s.e.m. Cumulative data of 2 independent experiments.  $n = 8$  (both groups). **c**, I.th. *E. coli* LPS administration ameliorates EAE. EAE was induced by transfer of T<sub>MBP</sub> cells. LPS was administered on D0, D2 and D4 after transfer. Clinical parameters. Mean  $\pm$  s.e.m. Representative data of 2 independent experiments.  $n = 5$  (both groups). **d**, Graphical abstract: Lung microbiota controls the immune reactivity of the CNS in steady state condition and in the case of autoimmunity. Created with BioRender.com. **a–c**, Statistical significance determined by unpaired two-tailed *t*-test (Gaussian distribution) and Mann–Whitney test (non-Gaussian distribution). \* $P < 0.05$ , \*\* $P < 0.01$ , \*\*\* $P < 0.001$ .

[Source data](#)

## Supplementary information

### [Supplementary Fig. 1](#)

Flow cytometry gating strategies for the characterization of immune and resident cells. **a**, Stromal and myeloid cells in lung EAE on D1 after immunization. **b**, IFN $\gamma$ , IL-17 and FOXP3 expression in T<sub>MBP</sub> cells, endogenous  $\alpha\beta$ TCR $^+$  CD4 $^+$  and CD8 $^+$  T cells in the spinal cord on D5 after transfer of T<sub>MBP</sub> cells. Proinflammatory cytokines are depicted in steady state condition (−PMA/I) and after stimulation with PMA and ionomycin (+PMA/I). **c**, Microglia and MΦ (comprising both recruited blood derived monocytes and resident macrophages) in the spinal cord of rats pre-treated with neomycin (D0) and on D5 after T<sub>MBP</sub> cell transfer. **d**, Myeloid cells and astrocytes in the spinal cord of rats pre-treated with neomycin (D0). **e**, Endothelial cells isolated from spinal cord meninges of rats pre-treated with

neomycin. Numbers indicate the percentage fraction of each cell population.

## **Reporting Summary**

### **Supplementary Table 1**

Genes differentially regulated in microglial cells isolated from PBS- or neomycin-treated rats. RNA-seq data. *P* values were extracted from Wald test statistics generated for differential gene expression analysis by the DESeq2 package for R. Multiple test correction was done with the FDR/Benjamini–Hochberg method.

### **Supplementary Video 1**

Lung dysbiosis does not affect T<sub>MBP</sub> cell motility at the CNS borders. Locomotion behaviour of T<sub>MBP</sub> cells in the leptomeningeal vessels of spinal cord of rats pre-treated with PBS or neomycin. D2.5 post transfer. Intravital TPLSM. 30 min time-lapse recordings and corresponding time-projections. Scale bar, 50  $\mu$ m. Time interval, 15 sec. Turquoise, T<sub>MBP</sub> cells; Red, 70 kDa Texas Red Dextran labelled vessels.

### **Supplementary Video 2**

Lung dysbiosis does not affect CNS-ignorant T<sub>OVA</sub> cell motility at the CNS borders. Intravascular and extravascular locomotion behaviour of T<sub>OVA</sub> cells in the leptomeninges recorded 3 or 4 days post transfer, respectively in rats pre-treated with PBS or neomycin. Intravital TPLSM recordings. 30 min time-lapse recordings and corresponding time-projections. Scale bar, 50  $\mu$ m. Time interval, 15 sec. Turquoise, T<sub>OVA</sub> cells; Red, 70 kDa Texas Red Dextran labelled vessels.

### **Supplementary Video 3**

Lung dysbiosis leads to morphological changes in brain and spinal cord microglia. 3D reconstructions of Iba1<sup>+</sup> microglial cells from cortical grey matter and lumbar spinal cord of rats pre-treated with PBS or neomycin. Confocal microscopy. Scheme of the experimental design created with BioRender.com.

## Source data

[Source Data Fig. 1](#)

[Source Data Fig. 2](#)

[Source Data Fig. 3](#)

[Source Data Fig. 4](#)

[Source Data Fig. 5](#)

[Source Data Extended Data Fig. 1](#)

[Source Data Extended Data Fig. 2](#)

[Source Data Extended Data Fig. 3](#)

[Source Data Extended Data Fig. 4](#)

[Source Data Extended Data Fig. 5](#)

[Source Data Extended Data Fig. 6](#)

[Source Data Extended Data Fig. 7](#)

[Source Data Extended Data Fig. 8](#)

## [Source Data Extended Data Fig. 9](#)

## [Source Data Extended Data Fig. 10](#)

## Rights and permissions

### [Reprints and Permissions](#)

## About this article

### Cite this article

Hosang, L., Canals, R.C., van der Flier, F.J. *et al.* The lung microbiome regulates brain autoimmunity. *Nature* **603**, 138–144 (2022).  
<https://doi.org/10.1038/s41586-022-04427-4>

- Received: 15 September 2020
- Accepted: 17 January 2022
- Published: 23 February 2022
- Issue Date: 03 March 2022
- DOI: <https://doi.org/10.1038/s41586-022-04427-4>

## Share this article

Anyone you share the following link with will be able to read this content:

[Get shareable link](#)

Sorry, a shareable link is not currently available for this article.

[Copy to clipboard](#)

Provided by the Springer Nature SharedIt content-sharing initiative

## Further reading

- [\*\*Lung microbes mediate spinal-cord autoimmunity\*\*](#)

- Aubrey M. Schonhoff
- Sarkis K. Mazmanian

*Nature* (2022)

### [\*\*Lung microbes mediate spinal-cord autoimmunity\*\*](#)

- Aubrey M. Schonhoff
- Sarkis K. Mazmanian

News & Views 23 Feb 2022

---

This article was downloaded by **calibre** from <https://www.nature.com/articles/s41586-022-04427-4>

| [Section menu](#) | [Main menu](#) |

- Article
- Open Access
- [Published: 19 January 2022](#)

# The cGAS–STING pathway drives type I IFN immunopathology in COVID-19

- [Jeremy Di Domizio](#) [ORCID: orcid.org/0000-0002-6281-3918<sup>1</sup>](#)<sup>na1</sup>,
- [Muhammet F. Gulen](#)<sup>2</sup><sup>na1</sup>,
- [Fanny Saidoune](#)<sup>1</sup><sup>na1</sup>,
- [Vivek V. Thacker](#) [ORCID: orcid.org/0000-0002-1681-627X<sup>2</sup>](#)<sup>na1</sup>,
- [Ahmad Yatim](#)<sup>1</sup><sup>na1</sup>,
- [Kunal Sharma](#) [ORCID: orcid.org/0000-0001-8086-3436<sup>2</sup>](#),
- [Théo Nass](#) [ORCID: orcid.org/0000-0002-5934-2895<sup>2</sup>](#),
- [Emmanuella Guenova](#) [ORCID: orcid.org/0000-0001-5478-8735<sup>1</sup>](#),
- [Martin Schaller](#)<sup>3</sup>,
- [Curdin Conrad](#) [ORCID: orcid.org/0000-0002-2547-3440<sup>1</sup>](#),
- [Christine Goepfert](#)<sup>4,5</sup>,
- [Laurence de Leval](#) [ORCID: orcid.org/0000-0003-3994-516X<sup>6</sup>](#),
- [Christophe von Garnier](#)<sup>7</sup>,
- [Sabina Berezowska](#)<sup>6</sup>,
- [Anaëlle Dubois](#) [ORCID: orcid.org/0000-0003-1260-9123<sup>8</sup>](#),
- [Michel Gilliet](#) [ORCID: orcid.org/0000-0002-4609-3762<sup>1</sup>](#)<sup>na2</sup> &
- [Andrea Ablasser](#) [ORCID: orcid.org/0000-0002-8475-8999<sup>2</sup>](#)<sup>na2</sup>

[Nature](#) volume 603, pages 145–151 (2022)

- 27k Accesses
- 2 Citations
- 102 Altmetric
- [Metrics details](#)

## Subjects

- [Infection](#)
- [Innate immunity](#)
- [SARS-CoV-2](#)

## Abstract

COVID-19, which is caused by infection with SARS-CoV-2, is characterized by lung pathology and extrapulmonary complications<sup>1,2</sup>. Type I interferons (IFNs) have an essential role in the pathogenesis of COVID-19 (refs [3,4,5](#)). Although rapid induction of type I IFNs limits virus propagation, a sustained increase in the levels of type I IFNs in the late phase of the infection is associated with aberrant inflammation and poor clinical outcome<sup>[5,6,7,8,9,10,11,12,13,14,15,16,17](#)</sup>. Here we show that the cyclic GMP-AMP synthase (cGAS)–stimulator of interferon genes (STING) pathway, which controls immunity to cytosolic DNA, is a critical driver of aberrant type I IFN responses in COVID-19 (ref. [18](#)). Profiling COVID-19 skin manifestations, we uncover a STING-dependent type I IFN signature that is primarily mediated by macrophages adjacent to areas of endothelial cell damage. Moreover, cGAS–STING activity was detected in lung samples from patients with COVID-19 with prominent tissue destruction, and was associated with type I IFN responses. A lung-on-chip model revealed that, in addition to macrophages, infection with SARS-CoV-2 activates cGAS–STING signalling in endothelial cells through mitochondrial DNA release, which leads to cell death and type I IFN production. In mice, pharmacological inhibition of STING reduces severe lung inflammation induced by SARS-CoV-2 and improves disease outcome. Collectively, our study establishes a mechanistic basis of pathological type I IFN responses in COVID-19 and reveals a principle for the development of host-directed therapeutics.

[Download PDF](#)

## Main

To obtain insight into aberrant immunological processes at the tissue level<sup>[19](#)</sup>, we profiled COVID-19-associated skin manifestations from 10 hospitalized patients with moderate-to-severe COVID-19 disease and compared the resultant signatures with those obtained from skin lesions of patients with inflammatory skin diseases<sup>[20](#)</sup> (Extended Data Fig. [1](#)). Transcriptome analysis revealed that COVID-19 profiles clustered with profiles from cutaneous lupus erythematosus (CLE), but separated from signatures of other skin diseases, such as psoriasis, atopic dermatitis and lichen planus (Fig. [1a](#), Extended Data Fig. [2](#)). Transcriptional similarities between COVID-19 and CLE samples were based on the expression of IFNs (*IFNA2*, *IFNA4*, *IFNA1*, *IFNA13*, *IFNB1*, *IFNL2* and *IFNL3*) in purpuro-necrotic COVID-19 skin lesions and IFN-

stimulated genes (ISGs) (*IFIT2*, *BST2*, *IRF7*, *OASL*, *MX1*, *IFITM1*, *IFIT2*, *IFI35*, *IFIH1*, *ISG15*, *CXCL10* and *CXCL9*) in those with a maculo-papular phenotype (Fig. 1a). Notably, both COVID-19 skin phenotypes—but not CLE—showed a marked upregulation of genes related to macrophage function, including macrophage receptors (*CD209*, *CLU*, *MARCO*, *FCGR2A*, *CLEC5A*, *CD163*, *MRC1* and *BST1*), differentiation factors (*IL32*) and monocyte-recruiting chemokines (*CXCL2* and *CCL2*) (Fig. 1a, Extended Data Fig. 2). Pro-inflammatory cytokines (*TNF*, *IL6*, *IL1B* and *IL1A*) were also induced in COVID-19 skin biopsies (Fig. 1a). The immune correlates detected in skin lesions of patients with moderate-to-severe COVID-19 therefore resemble those reported for the lung<sup>8,17</sup>, suggesting a shared mechanism of immunopathology across different organs.

**Fig. 1: Type I IFN-producing macrophages surround damaged endothelial cells in COVID-19 skin lesions.**

 figure 1

- a**, Immune gene expression profiles of skin lesions from individuals with COVID-19 ( $n = 10$ ) and individuals with CLE ( $n = 11$ ), and skin from healthy donors (HD;  $n = 5$ ). Unbiased clustering was performed. **b**, Immunohistochemistry quantification of macrophages, neutrophils, plasmacytoid dendritic cells (pDCs) and T cells (stained for CD163, MPO, CD123 and CD3) in CLE ( $n = 5$ ) and COVID-19 ( $n = 10$ ) skin lesions. **c**, Confocal microscopy images of representative COVID-19 skin lesion stained for CD163 (green) and IFN $\beta$  (red). Scale bars, 20  $\mu\text{m}$ . **d**, Contribution of CD163 $^{+}$  macrophages and CD31 $^{+}$  endothelial cells to IFN $\beta$  expression in CLE ( $n = 5$ ) and

COVID-19 ( $n=10$ ). **e**, Confocal microscopy images of representative COVID-19 skin lesion stained for CD31 (green) and IFN $\beta$  (red). Scale bars, 20  $\mu\text{m}$ . **f**, Proportions of CD163 $^+$  macrophages, CD31 $^+$  endothelial cells and other cells among IFN $\beta$ -producing cells for each CLE and COVID-19 sample. **g**, Confocal microscopy images of a representative COVID-19 skin sample stained for CD163 (green) and CD31 (red) to depict macrophages and endothelial cells. Scale bar, 50  $\mu\text{m}$ . **h**, Transmission electron microscopy of dermal vessels in purpuro-necrotic (left) and maculopapular (middle) COVID-19 skin lesions, and in healthy skin (right). Arrows show disrupted endothelial cells (COVID-19 skin lesions) and intact endothelial cells (healthy skin). Scale bars, 2  $\mu\text{m}$  (left); 5  $\mu\text{m}$  (middle); 1  $\mu\text{m}$  (right). **i**, Immunohistochemistry for cleaved caspase-3 (cl. caspase-3) in COVID-19 skin lesions (nuclear staining indicated by arrow). Scale bar, 20  $\mu\text{m}$ . **j**, Percentage of CD31 $^+$  endothelial cells with cleaved caspase-3 staining in healthy skin ( $n=8$ ) and in CLE ( $n=6$ ) and COVID-19 ( $n=10$ ) skin lesions. **k**, Correlation between cleaved-caspase-3-positive nuclei and overall staining intensity of IFN $\beta$  measured in COVID-19 skin samples ( $n=8$ ). Spearman correlation and two-tailed statistical significance were performed. Data are mean  $\pm$  s.d. (**b**, **d**, **j**).  $P$  values obtained with two-tailed Student's *t*-test and one-way ANOVA followed by Tukey's multiple comparisons test (**b**, **d**, **j**).

[Source data](#)

## Vascular damage and type I IFNs in skin lesions

Next, we comparatively analysed the immune cell composition in skin lesions of patients with COVID-19 and patients with CLE by immunostaining. Consistent with the specific expression of macrophage signature genes, the numbers of CD163 $^+$  macrophages were higher in COVID-19 skin lesions relative to CLE (Fig. [1b](#), Extended Data Fig. [3a](#)). By contrast, plasmacytoid dendritic cells—but not macrophages—were enriched in CLE samples, whereas the numbers of neutrophils and T cells were similar in the two conditions (Fig. [1b](#), Extended Data Fig. [3a](#)). Further examination of macrophages revealed that these cells consistently showed a robust IFN $\beta$  response across all samples (Fig. [1c,d,f](#)). Endothelial cells and other cell types also showed a marked IFN $\beta$  signal, albeit with a higher degree of inter-sample variability (Fig. [1e,f](#)). We observed that IFN $\beta$ -producing macrophages frequently surrounded injured vessels (Fig. [1g](#), Extended Data Fig. [3b](#)), a well-recognized pathophysiological feature in COVID-19 (refs. [21,22](#)). Accordingly, we found several characteristics of endotheliopathy in COVID-19 skin lesions, including endothelial cell swelling (Extended Data Fig. [3c,d](#)), disruption of endothelial cell integrity (Fig. [1h](#)) and nuclear accumulation of cleaved caspase-3 (Fig. [1i,j](#)), a marker for cell death. Notably, the relative amounts of cleaved caspase-3 significantly correlated with levels of IFN $\beta$  (Fig. [1k](#)).

## Activation of STING in skin and lung pathology

We therefore focused on the possibility that signals derived from dying (endothelial) cells promote the production of type I IFNs by macrophages. Consistent with the engulfment of dying endothelial cells, immunostaining revealed that cleaved caspase-3 fragments accumulated inside macrophages, especially in cells adjacent to the vasculature (Extended Data Fig. 4). In addition, we observed intracellular DNA foci accumulating inside IFN $\beta$ -producing macrophages (Fig. 2a,b, Extended Data Fig. 4b). On the basis of these findings, we considered that engagement of the cGAS-STING pathway, a pivotal cytosolic DNA sensing mechanism, triggers the activation of macrophages<sup>18</sup>. After binding DNA, cGAS synthesizes the second messenger cyclic GMP-AMP (cGAMP), which activates STING to induce cytokine responses, including type I IFNs<sup>18</sup>. To directly address the involvement of cGAS, we measured levels of cGAMP in whole skin extracts. Samples from patients with COVID-19, but not those from healthy donors, showed increased levels of cGAMP (Fig. 2c). Consistent with the activation of cGAS-STING signalling, phosphorylated STING (p-STING)—a selective marker of activated STING<sup>23</sup>—was observed in perivascular macrophages in COVID-19 lesions, but not in healthy controls (Fig. 2d,e). In addition, STING was phosphorylated in endothelial cells (Fig. 2f,g), which also contribute to type I IFN production (see above). Finally, we cultured COVID-19 skin explants overnight in the presence or absence of a small-molecule STING inhibitor, H-151 (ref. 24). Compared to healthy skin, COVID-19 explants exhibited significant expression of ISGs (*IFI35*, *IRF7* and *MX1*), and this response was strongly reduced by H-151 (Fig. 2h). Thus, the cGAS-STING pathway is a crucial driver of type I IFN responses in COVID-19 skin lesions.

**Fig. 2: cGAS-STING-dependent type I IFN signature in COVID-19 skin and lung pathology.**

---

 **figure 2**

**a**, Confocal microscopy images of a representative COVID-19 skin sample stained for CD163 (green), *IFNB1* mRNA (red) and DNA (blue). Scale bars, 10 µm. Arrows indicate cytosolic DNA particles. **b**, Quantification of CD163<sup>+</sup> macrophages containing cytosolic DNA particles in COVID-19 skin lesions ( $n = 10$ ) and in healthy skin ( $n = 9$ ). **c**, Quantification of cGAMP in lysates of COVID-19 skin lesions ( $n = 10$ ) and healthy skin ( $n = 3$ ). **d**, Confocal microscopy images of a representative COVID-19 skin sample stained for CD163 (green) and p-STING (red). Blood vessels, dashed line. Arrows show p-STING<sup>+</sup> endothelial cells. Scale bars, 20 µm (left); 5 µm (right two images). **e**, Quantification of p-STING<sup>+</sup> macrophages in COVID-19 skin lesions ( $n = 10$ ) and in healthy skin ( $n = 10$ ). **f**, Confocal microscopy images of a representative COVID-19 skin sample stained for CD31 (green) and p-STING (red). Blood vessels, dashed line. Scale bars, 20 µm. **g**, Proportions of CD163<sup>+</sup> macrophages and CD31<sup>+</sup> endothelial cells among p-STING<sup>+</sup> cells in COVID-19 skin lesions ( $n = 7$ ). **h**, Expression of ISGs (*IFI35*, *IRF7* and *MX1*) in cultured healthy skin ( $n = 3$ ) and COVID-19 skin explants ( $n = 3$ ), treated or not with H-151. **i**, Confocal microscopy images of representative post-mortem lungs with early (fewer than 10 days; left) or late (more than 14 days, right) DAD, stained for p-STING (red) and CD163 (green). Scale bars (left to right): 20 µm, 10 µm, 50 µm, 10 µm. **j**, Quantification of p-STING<sup>+</sup>CD163<sup>+</sup> macrophages in post-mortem lungs with early and late DAD ( $n = 4$ ). **k**, Immunohistochemistry of representative post-mortem lungs with early (left) or late (right) DAD, stained for MxA. Scale bar, 50 µm. **l**, Percentage of tissue area with MxA

positivity in early and late DAD samples ( $n = 4$ ). Data are mean  $\pm$  s.d. (**b**, **c**, **e**, **h**, **j**, **l**).  $P$  values obtained with two-tailed Student's t-test (**c**, **e**, **h**, **j**, **l**) and with Mann–Whitney test (**b**).

### [Source data](#)

We next sought to determine whether cGAS–STING activation also occurs in severely damaged lungs of patients with COVID-19 by post-mortem analysis<sup>25</sup> (Extended Data Fig. [5a](#), [b](#)). We observed p-STING in macrophages and endothelial cells in some—but not all—of the lung autopsies that were analysed (Fig. [2i](#), [j](#), Extended Data Fig. [5c](#), [d](#)). Further histopathological examination showed that lung samples that exhibited p-STING expression belonged to patients with a rapidly lethal disease course (death at fewer than 10 days after disease onset), and were characterized by signs of early diffuse alveolar damage (DAD) with extensive hyaline membrane formation (Fig. [2i](#), [j](#), Extended Data Fig. [5a](#), [b](#)). By contrast, samples that lacked p-STING were from patients with a protracted disease course (death at more than 14 days after disease onset) and exhibited fibrotic changes that are characteristic of later phases of DAD<sup>25</sup> (Fig. [2i](#), [j](#), Extended Data Fig. [5a](#), [b](#)). In addition, samples with hallmarks for early DAD, but not late DAD, showed a type I IFN signature, as indicated by increased expression of MxA (Fig. [2k](#), [l](#)). Together, these analyses link SARS-CoV-2-induced tissue damage in the lung to the activation of the cGAS–STING pathway and type I IFN signalling.

## Endothelial STING response to infection

The above results suggested that, besides macrophages, endothelial cells might contribute to STING-dependent type I IFN responses in COVID-19. Although SARS-CoV-2 affects the vascular endothelium in patients, poor in vitro infection of endothelial cell cultures prevents the study of infection-associated processes in these cells<sup>26,27,28</sup>. To overcome this limitation and determine the role of STING in the endothelium, we used a lung-on-chip (LoC) model, which mimics the alveolar–capillary interface and allows for robust SARS-CoV-2-dependent activities in endothelial cells<sup>27</sup> (Fig. [3a](#), Extended Data Fig. [6a](#)). After infection of the alveolar epithelium, endothelial cells—but not epithelial cells—produced high levels of IFN $\beta$ , and this response was completely abolished when the STING inhibitor H-151 was perfused through the vascular channel (Fig. [3b](#), [c](#), Extended Data Fig. [6b](#), [c](#)). Consistent with a direct engagement of STING, endothelial cells contained perinuclear foci of p-STING after infection (Fig. [3d](#)). In addition, we verified that macrophages could contribute to the resultant type I IFN response on the vascular side in a manner that was dependent on cGAS (Fig. [3b](#), Extended Data Fig. [6d](#)). Of note, we observed that the prominent virus-induced cytopathic effect in endothelial cells was also sensitive to treatment with H-151 (Fig. [3c](#), Extended Data Fig. [6e](#)). By short hairpin

RNA (shRNA)-mediated knockdown, we confirmed that commitment to infection-induced cell death depended on STING in endothelial cells, whereas depleting STING in the epithelial layer did not affect cell viability (Extended Data Fig. [7a](#)). Further transcriptional analysis revealed changes of endothelial-specific activation markers (*F3*, *TFPI* and *CD31*), which were regulated by STING as H-151 effectively suppressed this response (Fig. [3e](#)). As a control, treatment with H-151 did not affect SARS-CoV-2 transcript expression in endothelial cells (Extended Data Fig. [6a](#)). We also tested the involvement of RNA-sensing RIG-I-like receptors and found that a knockdown of mitochondrial antiviral signalling protein (MAVS) in endothelial cells left the type I IFN response unaffected (Extended Data Fig. [7b](#)). Together, these data reveal that STING participates in the response of endothelial cells towards SARS-CoV-2 infection by controlling distinct effector programs; namely, type I IFN signalling and endothelial cell death.

**Fig. 3: STING-dependent type I IFN production and cell death after SARS-CoV-2 infection in endothelial cells.**

---

 **figure 3**

**a**, Schematic of the three-cell component LoC model. **b, c**, Representative 3D images of the vascular face of uninfected or SARS-CoV-2-infected LoCs with or without vascular H-151 perfusion. ‘3C’, three-cell component (epithelial cells, endothelial cells and macrophages) in **b**; ‘2C’, two-cell component (epithelial cells and endothelial cells) in **c**. CD45<sup>+</sup> macrophage (green), IFN $\beta$  (bright pink), cleaved caspase-3 (amber), actin (azure) and nuclear (purple) stainings are shown. Scale bars, 20  $\mu$ m. **d**, Representative 3D images of p-STING<sup>+</sup> endothelial cells (yellow). Scale bars, 20  $\mu$ m. **e**, Expression levels of the indicated genes in uninfected ( $n = 4$ ), infected ( $n = 5$ ) and H-151-treated ( $n = 5$ ) LoCs. *CD31* is also known as *PECAM1*. RE, relative expression. **f**, Representative volumetric electron microscopy images, 3D reconstructions and quantification of the surface-area-to-volume ratio of endothelial cell mitochondria from uninfected ( $n = 45$ ) and infected ( $n = 43$ ) LoCs. Solid line, mean; dashed lines, quartiles. Scale bars, 1  $\mu$ m (left images); grey hexagons (middle images) represent 1  $\mu\text{m}^3$ . **g**, Representative 3D images of the vascular face of infected LoCs with or

without vascular VBIT-4 perfusion. Scale bars, 50 µm. Statistics for quantification: **b**, IFN $\beta$ : uninfected ( $n = 6$  fields of view (FOV)), infected ( $n = 7$  FOV) and H-151-treated ( $n = 4$  FOV) LoCs,  $n = 2$  LoCs each; **c**, IFN $\beta$ /cleaved caspase-3: infected ( $n = 4$  FOV in each case) and H-151-treated ( $n = 4/n = 5$  FOV) LoCs,  $n = 2$  LoCs each for both markers; **f**, data from  $n = 4$  endothelial cells each from  $n = 1$  uninfected and  $n = 2$  infected LoCs; **g**, IFN $\beta$ : infected ( $n = 7$  FOV) and VBIT-4-treated ( $n = 6$  FOV) LoCs,  $n = 2$  LoCs each. Data acquired at 3 dpi; mean ± s.e.m.;  $P$  values calculated by one-way ANOVA followed by Tukey's multiple comparisons tests (**b**, **c**, **e**) or two-tailed Mann–Whitney test (**f**, **g**).

### Source data

We next investigated the mechanism that governs STING activation in endothelial cells. To this end, we profiled the cytosol of endothelial cells after LoC infection for changes in highly expressed proteins by mass spectrometry. Analysis of the mass spectrometry data identified differences in the abundance of 75 proteins at 3 days after infection, with a particular enrichment of mitochondrial proteins (that is, mitochondrial proteins linked to the Gene Ontology (GO) terms ‘thermogenesis’ or ‘oxidative phosphorylation’) (Extended Data Fig. [8a](#), Supplementary Table [3](#)). Time-course analysis confirmed a steady increase in altered expression of proteins linked to mitochondrial metabolism (Extended Data Fig. [8b](#)). Moreover, in volumetric ultrastructural imaging *in situ*, the mitochondria of endothelial cells showed disrupted cristae and appeared swollen after infection, with a pronounced reduction in the surface-area-to-volume ratio (Fig. [3f](#), Extended Data Fig. [8c](#)). Notably, endothelial cells containing damaged mitochondria were also detected in skin biopsies from patients with COVID-19 (Extended Data Fig. [8d](#)). On the basis of these findings, we hypothesized that mitochondrial DNA (mtDNA) released into the cytosol might trigger cGAS upstream of STING in endothelial cells. To test this idea, we incubated endothelial cells with 2',3'-dideoxycytidine (ddC) to deplete mtDNA ( $\rho^0$  cells) (Extended Data Fig. [8e](#)). Compared to control cells,  $\rho^0$  cells showed significantly less production of type I IFNs after epithelial infection with SARS-CoV-2 (Extended Data Fig. [8d](#)). In addition, inhibition of VDAC1 oligomerization by VBIT-4, which enables the passage of mtDNA fragments into the cytosol during mitochondrial stress<sup>29</sup>, decreased the production of type I IFNs in endothelial cells (Fig. [3g](#)). Therefore, extending previous findings<sup>30,31</sup>, SARS-CoV-2 can provoke mitochondrial dysfunction, which in endothelial cells connects to activation of the cGAS–STING pathway through the release of endogenous mtDNA.

## Targeting STING in a mouse model of COVID-19

To investigate the role of STING during SARS-CoV-2 infection *in vivo*, we used K18-hACE2 transgenic mice, which are highly susceptible to SARS-CoV-2 infection and

recapitulate important immunological features of severe COVID-19 in humans<sup>[32,33,34,35,36](#)</sup>. K18-hACE2 mice received one daily dose of H-151 starting at 16 h before SARS-CoV-2 infection and were euthanized at 3 days or 6 days post infection (dpi) (Fig. [4a](#)). Histological examination of the lungs showed a significant reduction of inflammatory cell infiltration in H-151-treated compared to vehicle-treated mice at 6 dpi (Fig. [4b](#)). As an independent measure of tissue pathology, we observed a prominent accumulation of dying cells (Extended Data Fig. [9a](#)). Cell death was efficiently blocked by treatment with H-151 at 6 dpi, but not at 3 dpi (Extended Data Fig. [9a](#)). These findings show that STING is a critical contributor to SARS-CoV-2-induced lung pathology.

**Fig. 4: STING inhibition reduces SARS-CoV-2-induced inflammation in mice.**

 figure 4

**a**, Schematic of SARS-CoV-2 infection (intranasal;  $1 \times 10^4$  plaque-forming units (PFU) per mouse) and intraperitoneal administration of vehicle or H-151 (starting at 1

day before infection), related to data from **b–d**. **b**, Left, representative haematoxylin and eosin (H&E) images of lungs from vehicle- and H-151-treated mice. Scale bars, 500 µm. Right, average inflamed area in SARS-CoV-2 infected mice. **c**, mRNA expression levels of the indicated genes in uninfected and infected lungs at 6 dpi, analysed by RT–qPCR. **d**, Relative weight loss in mice after SARS-CoV-2 infection. **e**, Schematic of SARS-CoV-2 infection (intranasal;  $1 \times 10^4$  PFU per mouse) and intraperitoneal administration of vehicle or H-151 (starting at 2 dpi), related to data from **f–h**. **f**, Left, representative H&E images of lungs from vehicle- and H-151-treated mice. Scale bars, 500 µm, Right, average inflamed area in SARS-CoV-2 infected mice. **g**, **h**, Relative weight loss (**g**) and survival (**h**) in mice after SARS-CoV-2 infection with post-infection regimen. Numbers are: **a–c**, uninfected ( $n = 4$ ), vehicle and H-151 ( $n = 7$ ); **d**, uninfected ( $n = 8$ ), vehicle and H-151 ( $n = 12$ ); **e–g**, uninfected, vehicle and H-151 ( $n = 5$ ); **h**, vehicle and H-151 ( $n = 15$ ). Throughout the figure, data are mean ± s.e.m.;  $P$  values calculated by one-way ANOVA followed by Tukey multiple comparison tests (**b**, **c**, **d**, **f**, **g**), or by Mantel–Cox survival analysis (**h**). Mice infected with SARS-CoV-2 were age-matched (12–16 weeks) female K18-hACE2 mice.

### Source data

When examining cytokine responses in the lungs after infection, we found that treatment with H-151 considerably decreased the expression of *Ifnb1* and ISGs (for example, *Gbp2*, *Irf5* and *Irf8*) at 6 dpi<sup>32,35</sup> (Fig. 4c, Extended Data Fig. 9b). Levels of pro-inflammatory genes (*Il6* and *Tnfrsf12a*), chemokines (*Ccl2*, *Ccl3*, *Ccl12* and *Cxcl9*) and markers of lung injury (*F3* and *Retnla*) were also significantly lower in H-151-treated compared to vehicle-treated mice<sup>35</sup> (Fig. 4c, Extended Data Fig. 9b). Furthermore, lung homogenates collected at 6 dpi showed strongly reduced activity of NF-κB and type I IFN signalling, as shown by decreased levels of p-p65 and p-STAT1, respectively (Extended Data Fig. 9c). Viral replication was similar in the presence or absence of H-151 at each time point, ruling out a significant effect of STING inhibition on viral replication (Extended Data Fig. 9d). Notably, at 3 dpi there was no appreciable difference in cytokine levels in the lungs between the two treatment groups (Extended Data Fig. 9b). Collectively, these data show that STING has a unique and critical function in eliciting type I IFN and inflammatory responses in the late phase of infection, which coincides with excessive tissue damage, but not with the peak of viral replication<sup>32</sup>. We also monitored body weight changes of infected mice over time. Compared to treatment with vehicle, treatment with H-151 significantly attenuated weight loss after infection, showing that STING has an essential role in the progression to severe disease (Fig. 4d).

Finally, we determined the effect of H-151 as a therapeutic agent in ongoing disease when viral loads are maximal<sup>32</sup> (Fig. 4e). Mice that received H-151 at 2 dpi showed

reduced pathology and decreased levels of type I IFNs and other cytokines in the lungs compared to those that were treated with vehicle only, whereas viral loads were similar between the two groups (Fig. 4f, Extended Data Fig. 10a, b). Therapeutic administration of H-151 also protected mice from weight loss and death after infection with SARS-CoV-2 (Fig. 4g, h). Together with the data above, these results corroborate the select role of STING in promoting detrimental inflammation during the late (or later) stages of the infection and highlight the therapeutic efficacy of STING inhibition, whether in a prophylactic or a therapeutic setting.

## Discussion

We have identified a central mechanism of innate immunopathology in COVID-19. Our study shows that engagement of the cGAS–STING pathway regulates two distinctive pathological features that are critically involved in the progression and severity of COVID-19—namely, endothelial dysfunction and type I IFN production (Extended Data Fig. 10c). Moreover, we establish endothelial cells and macrophages as cells at the root of maladapted cGAS–STING responses, which are driven in each cell type by a distinct underlying process. In a cell-intrinsic mode of activation, cGAS within endothelial cells is stimulated by the loss of mitochondrial homeostasis and associated accumulation of mtDNA to direct the expression of type I IFNs, activation of endothelial cells and, ultimately, cell death. By contrast, macrophage-dependent cGAS responses are more focused on type I IFN induction and result from the recognition of DNA from engulfed dying (endothelial) cells. Our finding that STING regulates endothelial cell death accords well with previous reports of endotheliopathy and vascular damage due to gain-of-function mutations in STING or after administration of highly potent STING agonists<sup>37,38</sup>. Consistent with previous reports in patients with COVID-19 (ref. 26), endothelial cells in our LoC studies contain viral elements, arguing for direct viral involvement in triggering mitochondrial dysfunction and, in turn, the activity of the cGAS–STING pathway. Along these lines, cell-autonomous activation of cGAS–STING signalling has recently been suggested to contribute to the NF-κB-dependent production of cytokines in SARS-CoV-2-infected human epithelial cell lines<sup>39</sup>, which indicates that the pathway could have a more extensive role in COVID-19-associated cytokine responses. Given the importance of vascular damage in COVID-19, establishing the precise upstream cause (or causes) of endothelial cell involvement in viral activities is an area that warrants future investigation<sup>21,40</sup>.

Many reports have pointed to the context-dependent roles of type I IFNs during infection with highly pathogenic coronaviruses<sup>3,5,6,9,10,11,17,41,42</sup>. Our study adds to these reports by indicating that the signalling mechanisms that underlie the induction of beneficial (early) versus detrimental (delayed) type I IFN responses are distinct. In a

direct mode of recognition, rapid detection of viral RNA by Toll-like receptors 3 and 7 and RIG-I-like receptors initiates a type I IFN response that confers antiviral protection to the host<sup>43,44,45,46,47</sup>. By contrast, activation of the cGAS–STING pathway by DNA emerges from a collateral host response to tissue damage. This explains the involvement of the pathway in type I IFN production at the later stages of infection, eventually sustaining deleterious inflammation. Notably, STING-dependent induction of type I IFNs is compromised in bats, which raises the possibility that this immunological adaption could account for the increased tolerance of these animals to highly pathogenic coronavirus infection<sup>48</sup>.

In summary, our study has implications both for the understanding of how the innate immune system contributes to detrimental outcomes of SARS-CoV-2 infection and for current efforts to define new therapeutic paradigms for more efficient treatment modalities in COVID-19.

## Methods

### Patient data and samples

Studies were approved by the institutional review and privacy boards of the Lausanne University Hospital CHUV, and the local ethics committee, in accordance with the Helsinki Declaration: CER-VD 2020-02204 for studies using skin samples, and CER-VD 2020-01257 for studies using post-mortem lungs. For COVID-19 skin samples, 10 consecutive patients presenting with moderate-to-severe COVID-19 disease and associated skin manifestations, hospitalized at CHUV from the beginning of the COVID pandemic in March 2020 were selected. All patients had positive PCR tests from nasal swab for SARS-CoV-2 and a clinical diagnosis of COVID-19.

Comprehensive information on comorbidities, immunosuppressive treatment, type of skin manifestation and time from first symptoms are given in Extended Data Fig. 1b. In addition, the maximal disease severity score, determined according to the NIH ordinal scale and Sequential Organ Failure Assessment (SOFA) is provided. The score is defined as (1) not hospitalized with no limitation of activities; (2) not hospitalized with limitation of activities and/or home oxygen requirement; (3) hospitalized but not requiring supplemental oxygen and no longer requiring ongoing medical care; (4) hospitalized and not requiring supplemental oxygen but requiring ongoing medical care; (5) hospitalized requiring supplemental oxygen; (6) hospitalized requiring non-invasive ventilation or the use of high-flow oxygen devices; (7) hospitalized receiving invasive mechanical ventilation or extracorporeal membrane oxygenation; and (8) death. Control skin samples included skin lesions from CLE ( $n = 11$ ), plaque-type psoriasis ( $n = 21$ ), atopic dermatitis ( $n = 16$ ), lichen planus ( $n = 5$ ) and healthy skin ( $n = 4$ ). All patient biopsies were taken after informed consent was obtained and clinical diagnosis of the disease was histologically confirmed.

For the lung studies, eight post-mortem examinations of patients who died from COVID-19 at CHUV since March 2020 were included. All patients had positive PCR-tests from nasal swabs for SARS-CoV-2 and a clinical diagnosis of COVID-19. Patient information including comorbidities, immunosuppressive treatment, type of DAD, duration of symptoms until death and days of mechanical ventilation are given in Extended Data Fig. 6 and in Berezowska et al.<sup>25</sup>.

## Assessment of the endotheliopathy index in skin lesions

For scoring the endotheliopathy in skin samples, the outer and inner diameters of the post-capillary vessels of the superficial and middle dermis were measured and the endothelial swelling index was calculated as the ratio of the two diameters.

## Mice

Twelve-to-sixteen-week-old female K18-hACE C57BL/6J transgenic mice (strain: 2B6.Cg-Tg(K18-ACE2)2Prlmn/J) were obtained from The Jackson Laboratory. Mice were housed in groups and fed standard chow diets. Mice were housed in groups of up to five mice per cage at 18 °C–24 °C ambient temperature with 40–60% humidity. Mice were maintained on a 12-h light–dark cycle from 06:00 to 18:00. Food and water were available ad libitum. Mice were administered  $1 \times 10^4$  PFU of SARS-CoV-2 by intranasal administration. Virus inoculations were performed under anaesthesia that was induced and maintained with ketamine hydrochloride and midazolam, and all efforts were made to minimize animal suffering. The cages were assigned randomly for vehicle and H-151 treatment groups after the SARS-CoV-2 infection, and the experimenter was not blinded afterwards. Mice intraperitoneally received daily either dimethyl sulfoxide (DMSO) as vehicle or 750 nmol H-151 in 200 µl PBS 5% Tween-80. Mice were euthanized on the indicated day and immediately dissected for transcardial perfusion with 20 ml ice-cold PBS. Lungs and brains were collected. Half of each lung lobe was fixed in 4% PFA for histological analysis, and the other half of the lobes was chopped and stored for further analysis. For the survival study, mice were administered SARS-CoV-2 by intranasal administration as described above. Mice were euthanized when they reach one of the humane end point criteria: (1) more than 25% weight loss; (2) paralysis; (3) severe dyspnea. Animal experiments were approved by the Service de la Consommation et des Affaires Vétérinaires of the canton of Vaud (Switzerland) and were performed in accordance with the respective legal regulations.

## Plaque-forming assay

Lung and brain of the mice were homogenized in Vero-E6 cell-culture medium (DMEM + 10% FBS + P/S). Homogenized mix was centrifuged at 400g for 10 min.

The supernatant was analysed for the viral content. Vero-E6 cells were seeded in a 12-well plate at a density of  $2.5 \times 10^5$  cells per well. Cells were washed with PBS and inoculated with viruses serially diluted in cell-culture medium. One hour after the infection, cells were washed with PBS, and overlaid with 0.8% Avicel (GP 3515) mixed at 1:1 with DMEM supplemented with 4% fetal bovine serum, 200 units ml<sup>-1</sup> penicillin and 200 µg ml<sup>-1</sup> streptomycin. After 72 h of incubation, the overlay was removed and cells were washed with PBS, fixed with 4% PFA and stained with crystal violet.

## Immunofluorescence and immunohistochemistry analysis

Formalin-fixed paraffin-embedded (FFPE) skin blocks were cut into 6-µm sections and placed on slides. Sections were first deparaffinized and rehydrated, then Heat-Induced Epitope Retrieval (HIER) was performed and sections were permeabilized with PBS 0.01% Triton. Samples were stained with primary antibodies (Supplementary Table 1) for 2 hours at room temperature. For immunofluorescence analysis, sections were then stained with fluorescently labelled secondary antibodies (Supplementary Table 1) for 30 min at room temperature. For immunohistochemistry, sections were stained with HRP-conjugated secondary antibodies followed by DAB staining and Mayer counterstaining. For RNA fluorescence in situ hybridization (FISH), *IFNB1* mRNA was detected in skin using RNAScope Multiplex Fluorescent V2 Assay following the manufacturer's instructions (Advanced Cell Diagnostics, Inc.). Co-staining of sections with mouse anti-human CD163 (Diagnostic Bio Systems) was performed as described above. Images were acquired with a Zeiss LSM 700 confocal microscope and analysed with Zen 2010 software. For cell quantification, slides were digitalized using the PANNORAMIC 250 Flash digital scanner (3DHISTECH Ltd) and cell types were quantified using the QuantCenter plug-in 2.2 of Caseviewer 2.4 software.

For LoC samples, the fixed LoCs were permeabilized with 0.1% Triton, 2% saponin and incubated with a blocking solution of 2% bovine serum albumin (BSA) for 1 h followed by overnight incubation with the primary antibody (1:100 dilution) in the blocking buffer at 4 °C. The chip was then incubated with secondary antibodies (1:300 dilution) for 1 h at room temperature. A list of the primary antibodies and concentrations used is included in Supplementary Table 1. F-actin was stained using Sir-Actin dye in the far-red (Spirochrome) at 1 µM for 30 min concurrently with Hoechst staining.

Mouse lungs were cut into 3-µm sections. The extent of lung inflammation was quantified as the average percentage of lung surface area in which the alveolar wall is thickened with at least 50% decreased airspace area and was assessed by two independent investigators using three lung sections per mouse. TUNEL staining was

performed using a commercially available kit (Promega) according to the manufacturer's instructions. Imaging was performed using the Zeiss Axioplan fluorescence microscope with the use of Axiovision software. Three fields were selected randomly from each lung piece. TUNEL-positive cells were quantified by automated counting performed by image analysis software (ImageJ).

## RNA extraction

Excised 4-mm skin biopsies were immediately snap-frozen in liquid nitrogen and stored at  $-80^{\circ}\text{C}$  until processing. RNA was isolated using the TRIzol/chloroform method and a tissue homogenizer (Thermo Fisher Scientific). All isolated RNA had an A260/A280 value  $\geq 1.7$  and RNA integrity was analysed on a Fragment analyser (Agilent). Mouse lung pieces were lysed in TRIzol (Thermo Fisher Scientific) and RNA was isolated according to the manufacturer's instructions. RNA from cells in lung-on-chip experiments was isolated by using the RNeasy Micro Kit (Qiagen) according to the manufacturer's instructions.

## NanoString analysis

mRNA expression of 600 targets was analysed with the nCounter Human Immunology V2 panel including 20 customized probes (Nanostring Technologies, Seattle, WA, USA) on the nCounter platform (Nanostring Technologies) using 100 ng of RNA per skin sample. This commercial panel was extensively validated in-house for accuracy, repeatability and reproducibility before analysing the study samples. A quality check was run for each sample before including it into the analysis. Data were normalized and analysed using either nSolver 4.0 (Nanostring Technologies) or ROSALIND (ROSALIND Inc., San Diego, CA). Housekeeping probes to be used for normalization are selected based on the geNorm algorithm as implemented in the NormqPCR R library<sup>49</sup>. Clustering of genes for the final heatmap of differentially expressed genes was done using the PAM (Partitioning Around Medoids) method using the fpc R library (<https://cran.r-project.org/web/packages/fpc/index.html>) that takes into consideration the direction and type of all signals on a pathway and the position, role and type of every gene. The z-scores of each gene were then calculated for the selected patients to generate heatmaps and determine specific classifiers.

## STING inhibition in skin explants

Six-millimetre skin biopsies from healthy individuals or patients with COVID-19 were cut into three equal pieces and one piece was snap-frozen to measure the baseline gene expression. The two remaining pieces were cultured in 200  $\mu\text{l}$  of DMEM 10% FBS, 1% penicillin–streptomycin in the presence or not of 0.5  $\mu\text{g ml}^{-1}$  of H-151 for 15 h.

Skin biopsies were then homogenized in TRIzol to perform RNA extraction followed by NanoString analysis as described above.

### **2'3'-cGAMP enzyme-linked immunosorbent assay**

Six-millimetre skin punch biopsies were lysed in Pierce RIPA Buffer using a tissue homogenizer (Thermo Fisher Scientific). Protease inhibitor cocktail (Sigma) was added to prevent protein degradation. Thirty micrograms of the lysate was used to measure 2'3'-cGAMP concentrations by enzyme-linked immunosorbent assay (ELISA) and according to the manufacturer's instructions (Cayman Chemical).

### **Ultrastructural analysis of the skin**

For transmission electron microscopy, the skin biopsies were fixed in 2% glutaraldehyde in 0.1M sodium cacodylate buffer, pH 7.4. Samples were then post-fixed in 1% OsO<sub>4</sub>/1.5% potassium ferrocyanide in aqua bidest for 2 h, block stained with uranyl acetate (2% in distilled water), dehydrated in alcohol (stepwise 50–100%), immersed in propylenoxide and embedded in glycidyl ether (polymerized 48 h at 60 °C; SERVA, Electrophoresis GmbH, Heidelberg, Germany). Semi-thin and ultra-thin sections were cut with an ultramicrotome (Ultracut, Reichert Inc., Vienna, Austria). Ultra-thin sections (30 nm) were mounted on copper grids and analysed on a Zeiss LIBRA 120 transmission electron microscope (Carl Zeiss, Oberkochen, Germany) operating at 120 kV.

### **RT-qPCR analysis**

For mouse lung samples, RNA was reverse-transcribed using the RevertAid First Strand cDNA Synthesis reagents (Thermo Fisher Scientific), and quantitative PCR with reverse transcription (RT-qPCR) was performed in duplicate using Maxima SYBR Green Master Mix (Thermo Fisher Scientific) on QuantStudio 6/7 qPCR instruments. For LoC samples, RNA was reverse-transcribed using the SuperScript IV First-Strand Synthesis System with random hexamers (Invitrogen), and RT-qPCR reactions were prepared with SYBR Green PCR Master Mix (Applied Biosystems) on the ABI PRISM 7900HT System (Applied Biosystems). Amplicon specificity was confirmed by melting-curve analysis. The primer sequences are listed in Supplementary Table 2.

### **Immunoblotting**

SDS-loading buffer was mixed with the lung lysates in RIPA buffer and denatured at 95 °C for 10 min. Lysates were separated by 10% SDS-PAGE and transferred onto nitrocellulose membranes. Blots were incubated with anti-p-p65 (Ser468) (1:1,000

dilution), and anti-p-STAT1 (Tyr 701) (1:1,000 dilution) (Cell Signaling) and anti- $\beta$ -actin-HRP (1:2,000 dilution) (Santa Cruz Biotechnology). Proteins were visualized with the enhanced chemiluminescence substrate ECL (Pierce, Thermo Fisher Scientific) and imaged using the ChemiDoc XRS Biorad Imager and Image Lab Software 5.1. Uncropped images are presented in [Supplementary Fig. 1](#).

## Primary human cell culture and culture of macrophage cell lines

Primary human alveolar epithelial cells (epithelial cells) and human lung microvascular endothelial cells (endothelial cells) were obtained from a commercial supplier (Cell Biologics). All chips were reconstituted with epithelial cells seeded directly on the LoC without any additional in vitro culture. Endothelial cells were passaged 3–5 times before seeding in the LoC devices. Experiments were performed with cells from at least two donors.

Peripheral blood mononuclear cells from buffy coat (Interregional Blood Transfusion SRC) were obtained from anonymized donors and isolated using a Biocol Separation procedure as per the manufacturer's instructions. One week before seeding the macrophages in the LoC devices, a cryopreserved aliquot was cultured in a T-75 flask (TPP) in RPMI supplemented with 10% FBS. CD14<sup>+</sup> monocytes were isolated using positive selection (CD14 ultrapure isolation kit, Miltenyi Biosciences), embedded in hemispherical domes of basement membrane extract (BME-2, Cultrex) in 24-well plates, and cultured in RPMI medium supplemented with 10% FBS, 20 ng ml<sup>-1</sup> recombinant human macrophage-colony stimulating factor protein (M-CSF) and 100 U l<sup>-1</sup> of penicillin–streptomycin solution (Thermo Fisher Scientific). The monocytes were differentiated for 7 days. On the day of seeding into the LoC, the BME domes were first disrupted by scraping with a P1000 pipette. The mechanically dissociated hydrogel was then brought to semi-liquid state by adding 500  $\mu$ l of ice cold RPMI medium per well. The BME-RPMI suspension was then centrifuged at 200g for 5 min in a 15-ml Falcon tube pre-coated with 1% BSA in PBS and resuspended in 4–5 ml of ice-cold Cell Recovery Solution (Corning) over ice for 20–30 min. Occasionally, the solution was sheared with a fire-polished glass pipette to ensure the complete removal of the macrophages from the BME hydrogel. The cell suspension was then washed twice with 10 ml of RPMI medium/10% FBS to remove remaining traces of the cell recovery reagent. If required, BME-2 suspension was sometimes incubated in 2–3 ml trypsin to remove remaining fragments of BME-2, and the washing step was repeated again. Isolated macrophages were resuspended in epithelial cell medium and passed through a 40- $\mu$ m filter to obtain a single-cell suspension of macrophages.

Wild-type and *cGAS*<sup>−/−</sup> THP-1 cells were cultured according to the suppliers' instructions. THP-1 cells were differentiated with 5 ng ml<sup>-1</sup> PMA for 3 days and transferred to the vascular channel of the LoC at 2 dpi.

## **Production of lentiviral vectors and transduction of primary epithelial and endothelial cells**

HEK-293T cells were a gift from the laboratory of D. Trono. HEK-293T cells were transfected with pCMVDR8.74, pMD2.G plasmids and the puromycin-selectable pLKO.1-puro lentiviral vector containing the shRNA for human STING (5'-CATGGTCATATTACATCGGAT-3') and human MAVS (5'-CAAGTTGCCAACTAGCTAAA-3') by the calcium phosphate precipitation method. The supernatant containing lentiviral particles was collected at 48 and 72 h, pooled and concentrated by ultracentrifugation. Primary endothelial cells (shRNA for STING and MAVS) and primary alveolar epithelial cells at passage 5 (shRNA for STING only) were transduced with the lentiviral vectors by directly adding 10 µl to the culture medium; transduced cells were selected by adding 1 µg ml<sup>-1</sup> puromycin to the medium 48 h after the transduction.

## **Generation of SARS-CoV-2 stocks**

VeroE6 cells and a clinical isolate of SARS-CoV-2 were a gift from the laboratory of C. Tapparel. SARS-CoV2/Switzerland/GE9586/2020 was isolated from a clinical specimen in the University Hospital in Geneva in Vero-E6 cells. Vero-E6 cells were infected and supernatant was collected at 3 dpi, clarified, aliquoted and frozen at -80 °C and subsequently titrated by plaque assay in Vero-E6. Viruses used for the LoC and animal experiments in this manuscript were at passage 2 and passage 4, respectively, in Vero-E6 cells.

## **Infection of the LoC model with SARS-CoV-2**

LoC devices were purchased from a commercial vendor (Emulate). For a small subset of experiments for RT-qPCR measurements in uninfected controls, devices fabricated in-house with similar dimensions (but without a stretching channel) using porous membranes supplied by a commercial vendor were used (BiOND). A detailed protocol for the establishment of the LoC model has been described previously<sup>24</sup>. In brief, devices were coated with ECM solution of 150 µg ml<sup>-1</sup> bovine collagen type I (AteloCell, Japan) and 30 µg ml<sup>-1</sup> fibronectin from human plasma (Sigma-Aldrich). For the three-component model with primary macrophages, differentiated primary human macrophages were seeded directly on the PDMS membrane 1–2 h before seeding of the endothelial cells on the basolateral side of the membrane and epithelial cells on the apical side. For experiments with ρ<sup>0</sup> endothelial cells, the endothelial cells were incubated with ddC for 3–5 days before infection. The chip was incubated overnight with complete epithelial and endothelial medium in the respective channels under static conditions. Thereafter, a reduced medium for the air–liquid interface

(ALI) was flowed through the vascular channel and the epithelial face was incubated with epithelial base medium supplemented with 1  $\mu$ M dexamethasone (Sigma-Aldrich). This medium was replaced daily for the following 2–3 days. Thereafter, the chips were maintained overnight at an ALI and then transferred to the biosafety level 3 (BSL-3) facility for SARS-CoV-2 infection. Here, an aliquot of virus-containing supernatant was diluted approximately 20-fold in epithelial cell medium without FBS to generate the inoculum that corresponded to an infectious dose of 400–600 PFU in a volume of 30  $\mu$ l. This volume was then added to the apical channel of each LoC, and the LoC was incubated for an hour at 37 °C and 5% CO<sub>2</sub>. Thereafter, the LoC was returned to ALI. For LoCs treated with the STING or the VDAC oligomerization inhibitor, H-151 (1  $\mu$ M) or VBIT-4 (1  $\mu$ M) was perfused through the vascular channel after infection and maintained over the course of 3 days. Infection was terminated at specified time points and the LoCs processed for RNA extraction or by fixation with freshly prepared 4% paraformaldehyde for a period of 30 min.

## Confocal imaging and image analysis of LoCs

Infected and control LoCs were imaged using a Leica SP8 confocal microscope with a white light laser. LoCs were imaged with a 25 $\times$  water immersion objective (NA = 0.95, Leica), with standard settings (voxel size 227.27  $\times$  227.27  $\times$  300 nm<sup>3</sup>) across chips labelled the same way. Z-stacks were subsequently deconvolved using the Huygens Deconvolution Software (Scientific Volume Imaging) and 3D views were rendered using Imaris (Bitplane). Maximum intensity projects were rendered using ImageJ. The following parameters were used for generation of the surfaces in Imaris for the visualization of IFN $\beta$ , cleaved caspase-3, macrophages and p-STING. In each case, uninfected control chips and/or infected chips and/or treated chips from the same experiment were immunostained and imaged together, to control for differences in the immunofluorescence intensities across antibody aliquots, imaging conditions, and microscopes. Chips from the same experiment were analysed using the same Imaris parameters. Three-cell component chips in Fig. 3b, Extended Data Fig. 6b, IFN $\beta$ : manual threshold: 110, smoothing: 0.455  $\mu$ m. Three-cell component chips in Extended Data Fig. 6d, IFN $\beta$ : manual threshold: 110, smoothing: 0.455  $\mu$ m. Two-cell component chips in Fig. 3c, Extended Data Fig. 7b, IFN $\beta$ : manual threshold: 45, smoothing: 0.455  $\mu$ m. Three-cell component chips in Extended Data Fig. 6e, cleaved caspase-3: manual threshold: 110, smoothing: 0.8  $\mu$ m. Two-cell component chips in Fig. 3c, cleaved caspase-3: manual threshold: 110, smoothing: 0.8  $\mu$ m. Two-cell component chips in Fig. 3d., p-STING: manual threshold: 110, smoothing: 0.8  $\mu$ m. Three-cell component chips in Fig 3b, CD45: manual threshold: 110, smoothing: 1  $\mu$ m. Two-cell component chips in Fig. 3g, Extended Data Fig. 8d, IFN $\beta$ ; manual threshold: 30; smoothing: 0.455  $\mu$ m.

## Sample preparation for proteomic analysis

Cells from the vascular and apical faces of the LoC devices were extracted in a sequential manner by instillation of 0.25% Trypsin-EDTA solution (Gibco) in the vascular channel followed by the apical channel. Cells were centrifuged at 300g for 5 min and washed twice with PBS solution to eliminate extracellular matrix components. Pelleted cells were then resuspended in a 20- $\mu$ l solution of 100 mM HEPES pH 8 and 5 mM tris(2-carboxyethyl)phosphine and heat-inactivated at 95 °C for 10 min before removal from the BSL-3 facility, and stored at –20 °C for subsequent processing at the Proteomics Core Facility. Here cells were vacuum-centrifuged to near dryness and resuspended in 9  $\mu$ l of 100 mM HEPES pH 8 and 10 mM tris(2-carboxyethyl)phosphine. Samples were first heated for 20 min at 95 °C with permanent shaking and then sonicated in a water bath for 15 min. Extracted proteins were alkylated with 1  $\mu$ l of 400 mM chloroacetamide for 30 min at 37 °C in the dark with permanent shaking. Proteins were digested overnight using 400 ng mass spectrometry grade trypsin with permanent shaking. The resulting peptides were desalted on C18 StageTips<sup>50</sup> and dried by vacuum centrifugation. Peptides were reconstituted in 8  $\mu$ l HEPES 100 mM pH 8 and labelled with 3  $\mu$ l of isobaric tags (TMT 20  $\mu$ g  $\mu$ l<sup>–1</sup> in pure acetonitrile) for 90 min at room temperature. The labelling reaction was stopped with addition of 50% hydroxylamine (final concentration 0.4% (v/v)) for 15 min. A small fraction of the labelled peptides was mixed in a 1:1 ratio across all samples and analysed with a single shot control liquid chromatography–tandem mass spectrometry (LC–MS/MS) run to evaluate the mixing accuracy. On the basis of the results of this control run, the remaining labelled peptides were mixed in equal amounts, vacuum-centrifuged and fractionated into eight fractions using the Pierce High pH Reversed-Phase Peptide Fractionation Kit following the manufacturer’s instructions. The eight fractions were dried by vacuum centrifugation and stored at –20 °C.

## Mass spectrometry

Peptides were resuspended in 2% acetonitrile, 0.1% FA and analysed on a Lumos Fusion Orbitrap Mass Spectrometer online connected to a Dionex Ultimate 3000 RSLC nano UPLC system. A capillary precolumn (Acclaim Pepmap C18, 3  $\mu$ m 100 Å, 2 cm × 75  $\mu$ m inner diameter) was used for sample trapping and cleaning. Analytical separations were performed at 250 nl min<sup>–1</sup> over 150-min biphasic gradients on a 50-cm-long in-house packed capillary column (75  $\mu$ m inner diameter, ReproSil-Pur C18-AQ 1.9  $\mu$ m silica beads, Dr. Maisch). Acquisitions were performed through the top speed data-dependent acquisition mode using a 3 s cycle time. First MS scans were acquired at a resolution of 120,000 (at 200 *m/z*) and the most intense parent ions were selected and fragmented by high energy collision dissociation (HCD) with a normalized collision energy (NCE) of 37.5% using an isolation window of 0.7 *m/z*. Fragmented ion scans were acquired with a resolution of 50,000 (at 200 *m/z*) and selected ions were then excluded for the following 120s.

## Mass spectrometry data analysis

Raw data were processed using SEQUEST, Mascot, MS Amanda<sup>51</sup> and MS Fragger<sup>52</sup> in Proteome Discoverer v.2.4 against a concatenated database consisting of the Uniprot human reference proteome (release 2020\_10) and Uniprot SARS-CoV-2 reference proteome (release 2020\_10). Enzyme specificity was set to trypsin and a minimum of six amino acids was required for peptide identification. Up to two missed cleavages were allowed and a 1% false discovery rate (FDR) cut-off was applied both at peptide and at protein identification levels. For the database search, carbamidomethylation (C) and TMT tags (K and peptide N termini) were set as fixed modifications whereas oxidation (M) was considered as a variable. The resulting text files were processed through in-house written R scripts (v.3.6.3). Two steps of normalization were applied: sample loading (SL) and trimmed mean of M-values (TMM) normalization. The SL normalization<sup>53</sup> assumes that total protein abundances are equal across the TMT channels; therefore, the reporter ion intensities of all spectra were summed and each channel was scaled according to this sum, so that the sum of reporter ion signals per channel equals the average of the signals across samples. Subsequently, the TMM normalization step was applied using the package EdgeR (v.3.26.8)<sup>54</sup>. This normalization step works on the assumption that most of the protein abundances do not change across samples therefore, it calculates normalization factors according to these presumed unchanged protein abundances. Differential protein expression analysis was performed using the R bioconductor package limma (v.3.40.6, 2020-02-29)<sup>55</sup>, followed by the Benjamini–Hochberg multiple-testing method<sup>56</sup>.  $P$  values lower than 0.00128 (FDR < 0.05) and absolute  $\log_2$ -transformed fold change ( $\log_2\text{FC}$ ) > 0.5 were considered as significant. For the time-course study, all quantified proteins were monitored. The significant temporal dynamics were defined with the timecourse package in R Bioconductor, which uses a multivariate empirical Bayes model to rank proteins<sup>57</sup>. Replicate time-course data can be compared allowing for variability both within and between time points. The mb.long method was used to calculate the moderated Hotelling  $T^2$  statistic, specifying a one-dimensional method (method = “1D”), in which significant proteins change over the time course. The null hypothesis is that the protein temporal profile is equal to 0.

## Statistics and reproducibility

Statistical analyses are described in each figure legend. For experiments combining several groups, an ordinary one-way ANOVA test was used. Statistical significance was determined using Prism v.8.0 software (GraphPad). Significant differences between groups were determined by post-hoc Tukey’s multiple comparisons tests, unless specified otherwise,  $P > 0.05$  was considered non-significant. The Student’s  $t$ -test or the Mann–Whitney test was used to assess the  $P$  value when comparing only

two groups. For LoC studies, fields of view from a given LoC are considered as biological replicates, and the number of LoCs corresponds to the number of times the experiment was repeated. Images of p-STING<sup>+</sup> endothelial cells in Fig. 3d are from  $n = 2$  fields of view from  $n = 1$  LoC. Data of mitochondria with loss of cristae morphology are representative slices from volumetric electron microscopy imaging of  $n = 4$  endothelial cells from  $n = 2$  infected LoCs. Data from patient samples were obtained from  $n = 3$  independent experiments and quantifications for histological analysis were performed by  $n = 2$  independent investigators.

## Reporting summary

Further information on research design is available in the [Nature Research Reporting Summary](#) linked to this paper.

## Data availability

Full scans for all western blots and the in-gel fluorescence images are provided in Supplementary Fig. 1 and the limma and timecourse analyses of the proteomics data are provided in Supplementary Table 3. Raw data supporting the findings of this study have been deposited at Zenodo and are publicly available at <https://doi.org/10.5281/zenodo.5818157>. The proteomics dataset generated during this study has been deposited in the PRIDE database with accession code PXD030753. The NanoString dataset generated during this study has been deposited at the Gene Expression Omnibus (GEO) database with accession code [GSE193068](#). Source data are provided with this paper.

## Code availability

Custom scripts in R for the analysis of proteomics data have been deposited at Zenodo and are publicly available at <https://doi.org/10.5281/zenodo.5818157>.

## References

1. Huang, C. et al. Clinical features of patients infected with 2019 novel coronavirus in Wuhan, China. *Lancet* **395**, 497–506 (2020).
2. Gupta, A. et al. Extrapulmonary manifestations of COVID-19. *Nat. Med.* **26**, 1017–1032 (2020).
3. Lucas, C. et al. Longitudinal analyses reveal immunological misfiring in severe COVID-19. *Nature* **584**, 463–469 (2020).

4. Nienhold, R. et al. Two distinct immunopathological profiles in autopsy lungs of COVID-19. *Nat. Commun.* **11**, 5086 (2020).
5. Park, A. & Iwasaki, A. Type I and type III interferons—induction, signaling, evasion, and application to combat COVID-19. *Cell Host Microbe* **27**, 870–878 (2020).
6. Lee, J. S. & Shin, E.-C. The type I interferon response in COVID-19: implications for treatment. *Nat. Rev. Immunol.* **20**, 585–586 (2020).
7. Hadjadj, J. et al. Impaired type I interferon activity and inflammatory responses in severe COVID-19 patients. *Science* **369**, 718–724 (2020).
8. Chua, R. L. et al. COVID-19 severity correlates with airway epithelium–immune cell interactions identified by single-cell analysis. *Nat. Biotechnol.* **38**, 970–979 (2020).
9. Zhou, Z. et al. Heightened innate immune responses in the respiratory tract of COVID-19 patients. *Cell Host Microbe* **27**, 883–890 (2020).
10. Wilk, A. J. et al. A single-cell atlas of the peripheral immune response in patients with severe COVID-19. *Nat. Med.* **26**, 1070–1076 (2020).
11. Lee, J. S. et al. Immunophenotyping of COVID-19 and influenza highlights the role of type I interferons in development of severe COVID-19. *Sci. Immunol.* **5**, eabd1554 (2020).
12. Schulte-Schrepping, J. et al. Severe COVID-19 is marked by a dysregulated myeloid cell compartment. *Cell* **182**, 1419–1440 (2020).
13. Galani, I.-E. et al. Untuned antiviral immunity in COVID-19 revealed by temporal type I/III interferon patterns and flu comparison. *Nat. Immunol.* **22**, 32–40 (2021).
14. Wolfel, R. et al. Virological assessment of hospitalized patients with COVID-2019. *Nature* **581**, 465–469 (2020).
15. Wang, N. et al. Retrospective multicenter cohort study shows early interferon therapy is associated with favorable clinical responses in COVID-19 patients. *Cell Host Microbe* **28**, 455–464 (2020).
16. Israelow, B. et al. Mouse model of SARS-CoV-2 reveals inflammatory role of type I interferon signaling. *J. Exp. Med.* **217**, e20201241 (2020).

17. Liao, M. et al. Single-cell landscape of bronchoalveolar immune cells in patients with COVID-19. *Nat. Med.* **26**, 842–844 (2020).
18. Ablasser, A. & Chen, Z. J. cGAS in action: expanding roles in immunity and inflammation. *Science* **363**, eaat8657 (2019).
19. Farber, D. L. Tissues, not blood, are where immune cells function. *Nature* **593**, 506–509 (2021).
20. Freeman, E. E. et al. The spectrum of COVID-19-associated dermatologic manifestations: an international registry of 716 patients from 31 countries. *J. Am. Acad. Dermatol.* **83**, 1118–1129 (2020).
21. Goshua, G. et al. Endotheliopathy in COVID-19-associated coagulopathy: evidence from a single-centre, cross-sectional study. *Lancet Haematol.* **7**, e575–e582 (2020).
22. Bonaventura, A. et al. Endothelial dysfunction and immunothrombosis as key pathogenic mechanisms in COVID-19. *Nat. Rev. Immunol.* **21**, 319–329 (2021).
23. Liu, S. et al. Phosphorylation of innate immune adaptor proteins MAVS, STING, and TRIF induces IRF3 activation. *Science* **347**, aaa2630 (2015).
24. Haag, S. M. et al. Targeting STING with covalent small-molecule inhibitors. *Nature* **559**, 269–273 (2018).
25. Berezowska, S. et al. Postmortem cardiopulmonary pathology in patients with COVID-19 infection: single-center report of 12 autopsies from Lausanne, Switzerland. *Diagnostics* **11**, 1357 (2021).
26. Varga, Z. et al. Endothelial cell infection and endotheliitis in COVID-19. *Lancet* **395**, 1417–1418 (2020).
27. Thacker, V. V. et al. Rapid endotheliitis and vascular damage characterize SARS-CoV-2 infection in a human lung-on-chip model. *EMBO Rep.* **22**, e52744 (2021).
28. Nascimento Conde, J., Schutt, W. R., Gorbunova, E. E. & Mackow, E. R. Recombinant ACE2 expression is required for SARS-CoV-2 to infect primary human endothelial cells and induce inflammatory and procoagulative responses. *mBio* **11**, e03185–20 (2020).
29. Kim, J. et al. VDAC oligomers form mitochondrial pores to release mtDNA fragments and promote lupus-like disease. *Science* **366**, 1531–1536 (2019).

30. Stukalov, A. et al. Multilevel proteomics reveals host perturbations by SARS-CoV-2 and SARS-CoV. *Nature* **594**, 246–252 (2021).
31. Gibellini, L. et al. Altered bioenergetics and mitochondrial dysfunction of monocytes in patients with COVID-19 pneumonia. *EMBO Mol. Med.* **12**, e13001 (2020).
32. Winkler, E. S. et al. SARS-CoV-2 infection of human ACE2-transgenic mice causes severe lung inflammation and impaired function. *Nat. Immunol.* **21**, 1327–1335 (2020).
33. McCray, P. B. Jr. et al. Lethal infection of K18-hACE2 mice infected with severe acute respiratory syndrome coronavirus. *J. Virol.* **81**, 813–821 (2007).
34. Bao, L. et al. The pathogenicity of SARS-CoV-2 in hACE2 transgenic mice. *Nature* **583**, 830–833 (2020).
35. Golden, J. W. et al. Human angiotensin-converting enzyme 2 transgenic mice infected with SARS-CoV-2 develop severe and fatal respiratory disease. *JCI Insight* **5**, e142032 (2020).
36. Muñoz-Fontela, C. et al. Animal models for COVID-19. *Nature* **586**, 509–515 (2020).
37. Liu, Y. et al. Activated STING in a vascular and pulmonary syndrome. *N. Engl. J. Med.* **371**, 507–518 (2014).
38. Prantner, D. et al. 5,6-Dimethylxanthenone-4-acetic acid (DMXAA) activates stimulator of interferon gene (STING)-dependent innate immune pathways and is regulated by mitochondrial membrane potential. *J. Biol. Chem.* **287**, 39776–39788 (2012).
39. Neufeldt, C. J. et al. SARS-CoV-2 infection induces a pro-inflammatory cytokine response through cGAS-STING and NF-κB. *Commun. Biol.* **5**, 45 (2022).
40. Teuwen, L.-A., Geldhof, V., Pasut, A. & Carmeliet, P. COVID-19: the vasculature unleashed. *Nat. Rev. Immunol.* **20**, 389–391 (2020).
41. Channappanavar, R. et al. Dysregulated type I interferon and inflammatory monocyte–macrophage responses cause lethal pneumonia in SARS-CoV-infected mice. *Cell Host Microbe* **19**, 181–193 (2016).
42. Cameron, M. J. et al. Interferon-mediated immunopathological events are associated with atypical innate and adaptive immune responses in patients with

- severe acute respiratory syndrome. *J. Virol.* **81**, 8692–8706 (2007).
43. Zhang, Q. et al. Inborn errors of type I IFN immunity in patients with life-threatening COVID-19. *Science* **370**, eabd4570 (2020).
  44. Yang, D. M., Geng, T. T., Harrison, A. G. & Wang, P.-H. Differential roles of RIG-I-like receptors in SARS-CoV-2 infection. *Military Med. Res.* **8**, 49 (2021).
  45. Mazaleuskaya, L., Veltrop, R., Ikpeze, N., Martin-Garcia, J. & Navas-Martin, S. Protective role of Toll-like receptor 3-induced type I interferon in murine coronavirus infection of macrophages. *Viruses* **4**, 901–923 (2012).
  46. van der Made, C. I. et al. Presence of genetic variants among young men with severe COVID-19. *JAMA* **324**, 663–673 (2020).
  47. Asano, T. et al. X-linked recessive TLR7 deficiency in ~1% of men under 60 years old with life-threatening COVID-19. *Sci. Immunol.* **6**, eabl4348 (2021).
  48. Xie, J. et al. Dampened STING-dependent interferon activation in bats. *Cell Host Microbe* **23**, 297–301 (2018).
  49. Perkins, J. R. et al. ReadqPCR and NormqPCR: R packages for the reading, quality checking and normalisation of RT–qPCR quantification cycle (Cq) data. *BMC Genomics* **13**, 296 (2012).
  50. Rappsilber, J., Mann, M. & Ishihama, Y. Protocol for micro-purification, enrichment, pre-fractionation and storage of peptides for proteomics using StageTips. *Nat. Protoc.* **2**, 1896–1906 (2007).
  51. Dorfer, V. et al. MS Amanda, a universal identification algorithm optimized for high accuracy tandem mass spectra. *J. Proteome Res.* **13**, 3679–3684 (2014).
  52. Kong, A. T., Leprevost, F. V., Avtonomov, D. M., Mellacheruvu, D. & Nesvizhskii, A. I. MSFragger: ultrafast and comprehensive peptide identification in mass spectrometry-based proteomics. *Nat. Methods* **14**, 513–520 (2017).
  53. Plubell, D. L. et al. Extended multiplexing of tandem mass tags (TMT) labeling reveals age and high fat diet specific proteome changes in mouse epididymal adipose tissue. *Mol. Cell Proteomics* **16**, 873–890 (2017).
  54. Robinson, M. D., McCarthy, D. J. & Smyth, G. K. edgeR: a Bioconductor package for differential expression analysis of digital gene expression data. *Bioinformatics* **26**, 139–140 (2010).

55. Ritchie, M. E. et al. limma powers differential expression analyses for RNA-sequencing and microarray studies. *Nucleic Acids Res.* **43**, e47 (2015).
56. Klipper-Aurbach, Y. et al. Mathematical formulae for the prediction of the residual beta cell function during the first two years of disease in children and adolescents with insulin-dependent diabetes mellitus. *Med. Hypotheses* **45**, 486–490 (1995).
57. Tai, Y. C. & Speed, T. P. A multivariate empirical Bayes statistic for replicated microarray time course data. *Ann. Statist.* **34**, 2387–2412 (2006).

## Acknowledgements

We thank the Genomic Technologies Facility (GTF) at University of Lausanne (UNIL) and the Immune Landscape Laboratory (Oncology department, CHUV) for accessing the NanoString platform; A. Jonicic and I. Surbeck for technical assistance with the histological analysis; B. Fehrenbacher for technical assistance with transmission electron microscopy studies of COVID-19 skin samples; J. Blanc and G. Knott for technical assistance with serial block scanning electron microscopy of LoC devices and data analysis and volumetric reconstruction; R. Hamelin, F. Armand and M. Pavlou for technical assistance for the proteomic analysis studies in the LoC devices; F. Signorino-Gelo for LoC device fabrication; and N. Samson for help with BioRender. This work was supported by the COVID-19 National Research Program (NRP-78) to M.G. and A.A. (4078P0\_198470) with additional support by the Leenaards Foundation to M.G. and A.A. and the Fondation Acteria and European Union’s Horizon 2020 Research and Innovation program grant agreement (grant no. 804933, ImAgine) to A.A. V.V.T. received support from the Novartis Foundation for Medical-Biological Research (grant no. 20C240).

## Author information

### Author notes

1. These authors contributed equally: Jeremy Di Domizio, Muhammet F. Gulen, Fanny Saidoune, Vivek V. Thacker, Ahmad Yatim
2. These authors jointly supervised this work: Michel Gilliet, Andrea Ablasser

## Affiliations

1. Department of Dermatology, CHUV University Hospital and University of Lausanne (UNIL), Lausanne, Switzerland

Jeremy Di Domizio, Fanny Saidoune, Ahmad Yatim, Emmanuella Guenova, Curdin Conrad & Michel Gilliet

2. Global Health Institute, Swiss Federal Institute of Technology Lausanne (EPFL), Lausanne, Switzerland

Muhammet F. Gulen, Vivek V. Thacker, Kunal Sharma, Théo Nass & Andrea Ablasser

3. University Department of Dermatology, Eberhard Karls University of Tübingen, Tübingen, Germany

Martin Schaller

4. Institute of Animal Pathology, COMPATH, University of Bern, Bern, Switzerland

Christine Goepfert

5. Histology Core Facility, Swiss Federal Institute of Technology Lausanne (EPFL), Lausanne, Switzerland

Christine Goepfert

6. Institute of Pathology, CHUV University Hospital and University of Lausanne (UNIL), Lausanne, Switzerland

Laurence de Leval & Sabina Berezowska

7. Division of Pulmonology, CHUV University Hospital and University of Lausanne (UNIL), Lausanne, Switzerland

Christophe von Garnier

8. Biological Electron Microscopy Facility, Swiss Federal Institute of Technology Lausanne (EPFL), Lausanne, Switzerland

Anaëlle Dubois

## Contributions

J.D.D., F.S. and A.Y. conducted the experiments and associated analysis involving human tissues. A.Y., C.C. and M.G. selected patients and provided skin samples. C.v.G., L.d.L. and S.B. provided post-mortem lung samples. E.G. and M.S. performed electron microscopy analysis of COVID-19 skin lesions. V.V.T., M.F.G., K.S. and T.N.

conducted in vitro LoC cell culture studies and the associated analysis. A.D. performed electron microscopy analysis of the LoC devices. M.F.G. performed the animal study and associated analysis and C.G. helped with the histopathological analysis. M.G. and A.A conceived and supervised the work and wrote the manuscript with comments from co-authors.

## Corresponding authors

Correspondence to [Michel Gilliet](#) or [Andrea Ablasser](#).

## Ethics declarations

## Competing interests

A.A. is a scientific co-founder of IFM Due. The other authors declare no competing interests.

## Peer review

### Peer review information

*Nature* thanks Zhijian (James) Chen, Michael Matthay, Stanley Perlman and the other, anonymous, reviewer(s) for their contribution to the peer review of this work.

## Additional information

**Publisher's note** Springer Nature remains neutral with regard to jurisdictional claims in published maps and institutional affiliations.

## Extended data figures and tables

### [Extended Data Fig. 1 Clinical characteristics of patients with COVID-19 with associated skin manifestations.](#)

**a**, Photographs of the skin lesions. **b**, Clinical parameters and demographics of the 10 patients with COVID-19 selected for this study. HRD, Heart Rhythm Disorder; Overweight ( $BMI > 25 \text{ kg/m}^2$ , but  $< 30 \text{ kg/m}^2$ ); COPD, chronic obstructive pulmonary disease; CKD, chronic kidney disease; DM, diabetes mellitus; AIH, autoimmune hepatitis.

## Extended Data Fig. 2 Immune gene expression profiling of COVID-19 skin lesions and common inflammatory skin diseases.

**a**, Immune gene expression profiles of patients with lichen planus ( $n = 5$ ), cutaneous lupus erythematosus (CLE,  $n = 10$ ), COVID-19 associated skin lesions ( $n = 10$ ), plaque-type psoriasis ( $n = 21$ ), and atopic dermatitis (AD,  $n = 16$ ) compared to healthy skin (HD,  $n = 4$ ) assessed by NanoString assay. Differentially expressed genes between different pairwise comparisons (i.e. each disease group vs other skin inflammatory diseases) were used to generate disease-related gene signatures.  $P$  value  $< 0.05$ , and fold change  $> 2$  were used as cutoffs to choose specific classifiers. **b**, Volcano plot of upregulated genes in COVID-19 compared with CLE skin lesions.

[Source data](#)

## Extended Data Fig. 3 Macrophages accumulate around vessels exhibiting prominent endotheliopathy in COVID-19 skin lesions.

**a**, Confocal microscopy images of CD3<sup>+</sup> T cells, CD123<sup>+</sup> plasmacytoid dendritic cells, MPO<sup>+</sup> neutrophils, and CD163<sup>+</sup> macrophages in skin lesions from CLE (top row) and COVID-19 (bottom row). Images are representative of 10 patients with COVID-19 and 5 patients with CLE. **b**, Percentages of CD163<sup>+</sup> macrophages present at different distances from blood vessel in COVID-19 skin lesions ( $n = 9$ ). **c**, Representative histopathology image of a dermal blood vessel in COVID-19 skin lesions (H&E stain). Blood vessel, dashed line. **d**, Endothelial cell swelling index, a measure of endotheliopathy, quantified in COVID-19 ( $n = 10$ ) and CLE skin lesions ( $n = 6$ ).  $P$  values were obtained with one-way ANOVA followed by Tukey's multiple comparison test (**b**) and two-tailed Student's *t*-test (**d**).

[Source data](#)

## Extended Data Fig. 4 Perivascular macrophages engulf dying cells.

**a, b**, Confocal microscopy images of representative COVID-19 skin lesion stained for CD163 (green), cleaved caspase-3 (red) and DNA (DAPI). Images are representative of 10 patients with COVID-19. Blood vessel, dashed line.

## Extended Data Fig. 5 Patient characteristics and histopathological analyses of a post-mortem COVID-19-affected lung.

**a**, Representative histopathology image of a COVID-19 lung in the early phase of DAD with extensive hyaline membranes (left) or in the late phase of DAD with

fibrosis obliterating the alveolar lumina (right) (H&E stain). Arrows indicate hyaline membranes. **b**, Clinical parameters of the 8 patients with COVID-19 selected for the study. HC, hydroxychloroquine; Phase of the diffuse alveolar damage defined based on pure presence of hyaline membranes (exudative) or fibrotic changes (proliferative); \* limit of detection is 20.8 copies per reaction (c/r) for RdRp gene, and 5.4 c/r for E gene; \*\* spike and nucleocapsid antibody; MxA-staining defined as high (>50% cells with intermediate to strong positive staining), or low (< 50%). **c**, Confocal microscopy images of representative COVID-19 lung section stained for CD31 (green) and p-STING (red). Arrow indicates an endothelial cell with activated STING. **d**, Proportions of CD163<sup>+</sup> macrophages and CD31<sup>+</sup> endothelial cells among p-STING<sup>+</sup> cells in COVID-19 lungs ( $n = 4$ ).

[Source data](#)

### [Extended Data Fig. 6 Responses from distinct cell types after SARS-CoV-2 infection in the LoC system.](#)

**a**, mRNA expression levels of SARS-CoV-2 *N* gene in epithelial and endothelial cells at 3 dpi in 2-cell component LoCs. **b**, Representative 3D views of the airway surface of a LoC infected with SARS-CoV-2 at 3 dpi. Areas with high levels of IFN $\beta$  (bright pink) are shown as surfaces. Macrophage surfaces are depicted in green, and nuclear labelling in purple. **c**, mRNA expression levels of indicated genes in the epithelial cells at 3 dpi in uninfected ( $n = 3$ ), infected ( $n = 5$ ), and H-151-treated ( $n = 5$ ) 2-cell component LoCs. **d**, Representative 3D views of the vascular face from uninfected and infected LoCs; PMA-activated WT and *cGAS*<sup>-/-</sup> THP-1 cells were added to vascular layer 2 days after infection. LoCs were analysed at 3 dpi by quantifying the total volume with high IFN $\beta$  expression/volume with high IFN $\beta$  expression within macrophages from uninfected ( $n = 6$ /  $n = 4$  fields of view), infected chips with WT THP-1 cells added ( $n = 9$ /  $n = 6$  fields of view) and infected chips with *cGAS*<sup>-/-</sup> THP-1 cells added ( $n = 6$ /  $n = 5$  fields of view) across  $n = 2$  LoCs in each case. **e**, Representative 3D views of the vascular face from uninfected and infected 3-component LoCs; volumes with high levels of cleaved caspase-3 (amber) are shown as surfaces. Quantification of the total volume with high cleaved caspase-3 expression from uninfected ( $n = 3$  fields of view) and infected ( $n = 5$  fields of view) from  $n = 1$  LoC in each case. ‘3C’ refers to 3-cell component (epithelial cells, endothelial cells, and macrophages) LoCs. Bars represent mean  $\pm$  s.e.m.; *P* values were calculated by a two-tailed Mann–Whitney test (**a**) or one-way ANOVA followed by Tukey’s multiple comparison tests (**c**, **d**).

[Source data](#)

## Extended Data Fig. 7 Effect of innate immune sensors on endothelial cell response after SARS-CoV-2 infection in the LoC model.

**a**, Representative images of the epithelial and endothelial cells on LoC infected with SARS-CoV-2 at 3 dpi (above). Western blot characterization of STING expression in epithelial and endothelial cells treated with control (ctrl) and STING shRNAs (below, left). Modal value of CD31 expression in the endothelial layer of LoCs reconstituted with control or STING shRNA treated epithelial or endothelial cells (below, right). Each data point was calculated from a maximum intensity projection of CD31 expression from  $n = 7$  (sh Ctrl - epithelial/sh STING - endothelial),  $n = 8$  (sh Ctrl – epithelial/sh Ctrl – endothelial and sh STING – epithelial/sh Ctrl – endothelial) and  $n = 9$  (sh STING – epithelial/sh STING = endothelial) fields of view from  $n = 1$  LoC in each case. **b**, Representative 3D views at 3 dpi of the vascular surface of a LoCs reconstituted with endothelial cells treated with ctrl or MAVS shRNA and infected with SARS-CoV-2. Volumes with high levels of IFN $\beta$  (bright pink) are shown as surfaces. Quantification of the volume with high IFN $\beta$  expression from ctrl ( $n = 5$  fields of view) and MAVS shRNA ( $n = 4$  fields of view) from  $n = 1$  LoC in each case. Reduction of MAVS mRNA in endothelial cells after shRNA transduction (right). ‘2C’ refers to 2-cell component (epithelial cells, endothelial cells) LoCs. Bars represent mean  $\pm$  s.e.m.;  $P$  values were calculated by a one-way ANOVA test followed by Tukey multiple comparison tests (**a**) or a two-tailed Mann–Whitney test (**b**). For gel source data, see Supplementary Fig. 1.

[Source data](#)

## Extended Data Fig. 8 Disruption of mitochondrial homeostasis in endothelial cells after SARS-CoV-2 infection.

**a**, Functional interactions between proteins with significantly altered expression identified by a pairwise analysis depicted via an interaction network generated from StringDB and clustered with the MCL algorithm. Functional annotations (GO Biological Processes/ KEGG pathways) relevant to mitochondrial function are indicated. **b**, Heat map of data from mitochondrial proteins with significantly altered expression identified via a time-course analysis. **c**, **d**, Serial block scanning electron microscope image of endothelial cells in LoC system (**c**) or transmission electron microscopy image of endothelial cells in COVID-19 skin lesion (**d**). Arrows indicate damaged mitochondria with loss of cristae morphology with a magnified inset at bottom right. As control, arrowhead indicates an intact mitochondrion with a magnified inset at top right. **e**, Representative 3D views at 3 dpi of the vascular surface of a LoCs reconstituted with endothelial cells treated or untreated with 20  $\mu$ M ddC for 7 days in total and infected with SARS-CoV-2. Total mtDNA in endothelial cells was quantified by qPCR (right). Volumes with high levels of IFN $\beta$  (bright pink) are shown

as surfaces. Quantification of the volume with high IFN $\beta$  expression from infected ( $n = 11$  fields of view) and ddC treated infected ( $n = 8$  fields of view) from  $n = 1$  and  $n = 2$  LoCs respectively. ‘2C’ refers to 2-cell component (epithelial cells, endothelial cells) LoCs. Bars represent mean  $\pm$  s.e.m.;  $P$  values were calculated by a two-tailed Mann–Whitney test (e).

[Source data](#)

**Extended Data Fig. 9 Prophylactic STING inhibition reduces pathology and inflammatory gene expression in the late stages of SARS-CoV-2 infection.**

**a–d**, Mice were infected with SARS-CoV-2 infection (intranasal;  $1 \times 10^4$  PFU/mouse) and intraperitoneal administration of vehicle or H-151 was started at 1 day prior to infection. TUNEL assay performed on the infected lung sections collected at 3 or 6 dpi is shown (a). mRNA levels of indicated genes isolated from uninfected and infected mouse lungs at 6 dpi were analysed by RT–qPCR (b). Tissue lysates from the lungs were subjected to Western blotting (c). Viral burden in the lungs and brains was analysed at 6 dpi by plaque assay for infectious virus (d). Numbers are for a and b uninfected ( $n = 4$ ), day 3 samples ( $n = 4$ ), day 6 samples ( $n = 7$ ); for d, uninfected ( $n = 4$ ) and infected ( $n = 5$ ). Throughout the figure, bars represent mean  $\pm$  s.e.m.;  $P$  values were calculated by one-way ANOVA followed by Tukey multiple comparison tests. For gel source data, see Supplementary Fig. 1.

[Source data](#)

**Extended Data Fig. 10 Therapeutic inhibition of STING reduces pathology and inflammatory gene expression after SARS-CoV-2 infection.**

**a, b**, Mice were infected with SARS-CoV-2 infection (intranasal;  $1 \times 10^4$  PFU per mouse) and intraperitoneal administration of vehicle or H-151 was started at 2 dpi. mRNA was isolated from uninfected and infected mouse lungs and relative expression of indicated genes were analysed by RT–qPCR (a). Viral burden in the lungs and brains was analysed at 6 dpi by plaque assay for infectious virus (b). **c**, Model of the involvement of the cGAS–STING pathway in severe SARS-CoV-2 infection created with biorender.com. Numbers are uninfected ( $n = 4$ ), infected ( $n = 5$ ) (a, b). Throughout the figure, bars represent mean  $\pm$  s.e.m.;  $P$  values were calculated by one-way ANOVA followed by Tukey multiple comparison tests.

[Source data](#)

# **Supplementary information**

## **Supplementary Figure 1**

This file contains full scans for all western blots and the in-gel fluorescence images, in Supplementary Fig. 1.

## **Reporting Summary**

## **Supplementary Table 1**

A list of antibodies used in this study.

## **Supplementary Table 2**

A list of qRT–PCR primers and shRNA sequences in this study.

## **Supplementary Table 3**

Data for pairwise comparison (limma analysis) and timecourse analysis of the proteomics data in this study.

# **Source data**

## **Source Data Fig. 1**

## **Source Data Fig. 2**

## **Source Data Fig. 3**

## **Source Data Fig. 4**

## **Source Data Extended Data Fig. 2**

## **Source Data Extended Data Fig. 3**

## **Source Data Extended Data Fig. 5**

## **Source Data Extended Data Fig. 6**

[\*\*Source Data Extended Data Fig. 7\*\*](#)

[\*\*Source Data Extended Data Fig. 8\*\*](#)

[\*\*Source Data Extended Data Fig. 9\*\*](#)

[\*\*Source Data Extended Data Fig. 10\*\*](#)

## Rights and permissions

**Open Access** This article is licensed under a Creative Commons Attribution 4.0 International License, which permits use, sharing, adaptation, distribution and reproduction in any medium or format, as long as you give appropriate credit to the original author(s) and the source, provide a link to the Creative Commons license, and indicate if changes were made. The images or other third party material in this article are included in the article's Creative Commons license, unless indicated otherwise in a credit line to the material. If material is not included in the article's Creative Commons license and your intended use is not permitted by statutory regulation or exceeds the permitted use, you will need to obtain permission directly from the copyright holder. To view a copy of this license, visit <http://creativecommons.org/licenses/by/4.0/>.

[\*\*Reprints and Permissions\*\*](#)

## About this article

### Cite this article

Domizio, J.D., Gulen, M.F., Saidoune, F. *et al.* The cGAS–STING pathway drives type I IFN immunopathology in COVID-19. *Nature* **603**, 145–151 (2022).  
<https://doi.org/10.1038/s41586-022-04421-w>

- Received: 18 June 2021
- Accepted: 13 January 2022
- Published: 19 January 2022
- Issue Date: 03 March 2022
- DOI: <https://doi.org/10.1038/s41586-022-04421-w>

## Share this article

Anyone you share the following link with will be able to read this content:

[Get shareable link](#)

Sorry, a shareable link is not currently available for this article.

[Copy to clipboard](#)

Provided by the Springer Nature SharedIt content-sharing initiative

---

This article was downloaded by **calibre** from <https://www.nature.com/articles/s41586-022-04421-w>

| [Section menu](#) | [Main menu](#) |

- Article
- Open Access
- [Published: 16 February 2022](#)

# Twin study reveals non-heritable immune perturbations in multiple sclerosis

- [Florian Ingelfinger](#)<sup>1,2 na1</sup>,
- [Lisa Ann Gerdes](#)<sup>3,4,5 na1</sup>,
- [Vladyslav Kavaka](#)<sup>3,4</sup>,
- [Sinduya Krishnarajah](#)<sup>1</sup>,
- [Ekaterina Friebel](#)<sup>1</sup>,
- [Edoardo Galli](#) [ORCID: orcid.org/0000-0002-9760-2643](#)<sup>1 nAff12</sup>,
- [Pascale Zwicky](#) [ORCID: orcid.org/0000-0003-0419-2153](#)<sup>1</sup>,
- [Reinhard Furrer](#) [ORCID: orcid.org/0000-0002-6319-2332](#)<sup>6,7</sup>,
- [Christian Peukert](#)<sup>8</sup>,
- [Charles-Antoine Dutertre](#)<sup>9,10</sup>,
- [Klara Magdalena Eglseer](#)<sup>3,4</sup>,
- [Florent Ginhoux](#) [ORCID: orcid.org/0000-0002-2857-7755](#)<sup>11</sup>,
- [Andrea Flierl-Hecht](#)<sup>3,4,5</sup>,
- [Tania Kümpfel](#)<sup>3,4,5</sup>,
- [Donatella De Feo](#)<sup>1</sup>,
- [Bettina Schreiner](#)<sup>1,2</sup>,
- [Sarah Mundt](#)<sup>1</sup>,
- [Martin Kerschensteiner](#) [ORCID: orcid.org/0000-0003-4898-9383](#)<sup>3,4,5</sup>,
- [Reinhard Hohlfeld](#)<sup>3,4,5</sup>,
- [Eduardo Beltrán](#) [ORCID: orcid.org/0000-0002-7266-4098](#)<sup>3,4,5 na2</sup> &
- [Burkhard Becher](#) [ORCID: orcid.org/0000-0002-1541-7867](#)<sup>1 na2</sup>

*Nature* volume 603, pages 152–158 (2022)

- 15k Accesses
- 283 Altmetric

- [Metrics details](#)

## Subjects

- [Autoimmunity](#)
- [Multiple sclerosis](#)
- [Risk factors](#)
- [Systems analysis](#)

## Abstract

Multiple sclerosis (MS) is a chronic inflammatory disorder of the central nervous system underpinned by partially understood genetic risk factors and environmental triggers and their undefined interactions<sup>1,2</sup>. Here we investigated the peripheral immune signatures of 61 monozygotic twin pairs discordant for MS to dissect the influence of genetic predisposition and environmental factors. Using complementary multimodal high-throughput and high-dimensional single-cell technologies in conjunction with data-driven computational tools, we identified an inflammatory shift in a monocyte cluster of twins with MS, coupled with the emergence of a population of IL-2 hyper-responsive transitional naive helper T cells as MS-related immune alterations. By integrating data on the immune profiles of healthy monozygotic and dizygotic twin pairs, we estimated the variance in CD25 expression by helper T cells displaying a naive phenotype to be largely driven by genetic and shared early environmental influences. Nonetheless, the expanding helper T cells of twins with MS, which were also elevated in non-twin patients with MS, emerged independent of the individual genetic makeup. These cells expressed central nervous system-homing receptors, exhibited a dysregulated CD25–IL-2 axis, and their proliferative capacity positively correlated with MS severity. Together, our matched-pair analysis of the extended twin approach allowed us to discern genetically and environmentally determined features of an MS-associated immune signature.

[Download PDF](#)

## Main

MS is the most common neurological disorder affecting young adults with rising global incidence and prevalence, particularly in Western countries<sup>1</sup>. Despite numerous genome-wide association and epidemiological studies<sup>2,3,4</sup>, the aetiology of MS remains largely unknown. Yet, environmental cues associated with increased risk of developing MS have been established, and include factors acting prenatally<sup>5,6</sup>, during adolescence and adulthood (for example, viral infections, low levels of vitamin D, and

tobacco smoke)<sup>7</sup>. Conversely, a registry-based study investigated the familial recurrence rate of MS and revealed that monozygotic twin pairs displayed the highest familial risk (17% age-adjusted risk for the unaffected twin) of developing MS, indicating a strong heritable effect<sup>8</sup>. Accordingly, over 200 risk loci with moderate-to-subtle effects have been described, including *HLA-DRB1\*15:01*, *IL2RA* and *IL7R* genes<sup>3,9</sup>. Given that only 18–24% of MS heritability can be explained by known risk loci<sup>2,10</sup>, it is evident that the aetiology of MS involves a complex interplay between polygenic risk variants and environmental triggers. Hence, investigating how genetic predisposition and environmental triggers shape the interactions of individual immune cells is vital to understand the pathophysiology of autoimmune diseases including MS.

Previous attempts linking individual risk factors with functional perturbation on a single-cell level have given some insight into the inflammatory processes underlying MS<sup>8,11,12,13</sup>. Similarly, several studies have compared the immune profiles of patients with MS to healthy individuals or other control individuals with a disease<sup>14,15,16</sup>. Whereas these cross-sectional analyses revealed potential biomarkers, they cannot control for the effects of the genetic heterogeneity underlying MS susceptibility required for a patient to develop MS and its potential influence on immune cell perturbations.

Here we conducted an in-depth pairwise analysis of the systemic immune compartment of 61 monozygotic twin pairs discordant for MS, in which both siblings carry the same genetic and early-life environmental risk for the disease, yet only one is affected by MS. This approach thus eliminated the majority of bias attributed to variable genetic and early environmental influences in a heterogeneous population<sup>17,18</sup>. We combined the high-throughput of mass cytometry, facilitating the analysis of 57 twin pairs, with cellular indexing of transcriptomes and epitopes by sequencing (CITE-seq) of eight selected twin pairs to obtain a comprehensive overview of epitopes, transcriptome and T cell receptor (TCR) clonotypes. Substantial MS-associated alterations were largely restricted to the myeloid and helper T ( $T_H$ ) cell compartments. Our study thereby resolves how the immune systems of twins, who share the same genetic and early environmental risk factors, can diverge towards distinct clinical phenotypes.

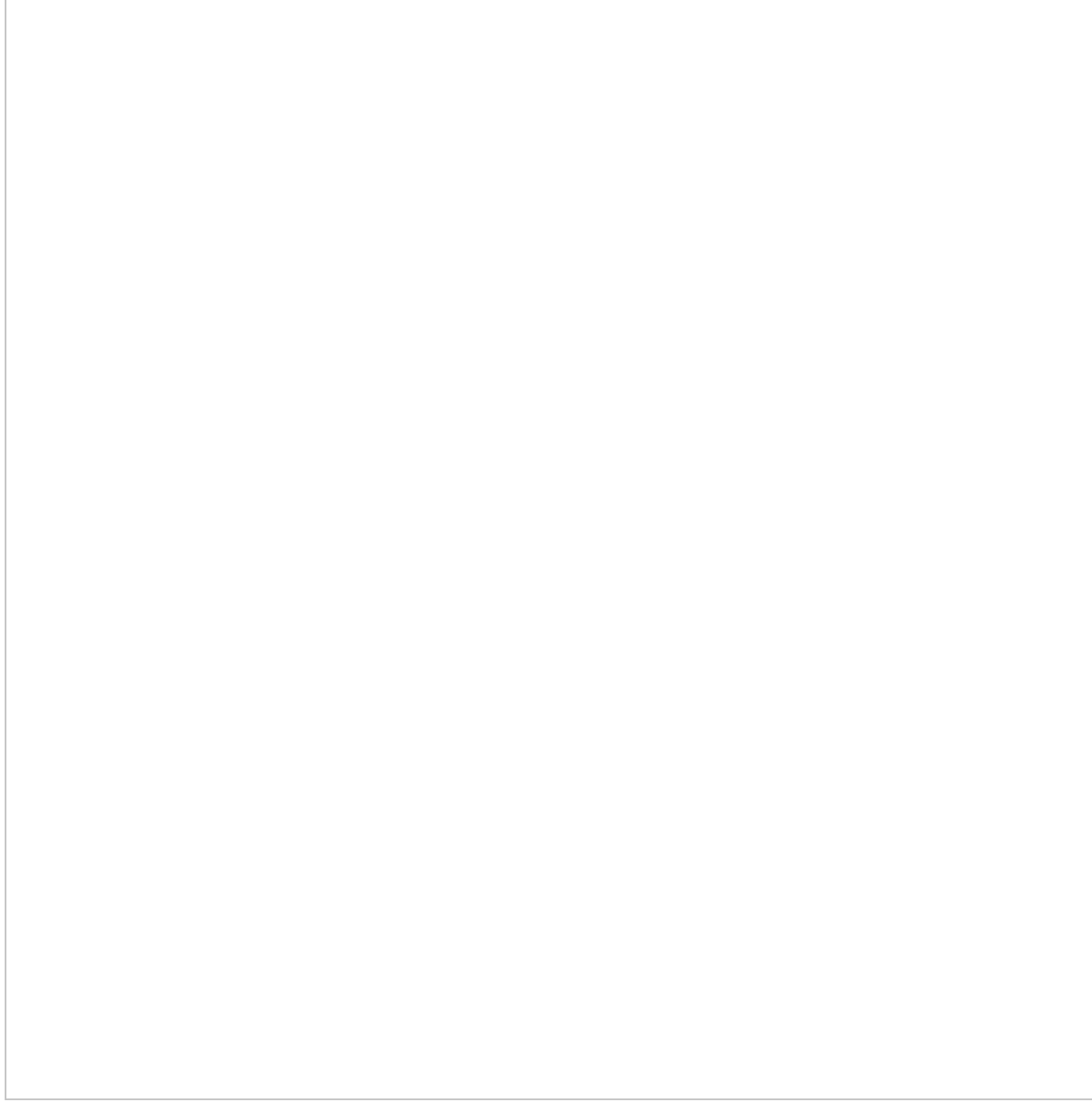
## MS signature in $T_H$ and myeloid cells

We began by comparing the peripheral blood immune cell populations of 57 patients with MS and their unaffected monozygotic twin siblings (Extended Data Table 1, Supplementary Tables 1, 2). We applied cytometry by time-of-flight (CyTOF) to samples of peripheral blood mononuclear cells (PBMCs) to define the abundance of different cell types capturing 59 cellular parameters at the single-cell level (Fig. 1a,

Supplementary Table 3). By combining data-driven and hypothesis-driven analyses, we created a cellular reference framework with well-defined canonical immune cell populations.

**Fig. 1: Twins discordant for MS exhibit differences in circulating T<sub>H</sub> cell and myeloid compartments.**

 figure 1



**a**, PBMCs from monozygotic twin pairs discordant for MS were analysed by CyTOF (MS;  $n = 57$ ) and CITE-seq ( $n = 8 + 2$  healthy twins) to reveal an environmentally triggered immune conversion in MS. **b**, Lollipop plot showing  $P$  values for the two-sided paired non-parametric Wilcoxon signed-rank test with a false discovery

correction according to the Benjamini–Hochberg approach of immune populations in the reference framework for untreated twins with MS ( $n = 20$ ) and controls ( $n = 20$ ). The dashed line indicates a 5% significance threshold. **c**, Automated analysis using diffcyt was performed by applying two filters screening for immune features that are different between all twin pairs ( $n = 57$ ) and twin pairs in which the twin with MS remained untreated ( $n = 20$ ) (left). Network visualization (right) of unsupervised FlowSOM clusters yielded by diffcyt analysis (beige; automated clustering nodes), the differential state nodes for twins with MS for which features appeared significantly different in both filters (red) and the nodes of the manually annotated reference framework defined in Extended Data Fig. 1c (green) are also shown. The dot size corresponds to the population frequency among total leukocytes. pDCs, plasmacytoid dendritic cells;  $T_{\text{eff}}$ , effector T cell;  $T_{\text{na}}$ , naive T cell;  $T_{\text{reg}}$ , regulatory T cell.

High-resolution clustering using FlowSOM and manual merging assigned all cells to a canonical immune subset, creating a framework of reference nodes that served as the basic substrate for the data-driven analysis (Extended Data Fig. 1a–c). Next, pairwise comparison of the frequencies of immune cell subsets in twins affected and unaffected by MS was performed, thereby controlling for the effects of genetic and shared early environmental (for example, prenatal and early childhood) influences. Although we uncovered significant differences in the frequency of classical monocytes in twins with MS (Extended Data Fig. 1d), we discovered that this was primarily driven by disease-modifying therapies (Fig. 1b). Thus, after eliminating genetic and early environmental sources of variance, monozygotic twins discordant for MS exhibit comparable frequencies of immune cell subsets in peripheral blood.

For a data-driven agnostic approach, which does not categorize cells into canonical subsets based on previous knowledge, the recently introduced diffcyt toolset based on the widely established Bayes moderated tests utilized in transcriptomic studies was applied. Markers were divided into lineage markers, which had served as the foundation for FlowSOM clustering, and cell-state markers including activation and trafficking molecules and cytokines (Supplementary Table 3). On the basis of this classification, diffcyt generated a list of 1,400 immune features, in which each feature represents the expression of a cell-state marker in a given immune cluster. Those features were then filtered by meeting two conditions: they distinguished twins with MS from their unaffected twin siblings across all twin pairs, and they were not elicited by disease-modifying therapy (Fig. 1c). Eighteen different immune features fulfilled both conditions in twins with MS and corresponding immune clusters were termed ‘differential state nodes’ (Extended Data Table 2). Twelve out of the 18 features localized within the  $T_H$  cell region, supporting previous observations<sup>13,14</sup>, one feature was close to the unconventional T cell reference nodes, three were close to the natural killer (NK) cell reference nodes and the remaining two were in the myeloid cell region (Fig. 1c, right). The most significant immune alterations were observed in the  $T_H$  cell

and myeloid cell compartment (Extended Data Table 2). The conjunction of data-driven and previous knowledge-driven approaches has thus demonstrated that the clinical manifestation of MS, independent of the genetic predisposition, is predominantly determined in the T<sub>H</sub> cell and myeloid compartments.

## CCR2–CSF2R are elevated in MS monocytes

Mononuclear phagocytes constitute a dominant fraction of leukocytes infiltrating the central nervous system (CNS) found in lesions of patients with MS<sup>19,20</sup> and their inhibition has been reported to prevent neuroinflammation in mice<sup>21,22,23</sup>. Both MS-related features of the myeloid compartment were found in the same differential state node and exhibited higher levels of the receptor for monocyte chemoattractant protein 2 (CCR2) and the granulocyte–macrophage colony-stimulating factor (GM-CSF) receptor-specific subunit (CD116) in twins with MS (Fig. 2a). This differential state phagocyte node in twins with MS phenotypically resembled classical monocytes (Fig. 2a, Extended Data Fig. 2a). However, CD14 expression was dim and CD16 was absent, obstructing their unambiguous assignment to a canonical immune population (Extended Data Fig. 2a). The strong positive correlation between CD116 and CCR2 expression in monocytes within the differential state phagocyte node suggests a common regulation of both molecules (Extended Data Fig. 2b). Elevated expression of CCR2 and CD116 was especially pronounced in untreated twin pairs, suggesting that this particular MS-related perturbation is susceptible to disease-modifying therapies (Fig. 2a, right, Extended Data Fig. 2c).

**Fig. 2: The myeloid landscape of twins with MS is shifted towards a monocyte population with increased expression of CCR2 and the GM-CSF receptor.**

 figure 2

**a**, Network visualization of unsupervised FlowSOM clusters in the myeloid compartment (beige); highlighted are the differential state nodes for twins with MS for which features appeared significantly different (red) and nodes of the manually annotated reference framework (green). The violin plots show the median expression levels of CCR2 and CD116 in monocytes within the differential state node from

untreated twin pairs and all combined twins enrolled in the study; the bold horizontal line depicts the respective group mean and the dashed line indicates twinship. **b**, Mapping of diffcyt-generated myeloid cell clusters (right) on InfinityFlow data from PBMCs of a healthy donor outside the cohort of twins with MS (left). The dot size in **a, b** corresponds to the population frequency among total leukocytes. cDC1s, conventional type 1 dendritic cells. **c**, Dot plot of CITE-seq data (a total of 21,043 cells) showing the expression profile of the top 15 differentially expressed genes for each cluster. The dot size corresponds to the fraction of cells within each cluster expressing the indicated transcript, and the colour indicates average expression. If not indicated, the differences between the experimental groups were statistically not significant ( $P > 5\%$ ) using the moderated limma-trend method implemented in diffcyt, performing a false discovery correction according to the Benjamini–Hochberg approach.

To fully understand the identity of the cells within the differential state myeloid node, we enriched the cohort of twins with MS with InfinityFlow data of PBMCs for 347 detected surface markers derived from a healthy control sample outside the cohort of twins with MS<sup>24</sup>. InfinityFlow combines traditional flow cytometry-based detection of hundreds of marker molecules, with machine learning analysis, facilitating the mapping of cellular subsets with single-cell resolution<sup>25</sup>. We applied FlowSOM clustering to identify the canonical myeloid cell subsets of the peripheral blood and retrieved their surface proteome (Extended Data Fig. [2d](#)). We next projected the differential state phagocyte node from the twin pairs with MS onto this map and identified their surface profile to be most similar to the classical monocyte and intermediate monocyte nodes (Fig. [2b](#), Extended Data Fig. [2e](#)).

To gain further insight into the functional properties of the differential state phagocyte node, we performed CITE-seq of the myeloid compartment of monozygotic twin pairs discordant for MS and obtained similar populations as present in the CyTOF data (Extended Data Fig. [3a](#), Extended Data Table [1](#)). CITE-seq confirmed that the phagocyte node characterized by the CD14<sup>dim</sup>CD16<sup>-</sup> phenotype showed transcriptional similarity to both classical monocytes and dendritic cells, as well as being characterized by the expression of *CIITA*, *ZEB2*, *JAK2* and *ITGAX* (Fig. [2c](#), Extended Data Fig. [3a, b](#)). In addition, we observed a trend towards increased signalling activity of *CSF2RA* with increased expression of *CSF2RB*, *PRKACA* and *STAT5A* transcripts in twins with MS compared with their unaffected twin siblings (Extended Data Fig. [3c](#)).

Exploring the monocyte reference nodes in proximity to the differential state node in the cohort of twins with MS, we further revealed that the frequency of non-classical monocytes among total myeloid cells was significantly reduced in twins with MS compared with their unaffected twin siblings. Again, this difference was more

pronounced in untreated twin pairs (Extended Data Fig. 3d), and indeed treatment with dimethyl fumarate, fingolimod or glatiramer acetate significantly reduced the disparity between twins with MS and their unaffected twin siblings (Extended Data Fig. 3e). Finally, investigation of the transcriptional circuits, which differentiate twins with MS from unaffected twin siblings in the reference nodes of the myeloid compartment, revealed increased expression of *FKBP5*, *CCND3*, *PER1* and *IRAK3* in classical monocytes of twins with MS compared with their unaffected twin siblings (Extended Data Fig. 3f, Supplementary Table 4). Moreover, we observed an overall reduction in the type 1 interferon gene signature in classical monocytes, dendritic cells and non-classical monocytes of twins with MS compared with twins without MS, providing a potential link towards the clinical efficacy of recombinant interferon- $\beta$  therapy in MS<sup>26</sup> (Extended Data Fig. 3f,g, Supplementary Table 4).

In conclusion, twins with MS manifested a population shift in the myeloid compartment, away from non-classical monocytes and towards their inflammatory classical monocyte counterparts with a concomitant decrease in the type 1 interferon gene signature. A subpopulation of monocytes exhibited elevated expression of CCR2 and the GM-CSF receptor, indicative of a sensitization towards inflammatory stimuli.

## T<sub>H</sub> cells display increased CD25 in MS

The unbiased feature extraction revealed the most prominent perturbations between twins with MS and unaffected twins within the lymphocyte compartment (Fig. 1c, Extended Data Table 2). Within the innate lymphocyte compartment, we observed increased expression of CCR6 and reduced amounts of CXCR3 and CD25 in NK cells and lower levels of CCR6 expression in an NKT cell node of twins with MS (Extended Data Fig. 4a). Significantly lower expression of CXCR3 and higher expression of CD69 were found in a node of CD4<sup>+</sup> effector memory T cells re-expressing CD45RA (T<sub>EMRA</sub>) in twins with MS (Fig. 3a, Extended Data Fig. 4b).

**Fig. 3: Transitional T<sub>H</sub> cells of twins with MS display IL-2 hypersensitivity and elevated expression of brain-homing markers compared with unaffected twin siblings.**

---

 **figure 3**

**a**, Network visualizations of  $T_H$  cell clusters yielded by diffcyt analysis; highlighted are the differential state nodes for twins with MS for which features appeared significantly different (red, differential markers annotated in bold, 8x indicates number of differential nodes for the same feature) and nodes of the manually annotated reference framework (green). The violin plots show the median expression level for CD127 in cells within the differential state  $T_{na}$  6 node and the median expression level for CD25 within the combined nodes for all twin pairs. **b**, Lollipop and violin plots showing the median expression levels of CD25 and the resulting *P* values across all T cell nodes in the reference framework of the naive  $T_H$  cell compartment for twin pairs discordant for MS ( $n = 57$ ). **c**, Mapping of CITE-seq nodes (78,531 cells) from eight twin pairs discordant for MS onto the mass cytometry dataset. The red nodes indicate significantly increased surface expression of CD25 between twin pairs. **d**, Diffusion map showing the trajectory of  $T_H$  cells. The arrow indicates the direction of trajectory and nodes highlighted in red demonstrated increased CD25 expression in twins with MS. DC, diffusion coefficients. **e**, Bar graph showing the fraction of expanded T cell clones ( $n > 2$  per clonotype) for twins discordant for MS (78,531 cells). **f**, PBMCs were activated in an antigen-independent manner, CD25-enriched  $T_H$  cell nodes were identified and analysed with regards to their cytokine and the trafficking profile in twin pairs discordant for MS ( $n = 25$ ). **g**, Violin plot showing the median expression levels of CD25 and IL-2 in cells within the differential state nodes in twins with MS for all twin pairs. **h**, Correlation between the inter-pair difference in median expression of IL-2 and expanded disability status scale (EDSS) of twins with MS. RRMS is shown in beige ( $n = 21$ ), and secondary progressive MS (SPMS) is

shown in red ( $n=4$ ). The dashed line indicates the smoothed conditional mean of the linear regression model with a 95% confidence interval in the shaded area. **i**, Effect size for the expression of the indicated trafficking molecules (left) and a violin plot showing the median expression level of VLA4 (right) in cells within the differential state  $T_H$  cell node of twin pairs discordant for MS ( $n=6$ ). The dot size of the networks corresponds to the population frequency among total leukocytes. In the violin plots, a bold horizontal line depicts the respective group mean and the dashed line indicates twinship. If not indicated, the differences between experimental groups were statistically not significant ( $P > 5\%$ ) using the moderated limma-trend method implemented in diffcyt (**a**, left) or a two-sided paired non-parametric Wilcoxon signed-rank test (**a**, right, **b**, **g**, **i**), both applying a false discovery correction according to the Benjamini–Hochberg approach or a paired two-way analysis of variance (ANOVA) (**e**).

However, the most dominant perturbations across our twin cohort were present in  $T_H$  cell nodes: we observed significantly higher expression of CD25, the IL-2 receptor high-affinity chain, in eight clusters phenotypically characterized as naive  $T_H$  cells that was accompanied by increased expression of CCR4 and decreased expression of CD127 in one node, respectively (Fig. 3a, Extended Data Fig. 4c). Although the overall expression of CD25 across naive  $T_H$  cells was relatively low, reducing the signal-to-noise ratio of the twin setup combined with barcoding and simultaneous acquisition revealed a robust increase in the expression of CD25 in twins with MS. This perturbation was the statistically most substantial change in the data-driven immune profiling of the cohort of twins with MS. CD25 represents a major genetic MS risk allele<sup>27</sup>. It is therefore of great interest that the unbiased analysis of twin siblings discordant for MS, with a shared genetic makeup, identified CD25 expression as one of the main features of the differential state node in  $T_H$  cells in siblings with MS.

When we mapped the eight differential state naive  $T_H$  cell nodes characterized by elevated expression of CD25 onto the reference  $T_H$  cell nodes for twins with MS, we found that they were phenotypically similar (Extended Data Fig. 4c, d). Binning of the eight clusters into a single naive  $T_H$  cell node also further increased the pairwise significance of the inter-twin difference in CD25 expression (Extended Data Fig. 4e). Investigation of our manually annotated canonical T cell reference nodes revealed that the expression of CD25 was low in naive  $T_H$  cells. However, the expression of CD25 in naive  $T_H$  cells was still higher than cytotoxic T cells (Extended Data Fig. 4f). Although significant differences in the expression of CD25 between pairs of twins with MS and their unaffected twins were restricted to  $T_H$  cells displaying a naive

phenotype, the most marked differences were limited to a very discrete set of T<sub>H</sub> cell nodes (Fig. 3b, Extended Data Fig. 4g).

Correlation analysis of significantly dysregulated immune traits in the cohort of twins with MS revealed that CD25 features in naive T<sub>H</sub> cells not only strongly correlated with each other but also with the expression of CD116 and CCR2 in monocytes, suggesting interconnectivity between these features during immunopathology (Extended Data Fig. 4h). Together, elevated expression of CD25 within a subgroup of phenotypically naive T<sub>H</sub> cells represented the most pervasive immune alteration in circulating immune cells of twins with MS.

## CD25 affects transitional T<sub>H</sub> cells in MS

To further expose the cellular identity of the CD25 differential state T<sub>H</sub> cell nodes in twins with MS, we performed CITE-seq, thereby retrieving the single-cell transcriptome in combination with single-cell TCR and surface epitope information.

We identified six T<sub>H</sub> cell clusters displaying a naive phenotype based on RNA (*CCR7*, *CD7*, *TCF7*, *LEF1* and *SELL*) and epitope expression (CD45RA<sup>+</sup> and CD45R0<sup>low</sup>) (Extended Data Fig. 5a). CITE-seq confirmed elevated surface expression of CD25 in two clusters of naive T<sub>H</sub> cells (T<sub>na</sub> 4 and T<sub>na</sub> 5), and a cluster of central memory T (T<sub>CM</sub>) cells (T<sub>CM</sub> 4) in twins with MS compared with unaffected twins (Extended Data Fig. 5b). These clusters mapped in close proximity to the differential CD25 nodes of the mass cytometry dataset of twins with MS, thereby validating the high-throughput discovery CyTOF approach using an independent single-cell technology (Fig. 3c, Extended Data Fig. 5c).

Although the differential state T<sub>H</sub> cell nodes in twins with MS displayed a naive phenotype, the increased surface expression of CD25 in twins with MS was indicative of cellular activation. Indeed, the transcriptomes of the T<sub>na</sub> 4 and T<sub>na</sub> 5 clusters placed these cells distant from bona fide naive T<sub>H</sub> cells based on pseudotime analysis and both clusters started to downregulate naive markers (CD45RA and CCR7) while upregulating activation or memory-associated proteins (CD45R0 and CD25) (Fig. 3d, Extended Data Fig. 5d). Next, we investigated whether the increased expression of CD25 in the transitional T<sub>H</sub> cell nodes of twins with MS is accompanied by an expansion of TCR clones. The fact that there was no indication for clonal expansion across T<sub>H</sub> cells of twins with MS compared with unaffected twin siblings does not support the notion that the observed activation is driven by a shared autoantigen (Fig. 3e, Extended Data Fig. 5e).

To uncover the underlying transcriptional circuits that drive the difference in CD25 expression, gene expression of transitional T<sub>H</sub> cell nodes was analysed. Apart from transcripts involved in IL-2 signalling such as *CISH*, increased expression of transcripts associated with protein synthesis and proliferation (*EEF1A1*, *EEF1B2*, *EIF3L*, *PIK3IP1* and *TPT1*) was found in twins with MS compared with unaffected twins (Extended Data Fig. 5f,g, Supplementary Table 5). The transcript showing the most significant induction in twins with MS compared with unaffected twins was *TXNIP*, which encodes thioredoxin-interacting protein (also known as vitamin D<sub>3</sub> upregulated protein 1), a key mediator of the cellular antioxidant system that has been reported to regulate the responsiveness of T cells to IL-2 (ref. 28) (Extended Data Fig. 5g, Supplementary Table 5).

In summary, the unbiased single-cell transcriptome and epitope analysis of T<sub>H</sub> cells across a selected group of twin pairs validated the specific increase of CD25 expression in a population of T<sub>H</sub> cells in twins with MS initially captured by high-throughput mass cytometry. The transcriptome and pseudotime profiling further suggests that this population is within a transitional differentiation state with increased expression of genes related to protein biosynthesis and IL-2-induced proliferation.

## Cytokine dysregulation in MS progression

As CD25 has a crucial function regulating T cell proliferation and activation<sup>29</sup>, we next investigated the possible functional implications of increased expression of CD25 in the differential state transitional T<sub>H</sub> nodes of twins with MS. Polyclonal stimulation of PBMCs from twin pairs discordant for MS using phorbol 12-myristate 13-acetate and ionomycin was followed by analysis of cytokines and trafficking-related markers (Fig. 3f). To anchor the CD25 differential state nodes in this additional dataset, a similar strategy as described above was applied. This revealed a T<sub>H</sub> cell node displaying a naive phenotype characterized by increased expression of CD25 as well as its ligand IL-2 (Fig. 3g, Extended Data Fig. 5h,i). We observed a strong positive correlation between the size of inter-twin difference in IL-2 expression in the transitional T<sub>H</sub> cell node and the severity of MS in the affected twin, assessed by the expanded disability status scale (Fig. 3h). Accordingly, the inter-twin difference in IL-2 expression was significantly higher in twin pairs in which the twin with MS had entered the more-advanced phase of disease progression known as secondary progressive MS, than twin pairs in which the affected twin was in a relapsing-remitting stage (RRMS) (Fig. 3h, Extended Data Fig. 5j).

To reveal early cytokine polarization across these transitional T<sub>H</sub> cells, we gated on T<sub>H</sub> cells that responded with IL-2 production to ex vivo reactivation (Extended Data Fig.

[5k](#)) and uncovered significantly lower production of IL-9 and higher production of IL-17A and IL-3 in twins with MS than in their unaffected twin sibling (Extended Data Fig. [5l, m](#)). Both, IL-17A and IL-3 were reported to be secreted by encephalitogenic T cells in MS<sup>[30,31](#)</sup>, suggesting that these transitional, CD25-expressing, IL-2-producing peripheral T<sub>H</sub> cells are the precursors to fully encephalitogenic T<sub>H</sub> cells found in CNS lesions in patients with MS. To investigate putative transcriptional networks that drive this early polarization fate, DoRothEA, a computational tool to assess transcription factor activities based on reported transcription factor–target interactions, was used. Significantly higher STAT4 activity in both transitional T<sub>H</sub> cell nodes that demonstrated increased expression of CD25 (T<sub>na</sub> 4 and T<sub>na</sub> 5) coincided with elevated RELA activity in T<sub>na</sub> 4 in twins with MS (Extended Data Fig. [5n](#), Supplementary Table [6](#)). RELA, which encodes the NF-κB p65 subunit, has been shown to promote differentiation of IL-17-producing T cells<sup>[32](#)</sup> and has been linked to MS in genome-wide association studies<sup>[33](#)</sup>. Similarly, mice deficient in STAT4 were resistant to experimental autoimmune encephalomyelitis, an animal model of neuroinflammation<sup>[34](#)</sup>.

## MS T<sub>H</sub> cells display a trafficking signature

To follow the hypothesis that the proliferative T<sub>H</sub> cell node in twins with MS could give rise to encephalitogenic T cells, we next measured the expression of trafficking molecules in the differential state T<sub>H</sub> cell node. Compared with cells from the unaffected twin siblings, the cells from twins with MS expressed significantly higher amounts of VLA4, which was further validated using our CITE-seq dataset (Fig. [3i](#), Extended Data Fig. [5o](#)). VLA4 is required for leukocyte migration into the CNS<sup>[35](#)</sup> and is directly targeted by natalizumab, an approved therapy for MS<sup>[36](#)</sup>. Finally, CXCR4 transcripts were enriched in the two T<sub>H</sub> cell nodes that demonstrated increased expression of CD25 (T<sub>na</sub> 5 and T<sub>CM</sub> 4) in twins with MS compared with unaffected twins, further supporting the CNS trafficking potential of the identified transitional T<sub>H</sub> cells (Extended Data Fig. [5g](#)).

Together, in the peripheral blood of twins with MS, a population of transitional T<sub>H</sub> cells is expanding due to increased expression of CD25. The level of expansion, determined by the production of IL-2 after ex vivo activation, correlates with disease severity. Expanding cells in twins with MS displayed early signs of encephalitogenic polarization, possibly driven by STAT4 and NF-κB activation, and demonstrated increased potential to traffic to the CNS.

## CD25 in naive T<sub>H</sub> cells is a heritable trait

Using the cohort of twins with MS, we were able to control for the genetic contribution to MS and thereby map immune alterations purely elicited by environmental cues. To extend this approach and estimate the respective effect of heritable, early environmental and late environmental influences on each immune trait in the reference framework, we next integrated flow cytometry data on PBMCs from a cohort of healthy monozygotic and dizygotic twin pairs (termed healthy twin cohort)<sup>17</sup> that was age-matched to the cohort of twins with MS (Fig. 4a, Extended Data Table 1). Manual gating was used to match the cell populations from the healthy twin cohort to those in the reference framework of the cohort of twins with MS (Extended Data Fig. 6a). Using OpenMx, a structural equation model commonly utilized in twin studies, the extent to which each immune trait was modulated by genetic, early-shared or later unique environmental sources of variance during adulthood was estimated. The predominant sources of variance in immune cell frequencies differed between individual leukocyte subsets; although variance in frequency of CD56<sup>bright</sup> NK cells and classical monocytes had a strong genetic component, plasmablasts and CD4<sup>+</sup> TEMRA cells were primarily influenced by unique environmental factors (Fig. 4b). Similar to previous reports<sup>17,37,38</sup>, we observed that approximately 50% of the variance across all identified immune populations was attributable to genetic influences, 40% to unique environmental factors and 10% to a shared early environment (Fig. 4c). Next, this method was applied to identify the influences associated with modulation of CD25 expression in T<sub>H</sub> cells overlapping with a naive phenotype. In naive T<sub>H</sub> cells, 51% of the variance in CD25 expression was regulated by genetics, 43% by shared (and thus early childhood) environmental factors and only 7% by unique environmental drivers (Fig. 4d, Extended Data Fig. 6b). Accordingly, analysis of the cohort of twins with MS eliminated 93% of the variance caused by heritable and early-childhood factors, thereby isolating disease-associated immune alterations that are unaffected by confounding variables.

**Fig. 4: The expression of CD25 in naive T<sub>H</sub> cells is regulated by genetic and early environmental factors and is increased in patients with MS in a cross-sectional validation cohort.**

---

 **figure 4**

**a**, Flow cytometry data of PBMCs from healthy monozygotic ( $n = 21$ ) and dizygotic ( $n = 22$ ) twin pairs age-matched to the cohort for twins with MS were used in a structural equation model to estimate the contribution of genetics and shared and non-shared environmental drivers on immune composition. **b–d**, Bar graphs (**b**) and pie charts (**c**, **d**) displaying the variance components for the populations in the manually annotated reference framework (**b**), the mean variance components across all detected immune subsets (**c**) and the variance components for the expression of CD25 in T<sub>H</sub>

cells displaying a naive phenotype (**d**). **e**, Data-driven analysis of twin pairs discordant for MS revealed MS-specific immune features that were validated within a cross-sectional validation cohort consisting of healthy donors (HD;  $n = 29$ ) and patients with RRMS ( $n = 30$ ). **f**, Violin plot showing the mean expression of CD25 in  $T_H$  cells displaying a naive phenotype of healthy donors and patients with RRMS. In the violin plots, the bold horizontal line depicts the respective group mean. If not indicated, differences between experimental groups were statistically not significant ( $P > 5\%$ ) using a two-sided unpaired non-parametric Mann–Whitney–Wilcoxon test with a false discovery correction according to the Benjamini–Hochberg approach.

## CD25 signature in non-twin patients with MS

Although the expression of CD25 in phenotypically naive  $T_H$  cells is largely regulated through heritable influences, the elevated expression of CD25 in transitional, quasi-naive  $T_H$  cells in MS is a disease-specific effect driven by unique environmental influences. To further solidify this concept, we analysed the expression of CD25 in a cross-sectional validation cohort of 30 untreated patients with RRMS and 29 genetically unrelated healthy donors<sup>14</sup> (cohort of non-twins with MS) (Fig. [4e](#), Extended Data Table [1](#)). Here the frequencies of canonical immune cell subsets were again comparable between patients with MS and non-familiarly related healthy donors<sup>14</sup> (Extended Data Fig. [6c,d](#)). Despite multiple sources of variation and the absence of enrichment for a familial MS susceptibility in controls of the cross-sectional cohort of non-twins with MS, we could observe that unfractionated naive  $T_H$  cells of patients with RRMS expressed higher levels of CD25 than healthy donors (Fig. [4f](#)).

In conclusion, we show that elevated expression of CD25 in  $T_H$  cells that display a naive phenotype is part of the heritable (cross-sectional) and non-heritable (twins) immune signature of MS.

## Discussion

Here we used deep immune profiling of monozygotic twin pairs discordant for MS using two highly complementary single-cell technologies to begin to explain how two people sharing the same genetic predisposition for this disease can demonstrate such divergent clinical phenotypes. Data-driven analysis revealed that mainly the  $T_H$  cell and, to a lesser extent, the myeloid cell compartment were phenotypically altered in the systemic immune compartment of twins with MS. This confirmed and refined the findings of previous MS immunophenotyping studies, which could not control for the effects of genetic predisposition<sup>13,14</sup>. The observation that some of the findings

revealed in this study have previously been reported in cross-sectional studies of MS (for example, increase in CCR2 expression in monocytes<sup>39</sup>), whereas other features demonstrated opposite trends of what has previously been described<sup>40</sup>, highlights the importance of discerning genetic predisposition from environmentally induced alterations in MS.

Compared with their unaffected twin siblings, the twins with MS exhibited a shift in their circulating monocyte compartment away from tissue-patrolling non-classical monocytes, and towards inflammatory monocytes. Analogously, ref. <sup>41</sup> reported that non-classical monocytes enter and patrol the CNS during the steady state, but are reduced and superseded by classical monocytes in the peripheral blood and cerebrospinal fluid of patients with RRMS. The role of inflammatory monocytes has been investigated intensively in the context of experimental autoimmune encephalomyelitis. Genetic ablation models have demonstrated that CCR2-expressing monocytes are the main executors of CNS immunopathology in this model, in which they sense T-cell-derived GM-CSF and adopt a pathological CNS-specific transcriptional signature that leads to tissue damage and neurological deficits<sup>21,23,42</sup>. We found that expression of both CCR2 and the GM-CSF receptor (CD116) was consistently increased in a subset of circulating monocytes in twins with MS. It is thus conceivable that T cell-orchestrated cytokine production leads to the observed phenotypic changes in the monocyte compartment, which may appear as an effect of the ongoing inflammation and ultimately contribute to tissue destruction in the CNS.

The most consistent pattern emerging from the pairwise analysis of monozygotic twins discordant for MS was significantly higher expression of CD25 in a population of T<sub>H</sub> cells in patients with MS and their hyper-proliferative state. This exclusively affected a cluster of T<sub>H</sub> cells transitioning from a naive to a memory or effector phenotype.

Altered expression of CD25 in transitional T<sub>H</sub> cells, predominantly under the influence of shared genetic and early environmental factors, highlights the crucial role of genetic predisposition in initiating MS. Despite eliminating the majority of heritable variance using the twin setting, the increase in the expression of CD25 in twins with MS still appeared as the most consistent immune dysregulation in the cohort of twins with MS. It is thus conceivable that polygenic risk variants, including single-nucleotide polymorphisms in the *IL2RA* gene<sup>27,43</sup>, confer genetic susceptibility that facilitates disease initiation by environmental challenges (for example, Epstein–Barr virus infection). Analogously, gene–phenotype correlations using clinically healthy high-risk allele carriers have revealed that the MS risk single-nucleotide polymorphism rs2104286 (in the *IL2RA* gene) resulted in increased expression of CD25 exclusively in naive T<sub>H</sub> cells<sup>44</sup>. The postulated hypersensitivity for IL-2 in T<sub>H</sub> cells in patients with MS has been shown to induce secretion of GM-CSF in high-risk allele carriers<sup>11</sup>,

which represents a hallmark of CNS inflammation in both experimental autoimmune encephalomyelitis and human MS<sup>14,45</sup>.

Functionally, the increased expression of CD25 and IL-2 responsiveness of transitional T<sub>H</sub> cells from patients with MS may provide the substrate for pathogenic CD4<sup>+</sup> effector memory T cells in the inflamed CNS, as previously proposed<sup>11,46</sup>. This hypothesis aligns with the cytokine profile and expression of CNS-homing molecules such as CXCR4 and VLA4 in these T<sub>H</sub> cells. Alternatively, homeostatically expanding CD25<sup>high</sup> naive T<sub>H</sub> cells<sup>47</sup> found in the peripheral blood of individuals with MS might contribute, as bystanders, to an antigen-specific immune response occurring in secondary lymphoid organs or the CNS, amplifying cytokine production up to the threshold required to start or maintain the neuroinflammatory cascade of MS. In support of this notion, IL-2-mediated STAT5 signalling is sufficient to induce the production of GM-CSF in naive human T<sub>H</sub> cells<sup>11,46</sup>. Accordingly, in the identified transitional T<sub>H</sub> cell node, the increased expression of CD25 was accompanied by increased IL-2 in twins with MS and correlated with disease severity. Together with the changes in the composition of the circulating mononuclear phagocyte population, this indicates that a cytokine dysregulation characterized by activation of the IL-2RA–IL-2–GM-CSF axis, triggered by a unique environmental challenge, may well be the immunological substrate for disease initiation and/or progression in MS.

## Methods

### Sample selection for the cohort of twins with MS

The cohort of twins with MS is part of the MS TWIN STUDY and represents a cohort of monozygotic twins with discordance for MS and is located at the Institute of Clinical Neuroimmunology at the LMU Klinikum Munich, Germany. Recruitment started in May 2012 and is still ongoing; samples used in the present study were collected up to May 2020.

Inclusion criteria for study participation were met if in one twin of a monozygotic twin pair an diagnosis of MS according to the revised McDonald criteria<sup>48,49</sup> was established, whereas the twin sibling was clinically healthy. Exclusion criteria were infection as well as treatment with antibiotics or high-dose intravenous glucocorticosteroids within 3 months before sampling. Monozygotic twin pairs clinically discordant for MS ( $n=61$ ) visited the outpatient department at the Institute of Clinical Neuroimmunology at the LMU Klinikum Munich for a detailed interview, neurological examination, blood sampling and MRI investigations (in a proportion of

twins only). To confirm a diagnosis of MS, medical records including MRI scans were obtained and reviewed (Extended Data Table 1, Supplementary Tables 1, 2).

As the current disease-modifying treatment at the time of blood sampling is known to have a strong effect on the peripheral immune signature<sup>38</sup>, we selected a subgroup, in which the twin with MS had not received treatment at the time of blood sampling ( $n = 20$ ) for further analyses (Extended Data Table 1, Supplementary Tables 1, 2). The expanded disability status scale (EDSS) was used as a measure of disease severity in twins with MS<sup>50</sup>.

The MS TWIN STUDY was approved by the local ethics committees of the Ludwig-Maximilians-University of Munich (ethics approval project number 267-13). All participants gave written informed consent, according to the principles of the Declaration of Helsinki.

## Blood sampling and PBMC preparation for the cohort of twins with MS

Blood samples of study participants of the MS TWIN STUDY were collected in EDTA-containing tubes. To exclude sample collection bias, blood samples were drawn from each twin pair before meals and at the same time on the same day. PBMCs were isolated as described before by density gradient centrifugation with Lymphoprep (STEMCELL technologies) and cryopreserved in liquid nitrogen using serum-free cryopreservation medium (CTL-Cryo ABC Media Kit, Immunospot) in concentrations of  $1 \times 10^7$  cells per ml.

## Ex vivo activation of PBMCs in the cohort of twins with MS

To measure cytokine expression by PBMC from the cohort of twins with MS, cells from 25 twin pairs (19 treated pairs and 6 untreated pairs) were activated in an antigen-independent manner as described previously<sup>51</sup>. In brief, leukocytes were taken from liquid nitrogen storage and thawed in a water bath at 37 °C. Cells were resuspended in cell culture medium (RPMI-1640, 10% FCS (Biochrom), 1× l-glutamine and 1× penicillin–streptomycin (both Life Technologies)) supplemented with 1:10,000 benzonase (Sigma-Aldrich), then centrifuged (350g for 7 min at 24 °C) and washed twice with cell culture medium. Samples subsequently underwent antibody labelling for mass cytometry, or, in the case of intracellular cytokine detection, were incubated overnight at 37 °C and 5% CO<sub>2</sub>, before stimulation with 50 ng ml<sup>-1</sup> phorbol 12-myristate 13-acetate (Sigma-Aldrich) and 500 ng ml<sup>-1</sup> ionomycin (Sigma-Aldrich) in the presence of 1× brefeldin A and 1× monensin (both BD Biosciences) for 4 h at 37 °C. Cells underwent surface marker antibody labelling, fixation, permeabilization and intracellular cytokine antibody labelling as described below.

## Antibodies

Antibodies used in mass cytometry experiments were either purchased already heavy-metal-conjugated (Fluidigm) or were conjugated in-house using the MaxPar X8 chelating polymer kit (Fluidigm) following the manufacturer's instructions. Antibody clones, corresponding heavy metal tags and suppliers are summarized in Supplementary Table 3. Antibodies used in CITE-seq experiments were purchased preconjugated and are summarized in Supplementary Table 7.

## Live-cell barcoding for mass cytometry

To eliminate technical variability during sample processing and data acquisition, a restricted combinatorial 9-choose-3 live-cell barcoding strategy was applied, as described previously<sup>14</sup>. To achieve this, anti-CD45 monoclonal antibodies (mAbs; BioLegend) were conjugated using MaxPar X8 polymers (Fluidigm) and palladium (<sup>104</sup>Pd, <sup>105</sup>Pd, <sup>106</sup>Pd, <sup>108</sup>Pd and <sup>110</sup>Pd), indium (<sup>113</sup>In and <sup>115</sup>In; all from Trace Sciences International) and tantalum (<sup>181</sup>Ta; Sigma) isotopes. In addition, Y89-conjugated anti-CD45 mAbs (Fluidigm) were used. Twin pairs were randomized and PBMCs of twins with MS and unaffected twin siblings were barcoded in two batches before acquisition during two independent mass cytometry runs. After sample thawing and/or ex vivo activation cells were labelled with heavy-metal-tagged CD45 antibodies at 37 °C for 25 min in cell labelling medium (CLM; RPMI-1640, 4% FCS) on an orbital shaker (500 rpm). Barcoded samples were washed twice in CLM and combined into a single-reaction vessel for surface marker and/or cytokine detection.

## Surface and intracellular cytokine detection by mass cytometry

After barcoding, the sample convolute was labelled in 400 µl CLM containing the antibody mix for surface marker detection (Supplementary Table 3) on an orbital shaker (500 rpm) at 37 °C for 40 min. Cisplatin (2.5 µM in PBS; Fluidigm) was added for 2 min on ice to enable live/dead cell discrimination and the reaction was stopped by adding 2% FCS in PBS and incubating for 2 min on ice.

For the detection of transcription factors, the barcoded sample convolute was fixed and permeabilized for 40 min at 4 °C in 1X FOXP3 fixation/permeabilization buffer (BioLegend) and was washed in permeabilization buffer (PBS, 0.5% saponin, 2% bovine serum albumin (BSA) and 0.01% sodium azide (all Sigma-Aldrich)). Labelling was performed in 400 µl permeabilization buffer containing the antibody mix for 1 h at 4 °C.

In case of intracellular cytokine detection, the sample convolute was fixed in 1.6% paraformaldehyde (Electron Microscopy Sciences) for 1 h at 4 °C and washed with

permeabilization buffer. The sample was labelled with antibodies recognizing intracellular cytokines in 400 µl permeabilization buffer for 1 h at 4 °C.

For both surface and nuclear antigen detection and intracellular cytokine detection, the labelled sample convolute was washed and incubated in 1X iridium intercalator solution (Fluidigm) at 4 °C overnight. The sample convolute was washed twice with PBS and twice with MaxPar water (Fluidigm) and following data were acquired.

## Mass cytometry data acquisition and preprocessing

Data were acquired on a CyTOF 2.1 mass cytometer (Fluidigm) with daily instrument quality control and tuning. Acquisitions from two independent CyTOF runs, each containing both of the twin siblings, were normalized using five-element beads (Fluidigm)<sup>52</sup>. To monitor potential batch effects, each independent run contained two normalization control samples that were present in both runs. Manual gating using FlowJo (TreeStar) was applied to identify live single cells in the sample convolute based on event length, centre, width, DNA (<sup>191</sup>Ir and <sup>193</sup>Ir) and live/dead (<sup>195</sup>Pt) channels. Following this, the sample convolute was debarcoded by utilizing Boolean gates of cells exclusively bearing three barcodes to prevent barcode mis-identification and facilitate doublet exclusion. Mass cytometry data were transformed in the R environment using an inverse hyperbolic sine (arcsine) function with varying cofactors to account for labelling variability between individual markers. To remove residual batch effects between the two independent mass cytometry runs, individual markers of the sample convolute were aligned by modifying the arcsine cofactor to achieve the same mean in labelling intensity for both normalization controls. A marker-based percentile normalization was applied using the 99.9th percentile of the transformed dataset. Analogously, individual cytokine positivity was determined by calculating the 99th percentile of the residual cytokine intensity using an unstimulated control.

## Algorithm-guided analysis of the cohort of twins with MS

The entire analysis was carried out in the statistical programming environment R in RStudio and Visual Studio Code (Microsoft). UMAPs were computed using the umap package with default parameters<sup>53</sup>. For the generation of the reference framework, FlowSOM was applied<sup>54</sup> in a similar manner as described previously<sup>51,55</sup>. In brief, 100 clusters of the combined dataset were generated and metaclustering was performed based on the elbow criterion determined by the ConsensusClusterPlus package. Resulting metaclusters were manually merged and annotated based on the median expression profile of individual metaclusters and localization on the UMAP. After initial clustering yielded the main populations such as CD4<sup>+</sup> T cells, CD8<sup>+</sup> T cells, B cells and myeloid cells, each main population was iteratively clustered into subpopulations that depicted the nodes of the reference framework.

The data-driven analysis was carried out using the diffcyt package<sup>56</sup>. For this, markers were separated into cell-state and cell-type markers (Supplementary Table 3) and the differential state diffcyt analysis was carried out using a design matrix considering the paired design. Significant immune features between all twins with MS and unaffected twin siblings were extracted using the moderated limma-trend method implemented in diffcyt, applying a false discovery correction according to the Benjamini–Hochberg approach<sup>57</sup>. To exclude treatment-induced immune alterations, a second filter was applied to identify significant immune features between only untreated twins with MS and unaffected twin siblings. Accordingly, immune features were extracted that fulfilled both conditions: (1) they appeared significantly different between all twins with MS and unaffected twin siblings, and (2) were not elicited by disease-modifying therapy of the twin with MS.

Network visualizations to map diffcyt-generated clusters onto the reference framework or to map different mass cytometry panels, InfinityFlow data or CITE-seq data were generated using modifications of the grappolo and vite packages of the Scaffold framework<sup>58</sup>. Resulting force-directed graphs were rearranged using the Fruchterman–Reingold and Kamada–Kawai algorithms implemented in the igraph package and modified and visualized using ggraph. Heatmaps were drawn using the pheatmap package. Correlograms were generated using the Hmisc and corrplot packages. All remaining plots were drawn using ggplot2.

## Mapping of myeloid cell populations using InfinityFlow

To fine-map the differential state phagocyte node, an extended myeloid reference framework was generated using the InfinityFlow data of healthy PBMCs containing 14 backbone markers and 332 predicted markers as published by ref. <sup>24</sup>. To generate the extended myeloid reference nodes, FlowSOM clustering was applied as described above using the backbone markers for clustering. The InfinityFlow dataset contained an overlap of 32 markers with the mass cytometry dataset of twins with MS that facilitated the mapping of the diffcyt-differential state node on the extended reference nodes using the grappolo and vite packages as described above.

## Sorting of twin samples and single-cell sequencing

Frozen PBMC samples from eight twin pairs with MS (16 samples; four pairs analysed by both CyTOF and CITE-seq and four additional pairs exclusively by CITE-seq) plus two additional healthy samples (total of 18 samples) were thawed quickly and washed twice with 1% BSA in PBS at 4 °C, followed by centrifugation at 300g for 10 min. The PBMC pellet was stained with Human TruStain FcX Fc Blocking Reagent (BioLegend) for 10 min and further stained with Fixable Viability Dye APC-eFluor 780, anti-CD3-AF700 (clone OKT3, Invitrogen), anti-CD4-pacific blue (clone S3.5,

Invitrogen), anti-CD11c-PE (clone BU15, BioLegend), and TotalSeq-C antibodies (Supplementary Table 2) for 30 min on ice. CD4<sup>+</sup> T cells were sort purified as a singlet, live, CD3<sup>+</sup> and CD4<sup>+</sup>, on a FACS Aria Fusion (BD). Simultaneously, a second population was sorted as a singlet, live, CD3<sup>-</sup> and CD11c<sup>+</sup>.

Sorted cells were washed in 0.04% BSA in PBS. Approximately 25,000 cells per population per sample were loaded on a 10x chip and run onto the 10x Chromium controller using Chromium NextGEM Single Cell V(D)J Reagent kits v1.1 with Feature Barcoding technology for Cell-Surface Protein (10x Genomics) according to the manufacturer's protocol. Gene expression, TCR enrichment and cell-surface protein expression were multiplexed using individual Chromium i7 Sample Indices. Gene expression and TCR enrichment libraries were sequenced on NovaSeq S4 Flowcells using 150-bp paired-end reads and 8 bp for the i7 index, aiming for 50,000 reads per cell for gene expression and 5,000 reads per cell for TCR enrichment. Cell-surface protein expression libraries were sequenced on NovaSeq S1 Flowcells using 50-bp paired-end reads and 8 bp for the i7 index, aiming for 10,000 reads per cell.

## Single-cell sequencing data processing

Cell Ranger software (10x Genomics, v.6.1) was used to demultiplex samples, process raw data, align reads to the GRCh38 human reference genome and summarize unique molecular identifier (UMI) counts. Filtered gene-barcode and cell-surface protein expression-barcode matrices that contained only barcodes with UMI counts that passed the threshold for cell detection were used for further analysis. Then, we processed the filtered UMI count matrices using the R package Seurat (version 4.0.3)<sup>59</sup>. Cells that expressed fewer than 500 genes and/or >15% mitochondrial reads, and genes expressed in fewer than three cells were removed from the count matrix. After quality control, only raw gene counts in high-quality singlets were submitted to: log-normalization; identification of high-variable genes by using the vst method; scaling; and regression against the number of UMIs and mitochondrial RNA content per cell. We applied an unbiased calculation of the  $k$ -nearest neighbours, generated the neighbourhood graph and embedding using UMAP. Differentially expressed genes between each cluster and all other cells were calculated using the FindAllMarkers function. Annotation of Seurat clusters was manually curated using a combination of upregulated genes for each cluster and visual inspection of key markers using UMAP visualization.

After initial cluster annotation, we subsetted all clusters containing myeloid cells and reanalysed this subset. After subsetting, integration using reciprocal principal component analysis was performed to remove batch effects and the integrated assay was used for principal component analysis and unsupervised clustering. Seurat subclusters were annotated using a combination of canonical protein and mRNA

markers. Similar to myeloid cells, only CD4<sup>+</sup> T cells in which a TCR clonotype was detected, were subsetted and reanalysed. Single-cell TCRs were computed from the TCR enrichment sequencing data using Cell Ranger vdj pipeline (10x Genomics, v.6.1). CD4<sup>+</sup> T cells containing more than two β-chains were removed.

Only samples with data for both the sibling with MS and the unaffected sibling were used for downstream analysis: seven and eight twin pairs for myeloid and T<sub>H</sub> cell populations, respectively.

## Downstream analysis of CITE-seq data

Differentially expressed genes between MS-affected and unaffected twin siblings were computed using a logistic regression model using the twinship as a latent variable. Mapping of CITE-seq data onto the mass cytometry data was accomplished by arcsine transformation of the raw counts obtained for each surface marker followed by percentile normalization similarly as performed for mass cytometry data. Resulting transformed and normalized data were combined with mass cytometry data to create a cellular network using the grappolo and vite packages as described above.

Transcription factor regulon activity was inferred based on the gene expression levels of its targets using DoRothEA<sup>60</sup>. Trajectory and pseudotime were computed based on the corresponding UMAP using Monocle 3 (ref. <sup>61</sup>). Subsequently, the Seurat object was converted into the .h5ad format for further trajectory analysis and calculation of diffusion maps using the SCANPY analysis framework implemented in Python<sup>62</sup>. Surface marker expression along pseudotime was smoothed using a generalized additive model from the mgcv package.

## Variance component analysis using the healthy twin cohort

To dissect genetic, early shared environmental and unique environmental sources of variance for frequencies of immune populations or median marker expressions within immune subsets, publicly available flow cytometry data from healthy monozygotic and dizygotic twin pairs were accessed<sup>17</sup>. Healthy monozygotic ( $n = 21$ ) and dizygotic ( $n = 22$ ) twin pairs were selected to be age-matched to the twin pairs in the cohort of twins with MS (Extended Data Table 1). A compensation matrix of the flow cytometry data was corrected using FlowJo (TreeStar) and populations matching the immune subsets of the reference framework in the cohort of twins with MS were retrieved using manual gating. Resulting immune subset frequencies or median marker expressions were imported into R. Variance components were estimated in a two-group Cholesky twin model using the umxACE function of the umx package applying default parameters—a framework commonly applied to twin studies<sup>63,64</sup>.

## Validation in the cross-sectional MS cohort

For the validation of the findings in the cohort of twins with MS, a publicly available cross-sectional cohort of non-twins with MS measured by mass cytometry was accessed<sup>14</sup> (Extended Data Table 1). The analysis was carried out using exclusively untreated patients with RRMS. A main population and T<sub>H</sub> cell subpopulation label for each cell was provided in the publicly available dataset.

## Statistical analysis

Immune cell frequencies and median marker expressions were compared using the unpaired non-parametric Mann–Whitney–Wilcoxon test or the paired non-parametric Wilcoxon signed-rank test implemented in the stats package with a false discovery correction according to the Benjamini–Hochberg approach<sup>57</sup>. For the validation cohort, the per-patient mean of CD25 expression was compared between patients with RRMS and health donors as a statistical parameter that is sensitive to outliers and could thus reflect variable CD25 expression by only a subset of naive T<sub>H</sub> cells. Mass cytometry analysis was carried out in two independent runs and was not repeated due to limited precious sample material. CITE-seq analysis was carried out once. Gene expression, module scores and transcription factor activity between cells of twins with MS and unaffected twin siblings were compared using a logistic regression model with the twinship as a latent variable and comparing each model to a null model with a likelihood ratio test and applying a Bonferroni correction. Linear regression analysis was performed using the base lm function. Inter-twin pair effect sizes were computed using the Wilcoxon two-sample paired signed-rank test implemented in the rstatix package.

## Reporting summary

Further information on research design is available in the [Nature Research Reporting Summary](#) linked to this paper.

## Data availability

Raw mass cytometry data can be accessed at <https://doi.org/10.17632/fzs5ph5p8s.1>. CITE-seq data are available at <https://doi.org/10.17632/278fy5m2yj.2>. Publicly available flow cytometry data of healthy monozygotic and dizygotic twin pairs<sup>17</sup> were accessed at <http://www.tinyurl.com/twinsFACSdata>. The publicly available cross-sectional MS mass cytometry dataset for non-twins<sup>14</sup> was accessed at <http://flowrepository.org/experiments/2166/>.

## Code availability

The code for the mass cytometry analysis and the variance component analysis of the healthy monozygotic and dizygotic twin pairs is available at <https://github.com/florianingelfinger/MStwins>. The code for the CITE-seq analysis of the cohort for twins with MS can be accessed at [https://github.com/beltranLab/twin\\_study\\_Nature\\_2021](https://github.com/beltranLab/twin_study_Nature_2021).

## References

1. Wallin, M. T. et al. Global, regional, and national burden of multiple sclerosis 1990–2016: a systematic analysis for the Global Burden of Disease Study 2016. *Lancet Neurol.* **18**, 269–285 (2019).
2. O’Gorman, C., Lin, R., Stankovich, J. & Broadley, S. A. Modelling genetic susceptibility to multiple sclerosis with family data. *Neuroepidemiology* **40**, 1–12 (2012).
3. Sawcer, S. et al. Genetic risk and a primary role for cell-mediated immune mechanisms in multiple sclerosis. *Nature* **476**, 214–219 (2011).
4. Simpson, S., Blizzard, L., Otahal, P., Van Der Mei, I. & Taylor, B. Latitude is significantly associated with the prevalence of multiple sclerosis: a meta-analysis. *J. Neurol. Neurosurg. Psychiatry* **82**, 1132–1141 (2011).
5. Nielsen, N. M. et al. Neonatal vitamin D status and risk of multiple sclerosis: a population-based case–control study. *Neurology* **88**, 44–51 (2017).
6. Gardener, H. et al. Prenatal and perinatal factors and risk of multiple sclerosis. *Epidemiology* **20**, 611–618 (2009).
7. Compston, A. & Coles, A. Multiple sclerosis. *Lancet* **372**, 1502–1517 (2008).
8. Westerlind, H. et al. Modest familial risks for multiple sclerosis: a registry-based study of the population of Sweden. *Brain* **137**, 770–778 (2014).
9. Patsopoulos, N. A. et al. Multiple sclerosis genomic map implicates peripheral immune cells and microglia in susceptibility. *Science* **365**, eaav7188 (2019).
10. International Multiple Sclerosis Genetics Consortium, Low-frequency and rare-coding variation contributes to multiple sclerosis risk. *Cell* **175**, 1679–1687.e7 (2018).

11. Hartmann, F. J. et al. Multiple sclerosis-associated IL2RA polymorphism controls GM-CSF production in human T<sub>H</sub> cells. *Nat. Commun.* **5**, 5056 (2014).
12. Smets, I. et al. Multiple sclerosis risk variants alter expression of co-stimulatory genes in B cells. *Brain* **141**, 786–796 (2018).
13. Jelcic, I. et al. Memory B cells activate brain-homing, autoreactive CD4<sup>+</sup> T cells in multiple sclerosis. *Cell* **175**, 85–100.e23 (2018).
14. Galli, E. et al. GM-CSF and CXCR4 define a T helper cell signature in multiple sclerosis. *Nat. Med.* **25**, 1290–1300 (2019).
15. Tzartos, J. S. et al. Interleukin-17 production in central nervous system-infiltrating T cells and glial cells is associated with active disease in multiple sclerosis. *Am. J. Pathol.* **172**, 146–155 (2008).
16. Duddy, M. et al. Distinct effector cytokine profiles of memory and naive human B cell subsets and implication in multiple sclerosis. *J. Immunol.* **178**, 6092–6099 (2007).
17. Roederer, M. et al. The genetic architecture of the human immune system: a bioresource for autoimmunity and disease pathogenesis. *Cell* **161**, 387–403 (2015).
18. Brodin, P. et al. Variation in the human immune system is largely driven by non-heritable influences. *Cell* **160**, 37–47 (2015).
19. Vogel, D. Y. S. et al. Macrophages in inflammatory multiple sclerosis lesions have an intermediate activation status. *J. Neuroinflammation* **10**, 35 (2013).
20. Frischer, J. M. et al. The relation between inflammation and neurodegeneration in multiple sclerosis brains. *Brain* **132**, 1175–1189 (2009).
21. Mildner, A. et al. CCR2<sup>+</sup>Ly-6C<sup>hi</sup> monocytes are crucial for the effector phase of autoimmunity in the central nervous system. *Brain* **132**, 2487–2500 (2009).
22. King, I. L., Dickendesher, T. L. & Segal, B. M. Circulating Ly-6C<sup>+</sup> myeloid precursors migrate to the CNS and play a pathogenic role during autoimmune demyelinating disease. *Blood* **113**, 3190–3197 (2009).
23. Croxford, A. L. et al. The cytokine GM-CSF drives the inflammatory signature of CCR2<sup>+</sup> monocytes and licenses autoimmunity. *Immunity* **43**, 502–514 (2015).

24. Dutertre, C. A. et al. Single-cell analysis of human mononuclear phagocytes reveals subset-defining markers and identifies circulating inflammatory dendritic cells. *Immunity* **51**, 573–589.e8 (2019).
25. Becht, E. et al. InfinityFlow: high-throughput single-cell quantification of 100s of proteins using conventional flow cytometry and machine learning. Preprint at <https://doi.org/10.1101/2020.06.17.152926> (2020).
26. Marrie, R. A. & Rudick, R. A. Drug insight: interferon treatment in multiple sclerosis. *Nat. Clin. Pract. Neurol.* **2**, 34–44 (2006).
27. The International Multiple Sclerosis Genetics Consortium. Risk alleles for multiple sclerosis identified by a genomewide study. *N. Engl. J. Med.* **357**, 851–862 (2007).
28. Ahsan, M. K. et al. Loss of interleukin-2-dependency in HTLV-I-infected T cells on gene silencing of thioredoxin-binding protein-2. *Oncogene* **25**, 2181–2191 (2006).
29. Boyman, O. & Sprent, J. The role of interleukin-2 during homeostasis and activation of the immune system. *Nat. Rev. Immunol.* **12**, 180–190 (2012).
30. Lee, P. W., Xin, M. K., Pei, W., Yang, Y. & Lovett-Racke, A. E. IL-3 is a marker of encephalitogenic T cells, but not essential for CNS autoimmunity. *Front. Immunol.* **9**, 1255 (2018).
31. Cao, Y. et al. Functional inflammatory profiles distinguish myelin-reactive T cells from patients with multiple sclerosis. *Sci. Transl. Med.* **7**, 287ra74 (2015).
32. Ruan, Q. et al. The Th17 immune response is controlled by the Rel–ROR $\gamma$ –ROR $\gamma$ T transcriptional axis. *J. Exp. Med.* **208**, 2321–2333 (2011).
33. Hussman, J. P. et al. GWAS analysis implicates NF- $\kappa$ B-mediated induction of inflammatory T cells in multiple sclerosis. *Genes Immun.* **208**, 2321–2333 (2016).
34. Chitnis, T. et al. Effect of targeted disruption of STAT4 and STAT6 on the induction of experimental autoimmune encephalomyelitis. *J. Clin. Invest.* **108**, 739–747 (2001).
35. Schneider-Hohendorf, T. et al. VLA-4 blockade promotes differential routes into human CNS involving PSGL-1 rolling of T cells and MCAM-adhesion of TH17 cells. *J. Exp. Med.* **211**, 1833–1846 (2014).

36. Rudick, R. A. et al. Natalizumab plus Interferon beta-1a for relapsing multiple sclerosis. *N. Engl. J. Med.* **354**, 911–923 (2006).
37. de Craen, A. J. M. et al. Heritability estimates of innate immunity: an extended twin study. *Genes Immun.* **6**, 167–170 (2005).
38. Gerdes, L. A. et al. Immune signatures of prodromal multiple sclerosis in monozygotic twins. *Proc. Natl Acad. Sci. USA* **117**, 21546–21556 (2020).
39. Chuluundorj, D., Harding, S. A., Abernethy, D. & La Flamme, A. C. Expansion and preferential activation of the CD14<sup>+</sup> CD16<sup>+</sup> monocyte subset during multiple sclerosis. *Immunol. Cell Biol.* **92**, 509–517 (2014).
40. Gjelstrup, M. C. et al. Subsets of activated monocytes and markers of inflammation in incipient and progressed multiple sclerosis. *Immunol. Cell Biol.* **96**, 160–174 (2018).
41. Waschbisch, A. et al. Pivotal role for CD16<sup>+</sup> monocytes in immune surveillance of the central nervous system. *J. Immunol.* **196**, 1558–1567 (2016).
42. Spath, S. et al. Dysregulation of the cytokine GM-CSF induces spontaneous phagocyte invasion and immunopathology in the central nervous system. *Immunity* **46**, 245–260 (2017).
43. Weber, F. et al. IL2RA and IL7RA genes confer susceptibility for multiple sclerosis in two independent European populations. *Genes Immun.* **9**, 259–263 (2008).
44. Dendrou, C. A. et al. Cell-specific protein phenotypes for the autoimmune locus IL2RA using a genotype-selectable human bioresource. *Nat. Genet.* **41**, 1011–1015 (2009).
45. Codarri, L. et al. ROR $\gamma$ T drives production of the cytokine GM-CSF in helper T cells, which is essential for the effector phase of autoimmune neuroinflammation. *Nat. Immunol.* **12**, 560–567 (2011).
46. Noster, R. et al. IL-17 and GM-CSF expression are antagonistically regulated by human T helper cells. *Sci. Transl. Med.* **6**, 241ra80 (2014).
47. Pekalski, M. L. et al. Postthymic expansion in human CD4 naive T cells defined by expression of functional high-affinity IL-2 receptors. *J. Immunol.* **190**, 2554–2566 (2013).

48. Thompson, A. J. et al. Diagnosis of multiple sclerosis: 2017 revisions of the McDonald criteria. *Lancet Neurol.* **17**, 162–173 (2018).
49. Polman, C. H. et al. Diagnostic criteria for multiple sclerosis: 2010 revisions to the McDonald criteria. *Ann. Neurol.* **69**, 292–302 (2011).
50. Bushnik, T. in *Encyclopedia of Clinical Neuropsychology* (eds Kreutzer, J. S., DeLuca, J. & Caplan, B.) [https://doi.org/10.1007/978-3-319-57111-9\\_1805](https://doi.org/10.1007/978-3-319-57111-9_1805) (Springer, 2018).
51. Hartmann, F. J. et al. High-dimensional single-cell analysis reveals the immune signature of narcolepsy. *J. Exp. Med.* **213**, 2621–2633 (2016).
52. Finck, R. et al. Normalization of mass cytometry data with bead standards. *Cytom. Part A* **83**, 483–494 (2013).
53. McInnes, L., Healy, J., Saul, N. & Großberger, L. UMAP: uniform manifold approximation and projection. *J. Open Source Softw.* **3**, 861 (2018).
54. Van Gassen, S. et al. FlowSOM: using self-organizing maps for visualization and interpretation of cytometry data. *Cytom. Part A* **87**, 636–645 (2015).
55. Ingelfinger, F. et al. Single-cell profiling of myasthenia gravis identifies a pathogenic T cell signature. *Acta Neuropathol.* **141**, 901–915 (2021).
56. Weber, L. M., Nowicka, M., Soneson, C. & Robinson, M. D. diffcyt: Differential discovery in high-dimensional cytometry via high-resolution clustering. *Commun. Biol.* **2**, 183 (2019).
57. Benjamini, Y. & Hochberg, Y. Controlling the false discovery rate: a practical and powerful approach to multiple testing. *J. R. Stat. Soc. Ser. B* **57**, 289–300 (1995).
58. Spitzer, M. H. et al. An interactive reference framework for modeling a dynamic immune system. *Science* **349**, 1259425 (2015).
59. Hao, Y. et al. Integrated analysis of multimodal single-cell data. *Cell* **184**, 3573–3587.e29 (2021).
60. Garcia-Alonso, L., Holland, C. H., Ibrahim, M. M., Turei, D. & Saez-Rodriguez, J. Benchmark and integration of resources for the estimation of human transcription factor activities. *Genome Res.* **29**, 1363–1375 (2019).
61. Trapnell, C. et al. The dynamics and regulators of cell fate decisions are revealed by pseudotemporal ordering of single cells. *Nat. Biotechnol.* **32**, 381–386 (2014).

62. Wolf, F. A., Angerer, P. & Theis, F. J. SCANPY: large-scale single-cell gene expression data analysis. *Genome Biol.* **19**, 15 (2018).
63. Bates, T. C., Maes, H. & Neale, M. C. Umx: twin and path-based structural equation modeling in R. *Twin Res. Hum. Genet.* **22**, 27–41 (2019).
64. Verweij, K. J. H., Mosing, M. A., Zietsch, B. P. & Medland, S. E. Estimating heritability from twin studies. *Methods Mol. Biol.* **850**, 151–170 (2012).

## Acknowledgements

We thank all study participants who took part in this study; L. Robinson from Insight Editing London for manuscript editing; the Core Facility Flow Cytometry unit at the Biomedical Center, Ludwig Maximilian University of Munich, for providing equipment; and the staff from CCGA Kiel for sequencing and transfer of data. This work was funded by the Deutsche Forschungsgemeinschaft (DFG; German Research Foundation) under Germany's Excellence Strategy within the framework of the Munich Cluster for Systems Neurology (EXC 2145 SyNergy: ID 390857198), the Gemeinnützige Hertie Stiftung, Bavarian association and National Association of the German MS Society (DMSG), Dr Leopold and Carmen Ellinger Foundation, and the association 'Verein zur Therapieforschung für MS Kranke e.V.'. This project received further funding from the European Research Council (ERC) under the European Union's Horizon 2020 research and innovation programme grant agreement no. 882424, the Swiss National Science Foundation (Ambizione PZ00P3\_193330 to S.M., and 733 310030\_170320, 310030\_188450 and CRSII5\_183478 to B.B.), as well as the Swiss MS Society Research grant to S.M. and F.I.; F.I. received a PhD fellowship from the Studienstiftung des deutschen Volkes.

## Author information

### Author notes

1. Edoardo Galli

Present address: Neurologic Clinic and Policlinic, University Hospital Basel, Department of Biomedicine, University of Basel, Basel, Switzerland

2. These authors contributed equally: Florian Ingelfinger, Lisa Ann Gerdes

3. These authors jointly supervised this work: Eduardo Beltrán, Burkhard Becher

## Affiliations

1. Institute of Experimental Immunology, University of Zurich, Zurich, Switzerland

Florian Ingelfinger, Sinduya Krishnarajah, Ekaterina Friebel, Edoardo Galli, Pascale Zwicky, Donatella De Feo, Bettina Schreiner, Sarah Mundt & Burkhard Becher

2. Department of Neurology, University Hospital Zurich, Zurich, Switzerland

Florian Ingelfinger & Bettina Schreiner

3. Institute of Clinical Neuroimmunology, University Hospital, LMU Munich, Munich, Germany

Lisa Ann Gerdes, Vladyslav Kavaka, Klara Magdalena Eglseer, Andrea Flierl-Hecht, Tania Kümpfel, Martin Kerschensteiner, Reinhard Hohlfeld & Eduardo Beltrán

4. Biomedical Center (BMC), Faculty of Medicine, LMU Munich, Martinsried, Germany

Lisa Ann Gerdes, Vladyslav Kavaka, Klara Magdalena Eglseer, Andrea Flierl-Hecht, Tania Kümpfel, Martin Kerschensteiner, Reinhard Hohlfeld & Eduardo Beltrán

5. Munich Cluster of Systems Neurology (SyNergy), Munich, Germany

Lisa Ann Gerdes, Andrea Flierl-Hecht, Tania Kümpfel, Martin Kerschensteiner, Reinhard Hohlfeld & Eduardo Beltrán

6. Department of Mathematics, University of Zurich, Zurich, Switzerland

Reinhard Furrer

7. Department of Computational Science, University of Zurich, Zurich, Switzerland

Reinhard Furrer

8. Department of Strategy, Globalization and Society, University of Lausanne, Lausanne, Switzerland

Christian Peukert

9. Gustave Roussy Cancer Campus, Villejuif, France

Charles-Antoine Dutertre

10. Institut National de la Santé Et de la Recherche Médicale (INSERM) U1015,  
Equipe Labellisée—Ligue Nationale contre le Cancer, Villejuif, France

Charles-Antoine Dutertre

11. Singapore Immunology Network, A\*STAR, Singapore, Singapore

Florent Ginhoux

## Contributions

F.I. designed and performed all of the mass cytometry experiments and performed the bioinformatic analysis of all cohorts. L.A.G., A.F.-H., T.K. and R.H. selected and characterized the cohort of twins with MS. V.K., E.B. and K.M.E. performed the CITE-seq analysis. E.G., S.K. and E.F. helped with the mass cytometry experiments. V.K., E.B., E.F., S.K. and P.Z. helped with the computational analysis. R.F. implemented the statistical model for the variance component analysis of healthy twins. C.P. provided statistical input. C.-A.D. and F.G. provided the InfinityFlow dataset and provided intellectual input. L.A.G., M.K., R.H., S.M., B.S., D.D.F. and P.Z. provided intellectual, scientific and clinical input. B.B., L.A.G., E.B., M.K. and R.H. supervised and funded the study. F.I. and B.B. wrote the manuscript. E.B., M.K., R.H. and L.A.G. edited the manuscript.

## Corresponding author

Correspondence to [Burkhard Becher](#).

## Ethics declarations

## Competing interests

The authors declare no competing interests.

## Peer review

## Peer review information

*Nature* thanks Vijay Kuchroo, Lawrence Steinman and the other, anonymous, reviewer(s) for their contribution to the peer review of this work.

## Additional information

**Publisher's note** Springer Nature remains neutral with regard to jurisdictional claims in published maps and institutional affiliations.

## Extended data figures and tables

### [Extended Data Fig. 1 Changes in canonical immune composition in twin pairs discordant for MS can be attributed to disease-modifying treatment.](#)

**a**, UMAP of 1500 cells randomly sampled per patient from the MS twin cohort (left panel). Color code indicates FlowSOM clustering and manual annotation using the lineage markers presented in the heatmap (right panel). **b**, Heatmap showing the combined expression profiles of antigens analyzed by two partially-overlapping mass cytometry panels for the indicated immune populations. **c**, Expression profiles in the CyTOF dataset of the indicated markers across the immune cell populations associated with each reference node, alongside their relative mean population frequencies across all individuals in the MS twin cohort ( $n = 114$ ). The FlowSOM-derived clusters were generated by iteratively clustering and manually merging the six main populations described in Extended Data Fig. [1a](#), [b](#). Network representation of immune cell subsets in the manually-annotated reference framework based on phenotypic similarity (right panel). **d**, Lollipop plot showing p-values for the two-sided paired non-parametric Wilcoxon signed-rank test with a false-discovery correction according to the Benjamini-Hochberg approach of immune populations in the reference framework for all MS twins ( $n = 57$ ) and controls ( $n = 57$ ).

### [Extended Data Fig. 2 MS-affected twins show functional perturbations in the monocyte compartment.](#)

**a**, UMAP of 1500 randomly sampled myeloid cells per patient with color code indicating nodes of the myeloid reference nodes. Red color indicates density overlay of the differential state phagocyte node that showed increased CCR2 and CD116 expression in MS-affected compared to unaffected twins (left panel). Heatmap (top right panel) displays expression profile of differential state phagocyte node and reference nodes in phenotypic proximity. UMAP with expression overlay of markers present in the myeloid reference nodes (bottom right panel). **b**, 2D lollipop plot showing the median expression of CCR2 and CD116 levels in the differential state phagocyte node from unaffected twins (green) and MS-affected twins (red) that did not receive disease modifying treatment. Twin pairs are indicated by a solid line.

Dashed line indicates smoothed conditional mean of the linear regression model with 95% confidence interval in shaded area. **c**, Violin plots showing the inter-twin-pair difference for median CCR2 (left panel) and CD116 (right panel) expression level in cells within the differential state phagocyte node, separated by treatment of the MS-affected twin. ALZ = Alemtuzumab (n = 3); DMF = Dimethyl Fumarate (n = 2); FTY = Fingolimod (n = 4); GLAT = Glatiramer Acetate (n = 8); IFN = Type 1 Interferons (n = 14); NAT = Natalizumab (n = 4); TFM = Teriflunomide (n = 2). **d**, UMAP of the myeloid cell compartment within healthy PBMCs outside the MS twin cohort from InfinityFlow data used to map the differential state phagocyte node of the MS twin dataset (top left panel). Color code indicates FlowSOM clustering and manual merging of the extended myeloid reference nodes by using the backbone markers presented in the heatmap showing the expression values (top right panel). The heatmap in the bottom panel displays the 100 most differentially expressed markers between the manually-annotated reference nodes. InfinityFlow backbone markers are presented in bold. **e**, Mapping of diffcyt-generated myeloid cell clusters in the MS twin dataset (left panel) on InfinityFlow data of healthy PBMCs (right panels) showing the overlay expression of CD88, CD89, Fc $\epsilon$ R1a, HLA-DQ. Dot size corresponds to population frequency among total leukocytes. Violin plots contain a bold horizontal line depicting the respective group mean. If not indicated, differences between experimental groups were statistically not significant ( $p > 5\%$ ) using a two-sided unpaired nonparametric Mann-Whitney-Wilcoxon test with a false-discovery correction according to the Benjamini-Hochberg approach.

### Extended Data Fig. 3 Transcriptional profiling of phagocytes of MS-affected twins and unaffected twin siblings.

**a**, Dot plot showing the expression profile of selected signature markers in CITE-seq data of phagocytes derived from 7 twin pairs discordant for MS (21 043 cells; left panel). Dot size corresponds to the fraction of cells within each cluster expressing the indicated transcript and color indicates average expression. UMAP showing (middle panel) the expression overlay of indicated markers and cell type yielded by clustering. Heatmap showing the expression profiles of the indicated clusters determined by CITE-seq (right panel). **b**, Violin plots (of 20 678 cells) showing the module score for genes involved in phagocytosis, antigen presentation and reactive oxygen species (ROS) production for the indicated phagocyte clusters. **c**, Heatmap showing the module score for genes involved in *CSF2RA* signaling (left box) and normalized expression of individual selected genes involved in *CSF2RA* signaling (right box) for individual MS-affected and unaffected twins in the differential state phagocyte node (162 cells). **d**, Violin plots showing the frequency of manually-annotated reference nodes in proximity to the differential state phagocyte node determined by mass cytometry for all twin pairs (n = 57) and untreated twin pairs (n = 20). **e**, Violin plots showing the inter-twin-pair difference in non-classical monocyte frequency, separated

by treatment of the MS-affected twin. **f**, Volcano plots showing the differentially expressed genes for the indicated clusters (a total of 18 024 cells) of MS-affected twins compared to unaffected twin siblings. The top 20 significant genes were annotated. Red color indicates increased and green color decreased gene expression in MS twins. **g**, Violin plots of CITE-seq data (a total of 18 024 cells) showing the module score of individual cells for type 1 IFN signature in clusters for which significant differences between MS-affected and unaffected twins were identified. Violin plots contain a bold horizontal line depicting the respective group mean. If not indicated, differences between experimental groups were statistically not significant ( $p > 5\%$ ) using a two-sided paired non-parametric Wilcoxon signed-rank test (**d**) or two-sided unpaired non-parametric Mann-Whitney-Wilcoxon test (**e**; both applying a false-discovery correction according to the Benjamini-Hochberg approach) or using a logistic regression model with the twinship as a latent variable and comparing each model to a null model with a likelihood ratio test and applying a Bonferroni correction (**f, g**).

#### **Extended Data Fig. 4 MS-affected twins are characterized by a transitional Th cell node displaying increased CD25 expression.**

**a**, Network visualization of unsupervised FlowSOM clusters in the unconventional T cell and NK cell compartment (left panel) yielded by diffcyt analysis (beige; automated clustering nodes); highlighted are MS twin differential state nodes for which features appeared significantly different in both filters (red) and nodes of the manually-annotated reference framework (green). Dot size corresponds to population frequency among total leukocytes. Heatmap showing the expression profile of MS twin differential state nodes for immune features present in the unconventional T cell and NK cell compartment and manually-annotated reference nodes in phenotypic proximity (middle panel). Violin plots showing the indicated median marker expression level in cells within the differential state NK and NKT cell nodes for all twin pairs enrolled in the study ( $n = 57$ ; right panel). **b**, Heatmap showing the expression profile of MS twin differential state Temra node and manually-annotated reference nodes in phenotypic proximity (left panel). Violin plots showing the median CD69 and CXCR3 expression level in cells within the differential state Temra nodes for all twin pairs enrolled in the study ( $n = 57$ ; right panel). **c**, Heatmap showing the expression profile of MS twin differential state nodes for immune features present in the naïve Th cell compartment and manually-annotated reference nodes in phenotypic proximity (left panel). Violin plots showing the median CD25 and CCR4 expression level in cells within the differential state naïve Th cell nodes for all twin pairs (right panel). **d**, UMAP of 1500 randomly sampled Th cells per patient with color code indicates FlowSOM clustering and manual merging of the Th cell reference nodes presented in Extended Data Fig. [1c](#). Red color indicates density overlay of the differential state naïve Th cell nodes that showed significantly increased CD25

expression between MS-affected twins and unaffected twin siblings. **e**, Lollipop plot showing p-values for the median CD25 expression levels across all differential state naïve Th cell nodes individually and combined for all MS-affected twins ( $n = 57$ ) and unaffected twin siblings ( $n = 57$ ; left panel). **f**, Dot plot showing the median CD25 expression level among cells within all T cell reference nodes for all patients enrolled in the study ( $n = 114$ ). **g**, Effect size for the twin-pair difference in median CD25 expression across cells from the manually-annotated reference Th cell (left panel) or cytotoxic T cell nodes (right panel) for all twin pairs ( $n = 57$ ). **h**, Correlogram showing the correlations between significant immune features for all individuals ( $n = 114$ ). Dot size indicates the magnitude of correlation coefficient, green dots indicate a positive correlation and red dots a negative correlation. Violin plots contain a bold horizontal line depicting the respective group mean and dashed line indicates twinship. If not indicated, the differences between experimental groups were statistically not significant ( $p > 5\%$ ) using a two-sided paired non-parametric Wilcoxon signed-rank test (**e, g**) or using the moderated *limma-trend* method implemented in *diffcyt* applying a false discovery correction according to the Benjamini-Hochberg approach (**a–c**).

### Extended Data Fig. 5 Transitional Th cells from MS-affected twins respond with increased IL-2 expression upon ex vivo reactivation.

**a**, UMAP showing CITE-seq data of Th cells (78 531 cells) derived from 8 twin pairs discordant for MS (left panel). Color coding indicates cell type yielded by clustering using the transcriptome. Heatmap showing the expression profile of the top differentially expressed genes across the different clusters (middle panel). UMAP showing the expression overlay for surface CD45RA and CD45R0 and *FOXP3* and *CX3CR1* transcripts. **b**, Lollipop plot showing p-values for increase in CD25 surface epitope expression between MS-affected twins and unaffected twins for the indicated clusters determined by CITE-seq (45 146 cells). **c**, UMAP of CITE-seq and CyTOF data with an overlay showing the transitional Th cell nodes that demonstrated a differential CD25 expression in MS-affected versus unaffected twins. **d**, Diffusion map Th cells (78 531 cells) with pseudotime overlay (left panel). Line plot (right panel) showing the indicated surface markers expression across the computed pseudotime. Horizontal lines indicate mean pseudotime for Tna 4 and Tna 5 respectively. **e**, UMAP of CITE-seq data (78 531 cells) showing expanded cells (orange;  $> 2$  TCR sequences in same patient) and non-expanded cells (grey). **f**, Heatmap and violin plots of selected genes within the IL2RA signaling pathway in Tna 4 and Tna 5 (11 343 cells) for MS-affected and unaffected twins. **g**, Volcano plots showing the differentially expressed genes of the indicated clusters (16 439 total cells) of MS-affected twins compared to unaffected twin siblings. The top 20 significant genes were annotated. Red color indicates increased and green color decreased gene expression in MS-affected twins. **h**, Network visualization (top left panel) of unsupervised FlowSOM clusters (beige); highlighted are MS twin differential nodes

for which CD25 and IL-2 expression appeared significantly (red) and nodes of the manually-annotated reference framework (green). Dot size corresponds to population frequency among total leukocytes. Heatmap (bottom panel) displays marker expression profile of differential state naïve Th cell node and manually-annotated reference nodes in phenotypic proximity. Violin plots (right panel) showing the median CD25 and IL-2 expression levels in cells within the differential state naïve Th cell nodes in untreated twin pairs ( $n = 6$ ). **i**, 2D lollipop plot showing the median expression of CD25 and IL-2 for unaffected twin siblings (green) and MS-affected twin siblings (red;  $n = 25$ ). Twin pairs are indicated by solid line. **j**, Violin plots showing the inter-twin-pair difference in median IL-2 expression level in the differential state naïve Th cell node, separated according to disease stage of the MS-affected twin. RRMS = relapsing-remitting MS ( $n = 21$ ); SPMS = secondary progressive MS ( $n = 4$ ). **k**, Biaxial plot showing the IL-2 and CD4 expression levels for cells in the differential state naïve Th cell node. The dashed line indicates the gate to determine IL-2-positive cells. **l, m**, Effect size for the twin-pair difference of indicated cytokines in IL-2 expressing cells in the MS twin differential state node for untreated twin pairs ( $n = 6$ ; **l**, left panel). Violin plots showing the median IL-17A and IL-3 (**l**, right panel) or IL-10 and IL-9 (**m**) expression level in IL-2-expressing cells within the differential state transitional Th cell node for MS-unaffected twins and untreated MS-affected twins. **n**, Heatmap displaying the transcription factor regulon activity for *STAT4* and *RELA* in Tna 4 and Tna 5 (11 343 cells) determined by CITE-seq for individual twins. **o**, Lollipop plot showing p-values for increase in VLA4 surface epitope expression between MS-affected and unaffected twins for the indicated clusters (75 856 cells) determined by CITE-seq. Violin plots contain a bold horizontal line depicting the respective group mean and dashed line indicates twinship. If not indicated, the differences between experimental groups were statistically not significant ( $p > 5\%$ ) using an two-sided unpaired nonparametric Mann-Whitney-Wilcoxon test (**j**) or a two-sided paired non-parametric Wilcoxon signed-rank test (**h, l, m**) with false discovery correction according to the Benjamini-Hochberg approach or a logistic regression model using the twinship as a latent variable and comparing each model to a null model with a likelihood ratio test and applying a Bonferroni correction (**b, g, o**).

## [Extended Data Fig. 6 Monozygotic and dizygotic non-MS twin pairs facilitate dissection of genetic and environmental influences on immune composition.](#)

**a**, Biaxial plots displaying the gating strategy for cells from monozygotic and dizygotic twin pairs of the non-MS twin cohort in order to obtain comparable cell populations as present in the reference framework of the MS twin cohort. **b**, Pie chart displaying the variance components for CD25 expression in memory Th cells (left panel) and regulatory T cells (Treg; right panel) using the structural equation model

and the median CD25 expression in the non-MS twin cohort. **c**, Heatmap (top left panel) displays expression profile of canonical subsets detected in the validation cohort. Network visualization of unsupervised FlowSOM nodes of the validation cohort and mapping onto the manually-annotated reference framework (grey dots; bottom left panel). Annotation provided in the publicly available mass cytometry dataset was used to match the main clusters in the reference nodes and indicated by the respective color. Dot size corresponds to population frequency among total leukocytes. Violin plots (right panel) showing the frequency of major canonical immune subsets in the validation cohort for HD ( $n = 29$ ) and RRMS patients ( $n = 30$ ). **d**, Violin plots showing the frequency of annotated Th cell nodes in the validation cohort for HD and RRMS patients (right panel). Heatmap (left panel) displaying the expression profile for the indicated Th cell populations. Violin plots contain a bold horizontal line depicting the respective group mean. If not indicated, differences between experimental groups were statistically not significant ( $p > 5\%$ ) using a two-sided unpaired nonparametric Mann-Whitney-Wilcoxon test with a false discovery correction according to the Benjamini-Hochberg approach.

**Extended Data Table 1 Clinical and demographic baseline characteristics of all study cohorts**

**Extended Data Table 2 Overview of results for data-driven analysis of mass cytometry data using diffcyt**

## Supplementary information

### Reporting Summary

### 41586\_2022\_4419\_MOESM2\_ESM.xlsx

Supplementary Table 1 **Clinical and demographic characteristics of all the patients in the MS twin cohort used for mass cytometry**. Disease state indicates whether the twin was affected by MS or unaffected. MS = Multiple Sclerosis; ALZ = Alemtuzumab; DMF = Dimethyl Fumarate; FTY = Fingolimod; GLAT = Glatiramer Acetate; IFN = Type 1 Interferons; NAT = Natalizumab; TFM = Teriflunomide; f = female; m = male; RRMS = relapsing-remitting MS; SPMS = secondary progressive MS; PPMS = primary progressive MS; EDSS = Expanded disability status scale; NA = not applicable; unk = unknown..

### 41586\_2022\_4419\_MOESM3\_ESM.xlsx

Supplementary Table 2 **Clinical and demographic characteristics of untreated patients in the MS twin cohort used for mass cytometry**. Disease state indicates

whether the twin was affected by MS or unaffected. MS = Multiple Sclerosis; female; m = male; RRMS = relapsing-remitting MS; SPMS = secondary progressive MS; PPMS = primary progressive MS; EDSS = Expanded disability status scale; NA = not applicable; unk = unknown.

### **41586 2022 4419 MOESM4 ESM.xlsx**

**Supplementary Table 3 Heavy metal labeled antibodies used in the mass cytometry experiments.** Metal tagged antibodies were either purchased preconjugated (Fluidigm) or conjugated using the MaxPar X8 polymer (for other suppliers). NA = non-applicable; ICS = intracellular cytokine staining.

### **41586 2022 4419 MOESM5 ESM.xlsx**

**Supplementary Table 4 Differentially expressed genes in phagocyte clusters determined by CITE-seq.** Shown are cluster-gene combinations that were statistically significant ( $p \text{ adj} < 0.05$ ) comparing MS twins to their non-MS twin siblings using a logistic regression model with twinship as a latent variable, comparing each model to a null model with a likelihood ratio test and applying a Bonferroni correction. Pct indicates the fraction of cells within each cluster that expressed the respective gene. FC = fold change; pct = percent expressed.

### **41586 2022 4419 MOESM6 ESM.xlsx**

**Supplementary Table 5 Differentially expressed genes in Th cell clusters determined by CITE-seq.** Shown are cluster-gene combinations that were statistically significant ( $p \text{ adj} < 0.05$ ) comparing MS twins to their non-MS twin siblings using a logistic regression model with twinship as a latent variable, comparing each model to a null model with a likelihood ratio test and applying a Bonferroni correction. Pct indicates the fraction of cells within each cluster that expressed the respective gene. FC = fold change; pct = percent expressed.

### **41586 2022 4419 MOESM7 ESM.xlsx**

**Supplementary Table 6 Differential transcription factor activity in naive Th cell clusters determined by CITE-seq.** Shown are cluster-transcription factor combinations for which transcription factor activity was statistically significant ( $p \text{ adj} < 0.05$ ) comparing MS twins to their non-MS twin siblings using a logistic regression model with twinship as a latent variable, comparing each model to a null model with a likelihood ratio test and applying a Bonferroni correction. Transcription factor activity was estimated using DoRothEA, a tool that computes regulon activity based on reported transcription factor - target gene interaction. Pct indicates the fraction of cells

within each cluster that were positive for the respective transcription factor activity. FC = fold change; pct = percent expressed.

## **41586\_2022\_4419\_MOESM8\_ESM.xlsx**

**Supplementary Table 7 Oligonucleotide labeled antibodies used in the CITE-seq experiments.** Oligonucleotide tagged antibodies (TotalSeq-C) were purchased preconjugated from Biolegend. NA = non-applicable.

## **Rights and permissions**

**Open Access** This article is licensed under a Creative Commons Attribution 4.0 International License, which permits use, sharing, adaptation, distribution and reproduction in any medium or format, as long as you give appropriate credit to the original author(s) and the source, provide a link to the Creative Commons license, and indicate if changes were made. The images or other third party material in this article are included in the article's Creative Commons license, unless indicated otherwise in a credit line to the material. If material is not included in the article's Creative Commons license and your intended use is not permitted by statutory regulation or exceeds the permitted use, you will need to obtain permission directly from the copyright holder. To view a copy of this license, visit <http://creativecommons.org/licenses/by/4.0/>.

## Reprints and Permissions

## **About this article**

### **Cite this article**

Ingelfinger, F., Gerdes, L.A., Kavaka, V. *et al.* Twin study reveals non-heritable immune perturbations in multiple sclerosis. *Nature* **603**, 152–158 (2022). <https://doi.org/10.1038/s41586-022-04419-4>

- Received: 18 March 2021
- Accepted: 04 January 2022
- Published: 16 February 2022
- Issue Date: 03 March 2022
- DOI: <https://doi.org/10.1038/s41586-022-04419-4>

## Share this article

Anyone you share the following link with will be able to read this content:

[Get shareable link](#)

Sorry, a shareable link is not currently available for this article.

[Copy to clipboard](#)

Provided by the Springer Nature SharedIt content-sharing initiative

## [Twin study probes non-heritable immune aspects of multiple sclerosis](#)

- Heather Wood

Research Highlight 03 Mar 2022

---

This article was downloaded by **calibre** from <https://www.nature.com/articles/s41586-022-04419-4>

| [Section menu](#) | [Main menu](#) |

- Article
- Open Access
- [Published: 23 February 2022](#)

# Low-dose metformin targets the lysosomal AMPK pathway through PEN2

- [Teng Ma<sup>1</sup>](#), [na1](#),
- [Xiao Tian<sup>1</sup>](#), [na1](#),
- [Baoding Zhang<sup>1</sup>](#), [na1](#),
- [Mengqi Li<sup>1</sup>](#),
- [Yu Wang<sup>1</sup>](#),
- [Chunyan Yang<sup>1</sup>](#),
- [Jianfeng Wu<sup>2</sup>](#),
- [Xiaoyan Wei<sup>1</sup>](#),
- [Qi Qu<sup>1</sup>](#),
- [Yixin Yu<sup>1</sup>](#),
- [Shating Long<sup>1</sup>](#),
- [Jin-Wei Feng<sup>1</sup>](#),
- [Chun Li<sup>1</sup>](#),
- [Cixiong Zhang<sup>1</sup>](#),
- [Changchuan Xie](#) [ORCID: orcid.org/0000-0002-1078-0464<sup>1</sup>](#),
- [Yaying Wu<sup>1</sup>](#),
- [Zheni Xu](#) [ORCID: orcid.org/0000-0001-7926-0259<sup>1</sup>](#),
- [Junjie Chen<sup>3</sup>](#),
- [Yong Yu<sup>1</sup>](#),
- [Xi Huang<sup>1</sup>](#),
- [Ying He<sup>1</sup>](#),
- [Luming Yao](#) [ORCID: orcid.org/0000-0002-9417-4356<sup>1</sup>](#),
- [Lei Zhang<sup>1</sup>](#),
- [Mingxia Zhu](#) [ORCID: orcid.org/0000-0002-1858-5655<sup>1</sup>](#),
- [Wen Wang<sup>4</sup>](#),
- [Zhi-Chao Wang<sup>4</sup>](#),

- [Mingliang Zhang<sup>5</sup>](#),
- [Yuqian Bao<sup>5</sup>](#),
- [Weiping Jia ORCID: orcid.org/0000-0002-6244-2168<sup>5</sup>](#),
- [Shu-Yong Lin ORCID: orcid.org/0000-0002-4419-1713<sup>1</sup>](#),
- [Zhiyun Ye<sup>1</sup>](#),
- [Hai-Long Piao ORCID: orcid.org/0000-0001-7451-0386<sup>4</sup>](#),
- [Xianming Deng ORCID: orcid.org/0000-0002-9354-5864<sup>1</sup>](#),
- [Chen-Song Zhang ORCID: orcid.org/0000-0001-5218-0101<sup>1</sup>](#) &
- [Sheng-Cai Lin ORCID: orcid.org/0000-0003-1993-8376<sup>1</sup>](#)

[Nature](#) volume 603, pages 159–165 (2022)

- 32k Accesses
- 204 Altmetric
- [Metrics details](#)

## Subjects

- [Cell signalling](#)
- [Metabolism](#)

## Abstract

Metformin, the most prescribed antidiabetic medicine, has shown other benefits such as anti-ageing and anticancer effects<sup>1,2,3,4</sup>. For clinical doses of metformin, AMP-activated protein kinase (AMPK) has a major role in its mechanism of action<sup>4,5</sup>; however, the direct molecular target of metformin remains unknown. Here we show that clinically relevant concentrations of metformin inhibit the lysosomal proton pump v-ATPase, which is a central node for AMPK activation following glucose starvation<sup>6</sup>. We synthesize a photoactive metformin probe and identify PEN2, a subunit of  $\gamma$ -secretase<sup>7</sup>, as a binding partner of metformin with a dissociation constant at micromolar levels. Metformin-bound PEN2 forms a complex with ATP6AP1, a subunit of the v-ATPase<sup>8</sup>, which leads to the inhibition of v-ATPase and the activation of AMPK without effects on cellular AMP levels. Knockout of *PEN2* or re-introduction of a *PEN2* mutant that does not bind ATP6AP1 blunts AMPK activation. In vivo, liver-specific knockout of *Pen2* abolishes metformin-mediated reduction of hepatic fat content, whereas intestine-specific knockout of *Pen2* impairs its glucose-lowering effects. Furthermore, knockdown of *pen-2* in *Caenorhabditis elegans* abrogates metformin-induced extension of lifespan. Together, these findings reveal

that metformin binds PEN2 and initiates a signalling route that intersects, through ATP6AP1, the lysosomal glucose-sensing pathway for AMPK activation. This ensures that metformin exerts its therapeutic benefits in patients without substantial adverse effects.

[Download PDF](#)

## Main

Metformin is the usual first-line drug of choice to reduce blood glucose levels in patients with type 2 diabetes mellitus. It also has other clinically beneficial effects such as reductions in body weight and hepatic fat content, and decreased cancer incidence in patients with diabetes who take the drug<sup>1,3</sup>. Administration of metformin to various organisms, including nematodes (*C. elegans*) and mice, can also extend lifespan and health span<sup>9,10</sup>. Metformin requires transporters of the OCT family to enter cells, which restricts its primary target organs to the liver, the kidney and the intestine<sup>5,11</sup>. Various mechanisms of action for metformin to exert its roles have been proposed. Metformin can inhibit complex I of the mitochondrial electron transport chain in hepatocytes<sup>12,13</sup>, which leads to decreases in ATP and increases in AMP levels and in turn activates AMPK through the canonical adenine-nucleotide-dependent mechanism<sup>14</sup>. Increased AMP also inhibits fructose-1,6-bisphosphatase-1 and adenylate cyclase to block gluconeogenesis<sup>15,16</sup>. Metformin has also been proposed to alter cellular redox status, which increases NAD<sup>+</sup>/NADH ratios and leads to the suppression of the utilization of gluconeogenic substrates. Metformin may also exert its glucose-lowering effects in the gut by promoting the secretion of glucagon-like peptide 1 (GLP-1)<sup>1</sup>.

Among the various potential effectors of metformin identified, AMPK, a master controller of metabolic homeostasis, has been placed at centre stage<sup>17,18</sup>. AMPK, through phosphorylating acetyl-CoA carboxylase 1 (ACC1) and ACC2, is indispensable for the attenuation of hepatic steatosis and atherosclerosis in diabetic mice that have been given chronic metformin treatment<sup>19,20</sup>. Duodenal activation of AMPK is essential for GLP-1 secretion in L cells, and is required for the acute glucose-lowering effect of metformin when orally administered<sup>21</sup>. Furthermore, the metformin-mediated retardation of ageing in *C. elegans* is through an AMPK-dependent mechanism<sup>9,18</sup>.

It has been widely accepted that metformin activates AMPK by inhibiting complex I of the mitochondrial electron transport chain, which impairs ATP synthesis and in turn increases AMP/ATP and ADP/ATP ratios<sup>12,13,14</sup>. However, the decrease in energy levels could only be observed at peak concentrations after high doses of metformin in

mice ( $\geq 250$  mg kg $^{-1}$  orally, which yields peak plasma concentrations of 125–150  $\mu$ M after 1–2 h and rapidly decreases thereafter<sup>16</sup>). By comparison, the plasma metformin concentrations in patients taking standard clinical doses of 1.5–2 g per day (Glucophage, 0.5 g three times a day or four times a day) have been reported to be only 5–30  $\mu$ M (ref. <sup>11</sup>) (Extended Data Fig. <sup>1a</sup>), which may not be sufficient to increase AMP/ATP and ADP/ATP ratios<sup>22,23</sup>. Therefore, it is necessary to explore how clinically relevant doses of metformin activates AMPK.

## PEN2 binds to metformin

We found that metformin at clinical doses sufficiently inhibited the vacuolar H $^{+}$ -ATPase (v-ATPase) on the lysosome (Fig. <sup>1a,b</sup> and Extended Data Fig. <sup>1</sup>, with detailed discussions in Supplementary Note <sup>1</sup>). We therefore used an affinity-based approach to analyse protein extracts of purified lysosomes to identify potential direct targets for metformin (Fig. <sup>2a</sup>). Two types of photoactive metformin probes, Met-P1 and Met-P2, were synthesized (Extended Data Fig. <sup>2a</sup>), but only Met-P1 was able to inhibit lysosomal acidification; Met-P2 had no effect and was therefore discarded (Extended Data Fig. <sup>2b</sup>). After incubation with lysosome lysates, Met-P1 was conjugated to proteins by ultraviolet irradiation and then biotinylated (chemical reactions shown in Extended Data Fig. <sup>2c</sup>). NeutrAvidin beads were used to pull down the conjugates for analysis by mass spectrometry (MS). As listed in Supplementary Table <sup>1</sup>, we engineered expression plasmids for a total of 367 proteins, and verified that 113 proteins of them could be pulled down by Met-P1 when individually expressed in HEK293T cells (Supplementary Note <sup>2</sup>). Next, we individually knocked down those 113 proteins in mouse embryonic fibroblasts (MEFs) through lentivirus-mediated short hairpin RNA (shRNA) silencing. We observed that depletion of PEN2, but not others, rendered the cells insensitive to metformin treatment, as assessed by levels of AMPK activation and inhibition of v-ATPase (Extended Data Figs. <sup>2d</sup> and <sup>3a,b</sup>). Consistently, knockout of *PEN2* blocked low-dose metformin-induced AMPK activation and v-ATPase inhibition in primary hepatocytes, MEFs and HEK293T cells (Fig. <sup>2b,c</sup> and Extended Data Fig. <sup>3c–i,k,l</sup>; note that knockout of *PEN2* did not affect basal lysosomal pH levels (Supplementary Note <sup>2</sup>)). Of note, depletion of PEN2 in all three cell types did not affect the transport of metformin into cells (Extended Data Fig. <sup>3j</sup>). PEN2 was originally identified as a component of  $\gamma$ -secretase<sup>7</sup>. Unlike PEN2, other subunits of  $\gamma$ -secretase did not directly participate in AMPK activation for low-dose metformin (Extended Data Figs. <sup>3m–s</sup>, <sup>4a,b</sup> and <sup>6m–o</sup>; detailed discussions on the relationship between metformin and  $\gamma$ -secretase are provided in Supplementary Note <sup>3</sup>). Imaging by confocal microscopy (Extended Data Fig. <sup>4c</sup>), stochastic optical reconstruction microscopy (STORM; Fig. <sup>2d</sup>) and APEX tag-based transmission electron microscopy (Fig. <sup>2e</sup>, with validation data in Extended Data Fig. <sup>4d</sup>) showed that a portion of PEN2 (approximately 40%; Extended Data Fig. <sup>4c</sup>) was localized on

the lysosome. This finding was confirmed in subcellular fractionation assays (Extended Data Fig. 4e, with detailed discussions on PEN2 localization provided in Supplementary Note 4 and Extended Data Figs. 4f,g and 5a), and metformin did not alter the subcellular localization of PEN2 (Extended Data Fig. 5b,c). These results indicate that the pool of lysosomally localized PEN2 may have a distinct role, whereby it participates in metformin-induced AMPK activation (discussed in Supplementary Note 5). Indeed, constructs of PEN2 fused to other organelle-specific proteins did not restore AMPK activation by metformin when re-introduced into *Pen2*<sup>-/-</sup> MEFs (Extended Data Fig. 5d, with validation data in Extended Data Fig. 5d,e).

**Fig. 1: Metformin activates AMPK without increasing AMP/ADP levels.**



**a.** Low-dose metformin deacidifies lysosomes in mouse primary hepatocytes (left). Cells were treated with 5  $\mu$ M metformin (Met) for 2 h, and the relative fluorescence

intensities of Lysosensor are shown (right). **b**, Metformin does not increase AMP/ADP levels in mouse primary hepatocytes. Cells were treated with 5  $\mu$ M metformin for the indicated time periods followed by analysis of phosphoAMPK $\alpha$  and p-ACC by immunoblotting (IB; left), AMP/ATP and ADP/ATP ratios, and the absolute concentrations of AMP, ADP and ATP by mass spectrometry (bottom right). After washing three times with PBS, the intracellular metformin concentrations (conc.) were measured by mass spectrometry (top right). For gel source data, see Supplementary Fig. 1. Data are the mean  $\pm$  s.e.m.,  $n$  values are labelled on each panel.  $P$  values were calculated using two-sided Mann–Whitney test (**a**) or one-way analysis of variance (ANOVA) followed by Tukey’s (**b**, bottom right) or Sidak’s test (**b**, top right). Experiments in **a** were performed three times and experiments in **b** were performed five times.

[Source data](#).

**Fig. 2: PEN2 binds to metformin and is required for low-dose metformin-induced AMPK activation.**

---

 **figure 2**

**a**, A schematic depicting the procedure of the affinity-based approach that used a photoactive metformin probe (Met-P) to identify target(s) of metformin from protein extracts of lysosomes purified from MEFs. MS, mass spectrometry. **b, c**, Knockout of *Pen2* blocks the activation of AMPK by low-dose metformin. Mouse primary hepatocytes (**b**) and MEFs (**c**; clone 1, and same hereafter, unless stated otherwise) were treated with 5  $\mu$ M and 200  $\mu$ M metformin for 2 h and 12 h, respectively, followed by analysis of p-AMPK $\alpha$  and p-ACC. WT, wild type. **d, e**, STORM image of MEFs (**d**) and TEM image of HEK293T cells (**e**) showing that a portion of PEN2 is localized to the lysosome (**e**, black arrowheads) and overlaps with the lysosome marker LAMP2 (**d**). **f, g**, PEN2 is able to bind metformin. **f**, In SPR assays, PEN2 was incubated with metformin at the indicated concentrations. **g**, In Met-P1-binding assays, HEK293T cells transfected with PEN2 or PEN2-2A were lysed, incubated with 10  $\mu$ M Met-P1 and then biotinylated, and then affinity pull-down (AP) of biotinylated proteins was performed. TCL, total cell lysate. **h**, PEN2-2A does not mediate AMPK activation by metformin. *Pen2*<sup>-/-</sup> MEFs re-introduced with haemagglutinin (HA)-tagged PEN2-2A

were treated with 200  $\mu$ M metformin for 12 h, followed by analysis of p-AMPK $\alpha$  and p-ACC. For gel source data, see Supplementary Fig. 1. Experiments in this figure were performed three times, except those in **b** and **c**, which were performed four times.

High concentrations of metformin can increase cellular levels of AMP, which can allosterically activate AMPK; therefore, it was anticipated that AMPK activation induced by high metformin levels would be lysosome-independent. Indeed, high concentrations of metformin, which increased AMP/ATP and ADP/ATP ratios (Extended Data Fig. 1m–p), bypassed the requirement of PEN2 for AMPK activation, as did phenformin and buformin (Extended Data Fig. 5f). Moreover, PEN2 deficiency did not affect glucose-starvation-induced AMPK activation (Extended Data Fig. 5g) or other agonists (Extended Data Fig. 5g, h).

We next investigated the biophysical nature that underlies the binding of PEN2 to metformin. Differential scanning calorimetry assays showed a shift in the thermal transition midpoint in the presence of metformin (Extended Data Fig. 6a). Isothermal calorimetry (ITC) and surface plasmon resonance (SPR) measurements further gave estimated dissociation constant ( $K_D$ ) values of 1.7  $\mu$ M and 0.15  $\mu$ M (with an association rate constant ( $k_a$ ) value of  $2,815\text{ M}^{-1}\text{s}^{-1}$ ), respectively. These values are within the range of detected intracellular metformin concentrations in animals or human patients administered with regular doses (Fig. 2f and Extended Data Fig. 6b, f, with detailed discussions in Supplementary Note 6). The ITC measurement gave an additional metformin binding site, with a much higher  $K_D$  of 98  $\mu$ M, which is beyond the ranges of clinically relevant intracellular concentrations of metformin (Extended Data Fig. 6b). As a control, other  $\gamma$ -secretase subunits did not show apparent binding affinity to metformin (Extended Data Fig. 6c). We also performed mass spectrometry on purified PEN2 conjugated to Met-P1 to identify the residue(s) responsible for binding metformin. As a result, the Y47 residue of PEN2 was identified (Extended Data Fig. 6d), which indicates that metformin may be able to bind the amino-terminal cytosolic face. In silico modelling further illustrated that at the N-terminal region of PEN2, metformin forms direct contacts with PEN2 through the F35 and E40 residues on PEN2 (Extended Data Fig. 6e). Indeed, mutation of both F35 and E40 to alanine on PEN2 (PEN2-2A) blocked its interaction with metformin (Fig. 2g and Extended Data Fig. 6f). Re-introduction of PEN2-2A into *Pen2*<sup>−/−</sup> MEFs did not restore metformin-induced AMPK activation, or v-ATPase inhibition, even though PEN2-2A shares a similar subcellular localization with wild-type PEN2 (Fig. 2h and Extended Data Fig. 6h, with validation data in Extended Data Fig. 6g, i). The mass spectrometry results also revealed an additional, but much weaker, metformin-binding site at the carboxy-terminal (luminal) face of PEN2. Given that metformin may be transported through endocytosis and may be present in the lumen of lysosomes, we examined possible binding of metformin to the C terminus of PEN2. We found that mutation of residues

at this site did not block metformin binding or dampen AMPK activation (Extended Data Fig. 6d, j–l).

## ATP6AP1 tethers PEN2 to v-ATPase

We next investigated how metformin binding causes PEN2 to interact with and inhibit v-ATPase. We analysed PEN2 that was immunoprecipitated after incubation with protein extracts of lysosomes by mass spectrometry. A total of 1,881 proteins were detected in the PEN2 prey, among which 889 were changed after metformin treatment. Of these 889 proteins, 123 are lysosome-resident proteins (Supplementary Table 2). Among these 123 candidates, we were particularly interested in ATP6AP1 (also known as Ac45), an accessory factor of v-ATPase<sup>8</sup>, because its metformin-dependent interaction with PEN2 could be verified by co-immunoprecipitation assays in cells and in vitro (Fig. 3a–c and Extended Data Fig. 7a, b). Domain-mapping experiments identified that amino-acid residues from 420 to 440, which constitute the transmembrane domain of ATP6AP1, were responsible for PEN2 binding (Extended Data Fig. 7c). This finding was reinforced by results from experiments that used the chimeric construct LAMP2<sup>TM</sup>–ATP6AP1, which has the ATP6AP1 transmembrane domain replaced by the transmembrane domain of the lysosomal protein LAMP2. This construct did not interact with PEN2 (Extended Data Fig. 7d). In addition, PEN2 mutations on its interface towards ATP6AP1 (based on in silico docking assays; PEN2-20A), impaired the interaction between PEN2 and ATP6AP1 (Fig. 3d and Extended Data Fig. 7e–g). Of note, ATP6AP1 itself did not bind Met-P1 (Extended Data Fig. 7h). Together, these results indicate that after binding to metformin, lysosomal PEN2 is recruited to ATP6AP1 of the v-ATPase complex.

**Fig. 3: ATP6AP1 tethers PEN2 to v-ATPase for AMPK activation.**

---

 **figure 3**

**a–c**, Identification of ATP6AP1 as an interacting protein of PEN2. Lysates of HEK293T cells expressing HA–PEN2 or Myc–ATP6AP1 (**a**), and lysates from wild-type MEFs, *Pen2*<sup>−/−</sup> MEFs (**b**) or *Atp6ap1*<sup>−/−</sup> MEFs (**c**) were incubated with 10 µM metformin and immunoprecipitated (IP) for the PEN2 and AP1 proteins. **d**, Metformin does not promote the interaction between ATP6AP1 and PEN2-20A. HEK293T cells transfected with HA-tagged PEN2 or PEN2-20A were lysed and treated as in **a**. The interaction between ATP6AP1 and PEN2 was analysed by IP followed by IB. **e–i**, Loss of the PEN2–ATP6AP1 interaction abolishes the effects of metformin on AMPK activation. *Atp6ap1*<sup>−/−</sup> MEFs re-introduced with ATP6AP1<sup>Δ420–440</sup> (**e**) or *Pen2*<sup>−/−</sup> MEFs re-introduced with the PEN2-20A mutant (**f**) were treated with 200 µM metformin for 12 h followed by analysis of p-AMPK and p-ACC. **g–i**, The effects of ATP6AP1 and PEN2 mutants on the lysosomal translocation of AXIN (**g**), and the formation of the AXIN-based complex (**h, i**) were analysed. Concanamycin A (conA; 5 µM for 2 h) was used as a control. FL, full length. **j**, A schematic depicting that the

metformin–PEN2–ATP6AP1 and the FBP–aldolase axes constitute two incoming shunts that converge at v-ATPase to elicit AMPK activation through the lysosomal pathway. For gel source data, see Supplementary Fig. 1. Data are the mean  $\pm$  s.e.m.,  $n$  values are labelled on each panel, and  $P$  values were calculated using two-sided Student's  $t$ -test (**a**, for Myc–ATP6AP1), two-sided Student's  $t$ -test with Welch's correction (**a**, for HA–PEN2) or two-way ANOVA, followed by Tukey's test (**g**). Experiments in this figure were performed three times, except for **a** (four times), and **h** and **i** (five times).

### Source data

We next examined how ATP6AP1 mediates the inhibition of v-ATPase by metformin. First, as an integral member of v-ATPase, knockout of ATP6AP1 led to constitutive activation of AMPK (Extended Data Fig. 7*i–k*). When we re-introduced the truncated ATP6AP1 mutant ( $\Delta 420\text{--}440$ ), which lacks the transmembrane domain required for its interaction with PEN2, into *Atp6ap1*<sup>−/−</sup> MEFs, the basal activity of v-ATPase was restored (Extended Data Fig. 8*a*, with validation data in Extended Data Fig. 7*l*). Of note, the ATP6AP1 $^{\Delta 420\text{--}440}$  mutant did not mediate metformin-induced v-ATPase inhibition or AMPK activation (Fig. 3*e* and Extended Data Fig. 8*b,c*). Similar restoration of v-ATPase activity, as well as blockade of AMPK activation, was observed when the LAMP2<sup>TM</sup>–ATP6AP1 chimeric construct was re-introduced into *Atp6ap1*<sup>−/−</sup> MEFs (Extended Data Fig. 8*a,d*, with validation data in Extended Data Fig. 7*l*). Furthermore, re-introduction of PEN2-20A, which cannot interact with ATP6AP1 even though it is localized in a similar manner as wild-type PEN2 (Extended Data Fig. 8*e*), into *Pen2*<sup>−/−</sup> MEFs blocked the activation of AMPK and the inhibition of v-ATPase (Fig. 3*f* and Extended Data Fig. 8*f*). These results indicate that metformin-bound PEN2, by gaining affinity to ATP6AP1, inhibits v-ATPase to activate AMPK.

We previously reported that glucose deprivation can activate lysosomal AMPK without increasing AMP/ADP levels through v-ATPase, Ragulator and AXIN<sup>24</sup>, which are downstream of the fructose-1,6-bisphosphate sensor aldolase. Knockout of *AXIN*, *LAMTOR1* (a subunit of Ragulator) or the v0c subunit of v-ATPase (*ATP6v0c*) in the liver, MEFs or HEK293T cells blocked the activation of AMPK by low-dose metformin (Extended Data Fig. 9*a–h*). Re-introduction of the AMPK $\beta 1$ -G2A mutant, which cannot localize on lysosomes, into MEFs that are deficient in both AMPK $\beta 1$  and AMPK $\beta 2$  also blocked the activation of AMPK by low-dose metformin (Extended Data Fig. 9*a–h*). Moreover, high concentrations of metformin bypassed the requirement for AXIN and LAMTOR1 in AMPK activation (Extended Data Fig. 9*a–c, h*). PEN2 and ATP6AP1 seem to act as factors upstream of AXIN and LAMTOR1 through their regulation of v-ATPase. This is based on the fact that the lysosomal translocation of AXIN—and the formation of the AXIN-based complex—was

dampened in *Pen2*<sup>-/-</sup> MEFs, in *Pen2*<sup>-/-</sup> MEFs expressing PEN2-2A or PEN2-20A mutants, and in *Atp6ap1*<sup>-/-</sup> MEFs expressing the ATP6AP1<sup>Δ420–440</sup> mutant when treated with metformin (Fig. 3g–i, Extended Data Figs. 9i–l and 10a, b). Blockade of v-ATPase by its inhibitor concanamycin A restored these phenotypes (Fig. 3g–i, Extended Data Figs. 9i, k, 10a, b and 11a, b). As additional controls, aldolase and TRPV, which are required for signalling of low glucose to v-ATPase and AMPK<sup>6,25</sup>, were dispensable for the PEN2-sensed AMPK activation by metformin. This result was supported by the following lines of evidence: (1) expression of ALDOA-D34S, which mimics a high glucose state and blocks glucose-deprivation-induced AMPK activation in both mouse liver and cultured cells<sup>6</sup> (Extended Data Fig. 11c), did not block metformin-induced AMPK activation (Extended Data Fig. 11d, e); and (2) a quadruple knockout of *Trpv1*–*Trpv4* in MEFs, or knockdown of *Trpv2*–*Trpv4* in the liver of *Trpv1*<sup>-/-</sup> mice (leaving those cells or tissues with scarce TRPV expression<sup>25</sup>), did not affect the activation of AMPK when treated with metformin (Extended Data Fig. 11f, g). Together, PEN2–ATP6AP1 relays the signal of metformin, as an intersecting shunt, to inhibit v-ATPase, which primes the lysosomal translocation of AXIN and LKB1 to the lysosomal surface for phosphorylation and activation of AMPK (schematically represented in Fig. 3j).

## Phenotypes in animal models

We next explored the functions of PEN2 and ATP6AP1 to mediate the beneficial effects of metformin in animal models. We observed that mice that had PEN2 depleted specifically in the intestine (PEN2-IKO mice; generated as illustrated in Extended Data Fig. 12c, d), had impaired postprandial glucose-lowering effects of metformin, similar to those observed in intestine-specific *Ampka* knockout (AMPKα-IKO) mice (Extended Data Fig. 12a, b). We also observed impaired promotion of GLP-1 and insulin secretion by metformin (Fig. 4a, b and Extended Data Fig. 12e). Meanwhile, hepatic-specific depletion of PEN2 (PEN2-LKO mice; generated as illustrated in Extended Data Fig. 12f) led to strong impairments in the activation of AMPK in mouse liver. The effects of administration of metformin for 4 months to decrease levels of hepatic triglycerides (TAGs), as well as glucose tolerance in high-fat diet (HFD)-induced obese mice, were also impaired (Fig. 4c, d and Extended Data Fig. 12g–k). Similarly, re-introduction of ATP6AP1<sup>Δ420–440</sup> into mouse liver with *Atp6ap1* knocked out did not rescue the metformin effects on AMPK activation or on TAG level reduction (Fig. 4e, f and Extended Data Fig. 12l–r). Therefore, PEN2 and ATP6AP1 are required for the effect of metformin to reduce hepatic fat by activating the lysosomal AMPK pathway.

**Fig. 4: PEN2 and ATP6AP1 are required for the biological effects of metformin.**

---

 **figure 4**

**a, b**, Intestinal PEN2 is required for the metformin-induced glucose-lowering effect. PEN2-IKO mice were administered with metformin as depicted in Extended Data Fig. 12d. Oral glucose tolerance test analysis (**a**), measurements of duodenal metformin concentrations (**b**, left) and measurements of plasma GLP-1 levels before and after 15 min of glucose gavaging (**b**, right) were then performed. **c, d**, PEN2 is required for metformin-induced reduction in hepatic fat. Mice in which *Pen2* was specifically knocked out in the liver (LKO) were treated with metformin as depicted in Extended Data Fig. 12f. Intraperitoneal glucose tolerance test results (**c**) and hepatic TAG levels (**d**) in mice after 16 weeks of treatment of metformin are shown. **e, f**, ATP6AP1 is required for metformin-induced reduction in hepatic fat. Mice were treated as depicted in Extended Data Fig. 12m. Intraperitoneal glucose tolerance test results (**e**) and hepatic TAG levels (**f**) in mice after 16 weeks of treatment of metformin are shown. **g, h**, PEN2 and ATP6AP1 are required for metformin-induced lifespan extension in *C. elegans*. WT (N2) nematodes with *pen-2* (T28D6.9) knocked down using siRNA (*sipen-2*) (**g**) or *ATP6API<sup>-/-</sup>* (*vha-19*) nematodes with full-length ATP6AP1 or ATP6AP1<sup>Δ420–440</sup> stably expressed (**h**) were treated with 50 mM metformin. Lifespan data are shown as Kaplan–Meier curves (statistical analyses are provided in Supplementary Table 3). Ctrl, control. **i, j**, PEN2 and ATP6AP1 are required for AMPK activation induced by 0.1% metformin in the diet. The 5-week-old PEN2-LKO mice (**i**; tamoxifen was injected at 4 weeks old) or 8-week-old ATP6AP1-LKO mice expressing ATP6AP1<sup>Δ420–440</sup> (**j**; viruses injected at 4 weeks old, and tamoxifen was injected at 5 weeks old), were fed with normal chow diet containing 0.1% metformin for 1 week, as previously described<sup>10</sup>. Hepatic AMPK activation was then analysed by IB. For gel source data, see Supplementary Fig. 1. Data are shown as the mean ± s.e.m., *n* values are labelled on each panel, and *P* values were calculated using two-

way repeated-measures ANOVA followed by Tukey's test (**a**, **c** and **e** compared blood glucose between the WT/ATP6AP1-FL + Met group and the PEN2-IKO/LKO/ATP6AP1 $\Delta^{420-440}$  + Met group at each time point; see also insets of **a**, **c** and **e** for area under the receiver operator characteristic curve (AUC) values, and *P* values by two-way ANOVA, followed by Tukey's test), two-sided Student's *t*-test (**b**, left), and two-way ANOVA, followed by Tukey's test (right panel of **b**, and **d**, **f**). Experiments in this figure were performed three times.

### Source data

We also tested whether lifespan extension induced by metformin depends on PEN2 and ATP6AP1. Consistent with previous reports<sup>9</sup>, metformin at 50 mM was able to extend the lifespan of *C. elegans* (Extended Data Fig. [13a](#)), and no increases in AMP/ATP and ADP/ATP ratios were observed (Extended Data Fig. [13b](#)). Knockdown of T28D6.9, the nematode orthologue of *PEN2*, blocked the metformin-induced lifespan extension effect in *C. elegans* (Fig. [4g](#), Extended Data Fig. [13b,c](#) and Supplementary Table [3](#), with validation data in Extended Data Fig. [13d](#)). Similarly, expression of mammalian ATP6AP1 $\Delta^{420-440}$  in *ATP6AP1* $^{-/-}$  *C. elegans* impaired the metformin-induced AMPK activation and lifespan extension effects (Fig. [4h](#), Extended Data Fig. [13f,i](#) and Supplementary Table [3](#)). Of note, genetic manipulation of *pen-2* and *ATP6AP1* or the living bacteria (OP50 and HT115) on the culture plates did not affect the cellular uptake of metformin (Extended Data Fig. [13e,j,k](#)). Finally, we examined the effects of normal chow diet that contained 0.1% metformin—a diet that has been shown to extend the lifespan and retard the ageing of mice through the activation of AMPK<sup>10</sup>—on the activation of AMPK in mice with hepatic depletion of PEN2 or expression of ATP6AP1 $\Delta^{420-440}$ . The activation of AMPK was strongly dampened in both of these mouse strains (Fig. [4i,j](#) and Extended Data Fig. [13l](#)). Taken together, PEN2, in conjunction with ATP6AP1, appears to be responsible for the three main biological benefits of metformin: lowering glucose levels, reducing hepatic fat content and extending lifespan.

## Discussion

Here we identified that PEN2 is a target of metformin. After stimulation, PEN2 binds to the ATP6AP1 subunit of and inhibits the activity of v-ATPase without increasing AMP or ADP, which then activates lysosomal AMPK. The PEN2–ATP6AP1 axis therefore constitutes a signalling shunt that intersects the lysosomal v-ATPase–AXIN–AMPK axis, which enables metformin at low concentration to make use of the AMP-independent AMPK-activation pathway, which is can also be triggered by glucose starvation. We also established that the PEN2–ATP6AP1 pathway is not involved in AMPK activation at low glucose levels, which indicates that the PEN2–ATP6AP1 axis is a parallel route to the v-ATPase complex. Therefore, the two axes, PEN2–ATP6AP1

and aldolase–TRPV, sense the presence of metformin and the lowered levels of glucose, respectively, and impinge on v-ATPase to control the activation of AMPK. This finding underscores the important role of v-ATPase as a signalling node for lysosomal AMPK activation (Extended Data Fig. [13m](#)).

We also showed that the PEN2–ATP6AP1 axis is required for the three main beneficial effects of metformin: postprandial glucose reduction, hepatic fat reduction and lifespan extension, all of which strictly depend on AMPK<sup>[9,20](#)</sup> (Extended Data Fig. [13g, h, 14a–i](#) and Supplementary Notes [7–9](#)). Our data are also consistent with previous findings that metformin can promote GLP-1 secretion in the intestine to lower blood glucose in an AMPK-dependent manner<sup>[21](#)</sup>, unless high doses of metformin are administered<sup>[26](#)</sup>. However, although it has been shown that metformin can also inhibit hepatic gluconeogenesis<sup>[1](#)</sup>, we found that low doses of metformin did not do so, as assessed by pyruvate tolerance tests and the quantification of gluconeogenic genes (Extended Data Fig. [14j, k](#)). Moreover, we also found that the PEN2–ATP6AP1 axis is required for the inhibition of mTORC1 signalling by metformin (Extended Data Fig. [14l–n](#)), in addition to the activation of AMPK. However, mTORC1 inhibition did not seem to be involved in the abovementioned beneficial effects mediated by AMPK (Supplementary Note [10](#)).

The intersection of metformin signalling to the lysosomal AMPK pathway, without perturbing AMP/ADP levels, might underlie the reason why metformin exerts many benefits with few side effects. This pathway only allows the activation of a small pool of AMPK<sup>[6,27](#)</sup>, and this innate pathway is perhaps related to calorie restriction and would be less likely to cause adverse effects compared with global AMPK activation. It has been shown that indiscriminate AMPK activation results in harmful rather than beneficial effects. For example, the AMPK activator MK-8722, which appears to activate all AMPK subunit isoform combinations, can cause cardiac hypertrophy<sup>[28](#)</sup>. Moreover, naturally occurring mutations in *PRKAG2* (encoding AMPK $\gamma$ 2), which cause increases in the basal activity of AMPK, are associated with cardiac disorders<sup>[29,30](#)</sup>. In summary, we identified that PEN2 is the molecular target for metformin and it intersect the glucose-sensing pathway to activate AMPK, which elicits benefits that resemble those induced by glucose starvation or calorie restriction. The PEN2–ATP6AP1 axis offers potential targets for screening for substitutes for metformin, which may be available to a wider range of tissues, such as muscle, thereby engendering better efficacy in treating diabetes and other metabolic diseases.

## Methods

### Data reporting

The following sample sizes were similar to those previously used by us and others in this field:  $n = 4$ – $6$  human participants or mice were used to determine the pharmacokinetics of metformin<sup>16,31,32</sup>;  $n = 5$ – $7$  mice were usually used to determine the effects of metformin on blood glucose<sup>33,34</sup> and fatty liver<sup>20,35</sup>;  $n = 100$ – $300$  worms were used to determine lifespan<sup>36,37</sup>;  $n = 20$ – $42$  cells from 2–6 dishes or experiments were included when conclusions were based on immunofluorescence staining<sup>6,25</sup>;  $n = 3$ – $5$  samples were used for evaluation of the levels of AMP, ADP and ATP in cells and tissues<sup>6,15,25,27</sup>;  $n = 3$  samples to determine the expression levels and phosphorylation levels of a specific protein<sup>24,38</sup>;  $n = 3$  samples to determine the mRNA levels of a specific gene<sup>20,24,39</sup>; and  $n = 3$  samples to determine the activity of v-ATPase in vitro<sup>25</sup>. No statistical methods were used to predetermine sample sizes. All experimental findings were repeated as stated in the figure legends, and all additional replication attempts were successful. For animal experiments, mice or nematodes in each genotype were housed under the same condition or place. For cell experiments, cells of each genotype were cultured using the same condition. Each experiment was designed and performed along with proper controls, and samples for comparison were collected and analysed under the same conditions for the same batch of experiments. Randomization was applied wherever possible. For example, during MS analyses, samples were processed and subjected to the mass spectrometer in random order. For the animal experiments, sex-matched (only for mice), age-matched littermate mice in each genotype were randomly assigned to pharmacological or diet treatments. In cell experiments, cells of each genotype were parallel seeded and randomly assigned to different treatments. Otherwise, randomization was not performed. For example, when performing immunoblotting, samples needed to be loaded in a specific order to generate the final figures. Blinding was applied wherever possible. For example, samples, cages or agar plates during sample collection and processing were labelled as code names that were later revealed by the individual who picked and treated the animals or the cells, but did not participate in sample collection and processing until assessing the outcomes. Similarly, during microscopy data collection and statistical analyses, the fields of view were chosen on a random basis, and were often performed by different operators, thereby preventing potentially biased selection for desired phenotypes. Otherwise, blinding was not performed, such as the measurement of v-ATPase activity and the determination of metformin binding to PEN2 in vitro, for which operators had to know the conditions of each well and added reagents to the well accordingly during the measurement.

## Determination of metformin pharmacokinetics in human participants

Women with obesity and diagnosed with polycystic ovary syndrome (PCOS) between September 2017 and July 2020 at Shanghai Jiao Tong University Affiliated Sixth People's Hospital were recruited. This study was approved by the Ethics Committee of

Shanghai Sixth People's Hospital and was in accordance with the Declaration of Helsinki and Good Clinical Practice. All participants signed an informed consent form before enrolment. This study was registered on the Chinese Clinical Trial Registry (ChiCTR-IOR-17013169; <http://www.chictr.org.cn/showproj.aspx?proj=21769>).

Participants included in the study fulfilled the following criteria: (1) aged 18–40 years (inclusive); (2) body-mass index (BMI) higher than  $27.5 \text{ kg m}^{-2}$ ; and (3) meeting the diagnostic criteria of PCOS. The diagnostic criteria of PCOS were as follows: (1) irregular menstruation over the past year; (2) hyperandrogenism; and/or (3) ultrasound examination of polycystic ovaries. Participants with the following conditions were excluded: (1) after hysterectomy; (2) congenital adrenal hyperplasia, Cushing's syndrome or androgen-secreting tumours within 5 years; (3) mothers pregnant or lactating; (4) thrombosis-related history or risk factors, such as deep vein thrombosis, pulmonary embolism, myocardial infarction (angina), valvular heart disease, atrial fibrillation or cerebrovascular accident (transient ischaemic attack); (5) abnormal liver function (for example, caused by viral hepatitis); (6) a history of liver malignancy or adenoma, or a history of genital or breast malignancies; (7) a history of severe or frequent migraine attacks; (8) renal insufficiency; and (9) other factors that may affect the efficacy of the drug or cause complications by the drug.

Participants were administered with Diane 35 (Bayer), one tablet per day, plus metformin (Bristol-Myers Squibb) at  $2,000 \text{ mg day}^{-1}$ . Such a combined treatment lasted 6 months, which was then switched to metformin-alone treatment for another 6 months. At the endpoint of the treatment, six participants with the lowest BMI were selected to determine pharmacokinetics. A potential selection bias may be introduced. However, they were characterized as follows (mean  $\pm$  s.d.), and were therefore able to represent the general population: aged  $25.5 \pm 6.2$  years; weight,  $69.0 \pm 6.4 \text{ kg}$ ; BMI,  $26.5 \pm 1.1 \text{ kg m}^{-2}$ ; waist circumference,  $89.8 \pm 5.8 \text{ cm}$ ; hip circumference,  $102.2 \pm 11.4 \text{ cm}$ ; waist/hip ratio,  $0.89 \pm 0.12$ ; fasting plasma glucose,  $5.1 \pm 0.7 \text{ mM}$ ; fasting serum insulin  $28.2 \pm 15.3 \mu\text{U ml}^{-1}$ ; HbA1c,  $5.1 \pm 0.2\%$ ; total cholesterol,  $5.1 \pm 1.0 \text{ mM}$ ; TAGs,  $1.4 \pm 0.7 \text{ mM}$ ; high-density lipoprotein cholesterol,  $1.4 \pm 0.3 \text{ mM}$ ; low-density lipoprotein cholesterol,  $3.0 \pm 0.6 \text{ mM}$ . Participants were fasted for 12 h before experiments (starting from 22:00 of the previous day), followed by taking orally 0.5 g of metformin hydrochloride extended-release tablets (Bristol-Myers Squibb) per person. Blood samples were taken at 1, 3, 6 and 12 h after metformin intake, followed by serum preparation.

## Mouse strains

*AXIN*<sup>F/F</sup>, *LAMTOR1*<sup>F/F</sup>, *AXIN*<sup>LKO</sup> and *LAMTOR1*<sup>LKO</sup> mice were generated and maintained as previously described<sup>24</sup>. Wild-type C57BL/6 mice (000664), DBA2 mice (000671) and ROSA26-FLPe mice (016226) were obtained from The Jackson

Laboratory. ICR mice (N000294) were obtained from GemPharmatech. *TRPV1*<sup>-/-</sup> mice were obtained from The Jackson Laboratory provided by D. Julius (003770). *TRPV1*<sup>-/-</sup> mice with knockdown of *TRPV2*–*TRPV4* or *GFP* were generated as previously described<sup>25</sup>. *APH1A*<sup>F/F</sup> *APH1B*<sup>-/-</sup> *APH1C*<sup>F/F</sup> mice were obtained from The Jackson Laboratory provided by B. De Strooper (030985). *ATG5*<sup>F/F</sup> mice were obtained from RIKEN, provided by N. Mizushima (BRC no. RBRC02975). *AMPKA1*<sup>F/F</sup> (014141) and *AMPKA2*<sup>F/F</sup> mice (014142) were obtained from Jackson Laboratory, provided by S. Morrison.

The *Pen2*<sup>F/F</sup> mouse strain was generated according to an androgenetic haploid embryonic stem cell (AG-haESC)-based, CRISPR–Cas9-mediated genomic editing strategy as previously described<sup>40</sup>, but with minor modifications. The AG-haESCs carrying deletions in the differentially DNA methylated regions (DKO-AG-haESCs) were a gift from J.-S. Li (Shanghai Institute of Biochemistry and Cell Biology, CAS). The single guide RNAs (sgRNAs) targeting *Pen2*, 5'-GTGGTACTACTGCGCACGCG-3' and 5'-GAAAGAATGAGCGAACGCCCT-3' (at intron 1 and intron 2, respectively) were cloned into a pSpCas9(BB)-P2A-mCherry-puromycin-sgRNA vector that was modified from the pSpCas9(BB)-2A-GFP vector (Addgene, 48138). The editing efficiency of each sgRNA was examined by transfecting into L929 cells followed by sequencing the targeted genomic segments before experiments. The template plasmid was constructed by inserting a 0.6-kb genomic fragment (containing exon 1 between the two *loxP* sites), along with a 1-kb fragment as a 5'-homology arm and a 1-kb fragment as 3'-homology arm into a pBKS vector. Approximately  $1 \times 10^6$  DKO-AG-haESCs in a 6-well dish were transfected with 2 µg per well of each sgRNA (0.1 µg µl<sup>-1</sup>) and 4 µg of template plasmids (0.2 µg µl<sup>-1</sup>) with Lipofectamine 2000 transfection reagent. At 24 h after transfection, cells were trypsinized, washed with PBS and stained with 5 mg ml<sup>-1</sup> Hoechst for 5 min. Those within the haploid 1C peak (haploid cells at G1 phase), mCherry-positive cells, were sorted on a FACS Aria III flow cytometer (BD). Approximately 7,000 sorted cells were then cultured in a well of a gelatin-coated 6-well dish in EmbryoMax DMEM medium containing 10% ES-FBS and non-essential amino acids. Genotypes of individual clones were verified by sequencing, and the *loxP*-flanked *Pen2* clones were selected for generating diploid ESCs. The verified clones were first treated with 0.05 µg ml<sup>-1</sup> demecolcine for 10 h, digested to single cells and then intracytoplasmically injected into the mature oocyte (cultured in M2 medium) derived from the F<sub>1</sub> generation of C57BL/6 × DBA2 female mice at 8–10 weeks old. After 24 h, 2-cell ESCs were transplanted into pseudopregnant ICR female mice (8–10 weeks old, >26 g), and the offspring carrying the *loxP*-flanked *Pen2* allele were further outcrossed 6 times to C57BL/6 mice before experiments.

*Atp6ap1*<sup>F/F</sup> mice were generated according to the traditional, homologous recombination method<sup>41</sup>. In brief, a targeting vector was generated by inserting a 1-kb genomic fragment (containing exon 3 and exon 4) and an *FRT*-flanked *PGK-Neo-polyA* sequence (as a positive selection marker), along with a 3-kb fragment as 5'-homology arm and a 3-kb fragment, followed by a *MC1-TK-polyA* sequence (as a negative selection marker), as a 3'-homology arm, into a pBKS vector. The targeting vector was then linearized and purified. A total of 10 µg of the linearized vector (1 µg µl<sup>-1</sup>) was electroporated into 1 × 10<sup>10</sup> JM8A3 ESCs, followed by selection with G418, and genotyped by Southern blotting. *Atp6ap1*<sup>F/F</sup> chimeric mice were obtained by microinjecting *loxP*-flanked *Atp6ap1* ESC clones into C57BL/6 blastocysts (10–15 ESCs to a blastocyst), then transplanted into a pseudopregnant ICR female mice. The *PGK-Neo* allele was removed by crossing chimeric mice with ROSA26-FLPe mice, and was further outcrossed six times to C57BL/6 mice before experiments.

The *Pen2*<sup>F/F</sup> mice were then crossed with *Alb-CreERT2* or *Villin-CreERT2* mice to generate inducible liver-specific *Pen2* knockout mice (PEN2-LKO) or inducible intestine-specific *Pen2* knockout mice (PEN2-IKO). The *Atp6ap1*<sup>F/F</sup> mice were crossed with *Alb-CreERT2* to generate inducible liver-specific *Atp6ap1* knockout mice (ATP6AP1-LKO). *Ampka1/2*<sup>F/F</sup> mice were crossed with *Villin-CreERT2* mice to generate inducible intestine-specific *Ampka* knockout mice (AMPKa-IKO). *Pen2*, *Atp6ap1* and *Ampka* were deleted by intraperitoneally injecting mice with tamoxifen (dissolved in corn oil) at 200 mg kg<sup>-1</sup>, 3 times a week. Knockout efficiencies were analysed 1 week after the last injection by western blotting. ATP6AP1-LKO mice expressing wild-type ATP6AP1 or ATP6AP1<sup>Δ420–440</sup> were generated by injection into the tail vein different adeno-associated viruses (AAVs) carrying indicated inserts before knockout of the endogenous ATP6AP1 by tamoxifen. Levels of the re-introduced ATP6AP1 proteins were analysed 4 weeks after virus injection.

To generate Tg-ALDOA and Tg-ALDOA-D34S mice strains, human ALDOA or human ALDOA-D34S was cloned into the pLiv-Le6 vector (containing the constitutive human *APOE* gene promoter and its hepatic control region) between *Cla* I and *Xho* I sites. Vectors were then linearized with *Not* I and *Spe* I restriction enzymes. A 6.12-kb fragment was recovered using a QIAquick Gel Extraction kit (28706, Qiagen), followed by removal of endotoxin using an EndoFree Plasmid Maxi kit (12362, Qiagen). Plasmids were diluted to 2.5 ng µl<sup>-1</sup>, and 1 pl was injected intranuclearly into the male pronucleus in zygote at embryonic day 0.5 of C57BL/6 mice. Two-cell embryos were transplanted into the pseudopregnant ICR female mice. The positive F<sub>0</sub> offspring were identified by sequencing and crossed with C57BL/6 mice. The F<sub>1</sub> mice carrying the transgenic genomic were selected by PCR, and ALDOA or ALDOA-D34S expression was examined by immunoblotting. One

verified F<sub>1</sub> mouse of each genotype was chosen to set up the transgenic mouse strain, which was then outcrossed six times to C57BL/6 mice before experiments.

## Metformin treatment of mice

The protocols described below for all mouse experiments were approved by the Institutional Animal Care and the Animal Committee of Xiamen University (XMULAC20180028). Unless stated otherwise, mice were housed with free access to water and standard diet (65% carbohydrate, 11% fat, 24% protein) under specific pathogen-free conditions. The light was on from 8:00 to 20:00, with the temperature kept at 21–24 °C and humidity at 40–70%. Male littermate controls were used throughout the study. Metformin was supplied either in drinking water at desired concentrations or in standard diet at 0.1% (w/w) for 1 week. For creating the diabetic mouse model, mice were fed a HFD (60% calories from fat; D12492, Research Diets) for desired time periods starting at 4 weeks old.

The following ages of mice were used. (1) For isolating primary hepatocytes: normal-chow-diet-fed wild-type and *loxP*-flanked *Ampka* mice aged 4 weeks (Fig. [1a, b](#), Extended Data Figs. [1c, e–g](#), [13g, h](#) and [14f–h, n](#)); normal-chow-diet-fed PEN2-LKO mice aged 6 weeks (Fig. [2b](#), Extended Data Figs. [3c, j](#) and [14l, j](#); into which tamoxifen was injected at 4 weeks old); HFD-fed wild-type mice aged 38 weeks (Extended Data Fig. [12i](#); fed with a HFD for 34 weeks starting from 4 weeks old); HFD-fed PEN2-LKO mice aged 38 weeks (Extended Data Fig. [12i](#); into which tamoxifen was injected at 35 weeks old after 31 weeks of HFD treatment starting from 4 weeks old); normal-chow-diet-fed ATP6AP1-LKO mice expressing full-length ATP6AP1 or ATP6AP1<sup>Δ420–440</sup> aged 8 weeks (Extended Data Fig. [14m, j](#); into which an AAV carrying ATP6AP1 was injected at 4 weeks old and tamoxifen at 5 weeks old); and HFD-fed ATP6AP1-LKO mice expressing full-length ATP6AP1 or ATP6AP1<sup>Δ420–440</sup> aged 38 weeks (Extended Data Fig. [12p](#); into which an AAV was injected at 34 weeks old and tamoxifen at 35 weeks old, after 34 weeks of HFD treatment starting from 4 weeks old). (2) For glucose tolerance tests (GTTs), insulin tolerance tests (ITTs) and measurements of metformin, GLP-1, insulin and TAG contents: wild-type mice aged 5 weeks (Extended Data Fig. [1h, l, m](#)); PEN2-IKO and AMPK $\alpha$ 1/2-IKO mice aged 6 weeks (Fig. [4a, b](#) and Extended Data Fig. [12b, e](#); mice at 4 weeks old were injected with tamoxifen and were fed a HFD for 1 week, and then treated with metformin for another week); HFD-fed PEN2-LKO mice aged 54 weeks (Fig. [4c, d](#) and Extended Data Fig. [12g, h](#); mice at 4 weeks old were fed a HFD for 31 weeks, and then injected with tamoxifen; at 38 weeks old, mice were treated with metformin for 16 weeks); HFD-fed ATP6AP1-LKO mice expressing full-length ATP6AP1 or ATP6AP1<sup>Δ420–440</sup> aged 54 weeks (Fig. [4e, f](#) and Extended Data Fig. [12n, o](#); mice at 4 weeks old were fed a HFD for 30 weeks, and were injected with an AAV at 34 weeks old; at 35 weeks old, the mice were injected with tamoxifen and then treated with metformin for 16 weeks).

(3) For pyruvate tolerance tests (PTTs): PEN2-LKO mice aged 6 weeks (Extended Data Fig. 14k; mice at 4 weeks old were injected with tamoxifen and then treated with metformin for 1 week starting from 5 weeks old). (4) For immunoblotting and measurement of adenylates: wild-type mice aged 5 weeks (Extended Data Figs. 1j, k, m, n and 13l; mice were treated with metformin for 1 week starting from 4 weeks old); PEN2-LKO mice aged 6 weeks (Fig. 4i; mice at 4 weeks old were injected with tamoxifen and then treated with metformin for 1 week starting from 5 weeks old); ATP6AP1-LKO mice expressing full-length ATP6AP1 or ATP6AP1 $\Delta$ 420–440 aged 9 weeks (Fig. 4j; mice at 4 weeks old were injected with an AAV; at 5 weeks old, the mice were injected with tamoxifen and then treated with metformin for 1 week starting from 8 weeks old); HFD-fed PEN2-LKO mice aged 39 weeks (Extended Data Fig. 12j; mice at 4 weeks old were fed a HFD for 31 weeks and then injected with tamoxifen; at 38 weeks old, mice were treated with metformin for 1 week); HFD-fed ATP6AP1-LKO mice expressing full-length ATP6AP1 or ATP6AP1 $\Delta$ 420–440 aged 39 weeks (Extended Data Fig. 12q; mice at 4 weeks old were fed a HFD for 30 weeks and then injected with an AAV at 34 weeks old; at 35 weeks old, the mice were injected with tamoxifen and then treated with metformin for 1 week starting from 38 weeks old); AXIN-LKO mice, LAMTOR1-LKO mice and Tg-ALDOA-D34S aged 7 weeks (Extended Data Figs. 9d, e and 11e; mice were treated with metformin for 1 week starting from 6 weeks old); Tg-ALDOA-D34S aged 6 weeks (Extended Data Fig. 11c; mice were starved for 16 h); hepatic *ATP6v0c* knockdown mice aged 7 weeks (Extended Data Fig. 9f; mice were treated with metformin 1 week starting from 6 weeks old, into which an AAV carrying a short interfering siRNA (siRNA) against *ATP6v0c* was intravenously injected at 4 weeks old); and *TRPV1* $^{−/−}$  and hepatic *TRPV2*–*TRPV4* knockdown mice aged 8 weeks (Extended Data Fig. 11g; mice were treated with metformin for 1 week starting from 7 weeks old, into which an AAV carrying siRNAs against *TRPV*–*TRPV4* was intravenously injected at 5 weeks old). (5) For hepatic haematoxylin and eosin (H&E) staining: HFD-fed PEN2-LKO mice aged 54 weeks (Extended Data Fig. 12k; mice at 4 weeks old were fed a HFD for 31 weeks and then injected with tamoxifen; at 38 weeks old, mice were treated with metformin for 16 weeks); HFD-fed ATP6AP1-LKO mice expressing full-length ATP6AP1 or ATP6AP1 $\Delta$ 420–440 aged 54 weeks (Extended Data Fig. 12r; mice at 4 weeks old were fed a HFD for 30 weeks and then injected with an AAV at 34 weeks old; at 35 weeks old, the mice were injected with tamoxifen and then treated with metformin for 16 weeks). (6) For all the other experiments, mice aged 4 weeks were used.

## Serology, GTTs, ITTs and PTTs

Mice were individually caged for 1 week before each experiment. For GTTs, mice were fasted for 6 h (8:00 to 14:00), then gavaged or intraperitoneally injected with glucose at 1.5 g kg $^{-1}$  (for lean mice) or 1 g kg $^{-1}$  (for HFD-induced diabetic mice). Blood glucose was measured at the indicated time points through tail-vein bleeding

using a OneTouch UltraVue automatic glucometer (LifeScan). ITTs were performed as per the GTTs, except that 1 U kg<sup>-1</sup> insulin was intraperitoneally injected. PTTs were performed as GTTs, except that 1 g kg<sup>-1</sup> sodium pyruvate was intraperitoneally injected into 16-h fasted (18:00 previous day to 10:00) mice. GTTs, ITTs and PTTs were performed using different batches of mice.

For measuring GLP-1 levels, 300 µl of blood from each mouse was collected in an ice-cold, K<sub>2</sub>EDTA spray-coated tube (366420, BD P800 blood collection system) containing pre-added 50 µl aprotinin (5 mg ml<sup>-1</sup>) and 50 µl diprotin A (5 mg ml<sup>-1</sup>) as previously described<sup>42,43</sup> (with modifications of concentrations of aprotinin and diprotin A used). Plasma was then prepared by centrifugation at 3,000g for 10 min at 4 °C, and 100 µl was used to determine the levels of GLP-1 using a GLP-1 EIA kit according to the manufacturer's instructions.

For measuring insulin levels, approximately 100 µl of mouse blood was collected at each time point (from the submandibular vein plexus) and was placed at room temperature for 20 min, followed by centrifugation at 3,000g for 10 min at 4 °C. A total of 5 µl of serum (the supernatant) was used to determine the levels of insulin using a Mouse Ultrasensitive Insulin ELISA kit according to the manufacturer's instructions. The five-parameter logistic fitted standard curve for calculating the concentration of insulin was generated from the Arigo Biolaboratories website (<https://www.arigobio.cn/ELISA-calculator>).

## Histology

For H&E staining, liver tissues were fixed in 4% (v/v) paraformaldehyde for 24 h at room temperature then transferred to embedding cassettes. The cassettes were then washed in running water for 12 h, followed by successive soaking, each for 1 h, in 70% ethanol (v/v in water), 80% ethanol and 95% ethanol. The fixed tissues were further dehydrated in anhydrous ethanol for 1 h twice, followed by immersing in 50% xylene (v/v in ethanol) for 30 min, with two changes of xylene (15 min each) and two changes of paraffin wax (58–60 °C; 1 h each). The dehydrated tissues were embedded in paraffin on a HistoCore Arcadia paraffin embedding machine (Leica). Paraffin blocks were then sectioned at a thickness of 3 µm, dried on an adhesion microscope slide, followed by rehydrating in the following order: two changes of xylene at 70 °C 10 min each; two changes of anhydrous ethanol 5 min each; two changes of 95% ethanol 5 min each; one change of 80% ethanol for 5 min; one change of 70% ethanol for 5 min; one change of 50% ethanol for 5 min; and briefly in water. The sections were then stained in haematoxylin solution for 8 min, then washed in running water for 5 min, differentiated in 1% hydrochloric acid (in ethanol) for 30 s, washed in running water for 1 min, immersed in 0.2% (v/v in water) ammonium hydroxide solution for 30 s, washed in running water for 1 min and stained in eosin Y solution for

30 s. The stained sections were dehydrated in 70% ethanol for 5 min, twice in 95% ethanol for 5 min each, twice in anhydrous ethanol for 5 min each and two changes of xylene for 15 min each. The stained sections were mounted with Canada balsam and visualized on a Leica DM4 B microscope. Images were processed using LAS X software (v.3.0.2.16120, Leica), and formatted using Photoshop 2021 software (Adobe).

For measuring the TAG content, mice were euthanized, and the livers were immediately removed and rinsed in PBS for three times. Approximately 50 mg tissue was homogenized in 1 ml of PBS containing 5% (v/v) Triton X-100. The homogenates were boiled for 5 min followed by centrifugation at 20,000g at 25 °C for 10 min. The TAG content (from the supernatant) was determined using Labassay triglyceride reagent.

### ***C. elegans* strains**

Wild-type (N2 Bristol), *aak-2(ok524)* and *unc-76(e911)* strains were obtained from the *Caenorhabditis* Genetics Center. Unless stated otherwise, worms were maintained on nematode growth medium (NGM) plates (1.7% (w/v) agar, 0.3% (w/v) NaCl, 0.25% (w/v) bacteriological peptone, 1 mM CaCl<sub>2</sub>, 1 mM MgSO<sub>4</sub>, 25 mM KH<sub>2</sub>PO<sub>4</sub>-K<sub>2</sub>HPO<sub>4</sub>, pH 6.0, 0.02% (w/v) streptomycin and 5 µg ml<sup>-1</sup> cholesterol) spread with *Escherichia coli* OP50 as standard food. Metformin of desired concentrations was added to the autoclaved NGM (cooled down to 50 °C) before pouring onto plates. All worms were cultured at 20 °C.

*pen-2* was knocked down instead of knocked out in *C. elegans* because complete depletion of PEN-2 is lethal to *C. elegans*<sup>7</sup>. To knock down *pen-2*, the growth of nematodes was first synchronized: worms were washed off from agar plates with 15 ml M9 buffer (22.1 mM KH<sub>2</sub>PO<sub>4</sub>, 46.9 mM Na<sub>2</sub>HPO<sub>4</sub>, 85.5 mM NaCl and 1 mM MgSO<sub>4</sub>) supplemented with 0.05% (v/v) Triton X-100 per plate, followed by centrifugation at 1,000g for 2 min. The worm sediment was suspended with 6 ml of M9 buffer containing 50% synchronizing bleaching solution (by mixing 25 ml of NaClO solution (5% active chlorine), 8.3 ml of 25% (w/v) NaOH and 66.7 ml of M9 buffer, for a total of 100 ml), followed by vigorous shaking for 2 min and centrifugation for 2 min at 1,000g. The sediment was washed with 12 ml of M9 buffer twice, then suspended with 6 ml of M9 buffer, followed by rotating at 20 °C, 30 r.p.m. for 12 h. Synchronized worms (around the L1 stage) were then placed on RNAi plates (NGM containing 1 mg ml<sup>-1</sup> IPTG and 50 µg ml<sup>-1</sup> carbenicillin) spread with HT115 *E. coli* stains containing RNAi against *pen-2* (well A05 on plate 86 from *C. elegans* RNAi Collection (Ahringer)) for 2 days. The knockdown efficiency was examined by determining the levels of *pen-2* mRNA by real-time quantitative PCR (qPCR). Approximately 1,000 worms were washed off a RNAi plate with 15 ml of M9 buffer

containing Triton X-100, followed by centrifugation for 2 min at 1,000g. The sediment was then washed with 1 ml of M9 buffer twice, and then lysed with 1 ml of TRIzol. The worms were then frozen in liquid nitrogen, thawed at room temperature and then subjected to repeated freeze–thaw for another two times. The worm lysates were then placed at room temperature for 5 min, then mixed with 0.2 ml of chloroform followed by vigorous shaking for 15 s. After 3 min, lysates were centrifuged at 20,000g at 4 °C for 15 min, and 450 µl of the aqueous phase (upper layer) was transferred to a new RNase-free centrifuge tube, followed by mixing with 450 µl of isopropanol, then centrifuged at 20,000g at 4 °C for 10 min. The sediment was washed with 1 ml of 75% ethanol (v/v) followed by centrifugation at 20,000g for 10 min, and then with 1 ml of anhydrous ethanol followed by centrifugation at 20,000g for 10 min. The sediment was dissolved with 20 µl of RNase-free water after the ethanol was evaporated. The dissolved RNA was then reverse-transcribed to cDNA using ReverTra Ace qPCR RT master mix with a gDNA Remover kit, followed by performing real-time qPCR using Maxima SYBR Green/ROX qPCR master mix on a CFX96 thermocycler (Bio-Rad). Data were analysed using CFX Manager software (v.3.1, Bio-Rad). Knockdown efficiency was evaluated according to the CT value obtained. The primers for *pen-2* are 5'-TACGTGATGCCAGCATTGT-3' and 5'-CGTGTGGACCGATTCCCTGA-3'. The primers for *ama-1* (the internal control) are 5'-GACATTGGCACTGCTTG-3' and 5'-ACGATTGATTCCATGTCTCG-3'.

The *ATP6AP1*<sup>−/−</sup> *C. elegans* strains expressing ATP6AP1 or its Δ420–440 mutant were established as follows: ATP6AP1 or its Δ420–440 mutant was introduced to the *unc-76(e911)* *C. elegans* strain, which had been outcrossed six times to the N2 strain; such generated strains were then subjected to knockout of the *ATP6AP1* (*vha-19*) gene, and the uncoordinated phenotype of *unc-76* was rescued. To generate *unc-76* strains expressing ATP6AP1 or the Δ420–440 mutant, cDNA of ATP6AP1 or ATP6AP1<sup>Δ420–440</sup> was inserted into a pJM1 vector, with GFP as a selection marker, between the *Nhe* I and *Kpn* I sites (expressed under control by a *sur-5* promoter), then injected into the syncytial gonad of the worm. Microinjection was performed using a Leica DMI8 microscope equipped with a M-152 manipulator (Narishige) and a microinjector system (Tritech). The injection pad was prepared by placing 2 drops (approximately 50 µl) of boiling 2% agarose (w/v) onto the centre of a glass coverslip (24 × 50 mm, 0.13–0.15 mm thickness), immediately followed by flattening with another coverslip, then dried at room temperature for 24 h. The injection needle was processed from a glass capillary (Borosil 1.0 × 0.75 mm ID/Fibre with Omega dot fibre, FHC) by a PC-100 Puller (Narishige) using the Step 2 programme (with heater no. 1 at 66 °C, and no. 2 at 75 °C), and was then loaded with 0.5 µl of pJM1-ATP6AP1 or ATP6AP1<sup>Δ420–440</sup> plasmid (200 ng µl<sup>−1</sup>, centrifuged at 20,000g for 15 min before loading), and then connected to the nitrogen gas source at a pressure adjusted to 20 psi. Successful loading of plasmid was checked using a dissection microscope before loading onto the manipulator at a 45° angle in relation to the injection pad. All equipment was adjusted

and aligned to make sure that a clear, centred view of the pad and the needle was obtained. The sealed needle tip was then opened by gentle tapping on the lateral side of the coverslip to a size that allowed a five-times broader droplet to be made during each injection. A young adult *unc-76* worm with well distinguishable gonads was then gently anchored on an injection pad covered with a thin layer of microinjection oil (Halocarbon oil 700). The pJM1-ATP6AP1 or ATP6AP1 $\Delta^{420-440}$  plasmid was then injected into the syncytial arm of the gonad (gonadal sheath) until a slightly visible swelling was achieved. A drop of M9 buffer was then added to the injected worm, and the worm was floated on microinjection oil then picked and recovered on a NGM plate for 2 days. The F<sub>1</sub> GFP-expressing hermaphrodite was selected for further culture. The genomic sequence encoding *ATP6AP1* (*vha-19*) was then knocked out from this strain by injecting a mixture of a pDD122 (Peft-3::Cas9 + ttTi5605 sgRNA) vector carrying sgRNAs against *vha-19* (5'-CGTCGAAAAAA CCCGATTGTTGG-3' for intron 2, and 5'-AATGATGTCAGGTTTTCTGG-3' for intron 3, designed using the CHOPCHOP website <http://chopchop.cbu.uib.no/>), and the p7616B (*unc-76* (+)) rescue plasmid (100 µg ml<sup>-1</sup> each) into young adult worms. The F<sub>1</sub> hermaphrodite worms with normal postures were individually cultured on a NGM plate. After egg-laying, worms were lysed using Single Worm lysis buffer (50 mM HEPES, pH 7.4, 1 mM EGTA, 1 mM MgCl<sub>2</sub>, 100 mM KCl, 10% (v/v) glycerol, 0.05% (v/v) NP-40, 0.5 mM DTT and protease inhibitor cocktail), followed by PCR with the primers 5'-AACTGCTTTGGCTCGAAAATA-3' and 5'-AAGTAAAAAGGGACAAAAGTCG-3' for genotyping. The offspring generated from knockout-assured individuals were outcrossed six times to the N2 strain, and the expression levels of ATP6AP1 or ATP6AP1 $\Delta^{420-440}$  were examined by immunoblotting. Strains expressing ATP6AP1 or ATP6AP1 $\Delta^{420-440}$  at similar levels were chosen for further experiments.

The ages of the nematodes used in this study were as follows: (1) for lifespan assays, worms at L4 stage were used (Fig. 4g, h, Extended Data Figs. 13a and 14d, e; treated with metformin or *N*-acetylcysteine until death); (2) for analysis of adenylates and pharmacokinetics of metformin, p-AMPK $\alpha$  and reactive oxygen species (ROS) levels (Extended Data Figs. 13b, c, e, f, i–k and 14c, i), worms at L4 stage (after treatment of metformin for 1 day) were used; and (3) for the experiments using *pen-2* knock down worms, worms at L1 stage were used (Extended Data Fig. 13d; fed with HT115 *E. coli* strain containing RNAi against *pen-2*).

## Evaluation of nematode lifespan

Synchronized worms were cultured to the L4 stage before transfer to the desired agar plates. Worms were transferred to new plates every 2 days. Live and dead worms were counted during the transfer. Worms that displayed no movement after gentle touching with a platinum picker were judged as dead. Kaplan–Meier curves were generated

using Prism 9 (GraphPad software), whereas the statistical analysis data were analysed using SPSS 27.0 (IBM).

## Reagents

Rabbit polyclonal antibody against LAMTOR1 was raised and validated as previously described<sup>24</sup>, and was diluted 1:100 for immunoprecipitation (IP) or 1:500 for immunoblotting (IB). Rabbit polyclonal antibody against ATP6AP1 was raised with bacterially expressed and purified ATP6AP1 (amino acids 440–470, GST-tagged), and was diluted 1:100 for IP. The following antibodies were purchased from Cell Signaling Technology: rabbit anti-phospho-AMPK $\alpha$ -T172 (cat. 2535, 1:1,000 for IB), anti-AMPK $\alpha$  (cat. 2532, 1:1,000 for IB), anti-AMPK $\beta$ 1/2 (cat. 4150, 1:1,000 for IB), anti-phospho-ACC-Ser79 (cat. 3661, 1:1,000 for IB), anti-ACC (cat. 3662, 1:1,000 for IB), anti-phospho-p70 S6K-S389 (cat. 9234, 1:1,000 for IB), anti-p70 S6K (cat. 2708, 1:1,000 for IB), anti-LKB1 (cat. 3047, 1:1,000 for IB), anti-AXIN1 (cat. 2074, 1:1,000 for IB), anti-presenilin 1 (cat. 3622, 1:1,000 for IB), anti-presenilin 2 (cat. 2192, 1:1,000 for IB), anti-nicastrin (cat. 3632, 1:1,000 for IB), anti- $\beta$ -tubulin (cat. 2128, 1:1,000 for IB), anti-HA-tag (cat. 3724, 1:1,000 for IB or 1:120 for immunofluorescent (IF) staining), anti-PDI (cat. 3501, 1:1,000 for IB), anti-cytochrome *c* (cat. 4280, 1:1,000 for IB), anti-clathrin (cat. 4796, 1:1,000 for IB), anti-p62 (cat. 23214, 1:1,000 for IB), anti-ATG5 (cat. 12994, 1:1,000 for IB), anti-PDI (Alexa Fluor 488-conjugated, cat. 5051, 1:60 for IF), HRP-conjugated mouse anti-rabbit IgG (conformation-specific, cat. 5127, 1:2,000 for IB), HRP-conjugated goat anti-rat IgG (conformation-specific, cat. 98164, 1:2,000 for IB) and mouse anti-Myc-tag (cat. 2276, 1:500 for IB). Rabbit anti-ATP6v0c (cat. NBP1-59654, 1:1,000 for IB or 1:100 for IP) antibody was purchased from Novus Biologicals. Mouse anti-FLAG M2 (cat. F1804, 1:1,000 for IB), goat anti-rabbit IgG antibody and anti-FLAG M2 affinity gel (cat. A2220, 1:500 for IP) were purchased from Sigma. Rabbit anti-PEN2 (cat. ab154830, 1:1,000 for IB or 1:100 for IP and IF), anti-ATP6AP1 (cat. ab176609, 1:500 for IB), anti-transferrin (cat. ab1223, 1:500 for IB), anti-TGN46 (cat. ab76282, 1:60 for IF) and rat anti-LAMP2 (cat. ab13524; 1:1000 for IB or 1:120 IF) antibodies were purchased from Abcam. Goat anti-AXIN (cat. sc-8567, 1:120 for IF), mouse anti-HA (cat. sc-7392, 1:1,000 for IB, 1:500 for IP or 1:120 for IF), mouse anti-goat IgG-HRP antibody were purchased from Santa Cruz Biotechnology. Normal rabbit control IgG (cat. CR1, 1:100 for IP) was purchased from Sino Biological. Goat anti-mouse IgG (cat. 115-035-003, 1:1,000 for IB) and anti-rabbit (cat. 111-035-003, 1:1,000 for IB) antibodies were purchased from Jackson ImmunoResearch. Donkey anti-goat IgG (cat. A-11055, 1:1,000 for IB), anti-rabbit IgG (cat. A-21206, 1:1,000 for IB), anti-rat IgG (cat. A21209, 1:1,000 for IB), goat anti-rat IgG (cat. A-21247, 1:1,000 for IB), rabbit anti-APH1 (cat. PA1-2010, 1:1,000 for IB), mouse anti-Strep-tag (cat. MA5-17283, 1:1,000 for IB) antibodies were purchased from Thermo

Scientific. Rabbit anti-ATP1A1 (cat. 14418-1-AP, 1:60 for IF) and anti-TOMM20 (cat. 11802-1-AP, 1:60 for IF) antibodies were purchased from Proteintech.

Glucose (cat. G7021), HEPES (cat. H4034), lysosome isolation kit (cat. LYSISO1), CaCl<sub>2</sub> (cat. C5670), PEP (cat. P7002), β-NADH (cat. N8129), pyruvate kinase (cat. P9136), LDHA (cat. SAE0049), FITC–dextran (cat. FD10S), H<sub>2</sub>O<sub>2</sub> (cat. 323381), metformin (cat. D150959), KCl (cat. P9333), MgSO<sub>4</sub> (cat. M2643), KH<sub>2</sub>PO<sub>4</sub> (cat. P5655), NaH<sub>2</sub>PO<sub>4</sub> (cat. S8282), Na<sub>2</sub>HPO<sub>4</sub> (cat. S7907), DAB (cat. D8001), ethanol (cat. 459836), acetonitrile (cat. 34888), isopropanol (cat. 34863), dichloromethane (cat. 650463), SDS (cat. 436143), sodium acetate (cat. S2889), EmbryoMax DMEM (cat. SLM-220-M), demecolcine (cat. D7385), M2 medium (cat. M7167), corn oil (cat. C8267), insulin (cat. I1882), sodium pyruvate (cat. P2256), halocarbon oil 700 (cat. H8898), agar (cat. A1296), tryptone (cat. T9410), cholesterol (cat. C3045), sodium hypochlorite solution (cat. 239305), IPTG (cat. I6758), carbenicillin (cat. C1613), agarose (cat. A9539), collagenase type IV (cat. C5138), BSA (cat. A2153), CH<sub>3</sub>COOK (cat. P1190), magnesium acetate tetrahydrate (cat. M5661), digitonin (cat. D141), oligomycin A (cat. 75351), FCCP (cat. C2920), antimycin A (cat. A8674), rotenone (cat. R8875), ethanolamine (cat. 411000), acetone (cat. 650501), Coomassie Brilliant Blue R-250 (cat. 1.12553), GLP-1 EIA kit (cat. RAB0201), aprotinin (cat. A1153), diprotin A (cat. I9759), trypsin (cat. T1426), 2-mercaptoethanol (cat. M6250), biotin (cat. 14400), NaN<sub>3</sub> (cat. S2002), CH<sub>2</sub>Cl<sub>2</sub> (cat. 270997), pyridine (cat. 270970), l-glutamine (cat. G3126), paraformaldehyde (cat. 158127), haematoxylin solution (cat. 03971), eosin Y solution (cat. 318906), Canada balsam (cat. C1795), xylene (cat. 214736), hydrochloric acid in ethanol (cat. 1.00327), PEG (cat. 89510), phenol red solution (cat. P0290), sucrose (cat. S7903), CsCl (cat. 289329), Na<sub>2</sub>H<sub>2</sub>P<sub>2</sub>O<sub>7</sub> (cat. P8135), β-glycerophosphate (cat. 50020), AICAR (cat. A9978), A23187 (cat. C7522), A-769662 (cat. SML2578), tamoxifen (cat. T5648), NaHCO<sub>3</sub> (cat. S5761), EGTA (cat. E3889), poly-l-lysine solution (cat. P8920), formaldehyde solution (formalin, cat. F8775), OptiPrep (cat. D1556), MgCl<sub>2</sub> (cat. M8266), tetramethylsilane (cat. T24007), Trizma base (Tris, cat. T1503), glycerol (cat. G5516), DMSO (cat. D2650), TCEP (cat. C4706), TBTA (cat. 678937), CuSO<sub>4</sub> (cat. C1297), IGEPAL CA-630 (NP-40, cat. I3021), methanol (cat. 646377), CHCl<sub>3</sub> (cat. C7559), buformin hydrochloride (cat. SML1496), octyl β-d-glucopyranoside (cat. O8001), Triton X-100 (cat. T9284), concanamycin A (cat. C9705), DTT (cat. 43815), MEA (cat. 30070), glucose oxidase (cat. G2133), catalase (cat. C40), ammonium hydroxide solution (cat. 338818), FLAG peptide (cat. F3290), EDTA (cat. E6758), polybrene (cat. H9268), HCl (cat. 320331), NaCl (cat. S7653), NaOH (cat. S8045), ATP disodium salt (cat. A2383), ATP magnesium salt (cat. A9187), d-mannitol (cat. M4125), Percoll (cat. P4937), imidazole (cat. I5513), chloroquine (cat. C6628), cytochalasin D (cat. C2618), N-acetyl-l-cysteine (cat. A9165), phenformin hydrochloride (cat. P7045), formic acid (cat.

5.43804), ammonium formate (cat. 70221), glucagon (cat. 05-23-2700), DEPC-treated water (cat. 693520), glutaraldehyde solution (cat. G5882), glycine (cat. G8898), streptavidin agarose (cat. 16-126), d-desthiobiotin (cat. 71610-M), myristic-d27 acid (cat. 68698), methoxyamine hydrochloride (cat. 89803), MTBSTFA (with 1% t-BDMCS, cat. M-108), hexane (cat. 34859), fatty acid-free BSA (cat. SRE0098), APS (cat. A3678), TEMED (cat. T9281) and Tween-20 (cat. P9416) were purchased from Sigma. WesternBright ECL and peroxide solutions (cat. 210414-73) were purchased from Advansta. Acrylamide/Bis solution, 30%, 29:1 (cat. 1610156) was purchased from Bio-Rad. TAG (15:0/15:0/15:0, cat. 26962) was purchased from Cayman. Protease inhibitor cocktail (cat. 70221) was purchased from Roche. Hoechst (cat. H1399), LysoSensor Green DND-189 (cat. L7535), ProLong Diamond antifade mountant (cat. P36970), ProLong Live Antifade reagent (cat. P36975), NeutrAvidinTM agarose (cat. 29204), Lipofectamine 2000 (cat. 11668500), DMEM, high glucose (cat. 11965175), DMEM, no glucose (cat. 11966025), DMEM without phenol red (cat. 21063045), MEM amino acids solution (cat. 11130077), MEM non-essential amino acids solution (cat. 11140050), JC-1 (cat. T3168), CM-H<sub>2</sub>DCFDA (cat. C6827), CellROX Deep Red (cat. C10422), ESC-qualified fetal bovine serum (FBS) (cat. 30044333), Maxima SYBR Green/ROX qPCR master mix (cat. K0223), Trypan Blue stain (cat. T10282), FBS (cat. 10099141C), penicillin–streptomycin (cat. 15140163), William's E medium, no glutamine (cat. 12551032), liver perfusion medium (cat. 17701), liver digest medium (cat. 17703), GlutaMAX (cat. 35050061), sodium pyruvate (cat. 11360070) and TRIzol (cat. 15596018) were purchased from Thermo Scientific. Internal Standards 1 (cat. H3304-1002) and Internal Standards 3 (cat. H3304-1104) were purchased from Human Metabolome Technologies. rProtein A Sepharose Fast Flow (cat. 17127904), Protein G Sepharose 4 Fast Flow (cat. 17061806), Series S Sensor Chip CM5 (cat. BR100530), Amine Coupling kit (with EDC and NHS included, cat. BR100050) were purchased from Cytiva. OsO<sub>4</sub> (cat. 18465), uranyl acetate (cat. 19481) were purchased from Tedpella. SPI-Pon 812 Embedding kit (cat. 02660-AB) was purchased from SPI. DAPT (cat. S2215), RO4929097 (cat. S1575), bafilomycin A1 (cat. S1413), 3-MA (cat. S2767), Dynasore (cat. S8047), Dyngo-4a (cat. S7163) and nystatin (cat. S1934) were purchased from Selleck. Methyl-β-cyclodextrin (cat. HY-101461) was purchased from MedChemExpress. Labassay triglyceride reagent (cat. 290-63701) was purchased from Wako Pure Chemical Industries. Mouse Ultrasensitive Insulin ELISA kit (cat. 80-INSMSU-E10) was purchased from ALPCO. ReverTra Ace qPCR RT master mix with gDNA remover (cat. FSQ-301) was purchased from Toyobo. 3-(But-3-yn-1-yl)-3-(2-iodoethyl)-3H-diazirine (cat. BD627886) was purchased from Bide Pharmatech. SMM 293-TII expression medium (cat. M293TII) was purchased from Sino Biological. Seahorse XF base medium (cat. 103334) was purchased from Agilent. Paraplast high melt paraffin (cat. 39601095) was purchased from Leica. [U-<sup>13</sup>C]-glutamine (cat. 184161-19-1), [U-<sup>13</sup>C]-palmitic acid (cat. CLM-409) and [U-<sup>13</sup>C]-glucose (cat. CLM-1396) were purchased from Cambridge Isotope Laboratories.

## Plasmids

Full-length cDNAs used in this study were obtained either by PCR using cDNA from MEFs or by purchasing from Origene, Sino Biological or Genescrypt. Mutations of *PEN2* and *ATP6AP1* were performed by PCR-based site-directed mutagenesis using PrimeSTAR HS polymerase (Takara). Expression plasmids for various epitope-tagged proteins were constructed in the pcDNA3.3 vector for transfection (ectopic expression) or in the pBOBI vector for lentivirus packaging (stable expression). To express Strep-tagged ATP6AP1, the *ATP6AP1* cDNA was inserted into a modified pcDNA3.3-C-HA vector with the sequence encoding the HA epitope tag replaced by the sequence of the Strep tag<sup>44</sup>. PCR products were verified by sequencing (Invitrogen). The lentivirus-based vector pLV-H1-EF1a-puro was used for expression of siRNA in MEFs and HEK293T cells, and the AAV-based vector pAAV2 for mouse liver. The sequences for siRNAs of mouse *Pen2* were as follows: 5'-GCCTGTGCCGGAAAGTACTAT-3' (1) and 5'-GTTCTTGTTAGTC AACATT-3' (2). All plasmids, except those used for adenovirus packaging (see below, the 'Packaging and injection of adenovirus and AAV' section), were purified using the caesium chloride density gradient ultracentrifugation method.

## Primary hepatocytes

Human primary hepatocytes were isolated from surgically removed liver tissues. Fresh tissues were minced followed by digesting in 0.25% (w/v) trypsin supplemented with 0.5 mg ml<sup>-1</sup> collagenase type IV for 10 min at 37 °C. Cells were then immediately plated (at 60–70% confluence) in collagen-coated 6-well plates in William's medium E plus 10% FBS, 100 IU penicillin and 100 mg ml<sup>-1</sup> streptomycin. After 4 h of attachment, the medium was replaced with fresh William's medium E with 1% (w/v) BSA for another 12 h before further use. This study was approved by the Human Research Ethics Committee of the Shanghai Sixth People's hospital following the principles of the Declaration of Helsinki. Written informed consent was obtained from all participants.

Mouse primary hepatocytes were isolated with a modified two-step perfusion method using liver perfusion medium and liver digest buffer. Before isolation of hepatocytes, mice were first anaesthetized followed by the insertion of a 0.72 × 19 mm intravenous catheter into the postcava. After cutting off the portal vein, mice were perfused with 50 ml of liver perfusion medium at a rate of 5 ml min<sup>-1</sup>, followed by 50 ml of liver digest buffer at a rate of 2.5 ml min<sup>-1</sup>. The digested liver was then briefly rinsed with PBS and then dissected by gently tearing apart the Glisson's capsule with two sterilized, needle-pointed tweezers on a 6-cm dish containing 3 ml of PBS. The dispersed cells were mixed with 10 ml of ice-cold William's medium E plus 10% FBS and were filtered by passing through a 100-μm cell strainer (BD Falcon). Cells were

then centrifuged at 50g at 4 °C for 2 min, followed by washing twice with 10 ml of ice-cold William's medium E plus 10% FBS. Cells were then plated and cultured as for human primary hepatocytes. *Pen2*<sup>-/-</sup> hepatocytes were established by infecting *Pen2*<sup>F/F</sup> hepatocytes (isolated from *loxP*-flanked *Pen2* mice) with adenoviruses expressing the Cre recombinase (or GFP as a control) for 6 h, followed by incubating in William's medium E with 1% (w/v) BSA for another 12 h before experiments.

## Cell lines

HEK293T, AD293 (Adeno-X 293) cells, MEFs and L929 cells were maintained in Dulbecco's modified Eagle's medium supplemented with 10% FBS, 100 IU penicillin, 100 mg ml<sup>-1</sup> streptomycin at 37 °C in a humidified incubator containing 5% CO<sub>2</sub>. The suspension HEK293T cell line, which was established from HEK293T cells, was a gift from Z. Wang (Xiamen Immocell Biotechnology). Cells were cultured in 400 ml of SMM 293-TII medium in a 2-litre conical glass flask at 37 °C, 160 r.p.m. on a CO<sub>2</sub>-resistant shaker (cat. 88881101, Thermo Scientific) in a humidified incubator containing 5% CO<sub>2</sub>. All cell lines were verified to be free of mycoplasma contamination. HEK293T cells were authenticated by STR sequencing. Polyethylenimine (PEI) at a final concentration of 10 µM was used to transfect HEK293T cells. Total DNA to be transfected for each plate was adjusted to the same amount by using a relevant empty vector. Transfected cells were collected 24 h after transfection.

Lentiviruses, including those for knockdown or stable expression, were packaged in HEK293T cells by transfection using Lipofectamine 2000. At 30 h after transfection, medium (approximately 2 ml) was collected and centrifuged at 5,000g for 3 min at room temperature. The supernatant was mixed with 10 µg ml<sup>-1</sup> (final concentration) polybrene, and this was added to MEFs or HEK293T cells followed by centrifuging at 3,000g for 30 min at room temperature (spinfection). Cells were incubated for another 24 h (MEFs) or 12 h (HEK293T cells) before further treatments.

*LAMTOR1*<sup>F/F</sup>, *AXIN*<sup>F/F</sup> and *ATG5*<sup>F/F</sup> MEFs were established by introducing SV40 T antigen using lentivirus into cultured primary embryonic cells from mouse litters. *LAMTOR1*<sup>-/-</sup> MEFs were generated by infecting *LAMTOR1*<sup>F/F</sup> MEFs with adenoviruses expressing the Cre recombinase for 12 h, as for *AXIN*<sup>-/-</sup> MEFs, *ATG5*<sup>-/-</sup> MEFs and *APH1A-APH1C* triple knockout MEFs. The infected cells were then incubated in fresh DMEM for another 12 h before further treatments. *TRPV1-TRPV4* quadruple knockout MEFs were generated as previously described<sup>25</sup>.

The genes (*PEN2*, *ATP6API*, *PSEN1*, *PSEN2*, *NCSTN*, *PRKAB1* and *PRKAB2*) were deleted from MEFs or HEK293T cells using the CRISPR–Cas9 system. Nucleotides

were annealed to their complements containing the cloning tag aaac, and inserted into the back-to-back *BsmB* I restriction sites of lentiCRISPRv2 vector. The sequence for each sgRNA is as follows: 5'-ATGAGGAGAACCTG-3' (1) and 5'-CAGATCTACCGGCCCGCTG-3' (2) for mouse *Pen2*; 5'-CATCTTCTGGTTCTTCGAG-3' (1) and 5'-CCGGAAGTACTACCTGGGTA-3' (2) for human *PEN2*; 5'-GGTGGCCCGTGATATAACCA-3' for mouse *Atp6ap1*; 5'-GATGTAGCCGTGGTGGCCGGA-3' for human *ATP6AP1*; 5'-CTGAGCCAATATCT AATGGG-3' for mouse *Psen1*; 5'-CACGCTGTGTATGATCG-3' for mouse *Psen2*; 5'-CTGTGG AATGAACGGCAA-3' for mouse *Nestn*; 5'-GAGATCCTTACC TTCTCGTG-3' for mouse *Prkab1*; and 5'-AGCTCGGAGACG TCATGTGCG-3' for mouse *Prkab2*. The constructs were then subjected to lentivirus packaging using HEK293T cells that were transfected with 2 µg of DNA in Lipofectamine 2000 transfection reagent per well of a 6-well plate. At 30 h after transfection, the virus (approximately 2 ml) was collected and used for infecting MEFs or HEK293T cells as described above, except cells cultured to 15% confluence were incubated with the virus for 72 h. In particular, for HEK293T cells, 0.5 ml of fresh DMEM was supplemented to each well after 36 h of infection. When cells were approaching confluence, they were single-cell-sorted into 96-well dishes. Clones were expanded and evaluated for knockout status by sequencing. For glucose starvation, cells were rinsed twice with PBS and then incubated in glucose-free DMEM supplemented with 10% FBS and 1 mM sodium pyruvate for desired periods of time at 37 °C.

## Packaging and injection of adenovirus and AAV

Adenoviruses (AV) carrying Cre recombinase (Ad-Cre) were packaged using the AdEasy Adenoviral Vector system (240009, Agilent) in AD293 (Adeno-X 293) cells. In brief, pAdEasy vector carrying Cre recombinase was linearized with *Pac* I for 12 h, and the efficiency was confirmed by subjecting 0.2 µg of each linearized vector to 0.8% agarose gel (w/v, showing an approximately 30-kb band and a 4.5-kb band). The linearized vector was precipitated with two volumes of ethanol then dissolved with 20 µl of sterile water. A total of 5 µg of linearized vector was transfected into  $3 \times 10^6$  AD293 cells cultured in a 60-mm dish by Lipofectamine 2000, and 3 ml of medium was refreshed after 12 h of transfection. Cells were cultured for another 7 days, with 1.5 ml of fresh medium added (not refreshed) every other day. Cells were collected together with the culture medium followed by three rounds of freeze–thaw cycles. Cell debris was removed by centrifugation at 20,000g for 10 min, and the supernatant was used to infect two 6-cm dishes of AD293 cells followed by 3 rounds of amplification to produce a 10-fold increase in titre. Viral particles were loaded on the top of 5 ml of 15% CsCl (dissolved in TBS (10 mM Tris, 0.9% (w/v) NaCl, 2.5% (w/v) sucrose, pH 8.1)) cushion over 4.5 ml of 40% CsCl cushion (w/v, dissolved in TBS) in an ultracentrifuge tube (cat. 344059, Beckman). The sample was centrifuged at 30,000 r.p.m. in a SW41 rotor (Beckman) for 16 h at 4 °C. The heavier band was collected

followed by dialysis in TBS for 1 h at 4 °C. Purified Ad-Cre viruses were stored at –80 °C.

AAVs were packaged in HEK293T cells using the protocol from Grieger et al.<sup>45</sup>. In brief, cells used for in-house viral production were maintained in 150-mm dishes. A total of 7 µg of pAAV-RC2/9 (AAV2 inverted terminal repeat (ITR) vectors pseudotyped with AAV9 capsid) plasmid, 21 µg of pAAV-helper plasmid and 7 µg of pAAV2 plasmid (carrying ATP6AP1 or its mutant, or siRNAs against mouse *Trpv2* to *Trpv4*) were added to 4 ml of DMEM without phenol red, followed by mixing with 175 µl of PEI solution (1 mg ml<sup>-1</sup>, pH 7.5). The mixture was then incubated at room temperature for 20 min and then added to the dishes. At 60 h after transfection, cells were collected by scraping and centrifugation. The viral particles were purified from the pellet using an Optiprep gradient as previously described<sup>45</sup>. The titres of purified AAV were determined by real-time qPCR (see below). Viruses were stored at –80 °C before use, and were delivered to mice intravenously by lateral tail-vein injection. For each mouse, 1 × 10<sup>11</sup> particles of virus, adjusted to 200 µl of final volume (with PBS, pH 7.4), was injected.

## IP and IB assays

For IP endogenous proteins, LAMTOR1, PEN2 and ATP6AP1 were immunoprecipitated and analysed as previously described<sup>24</sup>, but with minor modifications. In brief, ten 15-cm dishes of MEFs (grown to 80% confluence) were collected for IP of LAMTOR1, or two 10-cm dishes of MEFs (grown to 80% confluence) were collected for IP of PEN2 and ATP6AP1. Cells were lysed with 750 µl per dish of ice-cold ODG buffer (for LAMTOR1; 50 mM Tris-HCl, pH 8.0, 50 mM NaCl, 1 mM EDTA, 2% (w/v) ODG, 5 mM β-mercaptoethanol with protease inhibitor cocktail) or lysis buffer (for PEN2 and ATP6AP1; 20 mM Tris-HCl, pH 7.5, 150 mM NaCl, 1 mM EDTA, 1 mM EGTA, 1% (v/w) Triton X-100, 2.5 mM sodium pyrophosphate, 1 mM β-glycerophosphate, with protease inhibitor cocktail), followed by sonication and centrifugation at 4 °C for 15 min. Cell lysates were incubated with respective antibodies overnight. Overnight protein aggregates were pre-cleared by centrifugation at 20,000g for 10 min, and protein A/G beads (1:250, balanced with ODG buffer or lysis buffer) were then added into the lysate–antibody mixture for another 3 h at 4 °C. The beads were centrifuged and washed with 100 times volume of ODG buffer or lysis buffer for 3 times (by centrifuging at 2,000g) at 4 °C and then mixed with an equal volume of 2× SDS sample buffer and boiled for 10 min before immunoblotting.

For IP of ectopically expressed PEN2 or ATP6AP1, a 6 cm-dish of HEK293T cells was transfected with different expression plasmids. At 24 h after transfection, cells were collected and lysed in 500 µl of ice-cold lysis buffer, followed by sonication and

centrifugation at 4 °C for 15 min. Anti-HA (1:100) or anti-Myc (1:100) antibodies, along with protein A/G beads (1:100), or anti-FLAG M2 Affinity Gel (1:200, pre-balanced in lysis buffer) was added into the supernatant and mixed for 4 h at 4 °C. The beads were washed with 200 times volume of lysis buffer for 3 times at 4 °C and then mixed with an equal volume of 2× SDS sample buffer and boiled for 10 min before immunoblotting. Samples for probing APH1A and OCT1 were not boiled to avoid the formation of insoluble aggregates.

To analyse the levels of p-AMPK $\alpha$  and p-ACC in MEFs, HEK293T cells and primary hepatocytes, cells grown to 70–80% confluence (except for hepatocytes, which were grown to 60–70% confluence) in a well of a 6-well dish were lysed with 250  $\mu$ l of ice-cold lysis buffer. The lysates were then centrifuged at 20,000g for 10 min at 4 °C and an equal volume of 2× SDS sample buffer was added into the supernatant. Samples were then boiled for 10 min and then directly subjected to IB.

To analyse the levels of p-AMPK $\alpha$  and p-ACC in liver, mice were anaesthetized after indicated treatments. Freshly excised (or freeze-clamped) tissue was lysed with ice-cold lysis buffer (10  $\mu$ l mg $^{-1}$  liver weight) followed by homogenization and centrifugation as described above. The lysates were then mixed with 2× SDS sample buffer and subjected to IB. To analyse the levels of p-AMPK $\alpha$  and p-ACC in nematodes, about 150 nematodes cultured on a NGM plate were collected for each sample. Worms were quickly washed with ice-cold M9 buffer containing Triton X-100, and were lysed with 150  $\mu$ l of ice-cold lysis buffer. The lysates were then mixed with 5× SDS sample buffer, followed by homogenization and centrifugation as described above, and then subjected to IB. Analysis of PEN2 expression in mouse intestine was performed as previously described<sup>46</sup>. In brief, duodenal segments of intestine were removed immediately after euthanasia, and washed twice with pre-cold PBS containing inhibitor mix (1 mM PMSF, 5  $\mu$ g ml $^{-1}$  aprotinin, 1  $\mu$ g ml $^{-1}$  pepstatin A, 2  $\mu$ g ml $^{-1}$  leupeptin, 1 mM Na<sub>3</sub>VO<sub>4</sub> and 1 mM NaF). The tissues were then homogenized and sonicated in lysis buffer, followed by homogenization and centrifugation as described above. All samples, as described above, were subjected to IB on the same day of preparation, and any freeze-thaw cycle was avoided.

For IB, the SDS-polyacrylamide gels were prepared in house. In brief, the resolving gel solution (8%, 10 ml) was prepared by mixing 1.9 ml of 30% Acryl/Bis solution, 1 ml of 10× lower buffer (3.5 M Tris, 1% (w/v) SDS, pH 8.8), and 0.48 ml of 65% (w/v) sucrose (dissolved in water) with 6.62 ml of water; and the stacking gel solution (4%, 5 ml) was prepared by mixing 668  $\mu$ l of 30% Acryl/Bis solution and 1.25 ml of 4× stacking buffer (0.5 M Tris, 0.4% (w/v) SDS, pH 6.8) with 3.08 ml water. For each glass gel plate (with 1.0-mm spacer, cat. 1653308 and 1653311, Bio-Rad), approximately 7 ml of resolving gel solution and 2.5 ml of stacking gel solution were required. APS (to 0.1% (w/v) final concentration) and TEMED (to 0.1% (v/v) final

concentration) were added to the resolving gel solution. The resolving gel was overlaid with 2 ml of 75% (v/v) ethanol before acrylamide polymerization. After around 20 min (when a clear line between the resolving gel and ethanol is seen), the overlaid ethanol was poured off, dried using filter paper and then placed at room temperature for another 15 min to let the ethanol evaporate completely. The gel cassette was then filled with APS/TEMED-supplemented stacking gel solution, followed by placing a 15-well comb, and then placed at room temperature for 20 min. After removing the comb, the gel was rinsed with running buffer (25 mM Tris, 192 mM glycine, 1% (w/v) SDS, pH 8.3) before sample loading. Samples of less than 10 µl were loaded into wells, and the electrophoresis was run at 100 V by a Mini-PROTEAN Tetra Electrophoresis Cell (Bio-Rad). In this study, all samples were resolved on 8% resolving gels, except those for PEN2, APH1A–APH1C, PS1, PS2, LAMTOR1, cytochrome *c* and ATP6v0c, which were on 15% gels (prepared as those for 8%, except that a final concentration of 15% Acryl/Bis was added to the resolving gel solution), and AMPK $\beta$ 1/2 and ALDOA, which were on 10% gels. To transfer the resolved proteins, the pre-cut PVDF membrane (0.45 µm, cat. IPVH00010, Merck) was incubated in methanol for 1 min, followed by equilibrating and soaking in pre-cooled transfer buffer (25 mM Tris, 192 mM glycine, 10% (v/v) methanol) for more than 5 min. After preparing the gel/membrane sandwich, the transfer was performed using a voltage at 100 V in a Mini Trans-Blot Cell (Bio-Rad) for 1 h at 4 °C. The blotted PVDF membrane was then incubated in blocking buffer (5% (w/v) BSA or 5% (w/v) non-fat milk (according to the instructions from the antibody suppliers) dissolved in TBST, which is composed of 40 mM Tris, 275 µM NaCl, 0.2% (v/v) Tween-20, pH 7.6) for another 2 h on an orbital shaker at room temperature, followed by rinsing with TBST twice, for 5 min each. The PVDF membrane was incubated with the desired primary antibody (diluted in TBST supplemented with 5% BSA and 0.01% (m/v) NaN<sub>3</sub>) overnight at 4 °C on an orbital shaker with gentle shaking, followed by rinsing with TBST 3 times, 5 min each at room temperature, and then the secondary antibodies were incubated for 3 h at room temperature with gentle shaking. The secondary antibody (diluted in TBST) was then removed, and the PVDF membrane was further washed with TBST 3 times, 5 min each at room temperature. PVDF membranes were incubated in ECL mixture (by mixing equal volumes of ECL solution and peroxide solution for 5 min), then each membrane was placed onto a plastic wrap and laid with medical X-ray film (Fujifilm) in a light-proof cassette for the desired period of time. The films were then developed with X-OMAT MX developer and replenisher and X-OMAT MX fixer and replenisher solutions (Carestream) on a medical X-ray processor (Model 002, Carestream). The developed films were scanned using a Perfection V850 Pro scanner (Epson) using Epson scan software (v.3.9.3.4), and were cropped using Photoshop 2021 software (Adobe). Levels of total proteins and phosphorylated proteins were analysed on separate gels, and representative immunoblots are shown. The band intensities on developed films

were quantified using Image J software (v.1.8.0, National Institutes of Health Freeware).

### **Quantification of *G6pc1* and *Pck1* mRNA levels by real-time PCR**

Mouse primary hepatocytes cultured in 10-cm dishes were treated with metformin or with glucagon as a control. Total RNA was then prepared by lysing cells with 1 ml of TRIzol (for each 10-cm dish), followed by the addition of 270 µl of chloroform and vigorous mixing. After centrifugation at 12,000g for 15 min at 4 °C, 510 µl of the upper aqueous layer was transferred to a clean tube. The RNA was then precipitated by adding 675 µl of isopropanol followed by centrifugation at 12,000g for 15 min at 4 °C. The pellet was washed with 75% ethanol for 3 times by centrifugation at 12,000g for 5 min, and was dissolved in 30 µl of DEPC-treated water. The concentration of RNA was determined using a NanoDrop 2000 spectrophotometer (Thermo Scientific). A total of 4 µg of RNA was diluted with DEPC-treated water to a final volume of 10 µl at 65 °C for 5 min, and immediately chilled on ice. Random Primer Mix, Enzyme Mix and 5× RT buffer (all from the ReverTra Ace qPCR RT kit) were then added to the RNA solution, followed by incubation at 37 °C for 15 min, and then at 98 °C for 5 min on a thermocycler. The reverse-transcribed cDNA was quantified with Maxima SYBR Green/ROX qPCR master mix on a LightCycler 96 system (Roche) with the following programmes: pre-denaturing at 95 °C for 10 min; denaturing at 95 °C for 10 s, then annealing and extending at 60 °C for 30 s in each cycle; cycle number: 40. The following primer pairs were used for qPCR: mouse *Actin*, 5'-TTTGTCACCACAGCTGAGAGA-3' and 5'-TGCCCATTAGGCAACTCG-3'; mouse *G6pc1*, 5'-TTGTGGCTTCCTTGGTCCTC-3' and 5'-CAAAGGGAACTGTTGCGCTC-3'; mouse *Pck1*, 5'-CTCCTCAGCTGCATAACGGT-3' and 5'-GTGGATA TACTCCGGCTGGC-3'. Data were analysed using LightCycler 96 software (v.1.1, Roche).

## **Identification of metformin-binding proteins**

Lysosomes purified from sixty 10-cm dishes of MEFs (see below, ‘Purification of lysosomes’ section, for a detailed procedure) were lysed with 500 µl of ice-cold HEPES lysis buffer (50 mM HEPES, pH 8.0, 150 mM NaCl, 1% (v/v) NP40 with protease inhibitor cocktail), followed by sonication. After centrifugation, supernatants were incubated with 10 µM synthesized metformin probes (Met-Ps) at 4 °C for 2 h, then exposed to 365-nm wavelength UV (CX-2000, UVP) for 10 min. Supernatants were then adjusted to final concentrations of 1 mM TCEP, 0.1 mM TBTA, 1 mM CuSO<sub>4</sub> and 1 mM biotin-N<sub>3</sub> linker, and were incubated at 4 °C for 1 h.

Protein aggregates were cleared by centrifugation at 20,000g for 15 min, and NeutrAvidin beads (1:100) were then added to the lysates for 2 h with gentle rotation. Beads were then washed with 100× volume of HEPES lysis buffer for 3 times at 4 °C, and then mixed with an equal volume of 2× SDS sample buffer, followed by SDS gel electrophoresis. The gels were stained with staining solution (1% (m/v) Coomassie Brilliant Blue R-250 dye dissolved in 45% (v/v) methanol and 10% (v/v) acetic acid in water) for 30 min, followed by decolouring with staining solution without R-250 dye before subjecting to MS analysis.

For validation of metformin binding by pull down, proteins were prepared from a 10-cm dish of HEK293T cells (grown to 80% confluence) transfected with 10 µg of indicated plasmids per dish for 24 h. Samples were similarly prepared as those using lysosomes, and were subjected to immunoblotting using the indicated antibodies.

For identification of metformin-binding sites on PEN2 by MS, 10 µg of FLAG-tagged PEN2 (expressed and purified from HEK293T cells) was used. Samples were similarly prepared as those using lysosomes except sonication.

## **Confocal microscopy**

For determining the lysosomal localization of AXIN, cells grown to 80% confluence on coverslips in 6-well dishes were fixed for 20 min with 4%

(v/v) formaldehyde in PBS at room temperature. The coverslips were rinsed twice with PBS and permeabilized with 0.1% (v/v) Triton X-100 in PBS for 5 min at 4 °C. After rinsing twice with PBS, the coverslips were incubated with anti-AXIN and anti-LAMP2 antibodies (both at 1:100, diluted in PBS) overnight at 4 °C. The cells were then rinsed 3 times with 1 ml of PBS, and then incubated with secondary antibody for 8 h at room temperature in the dark. Cells were washed for another 4 times with 1 ml of PBS, and then mounted on slides using ProLong Diamond antifade mountant. Confocal microscopy images were taken on a Zeiss laser scanning microscope (LSM) 780 with a ×63, 1.4 NA oil objective.

For detecting the pH of lysosomes, cells were grown on 35-mm glass-bottom dishes, and were cultured to 60–80% confluence. Cells were treated with 1 µM (final concentration) LysoSensor Green DND-189 for 1 h, then washed twice with PBS and incubated in fresh medium for another 30 min. In the meantime, 2 µg ml<sup>-1</sup> (final concentration) Hoechst, along with ProLong Live antifade reagent, was added into the medium for staining the nucleus before taking images. For determining the mitochondrial membrane potential, cells were incubated with 10 µM JC-1 dye for 20 min at 37 °C, washed twice with PBS and then incubated in fresh medium before taking images. Mitochondrial membrane potentials were analysed by the red (emitted at 590 nm):green (emitted at 529 nm) fluorescence intensity ratio of JC-1 dye (excited at 488 nm). For determining ROS in MEFs, cells were incubated with 5 µM CellROX Deep Red for 30 min at 37 °C, washed twice with PBS and then incubated in fresh medium before taking images. During imaging, live cells were kept at 37 °C, 5% CO<sub>2</sub> in a humidified incubation chamber (Zeiss, Incubator PM S1). Images were taken using a Zeiss LSM 780 with a ×63, 1.4 NA oil objective.

For detecting ROS in *C. elegans*, synchronized worms cultured to L4 stage were treated with metformin for 24 h. Approximately 50 worms were soaked in 100 µl of M9 buffer containing 0.05% Triton X-100 and 10 µM CM-H<sub>2</sub>DCFDA for 30 min at 20 °C, followed by washing with M9 buffer containing 0.05% Triton X-100 three times. Worms were then placed on an injection pad prepared as described in the ‘*C. elegans* strains’ section, except that the 4% (w/v) agarose was used. Images were taken with a Zeiss LSM 900 with a ×20, 0.8 NA plan-APOCHROMAT air objective.

For imaging PEN2, the Semi-intact IF protocol<sup>47</sup> was used. MEFs were grown on a 35 mm dish (cat. D35-20-10-N, In Vitro Scientific) to 50–60% confluence. Cells were rinsed with PBS once, and treated with buffer I (25 mM HEPES, pH 7.2, 125 mM potassium acetate, 5 mM magnesium acetate, 1 mM DTT, 1 mg l<sup>-1</sup> glucose and 25 µg ml<sup>-1</sup> digitonin) for 2 min on ice, and then buffer II (25 mM HEPES, pH 7.2, 125 mM potassium acetate, 5 mM magnesium acetate, 1 mM DTT and 1 mg l<sup>-1</sup> glucose) for another 15 min on ice. The cells were then treated with 4% (v/v) formaldehyde in PBS at room temperature for 10 min. The slides were rinsed twice with PBS and then permeabilized with 0.05% (v/v) Triton X-100 in PBS for 5 min at 4 °C. After rinsing twice with PBS, the slides were blocked in block buffer (10% FBS (v/v) in PBS, with 0.1% (m/v) saponin) for 30 min. The slides were washed twice with PBS and incubated with primary antibodies diluted in block buffer overnight at 4 °C. The cells were then rinsed three times with PBS, and then incubated with a secondary antibody for another 8 h at 4 °C in the dark, followed by washing for four times with PBS and then mounted on slides using ProLong Diamond antifade mountant. Images were taken on a Zeiss LSM 780 with a ×63, 1.4 NA oil objective.

For taking images using the Zeiss LSM 780 system, the following lasers were used: Hoechst dye was excited with a Diode laser set at 405 nm; Lysosensor, JC-1, Alexa 488 and CM-H<sub>2</sub>DCFDA were visualized with an Ar gas laser (laser module LGK 7812) at 488 nm; Alexa 594 was visualized with a HeNe gas laser (LGK 7512 PF) at 594 nm; and CellROX Deep Red with a HeNe gas laser (LGK 7634) at 633 nm. When images were taken using the Zeiss LSM 900, CM-H<sub>2</sub>DCFDA was excited with laser module URGB (cat. 400102-9301-000, Toptica) using a 10-mW laser line. The parameters, including ‘PMT voltage’, ‘Offset’, ‘Pinhole’ and ‘Gain’, were kept unchanged between each picture taken. The resolution of images was 1,024 × 1,024 pixels. Images were processed using Zen 2012 software (for Zeiss LSM 780) or Zen 3.1 (for Zeiss LSM 900), and formatted using Photoshop 2021 software (Adobe). The intensities of CM-H<sub>2</sub>DCFDA in nematode intestines were quantified using ImageJ software (v.1.8.0, National Institutes of Health Freeware).

## STORM imaging

MEFs stably expressing HA–PEN2 were cultured in a Lab-Tek II chambered no. 1.5 German coverglass system (155409, 8 Chamber, Nunc) to 50% confluence, and were treated following the Semi-intact IF protocol as described above, except that the cells were incubated in rabbit anti-HA tag primary antibody and rat anti-LAMP2 primary antibody, and then with the Atto 488 goat anti-rabbit IgG and Alexa-Fluor 647 donkey anti-mouse IgG secondary antibodies. The slides were then fixed with 4% (v/v) formaldehyde for another 10 min, and washed twice with PBS. The STORM imaging buffer with MEA was then prepared according to the manufacturer's instructions. In brief, 7 µl of GLOX (14 mg of glucose oxidase, 50 µl catalase (17 mg ml<sup>-1</sup>), 200 µl buffer A (10 mM Tris, pH 8.0 and 50 mM NaCl), vortexed to dissolve and cooled on ice) and 70 µl 1 M MEA (77 mg MEA dissolved in 1.0 ml of 0.25 M HCl) were added to 620 µl buffer B (50 mM Tris, pH 8.0, 10 mM NaCl and 10% (m/v) glucose) in a 1.5-ml Eppendorf tube, followed by a brief vortex. The mixture was then added to each well, and images were taken on an N-STORM (Nikon). The imaging was performed using an inverted microscope system (Ti-E Perfect Focus; Nikon) equipped with a monolithic laser combiner (MLC400, Agilent) containing solid-state lasers of wavelengths 405 nm, 488 nm and 561 nm at 50 mW (maximum fibre output power) and a 647-nm laser at 125 mW. After locating a suitable field, a diffraction-limited TIRF image was acquired for reference, followed by a STORM acquisition. The 647-nm laser was then sequentially fired at 100% power to excite all possible fluorophore molecules and photoswitch them into a non-emitting dark state, and then the 488-nm laser. The emitted wavelengths from Alexa Fluor 647 and Atto 488 fluorophores were then sequentially collected by the plan-APOCHROMAT ×100/1.49 TIRF objective (Nikon), filtered by an emission filter set (Nikon TIRF Cube consisting of a TRF89902-EM filter set, Chroma Technology), and detected on an electron-multiplying charge-coupled device camera (Ixon DU-897, Andor Technology). During imaging, 20,000 sequential frames of each channel were acquired. The image acquisition, lateral drift correction and data processing were performed using NIS Elements software with STORM package (v.4.30 build 1053, Nikon) as previously described<sup>48,49</sup>.

## Measurement of oxygen consumption rates

Cells were plated on a 96-well Seahorse XF cell culture microplate (Agilent). For primary hepatocytes, the microplates were pre-coated with collagen. Primary hepatocytes were plated at a density of 1,000 cells per well, whereas MEFs and HEK293T cells were plated at 10,000 cells per well. Cells were incubated in full medium (Williams' medium E containing 1% (w/v) BSA for hepatocytes, and DMEM containing 10% FBS for MEFs and HEK293T cells) overnight before experiments. Medium was then changed to Seahorse XF base medium (Agilent) supplemented with glucose (25 mM for MEFs and HEK293T cells, and 10 mM for hepatocytes), glutamine (4 mM) and pyruvate (1 mM), 1 h before the experiment. Cells were then placed in a CO<sub>2</sub>-free, XF96 Extracellular Flux Analyzer Prep Station (Agilent) at 37 °C for 1 h. The oxygen consumption rate was then measured at 37 °C in an XF96 Extracellular Flux Analyzer (Agilent), with a Seahorse XFe96 sensor cartridge (Agilent) pre-equilibrated in Seahorse XF Calibrant solution (Seahorse Bioscience, Agilent) in a CO<sub>2</sub>-free incubator at 37 °C overnight. Respiratory chain inhibitors (10 µM oligomycin, 10 µM FCCP, and a mixture of 1 µM antimycin A and 1 µM rotenone; all final concentrations) were then sequentially added to cells during the assay. Data were collected using Wave 2.6.1 Desktop software (Agilent) and exported to Prism 9 (GraphPad) for further analysis according to the manufacturer's instructions.

## APEX-based TEM imaging

APEX2 imaging was performed as previously described<sup>50</sup>, but with minor modifications. In brief, HEK293T cells stably expressing APEX2-tagged proteins were grown on a 3.5-cm dish containing 1 ml of DMEM to approximately 70% confluence. Cells were fixed by gently adding 1 ml of 4% (v/v) glutaraldehyde solution (diluted in 1× phosphate buffer (0.1 M Na<sub>2</sub>HPO<sub>4</sub>:0.1 M NaH<sub>2</sub>PO<sub>4</sub> = 81:19, in water, pH 7.4), freshly prepared) pre-warmed to 37 °C. Cells were incubated in glutaraldehyde solution for 10 min, then substituted to 1 ml of ice-cold 2% (v/v) glutaraldehyde solution (freshly prepared) on ice for another 1 h, followed by 0.67% (v/v) glutaraldehyde (freshly prepared) solution at 4 °C overnight. Cells were then washed with 1 ml of ice-cold 1× phosphate Buffer for 5 times, 2 min each, followed by the addition of 1 ml of ice-cold 20 mM glycine solution

(in 1× phosphate buffer) for 10 min on ice, and were then washed with 1× phosphate buffer for 5 times, 2 min each. Cells were then incubated in 1 ml of freshly prepared 1× DAB solution ( $0.5 \text{ mg ml}^{-1}$ ) supplemented with 10 mM H<sub>2</sub>O<sub>2</sub> (all dissolved in 1× phosphate buffer) for 40 min, followed by washing with 1× phosphate buffer for 5 times, 2 min each. Cells were then stained with 2% (w/v) OsO<sub>4</sub> solution in 1× phosphate buffer on ice for 30 min, followed by washing for 5 times, 2 min each with ice-cold water. Cells were then stained in ice-cold 2% (w/v) uranyl acetate solution overnight at 4 °C in the dark, and were then washed for 5 times, 2 min each, with ice-cold water. Dehydration was then performed by sequentially incubating cells in the following ice-cold solutions: 20, 50, 70, 90 and 100% (v/v) ethanol (in water), each for 5 min, followed by incubation in anhydrous ethanol at room temperature for another 5 min. Cells were then quickly submerged ethanol/Spon 812 resin (3:1) mixture at room temperature for a 45-min incubation, and then in ethanol/resin (1:1) mixture at room temperature for 2 h, followed by ethanol/resin (1:3) at room temperature for 2 h, and finally 100% resin at room temperature for two rounds: first round overnight, and next round for 4 h. Resin was then completely drained, and the cells were spread with a thin layer of resin (with a total volume of approximately 400 µl, and below the thickness of 1 mm), followed by baking at 60 °C in a hot-wind drying oven for 48 h. The embedded cells were then sectioned into 75 nm slices after cooling down to room temperature. Images were taken on an electron microscope (Hitachi, HT-7800).

## Purification of lysosomes

Lysosomes were purified using a lysosome isolation kit according to the manufacturer's instructions, but with minor modifications. In brief, MEFs from sixty 10-cm dishes (60–80% confluence), or 200 mg of mouse livers, were collected by directly scrapping at room temperature, followed by centrifugation for 5 min at 500g at 37 °C. Cells were resuspended in 7 ml of 1× extraction buffer containing protease inhibitor cocktail at room temperature, and were dounced in a 7-ml Dounce homogenizer (Sigma, cat. P0610) for 120 strokes on ice followed by centrifugation for 10 min at 1,000g, 4 °C, yielding post-nuclear supernatant (PNS). The PNS was then centrifuged for 20 min at 20,000g and the pellet was suspended in 1×

extraction buffer by gentle pipetting, generating the crude lysosomal fraction (CLF). The volume of CLF was adjusted to 2.4 ml and then equally divided into six 1.5-ml Eppendorf tubes (400 µl per tube). A volume of 253 µl of OptiPrep and 137 µl of 1× OptiPrep dilution buffer were added to each CLF, and mixed by gentle pipetting. The mixture is defined as the diluted OptiPrep fraction (DOF). Each DOF (0.8 ml) was loaded into an 11 × 60 mm centrifuge tube at the top of 27% (0.4 ml) and 22.5% (0.5 ml) OptiPrep solution cushions, and then overlaid with 16% (1 ml), 12% (0.9 ml) and 8% (0.3 ml) OptiPrep solutions. The tube was then centrifuged on an SW60 Ti rotor (Beckman) at 150,000g for 4 h at 4 °C, and the fraction at the top of 12% OptiPrep solution was collected as the CLF. The fraction was diluted with two volumes of PBS, followed by centrifugation at 20,000g for 20 min. The supernatant was then aspirated, and the sediment was the lysosome fraction.

## Measurement of v-ATPase activity in vitro

For each assay, lysosomes purified from two 10-cm dishes of MEFs were used. ATP hydrolysis activity was measured using a coupled spectrophotometric method as previously described<sup>51</sup>, but with some modifications. In brief, lysosomes were suspended in ATPase assay buffer (50 mM NaCl, 30 mM KCl, 20 mM HEPES-NaOH, pH 7.0, 10% (v/v) glycerol, 1 mM MgCl<sub>2</sub>, 1.5 mM phosphoenolpyruvate, 0.35 mM NADH, 20 U ml<sup>-1</sup> pyruvate kinase and 10 U ml<sup>-1</sup> lactate dehydrogenase) with 5 µM concanamycin A (for calculating v-ATPase-specific ATP hydrolysis activity) or DMSO, and pre-warmed at 37 °C for 10 min. The assay was initiated by the addition of 5 mM ATP, and the OD<sub>341</sub> was continuously recorded by a SpectraMax M5 microplate reader.

ATP-dependent proton transport activity was assessed by measuring the initial velocity (early reaction periods during the assay, before levelling off due to depletion of substrate) of ATP-dependent fluorescent quenching of FITC-dextran, as previously described<sup>52,53</sup>. In brief, lysosomes were loaded with FITC-dextran by incubating cells in DMEM supplemented with 2 mg ml<sup>-1</sup> FITC-dextran (final concentration) on ice for 5 min, then transferred to a 37 °C incubator for 30 min. Cells were washed with DMEM for 3 times

and incubated with DMEM for another 30 min at 37 °C to allow transport of FITC–dextran to lysosomes. Cells were collected and lysosomes were purified as described above. The lysosomes were resuspended in assay buffer (125 mM KCl, 1 mM EDTA, 20 mM HEPES, pH 7.5, with KOH) and were balanced on ice for 1 h, then mixed with 5 µM concanamycin A (for calculating the v-ATPase-specific proton transport activity) or DMSO, then warmed at 37 °C for 10 min. Fluorescence of FITC was recorded with excitation at 490 nm and emission at 520 nm using a SpectraMax M5 microplate reader. The initial slope of fluorescence quenching was measured after the addition of 5 mM Mg-ATP (final concentration).

## Purification of mitochondria

Mitochondria were purified as previously described<sup>54</sup>, but with minor modifications<sup>27</sup>. In brief, forty 10-cm dishes of metformin-treated MEFs (60–80% confluence) were collected by direct scrapping at room temperature, followed by centrifugation for 5 min at 500g at 37 °C. Cells were then resuspended in 20 ml of ice-cold IB<sub>cells</sub>-1 buffer (225 mM mannitol, 75 mM sucrose, 0.1 mM EGTA and 30 mM Tris-HCl, pH 7.4), and dounced for 100 strokes in a 40-ml Dounce homogenizer (Sigma, cat. D9188), followed by two centrifugation rounds of 5 min at 600g at 4 °C. The supernatants were then collected and centrifuged for 10 min at 7,000g at 4 °C. The pellets were then washed twice with 20 ml of ice-cold IB<sub>cells</sub>-2 buffer (225 mM mannitol, 75 mM sucrose and 30 mM Tris-HCl pH 7.4). The suspensions were centrifuged at 7,000g, and again at 10,000g, both for 10 min at 4 °C. The pellets were then resuspended in 2 ml of ice-cold MRB buffer (250 mM mannitol, 5 mM HEPES pH 7.4 and 0.5 mM EGTA), and were loaded on top of 10 ml of Percoll medium (225 mM mannitol, 25 mM HEPES pH 7.4, 1 mM EGTA and 30% Percoll (v/v)) in 14 × 89-mm centrifuge tubes (cat. 344059, Beckman). The tubes were then centrifuged on a SW41 rotor (Beckman) at 95,000g for 0.5 h at 4 °C, and the dense band located approximately at the bottom of each tube was collected. The collected fractions were diluted with 10 volumes of MRB buffer, followed by centrifugation at 6,300g for 10 min at 4 °C; the pellets were resuspended and washed with 2 ml of MRB buffer, followed with centrifugation at 6,300g for 10 min at 4 °C. The pellets contained pure mitochondria.

## Purification of cytosol

Cytosol was purified as previously described<sup>55</sup>. In brief, ten 10-cm dishes of cells were homogenized in 800  $\mu$ l of the homogenization buffer (HB) containing 250 mM sucrose, 3 mM imidazole, pH 7.4. Homogenates were then passed through a 22-gauge needle attached to a 1-ml syringe for 6 times, and were then centrifuged at 2,000g for 10 min to yield PNS. PNS samples were then loaded on to the top of 11  $\times$  60-mm centrifuge tubes that had been sequentially loaded with 1 ml of 40.6% sucrose (dissolved in HB), 1 ml of 35% sucrose (dissolved in HB), and 1 ml of 25% sucrose (dissolved in HB). Tubes were then centrifuged on an SW60 Ti rotor (Beckman) at 35,000 r.p.m. for 1 h at 4 °C, and the top fractions (about 200  $\mu$ l) were collected as cytosolic fraction.

## Protein expression

FLAG-tagged PEN2, as well as Strep-tagged ATP6AP1, was expressed in suspension HEK293T cells. A total of 200 ml cells at  $5 \times 10^6$  per ml (with viability higher than 90%, as determined by Trypan Blue staining) were transfected with 200  $\mu$ g of each plasmid dissolved in 2 ml of SMM 293-TII medium containing 1,500  $\mu$ g of PEI. After 48 h, cells were collected by centrifugation at 2,000g, and then lysed with 100 ml of ice-cold lysis buffer. The lysates were then sonicated and centrifuged at 20,000g for another 30 min at 4 °C. Anti-FLAG M2 Affinity Gel (1:100, balanced in lysis buffer), or streptavidin agarose (1:100, balanced in lysis buffer) was added into the supernatant and mixed for 4 h at 4 °C. The beads were then washed with 200 times volume of lysis buffer for 3 times at 4 °C. Proteins were then eluted with 1 ml of FLAG peptide (400  $\mu$ g ml<sup>-1</sup> final concentration) or desthiobiotin (2.5 mM final concentration) for another 1 h at 4 °C. Eluent was further diluted with 15 ml of PBS buffer, then concentrated to 1 ml using an Amicon Ultra-15 centrifugal filter unit with Ultracel-10 regenerated cellulose membrane. Such a process for buffer exchanging was performed for another two times before experiments. Of note, experiments involving proteins expressed and purified described above should be performed on the same day after the purification, and any freeze-thaw cycle should be avoided.

## Differential scanning calorimetry

Differential scanning calorimetry assays were performed on a VP-DSC (GE Healthcare). The VP-DSC was run on a mode without feedback, and 15 min of equilibration at 20 °C was performed before and between each scan. The scanning range was set from 20 to 80 °C, and heating rate at 90 °C h<sup>-1</sup>. The instrument was pre-equilibrated by running for five heating–cooling cycles with both the sample cell and the reference cell loaded with PBS. The sample cell was then loaded with 380 µl of FLAG-tagged PEN2 protein at 1 mg ml<sup>-1</sup> in 20 µM metformin (in PBS) or PBS, and curves of heat capacity (Cp) versus temperature were recorded. Data were collected using VPViewer 2000 software (v2.66.7, GE Healthcare), and were then corrected for PBS baselines and normalized for scan rate and protein concentration<sup>56</sup> using Origin 7 software (v.7.0552, OriginLab).

## ITC

ITC was performed using a MicroCal iTC200 isothermal titration calorimeter (GE Healthcare), with the sample cell and the reference cell maintained at 25 °C. The instrument was pre-equilibrated before the experiment. A total of 280 µl of FLAG-tagged PEN2 (at 60 µM) and 40 µl of metformin (2 mM stock solution), all in PBS buffer, were loaded into the sample cell and the injector, respectively, and PBS to the reference cell. Metformin was then titrated stepwise (0.4 µl during 0.8 s for the first injection, and 2 µl during 4 s for the rest of 19 injections, all injected at constant velocity, and with an interval of 150 s between each injection) into the PEN2 solution, or PBS as a control. During titration, the sample cell was continuously stirred at 1,000 r.p.m. Data of heat changes acquired during metformin–PEN2 titration were collected using ITC200 software (v.1.26.1, GE Healthcare), and were subtracted by those of metformin–PBS, then analysed using Origin 7 software (v.7.0552, OriginLab), which fits a ‘Two Set of Sites’ model.

## SPR

Experiments were performed in triplicate at 25 °C on a BIACore T200 using CM5 sensor chips, and data were analysed using BIACore T200 Evaluation software (GE Healthcare) following the manufacturer's instruction. In brief, a cell on the CM5 sensor chip was activated with a mixture of 200 µM 1-ethyl-3-(3-dimethylaminopropyl)carbodiimide (EDC) and 50 µM *N*-hydroxysuccinimide (NHS) at 10 µl min<sup>-1</sup> for 10 min. A total of 20 µl of FLAG-tagged PEN2 or PEN2-2A protein (1 mg ml<sup>-1</sup>) purified as described above and adjusted to pH 4.0 (by mixing with 180 µl of 10 mM sodium acetate solution, pH 4.0) was then immobilized on the surface of the cell at 10 µl min<sup>-1</sup> for 5 min for two repetitive runs. The cell was then blocked with 1 M ethanolamine (10 µl min<sup>-1</sup> for 10 min). A neighbouring cell that served as a reference was similarly activated and blocked, except that PBS adjusted to pH 4.0 was used for immobilization. Both of the cells were then equilibrated with PBS. Metformin stock solution (2 mM) was diluted to a series of concentrations (6.25, 3.125, 1.5625, 0.78125 and 0.05 µM (all in PBS)), and was flowed at 30 µl min<sup>-1</sup> for 150 s in each run. At the end of each flow, cells were regenerated for 5 min with 10 mM glycine-HCl (pH 2.0) solution at 10 µl min<sup>-1</sup>. Data from the sample cell were collected using BIACore T200 Control software (v. 2.0, GE Healthcare), and were subtracted by those from the reference cell. Association and dissociation constants were obtained by global fitting of the data to a 1:1 Langmuir binding model using BIACore T200 Evaluation software (v.2.0, GE Healthcare). Data were exported to Origin 7 software (v.7.0552, OriginLab) for generating the final figures.

## Synthesis of metformin probes

Compounds were purified using a preparative HPLC (Sail 1000, Welch Materials) equipped with an XB-C18 column (30 × 250 mm, 5 µm, Welch Materials). Mass spectra for compound characterization were collected using an Autopurification LC Prep system equipped with an ACQUITY QDa detector (Waters) with the ESI mode. High-resolution mass spectra were obtained on a Q Exactive Orbitrap mass spectrometer (Thermo Scientific). NMR spectra were measured on an Avance III 600 MHz NMR spectrometer (Bruker) using tetramethylsilane as the internal standard, and the chemical shift was reported in δ (ppm), multiplicities (s = singlet, d =

doublet, t = triplet, q = quartet, p = pentet, m = multiplet and br = broad), integration and coupling constants ( $J$  in Hz).  $^1\text{H}$  and  $^{13}\text{C}$  chemical shifts are relative to the solvent:  $\delta_{\text{H}}$  2.50 and  $\delta_{\text{C}}$  39.5 for DMSO- $d_6$ .

The biotin-N<sub>3</sub> linker was synthesized as previously described<sup>57</sup>, and photoactive metformin probes as previously described<sup>58</sup>. In brief, metformin (converted from its hydrochloride form as previously described<sup>59</sup>; 50 mg, 0.387 mM, 1.0 eq), 3-(but-3-yn-1-yl)-3-(2-iodoethyl)-3*H*-diazirine (189.8 mg, 0.120 ml, 0.765 mM, 1.98 eq) and anhydrous acetone (1.0 ml) were stirred at 23 °C for 18 h. The mixture was then evaporated under reduced pressure at room temperature, followed by purification on a preparative HPLC. Mobile phase buffer A was H<sub>2</sub>O, and mobile phase buffer B was methanol. The gradients were as follows:  $t = 0$  min, 0% B;  $t = 3$  min, 0% B;  $t = 18$  min, 100% B;  $t = 30$  min, 100% B with a constant flow rate at 20 ml min<sup>-1</sup>. Type I (eluted at 80% phase B, referred to as Met-P1) and type II (eluted at 93% phase B, Met-P2) forms of metformin probes were obtained as a white solid with yields of 12.7% (18.5 mg) and 3.2% (4.7 mg), respectively.

Type I (Met-P1),  $^1\text{H}$ -NMR (600 MHz, DMSO- $d_6$ ):  $\delta$  7.52 (t,  $J = 5.4$  Hz, 1H), 6.57 (s, 4H), 2.97 (dt,  $J = 7.5, 5.4$  Hz, 2H), 2.90 (s, 6H), 2.85 (t,  $J = 2.7$  Hz, 1H), 2.00 (dt,  $J = 7.3, 2.7$  Hz, 2H), 1.62 (t,  $J = 7.4$  Hz, 2H), 1.58 (t,  $J = 7.3$  Hz, 2H);  $^{13}\text{C}$ -NMR (150 MHz, DMSO- $d_6$ ):  $\delta$  159.45, 156.58, 83.14, 71.90, 37.95, 37.45, 32.18, 31.25, 27.05, 12.71; HRMS ( $m/z$ ): [M-I]<sup>+</sup> calculated for C<sub>11</sub>H<sub>20</sub>N<sub>7</sub><sup>+</sup>, 250.1775; found, 250.1772.

Type II (Met-P2),  $^1\text{H}$ -NMR (600 MHz, DMSO- $d_6$ ):  $\delta$  7.22 (s, 2H), 6.96–6.26 (br m, 3H), 2.97–2.93 (m, 2H), 2.92 (s, 6H), 2.85 (t,  $J = 2.7$  Hz, 1H), 2.00 (dt,  $J = 7.4, 2.7$  Hz, 2H), 1.60 (dt,  $J = 7.4, 2.2$  Hz, 4H);  $^{13}\text{C}$ -NMR (150 MHz, DMSO- $d_6$ ):  $\delta$  154.20, 109.53, 83.14, 71.82, 37.48, 31.99, 31.41, 27.13, 12.70; HRMS ( $m/z$ ): [M-I]<sup>+</sup> calculated for C<sub>11</sub>H<sub>20</sub>N<sub>7</sub><sup>+</sup>, 250.1775; found, 250.1770.

## Protein and peptide MS

To identify metformin-interacting proteins, the pulled down, biotinylated proteins were subjected to SDS-PAGE. After staining with Coomassie Brilliant Blue R-250 dye, gels were decoloured and the excised gel segments were subjected to in-gel trypsin digestion and dried. Samples were analysed on a nanoElute (Bruker) coupled to a timsTOF Pro (Bruker) equipped with a CaptiveSpray source, or a NanoLC 425 System (SCIEX) coupled to a TripleTOF 5600+ mass spectrometer (SCIEX). Peptides were dissolved in 10 µl 0.1% formic acid (v/v) and were loaded onto a homemade C18 column (35 cm × 75 µm, ID of 1.9 µm, 100 Å). Samples were then eluted for 60 min with linear gradients of 3–35% acetonitrile (v/v, in 0.1% formic acid) at a flow rate of 0.3 µl min<sup>-1</sup>. MS data were acquired with a timsTOF Pro mass spectrometer (Bruker) operated in PASEF mode, and were analysed using Peaks Studio software (X<sup>+</sup>, Bioinformatics Solutions), or a TripleTOF 5600+ mass spectrometer, and were analysed using ProteinPilot software (v.5.0, SCIEX). The mouse UniProt Reference Proteome database was used during data analysis.

To determine the PEN2-interacting proteins, the HA-tagged PEN2 immunoprecipitants (immunoprecipitated from twenty 10-cm dishes of MEFs stably expressing HA-tagged PEN2) were subjected to SDS-PAGE, and were processed as described above. Data acquisition was performed as described above, except that an EASY-nLC 1200 System (Thermo Scientific) coupled to an Orbitrap Fusion Lumos Tribrid spectrometer (Thermo Scientific) equipped with an EASY-Spray Nanosource was used. Data were analysed using Proteome Discoverer (v.2.2, Thermo Scientific) against the mouse UniProt Reference Proteome database.

For identifying metformin-binding sites on PEN2, the Met-P1-conjugated FLAG-tagged PEN2 (purified from suspension HEK293T cells) were subjected to SDS-PAGE, and were processed as described above. MS analysis was performed as that for timsTOF Pro, except that the following parameters of Peaks Studio X<sup>+</sup> software were set: (1) precursor ion mass tolerance: 15 ppm; (2) fragment ion mass tolerance (error tolerance): 0.05 Da; (3) tryptic enzyme specificity with two missed cleavages: allowed; (4) mode of monoisotopic precursor mass and fragment ion mass was chosen; (5) mode of a fixed modification of cysteine carbamidomethylation was

chosen; and (6) variable modifications including *N*-acetylation of proteins, oxidation@M and 222.17@X.

## Measurement of adenylates

ATP, ADP and AMP from cells or tissues were analysed by capillary electrophoresis-based MS as previously described<sup>6</sup>. In brief, each measurement required cells collected from a 10-cm dish (60–70% confluence) or 100 mg of liver tissue dissected by freeze clamp. For analysis of metabolites, cells were rinsed with 20 ml of 5% (m/v) mannitol solution (dissolved in water) and instantly frozen in liquid nitrogen. Cells were then lysed with 1 ml of methanol containing Internal Standards 1 (IS1 (Human Metabolome Technologies, H3304-1002, 1:200), used to standardize the metabolite intensity and to adjust the migration time), and were scraped from the dish. For analysis of metabolites in liver, mice were anaesthetized after indicated treatments. The tissue was excised by freeze-clamping, then ground in 1 ml of methanol with 50 µM IS1. The lysate was then mixed with 1 ml of chloroform and 400 µl of water by 20 s of vortexing. After centrifugation at 15,000g for 15 min at 4 °C, 450 µl of aqueous phase was collected and was then filtrated through a 5-kDa cut-off filter (Millipore, cat. UFC3LCCNB-HMT) by centrifuging at 12,000g for 3 h at 4 °C. In parallel, quality control (QC) samples were prepared by combining 100 µl of the aqueous phase from each sample and then similarly filtered. The filtered aqueous phase was then freeze-dried in a vacuum concentrator (Labconco, CentriVap Benchtop centrifugal vacuum concentrator, equipped with a CentriVap –84 °C Cold Trap and a Scroll vacuum pump) at 4 °C, and then dissolved in 100 µl of water containing Internal Standards 3 (IS3 (Human Metabolome Technologies, H3304-1104, 1:200), to adjust the migration time). A total of 20 µl of redissolved solution was then loaded into an injection vial with a conical insert for CE-QTOF MS (Agilent Technologies 7100, equipped with 6545 mass spectrometer) analysis. Data were collected using MassHunter LC/MS acquisition 10.1.48 (Agilent), and were processed using Qualitative Analysis B.06.00 (Agilent). Levels of AMP, ADP and ATP were measured using full scan mode with *m/z* values of 346.0558, 426.0221, and 505.9885, respectively. Note that a portion of ADP and ATP could lose one phosphate group during in-source fragmentation, thus leaving the same *m/z* ratios as AMP and ADP, and

should be corrected according to their different retention times in the capillary. Therefore, the total amount of ADP is the sum of the latter peak of the *m/z* 346.0558 spectrogramme and the former peak of the *m/z* 426.0221 spectrogramme, and the same is applied for ATP.

To analyse ATP, ADP and AMP in nematodes, HPLC–MS was performed. In brief, 150 nematodes maintained on NGM or siRNA plates (with or without 50 mM metformin) for 48 h were washed with ice-cold M9 buffer containing Triton X-100. Bacteria were removed by quickly spinning down the slurry at 100g for 5 s. Nematodes were then instantly lysed in 1 ml of methanol, then mixed with 1 ml of chloroform and 400 µl of water (containing 4 µg ml<sup>-1</sup> [ $\text{U}-^{13}\text{C}$ ]-glutamine), followed by 20 s of vortexing. After centrifugation at 15,000g for another 15 min at 4 °C, 800 µl of aqueous phase was collected, lyophilized in a vacuum concentrator at 4 °C, and then dissolved in 30 µl of 50% (v/v, in water) acetonitrile. Measurement of AMP and ATP level was based on ref. <sup>60</sup> using a QTRAP MS (SCIEX, QTRAP 5500) interfaced with a UPLC system (SCIEX, ExionLC AD). A total of 2 µl of each sample was loaded onto a HILIC column (ZIC-pHILIC, 5 µm, 2.1 × 100 mm, PN: 1.50462.0001, Millipore). The mobile phase consisted of 15 mM ammonium acetate containing 3 ml l<sup>-1</sup> ammonium hydroxide (>28%, v/v) in the LC–MS-grade water (mobile phase A) and LC–MS-grade 90% (v/v) acetonitrile in LC–MS-grade water (mobile phase B) run at a flow rate of 0.2 ml min<sup>-1</sup>. AMP, ADP and ATP were separated with the following HPLC gradient elution programme: 95% B held for 2 min, then to 45% B in 13 min, held for 3 min, and then back to 95% B for 4 min. The mass spectrometer was run on a Turbo V ion source in negative mode with a spray voltage of -4,500 V, source temperature at 550 °C, gas no.1 at 50 psi, gas no.2 at 55 psi, and curtain gas at 40 psi. Metabolites were measured using the multiple reactions monitoring mode, and declustering potentials and collision energies were optimized using analytical standards. The following transitions were used for monitoring each compound: 505.9/158.9 and 505.9/408.0 for ATP; 425.9/133.9, 425.9/158.8 and 425.9/328.0 for ADP; 345.9/79.9, 345.9/96.9 and 345.9/133.9 for AMP; and 149.9/114 for [ $\text{U}-^{13}\text{C}$ ]-glutamine. Data were collected using Analyst 1.7.1 software (SCIEX), and the relative amounts of metabolites were analysed using MultiQuant 3.0.3 software (SCIEX). Note that a portion of ADP and ATP could lose one or two phosphate groups during in-source

fragmentation, thus leaving same *m/z* ratios as AMP and ADP, which was corrected according to their different retention times in the column.

For quantification of AMP, ADP and ATP in cells, tissues or nematodes, [ $^{13}\text{C}$ ,  $^{15}\text{N}$ ]AMP, [ $^{13}\text{C}$ ,  $^{15}\text{N}$ ]ADP and [ $^{13}\text{C}$ ,  $^{15}\text{N}$ ]ATP dissolved in individual lysates were used to generate corresponding standard curves by plotting the ratios of detected labelled AMP, ADP or ATP (areas) to the products of IS1 and IS3 (for CE-MS), or [ $^{13}\text{C}$ ]-glutamine (for HPLC-MS), against the added concentrations of labelled AMP, ADP or ATP. The amounts of AMP, ADP and ATP were estimated according to standard curves, and were then divided by protein wet weight. The protein wet weight of each sample was determined by Bradford assay after dissolving the naturally dried protein sediment with 0.2 M KOH at room temperature.

## Determination of metformin concentration

To measure metformin concentrations in serum, 50  $\mu\text{l}$  of serum collected from each mouse or human participant was mixed with 80% methanol (v/v) in water using buformin at 100  $\mu\text{g l}^{-1}$  as an internal standard. The aqueous phase was then collected after centrifugation at 15,000g for 15 min at 4 °C. Cells, liver tissues or intestinal tissues were prepared as in CE-MS measurement of adenylates, except that liver and intestinal tissues (50 mg each) were collected from anaesthetized, blood-drained mice, and no ultrafiltration was required. In addition, cells or liver tissues were rinsed with PBS before homogenization. Nematode samples were prepared as in for the HPLC-MS measurement of adenylates. Measurement was performed on a QTRAP MS (SCIEX, QTRAP 6500+) connected to a UPLC system (SCIEX, ExionLC AD). A total of 2  $\mu\text{l}$  of each sample was loaded onto a pHILIC column (ZIC-pHILIC, 5  $\mu\text{m}$ , 2.1  $\times$  100 mm, PN: 1.50462.0001, Millipore). The mobile phase consisted of 10 mM ammonium formate containing 0.1% formate (v/v) in the LC-MS-grade water (mobile phase A) and LC-MS-grade acetonitrile containing 0.1% (v/v) formate in LC-MS-grade water (mobile phase B) run at a flow rate of 0.3 ml  $\text{min}^{-1}$ . The HPLC gradient was as follows: 95% B held for 1 min, then to 40% B in 6 min, held for 1 min, then to 95% B within 7.5 min, and held for 2.5 min. The QTRAP mass spectrometer was run on a Turbo V ion source and running in negative mode run in a spray voltage of -5,500 V,

with source temperature at 500 °C, gas no.1 at 50 psi, gas no.2 at 55 psi, and curtain gas at 40 psi. Compounds were measured using the multiple reactions monitoring mode, and declustering potentials and collision energies were optimized using analytical standards. The following transitions were used for monitoring each compound: 130/71 for metformin and 158.1/60 for buformin. A standard curve was generated in each experiment for quantification. Data were collected using Analyst 1.6.3 software (SCIEX), and the relative amounts of metabolites were analysed using MultiQuant 3.0.2 software (SCIEX). The average cell volume of MEFs was estimated to be 2,263  $\mu\text{m}^3$ , HEK293T cells 4,240  $\mu\text{m}^3$  and primary hepatocytes 17,062  $\mu\text{m}^3$  using Imaris 7.4.0 software (Bitplane) from the axial image stacks of CDFA-SE labelled cells taken using a Zeiss LSM780.

## Determination of TAG synthesis

TAG synthesis rates were determined by analysing the contents of labelled TAG in cells treated with [ $\text{U}-^{13}\text{C}$ ] glucose or [ $\text{U}-^{13}\text{C}$ ] palmitic acid (PA). Glucose was dissolved in PBS, and PA was conjugated to BSA before use. To conjugate PA, 200 mg of PA was first dissolved in 20 ml of ethanol in a conical flask by stirring, followed by dropwise mixing with 156  $\mu\text{l}$  of 5 M NaOH. The slurry was constantly stirred for 12 h, which leads to a complete evaporation of ethanol. The dried sediment was then dissolved with 10% fatty-acid-free BSA to a final concentration of 2 mM.

Primary hepatocytes were isolated and cultured in DMEM containing 1% BSA for 12 h before the experiment. Cells were then incubated in glucose-free DMEM supplemented with 25 mM [ $\text{U}-^{13}\text{C}$ ] glucose and 1% BSA, or DMEM containing 100  $\mu\text{M}$  [ $\text{U}-^{13}\text{C}$ ] PA and 1% BSA for another 12 h. Cells on a 10-cm dish were rinsed with 25 ml of PBS twice, and instantly frozen in liquid nitrogen. Cells were then lysed with 1 ml of methanol containing TAG (15:0/15:0/15:0) as an internal standard, and were scraped from the dish. The lysate was then quickly mixed with 1 ml of chloroform and 400  $\mu\text{l}$  of water by 20 s of vortexing. After centrifugation at 15,000g for 15 min at 4 °C, 700  $\mu\text{l}$  of organic phase was collected, followed by lyophilization with nitrogen blow on a pressured gas blowing concentrator (MGS-2200, EYELA) at room temperature. Analysis of TAG was performed on a

Shimadzu Prominence UPLC system (Nexera UHPLC LC-30A) interfaced with a TripleTOF 5600+ system (SCIEX) equipped with an ESI source. Lyophilized samples were dissolved in 20 µl of dichloromethane/methanol solution (2/1, v/v), and was diluted with 380 µl of methanol/isopropanol/H<sub>2</sub>O solution (65/30/5, v/v/v). The injection volume was 5 µl. TAGs were separated through a C8 column (2.1 × 100 mm with 1.7 µm particle size, cat. 186002878, Waters) with column temperature maintained at 55 °C. Mobile phases consisted of 10 mM ammonium formate in acetonitrile/H<sub>2</sub>O (60/40, v/v) (mobile phase A) and 10 mM ammonium formate in isopropanol/acetonitrile (90/10, v/v) (mobile phase B) and was run at a flow rate of 0.26 ml min<sup>-1</sup>. The gradient was as follows: 32% B for 1.5 min, then increased to 97% B within 19.5 min and held for 4 min, then back to 32% B and held for another 5 min. The flow rate for mobile phases was set at 0.26 ml min<sup>-1</sup>. The mass spectrometer was run in positive, information-dependent acquisition (IDA) mode, with the source temperature of 550 °C, the ion source gas 1 and 2 at 55 psi, the curtain gas at 35 psi, the collision energy at 40 eV, the ion spray voltage floating at 5.5 kV, and the mass range at 500–1,250 *m/z*. The accumulation time for full scan was set at 150 ms, and the accumulation time for each IDA scan was 45 ms. Peaks of metabolites with intensities larger than 100 c.p.s. after adding up the signal from 10 rounds of IDA scans were chosen for further analysis. Data were collected using Analyst TF 1.6 software (SCIEX), and were analysed using MS-DIAL 4.7 software (RIKEN), through which the deconvolution and streamline criteria were used for peak/TAG identification.

## Determination of β-oxidation rates

The rates of β-oxidation were determined through the labelled intermediates of the TCA cycle in cells treated with [U-<sup>13</sup>C] PA for a certain time duration. Primary hepatocytes were cultured and treated as those used for the determination of TAG synthesis. Cells were rinsed with PBS twice, froze in liquid nitrogen and then lysed with 1 ml of 80% methanol (v/v) in water containing 10 µg ml<sup>-1</sup> myristic-*d*27 acid as an internal standard, followed by 20 s of vortexing. After centrifugation at 15,000g for 1 min at 4 °C, 600 µl of supernatant (aqueous phase) was freeze-dried at 4 °C. The

lyophilized sample was then vortexed for 1 min after mixing with 50 µl of freshly prepared methoxyamine hydrochloride (20 mg ml<sup>-1</sup> in pyridine), followed by incubating at 4 °C for 1 h. The mixture was sonicated at 0 °C by bathing in an ice slurry for 10 min, and was then incubated at 37 °C for 1.5 h, followed by mixing with 50 µl of MTBSTFA and incubated at 55 °C for 1 h. Before subjecting to GC–MS, samples were centrifuged at 15,000g for 10 min, and 60 µl of supernatant was loaded into an injection vial. GC was performed on a HP-5MS column (30 m × 0.25 mm i.d., 0.25 µm film thickness) using a GC/MSD instrument (7890-5977B, Agilent). The injector temperature was 260 °C. The column oven temperature was first held at 70 °C for 2 min, then increased to 180 °C at the rate of 7 °C min<sup>-1</sup>, then to 250 °C at the rate of 5 °C min<sup>-1</sup>, then to 310 °C at the rate of 25 °C min<sup>-1</sup>, where it was held for 15 min. The MSD transfer temperature was 280 °C. The MS quadrupole and source temperature were maintained at 150 °C and 230 °C, respectively. Data were collected using MassHunter GC/MS Acquisition software (B.07.04.2260, Agilent), and were analysed using GC-MS MassHunter Workstation Qualitative Analysis software (v.B.07.01SP1, Agilent).

## Statistical and reproducibility

Statistical analyses were performed using Prism 9 (GraphPad software), except for the survival curves, which were analysed using SPSS 27.0 (IBM). Each group of data was subjected to Kolmogorov–Smirnov test, Anderson–Darling test, D’Agostino–Pearson omnibus test or Shapiro–Wilk test for normal distribution where applicable. Unpaired two-tailed Student’s *t*-test was used to determine significance between two groups of normally distributed data. Welch’s correction was used for groups with unequal variances. Unpaired two-tailed Mann–Whitney test was used to determine significance between data without a normal distribution. For comparisons between multiple groups, an ordinary one-way or two-way analysis of variance (ANOVA) was used, followed by Tukey’s, Sidak’s, Dunnett’s or Dunn’s test as specified in the figure legends. The assumptions of homogeneity of error variances were tested using *F*-test (*P*>0.05). For comparison between multiple groups with two fixed factors, an ordinary two-way ANOVA or two-way repeated measures ANOVA (for GTT, ITT and PTT data) was used, followed by Tukey’s or Sidak’s multiple

comparisons test as specified in the legends. Geisser–Greenhouse's correction was used where applicable. The adjusted means and s.e.m. or s.d. were recorded when the analysis met the above standards. Differences were considered significant when  $P < 0.05$ , or  $P > 0.05$  with large differences of observed effects (as suggested in refs. [61,62](#)). All specific statistical details can be found in the figure captions and source data. All images shown without biological replicates are representative of a minimum of three independent experiments.

## Reporting summary

Further information on research design is available in the [Nature Research Reporting Summary](#) linked to this paper.

## Data availability

The data supporting the findings of this study are available within the paper and its [Supplementary Information](#) files. The MS proteomics data have been deposited to the ProteomeXchange Consortium (<http://proteomecentral.proteomexchange.org>) through the iProX partner repository<sup>63</sup> with the dataset identifier [PXD030090](#). Materials, reagents or other experimental data are available upon request. Full immunoblots are provided as Supplementary Information Fig. 1. [Source data](#) are provided with this paper.

## References

1. Foretz, M., Guigas, B. & Viollet, B. Understanding the glucoregulatory mechanisms of metformin in type 2 diabetes mellitus. *Nat. Rev. Endocrinol.* **15**, 569–589 (2019).
2. Barzilai, N., Crandall, J. P., Kritchevsky, S. B. & Espeland, M. A. Metformin as a tool to target aging. *Cell Metab.* **23**, 1060–1065 (2016).

3. Morales, D. R. & Morris, A. D. Metformin in cancer treatment and prevention. *Annu Rev Med* **66**, 17–29 (2015).
4. Rena, G., Hardie, D. G. & Pearson, E. R. The mechanisms of action of metformin. *Diabetologia* **60**, 1577–1585 (2017).
5. Foretz, M., Guigas, B., Bertrand, L., Pollak, M. & Viollet, B. Metformin: from mechanisms of action to therapies. *Cell Metab.* **20**, 953–966 (2014).
6. Zhang, C. S. et al. Fructose-1,6-bisphosphate and aldolase mediate glucose sensing by AMPK. *Nature* **548**, 112–116 (2017).
7. Francis, R. et al. *aph-1* and *pen-2* are required for Notch pathway signaling,  $\gamma$ -secretase cleavage of  $\beta$ APP, and presenilin protein accumulation. *Dev. Cell* **3**, 85–97 (2002).
8. Supek, F. et al. A novel accessory subunit for vacuolar H<sup>+</sup>-ATPase from chromaffin granules. *J. Biol. Chem.* **269**, 24102–24106 (1994).
9. Onken, B. & Driscoll, M. Metformin induces a dietary restriction-like state and the oxidative stress response to extend *C. elegans* healthspan via AMPK, LKB1, and SKN-1. *PLoS ONE* **5**, e8758 (2010).
10. Martin-Montalvo, A. et al. Metformin improves healthspan and lifespan in mice. *Nat. Commun.* **4**, 2192 (2013).
11. Graham, G. G. et al. Clinical pharmacokinetics of metformin. *Clin. Pharmacokinet.* **50**, 81–98 (2011).
12. El-Mir, M. Y. et al. Dimethylbiguanide inhibits cell respiration via an indirect effect targeted on the respiratory chain complex I. *J. Biol. Chem.* **275**, 223–228 (2000).
13. Owen, M. R., Doran, E. & Halestrap, A. P. Evidence that metformin exerts its anti-diabetic effects through inhibition of complex 1 of the mitochondrial respiratory chain. *Biochem. J.* **348**, 607–614 (2000).

14. Hawley, S. A. et al. Use of cells expressing  $\gamma$  subunit variants to identify diverse mechanisms of AMPK activation. *Cell Metab.* **11**, 554–565 (2010).
15. Miller, R. A. et al. Biguanides suppress hepatic glucagon signalling by decreasing production of cyclic AMP. *Nature* **494**, 256–260 (2013).
16. Hunter, R. W. et al. Metformin reduces liver glucose production by inhibition of fructose-1-6-bisphosphatase. *Nat. Med.* **24**, 1395–1406 (2018).
17. Steinberg, G. R. & Kemp, B. E. AMPK in health and disease. *Physiol. Rev.* **89**, 1025–1078 (2009).
18. Burkewitz, K., Zhang, Y. & Mair, W. B. AMPK at the nexus of energetics and aging. *Cell Metab.* **20**, 10–25 (2014).
19. Li, Y. et al. AMPK phosphorylates and inhibits SREBP activity to attenuate hepatic steatosis and atherosclerosis in diet-induced insulin-resistant mice. *Cell Metab.* **13**, 376–388 (2011).
20. Fullerton, M. D. et al. Single phosphorylation sites in ACC1 and ACC2 regulate lipid homeostasis and the insulin-sensitizing effects of metformin. *Nat. Med.* **19**, 1649–1654 (2013).
21. Duca, F. A. et al. Metformin activates a duodenal AMPK-dependent pathway to lower hepatic glucose production in rats. *Nat. Med.* **21**, 506–511 (2015).
22. Madiraju, A. K. et al. Metformin suppresses gluconeogenesis by inhibiting mitochondrial glycerophosphate dehydrogenase. *Nature* **510**, 542–546 (2014).
23. Cao, J. et al. Low concentrations of metformin suppress glucose production in hepatocytes through AMP-activated protein kinase (AMPK). *J. Biol. Chem.* **289**, 20435–20446 (2014).

24. Zhang, C. S. et al. The lysosomal v-ATPase–Ragulator complex is a common activator for AMPK and mTORC1, acting as a switch between catabolism and anabolism. *Cell Metab.* **20**, 526–540 (2014).
25. Li, M. et al. Transient receptor potential V channels are essential for glucose sensing by aldolase and AMPK. *Cell Metab.* **30**, 508–524.e12 (2019).
26. Olivier, S. et al. Deletion of intestinal epithelial AMP-activated protein kinase alters distal colon permeability but not glucose homeostasis. *Mol. Metab.* **47**, 101183 (2021).
27. Zong, Y. et al. Hierarchical activation of compartmentalized pools of AMPK depends on severity of nutrient or energy stress. *Cell Res.* **29**, 460–473 (2019).
28. Myers, R. W. et al. Systemic pan-AMPK activator MK-8722 improves glucose homeostasis but induces cardiac hypertrophy. *Science* **357**, 507–511 (2017).
29. Salt, I. P. & Hardie, D. G. AMP-activated protein kinase: an ubiquitous signaling pathway with key roles in the cardiovascular system. *Circ. Res.* **120**, 1825–1841 (2017).
30. Yavari, A. et al. Chronic activation of  $\gamma$ 2 AMPK induces obesity and reduces  $\beta$  cell function. *Cell Metab.* **23**, 821–836 (2016).
31. Tucker, G. T. et al. Metformin kinetics in healthy subjects and in patients with diabetes mellitus. *Br. J. Clin. Pharmacol.* **12**, 235–246 (1981).
32. Lalau, J. D. et al. Metformin treatment in patients with type 2 diabetes and chronic kidney disease stages 3A, 3B, or 4. *Diabetes Care* **41**, 547–553 (2018).
33. Foretz, M. et al. Metformin inhibits hepatic gluconeogenesis in mice independently of the LKB1/AMPK pathway via a decrease in hepatic energy state. *J. Clin. Invest.* **120**, 2355–2369 (2010).

34. He, L. et al. Metformin and insulin suppress hepatic gluconeogenesis through phosphorylation of CREB binding protein. *Cell* **137**, 635–646 (2009).
35. Fu, L. et al. Interaction between metformin and leucine in reducing hyperlipidemia and hepatic lipid accumulation in diet-induced obese mice. *Metabolism* **64**, 1426–1434 (2015).
36. Espada, L. et al. Loss of metabolic plasticity underlies metformin toxicity in aged *Caenorhabditis elegans*. *Nat. Metab.* **2**, 1316–1331 (2020).
37. Wu, L. et al. An ancient, unified mechanism for metformin growth inhibition in *C. elegans* and cancer. *Cell* **167**, 1705–1718.e13 (2016).
38. Howell, J. J. et al. Metformin inhibits hepatic mTORC1 signaling via dose-dependent mechanisms involving AMPK and the TSC complex. *Cell Metab.* **25**, 463–471 (2017).
39. Zhou, G. et al. Role of AMP-activated protein kinase in mechanism of metformin action. *J. Clin. Invest.* **108**, 1167–1174 (2001).
40. Zhong, C. et al. CRISPR–Cas9-mediated genetic screening in mice with haploid embryonic stem cells carrying a guide RNA library. *Cell Stem Cell* **17**, 221–232 (2015).
41. Griep, A. E., John, M. C., Ikeda, S. & Ikeda, A. Gene targeting in the mouse. *Methods Mol. Biol.* **770**, 293–312 (2011).
42. Gribble, F. M., Williams, L., Simpson, A. K. & Reimann, F. A novel glucose-sensing mechanism contributing to glucagon-like peptide-1 secretion from the GLUTag cell line. *Diabetes* **52**, 1147–1154 (2003).
43. Simpson, A. K. et al. Cyclic AMP triggers glucagon-like peptide-1 secretion from the GLUTag enteroendocrine cell line. *Diabetologia* **50**, 2181–2189 (2007).

44. Schmidt, T. G. & Skerra, A. The Strep-tag system for one-step purification and high-affinity detection or capturing of proteins. *Nat. Protoc.* **2**, 1528–1535 (2007).
45. Grieger, J. C., Choi, V. W. & Samulski, R. J. Production and characterization of adeno-associated viral vectors. *Nat. Protoc.* **1**, 1412–1428 (2006).
46. Luo, H. et al. AIDA selectively mediates downregulation of fat synthesis enzymes by ERAD to retard intestinal fat absorption and prevent obesity. *Cell Metab.* **27**, 843–853.e6 (2018).
47. Du, W. et al. Kinesin 1 drives autolysosome tubulation. *Dev. Cell* **37**, 326–336 (2016).
48. Dempsey, G. T., Vaughan, J. C., Chen, K. H., Bates, M. & Zhuang, X. Evaluation of fluorophores for optimal performance in localization-based super-resolution imaging. *Nat. Methods* **8**, 1027–1036 (2011).
49. Jones, S. A., Shim, S. H., He, J. & Zhuang, X. Fast, three-dimensional super-resolution imaging of live cells. *Nat. Methods* **8**, 499–508 (2011).
50. Martell, J. D., Deerinck, T. J., Lam, S. S., Ellisman, M. H. & Ting, A. Y. Electron microscopy using the genetically encoded APEX2 tag in cultured mammalian cells. *Nat. Protoc.* **12**, 1792–1816 (2017).
51. Shao, E. & Forgac, M. Involvement of the nonhomologous region of subunit A of the yeast V-ATPase in coupling and in vivo dissociation. *J. Biol. Chem.* **279**, 48663–48670 (2004).
52. Liberman, R., Bond, S., Shainheit, M. G., Stadecker, M. J. & Forgac, M. Regulated assembly of vacuolar ATPase is increased during cluster disruption-induced maturation of dendritic cells through a phosphatidylinositol 3-kinase/mTOR-dependent pathway. *J. Biol. Chem.* **289**, 1355–1363 (2014).

53. Trombetta, E. S., Ebersold, M., Garrett, W., Pypaert, M. & Mellman, I. Activation of lysosomal function during dendritic cell maturation. *Science* **299**, 1400–1403 (2003).
54. Wieckowski, M. R., Giorgi, C., Lebiedzinska, M., Duszynski, J. & Pinton, P. Isolation of mitochondria-associated membranes and mitochondria from animal tissues and cells. *Nat. Protoc.* **4**, 1582–1590 (2009).
55. Kobayashi, T. et al. Separation and characterization of late endosomal membrane domains. *J. Biol. Chem.* **277**, 32157–32164 (2002).
56. Kurganov, B. I., Lyubarev, A. E., Sanchez-Ruiz, J. M. & Shnyrov, V. L. Analysis of differential scanning calorimetry data for proteins. Criteria of validity of one-step mechanism of irreversible protein denaturation. *Biophys. Chem.* **69**, 125–135 (1997).
57. Umeda, N., Ueno, T., Pohlmeyer, C., Nagano, T. & Inoue, T. A photocleavable rapamycin conjugate for spatiotemporal control of small GTPase activity. *J. Am. Chem. Soc.* **133**, 12–14 (2011).
58. Li, Z. et al. Design and synthesis of minimalist terminal alkyne-containing diazirine photo-crosslinkers and their incorporation into kinase inhibitors for cell- and tissue-based proteome profiling. *Angew. Chem. Int. Ed. Engl.* **52**, 8551–8556 (2013).
59. Huttunen, K. M. et al. The first bioreversible prodrug of metformin with improved lipophilicity and enhanced intestinal absorption. *J. Med. Chem.* **52**, 4142–4148 (2009).
60. Bajad, S. U. et al. Separation and quantitation of water soluble cellular metabolites by hydrophilic interaction chromatography–tandem mass spectrometry. *J. Chromatogr. A* **1125**, 76–88 (2006).
61. Amrhein, V., Greenland, S. & McShane, B. Scientists rise up against statistical significance. *Nature* **567**, 305–307 (2019).

62. Wasserstein, R. L., Schirm, A. L. & Lazar, N. A. Moving to a world beyond “ $p < 0.05$ ”. *Am. Stat.* **73**, 1–19 (2019).
63. Ma, J. et al. iProX: an integrated proteome resource. *Nucleic Acids Res.* **47**, D1211–D1217 (2019).

## Acknowledgements

We thank D. Julius for providing *Trpv*<sup>-/-</sup> mice (The Jackson Laboratory, 003770); B. De Strooper for the *Aph1a*<sup>F/F</sup>*Aph1b*<sup>-/-</sup>*Aph1c*<sup>F/F</sup> mice (The Jackson Laboratory, 030985); N. Mizushima for the *Atg5*<sup>F/F</sup> mice (RIKEN, RBRC02975); B. Viollet for the *Ampka1/2*-DKO MEFs; S. Morrison for the *Ampka1*<sup>F/F</sup> (The Jackson Laboratory, 014141) and *Ampka2*<sup>F/F</sup> mice (The Jackson Laboratory, 014142); J. Taylor for providing the pLiv-Le6 vector; Z. Wang for providing the suspension HEK293T cell line; the *Caenorhabditis* Genetics Center for supplying nematode strains; S.-Q. Wu for mouse in vitro fertilization; all the other members of the S.-C.L. laboratory for technical assistance; G. Hardie for critical reading and comments; Z.-X. Wang for instructions on ITC assays; and M. Hu for the discussions and suggestions on electrophysiological properties of lysosomes. The artworks shown in Fig. 2a and Extended Data Fig. 13m were modified from elements created by Servier Medical Art (<https://smart.servier.com/>) licenced under a Creative Commons Attribution 3.0 Unported Licence (<https://creativecommons.org/licenses/by/3.0/>). This work was supported by grants from the National Natural Science Foundation of China (82088102, 91854208, 31922034, 32070753, 31730058, 22025702 and 91853203), the Natural Science Foundation of Fujian Province of China (2020J02003), the Fundamental Research Funds for the Central Universities (20720200069, 20720200014 and 20720190101), the Programme of Introducing Talents of Discipline to Universities (BP2018017), and the XMU Training Programme of Innovation and Entrepreneurship for Undergraduates (202010384190, 2020X901 and 2020X895).

## Author information

## Author notes

1. These authors contributed equally: Teng Ma, Xiao Tian, Baoding Zhang

## Affiliations

1. State Key Laboratory for Cellular Stress Biology, Innovation Centre for Cell Signalling Network, School of Life Sciences, Xiamen University, Fujian, China

Teng Ma, Xiao Tian, Baoding Zhang, Mengqi Li, Yu Wang, Chunyan Yang, Xiaoyan Wei, Qi Qu, Yaxin Yu, Shating Long, Jin-Wei Feng, Chun Li, Cixiong Zhang, Changchuan Xie, Yaying Wu, Zheni Xu, Yong Yu, Xi Huang, Ying He, Luming Yao, Lei Zhang, Mingxia Zhu, Shu-Yong Lin, Zhiyun Ye, Xianming Deng, Chen-Song Zhang & Sheng-Cai Lin

2. Laboratory Animal Research Centre, Xiamen University, Fujian, China

Jianfeng Wu

3. Analysis and Measurement Centre, School of Pharmaceutical Sciences, Xiamen University, Fujian, China

Junjie Chen

4. CAS Key Laboratory of Separation Science for Analytical Chemistry, Dalian Institute of Chemical Physics, Chinese Academy of Sciences, Liaoning, China

Wen Wang, Zhi-Chao Wang & Hai-Long Piao

5. Department of Endocrinology and Metabolism, Shanghai Clinical Centre for Diabetes, Shanghai Diabetes Institute, Shanghai Key Laboratory of Diabetes Mellitus, Shanghai Jiao Tong University Affiliated Sixth People's Hospital, Shanghai, China

Mingliang Zhang, Yuqian Bao & Weiping Jia

## Contributions

T.M., X.T., B.Z., X.D., C.-S.Z. and S.-C.L. conceived the study and designed the experiments. T.M. and X.T. identified lysosomal metformin-binding proteins and the PEN2-interacting proteins, generated the cell strains and performed the IP, confocal imaging acquisition, in vitro reconstitution and the associated western blot analyses (with assistance from M.L., X.W., Q.Q., S.L., J.-W.F. and C.L.). B.Z. and X.D. designed, synthesized and purified the photoactive metformin probe and performed in silico modelling assays. Y. Wang and Yixin Yu performed the nematode experiments (under the guidance of Yong Yu), and T.M. and X.T. performed the mouse experiments. M.L. performed STORM imaging acquisition, and X.W. and L.Y. performed APEX-based TEM imaging acquisition. C.Y. and J.C. determined the binding affinity of metformin to PEN2. J.W. generated the *Pen2*-floxed and *Atp6ap1*-floxed mouse strains. C.Z. analysed the pharmacokinetics of metformin and performed the HPLC–MS-based analysis of adenylates. X.T., Z.-C.W. and W.W. performed the CE–MS-based analysis of adenylates (under the guidance of H.-L.P.). C.X., Y. Wu and Z.X. performed protein-related mass spectrometry analysis. X.H. generated the antibody for immunoprecipitating endogenous ATP6AP1. Y.H. generated the liver-specific Tg-ALDOA and Tg-ALDOA-D34S mouse strains. L.Z. analysed the rates of TAG synthesis by HPLC–MS, and M. Zhu analysed the rates of β-oxidation by GC–MS. M. Zhang, Y.B. and W.J. enrolled human participants and analysed metformin concentrations in human serum. S.-Y.L. and Z.Y. helped supervise the project. C.-S.Z. and S.-C.L. wrote the manuscript.

## Corresponding authors

Correspondence to [Xianming Deng](#), [Chen-Song Zhang](#) or [Sheng-Cai Lin](#).

## Ethics declarations

### Competing interests

The authors declare no competing interests.

## Peer review

## Peer review information

*Nature* thanks Michael Ristow, Peter Vangheluwe, and the other, anonymous, reviewer(s) for their contribution to the peer review of this work. Peer reviewer reports are available.

## Additional information

**Publisher's note** Springer Nature remains neutral with regard to jurisdictional claims in published maps and institutional affiliations.

## Extended data figures and tables

### [Extended Data Fig. 1 Low metformin can activate AMPK without altering energy levels.](#)

**a**, Serum metformin concentrations in human subjects. Serum samples were collected at indicated time points from subjects after taking 0.5 g of Metformin Hydrochloride Extended-release Tablets. Data are shown as mean  $\pm$  s.e.m.;  $n = 6$ . **b, c, e**, Low metformin activates AMPK in primary hepatocytes without elevating AMP. Human (**b**) or mouse (**c, e**) primary hepatocytes were treated with metformin (Met), or PBS (Saline) for 2 h, and the levels of p-AMPK $\alpha$  and p-ACC (**b, c**), as well as the AMP:ATP and ADP:ATP ratios (**b, e**) were determined [ shown as mean  $\pm$  s.e.m.;  $n = 5$  (**b**) or 4 (**e**) cells for each condition, and  $P$  value by two-sided Student's *t*-test (**b**), or one-way ANOVA followed by Sidak (**e**)]. **d**, Metformin inhibits v-ATPase in purified lysosomes. Lysosomes purified from mouse livers were incubated with 5  $\mu$ M metformin for 1 h. The activity of v-ATPase was determined by the rates to hydrolyse ATP (left panel) and to transport protons (right panel). Data are shown as mean  $\pm$  s.e.m.;  $n = 3$ ;  $P$  value by two-sided Student's *t*-test. **f, s**, Low metformin does not affect mitochondrial membrane potential. Mouse primary hepatocytes (**f**), MEFs (**s**, left panel), or HEK293T cells (**s**, right panel) were treated with 5  $\mu$ M metformin for 2 h (**f**), 200  $\mu$ M metformin for 12 h (**s**, left panel) or 300  $\mu$ M metformin for 12 h (**s**, right panel) (higher concentrations and longer treatment times were used in MEFs and HEK293T cells because of lack of

OCTs), and were loaded with JC-1 dye for another 30 min. After normalisation to the group without metformin treatment, the data are shown as mean  $\pm$  s.e.m.;  $n = 37$  (control) and 34 (metformin-treated) with mouse primary hepatocytes,  $n = 36$  (control) and 40 (metformin-treated) for MEFs, and  $n = 35$  (control) and 36 (metformin-treated) with HEK293T cells; and  $P$  value by two-sided Mann-Whitney (**f** and **s**, left panel) or two-sided Student's *t*-test (**s**, right panel). **g, t**, Low metformin does not affect mitochondrial respiration. Mouse primary hepatocytes (**g**, approximately 3,000 cells in total), MEFs (**t**, left panel, approximately 10,000 cells in total), or HEK293T cells (**t**, right panel, approximately 10,000 cells in total) were treated as in **f**, left panel of **s**, and right panel of **s**. ATP production-coupled OCR was determined by subtracting basal OCR from that treated with 10  $\mu$ M oligomycin. Data are mean  $\pm$  s.e.m.;  $n = 6$  with hepatocytes and MEFs, and  $n = 4$  with HEK293T cells; and  $P$  value by two-sided Student's *t*-test. **h, i, l**, Mice taking 1 g/l metformin from drinking water resembles the situation of human patients taking standard clinical doses of metformin. As depicted in **i**, mice at 4-week old were treated with metformin in drinking water for 7 days. At day 8, mice were sacrificed at indicated times of the day. The mice were then divided into two groups, one for sacrifice to collect serum, and the others for the liver tissue. Results are mean  $\pm$  s.e.m.;  $n = 5$  for each time point, except  $n = 4$  for the 2 g/l group at 0:00, 4:00 and 18:00. Note that perhaps owing to the bitterness of metformin at higher doses (10 g/l), some of the mice showed a decreased water intake (hence metformin), and larger variations of the serum metformin concentrations than those of 1 g/l and 2 g/l were observed. **j, k, m, n**, High doses of metformin leads to increased AMP/ADP levels, and bypasses the requirement of PEN2 for AMPK activation. Mice were treated as in **i**, followed by analysis of p-AMPK $\alpha$  and p-ACC (**j, m, n**) and hepatic AMP:ATP and ADP:ATP ratios, the absolute concentrations of AMP, ADP and ATP, and the hepatic metformin concentrations. Results are mean  $\pm$  s.e.m.;  $n = 5$  (**k, m**) and  $n = 16$  (**n**) for each treatment, and  $P$  value by one-way ANOVA followed by Dunn (**k**) or Tukey (**m**). Isc; hepatic ischemia (for 5 sec). Note that in **m, n**, readouts were determined in the liver from the mice that did not undergo the step of blood draining (different from **h**), because ischemia will increase AMP and ADP, and will cause AMPK activation unrelated to the lysosomal pathway<sup>27</sup>. The legitimacy for skipping the step of blood draining was based on the observation that hepatic metformin concentration is similar to

that in the serum in our animal setting, as shown in **h** - the residual blood would not significantly interfere with the readout of the hepatic metformin concentration. **o, p, v, w**, AMPK can be activated in MEFs and HEK293T cells in AMP/ADP-independent manner in low metformin. MEFs (**o**), HEK293T cells (**p**), and the OCT1-expressing MEFs (**v**) and HEK293T cells (**w**) were treated with metformin at indicated concentrations for 12 h (**o, p**) or 2 h (**v, w**), followed by analysis of intracellular metformin concentrations [ shown as mean  $\pm$  s.e.m.;  $n = 4$  (for each metformin concentration in **o, p** and **w**, except  $n = 3$  for the 0.2 mM metformin in **o** and **p**) or 5 (**v**)], p-AMPK $\alpha$  and p-ACC, and AMP:ATP, and ADP:ATP ratios [shown as mean  $\pm$  s.e.m.;  $n = 4$  (for each metformin concentration in **o** and **p**, except  $n = 3$  for the ratios at 5 mM metformin in **o**) or 5 (**v, w**); and  $P$  values by one-way ANOVA, followed by Sidak (**o**, and AMP:ATP of **p**), Tukey (ADP:ATP of **p**, and **w**), or Dunn (**v**)], as well as the absolute concentrations of AMP, ADP and ATP. **q, r**, Low metformin deacidifies lysosomes. MEFs (**q**) and HEK293T cells (**r**) pre-labelled with Lysosensor Green DND-189 and Hoechst were treated as in **s**. Representative images are shown (left panel); the relative fluorescent intensities of Lysosensor (normalised to the intensity of Hoechst) are shown on the right. Results are mean  $\pm$  s.e.m.;  $n = 28$  (control) and 27 (metformin-treated) from 3 dishes/experiments for MEFs, and  $n = 21$  (control) and 20 (metformin-treated) from 3 dishes/experiments for HEK293T cells; and  $P$  value by two-sided Mann-Whitney test. **u**, Metformin is not accumulated in mitochondria. MEFs were treated as in **s**, and metformin concentrations in mitochondria and cytosol fractions (normalised to protein concentration) are shown as mean  $\pm$  s.e.m.;  $n = 4$ , and  $P$  value by two-sided Student's  $t$ -test. Experiments in this figure were performed three times, except **c, h, j, k** and **o** four times.

#### [Source data](#)

#### [Extended Data Fig. 2 Identification of metformin-interacting proteins by the metformin probe.](#)

**a**, Synthesis and purification of photoactive metformin probes (Met-Ps). Reactions for conjugating 3-(but-3-yn-1-yl)-3-(2-iodoethyl)-3H-diazirine to metformin that introduced a diazirine with a terminal alkyne moiety at

either the N4 or N1/N2 position of metformin yields two types of Met-P (Met-P1 and Met-P2) products (upper panel). The two products were further separated on a preparative HPLC (lower panel). See detailed procedures, HSMS data, and NMR data in Methods section and Supplementary Fig. 2. **b**, Met-P1 is able to inhibit v-ATPase. Lysosomes purified from MEFs were incubated with the two Met-Ps at 10 µM for 1 h. The activity of v-ATPase was determined by its rate to hydrolyse ATP as in Extended Data Fig. 1d. After normalisation to the group without Met-P added, the data are shown as mean ± s.e.m.;  $n = 3$  for each condition, and  $P$  value by one-way ANOVA, followed by Dunnett. **c**, Reactions taking place to form the Met-P1 and proteins conjugates. First, proteins were incubated with Met-P1. The metformin probe-protein mixture was exposed to UV light, followed by addition of Cu(II) salt, which catalyses a [3 + 2] azide-alkyne cycloaddition with biotin-azide, thus biotinylation probe-target complexes, allowing for the pull down of such complexes with NeutrAvidin beads. **d**, Interaction between PEN2 and metformin probe. HEK293T cells transfected with HA-tagged PEN2 were lysed. Total cell lysates (TCL) were incubated with 10 µM Met-P1, and subsequent exposure to UV, and were then mixed with 1 mM biotin-N<sub>3</sub> linker. The biotinylated proteins were then affinity-pulldown (AP) by NeutrAvidin beads, followed by immunoblotting with antibody against HA tag. Experiments in this figure were performed three times, except **a** seven times.

#### [Source data](#)

#### [Extended Data Fig. 3 PEN2 is required for AMPK activation by low metformin.](#)

**a, b**, Knockdown of *PEN2* impairs the activation of AMPK, and inhibition of v-ATPase by metformin. MEFs infected with lentivirus carrying two distinct siRNAs (#1 or 2#) against *PEN2*, or *GFP* as a control, were treated with 200 µM metformin for 12 h, representative images of the experiments shown in **a** upper, followed by analysis of the lysosomal pH [**a** lower, shown as mean ± s.e.m.,  $n = 20$  (control) and 21 (metformin-treated) cells for *siGFP*,  $n = 25$  cells for *siPEN2#1*, and  $n = 29$  (control) and 22 (metformin-treated) cells for *siPEN2#2*, all from 2 dishes/experiments; and  $P$  value by two-way ANOVA, followed by Tukey] and the determination of

p-AMPK $\alpha$  and p-ACC (**b**). **c**, Knockout of *PEN2* abrogates the inhibition of v-ATPase by metformin in mouse primary hepatocytes (left panel), MEFs (middle panel), and HEK293T cells (right panel). MEFs, HEK293T cells were treated with 200, 300  $\mu$ M metformin for 12 h, mouse primary hepatocytes were treated with 5  $\mu$ M metformin for 2 h, and then labelled with Lysosensor, along with Hoechst. The lysosomal pH was determined as in Fig. [1a](#). Data are shown as mean  $\pm$  s.e.m.,  $n = 26$  (control) and 31 (metformin-treated) from 6 dishes/experiments for primary hepatocytes,  $n = 25$  (control) and 22 (metformin-treated) from 4 dishes/experiments for MEFs, and  $n = 30$  (control) and 29 (metformin-treated) from 6 dishes/experiments for HEK293T cells;  $P$  value within each cell type was determined by two-sided Student's *t*-test. **d**, **g**, **h**, **k**, Knockout of *PEN2* blocks AMPK activation by low metformin. Clone #2 of *PEN2*<sup>-/-</sup> MEFs (**d**) treated with 200  $\mu$ M (low concentration) metformin, or clone #1 and clone #2 of *PEN2*<sup>-/-</sup> HEK293T cells (**g** and **h**), treated with 300  $\mu$ M (low concentration for the cell line) metformin, or OCT1-expressing *PEN2*<sup>-/-</sup> MEFs and HEK293T cells treated with 5  $\mu$ M (low concentration) metformin (**k**) or 5 mM (high concentration, as a control for **d**, **g** and **h**), 500  $\mu$ M metformin (high concentration, for **k**), for 12 h (**d**, **g** and **h**) or 2 h (**k**), were subjected to immunoblotting for the analysis of p-AMPK $\alpha$  and p-ACC. See also results with clone #1 of *PEN2*<sup>-/-</sup> MEFs in Fig. [2c](#). **e**, **f**, Strategies to generate MEFs (**e**) and HEK293T cells (**f**) with knockout of *PEN2*. Two distinct sets of sgRNAs for each cell line, whose sequences are listed in Methods section, were applied to generate *PEN2*<sup>-/-</sup> cells. Two clones (#1 and #2) for each cell line type were established. **i**, Knockout of *PEN2* blocks the inhibition of v-ATPase by metformin in purified lysosomes. Lysosomes purified from *PEN2*<sup>-/-</sup> MEFs were incubated with 5  $\mu$ M metformin for 1 h. The activity of v-ATPase was determined as in Extended Data Fig. [1d](#). Data are shown as mean  $\pm$  s.e.m.;  $n = 3$  for each condition, and  $P$  value by two-sided Student's *t*-test. **j**, Knockout of *PEN2* does not affect metformin uptake. Mouse primary hepatocytes, MEFs and HEK293T cells were treated as in **c**, followed by determining intracellular metformin concentrations. Data are shown as mean  $\pm$  s.e.m.,  $n = 4$  for each genotype, and  $P$  value within each cell type by two-sided Student's *t*-test. **l**, Re-introduction of *PEN2* into *PEN2*<sup>-/-</sup> MEFs or HEK293T cells restores AMPK activation. *PEN2*<sup>-/-</sup> MEFs (left panel) or HEK293T cells (right

panel) were infected with lentiviruses expressing HA-tagged PEN2 (all expressed at close-to-endogenous levels driven by pBOBI vector). Cells were treated with 200 or 300  $\mu$ M (low concentration), or 5 mM (high concentration, as a control) metformin for 12 h, followed by analysis of p-AMPK $\alpha$  and p-ACC. **m**, Activity of the  $\gamma$ -secretase holoenzyme is dispensable for metformin-induced AMPK activation. MEFs were treated with DAPT (left panel) or RO4929097 (RO, right panel) at indicated concentrations for 12 h or 48 h. Twelve hours before lysis, cells were treated with 200  $\mu$ M metformin, then lysed for analysis of p-AMPK $\alpha$  and p-ACC. **n**, Loss of APH1 does not affect metformin-induced activation of AMPK. MEFs with *APH1A*, *APH1B* and *APH1C* triple knockout were treated with 200  $\mu$ M or 5 mM metformin for 12 h, followed by analysis of p-AMPK $\alpha$  and p-ACC. **o**, Strategies to generate MEFs with knockout of nicastrin. sgRNAs against *NCSTN*, whose sequences are listed in Methods section, were applied to generate *NCSTN*<sup>-/-</sup> MEFs. **p**, **q**, Knockout of *NCSTN*, through decreasing the protein levels of PEN2, impairs metformin-induced activation of AMPK. *NCSTN*<sup>-/-</sup> MEFs (**p**) or *NCSTN*<sup>-/-</sup> MEFs with HA-tagged PEN2 expressed (**q**, expressed at close-to-endogenous levels driven by the lentiviral system using pBOBI vector, as validated in **r**) were treated with 200  $\mu$ M (low concentration) or 5 mM (high concentration, as a control) metformin for 12 h, followed by analysis of p-AMPK $\alpha$  and p-ACC. **r**, Protein levels of PEN2 in MEFs with knockout of *NCSTN*. Cells were lysed for analysis of PEN2 protein levels by immunoblotting, followed by densitometry analysis. **s**, Strategies to generate MEFs with knockout of presenilins. sgRNAs against *PS1* (left panel) and *PS2* (right panel), whose sequences are listed in Methods section, were applied to generate *PS1*- or *PS2*-KO MEFs. Experiments in this figure were performed three times, except **b**, **h**, **i**, four times.

#### [Source data](#)

#### [Extended Data Fig. 4 Other subunits of \$\gamma\$ -secretase are not required for AMPK activation by low metformin.](#)

**a**, Loss of presenilins does not affect metformin-induced activation of AMPK. MEFs with *PS1* and *PS2* double knocked out were treated with 200  $\mu$ M or 5 mM metformin for 12 h, followed by analysis of p-AMPK $\alpha$  and p-

**ACC.** **b**, Protein levels of PEN2 in MEFs with knockout of presenilins (left panel) or *APH1* (right panel). Cells were lysed for analysis of PEN2 protein levels by immunoblotting, followed by densitometry analysis. Statistical analysis results were shown as mean  $\pm$  s.e.m.;  $n = 6$ . **c**, A portion of PEN2 is localised on the surface of lysosome. MEFs were stained with rabbit anti-PEN2 antibody and rat anti-LAMP2 antibody, followed by staining with Alexa Fluor 488 goat anti-rabbit IgG and Alexa Fluor 594 donkey anti-rat IgG secondary antibodies. The areas defined by dashed boxes on each representative image are enlarged as insets. Mander's overlap coefficients are plotted as mean  $\pm$  s.e.m.,  $n = 20$ . **d**, As a control for Fig. 2e, APEX-tagged TOMM20-PEN2 chimeric construct shows mitochondrial localisation. HEK293T cells stably expressing APEX-tagged TOMM20-PEN2 fused protein (APEX-PEN2 Mito, expressed at close-to-endogenous levels) were imaged under a transmission electron microscope. **e**, Subcellular fractionation assays show that the lysosomal fraction contains PEN2. The lysosome fractions (purified as described in Methods section), along with total cell lysates of MEFs, or *PEN2*<sup>-/-</sup> MEFs as a control, were subjected to immunoblotting using the indicated antibodies (Lyso, lysosome; ER, endoplasmic reticulum; PM, plasma membrane; Mito, mitochondrion; Cyto, cytosol). **f**, The PEN2 lysosomal localisation is not altered when autophagy is blocked. The lysosomal localisation of PEN2 was determined by staining PEN2 and LAMP2 in WT MEFs and *ATG5*<sup>-/-</sup> MEFs, or WT MEFs treated with 20  $\mu$ M chloroquine (CQ), 4 mM 3-MA, or 0.5  $\mu$ M bafilomycin A (bafA) for 12 h. Mander's overlap coefficients are plotted as mean  $\pm$  s.e.m.,  $n = 20$  for each genotype/treatment, with  $P$  values calculated by one-way ANOVA, followed by Dunn (for autophagy inhibitors) or by two-sided Student's *t*-test (for *ATG5*<sup>-/-</sup> MEFs). **g**, Inhibition of endocytosis does not alter the lysosomal PEN2 localisation. MEFs were treated with 60  $\mu$ M Dynasore for 0.5 h, 10  $\mu$ M Dyngo-4a for 30 h, 20  $\mu$ M Nystatin for 1 h, 2 mM methyl- $\beta$ -cyclodextrin for 6 h, or 1  $\mu$ M cytochalasin D for 0.5 h. Co-localisation of HA-tagged PEN2 and LAMP2 was then determined by immunofluorescent staining, and the Mander's overlap coefficients are plotted as mean  $\pm$  s.e.m.,  $n = 20$  for each genotype/treatment, with  $P$  values calculated by one-way ANOVA, followed by Dunnett. Experiments in this figure were performed three times.

[Source data](#)

**Extended Data Fig. 5 Lysosomal localisation of PEN2 is required for AMPK activation by low metformin.**

**a**, Other  $\gamma$ -secretase subunits play no role in regulating lysosomal PEN2 localisation. MEFs with *PS1* and *PS2* double knockout or *APH1A/B/C* triple knockout were stained with antibodies against PEN2 and LAMP2. MEFs with *NCSTN* knockout were infected with lentivirus expressing HA-tagged PEN2 (at a close-to-endogenous level), and were stained with HA-tag and LAMP2 antibodies. Mander's overlap coefficients are plotted as mean  $\pm$  s.e.m.,  $n = 20$  for each genotype/treatment, with  $P$  values calculated by two-sided Student's  $t$ -test (for *APH1A/B/C* triple knockout MEFs) or by two-sided Student's  $t$ -test with Welch's correction (*PS1* and *PS2* double knockout MEFs and *NCSTN* knockout MEFs). **b, c**, Metformin does not alter the PEN2 lysosomal localisation. MEFs were treated with 200  $\mu$ M metformin for 12 h, followed by determination of PEN2 and LAMP2 co-localisation (**b**) or PEN2 protein levels on the lysosomal fractions (**c**). In **b**, Mander's overlap coefficients are plotted as mean  $\pm$  s.e.m.,  $n = 20$  for control and 21 for metformin treatment, with  $P$  values calculated by two-sided Student's  $t$ -test. **d, e**, Disruption of lysosomal localisation of PEN2 impairs AMPK activation by metformin. *PEN2<sup>-/-</sup>* MEFs were infected with lentiviruses carrying PEN2 constructs fused to N-terminus to TOMM20 (for tethering to the mitochondrial outer membrane), SEC61B (for tethering to the endoplasmic reticulum), LAMP2 (for tethering to the cytoplasmic face of lysosome) or GOLGA2 (for tethering to the cytoplasmic face of cis-Golgi complex), or at their C-terminus to LCK (for tethering to the cytoplasmic face of plasma membrane) (diagrammed on upper panel of **d**, and validated in **e**). Cells were treated with 200  $\mu$ M metformin for 12 h, followed by analysis of p-AMPK $\alpha$  and p-ACC (lower panel of **d**). **f**, Phenformin and buformin, two biguanides that increase AMP levels, activate AMPK independently of PEN2. *PEN2<sup>-/-</sup>* MEFs were treated with 1 mM of phenformin or buformin for 2 h, followed by analysis of p-AMPK $\alpha$  and p-ACC (left panel), as well as the AMP:ATP and ADP:ATP ratios (right panel, results are shown as mean  $\pm$  s.e.m.;  $n = 4$  for each genotype/treatment, and  $P$  value by two-way ANOVA followed by Tukey). **g, h**, PEN2 plays a specific role in the metformin-induced AMPK

activation. *PEN2*<sup>-/-</sup> MEFs were treated with glucose-free DMEM (GS, shown in **g**), 1 mM AICAR (as an AMP mimetic, **g**), 5 µM A23187 (to release calcium for AMPK activation via CaMKK2, **h**), or 200 µM A769662 (acting downstream by directly binding to AMPK, **h**) for 2 h, followed by analysis of p-AMPK $\alpha$  and p-ACC. Experiments in this figure were performed three times, except **f**, **g** and **h** four times.

### [Source data](#)

### **Extended Data Fig. 6 PEN2 binds to metformin.**

**a**, Incubation with metformin decreases the thermal transition midpoint (Tm) of PEN2. FLAG-tagged PEN2 was ectopically expressed in HEK293T cells and purified. Some 10 µM of the purified PEN2 was then incubated with 10 µM metformin in PBS buffer, followed by determining the Tm on a differential scanning calorimetre. Enthalpy changes of PEN2, and PEN2 incubated with metformin at indicated temperatures are shown. **b**, ITC assay showing that PEN2 is able to bind metformin. Metformin (2 mM stock concentration) was loaded stepwise to 60 µM PEN2 (purified as in **a**) in PBS buffer. Integrated data (lower panel) were obtained by fitting raw data (upper panel) with the two sets of sites model. **c**, Unlike PEN2, other  $\gamma$ -secretase subunits do not bind metformin. HEK293T cells transfected with HA-tagged PS1 (either its NTD or CTD), PS2 (either its NTD or CTD), NCSTN, APH1A, APH1B, APH1C, or PEN2 as a control, were lysed, followed by incubation with 10 µM Met-P1, exposure to UV, and were then mixed with 1 mM biotin-N<sub>3</sub> linker. The biotinylated proteins were then pulled down by NeutrAvidin beads, followed by immunoblotting with antibody against HA tag. **d**, Determination of the binding sites of PEN2 for metformin by mass spectrometry. HEK-293T cells expressing HA-tagged PEN2 were lysed, followed by incubation with 10 µM Met-P1, exposure to UV, and the potential modified residues (conjugated with biotinylated Met-P1, with an increase of m/z by 222.17) were determined by mass spectrometry, revealing two Met-P1-conjugated residues, Y47 and Y91, as shown by the typical spectrograms, with Y91 conjugated at a much lower efficiency. **e**, *In silico* modelling of metformin bound to the N-terminal, cytosolic face of PEN2. Modelling was performed according to the reported cryo-electron microscopy structure (PDB ID: 6IYC). As shown

in this figure, metformin could be protonated by carboxyl groups from residue E40 of PEN2, and then be docked onto PEN2 via salt bridges formed between N2-E40 (position of metformin to the residue of PEN2, and the same below) (2.3 Å) and N4-E40 (2.3 Å). Furthermore, two potential hydrogen bonds formed between N1-F35 (2.0 Å), N2-W36 (2.7 Å) may further strengthen the interaction between metformin and PEN2. **f**, PEN2-2A fails to bind metformin. PEN2-2A (F35A and E40A, purified as in **a**) was immobilised on a BIACore CM5 sensor chip, followed by analysing its interaction with metformin by an SPR assay as in Fig. [2f](#). Sensorgrams of each measurement are shown. See also sensorgrams from another two repeats of Fig. [2f](#) below. **g**, Validation data showing that re-introduced PEN2 and its mutants are expressed at a close-to-endogenous level in *PEN2*<sup>-/-</sup> MEFs and HEK293T cells. **h**, PEN2-2A fails to mediate the effect of metformin on v-ATPase inhibition. MEFs were treated as in Extended Data Fig. [1q](#), followed by analysis of lysosomal pH as in Fig. [1a](#). After normalisation to the group without metformin treatment within each genotype (same hereafter), results are shown as mean ± s.e.m.;  $n = 20$  (control) and 23 (metformin-treated) from 4 dishes/experiments for PEN2-WT, and  $n = 20$  (normal) and 23 (metformin-treated) from 6 dishes/experiments for PEN2-2A; and  $P$  value within each genotype was determined by two-sided Student's  $t$  test with Welch's correction (for re-introduction of wild type PEN2) or by two-sided Student's  $t$  test (for re-introduction of PEN2-2A). **i**, PEN2-2A mutant retains proper subcellular localisation as wildtype PEN2. *PEN2*<sup>-/-</sup> MEFs were infected with lentivirus expressing HA-tagged PEN2-2A or wildtype PEN2. Cells were then stained with mouse anti-HA antibody and rat anti-LAMP2 antibody, followed by incubation with Alexa Fluor 488 goat anti-mouse IgG and Alexa Fluor 594 donkey anti-rat IgG secondary antibodies (upper panel), or mouse anti-HA antibody and Alexa Fluor 594 goat anti-mouse IgG secondary antibody, followed with Alexa Fluor 488-conjugated rabbit anti-PDI antibody (lower panel). Mander's overlap coefficients are plotted as mean ± s.e.m.,  $n = 20$  for each genotype, with  $P$  values calculated by two-sided Student's  $t$ -test. The areas defined by dashed boxes on each representative image are enlarged as insets. **j**, *In silico* modelling of metformin bound to the C-terminal of PEN2. Residues D90 with the top-ranked score, as well as salt bridges and hydrogen bonds formed, are shown. **k**, PEN2-D90A displays full affinity for metformin. HEK293T cells transfected with HA-tagged

PEN2-D90A or wild type PEN2 were lysed, followed by incubation with 10  $\mu$ M Met-P1, exposure to UV, and were then mixed with 1 mM biotin-N<sub>3</sub> linker. The biotinylated proteins were then pulled down by NeutrAvidin beads, followed by immunoblotting with antibody against HA tag. **I**, Residue D90 in PEN2 is not involved in metformin-induced AMPK activation. *PEN2*<sup>-/-</sup> MEFs re-introduced with HA-tagged PEN2-D90A or wild type PEN2 (both were expressed at close-to-endogenous levels) were treated with 200  $\mu$ M (low concentration) or 5 mM (high concentration, as a control) metformin for 12 h, followed by analysis of p-AMPK $\alpha$  and p-ACC.

**m, o**, Effects of PEN2 mutant and metformin on the activity of  $\gamma$ -secretase. HEK293T cells (**o**) or *PEN2*<sup>-/-</sup> HEK293T cells (**m**) were infected with lentivirus expressing Myc-tagged Notch $\Delta$ E (N $\Delta$ E). In **m**, cells were also infected with lentivirus expressing HA-tagged PEN2-2A, PEN2-20A or wildtype PEN2, in addition to the Myc-tagged Notch $\Delta$ E (N $\Delta$ E). Cells were then treated with 300  $\mu$ M metformin for 12 h (**o**), or 100  $\mu$ M DAPT for 12 h, the inhibitor to  $\gamma$ -secretase as a control (**m**). The cleavage of Notch $\Delta$ E was determined by the protein levels of its NICD domain by immunoblotting. LE, long exposure; SE, short exposure. **n**, The PEN2 mutations or metformin do not affect the complex formation of  $\gamma$ -secretase. *PEN2*<sup>-/-</sup> MEFs infected with lentivirus expressing HA-tagged PEN2-2A, PEN2-20A (residues 27, 28, 30, 31, 34, 38, 42, 43, 57, 58, 60, 63 to 65, 67, 68, 71, 72, 74 and 75 of PEN2 mutated to alanine, see Extended Data Fig. 7e) or wildtype PEN2, were treated with 200  $\mu$ M metformin for 12 h and lysed, followed by immunoprecipitation (IP) with antibodies against HA. Immunoprecipitants were then subjected to immunoblotting with antibodies against PS1, PS2, NCSTN, APH1A/B/C, as well as HA (PEN2). Experiments in this figure were performed three times, except **g, k** and **l** four times.

### Source data

### Extended Data Fig. 7 ATP6AP1 tethers PEN2 to v-ATPase.

**a**, PEN2 interacts with ATP6AP1. HEK293T cells were transfected with HA-tagged PEN2 and Myc-tagged ATP6AP1 (AP1). Cells were lysed, and 10  $\mu$ M metformin (final concentration) or PBS was added to the lysates. Immunoprecipitation (IP) was performed using antibodies against HA,

followed by immunoblotting with antibodies indicated. **b**, PEN2 interacts with ATP6AP1 *in vitro*. Some 1 µg of FLAG-tagged PEN2 (expressed in HEK293T cells, and purified through eluting with FLAG® peptide) were incubated with 1 µg of Strep-tagged ATP6AP1 (expressed in HEK293T cells, and purified through eluting with desthiobiotin) (input) in lysis buffer, then with metformin at indicated concentrations for 2 h.

Immunoprecipitation was performed using ANTI-FLAG® M2 Affinity Gel, followed by immunoblotting with antibodies indicated. **c**, Domain mapping for the region on ATP6AP1 responsible for PEN2-binding. HA-tagged PEN2 was co-transfected with Myc-tagged ATP6AP1, or its deletion mutants into HEK293T cells. Immunoprecipitation was performed using antibody against Myc-tag, followed by immunoblotting with antibodies indicated. **d**, Replacement of ATP6AP1 transmembrane domain with that of LAMP2, blocks its interaction with PEN2. HEK293T cells transfected with HA-tagged PEN2-D90A, along with Myc-tagged LAMP2<sup>TM</sup>-ATP6AP1 or wildtype ATP6AP1, were lysed, and 10 µM metformin was added to the lysates, followed by immunoprecipitation with antibody against HA, and immunoblotting with antibodies indicated. **e**, *In silico* modelling of ATP6AP1 (cyan) bound to PEN2 (magenta). Circled area indicates the predicted interface, in which residues 27, 28, 30, 31, 34, 38, 42, 43, 57, 58, 60, 63 to 65, 67, 68, 71, 72, 74 and 75, within the transmembrane domain of PEN2, are involved. **f**, ATP6AP1 shows much weaker interaction with other γ-secretase subunits than PEN2. MEFs were lysed and incubated with metformin as in **a**, followed by immunoprecipitation with antibodies against ATP6AP1, or PEN2 as a control. Immunoprecipitants were then subjected to immunoblotting with antibodies against PS1, PS2, NCSTN, APH1A/B/C, as well as PEN2 and ATP6AP1. **g**, Metformin, through promoting the association between PEN2 and ATP6AP1, enhances association of ATP6AP1 and γ-secretase. *PEN2*<sup>-/-</sup> MEFs infected with lentivirus expressing HA-tagged PEN2 or its 20A mutant (lacking the interface for ATP6AP1) were lysed and incubated with metformin as in **a**, followed by immunoprecipitation with antibodies against ATP6AP1. Immunoprecipitants were then subjected to immunoblotting with antibodies against PS1, PS2, NCSTN, APH1A/B/C, as well as PEN2 and ATP6AP1. **h**, ATP6AP1 does not interact with metformin. HEK293T cells transfected with HA-tagged ATP6AP1, or HA-tagged PEN2 as a control, were lysed, followed by analysing the interaction between ATP6AP1 or PEN2 with

Met-P1 as in Extended Data Fig. 2d. **i**, Strategies to generate MEFs (lower panel) or HEK293T cells (upper panel) with knockout of *ATP6AP1*. sgRNAs against *ATP6AP1*, whose sequences are listed in Methods section, were applied to generate *ATP6AP1*<sup>-/-</sup> MEFs and HEK293T cells. **j**, Knockout of ATP6AP1 leads to constitutive activation of AMPK. MEFs with *ATP6AP1* knocked out, along with its wildtype control, were incubated with metformin at indicated concentrations for 12 h, followed by analysing p-AMPK and p-ACC. **k**, Knockout of ATP6AP1 renders v-ATPase inactive. *ATP6AP1*<sup>-/-</sup> MEFs were treated with 200 μM metformin for 12 h, followed by analysis of lysosomal pH with the Lysosensor dye. Data (relative intensity of Lysosensor, processed as in Fig. 1a) were graphed as mean ± s.e.m.,  $n = 29$  (control) and 26 (metformin-treated) cells from 6 dishes/experiment for WT MEFs, and 28 (control) and 23 (metformin-treated) cells from 4 dishes/experiments for *ATP6AP1*<sup>-/-</sup> MEFs,  $P$  value within each genotype was determined by two-sided Mann-Whitney test (for WT MEFs), or by two-sided Student's *t*-test (for *ATP6AP1*<sup>-/-</sup> MEFs). **l**, Validation data showing that the re-introduced ATP6AP1 and its mutants are expressed at a close-to-endogenous level in *ATP6AP1*<sup>-/-</sup> MEFs (upper panel) and HEK293T cells (lower panel). Experiments in this figure were performed three times, except **b**, **f**, **h**, four times and **l** five times.

#### Source data

#### Extended Data Fig. 8 The interaction between PEN2 and ATP6AP1 is required for metformin-induced AMPK activation.

**a, b**, The truncated ATP6AP1 mutant ( $ATP6AP1^{\Delta 420-440}$ ) or the chimeric construct LAMP2<sup>TM</sup>-ATP6AP1, which are able to maintain the basal activity of v-ATPase, fails to mediate metformin to inhibit v-ATPase. *ATP6AP1*<sup>-/-</sup> MEFs re-introduced with full length (FL) ATP6AP1,  $ATP6AP1^{\Delta 420-440}$  or LAMP2<sup>TM</sup>-ATP6AP1 (all expressed at close-to-endogenous levels) were treated with 200 μM metformin for 12 h (or 5 μM conA for 2 h as a control, right panel of **a**), followed by analysis of lysosomal pH by labelling cells with Lysosensor, along with Hoechst. Data (relative intensity of Lysosensor, processed as in Fig. 1a) were graphed as

mean  $\pm$  s.e.m.,  $n = 20$  cells from 3 dishes/experiment (**a**) and  $n = 28$  (control) and 23 (metformin-treated) for *ATP6AP1*<sup>-/-</sup> MEFs re-introduced with full length ATP6AP1, and  $n = 26$  (control) and  $n = 25$  (metformin-treated) for *ATP6AP1*<sup>-/-</sup> MEFs re-introduced with ATP6AP1<sup>Δ420-440</sup>, from 4 dishes/experiment (**b**) for each genotype/treatment. Results are mean  $\pm$  s.e.m.;  $P$  value was determined by one-way ANOVA followed by Dunn (**a**, left panel) or by two-sided Student's *t* test with Welch's correction (**a**, right panel) or by two-sided Mann-Whitney test (**b**). **c**, ATP6AP1<sup>Δ420-440</sup> mutant fails to mediate the effects of metformin on AMPK activation. *ATP6AP1*<sup>-/-</sup> MEFs (left panel) or HEK293T cells (right panel) stably expressing Myc-tagged OCT1 were re-introduced with full length (FL) ATP6AP1 or its Δ420-440 mutant (expressed at close-to-endogenous levels). Cells were treated with 5  $\mu$ M metformin or 500  $\mu$ M metformin (high concentration, as a control) for 2 h, followed by analysis of p-AMPK and p-ACC. **d**, ATP6AP1 mutant that cannot interact with PEN2 fails to mediate AMPK activation by metformin. *ATP6AP1*<sup>-/-</sup> MEFs re-introduced with full length ATP6AP1 or LAMP2<sup>TM</sup>-ATP6AP1 (expressed at close-to-endogenous levels) were treated with 200  $\mu$ M metformin for 12 h, followed by analysis of p-AMPK $\alpha$  and p-ACC by immunoblotting. **e**, PEN2-20A mutant retains proper subcellular localisation. *PEN2*<sup>-/-</sup> MEFs were infected with lentivirus expressing HA-tagged PEN2-20A or wildtype PEN2. Cells were then stained with mouse anti-HA antibody and rat anti-LAMP2 antibody, followed by incubation with Alexa Fluor 488 goat anti-mouse IgG and Alexa Fluor 594 donkey anti-rat IgG secondary antibodies (upper panel), or mouse anti-HA antibody and Alexa Fluor 594 goat anti-mouse IgG secondary antibody, and subsequently with Alexa Fluor 488-conjugated rabbit anti-PDI antibody (lower panel). Mander's overlap coefficients are plotted as mean  $\pm$  s.e.m.,  $n = 20$  for each genotype, with  $P$  values calculated by two-sided Student's *t*-test. The areas defined by dashed boxes on each representative image are enlarged as insets. **f**, *PEN2*<sup>-/-</sup> MEFs re-introduced with wildtype PEN2 or PEN2-20A mutant were treated like Extended Data Fig. 6h, followed by analysis of the lysosomal pH [shown as mean  $\pm$  s.e.m.,  $n = 29$  (control) and 27 (metformin-treated) from 6 dishes/experiments for *PEN2*<sup>-/-</sup> MEFs re-introduced with wildtype PEN2,  $n = 20$  (control) and 23 (metformin-treated) from 4 dishes/experiments for *PEN2*<sup>-/-</sup> MEFs re-introduced with PEN2-20A; and  $P$  value within each genotype by two-sided

Student's *t* test with Welch's correction (wildtype PEN2) or two-sided Student's *t* test (PEN2-20A)]. Experiments in this figure were performed three times, except **d** four times.

[Source data](#)

**Extended Data Fig. 9 PEN2 and ATP6AP1 act as upstream factors of v-ATPase.**

**a–c**, v-ATPase and its downstream factors AXIN and Ragulator, are required for AMPK activation by low metformin in cells. MEFs with *AXIN* (**a**) or *LAMTOR1* (**b**) knocked out, or HEK293T cells with *ATP6v0c* knocked down (**c**), were treated with metformin at indicated concentrations for 12 h, followed by analysis of p-AMPK $\alpha$  and p-ACC by immunoblotting. **d–f**, v-ATPase, AXIN and Ragulator are required for AMPK activation by low metformin in mouse liver. Mice at 6 weeks old with hepatic *AXIN* knocked out (**d**, AXIN-LKO, by crossing *AXIN*-floxed mice with mice carrying *albumin*-Cre, and those not carrying Cre as controls), hepatic *LAMTOR1* knocked out (**e**, LAMTOR1-LKO, generated same as in **d**, except that *LAMTOR1*-floxed mice were used), or hepatic *ATP6v0c* knocked down (**f**, si*ATP6v0c*, by intravenously injected with AAVs carrying siRNA against *ATP6v0c*, or *GFP* as a control, two weeks before experiments), were treated with metformin in drinking water (1 g/l) for 7 days. At the day 8, mice livers were quickly dissected from euthanised mice, and p-AMPK $\alpha$  and p-ACC levels in livers were determined by immunoblotting. **g**, Strategies to generate MEFs with knockout of *PRKAB1* and *PRKAB2* (*AMPK $\beta$ 1* and *AMPK $\beta$ 2*). sgRNAs against these two genes, whose sequences are listed in Methods section, were applied to generate *AMPK $\beta$ 1/2*<sup>-/-</sup> MEFs. See also knockout efficiency of *AMPK $\beta$ 1* and *AMPK $\beta$ 2*, as determined by immunoblotting using antibodies against pan-AMPK $\beta$ . **h**, Membrane localisation of AMPK is required for AMPK activation by low metformin. *AMPK $\beta$ 1/2*<sup>-/-</sup> MEFs were infected with lentivirus carrying *AMPK $\beta$ 1* or its G2A mutant (defective in N-myristoylation and hence preventing membrane/lysosomal localization of AMPK). Cells were treated with 200  $\mu$ M metformin or 5 mM for 12 h, followed by determining p-AMPK $\alpha$  and p-ACC levels by immunoblotting. **i**, Representative images of the experiments shown in Fig. 3g, indicate that

PEN2 is required for the lysosomal translocation of AXIN. *PEN2*<sup>-/-</sup> MEFs and its wildtype control were treated with 200 μM metformin for 12 h, or with the v-ATPase inhibitor concanamycin A (conA, 5 μM) for 2 h as a control. AXIN and the lysosomal marker LAMP2 were stained with goat anti-AXIN antibody (green) and rat anti-LAMP2 antibody (red), respectively. Images were taken by confocal microscopy after incubating cells with Alexa Fluor 488 donkey anti-goat IgG and Alexa Fluor 594 donkey anti-rat IgG. The areas defined by dashed boxes on each representative image are enlarged as insets. **j, k, l**, Loss of PEN2, hence PEN2-ATP6AP1 interaction, abolishes the formation of the AXIN-based lysosomal complex by metformin. *PEN2*<sup>-/-</sup> MEFs (**j**), or *PEN2*<sup>-/-</sup> MEFs re-introduced with PEN2 (**k**), or *ATP6AP1*<sup>-/-</sup> MEFs re-introduced with full length (FL) ATP6AP1 or its Δ420-440 mutant (**l**, all expressed at close-to-endogenous levels) were treated with 200 μM metformin for 12 h, or treated with 5 μM concanamycin A (**k**, conA) for 2 h as a control. Endogenous LAMTOR1 was immunoprecipitated with rabbit anti-LAMTOR1 antibody, and IgG as control, followed by immunoblotting using the indicated antibodies. Experiments in this figure were performed three times, except **a-c** four times.

### Extended Data Fig. 10 PEN2 and ATP6AP1 control the lysosomal translocation of AXIN.

**a, b**, Representative images of the experiments shown in Fig. 3g, indicate that PEN2, along with its interaction with ATP6AP1, is required for the lysosomal translocation of AXIN. *PEN2*<sup>-/-</sup> MEFs, along with *PEN2*<sup>-/-</sup> MEFs re-introduced with wildtype PEN2, its mutant 2A or mutant 20A (**a**), and *ATP6AP1*<sup>-/-</sup> MEFs, along with its wildtype control, or those re-introduced with full length (FL) ATP6AP1, or ATP6AP1<sup>Δ420-440</sup> (**b**, Re-introduced proteins were all expressed at close-to-endogenous levels), were treated with 200 μM metformin for 12 h, or with the v-ATPase inhibitor concanamycin A (conA, 5 μM) for 2 h as a control. AXIN and the lysosomal marker LAMP2 were stained with goat anti-AXIN antibody (green) and rat anti-LAMP2 antibody (red), respectively. Images were taken by confocal microscopy after incubating cells with Alexa Fluor 488 donkey anti-goat IgG and Alexa Fluor 594 donkey anti-rat IgG. The areas defined

by dashed boxes on each representative image are enlarged as insets. Experiments in this figure were performed three times.

### Extended Data Fig. 11 Aldolase-TRPV act as a separate route from PEN2-ATP6AP1.

**a, b**, Inhibition of v-ATPase by conA activates AMPK in cells lacking the PEN2 and ATP6AP1 axis. *PEN2<sup>-/-</sup>* MEFs (**a**) or *ATP6AP1<sup>-/-</sup>* MEFs re-introduced with full length (FL) ATP6AP1 or its Δ420-440 mutant (**b**; expressed at close-to-endogenous levels) were treated with 5 μM conA for 2 h, followed by determining p-AMPKα and p-ACC levels by immunoblotting. **c**, Liver-specific ALDOA-D34S transgenic (Tg) mice renders hepatic AMPK inactive under starvation. Tg mice (6-week-old) expressing ALDOA-D34S (expressed under an *ApoE* promoter and its hepatic control region included in the pLiv-Le6 vector), which can still bind FBP in low glucose, and therefore mimics a high glucose state in which AMPK is inactivated (see cell-based data in ref. <sup>6</sup>), were starved for 16 h. P-AMPKα and p-ACC levels in livers were then determined by immunoblotting. **d**, Aldolase is dispensable for low metformin-induced AMPK activation in HEK293T cells. Cells stably expressing HA-tagged ALDOA-D34S mutant, or wildtype ALDOA were treated with 300 μM metformin (low concentration) or 5 mM (high concentration, as a control) for 12 h, followed by analysis of p-AMPKα and p-ACC levels by immunoblotting. **e**, Aldolase is dispensable for low metformin-induced AMPK activation in mouse liver. Mice with Tg-ALDOA-D34S at 6 weeks old were treated with metformin in drinking water (1 g/l) for another 7 days. At the day 8, mice were sacrificed, and hepatic p-AMPKα and p-ACC levels were determined by immunoblotting. **f, g**, TRPV is dispensable for low metformin-induced AMPK activation. Experiments pertaining to TRPV dependency were performed in MEFs (**f**) as well as in mouse livers (**g**) as described in **d** (except 200 μM metformin was used) and **e**, respectively, except that MEFs with quadruple knockout of *TRPV1-4* (**f**, TRPV-QKO), or the *TRPV1<sup>-/-</sup>* mice injected with a combination of AAV-carried siRNAs against *TRPV2*, *TRPV3* and *TRPV4* (**g**, si*TRPV2-4*, at 8 weeks old, which had been validated to show little expression of TRPVs, see ref. <sup>25</sup>), were used (viruses were injected at 4 weeks old, and metformin was supplied at 8

weeks old). Experiments in this figure were performed three times, except **d** five times.

**Extended Data Fig. 12 PEN2-ATP6AP1 axis is required for metformin-mediated glucose absorption and hepatic fat reduction.**

**a**, Verification of AMPK $\alpha$  knockout efficiency in the duodenum of AMPK $\alpha$  intestine-specific knockout (IKO) mice. Mouse offsprings carrying floxed *AMPK $\alpha$ 1* and *AMPK $\alpha$ 2*, as well as *vilERT2*-Cre (tamoxifen-sensitive, ERT2-fused Cre recombinase expressed under the control of the *villin* promoter, for deletion of *AMPK $\alpha$*  in intestine), along with their wildtype littermates (carrying floxed *AMPK $\alpha$ 1* and *AMPK $\alpha$ 2*, but not *vilERT2*-Cre) were injected with tamoxifen (as described in Method section) for knockout of *AMPK $\alpha$* . Protein levels of AMPK $\alpha$  in duodenum were then analysed by immunoblotting. **b**, Intestinal AMPK is required for metformin to induce glucose lowering. Mice at 5 weeks old with intestinal *AMPK $\alpha$ 1/2* double knockout (AMPK $\alpha$ 1/2-IKO), along with its wildtype littermates, were treated with metformin in drinking water (+ Met, 1 g/l) for 7 days (tamoxifen was injected at 4 weeks old). At day 8, mice were starved for 6 h, followed by oral glucose tolerance test (OGTT, results are shown as mean  $\pm$  s.e.m.,  $n = 7$  for each genotype/treatment, except for WT mice treated with drinking water without metformin,  $n = 6$ ; and  $P$  value by two-way RM ANOVA, followed by Tukey, compared blood glucose levels between WT + Met group and AMPK $\alpha$ 1/2-IKO + Met group at the same time point; see also inset for AUC values,  $P$  value by two-way ANOVA, followed by Tukey). **c, l**, Strategies to generate *PEN2*-floxed (**c**) or *ATP6AP1*-floxed (**l**) allele. **d, f**, Depletion of *PEN2* in the intestine or liver in *PEN2*-floxed mice. PCR analysis results of mouse offsprings carrying floxed *PEN2*, as well as *vilERT2*-Cre (**d**) or *albERT2*-Cre (**f**, same as in **d**, except Cre under *albumin* promoter, for deletion of *PEN2* in liver) allele are shown on the upper panels. Protein levels of *PEN2* in duodenal (**d**), or hepatic (**f**) tissues in *PEN2* intestine- or liver-specific knockout (IKO or LKO) mice are also shown. See also panels of **d** and **f** for the experimental timeline of the analysis of phenotypes of *PEN2*-IKO (**d**) and *PEN2*-LKO (**f**) mice. **e**, Intestinal *PEN2* is required for metformin-induced glucose-lowering effect. Mice were fed with HFD as in Fig. [4a](#). Serum insulin levels

are shown as mean  $\pm$  s.e.m.,  $n = 5$  for each genotype/treatment, and  $P$  value by two-way RM ANOVA, followed by Tukey, compared insulin levels between WT + Met group and PEN2-IKO + Met group at the same time point; see also inset for AUC values,  $P$  value by two-way ANOVA, followed by Tukey. **g, h**, PEN2 is required for metformin-induced reduction of hepatic fat. As depicted in **f**, mice at 38 weeks old with hepatic *PEN2* knockout (PEN2-LKO), along with its wildtype littermates, were treated with metformin in drinking water (+ Met, 1 g/l) for 16 weeks. At week 54, mice were starved for 6 h, followed by intraperitoneal glucose tolerance test (**g**, IPGTT; serum insulin levels are shown as mean  $\pm$  s.e.m.,  $n = 5$  for each genotype/treatment, and  $P$  values by two-way RM ANOVA, followed by Tukey, compared blood glucose or insulin levels between WT + Met group and PEN2-LKO + Met group at the same time point; see also inset for AUC values,  $P$  values by two-way ANOVA, followed by Tukey), insulin tolerance test (**h**, ITT, results are shown as mean  $\pm$  s.e.m.,  $n = 6$  for each genotype/treatment, and  $P$  value by two-way RM ANOVA, followed by Tukey, compared as in **c**; see also inset for AUC values,  $P$  value by two-way ANOVA, followed by Tukey). **i, p**, The PEN2-ATP6AP1 axis is required for AMPK activation by metformin in primary hepatocytes from HFD-fed mice. *PEN2*-LKO mice were generated as in Fig. [4c](#) (**i**), and ATP6AP1 or ATP6AP1 $^{\Delta 420-440}$  mutant was reintroduced to in the liver of mice lacking hepatic *ATP6AP1* as in Fig. [4e](#) (**p**), and the resultant mice were fed with HFD for 35 weeks. Primary hepatocytes were then isolated, and treated with 5  $\mu$ M metformin or 500  $\mu$ M metformin for 2 h, and then subjected to analysis p-AMPK $\alpha$  and p-ACC levels by immunoblotting. **j, q**, The PEN2-ATP6AP1 axis is required for AMPK activation in the liver of HFD-fed mice. Mice were treated as in Fig. [4c](#) (**j**) or [4e](#) (**q**). Hepatic AMPK activation (immunoblots), AMP:ATP and ADP:ATP ratios (scatter plots, left panel), as well as the absolute concentrations of AMP, ADP and ATP [scatter plots, middle panel, shown as mean  $\pm$  s.e.m.,  $n = 5$  (**j**) and  $n = 5$  (**q**) for each genotype/treatment, except for ischemic treatment,  $n = 4$ ;  $P$  value by one-way ANOVA, followed by Tukey], and metformin concentrations [scatter plots, right panel, shown as mean  $\pm$  s.e.m. on right panel,  $n = 6$  (**j**) and  $n = 5$  (**q**) for each genotype, and  $P$  value by two-sided Student's *t*-test] in mice after 1-week treatment of metformin (1 g/l in drinking water) are shown. **k, r**, The PEN2-ATP6AP1 axis is required for the reduction of hepatic fat by metformin. Mice were fed with HFD as in Fig. [4c](#) (**k**) or [4e](#)

(r), and images from H&E staining of the liver in mice after 16-week treatment of metformin are shown. **m**, Depletion of ATP6AP1, and re-introduction of ATP6AP1 or ATP6AP1<sup>Δ420-440</sup> in liver in ATP6AP1-LKO mice. PCR analysis results of mouse offsprings carrying floxed *ATP6AP1*, as well as *albERT2-Cre* are shown on the upper panel. Protein levels of endogenous ATP6AP1, as well as full length (FL) ATP6AP1, or ATP6AP1<sup>Δ420-440</sup> mutant expressed via AAVs, are shown on the middle panel. Experimental timeline of the analysis of the phenotypes of liver-specific ATP6AP1 (FL) and ATP6AP1<sup>Δ420-440</sup>-expressing mice were shown on the lower panel. **n**, **o**, ATP6AP1 is required for metformin-induced reduction of hepatic fat. As depicted in **m**, mice at 38 weeks old with hepatic depletion of ATP6AP1, and re-introduction of ATP6AP1 or ATP6AP1<sup>Δ420-440</sup> (FL or Δ420-440) were treated with metformin in drinking water (+ Met, 1 g/l) for 16 weeks. At week 54, mice were starved for 6 h, followed by intraperitoneal glucose tolerance test (**n**, serum insulin levels are shown as mean ± s.e.m.,  $n = 5$  for each genotype/treatment, and  $P$  value by two-way RM ANOVA, followed by Tukey, compared insulin levels between ATP6AP1 (FL) + Met group and ATP6AP1<sup>Δ420-440</sup> + Met group at the same time point; see also inset for AUC values,  $P$  value by two-way ANOVA, followed by Tukey), insulin tolerance test (**o**, shown as mean ± s.e.m.,  $n = 6$  for each genotype/treatment, and  $P$  value by two-way RM ANOVA, followed by Tukey, compared as in **n**; see also inset for AUC values, and  $P$  value by two-way ANOVA, followed by Tukey). Experiments in this figure were performed three times, except **i** four times.

#### [Source data](#)

#### [Extended Data Fig. 13 PEN2-ATP6AP1 axis is required for metformin-mediated lifespan extension in nematodes.](#)

**a**, Metformin extends lifespan of *C. elegans*. Wildtype nematodes (N2) were cultured on NGM plates containing metformin at different concentrations. Lifespans were determined, and results are shown as Kaplan-Meier curves, see also statistical analysis data on Supplementary Table 3. **b**, **d**, Metformin at 50 mM does not elevate AMP/ADP levels in *C. elegans* with knockdown of *PEN2*. Nematodes were knocked down of

*PEN2* (**b**, generated as in Fig. 4g by culturing on RNAi plates containing *E. coli* expressing siRNA against *PEN2*; the knockdown efficiency was assessed by determining mRNA levels of *PEN2* as shown in **d**; results are mean  $\pm$  s.e.m.,  $n = 3$  for each genotype; and  $P$  value by two-sided Student's *t*-test), and were maintained on RNAi plates containing 50 mM metformin for 2 more days. Worms were then subjected to the analysis of AMP:ATP and ADP:ATP ratios. Data are shown as mean  $\pm$  s.e.m.,  $n = 4$  for each genotype/treatment, and  $P$  value by two-way ANOVA, followed by Tukey. **c**, *PEN2* is required for metformin-induced lifespan extension in *C. elegans*. Nematodes were generated as in Fig. 4g and AMPK activation after 2-day treatment of metformin, were determined. **e**, **j**, Metformin uptake is not altered in nematodes lacking *PEN2* or *ATP6AP1*. L4 larvae of nematodes with *PEN2* knockdown (**e**, generated as in Fig. 4g), or of nematodes with knockout of *ATP6AP1* and stable expression of full length *ATP6AP1* or *ATP6AP1* $^{\Delta 420-440}$  mutant (**j**, generated as in Fig. 4h), were cultured on RNAi plates (**e**) or NGM plates (**j**) containing 50 mM metformin, for 2 days. Metformin concentrations were determined by HPLC-MS, and normalised to protein concentrations. Data are shown as mean  $\pm$  s.e.m.,  $n = 4$  for each genotype; and  $P$  value by two-sided Student's *t*-test. **f**, Metformin at 50 mM does not elevate AMP/ADP levels in *ATP6AP1* $^{-/-}$  *C. elegans* re-introduced with *ATP6AP1* $^{\Delta 420-440}$ . Nematodes were knocked out of *ATP6AP1* (*vha-19*), then re-introduced with *ATP6AP1* $^{\Delta 420-440}$  or *ATP6AP1* as a control, as shown in Fig. 4h, and then cultured on NGM plates containing 50 mM metformin for 2 more days before subjecting to analysis of AMP:ATP and ADP:ATP ratios. Data are shown as mean  $\pm$  s.e.m.,  $n = 4$  for each genotype/treatment; and  $P$  value by two-way ANOVA, followed by Tukey. **g**, Low metformin fails to promote fatty acid  $\beta$ -oxidation.

*AMPK $\alpha 1/2$  $^{-/-}$*  mouse primary hepatocytes were treated with 100  $\mu$ M BSA-conjugated [ $U-^{13}C$ ]-palmitic acid and 5  $\mu$ M or 500  $\mu$ M metformin for 4 h. Relative contents of labelled citrate, succinate and fumarate were determined by GC-MS. Data are shown as mean  $\pm$  s.e.m.,  $n = 4$  for each genotype/treatment; and  $P$  value by two-way ANOVA, followed by Tukey. **h**, Low metformin inhibits de novo lipogenesis, but does not affect TAG synthesis from fatty acids. Mouse primary hepatocytes were isolated as in **g**, and were treated with 100  $\mu$ M BSA-conjugated [ $U-^{13}C$ ]-palmitic acid (left panel) and 25 mM [ $U-^{13}C$ ]-glucose (right panel) for 12 h for determining

the TAG synthesis from fatty acids and de novo lipogenesis, respectively. Metformin at 5  $\mu$ M or 500  $\mu$ M was added to the culture medium along with labelled palmitic acid or glucose. Relative contents of labelled TAG were determined by LC-MS. Data are shown as mean  $\pm$  s.e.m.,  $n = 4$  for the determination of TAG synthesis and  $n = 5$  for the determination of de novo lipogenesis; and  $P$  value by two-way ANOVA, followed by Tukey. **i**, ATP6AP1 is required for metformin-induced lifespan extension in *C. elegans*. Nematodes were treated as in Fig. 4h, AMPK activation after 2-day treatment of metformin, were determined. **k**, The presence of living bacteria on the culture plates does not affect metformin uptake by nematodes. The L4 larvae of N2 were cultured on NGM plates (left panel) or RNAi plates (right panel) containing 50 mM metformin. Metformin concentrations of nematodes at day 1 and day 3 (before culture plate refreshing) were measured by HPLC-MS. Data are shown as mean  $\pm$  s.e.m.,  $n = 4$  for each treatment, and  $P$  value by two-sided Student's *t*-test. **l**, No changes in AMP:ATP and ADP:ATP ratios in the liver from mice fed with 0.1% metformin in diet. Mice at 4 weeks old were fed with normal chow (NC) diet, or normal chow diet containing 0.1% metformin (This way of giving metformin has been shown to be effective in extending the lifespan of mice<sup>10</sup>) for a week. Hepatic AMP:ATP and ADP:ATP ratios were then determined. Results are shown as mean  $\pm$  s.e.m.,  $n = 9$  for normal chow or  $n = 7$  for 0.1% metformin; and  $P$  value by two-sided Student's *t*-test. **m**, Schematic diagramme showing that the FBP-unoccupied aldolase-triggered glucose sensing and the PEN2-mediated metformin signalling axes converge at the v-ATPase complex to trigger AMPK activation. In response to lowering glucose levels, aldolase inhibits the cation channel TRPV, the latter of which then disrupts the association of the former with, and inhibits, v-ATPase. Metformin at low concentrations binds to PEN2, and metformin-bound PEN2 is recruited to v-ATPase via interacting with ATP6AP1, thereby inhibiting the activity of v-ATPase. Also shown is that high concentrations of metformin activates AMPK via elevating cellular AMP levels. Experiments in this figure were performed three times, except **l** five times.

## Source data

## Extended Data Fig. 14 Autophagy and ROS elevation are downstream events of AMPK, and are not involved in metformin-induced AMPK activation.

**a, b**, Autophagy occurs in MEFs treated with metformin. MEFs were treated with 200  $\mu$ M metformin for indicated durations. Protein levels of the autophagy reporter p62 and the phosphorylation levels of AMPK and ACC (**b**), as well as the lysosomal pH (**a**), were determined by immunoblotting using the indicated antibodies (**b**) or by visualisation with Lysosensor dye (**a**). Results of **a** (relative intensities of Lysosensor, processed as in Fig. 1a) are shown as mean  $\pm$  s.e.m.,  $n = 40$  cells from 4 dishes/experiment for 0 h, and  $n = 40$  cells for 4 h, 24 h and 48 h,  $n = 41$  cells for 8 h, and  $n = 42$  cells for 72 h, all from 6 dishes/experiments; and  $P$  value by one-way ANOVA, followed by Dunn. **c, f**, Metformin elevates ROS levels in *C. elegans*, but not in MEFs, HEK293T cells and mouse primary hepatocytes. In **c**, L4 larvae of N2 were cultured on NGM plates containing 50 mM metformin, 5 mM NAC for one day, and were then stained with 10  $\mu$ M CM-H<sub>2</sub>DCFDA followed by determination of ROS by imaging. Data are shown as mean  $\pm$  s.e.m.,  $n = 30$  worms for control (untreated) condition or  $n = 25$  worms for other conditions; and  $P$  value by two-way ANOVA, followed by Tukey (**c**). In **f**, MEFs and HEK293T cells were treated with 200 or 300  $\mu$ M metformin for 12 h, and mouse primary hepatocytes were treated with 5  $\mu$ M metformin for 2 h. Cells were stained with 5  $\mu$ M CellROX Deep Red, followed by determination of ROS by imaging. Data are shown as mean  $\pm$  s.e.m.,  $n = 20$  (for hepatocytes and HEK293T cells) or 40 (for MEFs) cells from 4 dishes/experiment; and  $P$  value by two-sided Student's *t*-test (hepatocytes) or two-sided Mann-Whitney test (MEFs and HEK293T cells). **d, e**, ROS and AMPK are both required for the metformin-mediated lifespan extension of *C. elegans*. L4 larvae of N2 or AMPK-deficient (*aak-2*) strain were cultured on NGM plates containing 50 mM metformin, 5 mM NAC (in **d**, for inhibiting ROS), or 0.1  $\mu$ M rotenone (in **d**, as a positive control for ROS induction). Lifespans were determined, and results are shown as Kaplan-Meier curves, see also statistical analysis data on Supplementary Table 3. **g, i**, NAC does not affect metformin-induced AMPK activation. Mouse primary hepatocytes, MEFs, HEK293T cells (**g**), or nematodes (**i**) were pre-treated with 5 mM NAC for 24 h, followed by treating with 5  $\mu$ M

metformin for 2 h, 200  $\mu$ M metformin for 12 h, 300  $\mu$ M metformin for 12 h, or 50 mM metformin for 2 days. Levels of p-AMPK $\alpha$  and p-ACC were then determined by immunoblotting. **h**, NAC does not affect metformin-induced v-ATPase inhibition. Primary hepatocytes, MEFs, or HEK293T cells were treated as in **g**, followed by analysis of lysosomal pH with the Lysosensor dye. Data (relative intensity of Lysosensor, processed as in Fig. **1a**) were graphed as mean  $\pm$  s.e.m.,  $n = 20$  cells from 3 dishes/experiment (for hepatocytes),  $n = 20$  cells from 3 dishes/experiment (for MEFs), or  $n = 24$  cells for normal condition and normal condition with NAC, and  $n = 25$  for metformin treatment and metformin plus NAC treatment, all from 4 dishes/experiment (for HEK293T cells).  $P$  value within each treatment was determined by two-way ANOVA, followed by Tukey. **j**, Low metformin does not alter the expression of gluconeogenic genes. Mouse primary hepatocytes isolated from PEN2-LKO mice or its wildtype littermates, or ATP6AP1-LKO mice re-introduced full length ATP6AP1 or ATP6AP1 $^{\Delta 420-440}$  mutant were treated with 5  $\mu$ M metformin, 500  $\mu$ M metformin (high dose, as a control), or 100 nM of glucagon (as a positive control for elevation of the expression of gluconeogenic genes) for 2 h, followed by analysis of mRNA levels of *PCK1* and *G6PC1* by real-time PCR. Data are shown as mean  $\pm$  s.e.m.;  $n = 3$  for each genotype/treatment, and  $P$  value by two-way ANOVA, followed by Tukey. **k**, Hepatic PEN2 is not required for the inhibition of gluconeogenesis by metformin. Mice at 5 weeks old with hepatic *PEN2* knocked out, along with its wildtype littermates, were treated with metformin in drinking water (1 g/l) for another 7 days (tamoxifen was injected at 4 weeks old). At the day 8, mice were starved for 16 h, followed by pyruvate tolerance test. Results are shown as mean  $\pm$  s.e.m.,  $n = 7$  for each genotype/treatment, and  $P$  value by two-way RM ANOVA followed by Tukey; see also inset for AUC values,  $P$  value by two-way ANOVA followed by Tukey. **l, m**, The PEN2-ATP6AP1 axis is required for the inhibition of mTORC1 by low metformin. MEFs, HEK293T cells and mouse primary hepatocytes with *PEN2* knockout (**l**), *ATP6AP1* knockout and with re-introduced full length ATP6AP1 or ATP6AP1 $^{\Delta 420-440}$  (**m**), were treated with 200  $\mu$ M and 5 mM metformin (for MEFs), 300  $\mu$ M and 5 mM metformin (for HEK293T cells) for 12 h, 5  $\mu$ M and 500  $\mu$ M metformin (for mouse primary hepatocytes). Cells were then lysed, and the activity of mTORC1 was determined by immunoblotting the phosphorylation levels of its substrate S6K (p-S6K). **n**, AMPK is required for the inhibition of

mTORC1 by low metformin. *AMPK $\alpha 1/2^{-/-}$*  mouse primary hepatocytes were treated with 5  $\mu$ M and 500  $\mu$ M metformin for 2 h. Cells were then lysed, and the activity of mTORC1 was determined by immunoblotting the phosphorylation levels of its substrate S6K (p-S6K). Experiments in this figure were performed three times, except **a, j, l, m** four times.

## [Source data](#)

# **Supplementary information**

## [Supplementary Information](#)

This file contains Supplementary Notes 1–10, Supplementary References and Supplementary Fig. 1.

## [Reporting Summary](#)

## [Peer Review File](#)

## [Supplementary Table 1](#)

A list of potential Met-P1-binding proteins.

## [Supplementary Table 2](#)

A list of potential PEN2-binding proteins.

## [Supplementary Table 3](#)

Summary of lifespan analysis for PEN2 and ATP6AP1 worms.

# **Source data**

## [Source Data Fig. 1](#)

[\*\*Source Data Fig. 3\*\*](#)

[\*\*Source Data Fig. 4\*\*](#)

[\*\*Source Data Extended Data Fig. 1\*\*](#)

[\*\*Source Data Extended Data Fig. 2\*\*](#)

[\*\*Source Data Extended Data Fig. 3\*\*](#)

[\*\*Source Data Extended Data Fig. 4\*\*](#)

[\*\*Source Data Extended Data Fig. 5\*\*](#)

[\*\*Source Data Extended Data Fig. 6\*\*](#)

[\*\*Source Data Extended Data Fig. 7\*\*](#)

[\*\*Source Data Extended Data Fig. 8\*\*](#)

[\*\*Source Data Extended Data Fig. 12\*\*](#)

[\*\*Source Data Extended Data Fig. 13\*\*](#)

[\*\*Source Data Extended Data Fig. 14\*\*](#)

## Rights and permissions

**Open Access** This article is licensed under a Creative Commons Attribution 4.0 International License, which permits use, sharing, adaptation, distribution and reproduction in any medium or format, as long as you give appropriate credit to the original author(s) and the source, provide a link to the Creative Commons license, and indicate if changes were made. The images or other third party material in this article are included in the article's Creative Commons license, unless indicated

otherwise in a credit line to the material. If material is not included in the article's Creative Commons license and your intended use is not permitted by statutory regulation or exceeds the permitted use, you will need to obtain permission directly from the copyright holder. To view a copy of this license, visit <http://creativecommons.org/licenses/by/4.0/>.

## [Reprints and Permissions](#)

## About this article

### Cite this article

Ma, T., Tian, X., Zhang, B. *et al.* Low-dose metformin targets the lysosomal AMPK pathway through PEN2. *Nature* **603**, 159–165 (2022).  
<https://doi.org/10.1038/s41586-022-04431-8>

- Received: 30 March 2021
- Accepted: 10 January 2022
- Published: 23 February 2022
- Issue Date: 03 March 2022
- DOI: <https://doi.org/10.1038/s41586-022-04431-8>

### Share this article

Anyone you share the following link with will be able to read this content:

[Get shareable link](#)

Sorry, a shareable link is not currently available for this article.

[Copy to clipboard](#)

Provided by the Springer Nature SharedIt content-sharing initiative

This article was downloaded by **calibre** from <https://www.nature.com/articles/s41586-022-04431-8>

| [Section menu](#) | [Main menu](#) |

- Article
- Open Access
- [Published: 23 February 2022](#)

# Effective drug combinations in breast, colon and pancreatic cancer cells

- [Patricia Jaaks<sup>1</sup>](#), [nal](#),
- [Elizabeth A. Coker<sup>1</sup>](#), [nal](#),
- [Daniel J. Vis<sup>2,7</sup>](#),
- [Olivia Edwards](#) [ORCID: orcid.org/0000-0001-8753-9348<sup>1</sup>](#),
- [Emma F. Carpenter](#) [ORCID: orcid.org/0000-0002-1911-6842<sup>1</sup>](#),
- [Simonetta M. Leto](#) [ORCID: orcid.org/0000-0001-7580-6584<sup>3</sup>](#),
- [Lisa Dwane<sup>1</sup>](#),
- [Francesco Sassi<sup>3</sup>](#),
- [Howard Lightfoot<sup>1</sup>](#),
- [Syd Barthorpe<sup>1</sup>](#),
- [Dieudonne van der Meer<sup>1</sup>](#),
- [Wanjuan Yang<sup>1</sup>](#),
- [Alexandra Beck<sup>1</sup>](#),
- [Tatiana Mironenko<sup>1</sup>](#),
- [Caitlin Hall](#) [ORCID: orcid.org/0000-0002-5713-5980<sup>1</sup>](#),
- [James Hall](#) [ORCID: orcid.org/0000-0002-8124-5434<sup>1</sup>](#),
- [Iman Mali<sup>1</sup>](#),
- [Laura Richardson](#) [ORCID: orcid.org/0000-0002-8075-3816<sup>1</sup>](#),
- [Charlotte Tolley](#) [ORCID: orcid.org/0000-0002-1119-7983<sup>1</sup>](#),
- [James Morris<sup>1</sup>](#),
- [Frances Thomas](#) [ORCID: orcid.org/0000-0003-2345-0912<sup>1</sup>](#),
- [Ermira Lleshi<sup>1</sup>](#),
- [Nanne Aben<sup>2</sup>](#),
- [Cyril H. Benes<sup>4</sup>](#),
- [Andrea Bertotti<sup>3,5</sup>](#),
- [Livio Trusolino](#) [ORCID: orcid.org/0000-0002-6379-3365<sup>3,5</sup>](#),
- [Lodewyk Wessels](#) [ORCID: orcid.org/0000-0002-1656-6995<sup>2,6,7</sup>](#) &
- [Mathew J. Garnett](#) [ORCID: orcid.org/0000-0002-2618-4237<sup>1</sup>](#)

*Nature* volume 603, pages 166–173 (2022)

- 27k Accesses
- 137 Altmetric
- [Metrics details](#)

## Subjects

- [Breast cancer](#)
- [Colorectal cancer](#)
- [High-throughput screening](#)
- [Pancreatic cancer](#)
- [Targeted therapies](#)

## Abstract

Combinations of anti-cancer drugs can overcome resistance and provide new treatments<sup>1,2</sup>. The number of possible drug combinations vastly exceeds what could be tested clinically. Efforts to systematically identify active combinations and the tissues and molecular contexts in which they are most effective could accelerate the development of combination treatments. Here we evaluate the potency and efficacy of 2,025 clinically relevant two-drug combinations, generating a dataset encompassing 125 molecularly characterized breast, colorectal and pancreatic cancer cell lines. We show that synergy between drugs is rare and highly context-dependent, and that combinations of targeted agents are most likely to be synergistic. We incorporate multi-omic molecular features to identify combination biomarkers and specify synergistic drug combinations and their active contexts, including in basal-like breast cancer, and microsatellite-stable or *KRAS*-mutant colon cancer. Our results show that irinotecan and CHEK1 inhibition have synergistic effects in microsatellite-stable or *KRAS*–*TP53* double-mutant colon cancer cells, leading to apoptosis and suppression of tumour xenograft growth. This study identifies clinically relevant effective drug combinations in distinct molecular subpopulations and is a resource to guide rational efforts to develop combinatorial drug treatments.

[Download PDF](#)

## Main

Single-agent targeted therapies for patients with molecularly defined tumours are transforming cancer treatment. Nonetheless, many patients still lack effective

treatments and pre-existing or acquired resistance limits the clinical benefit of even the most advanced medicines<sup>2</sup>. Empirically developed combinations of chemotherapy drugs are used to treat cancer patients<sup>1</sup>. Combination therapies using targeted anti-cancer agents have the potential to overcome resistance, enhance the response to existing drugs, reduce dose-limiting single agent toxicity and expand the range of treatments<sup>2</sup>, as exemplified by triple combination therapy for patients with BRAF-mutant colorectal cancer<sup>3</sup>. However, our ability to predict effective combinations is limited<sup>4</sup>. Molecularly annotated cancer cell line panels<sup>5</sup> are increasingly being used to identify active drug combinations<sup>4,6,7,8</sup>. Studies performed so far have limitations, including testing relatively few combinations, using few molecularly targeted drugs, or using a limited number and sub-optimal range of drug concentrations. Furthermore, previous studies have employed a limited number of cell lines<sup>4</sup> (a maximum of 85), making it difficult to link combination activity and molecular context.

## Drug combination screens in cancer cells

To systematically identify active drug combinations, we used the Genomics of Drug Sensitivity in Cancer (GDSC) cell line screening platform<sup>5</sup> to measure the effects of 2,025 pairwise drug combinations (Supplementary Table 1) in 125 cell lines (Supplementary Table 2), including breast ( $n = 51$ ), colorectal ( $n = 45$ ; hereafter referred to as colon) and pancreatic ( $n = 29$ ) cancer (Fig. 1a). We produced 296,707 drug combination viability measurements for 108,259 combination–cell line pairs, making it the second largest drug combination dataset by number of combinations and experiments, with the largest number of cell lines tested<sup>4,6,7,8</sup>.

**Fig. 1: A large-scale drug combination screen.**

---

 **figure 1**

---

**a**, 2,025 drug combinations were screened in breast, colon and pancreas cancer cell lines ( $n = 125$ ). Synergy was evaluated on the basis of efficacy ( $\Delta E_{\max}$ ) and potency ( $\Delta IC_{50}$ ) for 108,259 drug responses and integrated with cell line molecular features to identify biomarkers. **b**, Heat map of  $\Delta IC_{50}$  values for 1,275 combinations in 51 breast cancer cell lines: clustering by combination and annotation by combination type, anchor and library pathway.  $\Delta IC_{50}$  limits are clipped to -4 and 4, rows are sorted by conditional mean  $\Delta IC_{50}$  on cell line identity. Chemo., chemotherapeutic agent.

Each cell line has mutation, copy number alteration, methylation and gene expression data available (Extended Data Fig. [1a](#), Supplementary Table [2](#)). We selected drugs for each tissue including chemotherapeutics and targeted agents approved by the United States Food and Drug Administration (FDA), drugs in clinical development and investigational compounds (Extended Data Fig. [1b,c](#)). We enriched for drugs against key targets and pathways ( $n = 20$ ), such as ERBB2 inhibitors in breast and drugs targeting MAPK signalling in colon and pancreas (Extended Data Fig. [1d](#), Supplementary Table [1](#)). We tested 121 combinations in all three tissues.

To screen efficiently we used a  $2 \times 7$  concentration matrix, or ‘anchored’ approach. We screened each anchor compound at two optimised concentrations and a discontinuous 1,000-fold (7-point) dose–response curve of the library compound (Extended Data Fig. [1e](#)). Single-agent and combination viability measurements were fitted per cell line and multiple parameters derived including: (1) anchor viability effect, (2) library and combination viability effect at the highest-used library concentration (library  $E_{\max}$  and combination  $E_{\max}$ , respectively), and (3) the estimated library drug concentration producing a 50% viability reduction ( $IC_{50}$ ) for the library

and combination (Extended Data Fig. 1f). We compared observed combination response of cells to the Bliss independence-predicted response<sup>9</sup> based on monotherapy activity, and classified drug combinations on the basis of shifts beyond Bliss in potency ( $\Delta IC_{50}$ ; that is, increased sensitivity) or efficacy<sup>10</sup> ( $\Delta E_{max}$ ; that is, reduced cell viability) (Extended Data Fig. 1g). We classified combination-cell line pairs as synergistic if, at either anchor concentration, combination  $IC_{50}$  or  $E_{max}$  was reduced eightfold or 20% viability over Bliss, respectively (Extended Data Fig. 1h). Stringent quality control was applied to all screening data: technical and biological replicates were highly correlated and library  $IC_{50}$  values were highly correlated with  $IC_{50}$  values from independent screens (Extended Data Fig. 2a–e, Supplementary Table 2).

Dimensional reduction (using *t*-distributed stochastic neighbour embedding (*t*-SNE)) on the 121 pan-tissue combinations showed moderate mixing of cell lines by tissue, indicating that tissue has some effect on combination response, but is not on its own a major driver of variation (Extended Data Fig. 2f), as previously described by others<sup>8</sup>. Clustering by  $\Delta IC_{50}$  for all tissue-specific and pan-tissue combinations, we observed that combinations fall into three major groups: (1) broadly active, (2) minimally active, and (3) variable activity (Fig. 1b, Extended Data Fig. 2g–i). All data are available for download or exploration through GDSC Combinations, <https://gdsc-combinations.depmap.sanger.ac.uk/>.

## The landscape of drug interactions

Overall, 5.2% of the 108,259 combination–cell line pairs showed synergy, with the highest rate in pancreas (7.2%), then colon (5.4%) and breast (4.4%). Only 27.5% of synergistic combination–cell line pairs were observed at both high and low anchor concentrations, suggesting that synergy is detected within a specific range of concentrations (Fig. 2a) and pointing to the utility of aggregating synergy calls from both anchor concentrations. Synergy occurred most frequently in a background of weak to moderate single-agent activity, enhancing existing drug responses (Extended Data Fig. 3a). 54.9% of synergistic measurements affected either efficacy (22.2%) or potency (32.7%), whereas 45.1% affected both, indicating that these two metrics describe complementary responses (Fig. 2b). Although synergy overall was rare, most frequently observed in less than 3 cell lines per tissue, 192 combination–tissue pairs (7.8%; 60 breast, 52 colon and 80 pancreas) were synergistic in at least 20% of cell lines from their respective tissue (Supplementary Table 1). The relative frequency and context specificity of synergy was retained independent of the synergy threshold applied (Extended Data Fig. 3b).

**Fig. 2: Synergy is rare and highly context-dependent.**

 figure 2

**a**, Overlap of synergy identified at two anchor concentrations.  $n = 5,541$  synergistic combination-cell line pairs. **b**, Synergy calls by  $\Delta\text{IC}_{50}$  and  $\Delta E_{\max}$  are complementary.  $n = 9,402$  synergistic measurements. **c**, Navitoclax combination partners and tissue-specific enrichment in synergy (hypergeometric test). Enriched navitoclax partners ( $P \leq 0.005$ , FDR  $\leq 5\%$ ) are labelled. **d**, Combinations of navitoclax with AURK inhibitors are frequently synergistic in breast cancer cell lines, with exception of HER2 cells. Binary synergy for navitoclax (anchor) paired with three AURK inhibitors with indicated specificity across PAM50 subtypes. **e**, Synergy rates for 1,736 combinations of two targeted drugs by minimum (min.) network distance between drug targets. Two-sided Student's *t*-test. **f**, Twenty-four unique target pathway pairs enriched in synergy in at least one tissue (136 unique pairs tested; hypergeometric test,  $P \leq 0.005$ , FDR  $\leq 5\%$ ). Red denotes pathway pairs that are enriched in all three tissues.

Rescreening a subset of 45–59 frequently synergistic combinations (51 breast, 45 colon and 59 pancreas) in 30 cell lines per tissue resulted in a validation dataset of 4,881 combination–cell line pairs. Primary and validation datasets correlated well for single-agent and combination response metrics ( $r = 0.69$ – $0.84$ , all  $P < 0.001$ ), and synergy classifications were consistent for all tissues (*F*-score: 0.62–0.7; recall: 0.61–0.76; precision rate: 0.56–0.77; original screening set defined as ‘positive’) (Extended Data Fig. 3c–e). Differences in classifications were frequently borderline cases and larger synergy effects were most reproducible (Extended Data Fig. 3f).

Of the 65 drugs in our screen, 10 were chemotherapeutic agents and 31.2% of all combinations contained one (28.7%) or two (2.5%) chemotherapeutic agents. Chemotherapeutic–chemotherapeutic combinations had lower  $\Delta\text{IC}_{50}$  and  $\Delta E_{\max}$  shifts than combinations with targeted compounds (Extended Data Fig. 3g), resulting in low synergy rates (21 out of 2,337 combination–cell line pairs (0.9%)) compared with

3.2% and 6.1% for chemotherapeutic–targeted and targeted–targeted combinations, respectively.

We observed significant enrichment of synergy when chemotherapeutics were paired with drugs targeting apoptotic signalling and cell cycle inhibitors (hypergeometric test, adjusted  $P \leq 0.05$ ). More than 76% of synergies between chemotherapeutics and cell cycle inhibitors per tissue occurred with AZD7762 (CHEK1/2), pairing well with 5-fluorouracil, gemcitabine, cisplatin and irinotecan (Extended Data Fig. [3h](#)).

Combinations with the apoptosis regulator navitoclax (an inhibitor of BCL-2, BCL-XL and BCL-W) comprised 25.4% of all synergistic combination–cell line pairs (1,418 out of 5,580), despite only representing 5.4% of combinations (109 out of 2,025). Seventy-eight per cent (137 out of 175) of combination–tissue pairs with navitoclax were synergistic in at least three cell lines (average per combination–tissue: 19.6% synergy). Navitoclax showed a synergy rate of more than 50% when combined with TOP1 inhibitors (irinotecan in pancreas and camptothecin in breast and colon) or microtubule stabilisers (docetaxel or paclitaxel) and destabilisers (vinorelbine) (Extended Data Fig. [3i](#)). Targeted drugs that were synergistic with navitoclax were mostly tissue-specific (Fig. [2c](#)). Navitoclax had particularly high synergy rates in breast when combined with either of the three aurora kinase (AURK) inhibitors alisertib, tozasertib or ZM447439 (61%, 60% and 53%, respectively). Navitoclax with alisertib and ZM447439 were tested and had reproducible synergy in the validation screen (94% and 88%, respectively). Notably, synergy was frequently observed for at least two out of three navitoclax–AURKi combinations in all PAM50 subtypes (63% (12 out of 19 cell lines) in basal-like, 73% (8 out of 11) in LumA and 75% (3 out of 4) in LumB), with the exception of HER2 cell lines (17%, 1 out of 6 cell lines) (Fig. [2d](#)). These data support ongoing efforts to use combinations suppressing anti-apoptotic adaptation in cancer<sup>[11](#)</sup>, but indicate that in defined cancer types, pairing with specific targeted drugs is most likely to be effective.

For the 67% of combinations involving two targeted compounds, we investigated pathway relationships between drug targets and their synergy rate. We overlaid drug targets for all 57 targeted compounds onto a protein–protein interactome of 14,431 protein nodes and 110,118 edges based on the IntAct<sup>[12](#)</sup> database, filtered to unique human protein–protein interactions (confidence threshold: 0.5). We calculated the shortest finite network distance between the drug target nodes and found that on average combinations whose targets are between one and two nodes away from each other yield the most synergy (Fig. [2e](#)), as reported previously<sup>[4](#)</sup>, which indicates that there is an optimal average target distance to induce synergy.

To further understand how targeted–targeted drug combinations work at the pathway level, we grouped combinations into unique curated pathway pairs by tissue on the basis of the nominal therapeutic target(s) of each drug (excluding navitoclax

combinations, as discussed separately, Supplementary Table 1). Eighteen per cent (25 out of 136) of pathway pairs were significantly enriched in synergy in at least one tissue (hypergeometric test,  $P \leq 0.005$ , false discovery rate (FDR)  $\leq 5\%$ ) (Fig. 2f). Five pathway pairs were enriched in synergy in all three tissues, including dual targeting of receptor tyrosine kinase (RTK) signalling, targeting of RTK signalling with downstream PI3K or MAPK pathways, or targeting of PI3K and MAPK pathways. Taking PI3K and MAPK pathways as examples, we examined inter-pathway versus intra-pathway combinations. Inter-pathway targeting of PI3K and MAPK pathways resulted in 2–5 times higher synergy rates than the tissue average: breast: 10.1% (versus 4.4%), colon: 17.1% (versus 5.4%) and pancreas: 36.4% (versus 7.2%). Conversely, intra-pathway targeting of the MAPK or PI3K pathways showed below or close to average rates of synergy (MAPK combinations: 2.2%; PI3K combinations: 6.7%; all combinations: 5.2%) (Extended Data Fig. 3j). Despite low intra-PI3K pathway synergy, we detected a distinct combination-specific synergy of MK-2206 (AKT1/2) combined with MTOR inhibitors OSI-027 or AZD8055 in breast (24% and 25% synergy rates, respectively), particularly in the PAM50 subtype HER2 (50–75%; 4 or 6 out of 8 cell lines) (Extended Data Fig. 3k). This combination may work by inhibiting feedback activation of AKT in HER2 breast cancer due to mTOR inhibitor-induced activation of PI3K signalling<sup>13</sup>. Numerous MAPK and PI3K inter-pathway combinations are currently in clinical trials, and preliminary data suggest that intermittent drug administration, isoform-selective PI3K inhibitors and site-specific delivery of drugs could maximise clinical activity while increasing tolerability<sup>14</sup>.

Overall, we find that drug synergy, on the basis of complementary potency and efficacy metrics, is rare but frequent for a subset of combinations. Synergy most frequently enhances weak to modest single-agent drug response and rates are highest for combinations of targeted compounds. Combinations containing the apoptosis regulator navitoclax show high synergy rates. Whereas some trends are universal across all three tissues, such as high synergy rates for inter-pathway targeting of MAPK and PI3K pathways, other synergistic effects are tissue-specific, including navitoclax plus AURK inhibition in breast.

## Combination response molecular markers

Associations between molecular features and drug response, referred to here as biomarkers, can provide insights into the cellular behaviour that dictates response to drug treatment and can inform clinical development of therapies. We used GDSCTools<sup>15</sup> to identify multi-omics biomarkers of combination ( $\Delta IC_{50}$ ,  $\Delta E_{max}$  and combination  $E_{max}$ ) and single-agent ( $IC_{50}$ ) responses. Multiple analyses were performed, grouping cell lines in molecular contexts, including pan-tissue (3 tissues), individual tissues and seven molecular ‘baskets’ representing specific molecular

subgroups (*TP53*, *KRAS*, *PIK3CA*, breast *PIK3CA*, basal-like breast cancers, colon *KRAS* and colon microsatellite-stable (MSS)) (Fig. 1a). *TP53*, *KRAS* and *PIK3CA* are the most frequently mutated genes across the cell lines, and the intra-tissue molecular baskets represent cancers with unmet clinical need.

We performed 7,941,266 analysis of variance (ANOVA) tests, out of which 8,078 associations were significant and of large effect size ( $P \leq 0.001$ , FDR  $\leq 5\%$ , Glass deltas for positive and negative populations both  $\geq 1$ ) (Fig. 1a, Supplementary Table 3). Biomarkers of all feature types were found for all drug response inputs, except for CRIS and PAM50 classifications (Extended Data Fig. 4a). Some 3,280 biomarkers (40.6%) were significantly associated with monotherapy IC<sub>50</sub> including multiple previously described associations<sup>5</sup> such as taselisib (PI3K inhibitor) sensitivity in *PIK3CA*-mutant cell lines (Extended Data Fig. 4b). We identified 4,798 significant combination response biomarkers, of which 18.4%, 15.8% and 65.7% were associated with potency ( $\Delta IC_{50}$ ), efficacy ( $\Delta E_{max}$ ) and combination activity (combination  $E_{max}$ ), respectively (Fig. 3a, Extended Data Fig. 4c). Of note, 76.8% of the  $\Delta IC_{50}$  and  $\Delta E_{max}$  biomarkers are associated with either  $\Delta IC_{50}$  (43.0%) or  $\Delta E_{max}$  (33.8%) but not with both, consistent with the complementary nature of these synergy metrics. Of the 2,025 combinations, 28.7% had at least one combination response biomarker (for combinations with one or more biomarkers: median: 2, range: 1–152; Extended Data Fig. 4d). We identified more than 2,050 combination biomarkers unique to the molecular basket analyses, demonstrating the benefit of testing for biomarkers within defined molecular subgroups.

**Fig. 3: A biomarker pipeline incorporating multi-omics features identifies context-specific associations.**

 figure 3

**a**, Volcano plot of biomarkers associated with  $\Delta\text{IC}_{50}$  ( $n = 2,006,328$ ). Statistically significant large effect-size biomarkers ( $n = 884$ ) are coloured by analysis type. Examples discussed in the text and selected outliers are labelled. Exp., expression; mut., mutant. **b**, Schematic of MAPK pathway showing the relationship between NRAS and BRAF. Low expression of NRAS is a biomarker of certain dabrafenib-containing combinations. **c**, Network of interactors of PIK3CA, showing its position two nodes away from targets of MK-2206 and linsitinib. *PIK3CA* mutation is predictive of the linsitinib + MK-2206 combination response in the *KRAS*-mutant molecular context. **d**, Number of combinations with at least three synergistic cell lines and combination response biomarkers ( $\Delta E_{\max}$  or  $\Delta\text{IC}_{50}$ ). **e**, Gain of *ERBB2* is associated with sapitinib + JQ1 combination response in breast and all synergistic cell lines have an *ERBB2* amplification. **f**, *KRAS* mutation is associated with trametinib + MK-2206 combination response in a pan-tissue setting (left, two-sided Welch's *t*-test) and most synergistic cell lines harbour mutated *KRAS* (right). In box plots, the horizontal line shows the median, boxes extend across first and third quartiles, and whiskers extend to  $1.5 \times$  interquartile range.

Of the 1,645  $\Delta\text{IC}_{50}$  and  $\Delta E_{\max}$  associations, we identified only three in pancreas-specific analyses: of these, low *CDH1* gene expression, which is associated with epithelial-to-mesenchymal transition, sensitised cells to irinotecan (TOP1 inhibitor) plus AZD7762 (CHEK1/2 inhibitor) (Extended Data Fig. 4e). Among known combination biomarkers, we identified *BRAF* mutation as a biomarker for dabrafenib (BRAF) paired with EGFR inhibitors afatinib and sapitinib screened in colon (Extended Data Fig. 4f), with synergy occurring exclusively in *BRAF*-mutant cell lines<sup>16</sup> (4 or 6 synergistic cell lines, respectively). Combinations of EGFR antibodies and BRAF inhibitors are a clinically approved regimen in *BRAF*-mutant metastatic colorectal cancer<sup>17</sup>. These examples show that our screen can identify known clinical biomarkers and candidate markers of combination response warranting further investigation.

To understand the relationship between drug targets and the molecular features in cells that influence drug synergy, we overlaid single-agent and combination biomarkers onto the previously described IntAct protein–protein interactome. We mapped 42.2% (633 out of 1,501) of features onto protein nodes; mapping was impossible for certain features such as clinical subtyping. We calculated the shortest finite network distance between each of the drug target and feature nodes for 582 and 124 unique combination and single-agent biomarkers, respectively (Extended Data Fig. 5a). Both types of biomarkers have a median shortest node distance of 3 (interactome diameter or maximum distance = 12); however, sensitivity biomarkers that were the drug target themselves (that is, a shortest distance of zero) were rarer for combinations (2.75%) than for single-agents (12.33%; Extended Data Fig. 5a). This was confirmed using Reactome<sup>18</sup>, an alternative interactome (Extended Data Fig. 5b), and randomly

shuffling biomarkers to simulate entirely false-positive associations eliminated the observation (Extended Data Fig. 5c for IntAct and Extended Data Fig. 5d for Reactome). These data are consistent with synergy being mediated through combined drug activity and indicate that drug combination biomarkers can be difficult to determine by single-agent activity alone.

Examples of combination biomarkers that are drug targets are high gene expression of *PARP1* in olaparib (PARP1/2 inhibitor) combinations, and a copy number gain of *CDK12*, *ERBB2* and *MED24* (feature: ‘gain:cnaPANCAN301’) as predictor of sensitivity to ERBB2-targeting combinations such as lapatinib (targeting EGFR and ERBB2) with vorinostat (a histone deacetylase inhibitor) in breast. Low expression of *NRAS* predicted response to dabrafenib (BRAF inhibitor) plus trametinib (MEK1/2 inhibitor) in breast, consistent with *NRAS* expression modulating BRAF inhibitor sensitivity<sup>19</sup>. This represents a biomarker one node away from a combination drug target (Fig. 3b). Mutation of *PIK3CA* predicted response to linsitinib (which targets IGF1R) + MK-2206 (AKT1/2 inhibitor) in a pan-tissue *KRAS*-mutant context, and is two nodes away from targets of both drugs (Fig. 3c).

Considering the combination–tissue pairs with more than three synergistic cell lines, we find that 164 out of 662 (24.8%) have at least one associated  $\Delta E_{\max}$  or  $\Delta IC_{50}$  biomarker (Fig. 3d, Supplementary Table 4). We found several examples in which the identified feature associated with combination response is closely associated with synergy. For instance, all seven breast cell lines synergistic for the combination of sapitinib (EGFR and ERBB2/3 inhibitor) and JQ1 (an inhibitor of BRD2, BRD3, BRD4 and BRDT) show a gain in *ERBB2* (Fig. 3e). Similarly, six out of nine breast cell lines that show synergy for MK-2206 (AKT1/2 inhibitor) and alpelisib (PI3K $\alpha$  inhibitor) have a mutation in *PTEN*. In a pan-tissue setting, *KRAS* mutation significantly associates with sensitivity to trametinib (MEK1/2 inhibitor) and MK-2206 (AKT1/2 inhibitor), and 74% of synergistic cell lines are *KRAS* mutants (Fig. 3f). These examples demonstrate that many synergistic combinations can be linked with a biomarker.

Our comprehensive analysis identified drug combination response biomarkers, including for many synergistic combinations, which could be used for patient stratification in pre-clinical and clinical follow-up. Combination biomarkers are more likely than single agents to be emergent properties arising from combinatorial drug activity in the context of signalling networks.

## Combinations in cancers with unmet need

We leveraged the number and molecular diversity of the cell lines to investigate synergy rate, biomarkers and clinical trials for combinations screened in three

populations with unmet clinical need: patients with basal-like breast cancer ( $n = 22$ ), MSS colon cancer ( $n = 31$ ) or *KRAS*-mutant colon cancer ( $n = 25$ ).

We compared combination synergy rates within each of these populations with the other cell lines from the same tissue (Fig. 4a, Extended Data Fig. 6a, b). Between 3% and 5% ( $n = 107$ ) of all combinations have synergy in at least 25% of cell lines from these populations (41 combinations for basal-like breast cancer, and 28 and 38 for MSS and *KRAS*-mutant colon cancer, respectively), with some having exquisite specificity of synergy in the population of interest. Of these 75 unique combinations, we identified 11 combinations with matching trials on clinicaltrials.gov for basal-like breast (10 trials) or MSS colon (1 trial) cancer (Fig. 4b, Supplementary Table 5). Cisplatin (a DNA crosslinker) combined with gemcitabine (a pyrimidine antimetabolite) or MK-1775 (WEE1 and PLK1 inhibitor; using MK-1775 as anchor) was highly synergistic in basal-like breast cancer (47% and 59% synergy rate, respectively) and both combinations are in clinical trials in clinically related triple-negative breast cancer (Fig. 4a). Synergy for cisplatin + gemcitabine was tested and robust in the validation screen (88% synergy overlap). Furthermore, several combinations showed repurposing potential: for instance, combined MK-1775 (WEE1 and PLK1 inhibitor) and irinotecan (TOP1 inhibitor) treatment, screened with camptothecin as the TOP1 inhibitor, had a 26.7% synergy rate in MSS colon cancer (versus 6.7% in microsatellite unstable (MSI)), is currently in a trial in rhabdomyosarcoma and blastomas (NCT02095132). Phase 1 safety studies of navitoclax (BCL2, BCL-XL and BCL-W inhibitor) paired with chemotherapeutics such as gemcitabine, docetaxel and paclitaxel are ongoing, all of which had high synergy rates in basal-like breast (63%, 41%, and 38%; Fig 4a), with navitoclax + gemcitabine, the only one of the three that was part of the validation screen, having robust synergy (100% overlap between screens).

**Fig. 4: Populations of unmet clinical need and validation of combined irinotecan and CHEK1 inhibitor treatment.**

 figure 4

**a**, Synergy rates of combination treatments for breast cancer, comparing basal-like ( $x$ -axis) against other PAM50 subtypes ( $y$ -axis). Dashed line indicates a 25% synergy rate.  $R$ , Pearson correlation coefficient. Combinations with biomarkers or clinical trials are indicated. **b**, Combinations with at least 25% synergy with biomarkers or ongoing trials. **c**, AZD7762 (CHEK1/2 inhibitor) and camptothecin (TOP1 inhibitor) show higher potency ( $\Delta\text{IC}_{50}$ ) in colon MSS cells. Replicates averaged and both combination anchor–library configurations pooled. Two-sided Welch's  $t$ -test. **d**, The response to combination treatment is CHEK1-specific. Activity of camptothecin combined with six CHEK inhibitors in 4 colon cell lines for 72 h. **e**, In most cases, combined TOP1 and CHEK1 inhibition produces cell death that is greater than the additive effect. CellTox green (CTOX) signal (in green calibrated units (GCU)) after 72 h of treatment with SN-38 (TOP1 inhibitor) and rabusertib (CHEK1 inhibitor). Mean of 3 or 4 biological replicates. Additive is defined as the sum of single-agent responses. Delta is observed response minus additive response. **f**, Inhibition of TOP1 and CHEK1 for 72 h induces caspase-dependent cell death in SW837 cells. CTOX and caspase 3/7 (Cas3/7) activity is shown as the mean of 3 biological replicates. PARP western blot is representative of three independent experiments (+, positive control; −, DMSO-only negative control); rabu, rabusertib; CCT, CCT241533. **g**, Rabusertib increases irinotecan response in vivo in colon cancer cells engrafted in NOD/SCID mice. Two-tailed unpaired Welch's  $t$ -test. **h**, Addition of rabusertib to irinotecan treatment

improves survival of mice. SNU-81 cells were engrafted in NOD/SCID mice; mice were treated with irinotecan ( $n = 10$  mice) or irinotecan + rabusertib ( $n = 4$ ) for 35 days and monitored for 42 days after treatment discontinued. Log-rank Mantel–Cox test;  $P$  value shown. **i**, Combined rabusertib and irinotecan treatment increases genotoxic stress. LS-1034 cells were treated as in **g**. Tumours were collected 72 h after start of treatment and stained for phospho-H2AX ( $n = 30$ ) and active caspase 3 (rabusertib,  $n = 10$ ; other groups,  $n = 15$ ). Data are mean  $\pm$  s.d. Two-tailed unpaired Welch's  $t$ -test. In box plots, the horizontal line shows the median, boxes extend across first and third quartiles, and whiskers extend to 1.5 $\times$  interquartile range.

#### Source data

A third or more of top-ranking combinations in populations of unmet need had at least one  $\Delta E_{\max}$  or  $\Delta IC_{50}$  biomarker, some of which were identified within the molecular basket that defines the population (Fig. **4b**, Supplementary Table **5**). For example, in the *KRAS*-mutant colon group, cell lines with loss of *ERCC3* were associated with sensitivity to linsitinib (IGF1R inhibitor) plus MK-2206 (AKT1/2 inhibitor) (Extended Data Fig. **6c**). Our data can identify specific combinations in populations of unmet need, provide support for ongoing clinical trials, and identify biomarkers and repurposing opportunities for combinations already in trials.

## Irinotecan and CHEK1i synergize in colon

One of the top synergistic combinations was camptothecin (TOP1 inhibitor) with AZD7762 (CHEK1/2 inhibitor). Camptothecin is an analogue of the standard-of-care chemotherapeutic irinotecan used to treat colon cancer, and CHEK1 inhibitors can potentiate responses of DNA-damaging compounds through abrogation of DNA damage-induced cell cycle arrest<sup>20,21,22</sup>. This combination yielded high synergy rates in MSS colon cancer cell lines (62.1% and 53.3% for both orientations), with significantly higher potency and efficacy in MSS cell lines than in MSI cell lines (Student's  $t$ -test,  $P < 0.005$ ; Fig. **4c**, Extended Data Fig. **6d**, Supplementary Table **5**). Furthermore, *KRAS*-mutant colon cell lines showed high synergy rates for this combination (46% and 48%) and *KRAS*–*TP53* double-mutant cell lines had significantly stronger combination responses than *KRAS* single-mutant cell lines (Extended Data Fig. **6e**, Supplementary Table **5**). Thus, we identified two potential patient populations, MSS and *KRAS*–*TP53* double-mutant colon cells, showing notable benefit from inhibition of both CHEK1/2 (CHEKi) and TOP1 (TOP1i).

We next combined camptothecin with six CHEK1/2 inhibitors with different selectivity. CHEK1-selective inhibitors SAR-020106 and rabusertib produced large shifts in potency (median  $\Delta IC_{50}$ : 8.5- to 10.5-fold shift) and efficacy (median  $\Delta E_{\max}$ : 0.22–0.24) in combination with camptothecin in 4 cell lines, whereas the CHEK2-

selective inhibitor CCT-241533 did not (Fig. 4d). Combining SN-38, the active metabolite of the TOP1 inhibitor irinotecan, with small interfering RNA (siRNA) against CHEK1, but not CHEK2, resulted in a synergistic viability reduction (Extended Data Fig. 7a–d), and at least sevenfold reduction in the IC<sub>50</sub> of SN-38 (Extended Data Fig. 7e). Our results indicate that combination effects of TOP1i + CHEKi are primarily mediated through inhibition of CHEK1. This is corroborated by reports of the potentiating effect of CHEK1 inhibition, but not CHEK2 inhibition, with DNA-damaging agents such as topoisomerase 1 inhibitors<sup>23</sup>.

In colony formation assays, combining low concentrations of SN-38 with rabusertib (CHEK1 inhibitor) resulted in fewer colonies and increased cell death (Fig. 4e, Extended Data Fig. 7f–i) than either drug alone, or when combining SN-38 with CCT241533 (CHEK2). Cell death effects of SN-38 + rabusertib surpassed an additive response for many colon cell lines (Fig. 4e), particularly in cell lines with weak to moderate response to SN-38 alone, consistent with CHEK1 inhibition potentiating the effect of TOP1 inhibition. The combination effects ranged from less than additive to robust potentiation, with all MSS and most KRAS–TP53 double-mutant cell lines showing at least additive response (Fig. 4e). The combination induced activation of the apoptosis markers caspase 3/7 and PARP cleavage (Fig. 4f, Extended Data Fig. 7g,i; For gel source data, see Supplementary Fig. 1).

We engrafted three colon cancer cell lines (LS-1034, SW837 and SNU-81) in NOD/SCID mice and treated them for 24–35 days with irinotecan (TOP1 inhibitor), rabusertib (CHEK1 inhibitor), or with a combination of the two drugs. In LS-1034 and SW837, which showed more cell death with combined TOP1i and CHEK1 inhibition than SNU-81 in vitro (Fig. 4e), the effect of the combination therapy on end-of-treatment tumour volumes and on tumour growth inhibition over time was more pronounced than that for irinotecan alone (Welch's *t*-test,  $P < 0.05$ ) (Fig. 4g, Extended Data Fig. 8a). In SNU-81, although the response to combination therapy was more similar to treatment with irinotecan alone, the resumption of tumour growth after drug withdrawal was delayed in mice treated with the combination compared to those treated with irinotecan alone (log-rank Mantel–Cox test; end point 750 mm<sup>3</sup>), suggesting a fitness disadvantage (Fig. 4h). Combination treatment led to more DNA double strand breaks (phospho-H2AX positive cells), less proliferative and more apoptotic tumour cells than in irinotecan-treated LS-1034 tumours 72 h after treatment start (Fig. 4i; Extended Data Fig. 8b).

These data validated combined TOP1 and CHEK1 inhibition as a potent combination in MSS and KRAS–TP53 double-mutant colon cancer cells, and demonstrate the potential for follow-up of other synergistic drug combinations identified here.

## Discussion

The scale and breadth of our study provides insights into combination response. We establish that evaluating combination potency and efficacy are complementary, a recently introduced concept<sup>10</sup>, and could identify combinations leading to dose reduction, improved efficacy or both, relative to single agents. We demonstrate that synergy is rare, as has been described<sup>6,7</sup>, that it varies within tissues and between molecular backgrounds, and that combinations of targeted drugs are more likely to synergise than combinations involving chemotherapy. This indicates that combinations of targeted agents in molecularly defined patient populations are most likely to be synergistic. We identified many highly synergistic combinations, notably for cancers of unmet clinical need. We recommend detailed validation of promising drug combinations reported here. As proof of concept, we validated in vitro and in vivo a combined irinotecan and CHEK1 inhibition. Although combinations of CHEK1i with DNA-damaging agents have been linked to *TP53*- and *KRAS*-mutant cancer<sup>24,25</sup>, to our knowledge, this is the first report of notable activity in MSS and *KRAS*–*TP53* double-mutant colon cancer. Clinical trials combining CHEKi with chemotherapy show variable toxicity and anti-tumour activity, particularly for unstratified patient populations. Since irinotecan is approved for the treatment of colon cancer, and rabusertib (a CHEK1-selective inhibitor) has an acceptable safety profile in phase 1 trials<sup>26</sup>, our data indicate that this combination—with appropriate consideration of potential toxicity—could be particularly effective for patients with MSS or *KRAS*–*TP53* double-mutant colon cancer.

The data presented here are a rich resource and augment existing genomic, transcriptomic and functional datasets for cell lines available as part of the Cancer Dependency Map<sup>27</sup>. Future screens in additional cancer types, focused studies using more complex culture models, and screening of higher-order combinations, will support and extend our observations. The testing of combinations in non-cancer cell lines may help to estimate clinical toxicity. Our findings that drugs with weak single-agent activity, and those separated by one or two nodes in a protein–protein interaction network are most likely to yield a synergistic interaction could improve the design of future screens. Similarly, our data could improve computational approaches, which currently lack training datasets, for predicting effective drug combinations in different contexts<sup>4,28,29</sup>. In conclusion, the data and analyses presented here are fertile ground for catalysing new discoveries and a basis for effective rational combinatorial therapies.

## Methods

### Statistics

Statistical tests are two-sided Welch's *t*-tests unless otherwise specified. Enrichment analyses were performed using the phyper function for hypergeometric tests in R. Multiple testing correction was performed based on the Benjamini–Hochberg method. Biomarker analysis was performed using GDSCTools as described below. Box plots depict the median value as the centre bar, first and third quartiles as box boundaries, and whiskers extending to either first quartile minus  $1.5 \times$  the inter-quartile range (lower boundary), or third quartile plus  $1.5 \times$  the inter-quartile range (upper boundary). Points beyond this region are individually plotted.

## Cell lines

Cell lines were acquired from commercial cell banks. All cells were grown in RPMI medium (supplemented with 10% FBS, 1% penicillin/streptomycin, 1% glucose, 1 mM sodium pyruvate) or DMEM/F12 medium (supplemented with 10% FBS, 1% penicillin/streptomycin) (Supplementary Table 2) at 37 °C in a humidified atmosphere at 5% CO<sub>2</sub>. To prevent cross-contamination or misidentification, all cell lines were profiled using a panel of 94 single nucleotide polymorphisms (Fluidigm, 96.96 Dynamic Array IFC). Short tandem repeat (STR) analysis was also performed, and cell line profiles were matched to those generated by the cell line repository. All cell lines are routinely tested for mycoplasma and are negative for mycoplasma. Further information on the cell lines used in this study, including their source and molecular profiling datasets can be found in Supplementary Table 2 and in the Cell Model Passports database<sup>30</sup> (<https://cellmodelpassports.sanger.ac.uk>).

## Compounds

Compounds were sourced from commercial vendors (Supplementary Table 1). DMSO-solubilized compounds were stored at room temperature in low humidity (<12% relative humidity), low oxygen (<2.5%) environment using storage pods (Roylan Developments). Water-solubilized compounds were maintained at 4 °C. For 8 compounds their identities and purity were confirmed by UHPLC-MS. Identity was confirmed by mass spectrometry (6550 iFunnel Q-TOF LC/MS, Agilent Technologies) using electrospray ionization in positive and/or negative modes. Anchor and library concentrations were drug- and tissue-specific and determined using a two-step process. First, drug concentrations were selected based on primary literature, in vitro data of minimum concentrations inhibiting relevant target activity and viability<sup>31</sup>, clinical data indicating achievable human plasma concentrations, or where known concentrations that induce sensitivity in a biomarker positive cell line. Additionally, a pilot screen, testing a 1,000-fold concentration range of each drug in 9–13 cell lines per tissue (breast: 13, colon: 9, pancreas: 12), was performed and concentrations optimized to give a range of sensitivities across the cell lines. Anchor drugs were screened at two fixed concentrations with a 2-, 4- or 10-fold difference between them

to give moderate activity (50–90% viability) across the cell lines within each cancer type. Screening concentrations (Supplementary Table 1) typically did not exceed 10  $\mu\text{M}$  and were in the range of human plasma exposures achievable in patients<sup>32</sup>. Library drugs were screened at seven concentrations spanning a 1,000-fold range with a non-equidistant  $\log_2$  design of four 4-fold steps followed by two 2-fold dilution steps starting at the lowest used concentration. The use of this design was based on the observation that higher concentrations were most informative and would benefit from denser profiling. As an alternative to  $\mu\text{M}$  concentration ranges, drug concentrations and  $\text{IC}_{50}$  values can be visualized on a standardized  $\log_2$  scale, with 9 being equivalent to the highest screened concentration. Each screening plate contained five replicates of the anchor alone (high and low concentrations) and four replicates of the library alone (full dose response). A single replicate of the combination dose response was performed in the primary screen.

## Screening

Cells were transferred into 1,536-well plates in 7.5  $\mu\text{l}$  of their respective growth medium using XRD384 (FluidX) dispensers. The seeding density was optimised prior to screening to ensure that each cell line was in the exponential growth phase at the end of the assay. For this, six seeding densities with a two-fold dilution step were each dispensed into 224 wells of a single 1,536-well assay plate (XRD384 (FluidX) dispenser) and cells were incubated for 96 h. Cell number was quantified using CellTiter-Glo 2.0 (Promega). The maximum density tested varied based on cell type, typically 5,000 cells per well for suspension cells and 1,250 cells per well for adherent cells (Supplementary Table 1). Assay plates were incubated at 37 °C in a humidified atmosphere at 5%  $\text{CO}_2$  for 24 h then dosed with the test compounds using an Echo555 (Labcyte). Final DMSO concentration was typically 0.2%. Following dosing with compounds assay plates were incubated, and the drug treatment duration was 72 h. To monitor cell growth over the duration of drug treatment, a parallel undrugged control plate was assayed at the time of drug treatment and referred to as a ‘day = 1’ plate. This was repeated each time that a cell line was screened. To measure cell viability, 2.5  $\mu\text{l}$  of CellTiter-Glo 2.0 (Promega) was added to each well and incubated at room temperature for 10 min; quantification of luminescence was performed using a Paradigm (Molecular Devices) plate reader.

## Assay plate quality control

All screening plates contained negative control wells (untreated wells,  $n = 6$ ; DMSO-treated wells,  $n = 126$ ) and positive control wells (blanks—that is, medium-only wells,  $n = 28$ ; staurosporine-treated wells,  $n = 20$ ; and MG-132 treated wells,  $n = 20$ ) distributed across the plate. We used these positive and negative control wells to test

whether the plates meet defined quality control criteria. A maximum threshold of 0.18 was applied to the coefficient of variation (CV) of the DMSO-treated negative controls ( $CV = \sigma_N / \mu_N$ , where  $\sigma_N$  is the s.d. of the negative control and  $\mu_N$  is the mean of the negative control). Using the DMSO-treated negative control (NC1) and the two positive controls (PC1 and PC2), we determined Z-factors (also known as  $Z'$ ; Z-factor =  $1 - 3 \times (\sigma_P + \sigma_N) / (|\mu_P - \mu_N|)$ , where  $\sigma_N$  and  $\sigma_P$  are the s.d. of the negative and positive controls, respectively, and  $\mu_N$  and  $\mu_P$  are the mean of the negative and positive controls, respectively). The Z-factors were calculated for all plates that indicate sensitivity of the cell lines to the positive control (ratio of NC1:PC  $\geq 4$ ). In case a cell line is insensitive to both positive control drugs, the Z-factors were calculated based on blank wells instead. Z-factors were required to exceed a minimum threshold of 0.3 for individual plates and a mean of 0.4 across all plates within a screening set. Where a cell line was sensitive to both positive controls, it had to pass Z-factor thresholds for both positive controls. Plates that did not meet these requirements were excluded from the study. Overall, 3,106 (>70%) of 1,536-well microtitre screening plates passed coefficient of variation and Z-factor thresholds. Wherever possible, failed plates were repeated, leading to dataset completeness of more than 96% for all three tissues (breast: 96.5%, colon: 99.8% and pancreas: 99%).

## Curve fitting

For each plate, the raw fluorescent intensity values were normalised to a relative viability scale (ranging from 0 to 1) using the blank ( $B$ ) and negative control (NC) values (viability = (Fluorescence of treated cells –  $B$ )/(NC –  $B$ )). Anchor viability was determined from the mean across the five replicate wells screened on each plate. All library drug dose responses were fitted as a two-parameter sigmoid function<sup>33</sup>. The dose–response curves for the combinations were fitted similarly, but with two notable differences: (1) the cell line parameters were obtained from the library drug fits; (2) the maximum viability was capped at the anchor viability (rather than from 0 to 1). We use the 50% (inflection) point of the sigmoidal curve between zero and the anchor viability for both the expected Bliss and the observed combination. We extended the model to nest each replicate within the drug or cell line to obtain stable estimates from the replicate experiments. To assess the quality of the fits, we computed the root mean square error (RMSE) and excluded curves with RMSE > 0.2 (equalling 1.5% of measurements). The  $E_{\max}$  and the  $IC_{50}$  are based on the fitted curves.  $E_{\max}$  is reported at the highest tested concentration for the drug.

## Classifying synergy

To detect synergy we compared observed combination responses to expected combination responses. For the latter, we used Bliss independence<sup>9</sup> of the response to

the anchor and the library drug alone. Conceptually, every point on the Bliss dose response curve is defined as the product between the anchor viability and the corresponding point on the library dose response curve. Shifts in potency ( $\Delta\text{IC}_{50}$ ) and in efficacy ( $\Delta E_{\max}$ ) were calculated as the difference between the observed combination response and expected Bliss ( $\Delta\text{IC}_{50} = \text{Bliss IC}_{50} - \text{combination IC}_{50}$ , and  $\Delta E_{\max} = \text{Bliss } E_{\max} - \text{combination } E_{\max}$ ).  $\Delta\text{IC}_{50}$  is reported on a  $\log_2$  scale.

A given measurement was synergistic if the combination  $\text{IC}_{50}$  was less than twice the highest screened library concentration and either the  $\Delta\text{IC}_{50}$  or the  $\Delta E_{\max}$  was above a specific threshold:  $\Delta\text{IC}_{50} \geq 3$  ( $2^3$  is equivalent to an 8-fold shift in  $\text{IC}_{50}$ ) or the  $\Delta E_{\max} \geq 0.2$  (20% shift in viability). Replicate measurements of ‘anchor–library–cell line’ tuples were summarized as synergistic if half or more of the replicate measurements showed synergy. To summarize both anchor concentrations, we considered a ‘combination–cell line’ pair as synergistic if synergy was observed at either anchor concentration.

## Reproducibility

To assess the reproducibility within a screen, we generated 2–18 biological replicates for 4–5 cell lines per tissue (breast: 5 (AU565, BT-474, CAL-85-1, HCC1937, MFM-223); colon: 4 (HCT-15, HT-29, SK-CO-1, SW620); pancreas: 5 (KP-1N, KP-4, MZ1-PC, PA-TU-8988T, SUIT-2)). Single-agent and combination responses were averaged across technical replicates (typically 3 per biological replicate) and correlated (Pearson correlation coefficient; minimum of 322 biological replicate pairs per ‘metric-tissue’ pair).

To assess the reproducibility of the screen, we rescreened a subset of combinations in each tissue (breast: 51 combinations in 34 cell lines; colon: 45 combinations in 37 cell lines; pancreas: 59 combinations in 29 cell lines; Supplementary Table 2). Drug combination responses were averaged across replicates within a screen and key metrics of single-agent and combination response were correlated between the two screens (Pearson correlation coefficient). To determine the quality of synergy calls, the original screen was considered as ground truth and numbers of true positive (TP), false positive (FP), true negative (TN) and false negative (FN) synergistic combination–cell line pairs were calculated. These were used to calculate *F*-score ( $F\text{-score} = \text{TP}/(\text{TP} + 0.5 \times (\text{FP} + \text{FN}))$ ), recall (recall =  $\text{TP}/(\text{TP} + \text{FN})$ ), and precision (precision =  $\text{TP}/(\text{TP} + \text{FP})$ ) per tissue. To investigate the strength of effects of  $\Delta E_{\max}$  and  $\Delta\text{IC}_{50}$  of FP and FN measurements, the distance to  $\Delta E_{\max}$  and  $\Delta\text{IC}_{50}$  synergy thresholds was calculated for each ‘anchor concentration–library–cell line’ tuple based on combination responses averaged across replicates ( $n = 9,570$  tuples).

## Biomarker analysis

Matrices of single-agent (library IC<sub>50</sub>) and combination response (combination E<sub>max</sub>, ΔIC<sub>50</sub>, ΔE<sub>max</sub>) metrics were used as input for GDSCTools ANOVAs<sup>15</sup>. To obtain a single combination E<sub>max</sub>, ΔIC<sub>50</sub> and ΔE<sub>max</sub> value per cell line–combination pair, responses were averaged across replicates for each anchor concentration–library–cell line tuple and the combination metrics were compared for the two anchor concentrations: the larger of the two ΔIC<sub>50</sub> and ΔE<sub>max</sub> values and the smaller of the two combination E<sub>max</sub> values were used for biomarker discovery in order to capture the largest effects of the combination. A range of binary feature files were used, including multi-omics binary event matrices (MOBEMs) composed of genes known to be mutated, amplified or homozygously deleted in human cancers<sup>5</sup> (number of features = 1,073), CELLector signatures<sup>34</sup> ( $n = 227$  for breast,  $n = 261$  for colon), RNA-seq gene expression<sup>35</sup> ( $n = 1,184$ ; original dataset accession number E-MTAB-3983), CRIS<sup>36</sup> and PAM50<sup>37,38</sup> classifications. Gene expression was limited to a curated panel of genes composed of targets of the drugs used, additional members of the *BCL2* family and apoptosis-associated genes<sup>39</sup>, genes annotated as clinically relevant for cancer<sup>40</sup>, and genes whose mutations were listed as features in the MOBEMs<sup>5,40</sup> and CELLector<sup>5,34,40</sup> feature files. Continuous values of gene expression were binarized by z-scoring each variable across the subset of cell lines used for the molecular context tested, and substituting a z-score  $\geq 2$  for a binary value representing that feature being elevated (that is, ‘Gene\_up’), and a z-score  $\leq -2$  for a binary feature representing that feature being decreased (that is, ‘Gene\_down’). Overall significance thresholds were  $P \leq 0.001$  and FDR  $\leq 5\%$ .

## Network overlays

An interactome of binary, undirected interactions was built in the iGraph R package (<https://cran.r-project.org/web/packages/igraph/citation.html>) using the Reactome<sup>18</sup> human interactions file (accessed April 2021), and all human interactions reported in IntAct<sup>12</sup> (accessed July 2021). All non-protein nodes and duplicated interactions were removed, resulting in a non-directed network of 5,556 Uniprot protein nodes and 25,731 edges for the Reactome interactome. For the IntAct interactome, an evidence filter of 0.5 was applied, and all non-protein nodes and duplicate interactions were removed, resulting in a non-directed network of 14,431 protein nodes and 110,118 edges. Drug targets and biomarkers features were manually mapped to their Uniprot proteome identifiers (UPID), with overall 57 out of 66 (86.3%) drug target profiles being mapped to one or more UPIDs, and 633 out of 1,501 (42.2%) biomarker features being mapped for one or more UPIDs. UPID mapping was not possible for chemotherapeutics, PAM50, CRIS, and not done for methylation sites not associated

with a cancer driver gene. A distance matrix between all nodes was calculated using iGraph: infinite values were reported for nodes that did not exist in the same network. When calculating the shortest distance between drug targets or drug targets and biomarkers, distances were calculated for all target-target or target-biomarker pairs and the smallest distance was reported. For example, for a drug with two targets combined with a drug with three targets, the shortest of six target-target distances would be reported. To simulate false positive biomarker associations, the biomarker features used in the genuine distance plot were randomly shuffled without replacement, before re-calculating the shortest distance between the new, ‘false’ biomarker and drug targets.

## Clinical trials

Clinical trials data were extracted from the API at <https://clinicaltrials.gov/> (accessed March 2021) using an R script and searches in the format ‘drug1 + drug2 + cancer + tissue’. Obtained lists of trials were manually curated to ensure that drugs were exact matches and to remove trials using radiotherapy alongside drug combination treatment. Searches were limited to 81 combinations with  $\geq 25\%$  synergy in populations of clinical need.

## Specificity of CHEK inhibition

To test CHEK specificity we seeded SW620, SW837, SNU-81 or LS-1034 cells in 96-well plates (770–2,750 cells per well) and treated them with camptothecin (anchor, 0.025  $\mu\text{M}$ ) in combination with six CHEK inhibitors (libraries, all dosed at 1  $\mu\text{M}$  highest used concentration unless indicated): AZD7762 (CHEK1, CHEK2), prexasertib (CHEK1, CHEK2), MK-8776 (CHEK1, CHEK2, CDK2), SAR-020106 (CHEK1), rabusertib (CHEK1) and CCT241533 (CHEK2; 2  $\mu\text{M}$ ). After 96 h of drug treatment viability was measured with CellTiter-Glo 2.0 (CTG; Promega). Drug response curves were fitted as described above.

For siRNA experiments, SW837 and SNU-81 cells (8,000 and 16,000 cells per well, respectively) were reverse transfected with siRNAs of a non-targeting pool as negative control (siNT; Dharmacon, D-001810-10-05), polo-like kinase 1 (PLK1) pool as positive control (Dharmacon, L-003290-00-0010), CHEK1 pool (Dharmacon, L-003255-00-0005) or CHEK1 individual siRNAs (LQ-003255-00-0005), and CHEK2 pool (Dharmacon, L-003256-00-0005) using lipofectamine RNAiMax (Thermofisher). After 30h, 0.025  $\mu\text{M}$  or a dose range of 0.001–9  $\mu\text{M}$  SN-38 or DMSO were added and viability was measured 72 h later with CTG. Signal was normalised to siNT+DMSO controls. Statistical significance between conditions was tested using a two-sided Welch’s *t*-test.

## **Real time cell death and caspase-3/7 activity**

Cells were seeded in 96-well plates (typically 5,000–16,000 cells per well). After 24 h drugs (0.125 µM staurosporine (positive control), 0.025 µM SN-38, 0.75 µM rabusertib, 0.75 µM CCT241533) or DMSO and real-time fluorescent reagents for detection of cell death (CellTox Green; 1:1,000; Promega) or caspase-3/7 activity (Incucyte Caspase-3/7 Red; 1:1,000; Essen Bioscience) were added. Pictures were recorded every 2 h for 96 h using an Incucyte (Essen Bioscience). Recorded fluorescent signals were measured as mean intensity per cell area and normalised to time 0 h.

## **Colony formation**

Cells were seeded in 6-well plates at 50,000 cells per well. Drugs (0.1 nM SN-38, 0.5 µM rabusertib, 0.5 µM CCT241533) or DMSO were added on day 1 and were refreshed through medium change on day 8. 14 days after drug treatment started the cells were fixed in 4% paraformaldehyde (Sigma-Aldrich) in PBS for 10 min at room temperature, and then stained with Giemsa (10%; Sigma-Aldrich) for at least 30 min at room temperature.

## **Western blot**

SW837 (1 million) or SNU-81 (1.5 million) cells were seeded in 10 cm dishes and treated with drugs (0.025 nM SN-38, 1.5 µM rabusertib, 1.5 µM CCT241533, 2 µM MG-132 (positive control)) or DMSO the day after. After 72 h, live and dead cells were collected and lysed in RIPA buffer (Sigma-Aldrich) supplemented with 1 mM DTT (Cayman Chemicals) and protease and phosphatase inhibitors (Roche). Total protein content was determined using Bradford reagent (ThermoFisher) and around 20 µg of lysate were loaded onto a 4–12% Bis-Tris gel (Invitrogen) for SDS-PAGE followed by protein transfer from the gel onto a PVDF membrane. Membranes were blocked in 5% milk (in TBST) and incubated overnight with the appropriate antibodies. Blots were washed in TBST and incubated with secondary antibody for 1 h at room temperature. Blots were washed in TBST before the signal was enhanced with Super Signal Dura and visualised. The following primary antibodies were used for immunoblot analysis: anti-PARP (Cell Signaling Technologies, 9542, 1:1,000; rabbit), and anti-β-tubulin (Sigma-Aldrich, T4026, 1:5,000; mouse) as loading control.

For experiments with knockdown of *CHEK1* and *CHEK2*, SW837 or SNU-81 cells were reverse transfected with siNT, siCHEK1 or siCHEK2 as described above. Cells were collected 72 h after transfection and lysed in RIPA buffer (Sigma-Aldrich, R0278) and protein concentrations were determined using the BCA assay (Novagen, 71285-3) as per manufacturer's instructions. SDS-PAGE and western blots were

conducted as described above and the following primary antibodies were used for immunoblot analysis: anti-CHEK1 (Santa Cruz Biotechnology, sc-8408, 1:200; mouse), anti-CHEK2 (Cell Signaling Technologies, D9C6, 1:1,000; rabbit), and anti- $\beta$ -actin (Abcam, ab6276, 1:5,000; mouse) as a loading control. Anti-Mouse IgG (GE Healthcare, NA931) and anti-rabbit (GE Healthcare, NA934; 1:2,000) HRP-linked secondary antibodies were used as secondary antibodies. PageRuler Plus Prestained Protein Ladder, 10–250 kDa (ThermoFisher, 26620) was used as a molecular weight marker.

## In vivo tumour xenograft studies

A total of  $4.5 \times 10^6$  LS-1034 cells,  $5 \times 10^6$  SW837 cells or  $2.5 \times 10^6$  SNU-81 cells in 30% Matrigel were injected subcutaneously into the right flank of male and female 6-week-old NOD/SCID mice. Once tumours reached an average volume of approximately 300–400 mm<sup>3</sup>, mice were randomized into treatment arms, with  $n = 12$  (irinotecan and irinotecan + rabusertib) or  $n = 6$  (vehicle and rabusertib) per group. Rabusertib was administered orally, 200 mg kg<sup>-1</sup> daily (vehicle: 16.66% Captisol; CyDex, in 25 mM phosphate buffer, pH 4); irinotecan was administered intraperitoneally, 25 mg kg<sup>-1</sup> twice a week (vehicle: physiological saline). Tumour size was evaluated once weekly by calliper measurements, and the approximate volume of the mass was calculated using the formula  $(4\pi/3) \times (d/2)^2 \times (D/2)$ , where  $d$  is the minor tumour axis and  $D$  is the major tumour axis. Results were considered interpretable when a minimum of 4 mice per treatment group reached the prespecified endpoints (at least 3 weeks on therapy or development of tumours with average volumes larger than 2,000 mm<sup>3</sup> within each treatment group in trials aimed to assess drug efficacy; at least 3 weeks after treatment cessation or development of individual tumours with volumes larger than 750 mm<sup>3</sup> in survival experiments aimed to assess tumour control by therapy). A major tumour axis of 20 mm is the endpoint permitted by the Italian Ministry of Health in authorization no. 806/2016-PR, in accordance with national guidelines and regulations. This endpoint was not exceeded in any experiment. Operators were blinded during measurements. In vivo procedures and related biobanking data were managed using the Laboratory Assistant Suite<sup>41</sup>. All animal procedures were approved by the Institutional Animal Care and Use Committee of the Candiolo Cancer Institute and by the Italian Ministry of Health.

Statistical significance for tumour volume changes during treatment was calculated using a two-way ANOVA. For endpoint comparisons, statistical analysis was performed by two-tailed unpaired Welch's *t*-test. Statistical analyses in the survival experiments were performed by log-rank (Mantel–Cox) test. For all tests, the level of statistical significance was set at  $P < 0.05$ . Graphs were generated and statistical analyses were performed using the GraphPad Prism (v9.0) statistical package.

## Immunohistochemistry

Morphometric quantitation of Ki67, active caspase-3, and phospho-H2AX immunoreactivity was performed in xenografts from mice treated with vehicle (until tumours reached an average volume of 1,500 mm<sup>3</sup>) or the indicated compounds (after 72 h). Tumours ( $n = 1–3$  for each treatment arm) were explanted and subjected to histological quality check and immunohistochemical analysis with the following antibodies: mouse anti-Ki-67(MIB-1) (Dako, GA626, 1:100), rabbit anti-cleaved caspase-3 (Asp175) (Cell Signaling, 9661, 1:200) and rabbit anti-phospho-histone H2AX (Ser139) (20E3) (Cell Signaling, 9718, 1:400). After incubation with secondary antibodies, immunoreactivities were revealed by DAB chromogen (Dako). Images were captured with the Leica LAS EZ software using a Leica DM LB microscope. Morphometric quantitation was performed by ImageJ software using spectral image segmentation. Software outputs were manually verified by visual inspection of digital images. Each dot represents the value measured in one optical field (40 $\times$  for Ki67 and phospho-H2AX; 20 $\times$  for active caspase-3), with 2–10 optical fields (Ki67 and phospho-H2AX) and 3–5 optical fields (active caspase-3) per tumour depending on the extent of section area ( $n = 12–30$  for Ki67 and phospho-H2AX;  $n = 8–15$  for active caspase-3). The plots show mean  $\pm$  s.d. Statistical analysis by two-tailed unpaired Welch's *t*-test.

## Reporting summary

Further information on research design is available in the [Nature Research Reporting Summary](#) linked to this paper.

## Data availability

All drug sensitivity data generated for this study are included in this published article (and its supplementary information files) or available in a Figshare repository (<https://doi.org/10.6084/m9.figshare.16895371>, <https://doi.org/10.6084/m9.figshare.16843600> and <https://doi.org/10.6084/m9.figshare.16843597>) and GDSC Combinations database (<https://gdsc-combinations.depmap.sanger.ac.uk/>). The cell line genomic datasets are available from the Cell Model Passports database (<http://cellmodelpassports.sanger.ac.uk/>). The following databases were accessed for this study: IntAct database (<http://www.ebi.ac.uk/intact>), the Reactome database (<https://reactome.org/>), the Cell Model Passports database (<http://cellmodelpassports.sanger.ac.uk/>) and the GDSC database (<http://www.cancerrxgene.org/>). Users have a non-exclusive, non-transferable right to use data files for internal proprietary research and educational purposes, including

target, biomarker and drug discovery. Excluded from this licence are use of the data (in whole or any significant part) for resale either alone or in combination with additional data/product offerings, or for provision of commercial services. [Source data](#) are provided with this paper.

## References

1. Al-Lazikani, B., Banerji, U. & Workman, P. Combinatorial drug therapy for cancer in the post-genomic era. *Nat. Biotechnol.* **30**, 679–692 (2012).
2. Lopez, J. S. & Banerji, U. Combine and conquer: challenges for targeted therapy combinations in early phase trials. *Nat. Rev. Clin. Oncol.* **14**, 57–66 (2017).
3. Kopetz, S. et al. Encorafenib, binimetinib, and cetuximab in BRAF V600E-mutated colorectal cancer. *N. Engl. J. Med.* **381**, 1632–1643 (2019).
4. Menden, M. P. et al. Community assessment to advance computational prediction of cancer drug combinations in a pharmacogenomic screen. *Nat. Commun.* **10**, 2674 (2019).
5. Iorio, F. et al. A landscape of pharmacogenomic interactions in cancer. *Cell* **166**, 740–754 (2016).
6. O’Neil, J. et al. An unbiased oncology compound screen to identify novel combination strategies. *Mol. Cancer Ther.* **15**, 1155–1162 (2016).
7. Flobak, Å. et al. A high-throughput drug combination screen of targeted small molecule inhibitors in cancer cell lines. *Sci. Data* **6**, 237 (2019).
8. Holbeck, S. L. et al. The National Cancer Institute ALMANAC: a comprehensive screening resource for the detection of anticancer drug pairs with enhanced therapeutic activity. *Cancer Res.* **77**, 3564–3576 (2017).
9. Bliss, C. I. The toxicity of poisons applied jointly 1. *Ann. Appl. Biol.* **26**, 585–615 (1939).
10. Meyer, C. T. et al. Quantifying drug combination synergy along potency and efficacy axes. *Cell Syst.* **8**, 97–108.e16 (2019).
11. Montero, J. & Letai, A. Why do BCL-2 inhibitors work and where should we use them in the clinic? *Cell Death Differ.* **25**, 56–64 (2018).

12. Orchard, S. et al. The MIntAct project-IntAct as a common curation platform for 11 molecular interaction databases. *Nucleic Acids Res.* **42**, D358–D363 (2014).
13. Shi, Y., Yan, H., Frost, P., Gera, J. & Lichtenstein, A. Mammalian target of rapamycin inhibitors activate the AKT kinase in multiple myeloma cells by up-regulating the insulin-like growth factor receptor/insulin receptor substrate-1/phosphatidylinositol 3-kinase cascade. *Mol. Cancer Ther.* **4**, 1533–1540 (2005).
14. Tolcher, A. W., Peng, W. & Calvo, E. Rational approaches for combination therapy strategies targeting the MAP kinase pathway in solid tumors. *Mol. Cancer Ther.* **17**, 3–16 (2018).
15. Cokelaer, T. et al. GDSCTools for mining pharmacogenomic interactions in cancer. *Bioinformatics* **34**, 1226–1228 (2018).
16. Prahallad, A. et al. Unresponsiveness of colon cancer to BRAF(V600E) inhibition through feedback activation of EGFR. *Nature* **483**, 100–103 (2012).
17. Tabernero, J. et al. Encorafenib plus cetuximab as a new standard of care for previously treated BRAF V600E-mutant metastatic colorectal cancer: updated survival results and subgroup analyses from the BEACON study. *J. Clin. Oncol.* **39**, 273–284 (2021).
18. Jassal, B. et al. The reactome pathway knowledgebase. *Nucleic Acids Res.* **48**, D498–D503 (2020).
19. Lidsky, M. et al. Mitogen-activated protein kinase (MAPK) hyperactivation and enhanced NRAS expression drive acquired vemurafenib resistance in V600E BRAF melanoma cells. *J. Biol. Chem.* **289**, 27714–27726 (2014).
20. Zabludoff, S. D. et al. AZD7762, a novel checkpoint kinase inhibitor, drives checkpoint abrogation and potentiates DNA-targeted therapies. *Mol. Cancer Ther.* **7**, 2955–2966 (2008).
21. Tse, A. N. et al. CHIR-124, a novel potent inhibitor of Chk1, potentiates the cytotoxicity of topoisomerase I poisons in vitro and in vivo. *Clin. Cancer Res.* **13**, 591–602 (2007).
22. Walton, M. I. et al. The preclinical pharmacology and therapeutic activity of the novel CHK1 inhibitor SAR-020106. *Mol. Cancer Ther.* **9**, 89–100 (2010).
23. Garrett, M. D. & Collins, I. Anticancer therapy with checkpoint inhibitors: what, where and when? *Trends Pharmacol. Sci.* **32**, 308–316 (2011).

24. Lee, H. J., Cao, Y., Pham, V., Blackwood, E. & Wilson, C. Ras-MEK signaling mediates a critical Chk1-dependent DNA damage response in cancer cells. *Mol. Cancer*. **16**, 694–704 (2017).
25. Shao, R. G. et al. Abrogation of an S-phase checkpoint and potentiation of camptothecin cytotoxicity by 7-hydroxystaurosporine (UCN-01) in human cancer cell lines, possibly influenced by p53 function. *Cancer Res.* **57**, 4029–4035 (1997).
26. Weiss, G. J. et al. Phase I dose-escalation study to examine the safety and tolerability of LY2603618, a checkpoint 1 kinase inhibitor, administered 1 day after pemetrexed 500 mg/m<sup>2</sup> every 21 days in patients with cancer. *Invest. New Drugs* **31**, 136–144 (2013).
27. Boehm, J. S. et al. Cancer research needs a better map. *Nature* **589**, 514–516 (2021).
28. Sidorov, P., Naulaerts, S., Ariey-Bonnet, J., Pasquier, E. & Ballester, P. J. Predicting synergism of cancer drug combinations using NCI-ALMANAC data. *Front. Chem.* **7**, 509 (2019).
29. Preuer, K. et al. DeepSynergy: predicting anti-cancer drug synergy with deep learning. *Bioinformatics* **34**, 1538–1546 (2018).
30. van der Meer, D. et al. Cell Model Passports—a hub for clinical, genetic and functional datasets of preclinical cancer models. *Nucleic Acids Res.* **47**, D923–D929 (2019).
31. Yang, W. et al. Genomics of Drug Sensitivity in Cancer (GDSC): a resource for therapeutic biomarker discovery in cancer cells. *Nucleic Acids Res.* **41**, D955–D961 (2013).
32. Liston, D. R. & Davis, M. Clinically relevant concentrations of anticancer drugs: a guide for nonclinical studies. *Clin. Cancer Res.* **23**, 3489–3498 (2017).
33. Vis, D. J. et al. Multilevel models improve precision and speed of IC50 estimates. *Pharmacogenomics* **17**, 691–700 (2016).
34. Najgebauer, H. et al. CELLector: genomics-guided selection of cancer in vitro models. *Cell Syst.* **10**, 424–432.e6 (2020).
35. Garcia-Alonso, L. et al. Transcription factor activities enhance markers of drug sensitivity in cancer. *Cancer Res.* **78**, 769–780 (2018).

36. Isella, C. et al. Selective analysis of cancer-cell intrinsic transcriptional traits defines novel clinically relevant subtypes of colorectal cancer. *Nat. Commun.* **8**, 15107 (2017).
37. Parker, J. S. et al. Supervised risk predictor of breast cancer based on intrinsic subtypes. *J. Clin. Oncol.* **27**, 1160–1167 (2009).
38. Ebbert, M. T. W. et al. PAM50 breast cancer intrinsic classifier: Clinical validation of a multianalyte laboratory developed test. *J. Clin. Orthod.* **29**, 10597–10597 (2011).
39. UniProt Consortium. UniProt: the universal protein knowledgebase in 2021. *Nucleic Acids Res.* **49**, D480–D489 (2021).
40. Griffith, M. et al. CIViC is a community knowledgebase for expert crowdsourcing the clinical interpretation of variants in cancer. *Nat. Genet.* **49**, 170–174 (2017).
41. Baralis, E., Bertotti, A., Fiori, A. & Grand, A. LAS: a software platform to support oncological data management. *J. Med. Syst.* **36**, S81–S90 (2012).

## Acknowledgements

We thank M. Michaut and R. Rahman for their work on CombiXplorer, a Shiny app initially used to explore combination drug response curves; G. Bounova for her CMS subtyping of colorectal cancer cell lines. Part of Fig. [1a](#) was created using BioRender.com. We thank J. Mettetal, C. Crafter, A. Cheraghchi-Bashi and K. Bulusu for feedback on a precursor to the GDSC Combination data visualisation website, and U. McDermott for contributing to the original design of screens. This research was funded in whole, or in part, by Wellcome Trust Grant 206194. For the purpose of open access, the author has applied a CC BY public copyright licence to any Author Accepted Manuscript version arising from this submission. A. Bertotti and L.T. are supported by AIRC, Associazione Italiana per la Ricerca sul Cancro, Investigator Grants 20697 (to A. Bertotti) and 22802 (to L.T.); AIRC 5x1000 grant 21091 ; AIRC/CRUK/FC AECC Accelerator Award 22795 (to L.T.); European Research Council Consolidator Grant 724748—BEAT (to A. Bertotti); H2020 grant agreement no. 754923 COLOSSUS (to L.T.); H2020 INFRAIA grant agreement no. 731105 EDIReX (to A. Bertotti); and Fondazione Piemontese per la Ricerca sul Cancro-ONLUS, 5x1000 Ministero della Salute 2016 (to L.T.).

## Author information

## Author notes

1. These authors contributed equally: Patricia Jaaks, Elizabeth A. Coker

## Affiliations

1. Wellcome Sanger Institute, Cambridge, UK

Patricia Jaaks, Elizabeth A. Coker, Olivia Edwards, Emma F. Carpenter, Lisa Dwane, Howard Lightfoot, Syd Barthorpe, Dieudonne van der Meer, Wanjuan Yang, Alexandra Beck, Tatiana Mironenko, Caitlin Hall, James Hall, Iman Mali, Laura Richardson, Charlotte Tolley, James Morris, Frances Thomas, Ermira Lleshi & Mathew J. Garnett

2. Division of Molecular Carcinogenesis, The Netherlands Cancer Institute, Amsterdam, The Netherlands

Daniel J. Vis, Nanne Aben & Lodewyk Wessels

3. Candiolo Cancer Institute, FPO–IRCCS, Turin, Italy

Simonetta M. Leto, Francesco Sassi, Andrea Bertotti & Livio Trusolino

4. Massachusetts General Hospital, Harvard Medical School, Boston, MA, USA

Cyril H. Benes

5. Department of Oncology, University of Torino School of Medicine, Turin, Italy

Andrea Bertotti & Livio Trusolino

6. Department of EEMCS, Delft University of Technology, Delft, The Netherlands

Lodewyk Wessels

7. Oncode Institute, Amsterdam, The Netherlands

Daniel J. Vis & Lodewyk Wessels

## Contributions

M.J.G., S.B., P.J., D.J.V., C.H.B. and N.A. contributed to the screening design. A. Beck, C.H., C.T., E.L., F.T., I.M., J.H., J.M., L.R., S.B. and T.M. contributed to screening data collection. H.L., D.J.V. and D.v.d.M. contributed to the data processing.

S.B., H.L. and P.J. contributed to the quality control of the data. P.J. and E.A.C. contributed to the data analysis of drug interactions. E.A.C. and P.J. contributed to the biomarker analysis. P.J., O.E. and E.F.C. conducted siRNA experiments and colony formation and apoptosis assays. L.D. conducted siRNA experiments including western blots. S.M.L., F.S., A. Bertotti and L.T. conducted the *in vivo* follow-up experiments, including immunohistochemical stainings. D.v.d.M., W.Y., H.L., E.A.C. and P.J. designed and implemented the drug combination website. P.J., E.A.C., D.J.V., L.W. and M.J.G. wrote the manuscript. All authors read and approved the manuscript.

## Corresponding author

Correspondence to [Mathew J. Garnett](#).

## Ethics declarations

## Competing interests

M.J.G. has received research grants from AstraZeneca, GlaxoSmithKline, and Astex Pharmaceuticals, and is founder of Mosaic Therapeutics. C.H.B is an employee of Novartis and previously received research funding from Novartis. L.T. reports research grants from Symphogen, Servier, Pfizer, Menarini, Merck KGaA and Merus. Drug combinations described in this study are subject to patents filed by Genome Research Limited, which is the name under which the Sanger Institute operates.

## Peer review

### Peer review information

*Nature* thanks Steven Corsello and the other, anonymous reviewers for their contribution to the peer review of this work. Peer review reports are available.

## Additional information

**Publisher's note** Springer Nature remains neutral with regard to jurisdictional claims in published maps and institutional affiliations.

## Extended data figures and tables

[Extended Data Fig. 1 Information on cell lines, drugs and screen design.](#)

**a**, OncoPrint detailing mutation status of three key mutations (*TP53*, *KRAS*, *PIK3CA*), MSI status, and clinical subtyping (PAM50 or CRIS where available) for all 125 cancer cell lines. **b**, Proportion of chemotherapeutic and targeted drugs screened. **c**, Proportion of drugs that are FDA-approved, in clinical trials, or are in development. **d**, Number of drugs screened per pathway and tissue. **e**, Schematic of anchored screening design. An anchor is tested at two fixed concentrations against a library screened at a 7-point, discontinuous 1,000-fold concentration range (two 2-fold dilution steps from the highest used concentration, all other dilution steps are 4-fold). **f**, Schematic of drug response curve fits of single-agent and combination responses. Vertical and horizontal lines are helper lines facilitating the reading of drug response metrics from the x-axis (concentration) and y-axis (viability), respectively. **g**, Schematic of synergy quantification based on efficacy ( $\Delta E_{\text{max}}$ ) or potency ( $\Delta IC_{50}$ ). **h**,  $\Delta E_{\text{max}}$  and  $\Delta IC_{50}$  are normally distributed and only a minority meet synergy thresholds. Density distribution of  $\Delta E_{\text{max}}$  (viability in %; left) and  $\Delta IC_{50}$  (log<sub>2</sub>; right) across all combination responses. Vertical dashed lines represent synergy thresholds ( $\Delta E_{\text{max}} \geq 20\%$  and  $\Delta IC_{50} \geq 3$ ). n = 156,065 measurements in breast, n = 74,525 in colon, n = 66,117 in pancreas.

## Extended Data Fig. 2 Screen quality control, single-agent response and combination response trends.

**a**, The coefficient of variation of the negative control DMSO across all 3,106 drug screening plates is low. Grey dashed line represents the quality control threshold of CV < 0.18. Median and interquartile range (IQR). **b**, The plate Z-factor scores for positive control drugs (MG-132, staurosporine) and blank wells across all drug screening plates. Grey dashed line represents the plate threshold of Z-factor > 0.3. Median and IQR. **c**, Single-agent and combination responses are well correlated across biological replicates ( $r > 0.6$ , p-value < 0.05). Replicate data was collected over the duration of screening at various time points for 4–5 cell lines per tissue. Drug responses were averaged across technical replicates and correlated across biological replicates (n = 2–18, median = 4 biological replicates per ‘anchor concentration–library–cell line’ tuple) using Pearson correlation coefficient with Fisher’s Z transform as statistical test. **d**, Monotherapies captured an informative range of drug response at the concentration selected, generally having weak to moderate activity in cell lines. Median anchor (anchor viability by anchor concentration) and library (library Emax) responses across cell lines within a tissue. n = 26 drugs in colon and pancreas, n = 25 anchors and n = 52 libraries in breast. Median and IQR. **e**, Library IC50s were highly correlated with corresponding drug responses from the Genomics of Drug Sensitivity in Cancer, with IC50 on natural log scale. Pearson correlation coefficient, n = 4,338 drug-cell line pairs. **f**, Tissue accounts for some, but not all, variance in combination response. Dimensional reduction using t-SNE analysis on combination responses ( $\Delta IC_{50}$ ) of 121 pan-tissue combinations across 125 cancer cell lines. **g, h**, Heatmaps

of combination responses ( $\Delta\text{IC50}$ ) in 45 colon (**g**) or 29 pancreas (**h**) cell lines. Drug responses were clustered by combination and are annotated by combination type and anchor (An.) and library (Lib.) pathway. Rows are sorted by conditional mean  $\Delta\text{IC50}$  on cell line identity.  $n = 650$  combinations. **i**, Heatmap of combination responses ( $\Delta\text{IC50}$ ) for 121 pan-tissue combinations across 125 breast, colon and pancreas cancer cell lines, clustered by combination and cell line. For all heatmaps  $\Delta\text{IC50}$  limits were clipped to  $-4$  and  $4$ .

### Extended Data Fig. 3 Landscape of synergy.

**a**, Synergy is associated with weak to moderate single-agent drug activity. Single-agent activity (anchor low and high, library) of synergistic ( $n = 9,402$ ) and non-synergistic ( $n = 287,305$ ) measurements. Single-agent activity of synergistic measurements: Anchor high:  $52 - 86\%$  interquartile range (IQR), anchor low:  $69 - 92\%$  IQR, library:  $53 - 80\%$  IQR. Median and IQR. Two-sided Welch's t-test. **b**, The relative rate of synergy for the 27 pan-tissue combinations with  $> 20\%$  synergy in at least one tissue remains context-dependent upon variation of synergy thresholds. Three different synergy thresholds of  $\Delta\text{Emax}$  ( $\Delta E$ ) and  $\Delta\text{IC50}$  ( $\Delta I$ ) were applied. Thresholds used in this study were, at either anchor concentration, combination IC50 or Emax was reduced 8-fold or 20% viability over Bliss, respectively (central panel), and here compared to less (left) or more (right) stringent thresholds. **c**,  $\Delta\text{IC50}$  correlates well between the original and the validation screen. Drug responses were averaged across replicates within a screen.  $n = 9,719$  'library-anchor concentration-cell line' tuples. Orange line represents linear fit. Pearson correlation coefficient and p-value. **d**, Single-agent and combination responses are well correlated between the original and validation screens. Drug responses were averaged across technical and biological replicates within a screen and correlated across screens.  $n > 3,000$  'anchor concentration-library-cell line' tuples. **e**, Synergy classification is consistent. The F-score as well as the recall and precision rates were calculated for validated responses in breast (yellow;  $n = 1,651$ ), colon (green;  $n = 1,597$ ) and pancreas (blue;  $n = 1,633$ ). **f**, False positives (FP) and false negative (FN) synergistic measurements have borderline  $\Delta\text{IC50}$  and  $\Delta\text{Emax}$  values close to the threshold for calling synergy (compared to true positive (TP) and true negative (TN)). Drug responses were averaged across replicates for each 'anchor concentration-library-cell line' tuple. Distance to the synergy threshold ( $\log_2$  normalised  $\Delta\text{IC50} \geq 3$  or  $\Delta\text{Emax} \geq 0.2$ ) was determined for each synergistic measurement. Median and interquartile range (IQR). Two-sided Welch's t-test. **g**, Combinations of two chemotherapeutics have lower combination responses.  $\Delta\text{IC50}$  and  $\Delta\text{Emax}$  for chemotherapeutic+chemotherapeutic (C+C;  $n = 50$ ), chemotherapeutic+targeted (C+T;  $n = 581$ ) and targeted+targeted (T+T;  $n = 1,394$ ) combinations. Median and IQR. ANOVA. **h**, AZD7762 has high synergy rates paired with certain chemotherapeutics. Synergy rate per tissue for AZD7762 paired with five chemotherapeutics in both anchor orientations. **i**, Several

navitoclax+chemotherapeutic combinations have high synergy rates. Synergy rate per tissue for all combinations of navitoclax (anchor) paired with a chemotherapeutic (library). **j**, Inter-pathway targeting of MAPK and PI3K signalling leads to increased synergy effects.  $\Delta$ IC50 per tissue for all combinations (All), inter-pathway MAPK and PI3K combinations (Inter), and intra-pathway combinations (Intra). Median and IQR. Two-sided Welch's t-test, \*: p-value  $\leq 0.05$ , \*\*: p-value  $\leq 0.01$ , \*\*\*: p-value  $\leq 0.001$ , \*\*\*\*= p < 0.0001. **k**, Combinations of MK-2206 (AKT1, AKT2) and MTOR inhibitors are highly synergistic in Her2 breast cancer cell lines. Synergy rate of MK-2206 (anchor) paired with OSI-027 or AZD8055 (libraries) across all breast cancer cell lines and PAM50 subtypes.

### Extended Data Fig. 4 Landscape of biomarkers I.

**a**, Heatmap showing the distribution of 8,078 significant biomarkers across four inputs and four feature types. MOBEM: binary matrix of mutations, copy number alterations and methylations present in cell lines (see [Methods](#) for feature selection). **b**, Volcano plot of single-agent response biomarker associations tested (library IC50; n = 1,922,552; significant and large-effect biomarkers n = 3,280), with select statistically significant large-effect size biomarkers showing known single agent examples highlighted, namely *BRAF* mutation and dabrafenib sensitivity (purple), *ERBB2* amplification and afatinib sensitivity (turquoise), *PIK3CA* mutation and taselisib sensitivity (orange), and *TP53* mutation and resistance to nutlin-3a (yellow). Biomarkers identified using ANOVA test, p  $\leq 0.001$ , FDR  $\leq 5\%$ , Glass deltas for positive and negative populations both  $\geq 1$ . **c**, Volcano plot of biomarkers tested for associations with  $\Delta$ Emax (n = 2,006,328), with significant and large-effect biomarkers (n = 761) coloured by analysis type. Examples discussed in the text and selected outliers are labelled. Biomarkers identified using ANOVA test, p  $\leq 0.001$ , FDR  $\leq 5\%$ , Glass deltas for positive and negative populations both  $\geq 1$ . **d**, Number of significant and large-effect biomarkers found per combination per context. Median and interquartile range (IQR). **e**,  $\Delta$ IC50 drug combination response for irinotecan+AZD7762 in pancreatic cell lines with low expression of CDH1. n = 3 CDH1\_down, n = 27 not CDH1\_down. ANOVA, p  $\leq 0.001$ , FDR  $\leq 5\%$ . Median and IQR. **f**, Drug combination responses for dabrafenib paired with EGFR inhibitors afatinib or sapitinib in *BRAF* wild-type (wt; n = 36) and mutant (mut, n = 11) colon cell lines.  $\Delta$ Emax and  $\Delta$ IC50 were averaged across replicates and highest response between anchor concentrations is reported. Two-sided Welch's t-test. Median and IQR.

### Extended Data Fig. 5 Landscape of biomarkers II.

**a**, Shortest distance in IntAct interactome between unique drug targets and biomarker features for combination metrics ( $\Delta$ IC50 and  $\Delta$ Emax biomarkers, n = 582) and single-agent library IC50 biomarkers (n = 124), split by whether the biomarker is associated

with sensitivity or resistance. **b**, Shortest distance in Reactome interactome between unique drug targets and biomarker features for combination metrics ( $\Delta\text{IC50}$  and  $\Delta\text{Emax}$  biomarkers,  $n = 420$ ) and single-agent library IC50 biomarkers ( $n = 68$ ), split by whether the biomarker is associated with sensitivity or resistance. **c**, Shortest distance in IntAct interactome between randomly shuffled unique drug targets and biomarker features for combination metrics ( $\Delta\text{IC50}$  and  $\Delta\text{Emax}$  biomarkers,  $n = 589$ ) and single-agent library IC50 biomarkers ( $n = 985$ ), split by biomarker effect. **d**, Shortest distance in Reactome interactome between randomly shuffled unique drug targets and biomarker features for combination metrics ( $\Delta\text{IC50}$  and  $\Delta\text{Emax}$  biomarkers,  $n = 422$ ) and single-agent library IC50 biomarkers ( $n = 569$ ), split by biomarker effect.

### Extended Data Fig. 6 Populations of unmet clinical need.

**a, b**, 28 and 38 combinations are highly synergistic in *KRAS* mut (**a**) or MSS (**b**) colon cancer cell lines and some have  $\Delta\text{Emax}$  or  $\Delta\text{IC50}$  biomarkers or are in clinical trials. Synergy rates of all colon combinations shown by *KRAS* mutant (mut; x-axis) versus wild-type (wt; y-axis). **b** or MSS (x-axis) versus MSI (y-axis; **a**). Colours represent biomarker or clinical trial presence. Vertical dashed line represents a synergy rate of 25% in MSS or *KRAS* mutant cell lines.  $n = 650$  combinations. Pearson correlation with Fisher's Z transform as statistical test. **c**, Loss of *ERCC3* is associated with increased efficacy ( $\Delta\text{Emax}$ ) of linsitinib+MK-2206 in *KRAS* mutant colon ( $n = 20$  wt;  $n = 5$  loss). Median and interquartile range.  $p\text{-value} < 0.001$ ,  $\text{FDR} < 0.05$ . **d**, Colon MSS cells show higher efficacy ( $\Delta\text{Emax}$ ) for AZD7762 (CHEK1/2) and camptothecin (TOP1). Drug combination responses were averaged across replicates and both anchor-library combination configurations were pooled ( $n = 31$  MSS cell lines;  $n = 15$  MSI cell lines). Median and interquartile range. Two-sided Welch's t-test. **e**, AZD7762 and camptothecin have greater potency ( $\Delta\text{IC50}$ ) and efficacy ( $\Delta\text{Emax}$ ) in *KRAS*-*TP53* double mutant colon cancer cells ( $n = 8$  *KRAS* mutant & *TP53* wild-type cell lines (wt);  $n = 16$  *KRAS*-*TP53* double mutant cell lines (mut)). Drug combination responses were averaged across replicates and both combination configurations were pooled. Median and interquartile range. Two-sided Welch's t-test.

### Extended Data Fig. 7 In vitro validation of combined targeting of TOP1 and CHEK1 in colon cancer.

**a**, Combination response is mostly CHEK1 specific. SW837 and SNU-81 cells were reverse transfected with pooled siRNA against CHEK1, CHEK2 or PLK1 (positive control), and 0.025  $\mu\text{M}$  SN-38 was added 30 h later. Viability was measured with CellTiter-Glo (CTG) after 72 h of drug treatment. Signal was normalised to non-targeting siRNA (siNT)+DMSO controls. Median and interquartile range. Two-sided Welch's t-test, \* $= p \leq 0.05$ , \*\* $= p \leq 0.01$ , \*\*\* $= p \leq 0.001$ , \*\*\*\* $= p \leq 0.0001$ . **b**, CHEK1

and CHEK2 knockdown confirmation by Western blotting. SW837 and SNU-81 cells were reverse transfected with siRNAs (40 nM) and knockdown was examined after 72 h. Western blot is a representative of two independent experiments. For gel source data, see Supplementary Fig. 1. Some knockdown of CHEK2 was observed in SW837 cells with CHEK1 siRNA pool. **c**, CHEK1 specificity of combination response is confirmed with individual siRNAs against CHEK1. SW837 and SNU-81 cells were reverse transfected with pooled or four individual siRNA against CHEK1 and 0.025  $\mu$ M SN-38 were added 30 h later. Viability was measured with CellTiter-Glo after 72 h of drug treatment. Signal was normalised to siNT+DMSO controls. Median and interquartile range. Two-sided Welch's t-test, \* $= p \leq 0.05$ , \*\* $= p \leq 0.01$ , \*\*\* $= p \leq 0.001$ , \*\*\*\* $= p \leq 0.0001$ . **d**, CHEK1 knockdown confirmation by Western blotting. SW837 and SNU-81 cells were reverse transfected with pooled or four individual siRNAs (40 nM) against CHEK1 and knockdown was examined after 72 h. Western blot is a representative of two independent experiments. For gel source data, see Supplementary Fig. 1. **e**, CHEK1 (but not CHEK2) silencing by siRNA significantly shifts and reduces the IC50 of SN-38 (SNU-81: 7.2-fold (IC50 siNT: 611.1 nM; siCHEK1: 84.4 nM ( $p = 0.0013$ ); siCHEK2: 714.7 nM ( $p = 0.339$ )); SW837: 120-fold (IC50 siNT: 84.4 nM; siCHEK1: 0.69 nM ( $p = 0.0019$ ); siCHEK2: 66.6 nM ( $p = 0.091$ ))). SW837 and SNU-81 cells were reverse transfected with siRNAs and the following day cells were treated with a dose range of SN-38 (0.001–9  $\mu$ M). Viability was assessed after 72 h using CellTiter-Glo. Signal was normalised to siNT+DMSO controls. Mean  $\pm$  SD. Two-way ANOVA. **f**, Combination of rabusertib (CHEK1) and SN-38 reduces colony formation. Colon cancer cells were seeded and treated with drugs (0.1 nM SN-38, 0.5  $\mu$ M rabusertib, 0.5  $\mu$ M CCT241533) or DMSO for 14 days. CCT241533 is a CHEK2 selective inhibitor. Representative pictures of three experiments. **g**, Combination of rabusertib and SN-38 leads to caspase-mediated cell death. Colon cancer cells were seeded and treated with drugs (0.125  $\mu$ M staurosporine (positive control), 0.025  $\mu$ M SN-38, 0.75  $\mu$ M rabusertib, 0.75  $\mu$ M CCT241533) or DMSO in the presence of fluorescent reagents (CellTox-Green for cell death and IncuCyte Caspase-3/7 Red for caspase activity). Pictures were taken every 2 h for 96 h on the IncuCyte and fluorescent signals were measured as mean intensity per area and normalised to time 0 h. Mean of three independent experiments. **h**, Combined TOP1 and CHEK2 inhibition leads to mostly less than additive combination response. Cell death was measured by CellTox-Green signal (CTOX; in green calibrated units (GCU)) after 72 h of treatment with SN-38 (TOP1; 0.025  $\mu$ M) and CCT241533 (CHEK2; 0.75  $\mu$ M). Drug responses are mean across 3–4 biological replicates. Additive response: sum of SN-38 and rabusertib responses. Delta: observed - additive response. **i**, Combined TOP1 and CHEK1 inhibition results in PARP cleavage in SNU-81 cells. SNU-81 cells were treated with drugs for 96 h. Western blot is a representative of three repeated experiments. +: positive control (MG-132; 2  $\mu$ M); -: negative control (DMSO; 1:1,000); SN-38 (0.025  $\mu$ M); Rab: rabusertib (1.5  $\mu$ M); CCT: CCT241533 (1.5  $\mu$ M).

[Source data](#)

## [Extended Data Fig. 8 In vivo validation of combined targeting of irinotecan and CHEK1 in colon cancer.](#)

**a**, Addition of rabusertib increases irinotecan response in two of three colon cancer xenograft models. NOD/scid mice were engrafted with colon cancer cell lines and treated with irinotecan (25 mg/kg twice a week) +/- rabusertib (200 mg/kg daily) for 24–35 days. Shown is average tumour volume change under treatment. LS-1034: n = 6 mice for vehicle, n = 11 for irinotecan, n = 12 for rabusertib and irinotecan+rabusertib. SW837: n = 6 mice for vehicle and rabusertib, n = 8 for irinotecan, n = 4 for irinotecan+rabusertib. SNU-81: n = 5 mice for vehicle and irinotecan+rabusertib, n = 6 for rabusertib, n = 10 for irinotecan. Two-way ANOVA. **b**, Treatment of rabusertib with irinotecan decreases proliferation. LS-1034 cells were engrafted and treated as described in (a). Tumours were collected 72 h after treatment start and stained for Ki67 (proliferative cells). n = 30 for vehicle, rabusertib and irinotecan+rabusertib; n = 25 for irinotecan. Mean ± SD. Two-tailed unpaired Welch's t-test.

[Source data](#)

## Supplementary information

### [Supplementary Fig. 1](#)

This file contains images of Western blots described in the paper.

### [Reporting Summary](#)

### [Peer Review File](#)

### [Supplementary Table 1](#)

2,575 drug combination-tissue pairs.

### [Supplementary Table 2](#)

Detail of 125 cancer cell lines used in this study.

### [Supplementary Table 3](#)

All significant and large effect biomarkers.

## Supplementary Table 4

Synergy and biomarkers: all combinations.

## Supplementary Table 5

Synergy and biomarkers: populations of unmet clinical need.

## Source data

### Source Data Fig. 4

### Source Data Extended Data Fig. 7

### Source Data Extended Data Fig. 8

## Rights and permissions

**Open Access** This article is licensed under a Creative Commons Attribution 4.0 International License, which permits use, sharing, adaptation, distribution and reproduction in any medium or format, as long as you give appropriate credit to the original author(s) and the source, provide a link to the Creative Commons license, and indicate if changes were made. The images or other third party material in this article are included in the article's Creative Commons license, unless indicated otherwise in a credit line to the material. If material is not included in the article's Creative Commons license and your intended use is not permitted by statutory regulation or exceeds the permitted use, you will need to obtain permission directly from the copyright holder. To view a copy of this license, visit <http://creativecommons.org/licenses/by/4.0/>.

### Reprints and Permissions

## About this article

### Cite this article

Jaaks, P., Coker, E.A., Vis, D.J. *et al.* Effective drug combinations in breast, colon and pancreatic cancer cells. *Nature* **603**, 166–173 (2022). <https://doi.org/10.1038/s41586-022-04437-2>

- Received: 02 July 2021

- Accepted: 18 January 2022
- Published: 23 February 2022
- Issue Date: 03 March 2022
- DOI: <https://doi.org/10.1038/s41586-022-04437-2>

## Share this article

Anyone you share the following link with will be able to read this content:

[Get shareable link](#)

Sorry, a shareable link is not currently available for this article.

[Copy to clipboard](#)

Provided by the Springer Nature SharedIt content-sharing initiative

---

This article was downloaded by **calibre** from <https://www.nature.com/articles/s41586-022-04437-2>

| [Section menu](#) | [Main menu](#) |

- Article
- [Published: 16 February 2022](#)

# Structure and receptor recognition by the Lassa virus spike complex

- [Michael Katz](#)<sup>1</sup>,
- [Jonathan Weinstein](#)<sup>2</sup>,
- [Maayan Eilon-Ashkenazy](#), ORCID: [orcid.org/0000-0003-0796-5422](https://orcid.org/0000-0003-0796-5422)<sup>1</sup>,
- [Katrin Gehring](#)<sup>1</sup>,
- [Hadas Cohen-Dvashi](#)<sup>1</sup>,
- [Nadav Elad](#), ORCID: [orcid.org/0000-0001-6222-2280](https://orcid.org/0000-0001-6222-2280)<sup>3</sup>,
- [Sarel J. Fleishman](#)<sup>2</sup> &
- [Ron Diskin](#), ORCID: [orcid.org/0000-0002-2837-5897](https://orcid.org/0000-0002-2837-5897)<sup>1</sup>

[Nature](#) volume 603, pages 174–179 (2022)

- 4906 Accesses
- 43 Altmetric
- [Metrics details](#)

## Subjects

- [Cryoelectron microscopy](#)
- [Virology](#)

## Abstract

Lassa virus (LASV) is a human pathogen, causing substantial morbidity and mortality<sup>1,2</sup>. Similar to other *Arenaviridae*, it presents a class-I spike complex on its surface that facilitates cell entry. The virus's cellular receptor is matriglycan, a linear carbohydrate that is present on  $\alpha$ -dystroglycan<sup>3,4</sup>, but the molecular mechanism that LASV uses to recognize this glycan is unknown. In addition, LASV and other arenaviruses have a unique signal peptide that forms an integral and functionally important part of the mature spike<sup>5,6,7,8</sup>; yet the structure, function and topology of the

signal peptide in the membrane remain uncertain<sup>9,10,11</sup>. Here we solve the structure of a complete native LASV spike complex, finding that the signal peptide crosses the membrane once and that its amino terminus is located in the extracellular region. Together with a double-sided domain-switching mechanism, the signal peptide helps to stabilize the spike complex in its native conformation. This structure reveals that the LASV spike complex is preloaded with matriglycan, suggesting the mechanism of binding and rationalizing receptor recognition by  $\alpha$ -dystroglycan-tropic arenaviruses. This discovery further informs us about the mechanism of viral egress and may facilitate the rational design of novel therapeutics that exploit this binding site.

[Download PDF](#)

## Main

Lassa haemorrhagic fever (LF) is a devastating disease caused by LASV infection. LASV is endemic to West Africa but has spread to new territories in recent years<sup>2</sup>. Although zoonotic transmission from rodents is the main route of infection, a substantial number of cases have resulted from human-to-human transmission, increasing the risk of large outbreaks. So far, the only therapy for Lassa haemorrhagic fever approved by the US Food and Drug Administration is ribavirin, but this treatment has adverse effects and its efficacy is uncertain<sup>12</sup>. Thus, there is an urgent need to fill the gaps in our knowledge regarding this lethal pathogen to guide the development of improved therapies.

The spike complex of all Arenaviruses undergoes substantial cellular processing before reaching its mature form. The protomers that constitute the homotrimeric complex are first expressed as glycoprotein precursor proteins (GPCs) and are then cleaved twice by a signal peptidase (SPase) and a subtilisin kexin isozyme-1/site-1 (SKI-1) protease. This processing yields three functional subunits: the stable signal peptide (SSP), glycoprotein 1 (GP1) and glycoprotein 2 (GP2) (Fig. 1a). GP1 is the receptor-binding domain that mediates attachment to the cell receptor. GP2 is the transmembrane domain that is responsible for host and viral membrane fusion. Unique to Arenaviruses, the SSP translocates with the spike, forms part of the mature complex, can be added in *trans*, and is important for the maturation and function of the spike<sup>5,6,7,8</sup>. Despite its critical role in generating a functional spike, it is unknown how the SSP interacts with the other GPC subunits. Although the general architecture of the spike is common to all Arenaviruses, different viruses utilize distinct cellular receptors: Arenaviruses that infect mammals (mammarenaviruses) can be classified into two serogroups: the Old World (OW) and the New World (NW) groups. Clades B and D of NW Arenaviruses use transferrin receptor protein 1 (TfR1) as a cellular receptor<sup>13,14</sup>, Lujo virus, which differs from the OW and NW viruses, uses neuropilin-2<sup>15</sup> (NRP2); and OW viruses

such as LASV and clade-C NW arenaviruses use  $\alpha$ -dystroglycan<sup>3,4</sup> ( $\alpha$ -DG). Recognition of  $\alpha$ -DG depends on matriglycan<sup>16</sup>, which is a unique linear carbohydrate modification synthesized by LARGE1<sup>17</sup>. Matriglycan comprises repeating units of xylose (Xyl) and glucuronic acid<sup>18</sup> (GlcA) that are linked together in the form of  $[-3\text{Xyl}-\alpha 1,3-\text{GlcA}-\beta 1-]_n$ . The linear chains of matriglycan consist of many such repeats, enabling them to project to substantial distances from the cell surface.

**Fig. 1: Structure and membrane organization of the LASV spike complex.**

---

 **figure 1**

---

**a**, A schematic view of the spike complex subunit organization. **b**, Overview of the structure. Top left, LASV spike electron density map. The trimeric spike is shown with a different colour (blue, grey or pink) for each protomer and with different tones for the SSP, GP1 and GP2 subunits. *N*-linked glycans are shown as spheres. The rough

boundaries of the membrane bilayer and the visible termini are indicated. **c**, Organization of the transmembrane helices. The six transmembrane helices are shown along the three-fold symmetry axis of the spike (marked with a triangle) from an intracellular viewpoint. **d**, Energy profiles (in Rosetta energy units (REU)) for the different registers of SSP. This graph shows a focused view of registers that place the first hydrophobic region of SSP, or part of it, in the membrane. Blue and red lines indicate threading the SSP with its C terminus out and N terminus out, respectively. The lowest-energy global solution is indicated with a large red dot. **e**, Side view of the transmembrane helices indicates their membrane-crossing angle. **f**, Close-up view of the SSP. One SSP is shown as a green ribbon, and the rest of the spike is shown as a surface coloured by the electrostatic potential: blue,  $5 \text{ kT e}^{-1}$ ; white, 0; red,  $-5 \text{ kT e}^{-1}$ . **g**, Multiple sequence alignment of the SSPs from the indicated viruses. The first (h1) and second (h2) helices of SSP are indicated as well as the extracellular region. The transmembrane region is shown in red and the unmodelled cytoplasmic tail is in grey. Previously identified hydrophobic regions are noted. Fully conserved residues are highlighted with a yellow background. DANV, Dandenong virus; GTOV, Guanarito virus; JUNV, Junín virus; LATV, Latino virus; MORV, Morogoro virus; OLVV, Oliveros virus; W WAV, Whitewater Arroyo virus.

Although it is known how TfR1 and NRP2 are recognized by arenaviruses<sup>19,20</sup>, the structural basis for  $\alpha$ -DG recognition remains unknown. An important step was made by Hastie et al., who determined the structure of a mutationally stabilized ectodomain of the LASV spike complex<sup>21</sup>. This enabled the mapping of residues that were previously found to influence binding to  $\alpha$ -DG by the OW lymphocytic choriomeningitis virus<sup>22,23,24</sup> (LCMV) onto the LASV spike. One of these residues, Tyr150, was found at the interface between two adjacent GP1 subunits at the apex of the spike, but the actual mechanism for binding  $\alpha$ -DG remained unknown. Other structural studies on components of the LASV spike complex and related proteins<sup>25,26</sup> have provided further clues regarding the basis of receptor recognition, yet key questions remain. Here we address these questions using a more holistic approach, investigating the structure of the complete, membrane-embedded, spike complex carrying only minimal modifications. We present the cryo-electron microscopy (cryo-EM) structure of the LASV spike complex, which provides fundamental information regarding the SSP, receptor recognition and the stability of this trimeric complex.

## Topology and structure of the SSP

To determine the structure of the LASV spike complex, we produced the full-length GPC of LASV fused to a C-terminal Flag tag in HEK 293F cells. Single-particle cryo-EM analysis using detergent-solubilized, purified spike provided a three-fold symmetric density (Extended Data Figs. 1, 2). Gold-standard Fourier shell correlation

(GSFSC) indicated a resolution of 2.5 Å (Extended Data Fig. 1), but the map quality suggested a lower resolution, and the map model Fourier shell correlation (FSC) extended to 3.3 Å (Extended Data Fig. 2). We thus low-pass filtered the map to 3.3 Å to avoid high-frequency noise. The map reveals that the spike has six transmembrane helices organized in a bundle (Fig. 1b, Extended Data Fig. 1). We used the available structure of the LASV ectodomain<sup>21</sup> (Protein Data Bank (PDB): 5VK2) as a starting model, and manually completed and refined the model (Fig. 1b, Extended Data Fig. 2, Extended Data Table 1). The membrane domain is organized such that the central three helices belong to GP2 subunits (Fig. 1a,c), and the outer three helices belong to the SSPs (Fig. 1c). Modelling the central GP2-helices was straightforward, as their register is dictated by the extracellular portion of the spike. Density for side chains of the SSP transmembrane helices point toward the extracellular side (Extended Data Fig. 3a), a directionality that is apparent even in the low-pass-filtered map (Extended Data Fig. 3b), clearly establishing that the N terminus is extracellular.

We were further able to trace the main chain of about 12 residues of SSP outside the membrane. However, the quality of the density in this region was not sufficient to unambiguously determine the register. To address this, we used an unbiased computational modelling approach using Rosetta all-atom modelling. First, the transmembrane region was embedded in a virtual membrane. Then, we threaded all possible registers of SSP (37 possibilities for each direction) on the 6-helix bundle, while maintaining the register of the central GP2-helices. In each modelling trajectory, the sidechain conformations were packed and the sidechains and backbone were minimized using an energy function dominated by van der Waals interactions, hydrogen bonds, electrostatic forces and membrane-depth-dependent solvation<sup>27</sup> (Extended Data Fig. 3c). Placing the first hydrophobic region of the SSP in the membrane provided the lowest-energy model, with a significant energy gap compared to all other possibilities (Fig. 1d, Extended Data Fig. 3c). Models with threaded sequences in reverse (that is, with the C terminus outside) exhibited much higher energies overall (Fig. 1d, Extended Data Fig. 3c). This analysis favoured a single solution (Extended Data Fig. 3d) which we then adopted for completion of our model.

The SSP starts with a short helical segment (h1) that lies parallel to and is probably partially embedded in the membrane (Fig. 1b) before its transmembrane helix enters the membrane at an angle of around 70° (Fig. 1b,e). Hydrophobic residues in h1—such as Ile4—seem to face and probably penetrate into the membrane (Fig. 1f). The highly conserved Pro12 serves as a helix breaker and seems to terminate h1 (Fig. 1b,f). Glu16 and the conserved Glu17 are predicted to face a positively charged patch that is formed by residues in GP2, and potentially interact with it (Fig. 1f,g). Lys33, which is highly conserved and was previously linked to pH-induced membrane fusion<sup>8</sup>, is located at the very end of the transmembrane helix of SSP (Fig. 1f) and is either exposed to, or snorkels with its side-chain toward the cytoplasm.

Previous experimental studies corroborate our model of SSP. Specifically, the conserved Pro12 is important for allowing the break between h1 and h2, and other residues may disfavour the observed bound conformation of SSP. Indeed, mutating Pro12 in LCMV spike (Fig. 1g) to either alanine or glycine does not affect the surface expression of the protein, but completely abrogates infectivity of pseudotyped viruses<sup>28</sup>, suggesting a premature dissociation of the SSP from the spike. Furthermore, in our structure, Glu16 and Glu17 of SSP point toward a positively charged patch on GP2 (Fig. 1f). Mutating the equivalent negatively charged residues of LCMV (Asp16 and Glu17) to alanine does not affect surface expression but, as in the case of Pro12, abrogates the infectivity of pseudotyped viruses<sup>28</sup>. Reverting the charge of these two residues by mutating them to lysine (that is, D16K/E17K) results in a more deleterious effect that reduces surface expression and maturation of the spike on top of abrogating infectivity of pseudotyped viruses<sup>28</sup>. This indicates that SSP has reduced association with the spike even inside the endoplasmic reticulum–Golgi network, since this interaction is needed for the proper maturation of the spike<sup>6</sup>. Our structure explains not only the deleterious effects, but also the lack of effect of mutating some residues. Specifically, mutating either Gln3 or Thr6 of LCMV (corresponding to Gln3 and Val6 in LASV) to alanine does not have any functional consequence for the spike<sup>28</sup>. Both of these SSP residues are predicted by our structure to be solvent-exposed (Fig. 1f), rationalizing this observation.

Different models for the topology of SSP have been proposed<sup>9,10,11,29</sup>, including a bitopic model in which the two hydrophobic regions cross the membrane<sup>9</sup>. Our structural data, however, indicate the presence of only six transmembrane helices (Fig. 1c, Extended Data Fig. 2), and not nine as predicted by the bitopic model. Further, our structure indicates that the N terminus of SSP is located on the outer side of the membrane (Fig. 1e, Extended Data Fig. 3a), which also differs from the bitopic model<sup>9</sup>. Although the observed configuration of the SSP does not support the previously proposed models, it is consistent with some published biochemical data. Specifically, Cys57 was shown to participate in zinc coordination together with the cytoplasmic tail of GP2<sup>30</sup>, an observation that is consistent with the observed topology of SSP in our structure. Furthermore, it has been demonstrated that the first hydrophobic region of the SSP interacts with GP2 inside the membrane<sup>31</sup>, which is also consistent with our structure. Last, our structure indicates that the positively charged residues of SSP are indeed on the cytoplasmic side of the membrane (Fig. 1g), an organization that is favoured<sup>32</sup> (that is, the ‘positive inside rule’).

## Double-sided stabilization of the spike

The modified ectodomain of LASV was found to be labile and unstable in the absence of ‘stapling’ antibodies<sup>21</sup>. This observation was surprising considering that LASV is

transmitted through aerosolized animal excreta and should therefore withstand harsh environmental conditions. By contrast, the detergent-solubilized native spike is stable without the addition of any binding partners. Several structural factors contribute to this apparent stability; at the apex of the trimer, the C termini of the GP1 subunits are mutually swapped and interlocked with the neighbouring protomers (Fig. 2a). This GP1 region contains the RRLL recognition motif of SKI-I<sup>33</sup> (Fig. 1a). It engages a neighbouring GP1 subunit via hydrophobic interactions through Ile254, Leu258 and Leu259, as well as polar interactions between Arg257 and 3 main-chain carbonyl groups (Fig. 2a). Tyr150 is an important residue for this interaction, as it is engulfed by the aliphatic part of Arg257 and by Leu258 (Fig. 2a). Leu258 reaches to and interacts with the interface between the two other GP1 subunits (Fig. 2a).

**Fig. 2: A double domain-swapping mechanism stabilizes the LASV spike complex.**

 figure 2

**a**, A domain swap at the apex of the trimer. A top view of the trimer using a surface representation for the three individual GP1 subunits, shown in pink, blue and grey. Inset, magnified view of the domain-swapped element. Key interacting residues are labelled and shown as sticks. Yellow dashed lines represent polar interactions between the Arg guanidino group and main-chain carbonyl oxygens. **b**, Domain swapping at the membrane-proximal region of the trimer. Main image, the three GP2 subunits are shown using ribbon and surface representations. The SSPs were omitted for clarity. The transmembrane (TM) region is indicated. Bottom left, the organization of

secondary structures in GP2. Right, magnified view of the interaction between the GP2 subunits. Key interacting residues are labelled and shown as sticks. Yellow dashed lines represent polar interactions. **c**, A similar view as in **b**, right, with the addition of one SSP.

On the opposite side of the trimer, at the membrane-proximal region, we found an additional domain swap that involves the GP2 subunits. The transmembrane helix of each of the GP2 subunits does not penetrate the membrane in proximity to its cognate subunit. Instead, a long  $\alpha$ -helix (h5) is projected toward its neighbouring GP2, interacts with the adjacent h5 helix, and penetrates into the membrane such that the transmembrane helices are twisted around each other (Fig. 2b). The h5–h5 interaction includes hydrophobic contacts between Leu415 and Pro427 (which also serves as a helix breaker) and between Tyr419 and the aliphatic part of Gln423 (Fig. 2b). In addition, Gln416 makes a hydrogen bond with the main-chain carbonyl of Met420, and Arg422 makes a salt bridge with Asp432 (Fig. 2b). The mutual h5-swapping of the GP2s is locked in place by the SSPs that prevent the h6 transmembrane helices of GP2 from unwinding (Fig. 2c). The transmembrane helices of the SSP are in grooves between each two central GP2 helices, forming multiple hydrophobic interactions (Fig. 1b,c,e). The extracellular h1 of SSP (Fig. 1b) makes hydrophobic interactions with its cognate GP2 h5 and a neighbouring GP2 h6 through Phe7 and Val11 (Fig. 2c). In addition, Glu16 of the SSP forms a polar interaction with Arg422 of the neighboring GP2 h5 (Fig. 2c). Of note, the mutual swapping at the apex and at the membrane-proximal region of the spike have opposite directionalities (Extended Data Fig. 4), in a configuration that could be envisioned as a sweet wrapper with two twisted ends.

## Recognition of matriglycan by LASV

A key open question is how matriglycan-dependent recognition of  $\alpha$ -DG is achieved. While solving the structure, we noticed elongated density blobs in deep pockets formed by the C terminus of GP1 and Tyr150 (Fig. 3a). These densities do not resemble in size and shape any of the compounds used for producing the spike. The proximity to Tyr150, which influences  $\alpha$ -DG binding<sup>24</sup>, suggests that these densities may belong to matriglycan. Indeed, segments of matriglycan [-Xyl- $\alpha$ 1,3-GlcA- $\beta$ 1,3-Xyl-] moieties readily fit into these density blobs (Fig. 3a). We generated a locally focused C3-symmetric map (Extended Data Fig. 5a) to provide a more detailed view of these densities (Fig. 3a). The size and shape of the densities agree well with the model of matriglycan. To confirm the presence of matriglycan, we used the IIH6 anti-matriglycan antibody<sup>34</sup>. Detergent-solubilized LASV spike that is captured on anti-Flag beads is able to pull down IIH6, whereas the spike of the TfR1-tropic arenavirus Machupo virus<sup>13</sup> (MACV) cannot (Fig. 3a, Extended Data Fig. 6a). The presence of matriglycan is further evident in MLV-based pseudotyped viruses that bear the spike

complexes of LASV but not of the neuropilin-2-tropic<sup>15,20</sup> LUJV (Extended Data Fig. 6b).

**Fig. 3: Matriglycan recognition by the LASV spike complex.**

 figure 3



**a**, Left, top view showing the apex of the trimer using surface representation for the different GP1 subunits (pink, blue and grey). *N*-linked glycans are shown as spheres. Blobs of density next to Tyr150 are shown as a blue mesh at  $\sigma = 4$ , carved at 2 Å around the Xyl- $\alpha$ 1,3-GlcA- $\beta$ 1,3-Xyl moieties, which are shown as sticks. Top right, a closeup view of the density around the Xyl- $\alpha$ 1,3-GlcA- $\beta$ 1,3-Xyl moiety (carved at 2 Å,  $\sigma = 4$ ) in a focused C3-symmetric map. Bottom right, dot blot analysis of membrane-solubilized Flag-tagged GPCs of LASV and MACV, co-purified in the presence of the anti-matriglycan IIH6 antibody. Top blot shows detection of IIH6; bottom blot shows detection of Flag tag. Representative image from three independent repeats. **b**, Detailed view of the matriglycan-binding site at two angles, using the same colour scheme as in **a**. Polar interactions are shown as dashed lines in yellow for spike–matriglycan, in green for inner spike, and in purple for inner matriglycan. Grey dashed line shows hydrophobic interaction. **c**, A continuous matriglycan chain in a focused C1-symmetric map. Density is shown as a blue mesh (carved at 2 Å,  $\sigma = 4.5$ ) around the matriglycan. Colour scheme as **a**. The Xyl–GlcA–Xyl triad in the

symmetric sites is shown in orange. Linker GlcA at the asymmetric sites and the first Xyl (marked with a red asterisk) are in green. N-linked glycans (N-Gly) are shown as spheres. **d**, Detailed view of the binding of GlcA at the asymmetric sites. Polar interactions are shown as dashed lines. **e**, Amino-acid frequency plots of the six terminal GP1 residues from  $\alpha$ -DG- and TfR1-tropic arenaviruses. AMAV, Amapari virus; CHAPV, Chapare virus; IPPYV, Ippy virus; LUAV, Luna virus; MOPV, Mopeia virus; SABV, Sabiá virus; TCRV, Tacaribe virus.

Matriglycan recognition by the spike is mediated by multiple polar interactions. The central sugar in the pocket is GlcA, and its carboxyl group makes polar interactions with the main-chain amines of Arg257 and Leu258, and a salt bridge with the guanidino group of Arg257 (Fig. 3b). Arg257, which is pre-positioned for binding by the three polar interactions it makes with the main-chain carbonyls, forms additional polar bonds with the ring-forming GlcA-O5, with the glycosidic bond of GlcA–Xyl, and the hydroxyl group on Xyl-C2 (Figs. 2a, 3b). Tyr150 is stabilized by polar interactions with Glu151 and Lys125 from a neighbouring GP1 and forms hydrophobic interactions with GlcA (Fig. 3b), thus rationalizing its previously assigned contribution for binding  $\alpha$ -DG in LCMV<sup>24</sup> and in LASV<sup>35</sup>. In addition, Arg256 forms two polar interactions with the hydroxyl group on Xyl-C2. Notably, the observed bound conformation of matriglycan may represent a low-energy conformer, since it is stabilized by several intra-matriglycan polar interactions (Fig. 3b). In addition, the formation of the binding site for matriglycan by a RRLL motif from one GP1 subunit that is packed against another GP1 subunit (Figs. 2a, 3b) explains why monomeric LASV GP1 subunits do not form detectable interactions with  $\alpha$ -DG<sup>25</sup>.

Next to each of the three Xyl–GlcA–Xyl moieties, we observed density that indicated a continuation of the chain but was not sufficiently clear for modelling. We hence further classified our data in C1 and created focused C1-symmetric maps for this region (Extended Data Fig. 5b). The main class clearly showed that the three densities comprise, in fact, parts of a single continuous linear chain of matriglycan (Fig. 3c, Extended Data Fig. 6c). We were able to model linking-GlcA moieties at two of the asymmetric sites (Fig. 3c, Extended Data Fig. 6c, Extended Data Table 1). In addition, we were able to model additional Xyl–GlcA at the entrance point of the matriglycan (Fig. 3c). The terminal Xyl moiety in our model stacks parallel to a *N*-acetylglucosamine attached to Asn119 (Fig. 3c). All the extra GlcA moieties form favourable contacts with the LASV spike; the carboxyl groups of the GlcA in the asymmetric sites serve as N-terminal caps for  $\alpha$ -helices of GP1 by forming hydrogen bonds with the main-chain amines of Leu120 and Ser121 (Fig. 3d). In addition, at least for one linking GlcA, the hydroxyl of Ser121 seems to form a hydrogen bond with the ring oxygen atom and with the carboxyl group of GlcA. In total, we observe 13 sugar monomers bound to the spike of LASV with a total buried surface area of 2,113 Å<sup>2</sup> (903 Å<sup>2</sup> on the spike and 1,210 Å<sup>2</sup> on the matriglycan chain) for complex formation.

Thus, extensive network of polar interactions, large buried surface area and additional factors such as degeneracy in binding states, drive the recognition of matriglycan by LASV. Of note, the role of the SKI-I RRLL recognition motif in binding matriglycan, and particularly the contribution of Arg257 (Fig. 3b), explain the conservation of this residue in  $\alpha$ -DG-tropic but not in TfR1-tropic arenaviruses (Fig. 3e), a difference that has been noted before<sup>33</sup>. This structure further explains how mutating His141 and Phe147 to alanine abrogates the interaction of the LASV spike with  $\alpha$ -DG<sup>35</sup>, as these two residues are located directly below the RRLL motif (Extended Data Fig. 7a) and thus contribute to the stabilization of the matriglycan-binding site.

## Spike inhibition by free matriglycan

The discovery that the LASV spike complex is generated preloaded with matriglycan raises questions about the source of this molecule and its role in the biology of LASV. Matriglycan is thought to be a unique modification of  $\alpha$ -DG<sup>16,17</sup>. To test whether the LASV-bound matriglycan is attached to  $\alpha$ -DG, we spotted a nitrocellulose membrane with detergent-solubilized Flag-tagged LASV spike and probed it with the IIH6 antibody (Fig. 4a). Although matriglycan signal is apparent in a total cell lysate that contains  $\alpha$ -DG, no signal was observed in the LASV spike (Fig. 4a), indicating that matriglycan was washed away. This implies that the spike-carried matriglycan is not covalently attached to a protein mass that could have retained it on the membrane, a notion that is further corroborated by the uniform appearance of particles in the electron micrographs (Extended Data Fig. 1) and the lack of unaccounted 2D classes in our data. These results further suggest that cells produce matriglycan that is not covalently linked to  $\alpha$ -DG.

**Fig. 4: Excess of matriglycan inhibits cell entry of LASV.**



**a**, Dot blot analysis of membrane-immobilized matriglycan. Purified LASV GPC and total cell lysate (TCL) of HEK 293T cells were spotted on a nitrocellulose membrane. The presence of matriglycan (top) was detected using IIH6 antibody. After stripping, the presence of Flag was detected using anti-Flag antibody (bottom). One representative experiment out of three independent repeats. **b**, Excess of matriglycan reduces infectivity of LASV. Infectivity of MLV-pseudotyped viruses carrying the spike complexes of LASV or of the TfR1-tropic MACV was measured in the presence or in the absence of excess matriglycan. Dots represent technical repeats ( $n = 5$ ) and  $P$  values (two tailed Student's  $t$ -test) are indicated. Whiskers indicate the minimum and maximum values, the central line indicates the mean, and the box shows the interquartile range. One representative experiment out of three independent repeats. **c**, Schematic model for the effect of soluble matriglycan on the cell-attachment potential of LASV. The red curve represents the decay in the number of spike complexes that are bound to soluble matriglycan following the transition of the viruses into an environment with low free matriglycan concentration (that is, much lower than the  $K_D$  for complex formation). The cell-attachment potential is indicated by a grey curve, and is cooperatively growing, owing to the high-avidity potential of binding to the target cell. A window of opportunity in which viruses can diffuse before their attachment potential becomes high and causes them to adhere to a target cell is indicated with a blue rectangle.

Soluble free matriglycan that occupies the spike binding site may serve as a competitive inhibitor for binding cells. Indeed, supplementing MLV-based LASV pseudotyped viruses with in vitro-produced matriglycan significantly inhibits infectivity (Fig. 4b). Therefore, once newly formed viruses are exposed to a low free-matriglycan concentration environment (that is, below the dissociation constant ( $K_D$ ) for complex formation), the number of blocked spikes will decay (Fig. 4c) until there would be a sharp increase in the attachment potential of the viruses to cells owing to the high avidity potential of attachment (Fig. 4c). We postulate that under such conditions, newly formed viruses will have a window of opportunity to escape the cell from which they originated before their attachment potential becomes too high. Thus, binding of free matriglycan by the LASV spike probably aids viral egress.

## Discussion

The structural role of the unusually long SSP of arenaviruses has so far remained unknown. Owing to the high conservation of SSP in arenaviruses (Fig. 1g), it is highly likely that they all share the same SSP configuration, as we discovered here. Our data indicate that the second hydrophobic region of SSP (Fig. 1g) is not associated with the central transmembrane region of the spike, and is located at the cytoplasm or inside the virion. The organization of the SSP indicates that besides the 38 residues of GP2

that form a cytoplasmic zinc-binding domain<sup>30</sup>, there are also around 25 residues of SSP inside the cell (Fig. 1f,g). Thus, the spike complexes of arenaviruses have a substantial protein mass located at the intraviral–inner-cellular region. The separation of the C terminus of SSP and the N terminus of GP1 across the membrane indicates a topological rearrangement event that probably occurs after cleavage by SPase. It is noteworthy that topological changes of signal peptides have been observed previously<sup>36,37</sup>, and this phenomenon might explain the difficulty of experimentally determining the topology of the SSP. The association mode of SSP with the trimeric spike (Fig. 1b) suggests that it helps in maintaining the stability of the native structure by locking in place the transmembrane helices of GP2 (Fig. 2c). We speculate that structural rearrangements of the spike probably occur during priming<sup>38</sup> and may involve changes in the way SSP interacts with the spike. This may help rationalizing the role of SSP residues, such as Lys33, in affecting pH-induced triggering of the spike<sup>8</sup>.

In addition to the multiple polar interactions and the extended buried surface area that drive the binding of matriglycan by the LASV spike complex, other factors may influence the binding strength. The interaction of the LASV spike complex, which exhibits three-fold symmetry and harbours a linear asymmetric form of matriglycan, gives rise to multiple degenerate binding states (Extended Data Fig. 8a). Although these states are fully equivalent and indistinguishable, their existence effectively reduces the entropic cost of binding. Besides the observed conformation in our structure (Fig. 3c), additional states might be accommodated using similar geometry. Two or even three separate matriglycan chains could potentially bind to a single trimer at the same time, and with multiple degenerate states (Extended Data Fig. 8b,c). Simultaneous binding of more than one chain may be important for establishing the initial interaction of the virus with the host cell and should also benefit from avidity if the matriglycan chains are anchored together to the same surface. The spike complex could also possibly bind in the middle of a long matriglycan chain. A proposed geometry for such binding is shown in Extended Data Fig. 8d. This putative interaction may allow the virions to slide along the long matriglycan chains, similarly to sliding of various proteins along other biological polymers<sup>39</sup>.

The finding that the RRLL–SKI-I recognition motif has important structural roles in stabilizing the spike (Fig. 2a) and in forming the matriglycan-binding site (Fig. 3a), provides an explanation for the evolutionarily conserved function of SKI-I in cleaving the GPC. For other viruses that utilize class-I spike complexes, such as SARS-CoV-2, acquiring a furin cleavage site increases their virulence<sup>40,41</sup> by achieving a more efficient cleavage as well as enabling the recognition of the newly formed C' by NRP1 and NRP2, which become attachment factors<sup>41</sup>. To enable binding by the NRPs, the newly formed C' must stay exposed in the mature spike, which is true for SARS-CoV-2, but not for LASV (Extended Data Fig. 9). Artificially introducing a furin site to the

spike complex of LASV results in a cleaved trimer<sup>21</sup> that lacks the stabilizing swapping mechanism as we observed, and has a malformed receptor binding site (Fig. 2a, Extended Data Fig. 7b).

Viruses are known to ‘borrow’ molecules from their host cells during biogenesis. A known example is the ‘pocket factor’, a cellular-derived fatty acid that binds and stabilizes the coat proteins of rhinoviruses<sup>42,43</sup>. A recent example includes the spike complex of SARS-CoV-2, which uses linoleic acid from its host cell to stabilize a ‘closed’ conformation<sup>44</sup>. After maturation, the LASV spike complex latches on to what appears to be a free matriglycan polymer (Fig. 4a). For this to happen, there are two important prerequisites: (1) the spike complexes need to be able to bind matriglycan, and (2) matriglycan should be available. SKI-I is localized to the Golgi<sup>45</sup> and the processing of the LASV GPC by SKI-I occurs at the endoplasmic reticulum–*cis*-Golgi<sup>46</sup>. The enzyme that produces matriglycan is LARGE1<sup>16,18</sup> and is also located at the Golgi<sup>47</sup>. However, LARGE1 is known to synthesize matriglycan on α-DG and not as a free polymer in solution. Notably, incubating the enzyme β1,4-glucuronyltransferase (B4GAT1)<sup>48</sup> with Xyl and UDP-GlcA in vitro produces a GlcA-β1-4-Xyl that is recognized and elongated by LARGE1<sup>49</sup>. Hence, B4GAT1 that is found in the Golgi<sup>48</sup> could potentially produce free substrates that LARGE1 would subsequently elongate to form free polymers of matriglycan. We therefore postulate that following SKI-I-dependent maturation at the endoplasmic reticulum–*cis*-Golgi, the LASV spike reaches a Golgi compartment where free matriglycan polymers are available, and that this is where loading occurs. The bound matriglycan then serves as a competitive inhibitor for the binding of matriglycan on cells (Fig. 4b). Inhibiting cell attachment for a certain duration using free matriglycan provides a mechanism that reduces the probability of newly formed α-DG-tropic arenaviruses adhering back to their host cells, and thereby facilitates viral egress. Moreover, since the LASV spike complex undergoes priming in a low-pH endocytic environment during cell entry<sup>38</sup>, the presence of free matriglycan in the *trans*-Golgi network—also characterized by low pH<sup>50</sup>—could help stabilize the spike to reduce premature priming.

Introducing various modifications, such as truncations, point mutations and alterations to viral spike proteins has been an essential approach for obtaining important structural information. Our study demonstrates that such modifications may unintentionally alter essential structural features, such as the formation of the matriglycan-binding site (Extended Data Fig. 7b), as in the case of the LASV spike. Using single-particle cryo-EM may circumvent or at least reduce the need to introduce such modifications. The structure of a stable LASV spike and the identification of the matriglycan-binding site may facilitate the design of improved therapies targeting this high-priority human pathogen.

## Methods

### LASV GPC production and purification

Expression of the full-length LASV GPC was carried out in HEK 293F cells (Invitrogen) using FreeStyle Medium (Life Technologies). Cells were grown to a density of approximately  $1.0 \times 10^6$  cells per ml before transfection. HEK 293F cells were transfected using 40 kDa polyethylenamine (PEI-MAX) (Polysciences) at 1 mg ml<sup>-1</sup>, pH 7 with DNA at a ratio of 1:2.5 (DNA:PEI solution). Codon-optimized LASV GPC (Josiah strain) was chemically synthetized (Genescrypt) and then subcloned with a C-terminal Flag tag into pcDNA3.1 using BamHI–NotI restriction sites. The LASV GPC-expressing cells were collected at 48 h post-transfection by centrifugation at 600g, 4 °C for 10 min. Membranes were then resuspended in a cold lysis buffer (10 mM Tris, 100 µM MgCl<sub>2</sub>, 100 µM phenylmethyl sulfonyl fluoride (PMSF), 15% glycerol) and homogenized for 5 min on ice. The lysis mixture was then incubated while rotating for 1 h at 4 °C. A second homogenization was carried out and the lysis mixture was centrifuged at 21,000g for 25 min, 4 °C. The supernatant was discarded and pellets were dissolved in solubilization buffer (20 mM Tris, 150 NaCl, 50 µM ZnCl<sub>2</sub>, 100 µM PMSF, 15% glycerol, 2% (% w/v) *n*-dodecyl-β-d-maltoside (DDM; Anatrace), 0.2% (% w/v) cholesteryl hemisuccinate (CHS; Anatrace). The solubilization mixture was then homogenized and incubated for 4 h; after which it was centrifuged at 265,000g for 25 min, 4 °C. The supernatant of this solubilization step was then incubated overnight with 40 µl of EZview red anti-Flag beads (Sigma Aldrich). The insoluble material from the solubilization step was discarded. The anti-Flag beads were then spun down (800g, 1 min) and washed by subsequently decreasing amounts of glycerol to 0.3% while replacing the DDM and CHS with increasing amounts of lauryl maltose neopentyl glycol (LMNG; Anatrace) to 0.03%. The protein was eluted after the last washing step with 120 µl of 0.40 mg/ml of 1× Flag peptide (Genescrypt) in a buffer containing 0.03% LMNG, 0.3% glycerol, 20 mM Tris-HCl, 150 mM NaCl, 50 µM ZnCl<sub>2</sub>, 100 µM PMSF, from a 2-hour incubation on ice with periodic mixing. For western blot analysis, anti-Flag primary antibody (Thermo Fischer) was used at 1:1,000 dilution with horseradish peroxidase (HRP)-conjugated anti-rabbit secondary antibody (Jackson) at a 1:10,000 dilution.

### Cryo-EM image acquisition, data analysis and 3D reconstruction

Purified LASV GPC sample (3.5 µl) was applied on glow-discharged (10 s, 12 mA; Pelco easiGlow, Ted Pella) graphene oxide Quantifoil copper grids, R1.2/1.3, (Electron Microscopy Sciences) using a Vitrobot system (Thermo Fischer/FEI) (3 s blotting time, 4 °C, 100% humidity). Samples were incubated on the grid for 2 min before blotting was carried out. cryo-EM data was then collected on the Titan Krios

microscope (FEI) operated at 300 kV, using a Gatan K3 direct detection camera. The beam size was 900  $\mu\text{m}$  diameter, the exposure rate was  $20 \text{ e}^- \text{ s}^{-1} \text{ pixel}^{-1}$ , and movies were then obtained at  $165,000\times$  magnification with a pixel size of 0.519 Å. The nominal defocus range was  $-0.6$  to  $-1.8 \mu\text{m}$ . A total of 4,072 movies were automatically collected using EPU.

Data processing was carried out with the cryoSPARC v3 suite<sup>51</sup>. Patch motion correction and patch CTF estimation were carried using cryoSPARC Live. Blob picking was used to pick 1,208,607 particles. Particles were extracted using a 512-pixel box, and were Fourier-cropped to a 256-pixel box with a pixel size of 1.038 Å. The dataset was cleared using several rounds of 2D classification, followed by 3D classification using C1 symmetry, and ab initio-created models. Some 97,542 particles belonging to a single class with the most visible transmembrane region were selected and further refined using 2D classification to yield a final data set of 91,903 particles that was used for reconstructing the density map while imposing a C3 symmetry. The final map was low-pass filtered to the map-model FSC value (see Extended Data Fig. 2).

To reconstruct focused maps, 234,687 particles belonging to classes 2, 3 and 4 that exhibited an apparent complete ectodomain were pooled together and reconstructed with C3 symmetry followed by local C3-symmetric reconstruction with a mask around the ectodomain (first map). The same pool of particles was further 3D-classified using a C1 symmetry, and a subset of 103,416 particles was used to first reconstruct and then to refine using local reconstruction a C1-symmetric map (second map). The final map was low-pass filtered to the map-model FSC value (see Extended Data Fig. 6c).

## Model building, refinement and analysis

An initial model was generated by docking the ectodomain structure obtained by Hastie et al. <sup>21</sup> (5VK2) into the density map using Chimera<sup>52</sup>. Then, using Coot<sup>53</sup> and real-space refinement in Phenix<sup>54</sup>, we manually completed and refined the model of the spike. We used PyMol<sup>55</sup> for structural analysis and generation of graphics. We used Areamol within the CCP4 suite<sup>56</sup> to calculate buried surface area.

## Structure modelling of the signal peptide

Membrane-spanning segments were identified manually. The structure was embedded in a virtual membrane using the PPM server<sup>57</sup>. The region encompassing the signal peptide (positions 1–58) was segmented into all possible 22 amino acid windows, generating 37 possible sequences. Each sequence was modelled in Rosetta in an orientation corresponding to a C terminus in the cytoplasm or out. Each sequence was threaded on the backbone coordinates as observed in the experimental structure,

followed by side-chain packing and side-chain and backbone minimization. All calculations were done using the membrane protein energy function ref2015\_memb<sup>27,58</sup>, which is dominated by van der Waals interactions, environment-dependent hydrogen bonding, electrostatics, and a depth- and orientation-dependent membrane solvation potential derived from the dsT $\beta$ L experiment<sup>58</sup>. Each window was modelled ten times in each orientation, retaining the model with the lowest computed energy for each window. See [Supplementary Information](#) for the RosettaScript<sup>59</sup> and command line for executing calculations.

## UniProtKB accession codes for GPC sequences and viruses abbreviations

The virus name abbreviations and the sequence entry codes for the relevant sequences that were used in this study are: Lassa (LASV, P08669), Dandenong (DANV, B1NX58), Guanarito (GTOV, Q8AYW1), Junín (JUNV, P26313), Latino (LATV, Q8B121), Lymphocytic choriomeningitis (LCMV, Lymphocytic choriomeningitis), Lujo (LUJV, C5ILC1), Morogoro (MORV, C6ZK00), Oliveros (OLVV, Q84168), Mopeia (MOPV, P19240), Ippy (IPPYV, Q27YE4), Luna (LUAV, A0A6B7EQ86), Mobala (MOBV, Q2A069), Sabiá (SABV, Q90037), Chapare (CHAPV, B2C4J0), Amapari (AMAV, Q8B122), Tacaribe (TCRV, P18141), Machupo (MACV, Q6IUF7) and Whitewater Arroyo (WWAV, Q911P0).

## Biochemical analysis for the presence of matriglycan

For detecting matriglycan we made use of the anti-matriglycan IIH6 monoclonal antibody. The IIH6 C4 monoclonal antibody developed by K. P. Campbell was obtained from the Developmental Studies Hybridoma Bank (DSHB), created by the NICHD of the NIH and maintained at The University of Iowa. Flag-LASV GPC was solubilized from membranes and immobilized on anti-Flag beads as described above for the purification of the spike. Following a wash at a buffer containing 7.5% glycerol, 50  $\mu$ l of 30  $\mu$ g ml<sup>-1</sup> IIH6 C4 was added to 250  $\mu$ l of the anti-Flag beads in a 5% glycerol wash buffer (with 0.04% LMNG and residual DDM). The anti-Flag beads were then incubated for 1 h with IIH6 with intermittent mixing. The remainder of the washing and elution steps were carried out exactly as described for the purification of the spike. Upon elution by the Flag 1 $\times$  peptide, protein samples were then directly used for immunoblotting on a nitrocellulose membrane. To detect IIH6, we blocked the membrane with 3% skim milk and used goat anti-mouse IgM-HRP (Santa Cruz; 1:2,500 dilution) in TBST with EZ-ECL (Biological Industries) for visualization. For detecting Flag, the membrane was washed with transfer buffer (25 mM Tris-HCl, 200 mM glycine, 20% methanol), blocked with 3% BSA in TBST, incubated with rabbit anti-Flag polyclonal antibody (Thermo Fisher; 1:2,000) for 1 h, and with anti-rabbit

HRP-conjugated IgG (Jackson ImmunoResearch Laboratories; 1:10,000), prior to the visualization with EZ-ECL.

### **Production of pseudotyped virus-like particle**

Murine leukaemia virus (MLV)-based, virus-like particles (VLPs) pseudotyped with the GPC spike complexes of LASV, Lujo virus (LUJV) and Machupo virus (MACV) were produced by co-transfected retroviral transfer vector pLXIN-Luc encoding a luciferase reporter gene together with a pcDNA3.1 encoding either MACV, LUJV or LASV GPC into the GP2-293 packaging cell line (Clontech). A total of  $5 \times 10^6$  GP2-293 cells were seeded on 10-cm plates and transfected 24 h later with 10 µg of DNA (5 µg of spike encoding plasmid and 5 µg of luciferase-encoding plasmid) using Lipofectamine 2000 (Invitrogen). Medium was replaced 5 h later with DMEM (Biological Industries) supplemented with 1% Pen-Strep (v/v), 1% glutamine (v/v), and 1% sodium pyruvate (v/v) and 10% fetal calf serum (FCS). At 48 h post-transfection, media containing pseudotyped viruses were collected, and VLPs were concentrated 10 times by the addition of PBS/8 % (w/v) PEG 6000 (Sigma), incubation at 4 °C for 24 h, centrifugation at 10,000g for 20 min and resuspension in full medium for viral depletion experiments or in plain DMEM for matriglycan inhibition assays. Concentrated VLPs were stored at -80 °C until use.

### **Generation of synthetic matriglycan in vitro**

The LARGE1 (xylosyl- and glucuronyl-transferase I) gene (Forchheimer plasmid bank, Weizmann Institute of Science, Clone ID 100000367), without its cytosolic or transmembrane domains (residues 28–756) and with a 6× His tag at its N terminus, in *pENTR223*, was subcloned into a modified pHsec downstream to a signal peptide, via its BglII and NotI restriction sites. Expression of LARGE1 was carried out in HEK 293F cells (Invitrogen) using FreeStyle Medium (Life Technologies). Cells were grown to a density of about  $1.0 \times 10^6$  cells per ml before transfection. HEK 293F cells were transfected using 40 kDa polyethylenamine (PEI-MAX) (Polysciences) at 1 mg ml<sup>-1</sup>, pH 7 with DNA at a ratio of 1:2.5 (DNA:PEI solution). Soluble LARGE1 was collected from cell medium one week post-transfection. Cells were removed by centrifuged at 600g for 10 min and then the supernatant was spun down at 15,800g for 30 min to remove residual cellular debris. The supernatant was then supplemented with 100 µM PMSF and 0.02% sodium azide and filtered through a 0.45 µm Stericup (Merck Millipore). Buffer exchange to TBS (20 mM Tris-HCl, pH 8, 150 mM NaCl) was carried out using a Pellicon Tangential Flow Filtration system (Merck Millipore). LARGE1 was then captured using affinity chromatography on a 5 ml HiTrap IMAC FF Ni<sup>2+</sup> column (GE Healthcare), and further purified using size-exclusion chromatography on a Superdex 200 10/300 GL column (GE Healthcare). Purified

LARGE1 was concentrated using a 4 ml 30 kDa Amicon centrifugal unit (Sigma) and aliquots were flash frozen and stored at  $-80^{\circ}\text{C}$ .

Matriglycan was prepared in a reaction mixture containing 100 mM MES pH 5.8, 3.3 mM MgCl<sub>2</sub>, 3.3 mM MnCl<sub>2</sub>, 200  $\mu\text{M}$  UDP-glucuronic acid (Promega), 200  $\mu\text{M}$  UDP-xylose (CarboSource Services), 1.5 mM 4-nitrophenyl- $\alpha$ -d-xylopyranoside (used as a substrate for matriglycan elongation; Megazyme), and about 100  $\mu\text{g ml}^{-1}$  of purified LARGE1. The reaction mixture was incubated at  $37^{\circ}\text{C}$  for 60 h before flash freezing in liquid N<sub>2</sub>. To monitor matriglycan synthesis we used Promega's glycosyltransferase kit. Specifically, 25  $\mu\text{l}$  of a reaction mixture was mixed with 25  $\mu\text{l}$  of UDP detection reagent and incubated for 1 h at room temperature. A calibration curve was derived using free UDP. Free UDP was then quantified by detecting bioluminescence signal following the addition of a UDP-Glo enzyme (Promega).

### **Inhibition of infectivity by matriglycan**

For infectivity assays, HEK 293T cells (for LASV) or HEK 293T cells that overexpress human transferrin receptor<sup>60</sup> (for MACV) were seeded on a poly-l-lysine-precoated white, chimney 96-well plate (Greiner Bio-One) at 50,000 cells per well. Cells were left to adhere for 3 h, followed by the addition of the supernatant containing the VLPs either with matriglycan (0.3 nmol of polymerized matriglycan units) or with matriglycan-generation buffer only as a control. Cells were washed from the viruses at 2 h post-infection, and luminescence from the activity of luciferase was measured at 48 h post-infection using Tecan Infinite M200 Pro plate reader after applying Bright-Glo reagent (Promega) to cells.

### **Depletion of pseudotyped viruses by IIH6**

Protein-L beads (SCBT) were either loaded with IIH6 (40  $\mu\text{l}$  of beads incubated with 150  $\mu\text{l}$  of IIH6 at a concentration of 125  $\mu\text{g ml}^{-1}$  for 30 min at room temperature), or washed using full medium (see above). Excess IIH6 was washed with 200  $\mu\text{l}$  of full medium after centrifugation of the beads at 1,000g for 2 min, followed by 30 min incubation with 125  $\mu\text{l}$  of either LASV or LUJV VLPs at room temperature. The supernatants containing the VLPs were separated using centrifugation at 1,000g for 2 min and transferred to a new tube for quantification by quantitative PCR with reverse transcription (RT-qPCR).

### **Quantifying pseudotyped viruses with RT-qPCR**

A sample of 5  $\mu\text{l}$  from previously described pulled-down pseudo-typed viruses was used to quantify RNA levels of the luciferase reporter gene using RT-qPCR. Viruses

were first diluted 10× in PBS buffer, and clarified by centrifugation at 19,000g at 4 °C for 10 min. Supernatants were then treated with 2 mg ml<sup>-1</sup> RNase A (Bio Basic) and RNase-free DNase I (NEB) for 10 min at 37 °C to eliminate nucleic acids contaminations that are not protected inside the VLPs. To inhibit RNase A activity, 40 units of RNase inhibitor (NEB) were added, and the reaction was incubated for 10 min at 37 °C. RNA was then extracted from viral-particles using the RNAeasy mini kit (Qiagen). Thereafter, cDNA was prepared from RNA using the High Capacity cDNA Reverse Transcription Kit (Applied Biosystems). cDNA was diluted 1:40, and subjected to quantitative PCR (qPCR) using specific primers for luciferase, and Fast SYBR green master mix (Applied Biosystems).

## Creating amino acid frequency plot

The amino acid frequency plot was generated using WebLogo<sup>61</sup>.

## Reporting summary

Further information on research design is available in the [Nature Research Reporting Summary](#) linked to this paper.

## Data availability

Coordinate files and experimental density maps for the C3-symmetric and C1-symmetric reconstructions were deposited at PDB (Electron Microscopy Data Bank (EMDB)) under accession codes [7PUY \(EMD-13662\)](#) and [7PVD \(EMD-13667\)](#), respectively. The C3-focused map was deposited to EMDB under accession code ([EMD-13668](#)).

## Code availability

The complete script that was used to execute the Rosetta calculation is included in Supplementary Data.

## References

1. McCormick, J. B., Webb, P. A., Krebs, J. W., Johnson, K. M. & Smith, E. S. A prospective study of the epidemiology and ecology of Lassa fever. *J. Infect. Dis.* **155**, 437–444 (1987).

2. Bell-Kareem, A. R. & Smither, A. R. Epidemiology of Lassa fever. *Cur. Top. Microbiol. Immunol.* [https://doi.org/10.1007/82\\_20](https://doi.org/10.1007/82_20) (2021).
3. Cao, W. et al. Identification of  $\alpha$ -dystroglycan as a receptor for lymphocytic choriomeningitis virus and Lassa fever virus. *Science* **282**, 2079–2081 (1998).
4. Kunz, S., Rojek, J. M., Perez, M., Spiropoulou, C. F. & Oldstone, M. B. Characterization of the interaction of Lassa fever virus with its cellular receptor  $\alpha$ -dystroglycan. *J. Virol.* **79**, 5979–5987 (2005).
5. Bederka, L. H., Bonhomme, C. J., Ling, E. L. & Buchmeier, M. J. Arenavirus stable signal peptide is the keystone subunit for glycoprotein complex organization. *mBio* **5**, e02063 (2014).
6. Eichler, R. et al. Identification of Lassa virus glycoprotein signal peptide as a *trans*-acting maturation factor. *EMBO Rep.* **4**, 1084–1088 (2003).
7. York, J., Romanowski, V., Lu, M. & Nunberg, J. H. The signal peptide of the Junin arenavirus envelope glycoprotein is myristoylated and forms an essential subunit of the mature G1–G2 complex. *J. Virol.* **78**, 10783–10792 (2004).
8. York, J. & Nunberg, J. H. Role of the stable signal peptide of Junin arenavirus envelope glycoprotein in pH-dependent membrane fusion. *J. Virol.* **80**, 7775–7780 (2006).
9. Agnihothram, S. S., York, J., Trahey, M. & Nunberg, J. H. Bitopic membrane topology of the stable signal peptide in the tripartite Junin virus GP-C envelope glycoprotein complex. *J. Virol.* **81**, 4331–4337 (2007).
10. Froeschke, M., Basler, M., Groettrup, M. & Dobberstein, B. Long-lived signal peptide of lymphocytic choriomeningitis virus glycoprotein pGP-C. *J. Biol. Chem.* **278**, 41914–41920 (2003).
11. Eichler, R. et al. Lassa virus glycoprotein signal peptide displays a novel topology with an extended endoplasmic reticulum luminal region. *J. Biol. Chem.* **279**, 12293–12299 (2004).
12. Salam, A. P. et al. Time to reconsider the role of ribavirin in Lassa fever. *PLoS Negl. Trop. Dis.* **15**, e0009522 (2021).
13. Radoshitzky, S. R. et al. Transferrin receptor 1 is a cellular receptor for New World haemorrhagic fever arenaviruses. *Nature* **446**, 92–96 (2007).

14. Abraham, J. et al. Host-species transferrin receptor 1 orthologs are cellular receptors for nonpathogenic new world clade B arenaviruses. *PLoS Pathog.* **5**, e1000358 (2009).
15. Raaben, M. et al. NRP2 and CD63 are host factors for Lujo virus cell entry. *Cell Host Microbe* **22**, 688–696 e685 (2017).
16. Yoshida-Moriguchi, T. & Campbell, K. P. Matriglycan: a novel polysaccharide that links dystroglycan to the basement membrane. *Glycobiology* **25**, 702–713 (2015).
17. Kunz, S. et al. Posttranslational modification of alpha-dystroglycan, the cellular receptor for arenaviruses, by the glycosyltransferase LARGE is critical for virus binding. *J. Virol.* **79**, 14282–14296 (2005).
18. Inamori, K. et al. Dystroglycan function requires xylosyl- and glucuronyltransferase activities of LARGE. *Science* **335**, 93–96 (2012).
19. Abraham, J., Corbett, K. D., Farzan, M., Choe, H. & Harrison, S. C. Structural basis for receptor recognition by New World hemorrhagic fever arenaviruses. *Nat. Struct. Mol. Biol.* **17**, 438–444 (2010).
20. Cohen-Dvashi, H., Kilimnik, I. & Diskin, R. Structural basis for receptor recognition by Lujo virus. *Nat. Microbiol.* **3**, 1153–1160 (2018).
21. Hastie, K. M. et al. Structural basis for antibody-mediated neutralization of Lassa virus. *Science* **356**, 923–928 (2017).
22. Sullivan, B. M. et al. Point mutation in the glycoprotein of lymphocytic choriomeningitis virus is necessary for receptor binding, dendritic cell infection, and long-term persistence. *Proc. Natl Acad. Sci. USA* **108**, 2969–2974 (2011).
23. Smelt, S. C. et al. Differences in affinity of binding of lymphocytic choriomeningitis virus strains to the cellular receptor  $\alpha$ -dystroglycan correlate with viral tropism and disease kinetics. *J. Virol.* **75**, 448–457 (2001).
24. Hastie, K. M. et al. Crystal structure of the prefusion surface glycoprotein of the prototypic arenavirus LCMV. *Nat. Struct. Mol. Biol.* **23**, 513–521 (2016).
25. Cohen-Dvashi, H., Cohen, N., Israeli, H. & Diskin, R. Molecular mechanism for LAMP1 recognition by Lassa virus. *J. Virol.* **89**, 7584–7592 (2015).
26. Israeli, H., Cohen-Dvashi, H., Shulman, A., Shimon, A. & Diskin, R. Mapping of the Lassa virus LAMP1 binding site reveals unique determinants not shared by

- other old world arenaviruses. *PLoS Pathog.* **13**, e1006337 (2017).
27. Weinstein, J. Y., Elazar, A. & Fleishman, S. J. A lipophilicity-based energy function for membrane-protein modelling and design. *PLoS Comput. Biol.* **15**, e1007318 (2019).
  28. Saunders, A. A. et al. Mapping the landscape of the lymphocytic choriomeningitis virus stable signal peptide reveals novel functional domains. *J. Virol.* **81**, 5649–5657 (2007).
  29. Schrempf, S., Froeschke, M., Giroglou, T., von Laer, D. & Dobberstein, B. Signal peptide requirements for lymphocytic choriomeningitis virus glycoprotein C maturation and virus infectivity. *J. Virol.* **81**, 12515–12524 (2007).
  30. Briknarova, K., Thomas, C. J., York, J. & Nunberg, J. H. Structure of a zinc-binding domain in the Junin virus envelope glycoprotein. *J. Biol. Chem.* **286**, 1528–1536 (2011).
  31. Messina, E. L., York, J. & Nunberg, J. H. Dissection of the role of the stable signal peptide of the arenavirus envelope glycoprotein in membrane fusion. *J. Virol.* **86**, 6138–6145 (2012).
  32. Heijne, G. The distribution of positively charged residues in bacterial inner membrane proteins correlates with the trans-membrane topology. *EMBO J.* **5**, 3021–3027 (1986).
  33. Burri, D. J. et al. Differential recognition of Old World and New World arenavirus envelope glycoproteins by subtilisin kexin isozyme 1 (SKI-1)/site 1 protease (S1P). *J. Virol.* **87**, 6406–6414 (2013).
  34. Ervasti, J. M. & Campbell, K. P. Membrane organization of the dystrophin–glycoprotein complex. *Cell* **66**, 1121–1131 (1991).
  35. Acciani, M. et al. Mutational analysis of Lassa virus glycoprotein highlights regions required for  $\alpha$ -dystroglycan utilization. *J. Virol.* **91**, e00574–17 (2017).
  36. Prod'homme, V. et al. Human cytomegalovirus UL40 signal peptide regulates cell surface expression of the NK cell ligands HLA-E and gpUL18. *J. Immunol.* **188**, 2794–2804 (2012).
  37. Cocquerel, L. et al. Topological changes in the transmembrane domains of hepatitis C virus envelope glycoproteins. *EMBO J.* **21**, 2893–2902 (2002).

38. Cohen-Dvashi, H., Israeli, H., Shani, O., Katz, A. & Diskin, R. Role of LAMP1 binding and pH sensing by the spike complex of Lassa virus. *J. Virol.* **90**, 10329–10338 (2016).
39. Bigman, L. S., Greenblatt, H. M. & Levy, Y. What are the molecular requirements for protein sliding along DNA? *J. Phys. Chem. B* **125**, 3119–3131 (2021).
40. Johnson, B. A. et al. Loss of furin cleavage site attenuates SARS-CoV-2 pathogenesis. *Nature* **591**, 293–299 (2021).
41. Cantuti-Castelvetri, L. et al. Neuropilin-1 facilitates SARS-CoV-2 cell entry and infectivity. *Science* **370**, 856–860 (2020).
42. Smith, T. J. et al. The site of attachment in human rhinovirus 14 for antiviral agents that inhibit uncoating. *Science* **233**, 1286–1293 (1986).
43. Rossmann, M. G. et al. Structure of a human common cold virus and functional relationship to other picornaviruses. *Nature* **317**, 145–153 (1985).
44. Toelzer, C. et al. Free fatty acid binding pocket in the locked structure of SARS-CoV-2 spike protein. *Science* **370**, 725–730 (2020).
45. Pullikotil, P., Benjannet, S., Mayne, J. & Seidah, N. G. The proprotein convertase SKI-1/S1P: alternate translation and subcellular localization. *J. Biol. Chem.* **282**, 27402–27413 (2007).
46. Burri, D. J. et al. Molecular characterization of the processing of arenavirus envelope glycoprotein precursors by subtilisin kexin isozyme-1/site-1 protease. *J. Virol.* **86**, 4935–4946 (2012).
47. Grewal, P. K., McLaughlan, J. M., Moore, C. J., Browning, C. A. & Hewitt, J. E. Characterization of the LARGE family of putative glycosyltransferases associated with dystroglycanopathies. *Glycobiology* **15**, 912–923 (2005).
48. Willer, T. et al. The glucuronyltransferase B4GAT1 is required for initiation of LARGE-mediated alpha-dystroglycan functional glycosylation. *eLife* **3**, e03941 (2014).
49. Osman Sheikh, M. et al. Cell surface glycan engineering reveals that matriglycan alone can recapitulate dystroglycan binding and function. Preprint at *bioRxiv* <https://doi.org/10.1101/2021.05.10.443358> (2021).

50. Paroutis, P., Touret, N. & Grinstein, S. The pH of the secretory pathway: measurement, determinants, and regulation. *Physiology* **19**, 207–215 (2004).
51. Punjani, A., Rubinstein, J. L., Fleet, D. J. & Brubaker, M. A. cryoSPARC: algorithms for rapid unsupervised cryo-EM structure determination. *Nat. Methods* **14**, 290–296 (2017).
52. Pettersen, E. F. et al. UCSF Chimera—a visualization system for exploratory research and analysis. *J. Comput. Chem.* **25**, 1605–1612 (2004).
53. Emsley, P., Lohkamp, B., Scott, W. G. & Cowtan, K. Features and development of Coot. *Acta Crystallogr. D* **66**, 486–501 (2010).
54. Adams, P. D. et al. PHENIX: a comprehensive Python-based system for macromolecular structure solution. *Acta Crystallogr. D* **66**, 213–221 (2010).
55. The PyMOL Molecular Graphics System. Version 1.8 (2016).
56. Winn, M. D. et al. Overview of the CCP4 suite and current developments. *Acta Crystallogr. D* **67**, 235–242 (2011).
57. Lomize, M. A., Pogozheva, I. D., Joo, H., Mosberg, H. I. & Lomize, A. L. OPM database and PPM web server: resources for positioning of proteins in membranes. *Nucleic Acids Res.* **40**, D370–D376 (2012).
58. Elazar, A. et al. Mutational scanning reveals the determinants of protein insertion and association energetics in the plasma membrane. *eLife* **5**, e12125 (2016).
59. Fleishman, S. J. et al. RosettaScripts: a scripting language interface to the Rosetta macromolecular modeling suite. *PLoS ONE* **6**, e20161 (2011).
60. Cohen-Dvashi, H. et al. Rational design of universal immunotherapy for TfR1-tropic arenaviruses. *Nat. Commun.* **11**, 67 (2020).
61. Crooks, G. E., Hon, G., Chandonia, J. M. & Brenner, S. E. WebLogo: a sequence logo generator. *Genome Res.* **14**, 1188–1190 (2004).

## Acknowledgements

The Diskin laboratory is supported by research grants from the Ernst I. Ascher foundation, Ben B. and Joyce E. Eisenberg Foundation, Estate of Emile Mimran, Jeanne and Joseph Nissim Center for Life Sciences Research, Dov and Ziva Rabinovich Endowed Fund for Structural Biology, Donald Rivin, Stanley and Tanya

Rossby Endowment Fund, Natan Sharansky, Dr. Barry Sherman Institute for Medicinal Chemistry, as well as from the Israel Science Foundation (grants No. 3147/19 and 209/20). Research in the Fleishman laboratory was supported by a Consolidator Award from the European Research Council (815379) and by a charitable donation in memory of Sam Switzer.

## Author information

### Affiliations

1. Department of Chemical and Structural Biology, Weizmann Institute of Science, Rehovot, Israel

Michael Katz, Maayan Eilon-Ashkenazy, Katrin Gehring, Hadas Cohen-Dvashi & Ron Diskin

2. Department of Biomolecular Sciences, Weizmann Institute of Science, Rehovot, Israel

Jonathan Weinstein & Sarel J. Fleishman

3. Department of Chemical Research Support, Weizmann Institute of Science, Rehovot, Israel

Nadav Elad

### Contributions

R.D. conceived this research. M.K. and K.G. produced and purified the protein. M.K., N.E. and R.D. collected electron microscopy data. M.K. and R.D. solved the structure. J.W. and S.J.F. computationally determined the SSP register. H.C.-D. performed qPCR experiments and provided reagents. M.E.-A. performed infectivity assays. All authors contributed to data analysis. M.K. and R.D. prepared the manuscript with help from all the other authors.

### Corresponding author

Correspondence to [Ron Diskin](#).

### Ethics declarations

## Competing interests

The authors declare no competing interests.

## Peer review

### Peer review information

*Nature* thanks Juha Huiskonen, Félix Rey and Yi Shi for their contribution to the peer review of this work.

## Additional information

**Publisher's note** Springer Nature remains neutral with regard to jurisdictional claims in published maps and institutional affiliations.

## Extended data figures and tables

### [Extended Data Fig. 1 Reconstruction of density map.](#)

The course of data processing and reconstruction of a C3-symmetric density map is visually summarized. Local resolution estimates, gold-standard FSC curve and orientational distribution are shown for the final map.

### [Extended Data Fig. 2 Overall fit of the model to the density map.](#)

Model is shown as a ribbon with or without stick-represented side chains. Density map is shown using a blue mesh at the indicated sigma levels. Asterisks indicate that the density map was carved around the model. Upper left side, the original model was fitted into a working map at GSFSC = 2.5 Å and achieved map-model FSC of 3.3 Å. Center, final refined model at a 3.3 Å low-passed filtered map with a map-model FSC of 3.3 Å. Around the central model, close-up views of regions of interest are indicated at the 3.3 Å low-passed filtered map. Key residues or structural elements are labeled. Bottom part, the six-helical transmembrane bundle is shown in a 6 Å low-pass filtered map at the indicated three different sigma levels.

### [Extended Data Fig. 3 Assigning the overall directionality and registry of the SSP.](#)

**a.** The amino-terminus of the SSP's trans-membrane  $\alpha$ -helix is facing extracellularly. The density map of the trans-membrane  $\alpha$ -helix is shown as a mesh, and two  $\alpha$ -helices are rendered as poly-ala; one has a carboxy-terminus facing up (left) and the second has an amino-terminus facing up (right). Densities for the side-chains are pointing toward the extracellular direction (up), indicating that the correct directionality of this  $\alpha$ -helix in the membrane is with its amino-terminus at the extracellular region (right). **b.** Side-chain densities are visible in low-pass filtered maps. Densities for the  $\alpha$ -helix of SSP are shown with maps that were low-pass (LP) filtered to the indicated resolution values. Dashed horizontal lines help to visualize the direction to which the side-chains are pointing. The directionality of the side-chains is apparent even at 4.5 Å LP-filtered map. **c.** Determining the registry of the SSP. On the left, superimposition of the 37 best-scoring computer-generated models for each threading (N-terminus out, only), shown in a 'top' view. The inner three  $\alpha$ -helices (yellow, brown, and gray) belong to the GP2 subunits and the outer three  $\alpha$ -helices (magenta, cyan, and green) belong to the SSP subunits. On the right, energy profiles (relative Rosetta energy units) of the best-scoring computed model for each threading option as a function of the register, starting with the indicated residue at the amino-terminus of the trans-membrane  $\alpha$ -helix (first methionine is considered as register "0"). The light-blue curve shows threading with the C-terminus out and the red curve shows threading with the N-terminus out. Large red dot indicates the lowest energy solution. **d.** The top-ranked model for the SSP registry.

#### [Extended Data Fig. 4 Domain swapping stabilization of the spike in a double-sided candy twist-wrap fashion.](#)

The directionality of the domain swapping in the trimer is illustrated. The domain swapping at the apex of the trimer (top) and at the membrane proximal region (bottom) have opposing directionalities, which is reminiscence to a candy's double-sided twist wrap (schematically shown on the right). Donation of a structural element from one subunit to another is marked by '-\*\*\*\*-'.

#### [Extended Data Fig. 5 Reconstruction of focused density maps.](#)

The process of reconstructing focused density maps is visually illustrated.

#### [Extended Data Fig. 6 Matriglycan on pseudotyped viruses and in density map.](#)

**a.** Free Flag peptide is not recognized by anti-Flag antibody in a dot-blot settings. To test if the anti-Flag antibody could recognize the Flag peptide that was used to elute the spike complexes, we spotted on a nitrocellulose membrane the LASV and MACV spike complexes as well as the elution buffer alone, or the elution buffer with the Flag

peptide (FLAG 1x). The elution buffer with the free Flag peptide produces only slight background, indicating that the Flag peptide is not adhering to the membrane, and hence does not contribute to the signal of the anti-Flag antibody. **b.** LASV pseudotyped viruses are depleted from solution by IIH6 conjugated to beads. To test if LASV spike complex is loaded with matriglycan in the context of pseudotyped viruses, we incubated MLV-based pseudotyped viruses bearing the spikes of LASV or of the neuropilin-2-tropic Lujo virus (LUJV) with protein-L beads alone, or after coating the beads with the IIH6 antibody. The amount of RNA encoding a luciferase reporter gene was then quantified in the supernatants of each sample using RT-qPCR. Each dot represents an average normalized value of three technical replicates in a single independent experiment ( $n = 5$  of independent experiments). The measurements in each experiment were normalized to the respective uncoated-beads control. Pseudotyped viruses with the LASV spike are significantly (two tailed Student's t-test) depleted from solution by IIH6 on beads. Whiskers indicate the min and max values, central line indicates the mean value, and the box indicates the interquartile range. The slight increase in the amount of LUVJ results from minor unspecific absorption of viral particles to uncoated protein-L beads, which lowers the amount of particle in the reference control. **c.** The ectodomain portion of the spike was fitted into the C1-focused map and yielded a map-model FSC of 3.7 Å. The map was low-passed filtered to 3.7 Å and the model was refined again using this map. The linear matriglycan chain is shown by its top and side views. The density map is shown as a blue mesh at  $\sigma = 4$ , carved at 2.5 Å around the matriglycan. The Xyl-GlcA-Xyl moieties in the symmetric sites are in orange. The GlcA moieties in the asymmetric sites as well as the termini Xyl-GlcA are shown in green.

### [Extended Data Fig. 7 Residues that affect matriglycan binding and a comparison of the cryo-EM structure of LASV spike with the crystal structure of its ectodomain.](#)

**a.** His141 and Phe147 (blue) that were found to be important for matriglycan binding via mutagenesis studies are located directly below the “RRLL” motif (magenta) that binds matriglycan (orange). The conformation of the “RRLL” motif is partially shaped by the interactions it makes with His141 and Phe147. **b.** The cryo-EM model from this study (similar color scheme as in Fig. 1) is show with the crystal structure of the spike’s ectodomain (PDB: 5VK2, green). The two structures are shown as ribbons from a side view (left) and from a top view (top right). Overall, the structures are similar (RMSD = 2.04 Å, for 1009 shared Ca atoms). Key differences are near the membrane spanning domain that is missing from the crystal structure and at the receptor binding site that is not formed (enlarged view, bottom right), following the replacement of the “RRLL”-SKI-I recognition site with a furin recognition sequence. Tyr150, Arg256, and Arg257 that participate in binding of matriglycan are labeled.

## [Extended Data Fig. 8 Degenerate and alternative states for matriglycan binding.](#)

A top view of the LASV trimeric spike showing a surface representation of the three GP1 subunits in pink, blue, and gray. Colored dots represent the potential traces of bound matriglycan chains. Different colors represent different individual chains of matriglycan.

## [Extended Data Fig. 9 Cleavage sites between the receptor binding modules and the transmembrane modules in different viruses.](#)

The trimeric spike complexes of LASV (left) and of SARS-CoV-2 (right, PDB: 6VXX), are shown in a relative scale using surface representations and in three different colors for their three protomers. The protease cleavage sites (i.e., a SKI-I site for LASV and a furin site for SARS-CoV-2) or their immediate vicinities are colored in orange and are pointed with red arrows.

## **Extended Data Table 1 Cryo-EM data collection, refinement and validation statistics**

## **Supplementary information**

### [Supplementary Information](#)

This file contains the Supplementary Methods, which includes the command line and script for Rosetta modelling.

### [Reporting Summary](#)

## **Rights and permissions**

### [Reprints and Permissions](#)

## **About this article**

### **Cite this article**

Katz, M., Weinstein, J., Eilon-Ashkenazy, M. *et al.* Structure and receptor recognition by the Lassa virus spike complex. *Nature* **603**, 174–179 (2022).  
<https://doi.org/10.1038/s41586-022-04429-2>

- Received: 25 July 2021
- Accepted: 17 January 2022
- Published: 16 February 2022
- Issue Date: 03 March 2022
- DOI: <https://doi.org/10.1038/s41586-022-04429-2>

## Share this article

Anyone you share the following link with will be able to read this content:

[Get shareable link](#)

Sorry, a shareable link is not currently available for this article.

[Copy to clipboard](#)

Provided by the Springer Nature SharedIt content-sharing initiative

---

This article was downloaded by **calibre** from <https://www.nature.com/articles/s41586-022-04429-2>

| [Section menu](#) | [Main menu](#) |

- Article
- [Published: 20 December 2021](#)

# Structural architecture of the human NALCN channelosome

- [Marc Kschonsak](#)<sup>1</sup>,
- [Han Chow Chua](#) [ORCID: orcid.org/0000-0003-4477-174X](#)<sup>2</sup>,
- [Claudia Weidling](#)<sup>2</sup> [na1](#),
- [Nourdine Chakouri](#) [ORCID: orcid.org/0000-0002-8809-8684](#)<sup>3</sup> [na1](#),
- [Cameron L. Noland](#) [ORCID: orcid.org/0000-0001-6364-3167](#)<sup>1</sup> [na1](#) [nAff6](#),
- [Katharina Schott](#)<sup>2</sup>,
- [Timothy Chang](#)<sup>4</sup>,
- [Christine Tam](#)<sup>4</sup>,
- [Nidhi Patel](#)<sup>4</sup>,
- [Christopher P. Arthur](#)<sup>1</sup>,
- [Alexander Leitner](#) [ORCID: orcid.org/0000-0003-4126-0725](#)<sup>5</sup>,
- [Manu Ben-Johny](#) [ORCID: orcid.org/0000-0002-5645-0815](#)<sup>3</sup>,
- [Claudio Ciferri](#) [ORCID: orcid.org/0000-0002-0804-2411](#)<sup>1</sup>,
- [Stephan Alexander Pless](#) [ORCID: orcid.org/0000-0001-6654-114X](#)<sup>2</sup> &
- [Jian Payandeh](#) [ORCID: orcid.org/0000-0002-4015-9716](#)<sup>1</sup> [nAff7](#)

[Nature](#) volume **603**, pages 180–186 (2022)

- 6167 Accesses
- 75 Altmetric
- [Metrics details](#)

## Subjects

- [Electron microscopy](#)
- [Ion channels in the nervous system](#)
- [Supramolecular assembly](#)

## Abstract

Depolarizing sodium ( $\text{Na}^+$ ) leak currents carried by the NALCN channel regulate the resting membrane potential of many neurons to modulate respiration, circadian rhythm, locomotion and pain sensitivity<sup>1,2,3,4,5,6,7,8</sup>. NALCN requires FAM155A, UNC79 and UNC80 to function, but the role of these auxiliary subunits is not understood<sup>3,7,9,10,11,12</sup>. NALCN, UNC79 and UNC80 are essential in rodents<sup>2,9,13</sup>, and mutations in human *NALCN* and *UNC80* cause severe developmental and neurological disease<sup>14,15</sup>. Here we determined the structure of the NALCN channelosome, an approximately 1-MDa complex, as fundamental aspects about the composition, assembly and gating of this channelosome remain obscure. UNC79 and UNC80 are massive HEAT-repeat proteins that form an intertwined anti-parallel superhelical assembly, which docks intracellularly onto the NALCN–FAM155A pore-forming subcomplex. Calmodulin copurifies bound to the carboxy-terminal domain of NALCN, identifying this region as a putative modulatory hub. Single-channel analyses uncovered a low open probability for the wild-type complex, highlighting the tightly closed S6 gate in the structure, and providing a basis to interpret the altered gating properties of disease-causing variants. Key constraints between the UNC79–UNC80 subcomplex and the NALCN DI–DII and DII–DIII linkers were identified, leading to a model of channelosome gating. Our results provide a structural blueprint to understand the physiology of the NALCN channelosome and a template for drug discovery to modulate the resting membrane potential.

This is a preview of subscription content

## Access options

Subscribe to Nature+

Get immediate online access to the entire Nature family of 50+ journals

\$29.99

monthly

[Subscribe](#)

Subscribe to Journal

Get full journal access for 1 year

\$199.00

only \$3.90 per issue

[Subscribe](#)

All prices are NET prices.

VAT will be added later in the checkout.

Tax calculation will be finalised during checkout.

Buy article

Get time limited or full article access on ReadCube.

\$32.00

[Buy](#)

All prices are NET prices.

### **Additional access options:**

- [Log in](#)
- [Learn about institutional subscriptions](#)

**Fig. 1: Overall structure of the human NALCN channelosome.**

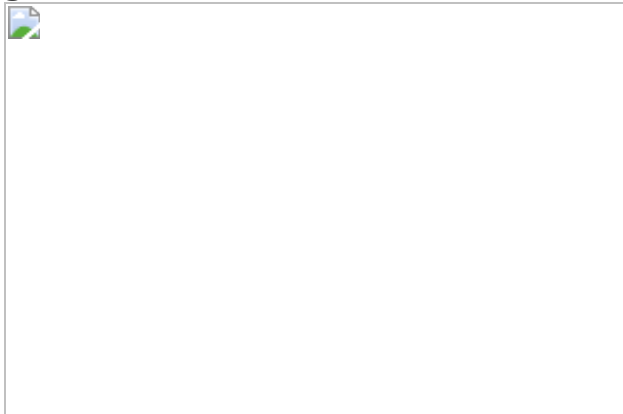


**Fig. 2: Overall structure of the UNC79–UNC80 subcomplex.**

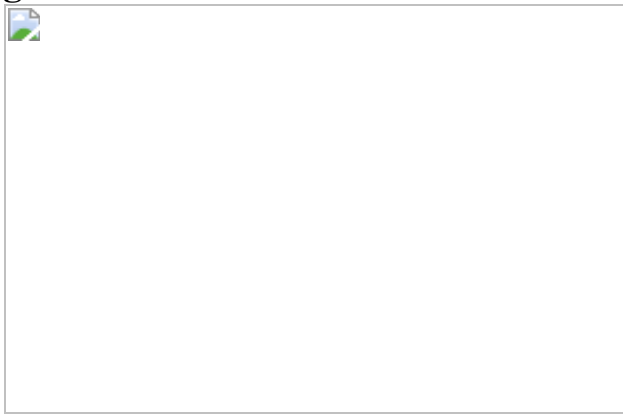


**Fig. 3: NALCN interactions with the UNC79–UNC80 subcomplex.**

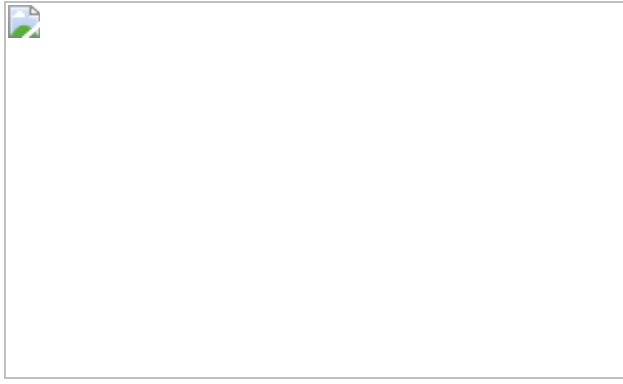
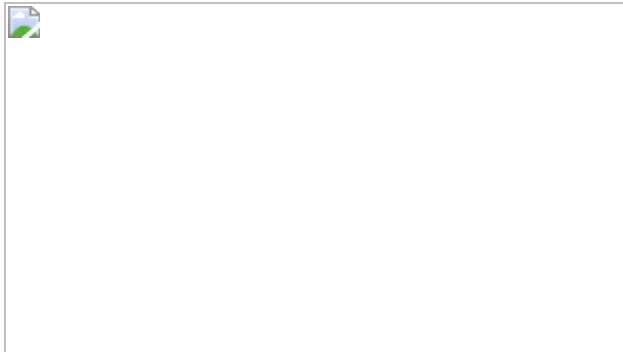


**Fig. 4: The pore structure and gating model of the NALCN channelosome.**



## Data availability

The NALCN–FAM155A–UNC79–UNC80–CaM coordinates are deposited in the PDB ([7SX3](#) and [7SX4](#)) and cryo-EM data are deposited in the Electron Microscopy Data Bank ([EMD-25492](#) and [EMD-25493](#)) for conformation 1 and conformation 2, respectively. Mass spectrometry proteomics data have been deposited to the ProteomeXchange Consortium via the PRIDE<sup>54</sup> partner repository with the dataset identifier [PXD027213](#) and details are included in the [Supplementary Information](#). Source data are provided with this paper.

## References

1. Lear, B. C. et al. The ion channel narrow abdomen is critical for neural output of the *Drosophila* circadian pacemaker. *Neuron* **48**, 965–976 (2005).
2. Lu, B. et al. The neuronal channel NALCN contributes resting sodium permeability and is required for normal respiratory rhythm. *Cell* **129**, 371–383 (2007).
3. Jospin, M. et al. UNC-80 and the NCA ion channels contribute to endocytosis defects in synaptojanin mutants. *Curr. Biol.* **17**, 1595–1600 (2007).
4. Xie, L. et al. NLF-1 delivers a sodium leak channel to regulate neuronal excitability and modulate rhythmic locomotion. *Neuron* **77**, 1069–1082 (2013).

5. Flourakis, M. et al. A conserved bicycle model for circadian clock control of membrane excitability. *Cell* **162**, 836–848 (2015).
6. Lutas, A., Lahmann, C., Soumillon, M. & Yellen, G. The leak channel NALCN controls tonic firing and glycolytic sensitivity of substantia nigra pars reticulata neurons. *eLife* **5**, e15271 (2016).
7. Shi, Y. et al. Nalcn is a “leak” sodium channel that regulates excitability of brainstem chemosensory neurons and breathing. *J. Neurosci.* **36**, 8174–8187 (2016).
8. Philippart, F. & Khaliq, Z. M. Gi/o protein-coupled receptors in dopamine neurons inhibit the sodium leak channel NALCN. *eLife* **7**, e40984 (2018).
9. Lu, B. et al. Extracellular calcium controls background current and neuronal excitability via an UNC79-UNC80-NALCN cation channel complex. *Neuron* **68**, 488–499 (2010).
10. Chua, C. H., Wulf, M., Weidling, C., Rasmussen, L. P. & Pless, S. A. The NALCN channel complex is voltage sensitive and directly modulated by extracellular calcium. *Sci. Adv.* **6**, eaaz3154 (2020).
11. Bouasse, M., Impheng, H., Servant, Z., Lory, P. & Monteil, A. Functional expression of CLIFAHDD and IHPRF pathogenic variants of the NALCN channel in neuronal cells reveals both gain- and loss-of-function properties. *Sci. Rep.* **9**, 11791 (2019).
12. Wie, J. et al. Intellectual disability-associated UNC80 mutations reveal inter-subunit interaction and dendritic function of the NALCN channel complex. *Nat. Commun.* **11**, 3351 (2020).
13. Nakayama, M., Iida, M., Koseki, H. & Ohara, O. A gene-targeting approach for functional characterization of KIAA genes encoding extremely large proteins. *FASEB J.* **20**, 1718–1720 (2006).
14. Cochet-Bissuel, M., Lory, P. & Monteil, A. The sodium leak channel, NALCN, in health and disease. *Front. Cell. Neurosci.* **8**, 132 (2014).

15. Bramswig, N. C. et al. Genetic variants in components of the NALCN-UNC80-UNC79 ion channel complex cause a broad clinical phenotype (NALCN channelopathies). *Hum. Genet.* **137**, 753–768 (2018).
16. Lee, J. H., Cribbs, L. L. & Perez-Reyes, E. Cloning of a novel four repeat protein related to voltage-gated sodium and calcium channels. *FEBS Lett.* **445**, 231–236 (1999).
17. Kang, Y., Wu, J. X. & Chen, L. Structure of voltage-modulated sodium-selective NALCN-FAM155A channel complex. *Nat. Commun.* **11**, 6199 (2020).
18. Kschonsak, M. et al. Structure of the human sodium leak channel NALCN. *Nature* **587**, 313–318 (2020).
19. Xie, J. et al. Structure of the human sodium leak channel NALCN in complex with FAM155A. *Nat. Commun.* **11**, 5831 (2020).
20. Lu, B. et al. Peptide neurotransmitters activate a cation channel complex of NALCN and UNC-80. *Nature* **457**, 741–744 (2009).
21. Yeh, E. et al. A putative cation channel, NCA-1, and a novel protein, UNC-80, transmit neuronal activity in *C. elegans*. *PLoS Biol.* **6**, e55 (2008).
22. Lear, B. C. et al. UNC79 and UNC80, putative auxiliary subunits of the NARROW ABDOMEN ion channel, are indispensable for robust circadian locomotor rhythms in *Drosophila*. *PLoS ONE* **8**, e78147 (2013).
23. Speca, D. J. et al. Conserved role of unc-79 in ethanol responses in lightweight mutant mice. *PLoS Genet.* **6**, e1001057 (2010).
24. Stray-Pedersen, A. et al. Biallelic mutations in UNC80 cause persistent hypotonia, encephalopathy, growth retardation, and severe intellectual disability. *Am. J. Hum. Genet.* **98**, 202–209 (2016).

25. Perez, Y. et al. UNC80 mutation causes a syndrome of hypotonia, severe intellectual disability, dyskinesia and dysmorphism, similar to that caused by mutations in its interacting cation channel NALCN. *J. Med. Genet.* **53**, 397–402 (2016).
26. Shamseldin, H. E. et al. Mutations in UNC80, encoding part of the UNC79-UNC80-NALCN channel complex, cause autosomal-recessive severe infantile encephalopathy. *Am. J. Hum. Genet.* **98**, 210–215 (2016).
27. Humphrey, J. A. et al. A putative cation channel and its novel regulator: cross-species conservation of effects on general anesthesia. *Curr. Biol.* **17**, 624–629 (2007).
28. Holm, L. Benchmarking fold detection by DaliLite v.5. *Bioinformatics* **35**, 5326–5327 (2019).
29. Wang, H. & Ren, D. UNC80 functions as a scaffold for Src kinases in NALCN channel function. *Channels (Austin)* **3**, 161–163 (2009).
30. Topalidou, I. et al. The NCA-1 and NCA-2 ion channels function downstream of Gq and Rho to regulate locomotion in *Caenorhabditis elegans*. *Genetics* **206**, 265–282 (2017).
31. Mastronarde, D. N. Automated electron microscope tomography using robust prediction of specimen movements. *J. Struct. Biol.* **152**, 36–51 (2005).
32. Scheres, S. H. RELION: implementation of a Bayesian approach to cryo-EM structure determination. *J. Struct. Biol.* **180**, 519–530 (2012).
33. Grant, T., Rohou, A. & Grigorieff, N. cisTEM, user-friendly software for single-particle image processing. *eLife* **7**, e35383 (2018).
34. Zheng, S. Q. et al. MotionCor2: anisotropic correction of beam-induced motion for improved cryo-electron microscopy. *Nat. Methods* **14**, 331–332 (2017).

35. Rohou, A. & Grigorieff, N. CTFFIND4: fast and accurate defocus estimation from electron micrographs. *J. Struct. Biol.* **192**, 216–221 (2015).
36. Rosenthal, P. B. & Henderson, R. Optimal determination of particle orientation, absolute hand, and contrast loss in single-particle electron cryomicroscopy. *J. Mol. Biol.* **333**, 721–745 (2003).
37. Pettersen, E. F. et al. UCSF Chimera—a visualization system for exploratory research and analysis. *J. Comput. Chem.* **25**, 1605–1612 (2004).
38. Cardone, G., Heymann, J. B. & Steven, A. C. One number does not fit all: mapping local variations in resolution in cryo-EM reconstructions. *J. Struct. Biol.* **184**, 226–236 (2013).
39. Afonine, P. V. et al. Real-space refinement in PHENIX for cryo-EM and crystallography. *Acta Crystallogr. D* **74**, 531–544 (2018).
40. Emsley, P., Lohkamp, B., Scott, W. G. & Cowtan, K. Features and development of Coot. *Acta Crystallogr. D* **66**, 486–501 (2010).
41. Goddard, T. D. et al. UCSF ChimeraX: meeting modern challenges in visualization and analysis. *Protein Sci.* **27**, 14–25 (2018).
42. Croll, T. I. ISOLDE: a physically realistic environment for model building into low-resolution electron-density maps. *Acta Crystallogr. D* **74**, 519–530 (2018).
43. Afonine, P. V. et al. New tools for the analysis and validation of cryo-EM maps and atomic models. *Acta Crystallogr. D* **74**, 814–840 (2018).
44. Williams, C. J. et al. MolProbity: more and better reference data for improved all-atom structure validation. *Protein Sci.* **27**, 293–315 (2018).
45. Sievers, F. et al. Fast, scalable generation of high-quality protein multiple sequence alignments using Clustal Omega. *Mol. Syst. Biol.* **7**,

539 (2011).

46. Waterhouse, A. M., Procter, J. B., Martin, D. M., Clamp, M. & Barton, G. J. Jalview version 2—a multiple sequence alignment editor and analysis workbench. *Bioinformatics* **25**, 1189–1191 (2009).
47. Robert, X. & Gouet, P. Deciphering key features in protein structures with the new ENDscript server. *Nucleic Acids Res.* **42**, W320–W324 (2014).
48. Banerjee, R. et al. Bilobal architecture is a requirement for calmodulin signaling to CaV1.3 channels. *Proc. Natl Acad. Sci. USA* **115**, E3026–E3035 (2018).
49. Kang, P. W. et al. Elementary mechanisms of calmodulin regulation of NaV1.5 producing divergent arrhythmogenic phenotypes. *Proc. Natl Acad. Sci. USA* **118**, e2025085118 (2021).
50. Leitner, A., Walzthoeni, T. & Aebersold, R. Lysine-specific chemical cross-linking of protein complexes and identification of cross-linking sites using LC-MS/MS and the xQuest/xProphet software pipeline. *Nat. Protoc.* **9**, 120–137 (2014).
51. Mohammadi, A., Tschanz, A. & Leitner, A. Expanding the cross-link coverage of a carboxyl-group specific chemical cross-linking strategy for structural proteomics applications. *Anal. Chem.* **93**, 1944–1950 (2021).
52. Walzthoeni, T. et al. False discovery rate estimation for cross-linked peptides identified by mass spectrometry. *Nat. Methods* **9**, 901–903 (2012).
53. Rinner, O. et al. Identification of cross-linked peptides from large sequence databases. *Nat. Methods* **5**, 315–318 (2008).
54. Perez-Riverol, Y. et al. The PRIDE database and related tools and resources in 2019: improving support for quantification data. *Nucleic Acids Res.* **47**, D442–D450 (2019).

55. Smart, O. S., Neduvvelil, J. G., Wang, X., Wallace, B. A. & Sansom, M. S. HOLE: a program for the analysis of the pore dimensions of ion channel structural models. *J. Mol. Graph.* **14**, 354–360 (1996).
56. Ashkenazy, H. et al. ConSurf 2016: an improved methodology to estimate and visualize evolutionary conservation in macromolecules. *Nucleic Acids Res.* **44**, W344–W350 (2016).

## Acknowledgements

We thank members of the Pless and Ben-Johny laboratories, P. Picotti, and Genentech colleagues in the BioMolecular Resources and Structural Biology departments for their support, and appreciate the encouragement of A. Rohou, C. Koth, S. Hymowitz, V. Dixit and A. Chan. Members of the Ben-Johny group acknowledge support from the NIH National Institute of Neurological Disorders and Stroke (R01 NS110672). Members of the Pless group acknowledge the Carlsberg Foundation (CF16-0504), the Independent Research Fund Denmark (7025-00097A and 9124-00002B) and the Lundbeck Foundation (R252-2017-1671) for financial support. Reagents are available under a material transfer agreement with Genentech or the appropriate party.

## Author information

### Author notes

#### 1. Cameron L. Noland

Present address: Department of Computational and Structural Chemistry, Merck & Co., Inc., South San Francisco, CA, USA

#### 2. Jian Payandeh

Present address: Department of Proteomics and Bioinformatics, Interline Therapeutics, South San Francisco, CA, USA

3. These authors contributed equally: Claudia Weidling, Nourdine Chakouri, Cameron L. Noland

## Affiliations

1. Department of Structural Biology, Genentech Inc., South San Francisco, CA, USA

Marc Kschonsak, Cameron L. Noland, Christopher P. Arthur, Claudio Ciferri & Jian Payandeh

2. Department of Drug Design and Pharmacology, University of Copenhagen, Copenhagen, Denmark

Han Chow Chua, Claudia Weidling, Katharina Schott & Stephan Alexander Pless

3. Department Physiology and Cellular Biophysics, Columbia University, New York, NY, USA

Nourdine Chakouri & Manu Ben-Johny

4. Department of BioMolecular Resources, Genentech Inc., South San Francisco, CA, USA

Timothy Chang, Christine Tam & Nidhi Patel

5. Department of Biology, Institute of Molecular Systems Biology, ETH Zürich, Zurich, Switzerland

Alexander Leitner

## Contributions

M.K. established protein purification and reconstitution methods with input from C.L.N. T.C., C.T. and N.P. generated key protein expression reagents. M.K and C.P.A. optimized cryo-EM sample preparation and data collection. M.K. determined the structure, with guidance from C.C. H.C.C. established

methods to record the function of the NALCN complex. H.C.C., C.W. and K.S. performed the molecular biology and two-electrode voltage clamp electrophysiology experiments. A.L. performed and analysed the crosslinking mass spectrometry experiments. N.C. and M.B.-J. performed the single-channel experiments and analyses. M.K., H.C.C., C.W., N.C., K.S., A.L., M.B.-J., C.C., S.A.P. and J.P. analysed the data. H.C.C. performed and analysed the linker competition experiments with input from M.K., S.A.P. and J.P. M.K., H.C.C., C.C., S.A.P. and J.P. wrote the manuscript with input from all authors. A.L., M.B.-J., C.C., S.A.P. and J.P. supervised the project and are co-senior authors.

## Corresponding authors

Correspondence to [Alexander Leitner](#), [Manu Ben-Johny](#), [Claudio Ciferri](#), [Stephan Alexander Pless](#) or [Jian Payandeh](#).

## Ethics declarations

### Competing interests

M.K., C.L.N., T.C., C.T., N.P., C.P.A., C.C. and J.P. are or were employees of Genentech/Roche; all remaining authors declare no competing interests.

## Peer review

### Peer review information

*Nature* thanks Paul DeCaen, Vera Moiseenkova-Bell and David Spafford for their contribution to the peer review of this work.

## Additional information

**Publisher's note** Springer Nature remains neutral with regard to jurisdictional claims in published maps and institutional affiliations.

# Extended data figures and tables

## Extended Data Fig. 1 Purification and structure determination of the NALCN channelosome.

**a**, NALCN channelosome protein expression and purification scheme. **b**, Example size exclusion chromatogram and SDS-PAGE of nanodisc-reconstituted NALCN channelosome sample. **c**, Example cryo-EM micrograph image of the NALCN channelosome-MSP1E3D1 complex. **d**, Representative 2D-class averages of selected particles from 200 classes and approximately 130,000 particles. **e**, Data collection and processing workflow. **f**, Conformation 1, FSC between two half datasets yields a global resolution estimate of approximately 3.1 Å resolution from the refinement using an overall mask of the NALCN channelosome, 3.2 Å resolution from the focused NALCN-CaM-FAM, 2.9 Å from the focused UNC crossover, 3.7 Å from the focused UNC N-C and 3.8 Å from the focused UNC C-N refinements. **g**, Conformation 1, heat map representation of the distribution of assigned particle orientations. **h**, Conformation 2, FSC between two half datasets yields a global resolution estimate of approximately 3.5 Å resolution. **i**, Conformation 2, heat map representation of the distribution of assigned particle orientations.

## Extended Data Fig. 2 Select cryo-EM map regions of the NALCN channelosome.

**a–g**, Example 3D map overlay for indicated regions.

## Extended Data Fig. 3 NALCN and FAM155A structures in the NALCN channelosome and NALCN-FAM155A subcomplex.

**a**, Comparison of the NALCN subunit in the NALCN-FAM155A subcomplex and NALCN channelosome (with UNC79 and UNC80 removed for clarity). **b**, Superposition of the FAM155A subunit in the NALCN-FAM155A subcomplex and NALCN channelosome. **c**, Pore radius of the ion conduction pathway in the NALCN channelosome or NALCN-FAM155A subcomplex structures (PDB 6XIW) calculated by HOLE<sup>55</sup>.

## Extended Data Fig. 4 UNC79 and UNC80 are HEAT-repeat proteins.

**a**, Side- and top-views of UNC79. Position of disordered loops >50 residues in length are indicated. **b**, Side- and top-views of UNC80. Position of disordered loops >50 residues in length are indicated. **c**, Open-book view of UNC79-UNC80 interface showing contact surface. **d**, Same as part **c**, showing electrostatic surface. **e**, Same as part **c**, showing surface conservation across selected vertebrate species calculated by ConSurf<sup>56</sup>.

## Extended Data Fig. 5 Structure-function analysis of UNC79 and UNC80.

**a**, Schematic of UNC79 and UNC80 with corresponding amino acid residues of fragments indicated. Example current traces from *Xenopus* oocytes expressing NALCN, FAM155A, UNC79 and UNC80, where various isolated ~500 residue fragments of either UNC79 or UNC80 are co-expressed in *trans*, with steps from +80 to -80 mV, 40 mV increments, in ND96 recording solution. Right shows summary of mean current amplitudes elicited at +80 mV (top bar graph) or -80 mV (bottom bar graph) from a holding potential of 0 mV for indicated construct combinations. Numbers of biological replicates (n) are indicated. Recordings were performed on four to five oocytes from two different batches. Data are shown as mean±SD. \*\*\*\*, \* and ns represent p value < 0.0001, < 0.05 and >0.05, respectively; one-way analysis of variance (ANOVA), Dunnett's test (against +H<sub>2</sub>O). P values are adjusted to account for multiple comparisons and are presented in Supplementary Table 5. For electrophysiological measurements, see Source Data. **b**, Schematic of UNC80 with corresponding truncated constructs indicated. Example current traces from *Xenopus* oocytes expressing NALCN, FAM155A, UNC79 and UNC80, where wild-type UNC80 or truncated constructs are expressed, with steps from +80 to -80 mV, 20 mV increments, in ND96 recording solution. Star (#) indicates constructs that contain fusion of a C-terminal GFP-Flag tag. Right shows summary of mean current amplitudes elicited at +80 mV (top bar graph) or -80 mV (bottom bar graph) from a holding potential of 0 mV for indicated construct combinations. Numbers of

biological replicates (n) are indicated. Recordings were performed on four to six oocytes from two different batches. Data are shown as mean $\pm$ SD. \*\*\*\*, \*\*, and \* represent p value < 0.0001, < 0.01 and < 0.05, respectively; one-way analysis of variance (ANOVA), Dunnett's test (against UNC80 $^{\#}$ ). P values are adjusted to account for multiple comparisons and are presented in Supplementary Table 5. For electrophysiological measurements, see Source Data. c, Schematic of UNC80 with corresponding nonsense mutation constructs indicated (note, R1265X, L2586X, and Y2796X mutations have been previously reported by us<sup>10</sup> and representative data are shown here for comparison). Example current traces from *Xenopus* oocytes expressing NALCN, FAM155A, UNC79 and UNC80, where wild-type UNC80 or nonsense mutation constructs are expressed, with steps from +80 to -80 mV, 20 mV increments, in ND96 recording solution. Right shows summary of mean current amplitudes elicited at +80 mV (top bar graph) or -80 mV (bottom bar graph) from a holding potential of 0 mV for indicated construct combinations. Numbers of biological replicates (n) are indicated. Recordings were performed on three to six oocytes from two to three different batches. Data are shown as mean $\pm$ SD. \*\*\* represents p value < 0.0001; one-way analysis of variance (ANOVA), Dunnett's test (against UNC80). P values are adjusted to account for multiple comparisons and are presented in Supplementary Table 5. For electrophysiological measurements, see Source Data. d, Example current traces from *Xenopus* oocytes expressing NALCN, FAM155A, UNC79 and UNC80, where wild-type UNC80 or missense mutation constructs are expressed, with steps from +80 to -80 mV, 20 mV increments, in ND96 recording solution. Right shows summary of mean current amplitudes elicited at +80 mV (top bar graph) or -80 mV (bottom bar graph) from a holding potential of 0 mV for indicated construct combinations. Numbers of biological replicates (n) are indicated. Recordings were performed on two to eight oocytes from two to three different batches. Data are shown as mean $\pm$ SD. \*\*\* and ns represent p value < 0.0001 and >0.05, respectively; one-way analysis of variance (ANOVA), Dunnett's test (against UNC80). P values are adjusted to account for multiple comparisons and are presented in Supplementary Table 5. For electrophysiological measurements, see Source Data. e, Close-in views of select missense mutations previously identified in UNC80 mapped onto the UNC79-UNC80 subcomplex structure. Note, exact p values are presented in Supplementary Table 5.

[Source data](#)

[Extended Data Fig. 6 Characterization of NALCN-Na<sub>V</sub>1.4 chimeras.](#)

**a**, Schematic of human NALCN and human NALCN-rat Na<sub>V</sub>1.4 chimeric constructs. Example current traces from *Xenopus* oocytes expressing NALCN, FAM155A, UNC79 and UNC80, where wild-type or chimeric truncated NALCN constructs are expressed, with steps from +80 to -80 mV, 20 mV increments, in ND96 recording solution. Numbers of biological replicates (n) are indicated in **b**. Recordings were performed on two to five oocytes from two to five different batches. For electrophysiological measurements, see Source Data. **b**, Summary of mean current amplitudes elicited at +80 mV (top bar graph) or -80 mV (bottom bar graph) from a holding potential of 0 mV for indicated constructs. Data are shown as mean±SD. \*\*\* and ns represent p value < 0.0001 and >0.05, respectively; one-way analysis of variance (ANOVA), Dunnett's test (against NALCN). P values are adjusted to account for multiple comparisons and are presented in Supplementary Table 5.

[Source data](#)

[Extended Data Fig. 7 Structure-function of the NALCN DI-DII and DII-DIII linkers.](#)

**a**, Current traces from *Xenopus* oocytes expressing NALCN, FAM155A, UNC79 and UNC80, where the NALCN subunit is wild-type or has indicated mutations, insertions or deletions in the DI-DII linker. Steps from +80 to -100 mV, 20 mV increments, in ND96 recording solution. Right shows summary of mean current amplitudes elicited at +80 mV (top bar graph) or -80 mV (bottom bar graph) from a holding potential of 0 mV for indicated constructs. **b**, Representative Western blot of total lysate and surface fraction proteins extracted from *Xenopus* oocytes expressing the indicated constructs where wild-type or mutant NALCN was co-expressed with wild-type UNC80, UNC79 and FAM155A. For gel source data, see Supplementary Fig. 3. **c**, Current traces from *Xenopus* oocytes expressing

NALCN, FAM155A, UNC79 and UNC80, where the NALCN subunit is wild-type or has indicated insertions and deletions in the DII-DIII linker. Steps from +80 to -100 mV, 20 mV increments, in ND96 recording solution. Right shows summary of mean current amplitudes elicited at +80 mV (top bar graph) or -80 mV (bottom bar graph) from a holding potential of 0 mV for indicated constructs. **a**, **c**, Numbers of biological replicates (n) are indicated. Recordings were performed on four to five oocytes from two different batches. Data are shown as mean $\pm$ SD. \*\*\*\*, \*\*\*, \*\*, \* and ns represent p value < 0.0001, < 0.001, < 0.01, < 0.05 and >0.05, respectively; one-way analysis of variance (ANOVA), Dunnett's test (against WT). P values are adjusted to account for multiple comparisons and are presented in Supplementary Table 5.

[Source data](#)

**Extended Data Fig. 8 Structure-function analysis of the NALCN C-terminal domain.**

**a**, Current traces from *Xenopus* oocytes expressing NALCN, FAM155A, UNC79 and UNC80, where the NALCN subunit is wild-type or has indicated CTD-deletions or mutations. Steps from +80 to -100 mV, 20 mV increments, in ND96 recording solution. Right shows summary of mean current amplitudes elicited at +80 mV (top bar graph) or -80 mV (bottom bar graph) from a holding potential of 0 mV for indicated constructs. Numbers of biological replicates (n) are indicated. Recordings were performed on three to six oocytes from two different batches. Data are shown as mean $\pm$ SD. \* and ns represent p value < 0.05 and >0.05, respectively; one-way analysis of variance (ANOVA), Dunnett's test (against WT). P values are adjusted to account for multiple comparisons and are presented in Supplementary Table 5. **b**, Current traces from *Xenopus* oocytes expressing NALCN, FAM155A, UNC79, UNC80 and control (H<sub>2</sub>O) or an isolated NALCN-CTD construct in *trans*. Steps from +80 to -100 mV, 20 mV increments, in ND96 recording solution. Right shows summary of mean current amplitudes elicited at +80 mV from a holding potential of 0 mV for indicated conditions. Numbers of biological replicates (n) are indicated. Recordings were performed on four to five oocytes from two different batches. Data are shown as mean $\pm$ SD. Two-

sided unpaired t-test,  $p = 0.1286$  (+80 mV),  $p = 0.0037$  (-80 mV). **c**, Current traces from *Xenopus* oocytes expressing wild-type NALCN (1-1738) or indicated C-terminal truncation constructs recorded in ND96 (top) and divalent cation ( $\text{X}^{2+}$ )-free buffer (bottom). Steps from +80 to -100 mV, 20 mV increments. Right shows fold-increase in inward current elicited at -100 mV for wild-type NALCN and indicated truncation mutants in response to removal of divalent cations. Numbers of biological replicates (n) are indicated. Recordings were performed on three to four oocytes from two different batches. Data are shown as mean $\pm$ SD. ns represents p value  $>0.05$ ; one-way analysis of variance (ANOVA), Dunnett's test (against WT). P values are adjusted to account for multiple comparisons and are presented in Supplementary Table 5. **d**, Current traces from *Xenopus* oocytes expressing wild-type NALCN, FAM155A, UNC79 and UNC80, where a "CaM-chelator" construct (which is composed of four tandem IQ motifs (IQ<sub>3-6</sub>: residues L766-K920) of mouse myosin Va (Uniprot Q99104) that diminishes free concentration of apo-CaM<sup>48,49</sup>) is co-expressed. Numbers of biological replicates (n) are indicated. Recordings were performed on four to five oocytes from three different batches. Data are shown as mean $\pm$ SD. Two-sided unpaired t-test,  $p = 0.0002$  (+80 mV),  $p = 0.0421$  (-80 mV).

### Source data

### Extended Data Fig. 9 Cell-attached single channel recordings of the NALCN channelosome.

**a**, Exemplar traces from an individual patch show absence of channel openings when HEK293 cells are transfected with only UNC79, UNC80, and FAM155A. Gray slanted line, unitary current relationship for wild-type NALCN. **b**, Ensemble average current obtained from 154 sweeps for the individual patch shown in panel a. No detectable channel activity was observed in a total of  $n = 8$  cells (852 sweeps). **c**, Exemplar traces show additional examples of single-channel openings of wild-type NALCN channelosome from the same patch shown in Fig. 4b. Gray slanted line, unitary current relationship. **d**, Ensemble average current obtained from 90 sweeps for the single-channel patch of NALCN channelosome as shown in

panel **c**. **e**, Diary plot of single-trial  $P_O$  values from the one-channel patch of wild-type NALCN, as shown in panel **c**, reveal distinct active (A; traces with brief and flickery openings) and quite (Q; traces with no discernible activity) gating modes. **f**, Exemplar traces show additional examples of single-channel openings of Y578S mutant channels from the individual patch shown in Fig. [4b](#). Gray slanted line, unitary current relationship. **g**, Ensemble average current obtained from 40 sweeps for the single-channel patch of Y578S mutant channel shown in panel **f**. **h**, Diary plot of single-trial  $P_O$  for the one-channel patch for Y578S mutant displayed in panel **f**. Y578S mutant channel also show switching between active and quite gating modes.

## [Source data](#)

### **Extended Data Table 1 Cryo-EM data collection, refinement and validation statistics**

## **Supplementary information**

### [Supplementary Information](#)

This file contains Supplementary Figures 1–3 and Supplementary Tables 1 and 3–5.

### [Reporting Summary](#)

### [Supplementary Table 2](#)

Complete cross-linking mass spectrometry of the NALCN channelosome.

## **Source data**

### [Source Data Fig. 1](#)

### [Source Data Fig. 2](#)

[\*\*Source Data Fig. 3\*\*](#)

[\*\*Source Data Fig. 4\*\*](#)

[\*\*Source Data Extended Data Fig. 5\*\*](#)

[\*\*Source Data Extended Data Fig. 6\*\*](#)

[\*\*Source Data Extended Data Fig. 7\*\*](#)

[\*\*Source Data Extended Data Fig. 8\*\*](#)

[\*\*Source Data Extended Data Fig. 9\*\*](#)

## Rights and permissions

[Reprints and Permissions](#)

## About this article

### Cite this article

Kschonsak, M., Chua, H.C., Weidling, C. *et al.* Structural architecture of the human NALCN channelosome. *Nature* **603**, 180–186 (2022).  
<https://doi.org/10.1038/s41586-021-04313-5>

- Received: 12 July 2021
- Accepted: 07 December 2021
- Published: 20 December 2021
- Issue Date: 03 March 2022
- DOI: <https://doi.org/10.1038/s41586-021-04313-5>

## Share this article

Anyone you share the following link with will be able to read this content:

[Get shareable link](#)

Sorry, a shareable link is not currently available for this article.

[Copy to clipboard](#)

Provided by the Springer Nature SharedIt content-sharing initiative

---

This article was downloaded by **calibre** from <https://www.nature.com/articles/s41586-021-04313-5>

| [Section menu](#) | [Main menu](#) |

# Amendments & Corrections

- **[Author Correction: Disruption of mitochondrial complex I induces progressive parkinsonism](#)** [ 11 February 2022]

Author Correction •

- Author Correction
- [Published: 11 February 2022](#)

# Author Correction: Disruption of mitochondrial complex I induces progressive parkinsonism

- [Patricia González-Rodríguez](#) ORCID: [orcid.org/0000-0002-2561-3984<sup>1</sup>](https://orcid.org/0000-0002-2561-3984),
- [Enrico Zampese](#) ORCID: [orcid.org/0000-0002-8851-2566<sup>1</sup>](https://orcid.org/0000-0002-8851-2566),
- [Kristen A. Stout<sup>1</sup>](#),
- [Jaime N. Guzman<sup>1</sup>](#),
- [Ema Ilijic<sup>1</sup>](#),
- [Ben Yang](#) ORCID: [orcid.org/0000-0003-0732-0237<sup>1</sup>](https://orcid.org/0000-0003-0732-0237),
- [Tatiana Tkatch<sup>1</sup>](#),
- [Mihaela A. Stavarache<sup>2</sup>](#),
- [David L. Wokosin<sup>1</sup>](#),
- [Lin Gao](#) ORCID: [orcid.org/0000-0002-1781-4671<sup>3</sup>](https://orcid.org/0000-0002-1781-4671),
- [Michael G. Kaplitt<sup>2</sup>](#),
- [José López-Barneo<sup>3</sup>](#),
- [Paul T. Schumacker](#) ORCID: [orcid.org/0000-0001-9591-2034<sup>4</sup>](https://orcid.org/0000-0001-9591-2034) &
- [D. James Surmeier](#) ORCID: [orcid.org/0000-0002-6376-5225<sup>1</sup>](https://orcid.org/0000-0002-6376-5225)

[Nature](#) volume 603, page E1 (2022)

- 1287 Accesses
- 2 Altmetric
- [Metrics details](#)

## Subjects

- [Parkinson's disease](#)

The [Original Article](#) was published on 03 November 2021

[Download PDF](#)

Correction to: *Nature* <https://doi.org/10.1038/s41586-021-04059-0>  
Published online 3 November 2021

In the version of this article initially published, the two bottom-left panels in Extended Data Fig. 8b duplicated the top-left and bottom-right panels of Fig. 4d presenting open field traces in mice. The panels have now been replaced with new images.

The errors have been corrected in the online version of the article.

## Author information

### Affiliations

1. Department of Neuroscience, Feinberg School of Medicine, Northwestern University, Chicago, IL, USA

Patricia González-Rodríguez, Enrico Zampese, Kristen A. Stout, Jaime N. Guzman, Ema Ilijic, Ben Yang, Tatiana Tkatch, David L. Wokosin & D. James Surmeier

2. Department of Neurological Surgery, Weill Cornell Medical College, New York, NY, USA

Mihaela A. Stavarache & Michael G. Kaplitt

3. Instituto de Biomedicina de Sevilla, Hospital Universitario Virgen del Rocío/CSIC/ Universidad de Sevilla and CIBERNED, Seville, Spain

Lin Gao & José López-Barneo

4. Department of Pediatrics, Northwestern University, Chicago, IL, USA

Paul T. Schumacker

## Corresponding author

Correspondence to [D. James Surmeier](#).

## Rights and permissions

[Reprints and Permissions](#)

## About this article

### Cite this article

González-Rodríguez, P., Zampese, E., Stout, K.A. *et al.* Author Correction: Disruption of mitochondrial complex I induces progressive parkinsonism. *Nature* **603**, E1 (2022). <https://doi.org/10.1038/s41586-021-04382-6>

- Published: 11 February 2022
- Issue Date: 03 March 2022
- DOI: <https://doi.org/10.1038/s41586-021-04382-6>

## Share this article

Anyone you share the following link with will be able to read this content:

[Get shareable link](#)

Sorry, a shareable link is not currently available for this article.

[Copy to clipboard](#)

Provided by the Springer Nature SharedIt content-sharing initiative

---

This article was downloaded by **calibre** from <https://www.nature.com/articles/s41586-021-04382-6>

| [Section menu](#) | [Main menu](#) |

# Nature Outline